FRP Composites

in Civil Engineering

CICE 2004

Edited by
R. Seracino

FRP COMPOSITES IN CIVIL ENGINEERING – CICE 2004

PROCEEDINGS OF THE SECOND INTERNATIONAL CONFERENCE ON FRP COMPOSITES IN CIVIL ENGINEERING – CICE 2004, 8–10 DECEMBER 2004, ADELAIDE, AUSTRALIA

FRP Composites in Civil Engineering – CICE 2004

Edited by

R. Seracino
School of Civil and Environmental Engineering, The University of Adelaide, Australia

A.A. BALKEMA PUBLISHERS LEIDEN / LONDON / NEW YORK / PHILADELPHIA / SINGAPORE

The official conference of the

International Institute for FRP in Construction

Organised by the

School of Civil and Environmental Engineering
The University of Adelaide

in conjunction with the

Department of Civil and Structural Engineering
The Hong Kong Polytechnic University

Published by: A.A. Balkema Publishers, Leiden, The Netherlands, a member of Taylor & Francis Group plc
www.balkema.nl and www.tandf.co.uk

ISBN 90 5809 638 6

Printed in Great Britain

FRP Composites in Civil Engineering – CICE 2004 – Seracino (ed)
© 2005 Taylor & Francis Group, London, ISBN 90 5809 638 6

Table of Contents

FRP research in Italy (special session)

FRP research in the Middle East (special session)

FRP research in Southeast Asia (special session)

Long-term monitoring (special session)

Materials and products

Confinement of concrete in compression

Bond and interfacial stresses between FRP and concrete

Flexural strengthening of concrete beams and slabs

Debonding failure in FRP strengthened beams

Shear and torsional strengthening of concrete beams

Durability

Practical applications

FRP Composites in Civil Engineering – CICE 2004 – Seracino (ed)

Preface

The significance of the inaugural fibre reinforced polymer (FRP) Composites in Civil Engineering (CICE) conference, organised by Professor J.G. Teng of The Hong Kong Polytechnic University in 2001, is unquestionable as it led to at least two pivotal outcomes. Firstly, it started an international conference series and has led to this, the Second International Conference on FRP Composites in Civil Engineering (CICE 2004) held at the University of Adelaide, Australia. Secondly, it was instrumental in the formation of the *International Institute for FRP in Construction* (IIFC). The link between the CICE conference series and the IIFC was later established when CICE became the official conference of the IIFC.

As a researcher, I am encouraged by the increasing number of papers being published internationally covering a wide range of FRP applications in civil engineering. This is an indication of the acceptance and practical significance of FRP in civil engineering practice. However, I am also aware of potential negative trends developing in this area that are wide spread in many 'traditional' areas of civil engineering. In part, these include: the absence of standardised testing techniques for fundamental properties; insufficient documentation of tests in the open literature; lack of consistent terminology; and unnecessary repetition of tests and research. To a certain degree this is to be expected in such a new and rapidly developing area. However, it may hinder the wide spread application and development of this exciting technology. Attendance at international forums such as CICE 2004, to broaden one's awareness of state-of-the-art research, is part of the solution. But, attendance in itself is not sufficient. It must be accompanied by constructive, yet critical, discussion. To encourage this discussion, I have challenged session chairs to play a proactive role in leading discussions during question periods of technical sessions. It is my hope that this will at least start to address some of the trends highlighted above and therefore become a measure of the success and contribution of CICE 2004 to the civil engineering FRP research community.

I was privileged to be the organiser of CICE 2004 and the editor of this book containing the proceedings of the Second International Conference on FRP Composites in Civil Engineering. One of the aims of CICE 2004 was to encourage the participation of researchers and practitioners from countries or regions of the world often underrepresented in such international forums. To this end, four special sessions were introduced in CICE 2004 to highlight the activities being undertaken in China, Italy, the Middle-East and Southeast Asia. The importance of long-term monitoring of existing FRP structures/components was also recognised by a special session. The strong international support for CICE 2004 was demonstrated by the contributions from nine keynote speakers, four invited speakers and over 100 delegates, from over 20 countries, presenting papers that cover a wide range of FRP applications in civil engineering.

CICE 2004 was a result of the efforts of many people worldwide. Special thanks are due to the keynote and invited speakers for their support and contribution. The International Advisory Committee and the Conference Organising Committee are also acknowledged for assisting with the promotion of the conference and for critically reviewing all of the papers published in these proceedings. The assistance provided by the secretarial staff of the School of Civil and Environmental Engineering at the University of Adelaide is also acknowledged. The IIFC must also be recognised for sponsoring the Best Paper Awards presented, for the first time in this conference series, at CICE 2004. Furthermore, the support and encouragement provided by Professor Teng and the Executive Committee members of the IIFC is also greatly appreciated. I must also thank my family, and in particular my wife Joanne, for their support during the many long hours devoted to the organisation of this conference. Finally, I thank all of the authors, presenters, delegates, sponsors, and the supportive staff of A.A. Balkema for their contributions, without which CICE 2004 would not have been possible.

Rudolf Seracino

Adelaide, Australia
December 2004

FRP Composites in Civil Engineering – CICE 2004 – Seracino (ed)
© 2005 Taylor & Francis Group, London, ISBN 90 5809 638 6

Message from the President of IIFC

Recent years have seen rapidly growing interests in the application of advanced fibre-reinforced polymer (FRP) composites in construction around the world, in terms of both research activities and practical implementations. Indeed, many have hailed FRP composites as a new generation of construction materials following steel and concrete. Against this background, the *International Institute for FRP in Construction* (IIFC) was formed in 2003 to promote and coordinate world-wide activities in this area. One of the important activities of IIFC is the organization of a biennial official conference series, and CICE 2004 was organized as the first official conference of IIFC, although it is the second in the CICE series which started in 2001 with its first conference (CICE 2001) in Hong Kong.

As the founding President of IIFC, I would like to take this opportunity to provide a brief report on the process that gave birth to IIFC. The first step towards the formation of IIFC was taken at the International Conference on FRP Composites in Civil Engineering held in December 2001 (CICE 2001) at which a meeting of leading researchers attending the conference was convened to discuss the possibility. The idea of forming an international organization dedicated to the application of FRP composites in construction was enthusiastically supported at that meeting. The meeting also led to the establishment of an Ad-Hoc Committee for the formation of the Institute, which consisted of 33 leading figures in the area drawn from 13 countries around the world.

Among the many tasks completed by this Committee was the development of the By-laws of the Institute. Following the finalization of the By-laws in March 2003, the Ad-Hoc Committee was immediately converted into the founding Council of the Institute based on the majority view of the Committee, which signified the formal establishment of IIFC. Elections of the Executive Committee, the first Fellows and the Advisory Committee of IIFC then followed. The Institute became fully functional and started to accept applications for membership on 1 January 2004. In this process, an official web site for IIFC was also established (www.iifc-hq.org). Readers interested in the activities of IIFC are encouraged to visit this web site regularly.

The founding of IIFC would not have been possible without the willing contributions of many individuals. On behalf of IIFC, I would like to express my sincere gratitude to all of them. The future success of IIFC will hinge on the support of individuals and organizations who share the aim of IIFC. In this connection, you are strongly encouraged to take an active part in IIFC activities.

Having organized conferences myself, I am fully aware of the amount of work required to organize a successful conference of this magnitude. On behalf of IIFC, I would like to express my sincere appreciation to Dr. Rudi Seracino, Chairman of the Organizing Committee of CICE 2004, for devoting so much of his time and energy to make this conference a great success and for looking after the interests of IIFC so well despite the many other constraints he had to operate with. I would also like to thank all others who contributed to this success in different ways, including members of the Organizing Committee, the International Advisory Committee and many others. The strong support to CICE 2004 shown by the international civil engineering FRP research community is testimony to the importance and significance of this conference.

Jin-Guang Teng

Hong Kong, China
December 2004

FRP Composites in Civil Engineering – CICE 2004 – Seracino (ed)
© 2005 Taylor & Francis Group, London, ISBN 90 5809 638 6

CICE 2004 Organising Committee

Chairman:

R. Seracino	University of Adelaide

Members:

G. Boully	VicRoads, Melbourne
M.C. Griffith	University of Adelaide
L. Lam	The Hong Kong Polytechnic University
P. Molloy	Transport SA, Adelaide
D.J. Oehlers	University of Adelaide
A. Sarkady	Degussa (Australia)
P. Simpson	Connell Wagner Pty Ltd, Brisbane
S.T. Smith	University of New South Wales
S.H. Xia	University of Adelaide

FRP Composites in Civil Engineering – CICE 2004 – Seracino (ed)
© 2005 Taylor & Francis Group, London, ISBN 90 5809 638 6

CICE 2004 International Advisory Committee

Chaiman:

J.G. Teng	The Hong Kong Polytechnic University	Hong Kong, China

Members:

M. Anson	The Hong Kong Polytechnic University	Hong Kong, China
M. Arduini	Composite for Civil Engineering	Italy
C.E. Bakis	Pennsylvania State University	USA
S. Bandyopadhyay	University of New South Wales	Australia
L.C. Bank	University of Wisconsin – Madison	USA
B. Benmokrane	University of Sherbrooke	Canada
M.A. Bradford	University of New South Wales	Australia
C.J. Burgoyne	University of Cambridge	UK
O. Buyukozturk	Massachussetts Institute of Technology	USA
J.F. Chen	University of Edinburgh	UK
M.R. Ehsani	University of Arizona	USA
M.A. Erki	Royal Military College of Canada	Canada
M.C. Forde	University of Edinburgh	UK
H. Fukuyama	Building Research Institute	Japan
N.F. Grace	Lawrence Tech University	USA
R.I. Gilbert	University of New South Wales	Australia
N. Gowripalan	University of New South Wales	Australia
L.C. Hollaway	University of Surrey	UK
V.M. Karbhari	University of California – San Diego	USA
J.M. Ko	The Hong Kong Polytechnic University	Hong Kong, China
G. Manfredi	University of Naples Frederico II	Italy
U. Meier	Swiss Federation Laboratories for Materials Research	Switzerland
A. Mirmiran	North Carolina State University	USA
G. Monti	Università La Sapienza di Roma	Italy
A.S. Mosallam	California State University – Fullerton	USA
J.T. Mottram	University of Warwick	UK
A.A. Mufti	University of Manitoba	Canada
A. Nanni	University of Missouri – Rolla	USA
K.W. Neale	University of Sherbrooke	Canada
D.J. Oehlers	University of Adelaide	Australia
P. Paramasivam	National University of Singapore	Singapore
M. Raoof	Loughborough University	UK
S.H. Rizkalla	North Carolina State University	USA
F.S. Rostasy	University of Braunschweig	Germany
H. Saadatmanesh	University of Arizona	USA
R.N. Swamy	University of Sheffield	UK
L. Taerwe	Ghent University	Belgium
B. Täljsten	Luleå University of Technology	Sweden
K.H. Tan	National University of Singapore	Singapore
H. Toutanji	University of Alabama – Huntsville	USA
T.C. Triantafillou	University of Patras	Greece
G.J. Turvey	Lancaster University	UK
T. Ueda	Hokkaido University	Japan
G. Van Erp	University of Southern Queensland	Australia

D. Van Gemert	Katholieke Universiteit Leuven	Belgium
P. Waldron	University of Sheffield	UK
Z.S. Wu	Ibaraki University	Japan
Y. Xiao	University of Southern California	USA
L.P. Ye	Tsinghua University	China
Q.R. Yue	Central Research Institute of Building and Construction of MMI	China
A. Zingoni	University of Cape Town	South Africa

FRP Composites in Civil Engineering – CICE 2004 – Seracino (ed)
© 2005 Taylor & Francis Group, London, ISBN 90 5809 638 6

IIFC Council

Professor V.M. Karbhari	University of California at San Diego
Professor A. Mirmiran	North Carolina State University
Professor A. Nanni	University of Missouri – Rolla
Professor S.H. Rizkalla	North Carolina State University
Professor F. Seible	University of California at San Diego

UK:

Dr. J.F. Chen	University of Edinburgh
Professor L.C. Hollaway	University of Surrey
Professor P. Waldron	University of Sheffield

FRP Composites in Civil Engineering – CICE 2004 – Seracino (ed)
© 2005 Taylor & Francis Group, London, ISBN 90 5809 638 6

IIFC Advisory Committee

L.C. Hollaway	University of Surrey	UK
A. Machida	Saitama University	Japan
U. Meier	EMPA	Switzerland
A.A. Mufti	University of Manitoba	Canada
A. Nanni	University of Missouri – Rolla	USA
S.H. Rizkalla	North Carolina State University	USA

FRP Composites in Civil Engineering – CICE 2004 – Seracino (ed)
© 2005 Taylor & Francis Group, London, ISBN 90 5809 638 6

IIFC Executive Committee

President:		
Professor J.G. Teng	The Hong Kong Polytechnic University	China
Vice-Presidents:		
Dr. B. Bakht	JMBT Structures Research Inc.	Canada
Professor L.C. Bank	University of Wisconsin – Madison	USA
Professor T. Keller	Swiss Federal Institute of Technology	Switzerland
Dr. T. Ueda	Hokkaido University	Japan
Newsletter Editor:		
Professor V.M. Karbhari	University of California at San Diego	USA
Treasurer:		
Professor N. Banthia	University of British Columbia	Canada
Secretary:		
Dr. J.F. Chen	University of Edinburgh	UK
Conference Coordinator:		
Dr. R. Seracino	University of Adelaide	Australia
Members-at-Large:		
Dr. J.T. Mottram	University of Warwick	UK
Professor Z.S. Wu	Ibaraki University	Japan

Keynote papers

FRP Composites in Civil Engineering – CICE 2004 – Seracino (ed)
© 2005 Taylor & Francis Group, London, ISBN 90 5809 638 6

Mechanically-fastened FRP (MF-FRP) – a viable alternative for strengthening RC members

L.C. Bank
Department of Civil and Environmental Engineering, University of Wisconsin, Madison, WI, USA

ABSTRACT: A method for strengthening reinforced concrete members using mechanical fasteners has recently been developed. The strengthening is obtained by attaching FRP strips, having high bearing and longitudinal strengths, to concrete elements using many closely spaced steel Power Actuated (PA) fastening "pins" and a limited number of steel expansion anchors. The method, known as the Mechanically-Fastened FRP (MF-FRP) method, is rapid, uses conventional typically available hand-tools, lightweight materials and unskilled labor. In addition, unlike the bonded method, the MF-FRP method requires minimal surface preparation and permits immediate use of the strengthened structure. Previous research on this method on a variety of beam sizes has shown promising results in terms of installation efficiency, level of strengthening achieved, and preventing strip delamination before concrete crushing. This paper presents an overview of the work conducted over the last 5 years at the University of Wisconsin-Madison on the experimental, theoretical and design aspects of the MF-FRP method.

1 INTRODUCTION

A method for strengthening reinforced concrete beams (or slabs) by attaching FRP (fiber reinforced polymer) strengthening strips to the underside of the beam using powder actuated fasteners and mechanical anchors has been developed at the University of Wisconsin-Madison. The method is known as the Mechanically Fastened (MF) Fiber-Reinforced Polymer (FRP), or the MF-FRP method, to distinguish it from the traditional Externally-Bonded FRP (EB-FRP) method (ACI 440.2R 2002; FIB 2001, Teng et al. 2001). This method relies on mechanical attachment of the FRP strip, and is a rapid procedure that uses simple hand tools, lightweight materials, and unskilled labor. Unlike the conventional method of adhesively bonding FRP strips to the concrete surface, this method does not require surface preparation and allows for immediate use of the strengthened structure. Bonded repair methods have been used in a number of full-scale bridge strengthening projects (e.g. Alkhrdaji et al. 2000; Nanni 1997). The conventional bonding method requires time consuming grinding, sand blasting, priming and smoothing of the concrete surface to make it suitable for bonding the strip. In addition, it is often recommended that the bonded strip not be disturbed for a minimum of 24 hours following the application of the adhesive and the structure not be used for up to a week.

Even with FRP bonded systems a number of authors have recommended that in order to prevent a catastrophic brittle failure of the strengthened beam by strip detachment, mechanical anchorage should be provided at the strip ends (Spadea et al. 1998, Garden & Holloway 1998). This type of anchorage is usually provided with steel anchor bolts or cover plates or with "fiber anchors" (Lam & Teng 2001). In addition to being rapid and easy to install, the MF-FRP method provides the necessary anchoring mechanism as part of the procedure, since it is based entirely on mechanical fastening systems. Moreover, the multiple small fasteners used in the MFFRP method, in contrast to large diameter bolts typically used for anchorages, distribute the load uniformly over the FRP strip and reduce stress concentrations which can lead to premature failure.

This research activity began in 1998. A number of experiment and theoretical studies on the MFFRP method have been conducted. Experimental laboratory studies have been conducted on small 1.2 m long rectangular beams, moderate-length 3.7 m long rectangular long beams, 8.8 m long T-beams, and 7.3 m long rectangular beams (Bank et al. 2002a, 2002b; Lamanna et al. 2001, Lamanna, et al. 2004). In addition, a 1930s era reinforced concrete flat-slab bridge with a 7.3 m span was strengthened with the MF-FRP method (Bank et al. 2003, Bank et al. 2004). An analytical method has been developed to predict the strength of concrete beams strengthened with the MF-FRP method (Bank & Arora, 2004; Arora 2003). This paper presents an overview of the work conducted over the last 5 years on the experimental, theoretical and design aspects of the MF-FRP method.

2 DESCRIPTION OF THE MF-FRP METHOD

In the MF-FRP method, the strengthening is obtained by attaching FRP strips, having high bearing strength and high longitudinal strength and stiffness, to concrete elements using many closely spaced steel Power Actuated (PA) fastening "pins" and, if necessary, steel expansion anchors (EA). The expansion anchors are typically only used at the ends of the strip to prevent end-delamination.

The fastening pins are embedded using a Powder Actuated Fastening (PAF) "gun." Several PAF systems are available commercially from vendors such as Hilti, Ramset, Powers and Simpson. Hilti DX A41 and Hilti DX 460 powder actuated fastening systems were used in the testing reported in this paper. The system consists of fasteners (called "pins") and the "gun" which uses a 6.8 mm gunpowder charge to shoot the fastener into the base material. Adequate embedment of the powder-actuated fastener is required in order to secure the FRP strip to the reinforced concrete member. The effects of fastener type, washer, diameter, length, embedment depth and the use of predrilled holes have been investigated in a number of studies described in what follows (Bank et al. 2002a,b; Lamanna et al. 2001a,b; Lamanna et al. 2004).

Based on these studies hardened galvanized steel fasteners with neoprene backed steel washers, and shallow 12 mm pre-drilled holes are recommended for use with FRP strips. Use of shallow pre-drilled holes was shown to significantly reduce spalling during fastener driving and to increase tensile and shear capacity of the embedded fasteners. For embedment in high strength concrete pre-drilling is recommended by manufacturers of PAF systems and special drill bits with stoppers are available for this purpose (e.g. Hilti DX-Kwik). A minimum embedment of 25 mm beyond the pre-drilled hole is recommended. Based on the results of the studies conducted, 45 to 50 mm long fasteners (such as the Hilti X-ALH 47 high strength steel fastener) are recommended for use with 3.2 mm thick FRP strips.

Pultruded Fiber Reinforced Polymer (FRP) strips are used with the MF-FRP system. A number of different strips, ranging from standard glass fiber pultruded strips to custom hybrid carbon and glass fiber strips have been used in the laboratory studies. Based on the work to-date a custom FRP strengthening strip, called SafStrip™, has been designed and produced. The strip has a high longitudinal tensile strength and stiffness and a high bearing strength and is manufactured by Strongwell (Chatfield, Minnesota, USA). Currently produced FRP strips are 102 mm wide and 3.2 mm thick. The reinforcing fibers in the FRP strip are a combination of unidirectional carbon and E-glass fibers and E-glass continuous strand mats. The resin system is a vinylester system formulated for the pultrusion process. It is important to point out that conventional unidirectionally reinforced pultruded carbon FRP strips currently available on the market cannot be used with the MF-FRP method, since they do not have sufficient bearing strength and will split longitudinally.

Figure 1. 30.5 m-long roll of SafStrip™.

The strips are supplied in rolls (Figure 1) and cut to the required length. If the concrete is to be predrilled (as recommended) the strips are then also pre-drilled at the required fastener spacing with holes to receive the fasteners. The strip is then used as a template for predrilling the concrete and for inserting the fasteners. If the concrete is not predrilled then the fasteners can be "shot" directly through the FRP strip into the concrete.

The drilled holes in the strip should not be oversized. Holes should be drilled the same diameter as the fastener shaft. In addition, fasteners should not be "overdriven" such that they crush the FRP strip and prevent shear-out failure of the strip at the fastener locations. PAF guns can be used at different charge levels and many have fine power-level adjustment capabilities (ANSI 1995). Typically, the PAF gun operator makes a series of trial "shots" into the concrete substrate (through the FRP strip) to determine the charge level required to obtain the desired embedment with the chosen fastener.

3 LABORATORY TESTING

3.1 *1.2 m long rectangular beams*

In 1999 a preliminary investigation of the feasibility of the MF-FRP method of strip attachment was first

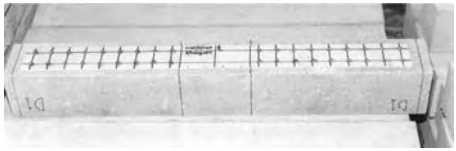

Figure 2. Standard FRP strip attached to underside of 1.2 m beam with powder-actuated fasteners.

Figure 3. Failure of 3.7 m beam with MF-FRP strip.

conducted on 35 small rectangular reinforced concrete beams (Lamanna 2002). The beams measured 152 × 152 × 1220 mm and were tested in four-point bending on a span of 1067 mm (shear span of 432 mm). The beams were reinforced with 2 #4 grade 60 deformed steel bars and #2 grade 40 smooth steel stirrups at a spacing of 58 mm on-center. A variety of fasteners and fastener layouts were considered with a number of different E-glass reinforced FRP strips. An example of a beam with an attached strip is shown in Figure 2. In this preliminary study, all the PA fasteners where shot through the FRP strip into the concrete with no pre-drilling of the strip or the concrete. The purpose of this study was to determine feasibility of the method using available glass FRP pultruded materials and not to obtain "maximum" strengthening. The longitudinal moduli of the FRP strips used in this study ranged from 14 to 27 GPa and the longitudinal strengths ranged from 232 to 561 MPa.

The strengthened small beams showed increases in yield and ultimate moments up to 34% and 30%, respectively, over the unstrengthened control beams (Lamanna et al. 2001). Strengthened beams generally failed due to concrete compression (after steel yielding) with the FRP strip still firmly attached to the beam with the fasteners. This led to a ductile failure mode of the strengthened beam. The MF-FRP method was shown to perform better with lower strength concrete beams (21 MPa) than with higher strength concrete beams (42 MPa) due to reduced spalling in the lower strength concrete when the fasteners were inserted.

3.2 *3.7 m long rectangular beams*

In 2000 the effect of increasing the scale of the beams on the MF-FRP method was investigated. Fifteen 3.7 m long reinforced concrete beams were tested. The purpose of this testing was to examine the effect of different types of FRP strips, fasteners, and fastener spacing on large-scale beams. The beams had dimensions of 305 × 305 × 3658 mm and were tested in four-point bending on a span of 3353 mm (shear span of 1118 mm) at the US Army Corps of Engineers laboratories in Vicksburg, MS (Bank et al. 2002a; Lamanna et al. 2001b; Lamanna et al. 2004). The beams were reinforced with 2 #8 grade 60 deformed steel bars and #4 grade 60 deformed steel stirrups at a spacing of 102 mm on-center in the shear spans. A pea-gravel concrete mix was used with a 28-day strength of 33 MPa. In this study the influence of the type and number of FRP strips, and the influence of fastener type and spacing were studied. In addition, the effect of pre-drilling the FRP strip and the concrete were investigated and the effect of a higher modulus custom carbon/glass FRP strip ($E_{frp} > 55$ GPa) was studied. The hybrid strip was pultruded with two layers of 108 mm wide 1.5 oz/ft^2 (450 g/m^2) continuous strand mat, 21-113 yield (4400 Tex) E-glass rovings, and 138-12k standard modulus ($E_{fiber} = 234$ GPa) carbon tows in a vinylester resin matrix. Detailed strain measurements of the strip were taken during some tests to determine the strain distribution in the strip and the loadtransfer mechanisms.

This study demonstrated that with the appropriate fastener layout and strip properties, strength increases equal to that of beams strengthened by bonding the strips were achieved with the MF-FRP method. The 3.7 m beam tests showed increases in yield and ultimate strength up to 13.8 and 20.1 percent for beams strengthened with pre-drilled fasteners. All beams with pre-drilled fasteners failed in a ductile manner, in which the tensile steel yielded first and then the concrete crushed with the strip still attached. Continued application of the load following the crushing of the concrete eventually caused the FRP strip to detach, either from the interior of the beam or from the end. Cover failure also occurred in some cases, however the strip still remained attached to the beam as shown in Figure 3.

The beam in Figure 3, beam H1.5-4-Y-AL47D, was reinforced with a 102 mm wide hybrid FRP strip, with 2 rows of Hilti X-ALH 47 fasteners (with neoprene backed washers and pre-drilled holes) at 51 mm spacing along the entire length of the strip. Figure 4 shows a comparison between the applied moment-midspan displacement of the beam, a control beam with no FRP strengthening, and a beam strengthened with an identical externally bonded FRP (EB-FRP) strip. The beam with the bonded strip failed due to end-delamination of the strip. It can be seen that the stiffness of the beam with the bonded strip was slightly higher than the strip with the MF-FRP beam in both the elastic and inelastic ranges. The beams both achieve similar strength increases but the beam with the MF-FRP

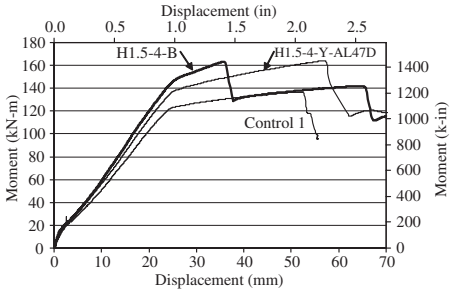

Figure 4. Comparison between control beam and beams strengthened with MF-FRP and EB-FRP methods.

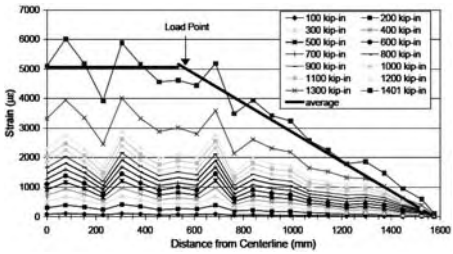

Figure 5. Axial strain distribution along the MF-FRP strip as a function of load level.

strengthening had a much high ductility than the beam with the bonded strip.

Figure 5 shows the distribution of axial strain along the length of the MF-FRP strip from the beam centerline to the end of the strip for a very similar beam to the one described above (fastener spacing was 76 mm as opposed to 51 mm and behavior was almost identical). It can be seen that the strain increases linearly along the length of the strip in the shear span and that the strain in the strip increases significantly following yielding of the internal steel at approximately 135 kN-m (1200 k-in) (Bank et al. 2002a).

In 2001 a second series of 3.7 m long beams was tested at the University of Wisconsin (Borowicz 2002; Bank et al. 2002b). 10 beams were tested in this series. The beams had the same internal steel reinforcing as the previous 3.7 m series. The 28 day concrete strength was 44.7 MPa; slightly higher than the previous series. The beams were tested in fourpoint bending. The purpose of this series of tests was to investigate the effect of end-termination length, shear spans, multiple strip layers, and fatigue loads. All constant moment spans were 762 mm. The shear spans were 1372 mm in eight of the beams, and were decreased in two of the beams to 940 mm and 686 mm, respectively. All FRP strips were attached with 2 rows of Hilti ALH 47 fasteners at a 51 mm spacing along the length of the beam. Two beams (UW3, UW10) were fatigue tested at 2 Hz and cycled between 20% and 80% of the unstrengthened control beam's yield moment. To investigate the effect of end-delamination the distance from the last row of PA fasteners to the support point (called the termination length) was taken as 102, 254 or 305 mm. One beam was tested with two strips placed (not bonded) on top of each other.

In addition, two different FRP strips were used in this series. One strip was pultruded with a grey pigment to make it more "visually compatible" with the concrete. The other strip was pultruded with no pigment and had a characteristic black color due to the carbon fibers. Both strips were pultruded with two layers of 108 mm wide 1.5 oz/ft^2 (450 g/m^2) continuous strand mat, 21-113 yield (4400 Tex) E-glass rovings, and 138-12 k standard modulus carbon tows in a vinylester resin matrix. The intent was to use only the grey strip that was produced before the black strip. However, after the first beam test it was discovered that the grey strip had a significantly lower strength than expected. The longitudinal strengths of the grey and black strips according to ASTM D3039 were 494 MPa and 743 MPa, respectively. The open-hole strengths according to ASTM D5766 were 358 MPa and 655 MPa, respectively. Although the strips had significantly different strengths, their longitudinal moduli (measured to 50% of ultimate only) were the same (56.5 GPa). It is believed that the low strength of the grey strips was due to the pigment in the resin that reduced the bond between the carbon fibers and the vinylester resin. Three beams (UW2, UW4, UW5) were tested with the grey strip at different shear spans (1372, 940 and 686 mm). All the remaining beams were tested with the higher strength black strip.

The beams tested over the 1372 mm shear span with a single the black strip failed due to concrete crushing with the strip still firmly attached and achieved strength increases of 22–24% regardless of the end distance (UW6, UW7, UW8). The beam with the double strip failed due to strip end delamination and achieved a strength increase of 37% (UW9). The moment-midspan displacement of the four beams and the control (UW1) are shown in Figure 6. Beam UW2 strengthened with the grey strip is also shown in this figure. The premature failure of UW2 due to strip rupture can be seen. After rupture of the strip, the moment capacity dropped to that of the unstrengthened beam (UW1).

Figure 7 shown moment versus the strain in the concrete and the FRP strip at midspan for beam UW7 which is representative of beams UW6 to UW9. At concrete failure the maximum strain in the FRP strip was close to 0.0075 which corresponds to a stress of 424 MPa in the strip which is 57% of the ultimate strength of the strip and 65% of the openhole strength

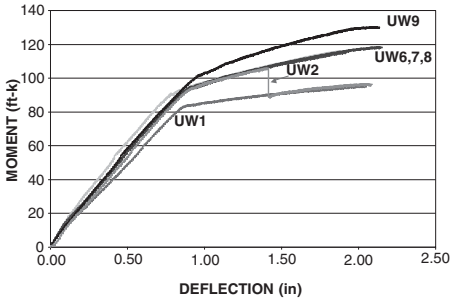

Figure 6. Comparison of MF-FRP beams with 1372 mm shear spans.

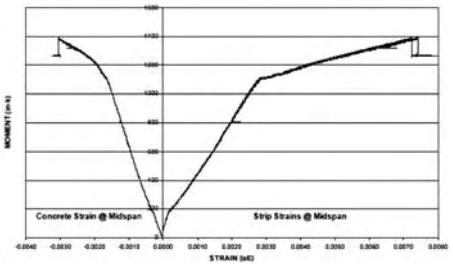

Figure 7. Moment vs strain in beam UW7.

of the strip. On the other hand the maximum strain achieved in the grey strip in beam UW2 was 0.0065 which correspond to a stress of 367 MPa which is very close to the open-hole strength of the grey strip (358 MPa).

The behavior of the beams with the different shear spans (UW2, UW4 and UW5) is shown in Figure 8. The beams with the longer shear spans (UW2 and UW5) failed due to strip rupture, however, the beam with the short shear span (UW4) failed due to concrete crushing. Since a control beam for this shear span was not tested it is not possible to draw meaningful conclusions regarding the strengthening of beams with short shear spans and further work is needed in this area, however, it appers that the MF-FRP method may be advantageous for strengthening short beams.

The beams (UW3 and UW10) subjected to fatigue load both failed due to rupture of the internal steel reinforcing bars and not due to failure of the FRP strip or the PA fasteners. Beam UW3 failed after 1,780,000 cycles (2,000,000 was the target) and beam UW10 failed after 759,00 cycles (using a slightly different set-up). After every 200,000 cycles the cyclic load was stopped and a static load-deflection test was performed. The static load-deflection tests for beam UW3

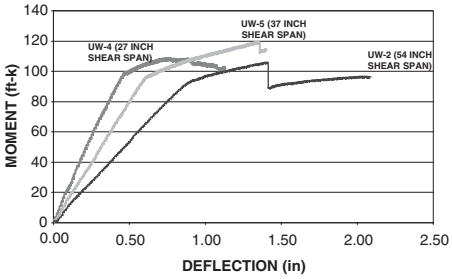

Figure 8. Comparison of MF-FRP beams with different shear spans.

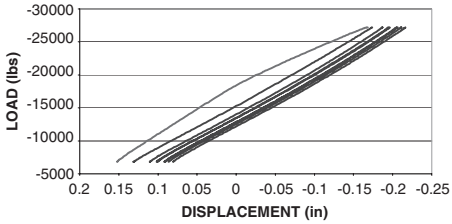

Figure 9. Stiffness change due to fatigue load in beam UW3.

are shown in Figure 9 (the initial static load cycle is the first line to the left of the figure). It can be seen that very little stiffness degradation occurred in the MF-FRP beam after the first 200,000 cycles.

3.3 *8.8 m long T-beams*

In 2001 a series of full-scale bridge T-beams strengthened with the MF-FRP method were tested at the US Army Corps of Engineers laboratories (Bank et al. 2002b, Borowicz 2002). The T-beams were 8839 mm long, with a 1524 × 203 mm flange and a 559 × 305 mm web (762 mm total depth). The beams were tested in four-point bending on a 8534 mm span with a 1524 moment span and 3510 shear spans. They were reinforced with #9 grade 60 deformed steel bars in the bottom of the web and #4 stirrups at 305 mm spacing. The flange was reinforced with a double layer of #4 bars at 305 mm in both directions. Beams were fabricated at the Corps of Engineers. The average 28 day concrete compressive strength was 30 MPa. At the time of the beam tests the average concrete strength was 36 MPa. Three different levels of tensile steel reinforcement were used, identified by the number of #9 main bars, A3, A5 and A8 (i.e. 3, 5 or 8 #9 bars, respectively). The objective of this testing was to determine if the MF-FRP method could be used to perform rapid (i.e. in a few hours) field strengthening of bridges

Figure 10. Attaching MF-FRP strip to T-beams.

for military purposes. The T-beam dimensions and steel reinforcement levels were taken to represent typical T-beam bridge girders constructed in the US in the 1960s.

For each reinforcement level 3 different strengthening levels were used – no strengthening (Control), one hybrid FRP strip (Test 1) and two hybrid FRP strips (Test 2) having the same properties as the "black" strips used on 3.7 m beams tested at UW. All beams had the FRP strips fastened with Hilti XALH powder actuated fasteners (47 or 52 mm long) in two rows 51 mm apart and spaced at 51 mm along the entire length. All strips and holes were predrilled. The strips were attached from the underside of the beams as shown in Figure 10 to simulate field conditions.

In the A3 and A5 controls it was not possible to achieve ultimate failure of the beams due to the large displacement required. Only the A8 beam reached its ultimate load. All the strengthened beams failed due to strip delamination before achieving compressive failure in the concrete. Beams with the single FRP strip were tested with a termination length of 482 mm, while beams with double strips were tested with a termination length of 76 mm. (The longer termination length for the single strips was to simulate field conditions where access to the support point would not be feasible for practical reasons.) Beams showed increases of between 10 and 20% in strength at yield and at ultimate load. Figure 11 shows the moment versus displacement data for all nine tests.

The beams with the single strips and the longer termination lengths failed due to end-delamination after significant shear-out failure in the strips (Figure 12),

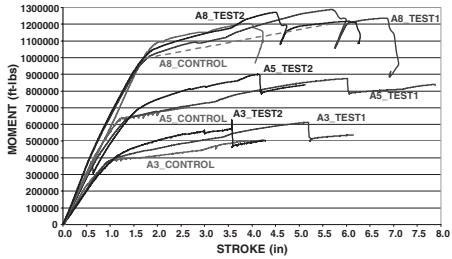

Figure 11. Test results for 8.8m long T-beams.

Figure 12. Shear-out failure at end of strip in A3-1.

Figure 13. Delamination failure of strip in A3-2.

while the beams with the double strips with the shorter termination lengths failed due to interior delamination at a flexural crack (Figure 13).

It can be seen that the bearing/shear-out delamination failure is significantly more ductile than the interior delamination failure and that the beams with the single strips ultimately achieved the same or greater strength increases as the beams with the double strips. The double strips were not as effective as the single strips due to premature delamination failures in the beams with the thicker (double) strips.

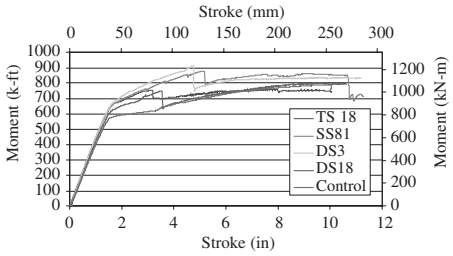

Figure 14. Test results for 2nd series of T-beams.

In order to investigate this issue further a second series of 8.8 m T-beams was tested at the US Army Corps of Engineers in 2002. The purpose of this series was to investigate the use of expansion anchors to prevent end-delamination failures, to try to improve the performance of beams with multiple strips (one, two or three), and to conduct a fatigue test on a T-beam (Bank et al. 2003). Six beams were tested in this series. All beams had 5 #9 main steel bars. Five beams were subjected to monotonic loading to failure and one beam was subjected to 2 million cycles of fatigue loading. The monotonically loaded beams were tested in the same manner as the first series of T-beams. The fatigue beam was tested in three-point bending with a single actuator at midspan cycled at 2 Hz between 96 and 284 kN-m (approximately 50% of the yield moment).

The monotonically loaded beams included one control beam, a beam with a single strip and 2 end anchor bolts at each end (SS18), a beam with a double strip and no anchor bolts (DS18), a beam with a triple strip with anchor bolts (TS18), and a beam with a double strip and a short termination length and no anchor bolts (DS3). Test results for these beams are shown in Figure 14.

In this series, increases in capacity over unstrengthened control beams of over 25% were obtained. All beams failed due to strip enddelamination (with shear-out failure in SS18). Ultimate compression failure of the control beam occurred at 250 mm of midspan deflection. Two 64 mm long by 13 mm diameter expansion anchors were seen to significantly delay end-delamination of the strips and to increase both the deflection and load at failure. Shorter termination lengths (3 inches versus 18 inches from the support) also increased strengthening by delaying end-delamination. The use of multiple FRP strips (in unbonded layers) did not yield significant increases in capacity of the strengthened beams over single strips due to premature end-delamination failures and the inability of the fasteners to transfer load into the outer strips.

The beam subjected to the fatigue loading (same as SS18) sustained the full 2 million cycles with almost no degradation of the strengthening system nor change in stiffness of the beam (Bank et al. 2003).

Table 1. Properties of FRP strips used in 7.3 m beams.

	Mean MPa	SD MPa	COV %
Ultimate Strength	844	77	9.2
Open-hole Strength	640	49	7.6
Sustained Bearing Strength	234	10	4.3
Modulus of Elasticity	61.3	5.3	8.6

3.4 *7.3 m long rectangular beams*

In 2002, four beams 7320 mm long with nominal cross section measurements of 508 × 508 mm were fabricated and tested at the University of Wisconsin-Madison (Arora 2003; Bank & Arora 2004). One beam (C-1) was used as an unstrengthened control beam, two beams (FRP 1 and FRP 2SS) were used to determine the behavior of the strengthened beam with two FRP strips fastened using galvanized steel fasteners or stainless steel (SS) fasteners, respectively. One beam (FRP 3) was used to determine the behavior of the beam strengthened with 3 strips.

The beams were reinforced with 3 #7 grade 60 deformed main bars and #4 closed stirrups at 200 mm spacing. On the day of testing the concrete strength was 34 MPa. Beams were strengthened with a second generation hybrid glass/carbon FRP strip and with Hilti ALH 47 galvanized steel fasteners or Hiti CRS 44 stainless steel fasteners. In each strip a single row of fasteners at 102 mm spacing along the length was used. In addition, either carbon steel or stainless steel end anchors (Hilti Kwik Bolt (KB) II Expansion Anchors) were used at the strip ends (also at 102 mm spacing). The beams were tested in fourpoint bending over a span of 6528 mm with a constant moment span of 762 mm. The beam geometry was chosen to represent a "unit width" of the fieldtested bridge described in what follows.

The second generation hybrid FRP strip, known as SafStrip™, was pultruded with two layers of 108 mm wide 1.5 oz/ft^2 (450 g/m^2) continuous strand mat, 16-113 yield (4400 Tex) E-glass rovings, and 40–48 k standard modulus carbon tows in a vinylester resin matrix. The FRP strips were tested at the University of Wisconsin for ultimate tensile strength, open-hole tensile strength, longitudinal tensile modulus, and longitudinal bearing strength as per ASTM standards D3039, D5766 and D5961, respectively. Five specimens were used for the longitudinal tests and 10 specimens were used for the bearing tests. The test results are shown in Table 1.

Strips were attached from the underside with the beams supported at their ends. The strips and concrete

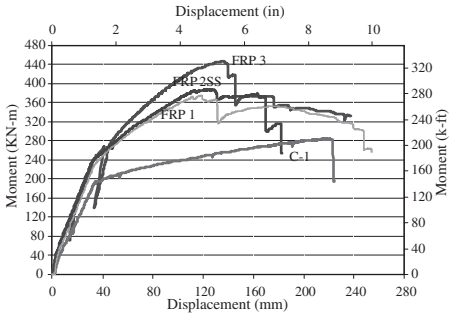

Figure 15. Test results for 7.3 m beams.

were pre-drilled as described previously. All the strengthened beams failed due to concrete compression crushing with the strips still firmly attached. At this point, a drop in load carrying capacity was seen, however, the beams continued to carry significantly more load than the unstrengthened beam. This indicates that the FRP strengthening system was active well beyond concrete compression failure. Ultimately the FRP strips failed due to bearing or splitting at very large displacements. The moment-midspan deflection plots for the four beams are shown in Figure 15.

The strengthened beams (FRP 1, FRP 2SS, and FRP 3) achieved increases in yield moments of 18, 23 and 25 percent, and increases in ultimate moments of 33, 38 and 58 percent, respectively over the control beam. It can be seen that the compression failure occurred at different ultimate displacements in the different beams. Therefore, the strengthening achieved at equivalent displacements is even higher than listed above. At a displacement of L/64 (102 mm), the strength increases were 50, 55 and 71 percent respectively.

Figure 16. Bridge P-53-702.

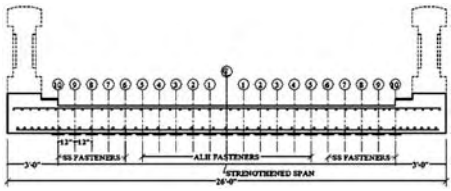

Figure 17. Cross-section of bridge.

Figure 18. Workers installing FRP strips under bridge.

4 FIELD TESTING

In 2002 a concrete bridge was strengthened in the field with the MF-FRP method (Bank et al. 2003; Arora 2003) The bridge was a 7.3 m long flat slab bridge (No. P-53-702) located on Stoughton Road over Saunders Creek in the City of Edgerton, Wisconsin, USA. The bridge was originally constructed in 1930 for an H15 truck loading and was 7.9 m wide. The bridge strengthening was designed to increase the bridge load rating from its existing insufficient HS17 to an HS25 rating. This required an increase of 29% in the nominal flexural capacity of the bridge (AASHTO 1996).

Figure 16 shows a picture of the bridge. The bridge was strengthened with 21 FRP strips spaced at 305 mm on-center across the bridge width. The 11 strips in the center were fastened with ALH 47 fasteners while the outer 10 strips were fastened with CRS 44 stainless steel fasteners. Figure 17 shows a cross-section of the bridge and the FRP strips.

The bridge slab was 508 mm thick. Over the years an asphalt overlay approximately 150 mm thick had been placed over the concrete. The bridge was severely deteriorated and had extensive cracking of the slab. The bridge was reinforced with 25 mm square ribbed steel rebars at 150 mm on center having a yield strength of 230 MPa. The FRP strips were attached in August 2002 and they remained in place until June 2003 when a failure load test was conducted on the bridge prior to its scheduled demolishion. Local county maintenance workers installing the strips are shown in Figure 18.

The bridge was strengthened for a total cost of (all materials and labor) of \$8000 or \$138/m^2 (includes 147 m of FRP strip at \$30/m). The strips remained

Figure 19. Failure load testing of the MF-FRP strengthened bridge.

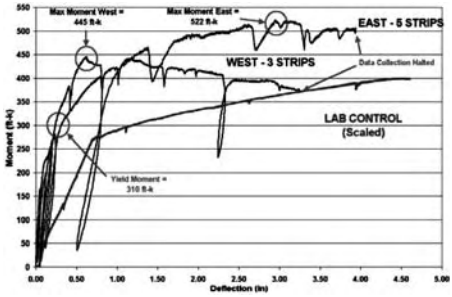

Figure 20. Results of field tests.

attached to the bridge throughout the winter of 2002–2003 while it was open to regular traffic. Average winter temperature in south-central Wisconsin is −10°C. Prior to the load testing in June 2004 the condition of the strips and the fasteners was examined. The qualitative examination revealed minor corrosion damage to the ALH fasteners and no corrosion to the CRS fasteners. All strips were still firmly attached to the underside of the bridge. No deterioration of the FRP strips was seen and laboratory testing of strips removed from the bridge showed no loss of longitudinal strength or stiffness (Borowicz et al. 2004). The concrete was tested using a rebound hammer and was found to have a compressive strength of approximately 15 MPa. This value was close to the AASHTO (2000) recommended value of 17 MPa for concrete of this era. Attempts to extract cores for compression testing were unsuccessful due to the poor condition of the concrete.

The failure load test was conducted by a team of researchers from the University of Missouri-Rolla under the supervision of Prof. A. Nanni. The bridge deck was sectioned into two approximately 1000 mm wide by 508 mm deep (not including the overlay) test sections and a load frame with hydraulic rams was used to apply load to the sections in four point bending with a 1524 mm constant moment span. Figure 19 shows the bridge during testing. A portion of the overlay was removed at the center of the test section to attach strain gages to the concrete and to observe the compression crushing of the concrete.

The first section (West section) to be tested was strengthened with the original 3 FRP strips installed in August 2002. Unfortunately, due to the concrete overlay (and the lack of a saw blade larger than 635 mm cut depth) two of the three longitudinal saw cuts did not cut completely through the full depth of the deck. A 20–30 mm deep part of the bottom cover remained attached between the two sections along the full length and between the East section and the remainder of the deck along a 4 m central section. This caused the West section to deflect with the East section until the steel yielded and the sections broke apart. This complicated the interpretation of the test. Because of this an additional two FRP strips were added to the second section (East section) to obtain additional data on the strengthening capability of the MF-FRP method. Unfortunately, this meant that a control section was not tested (as originally intended for the East section). However, the test data were compared with a scaled version of the control beam tested in the laboratory. Compassion between the moment and the midspan deflection of the two test sections tested together with a scaled (for width and moment span differences, but not for concrete strength) is shown in Figure 20. This gives an indication of the behavior of the strengthened sections. The behavior of the section with the 5 strips (East section) is felt to be a more reliable result. In this East section, we see clear evidence of yielding of the section which is followed by a non-linear regime corresponding to the strengthened section. This behavior can be compared qualitatively with that of the FRP strengthened 7.3 m beams tested in the laboratory and shown in Figure 15. The larger stiffness of the deck sections in the elastic range is attributed to the sections not being fully separated in this range.

In the field tests, the displacement gages (LVDTs) were removed from under the bridge at approximately 100 mm of midspan deflection. By this time compression failure in the top flange was clearly evident and FRP strips were still firmly attached. Load application was continued without data acquisition to attempt to achieve ultimate failure of the strengthening system. The West section failed due to shear failure of the concrete at a displacement of approximately 200 mm. At this time the FRP strip detached from one end. In the East section it was not possible to cause failure of the MF-FRP system. At approximately 175 mm of displacement, the loading was halted due to safety concerns as the previously tested West section had been dragged downwards by the East section and was in danger of completely collapsing into the riverbed.

Figure 21. Failure of the West section.

Figure 22. Failure of the East section (foreground) and West section (background).

Figure 21 shows a view from under the bridge after completion of the test on the West section. Figure 22 shows a view from under the bridge after completion of the test on the East section. The very large displacements of the sections can be seen.

5 ANALYTICAL MODEL

A strength model was developed to predict the ultimate flexural strength of reinforced concrete members strengthened with the MF-FRP system (Bank & Arora 2004; Arora 2003). A moment-curvature model was also developed for research purposes (Lamanna et al. 2002). It is assumed that concrete compression failure occurs at a strain of 0.003 and that plane sections remain plane. In addition, it is assumed that FRP strip has a pseudo elasticperfectly plastic behavior when attached with discrete mechanical fasteners. This assumption implies that the FRP strip behaves in a linear elastic fashion up until the bearing failure of the FRP strip and thereafter the strip carries a constant load as progressive shear-out failure occurs at each fastener location. This is quite different from the behavior of an externally-bonded FRP strip that has a linear elastic behavior up until strip rupture or delamination. This behavior is unique to the MF-FRP method and gives the strengthened beam its ductility. The tensile force in the FRP strip at any point along its length is equal to the shear force transferred into the strip by all the fasteners in the corresponding shear span (or shear transfer length) of the beam. The force transferred by each fastener is a function of the bearing stress at the hole in the FRP strip (σ_b), the fastener diameter (ϕ_b), and the strip thickness (t_{strip}).

$$P = \frac{\sigma_b}{\phi_b \, t_{strip}} \tag{1}$$

This means that the force transferred to the FRP strip (T_{frp}) is directly proportional to the number of fasteners (N) and end anchors (M) available at a point along the length of the strip and is given as,

$$T_{frp} = NP_f + MP_a \tag{2}$$

where P_f and P_a are the force transferred by the fasteners and the anchors, respectively. The tensile stress in the FRP strip at a point along the strip can be related to the tensile force in the strip. When shear-out failure occurs (denoted by the subscript b for bearing) the stress in strip ($f_{f,b}$) is given as,

$$f_{f,b} = \frac{NP_{f,b} + MP_{a,b}}{A_{strip}} \tag{3}$$

It is further assumed that when concrete compression failure occurs at the section flexural capacity, after the steel has yielded, the Whitney rectangular stress distribution can be used to determine the compressive force resultant in the concrete. Using ACI 440 notation, the flexural capacity can be determined from,

$$M_n = A_s f_y \left(d_s - \frac{a}{2} \right) + A_f f_{f,b} \left(d_f - \frac{a}{2} \right) \tag{4}$$

where, $A_f = n_s \times A_{strip}$, n_s is the number of strips, d_s and d_f are distances from the extreme compression fiber to the centroid of the steel and FRP, respectively. The neutral axis depth in this situation (i.e. steel and FRP strip "yielding" prior to concrete compression), $c = a/\beta_1$, is given as,

$$c = \frac{A_s f_y + A_f f_{f,b}}{0.85 f_c' \beta_1 b} \tag{5}$$

This is analogous to the situation of a conventional steel under-reinforced section. The MF-FRP strip can

Table 2. Comparison between model predictions and test results.

Beam	Fastener bearing load $P_{f,b}$ (N)	Anchor bearing load $P_{a,b}$ (N)	Stress in FRP strip $f_{f,b}$ (MPa)	Area of FRP strips A_{frp} (mm^2)	Ultimate moment (predicted) M_n^{calc} (kN-m)	Ultimate moment (experiment) M_n^{exp} (kN-m)	% Difference
C1	–	–	–	–	219	283	−22.6
F1	3345	9452	421	645	352	376	−6.5
F2	2989	9452	383	645	340	389	−12.7
F3	3345	9452	421	968	416	447	−6.9

$N = 35$ and $M = 2$ in each shear span for all beams.

be thought of as a secondary "yielding" layer of reinforcement that "yields" after the steel yields, on condition that the number and spacing of fasteners is correctly proportioned in the design procedure (described in what follows). What is unique about this "yielding" is that the designer can choose the "yield stress"; it is not only a function of the material properties as with conventional materials. A comparison between analytical predictions and the results of the tests on the 7.3 m long beams (renamed C1, F1, F2, and F3 respectively) are shown in Table 2. Note that in all cases the stress in the FRP strip at ultimate is less than the open-hole strength of the strip (640 MPa).

6 DESIGN PROCEDURE

The design procedure is to first determine the required (strengthened) ultimate moment and then to determine the number of fasteners their spacing, and the number of strips. The strengthened section must be designed as under-reinforced so that the strip will develop the sustained shear-out failure prior to concrete crushing. The balanced condition in which the concrete fails in compression at $\varepsilon_{cu} = 0.003$ when the FRP begins to fail in bearing at $f_{f,b}$ is given by the following equality,

$$\frac{A_f f_{f,b} + A_s f_y}{b d_f} = \frac{0.85 \beta_1 f_c' E_f \varepsilon_{cu}}{f_{f,b} + E_f \varepsilon_{cu}} \qquad (6)$$

with $f_{f,b}$ given by Eq. (3). Note that $f_{f,b}$ appears on both sides of the equation. For a selected number of strips this yields a quadratic equation for $f_{f,b}$. Eq. (3) is then used to determine the number of fasteners required in the shear span. It is recommended that the actual $f_{f,b}$ used in the design not exceed 0.75 the "balanced" $f_{f,b}$ given in Eq. (6) to ensure ductile failure of the MF-FRP strengthened beam.

Following ACI 440 (2002) recommendations an additional strength reduction factor ($\Psi_f = 0.85$) for the FRP is introduced and the nominal moment capacity is given as,

$$M_n = A_s f_y \left(d_s - \frac{a}{2} \right) + \psi_f A_f f_{f,b} \left(d_f - \frac{a}{2} \right) \qquad (7)$$

At this time the resistance factor, ϕ, is also taken following ACI 440 (2002). Since the design method requires a ductile shear-out failure of the FRP strip, ε_s will far exceed 0.005 so that $\phi = 0.9$. The factored moment capacity is then given as ϕM_n. Following ACI 440 recommendations, the guaranteed ultimate open-hole tensile strength should be determined from the mean minus 3 standard deviations of a minimum of 25 test specimens. It is important to ensure that the stress in the strip remain below the guaranteed open-hole strength of the strip to prevent rupture of the strip prior to sustained shear-out failure. At this time it is recommended that the mean sustained shear-out (bearing) strength of the strip (and not the mean minus 3 standard deviations) be used in design when calculating the stress in the strip at shear-out failure since this failure mode is desirable.

The remainder of the design is a function of detailing considerations. After the number of fasteners has been determined, the designer must ensure that there is sufficient shear transfer length to accommodate all of the fasteners. This depends on the available shear span length but also on the spacing between the fasteners. At this time, a fastener spacing of 100 mm is recommended to prevent pry-out failure of the fasteners. The use of only one row of fasteners along a 102 mm wide strip and the use of single strips (i.e. no double or triple layers) only is recommended. Pre-drilling of holes is recommended, as is the use of fasteners with neoprenebacked washers. Although many of the laboratory beams were successfully strengthened without end anchors, two end anchors at each end of the strip are recommended at this time. Extending the FRP strip as close as possible to the support or beyond a point of inflection is also recommended at this time to prevent peeling delamination failure at the strip end.

7 CONCLUSIONS

An overview of the experimental and theoretical research on the Mechanically-Fastened FRP method has been presented in this paper. Based on the experimental investigations conducted to date it appears that the MF-FRP method may be a promising method for strengthening concrete members, particularly where speed of installation and immediacy of use is imperative, and the strengthening is intended for a limited lifetime (e.g. when it is known that the structure will be replaced in the foreseeable future.) The method is particularly attractive since very little surface preparation of the concrete is needed and a ductile failure mode is obtained in the strengthened members.

Research is needed to determine the long-term durability of the MF-FRP method. Issues of galvanic corrosion, degradation of the strips at the holes, and environmental effects on pry-out failures of the concrete all need to be studied in greater depth. Design issues also need to be studied further to gain a better understanding of how to control the shear-out failure mode that gives the MF-FRP method its desirable ductile behavior. Further investigations of the effect of shear transfer length are needed, as are further tests on the FRP strips currently being produced for the MF-FRP method. The author encourages the research community to experiment with the MF-FRP method and to help to uncover its unique benefits.

ACKNOWLEDGEMENTS

The author would like to thank, (1) the US Army Corps of Engineers, (2) the Wisconsin Department of Transportation, (3) Strongwell, (4) graduate students (Anthony J. Lamanna, David T. Borowicz, Dushyant Arora), and, (5) colleagues (Prof. Michael G. Oliva, Prof. Jeffrey S. Russell, Prof. Antonio Nanni) for helping to make this work possible.

REFERENCES

AASHTO. 1996. Standard Specifications for Highway Bridges, 16th Edition. *American Association of State Highway and Transportation Officials,* Washington, DC.

AASHTO. 2000. Manual for Condition Evaluation of Bridges, 2nd Edition. *American Association of State Highway and Transportation Officials*, Washington, DC.

ACI Committee 440.2R. 2002. Guide for the Design and Construction of Externally Bonded FRP Systems for Strengthening Concrete Structures. *American Concrete Institute*, Farmington Hills, MI.

Alkhrdaji, T., Nanni, A., and Mayo, R. 2000. "Upgrading Missouri Transportation Infrastructure: Solid RC Decks Strengthened with FRP Systems," *Transportation Research Record 1740*, pp. 157–163.

Arora, D. 2003. Rapid Strengthening of Reinforced Concrete Bridge with Mechanically Fastened-Fiber Reinforced Polymer Strips. MS Thesis, University of Wisconsin-Madison.

ANSI A 10.3-1995. 1995. American National Standard for Construction and Demolition: Powder-Actuated Fastening Systems – Safety Requirements. *American National Standards Institute*, Chicago, IL.

ASTM D3039. "Standard Test Method for Tensile Properties of Polymer Matrix Composite Materials," *American Society for Testing and Materials*, West Conshohocken, PA.

ASTM D5766. "Standard Test Method for Open Hole Tensile Strength of Polymer Matrix Composite Laminates," *American Society for Testing and Materials*, West Conshohocken, PA.

ASTM D5961. "Standard Test Method for Bearing Response of Polymer Matrix Composite Laminates," *American Society for Testing and Materials*, West Conshohocken, PA.

Bank, L.C., and Arora, D., 2004. "Analysis and Design of RC Beams with Mechanically Fastened FRP(MF-FRP) Strips," *ACI Structures Journal*, under review.

Bank, L.C., Lamanna, A.J., Ray, J.C., and Velazquez, G.I. 2002a. Rapid Strengthening of Reinforced Concrete Beams with Mechanically Fastened, Fiber-Reinforced Polymeric Composite Materials. *US Army Corps of Engineers*. Report Number ERDC/GSL TR-02-4. 93 pages.

Bank, L.C., Borowicz, D.T., Lamanna, A.J., Ray, J.C., and Velazquez, G.I. 2002b. Rapid Strengthening of Full-Size Reinforced Concrete Beams with Powder-Actuated Fastening Systems and Fiber-Reinforced Polymer (FRP) Composite Materials. *US Army Corps of Engineers*. Report Number ERDC/GSL TR-02-12. 110 pages.

Bank, L.C., Borowicz, D.T., Arora D., and Lamanna, A.J. 2003. Strengthening of Concrete Beams with Fasteners and Composite Material Strips – Scaling and Anchorage Issues. *US Army Corps of Engineers*. Draft Final Report, Contract Number DACA42-02-P-0064.

Bank, L.C., Arora, D., Borowicz, D.T., and Oliva, M., 2003. Rapid Strengthening of Reinforced Concrete Bridges, *Wisconsin Highway Research Program*, Report Number 03–06. 166 pages.

Borowicz, D.T. 2002. Rapid Strengthening of Concrete Beams with Powder Actuated Fasteners and Fiber Reinforced Polymer (FRP) Composite Materials. MS Thesis, University of Wisconsin-Madison.

Borowicz, D.T., Bank, L.C., Nanni, A., Arora, D., Desa, U., and Rizzo, A. 2004. "Ultimate Load Testing and Performance of Bridge Strengthened with Fiber Reinforced Composite Materials and Powder-Actuated Fasteners," *Proceedings of the 83rd Annual Transportation Research Board Meeting*, CD-ROM, Washington, DC, January 11–14.

FIB (Féderation Internationale du Béton). 2001. "Externally Bonded FRP Reinforcement for RC Structures," *International Federation for Structural Concrete (fib)*, Switzerland.

Garden, H.N., and Holloway, L.C. 1998. "An Experimental Study of the Influence of Plate End Anchorage of Carbon Fibre Composite Plates Used to Strengthen Reinforced Concrete Beams," *Composite Structures*, Vol. 42, pp. 175–188.

Lam, L., and Teng, J.G. 2001. "Strength of RC Cantilever Slabs Bonded with GFRP Strips," *ASCE Journal*

of Composites for Construction, Vol. 5, No. 4, pp. 221–227.

Lamanna, A.J. 2002. Flexural strengthening of Reinforced Concrete Beams with Mechanically fastened Fiber-Reinforced Polymer Strips. PhD Thesis, University of Wisconsin – Madison.

Lamanna, A.J., Bank, L.C., and Scott, D.W. 2001a. "Flexural Strengthening of Reinforced Concrete Beams Using Fasteners and Fiber-Reinforced Polymer Strips," *ACI Structural Journal*, Vol. 98, No. 3, pp. 368–376.

Lamanna, A.J., Bank, L.C., and Scott, D.W. 2001b. "Rapid Flexural Strengthening of RC Beams Using Powder Actuated Fasteners and FRP Strips," *Proceedings of the 5th International Symposium of FRP in Reinforced Concrete Structures*, (ed. C. Burgoyne), Cambridge, UK, July 16–18, pp. 389–397.

Lamanna, A.J., Bank, L.C., and Scott, D.W. 2004. "Flexural Strengthening of RC Beams by Mechanically Attachinga FRP Strips," *ASCE Journal of Composites for Construction*, Vol. 8, in press.

Lamanna, A.J., Bank, L.C., Borowicz, D.T., and Arora, D. 2002. "Strengthening of Concrete Beams with Mechanically Fastened Strips," Proceedings of ICCI 2002, the *Third International Conference on Composites in Infrastructure*, San Francisco, CA, June 10–12, CD-ROM.

Nanni, A. 1997. "Carbon FRP Strengthening: New Technology Becomes Mainstream," *Concrete International*, Vol. 19, No., 6, pp. 19–23.

Spadea, G., Bencardino, F., and Swamy, R.N. 1998. "Structural Behavior of composite RC Beams with Externally Bonded CFRP," *ASCE Journal of Composites for Construction*, Vol. 2, No. 2, pp. 59–68.

Teng, J.G., Chen, J.F., Smith, S.T., and Lam, L. 2001. FRP-Strengthened RC Structures. *John Wiley & Sons*, NY.

FRP Composites in Civil Engineering – CICE 2004 – Seracino (ed)
© 2005 Taylor & Francis Group, London, ISBN 90 5809 638 6

Strengths and limitations of fibre reinforced polymers in the civil infrastructure, material advances and the influences on present and future developments

L.C. Hollaway & I. Hackman
School of Engineering – Civil Engineering, University of Surrey Guildford, Surrey, UK

ABSTRACT: The last thirty years has shown very great progress in the utilisation of polymer composites in the civil engineering infrastructure. This paper reviews the present uses and successes of fibre reinforced polymer (FRP) composites and gives possible reasons for this achievement; but, in addition and more importantly, investigates their limitations and how these might be improved or whether inevitably they must be accepted. The strengths and limitations of the composites are a function of two main property divisions, namely, their mechanical properties and their in-service overall durability under aggressive and changing environments. These two areas must be investigated, under static and fatigue loading from a short and a long term loading situation, before a proper assessment of the utilisation of the material for a specific structural application can be made. This paper demonstrates, through illustrative examples, that the over-riding concern for the future use of composites in construction is the durability of polymers associated with its permeability when it is exposed to adverse environmental conditions such as moisture and salt solutions over long periods of time. A potential technique, which utilises nanotechnology to improve the barrier properties, fire resistance and the strength of the polymer, is discussed. It is concluded that this technique could have positive advantages for adhesives and surface coatings as well as for FRP composites.

1 INTRODUCTION

1.1 *The current developments of fibre reinforced composites in the civil infrastructure*

Since they were first seriously considered for use in the construction industry some thirty-five years ago, advanced polymer composites have made great advances compared with the more conventional materials, these latter having evolved over the last century. The uses of fibre-reinforced polymer (FRP) composites in construction can be conveniently divided into specific areas, which will be discussed from their utilisation advantages and their limitation point of view associated with their in-service and mechanical characteristics.

- *All composite structures* – these systems can be divided into two specific categories, (a) the substitution of the traditional materials with the new FRP material, (b) the new material-adapted concepts.
- *External reinforcement of concrete structures*, (i) flexural and shear upgrading of RC beams and slabs, (ii) wrapping of concrete columns, (iii) near surface mounted (NSM) FRP rods or strips for upgrading RC, timber and masonry beams, (iv) flexural and shear upgrading of metallic structures, (v) seismic retrofit of RC and masonry structures.
- *FRP composite rebars* used as internal reinforcement to concrete.
- *Replacement of degraded bridge deck systems with fibre/matrix composites.*
- *Miscellaneous.*

2 'ALL FRP COMPOSITE' STRUCTURES

In civil engineering the manufacture of composite materials has generally been evolved from those used in the aircraft and marine industries. The manufacturing process, the intrinsic lightweight and the tailorability of composites have enabled the integration of form and function to be used to install large and unsupported systems. Furthermore, given time for the public acceptance of these changed structural forms and for a greater knowledge of the long term properties of the composite material it can be expected that these forms will be more extensively utilised into the 21st century. Composite structural systems, up to the present, have generally been designed by a consideration of the pristine mechanical and short term in-service properties

of the material and in some cases the performance of accelerated tests to provide long term durability estimates. The introduction of new structural systems involving new materials generally takes from 20 to 40 years to be completely accepted. Thus the 'all composite' systems produced to date have, in the main, tended to be single prestigious structures; one exception to this statement is the FRP composite bridge deck, this structural system is treated separately in Section 5. One building and one bridge structure will be given as illustrative examples of the 'all composites' technique. These structures have been chosen as both are more than 10 years old, but show little or no sign of deterioration and, in addition, are given as an illustrative example of the '*building block*' technique, which is an ideal system to be used to form 'all FRP composite' structures.

Figure 1. GFRP Composite Class Room System – 1974 conceived by Lancashire County Council UK.

Figure 2. Opening ceremony of the Bonds Mill Lift-bridge. Gloucestershire UK – May 1994 (by kind permission of FaberMaunsell, London).

2.1 *Building*

The Lancashire GFRP Class Room System, UK, 1974 (Figure 1) [this comes under the new material adaptive concept category]. This is one of the first, and is an excellent example of an 'all FRP composite' structure using identical lightweight '*building blocks*', manufactured from randomly orientated glass fibre in a polyester resin. The whole structure was then fabricated by bolting these units together; a watertight seal was placed between the units using a preparatory sealing compound. At the time of construction, the material was estimated to have durability advantages, but these were based upon relatively short-term tests and a possible lack of understanding of the causes of degradation. One disadvantage of this type of construction is its 'futuristic' architecture, which the general public, at present, may not be prepared to accept.

2.2 *Bridges*

Bonds Mill Bridge, UK, 1995 (Figure 2) [this system falls into the substitution category]. The bridge was manufactured from ten identical pultruded Maunsell Planks [*building blocks*] to form a box cell beam (ACCS-FRP elements forming the walls of the box beam). The planks were bonded together and special dog-bone units held the planks during adhesive curing. At the time of manufacture, this 9 metre span bridge attracted considerable interest, but in-spite of this, the structural concept has not progressed to any significant degree in the UK, but is being used more frequently in the USA. The continuing monitoring, at Bonds Mill Bridge, of the material to observe any degradation will be of scientific value.

The strengths of the '*building block*' systems lie in (a) the construction of identical units and therefore an utilisation of a production line. (b) The controlled mechanised/manual factory manufacture and fabrication of identical structural units. The transportation to site of the lightweight units presents no particular problem.

The limitations of the '*building block*' system (a) due to the layered and fibre dominated structure of the FRP composite its most efficient use is under in-plane stress which indicates a structural form of membrane or thin shell construction. However, most structures are required to take some moment and for the building block systems this would require a finite analysis and design approach, which does not lend itself to design code approaches. (b) The limited information available on the long term mechanical and physical properties of the FRP and adhesive joining materials of the components. Clearly, the durability of the material for civil engineering applications is equally important as that of the intrinsic strength and mechanical performance of the structure. One problem with these structural systems exposed to the natural environment is the ingress of moisture into a closed hollow section; this situation might not become apparent for a number of years after construction. Reducing the permeability of the composite will alleviate this problem, to a degree;

a possible method to enable the permeability of the material to be improved is given in Section 8.

3 EXTERNAL REINFORCEMENT TO CONCRETE AND STEEL STRUCTURES

3.1 *FRP plate bonding*

There is no doubt that during the last two decades the use of fibre-reinforced polymer (FRP) composite materials for external strengthening of civil engineering structures has emerged as one of the most promising techniques in materials and structural engineering. However, some mechanical properties such as the creep and fatigue of the FRP composite material, the long term behaviour of the adhesive and in-service properties such as durability and fire performance of the FRP composite, etc. require further investigative work.

The FRP material used for composite plate bonding to upgrade RC beams is generally fabricated by one of three methods, namely (a) the pultrusion technique (a pre-cast FRP plate), (b) the prepreg method (either a FRP pre-cast plate or a FRP system fabricated in place) and (c) the resin infusion method (a system fabricated in place). Currently, the preferred method is pultrusion and this implies that, (i) the material cannot be reformed and that (ii) a two-part epoxy adhesive for joining is most likely used. In applying external reinforcement to beam members, the effectiveness of the strengthening scheme is highly dependent upon the bond between the composite and the concrete member and the condition of the cover concrete. There are three major areas, which are currently receiving particular attention, these are (i) the long term bonding characteristics of the adhesive, (ii) the durability of the composite plate, and (iii) the effectiveness of the strengthening scheme when the plate is bonded on to a curved soffit formed under bending forces. Currently, items (i) and (ii) are the major concerns for the civil engineer.

To date, advanced polymer composite materials have been used to upgrade a relatively small number of steel structures compared to those of RC. Furthermore, only a limited amount of research has been conducted on the application of these materials to steel structures, (Mosallam & Chakrabarti 1997, Liu *et al*. 2001, Tavakkolizadeh & Saadatmanesh 2003 and Photiou *et al*. 2004a). Nevertheless, the tensile strength and modulus of elasticity of the ultra-high modulus carbon fibre/polymer (UHM-CFRP) or the high modulus carbon fibre/polymer (HM-CFRP) composites make them ideal potential candidates for upgrading steel structures but it is necessary to appreciate the possible restrictions of both their mechanical characteristics, (namely, the very low ultimate strain value of the UHM-CFRP, approximately 0.4% strain and the limited stiffness of the HM-CFRP compared with steel). Consequently, the mechanical properties of the carbon fibre used in the composite must be chosen carefully. Another potential problem using CFRP composites is the large differential coefficient of thermal expansion between the steel and the FRP composite when in a situation of temperature fluctuations.

The strengths of these rehabilitation systems for concrete, steel, timber and masonry structural members are associated with the favourable intrinsic properties possessed by the CFRP material such as, high specific strength, good corrosion resistance and magnetic neutrality, and they have proved advantageous over other upgrading materials. In addition, the advantage of prepreg materials, with a compatible film adhesive system for metallic and timber structures, over that of the precast plate with a two part adhesive system, lies in the site fabrication of the composite and the adhesive system, Photiou *et al*. (2004b). The curing procedure for this operation would invariably be undertaken at a slightly raised temperature above ambient and would allow the two resin components to surface mix, introducing a greater degree of molecular interlocking.

The limitations of a well-designed FRP plate bonding system to RC beams are a lack of long-term knowledge of the load carrying characteristics, and the long-term durability characteristics of the composite material and of the adhesion between the two dissimilar adherends. Furthermore, in the case of upgrading metallic systems there is very limited understanding of the consequence of the two vastly different coefficients of thermal expansion of the two adherends. Arguably, the area where there is the greatest dearth of well-documented data for FRP composite is associated with the durability, the ingress of moisture and salt solutions in regions of adverse environmental conditions. A discussion of a potential method of improving the barrier properties of composites is given in Section 8.

3.2 *Near surface mounted (NSM) FRP rods*

The introduction and utilisation of NSM rods is a valid alternative to the externally bonded FRP plates. It is used for the strengthening of deficit reinforced concrete or timber members and masonry walls. The application does not require the preparation of the concrete surface.

Whereas the composite material for strengthening concrete members is generally CFRP, the material used for timber and masonry is GFRP. NSM rods have also been use for structural repairing of masonry structures, Tinazzi *et al*. (2000) and DeLorenzis *et al*. (2000). Installations of FRP rods have been undertaken for the repair of historical monuments, La Tegola *et al*. (2000) and IMTCR (2004).

The strengths of these systems lie in (i) the fact that the rods are protected from the external environments;

they are completely surrounded in adhesive paste, (ii) the ease and speed of erection of the FRP rods due to their lightweight properties, (iii) the optimisation of the grooving process, and (iv) the bonding characteristics of the FRP rods. This implies that, in item (i), the alkaline and other salts in the cements do not influence the paste. If this is so, the rods will not be susceptible to chlorides or carbonation initiated corrosion in a concrete environment.

The limitations of the NSM FRP rods are that they are susceptible to failure by de-bonding, particularly when the grooves are cut into, say, the soffit of a *concrete* beam. Therefore, before this technique can be used with complete confidence, further investigative work is required to be undertaken on the end bond behaviour of NSM reinforcement, particularly, the development of anchorage lengths, the groove width-to-depth ratio and the possible use of FRP laminates to confine the NSM joint to increase its bond strength and ductility. Of vital importance is the understanding of the interaction between flexural/shear cracking and bond stresses. Research work is required to determine the most relevant geometrical shape of the FRP rod. Currently, little work has been undertaken on the dynamic behaviour or on the thermal and durability characterisations of such structural systems. The majority of the limitations mentioned above are issues that can only be addressed after significant testing and research has been undertaken into this technique. The real limitation of the system is associated with the long-term understanding of the adhesive properties of the bonding paste and degradation of the FRP rods from moisture ingress and alkaline attack.

3.3 *Seismic retrofit of RC structures*

FRP composite wraps are used for seismic retrofit purposes. The composite material can be applied to the columns in the form of a prepreg or by dry fibres, which are then impregnated with a resin. This technique is also used to repair reinforced concrete columns where steel corrosion has taken place. For protection of the polymerised composite material, an appropriate post fabrication surface treatment is invariably applied by painting or rendering.

The strengths and limitations are basically similar to those discussed for the external plate bonding techniques.

4 FRP COMPOSITE REBARS USED AS INTERNAL REINFORCEMENT TO CONCRETE

The mechanical properties of the anisotropic FRP rebars are considerably more difficult to obtain than those of the isotropic steel rebar. The strength and stiffness of FRP rebars are dependent upon (a) the fibre volume fraction, (b) the method of manufacture (including curing process and quality control) and (c) the sectional area, (the loading across the section of the rebar is not uniform due to shear lag effects, the larger the cross sectional area the greater will be this effect, indeed reductions in strength up to 40% for diameter increases of 9.5 to 20 mm have been reported (Faza & GangaRao 1993). Thus, the tensile strength and stiffness must be determined by experiment for every type and diameter of rebar used.

There are various different types of FRP rebars, all with their specific properties, some of the common ones are (i) ribbed bars manufactured by a 'hybrid-pultrusion' process, a combination of pultrusion and compression moulding, (ii) sand-blasted bars manufactured by the pultrusion process and then sand blasted to enhance the bond characteristics, and (iii) spirally wound and sand coated bars are manufactured by the pultrusion process, the surface of the bars are then spirally wound with a fibre tow and sand covered.

The strengths of FRP rebars lie in the fact that they do not corrode and are not susceptible to chloride or carbonation initiated corrosion in a concrete environment. A constant improvement of component parts of the rebar is continuously being undertaken. Saint-Gobain Vetrox (Almenara & Thornburrow 2004) has recently developed a glass fibre to resist alkali attack.

The limitations lie in the fact that the rebars are prone to deteriorate due to other degradation mechanisms. The concrete pore solution is a potential durability threat to GFRP reinforcement. Glass fibres in particular are susceptible to the high alkaline environment in the pore solution and in concrete the concentration has a pH value of 13–14. To overcome these limitations, the fibre and the fibre/matrix interface must be well protected by the matrix material to prevent rapid degradation; however, polymers are known to be susceptible to alkali ingress and attack. Although carbon fibres used in rebars are generally considered to be inert to the salt solutions associated with cements, the same situation regarding alkali ingress into the polymer and thence to the interface between the composite and concrete still exists. This is a further case where the barrier properties of the resin must be improved; this problem will be discussed in Section 8.

5 REPLACEMENT OF NEW BRIDGE DECK SYSTEMS

Composite bridge deck systems are made in different shapes and forms. Most decks are preparatory products that are manufactured from glass fibre and vinyl-ester polymer. They are made with either full depth sections to conveniently match the typical existing concrete bridge decks or partial depth section.

The strengths of the FRP deck panel system is its ability to, (i) be rapidly deployed and installed on site and (ii) reduce congestion in the work zone and to improve safety. The Federal Highway Administration (FHWA) of the USA is aiming to increase the use of FRP composite deck applications and is working with the AASHTO Technical Committee to develop guide specifications for testing and acceptance of the deck systems.

The limitations to the use of FRP composites for deck replacement are (i) the design of an FRP deck system is complicated and it requires to be undertaken using a finite element analysis. (ii) Its lightweight superstructure could become aerodynamically unstable especially for long span structures. As in any new innovation and considering the anisotropy of the material, the composite components and system requires validation testing to enable a database for each specific system. As stated earlier in reviewing other applications the problem of durability and ingress of moisture into the composite is possible, particularly during the winter months in the northern hemisphere when the bridge surface is treated with salt solution.

6 MISCELLANEOUS

There are numerous examples that could be cited under this heading; two specific examples will be given here.

Transmission towers. These systems can be fabricated using specially designed interlocking pultruded structural elements and are providing immense advantages over metallic incumbent structures due to increased durability and ease of installation especially in areas which are difficult to access.

Membrane structures. The structures, which have been illustrated in this paper thus far are composed, generally, of layers of multi-directional fibres embedded in a bonding matrix. This assembly leads to a composite system that, in-plane, is strong and stiff along the fibre orientations but is weak through-the-thickness where the structural behaviour is dominated by the polymer matrix. It is realised, therefore, that the most efficient use of composites are under global in-plane stress situations, such as cable-nets, membranes and thin shells. Burgueño & Wu (2004) have introduced a FRP composite membrane beam bridge system made from a FRP membrane working compositely with a reinforced concrete deck as a beam-slab bridge. Their system is an optimised hyperbolic paraboloid as the surface can be generated by straight-line segments, which permits principal stress directions to be closely aligned with the principal curvature for efficient use of the FRP reinforcement.

These future structures will require the development of efficient FRP structural forms, optimisation techniques and will challenge engineering intuition.

The strengths lie in the inventiveness of such systems leading to the efficient use of the FRP material. The imaginative uses of the FRP material must lead to its greater utilisation.

The limitations of new systems as discussed above are, the long-term durability and structural characteristics of the material, the joining techniques and the time required for acceptance of such techniques. The cable net and membrane systems would be relatively thin and will be particularly sensitive to aggressive environments.

7 METHOD TO ENHANCE THE DURABILITY OF CIVIL FRP COMPOSITE MATERIALS AGAINST INGRESS OF MOISTURE/ AQUEOUS SOLUTIONS AND FIRE

The various civil engineering structural examples illustrated in this paper have all shown that one of the major concerns with the use of polymer/fibre composites in the civil engineering environments are associated with the durability and the long-term characteristics of the FRP material. Durability from a civil engineering point of view may be divided into five groups:

- Moisture and aqueous solutions
- Alkaline environment
- Fire
- Thermal effects
- Ultra-violet radiation.

The long term loading conditions in which the material may have to function are

- Fatigue
- Creep.

The composite systems used in construction have shown that polymers can be engineered to provide resistance against moisture and aqueous solutions diffusing into them; however, moisture eventually will diffuse into all organic polymers leading to changes in mechanical and chemical characteristics. The primary effect of diffusion is through hydrolysis and plasticisation. This process may cause reversible and irreversible changes to a polymer. The characteristic of the polymer, which may occur, is a lowering of the T_g value and in a composite to cause deleterious effects to the fibre/matrix interface bond resulting in a loss of integrity. Possible solutions for the reduction of diffusion through the polymer are to:

(i) apply a protective coating/gel coat on to the system.
(ii) cure the product at an elevated temperature.
(iii) factory fabrication under controlled conditions, such as the pultrusion; these composites are manufactured at temperatures of 120°C–140°C. This

ensures low void content, full cure, high levels of overall integrity, a high glass transition temperature and greater resistance to moisture degradation compared with the cold curing polymers. Another effective method of enhancing durability of composites is through the use of appropriate sizing/finishes on the fibres.

A potential technique for enhancing the resistance of ingress of moisture and aqueous solutions is by the addition of nanoparticles into the polymer.

The following section will discuss the technique of introducing clay nanoparticles into a polymer. Clay nanocomposite materials are a new and developing area of nanotechnology that have the potential to offer many wide-ranging benefits to current matrix polymers. The ability of nanocomposites to increase the service life of materials subjected to aggressive environments could be utilised to increase the durability of glass and carbon fibre composites. The system has the potential for lowering the permeability and thus providing a barrier property to polymers to reduce the ingress of moisture and salt solutions into them and to improve the mechanical strengths and fire resistance of the polymer. These advantages would allow the use of composite materials in situations where their performance under aggressive environments is currently thought to be inadequate for the in-service conditions and to be used with more confidence in their long-term durability. The section will concentrate upon the first three environmental conditions mentioned above that cause FRP materials to degrade with time.

8 THE NANOCOMPOSITE MATERIALS

8.1 *Introduction*

Chemically treated layered silicates (clays) can be combined with polymer matrix materials to form a nanocomposite in which clay layers are evenly dispersed through the material. Research has shown that these high aspect ratio clays alter the properties of the composite by a number of mechanisms, to increase the strength and fire resistance and reduce permeability. A brief description of nanocomposite materials will be given to illustrate a future possible development for improved mechanical and in-service properties for composite systems in construction.

A nanocomposite can be formed from a combination of two or more materials, as with normal composites; however, one of the components has nanoscale dimensions. This allows the nanoparticles to bond and interact with the other constituent materials on a nanoscale. In this range the interaction between atoms and molecules occurs and from which all the observable material properties are derived. Therefore, being able to influence bonding and structure on this level will enable the properties of a material to be significantly altered. There are many nanoparticles that are being used in the nanocomposite field; however, the one that has the potential to improve the durability aspects highlighted is the polymer-layered silicate nanocomposite (PLSN).

8.2 *Clay type and structure*

Smectite clays are the most common form of nanoparticles used to produce nanocomposites. These clays are ideal for use as nanoparticles in nanocomposite materials due to:

- High strength and stiffness along their length, reported to be higher than glass fibres (Luo & Daniel 2003).
- High aspect ratios enable large surface areas (700 m^2/g) to be in contact and bond with the polymer.
- Can be modified more easily than most other types of clay, this high level of intercalation chemistry enables the clays to be chemically altered to aid their bonding and dispersion in the polymer.
- Are naturally occurring and can be purified at a relatively low cost.

Smectite clays naturally form layers of oxide sheets that only have weak van der Waals forces holding the layers together. These sheets are around 1 nm thick and vary from 20 nm to 2000 nm in length and width, depending on the type of smectite clay. Montmorillonite, the most widely used particle is typically about 250 nm in length and width, resulting in massive surface areas of 700 m^2/g. These large surface areas make them exceptional at altering the properties of a composite.

Between the layers is a gap known as the gallery layer, shown in Figure 3, unmodified clays will have a small gallery layer of around 1.2 nm. This spacing changes when used in nanocomposites, the way in which this gap changes varies the properties of the resulting nanocomposite.

8.3 *Chemical modification*

The clays are naturally hydrophilic and are immiscible in organic liquids; therefore, the clay must be altered

Figure 3. Structural representation of smectite clay layers.

to become organophilic, this modification is known as compatibilisation.

The most common compatibilisation process is onium-ion modification; a small hydrocarbon chain, known as a surfactant, is bonded to the surface of the clay layer (Figure 4). One end of the chain contains an ammonium functional group that bonds to the clay layer (Figure 4, End A); the other end has the required polarity to allow the clay and surfactant as a whole to be organophilic enough to mix with organic liquids (Figure 4, End B).

The type of surfactant applied to the clay layer will have a significant effect on the compatibility of the clay and polymer. After modification the clay gallery layer will have increased in size to accommodate the hydrocarbon chain, typically to 1.5–3.5 nm, depending upon surfactant type.

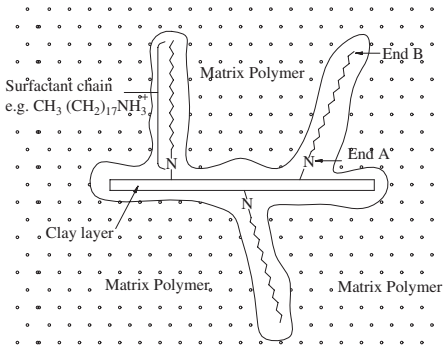

Figure 4. Modification of clay layers.

8.4 *Types of PLSN*

The way in which the clay layers are dispersed in the polymer will influence the level of interaction between the clay layers and the polymer, affecting the resulting properties. There are three distinct types of material that can be formed by the introduction of these clay layers into the matrix, clay filled composites, intercalated and exfoliated nanocomposites.

8.4.1 *Clay filled (conventional) composites*

In clay filled composites the clay acts only as inert filler, this is achieved if the clay has not undergone any compatibilisation treatment. The clay layers and polymer are not compatible so no polymer will penetrate the gallery layer (Figure 5). There will be no, or very little bonding between the clay and the polymer; therefore, the clay will provide little reinforcement. This type of composite is often used as a cheap way to fill out a polymer. As the clay has not undergone any treatment, it is an extremely cheap and effective filler, but offers no increase in durability.

8.4.2 *Intercalated nanocomposites*

An intercalated nanocomposite is formed when the clay layers are separated by a fixed amount (Figure 5). Only a small quantity of polymer molecules will enter this increased size gallery layer, causing a degree of interfacial bonding between the polymer and the clay layers. The clay layers will act as reinforcement for the polymer, although the fixed layer separation is unable to provide the maximum reinforcement. The distance between the clay layers will depend on the length of the surfactant; these types of nanocomposite are produced by quaternary and tertiary alkylammonium surfactants. These surfactants provide no acidity to catalyse the curing reaction, causing the cure rates between the

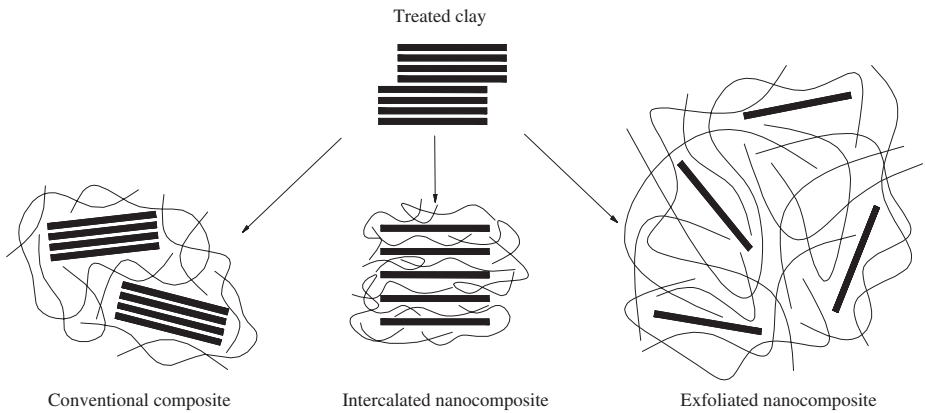

Figure 5. Types of PLSN.

clay layers and outside the clay layers in the bulk of the material to cure at the same speed. The resulting clay morphology is, therefore, unchanged from that after mixing, having a small amount of polymer penetrated between the clay layers.

8.4.3 *Exfoliated nanocomposites*

An exfoliated nanocomposite is formed when the clay layers are dispersed in the polymer with random separation and orientation (Figure 5). The distance between clay layers will depend on the clay loading, the higher the proportion of clay in the nanocomposite the closer the clay layers will be to each other. The clay layers will be sufficiently separated and randomly orientated to allow full interfacial bonding and to contribute all of their strength to improve the properties of the nanocomposite. These types of nanocomposites are produced with primary and secondary alkylammonium ion surfactants. They are slightly acidic and catalyse the curing reaction between the clay layers; therefore, curing occurs faster in the clay galleries than outside in the bulk of the material. This causes the clay layers to separate as cross-linking occurs and more resin components enter the clay galleries.

The effect that conventional, intercalated and exfoliated clay additives have on the tensile strength of a nanocomposite has been investigated by Wang *et al*. (2000). At 10 wt.% clay loading they reported increases of 350%, and 150% for exfoliated and intercalated nanocomposites respectively manufactured from an elastomeric epoxy polymer.

8.5 *Property improvements*

The property improvements generated by the inclusion of nanoparticles in a polymer have been well researched. The majority of polymers have all been used to construct nanocomposites and all have shown improvements in a few or many different areas. Recent global research has focussed on the use of thermoplastic resins as these types of nanocomposites are commercially viable for small-scale products such as food packaging etc. However, many thermosets have also been used; epoxy resins typically used are amine cured Bisphenol A and F resins.

8.5.1 *Mechanical properties*

Epoxy nanocomposites have been tested by researchers and it has been shown that extensive mechanical property improvements can be achieved with sub-ambient T_g (elastomeric) polymers and modest improvements in high T_g (glassy) polymers. Increases in tensile strengths and moduli of elasticity of 183% and 87% respectively with a 5 wt% addition of clay, a 466% and 250% increase respectively with 15 wt% addition of clay in Jeffamine D-2000 cured EPON 828 elastomeric polymer (Wang *et al*. 2000). However, in a civil engineering type glassy epoxy polymer the property increases would be less dramatic. Increases in flexural strength and moduli of 25%, 22% and 23% at a clay loading of 10 wt% have been reported (Becker *et al*. 2002) for diethyltoluenediamine cured DGEBA, TGAP and TGDDM epoxy resins respectively.

8.5.2 *Barrier property improvements*

The reduction in permeability that can be attained from the exfoliation of nanoparticles into polymers depends on the agent that is being investigated; the improvements recorded range from three fold to zero. The permeability reduction achieved also depends upon the specific aspect ratio of the clay being used. High aspect ratio clays have a higher surface area and therefore reduce the permeability by a larger amount than lower aspect ratio clays.

A (Montmorillonite) nanocomposite with an aspect ratio of 250 would be expected to achieve a reduction in permeability of one half compared to the pristine polymer. However, this reduction in permeability is also a function of the clay loading that is applied to the nanocomposite, the higher the clay content the greater the improvement.

Improvements in barrier properties have been reported by Beall (2000), of 400%, 240% and 144% compared to the pristine polymer for water vapour transmission rates for various different modified clay types with the same clay loading in HDPE nanocomposites.

The mechanism responsible for the improved barrier resistance can be described by a number of different models. The traditional model, Neilson (1967), used to describe the improved barrier resistance is one of increased path length through the composite that must be taken to negotiate around the clay layers. The torturous path that an ingressing agent must take can be made longer or shorter depending upon the clay loading applied to a nanocomposite. However, this model cannot totally explain the resulting reduction in permeability when nanoparticles are incorporated into composites. Beall (2000) introduced a model which assumes a number of regions in and around the clay layers, illustrated in Figure 6, that have undergone a change in permeability due to the inclusion of nanoparticles.

The clay layer has an extremely low permeability and for all practical purposes can be assumed to be impermeable, this region being the same size as the clay platelet. The first region is about 1–2 nm around the clay layer in each direction that contains the alkylammonium ions. These hydrocarbon chains and the effects of the bonding between the polymer and the surfactant chains result in the areas around the clay layers having a different permeability from either the clay layer or the pure polymer. The second region extends from the edge of the first region to approximately

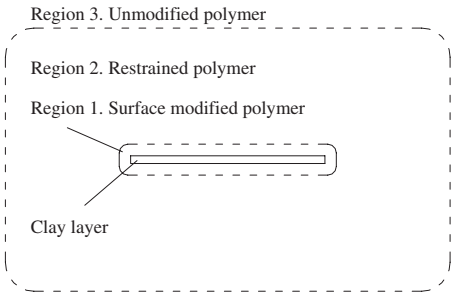

Figure 6. Regions in the conceptual model.

50–100 nm away from the surface. In this region the polymer is altered due to the bonding between the polymer and the surfactant; this interaction alters the permeability of the polymer in this region. The size and permeability of this region will depend on many different factors, such as the type of polymer, surfactant type and the bonding between the two. The third region extends beyond the edge of the second region and is that of the unmodified polymer, the properties of which are those of the pure polymer. The overall permeability of the model depends on the relative permeability of these two modified polymer regions, the clay layer and the unmodified polymer.

8.5.3 *Fire property improvements*

Composites are organic materials, they are composed of mainly carbon and hydrogen atoms, and therefore, they do not have a good resistance to fire. A considerable amount of research has been conducted into the fire properties of nanocomposites, the majority of which concentrates on the properties of heat distortion temperature (HDT, also known as heat deflection temperature), peak and mean heat release rate (HRR) and mass loss rate (MLR). Comprehensive research into the fire properties of a variety of different polymer nanocomposites has been conducted by Gilman and published in various papers (Gilman *et al*. 2000). It was found that the additions of nanoparticles to all polymers tested, resulted in large reductions in peak and mean HRR and mean MLR. However, the specific heat of combustion for some of the nanocomposites was decreased by a small amount. These increases in fire performance have been tested under laboratory conditions and using low temperature sources. In a real fire situation the benefits of the PLSN would be to form a protective network of char around the non-burnt polymer. However, this advantage would only be seen in thick sections in which an outer layer will be burnt and form a protective layer for the remaining polymer. In thin laminates, too much of the component cross section will be lost in the creation of this char protective network to sustain any of the structural properties of the original component.

8.5.4 *Fibre reinforced polymer composites*

The majority of research work undertaken to date relating to nanocomposites has been mainly associated with pure polymers, but investigations are now being extended to fibre/matrix composites. Some work has been carried out into glass/epoxy nanocomposites (Haque *et al*. 2003). This work shows some interesting property improvements such as a 24%, 14% and 44% increase in flexural strength, flexural modulus and interlaminar shear strength respectively with 1wt% clay loading.

9 CIVIL ENGINEERING ASPECTS OF NANOCOMPOSITES

From the results of previous research workers it is clear that the addition of nanoparticles to resin formulations can alter many properties of the polymer; however, a wide range of different curing agents (epoxy resins are commonly basic DGEBA or DGEBF), clay types and surfactant types has resulted in a huge amount of different combinations that are used to produce nanocomposites. All these different types of nanocomposites result in different property enhancements or alter the magnitude of similar property enhancements. This makes it difficult to assess which property improvements are universal for epoxy nanocomposites or whether the property enhancements will vary greatly between formulations.

It is necessary to confirm, (i) which resins offer the best compatibility for exfoliation of nanoparticles into polymers, and to identify if any currently used civil engineering resins will achieve this, (ii) which properties can be enhanced via the inclusion of nanoscale layered fillers and the extent to which these increases are achieved into the resins established in (i), (iii) whether the production of nanocomposite materials is feasible in the civil engineering field at its present state, or whether further advancements need to be made, and (iv) the situations where these materials may be of an advantage and offer a higher performing matrix polymer, whether this be an on site wet lay-up process, a factory processed pultrusion or a filament winding technique.

The civil engineering industry has specific requirements when forming polymer composites for site utilisation. The polymers that are used are generally standard ones with specified additives incorporated into them; these additives may cause problems when attempting to exfoliate nanoparticles into them. Polymer composites and adhesives that are fabricated on site must be polymerised at ambient temperatures or at a slightly elevated temperature and ideally they

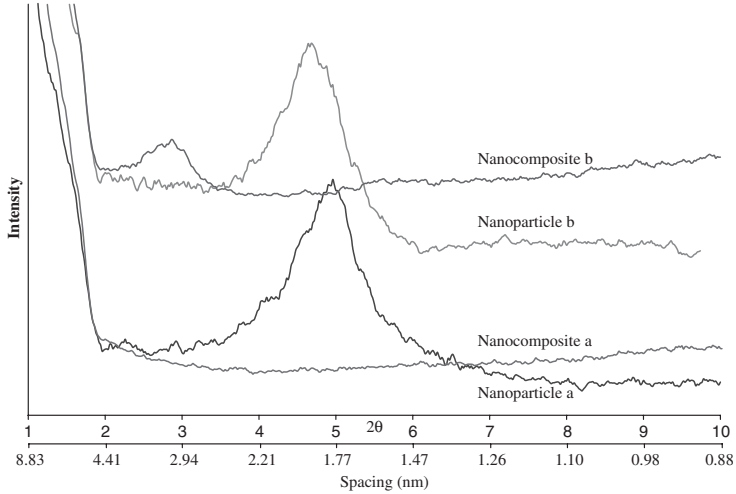

Figure 7. X-ray diffractographs for Ethacure 100 cured DER331 nanocomposites.

should be polymerised within minimum time, these low temperatures may not be suitable for exfoliating nanoparticles; there is of course no such limitations when producing pre-cast units made in the factory, allowing for higher temperature and longer curing cycles to be used where the exfoliation of nanoparticles could be achieved. Therefore, the manufacture of nanocomposite parts by pultrusion is most likely to be used first due to the controlled process required for exfoliation. However, as the technology becomes better understood their use can be transferred to prepreg and on site lay-up techniques.

10 RESEARCH AT THE UNIVERSITY OF SURREY

At the University of Surrey research investigations are currently concentrating on confirming the exfoliability of these layered silicates, this is being undertaken by using a number of (i) different resin systems, (ii) different surfactants and (iii) different loadings of the treated clay particles. The resin systems are, (i) a room temperature curing civil engineering laminating resin, made and possibly modified by the resin supplier to provide additional in-service properties; Exchem Mining and Construction, Selfix Carbofibre Laminating resin, (ii) a high temperature curing imidazole accelerated system that has a long work life is being used to create intercalated nanocomposites, (iii) a system that has been used in a number of published papers, DER 331 and Ethacure 100 (diethyltoluenediamine), and found to produce exfoliated nanocomposites is being used to directly test the claims made in these papers, and (iv) a system, Polypox E403 cured with Polypox H205, which is similar to a Jeffamine D230 cured DGEBA system used in a number of published papers.

In all cases the nanoparticles are required to be well mixed and dispersed in the resin and thus the time of mixing and the temperature of cure are two important parameters to be considered. Three stages of analysing the nanocomposite are being utilised to determine the degree of exfoliation, (i) X-ray diffraction, (ii) optical microscopy, and (iii) electron microscopy.

An example of typical intercalated and exfoliated X-ray diffractographs produced from Ethacure 100 cured DER331 containing 5 wt% nanoparticles are shown in Figure 7, compared to the original diffractograph for the pure nanoparticles used in each case. The nanoparticles used are, (a) a primary alkylammonium ion (octadecyl-ammonium), and (b) a quaternary alkylammonium ion (octadecylbenzyldimethyl-ammonium). Both nanoparticles (lines 'Nanoparticle a' and 'Nanoparticle b') have large peaks indicating a consistent spacing between the clay layers throughout the sample. 'Nanocomposite a' shows no peak, indicating that the consistent spacing has been lost and the clay layers have random spacing. 'Nanocomposite b' shows a peak at 3 2θ (around 2.9 nm), indicating an intercalated specimen with a consistent spacing of clay layers at this distance.

Electron microscopy also can provide a great amount of information about the morphology of a nanocomposite. Figure 8 shows an electron micrograph of a nanoparticle before being incorporated into a polymer; Figure 9 shows a typical electron

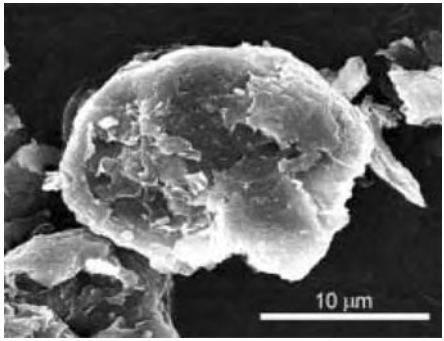

Figure 8. SEM micrograph of pure nanoparticles.

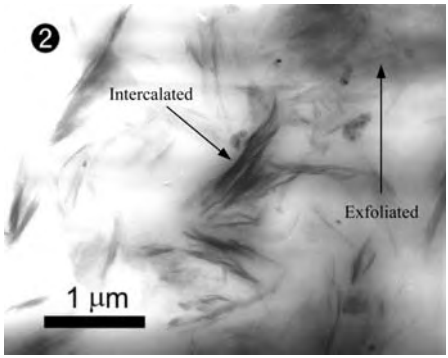

Figure 9. TEM micrograph showing intercalated/exfoliated clay layers. (Figures 8 & 9 reprinted from *Experimental Mechanics* with the permission of the Society for Experimental Mechanics, Inc., 7 School Street, Bethel, CT 06801, (203) 790-6373, www.sem.org.)

micrograph of a nanocomposite with areas of intercalation and exfoliation. These different areas are distinguishable by the darker areas with clear layer stacking in the intercalated areas and the randomly orientated low clay concentration lighter exfoliated areas.

11 INFLUENCES ON FUTURE DEVELOPMENTS OF FRP COMPOSITES

When nanocomposites have been successfully manufactured on a commercial scale for use in the civil engineering industry, the effect on the utilisation of composites in construction will be great. Although improved mechanical properties (i.e. modulus of elasticity and strength) of the polymer can be achieved, this improvement will not have a great influence on the overall strength of, for instance, CFRP. However, the advantage in the utilisation of nanocomposites in civil engineering will be:

- The improvement in the interlaminar shear strength, Haque & Shamsuzzoha (2003), have shown that for a 1 wt.% addition of nanoparticles to S2 glass/epoxy composite there is a 44.07% increase in the interlaminar shear strength over the conventional S2 glass/epoxy composite. It should be mentioned that improvement are very sensitive to the weight percent loading of the nanoparticle as the inclusion of a 2 wt.% addition to the composite will reduce this advantage by 50%.
- The improvement in the shear failure of adhesives, this will be particularly relevant to the rehabilitation of structural members.
- The barrier property improvement of composites and polymers in the construction industry. Although nanoparticles in composites will reduce the permeability of the pristine polymer and thereby improve the boundary properties, in some cases, eventually the ingress of solutions will penetrate the FRP composites. It will be realised, however, that all man-made materials do have a finite life and FRP polymer composites are no exception but the improvements that can be made by the addition of nanoparticles to these civil engineering composites will improve and extend their performance considerably.

REFERENCES

Almenara, P.C. & Thornburrow, P. (2004), A New Glass Fibre Reinforcement for Anti-corrosion Composites, in *Conference Proceedings 'Advanced Polymer Composites for Structural Applications in Construction – ACIC 2004', Ed. Hollaway, L.C., Chryssanthopoulos, M.K. & Moy, S.S.J.,* Pub. Woodhead Publishing Ltd. Oxford. pp 319–326.

Beall, G.W. (2000), 'New Conceptual Model for Interpreting Nanocomposite Behaviour', in Polymer-Clay Nanocomposites', Eds Pinnavaia, T.J. and Beall, G.W., Wiley & Sons Ltd 2000, pp 267–279.

Becker, O., Varley, R. & Simon, G. (2002), Morphology, Thermal Relaxations and Mechanical Properties of Layered Silicate Nanocomposites Based Upon High-Functionality Epoxy Resins, in *'Polymer', V.43*, Elsevier, pp 4365–4373.

Burgueño, R. & Wu, J. (2004), Membrane-based Structural Forms for FRP Bridge Systems *in Conference Proceedings 4th International Conference on Advanced Composite Materials in Bridges and Structures*, 20–23 July 2004.

Daniel, I., Miyagawa, H., Gdoutos, E. & Luo, J. (2003), Processing and Characterization of Epoxy/Clay Nanocomposites, in *'Experimental Mechanics', V.43 N.3, Society for Experimental Mechanics*, pp 348–354.

De Lorenzis, L.D., Tinazzi, A. & Nanni, A. (2000), Near Surface Mounted FRP Rods for Masonry Strengthening: Bond and Flexural Testing, *Symposium, Meccanica*

delle Strutture in Muratura Rinforzate con FRP Materials Ed. Ceriolo, L., Venezia, Italy, Dec. 7–8, 2000, pp 7–18.

Faza, S.S. & GangaRao, H.V.S. (1993), Glass FRP Reinforcing Bars for Concrete, in '*Fiber-Reinforced Plastic (FRP) Reinforcement for Concrete Structures: Properties and Applications', V. 42* A. Nanni, Ed. Elsevier, Amsterdam., pp 176–188.

Gilman, J.W., Kashiwagi, T., Morgan, A., Harris, R., Brassell, L., Van Landingham, M. & Jackson, C. (2000), Flammability of Polymer Clay Nanocomposites Consortium: Year One Annual Report, *National Institute of Standards and Technology, U.S. Department of Commerce*.

Goldsworthy, W.B. & Heil, C. (1998),Composite Structures are a Snap, *in 2nd international Conference on Composites in Infrastructure, Vol.2 Tucson, AZ*. 1998, pp 382–396.

Haque, A. & Shamsuzzoha, M. (2003), S2-Glass/Epoxy polymer Nanocomposites: manufacturing, structures, thermal and mechanical properties, *Journal of Composite materials*, Vol.37, No 20 pp 1821–1837. IMTCR 2004 Lecce 7–9 June 2004 Italy.

La Tegola, A., De Lorenzis, L. & Micelli, F. (2000), Confina mento di Pilastri in Muratura Mediante Barre e Nastri *In FRP, {poc. Symposium, Meccanica delle Strutture in Muratura Rinforzate con FRP Materials, Ed. Cerolo, L. Venezia, Italy*, Dec. 7–8, 2000, pp 41–52.

Liu X., Silva P.R. & Nanni, A. (2001), Rehabilitation of steel bridge members with FRP composite materials. In J. Figueiras, L. Juvandes and R. Furia. (Eds) *Proc. CCC, Composites in Construction – 2001*.

Luo, J. & Daniel, I. (2003), Characterization and Modelling of Mechanical Behaviour of Polymer/Clay Nanocomposites, in *Composites Science and Technology*, V.63, Elsevier, pp 1607–1616.

Mosallam, A.S. & Chakrabarti, P.R. (1997), 'Making connection', *Civil Engineering, ASCE*, pp 56–59.

Neilson, L.E. (1967), in *Journal of Macromolecular Science, A1(5)*, pp 929–942.

Photiou, N.K., Hollaway, L.C. & Chryssanthopoulos, M.K. (2004a), Strengthening of an Artificially Degraded Steel Beam Utilising a Carbon/Glass Composite System. In Hollaway, L.C., Chryssanthopoulos, M.K. & Moy, S.S.J (Eds), *Proc of the Conference Advanced Polymer Composites for Structural Applications in Construction – ACIC 2004*, Woodhead Publishing.

Photiou, N.K., Hollaway, L.C. & Chryssanthopoulos, M.K. (2004b), Selection of CFRP systems for Steelwork Upgrading. In Antonio La Tegola & Antonio Nanni (Eds), *Proc. of the Conference Innovative Materials and Technologies for Construction and Restoration (IMTCR)*, Liguori Editore.

Tavakkolizadeh, M. & Saadatmanesh, H. (2003), Strengthening of steel-concrete composite girders using carbon fibre reinforced polymer sheets, *Journal of Structural Engineering, ASCE*, January 2003, pp 30–40.

Tinazzi, D., Modena, C. & Nanni, A. (2000), Strengthening of Assemblages with Fiber Reinforced polymer Rods and Laminates, *in proceedings 'Advancing with Composites 2000', Milan, Italy*.

Wang, Z., Massam, J. & Pinnavaia, T.J. (2000), Epoxy–Clay Nanocomposites, in *Polymer-Clay Nanocomposites*, edited by Pinnavaia, T.J. and Beall, G.W., Wiley & Sons Ltd 2000, pp 127–149.

FRP Composites in Civil Engineering – CICE 2004 – Seracino (ed)
© 2005 Taylor & Francis Group, London, ISBN 90 5809 638 6

ISIS technologies for civil engineering smart infrastructure

A.A. Mufti
President, ISIS Canada Research Network

ABSTRACT: For more than a century, important civil engineering structures such as bridges, high-rise buildings, dams and marine platforms have contained iron or steel as the reinforcement for concrete or wood. The useful lives of these structures have often been severely limited by the corrosion of this ferrous component. Much thought has been given in recent years to constructing structures that are lighter, stronger and non-corrosive. ISIS Canada intends to significantly change the design and construction of civil engineering structures by developing innovative new structures. For these new structures to be accepted by the engineering community, it is mandatory that they be monitored and the results reported to the engineering community as well as being incorporated into civil engineering codes. ISIS Canada has been developing such structures and monitoring them through an innovative concept, which involves the development of the new discipline of Civionics where Civil Engineering and Electrophotonics are being integrated. In this paper, some of the innovations that have been implemented will be described.

1 INTRODUCTION

1.1 *Fibre Reinforced Materials*

Active research into the design of new highway bridges in Canada is focused on a number of specialty areas including; the replacement of steel reinforcing bars in concrete decks by randomly distributed chopped fibers, and the replacement of steel prestressing cables for prestressed concrete by tension elements which comprise longitudinally-oriented fibers embedded in a polymer (ISIS Canada-Strategic Plan 2nd Funding Cycle). For the repair and strengthening of existing structures by the addition of fibre-reinforced polymers (FRPs), research is being conducted into increased axial, bending and shear strength of concrete beams and columns, as well as applications to timber and masonry structures. There is a need to conduct basic research into FRP materials regarding durability, longevity and performance under fire conditions. Effectiveness under seismic loading is another area of needed research. This research is in progress on a variety of FRP products, as shown in Figure 1, in Canada under the directive of ISIS Canada.

Figure 1. A variety of FRP products used in ISIS Canada research and applications.

2 INTELLIGENT SENSING

For many years, engineers have been searching for ways to obtain information on how a structure is behaving in service by incorporating, at the time of construction or subsequently, sensing devices which can provide information about conditions such as strain, temperature, and humidity (Tennyson, 2001). The development of such structurally integrated fibre optic sensors (FOSs) has led to the concept of smart structures.

The current fibre Bragg grating (FBG) sensors are based on a passive spectral ratiometric approach using a low power, broad bandwidth light source. To interrogate many sensors, a multiplexing system has been used that involves sequential measurements, thus limiting dynamic response capability. However, the requirement to monitor many FOSs simultaneously over long distances with complete dynamic spectrum

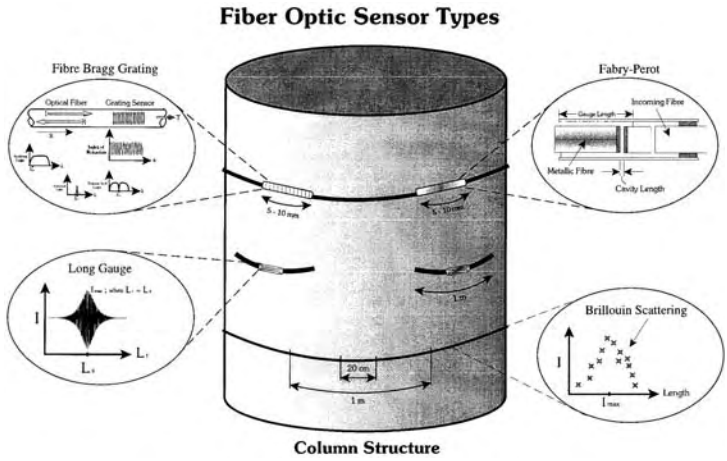

Figure 2. Fibre optic sensors being developed or utilized by ISIS Canada.

capability, necessitates a new approach involving tunable laser light sources.

ISIS Canada is developing new Long Gauge fibre optic sensors, which are based on Brillouin scattering as shown in Figure 2.

3 APPLICATION OF INNOVATIVE TECHNOLOGIES IN FIELD APPLICATIONS

For infrastructure owners, one of the greatest values of ISIS Canada research lies in its practical application. Over the past year, there have been many new opportunities for applying ISIS Canada technology as is evidenced in the growing number of field demonstration projects underway. The projects range from a new concrete steel-free bridge deck for the Salmon River Bridge in Nova Scotia, to the strengthening of a nuclear containment structure in Quebec, to the testing of timber piles for use in an Inuvik housing project in the cold, northern regions of Canada.

At least fifty projects are currently being monitored for health in Canada. Several of those are described in the following sections.

3.1 *Beddington Trail Bridge, Alberta (Calgary)*

In 1992, the Beddington Trail Bridge in Calgary (Rizkalla et al., 1994), Alberta, as shown in Figure 3(a), was one of the first bridges in Canada to be outfitted with fibre-reinforced polymer (FRP) tendons and a system of structurally integrated optical sensors for remote monitoring.

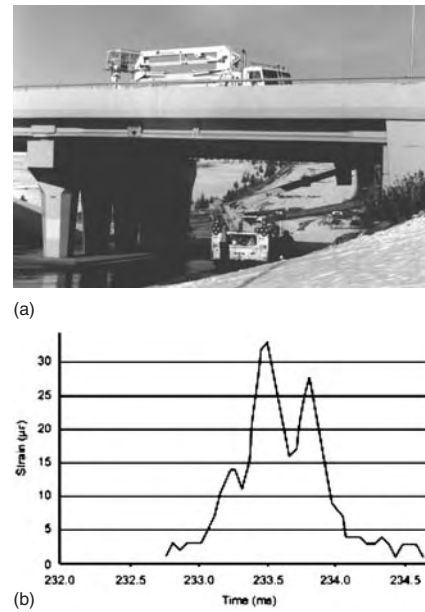

Figure 3. On-site monitoring (a) accessing fibre optic junction box (b) dynamic FBG response to three-axle truck load.

The bridge opened in 1993, before ISIS Canada was formed. It is significant to the ISIS network because, for the group of researchers involved, it confirmed the need for an organization, like ISIS Canada, that

could spearhead transferring this new technology to industry.

The Beddington Trail Bridge is a two-span, continuous skew bridge of 22.83 and 19.23 m spans, each consisting of 13 bulb-Tee section, pre-cast, prestressed concrete girders. Two different types of FRP tendons were used to pretension six precast concrete girders. Carbon fibre composite cables produced by Tokyo Rope of Japan were used to pretension four girders while the other two girders were pretensioned using two Leadline rod tendons produced by Mitsubishi Kasei.

Fibre optic Bragg grating strain and temperature sensors were used to monitor structural behaviour during construction and under serviceability conditions. The four-channel Bragg grating fibre laser sensing system was developed for this purpose at the University of Toronto Institute for Aerospace Studies.

Before constructing the bridge, an experimental program was conducted at the University of Manitoba's W.R. McQuade Laboratory to examine the behaviour of scale model beams pretensioned by the same type, size, and anchorage of the two different tendons used for the bridge girders. The tests compared results using the same optic sensor as used for the bridge in addition to electric resistance strain gauges (Fig. 3(b)).

Prestressing of carbon FRP was adapted by coupling the carbon fibre composite cables and Leadline rods to conventional steel strands. Couplers helped to minimize the length of carbon FRP tendons, and were staggered to allow use of the same spacing for the conventional steel reinforcing tendons.

The Leadline rods were cut at the site and two rods were used for each tendon. The carbon fibre composite cables were delivered precut to the specified length with 300 mm die cast at each end to distribute the stresses at the anchoring zone. Construction of the bridge and handling of the girders at the site was typical.

A four-channel Bragg grating fibre optic sensor system was used at different locations along the bridge girders that were pretensioned by the carbon FRP. Each fibre optic sensor was attached to the surface of the tendon to serve as a sensor. The sensors were connected, through a modular system, to a laptop computer used at the construction site to record the measurements at different stages of construction and after completion of the bridge. The optic sensor system measures the absolute strain rather than a strain relative to an initial calibration value similar to the electric resistance strain gauges and mechanical gauges.

In 1999 the bridge was tested statically and dynamically to assess the durability of fibre optic sensors. After six years, all FOSs were functioning. This finding validates the view that FOSs are durable and reliable for long term monitoring.

Figure 4. Casting of the steel free deck.

4 FIRST GENERATION STEEL-FREE DECKS

4.1 *Salmon River Highway Bridge, Nova Scotia*

The first steel-free deck-slab in Canada was cast on the Salmon River Bridge (Newhook et al., 2000a), part of the Trans Canada 104 Highway near Kemptown, Nova Scotia. Construction of the bridge, which consists of two, 31 m spans, includes a steel-free deck over one span and a conventional steel reinforced deck over the other. Internal arching in the slabs helps transfer the loads to the girders. Although the cost of the steel-free side was six percent more than the steel-reinforced side, the overall design tends to be less expensive than conventional decks. This is because steel-free decks do not suffer from corrosion, so traditional maintenance costs are greatly reduced. This concept has won six national and international awards including the prestigious NOVA award from the Construction Innovation Forum (CIF) of the United States.

The deck contains no rebar (Fig. 4). Instead, longitudinal beams or girders support it. The load is transferred from the deck to the supporting girders in the same way that an arch transfers loads to supporting columns. Although steel straps are applied to tie the girders together, because they are not embedded in the concrete they can be easily monitored and inexpensively replaced.

The Structural Health Monitoring (SHM) of the steel-free bridge deck was conducted by installing sensors, as shown in Figure 5. SHM indicates that the load sharing of the Salmon River Highway Bridge is similar to conventional decks as shown in Figure 6.

With no steel inside the concrete, no unnecessary weight is added, meaning thinner deck designs. The steel straps are welded to the top flanges of the girders thereby resisting any lateral movement. The Salmon River steel-free bridge deck has withstood a number of Canadian winters, and it appears to be defying the conventional approach to building steel-reinforced bridge decks. The Salmon River Bridge has four spans, and

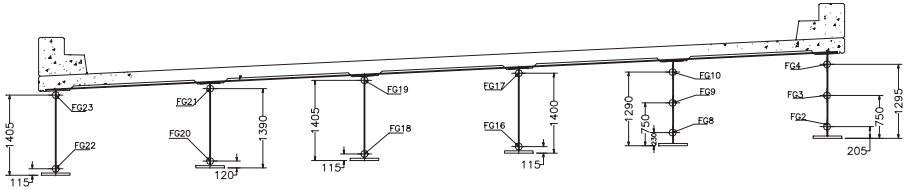

Figure 5. Sensor locations.

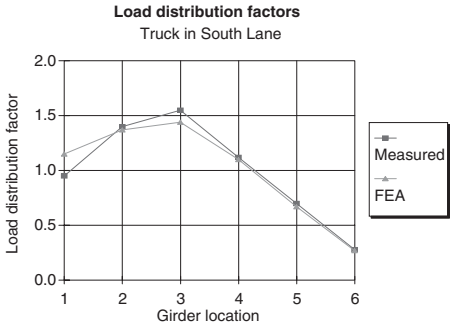

Figure 6. Load sharing of the Salmon River Highway Bridge.

one of these is a steel-free bridge deck. The adjacent bridge has a conventional bridge deck reinforced with steel. A recent visual inspection, on June 7, 2003, revealed that the conventional deck, built within the last eight years, is showing signs of deterioration and possibly the start of corrosion. This will be further investigated. It should be noted that there are six steel free bridge decks across Canada.

4.2 *Hall's Harbour Wharf, Hall's Harbour, NS*

Hall's Harbour Wharf (Newhook et al., 2000b) in Nova Scotia is a 96-year-old combination wharf/breakwater, shown in Figure 7(a). It is the world's first marine structure with fibre optic sensors embedded in a steel-free concrete deck for remote monitoring. It is designed to last 80 years – three times longer than traditional construction methods. This design received the "Award of Excellence" from the Canadian Consulting Engineer Association.

The new wharf consists of piles supporting concrete beams and deck elements above an armour stone and timber crib breakwater (Fig. 7(b)). The concrete beams are designed with a hybrid reinforcement scheme of steel and glass FRP rods. The outer durable layer of FRP protects the inner core of steel reinforcement, which was included for code considerations. The deck

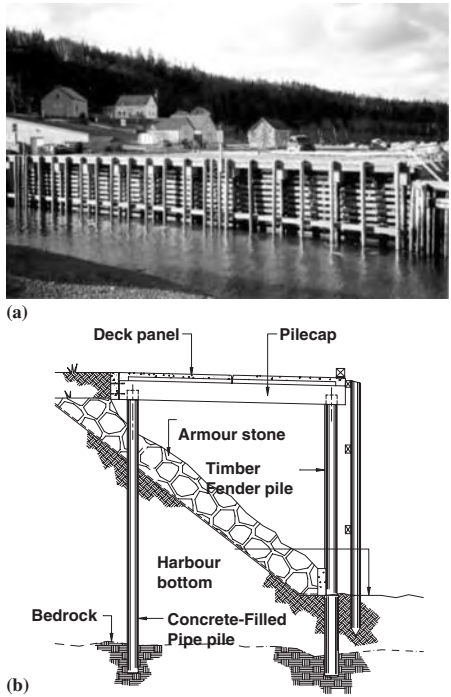

Figure 7. Hall's Harbour Wharf.

consists of precast steel-free concrete bridge deck panels modified to meet the durability needs of this structure (Fig. 8). It is the world's first marine structure with fibre optic sensors embedded in a steel-free concrete deck for remote monitoring (Fig. 9). The design is based on draft versions of both the *Canadian Highway Bridge Design Code* and the *American Concrete Institute Code*.

It is anticipated that rehabilitation of marine structures using FRPs will become standard practice through time, with the inner core of steel reinforcement considered unnecessary.

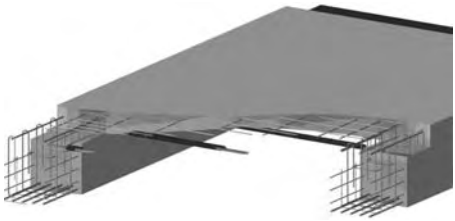

Figure 8. 3-D view of deck and beam details.

Figure 9. Installed sensors.

5 CIVIONICS

CIVIONICS (Mufti, 2003b) is a new term coined from Civil-Electronics, which is derived from the application of electronics to civil structures. It is similar to the term Avionics, which is used in the Aerospace Industry. For structural health monitoring to become part of civil structural engineering, it should include Civionics. Formal definitions and guidelines are given below to encourage the development of Civionics as an academic discipline in Canadian universities and technical colleges.

Realistically, it is true that consulting engineers and contractors will only invest in the development of the expertise created by graduates of the Civionics discipline when they can be assured that the prospects for business are good in this field. The ISIS Canada experience of integrating FOSs and FRPs into innovative structures that have been built across Canada demonstrates that these opportunities do exist. Following are some business opportunities that have been identified, as well as some recommendations for the Civil Structural Engineering Industries to develop the opportunities that currently exist.

In Canadian Universities and Technical Colleges, the research, academic and training courses are established or are in process of being developed. It is intent

Figure 10. Civionics specifications manual.

of ISIS Canada that future generations of structural engineers and technologists will be familiar with the requirements of industries related to Civionics. To that end, ISIS Canada has developed Civionics Specifications (Rivera et al., 2004), which are currently in the process of being printed (Fig. 10).

5.1 *Civionics application in a second generation steel free bridge deck*

In the spring of 2004 research engineers at the University of Manitoba constructed a full-scale second generation steel free bridge deck. The bridge deck is the first of its kind to fully incorporate a complete civionics structural health monitoring system to monitor the deck's behaviour during destructive testing.

Throughout the construction of the bridge deck the entire installation of the civionics system was carried out by research engineers to simulate an actual implementation of such a system in a large scale construction environment. One major concern that consulting engineers have raised is the impact that a civionics system that uses conduit, junction boxes, and other electrical ancillary protection, will have when embedded and installed externally on full-scale infrastructure. The full-scale destructive testing of the second generation steel free bridge deck that uses a civionics system designed and implemented using a civionics specification manual at the University of Manitoba will provide engineers with the information necessary to address the constructability and structural integrity issues.

The complete civionics system for the test bridge deck at the University of Manitoba includes rigid PVC conduit and junction boxes to provide protection for the network of sensors embedded within the deck and all of the sensors installed externally on the steel straps and steel bridge girders. The placement of the system of conduits and junction boxes is important because it should minimize its effect on the structural integrity of the bridge deck, as well as minimize the amount

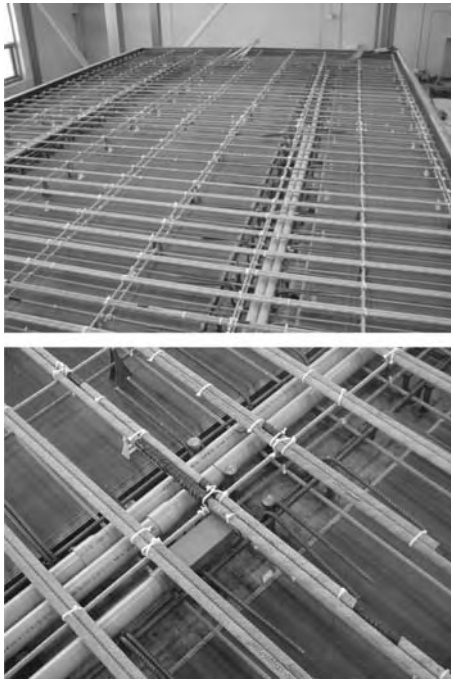

Figure 11. Rigid PVC conduit embedded with bridge deck haunches.

of conduit and exposed cable within the deck. In this case, the conduits were placed within the haunches of the deck (Fig. 11).

The sizing of the conduit was determined using the civionics specifications. The conduit size and junction boxes required for this project were 1½″ in diameter. It should be noted that for research purposes this bridge deck was equipped with several additional sensors and that the conduit was sized accordingly. A civionics system for an actual steel free bridge deck would contain a minimal number of embedded sensors, thus reducing the amount and size of conduit required. For a typical installation on an actual bridge the conduit would be placed by the local electrical contractor and all of the necessary wires would be terminated at the junction boxes. A short time prior to the casting of the bridge deck, and after all major placement of reinforcement has been completed, qualified personnel would be required to install the specified sensors and make the appropriate connections at the junction box to the wires already supplied and installed by the electrical contractor. Field installation of the sensors requires the application of several protective coatings and the exposed lead wires should be located in such

Figure 12. Protected sensors complete with properly located and secured lead wires.

Figure 13. Rigid PVC conduit and junction boxes for externally installed gauges.

a manner as to prevent damage during placement of concrete (i.e. wires should be placed on the underside of the reinforcement and properly secured – Fig. 12). The sensors embedded within the bridge deck on the reinforcing bars allow engineers to monitor live load stresses during and after construction.

Surface mounted sensors located on the external steel straps and on the steel girders also provide engineers with pertinent information relating to the bridges overall performance. However, these sensors must also be properly protected from vandalism and local environmental conditions. Therefore, a system of rigid PVC conduits and junction boxes were permanently installed on the steel girders and steel straps. The conduit and lead wires would be installed by an electrical contractor after all of the formwork has been removed. The wires must be properly labelled to ensure that the correct locations of all sensors are known at a later date. Once again, qualified personnel perform the installation of the necessary gauges within the PVC boxes and splice all lead wires.

The size of the conduit and junction boxes on the straps were 1″ in diameter to provide enough space in the junction box to install the sensor. The back of the PVC junction box had to be removed in order to facilitate surface mounting of the sensors (Fig. 13). Strain gauges installed on the straps will allow engineers to monitor live load strains. Flexible conduit measuring ¾″ in diameter was used with the junction boxes on the top and bottom flanges of the steel girder (Fig. 13).

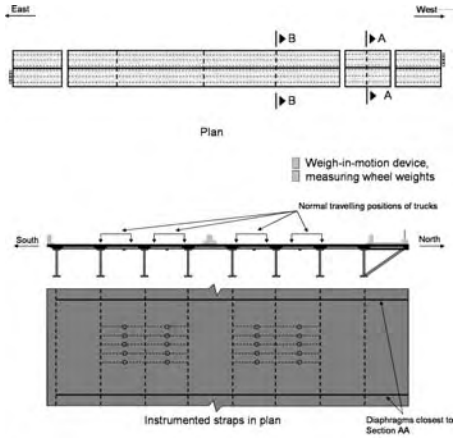

Figure 14. Location of weigh-in-motion sensors and electronic strain gauges on steel straps.

The purpose of the gauges installed on the girders is to determine the live load stress ranges and to determine the transverse load distribution pattern. Also, the gauges will allow engineers at the University of Manitoba to determine exactly if placement of the conduit within the haunches has any significant effect on the composite action between the girders and the deck.

5.2 *South perimeter bridge*

The Red River Bridge is located on the South Perimeter Highway that encircles the city of Winnipeg, Manitoba. It is a 250 m long, 7-span bridge, consisting of three simply supported spans and one continuous span. Over a period of two years, the entire bridge deck will be replaced with a second generation steel-free GFRP hybrid bridge deck. The installation of a civionic structural health monitoring system in this bridge will follow the requirements as outlined in the civionics specifications. Preliminary plans involve a minimal number of sensors including fibre optic sensors, accelerometers, conventional sensors and weigh in motion sensors (Fig. 14).

6 SMART FRP REINFORCED BRIDGE DECKS

6.1 *Joffre Bridge, Québec*

The Joffre Bridge (Benmokrane et al., 2000) located over the St-François River in Sherbrooke, Quebec, Canada, built in 1950, showed signs of deterioration of the concrete deck slab and girders primarily due to reinforcement corrosion. The City of Sherbrooke and the Ministry of Transport of Québec reconstructed a significant part of the bridge deck, sidewalk and traffic barrier using carbon and glass FRP reinforcements, and monitored the performance not only to answer the safety concerns, but also to generate valuable data for the research and development of FRP technology for reinforced concrete structures.

The selected CFRP reinforcement used to reinforce the concrete deck slab is manufactured by Autocon Composites Inc. in Ontario, Canada, and is commercially known as NEFMAC C19-R2 grid. The CFRP reinforcement was in the form of a rectangular cross-section 100 mm × 200 mm grid with a constant thickness of 19 mm. The grids were manufactured with longitudinal spacing of 200 mm and transverse spacing of 100 mm. The GFRP rebars used as reinforcement for the concrete sidewalk and traffic barrier are produced by Marshall Industries Composites Inc. and commercially known as GFRO C-BAR. The lightweight of the FRP reinforcements was very convenient for easy handling and placement during construction.

The bridge was extensively instrumented with several different types of gauges. A total of 180 critical locations were identified and instruments (fibre optic sensors, vibrating wire strain gauges, and electrical strain gauges) were installed at those locations in the concrete deck slab and on the steel girders.

A number of CFRP reinforcement grids were integrated with fibre optic sensors during the manufacturing process, as shown in Figure 15. Gauges were installed on the steel girders and embedded strain gauges were placed inside the concrete to measure the strain inside the concrete to provide information about the hidden structural damage in the concrete deck slab.

The bridge was opened to traffic on December 5, 1997. The dynamic responses of different components of the bridge are being regularly recorded using computer aided data logging systems. The interim results indicate confidence in the use of FRP reinforced concrete structures and the use of state-of-the-art instrumentation for continuous long-term structural performance monitoring. The variation of recorded strain with time and temperature clearly indicates, as shown in the Figure 16, that it is possible to obtain meaningful and consistent results from fibre optic sensors and that temperature is the most prominent factor influencing the strain variation in the bridge deck.

In November 1998, one year after the opening of the bridge to traffic, field dynamic and static tests, using calibrated heavy trucks (Fig. 17) were conducted on the bridge to evaluate the stress level in the FRP reinforcement, concrete deck, and steel girders. Figure 18 shows the results of strains recorded using FOS at the middle of the web of steel girders due to movement of the trucks. The data clearly show that during a 35 s duration, a large strain event (e.g. a truck) followed by

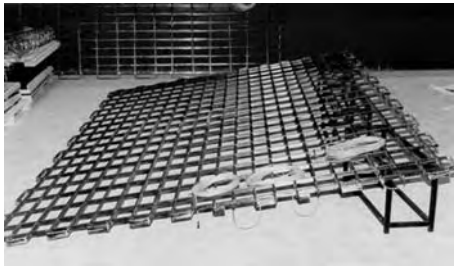

Figure 15. CFRP grid with integrated Fabry-Perot fibre optic sensors.

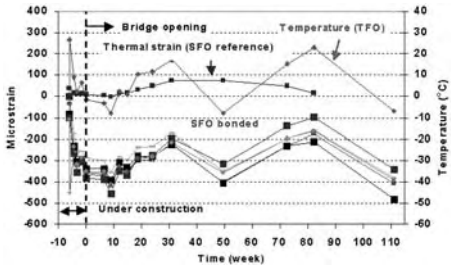

Figure 16. Data recorded by fibre optic sensors installed on CFRP grid.

Figure 17. Trucks being positioned for static load tests of Joffre Bridge.

two similar strain events (e.g. two consecutive trucks) took place on the bridge.

6.2 *Portage creek bridge – strengthening against earthquakes & field assessment, British Columbia*

The Portage Creek Bridge (Mufti et al., 2003) (Fig. 19(a)) in Victoria, British Columbia, was designed in 1982 by the British Columbia Department

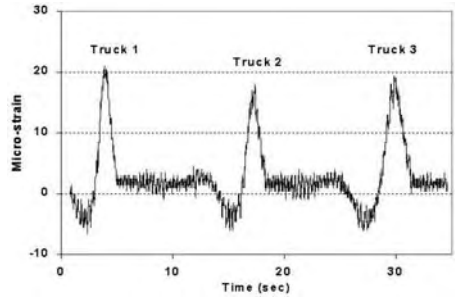

Figure 18. Strain responses from dynamic calibrated load testing.

Figure 19a. Portage Creek Bridge.

of Highways Bridge Engineering Branch. It crosses Interurban Road and the Colquitz River at McKenzie Avenue.

It is a 125 m (410 ft) long three-span steel structure with a reinforced concrete deck supported on two reinforced concrete piers and abutments on steel H piles. The deck has a roadway width of 16 m (52 ft) with two 1.5 m (5 ft) sidewalks and aluminum railings. The super structure is supported at the ends and has two intermediate supports along the length of the bridge called Pier No. 1 and Pier No. 2.

The Portage Creek Bridge is a relatively high profile bridge that has been classified a Disaster-Route Bridge. However, it was built prior to current seismic design codes and construction practices and would not resist potential earthquake forces as required by today's standards. Although some consideration has been given to seismic aspects as evidenced in the original drawings, it requires retrofitting to prevent collapse during a seismic event. The service life of the bridge can thus be increased to 475 years.

Most of the bridge is being strengthened by conventional materials and methods. The dynamic analysis of the bridge predicts the two tall columns of Pier No. 1

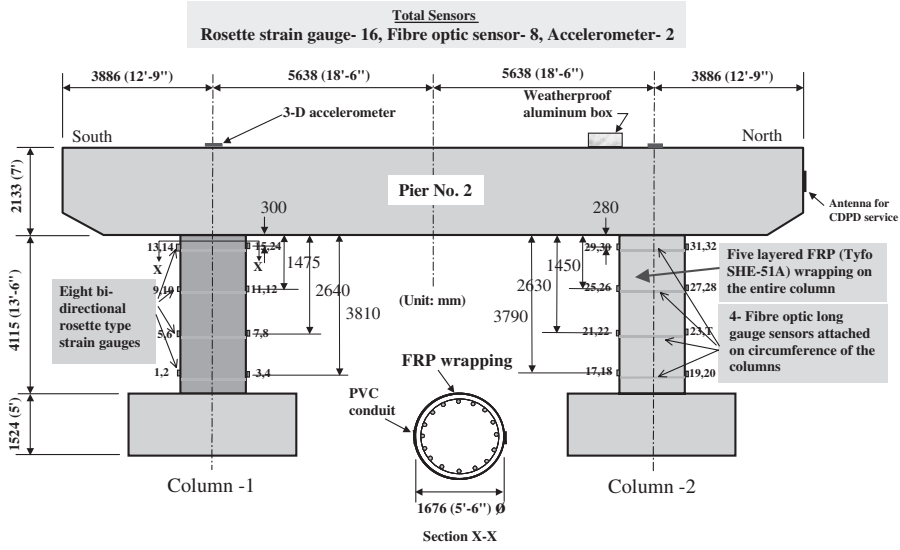

Figure 19b. Portage Creek FOS location.

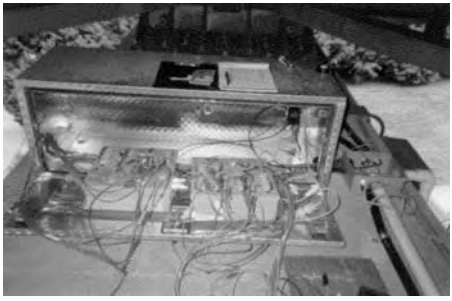

Figure 20a. Datalogger.

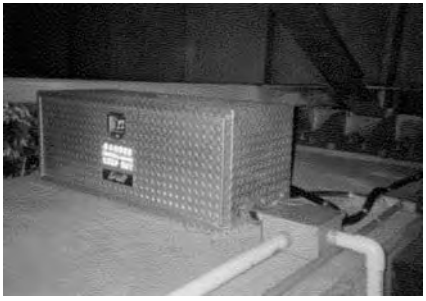

Figure 20b. Monitoring system.

will form plastic hinges under an earthquake. Once these hinges form, additional shear will be attracted by the short columns of Pier No. 2. A nonlinear static pushover analysis indicates that the short columns will not be able to form plastic hinges prior to failure in shear. Therefore, it was decided that FRP wraps should be used to strengthen the short columns for shear without increasing the moment capacity. The bridge is instrumented with 16 foil gauges, 8 fibre optic sensors and 2 accelerometers (Fig. 19(b)). The bridge is being remotely monitored and data collected with the datalogger and monitoring system shown in Figures 20(a) and 20(b). ISIS Canada is assisting with the structural health monitoring of this bridge.

6.3 *Brookside Cemetery – long-term performance of anchor assembly for marker in concrete at Veteran Affairs*

The rapid deterioration of the markers and the concrete beams supporting the markers at the grave of veterans at Brookside Cemetery (Fig. 21) in Manitoba and other cemeteries across Canada has become a major issue of concern for Veterans Affairs Canada National and International Memorials, and Heritage Conservation Services, Public Works and Government Services Canada.

Brookside Cemetery, located northwest of Winnipeg, is a very large cemetery with over 96,000 graves. A portion of the cemetery is designated for the

Figure 21. Brookside Cemetery, Winnipeg, Manitoba, Canada.

Figure 22. Longitudinal cracking of the pre-stressed hollow beams.

graves of Canadian veterans from World Wars I and II and from the Korean War. The rest of the cemetery is designated for the graves of civilians.

By 1999, a large proportion of the hollow core supports had fallen, about 5% in the military portion and about 40% in the civil area of the cemetery. Longitudinal cracking of the hollow concrete beams was noted in Figure 22, as well as the development of cracks at the edge of the beam and longitudinal cracks between grouted pockets were also observed.

The essential requirements for a durable marker anchor assembly include:

- Long-term physical and chemical stability of materials under service conditions;
- Structural stability under service conditions;
- Ease of assembly using existing, or new technique(s); and
- Resistance to cracking of concrete support beams under service conditions.

Different approaches have been suggested to improve the performance of the markers. Figure 23 lists the mechanical tests and specimen configurations included in this study. One of the recommendations was to improve the anchor methods used to attach

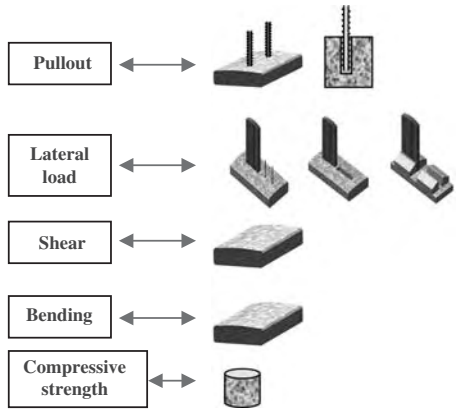

Figure 23. Mechanical tests and specimen configurations included in this study.

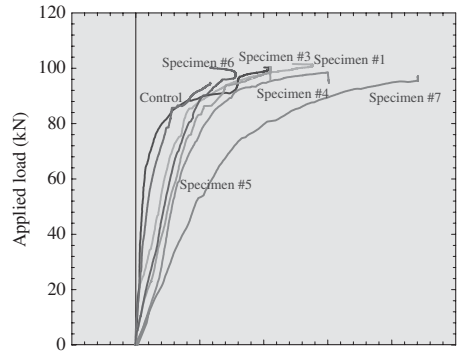

Figure 24. The load-slip behavior of the deformed GFRP rods anchored with Hilti RE 500 epoxy to the steel reinforced concrete beams after 50 freeze and thaw cycles.

the markers to the ground beam. Preliminary results from a series of freeze-thaw tests carried out at University of Manitoba under the supervision of Intelligent Sensing for Innovative Structures (ISIS) Canada, indicated that stainless steel and GFRP fiber reinforced polymer (GFRP) dowels in the Hilti 500 epoxy or Sika-212 grout are promising anchor methods and warrant further investigation (Mufti et al., 2004a&b).

The test program included multiple freeze/thaw cycles shown in Figure 24. Pullout, lateral loading, shear and bending tests were performed under carefully designed accelerated weathering conditions closely simulating the actual conditions at Brookside

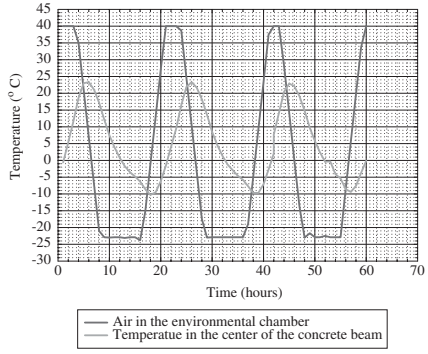

Figure 25. A segment of the freeze and thaw cycles established for the experimental program.

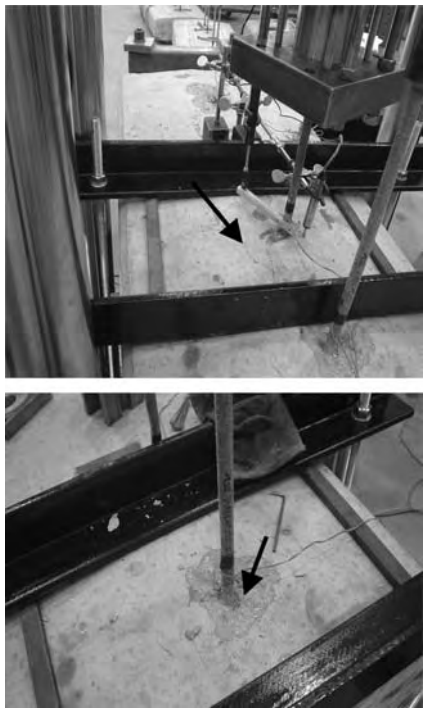

Figure 26. Cracking (A) & spalling (B) of concrete surrounding deformed GFRP rods during pullout tests.

Cemetery. Acceptance of a new marker anchor assembly will ultimately depend on its service life performance (i.e., durability) as compared with the existing marker mounting assembly, and economics.

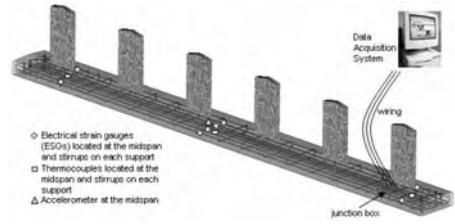

Figure 27. Schematic diagram of a 24 ft beam and SHM system.

The pullout test on the pin method using steel and GFRP bars (Fig. 25) demonstrated that GFRP gave a similar axial load to that given by steel. However, GFRP is more advantageous as it will not corrode (Fig. 26).

6.4 *Field application to FRP reinforced smart beam*

A 24 ft beam has been designed and instrumented as shown in Figure 27 to demonstrate the performance of FRPs in a field application.

7 STRUCTURAL HEALTH MONITORING DATA ON WEB SITE

For the structures that have been instrumented with remote monitoring capabilities, data is constantly collected at varying frequencies. As the data grows daily, so does the need for a sophisticated archival management system. It becomes one of the most vital aspects of structural monitoring. ISIS is developing an online archiving system whereby authorized researchers submit raw data that will be accessible to users. In a user-friendly, worldwide web interface, the site will offer access to sensor characteristics and locations, and response measurements from static and dynamic load tests. The archive will enable interested parties to browse the content, view the relevant documentation and down load data for their own analysis.

Several different strategies are being used for data collection. In some cases, the sensors are triggered manually at selected intervals of time, and the sensor data is stored on computer disks. In other cases sensor data is collected continuously at a specified scan rate and automatically transmitted to a remote location, where it is stored on a computer.

8 DESIGN GUIDELINES MANUALS AND CODES

The new *Canadian Highway Bridge Design Code* has recently been published (Bakht et al., 2001). The

Figure 28. Design codes CHBDC and CSA: design & construction of building components with FRP.

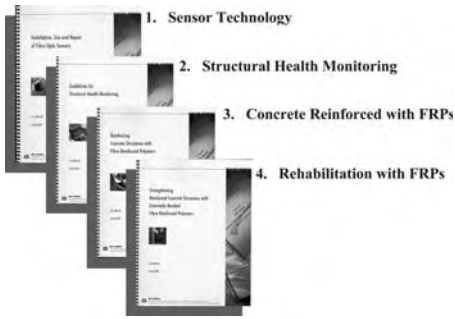

Figure 29. ISIS Canada Design Manuals.

Canadian Standards Association (CSA) code on the use of FRP in buildings and structures is also nearing completion. Members of both committees are well represented by ISIS Canada researchers.

Naturally, engineers are reluctant to use FRPs and FOSs in structures without approved design codes. A major step toward widespread use of FRPs has been the publishing of ISIS Canada's manuals for design engineers. The four manuals cover: Installation, Use and Repair of Fibre Optic Sensors (Tennyson, 2001); Guidelines for Structural Health Monitoring (Mufti, 2001), Reinforcing Concrete Structures with Fibre Reinforced Polymers (Rizkalla et al., 2001), and Strengthening Reinforced Concrete Structures with Externally-Bonded Fibre Reinforced Polymers (Neale, 2001). The codes are shown in Figure 28 and the manuals in Figure 29.

9 CONCLUSIONS AND RECOMMENDATIONS

As mentioned earlier, ISIS Canada intends to significantly change the design and construction of civil engineering structures. For changes in design and construction to be accepted, it is necessary that innovative structures be monitored for their health. To assist in achieving this goal, ISIS Canada is developing a new discipline, which integrates Civil Engineering and Electrophotonics under the combined banner of Civionics.

The new discipline of Civionics must be developed by Civil Structural Engineers and Electrophotonics Engineers to lend validity and integrity to the process. Civionics will produce engineers with the knowledge to build "smart" structures containing the SHM equipment to provide much needed information related to the health of structures before things go wrong. This discipline will, thereby, assist engineers and others to realize the full benefits of monitoring civil engineering structures.

ACKNOWLEDGMENTS

The financial assistance of NCE, ISIS Canada and NSERC is gratefully acknowledged. The assistance of Ms. Nancy Fehr, Executive Assistant to the President of ISIS Canada is also gratefully acknowledged.

REFERENCES

Bakht, B., Al-Bazi, G., Banthia, N., Cheung, M., Erki, M-A., Faoro, M., Machida, A., Mufti, A., Neale, K. and Tadros, G. 2001. Canadian Highway Design Code Provisions for Fibre-Reinforced Structures. Journal of Composites for Construction, ASCE: 4(1): 3–15.

Benmokrane, B., Zhang, B., Nicole, J.F. and Masmoudi, R. 2000. Application of Fibre Optic Sensors for Structural health Monitoring of bridges and Other Structures. Research Report, University of Sherbrooke.

ISIS Canada – Strategic Plan 2nd Funding Cycle. ISIS Canada Room 227 Engineering Building, University of Manitoba. Winnipeg, MB, Canada, R3T 5V6.

Mufti, A.A. 2001. Guidelines for Structural Health Monitoring. ISIS Canada Design Manual. Winnipeg, Manitoba, Canada.

Mufti, A.A. 2003b. Integration of Sensing in Civil Structures: Development of the New Discipline of Civionics. Proceedings for the First International Conference on Structural Health Monitoring and Intelligent Infrastructure (SHMII-1 2003): 119–129. Tokyo, Japan.

Mufti, A.A., Neale, K., Rahman, S. and Huffman, S. 2003. GFRP Seismic Strengthening and Structural Health Monitoring of Portage Creek Bridge Concrete Columns. Proceedings for the fib2003 Symposium – Concrete Structures in Seismic Regions. Athens, Greece.

Mufti, A.A., Onofrei, M. and Kroeker, A. 2004a. Long-Term Performance of Anchor Assembly for Marker in Concrete at Veteran Affairs Brookside Cemetery. ISIS Canada Technical Progress Report No. 2, June 2004.

Mufti, A.A., Onofrei, M. Kroeker, A. and Klowak, C. 2004b. Long-Term Performance of Anchor Assembly for Marker in Concrete at Veteran Affairs Brookside Cemetery. ISIS Canada Technical Progress Report No. 1 February 2004.

Neale, K. 2001. Strengthening Reinforced Concrete Structures with Externally-Bonded Fibre Reinforced Polymers. Winnipeg, Manitoba, Canada.

Newhook, J.P, Bakht, B., Tadros, G. and Mufti, A.A. 2000a. Design and Construction of a Concrete Marine Structure Using Innovative Technologies. ACMBS-III Conference Proceeding: 777–784. Ottawa, Ontario, Canada.

Newhook, J.P. and Mufti, A.A. 2000b. A Reinforcing Steel Free Concrete Bridge Deck for the Salmon River Bridge. Concrete International: Vol. 18(6): 30–34.

Rivera, E., Mufti A.A. and Thomson, D. 2004. Civionics Specifications Design Manual. ISIS Canada Research Network. Winnipeg, Manitoba, Canada.

Rizkalla, S. and Mufti, A.A. 2001. Reinforcing Concrete Structures with Fibre Reinforced Polymers. ISIS Canada Research Network. Winnipeg, Manitoba, Canada.

Rizkalla, S.H. and Tadros, G. 1994. A Smart Highway Bridge in Canada. Concrete International: 42–44.

Tennyson, R. 2001. Installation, Use and Repair of Fibre Optic Sensors. ISIS Canada Research Network. Winnipeg, Manitoba, Canada.

FRP Composites in Civil Engineering – CICE 2004 – Seracino (ed)
© 2005 Taylor & Francis Group, London, ISBN 90 5809 638 6

Strengthening of scaled steel–concrete composite girders and steel monopole towers with CFRP

D. Schnerch & S. Rizkalla
North Carolina State University, Raleigh, NC, USA

ABSTRACT: Cost-effective rehabilitation and/or strengthening of steel structures currently demanded by the telecommunications industry and transportation departments. Rehabilitation is often required due to cross-section losses resulting from corrosion damage and strengthening may be required due to changes in the use of a structure. Current strengthening techniques, have several disadvantages including their cost, poor fatigue performance and the need for ongoing maintenance due to continued corrosion attack. The current research program makes use of new high modulus types of carbon fiber for strengthening steel structures. The research program, currently in progress, includes phases to determine the appropriate resin and adhesive for wet lay-up of carbon fiber reinforced polymer (CFRP) sheets and bonding of CFRP strips, respectively. Test results of three scaled monopoles showed significant stiffness increases prior to yield. A significant stiffness as well as ultimate strength increase was found for the first steel–concrete composite girder tested in the program.

1 INTRODUCTION

1.1 *Research objective*

While FRP materials have been successfully used for flexural strengthening, shear strengthening and ductility enhancement of concrete bridge structures, far less research has been conducted in strengthening steel structures with fiber reinforced polymer (FRP) materials. Increasing number of cellular phone users and their requirement for improved service has required cellular phone companies to increase the number of antennas on monopole towers. This trend has been exasperated by the reluctance of communities to allow new monopoles to be built. Addition of new antennas increases the wind load acting on the monopole, therefore strengthening is required to match this demand. Existing techniques for strengthening monopoles with steel collars or with an additional lattice structure are costly and negatively affect the visual appearance of the structure. Repair and/or rehabilitation of steel bridge are also being demanded by transportation departments. The strengthening technique must be cost effective and should not cause major interruption of traffic. The purpose of this research is to determine the feasibility of using new types of high modulus carbon fiber reinforced polymer (CFRP) materials to provide stiffness and strength increases for steel–concrete composite girders and steel monopoles.

1.2 *Background*

1.2.1 *Advantages*

There are many advantages in favor of the use of FRP materials for repair and rehabilitation of bridges and structures. Cost savings may be realized through labor savings and reduced requirements for staging and lifting material. Due to the ease of application, disruption of service during construction may be reduced or eliminated. The dead weight added to a structure is minimal and there is typically little visual impact on the structure, such that good aesthetics can be maintained.

1.2.2 *Adhesive selection and surface preparation*

Previous work has illustrated the importance of surface preparation, adhesive working time, curing methods and prevention of the formation of galvanic couples in selecting an appropriate resin/adhesive system (Rajagoplan et al. 1996). Different types of adhesives have been used to bond CFRP to steel, but generally room-temperature cured epoxies have been chosen due to their superior performance and ease of use. Adhesion promoters, such as silanes, have been shown to increase the durability of steel–epoxy bonds without affecting the bond strength (McKnight et al. 1994). Since the study at this stage is focused mainly on the structural performance, silanes were not used in this program, but would be recommended for use in field applications.

Surface preparation of the steel must be undertaken to enhance the formation of chemical bonds between the adherend surface and the adhesive. This requires a chemically active surface that is free from contaminants. The most effective means of achieving this is by grit blasting (Hollaway and Cadei, 2002). For the CFRP strip, it is usually desirable that the strip would be fabricated with a peel-ply on one or both surfaces. However, for the small amount of CFRP produced for this program it was not economical to manufacture the CFRP strips with peel plys. As such, the procedure recommended by Hollaway and Cadei (2002) was followed, whereby the strips were abraded on the side to be bonded with sandpaper and cleaned with a solvent, which was methanol in this study.

1.2.3 *Previous work*

Previous work has shown the effectiveness of the technique in improving the ultimate strength of steel–concrete composite girders, although little enhancement to the stiffness has been shown. Sen et al. (2001) strengthened steel–concrete composite girders that were initially loaded past the yield strength of the tension flange. Ultimate strength increases were possible, however stiffness increases were small particularly for the thinner of the two types of CFRP laminate strips studied. It was noted that even for these specimens, the increase in the elastic region of the strengthened members might allow service load increases. Tavakkolizadeh and Saadatmanesh (2003a) also noted considerable ultimate strength increases and insignificant elastic stiffness increases. Potential to increase the elastic stiffness increase by strengthening with many plys of CFRP strips was discounted, since as the number of plys increase, the efficiency for utilizing the CFRP decreased. However, for girders that simulated corrosion damage with notches of the tension flange, Tavakkolizadeh and Saadatmanesh (2003c) found that elastic stiffness increases were possible.

Vatovec et al. (2002) performed tests on square tubular steel sections that were 152 mm in depth with a span of 3048 mm. After some early trials, the tubes were filled with concrete to prevent premature local buckling of the tubes. The reported increases of strength varied from 6 to 26 percent depending on the configuration and number of plys used. No meaningful difference in stiffnesses between the unstrengthened tubes and strengthened tubes could be found and it was claimed that strengthened steel elements could not develop the full ultimate tensile or compressive strength of the CFRP due to premature delamination.

Current techniques for strengthening and rehabilitation of steel structures often require bolting or welding steel plates to the existing structure. Welding is often not desirable due to the poor fatigue performance of welded connections. In contrast, the fatigue performance of repairs made to cracked steel cross-girders by bonding with CFRP has been shown to be effective up to 20 million cycles (Bassetti et al. 2000). For notched tensile specimens subjected to fatigue loading, Gillespie et al. (1997) has shown that CFRP patches applied across the notch have the effect of reducing the stress concentration at the notch, thereby substantially increasing the life of the specimen due to the slower rate of crack propagation. This finding was confirmed for notched flexural specimens subjected to fatigue loading (Tavakkolizadeh and Saadatmanesh, 2003b).

The durability of CFRP materials bonded to metallic surface has to be carefully considered due to the potential for galvanic corrosion to occur if three conditions are met: an electrolyte (such as salt water) must bridge the two materials, there must be electrical connection between the materials and there must be a sustained cathodic reaction on the carbon (Francis, 2000). Brown (1974) studied the corrosion of different metals connected to CFRP by adhesive bonding or bolting. For the specimens connected by adhesive bonding there was no accelerated corrosion attack. This behavior was claimed to be due to the insulating behavior of most structural adhesives in not allowing electrical contact between the two materials. Tavakkolizadeh and Saadatmanesh (2001) provided the most comprehensive study of galvanic corrosion between steel and CFRP to date. Thicker epoxy films between the steel and CFRP surfaces were shown to significantly slow the corrosion rate of steel. The proceeding study proposed placing a layer of nonconductive GFRP as an insulating layer between the steel and CFRP interface. However, Tucker and Brown (1989) have found that glass fibers placed within a carbon fiber composite result in the blistering of the composite by creating conditions favorable for the development of a strong osmotic pressure within the composite. Clearly, water being drawn within the bond line by osmotic pressure is not favorable for maintaining a durable bond.

1.3 *Carbon fiber material*

The work presented in this paper makes use of two types of carbon fiber with properties given in Table 1. The high modulus carbon fiber used, was in the form of unidirectional tow sheets or CFRP laminate strips. These sheets had a width of 330 mm and are suitable when a wet lay-up process is necessary to conform

Table 1. Fiber properties for two types of fiber used in the experimental program.

Fiber type	High modulus	Intermediate modulus
Tensile modulus (GPa)	640	438
Tensile strength (MPa)	2450	2550

to the exact surface configuration of the structure. The same fiber was also pultruded into unidirectional CFRP laminate strips using Resolution Performance Products Epon 9310 epoxy resin with Ancamine 9360 curing agent at a fiber volume content of 55 percent. These strips were expected to be more suitable for field applications where a greater degree of strengthening is required and flat uniform surfaces are available for bonding. An intermediate modulus fiber was also pultruded using the same epoxy and to the same fiber volume fraction. The properties of the CFRP strips, as determined by the manufacturer, are provided in Table 2.

2 EXPERIMENTAL PROGRAM

2.1 *Outline*

The main objective of the experimental program is to develop a system to increase the elastic stiffness and ultimate strength of steel structures. The program consists of three phases. The first phase was conducted to determine a suitable resin for the wet lay-up of unidirectional carbon fiber sheets bonded to steel. For applications requiring more strengthening material, adhesive bonding of CFRP laminate strips is more practical. As such, the second phase focused on selection of adhesives and continued to determine development lengths for both materials. The third phase of the program was conducted to investigate the performance of the strengthening technique using larger scale specimens, including steel monopoles and steel–concrete composite girders.

Table 2. CFRP strip properties for two types of strips used in the experimental program.

Strip type	High modulus	Intermediate modulus
Width (mm)	75	75
Thickness (mm)	1.4	3.2
Tensile modulus (GPa)	340	230
Compressive modulus (GPa)	317	177
Tensile strength (MPa)	1190	1230
Compressive strength (MPa)	355	470
Tensile rupture strain (millistrain)	3.32	5.08

2.2 *Phase I: resin selection*

Resin selection for the wet lay-up process was determined through testing of double lap shear coupons using ten different resins. Additional variables included different cure temperatures, use of a wetting agent and resin hybridization resulting in a total of twenty-two different trials. This work is presented in greater detail elsewhere, Schnerch et al. (2004).

2.3 *Phase II: adhesive selection and development length study*

2.3.1 *Test specimens*

Test specimens for adhesive selection and determining the development length for bonded laminate strips were Super Light Beams, designated SLB 100 × 4.8, as shown in Figure 1. The same beam specimens were also used to determine the development length for the CFRP sheets. An additional 6.4 mm thick, grade A36 steel plate was welded to the compression flange to simulate the strain profile of a bridge girder that acts compositely with a concrete deck, such that the neutral axis is located closer to the compression flange. The beams were then strengthened on the tension flange with either the CFRP laminate strips described previously, or by bonding one layer of the CFRP sheets. For this study, the width of the laminate strip was reduced to 35.8 mm to fit within the tensile flange of the test specimens. The width of the CFRP sheets used was 53.7 mm and its effective thickness was 0.19 mm.

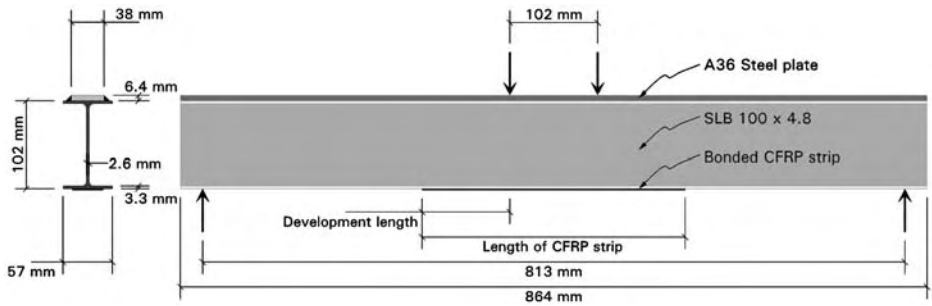

Figure 1. Cross-section dimensions and loading configuration of typical adhesive selection and development length specimen.

Table 3. CFRP laminate strip ultimate strain (millistrain) and failure mode for various development lengths.

		Development lengths						
Adhesive	Plys	254 mm	203 mm	152 mm	127 mm	102 mm	76 mm	51 mm
Weld-On SS620	1	–	3.08 rupture	2.96 rupture	–	3.16 rupture	2.80 rupture	1.55 debond
SP Spabond 345	1	–	2.88 rupture	2.93 rupture	–	3.11 rupture	2.43 rupture	1.83 debond
Vantico Araldite 2015	1	–	3.09 rupture	2.98 rupture	–	2.82 rupture	2.18 debond	–
Jeffco 121	1	–	2.98 rupture	3.28 rupture	2.66 rupture	3.01 debond	–	–
Fyfe Tyfo MB2	1	–	3.47 rupture	3.06 debond	–	2.10 debond	–	–
Sika Sikadur 30	1	–	2.81 debond	–	–	–	–	–
SP Spabond 345	2	–	3.09 rupture	–	–	–	–	–
Jeffco 121	2	2.02 debond	–	–	–	–	–	–

* note that underlined strain values are the average from repeated tests and dashed indicate that no tests were conducted.

Different laminate strip lengths, varied from 51 mm to 203 mm, were used to determine the approximate development length and most suitable adhesive for bonded laminate strips. A length of 51 mm was used for the CFRP sheet and shown to be conservative in developing the full strength of the fibers.

2.3.2 *Test procedure and instrumentation*

Six adhesives for bonding the laminate strips and two resins for bonding carbon fiber sheets were evaluated in the development length study. The six adhesives were: Fyfe Tyfo MB2, Jeffco 121, Sika Sikadur 30, SP Systems Spabond 345, Vantico Araldite 2015, and Weld-On SS620. The two resins were Degussa MBrace Saturant and Sika Sikadur 330. These two resins were selected from the ten resins evaluated using double lap-shear coupons in the first phase.

The beams were simply supported and loaded under four-point loading using a spherically seated bearing block over two 25 mm diameter steel rollers. Lateral bracing was provided by supporting the top flange of the beam over the supports with two steel angles fixed to each support. Load was applied at a constant displacement rate of 0.75 mm/min.

Strain and displacement were measured at mid-span of the beam. Strain was measured using foil strain gauges bonded on the inside of the compression flange, inside of the tension flange, and outside of the tension flange for the unstrengthened specimen and outside on the laminate strip, or carbon fiber sheet, for the strengthened beams. Displacement was measured using two linear voltage displacement transducers.

Table 4. CFRP sheet ultimate strain (millistrain) and failure mode for various development lengths.

		Development lengths		
Resin	Plys	102 mm	76 mm	51 mm
Degussa MBrace Saturant	1	–	–	3.57 rupture
Sika Sikadur 330	1	–	–	3.41 rupture
Degussa MBrace Saturant	2	3.24 rupture	2.04 debond	2.58 debond
Sika Sikadur 330	2	3.19 rupture	2.84 rupture	2.33 debond

* note that underlined strain values are the average from repeated tests and dashed indicate that no tests were conducted.

2.3.3 *Results and observations*

The results of the tests are shown in Tables 3 and 4 for the laminate strips and carbon fiber sheets respectively, indicating the ultimate strain at failure, either by rupture or debonding from the steel surface. The specimens fabricated using SP Spabond 345 and Weld-On SS620 adhesives had the shortest development lengths, developing the ultimate CFRP strip strain at a length of approximately 102 mm. Specimens tested with both Sika Sikadur 330 and Degussa MBrace Saturant achieved ultimate strain of the carbon fiber sheet at the development length of 51 mm. Certain development lengths were replicated to validate results. The average strains from these tests are underlined in both tables.

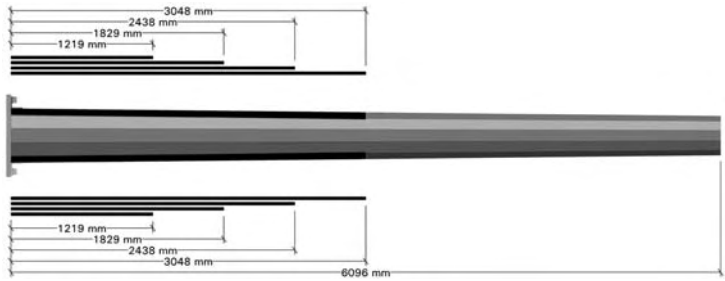

Figure 2. Longitudinal strengthening configuration of monopole (MWL).

Of the six adhesives tested, SP Spabond 345 and Weld-On SS620 achieved a development length of 102 mm, Jeffco 121 and Vantico Araldite 2015 reached 152 mm, Fyfe Tyfo MB2 was 203 mm, and Sika Sikadur 30 was greater than 203 mm. The development lengths were based on ultimate strain of the laminate strip and failure by rupture.

Two tests were completed to verify a linear relationship assumption between the thickness of the laminate strips and the development length. Using the laminate strips provided, thickness was doubled by bonding two layers with the adhesives SP Spabond 345 and Jeffco 121 at the development lengths of 203 mm and 254 mm respectively. As shown in Table 3, the ultimate strain for the beam bonded with SP Spabond 345 achieved 3.09 millistrain and a rupture failure mode, which was the same failure mode and almost the same strain measurement, 3.11 millistrain, as the 102 mm development length tested beam. Ultimate strain for the beam bonded with Jeffco 121 was 2.02 millistrain; which was a little less than the ultimate strain of the laminate strip at half the development length of 127 mm, which was 2.66 millistrain. No conclusive decisions can be drawn from these few tests, though the results did show that doubling the thickness of the laminate strip increased the development length by at least twice the length for one layer of CFRP strip.

The same study was completed using carbon fiber sheets for 51, 73, and 102 mm development lengths. The results from these tests showed that doubling the thickness of the carbon fiber sheets required at least twice the development length needed for one layer. At 102 mm development length, the ultimate strain of the carbon fiber sheet was achieved.

2.4 *Phase III: testing of scaled members*

2.4.1 *Scaled steel monopoles*

2.4.1.1 Test specimens

Three scaled steel monopoles were fabricated from A572 grade 60 steel with similar proportions to monopoles that are typically used as cellular phone towers. The length of the monopole was 6096 mm with a dodecagonal, or twelve-sided, cross-section. The cross-section depth as measured from outside to outside of two opposing sides was tapered uniformly along the length, with a maximum depth of 457 mm at the base and a minimum depth of 330 mm at the tip. Cold forming was used to fabricate the monopole from two equal halves, which were then welded together along their length near mid-depth of the monopole. The monopole was welded to a base plate that was 38 mm in thickness to allow mounting of the monopole to a fixed structural wall. Three different strengthening configurations were examined in this series of testing. Monopole (MWL) was strengthened by wet lay-up of the high modulus CFRP sheets. Monopole (MAB-H) was strengthened by bonding CFRP laminate strips pultruded using the same high modulus fibers. The final monopole (MAB-I) was strengthened by bonding pultruded strips using an intermediate modulus carbon fiber.

Monopole (MWL) was strengthened by wet lay-up of 330 mm wide unidirectional, CFRP sheets in both the longitudinal and transverse directions using Sika Sikadur 330 resin. This process allowed the composite material to exactly conform to the surface configuration of the monopole. Strengthening was performed to match the demand placed on the monopole due to the cantilever loading condition. From a preliminary analysis, it was found that most of the strengthening is required at the base of the monopole and no strengthening was required from mid-span to the tip. As such, the thickness of the applied CFRP sheets was tapered from four plys of the sheets at the base to one ply terminating at mid-length of the monopole as shown in Figure 2. Anchorage was provided for the sheets by continuing the fibers past the shaft of the monopole and bending the fibers up onto the base plate. More resin was applied to the surface of the fibers and several steel angles were used to mechanically anchor the fibers to the base plate.

Half-width sheets were used to wrap the longitudinal sheets transversely to prevent possible premature

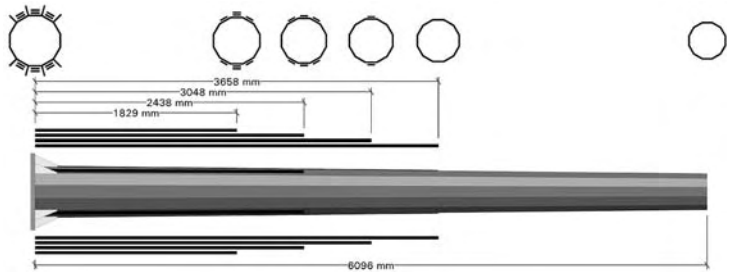

Figure 3. Longitudinal strengthening configuration of monopoles (MAB-H) and (MAB-I).

delamination of the strengthening applied to the compression side of the monopole. These sheets were wrapped around the cross-section in two halves such that they overlapped by 100 mm at mid-depth of the monopole. The transversely oriented sheets were applied continuously from the base to 1200 mm along the length to also delay the onset of local buckling of the steel on the compression side. From this point to the mid span, the transversely oriented sheets were spaced apart from each other.

The two remaining monopoles were strengthened by adhesive bonding of unidirectional CFRP laminate strips. Monopole (MAB-H) used high modulus CFRP strips and monopole (MAB-I) used intermediate modulus strips. For both monopoles, the adhesive used was Spabond 345 with a fast hardener, manufactured by SP Systems. Similar to monopole (MWL), due to the requirement for greatest strength increase at the base, six strips were applied to the three flat sides on both the tension and compression sides of the monopole and the amount of strengthening provided decreased with increasing distance from the base as shown in Figure 3. To allow comparison of the effectiveness between the two adhesive bonded systems, the applied strengthening had approximately equal values of the Young's Modulus multiplied by the cross-sectional area of the applied strips. To accomplish this, the width of the strips applied to the flats on the sides was reduced to 50 mm for monopole (MAB-I). Anchorage was provided by the addition of steel gusset plates welded from the base plate along the shaft at the corners of the cross-section. The length of the gusset plate was 200 mm to allow full development of two plys of the high modulus CFRP strips.

2.4.1.2 Test procedure and instrumentation

Each of the three monopoles was statically loaded to 60 percent of the specified yield stress and unloaded to determine the initial stiffness of each monopole. For monopole (MWL) this was completed before strengthening and for monopoles (MAB-H) and (MAB-I) this was completed after the addition of the gusset plates,

Figure 4. Test setup for scaled monopoles.

but before strengthening with the CFRP strips. The monopoles were tested as cantilevers using the test setup shown in Figure 4. The monopole was mounted horizontally to a rigid structural wall by bolting to a steel fixture. Load was applied with nylon straps near the tip of the monopole, pulling the tip of the monopole upward. This type of loading was used to most closely represent the loading condition of a field monopole, whereby most of the loading from wind pressure is concentrated at the location of the antennas.

After strengthening, each monopole was reloaded to the same mid-pole displacement as the same monopole before strengthening to determine the stiffness increase resulting from the applied strengthening. After unloading, nylon straps were exchanged for steel chains and the monopoles were loaded to failure.

Measurements were taken of the deflection and extreme fiber strains at quarter points of the monopoles in addition to the actuator load and displacement. Deflection was also recorded at the base to determine the uplift as well as the rotation of the base plate. From these displacements, the net deflection of the monopole was calculated.

2.4.1.3 Results and observations

Monopole (MWL): The result of strengthening by wet lay-up of CFRP sheets was that the net deflection

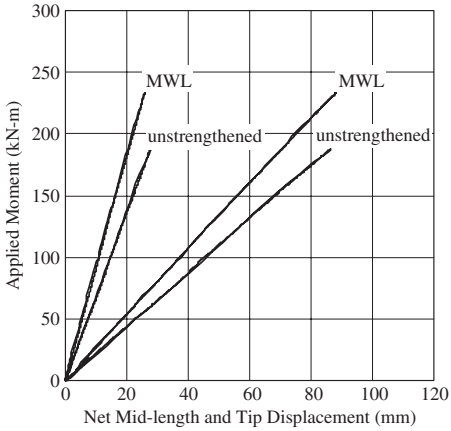

Figure 5. Comparison of net mid-length and tip displacements before and after strengthening of monopole (MWL).

of the monopole was reduced by 25 percent at the mid-length and the tip deflection was reduced by 17 percent compared to the unstrengthened monopole. The load-deflection behavior for both the strengthened monopole (MWL) and the same monopole before strengthening are given in Figure 5. The monopole was then reloaded to failure, which occurred due to rupture of the sheets on the tension side underneath the anchorage. Following rupture, redistribution of the stresses in the monopole resulted in local buckling of the monopole on the compression side about 150 mm from the base, as shown in Figure 6. This buckling ruptured the longitudinal and transverse fibers surrounding the buckled region. The ultimate moment capacity of the monopole was 548 kN-m with a maximum net deflection at the tip of 129 mm.

Monopole (MAB-H): The monopole was reloaded to the same mid-length displacement as before strengthening, but after welding of gusset plates. Figure 7 shows the load-deflection behavior at mid-length and at the tip. Net deflection of the monopole was reduced by 39 percent at mid-length and by 30 percent at the tip. Upon loading to failure, crushing of the laminate strips on the compression side preceded their debonding. Two of the strips on the tension side ruptured, while one debonded, as shown in Figure 8. Failure of the monopole was by local buckling near the base.

Monopole (MAB-I): Figure 7 also shows the behavior of the monopole strengthened with the intermediate modulus CFRP strips. This monopole showed the greatest stiffness increase, with a reduction of the net mid-length and tip deflection by 53 percent and 39 percent, respectively. Debonding of all the strips on the tension side occurred just after yielding of the monopole. Examination of the failure surface after

Figure 6. Detail of local buckling at base showing anchorage angles for sheets.

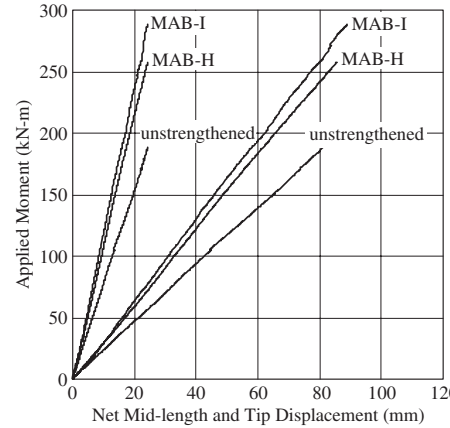

Figure 7. Comparison of net mid-length and tip displacements before and after strengthening monopoles (MAB-H) and (MAB-I).

testing showed that the strips were not fully wetted by the adhesive. This was likely due to their application being completed from underneath, together with their greater thickness in comparison to the previous strips resulting in possible sagging during adhesive curing. Near the ultimate strength of the monopole, but prior to local buckling, the strips on the compression side first crushed, and then began to debond.

2.4.2 *Scaled steel–concrete composite girders*

2.4.2.1 Test specimens

Three identical steel–concrete composite girders were fabricated, simulating the geometry of steel–concrete girders commonly used for bridge structures. These girders used grade A36 steel W310 × 45 sections, with shear studs welded along the length of the compression flange to ensure full composite action between

Figure 8. Rupture of CFRP strips at end of gusset plates for monopole (MAB-H).

the concrete deck and the steel section as shown in Figure 9. These studs were staggered to prevent longitudinal cracking of the deck. The concrete deck was 100 mm thick and 835 mm in width and was reinforced with grade 60 steel reinforcing bars with a diameter of 12.7 mm at a spacing of 100 mm in the longitudinal direction and 152 mm in the transverse direction. End blocks were cast with the deck and fully encasing the steel girder at the ends to provide lateral stability and to eliminate the possibility of web crippling at the supports during loading. The distance from inside to inside of the end blocks was 6250 mm.

Concrete for all the girders was cast simultaneously from a single batch to minimize differences among the three girders. A nominal concrete strength of 31 MPa was used in the design; however test results of four standard concrete cylinders after 28-days provided a compressive strength of 44 MPa with a standard deviation of 2 MPa. Results of an additional four concrete cylinders at the time of testing indicated no change in the concrete strength from the 28-day strength.

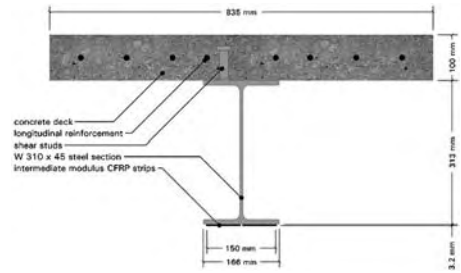

Figure 9. Cross-section of steel–concrete composite girder (CGAB-I).

The first steel–concrete composite girder (CGAB-I) represents one of the three different strengthening configurations considered in this investigation. The strengthening technique for this girder was achieved using the same intermediate modulus CFRP strips used for strengthening monopole (MAB-I). As shown in Figure 10, two strips with a length of 4000 mm were placed side by side to strengthen the middle of the girder. The effectiveness of a spliced connection was investigated by bonding additional 1000 mm strips on either side of the main longitudinal strips and spliced with 400 mm long pieces of the same type of strip. This allowed a development length of 200 mm (or twice the development length determined from the second phase of the study) to transfer the forces from the 4000 mm long strips into the 1000 mm long strips. As a precaution against debonding due to peeling, the strips were wrapped around the flange by wet lay-up of 330 mm unidirectional carbon fiber sheets at the splice locations and at the ends of the 1000 mm long pieces.

Strengthening of composite girder (CGAB-I) was completed immediately following grit blasting the tension flange with an abrasive consisting mainly of angular iron and aluminum silicates produced as a by-product of coal fired power-generating stations. Surface preparation of the strips followed the same procedure used for the monopoles. All the strip ends were detailed with a 20-degree reverse bevel. This type of end treatment has been shown by Adams (2001) to improve the bond performance of the CFRP to steel due to reduction of the stress concentration at these critical locations.

The second composite girder (CGAB-H) will be strengthened using three plys of the high modulus carbon fiber strips similar to the ones used for strengthening monopole (MAB-H). The third composite girder (CGAB-H-PS) will also make use of the high modulus strips, however using one prestressed ply to improve the initial stiffness of the girder. Test results of the last two girders will be presented at the conference.

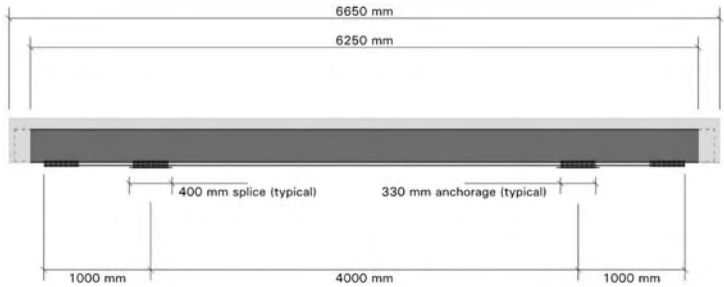

Figure 10. Reinforcement scheme for steel–concrete composite girder (CGAB-I).

2.4.2.2 Test procedure and instrumentation

All composite girders were initially subjected to a four-point flexural bending test with two equal loads applied symmetrically about the center of the girder as shown in Figure 11. The constant moment region was 1000 mm in length and load was applied across the entire width of the composite girder by means of two hollow square steel tubular sections with 25 mm thick neoprene pads placed between the tubes and the finished concrete surface. The girders spanned 6400 mm, center-to-center of the 75 mm thick neoprene support pads. Each girder was loaded to 60 percent of the specified yield stress and unloaded to determine the initial stiffness properties before strengthening. The girder was loaded under displacement control of the actuator at a rate of 0.5 mm/min.

After strengthening, the girder was reloaded to the same mid-span displacement using the same displacement rate to determine the stiffness increase. The girder was reloaded to failure using the same rate before yield, and then increased to 2.0 mm/min after yield.

Instrumentation consisted of wire potentiometers to measure the deflection at the quarter points of the girder and under the load points. Two potentiometers were also positioned at each end of the girder to measure the support settlement and the girder rotation. Strain gauge type displacement transducers were positioned above the top surface of the concrete and underneath the tension flange at each quarter point to determine the extreme fiber strains at these locations. For the strengthened girder, additional foil strain gauges were applied to the surface of the FRP at additional locations near the splice to determine its effectiveness.

Figure 11. Test setup for steel–concrete composite beam (CGAB-I) before strengthening.

2.4.2.3 Results and observations

The load deflection behavior for the three loadings of composite girder (CGAB-I) is shown in Figure 12. The first loading was completed to a load of 155 kN at a net mid-span deflection of 16.1 mm. The second loading, showed the effectiveness in providing stiffness increase to the girder, resulting in a load of 173 kN at the same mid-span deflection or a 12 percent increase compared to the predicted value of 19 percent using moment curvature analysis. No degradation of the stiffness was apparent for the third loading, which became only slightly nonlinear after yielding of the

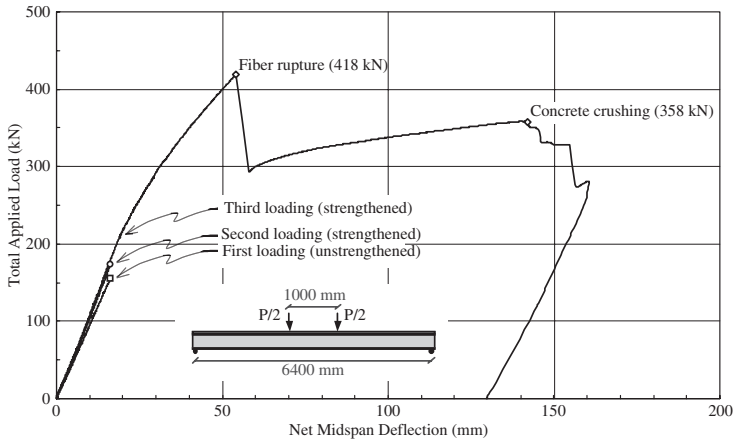

Figure 12. Load-deflection behavior of steel–concrete composite beam (CGAB-I) for three loadings.

Figure 13. Concrete crushing failure and CFRP strip rupture of steel–concrete composite girder (CGAB-I).

steel. The ultimate load, which was recorded prior to rupture of the CFRP strips, was 418 kN. The measured maximum CFRP strip strain, occurring at mid-span of the girder, was 4.50 millistrain. This is slightly less than the ultimate strain of the laminate subjected to pure tension conditions, determined by the manufacturer to be 5.08 millistrain. The load drop at failure was measured to be 42 percent, compared to a predicted value of 38 percent. Failure of the girder occurred at a load of 358 kN due to crushing of the concrete near one of the load points, as shown in Figure 13. This load represents the ultimate load of an unstrengthened girder, since at this point most of the strengthening material was no longer effective. As such, the ultimate load increase was 18 percent compared to an expected value of 24 percent. This difference was due to the higher measured concrete strain than the anticipated value for the girder.

Rupture of the fiber occurred within the constant moment region. Away from the rupture location, the strips partially debonded. The debonding surface was partially between the adhesive and the strip and partially within the strip itself, leaving a thin layer of fiber still bonded to the girder in some locations, as shown in Figure 14. No debonding or other distress was observed from the location of the splice to the ends of the girder, where the splice was wrapped transversely with sheets around the top of the tension flange.

3 CONCLUSIONS

A strengthening system for steel structures has been developed using high modulus CFRP sheets and high or intermediate modulus CFRP strips for providing stiffness increases and strength increases. Resins and adhesives for these materials have been selected. Typically development lengths for the CFRP sheets used are 50 mm, whereas for the strips, the development

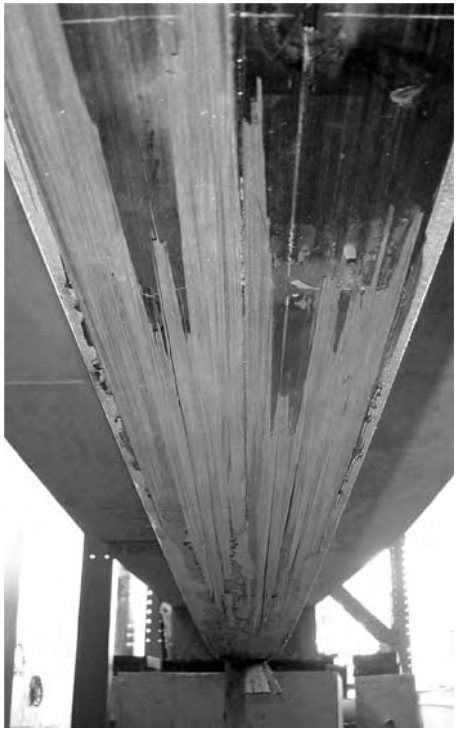

Figure 14. Soffit of girder (CGAB-I) showing interlaminar shear failure of CFRP strip away from midspan.

length varies between 100–200 mm based on the adhesive used. Substantial stiffness increases up to 39 percent at the tip have been shown for the three strengthened monopoles that were tested. The first steel–concrete composite girder tested in this program showed a stiffness increase of 12 percent and an ultimate strength increase of 18 percent. This strengthening technique achieved up to a 42 percent strength increase before rupture of the fibers.

ACKNOWLEDGEMENTS

The authors would like to acknowledge the financial support provided by the National Science Foundation Industry/University Cooperative Research Center and Mitsubishi Chemical for sponsoring this project. The assistance of Mr. Bryan Lanier in completing testing of the steel monopoles is greatly appreciated. Mr. Kirk Stanford and Mr. Mina Dawood are also acknowledged for their assistance in strengthening the first of the steel–concrete composite girders tested in this program.

REFERENCES

Adams, R.D. 2001. The design of adhesively-bonded lap joints: Modelling considerations. In, *A materials and processes odyssey, Proc. 46th intern. SAMPE symp. and exhib. Long Beach, California, 6–10 May 2001*.

Bassetti, Andrea, Alain Nussbaumer, and Manfred, A. Hirt. 2000. Fatigue life extension of riveted bridge members using prestressed carbon fiber composites. In, *Steel structures of the 2000's, ECCS, Istanbul, 11–13 September 2000*.

Brown, A.R.G. 1974. The corrosion of CFRP-to-metal couples in saline environments. In *Proc. 2nd intern. conference on Carbon Fibers, London, 18–20 February, 1974.*

Francis, R. 2000. *Bimetallic corrosion: Guides to good practice in corrosion control*. London: National Physical Laboratory.

Gillespie, John W., Jr., Dennis R. Mertz, William Edberg, and Nouredine Ammar. 1997. Steel girder rehabilitation through adhesive bonding of composite materials. In, *Annual Technical Conference – ANTEC conference proc. Toronto, 27 April-2 May 1997*.

Hollaway, L.C. and J. Cadei. 2002. Progress in the technique of upgrading metallic structures with advanced polymer composites. *Progress in Structural Engineering Materials* 4 (2): 131–148.

McKnight, Steven H., Pierre E. Bourban, John W. Gillespie, Jr., and Vistap Kharbari. 1994. Surface preparation of steel for adhesive bonding in rehabilitation applications. In Kim D. Bashim (ed.), *Infrastructure: New materials and methods of repair, proc. ASCE materials engineering conference*, New York: 13–16 November 1994.

Rajagoplan, G., K.M. Immordino, and J.W. Gillespie, Jr. 1996. Adhesive selection methodology for rehabilitation of steel bridges with composite materials. In, *proc. 11th technical conference of the American Society for Composites, Atlanta, Georgia*, 7–9 October 1996.

Schnerch, David, Kirk Stanford, Emmett A. Sumner, and Sami Rizkalla. 2004. Strengthening steel structures and bridges with high modulus carbon fiber reinforced polymers: Resin selection and scaled monopole behavior, accepted for publication in, *Transportation Research Record*.

Sen, Rajan, Larry Liby, and Gray Mullins. 2001. Strengthening steel bridge sections using CFRP laminates. *Composites: Part B* 32 (4): 309–322.

Tavakkolizadeh, Mohammadreza and Hamid. Saadatmanesh. 2001. Galvanic corrosion of carbon and steel in aggressive environments. *Journal of Composites for Construction* 5 (3): 200–210.

Tavakkolizadeh, M. and H. Saadatmanesh. 2003a. Strengthening of steel–concrete composite girders using carbon fiber reinforced polymer sheets. *Journal of Structural Engineering*. 129 (2): 30–40.

Tavakkolizadeh, M. and H. Saadatmanesh. 2003b. Fatigue strength of steel girders strengthened with carbon fiber reinforced polymer patch. *Journal of Structural Engineering*. 129 (2): 186–196.

Tavakkolizadeh, M. and H. Saadatmanesh. 2003c. Repair of damaged steel–concrete composite girders using carbon fiber-reinforced polymer sheets. *Journal of Composites for Construction*. 7 (4): 311–322.

Tucker, Wayne C. and Richard Brown. 1989. Blister formation on graphite/polymer composites galvanically coupled with steel in seawater. *Journal of Composite Materials* 23 (4): 389–395.

Vatovec, M., P.L. Kelley, M.L. Brainerd, and J.B. Kivela. 2002. Post strengthening of steel members with CFRP. In, *Proc. intern. SAMPE symp. and exhibition, v. 47 II, Long Beach, California, 12–16 May 2002*.

FRP Composites in Civil Engineering – CICE 2004 – Seracino (ed)
© 2005 Taylor & Francis Group, London, ISBN 90 5809 638 6

Bond-slip models for interfaces between externally bonded FRP and concrete

J.G. Teng
Department of Civil and Structural Engineering, The Hong Kong Polytechnic University, Hong Kong, China

X.Z. Lu, L.P. Ye & J.J. Jiang
Department of Civil Engineering, Tsinghua University, Beijing, China

ABSTRACT: An accurate local bond-slip model is of fundamental importance in the modelling of FRP-strengthened RC structures. This paper has two principal objectives: (a) to provide a critical review and assessment of existing bond-slip models to clarify the differences between existing bond-slip models and between these models and test results, a task that does not appear to have been properly undertaken so far; and (b) to present a set of three new bond-slip models of different levels of sophistication which are superior to existing models. A unique feature of the present work is that the new bond-slip models are not based on axial strain measurements or slip measurements on the FRP plate, but instead they are based on the predictions of a meso-scale finite element model, plus appropriate calibration with the experimental results of a few key parameters. Through comparisons with a large test database, the new bond-slip models are shown to provide accurate predictions of both the bond strength (i.e. ultimate load) and the strain distribution in the FRP plate.

1 INTRODUCTION

Over the past decade, external bonding of fibre reinforced polymer (FRP) plates or sheets (referred to as plates only here after for brevity) has emerged as a popular method for the strengthening of reinforced concrete (RC) structures (Teng et al. 2002, 2003a). An important issue in the strengthening of concrete structures using FRP composites is to design against various debonding failure modes, including: (a) cover separation (e.g. Smith and Teng 2002a, 2002b, 2003); (b) plate end interfacial debonding (Smith and Teng 2002a, 2002b); (c) intermediate (flexural or flexural-shear) crack (IC) induced interfacial debonding (Teng et al. 2003b); and (d) critical diagonal crack (CDC) induced interfacial debonding (Oehlers et al. 2003). The behaviour of the interface between the FRP and the concrete is the key factor controlling debonding failures in FRP-strengthened structures. Therefore, for the safe and economic design of externally bonded FRP systems, a sound understanding of the behaviour of FRP-to-concrete interfaces needs to be developed. In particular, a reliable local bond-slip model is of fundamental importance to the accurate modelling and hence understanding of debonding failures in FRP-strengthened RC structures.

In various debonding failure modes, the stress state of the interface is similar to that in a pull test specimen in which a plate is bonded to a concrete prism and is subject to tension (Figure 1). Such pull tests can be realized in laboratories in a number of ways with some variations (Chen and Teng 2001), but the results obtained are not strongly dependent on the set-up as long as the basic mechanics as illustrated in Figure 1 is closely represented (Yao et al. 2004).

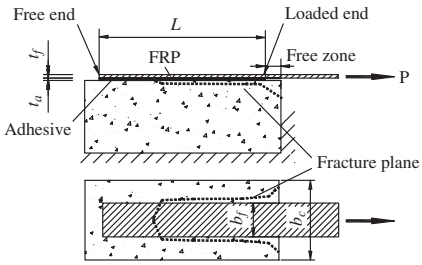

Figure 1. Schematic of pull test.

The pull test not only delivers the ultimate load (also referred to as the bond strength hereafter in this paper) of the FRP-to-concrete interface, but also has been used to determine the local bond-slip behaviour of the interface (Maeda et al. 1997, Brosens and van Gemert 1999, De Lorezis et al. 2001, Nakaba et al.

2001, Wu et al. 2001, Dai and Ueda 2003, Ueda et al. 2003, Savioa et al. 2003, Yuan et al. 2004). Local bond-slip curves from pull tests are commonly determined in two ways: (a) from axial strains of the FRP plate measured with closely spaced strain gauges (e.g. Nakaba et al. 2001); (b) from load–displacement (slip at the loaded end) curves (e.g. Ueda et al. 2003). In the first method, the shear stress of a particular location along the FRP-to-concrete interface can be found using a difference formula, while the corresponding slip can be found by the numerical integration of the measured axial strains of the plate. This method appears to be simple, but in reality cannot produce accurate local bond-slip curves. This is because the axial strains measured on the thin FRP plate generally show violent variations as a result of the discrete nature of concrete cracks, the heterogeneity of concrete and the roughness of the underside of the debonded FRP plate. For example, a strain gauge located above a crack will have a much greater strain than one that sits above a large aggregate particle. The shear stress deduced from such axial strains is thus not reliable although the slip is less sensitive to such variations. Consequently, bond-slip curves found from different tests for nominally the same interface may differ substantially. The second method is an indirect method and has its own problem: the local bond-slip curve is determined indirectly from the load-slip curve, but it is easy to show that rather different local bond-slip curves may lead to similar load–displacement curves.

This paper has two principal objectives: (a) to provide a critical review and assessment of existing bond-slip models, and (b) to present a set of three new bond-slip models. The former part aims to clarify the differences between existing bond-slip models and between these models and test results, a task that does not appear to have been properly undertaken so far. The former part also sets the stage for the latter part in which three new bond-slip models of different levels of sophistication are presented. A unique feature of the present work is that the new bond-slip models are not based on axial strain measurements or slip measurements on the FRP plate, but instead they are based on the predictions of a meso-scale finite element model with numerical smoothing, plus appropriate calibration with the experimental results of a few key parameters. The numerical results allow the use of a smoothing procedure and the smoothing procedure removes the effect of local fluctuations on the predicted local bond-slip curve. It should be noted that in experimental work, such smoothing is impossible because the axial strains in the FRP plate are generally available only at much wider spacings. The experimental calibration of the predicted bond behaviour is brought in through the comparison of key parameters such as the bond strength that are much more reliable than local strain measurements on the FRP plate. Therefore, the present approach for obtaining local bond-slip curves is advantageous over the two existing approaches in that it does not suffer from the random variations associated with strain measurements nor the indirectness of the load-slip curve approach.

2 EXISTING THEORETICAL MODELS FOR BOND BEHAVIOR

2.1 *Bond strength models*

Many theoretical models have been developed from 1996 onwards to predict the bond strengths of FRP-to-concrete bonded joints, generally on the basis of pull test results. These are commonly referred to as bond strength models. Altogether 12 bond strength models have been found in the existing literature, and 8 of them have been examined in detail by Chen and Teng (2001). These 8 models have been developed by Tanaka (1996), Hiroyuki and Wu (1997), van Gemert (van Gemert 1980, Brosens and Gemert 1997), Maeda et al. (1997), Neubauer and Rostasy (1997), Khalifa et al. (1998), Chaallal et al. (1998) and Chen and Teng (2001). The 4 models not covered by Chen and Teng (2001) include three models (Izumo, Sato, and Iso) developed in Japan and described in a recent JCI (2003) report and one developed by Yang

Table 1. Factors considered by existing bond strength models.

	Bond strength model	FRP Concrete strength	Effective plate stiffness	bond length	Width ratio
1	Tanaka (1996)	No	No	No	No
2	Hiroyuki and Wu (1997)	No	No	No	No
3	van Gemert (1980)	Yes	No	No	No
4	Maeda et al. (1997)	Yes	Yes	Yes	No
5	Neubauer and Rostasy (1997)	Yes	Yes	Yes	Yes
6	Khalifa et al. (1998)	Yes	Yes	Yes	No
7	Chaallal et al. (1998)	No	Yes	No	No
8	Chen and Teng (2001)	Yes	Yes	Yes	Yes
9	Izumo (JCI 2003)	Yes	Yes	No	No
10	Sato (JCI 2003)	Yes	Yes	Yes	No
11	Iso (JCI 2003)	Yes	Yes	Yes	No
12	Yang et al. (2001)	Yes	Yes	Yes	No

et al. (2001). Table 1 provides a summary of the key parameters considered by these 12 models, while an assessment of their accuracy is given later in the paper.

2.2 *Bond-slip models*

Despite the difficulty in obtaining local bond-slip curves from pull tests directly, local bond-slip models for FRP-to-concrete interfaces have been developed, based on strain measurements or load-slip curves. Six local bond-slip models available in the existing literature are summarized in the Appendix, where τ (MPa) is the local bond (shear) stress, s (mm) is the local slip, τ_{max} (MPa) is the local bond strength (i.e. the maximum bond/shear stress experienced by the interface), s_0 (mm) is the slip when the bond stress reaches τ_{max}, s_f (mm) is the slip when the bond stress reduces to zero, G_f (N/mm) is the interfacial fracture energy, β_w is the width ratio factor, b_c (mm) and b_f (mm) are the widths of the concrete prism and the FRP plate, E_c, f'_c and f_t (all in MPa) are the elastic modulus, cylinder compressive strength and tensile strength of concrete, E_f (MPa) and t_f (mm) are the elastic modulus and thickness of the FRP plate, E_a (MPa), G_a and t_a (mm) are the elastic and shear moduli and thickness of the adhesive layer, and the shear stiffness of the adhesive layer $K_a = G_a/t_a$. In addition, Sato (JCI 2003) proposed a model which was modified from an existing bond-slip model for rebar-concrete interfaces by replacing the yield strain of steel with the ultimate tensile strain of FRP, based on strain measurements on FRP-strengthened RC tension members. As a result, the model has included the effect of tensile cracks and is not a true local bond-slip model. This model is therefore not further discussed.

Of the 6 models, the recently proposed models by Dai and Ueda (2003) and Ueda et al. (2003) were based on test data which contained specimens with very soft adhesives. Their specimens had a shear stiffness of the adhesive layer K_a being between 0.14 to 1.0 GPa/mm. All other models did not consider such soft adhesives. Numerical results not presented here showed that for values of K_a in the range of about 2.5 GPa/mm to about 10 GPa/mm, the bond-slip curve is little dependent on the shear stiffness of the adhesive layer. A shear stiffness of 5 GPa/mm for the adhesive layer has been used in the present work to represent normal adhesives when it is needed.

3 ACCURACY OF EXISTING THEORETICAL MODELS

3.1 *Bond strength models*

Lu et al. (2004a) recently established a database of 253 pull tests and assessed the accuracy of existing bond strength models. The average value and coefficient of variation of the predicted-to-test bond strength ratios and the correlation coefficient of each model are given in Table 2. More detailed comparisons can be found in Lu et al. (2004a). Table 2 shows that the bond strength models of Maeda et al. (1997), Iso (JCI 2003), Yang et al. (2001) and Chen and Teng (2001) are the better models, with a good average ratio, a reasonably small coefficient of variation and a large correlation coefficient. Based on Tables 1 and 2, Chen and Teng's model is clearly the most accurate model among the 12 existing bond strength models. If Table 2 is examined together with Table 1, it can be found that the accuracy of a model improves as more significant parameters are considered, with the effective bond length being the most influential parameter. All the 4 better-performing models include a definition of the effective bond length. Of the other 8 models, 5 models do not take the effective bond length into consideration.

3.2 *Shapes of bond-slip models*

For a bond-slip model to provide accurate predictions, it needs to have an appropriate shape as well as a correct value for the interfacial fracture energy which is equal to the area under the bond-slip curve. The shape of the bond-slip model determines the predicted

Table 2. Predicted-to-test bond strength ratios: bond strength models.

	Bond strength model	Average Predicted-to-test bond strength ratio	Coefficient of variation	Correlation coefficient
1	Tanaka (1996)	4.470	0.975	0.481
2	Hiroyuki and Wu (1997)	4.290	0.611	−0.028
3	Sato (JCI 2003)	1.954	0.788	0.494
4	Chaallal et al. (1998)	1.683	0.749	0.240
5	Khalifa et al. (1998)	0.680	0.293	0.794
6	Neubauer and Rostasy (1997)	1.316	0.168	0.848
7	Izumo (JCI 2003)	1.266	0.506	0.656
8	Gemert (1980)	1.224	0.863	0.328
9	Maeda et al. (1997)	1.094	0.202	0.773
10	Iso (JCI 2003)	1.087	0.282	0.830
11	Yang et al. (2001)	0.996	0.263	0.766
12	Chen and Teng (2001)	1.001	0.163	0.903
13	Proposed, bilinear model	1.001	0.156	0.908

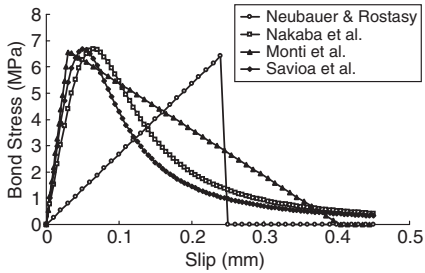

(a) Models by Neubauer and Rostasy, Nakaba et al., Savioa et al. and Monti et al.

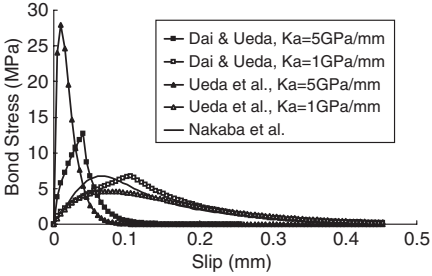

(b) Models by Dai and Ueda, Ueda et al. and Nakaba et al.

Figure 2. Bond-slip curves from existing bond-slip models.

distribution of axial strains in the plate. The predictions of the 6 existing bond-slip models are shown in Figure 2 for an FRP-to-concrete bonded joint with the following properties: $f_c' = 32$ MPa, $f_t = 3.0$ MPa, $b_f = 50$ mm, $b_c = 100$ mm, $E_f t_f = 16.2$ GPa · mm. An FRP-to-concrete width ratio of 0.5 was chosen for this comparison joint as some of the bond-slip models were based on test results of joints with similar width ratios and do not account for the effect of varying this ratio. It can be seen that the shapes of the predicted bond-slip curves differ greatly (Figures 2a and 2b). The fact that the bond stress reduces to zero at the ultimate slip dictates that there exists an effective bond length beyond which an increase in the bond length will not increase the ultimate load.

Existing studies (e.g. Nakaba et al. 2001) have shown that the bon-slip curve should have an ascending branch and a descending branch, similar to the curve from Nakaba et al.'s model shown in Figure 2. Other models with similar shapes include those by Savioa et al. (2003), Dai and Ueda (2003) and Ueda et al. (2003). The bilinear model can be used as an approximation (Yuan et al. 2004), but the linear-brittle model by Neubauer and Rostasy (1999) is unrealistic. Apart from the general shape, three key parameters, including the maximum bond stress, the slip at maximum bond stress and the ultimate slip at zero bond stress, determine the accuracy of the model. It is interesting to note that the models by Nakaba et al. (2001), Savioa et al. (2003) and Monti et al. (2003) are in reasonably close mutual agreement, and the linear-brittle model of Neubauer and Rostasy (1999) predicts a similar maximum bond stress. It may be noted that the model of Savioa et al. (2001) is only a slightly modified version of the model by Nakaba et al. (2001). By contrast, the recent models from Ueda's group (Dai and Ueda 2003, Ueda et al. 2003) may lead to rather unrealistic values for the maximum bond stress when a normal adhesive is assumed. Furthermore, the predictions by Dai and Ueda's (2003) model are very different from those by Ueda et al.'s (2003) model, despite that these two models are based on the same test database. This large discrepancy casts doubt on the reliability of these two models.

3.3 *Interfacial fracture energy of bond-slip models*

Existing research has shown that the bond strength P_u is proportional to the square root of the interfacial fracture energy G_f regardless of the shape of the bond-slip curve (Taljsten 1994, Wu et al. 2002, Neubauer and Rostasy 1997, Yuan et al. 2004), so a comparison of the bond strength is equivalent to a comparison of the interfacial fracture energy. As most bond-slip models do not provide an explicit formula for the ultimate load, the bond strengths of bond-slip models need to be obtained numerically. In the present work, they were obtained by numerical nonlinear analyses using MSC.Marc (2003) with a simple model consisting of 1 mm-long truss elements representing the FRP plate connected to a series of shear springs on a rigid base representing the bond-slip law of the interface. The nonlinear analyses were carried out with a tight convergence tolerance to ensure accurate predictions. The theoretical predictions of the bond strength were compared with the 253 results of Lu et al.'s (2004a) pull test database. The average and coefficient of variation of the predicted-to-test ratios together with the correlation coefficient for each model are given in Table 3. The correlation coefficients for all 6 bond-slip models are larger than 0.8, which demonstrates that the trends of the test data are reasonably well described by the bond-slip models. It is clearly seen that Dai and Ueda's (2003) model provides the most accurate predictions, while other models are either too conservative (Ueda et al. 2003) or too optimistic (all other 4 models). The coefficient of variation of this model is however still larger than that of Chen and Teng's model.

Of the 6 existing bond-slip models, only the model of Dai and Ueda (2003) provides close predictions of the bond strength. It should be noted that although

Table 3. Predicted-to-test bond strength ratios: bond-slip models.

	Bond-slip model	Average predicted-to-test bond strength ratio	Coefficient of variation	Correlation coefficient
1	Neubauer and Rostasy (1999)	1.330	0.209	0.873
2	Nakaba et al. (2001)	1.326	0.231	0.846
3	Savioa et al. (2003)	1.209	0.199	0.847
4	Monti et al. (2003)	1.575	0.164	0.888
5	Dai and Ueda (2003) $K_a = 5000$	1.008	0.228	0.807
6	Ueda et al. (2003) $K_a = 5000$	0.575	0.203	0.821
7	Proposed, precise model	1.001	0.155	0.910
8	Proposed, simplified model	1.001	0.155	0.910
9	Proposed, bilinear model	1.001	0.156	0.908

this model has the smallest average error in the predicted bond strength among the 6 existing bond-slip models, it predicts a grossly incorrect shape for the bond-slip curve with a very high maximum bond stress for normal adhesives (Figure 2b). This means that its predictions for the strain distribution in the FRP plate, the effective bond length, and the bond strength when the bond length is shorter than the effective bond length, will be in serious error. This illustrates the point that the accuracy of a bond-slip model for the bond strength alone is no guarantee of its overall performance.

3.4 *Additional remarks*

The comparisons presented in this section clearly illustrate the need for the development of a more accurate bond-slip model as none of the existing bond-slip models provides accurate predictions of both the shape of the bond-slip curve and the interfacial fracture energy. In the rest of the paper, a novel numerical method for the simulation of bond behaviour is first introduced, followed by the presentation of three new bond-slip models and their verification using test data.

4 MESO-SCALE FINITE ELEMENT MODEL

4.1 *General considerations*

In general, the debonding of FRP from concrete occurs within a thin layer of concrete adjacent to the adhesive layer unless the adhesive is rather weak. The thickness of this concrete layer is about 2∼5 mm. To simulate concrete failure within such a thin layer, with the shapes and paths of the cracks properly captured, the rotating angle crack model (RACM) (Lu et al. 2004b, Rots & Blaauwendraad 1989) should be used if elements with a size comparable to the thickness of the concrete layer are adopted. The RACM however has the major drawback that its constitutive parameters do not have clear physical meanings and have to be empirically derived from pull tests. Therefore, the present study employed a fixed angle crack model (FACM) (Rots and Blaauwendraad 1989) in conjunction with a very fine finite element mesh with element sizes being one order smaller than the thickness of the facture zone of concrete. This approach has the simplicity of the FACM for which the relevant material parameters have clear physical meanings and can be found from well established standard tests, but in the meantime retains the capability of tracing the paths of cracks as deformation progresses. The present model using very small elements is referred to as the meso-scale finite element model. To reduce the computational effort, the three-dimensional FRP-to-concrete bonded joint (Figure 1) was modeled as a plane stress problem using 4-node isoparametric elements. The effect of FRP-to-concrete width ratio was separately considered based on the work of Chen and Teng (2001).

It should be noted that the present model differs from those employed in existing finite element studies of FRP-to-concrete bond behavior in which an interface element is employed to simulate debonding (e.g. Wu and Yin 2003, Wu 2003). In such models, the interface element has to be based on a bond-slip model which needs to be pre-defined. Unlike the present meso-scale finite element model, such models are not true predictive models, although they may be used with test data to verify/identify interfacial behavior.

4.2 *Modeling of FRP*

As the element size adopted in the present work for the concrete prism is within the range of 0.25∼0.5 mm, while the actual thickness of the FRP plate per ply is about 1 mm, each ply was modeled using two layers of plane stress elements if the concrete element size was 0.5 mm, or four layers of plane stress elements if the concrete element size was 0.25 mm. The use of plane stress elements simplified the modeling procedure in terms of proper interaction between FRP and concrete. The FRP plate was treated as

an isotropic material for simplicity with the elastic modulus being that of the longitudinal direction, as only the longitudinal behavior of the FRP plate is of interest here.

4.3 *Modeling of concrete*

When concrete is modeled using small elements (here nearly square elements with sizes of 0.25∼0.5 mm), the element size effect should be considered. According to Bazant and Planas (1997), the compressive behavior of concrete does not depend significantly on element sizes, so the stress–strain relationship proposed by Hognestad (1951) was directly used in the present study to simulate the compressive behavior of concrete.

The tensile behavior of concrete was modeled using the crack band model (Bazant and Planas 1997). The essence of this approach is to control the post-cracking softening branch of the tensile stress–strain curve using the concept of fracture energy in which element sizes are considered. For the linear softening model proposed by Hillerborg, the ultimate tensile strain ε_{cr}^{u} at which the tensile stress decreases to zero is given by (Rots et al. 1985)

$$\varepsilon_{cr}^{u} = 2G_f^I/(b_{cr} f_t) \tag{1}$$

where G_f^I is the fracture energy of concrete; f_t is the tensile strength of concrete; and b_{cr} is the crack band width (ie the element size). According to the model code of CEB-FIP (1993), $G_f^I = \alpha(f_c'/10)^{0.7}$, where f_c' is the cylinder compressive strength of concrete. For concrete of normal aggregate size, $\alpha = 0.03$ (CEB-FIP 1993).

The modeling of the shear behavior of cracked concrete also needs to take into account the effect of element size. Eight different shear models for cracked concrete were compared in the present study, which identified the following model developed at Dalian University of Technology (Kang 1996) in China as the best performing model (Lu et al. 2004c):

$$\tau = (0.543w^{-0.585} + 0.1999)\sqrt{f_c}\,\Delta^{0.72} \tag{2}$$

where w is the crack width and Δ is the relative slip between the two sides of the crack, both in mm. Equation (2) was therefore adopted to model the shear behavior of cracked concrete in the present study.

4.4 *Implementation*

The concrete model described above was implemented into the general purpose finite element package MSC. MARC (2003) as a user subroutine. Before finalizing the finite element model, several issues were first examined for accurate predictions, including the post-peak softening scheme and the element size (Lu et al. 2004c). The final model employed an element size of 0.5 mm, with a linear softening branch for concrete subject to tension.

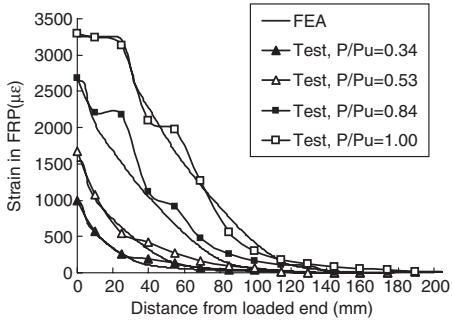

Figure 3. Comparison of strain distributions in the FRP plate.

The finite element model was verified by detailed comparison with the results of 10 pull tests (Lu et al. 2004c). A close agreement was achieved for all 10 specimens. A typical comparison of the distribution of longitudinal strain on the FRP plate for a specimen tested by Wu et al. (2001) is shown in Figure 3.

5 DEBONDING PROCESS

The process of crack propagation in a pull test is difficult to observe in laboratory tests but can be easily predicted by the meso-scale finite element model. It should however be noted that the actual process of debonding is more complicated than is predicted by the present finite element model, as real concrete is an inhomogeneous material. Nevertheless, the present finite results provide useful insight into the failure mechanism.

Figure 4 shows a set of diagrams of the contours of the larger crack strain (total tensile strain minus elastic strain) at each Gauss point for different slip values at the loaded end. The state each diagram represents can be identified by comparing its slip at the loaded end to the slip value s_0 when the local bond strength is reached at the loaded end and s_f when the ultimate load P_u is first attained. For this specimen, $s_0 = 0.0585$ mm and $s_f = 0.154$ mm.

Figure 4a shows that even at a load of 28% of the ultimate load, the concrete under the FRP plate near the loaded end has experienced extensive cracking. The cracks can be classified into 3 types: (a) interfacial shallow cracks; (b) interfacial deep cracks; and (c) micro-cracks within a cracked zone under the FRP

(a) s=0.017mm

(b) s=0.042mm

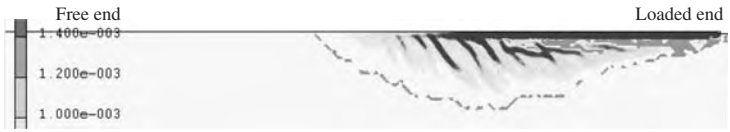

(c) s=0.067mm

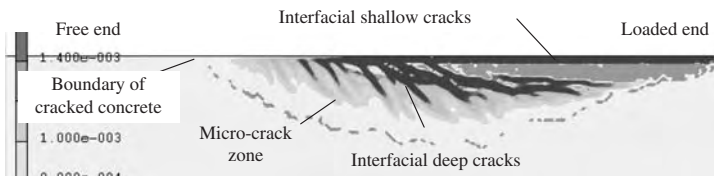

(d) s=0.117mm

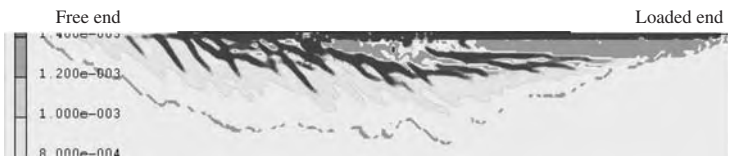

(e) s=0.192mm

Figure 4. Propagation of cracks in concrete.

plate. The same three types of cracks also exist at later stages of deformation as shown in Figures 4b~4e.

The depths of the interfacial shallow cracks are about 0.5~1 mm, whose widths are small and relatively uniform. This thin layer is subject to high tensile stresses as well as high shear stresses as it is directly bonded to the FRP. The depths of the interfacial deep cracks are 2~5 mm. The widths of these cracks are relatively large. They are caused by shear stresses and control the final debonding strength and the slip of the interface. The overall depth of the cracked zone of concrete is about 5~10 mm. They are also caused by shear stresses and some will develop into interfacial deep cracks as deformation further increases.

The above classification of crack patterns also helps explain the failure process. At a low level of loading, the formation of interfacial shallow cracks at angles of 45 ~ 60° to the interface leads to the appearance of small cantilever columns (i.e. meso-cantilevers). With further increases in loading, these cantilevers may grow longer as the shallow cracks grow into deep cracks or may fail if the shear force acting on the

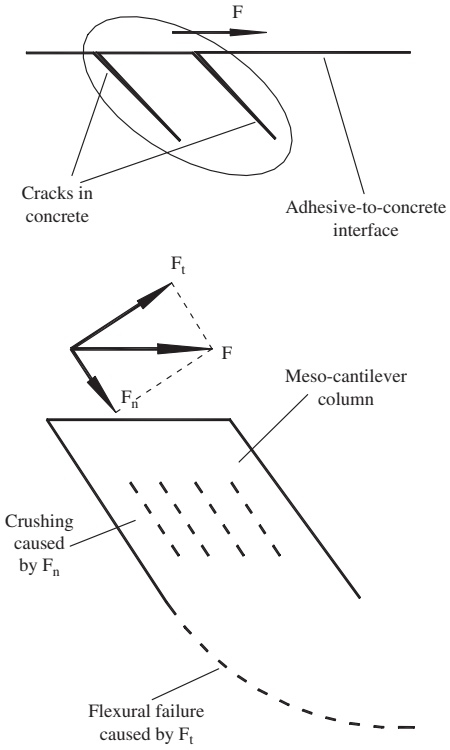

Figure 5. Meso-cantilever column and its failure modes.

cantilever reaches a critical value. The shear force F on the cantilever leads to axial compressive stresses which can cause crushing failure, or flexural tensile stresses at the root which are responsible for flexural failure at the root (Figure 5). It is worth noting that debonding as observed in laboratory tests corresponds to the progressive flexural failure of the meso-cantilevers, except near the loaded end where debonding is mainly due to the crushing of the meso-cantilevers.

6 LOCAL BOND-SLIP MODELS

6.1 *General*

The finite element model, following verification, was deployed to study the local bond-slip behavior, as the stress in and the slip of the FRP plate at any point along the interface under any level of loading can be obtained easily from this model. The interfacial shear stresses can be deduced from the longitudinal stresses in the FRP plate. Due to localization of cracks, the deduced

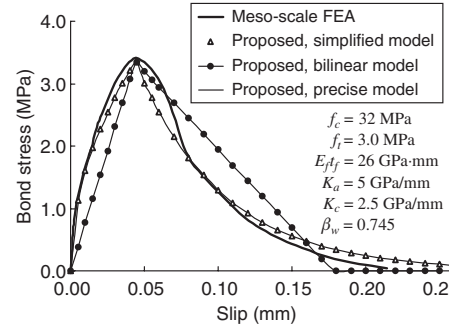

Figure 6. Bond-slip curves.

shear stresses show substantial local fluctuations so a smoothing procedure was applied (Lu et al. 2004a). A typical bond-slip curve obtained from this procedure is shown in Figure 6.

In order to develop bond-slip models, a finite element parametric study was carried out to establish the relationships between various bond parameters and geometric and material parameters. This parametric study showed that the local bond strength τ_{max} and the corresponding slip s_0 are almost linearly related to the tensile strength of concrete f_t, while the total interfacial fracture energy G_f is almost linearly related to $\sqrt{f_t}$. Based on such finite element bond-slip curves and some calibration with a large test database, three bond-slip models were developed (Lu et al. 2004a).

6.2 *Precise model*

The first of the three bond-slip models is referred to as the precise model as it takes explicit account of the effect of the adhesive layer, which is important when the adhesive is much softer than those currently in common use. It has been reported that very soft adhesive layers can increase the interfacial fracture energy (Dai and Ueda 2003). The prediction of the precise model is almost identical to that of the simplified model presented later for normal adhesives.

The precise model describes the ascending and descending branches separately using the following equations:

$$\tau = \tau_{max}\left(\sqrt{\frac{s}{s_0 A} + B^2} - B\right) \quad \text{if } s \le s_0 \tag{3a}$$

$$\tau = \tau_{max}\exp\left[-\alpha(s/s_0 - 1)\right] \quad \text{if } s > s_0 \tag{3b}$$

where $A = (s_0 - s_e)/s_0$, $B = s_e/[2(s_0 - s_e)]$.

The local bond strength τ_{max} and the corresponding slip s_0 are given by

$$\tau_{max} = 1.5\beta_w f_t \tag{3c}$$

$$s_0 = 0.0195\beta_w f_t + s_e \tag{3d}$$

where $s_e = \tau_{max}/K_0$ is the elastic component of s_0 and the FRP-to-concrete width ratio β_w can be expressed as

$$\beta_w = \sqrt{(2.25 - b_f/b_c)/(1.25 + b_f/b_c)} \tag{3e}$$

The initial stiffness of the bond-slip model is defined by

$$K_0 = K_a K_c/(K_a + K_c) \tag{3f}$$

where $K_a = G_a/t_a$ and $K_c = G_c/t_c$. G_c is the shear modulus of concrete and t_c is the effective thickness of concrete whose deformation forms part of the interfacial slip and may be taken as 5 mm unless this thickness is specifically measured during the test.

The parameter α controls the shape of the descending branch and is given by

$$\alpha = \tau_{max} s_0 / \left(G_f - G_f{}^a\right) \tag{3g}$$

where the total interfacial fracture energy can be expressed as:

$$G_f = 0.308\beta_w{}^2 \sqrt{f_t} f(K_a) \tag{3h}$$

while the fracture energy of the ascending branch G_f^a can be calculated as:

$$G_f{}^a = \int_0^{s_0} \tau ds = \tau_{max} s_0 \left[\frac{2A}{3}\left(\frac{1+B^2A}{A}\right)^{3/2} - B - \frac{2}{3}B^3 A \right] \tag{3i}$$

Here, $f(K_a)$ is a function of the stiffness of the adhesive layer. Based on finite element results, for normal adhesives with $K_a \geq 2.5$ GPa/mm, the effect of adhesive layer stiffness on G_f is very small, so it is proposed that $f(K_a) = 1$ for normal adhesives. A precise definition of $f(K_a)$ requires further work. The prediction of the precise model for an example FRP-to-concrete bonded joint is shown in Figure 6 and is seen to compare very well with the prediction of the meso-scale finite element analysis.

6.3 *Simplified model*

The precise model is accurate but complicated. For normal adhesives, a simplified model without a significant loss of accuracy can be easily obtained. This is because the initial stiffness of the bond-slip curve is much larger than the secant stiffness at the peak point when a normal adhesive of a reasonable thickness is used. Therefore, the initial stiffness can be approximated as infinity. Furthermore, the interfacial fracture energy G_f depends little on the stiffness of the adhesive layer. Based on these two simplifications, the following simplified bond-slip model can be obtained:

$$\tau = \tau_{max}\sqrt{\frac{s}{s_0}} \quad \text{if } s \leq s_0 \tag{4a}$$

$$\tau = \tau_{max} e^{-\alpha\left(\frac{s}{s_0}-1\right)} \quad \text{if } s > s_0 \tag{4b}$$

where

$$s_0 = 0.0195\beta_w f_t \tag{4c}$$

$$G_f = 0.308\beta_w{}^2\sqrt{f_t} \tag{4d}$$

$$\alpha = \frac{1}{\frac{G_f}{\tau_{max} s_0} - \frac{2}{3}} \tag{4e}$$

and τ_{max} and β_w can be found from Eqs 3(c) and 3(e).

The bond-slip curve of the example bonded joint predicted by the simplified model is also shown in Figure 6, where it can be seen that there is little difference between this model and the precise model as a normal adhesive is used in this bonded joint. For all practical purposes, the simplified model is sufficiently accurate for normal adhesive joints but much simpler than the precise model.

6.4 *Bilinear model*

Further simplification was made to the simplified model, leading to a simple bilinear model which can be used to derive an explicit design equation for the ultimate load. This bilinear model has the same local bond strength and total interfacial fracture energy, so the ultimate load remains unchanged if the bond length is longer than the effective bond length. This bilinear model is described by the following equations:

$$\tau = \tau_{max} s / s_0 \quad \text{if } s \leq s_0 \tag{5a}$$

$$\tau = \tau_{max}\left(s_f - s\right)/\left(s_f - s_0\right) \quad \text{if } s_0 < s \leq s_f \tag{5b}$$

where $s_f = 2G_f/\tau_{max}$ and τ_{max}, s_0 and β_w can be found using Eqs 3(c), 4(c) and 3(e). The prediction

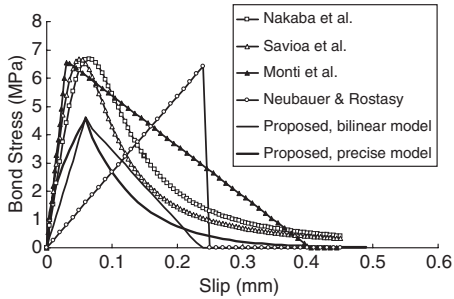

Figure 7. Proposed and existing bond-slip models.

of the bilinear model is also shown in Figure 6 to illustrate the differences between this and the other two models.

The predictions of the proposed models and 4 of the 6 existing models are compared in Figure 7 to show their differences. The two models by Dai and Ueda (2003) and Ueda et al. (2003) are not included in the comparison as they predict grossly incorrect shapes for interfaces with normal adhesives. It can be seen that the shapes of the proposed models are similar to those of models by Nakaba et al. (2001) and Sovioa et al. (2003), while the area under the curves of the proposed models is substantially smaller than those of the other models. The proposed models and the models by Monti et al. (2003) and Savioa et al. (2003) and Nakaba et al. (2001) give similar predictions for the early part of the bond-slip curve, which means that they will yield similar predictions of FRP strains in the early stage of deformation.

7 ACCURACY OF THE PROPOSED MODELS

7.1 *Bond strength*

In Figure 8, the bond strengths predicted using the proposed bond-slip models are compared with the results of the 253 pull tests in Lu et al.'s (2004a) database. It can be seen that the proposed bond-slip models give results in close agreement with the test results and perform better than any other bond-slip models (Table 3). The results of the precise model and the simplified model are almost the same, with the precise model performing very slightly better. Table 2 shows that the prediction of the proposed bi-linear model for the bond strength, which can be given as a closed-form expression (Lu et al. 2004a), performs significantly better than all existing bond strength models except Chen and Teng's (2001) model. For the prediction of bond strength, Chen and Teng's (2001) model is still

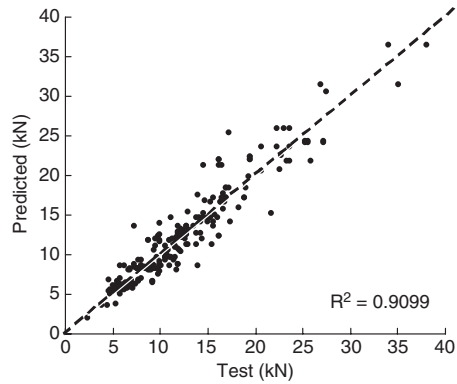

(a) Precise model

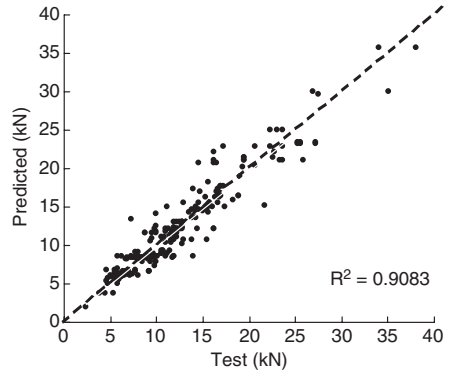

(b) Bilinear model

Figure 8. Bond strengths: test results versus predictions of proposed bond-slip models.

recommended for use in design due to its simple form and good accuracy.

7.2 *Strain distributions in the FRP plate*

The strain distributions in the FRP plate in a pull test can be found from the bond-slip models via a simple numerical approach (Lu et al. 2004a). The comparison of strain distributions between tests and predictions for specimens PG1-22 and PC1-1C2 tested by Tan (2002), specimen S-CFS-400-25 tested by Wu et al. (2001), and specimen B2 tested by Ueda et al. (1999), are shown in Figures 9a∼9d. It is clear that both the precise model and the bilinear model are in close agreement with the test results. The precise model does provide slightly more accurate predictions, which demonstrates that the curved shape of the precise model is closer to the real situation. Additional

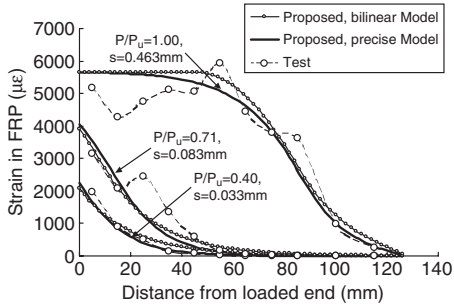

(a) Specimen PG1-22 of Tan (2002)

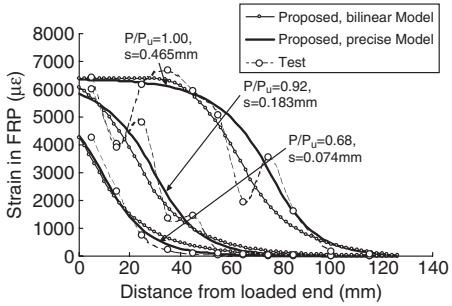

(b) Specimen PC1-1C2 of Tan (2002)

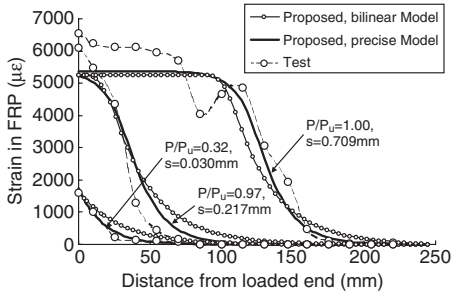

(c) Specimen S-CFS-400-25 of Wu et al. (2001)

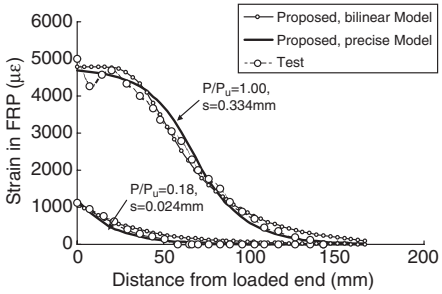

(d) Specimen B2 of Ueda et al. (1999)

Figure 9. Axial strains in FRP plate: test results versus predictions of proposed bond-slip models.

comparisons not reported here for a number of other specimens for which strain distributions are available also showed similar agreement.

Using specimen PG1-22 as an example, the strain distributions predicted with different bond-slip models are compared with the test results in Figure 10. Comparisons are made for the same applied load of $P/P_u = 0.40$ before debonding occurs (Figure 10a) and for the same effective stress transfer length of 125 mm in the stage of debonding propagation (Figure 10b). At a low load in the pre-debonding stage, the predicted strain distribution does not appear to be so sensitive to the bond-slip model used, with several models giving predictions close to the test results (Figure 10), including the proposed precise model and models by Nakaba et al. (2001), Savioa et al. (2003) and Monti et al. (2003). However, in the stage of debonding propagation, the differences between the models and between the model predictions and the test results are large. None of the existing models provides accurate predictions of test results (Figure 10).

8 CONCLUSIONS

This paper has provided a critical review and assessment of existing bond strength models and bond-slip models, and presented a set of three new bond-slip models. The assessment of theoretical models has been conducted using the test results of 253 pull specimens collected from the exiting literature. The development of the new bond-slip models employed a new approach in which meso-scale finite element results are exploited together with test results. Based on the results and discussions presented in this paper, the following conclusions may be drawn.

1. The interfacial debonding process in a pull test can be successfully simulated by a meso-scale finite element model. Such simulations provide not only useful insight into the debonding process but also a tool to predict the local bond-slip curve.
2. Among the 12 existing bond strength models, the model proposed by Chen and Teng (2001) is the most accurate. The bond strength model

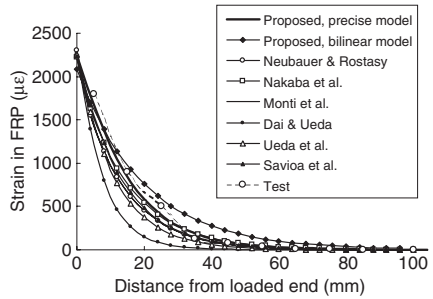

(a) Before debonding stage

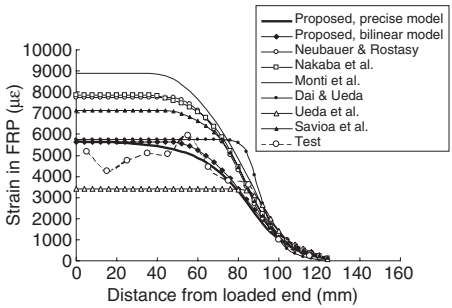

(b) Debonding propagation stage

Figure 10. Axial strains in FRP plate: test results versus predictions of all bond-slip models.

based on the proposed bilinear bond-slip model is as accurate as Chen and Teng's (2001) model but is more complicated. Chen and Teng's model therefore remains the model of choice for use in design.

3. Typical bond-slip curves should consist of an ascending branch with continuous stiffness degradation to the maximum bond stress and a curved descending branch reaching a zero bond stress at a finite value of slip.
4. While a precise bond-slip model should consist of a curved ascending branch and a curved descending branch, other shapes such as a bilinear model can be used as a good approximation. An accurate bond-slip model should provide close predictions of both the shape and the interfacial fracture energy (area under the bond-slip curve) of the bond-slip curve. None of the existing bond-slip models provides accurate predictions of both the shape and the interfacial fracture energy as found from tests.
5. The three new bond-slip models, based on a combination of finite element results and test results, predict both the bond strength and the strain distribution in the FRP plate accurately. These models are therefore recommended for future use in the numerical modelling of FRP-strengthened RC structures.

ACKNOWLEDGEMENTS

The authors gratefully acknowledge the financial support provided by the Research Grants Council of Hong Kong (Project No: PolyU 5151/03E), the Natural Science Foundation of China (National Key Project No. 50238030) and The Hong Kong Polytechnic University through the Area of Strategic Development (ASD) Scheme for the ASD in Mitigation of Urban Hazards.

REFERENCES

Bazant, Z.P. and Planas, J. (1997). *Fracture and size effect in concrete and other quasibrittle materials*, Boca Baton, CRC Press.

Brosens, K. and van Gemert, D. (1997). Anchoring stresses between concrete and carbon fiber reinforced laminates. *Non-Metallic (FRP) Reinforcement for Concrete Structures, Proc. of 3rd International Symposium*, Japan Concrete Institute, Sapporo, Vol. 1, 271–278.

Brosens, K. and van Gemert, D. (1999). Anchorage design for externally bonded carbon fiber reinforced polymer laminates. *Proc. of 4th International Symposium on Fiber Reinforced Polymer Reinforcement for Reinforced Concrete Structures, SP-188, ACI*, Farmington Hills, Michigan, 635–645.

CEB-FIP (1993). *Model Code 90*. Lausanne.

Chaallal, O., Nollet, M.J. and Perraton, D. (1998). Strengthening of reinforced concrete beams with externally bonded fiber-reinforced-plastic plates: Design guidelines for shear and flexure. *Canadian Journal of Civil Engineering*, 25(4), 692–704.

Chen, J.F. and Teng, J.G. (2001). Anchorage strength models for FRP and steel plates bonded to concrete. *Journal of Structural Engineering, ASCE*, 127(7), 784–791.

Dai, J.G. and Ueda, T. (2003). Local bond stress slip relations for FRP sheets-concrete interfaces. *Proc. of 6th International Symposium on FRP Reinforcement for Concrete Structures*, World Scientific Publications, Singapore, 143–152.

De Lorezis, L., Miller, B. and Nanni, A. (2001). Bond of fiber-reinforced polymer laminates to concrete. *ACI Material Journal*, 98(3): 256–264.

Hiroyuki, Y. and Wu, Z. (1997). Analysis of debonding fracture properties of CFS strengthened member subject to tension. *Non-Metallic (FRP) Reinforcement for Concrete Structures, Proc. of 3rd International Symposium*, Japan Concrete Institute, Sapporo, Vol. 1, 284–294.

Hognestad, E. (1951). *A study of combined bending and axial load in reinforced concrete members*, University of Illinois Engineering Experiment Station, Bulletin Series No. 399, Bulletin No.1.

JCI (2003). *Technical report of Technical Committee on Retrofit Technology*, Japan Concrete Institute.

Kang, Q.L. (1996) *Finite element analysis for reinforced concrete*, Beijing: China Water Power Press, 120–126.

Khalifa, A., Gold, W.J., Nanni, A. and Aziz, A. (1998). Contribution of externally bonded FRP to shear capacity of RC flexural members. *Journal of Composites for Construction, ASCE*, 2(4), 195–203.

Lu, X.Z., Teng, J.G., Ye, L.P. and Jiang, J.J. (2004a). Bond-slip models for FRP sheets/plates externally bonded to concrete, submitted for publication.

Lu, X.Z., Tan, Z., Ye, L.P. and Jiang, J.J. (2004b) Finite element analysis for debonding in the interface between FRP sheet and concrete, *Engineering Mechanics*, in press.

Lu, X.Z., Ye, L.P., Teng, J.G. and Jiang, J.J. (2004c). Meso-scale finite element model for FRP sheets/plates externally boned to concrete, submitted for publication.

Maeda, T., Asano, Y., Sato, Y., Ueda, T. and Kakuta, Y. (1997). A study on bond mechanism of carbon fiber sheet. *Non-Metallic (FRP) Reinforcement for Concrete Structures, Proc. of 3rd International Symposium*, Japan Concrete Institute, Sapporo, Vol. 1, 279–285.

Monti, M., Renzelli, M. and Luciani, P. (2003). FRP adhesion in uncracked and cracked concrete zones. *Proc. of 6th International Symposium on FRP Reinforcement for Concrete Structures*, World Scientific Publications, Singapore, 183–192.

MSC. MARC (2003). *User's manual*. MSC. Software Corporation.

Nakaba, K., Toshiyuki, K., Tomoki, F. and Hiroyuki, Y. (2001). Bond behavior between fiber-reinforced polymer laminates and concrete. *ACI Structural Journal*, 98(3), 359–367.

Neubauer, U. and Rostasy, F.S. (1997). Design aspects of concrete structures strengthened with externally bonded CFRP plates. *Proc. of 7th International Conference on Structural Faults and Repair*, ECS Publications, Edinburgh, Scotland, Vol. 2, 109–118.

Neubauer, U. and Rostasy, F.S. (1999). Bond failure of concrete fiber reinforced polymer plates at inclined cracks-experiments and fracture mechanics model. *Proc. of 4th International Symposium on Fiber Reinforced Polymer Reinforcement for Reinforced Concrete Structures, SP-188, ACI*, Farmington Hills, Michigan, 369–382.

Oehler, D.J., Park, S.M. and Mohamed Ali, M.S. (2003). A structural engineering approach to adhesive bonding longitudinal plates to RC beams and slabs. *Composites Part A – Applied Science and Manufacturing*, 34(12), 887–897.

Rots, J.G. and Blaauwendraad, J. (1989). Crack models for concrete: discrete or smeared? Fixed, multi-directional or rotating?, *HERON*, 34(1).

Rots, J.G., Nauta, P., Kusters, M.A. and Blaauwendraad, J. (1985). Smeared crack approach and fracture localization in concrete. *HERON*, 30(1).

Smith, S.T. and Teng, J.G. (2002a). FRP-strengthened RC structures-I: Review of debonding strength models. *Engineering Structures*, 24(4), 385–395.

Smith, S.T. and Teng, J.G. (2002b). FRP-strengthened RC structures-II: Assessment of debonding strength models. *Engineering Structures*, 24(4), 397–417.

Smith, S.T. and Teng, J.G. (2003). Shear-bending interaction in debonding failures of FRP-plated RC beams. *Advances in Structural Engineering*, 6(3), 183–199.

Savioa, M., Farracuti, B. and Mazzotti, C. (2003). Non-linear bond-slip law for FRP-concrete interface. *Proc. of 6th International Symposium on FRP Reinforcement for Concrete Structures*, World Scientific Publications, Singapore, 163–172.

Taljsten, B. (1994). *Plate bonding: strengthening of existing concrete structures with epoxy bonded plates of steel or fiber reinforced plastics*. PhD thesis, Lulea University of Technology, Sweden.

Tan, Z. (2002). *Experimental research for RC beam strengthened with GFRP*. Master degree thesis, Beijing: Tsinghua University (in Chinese).

Tanaka, T. (1996). *Shear resisting mechanism of reinforced concrete beams with CFS as shear reinforcement*. Graduation thesis, Hokkaido University, Japan.

Teng, J.G., Chen, J.F., Simth, S.T. and Lam, L. (2002). *FRP-strengthened RC structures*. UK:John Wiley & Sons.

Teng, J.G., Chen, J.F., Smith, S.T. and Lam, L. (2003a). Behaviour and strength of FRP-strengthened RC structures: a state-of-the-art review. *ICE Proceedings: Structures and Buildings*, 156(1), 51–62.

Teng, J.G., Smith, S.T., Yao, J. and Chen, J.F. (2003b). Intermediate crack-induced debonding in RC beams and slabs. *Construction and Building Materials*, 17 (6&7), 447–462.

Ueda, T., Dai, J.G. and Sato, Y. (2003). A nonlinear bond stress-slip relationship for FRP sheet-concrete interface. *Proc. of International Symposium on Latest Achievement of Technology and Research on Retrofitting Concrete Structures*. Kyoto, Japan, 113–120.

Ueda, T., Sato, Y. and Asano, Y. (1999). Experimental study on bond strength of continuous carbon fiber sheet. *Proc. of 4th International Symposium on Fiber Reinforced Polymer Reinforcement for Reinforced Concrete Structures, SP-188, ACI*, Farmington Hills, Michigan, 407–416.

van Gemert, D. (1980). Force transfer in epoxy-bonded steel-concrete joints. *International Journal of Adhesion and Adhesives*, 1, 67–72.

Wu, Z.S., Yuan, H. and Niu, H.D. (2002). Stress transfer and fracture propagation in different kinds of adhesive joints. *Journal of Engineering Mechanics, ASCE*, 128(5), 562–573.

Wu, Z.S. (2003). Element-level study on stress transfer based on local bond properties. *Technical Report of JCI Technical Committee on Retrofit echnology*, 44–56.

Wu, Z.S. and Yin, J. (2003) Fracture behaviors of FRP-strengthened concrete structures. *Engineering Fracture Mechanics*, 70(10) 1339–1355.

Wu, Z.S., Yuan, H., Hiroyuki, Y. and Toshiyuki, K. (2001). Experimental/analytical study on interfacial fracture energy and fracture propagation along FRP-concrete interface. *ACI International SP-201-8*, 133–152.

Yang, Y.X., Yue, Q.R. and Hu, Y.C. (2001). Experimental study on bond performance between carbon fiber sheets and concrete. *Journal of Building Structures*, 22(3), 36–42 (in Chinese).

Yao, J., Teng, J.G. and Chen, J.F. (2004) Experimental study on FRP-to-concrete bonded joints. *Composites Part B-Engineering*, in press.

Yuan, H., Teng, J.G., Seracino, R., Wu, Z.S. and Yao, J. (2004). Full-range behavior of FRP-to-concrete bonded joints. *Engineering Structures,* 26(5), 553–564.

APPENDIX: EXISTING BOND-SLIP MODELS

Bond-slip model	Ascending branch $s \le s_0$	Descending branch $s > s_0$	τ_{max}	s_0	s_f	β_w	Remarks
Neubauer and Rostasy (1999)	$\tau_{max}\left(\frac{s}{s_0}\right)$	0	$1.8\beta_w f_t$	$\beta_w \times 0.202$		$\sqrt{1.125\frac{2-b_f/b_c}{1+b_f/400}}$	A linear ascending branch and a sudden drop
Nakaba et al. (2001)	$\tau_{max}\left(\frac{s}{s_0}\right)\left[3/\left(2+\left(\frac{s}{s_0}\right)^3\right)\right]$		$3.5f_c'^{0.19}$	0.065			A single curve
Savioa et al. (2003)	$\tau_{max}\left(\frac{s}{s_0}\right)\left[2.86/\left(1.86+\left(\frac{s}{s_0}\right)^{2.86}\right)\right]$		$3.5f_c'^{0.19}$	0.051			A single curve
Monti et al. (2003)	$\tau_{max}\frac{s}{s_0}$	$\tau_{max}\frac{s_f-s}{s_f-s_0}$	$1.8\beta_w f_t$	$2.5\tau_{max}\left(\frac{t_a}{E_a}+\frac{50}{E_c}\right)$	$0.33\beta_w$	$\sqrt{\frac{1.5(2-b_f/b_c)}{1+b_f/100}}$	
Dai and Ueda (2003)*	$\tau_{max}\left(\frac{s}{s_0}\right)^{0.575}$	$\tau_{max}e^{-\beta(s-s_0)}$	$\frac{-1.575\alpha K_a+\sqrt{2.481\alpha^2K_a^2+6.3\alpha\beta^2K_aG_f}}{2\beta}$	$\tau_{max}/(\alpha K_a)$	$\alpha=0.028(E_ft_f/1000)^{0.254}$, $\beta=0.0035K_a(E_ft_f/1000)^{0.34}$ $K_a=G_a/t_a$, $G_f=7.554K_a^{-0.449}(f_c')^{0.343}$		
Ueda et al. (2003)*	$2UG_f(e^{-Us}-e^{-2Us})$ $[U=6.846(E_ft_f)^{0.108}(G_a/t_a/1000)^{0.833}$, $G_f=0.446(E_ft_f)^{0.023}(G_a/t_a/1000)^{-0.352}f_c'^{0.236}]$						A single curve

*: regressed from specimens with very soft adhesive layers.

FRP Composites in Civil Engineering – CICE 2004 – Seracino (ed)
© 2005 Taylor & Francis Group, London, ISBN 90 5809 638 6

New shear bond model for FRP–concrete interface – from modeling to application

T. Ueda & J.G. Dai
Hokkaido University, Sapporo, Japan

ABSTRACT: This paper presents a local bond stress–slip model for FRP–concrete interface (shear bond model). The shear bond model was derived based on a FRP stress–slip relationship at loaded end of pullout bond test, so that necessary measurement was simplified and the data scatter problem was minimized. The shear bond model needs only two material constants, interfacial fracture energy and interfacial ductility factor. The shear bond model was expanded to be bond stress–slip–FRP strain model to express cases with a short bond length. Both original and expanded shear bond models consider effects of mechanical properties of FRP, adhesive materials and concrete substrate. Besides the shear bond model, the prediction formula for interfacial fracture energy, effective bond length and bond strength for given anchorage length are presented.

1 INTRODUCTION

One of the unique features of externally bonding as strengthening is debonding (or delamination) as a failure mode. Debonding is practically less likely to be a cause of failure in conventional concrete structures although bonding between concrete and reinforcement is a primary concern. This fact clearly shows that model for the externally bonded material-concrete interface is vital to predict structural behavior of concrete structures strengthened by external bonding.

External bonding with FRP is a commonly applied strengthening method. There are various types of fibers and impregnating/adhesive resins, whose mechanical properties, such as strength and stiffness are quite different. In the past there was not enough study on bond model for FRP–concrete interface, which is applicable to various materials. Especially studies on effect of mechanical properties of resins are limited. In this paper, a new model for shear bond of FRP–concrete interface, in which material properties of FRP (fiber and impregnating resin), adhesive resin and concrete substrate are all considered together with interface fracture energy, is presented.

Major obstacles in experimentation for interface bond are the necessity of arrangement of many strain gages in a small interval and scatter in measured strains. In this paper a completely new approach for identifying a local bond-slip model is presented to eliminate those obstacles. Based on the presented shear bond model, prediction formula for effective bond length and pullout bond strength for a given bond length are presented.

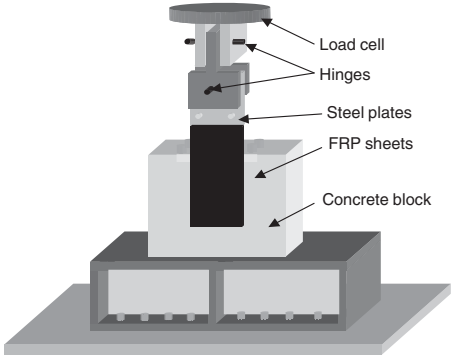

Figure 1. Pullout test setup.

Tension bond (or Mode I fracture) model and a combined tension and shear (or mixed Mode fracture) model are not discussed in this paper but in the authors' other papers (Dai et al. 2004a, b).

2 EXPERIMENTAL OUTLINE

2.1 *Test setup*

A single-lap pullout test setup (see Fig. 1), in which FRP sheets with a width of 100 mm were externally bonded to a concrete block with a size of 400 × 200 × 400 mm by wet-lay-up bonding system,

Table 1. Mechanical properties of FRP materials.

Fiber	Type	ρ (g/m^3)	f_t (MPa)	E_f (GPa)	t_f (mm)	ε_u (%)
Carbon	FTS-C1-20	200	3550	230	0.11	1.5
Aramid	At-90	530	3030	84	0.38	2.4
Glass	FTS-GE-30	300	1500	74	0.12	2.1

Note: ρ = fiber density; f_t = tensile strength; E_f = elastic modulus; t_f = thickness; ε_u = fiber fracturing strain; FTS-C1-20 and FTS-GE-30 sheets were offered by Nippon Steel Composite Co. Ltd; AT-90 was offered by Nippon Aramid Co. Ltd.

Table 2. Material properties of adhesives.

Types of adhesives	ρ (g/cm^3)	E (GPa)	v	f_t (MPa)	f_b (MPa)
CN-100	1.13	0.39	0.45	11.8	3.7
SX-325	1.15	1.0	0.38	15.9	29.6
FR-E3P	1.17	2.41	0.38	44.7	39.0
FP-NS (Primer)	1.16	2.45	0.38	48.1	39.0

Note: ρ = density; E = elastic modulus; v = Poisson's ratio; f_t = tensile strength; f_b = bending strength.

was applied in the study. A bond length of 330 mm was applied in order to observe a complete peeling-off process. In order to avoid local damage of the concrete block, an un-bonded length (50 mm) was set by using vinylon tape to separate the concrete surface from the FRP sheets.

During the pullout test, displacement control loading was applied. LVDT transducers were set at both the loaded and free ends of the bond area to obtain relative slips between the FRP sheets and concrete. Strain gages were mounted on the FRP sheets to measure FRP sheet strain distributions.

2.2 *Materials used*

Four types of adhesives (including one type of primer) and three types of FRP sheets were applied. The mechanical properties of adhesives and FRP sheets and the information of manufacturers are shown in Table 1 and Table 2 respectively. Due to the obvious non-linearity of the softer adhesive (see the tensile stress–strain relationships of adhesives in Fig. 2), the initial elastic modulus of adhesives is defined as the average secant modulus for the strain between 0.0005 and 0.0025 according to JIS K7113 (1995) "Testing Method for Tensile Properties of Plastics." Since both the elasticity modulus and thickness of bond layer affect the interfacial bond properties (Lee et al. 1999, Tripi et al. 2000, Dai et al. 2002), the property of bond

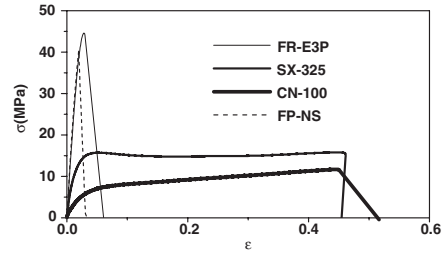

Figure 2. Tensile stress–strain relations of adhesives.

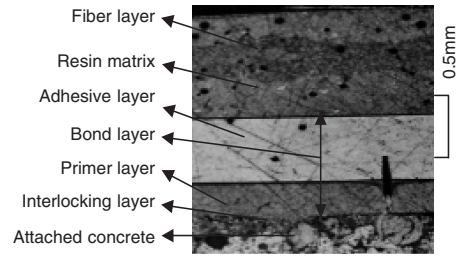

Figure 3. Microscopic observation of FRP sheets after pullout test (CR3L1).

layer can be quantified using its shear stiffness (shear modulus divided by thickness) as follows:

$$\frac{G_a}{t_a} = \frac{G_p \cdot G_{ad}}{G_p t_{ad} + G_{ad} t_p} \quad (1)$$

where $G_p = \frac{E_p}{2(1+\nu_p)}$, $G_{ad} = \frac{E_{ad}}{2(1+\nu_{ad})}$, G_a is the shear modulus of adhesive layer; t_a is the thickness of adhesive layer; E_P, E_{ad}; t_p, t_{ad} and v_p, v_{ad} are the elastic modulus, thickness and Poisson's ratio of primer and adhesive layer respectively. As indicated in Equation 1, the shear stiffness of bond layer is that of a combined layer of primer and adhesive.

To obtain the accurate geometrical information of the adhesive layer, the FRP sheets together with attaching thin concrete layer were cut out after the pullout tests. Then the thickness of primer and adhesive layer was measured using a microscope (see Fig. 3), and then the shear stiffness of adhesives was calculated with Equation 1 (see the values in Table 3). Ready-mixed concrete with a tested compressive strength of 35 MPa was prepared in order to keep a same strength for all the specimens.

To avoid reducing the tensile strength of FRP sheets due to a resin matrix with low elasticity modulus, the

Table 3. Details of specimens and pullout bond test results.

Specimen codes*	G_a/t_a (GPa/mm)	$E_f t_f$ (kN/mm)	•• (ε)	B mm^{-1}	G_f (N/mm)	R^2	τ_{max} (MPa)	s_{max} (mm)	P_{max} kN (Exp.)	P_{max} kN (Ana.)	P_{max} (Ana./Exp.)	Failure mode*
CR1L1	0.97	25.3	0.00904	10.79	1.034	0.985	5.58	0.064	23.4	22.9	0.98	CF
CR1L1	1.14	25.3	0.01046	10.44	1.384	0.996	7.22	0.066	23.1	26.5	1.15	CF
CR1L1	1.14	25.3	0.00908	10.38	1.043	0.982	6.80	0.053	24.9	22.3	0.92	CF
CR1L2	0.97	50.6	0.00664	10.01	1.115	0.991	5.58	0.069	33.5	33.6	1.00	CF
CR1L2	1.14	50.6	0.00682	11.34	1.177	0.992	6.67	0.061	39.3	34.5	0.88	CF
CR1L2	1.14	50.6	0.00732	9.04	1.356	0.991	6.13	0.077	39.3	37.0	0.94	CF
CR1L3	0.97	75.9	0.00509	10.91	0.983	0.975	5.36	0.064	42.9	38.6	0.90	CF
CR1L3	1.14	75.9	0.00554	11.13	1.165	0.987	6.47	0.057	38.4	42.1	1.10	CF
CR1L3	1.14	75.9	0.00525	12.25	1.042	0.987	6.40	0.062	38.4	39.7	1.03	CF
CR1L3	1.14	75.9	0.00496	11.69	0.930	0.994	5.45	0.059	36.9	37.5	1.02	CF
AR1L1	0.99	18.6	0.01260	9.83	1.476	0.986	7.26	0.070	25.5	23.4	0.92	CF
AR1L2	0.97	31.8	0.00955	9.47	1.450	0.979	6.87	0.073	33.6	30.4	0.90	CF
AR1L3	0.97	73.6	0.00606	10.18	1.351	0.990	6.88	0.068	39.9	44.6	1.12	CF
GR1L1	0.97	8.7	0.01443	9.66	NA	0.989	NA	0.072	13.5	NA	NA	FF
GR1L3	0.97	32.0	0.00848	8.12	1.444	0.995	4.88	0.062	28.6	27.1	0.95	CF
GR1L5	0.97	43.7	0.00732	11.13	1.171	0.980	6.52	0.062	33.4	32.0	0.96	CF
CR2L1	0.49	25.3	0.01124	6.24	1.598	0.993	4.99	0.111	28.1	28.4	1.01	CF
CR2L2	0.49	50.6	0.00809	5.66	1.656	0.997	4.68	0.123	43.2	40.9	0.95	CF
CR2L3	0.49	75.6	0.00596	6.71	1.343	0.993	4.51	0.103	47.4	45.1	0.95	CF
AR2L3	0.49	73.6	0.00668	6.26	1.642	0.989	5.14	0.111	47.1	49.2	1.04	CF
GR2L3	0.49	32.0	0.00869	7.70	1.208	0.986	4.65	0.090	31.0	27.8	0.90	CF
CR3L1	0.20	25.3	0.01791	2.07	NA	0.984	NA	0.335	31.8	NA	NA	FF
CR3L2	0.20	50.6	0.00980	2.39	2.430	0.976	2.91	0.290	47.7	49.6	1.04	CF
CR3L3	0.20	75.6	0.00732	3.06	2.205	0.993	2.81	0.227	57.6	55.3	0.96	CF
AR3L3	0.20	73.6	0.00923	2.24	3.135	0.991	3.52	0.309	60.9	67.9	1.12	CF
GR3L3	0.20	26.2	0.01820	1.70	NA	0.996	NA	0.408	33.4	NA	NA	FF

Note: (1) For specimen codes, first letter/C: carbon, A: aramid, G: glass; R + number/R1: FR-E3P, R2: SX-325, R3: CN-100; L + number/L1: 1 layer of sheet, L2: 2 layers, L3: 3 layers; (2) For failure mode, CF: concrete failure, FF: FRP fracture.

resins used in FRP layers and the adhesive layers were different. Adhesive FR-E3P, which is commercially used as the resin matrix and the bonding adhesive of carbon fiber sheets, was applied as the resin matrix of FRP in all specimens. The primer FP-NS was used in the bonding procedures of all specimens. After the adhesive bond layer was cured for 24 hours, resin FR-E3P was used to form FRP layers as shown in Figure 3. The details of the specimens can be found in Table 3.

3 SHEAR BOND MODEL

3.1 *Bond stress–slip model*

3.1.1 *Conventional methodology for modeling*

Usual method for obtaining local bond stress (τ_i) and slip (s_i) is to use the following equations:

$$\tau_i = \frac{E_f t_f (\varepsilon_i - \varepsilon_{i-1})}{\Delta x} \tag{2}$$

$$s_i = \frac{\Delta x}{2}(\varepsilon_0 + 2\sum_{j=1}^{i-1}\varepsilon_j + \varepsilon_i) \tag{3}$$

where τ_i is an average interfacial bond stress in section i; ε_i and ε_{i-1} are strain values of i th and $i-1$ th gages mounted on a FRP sheet respectively; E_f and t_f are the elastic modulus and thickness of the FRP sheet respectively; Δx is the length of each section; s_i is a local slip between FRP sheets and concrete at section i; ε_0 is the strain of FRP sheet at the free end of bond area; $\varepsilon_j (j = 1, i)$ is the strain value of j th gage mounted on the FRP sheet.

Applying Equations 2 and 3, the local $\tau-s$ relationships at different locations from the loaded end in a pullout test can be derived as shown in Figure 4. Obviously, fairly big irregular differences among those $\tau-s$ relationships are observed at different interfacial locations. The similar experimental observations can be found in other literatures (Yoshizawa et al. 2000, Nakaba et al. 2001, Sato et al. 2001). This big variation is probably a main reason why different shapes of bond stress–slip relationships were proposed or why researchers prefer a simplified bilinear bond stress–slip model even though numerous of pullout bond tests for FRP sheets–concrete interfaces have indicated that more reasonable configurations are needed. All the factors such as distribution of fine and coarse

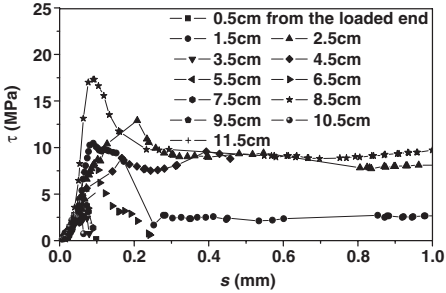

Figure 4. Calculated local bond stress–slip relationships at different locations from loaded end (specimen CR1L1).

aggregates along the concrete surface, concrete layer attached to FRP sheets after the initial debonding, and local bending of FRP sheets due to imperfect concrete surface treatment can contribute to the final scattering.

3.1.2 *New methodology and model*

It is assumed as for reinforcing bar in concrete (Shima et al. 1987) that at any location (x) of an FRP sheet–concrete bond interface under the boundary condition of zero free end slip, which can be easily attained using a long bond length, there exists a unique local bond stress–interfacial slip ($\tau - s$) relationship and a unique FRP sheet strain–interfacial slip relationship ($\varepsilon - s$). The latter can be expressed as follows:

$$\varepsilon = f(s) \tag{4}$$

A first order differential calculus of ε to x yields the following equation:

$$\frac{d\varepsilon}{dx} = \frac{df(s)}{ds} \cdot \frac{ds}{dx} = \frac{df(s)}{ds} \cdot \varepsilon = \frac{df(s)}{ds} \cdot f(s) \tag{5}$$

Therefore, for FRP sheet–concrete interfaces, the interfacial bond stress can be expressed as:

$$\tau = E_f t_f \cdot \frac{d\varepsilon}{dx} = E_f t_f \cdot \frac{df(s)}{ds} \cdot f(s) \tag{6}$$

It can be seen from Equation 4 to 6 that the bond stress-slip relationship can be determined if the relationship between local strain of FRP sheets and local slip is defined. During the pullout test, the pullout forces and the slips at the loaded end can be measured easily and accurately through load cell and displacement transducer. As a result, the relationship between the strains of FRP sheets and the slips at the loaded end, in other word, the function of $f(s)$ can be obtained directly from the simple pullout tests and then $\tau - s$ relationship can be obtained without arranging many strain gages.

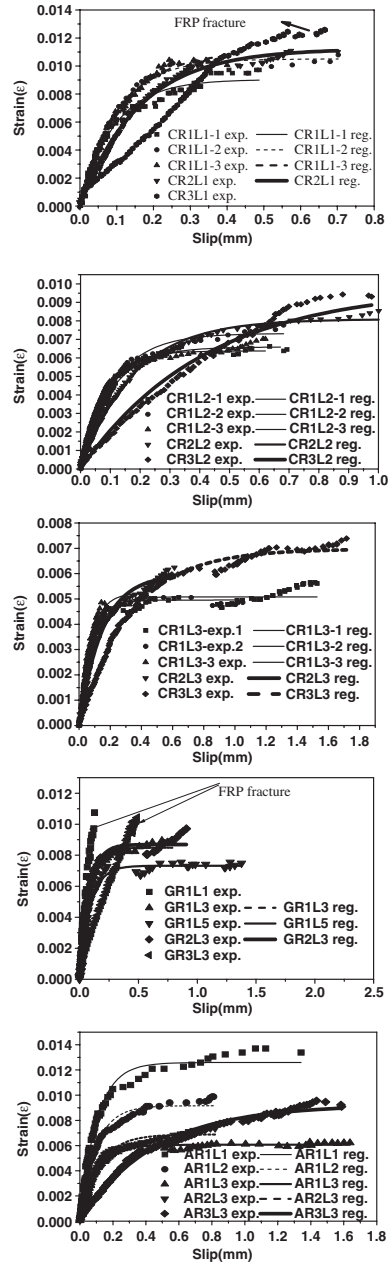

Figure 5. Experimental and regressed FRP sheet strain–slip curves at loaded ends.

Figure 5 shows the experimentally observed relationships between the strains of FRP sheets and the interfacial slips at the loaded ends of FRP sheet–concrete interfaces, which include cases of different FRP stiffnesses, different adhesive types and different types of FRP materials. It is found that an exponential expression (see Eq.7) can fit the experimental results very well (the values of correlative factors R^2 between the strains in FRP sheets and the slips at loaded ends lie between 0.975 and 0.997 for all specimens as shown in Table 3).

$$\varepsilon = f(s) = A(1-\exp(-Bs)) \tag{7}$$

where A and B are experimental parameters (the values for each specimen are given in Table 3). Substituting Equation 7 into Equation 6, the bond stress–slip relationship can be obtained as follows:

$$\tau = A^2 B E_f t_f \exp(-Bs)(1-\exp(-Bs)) \tag{8}$$

Based on the above-mentioned process, all the found bond stress–slip relationships derived from pull-out tests are shown in Figure 6. When the FRP fracture happens, the $\tau - s$ relationships are excluded because the peeling off process is interrupted and the interfacial fracture energy cannot be calculated correctly.

3.1.3 *Interfacial bond related parameters*
Interfacial fracture energy G_f is defined as:

$$G_f = \int_0^\infty \tau ds \tag{9}$$

By substituting Equation 8 into Equation 9, the following equations can be obtained:

$$G_f = \frac{1}{2} A^2 E_f t_f \tag{10}$$

Then the following expression for A is obtained:

$$A = \sqrt{\frac{2G_f}{E_f t_f}} \tag{11}$$

For FRP sheets bonded to concrete, the theoretical maximum interfacial pullout force can be expressed as follows:

$$P_{\max} = b_f E_f t_f \varepsilon_{\max} = b_f E_f t_f \lim_{s\to\infty} A(1-\exp(-Bs)) = b_f E_f t_f A \tag{12}$$

where b_f is bond width of FRP sheets; and $\varepsilon_{\max}$ is the maximum strain of FRP sheets corresponding to the maximum pullout force.

The comparisons between the calculated maximum pullout forces based on the regressed A (see Table 3) and the experimental ones are shown in Figure 7.

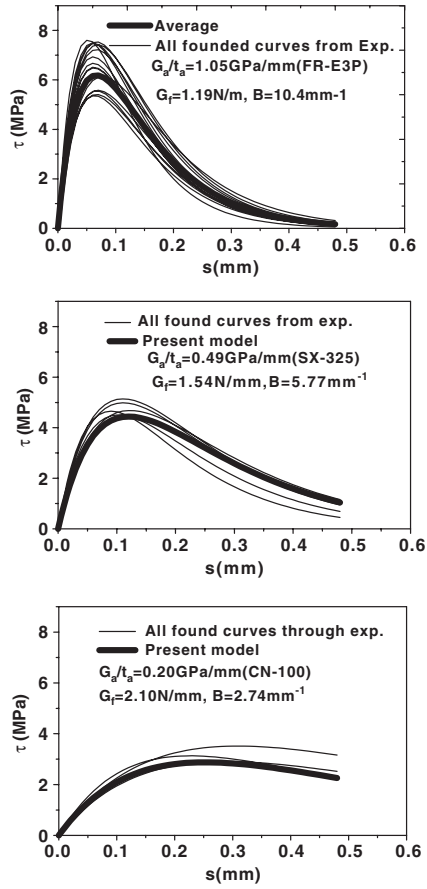

Figure 6. Experimentally found bond stress–slip relationships.

It is seen that good agreement can be reached. The agreement implies that the theoretical maximum interfacial pullout force predicted based on the assumption of zero end slip boundary condition can be reached using the bond length of 330 mm in the experiment.

With the substitution of Equation 11, Equation 12 can become:

$$P_{\max} = b_f E_f t_f A = b_f \sqrt{2E_f t_f G_f} \tag{13}$$

Based on energy method or force equilibrium method, Equation 13 was derived by many researchers (Täljsten et al. 1997, Yuan et al. 2001) and now is applied widely in predicting the ultimate bond forces of FRP sheet–concrete interfaces. And also, through

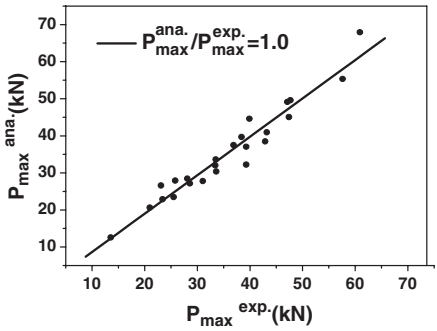

Figure 7. Comparison between analytical and experimental maximum pullout forces.

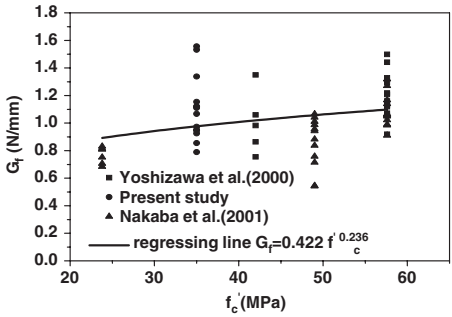

Figure 8. Effects of concrete strength on interfacial fracture energy.

experimental study, the authors found that Equation 13 is applicable for all types of FRP materials regardless of differences in their elastic modulus (Dai et al. 2002, Dai & Ueda 2003).

Shear stress flows due to interfacial bond stresses can spread to concrete in the vicinity of both sides of FRP sheets if the FRP sheets are attached to concrete whose width is wider than theirs. That makes the effective interfacial contact areas wider than the actual ones because interfacial debonding failure occurs in a thin concrete surface layer instead of FRP-adhesive interface. The authors observed effects of bond width of FRP sheets (from 1 cm to 20 cm) on the average bond strength in the previous studies (Sato et al. 2001). The experimentally obtained bond force per unit width of FRP sheets (P_{max}/b_f) is generally high when the width of FRP sheets used in the tests is narrow. When the bond width exceeds 10 cm, the value of P_{max}/b_f becomes almost constant. An additional width $2\Delta b_f$ (Δb_f is taken as 3.7 mm) can be added to the original bond width b_f for calculating the interfacial bond strength and quantifying the bond width's effects (Sato et al. 2001). Here a same $2\Delta b_f$ is introduced into Equation 13. Through that the back-calculated G_f obtained from P_{max} will not depend on the FRP sheet width used in the test. Therefore Equation 13 can be modified as follows:

$$P_{max} = (b_f + 2\Delta b_f)\sqrt{2E_f t_f G_f} \tag{14}$$

Equation 14 shows that the increase in FRP sheet stiffness ($E_f t_f$) and interfacial fracture energy enhances the interfacial load carrying capacity (P_{max}). However, efficiency of FRP sheet strength ($\varepsilon_{max}/\varepsilon_u$, ε_u is fracturing strain) is not improved by FRP stiffness, since ε_{max} is expressed as follows (see Equations 11 and 12):

$$\varepsilon_{max} = A = \sqrt{\frac{2G_f}{E_f t_f}} \tag{15}$$

With Equations 8 and 11, the interfacial $\tau - s$ relationship can be rewritten as:

$$\tau = 2BG_f(\exp(-Bs) - \exp(-2Bs)) \tag{16}$$

Slip s_{max} corresponding to the maximum bond stress τ_{max}, at which $d\tau/ds = 0$, can be determined as follows:

$$s_{max} = \ln 2 / B = 0.693 / B \tag{17}$$

By substituting Equation 17 into Equation 16, the maximum bond stress τ_{max} can be obtained as well:

$$\tau_{max} = 0.5BG_f \tag{18}$$

For every specimen in the present study, the material constant B and the interfacial fracture energy G_f can be obtained according to the processes proposed in 3.1.2 and 3.1.3 (see the results in Table 3). Then the values of τ_{max} and s_{max} are calculated and shown in Table 3. For the normal adhesive (FRP- E3P), Nakaba et al. (2001) observed experimentally that the values of s_{max} lie between 0.052 and 0.087 mm, with which the analytical results (0.053–0.077 mm) based on the present method show good agreement.

The interfacial fracture energy G_f is affected by the properties of concrete, adhesives and the FRP stiffness. It has been mentioned that, in the case of long bond lengths, G_f can be calculated based on either the value of A obtained from the regression analysis of the FRP sheet strain–slip curves at loaded ends (see Equation 7) or directly from the ultimate pullout forces (see Equation 13). Therefore, the authors collected more experimental data of the ultimate pullout forces published by other researchers (Nakaba et al. 2001, Yoshizawa et al. 2000) to evaluate the effects of concrete strength and FRP stiffness on G_f. Only those data with bond lengths exceeding 300 mm has

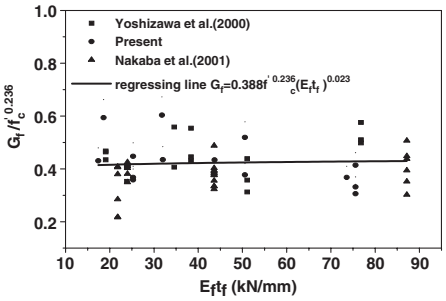

Figure 9. Effects of FRP stiffness on interfacial fracture energy.

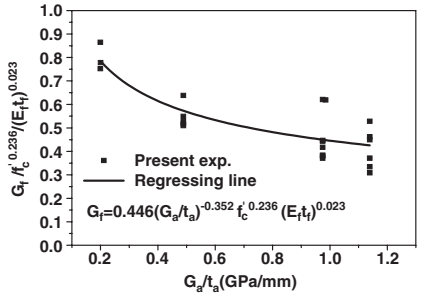

Figure 10. Effects of adhesive shear stiffness on interfacial fracture energy.

been selected. Through Equation 14 the effects of bond width on the G_f can be eliminated. Figures 8, 9 and 10 show the effects of concrete strength, FRP stiffness and adhesive properties on the G_f respectively. Since no researchers has studied the effects of adhesives, Figure 10 only shows the test results of only the authors' study in which the mechanical property of adhesives is provided. It can be found that the shear stiffness of adhesive layer affects the interfacial fracture energy most (see Fig. 10). The effect of the concrete strength is much less than that of the adhesive (see Fig. 8) but slightly greater than that of the FRP stiffness (see Fig. 9). Adhesives with lower shear stiffness can improve the interfacial fracture energy significantly due to their good toughness (Dai et al. 2002, Dai and Ueda 2003). Through regression analysis, the expression for the interfacial fracture energy can be obtained as follows:

$$G_f = 0.446(G_a/t_a)^{-0.352} f_c^{0.236}(E_f t_f)^{0.023} \quad (19)$$

The values of another interfacial parameter B are obtained from the regression analysis of the FRP

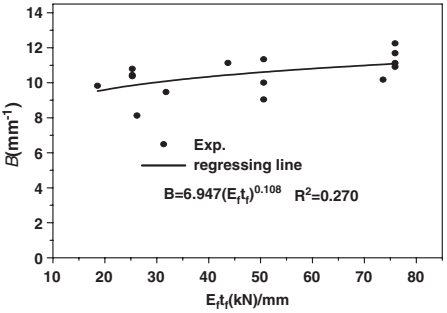

Figure 11. Effects of FRP stiffness on B.

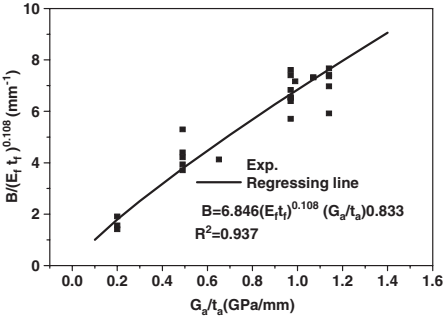

Figure 12. Effects of adhesive shear stiffness on B.

sheet strain–slip curves at the loaded end of each specimen in the Authors' study. The effects of FRP stiffness and adhesives on B are shown in Figures 11 and 12 respectively. It can be seen that B increases insignificantly with the FRP stiffness (see Fig. 11) whereas increases remarkably with the shear stiffness of adhesive layer (see Fig. 12). Through a similar regressing way, the expression for B can be obtained as follows:

$$B = 6.846(E_f t_f)^{0.108}(G_a/t_a)^{0.833} \quad (20)$$

Therefore, the $\tau-s$ relationships of FRP sheet–concrete interfaces with different properties of FRP, adhesives and concrete strength can be determined through the two calibrated material parameters G_f (Eq. 19) and B (Eq. 20).

3.1.4 *Effects of factors on $\tau-s$ relationship*

Figure 13 shows the effects of FRP stiffness on the $\tau-s$ relationships. It can be seen that both the initial stiffness of the $\tau-s$ relationships and the maximum bond stresses increase slightly with the increasing of FRP stiffness. Similar effects of FRP stiffness on the

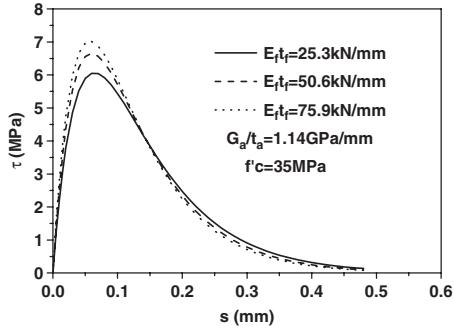

Figure 13. Effect of FRP stiffness on bond stress–slip relationship.

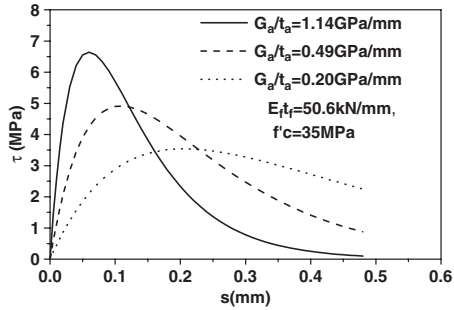

Figure 14. Effect of adhesive shear stiffness on bond stress–slip relationship.

maximum bond stress were included in the models proposed by Sato et al. (2001) and Lorenzis et al. (2001) in different extent. Tripi et al. (2000) also found that relative displacements between the FRP sheets and concrete are slightly affected by the elastic modulus of the sheets in their moiré interferometric analysis. The effects of FRP stiffness on the interfacial stiffness and maximum bond stress may be caused by the different strain condition in the thin concrete layer next to the adhesives. In the case of using same adhesives, higher FRP stiffness brings lower strain level in the concrete.

Figure 14 gives a group of $\tau-s$ relationships with different shear stiffness of adhesives but the same FRP stiffness (50.6 kN/mm) and concrete strength (35 MPa). The comparisons between the experimental $\tau-s$ relationships and predicted ones in cases of using adhesives (FR-E3P, SX325 and CN-100) with different stiffnesses are shown in Figure 6. It is obvious that the maximum interfacial bond stress increases with the shear stiffness of adhesives. When the FRP stiffness is same, this increase is caused by high strain

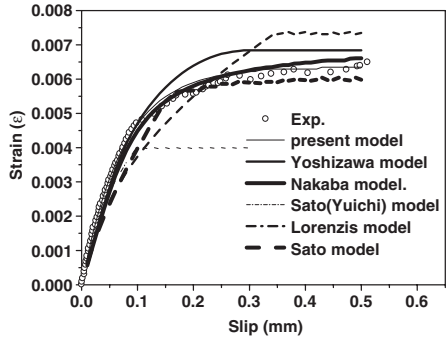

Figure 15. Comparison of predicted strain–slip relationships at loading point by different models with experimental results.

gradients in FRP sheets in the case of using high modulus adhesives (Nishida et al. 1999, Dai et al. 2002). In the present model, the maximum bond stress decreases with the shear stiffness of adhesive due to the significant decreasing B, although the interfacial fracture energy G_f can increase with the decreasing of adhesives' shear stiffness (see Eq. 18).

In fact, the value B can be regarded as an index of ductility of the $\tau-s$ relationships, which is mainly affected by the adhesive properties. Better ductility means slower softening after the peak bond stress. Smaller B means lower initial interfacial stiffness but better interfacial ductility and vice versa. In other words, it is difficult to obtain higher interfacial stiffness and ductility simultaneously. This short-coming is caused by the inherent properties of adhesives. However, it gives us a possibility to optimize the interface design according to the desirable structural performances.

3.1.5 *Verification of new model*

Table 3 gives comparisons of the ultimate interfacial loads of FRP–concrete interfaces predicted by the present proposed $\tau - s$ model and the authors' experimental data. The authors also selected data from the other researchers' pullout tests with bond lengths exceeding 30 cm (Yoshizawa et al. 2000, Nakaba et al. 2001 and the authors' study). A reasonable agreement of all data is found. The average and coefficient of variation of $P_{ana.}/P_{exp}$ are 1.0 and 0.11 respectively, indicating the good accuracy of the present models on predicting the bond capacity of FRP sheet–concrete interfaces.

Based on the authors' and other researchers' $\tau-s$ relationships, Figure 15 gives an example of comparing the predicted strain–slip relationships at the loaded end of a FRP sheet–concrete interface, of which the FRP stiffness, concrete strength and adhesive stiffness

are 50.6 kN/mm, 35 MPa and 1.14 GPa/mm (FR-E3P) respectively. It can be seen that the present model and Nakaba's model give good prediction on the whole period of pullout test (before and after initial peeling). Nakaba's model gives slight underestimation on the initial interfacial stiffness. Yoshizawa's simplified bilinear model gives a good prediction on the initial interfacial stiffness but shows a big deviation when the strain of FRP becomes higher. Sato's model gives a good prediction on the maximum strain but shows a big deviation during initial ascending period. The assumption of elasto-plastic bilinear $\tau - s$ relationships (Sato (Yui-chi) and Lorenzis) shows comparatively less fitting.

3.2 *Bond stress–slip–FRP strain model*

The local $\tau - s$ relationship of FRP sheet–concrete interfaces in Equation 8 is obtained from the $\varepsilon - s$ relationship (Eq. 7) at loaded point of a pullout test with long bond length, through which the interface can achieve the maximum bond capacity under the boundary condition of zero strain in FRP sheets and zero slip at free end. With this boundary condition, it can be assumed that the $\varepsilon - s$ and $\tau - s$ relationship are unique and independent of location along the interface (Shima et al. 1987). However, when bond length becomes short, slip at free end occurs although the strain in FRP sheets there is zero. Non-zero slip and zero strain condition at free end causes different shapes of strain distributions of reinforcing materials internally or externally bonded with concrete (see Figs. 16 and 17). So that $\tau - s$ relationships are considerably different at different locations from the free ends in pullout tests. For reinforcing bar in concrete, Shima et al. (1987) modeled successfully the different $\tau - s$ and strain distribution behaviors (see Fig. 16) under three boundary conditions, which are (i) zero bar strain and zero slip, (ii) zero bar strain and non-zero slip, and (iii) non-zero bar strain and zero slip, by considering the effects of reinforcing bar's strain in a $\tau - s$ relationship. They concluded that a bond stress–strain–slip ($\tau - \varepsilon - s$) model as the following Equation 21 can be used to unify the $\tau - s$ relationships under all the boundary conditions:

$$\tau = g(\varepsilon) \cdot \tau_0(s) \tag{21}$$

where $\tau_0(s)$ is the $\tau - s$ relationship under the condition of zero strain in reinforcing bar, or in other word, at the location of free end in a pullout bond test. $g(\varepsilon)$ is a function of reinforcing bar's strain, which can represent the effects of strain conditions in reinforcing bar on the $\tau - s$ behaviors at the different locations from the set boundary.

For FRP sheets externally bonded to concrete, the similar bonding phenomenon happens. Before the pullout force reaches the free end of FRP sheets in a

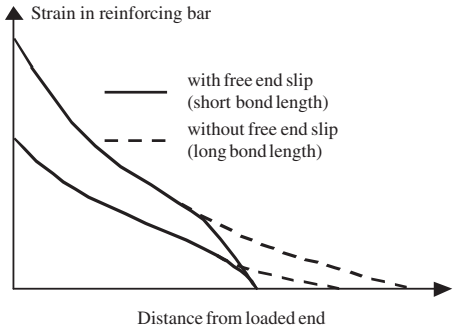

Figure 16. Strain distribution of reinforcing bar in concrete in a pullout test with or without free end slip.

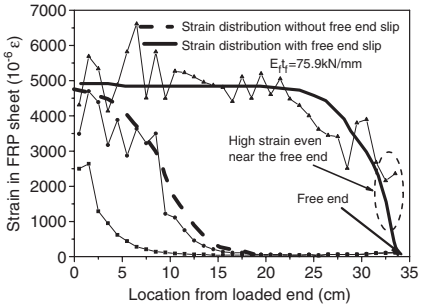

Figure 17. Observed strain distribution in FRP sheets in a pullout test with or without free end slip.

pullout test (zero slip and zero strain in FRP sheets at free end), the strain distribution in FRP sheets near the zero strain location is smooth and gradual (see Fig. 17). However, when the stress in FRP is transferred to the free end, end slip happens and the boundary condition makes the strain in FRP sheets there decrease rapidly to zero (see Fig. 17). Rather high FRP's strain can be observed even at the locations very close to the free end, implying that there is high bond stress within a short distance from the free end (see Fig. 17).

The local $\tau - s$ behaviors of FRP sheet–concrete interfaces near the free end can be observed in both long bond length and short bond length tests. However both ways are difficult. In the long bond length test, when the peeling of FRP sheets propagates toward the free end, the release of the strain energy stored in FRP sheets usually needs big slip at the free end, which causes the sudden separation of the FRP sheets from concrete and makes it difficult to record the strain distributions in FRP sheets at the final peeling stage. Using short bond length pullout tests can avoid the sudden releasing of strain energy in FRP sheets in

some extent. However, it is not easy for us to create a pure shear condition for the FRP sheet–concrete interfaces especially near the free end, where more brittle premature interface failure similar to plate end failure in FRP externally strengthened RC beams happens easily (Dai 2003).

It is assumed that a unified $\tau-\varepsilon-s$ expression like Equation 21 can be used for FRP sheet–concrete interface as well to describe the $\tau-s$ relationships obtained at the loaded point in a long bond length pullout test (Eq. 16) and those obtained at locations near the free end (see Fig. 18). Therefore,

$$\tau = g(\varepsilon)\tau_0(s) = 2G_f B(\exp(-Bs) - \exp(-2Bs)) = 2G_f B\exp(-Bs)(1-\exp(-Bs)) \quad (22)$$

Thus, the issue now is how to get expressions for $g(\varepsilon)$ and $\tau_0(s)$. It can be known from Equation 7, which is true for the boundary condition of $\varepsilon = 0$, $s = 0$, $\tau = 0$ (long bond length case), that:

$$\frac{\varepsilon}{A} = 1-\exp(-Bs)$$

$$\therefore \exp(-Bs) = 1-\frac{\varepsilon}{A} \quad (23)$$

Now the function for FRP strain, g(ε) is assumed as the following:

$$g(\varepsilon) = 1-\frac{\varepsilon}{A} \quad (24)$$

Substituting Equations 23 and 24 into Equation 23,

$$\tau = g(\varepsilon)\tau_0(s) = 2G_f B\left(1-\frac{\varepsilon}{A}\right)(1-\exp(-Bs)) = 2G_f Bg(\varepsilon)(1-\exp(-Bs)) \quad (25)$$

$$\therefore \tau_0(s) = 2G_f B(1-\exp(-Bs)) \quad (26)$$

In Equation 26, the peak interface shear stress at free end is governed by two parameters G_f and B, which are mainly affected by the properties of adhesives and concrete as shown in Equations 19 and 20.

According to the unified $\tau-\varepsilon-s$ model (Eq. 25), Figure 18 presents the $\tau-s$ relationships at different locations from the free end of a pullout test. It can be seen that the local $\tau-s$ relationships at the distances longer than 100 mm away from the free end show practically no difference, which means that strain effect is negligible. Then the $\tau-s$ model and $\tau-\varepsilon-s$ model become the same. On the other hand, when the bond length from free end is shorter than 50 mm the strain effects become noticeable. Particularly high bond stress occurs at the location of 0 to 20 mm from the free end in the pullout test.

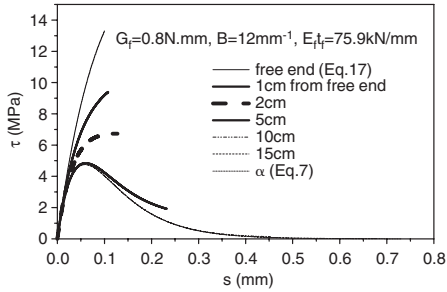

Figure 18. Obtained $\tau\sim s$ relationships at different locations from free end based on Equation 24.

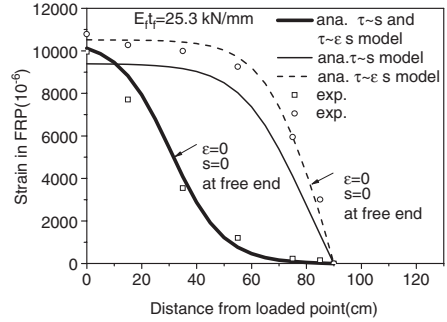

Figure 19. Strain distributions in FRP sheets predicted by $\tau-s$ and $\tau-\varepsilon-s$ models at different peeling stages.

Figure 19 shows experimentally observed strain distributions in FRP sheets ($E_f t_f = 25.3$ kN/mm) at different peeling stages in a pullout test with the bond length of 90 mm, as well as the predicted ones. It is indicated that the predicted strain distributions by $\tau-s$ and $\tau-\varepsilon-s$ models are same when the pullout force in FRP sheets has not been transferred to the free end, meaning that the interface has the boundary condition of zero strain and zero slip (or very small) at free end. But after the pullout force is transferred till the free end and free end slips appears, only the $\tau-\varepsilon-s$ models can explain well the experimentally observed high strain in FRP sheets near the free end.

3.3 *Effective bond length*

An important interfacial parameter named as effective bond length is needed for the anchorage design of FRP sheet–concrete interfaces. In order to define the effective bond length in a comprehensive way, we need to have good understanding on the strain distributions of FRP sheets or the interfacial shear stress distributions along the interfaces. At any location of an FRP

sheet–concrete interface under pullout force, the local bond stress can be expressed as:

$$\tau(x) = E_f t_f \frac{d\varepsilon(x)}{dx} \tag{27}$$

Since $\varepsilon(x) = ds(x)/dx$, the following differential equation governing the interfacial bond behaviors can be obtained using Equation 16:

$$\frac{d^2 s(x)}{dx^2} = \frac{\tau(x)}{E_f t_f} = \frac{2BG_f}{E_f t_f}\left(\exp(-Bs) - \exp(-2Bs)\right) \tag{28}$$

With a long bond length L, the solution for Equation 28 can be obtained as follows:

$$s(x) = \frac{1}{B}\ln[\exp B(Ax + c_2) + 1] \tag{29}$$

$$\therefore \varepsilon(x) = \frac{ds(x)}{dx} = A\frac{\exp B(AL + c_2)}{\exp B(AL + c_2) + 1} \tag{30}$$

where c_2 is a constant related to the boundary condition at loaded end. When pullout force P is exerted at the loaded end, the boundary condition of $\varepsilon = P/(b_f E_f t_f)$ at $x = L$ can be introduced into Equation 30, and the constant c_2 can be determined as follows:

$$c_2 = \frac{\ln\dfrac{P}{P_{\max} - P}}{B} - AL \tag{31}$$

By substituting Equation 31 into Equation 30, the strain distribution of FRP sheets under the pullout load P and a long bond length L can be expressed as:

$$\varepsilon(x) = \frac{ds(x)}{dx} = \frac{A}{1 + \dfrac{\exp(AB(L-x))(P_{\max} - P)}{P}} \tag{32}$$

Figure 20 shows the comparisons between experimentally obtained distributions of strains in FRP sheets obtained under different pullout forces (Dai et al. 2002) and the analytical ones drawn based on Equation 32. The good prediction on the distributions of strains in FRP sheets, in other words, the interfacial stress distributions under different pullout load levels, verifies the accuracy of the proposed local $\tau - s$ model.

Figure 21 shows the FRP strain distribution calculated by Equation 32. For each force level, there is an active bond zone at which the FRP strain changes much more greatly than the rest. The active bond zone is slightly more than 100 mm even for 99.99% of P_{max}. The size of this active bond zone is called effective bond length (L_e).

Mathematically, the L_e can be expressed as a distance between two locations x_1 and x_2 ($L_e = x_2 - x_1$), which bears the pullout force $\alpha P_{\max}$ (α can be taken as a constant percentage for anchorage design) as shown in Figure 21. At these two locations, the strains of FRP sheets are defined as follows:

$$\varepsilon_1 = \frac{1-\alpha}{2}A;\ \ \varepsilon_2 = \frac{1+\alpha}{2}A;\ \ \varepsilon_1 - \varepsilon_2 = \alpha A \tag{33}$$

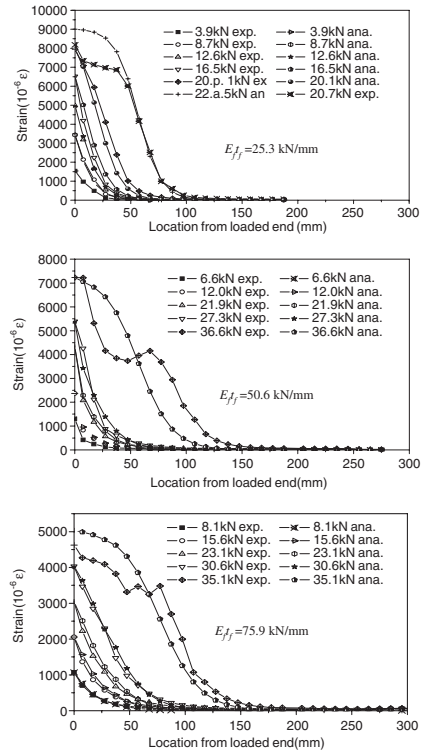

Figure 20. Comparison between experimental and analytical distributions in FRP sheets.

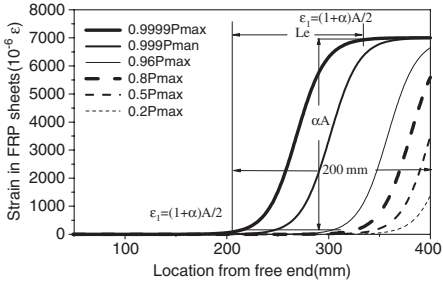

Figure 21. Calculated strain distributions in FRP sheets under different pullout forces.

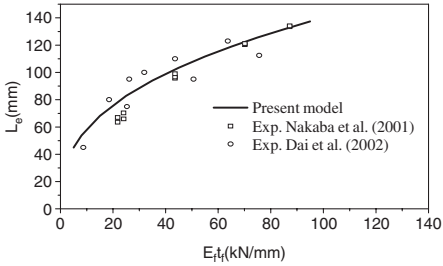

Figure 22. Increase of effective bond length with FRP stiffness.

The following equation can be obtained from Equation 32:

$$L - x = \frac{1}{AB}[\ln(\frac{A}{\varepsilon(x)} - 1) - \ln(\frac{P_{max} - P}{P})] \quad (34)$$

Substituting Equation 34 into Equation 33, the effective bond length can be derived as follows:

$$\begin{aligned} L_e &= x_2 - x_1 = (L - x_1) - (L - x_2) \\ &= \frac{1}{AB}\left[\ln\left(\frac{A}{\varepsilon_1} - 1\right) - \ln\left(\frac{A}{\varepsilon_2} - 1\right)\right] \\ &= \frac{1}{AB}\left[\ln\left(\frac{1+\alpha}{1-\alpha}\right) - \ln\left(\frac{1-\alpha}{1+\alpha}\right)\right] = \frac{2}{AB}\ln\left(\frac{1+\alpha}{1-\alpha}\right) \end{aligned} \quad (35)$$

Substituting Equation 19 for G_f and Equation 20 for B into Equation 35, the following equation can be obtained:

$$L_e = \frac{9.79(E_f t_f)^{0.38}}{(G_a / t_a)^{0.657} f_c^{0.118}} \ln(\frac{1+\alpha}{1-\alpha}) \quad (36)$$

The authors suggest here that a constant 0.96 can be given to α in Equation 36 to fit with experimentally observed effective bond length well (see Fig. 22) and lead to reasonable anchorage strength design.

The shear stiffness (shear modulus divided by thickness) of adhesive layers has significant effects on the effective bond length (see Fig. 23). That is a possible reason for the big differences existing in the different models as shown in Figure 23.

3.4 *Bond strength for a given anchorage length*

An ultimate pullout force (P_u) for an anchorage length (L_b or bond length) less than the effective bond length is less than that for an anchorage length equal to or longer than the effective bond length (P_{max}), which is calculated by Equation 12. When P_u is equal to αP_{max}, it is assumed that the relationship between L_b and α

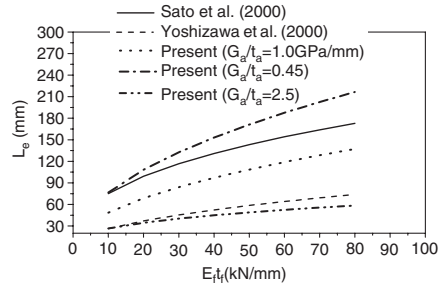

Figure 23. Effective bond length affected by adhesive stiffness.

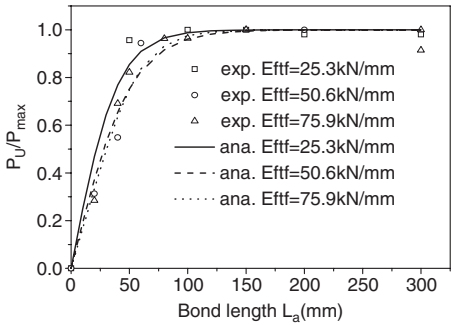

Figure 24. Comparison between the experimental and analytical bond strengths.

is the same as L_e–α relationship in Equation 35. Then the following equation can be obtained:

$$\alpha = \frac{\exp(\frac{L_b B\sqrt{G_f}}{\sqrt{2E_f t_f}}) - 1}{\exp(\frac{L_b B\sqrt{G_f}}{\sqrt{2E_f t_f}}) + 1} \quad (37)$$

Experimentally obtained bond strengths of FRP sheet–concrete interfaces with different bond length and FRP stiffness are compared with the predicted curves in Figure 24. It can be seen that the simplified closed-form model (Eq. 37) can predict the bond force capacity of FRP sheet–concrete interfaces with either long or short bond length satisfactorily.

4 CONCLUSIONS

This paper presents new shear bond model for FRP–concrete interface, which considers effects of not only FRP and concrete mechanical properties but also

adhesive ones, based on the new methodology, which eliminates strain gage arrangement on FRP and needs only FRP strain–slip relationship at loaded end. The shear bond model is expanded by introducing FRP strain effects on bond stress–slip relationship, so that the model can be applied to short bond length cases. Besides the shear bond model, formula for interfacial fracture energy, effective bond length and bond strength for a given anchorage length are presented as well. The presented bond model and formula were verified by the authors' and previous experimental data.

ACKNOWLEDGEMENTS

The authors are grateful to Dr Yasuhiko SATO of Hokkaido University for his valuable advice towards this study.

REFERENCES

Dai, J.G. 2003. Interfacial models for fiber reinforced polymer (FRP) sheets externally bonded to concrete. *Ph. D Dissertation*, Hokkaido University, Japan.

Dai, J.G. and Ueda, T. 2003. Local bond stress slip relations for FRP composites-concrete interfaces. In Tan, K. H. (ed), *Proceedings of FRPRCS-6*, 1: 143–152.

Dai, J.G., Sato, Y. and Ueda, T. 2002. Improving the load transfer and effective bond length for FRP composites bonded to concrete. *Proceedings of JCI*, 24(2): 1423–1428.

Dai, J., Sato, Y. and Ueda, T. 2004a. Dowel effects on interface shear bond force transfer in concrete beams strengthened with FRP sheets. *Proceedings of JCI*, 25.

Dai, J., Ueda, T., Sato, Y. and Jaqin, H. 2004b. Dowel resistances of bond interfaces between FRP sheets and concrete. *Proceedings of 2nd International Conference on FRP Composites in Civil Engineering (CICE2004), Adelaide, 8–10 December 2004*: Rotterdam, Balkema.

Lee, Y.J., Boothby T.E., Bakis, C.E. and Nanni, A. 1999. Slip modulus of FRP sheets bonded to concrete. *Journal of Composites for Construction*, ASCE, 3(4): 161–167.

Lorenzis, L. De., Miller, B. and Nanni, A. 2001. Bond of fiber-reinforced polymer laminates to concrete. *Material Journal*, ACI, 98(3): 256–264.

Nakaba, K., Kanakubo, T., Furuta, T. and Yoshizawa, H. 2001. Bond behavior between fiber-reinforced polymer laminates and concrete. *Structural Journal*, ACI, 98(3): 359–167.

Nishida, H., Simomura, T., Kamiharako, A. and Maruyama, K. 1999. Bond behaviors between the FRP Sheets and concrete. *Proceedings of JCI*, 21(3): 1507–1511 (in Japanese).

Sato, Y., Asano, Y. and Ueda, T. 2001. Fundamental study on bond mechanism of carbon fiber sheet. *Concrete Library International*, JSCE, 37: 97–115.

Täljsten, B. 1997. Defining anchor lengths of steel and CFRP plates bonded to concrete. *International Journal of Adhesion and Adhesives*, 17(4): 319–327.

Tripi, J.M., Bakis, C.E., Boothby, T.E. and Nanni, A. 2000. Deformation in concrete with externally CFRP sheet reinforcement. *Journal of Composites for Construction*, ASCE, 4(2): 85–94.

Yoshizawa, H., Wu, Z., Yuan, H. and Kanakubo, T. 2000. Study on FRP–concrete interface bond performance. *Journal of Materials, Concrete Structures and Pavements*, JSCE, 662/V-49: 105–119.

Yuan, H., Wu, Z. and Yoshizawa, H. 2001. Theoretical solutions on interfacial stress transfer of externally bonded steel/composite plates. *Journal of Structural Mechanics and Earthquake Eng.* JSCE, 18(1): 27–39.

FRP Composites in Civil Engineering – CICE 2004 – Seracino (ed)

The use of FRP as embedded reinforcement in concrete

P. Waldron
Centre for Cement and Concrete, University of Sheffield, Sheffield, UK

ABSTRACT: The increased use of FRP in construction is largely driven by the requirement for more durable solutions than steel for those applications subjected to the most severe environmental conditions. Adoption of FRP as embedded reinforcement in new structures has, however, been much slower than for other applications such as repair and strengthening. This is due to a number of factors including cost, availability (especially of bent bars), structural performance, lack of design guidance, and its own durability in highly alkaline environments such as that found in concrete. On-going research around the world has addressed, and continues to address, these various areas of concern. This Paper summarizes the research contributions made by the University of Sheffield over the past decade to this huge worldwide effort.

1 INTRODUCTION

For more than a century steel bars have been used as reinforcement in RC structures to compensate for the low tensile strength of the concrete. Although steel reinforcement is generally manufactured and used in straight lengths, it is readily cold formed in to 2-d and 3-d shapes for use in more complex structural elements and critical structural connections.

Nevertheless, when concrete structures come into contact with carbonic acid, resulting from the carbon dioxide present in the atmosphere, or are exposed to chloride rich environments, such as those created by the presence of seawater or the frequent use of deicing salts, steel reinforcement is susceptible to corrosion. Corrosion of the reinforcement can lead to premature deterioration of the mechanical performance of the structure and subsequent failure.

At present, corrosion of steel reinforced concrete structures is considered to be the most significant factor in limiting the life expectancy of RC structures in North America, Europe, the Middle-East and other parts of the world. In Europe alone, the annual cost of repair and maintenance of the infrastructure is estimated to be over €30 billion and, in the United States, the overall costs associated with damage due to reinforcing steel corrosion have been estimated at about $80 billion (Federal Highway Administrator 1997).

Over the past thirty years, different measures have been taken to combat the corrosion problem. These have included the specification of increased concrete cover, the introduction of additives and inhibitors to make the concrete more impermeable and non-conductive, and the use of different types of reinforcing materials such as stainless steel and epoxy coated steel bars. Research data, however, have shown the long-term performance of epoxy coated steel rebar to be questionable, while stainless steel, which exhibits excellent corrosion resistance, is too expensive for wide scale use (Federal Highway Administration, 2000). The on-going requirement for more durable structures is therefore the key driving force behind the introduction of advanced composites in the construction industry as reinforcing material for concrete.

Manufactured from a combination of mineral fibres within a polymeric matrix, fibre reinforced polymer (FRP) reinforcing bars display excellent resistance to environmental factors such as freeze-thaw cycles, chemical attack and temperature variations. Above all, composites can be engineered to be highly corrosion resistant providing a highly durable reinforcement material for increasing the design life of new concrete structures.

While composite materials have proven to possess superior mechanical properties and have been used extensively in the aerospace, automobile and defence industries, civil engineers are beginning only now to gain confidence and experience in applying this technology to the construction industry.

2 FRP PRODUCTS FOR CONCRETE STRUCTURES

The mechanical characteristics of FRP reinforcement are different in many respects from conventional steel reinforcement and depend very much on the type of fibres and resins used. Carbon, glass and aramid fibres, impregnated with a resin matrix, are the basic components for the manufacture of composite

Figure 1. Examples of various types of FRP reinforcement.

Table 1. Advantages and disadvantages of FRP reinforcement.

Advantages	Disadvantages
Higher strength to self-weight ratio (10–15 times greater than steel)	Higher raw material cost and relatively poor availability
Excellent fatigue characteristics (carbon and aramid FRPs only)	Lower elastic modulus (except some Carbon FRPs)
Excellent corrosion resistance and electromagnetic neutrality	Glass FRP reinforcement suffers from stress corrosion
Low axial coefficient of thermal expansion	Lack of ductility; durability issues in alkaline environments

reinforcement. Due to the non-structural contribution made by the resin, as well as its relatively high cost, a maximum fibre to resin volume fraction is always desirable. However, the maximum fibre content that can be achieved in practice is normally below 70% resulting in bars with an equivalent elastic modulus well below that of the constituent fibres.

FRP materials can be manufactured by using different techniques such as pultrusion, filament winding, moulding, braiding and manual lay-up and can be produced in various shapes. As for conventional steel reinforcement, however, non-ferrous composite materials are usually manufactured in the form of rebars, sheets, grids and links (Figure 1).

Composites can be engineered to meet the specific demands of each particular application and their overall performance and characteristics depend on the choice of materials (fibre and resin matrix), the volume fraction of fibre, fibre orientation and fabrication method. Furthermore, in order to enhance the bond characteristics of FRP reinforcing bars in concrete, several techniques are employed including the introduction of surface deformations, sand coating, over-moulding a new surface on the bar, or a combination thereof.

The main advantages and disadvantages of these advanced composite materials compared to steel are listed in Table 1.

High strength, light weight and low modulus of elasticity, together with the fact that FRP bars, unlike steel, do not display plasticity, are the key properties that differentiate the performance of these materials.

3 INTERNATIONAL RESEARCH EFFORT AND THE DEVELOPMENT OF GUIDELINES

The first research committee on Continuous Fiber Reinforcing Materials (CFRM) was established in 1989 by the Japan Society of Civil Engineers (JSCE). The work of this Committee was published in Japanese in the form of a State-of-the-Art report in 1992 addressing various issues such as applications, design guidelines, durability and test methods. The part of this first publication that dealt with design considerations was translated into English and published in 1993. Since the development of design guidelines was seen as crucial if the use of CFRM was to be encouraged, the work of the Committee focused specifically on this issue and fuller design recommendations were subsequently published in Japanese in 1996 and then in English in 1997.

Research activity in Canada on the use of FRP as reinforcement for concrete also began in 1989. The Canadian Society of Civil Engineers created a technical committee to study the use of advanced composite materials in bridges and structures. The efforts of this committee resulted in the publication of a State-of-the-Art report in 1991 (Mufti *et al.*) and lead to design recommendations that were published in February 1998 (Canadian Highway Bridge Design Code). The Canadian Network of Centres of Excellence on Intelligent Sensing for Innovative Structures (ISIS Canada), was established in 1995 largely to provide civil engineers with smarter ways to build, repair and monitor structures using high-strength, non-corroding, fibre reinforced polymers and fibre optic sensors. Within this framework, two design manuals, which deal with various aspects of reinforcing and strengthening concrete structures, were published in 2001 (ISIS Canada).

Mainstream FRP research in the U.S.A. and Europe commenced in 1991. In January of that year, the American Society of Civil Engineering sponsored a conference on Advanced Composites Materials in Civil Engineering Structures and in November, the 5-year BRITE/EURAM Project, "Fibre Composite Elements and Techniques as non Metallic Reinforcement for

Concrete", funded by the Commission of the European Communities, began in Europe (Taerwe, 1997).

Also in 1991, the American Concrete Institute (ACI) formed Committee 440, Fibre Reinforced Polymer Reinforcement, whose efforts lead to the publication of a State-of-the-Art report in 1996 (American Concrete Institute). This report was followed by the publication of their recommendations for externally bonded with FRP systems (American Concrete Institute 2002) and the design and construction of concrete reinforced with FRP bars (American Concrete Institute, 2003).

In December 1993, the EUROCRETE project (Clarke *et al*, 1996) began in Europe. This pan-European research programme was established with the aim of developing durable FRP reinforcement for concrete. Although many fundamental areas of research were progressed, one of the main objectives was the development of suitable design guidelines. Much of the work done by the task group that dealt with this particular issue is included in an interim guidance, which was published in 1999 by the British Institution of Structural Engineers.

The EU TMR Network, ConFibreCrete, was established in 1997 with the aim of developing guidelines for the design of concrete structures, reinforced, prestressed or strengthened with advanced composites. The Network comprised 11 teams from 9 different European countries and its work was closely linked to the work of the *fib* Task Group 9.3, FRP Reinforcement for Concrete Structures, which was established late in 1996. An outcome of the ConFibreCrete project was a bulletin on externally bonded FRP reinforcement for RC structures published through the International Federation of Concrete, *fib* (*fib* Task Group 9.3, 2001). These guidelines concern mainly flexure, shear and confinement, but they also deal with other issues such as execution, quality control, durability and environmental effects. A further bulletin dealing with state-of-the-art knowledge on FRP materials and their use in RC and PC structures is in the final stages of preparation and is expected to become available in 2005.

The most recent effort in trying to address some of the fundamental problems of using FRP in reinforced concrete in Europe is the 2 year CRAFT RTD project, CurvedNFR, which commenced in June 2003. This project aims to develop materials, methodology and manufacturing processes for a low cost, curved FRP rebar (CurvedNFR, 2003).

The University of Sheffield, having taken a key role in the Eurocrete project and having recently coordinated the ConFibreCrete Network, has had an ongoing involvement in FRP research in Europe. The main focus of its work has been to undertake fundamental research to support the development of design guidelines.

Although great strides have been made in research dealing with the use of FRPs in RC structures since its inception in 1989, there remains much work to be done. For example, internationally accepted codes of practice for FRP materials are still required and there are many specific research problems that remain to be more fully investigated, such as shear behaviour of FRP RC elements, detailing of FRP reinforcement and a unified design philosophy in general.

4 THE USE OF FRP IN THE CONSTRUCTION INDUSTRY

FRP products have made a dramatic entry into the construction industry over the past 20 years and, since demonstration projects were first constructed in the late 80's and early 90's, the interest in these materials has increased exponentially. The main reasons behind the rapid growth of the use of FRPs in construction were firstly related to the light weight of the reinforcing products and their electromagnetic neutrality. The earliest commercial applications were for non-magnetic or radio-frequency transparent reinforcement for advanced transport systems, specialised defence applications and structures housing magnetic resonance imaging medical equipment. Nowadays, the crucial need to find durable and cost effective solutions to the problem of corrosion in RC structures is perhaps the stronger driver responsible for the rapidly increasing interest in the use of advanced composite materials as reinforcement in concrete around the world.

The number of applications worldwide has increased substantially during the last decade and, although externally bonded applications of FRP reinforcement for the strengthening and rehabilitation of existing structures predominate, the use of FRP as internal reinforcement for newly built structures is receiving more and more attention.

When FRP reinforcement is specified for use in new concrete structures, durability is generally the primary concern. Because of its relatively high cost, the use of advanced composites is typically only likely to replace steel reinforcement in those applications where the superior corrosion resistance properties of FRP are required. For these special applications, FRP can be competitive with other corrosion resistant products such as stainless steel and epoxy coated reinforcement. Although these existing corrosion resistant products only account for about 3–4 % of the total reinforcement market, in Europe alone this represents about 0.5 million tonnes per year (Euro-Project Ltd. 1997). Even a relatively modest share of this corrosion resistant market coupled with the other niche markets where electro-magnetic neutrality or high strength are identified as key issues, is very attractive to the composites industry.

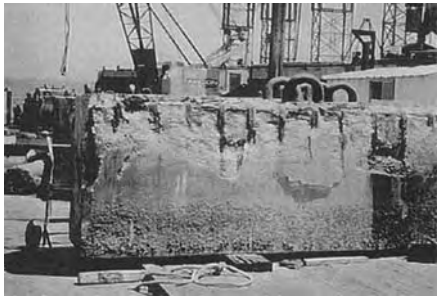

Figure 2. Damaged fender support beam, Qatar (courtesy EUROCRETE project).

Figure 3. FRP reinforced post and panel fencing around a transmitter (courtesy EUROCRETE project).

4.1 *Durability*

Currently, in Europe, more money is spent each year on repairing and strengthening existing structures than on new construction. A large proportion of this expenditure on the rehabilitation of existing infrastructure is incurred in resolving problems of reinforcement corrosion in concrete structures. When steel corrodes, it expands locally resulting in additional stresses accumulating in the concrete. These stresses are capable of cracking the concrete near the surface, allowing much faster ingress of water and corrosive chemicals ultimately resulting in spalling of the concrete cover (Figure 2).

FRP reinforcement represents a valid alternative for structures vulnerable to corrosive environments and has many possible applications in structures in or adjacent to the sea, in or near the ground, in chemical and other industrial plants and in places where good quality concrete can not easily be achieved.

Furthermore, the use of FRP reinforcement allows the concrete cover needed to protect the reinforcement to be reduced. This results in thinner sections of lower weight and has particular benefits in precast elements such as cladding panels.

Figure 4. Magnetic levitation train track in Japan.

Figure 5. Prestressed FRP cables used in a ribbon bridge in Japan.

4.2 *Electromagnetic neutrality*

Steel reinforcement is usually avoided when magnetic neutrality is required and in many applications, especially for the mobile telecommunications and defence industries, this can be a big concern. As a demonstration project in the Eurocrete Project, concrete posts and fence panels reinforced with FRP reinforcement were used to provide a secure boundary for a telecommunication facility (Figure 3).

Other possible applications include bases of large motors, hospital buildings containing magnetic resonance scanning equipment, power transmission towers and magnetic levitation systems such as the MAGLEV (Figure 4).

4.3 *High strength*

One of the more important properties of FRPs is the very high strength that can be developed, allowing a reduction in the area of reinforcement needed in certain applications. However, since high strength in the reinforcement can only be developed when accompanied by high strain, this property can only be fully exploited in prestressed concrete elements (Figure 5). Furthermore, when FRP is adopted for prestressing, considerably lower losses occur than those associated

Figure 6. FRP ground anchors.

with conventional steel tendons due to the lower elastic modulus of the FRP material. However, because of the stress corrosion that affects FRP materials, particularly glass fibre based products, only carbon and aramid are likely to be appropriate for applications in this field.

In addition, FRP cables can be used in cable stay bridges and in other anchoring applications such as ground anchors or rock bolts (Figure 6).

5 FRP IN REINFORCED CONCRETE: STRUCTURAL CONSIDERATIONS

Figure 7 shows the generic mechanical properties of FRP reinforcement according to the type of fibres used in their manufacture.

FRP products are characterized by perfectly elastic behaviour up to failure and can develop higher tensile strength than conventional steel in the direction of the fibres. This anisotropy, however, seriously affects the shear strength, which is very low, compared to the tensile strength, and depends on the properties of the matrix and orientation of the fibres. The elastic modulus of FRP materials used in construction generally varies between 20% of that of steel for glass fibres to 75% of that of steel for carbon fibres.

Although FRP materials, in general, have a low compressive strength, due to the low buckling strength of the individual fibres, this is not usually a major concern since, in the majority of civil engineering applications, FRP is predominantly used only in tension.

Due to the particular mechanical properties of the reinforcement, and especially due to their lack of ductility, FRP RC structures are normally governed by brittle modes of failure generally considered to be undesirable. Based on these considerations, both the construction techniques and the design philosophy need to be carefully reassessed (Pilakoutas, 2000). The behaviour of FRP RC members in flexure, shear and bond is therefore briefly examined and various approaches for the design of RC elements with FRP reinforcement are considered and commented upon.

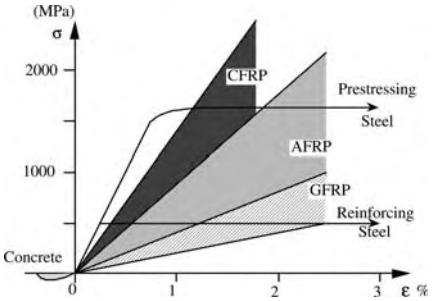

Figure 7. Stress–strain characteristics for concrete and reinforcing materials.

5.1 *Design philosophy*

Work at Sheffield (Pilakoutas *et al*, 2002) has looked at the issue of a suitable design philosophy and has arrived at a new approach. During this work it was revealed that the current partial safety factor approach does not lead to uniform safety levels and often results in conservative designs with larger than necessary amounts of reinforcement. In addition, the margins between the flexural mode of failure and the other modes of failure are quite variable and the designer has no reliable means of assessing them.

In the proposed approach, the main aim was to arrive at a design that has a predetermined safety level (a probability of failure of 10^{-6}) and for which the failure mode hierarchy could be selected by the designer at the design stage. This unified approach has been proposed since it enables new materials to be introduced as they are developed without the need for re-writing the design guide each time. Hence, as a result, the engineer not only selects whether, for example, concrete crushing, bond failure or shear failure is to be the dominant mode of failure for design purposes, but also the secondary failure mode. This approach will always ensure the desired safety level in a structure without undue conservatism.

To demonstrate this approach, the work at Sheffield has resulted in a proposal for a new set of partial safety factors for use with the Eurocrete bar. For this particular bar, the predominant mode of failure is chosen to be by concrete crushing, hence only relatively modest partial safety factors are imposed on the reinforcement material itself.

The above work has highlighted the problem that the use of high safety factors does not necessarily improve the safety of elements and can have the opposite effect by leading to failure in an undesirable mode.

5.2 *Flexure*

When dealing with FRP RC structures, the amount of reinforcement to be used depends on the stiffness

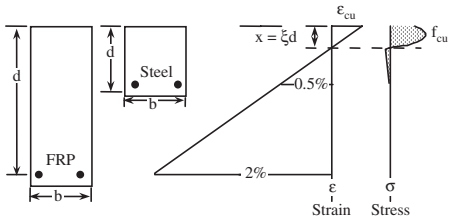

Figure 8. Strain distribution for a glass FRP RC section.

Figure 9. Deflection and cracking in FRP RC beams.

Figure 10. Shear failure of an FRP RC beam.

and strength of the composite material. For FRP reinforcement, the strength to stiffness ratio is an order of magnitude greater than that of steel and this greatly affects the distribution of stresses along the section. Hence, when considering a balanced section, as usually desired in steel RC design, the neutral axis depth for the equivalent FRP RC section would be relatively small and close to the compressive face. Moreover, due to the lower elastic modulus of FRPs, section depth will also need to be increased if deflections are to be maintained at a similar level, as shown in Figure 8. For such a section this implies that a larger proportion of the cross-section is subjected to tensile stress and that the compressive zone is subjected to a greater strain gradient. Hence, for a similar cross-section as that used for steel RC, much larger deflections and crack widths are to be expected, Figure 9.

Figure 11. Shear fracture surface of slab SCS1 after failure.

Furthermore, anchoring of the FRP rebars becomes more difficult due to the high strains developed in the tensile reinforcement.

If all the other modes of failure are avoided, flexural failure can be reached either by crushing of the concrete in compression or by rupture of the FRP reinforcement in tension.

Although both modes are brittle and undesirable, the approach currently adopted by most researchers in the field is to accept that FRP RC sections will be over-reinforced and that the ultimate failure will be by concrete crushing rather than by reinforcement failure.

5.3 *Cracking deformation*

Work by Zhao (1999) at the University of Sheffield has lead to the conclusion that, provided the FRP bars have good bond characteristics, then the crack widths in RC members can be calculated by existing equations that use the strain in the reinforcement as the basis for the calculation. However, the British Standard equation was found to be non-conservative and a modification has been proposed. Regarding short-term deflection calculations, the same work has concluded that existing equations such as those adopted by the ACI can be used directly without modification for the accurate prediction of deflections. The same applies to calculations for long-term deformation when the approach used is based on the fundamental properties of the materials.

5.4 *Shear and punching shear*

Shear transfer in RC beams relies on the tensile and compressive strength of concrete as well as the tensile properties of the longitudinal and, when provided, the transverse reinforcement. In most cases, failure due to shear (Figures 10 and 11) is brittle in nature and, therefore, should be avoided.

All of the shear-resisting mechanisms provided by conventional steel RC elements, such as aggregate

interlock, tooth bending and dowel action, are expected to be affected when using FRP reinforcement due to the higher strains that are generally mobilised in the reinforcement. The mechanical properties of the longitudinal reinforcement significantly affect the amount of concrete in compression and the overall deflections. Larger deflections and the absence of plasticity in the reinforcement always lead to a brittle failure and not much dowel strength is expected from the more flexible, anisotropic FRP materials. Furthermore FRP links cannot generally develop their full tensile potential also due to their anisotropic properties resulting in premature failure at the corners.

An important aim of researchers working in this field has been to provide simplified design equations to enable FRP reinforcement to be used in practice. This has resulted in the development of modification factors for inclusion in existing predictive code equations. This approach, although not ideal, has the perceived advantage that code committees are more likely to accept such modifications than they are to adopt fundamental changes to the underlying design philosophy. The proposed modifications of existing code equations are based on the fundamental principle that, assuming perfect bond, the concrete section experiences forces and strains that are independent of the type of reinforcement utilised. Hence, if a design using FRP reinforcement maintains the same strain as when conventional steel is used ($\varepsilon_{FRP} = \varepsilon_s$) and the same design forces are developed ($F_{FRP} = F_s$), then that design, by definition, will lead to the same safe result. Based on this assumption, an equivalent area of steel (A_e) is introduced to evaluate the concrete shear resistance by multiplying the actual area of FRP reinforcement (A_{FRP}) by the modular ratio of FRP to that of steel, as shown in Eqs. (1) and (2) (for example Nagasaka *et al*, 1989).

$$F_{FRP} = \varepsilon_{FRP} \cdot E_{FRP} \cdot A_{FRP} = \varepsilon_S \cdot E_S \cdot A_S = F_S \quad (1)$$

$$A_e = A_{FRP} \cdot \frac{E_{FRP}}{E_S} \quad (2)$$

When the shear force applied to a RC member exceeds the shear strength of the concrete itself, shear reinforcement is required. According to the proposed modifications, the required amount of FRP shear reinforcement is determined by limiting the maximum strain that it can develop. In some formulations, a maximum limit of 0.0025 (0.002 according to the ACI Committee 440 (2003) and the Canadian Standard Association (1996)), which is the value that corresponds to the yield strain of conventional steel bars, is suggested (for example Institution of Structural Engineers, 1999). By imposing this limit, however, FRP links will only be stressed to a fraction of their potential and thus the benefits of using such materials are not taken to their maximum mechanical and economic advantage (see for example Figure 12).

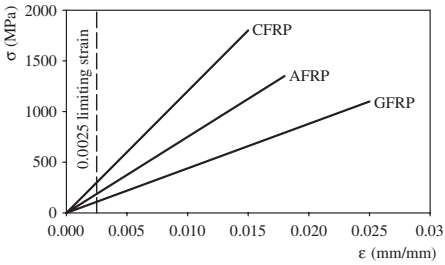

Figure 12. Limiting strain according to current design recommendations to include the use of non-ferrous reinforcement.

Experimental tests carried out on FRP RC beams at the University of Sheffield and by other researchers (Duranovic, 1997, Tottori and Wakui, 1993) have provided evidence that the restrictions imposed by the current modifications to design code equations on the value of maximum allowable strain that can be developed in FRP reinforcement are unnecessarily conservative (recorded values of up to 10,000 microstrain being reported).

Such a tendency was also observed during a series of tests focusing on punching shear and shear by El-Ghandour *et al* (2003) and Guadagnini *et al* (2003) respectively.

5.5 *Bond of FRP bars*

Bond between concrete and FRP reinforcing bars is a fundamental aspect of the composite action of FRP reinforced concrete and accordingly, needs to be adequately understood before FRP materials can be accepted widely in the construction industry.

In flexural structural elements, splitting of concrete in the tension zone is the most likely mode of bond failure. This type of failure is substantially different and more dangerous than the pull-out mode, since it happens at a much lower bond stress level and the residual bond strength of the reinforcing bar decreases rapidly to zero.

The bond splitting behaviour of FRP bars in concrete is expected to vary from that of conventional steel bars due to their lower modulus of elasticity, lower shear strength and stiffness in the longitudinal and transverse directions, and the high normal strains expected before failure. However, despite the fact that a lower maximum bond strength is expected from FRPs, the more ductile nature of the bonding mechanism can lead to a better distribution of the bond stresses and, hence, lead to reduced anchorage lengths.

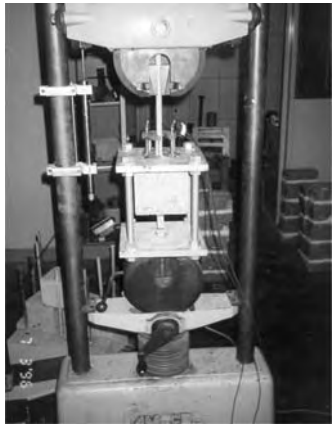

Figure 13. Pull-out test arrangement.

In order to investigate the bond behaviour of carbon and glass FRP bars in concrete, two major experimental series of tests were undertaken at the University of Sheffield (Achillides and Pilakoutas, 2004) as part of the EUROCRETE project. These included pull-out tests and beam tests.

In the pull-out tests, several parameters were examined such as the nature of the fibres, the diameter, shape and deformations of the bars, the embedment length and concrete strength. The pull-out test arrangement adopted is shown in Figure 13.

Beam testing was necessary to improve understanding of the splitting mode of failure. In fact, under flexural load conditions, splitting of concrete in the tension zone rather than pull-out is the most common mode of bond failure.

Pull-out tests are therefore useful for determining the pull-out bond strength, whilst beam tests offer a more realistic assessment of bond strength in structural applications.

The carbon FRP bars used in the beam tests developed a bond strength of more than 4 MPa. This is comparable to the bond strength of deformed steel bars and substantially higher than that of the glass FRP bars (3 MPa). However, in the pull-out tests, they produced similar results. This comparatively lower bond strength of glass FRP bars in the beam tests may be attributed to their higher deformability in the longitudinal direction which seems to play an important role in inducing the splitting mode of failure. Unexpectedly, splices with both carbon and glass EUROCRETE bars developed better bond characteristics than for single anchorage bars.

In general, the experimental results indicate that FRP reinforcing bars interface satisfactorily with the concrete matrix. Their bond behaviour depends on various factors, the full influences of which will need to be evaluated before the formulation of any design formulae. Attention has to be focused on the high deformability of FRP bars that seems to play an important role in the splitting mode of failure in concrete members.

As a step in the direction of increasing current knowledge of the bond properties of FRP bars and bond performance in concrete elements, an international round robin test (*i*RRT, 2002) programme was recently organised by the ConFibreCrete research network (1997) working together with the *fib* Task Group 9.3 and ISIS, Canada.

The *i*RRT was designed with the following objectives in mind:

1. To assess the merits of simple tests for material characterization.
2. To specify a standard methodology for determining relevant parameters such as average maximum bond strength and average maximum pull out load for FRP bars embedded in concrete. A uniform presentation of experimental data will facilitate comparison of the results and will enable the assessment of the reliability and replicability of the specified tests.
3. To generate a comprehensive database that will be made available to the scientific community. This will enable code committees to compare the bond strength developed by various types of FRP bars predicted by design relationships with an extensive set of test results and will assist researchers in evaluating the validity of their analytical and mechanical models.

Other indirect benefits that will result from this exercise are an increased familiarization with the range of FRP products available in the global market and a heightened awareness of the international efforts aimed towards the development of design guidelines and standardised tests to ensure reliable, replicable research.

The tests have now been concluded and the reports from the various laboratories are currently being compiled.

6 SHAPING: THE FUTURE OF FRPs

Although FRPs are already quite extensively adopted in various sectors of the construction industry (e.g. strengthening and repair of existing structures), their use as internal reinforcement for concrete is limited only to specific structural elements and does not extend to the whole structure. The reason for the limited use of FRPs as internal reinforcement can be partly related to the lack of commercially available curved or shaped reinforcing elements used for shear reinforcement or complex structural connections.

Most of the shaped steel reinforcing bars currently used in concrete structures are provided pre-bent and cut in the factory according to design specifications. These may be supplemented by a small quantity of special one-off shapes bent directly on site. Whether bending occurs on site or at the factory, conventional steel reinforcing bars have a major advantage since, due to their elastoplastic behaviour, they can be easily formed by cold bending, and hence, most detailing needs can be easily met speedily at very low cost.

The high production costs that are associated with the manufacturing of FRP curved elements, however, have generally reduced the interest in using FRPs for these types of applications. In addition, various studies have shown that the mechanical performance of bent portions of composite bars are reduced dramatically under a combination of tensile and shear stresses and that the maximum tensile strength that can be carried through the bend can be as low as 40% of the maximum tensile strength of the equivalent straight bar (Ehsani *et al*, 1995, Morphy *et al*, 1997). This phenomenon can become an issue whenever non-straight unidirectional composite elements are used in structural applications since premature failure can occur at the corner portion of the composite. The reduction in the strength of the composite, therefore, needs to be carefully taken into account since it has a major influence on the maximum value of strain that can be safely sustained by the reinforcement. To date, this reduction in strength has been quantified using empirical models such as that proposed by the Japanese Concrete Institute, which is described by Eq. (3) (JSCE, 1996). In this equation, the strength of the bent bar, f_{fb}, is expressed as a function of the uniaxial tensile strength, f_{fu}, the bar diameter, h, and the bend radius, r.

$$f_{fb} = \left(0.05\frac{r}{h} + 0.3\right) f_{fu} \leq f_{fu} \qquad (3)$$

All of these issues are being addressed in the 2 year CRAFT RTD project CurvedNFR (2003), funded by the European Commission. This was established with the aim of developing materials, methodology and manufacturing processes for low-cost, curved fibre reinforced plastic (FRP) rebars. The project partnership includes 8 small specialist industrial partners and 3 research providers across 6 European countries. Of many candidate materials being considered, thermoplastic resins that may be retrospectively softened and bent by the application of heat seem to offer a promising solution at this early stage of this project.

7 CONCLUSIONS

Although FRP materials have fundamentally different mechanical characteristics than steel, the design of FRP RC elements can be based on the same fundamental principles as far as flexural design, shear design, cracking and deflections are concerned. However, a different philosophy of design is needed which addresses the issue of safety at a more fundamental level.

FRP materials offer an effective solution to the problem of steel durability in aggressive environments and where the magnetic or electrical properties of steel are undesirable. They also appear to be highly suited for the manufacture of non-structural precast elements where the combined self weight of the reinforcement and concrete necessary to provide adequate cover is a major disadvantage. Using FRPs can allow a drastic reduction in the overall weight of these elements and facilitates cheaper handling and installation procedures.

FRP reinforcement will never totally replace steel reinforcement in RC structures but is likely to find increasing use in niche applications where its particular chemical, physical and mechanical properties lead to more practical or economic structural solutions.

Despite the extraordinary progress made to date in the use of these advanced composite materials as embedded reinforcement in concrete, many aspects of their structural behaviour still require further detailed examination before their full potential can be exploited in new construction.

ACKNOWLEDGMENTS

The author wishes to acknowledge the financial assistance of the European Union for the TMR Network ConFibreCrete, and the CRAFT RTD project CurvedNFR.

REFERENCES

Achillides Z. and Pilakoutas K. (2004). Bond Behaviour of Fiber Reinforced Polymer Bars Under Direct Pullout Conditions, *Journal of Composites for Construction*, vol 8 **(2)**: 173–181.

American Concrete Institute (1996). State-of-the-Art Report on fibre Reinforced Plastic Reinforcement for Concrete Structures, ACI Committee 440, Farmington Hills, MI, USA.

American Concrete Institute (2002). Design and Construction of Externally Bonded FRP Systems for Strengthening Concrete Structures 440.2R-02, ACI Committee 440, Farmington Hills, MI, USA.

American Concrete Institute (2003). Guide for the Design and Construction of Concrete Reinforced with FRP Bars ACI 440.1R-03, ACI Committee 440, Farmington Hills, MI, USA.

Canadian Highway Bridge Design Code (1996). Section 16: Fibre Reinforced Structures, Final Draft, CHBDC.

Clarke J.L., O'Regan D.P. and Thirugnanenedran C. (1996). "EUROCRETE Project, Modification of Design Rules to Incorporate Non-Ferrous Reinforcement", EUROCRETE Project, Sir William Halcrow & Partners, London.

ConFibreCrete (1997). "Development of Guidelines for the Design of Concrete Structures, Reinforced, Prestressed or Strengthened with Advanced Composites", Training and Mobility of Researchers, http://www.shef.ac.uk/∼tmrnet

CurvedNFR (2003). "Cost effective Curved Polymer Composite Rebar", CRAFT RTD European funded project, CRAFT G1ST-CT-2002-50365, www.curvednfr.com

Duranovic N., Pilakoutas K. and Waldron P. (1997). "Tests on Concrete Beams Reinforced with Glass Fibre Reinforced Plastic Bars", Third International Symposium on Non-Metallic (FRP) Reinforcement for Concrete Structures, Sapporo, Japan, vol. 2, pp 479–486.

Ehsani M.R., Saadatmanesh H. and Tao S. (1995). Bond of Hooked Glass Fiber Reinforced Plastic (GFRP) Reinforcing Bars to Concrete, *Materials Journal*, 122 **(3)**, 247–257.

El-Ghandour A.W., Pilakoutas K. and Waldron P. (2003). Punching Shear Behaviour of FRP RC Flat Slabs: Experimental Study and Predictive Model. *Journal of Composites for Construction*, ASCE, Vol. 7 **(3)**, pp 258–265.

Euro-Projects Ltd (1997), The development of non-ferrous reinforcement for concrete structures, section 10: marketing and costs, project funded by DTI/EPSRC Link Structural Composites programme under contract IL 12/2/120: Eurocrete – Development of Non-Ferrous Reinforcement for Concrete Structures, pp 91–97.

Federal Highway Administration (1997). "The Status of the Nation's Highway Bridges: Highway Bridge Replacement and Rehabilitation Program and National Bridge Inventory," Thirteenth Report to the United States Congress, Washington, D. C.

Federal Highway Administration (2000). Materials and Methods for Corrosion Control of reinforced and Prestressed Concrete Structures in New Construction, Publication No. 00-081, U.S. Department of Transportation, pp. 71.

International Federation of Concrete (2001). Bulletin 14 "Externally bonded FRP reinforcement for RC structures – Technical report on the design and use of externally bonded fibre reinforced polymer reinforcement for reinforced concrete structures", "EBR" working party of fib TG 9.3, pp. 138.

Guadagnini M., Pilakoutas K. and Waldron P. (2003). Shear Performance of FRP Reinforced Concrete Beams, *Journal of Reinforced Plastics and Composites*, Vol 22 **(13)**, pp 1389–1408.

Institution of Structural Engineers (1999). Interim guidance on the design of reinforced concrete structures using fibre composite reinforcement, Published by SETO Ltd, pp. 116.

International Federation of Concrete (1995). fib Task Group 9.3, FRP Reinforcement for Concrete Structures, http://allserv.rug.ac.be/∼smatthys/fibTG9.3

*i*RRT, International Round Robin Test for FRP Reinforcement (2002). http://www.shef.ac.uk/∼tmrnet/rrt

ISIS Canada (2001). Manual No. 3 "Reinforcing Concrete Structures with Fibre Reinforced Polymers (FRPs)", Winnipeg, Manitoba, Canada.

ISIS Canada (2001). Manual No. 4 "Strengthening Reinforced Concrete Structures with Externally-Bonded Fibre Reinforced Polymers (FRPs)", Winnipeg, Manitoba, Canada.

ISIS Canada, Intelligent Sensing for Innovative Structures (1998). http://www.isiscanada.com

Japan Society of Civil Engineers (1992). "Application of Continuous Fiber Reinforcing Materials to concrete Structures", Concrete Library, No. 72, published in Japanese.

Japan Society of Civil Engineers (1997). "Recommendation for Design and Construction of Concrete Structures using Continuous Fiber Reinforcing Materials", Concrete Engineering Series 23.

Japan Society of Civil Engineers (1993). "State-of-the-Art Report on Continuous Fiber Reinforcing Materials", Concrete Engineering Series 3.

Morphy R., Sheata E. and Rizkalla S. (1997). "Bent Effect on Strength of CFRP Stirrups", Third International Symposium on Non-Metallic (FRP) Reinforcement for Concrete Structures, Sapporo, Japan, 19–26.

Mufti A.A., Erki M.A. and Jaeger L.G. (eds) (1991). "Advanced composite Materials with Application to Bridges". The Canadian Society for Civil Engineering, Montreal, Quebec, pp. 297.

Nagasaka T., Fukuyama H. and Tanigaki M. (1989). Shear Performance of Concrete Beams Reinforced with FRP Stirrups. *Transactions of the Japan Concrete Institute*, 11.

Pilakoutas K., Neocleous K. and Guadagnini M. (2002). Design Philosophy Issues of FRP RC Structures. *Journal of Composites for Construction*, ASCE, Vol.6 **(3)**, pp 154–161.

Pilakoutas, K. (2000). Composites in Concrete Construction. In Gdoutos, E. E., Pilakoutas, K. and Rodopoulos C. A. (eds). Failure Analysis of Industrial Composite Materials. McGraw-Hill, London, pp 449–497.

Taerwe L. (1997). "FRP Activities in Europe: Survey of Research and Applications", Non-Metallic (FRP) Reinforcement for Concrete Structures, Proceedings of the Third International Symposium, Vol. 1, pp 59–74.

Tottori S. and Wakui H. (1993). "Shear Capacity of RC and PC Beams Using FRP Reinforcement". International Symposium on Fiber Reinforced Plastic Reinforcement for Concrete Structures, American Concrete Institute, pp 615–632.

Zhao W. (1999). Deformation of FRP RC Members, PhD Thesis, University of Sheffield, Department of Civil and Structural Engineering, UK.

FRP Composites in Civil Engineering – CICE 2004 – Seracino (ed)
© 2005 Taylor & Francis Group, London, ISBN 90 5809 638 6

Structural strengthening and integrity with hybrid FRP composites

Zhishen Wu
Department of Urban & Civil Engineering, Ibaraki University, Japan

ABSTRACT: To take full advantage of individual fibers and realize an innovative structure with integrated and synthesized structural performances, one feasible way is to hybridize several kinds of fibers of different stiffnesses and ultimate strains to behave as an elastic-pseudo-ductile material with also an appropriate stress hardening characteristics. In terms of strengthening purposes of structures, FRP composites can be hybridized to enhance the serviceability performances under service loads by using high modulus fibers, ultimate load-carrying capacities by utilizing high strength fibers and ductility behavior under seismic loads by using high ductile fibers. Hybrid fiber composites consisting of different kinds of fibers available in Japan have been developed for giving more advanced structural performances in strengthening and retrofitting structures by the author's research group. This paper introduces some achievements in structural rehabilitation by using the hybrid FRP composites. First, an idealized concept of FRP hybridization is introduced and some fundamental investigations are presented for confirming the effect of hybrid FRP composites through uniaxial tension tests. Then the flexural strengthening with hybrid composites is reviewed. Finally, numerical simulations of hybrid and strengthening effects are also discussed on both tension and flexural tests. Due to the lacking of space, the paper is limited only on the discussion of hybrid fiber sheets.

1 INTRODUCTION

Fiber-reinforced polymers (FRPs) have been increasingly used in structural strengthening through epoxy-bonding them to the tension face of structures. FRPs usually consist of glass, aramid, and carbon fibers in a polymer matrix and possess light weight, high strength, high resistance to corrosion and ease in handling as compared to steel. There are several types of carbon fibers with superior modulus higher than 2–4 times of steel reinforcement. Recently, new structural fiber materials like PBO (Zylon®) and ultra-high-strength polyethylene (Dyneema®) fibers are available in Japan and possess great energy absorption capacities and, superior strength higher than high strength type of carbon fibers (PBO fibers) and superior ultimate tensile strain higher than 3% (polyethylene fibers) (refer to Fig. 1). However, unlike the cold worked steel reinforcements, FRPs stay elastic until failure and fail in a noticeably brittle manner. Correspondingly, FRP-strengthened concrete structures may fail momentarily without any advanced warning

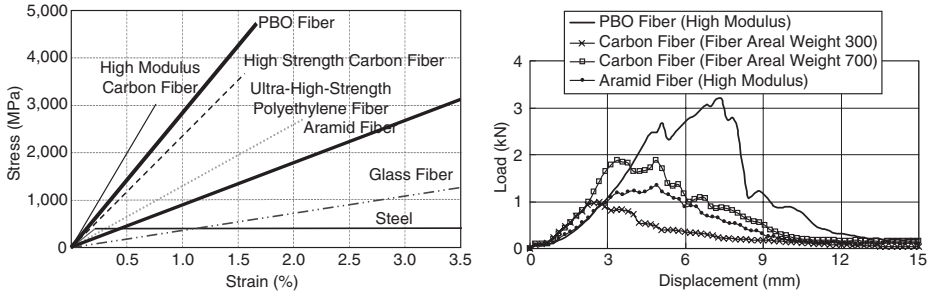

(a) Stress-strain relationships (b) Impact test

Figure 1. Mechanical properties of different continuous fibers.

of impending failure. In addition, limited bonding ability of FRP–concrete interface to transfer stresses from concrete substrate to FRP composites often greatly lowers the expected gains and results in a catastrophic and brittle failure such as debonding at cutoff point or flexural/shear cracks. This implies that advantages of FRP composites may not be fully utilized and enough ductility may not be gained before attaining the expected ultimate load due to interfacial debonding failure or brittle rupture of FRP composites. Moreover, gains in the stiffness and yield load are very limited for the strengthening effects of aramid or glass fiber composites. Even for the case of carbon fibers with a modulus similar to steel reinforcement, the strengthening effects are not yet enough due to the reason that the reinforcing ratio is relatively low (Fig. 2). Therefore, a significant enhancement can hardly be achieved in the service load. To improve the performance of the strengthened structures and efficiently utilize the advantages of FRPs, it is essential to either develop an efficient design guideline concerning such unfavorable failure modes or create some new effective

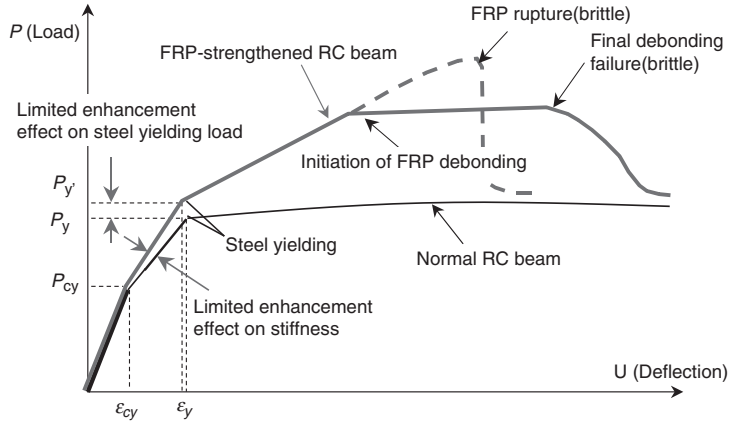

Figure 2. Drawbacks of normal FRP bonding technique for strengthening RC structures.

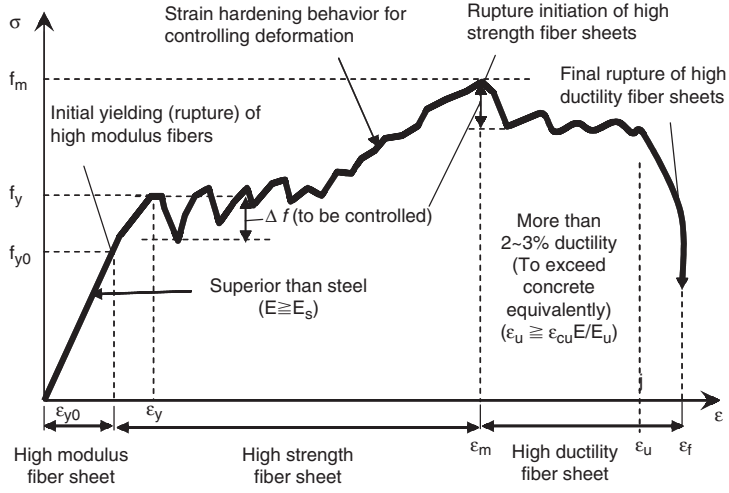

Figure 3. Idealized stress–strain behaviour of hybrid FRP composites.

strengthening techniques. One idea to incorporate the ductility and the stiffness is to use hybrid composites consisting of different types of fibers with different moduli and strengths, which fracture at different strains during loading, thereby allowing a gradual rupture of the composites. Such kind of gradual fracture processes is also very helpful to relieve the stress concentrations along the FRP–concrete interface thus the premature debonding can be prevented.

Generally, strengthening of structures aims to either enhance the serviceability performances such as cracking resistance behavior, ultimate load-arrying capacity or seismic resistance (ductility) etc.

Figure 3 demonstrates an idealized stress–strain relationship of hybrid FRP composites which compose of three types of high modulus, strength and ductility fibers. High modulus fibers can be used to ensure the enhancement in the stiffness, cracking resistance and yield loads. To enhance largely the structural strength, high strength fibers can be used together with high modulus fibers. The mixture of high modulus and high strength fibers presents a certain strain hardening behavior till the rupture of high strength fibers, which may be used to control the deformation of structures with a good restorability performance. In addition, the ductility can be increased by mixing some high ductility fibers. Theoretical studies showed that the stiffness can be enhanced by higher modulus fibers and the ductile behavior may be obtained by hybrid fibers where carbon fibers are mixed in certain proportion with aramid or glass fibers. But the practical problem often showed that premature failure or significant load drops of the hybrid composites occur due to that locally high stress concentrations at the location of fiber breakage damaged the surrounding fibers (Razaqpur and Ali 1996; Harris et al. 1998; Apinis et al. 1998; Wu et al. 2001, 2002). Therefore, the expected strengthening effects cannot be achieved simply by using the rule of mixture prediction. This needs rational mixture design and special efforts to control the stress drops.

2 FUNDAMENTAL INVESTIGATION OF HYBRID FRP COMPOSITES

To give a clear insight into the mechanical behavior of different hybrid fiber sheets, a series of uniaxial tension specimens were tested by composing different types of fiber sheets. The fiber sheets included in the investigation were higher modulus (C7), higher strength (C1) carbon fiber sheets, high strength PBO (P for short) fiber sheets, high ductility fiber sheets (D short for Dyneema fiber sheets) with different proportions. The hybrid ratios of different kinds of fibers are indicated as layer's ratio. The tension specimens of FRP sheets are manufactured through impregnation of epoxy resin according to JSCE (2001) as shown in Figure 4. The loading is controlled by displacement at a rate of 1 mm/min.

To calibrate the material properties provided by the manufacturer, single type of fiber sheets were tested. The results are also tabulated in Table 1, where most of the indices are higher than those in the specification by the manufacturer. Based on these values, it is easy to predict the mechanical behavior of hybrid fiber sheets following the rule of mixture (Wu et al. 2004a).

2.1 *Preliminary hybrid design following rules of mixtures*

Following rule of mixtures behavior, the stress σ_{ave} or load P_{ave} – strain ε relationships and the elastic

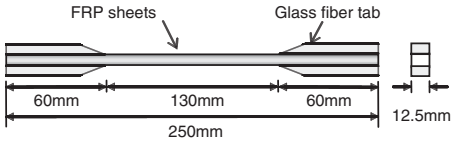

Figure 4. Details of tension specimens.

Table 1. Summary of mechanical properties of different fiber sheets.

Fiber ID	Types of fiber	Fiber aerial weight (g/m^2)	Thickness (mm)	Tensile strength*	Modulus of elasticity* (MPa)	Rupture strain* (%)
C1	High strength carbon Fiber	200 300	0.111 0.156	3400 (4232)	2.3×10^5 (2.43×10^5)	1.48 (1.74)
C7	High modulus carbon fiber	200	0.143	1900 (2507)	5.4×10^5 (5.54×10^5)	0.35 (0.45)
P	PBO fiber	200	0.128	3500 (4156)	2.4×10^5 (2.60×10^5)	1.67 (1.60)
G	E-glass	300	0.118	1500 (1793)	7.3×10^4 (8.0×10^4)	2.05 (2.23)
D	Polyethylene (Dyneema®)	250	0.258	1850 (1832)	7.0×10^4 (6.0×10^4)	2.64 (3.08)

* The values provided by the manufacturer are followed by the average values from experiment in parentheses.

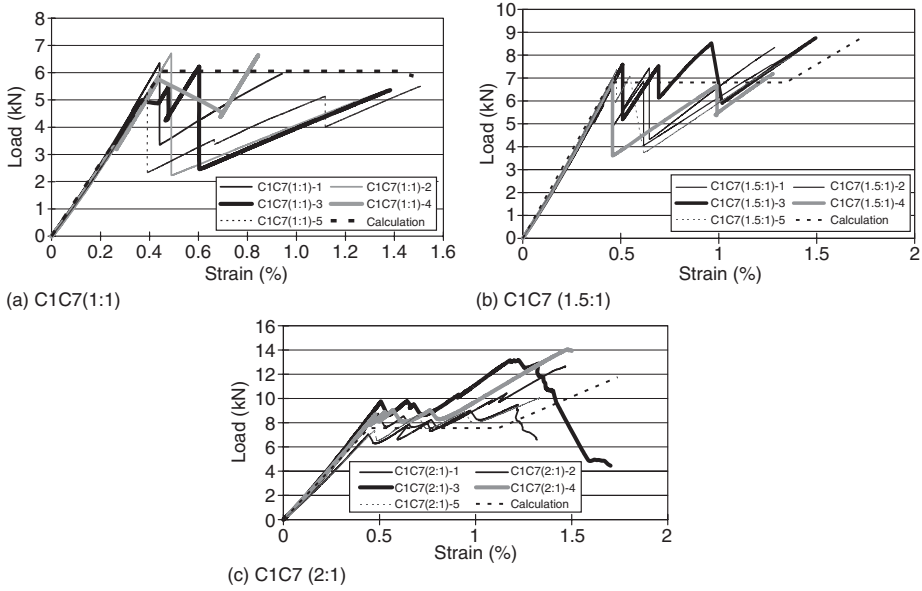

Figure 5. Hybrid fiber sheets composing of C1 and C7.

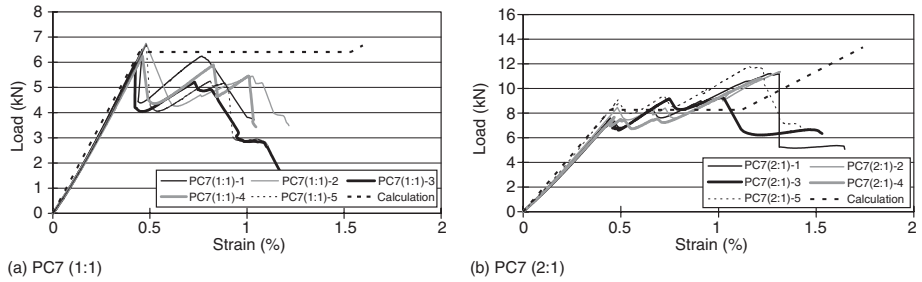

Figure 6. Hybrid fiber sheets composing of PBO and C7.

modulus E_{ave} of hybrid composites can be represented by the following equations:

$$\sigma_{ave} = \varepsilon\left(E_1A_1 + E_2A_2 + E_3A_3\right)/A$$
$$E_{ave} = \left(E_1A_1 + E_2A_2 + E_3A_3\right)/A$$
$$P_{ave} = F_{HM}A_1 + \varepsilon\left(E_2A_2 + E_3A_3\right)$$

where E_1, E_2, E_3 and A_1, A_2, A_3 are the elastic moduli and cross-sectional areas of high modulus, strength and ductility fiber sheets respectively. A is the entire cross-sectional area of the fiber sheets ($A = A_1 + A_2 + A_3$). F_{HM} is the tensile strength of high modulus fiber sheet.

After the rupture of the each individual fiber sheet, it is excluded in calculating the stiffness E_i and cross sectional area A_i of the hybrid composites. In order to discuss the stress (load) drops P_d due to the impact of gradual ruptures of fibers and to find an influencing factor to control the load drops, the ratio of load loss due to the current ruptured fibers, P_r and maximum load-carrying capacities of hybrid composites P_{max} is defined as P_r/P_{max}(%). Moreover, the load drop ratios at the ruptures of high modulus (HM) and high strength (HS) fibers are defined as P_d/P_y(%) and P_d/P_{max}(%) respectively.

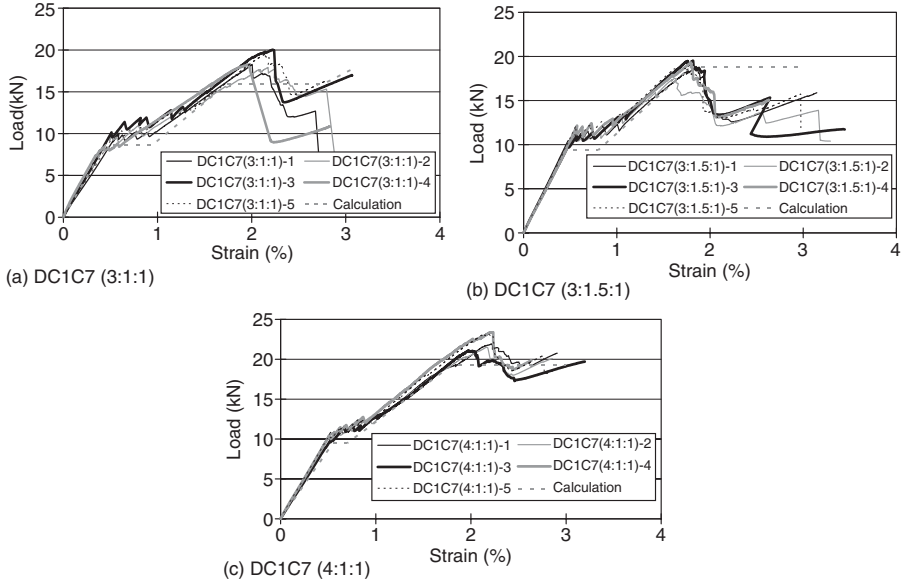

Figure 7. Hybrid fiber sheets consisting of D, C1 and C7.

2.2 *To enhance the serviceability performances of structures with hybrid fiber sheets composing of high modulus and high strength fiber sheets*

As expected in Figure 3, high modulus fibers combined with high strength, when subjected to loading, may exhibit high initial stiffness and then followed by some load drops due to gradual rupture of high modulus sheets till attaining the strength of high strength fiber sheets. Such hybridization may be helpful to enhance the structural stiffness, yielding load and cracking resistance when applied to repair or strengthen structures. However, as shown in Figure 5 and 6, load drops can be expected due to early and progressive rupture of high modulus and it may fail the structure if such load drops cannot be controlled within a small range. With the increase of hybrid ratio of high strength fiber sheets, load drops can be effectively controlled and a pseudo-plastic plateau can be achieved in hybrid sheets of C1/P with C7 fibers. This means that an optimum mix design can be made for practical application.

2.3 *To achieve a comprehensive structural behavior with hybrid fiber sheets composing of high modulus, high strength and high ductility fiber sheets*

Hybrid fiber sheets of high modulus, high strength and high ductility fibers may be composed together to present a required mechanical behavior in terms of initial stiffness, strength, ductility and other performances. Actually, ductility of FRP is one of major concerns in repairing/strengthening of structures.

Figure 7 demonstrates that increasing the hybrid ratio of high ductility fiber (D) may be helpful to control the load drops due to the rupture of C7 and C1 fibers and give a superior ductile behavior. The ratio of C1 only and slightly affects the behavior prior to the expected strength and after that load is successively transferred to D due to the failure of C1. High volume of C1 may smooth the load transfer in the hybrid fiber sheets. From the results of Figure 5–7, it is observed that there are good agreement between the experiments and prediction based on rule of mixtures for the initial stiffness, load at rupture of HM fibers and maximum load. Moreover, a hybrid composite with over 3% ultimate strain can be realized through an appropriate design of hybridization.

Table 2 and Table 3 summaries the tensile test results of hybrid fiber sheets composing of two or three types of fibers respectively. Each experimental value is an average one of five samples of specimens. Through the investigation on the stress (load) drop, it is realized that for the hybridization by composing two types of fibers, the load drop ratio is about under 10% while for the hybridization of composing three types of fibers the load drop ratio is about under 16% if the ratio of load loss is kept below 40%.

Table 2. Summary of tensile tests of hybrid fiber sheets (consisting of two types of fibers).

Type of specimen	Experiment or calculation	Load at HM sheet rupture P_y (kN)	Load loss due to HM sheet rupture P_r (kN)	Max. load P_{max} (kN)	Max. load drop due to HM sheet rupture P_d (kN)	$1–P_r/P_{max}$ (%)	P_d/P_y (%)	Ductility (%)
C7:C1 = 1:1		5.91		5.73	2.57		43	*
C7:C1 = 1:1.5		7.24	For	8.08	2.17	For	30	1.37
C7:C1 = 1:2	Experiment	8.31	calculation	11.90	0.90	calculation	11	1.35
C7:P = 1:1		6.44	only	5.44	2.21	only	34	*
C7:P = 1:2		8.03		10.01	0.75		9	1.28
C7:C1 = 1:1		6.05	4.53	5.87		23		1.48
C7:C1 = 1:1.5		6.81	4.53	8.81	For	49	For	1.48
C7:C1 = 1:2	Calculation	7.56	4.53	11.75	experiment	61	experiment	1.48
C7:P = 1:1		6.41	4.53	6.67	only	32	only	1.46
C7:P = 1:2		8.27	4.51	13.34		66		1.46

* These strains were not measured because extensometer was shifted due to impact at the HMC sheets rupture.

3 FLEXURAL STRENGTHENING OF STRUCTURES WITH EXTERNALLY BONDED HYBRID FIBER SHEETS

To investigate the effect of FRP hybridization on the flexural strengthening or repairing of RC structures, a series of beam specimens as shown in Figure 8 were constructed and tested under three point bending with one-point loading at the mid-span (Wu et al. 2004b). All the beams were designed to undergo enough shear strength for avoiding a brittle shear failure. The specimens were categorized into two groups: the first one was used for strengthening of virgin RC beams and the other one was for retrofitting of RC beams with existing damage.

3.1 *Load-deflection and crack width relationships of RC beams strengthened with hybrid composites*

3.1.1 *Strengthening of virgin RC beams*

Figure 9(a) and 9(b) show the experimental load-deflection curves of strengthened beams with both carbon fiber sheet (CFRP) and PBO fiber sheets (PFRP) by varying the FRP amount from 1 layer to 3 layers. Moreover, the control beam and examples of beam specimens strengthened with hybrid fiber sheets of C1C7 (1.5:1, 2:1) and PC7 (1.5:1, 2:1) are also drawn in Figure 9(a) and Figure 9(b) to make a comparison.

The observed test results showed that one layer of C1 or P sheets failed in rupture and with increase of FRP amounts, debonding failure may be caused from the end of a critical flexural crack around midspan with a brittle behavior. But by using hybrid fiber sheets, the failure mode may be shifted from debonding to gradual ruptures and the premature FRP debonding can be avoided and controlled by the FRP hybridization. As demonstrated in Figure 9 (a) and (b), hybrid fiber sheets with a hybridization of higher modulus type of carbon fiber sheets (C7) can achieve a higher initial stiffness. And a good ductility also can be realized because the gradual ruptures of fibers prevent the occurrence of FRP debonding. Due to the partial rupture of C7 in the hybrid fiber sheets, stresses may be redistributed and thus interfacial shear stress along FRP-concrete interface can be relieved, which is helpful to fully utilize the potentials of FRP composites and increase the ductility though final failure mode remains unchanged (debonding).

It is also found that the specimens strengthened with PBO fiber sheets yield higher strength and ductility than the ones with C1 fiber sheets, which lies in its higher energy absorption capacity in addition to its marginally high strength.

Figure 10(a) to Figure 10(c) represent the distribution of FRP strains with distance from the mid-span under different loading levels. It is observed from Figure 10(c) that the beam strengthened with hybrid fiber sheets can carry a very high ultimate stress near by the capacity of PBO fiber sheets. In the case of specimens strengthened with three layers of PBO sheets as shown in Fig 10 (b), the maximum FRP strains at the maximum load is below 10000 μ which is far away comparing with the ultimate strain of PBO fibers due to the premature debonding failure of FRP sheets.

Table 4 tabulates the various indices of performance evaluation of structural beams on steel yielding load, deflection load, ultimate load, ductility and FRP strain at final failure. All indices are defined as ratios i.e. the steel yielding load, inflection load and ultimate load of the control beam are considered as reference. Moreover, the index of the FRP strain is defined as a ratio between the FRP strain at final failure and the ultimate strain.

Table 3. Summary of tensile tests of hybrid fiber sheets (consisting of three types of fibers).

Type of specimen	Experiment or calculation	Load at HM sheet due to rupture P_y (kN)	Load loss due to HM sheet rupture P_r (kN)	Max. load P_{max} (kN)	Load drop due to HM sheet rupture P_{d1} (kN)	Load drop due to HS sheet rupture P_{d2} (kN)	$1-P_r/P_{max}$ (%)	P_{d1}/P_y (%)	P_{d2}/P_{max} (%)	Ductility (%)
C7:C1:G = 1:1:3		10.56		16.74	1.67	3.83		16	23	2.19
C7:C1:G = 1:1:4		9.79		14.77	1.89	2.60		19	18	2.22
C7:C1:G = 1:1.5:3		9.51	For	17.83	0.80	1.71	For	8	10	2.29
C7:C1:G = 1:1.5:4	Experiment	10.65	calculation	21.24	0.21	2.02	calculation	2	10	2.86
C7:C1:D = 1:1:3		9.64	only	18.80	0.51	3.16	only	5	17	2.90
C7:C1:D = 1:1:4		10.72		22.15	0.42	6.35		4	29	2.90
C7:C1:D = 1:1.5:3		11.42		18.75	0.53	6.38		5	34	3.10
C7:C1:G = 1:1:3		7.65	4.54	12.12			63			2.23
C7:C1:G = 1:1:4		8.17	4.53	14.13			68			2.23
C7:C1:G = 1:1.5:3		8.39	4.52	15.00	For	For	70	For	For	2.23
C7:C1:G = 1:1.5:4	Calculation	8.92	4.52	17.07	experiment	experiment	74	experiment	experiment	2.23
C7:C1:D = 1:1:3		8.63	4.50	15.91	only	only	72	only	only	3.07
C7:C1:D = 1:1:4		9.48	4.48	19.26			77			3.07
C7:C1:D = 1:1.5:3		9.38	4.49	18.85			76			3.07

Note: G stands for glass fiber and D stands for Dyneema fiber.

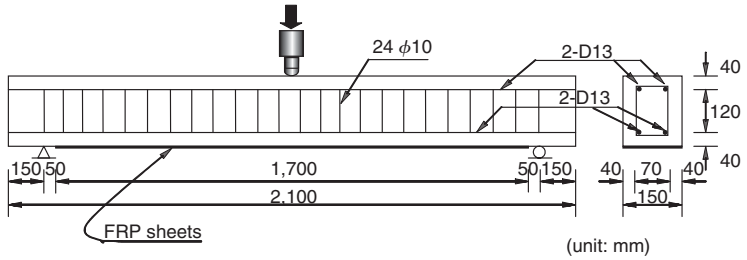

Figure 8. Dimensions of FRP-strengthened RC beams.

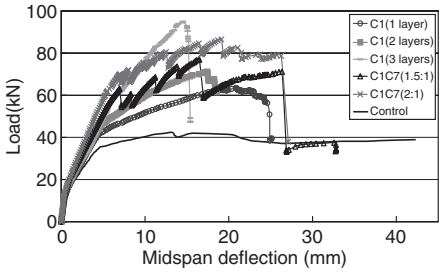

(a) C1 series

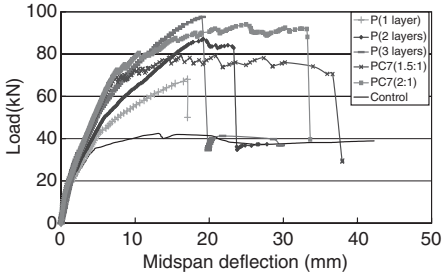

(b) PBO series

Figure 9. Load-deflection curves of strengthened virgin RC beams.

Through the comparison of different evaluation indeces, the hybridization of C1C7 or PC7 with a layer mixture of 2:1 can be considered being an optimum design for strengthening concrete beams as externally bonded reinforcements.

In Figure 11, two beam specimens were strengthened with hybrid fiber sheets composing of high modulus (C7), high strength (C1) and high ductility (D) fibers under a proportion of 1:1:3 by using 3 and 5 U-wrapping anchorages respectively. Because in this study different FRP layered hybridization is to use existing fiber sheets, it is difficult to have a mixture design by considering the constraints condition

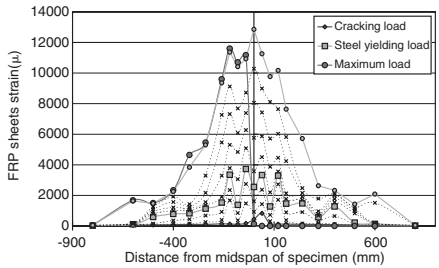

(a) Single PBO sheet (1 layer)

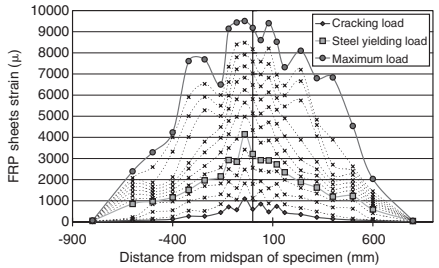

(b) Single PBO sheets (3 layers)

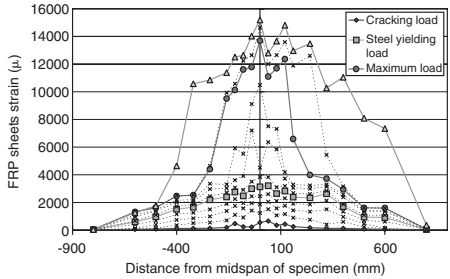

(C) PC7 hybrid sheet (1.5:1)

Figure 10. Strain distributions along beam axis of strengthened RC beams.

Table 4. Various indices of performance evaluation.

	Indices				
	Steel yielding load	Inflection load	Ultimate load	Ductility ratio	FRP strian at failure
C1(1 layer)	1.16	1.18	1.49	5.29	0.75
C1(2 layer)	1.40	1.33	1.91	6.25	0.94
C1(3 layer)	1.60	1.56	2.24	3.13	0.49
C1C7(1:1)	1.47	1.72	1.69	4.25	1.11
C1C7(1:5:1)	1.50	1.78	1.82	5.67	0.91
C1C7(2:1)	1.73	1.81	2.04	5.66	1.06
C1C7(2:5:1)	1.76	1.92	2.26	5.56	0.78
P(1 layer)	1.16	1.16	1.60	3.67	0.77
P(2 layer)	1.30	1.43	2.05	5.01	0.72
P(3 layer)	1.55	1.52	2.30	4.09	0.60
PC7(1:1)	1.41	1.61	1.84	3.34	0.98
PC7(1:5:1)	1.64	1.75	1.87	7.88	0.95
PC7(2:1)	1.72	1.85	2.22	7.13	0.84
PC7(2:5:1)	1.87	1.87	2.24	4.55	0.72

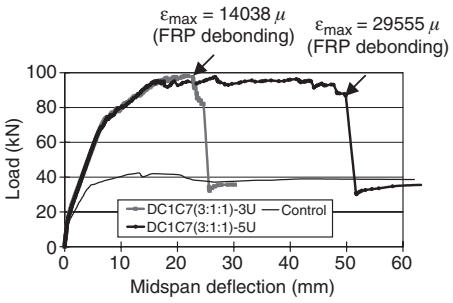

Figure 11. Load-deflection curves of strengthened RC beams with hybrid sheet composing of three types of fibers D, C1 and C7.

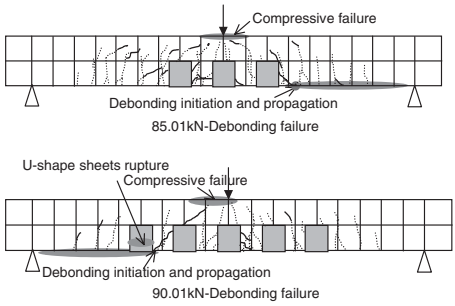

Figure 12. Performances of 3 and 5 U-wrapping anchorage to avoid debonding failure.

for avoiding FRP debonding. To prevent the premature debonding failure, a certain number of U-wrapping anchorages were used around the midspan of specimen (Fig. 12).

Although the debonding is predicted to initiate around the midspan, due to the large amount of flexural reinforcements of both rebars and hybrid composites, a diagonal flexural crack become a dominated one and the FRP debonding initiates from the end of this crack (Fig. 12). Therefore, as shown in Figure 12 for the spacing of 20 mm c/c, the performances of three U-wrapping anchorages to prevent debonding was also not satisfactory. However, a very desirable strengthening performance can be achieved by using hybrid fiber sheets consisting of three types of fiber sheets with five U-warpping anchorage [DC1C7(3:1:1)-5U]. Although the final failure is due to the FRP debonding, the full ability of the hybrid composites is also almost displayed because the FRP strain at final debonding failure reaches 29555 μ.

As explained previously, hybrid fiber sheets can relieve the stress concentration at cracks and thus to a certain degree, prevent the premature debonding failure. If an optimum design could be made for the fibers, the structure can behave in a desirable way even without anchorage.

3.1.2 *Strengthening of existing beams with initial damage*

In most of the practical cases, existing structures under service may have experienced some cracks or a certain degree of damage and the strengthening is performed without removing the service load. So it is necessary to investigate the strengthening performance of preloaded structures. The beam specimens were first preloaded to a percentage of the experimental yield

load of the control beam and then strengthened with CFRP sheets on the bottom, followed by using the electrical heaters to speed up the curing process for three hours at 80°C, while the preload was maintained.

When the temperature decreases to room temperature, loading was resumed till failure. The load was applied incrementally by a 200 kN-universal testing machine at the rate of 1 kN/min until failure (Sakamoto 2002). Figure 13(a–c) show the load-deflection curves while Fig. 3(d) shows the load-crack width curve for damaged RC beams strengthened with single or hybrid fiber sheets.

The experimental results showed that high predamage level yields more cracks in beams and thus a low stiffness, which may improve stress distributions in FRP composites and thus present a good ductility. It can also be concluded that no adverse effect of precracking has on the strengthening performance as compared to the corresponding virgin beams, which agrees with the experimental findings from other researchers (Arduini and Nanni, 1997). However, it can be identified that the hybridization by composing of high modulus type of fiber sheet has more effective and remarkable role in strengthening the structures with severe damage especially on different serviceability performances.

Some results of interests of RC beams have been mentioned in Figure 14 (a) to Figure 14(d). Figure 14 (a) gives yielding load vs. stiffness curve for different individual and hybrid fibers. From Figure 14(a), it is found that there is a linear relationship between the yielding load and the effective stiffness (Et) of FRP, although both cases of single types of fibers and hybrid fibers are not in one line. Because the yielding loads of specimens are determined based on the limited measurement points of strain gauges attached to the rebars, there is a difference between the judgment and real situation. Therefore the load at inflection points determined from the load-deflection curve is also discussed here. Due to the uses of hybrid fibers, the stiffness level of RC beams shifted to a higher range (110–160 kN/mm). Figure 14(b) shows the load at the inflection point vs. stiffness of various FRP sheets. A good linear variation between load at inflection point and stiffness is observed for both individual and hybrid fibers.

Figure 14 (c) shows the reationship between the maximum load and potential tensile ability of FRP sheets. The strengthening effect on load carrying capacity by using hybrid composites is higher than one by using single types of fibers. Moreover, there is a limit on strength enhancement by using single type of fiber sheets due to the limited ability of FRP–concrete interface. Figure 14(d) shows that for all the used fibers, the ductility increases within the range of potential tensile ability value of 0.6–1 kN/mm and then ductility decreases for higher value of f_t–t.

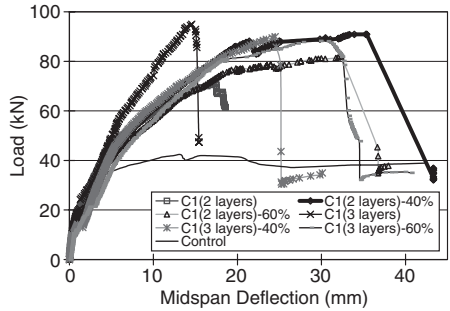

(a) Single type of C1 sheets

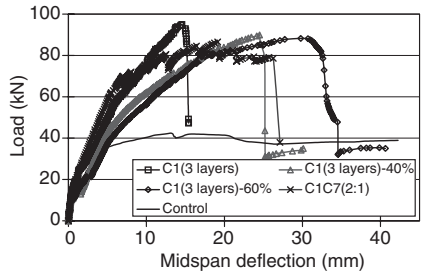

(b) Hybrid fiber sheets with two types of C1 and C7

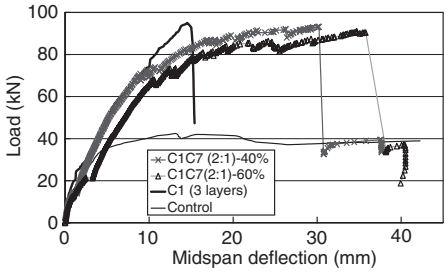

(c) Hybrid fiber sheets with two types of C1 and C7

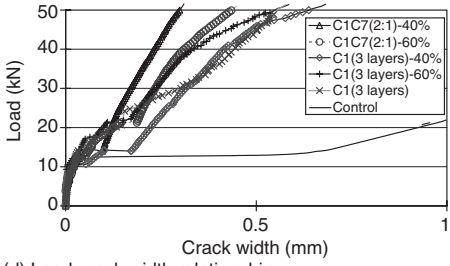

(d) Load-crack width relationship

Figure 13. Load-deflection (a–c) and crack width (d) curves of strengthened RC beams with damage.

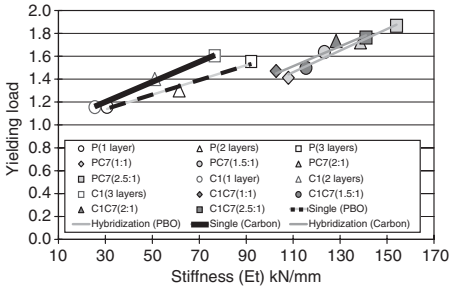

Figure 14(a). Yield load vs. stiffness of FRP sheets.

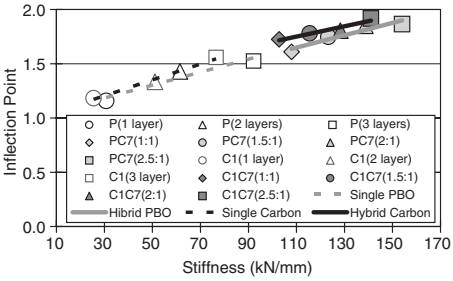

Figure 14(b). Load at inflection point vs. stiffness of FRP sheets.

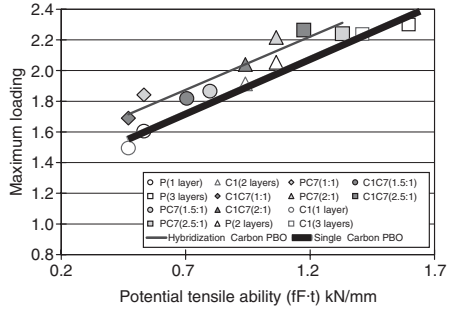

Figure 14(c). Load carrying capacity vs. tensile ability of FRP sheets.

4 NUMERICAL INVESTIGATION OF HYBRID STRENGTHENING EFFECT

Unlike steel reinforcement, FRP sheets of single type generally behave in linear elastic fashion until rupture. However, when hybrid fiber sheets are subjected to loading, some progressive damages such as matrix

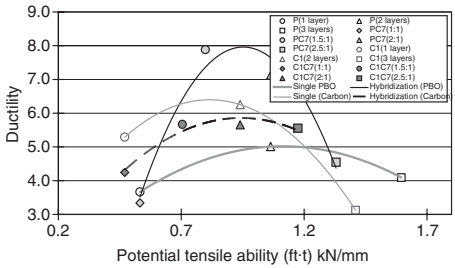

Figure 14(d). Ductility vs. potential tensile ability of FRP sheets.

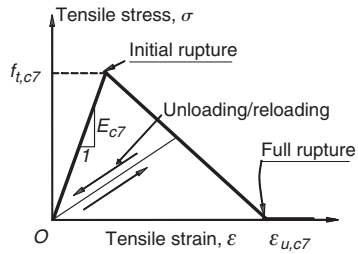

Figure 15. Modeling of progressive rupture of C7 in hybrid composite.

cracking, fiber-matrix debonding, fiber-rupture and delamination may lead to a different mechanical behavior, as shown in the experimental observations (Figs 5–7).

Considering that the shocks from such damages may rupture a portion of unimpaired fibers, it is very important to evaluate the stress transfer capacity upon the partial rupture of some fibers.

Herein, from a macroscopic point of view, a damage mechanical behavior shown in Figure 15 (Niu and Wu, 2003b) is used for simulating the stress transfer from C7 to C1 during progressive rupture of C7 fibers, where C7 and C1 sheets are expected to achieve initial high modulus and final high strength respectively.

By using this model, the effect of hybrid ratios can be found in Figure 16a. It is easy to conclude that load drop can be significantly reduced with the increase of the volume of C1 sheet on the whole, but there is no doubt a certain limit in the hybrid design over which it is not economical to achieve the expected effect. Fig. 16b demonstrates that the amount of load drop or the expected hybrid effect also depends on the stress transfer behavior caused by progressive rupture of C7 fibers. The slower rupture process is the desirable hybrid effect can be achieved.

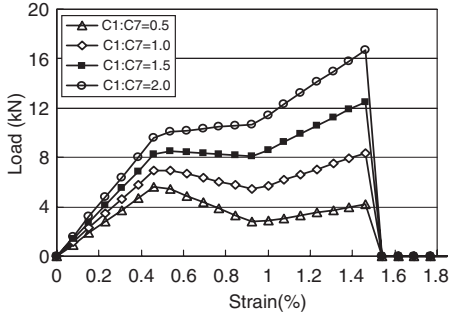

(a) Hybrid ratios of C1 to C7 sheets

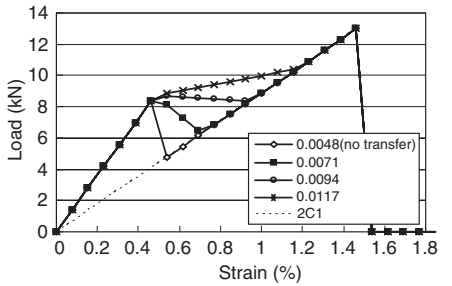

(b) Rupture strain of C7 sheet in 2C1/C7 sheets

Figure 16. Hybrid effects for different ratios and rupture strains of C7 sheet.

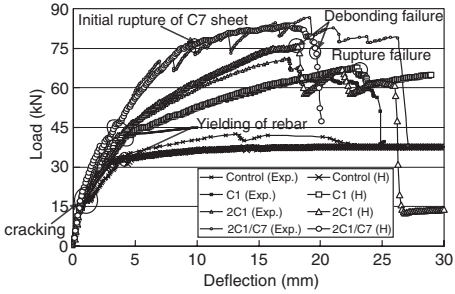

Figure 17. Comparison of numerical and experimental results.

To further investigate the strengthened RC beams, as shown in Figure 17, the overall numerical results were in good agreement with the experimental ones (Niu and Wu, 2003b). It should be noted that the proposed model is based on a macroscopic behavior not the local one, which makes it unable to capture load fluctuations in the experiment of hybrid fiber sheets.

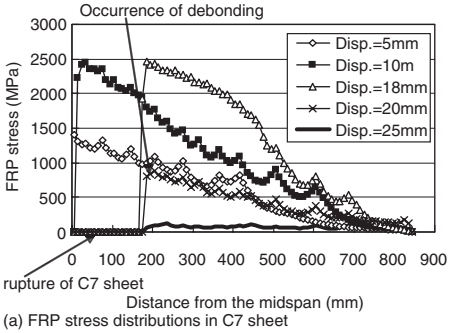

(a) FRP stress distributions in C7 sheet

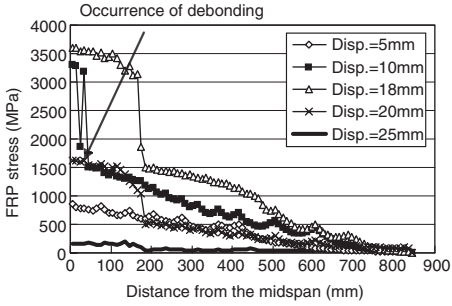

(b) FRP stress distributions in C1 sheet

Figure 18. FRP stress distribution of C1C7 (2:1) hybrid sheets.

5 CONCLUSIONS

FRP composites have been widely accepted as an effective mean to repair/strengthen civil infrastructures. However, the problems of debonding and brittle rupture limit the practical applications of FRP composites. To fully utilize the properties of these materials, hybrid design concept is one of the alternatives. This paper provides a review of using hybrid fiber sheets composing of high modulus, high strength and high ductility fibers to strengthen the structures. The research work on strengthening of columns and developing new composite structures by using hybrid concept and hybrid composite fibers is also carried out in Ibaraki University, Japan. The effectiveness and practicability of hybrid concept and hybridization of fibers have also been confirming.

REFERENCES

Razaqpur, A. G. & Ali, M. M. (1996), A new concept for achieving ductility in FRP-reinforced concrete, *Proceedings of the First International Conference on Composites in Infrastructure (ICCI'96)*, 401–413, Tucson, Arizona.

Harris, H. G., Somboonsong, W., Ko, F. K. & Huesgen, R. (1998), A second generation ductile hybrid fiber reinforced polymer (FRP) for concrete structures, *Proceedings of the Second International Conference on Composites in Infrastructure (ICCI'98)*, Vol. 2, 66–79, Tucson, Arizona.

Apinis, R., Modniks, J., Tamuzs, V. & Tepfers, R. (1998), Ductility of hybrid fiber composite reinforcement FRP for concrete, *Chalmers University of Technology, Göteborg, Div. of Building Tech.,* Publication No 1998:2, Work No 21, 8 pp.

Wu, Z. S., Sakamoto, K., Iwashita, K. & Yue Q. (2004a), Hybridization of continuous fiber sheets as structural composites. *Journal of the Japan Society for composite Materials (Submitted)*.

Wu, Z. S., Sakamoto, K., Iwashita, K. & Kobayashi, A. (2004b), Enhancement of flexural performances through FRP hybridization with high modulus type of carbon fibers, J. of materials, concrete struct. & pavements, JSCE (Submitted).

Wu, Z. S., Sakamoto, K., Niu, H. D. & Kurokawa, T. (2001), Retrofitting RC beams with innovative hybrid fiber sheets, *Proc. of The Seventh Japan Int.l SAMPE Sym.* 383–386, Tokyo.

Wu, Z. S., Sakamoto, K., Niu, H. D., Shimada, M. & Murakami, S. (2002), Strengthening effects of concrete flexural members retrofitted with hybrid FRP composites, *Proceedings of The Third International Conference on Composites in Infrastructure (ICCI'02)*, CD-ROM, California.

JSCE (2001), Recommendations for Upgrading of Concrete Structures with Use of Continuous Fiber Sheets, *Concrete Eng. Series 41*, JSCE.

Arduini, M. & Nanni, A. (1997), Behavior of precracked RC beams strengthened with Carbon FRP sheets. *J. of Compo. for Cons.* 1(2), 63–70.

Niu, H. D. & Wu, Z. S. (2003a), Strengthening of deteriorated RC beams with externally bonded FRP sheets, *Proceedings of the 8th Japan Int. SAMPE Symposium,* 1245–1251, Tokyo.

Niu, H. D. & Wu, Z. S. (2003b), Numerical investigation on strengthening behavior of concrete structures strengthened with hybrid fiber sheets, *J. of Applied Mechanics*, JSCE, 1217–1216.

FRP research in China (special session)

FRP Composites in Civil Engineering – CICE 2004 – Seracino (ed)
© 2005 Taylor & Francis Group, London, ISBN 90 5809 638 6

FRP in China: the state of FRP research, design guidelines and application in construction

L.P. Ye, P. Feng, X.Z. Lu, P. Qian, L. Lin, Y.L. Huang & W.H. Hu
Department of Civil Engineering, Tsinghua University, Beijing, China

Q.R. Yue, Y.X. Yang, Z. Tan, T. Yang, N. Zhang & R. Li
National Engineering Technique Research Center of Industrial Buildings, Beijing, China

ABSTRACT: This paper presents the state of FRP research and design guidelines in construction in the mainland of China. It covers structural strengthening with FRP sheets and plates, reinforced concrete structures with FRP bars and tendons, all FRP structures and bridges, and FRP-concrete composite structures.

1 INTRODUCTION

Research on FRP in construction in the mainland of China may be traced back to the end of 1950s when China was in short supply of steel. The purpose of the research was to explore the use of GFRP bars instead of steel bars in RC T-section beams. But the beam failed in a very brittle manner with a sudden rupture of the GFRP bars, and the research was not continued. In 1982, a highway bridge of 20.7 m in span and 9.2 m in width in the form of a box-beam made of GFRP honeycomb plates was built in Beijing, which was the first trial to use FRP in bridges in China. After about one year's service, a local depression was observed in the bridge due to the instability of the honeycomb and local buckling. The GFRP beam was then strengthened into a GFRP-concrete composite beam in 1987 and the bridge has performed well till now.

Systematic research on FRP in construction was begun in 1997 when the external bonded CFRP sheets strengthening technique for RC structures was introduced in China. The first test to demonstrate the effectiveness of this new strengthening method was conducted in 1997. Then, a series of experimental studies were conducted at Tsinghua University under the leadership of YE and YUE (Ref. 1–3). With the fundamental research results, FRP began to find its applications more and more in RC structure strengthening. It is estimated that about 600,000 m^2 of FRP sheet was used in 2003. In 1998, a sub-committee of FRP in construction was founded under the Chinese Civil Engineering Association. After that, there has been more and more research on FRP strengthening of structures. Figure 1 shows the growth in the number of technical papers on FRP in construction published in Chinese journals from 1997 to 2003. In 2002 and 2003, two key research projects on FRP in civil engineering were supported by the Chinese Science and Technology Ministry and the Chinese National Science Foundation. A design specification for RC structures strengthening with CFRP sheets was published in May, 2003. Now, a design code of FRP in civil engineering with a wider scope of application of FRP in addition to RC structure strengthening is under development and will be finished by the end of 2004.

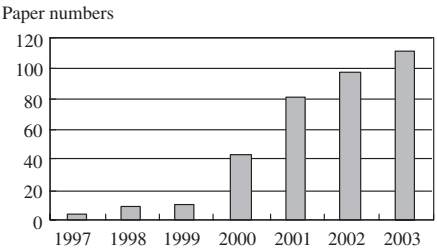

Figure 1. Numbers of technical papers published in chinese journals.

2 RC STRUCTURE STRENGTHENING

2.1 *Flexural strengthening*

Figure 2 shows the experimental research of RC bridge slab flexurally strengthened with CFRP sheets bonded to the soffit under sustained load. It was found that the initial load before strengthening has only a small influence on the ultimate strength (Ref. 4).

(a) Test set-up

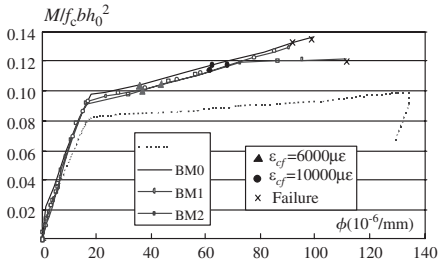

(b) Test results of M-ϕ relation

Figure 2. Test of RC bridge slabs strengthened with CFRP sheets under sustained load.

With the initial experimental research, it was found that debonding failure was one of the controlling failure modes. And then tests on fourteen beams, in addition with a series of FRP-to-concrete bond tests, were conducted on the debonding strength, and FRP U-jackets were suggested to increase the flexural debonding strength (Ref. 5). Figure 3 shows that the flexural debonding strength and the deformation capacity can be increased with a uniform arrangement of U-jackets. A thorough theoretical study with the finite element method on the debonding behavior was then undertaken (Ref. 6). A more detailed report on research on debonding is given in another paper to be presented at CICE 2004 (Ref. 7).

It is known from a lot of research that the strength of FRP can only be effectively developed after the yielding of tensile steel reinforcement in RC beams for flexural strengthening. And it is naturally to apply prestressed technique for flexural strengthening and a device to apply prestressing to FRP sheets was developed in 2003 (Ref. 8). Then, seven full scale beams strengthened with prestressed CFRP sheets, including five RC beams and two PC beams, were tested. Figure 4a shows the prestressed CFRP sheets before bonding to the bottom of the beam, and Figure 4c shows a comparison of the two PC beams, in which PB1 is the one strengthened with the conventional method and PB2 is the one strengthened with prestressed CFRP sheets.

(a) Test set-up

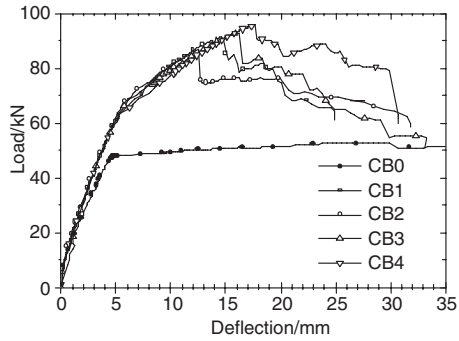

(b) Load-Deflection Relations

Figure 3. Flexural Debonding of CFRP-strengthened RC beams with U-jackets for anchorage.

(a) Prestressed CFRP sheet before bonding to the bottom of the beam and the test set-up

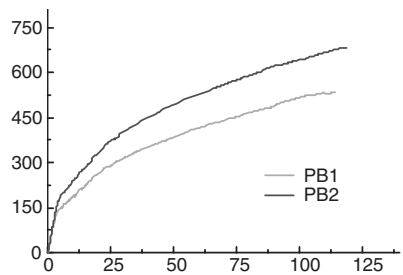

(b) Comparison of load-deflection relations

Figure 4. RC beams strengthened with prestressed CFRP sheets.

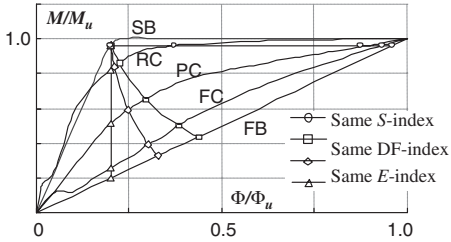

Figure 5. Comparison of design levels using different design indices.

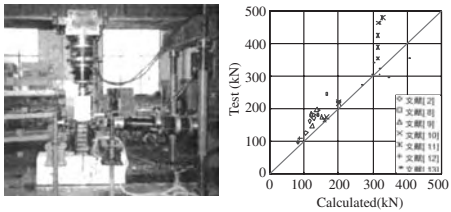

(a) Test set-up

(b) Comparison of calculation results with test results

Figure 6. Shear strengthening of RC column.

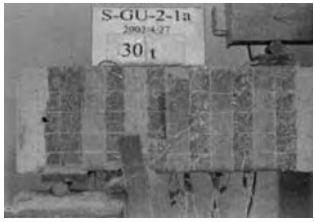

(a) Failure pattern

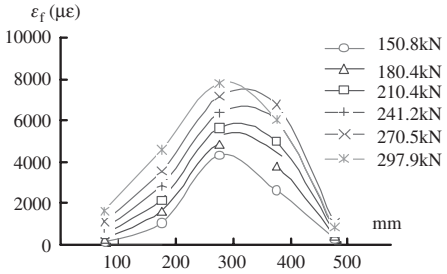

(b) The strain distribution in FRP

Figure 7. Debonding failure of RC beams shear strengthened with GFRP U-jackets.

To achieve the same safety degree as ordinary RC and steel beams, the design indices for strength, ductility and deformability for different load-deformation patterns obtained from different compositions of material were studied. Figure 5 shows the comparison of design levels using different design indices for normalized M-ϕ relations of steel, RC, PC, FRP-concrete and FRP beams, in which $S = M_u/M_d$ is the strength index; $D = \phi_u/\phi_d$ is the ductility index; $E = E_u/E_d$ is the energy index; $DF = (M_u/M_d)(\phi_u/\phi_d)$ is the deformability index. It was concluded that the deformability index and the energy index are reasonable for use to achieve the same safety degree for FRP and FRP–concrete beams as the RC and steel beams. Based on this design philosophy, the design criteria based on the reasonable design index is used for flexurally strengthened RC beams and the other of FRP application in construction.

2.2 *Shear strengthening*

In 1998, seven specimens of RC columns strengthened by wrapping CFRP sheets were first tested at Tsinghua University to investigate the shear strength enhancement (Figure 6a, Ref. 9). In the tests, the strains and their distributions in the CFRP sheets were carefully studied to determine the contribution of CFRP to the shear strength. It was found that the amount of CFRP, shear-span ratio and axial load ratio have effects on the contribution of CFRP to the shear strength (Ref. 9–11). Based on the analysis of test results, a simplified calculation formula to determine the contribution of CFRP to the shear strength is suggested (Ref. 12). Figure 6b shows the comparison of the calculated results and the test results.

For RC beams, U-jacket bonded strengthening is always used in construction and debonding is the main failure mode. In 2002, 15 beams were tested to investigate the shear debonding strength (Ref. 13). The strain distribution and its development in the FRP sheets were carefully studied to obtain the shear contribution of FRP when shear debonding occurs. Figure 7a is a photograph of shear debonding failure of GFRP U-jackets. Figure 7b shows the strain distribution and development in the GFRP sheets. Based on the test results and finite element analysis (Ref. 14), it was found that the shear contribution of FRP U-jackets only depends on the bonded area and the FRP-to-concrete interfacial shear strength. It was found that the shear-span ratio has some influence on the strain distribution, and the stiffness of FRP sheets has less effect on the shear contribution of FRP.

2.3 *Seismic strengthening of RC columns*

In 1998, eight specimens of RC columns, including two strengthened after being loaded to yield level with some damage and one strengthened under a sustained

(a) Circular columns (b) Square columns

Figure 8. Test set-up for RC columns under high axial load and cyclic lateral load.

axial load, with insufficient hoops according to the current Chinese seismic design code were tested under constant axial load and lateral cyclic load at Tsinghua University to investigate the improvement of seismic performance by wrapping CFRP sheets (Ref. 15–16). The ductility enhancement with the confinement of CFRP sheets was studied by the strain development and distribution in the CFRP sheets. Based on the experimental research, it was found that the strains in the wrapped CFRP sheets were mainly induced by the expanding concrete after the yielding of the columns. An equivalent confinement factor of the wrapped CFRP sheets was proposed to make up for the deficiency in the amount of steel hoops.

In the Chinese seismic design code, the axial load is limited for RC columns to ensure sufficient ductility. The limitation of the axial load is related to the amount of steel hoops. There is a demand in construction to increase the axial load limitation with the confinement of FRP for existing columns. A series of experiments, including six circular RC columns and seven square RC columns were conducted in 2003 under high axial load-to-concrete strength ratio ($\sigma_c/f_c = 0.7 - 1.0$) and cyclic lateral loads (Figure 8–9). Based on the experimental results, the relationship between steel reinforcement confinement and FRP confinement was calibrated, and a simple expression was proposed. As a result, the design method of FRP confinement can be easily implemented into the design code for RC columns.

2.4 *Compressive stress–strain behavior of FRP-confined concrete*

The compressive behavior of concrete confined by FRP and hybrid FRP jackets and tubes, including round, square and rectangular sections under uniaxial compression were researched in several universities in China. Figure 10 shows some photographs of specimens tested at Tsinghua University and some test results. A design-oriented stress–strain relation considering the effects of section type, size ratio and initial axial load ratio was suggested based on the test results.

In order to investigate the behavior of square concrete columns confined by FRP sheets, finite element analysis was used. The FEA method can effectively simulate the behavior of square columns confined by FRP sheets when a proper numerical model is adopted. Based on the test and FEA results, the stress distributions and the stress development were obtained (Figure 11a). And the strong constraint area at the corners, the weak constraint area at the edges and the average constraint area in the centre were determined (Figure 11b). These results provide a theoretical understanding for establishing a stress–strain model. Figure 12 shows a comparison of stress–strain curves from FEA and the test results.

A new analysis-oriented stress–strain model for FRP-confined concrete has been proposed for circular columns (Ref. 18). In this model the responses of the concrete, the FRP jacket and their interaction are explicitly considered. The key new feature of this model is a more accurate and widely applicable lateral strain equation based on careful interpretations of test results of unconfined, actively confined and FRP-confined concrete. Independent test data were compared with predictions of the proposed model to demonstrate its accuracy, as shown in Figure 13.

2.5 *Others*

The research on the strengthening of other RC structural elements with FRP sheets and plates in China includes two-way slabs, torsional members and beam-column joints. There has also been research on RC beams strengthened using external prestressed CFRP strands and fatigue behavior of RC beams strengthened with CFRP sheets and prestressed CFRP sheets.

3 STRENGTHENING OF OTHER KINDS OF STRUCTURES

3.1 *Steel structures*

To increase the fatigue strength of steel beams, a series of experimental studies on the strengthening of steel structures with CFRP were conducted at the National Engineering Technique Research Center of Industrial Buildings since 2001. The tensile tests showed that the tensile strength can be increased by 8∼21% with different amounts of CFRP. Figure 14 shows welded tensile specimens and a comparison of the S-N relation under fatigue cyclic loading. An increase in the fatigue strength was also obtained in a steel beam in which CFRP sheets were bonded to the round corners at the support of the steel beam.

3.2 *Masonry structures*

About sixty percent of the masonry buildings in China were built about 30 years ago and some were built more than 100 years ago. Many of them do not meet

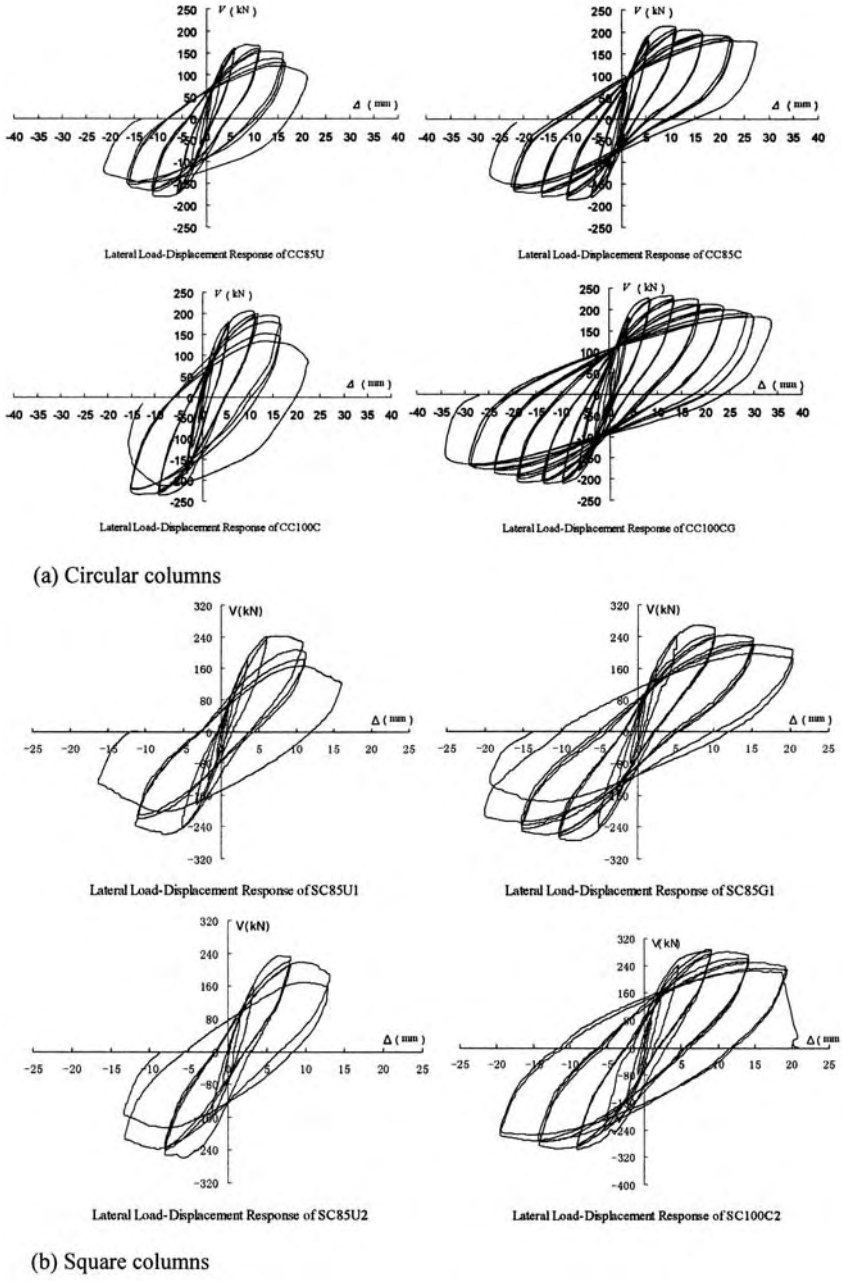

Figure 9. Load-displacement hysteresis relations of RC columns under high axial load and cyclic lateral load.

(a) Specimens of confined RC columns: square and rectangular section confined with CFRP and hybrid FRP; GFRP and hybrid C-G-FRP tube

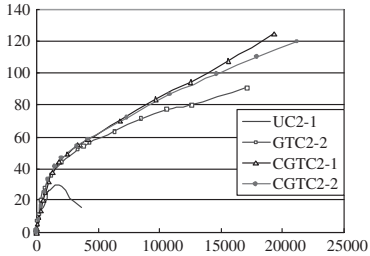

(c) Stress-strain relations of FRP tube confined concrete

Figure 10. Tests on FRP confined concrete.

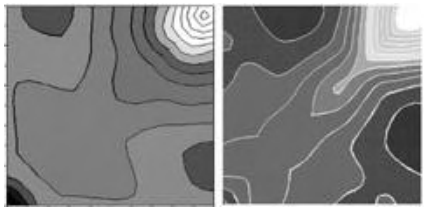

(a) Stress distribution in concrete (darker for lower stresses)

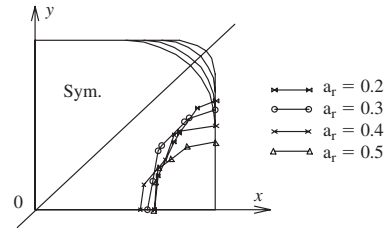

(b) Strong and weak confined regions

Figure 11. FE analysis results.

the requirements of the current design requirements, especially the seismic resistance of the masonry walls. About 40 masonry walls strengthened with GFRP and CFRP sheets were tested under cyclic lateral load in the wall plane to investigate seismic resistance behavior in China. Figure 15 shows the experimental research conducted at Tsinghua University. It was found that

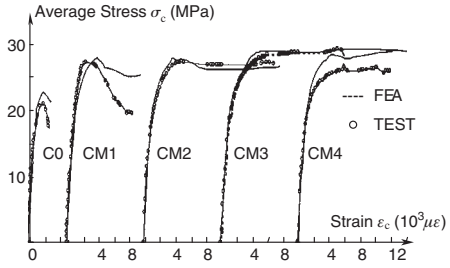

Figure 12. Comparison of stress–strain curves.

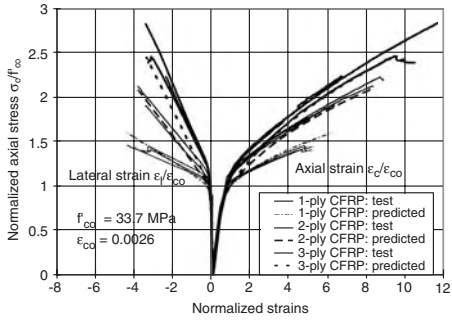

Figure 13. Comparison with test results of CFRP-wrapped specimens.

(a) Welded tensile steel specimens

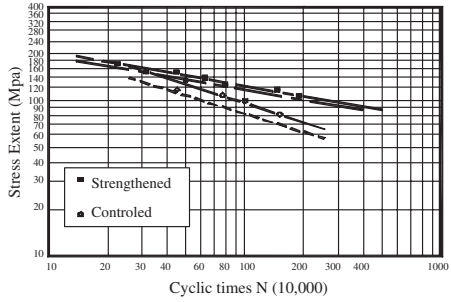

(b) Comparison of S-N relation

Figure 14. Fatigue behavior of tensile steel specimens.

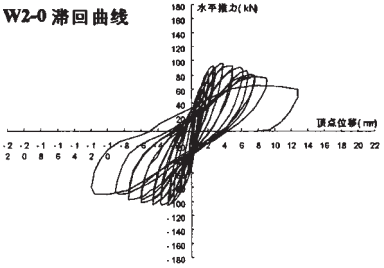

(a) W2-0

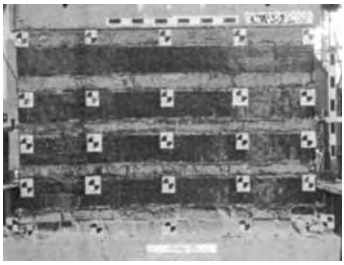

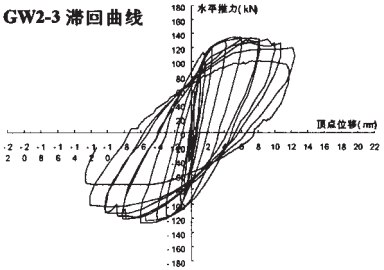

(b) CW2-3

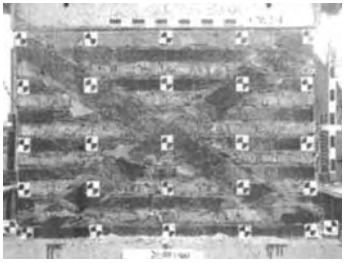

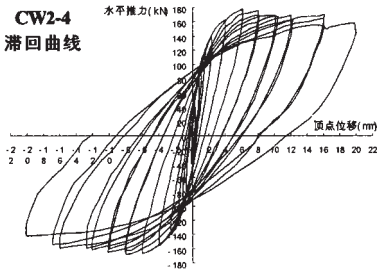

(c) CW2-4

Figure 15. Test of masonry walls strengthened with FRP sheets.

the seismic shear strength of masonry walls can be increased by the direct tensile stresses developed in the FRP sheets, and in addition, the integrity of the wall can be enhanced.

3.3 *Special structures*

Figure 16 shows a test of a containment shell structure of a nuclear power station strengthened with CFRP sheets conducted by the National Engineering Technique Research Center of Industrial Buildings. The one-tenth scale shell structure model was first loaded to failure under internal pressure and then strengthened with CFRP sheets. It was shown that the capacity can be recovered and a little increased to the level of the new one.

4 RC STRUCTURES WITH FRP BARS AND PRESTRESSED FRP TENDONS

Research on RC structures using FRP bars began at Southeast University, Nanjing, in 1999, and then at Tongji University, Shanghai. More than 40 beams were tested to determine the flexural behavior and to establish the flexural strength. To obtain high performance, Southeast University began to study RC beams prestressed with FRP tendons and developed

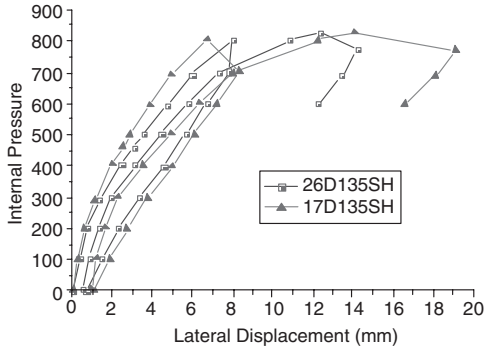

(a) Test model

(b) Test curves of internal pressure and lateral displacements

Figure 16. Test of containment shell structure of nuclear power station.

some anchorage devices for prestressed FRP tendons. The design methods are now well developed, but there has been no application so far, because there is not much demand in construction compared to FRP strengthening.

5 ALL FRP STRUCTURES AND FRP–CONCRETE COMPOSITE STRUCTURES

5.1 *GFRP bridges*

Besides the first GFRP highway bridge built in Beijing in 1982, about seven GFRP footbridges were completed in Sichuan province from 1986 to 1993. Figure 17 shows two of them built in Chongqin.

5.2 *FRP bridge deck*

In 2001, a research project on FRP bridge decks was undertaken at Tsinghua University. The initial test results showed that delamination and local buckling were the controlling failure modes. To enhance the deck's performance, the use of outside filament winding was proposed. Figure 18 shows obvious improvement as a result of filament winding. A pseudo-ductile behavior can be achieved by outside winding reinforcement. Based on the initial test results, an FRP deck product for traffic bridges was designed as shown in Figure 18.

5.3 *FRP space structures*

Due to its favorite properties of lightweight and high strength, it is reasonable to use FRP to construct super span space structures. Two types of all FRP super-span space structures are now under research at Tsinghua

(a) Chenjiawan bridge

Jiaoyuan Bridge

Figure 17. GFRP footbridges in Chongqin.

University. One is the latticed space structure using FRP tubes. Figure 20 shows CFRP tubes used to study their mechanical behavior under axial tensile and compressive forces. A linear behavior was found in the tests until debonding or buckling failure occurred.

Another innovative form of FRP super-span space structures is the FRP woven web structure (FRP WWS). A model is shown in Figure 21. In the FRP WWS, the high-strength FRP strips are woven like bamboo strips in a Chinese bamboo mat to form a plane web. The outer and the inner ring beams are provided to anchor the FRP strips, which are initially prestressed to establish sufficient stiffiness. The low self-weight, high tensile strength and corrosion-resistance of FRP

(a) FRP deck without outside filament winding

(b) FRP deck with outside filament winding

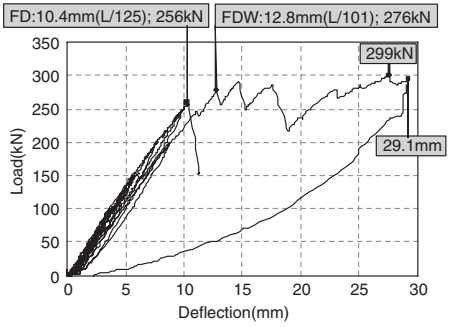

(c) Comparison of load-deflection of FD and FDW

(d) FRP deck product

Figure 18. FRP bridge deck for traffic bridges.

strips can be fully utilized in an FRP WWS. In addition, a significant amount of damping can be expected to arise from friction at joints between FRP strips. Special architectural configurations can be achieved by employing regular weaving patterns.

5.4 *Concrete filled FRP tubes*

More than 40 concrete filled GFRP tube columns were tested to determine their static and seismic behavior at Tongji university since 1999. The ductility of the

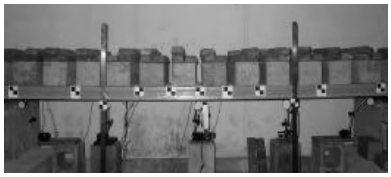

(a) Test set-up

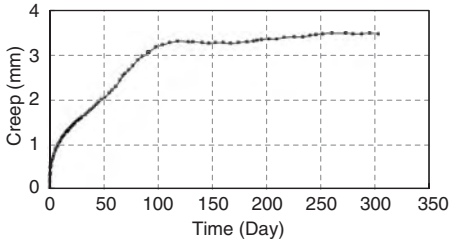

(b) Creep deformation

Figure 19. Long term test of FRP deck.

columns was much increased with the confinement of GFRP tube. It was found that GFRP tubes made with fibers in 45 degrees had pseudo-yielding properties under compression. A hybrid tube of GFRP and CFRP has been used in the research on compressive behavior of confined concrete at Tsinghua University in 2003, as shown in Figures 10c and 10d.

6 DESIGN SPECIFICATIONS AND STANDARDS

The development of the first design and construction specification for CFRP strengthening of RC structures began in 1998. The specification was formally approved by the Chinese Construction Standard Committee in May, 2003. Two material product standards, for CFRP sheets and resins respectively, were also published. With the increased field applications of FRP in civil engineering and based on the researches in recent years, a code of FRP application in civil engineering has been under development since 2002. The contents of the code are as below.

(1) FRP materials: CFRP, GFRP and AFRP and their products, such as FRP bars, strands and tubes, are included. The standard mechanical properties should have a reliability of 95% based on more than 15 standard tests. And lower bounds are imposed for each kind of FRP materials and the corresponding mechanical properties.
(2) Strengthening of RC structures: Flexural strengthening of beams and slabs with external bonded CFRP sheets and plates, both prestressed and

(a) CFRP tubes for latticed space structures

(b) Debonding failure under tension

(c) Debonding failure under compression

(d) Local buckling failure

Figure 20. CFRP tubes for space truss structures.

Figure 21. A model of the FRP woven web structure.

unprestressed. The use of GFRP and AFRP in flexural strengthening is not allowed due to their lower modulus; Shear strengthening of beams and columns; Strengthening of two-way slabs; Strengthening of torsional beams; Seismic strengthening of columns; and Quality control and checking procedures are also provided.

(3) Strengthening of masonry structures: seismic strengthening of masonry walls and a calculation method for the in-plane shear strength is provided.
(4) Strengthening of steel structures: fatigue strengthening and an evaluation method is provided.
(5) Concrete beams reinforced with FRP bars and prestressed with FRP strands.
(6) FRP and FRP-concrete composite structures: concrete filled FRP tubes and FRP slabs.

ACKNOWLEDGMENTS

The authors are very grateful to the Chinese Natural Science Foundation for supporting the key research project of FRP application in civil engineering in China (Grant No. 50238030).

REFERENCES

1. *Proceedings of first conference of Chinese FRP and application in civil engineering*, June, 2000, Beijing, China, Committee of Chinese FRP and application in civil engineering (in Chinese).
2. *Proceedings of 2nd conference of Chinese FRP and application in civil engineering*, July 25–28, 2002, Kunming, China, Tsinghua Press (in Chinese).
3. Ye L. P., Feng P., Zhang K., lin L., Hong W. H., FRP in Civil Engineering in China: Research and Applications, *Proceedings of* FRPRCS-6, Singapore, July, 2003, pp. 1401–1412.
4. Ye L. P., Cui W., Flexural strength analysis for RC beams strengthened with bottom bonded CFRP sheets, March. 2001, *Building Structure*, pp. 3–5 (in Chinese).
5. Ye L. P., Fang T. Q., etc, Experimental Research of Flexural Debonding behavior for RC Beams Strengthened with CFRP Sheets, *Building Structure*, Vol.33, No.2, pp. 61∼65 (in Chinese).
6. Huang Y. L., Ye L. P., Nonlinear Fe Analysis Of Bond Behaviors For Rc Beams Strengthened With Bottom Bonded Cfrp Sheets, *Engineering Mechanics*, Accepted (in Chinese).

7. Lu X. Z., Ye L. P., Teng J. G., etc, Study on Interfacial behaviors of external bonded FRP sheets for RC structures, *Proceedings of CICE*, Adelaide, Australia, Dec. 8–10, 2004.
8. Sawulet, B., Ye L. P., Technology of RC Beam Strengthened with Prestressed CFRP Sheets, *Construction Technology*, Accepted (in Chinese).
9. Zhao S. H., Li Q. W., Ye Lieping, Experimental Research on Shear Behaviors for Concrete Column Strengthened with CFS, *Industrial Construction*, Vol.30, No.2, 2000: 12–15 (in Chinese).
10. Zhao S. H., Ye L. P., Shear Strength Analysis of Concrete Column Retrofitted with CFRP Sheet Based on Strut-arch Model, *Engineering Mechanics*, Dec. 2001, Vol.18, pp. 134–140 (in Chinese).
11. Ye L. P., Yue Q. R., etc, Shear Strength of Concrete Columns Strengthened with Carbon Fiber Sheets, *Journal of ASCE*, Vol.128, No.12, 2002.12, pp. 1527–1534.
12. Hu W. H., Ye L. P., Analysis of Shear Strength of RC Columns Strengthened with Wrapped FRP Sheets, *Building Structure*, Accepted (in Chinese).
13. Tan Z., Ye L. P., Experimental Research On Shear Strength Of RC Beam Strengthened With External Bonded Of U-Type FRP Sheets, *Journal of CSCE*, Vol.36, No.11, 2003: 12–18 (in Chinese).
14. Zhang K., Yue Q. R., Ye L. P., Experimental Study on Ductility Improvement of Concrete Column Strengthened with CFRP Sheet. *Industrial Construction*, Vol.30, 2000, pp. 6–19 (in Chinese).
15. Ye L. P., Zhao S. H., etc, Experimental study on seismic strengthening of RC columns with wrapped CFRP sheet, *Proceedings of CICE*, Hong Kong, Dec. 12–15, 2001, pp. 885–891.
16. Li J., Qian J. R., Jiang J. B., Experimental Investigation on Axial Compressive Behavior of FRP Confined Concrete Columns. *Proceedings of the International Conference on Advances in Building Technology* (ABT 2002), Hong Kong, December 2002, pp. 289–296.
17. Lu X. Z., Feng P., Ye, L. P., Finite Element Analysis of FRP Confined Square Columns under Uniaxial Loading, *Journal of CSCE*, Vol.36, No.2, pp. 46–51, 2003 (in Chinese).
18. Huang, Y. L., Lam L., Teng J. G., Ye L. P., Analysis-oriented stress–strain model for concrete confined with FRP, *Proceedings, 8th Japan International SAMPE Symposiu*., Tokyo, Japan, 18–21 November, 2003, pp. 1265–1268.
19. Technical Specification for Strengthening Concrete Structure with Carbon Fiber Reinforced Polymer, Chinese Standard of Chinese Construction Standard Association, 2003.5.

FRP Composites in Civil Engineering – CICE 2004 – Seracino (ed)
© 2005 Taylor & Francis Group, London, ISBN 90 5809 638 6

Experimental and finite element studies on deteriorated steel members repaired with CFRP sheets

Q.R. Yue[1], F.M. Peng[2,1], Y.X. Yang[1] & N. Zhang[1]
[1] *National Diagnosis and Rehabilitation of Industrial Building Engineering Research Center, Beijing, China*
[2] *Dept. of Civ. Eng., Xi'an University of Architecture & Technology, Xi'an, China*

ABSTRACT: Defects and damage exist in many steel members because of corrosion, fatigue or mechanical damage, so cost-effective techniques for the rehabilitation and strengthening of these members are in urgent needs. There are several advantages of adhesively bonded fiber reinforced polymer (FRP) laminates to the deteriorated steel members over traditional retrofit methods. But to date, little research has been conducted on the steel members repaired with FRP laminates. The feasibility of using carbon fiber reinforced polymer (CFRP) sheets for repairing deteriorated steel members was discussed in this paper. The stress distribution between the CFRP sheets and the steel plates interface was also analyzed and the effective bond length of CFRP sheets was obtained. The 3D FEM software ANSYS was adopted to analyze the stress of the specimen and J-integral of the specimen.

1 INTRODUCTION

Defects and damage exist in many steel members because of corrosion, fatigue or mechanical damage. Traditional methods of repairing these deteriorated steel members are to attach cover plates to these members through bolts or welding. However, there are many disadvantages, such as labor intensive and time consuming, the sensitivity of the welded detail to fatigue, high stress concentrations near the bolts, increase in the weight of the member. Owing to the high strength and stiffness to weight ratio, excellent fatigue and durability, corrosion-resistant characteristics of FRP, the application of FRP is a preferable strengthening technique to conventional strengthening methods. To date, a vast majority of studies have been conducted into FRP strengthening concrete members, but with little research on the steel members [1,2,3,4].

In this paper, ten uniaxial tensile tests were conducted to investigate the efficiency of using CFRP sheets to rehabilitate damaged or undamaged steel members. The interfacial stress distribution between CFRP sheets and steel plates was measured in the tests and the effective bond length of CFRP sheet was obtained. Three-dimensional nonlinear finite element software ANSYS was adopted to analyze the stress of the steel plate, adhesive and CFRP sheets. The J-integral of the crack-tip of the steel plate was calculated by the use of ANSYS Parametric Design Language (APDL). The parameters, such as type of FRP, property of adhesive, dimension of the crack, which influence the J-integral were discussed in this paper.

2 EXPERIMENTAL STUDY

The main objectives of the research program were to investigate the effectiveness of adhesive bonding CFRP sheets to deteriorated steel plate, analyze the interfacial stress distribution of the interface and determine the effective bond length of the CFRP sheets when used to repair the deteriorated steel members.

2.1 *Materials*

The steel plate was of Q235 quality, which was used widely in civil engineering in China. A total of three dogbone coupons with a gauge length of 100 mm, gauge width of 19 mm, and thickness of 5.9 mm were tested in uniaxial tension to determine the actual yield and ultimate strength. The average yield strength and tensile strength were 388.2 MPa and 517.1 MPa, respectively. The average modulus of elasticity was 216.2 GPa.

The CFRP sheets used were fabricated by T700 carbon fibers. A total of five tensile coupons, with a length of 230 mm and width of 25 mm, were tested. The nominal thickness of the CFRP sheet was 0.167 mm and the fibre amount was 300 g/m^2 per sheet. The sheets had a unidirectional average tensile strength of 3788.0 MPa and tensile elastic modulus in the fiber direction of 217.6 GPa. The ultimate failure strain of the sheets was approximately 1.7%. The stress–strain relationship of the CFRP sheets was typically linear-elastic.

Material properties of the steel plates and CFRP sheets were given in Table 1.

Table 1. Material properties of steel plates and CFRP sheets.

Properties	Yield strength (MPa)	Tensile strength (MPa)	Elastic modulus (GPa)	Failure strain (%)
steel	388.2	517.1	216.2	28.5
CFRP	–	3788.0	217.6	1.7

Table 2. Material properties of the adhesive.

Properties	Tensile strength (MPa)	Elastic modulus (GPa)	Failure strain (%)	Shear* strength (MPa)
	42.6	2.57	1.7	16.42

*The shear strength of the epoxy adhesive was tested by stainless steel-to-steel single-lap tensile shear bonded joint.

A two-component, room temperature, less viscous epoxy adhesive was selected for bonding the CFRP sheets to the steel plate. The mixing ratio of the adhesive was four parts resin to one part hardener by volume. The adhesive had a pot life of 50 minutes at room temperature and was fully cured after seven days at 25°C. Properties of the epoxy adhesive were given in Table 2.

2.2 *Specimen details and preparation*

Two types of specimens were tested in the study (see Fig. 1). Specimens of type I were used to assess the feasibility of using CFRP sheets for strengthening damaged steel plate. There were two semicircular part-through holes at each side of the plate and the radius of the holes was 5 mm, which was introduced to simulate the loss of steel section area and to ensure that failure would occur at this location. The CFRP sheets were bonded on both sides of the steel plate, which was called as symmetric bonding. The difference of specimens of type II was that there was no damage in the steel plates and a transverse GFRP sheet was placed on one end to force debonding to occur at the other end.

The steel plates were first fabricated into the proper dimensions illustrated in Fig. 1, including the cut of the holes. Then the CFRP sheets were cut into the proper dimensions. After cleaning the dust, contamination, oxide and grease of the steel from the bonding area, a thin film of silane coupling agent was smeared on the clean surface of the steel plate. Twenty minutes later, the CFRP sheets were bonded to the surface of the steel plate through a layer of the epoxy adhesive. The CFRP sheets of series II were anchored at one end. Data collection was accomplished by a series of

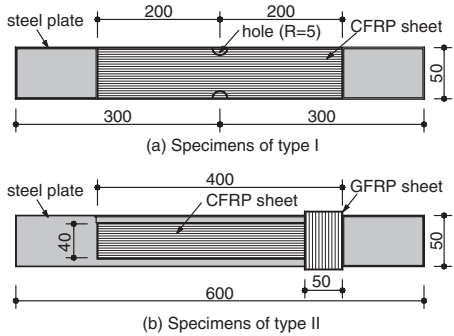

Figure 1. Specimen details.

strain gauges located along the length of CFRP sheet. Two days later, strain gauges were glued along the centerline of the CFRP sheet in the half-bonded region. In order to obtain the strain distribution in the steel plates, strain gauges were glued to the corresponding locations at the side of the steel plates of the type II specimens. The specimens were tested after a minimum period of seven days to guarantee full curing of the epoxy adhesive.

2.3 *Test setup and test procedure*

Uniaxial tensile tests were performed by a WE-600 testing machine. When loading was at a lower level, the steel plate was in elastic stage and no failure was observed. With the increase in loading, peel off initiated at the corner of the adhesive-steel interface at the end of the CFRP sheet without anchorage. When the loading was close to the yield load of the steel plate, peel off extended longer from the end to the center. When the peel off length was approximately a half, the steel plate ruptured suddenly. The typical failure modes of the specimens were illustrated in Fig. 2 and Fig. 3.

2.4 *Test Results*

Test results showed that the yield load of control specimen of type I was about 97.3 kN and the yield load of the retrofitted specimen without anchorage at both ends of the CFRP sheets increased to 112.1 kN. So increase in yield loads were approximately 15.1%. The reason was that the CFRP sheets shared a portion of the load transferred across the damaged section and the stress in the area of the steel plate reduced, which delay the yield of the steel plate. After peeling of the CFRP sheets, the load was transferred only by the steel plate. So the ultimate bearing capacities of retrofitted

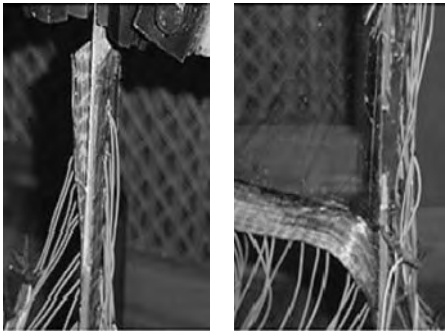

(a) Peel off of CFRP (b) Fracture of steel

Figure 2. Failure of specimen of type I.

(a) Peel off of CFRP (b) Fracture of steel

Figure 3. Failure of specimen of type II.

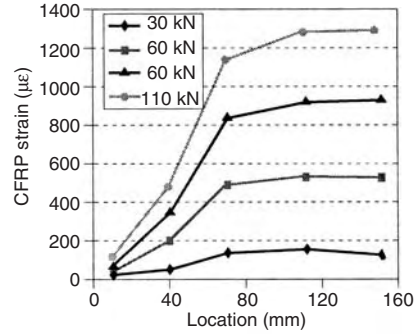

(a) Strain versus location

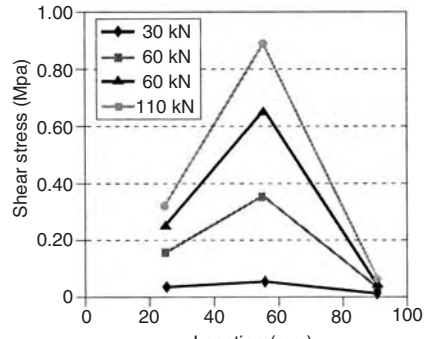

(b) Shear stress versus location

Figure 4. Specimen belonging to type I.

specimens were approximately the same as that of the control specimen.

The typical strain-location graphs for specimen were shown in Fig. 4 and Fig. 5, which illustrated the strain vs. the distance the strain gauge located from the free end of the CFRP sheets. Each curve was plotted for a given load level. It can be seen that at early stages of loading, the tensile strains of CFRP sheets were low near the end and the strain was horizontal. As the load increased, the curves tended to attain a non-linear shape and the strain curves became steep. But beyond a certain bond length the strain tended to become horizontal and the certain bond length was called effective bond length to develop stress in the CFRP sheets. From the plots, the development length of CFRP sheets was about 100 mm.

The interfacial shear stress of adhesive-CFRP sheets was calculated from the strain data along the CFRP sheet at different loading levels (see Fig. 4 and Fig. 5). Considering an elastic behavior for the CFRP sheets, the bond stress is obtained from the differences between the tensile forces at different sections along the CFRP sheets. It was observed from the test results that the bond stress was nearly equal to zero at early stages of loading. With the increase of loading, the bond stress increased. It should be pointed out that beyond the development length, the bond stress was approximately zero at every load level, which meant that the stress in the CFRP sheets was invariable.

The strain distribution of the CFRP sheet and the steel plate at the load level of 90 kN was illustrated in Fig. 6, in which the strain gauges of the CFRP sheet and the steel plate were located at the same coordinates in the longitudinal direction. It can be seen that at the location of the end of the CFRP sheets, the stress in the steel plate was maximal. The further from the end of the CFRP sheet, the larger the stress was in the CFRP sheet and the smaller in the steel plate. Beyond

a certain length the strains of the CFRP sheet and the steel plate were approximately the same. In other words, the strains in the steel plate and CFRP sheet at the central zone developed isochronously.

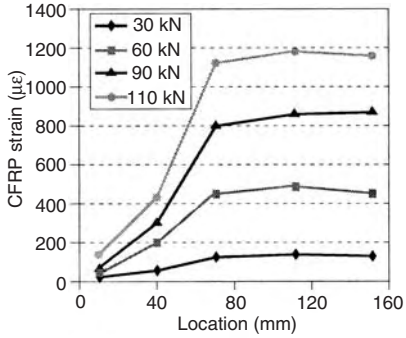

(a) Strain versus location

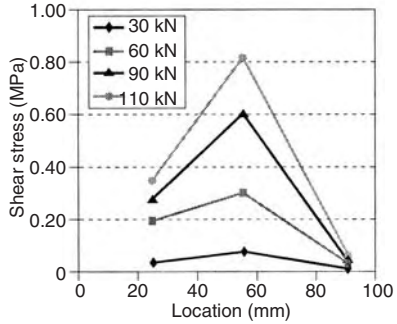

(b) Shear stress versus location

Figure 5. Specimen belonging to type II.

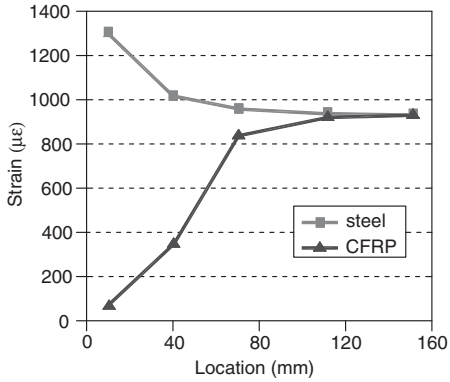

Figure 6. Strain of CFRP and steel.

3 NUMERICAL ANALYSIS

3.1 *Details of the model*

A typical configuration of a center-cracked steel plate repaired by bonded FRP sheets was shown in Fig. 7. The commercial three dimensional nonlinear finite element software package ANSYS was applied in the analysis [5]. Due to symmetry, only eighth of the specimen was modelled (see Fig. 8(a)). Symmetry boundary conditions were applied on the symmetry planes. The most important region in a fracture model was the region around the crack front and the detail of the finite model was shown in Fig. 8(b). In linear elastic problems, the stresses and strains are singular at the crack front, varying as $1/\sqrt{r}$. To pick up the singularity

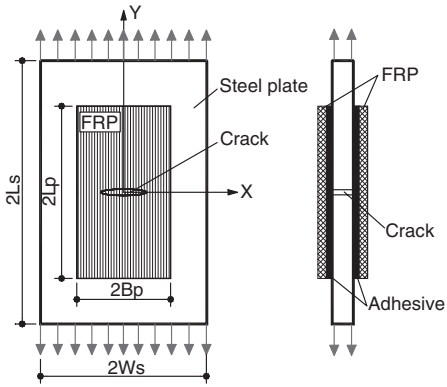

Figure 7. Configuration of a repaired center-cracked steel plate.

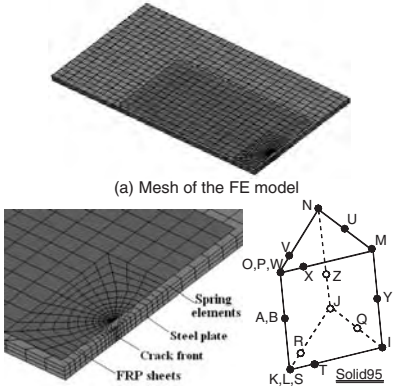

(a) Mesh of the FE model

(b) Detail around the crack (c) Singular element

Figure 8. Details of the finite element model.

in the strain, the elements around the crack front should be quadratic, with the midside nodes placed at the quarter points, which were called singular elements. The recommended element type for three-dimensional models in ANSYS is SOLID95, the 20-node brick element (see Fig. 8(c)). The shell41 element was used to model the CFRP sheets and solid45 element was used to model the steel plate. The adhesive layer was modeled by three springs (Combin39) for the transverse shear stiffness in the x-z and y-z planes and the axial stiffness in the z direction. The combin39 element is defined by two node points and a generalized force-deflection curve. The force-deflection curve of the axial spring elements was determined by the stress–strain relationship of the adhesive from the tensile tests. The force-deflection curve of the shear spring elements was determined by the shear stress-shear strain curve of the adhesive. The material properties of the model were the same as the previous tests. The adhesive was assumed to be isotropic and the CFRP sheet was orthotropic.

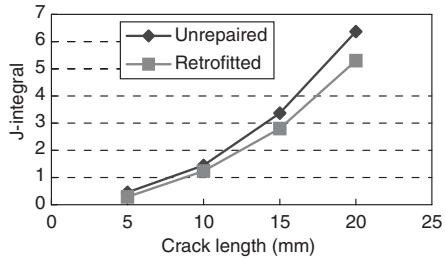

Figure 9. Variation of J-integral vs. crack length.

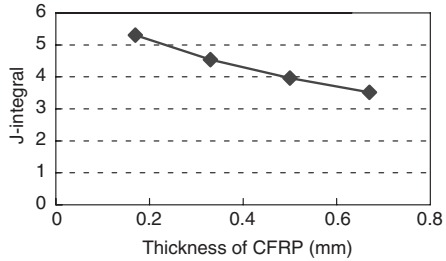

Figure 10. Variation of J-integral vs. CFRP thickness.

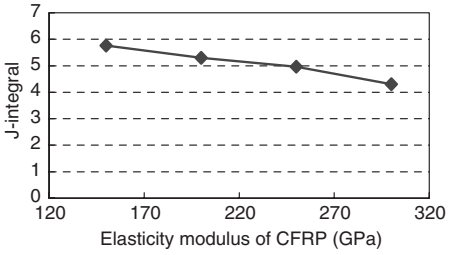

Figure 11. Variation of J-integral vs. CFRP elastic modulus.

3.2 *Analysis results*

The typical fracture parameter J-integral was calculated for both the steel plate without repair and the repaired steel plate bonded with CFRP sheets. Variation of the J-integral as a function of crack length for both specimens was shown in Fig. 9. It can be seen that the J-integral increased with the increase of the crack length. For retrofitted specimen, when the crack length was 20 mm, the J-integral reduced from 6.37 to 5.30.

Figure 10 showed the variation of J-integral for the retrofitted steel plate with the increase of CFRP sheet thickness. Increase the thickness of CFRP sheets can reduce the J-integral and so extend the crack propagation. The variation of J-integral versus the elasticity of the CFRP sheets was shown in Fig. 11, from which we can see that using high modulus CFRP sheets is an effective method to reduce the J-integral of the crack front.

4 CONCLUSIONS

From the test results and the numerical analysis, the major conclusions were as follows:

(a) Adhesively bonded CFRP sheets to the deteriorated steel members increased the yield loads obviously, but the increase of the ultimate loads was slightly because of the peel failure of the CFRP sheets.
(b) Stress concentration was serious at the end of the CFRP sheets and the effective bond length was about 100 mm.
(c) The CFRP sheets were effective in preventing the propagation of the crack. Increase of the thickness of CFRP sheets can reduce the stress of the crack front. Using high modulus CFRP sheets is an effective method to extend the fatigue crack growth life.

ACKNOWLEDGEMENTS

The authors gratefully acknowledge the financial support of the National High Technology Research and Development Program of China (The 863 Plan, #2001AA336010), the National Natural Science

Foundation of China (#50238030) and the Special Foundation for Institute of Science and Technology of China in 2003 (#2003EG213003).

REFERENCES

Mertz, D.R. and Gillespie, J.W. 1996. NCHPR-IDEA final report: Rehabilitation of steel bridge girders through the application of advanced composite materials, Transportation Research Board, Washington, D.C., 30 pp.

Zhang, N. and Yue, Q.R. 2003. Research on the Adhesive Interfacial Stress of CFRP for the Strengthened Steel Structure. *Industrial Construction* 33(1): 71–73.

Peng, F.M. and Yue, Q.R. 2003. CFRP for Strengthening and Repairing of Damaged Steel Structure. *Industrial Construction* 33(9): 7–10.

Liu, X., Silva, P.F. and Nanni, A. 2001. Rehabilitation of Steel Bridge Members with FRP Composite Materials. *Proc., CCCC, Composites in Construction*, *Porto, Portugal*: 613–617.

ANSYS. 1998. ANSYS User's Manual Revision 5.5, ANSYS, Inc., Canonsb urg, PA.

FRP Composites in Civil Engineering – CICE 2004 – Seracino (ed)

Behaviour of continuous RC beams strengthened with CFRP composites

J.W. Zhang
College of Civil Engineering, Southeast University, Nanjing, China

S.T. Smith
Centre for Built Infrastructure Research, Faculty of Engineering, University of Technology, Sydney, Australia

T.T. Zhang & Z.T. Lu
College of Civil Engineering, Southeast University, Nanjing, China

ABSTRACT: This paper reports the results of eight two-span continuous reinforced concrete (RC) beams strengthened with carbon fibre reinforced polymer (CFRP) composites that were tested to failure. Various strengthening arrangements were investigated, with the serviceability and strength limit states being carefully monitored. Crack propagation, deflections, and strains on the internal steel reinforcing bars, CFRP, and concrete, are reported. A novel pseudo plastic hinge concept that can be used to predict the behaviour of strengthened continuous beams up to failure, which correlates well with experimental results, is presented. The redistribution of internal forces is analyzed with this analytical procedure and the effectiveness of the various strengthening schemes with regards to strength, ductility and deformability is discussed. The strengthened beams display suitable deformability and ductility with the CFRP restraining the excessive opening of cracks.

1 INTRODUCTION

An increasing number of existing building structures and bridges all over the world are in need of strengthening, retrofit, or repair due to factors such as deterioration, construction or design faults, additional load, or functional change. Application of externally bonded high-strength fibre reinforced polymers (FRP) has become increasingly popular in the last decade. Their popularity has stemmed from lower labour costs for implementation compared to other strengthening techniques such as steel plating or jacketing. The FRPs are also resistant to corrosion and offer minimal section enlargement. One of the largest construction markets in the world is located in China, and the use of FRP for strengtheneing and repair in China is becoming widespread.

Strengthening of simply supported reinforced concrete (RC) beams or girders with externally bonded FRP composites has been extensively investigated since the early 1990s and a comprehensive review of exiting research is given in Teng et al. (2002). There have however been a limited number of studies on strengthening continuous RC beams with FRP composites. The few studies undertaken (i.e. Grace et al. 1999a, Grace 2001 and El-Refaie et al. 2003) have been predominantly experimental.

The negative moment (hogging) and positive moment (sagging) regions of four two-span continuous T-section RC beams were strengthened with carbon FRP (CFRP) and glass FRP (GFRP) composites by Grace et al. (1999a). Both wet lay-up formed FRP and pultruded FRP plates were investigated. No anchorage of the strengthening was provided although shear strengthening was applied. The FRP strengthening was found to increase the load carrying capacity, reduce deflections, and reduce the width of cracks over that of the control beam. Rupture, as well as debonding of the FRP was observed.

Grace (2001) investigated the response of five RC beams strengthened in the hogging moment region. Simply-supported RC concrete beams, with an overhanging (cantilever) end, were tested with load being applied near the free end of the beam in the overhanging region. Various amounts and configurations of CFRP plates were applied to the hogging moment region. The CFRP strengthening was found to increase the strength and stiffness of the beams in the negative moment region. All strengthened beams failed by separation, or debonding, of the CFRP from the concrete as no anchorage of the CFRP plates was provided.

El-Refaie et al. (2003) reported a series of experiments on eleven continuous two-span RC beams strengthened with various CFRP schemes in the

hogging and sagging moment regions. The CFRP strengthening increased the strength of the RC beams, as expected. The dominant mode of failure for the strengthened beams was debonding, prompting El-Refaie et al. (2003) to recognize the importance of anchoring the CFRP in future studies to prevent premature debonding failure.

This paper reports the results of an experimental and analytical study on CFRP-strengthened RC continuous beams. Eight two-span continuous RC beams were tested. Two were unstrengthened control beams and six beams were strengthened with various amounts and arrangements of CFRP bonded onto the hogging and sagging moment regions of the beams. End anchorage was also provided in order to prevent debonding failures. The serviceability and ultimate limit state behaviour of the beams is described as well as the failure modes. An analytical procedure is then described which can model the load and deflection response of FRP-strengthened continuous beams. The analytical predictions are found to be in good agreement with the experimental results.

2 EXPERIMENTAL PROGRAM

2.1 *Details of test beams*

The experimental program consisted of testing eight 1:3 scale two-span continuous RC beams (Figure 1). All beams were nominally 5150 mm long, 150 mm wide and 250 mm deep, with a span of 2500 mm between supports. Reinforcement ratios along the whole length of all beams of 1.25% for the top and 0.87% for the bottom steel were selected. Such ratios were consistent with practical continuous beams and correspond to two 16 mm and two 14 mm diameter steel reinforcing bars in the top and bottom of the beam respectively. The number and size of reinforcing bars were determined from multiplication of the appropriate reinforcement ratio by the width, b_c, and the effective depth of the beam, d_0 (d_0 is the distance from the compressive face of the section to the centre of the tension steel reinforcement). All beams were reinforced with 8 mm diameter steel stirrups placed at 100 mm centres and proportioned to ensure 20 mm of cover between the outside face of the beam to the outside of the stirrup. To prevent potential shear failure at each support region of the beam, stirrups were placed at 80 mm centres for a distance extending 800 mm beyond the supports.

The eight test beams were cast in two batches. The first batch of four beams was designated CBCF1-a (un-strengthened control beam), CBCF1-b, CBCF1-c, CBCF1-d, and the second batch as CBCF2-a (un-strengthened, control beam), CBCF2-b, CBCF2-c, CBCF2-d. Apart from the two control beams all six remaining beams were strengthened with varying amounts of CFRP bonded on both the top and bottom faces except beam CBCF2-c. For beam CBCF2-c, CFRP was not applied to the top face of the interior support region intentionally in order to simulate a situation where obstructions, such as walls, could inhibit placement. All strengthening arrangements are shown in Figure 2 where the width of FRP is the same as the width of the beams. To resist separation, or debonding, of the CFRP from the concrete substrate before the ultimate strength of the beam section was reached, close looped CFRP strips (herein referred to as *anchorage hoops*) were wrapped around the ends of the CFRP as shown in Figure 2. The width of each anchorage strip was 150 mm and the number of anchorage hoops applied to each plate end and the number of layers of CFRP forming each anchorage hoop are also given in Figure 2.

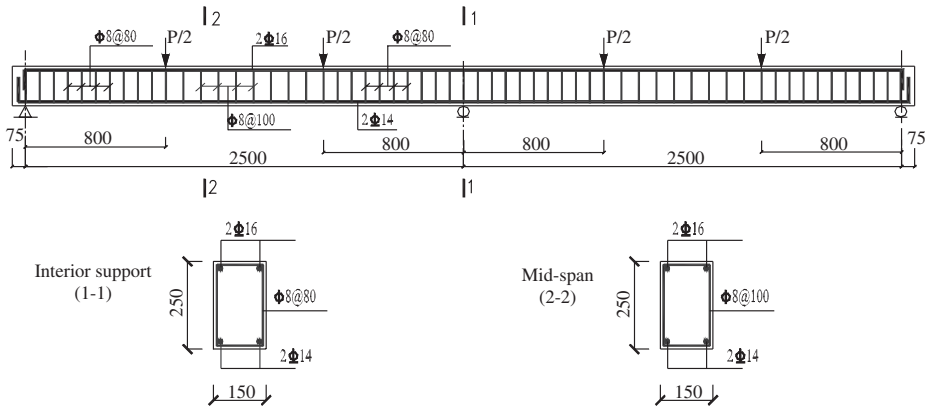

Figure 1. Test beam elevation and cross-sectional details (all dimensions in mm).

The CFRP composites were formed in a wet layup procedure, from 0.167 mm nominally thick carbon fibre sheets, in accordance with the manufactures specifications. To improve the bond between the CFRP and concrete the top few millimeters of the concrete substrate was removed and aggregate exposed by sandblasting prior to application of the CFRP.

Table 1 gives the effective reinforcement ratio ρ_{er}, at the mid-span and interior support. The effective reinforcement ratio of the strengthened beams is calculated by dividing the summation of the cross-sectional area of the tension steel reinforcement, A_s, and the effective cross-sectional area of the CFRP strengthening, $A_{frp,e}$, by the effective cross-sectional area of the beam ($b_c \times d_e$). The effective depth, d_e is the distance from the compressive face of the section to the centroid of the tension steel reinforcement and CFRP strengthening, where the centroid is a weighted

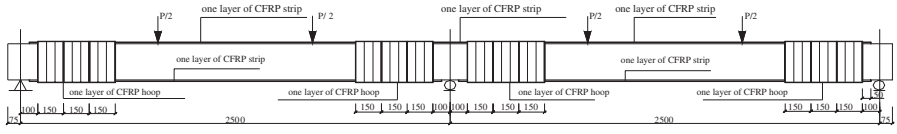

(a) Beam CBCF1-b

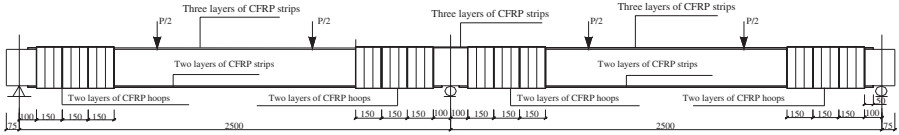

(b) Beam CBCF1-c

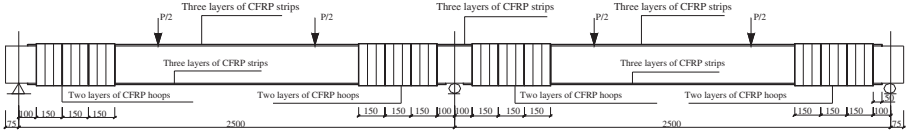

(c) Beam CBCF1-d

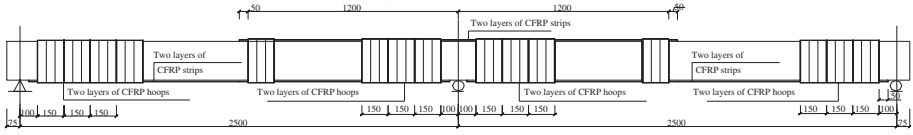

(d) Beam CBCF2-b

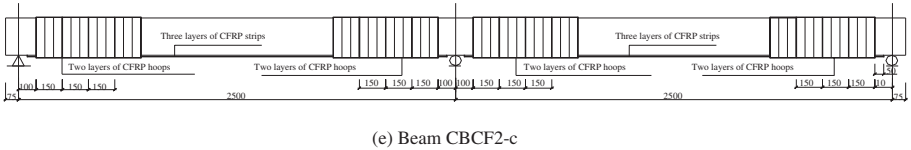

(e) Beam CBCF2-c

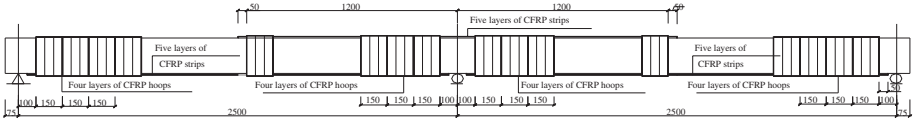

(f) Beam CBCF2-d

Figure 2. CFRP strengthening schemes (all dimensions in mm).

average based on the yield strength of the steel reinforcement and the tensile strength of the CFRP. The effective cross-sectional area of the CFRP, $A_{frp,e}$, is calculated by transforming the CFRP to an equivalent amount of steel based on the yield strength of the steel and the tensile strength of the CFRP. A tensile strength of 1500 MPa was initially adopted for the CFRP in the design stage, prior to tensile tests being undertaken. For the control test specimens with no bonded CFRP, ρ_{er} refers to the ratio of A_s to the effective cross-sectional area of the beam ($b_c \times d_0$).

2.2 *Load set-up and test procedure*

A typical test in progress is shown in Figure 3. Each span of each beam was simultaneously loaded by two symmetrically placed concentrated loads at a distance of 800 mm from the interior and exterior supports. All beams were placed on adjustable supports and the load was applied by hydraulic jacks. The supports were locked in position during loading but adjusted during pauses in the loading before cracking. All beams were loaded in a load-controlled manner that was applied monotonically up to failure. For the lower load levels, load was applied in increments of 10 kN and held stationary while measurements were taken and crack patterns observed. At the higher load range, including just prior to failure, the load increments were reduced to 5 kN. Prior to cracking, the beam is in an elastic state and all reactions can be calculated from elastic theory using a constant beam stiffness. After each increment of load, prior to cracking, the reaction forces were made consistent with those determined from elastic theory by altering the height of the appropriate supports. The reason for regulating the height of the supports arose from initial settling of the beam due to gaps between the bottom of the beam and supports, and the load points and the top of the beam. After the first concrete cracks were visually observed, the supports were no longer adjusted as the beam was beyond the elastic state and all settling was deemed to have taken place.

Table 1. Effective reinforcement ratio ρ_{er}.

	ρ_{er} (%)	
Test	Interior support	Mid-span
CBCF1-a[#]	1.25	0.87
CBCF1-b	1.58	1.20
CBCF1-c	2.25	1.54
CBCF1-d	2.25	1.87
CBCF2-a	1.25	0.87
CBCF2-b	1.92	1.54
CBCF2-c	1.25	1.87
CBCF2-d	2.92	2.54

[#] CBCF1-a = Continuous Beam, Carbon Fibre, batch 1, beam a.

Figure 3. Test set-up.

2.3 *Instrumentation*

Vertical deflection was measured directly over each support and beneath the middle of each span using dial gauges. Electrical resistance strain gauges were used to measure strain in the longitudinal tension steel reinforcement, steel stirrups, and CFRP plates. Strain gauges were attached on the surfaces of the top internal steel bars and CFRP at the interior support and the bottom steel bars and CFRP at the middle of each span. The mid-depth of one side of the first three stirrups either side of the interior support were also strain gauged. The total load applied to each span, P (where P is the summation of the two point loads applied to each span), was directly read from dial pressure meters connected to hydraulic jacks as can be seen in Figure 3. Electronic pressure transducers were installed between the beam base and each of the three supports to measure the reaction forces. Crack formation was monitored for each beam and crack widths were measured at the tension steel reinforcement level using a crack width micrometer with an accuracy of 0.02 mm (1 in 50).

The load was applied slowly and monotonically, and paused at regular intervals in order to record deflection, strain and crack width values and monitor crack progression. To ensure each beam was in a stable state when the load was paused and held constant, the beam was left for three minutes prior to taking measurements. No measurements were taken while load was being applied so it was important to pause the load right before failure to record peak measurements. This final pause was made when it was judged the specimens were on the verge of failure. In addition to recording the output of all instrumentation at each load level, the condition of the CFRP was also assessed. A simple FRP-to-concrete bond quality test, which involved tapping the CFRP with a metallic object, was undertaken to check for CFRP debonding. A hollow tapping sound indicated a breakdown of bond between the CFRP and

concrete, otherwise known as debonding. The interface between the CFRP and concrete was inspected by examining the edges of the CFRP.

2.4 *Material properties*

The properties of each batch of concrete were determined on the day of testing the control beam for that batch. The control beam was the first beam to be tested in each batch and each control beam was approximately forty-five days of age when tested. All four beams in each batch were tested over a period of approximately ten days and the concrete cylinder compressive strength of the control beams from batches 1 and 2, each averaged from three tests, were 53 MPa and 41 MPa respectively.

Steel reinforcing bars of 8 mm, 14 mm and 16 mm diameter were used in all beams for the longitudinal and shear reinforcement. Based on an average of three specimens, the yield strength and ultimate strength of the three different diameter bars was 294 MPa, 390 MPa, 397 MPa and 382 MPa, 560 MPa, 584 MPa respectively.

The tensile strength and elastic modulus of the CFRP was 3978 MPa and 235 GPa respectively. These were obtained by averaging the results of six flat coupon test specimens containing one layer of CFRP, and a nominal sheet thickness of 0.167 mm.

3 EXPERIMENTAL RESULTS

A summary of the experimental results is presented in this section while a more comprehensive review is given in Zhang et al. (2004).

3.1 *Deflection and stiffness*

Figure 4 shows the load versus the greater of the two mid-span deflections for the eight test beams. The CFRP did not appreciably increase the stiffness of the beam prior to concrete cracking. The stiffness of the strengthened beams was, however, significantly enhanced after concrete cracking, particularly after yielding of the internal longitudinal steel bars.

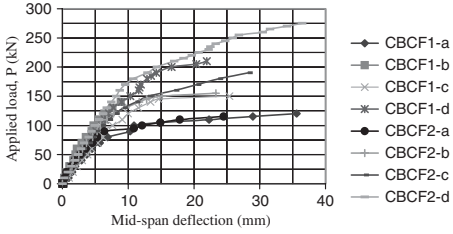

Figure 4. Load-deflection curves.

In general, and as expected, more layers of CFRP led to a greater increase in stiffness as compared to the unstrengthened control beams (CBCF1-a and CBCF2-a).

The two control beams exhibited excellent ductility as evidenced by relatively long and flat peak load plateaus due to yielding of the internal steel reinforcement. Ductility herein is related to the length and flatness of the peak region of the load-deflection curve. The beam with the least amount of strengthening (CBCF1-b with one layer of CFRP) deflected the least amount out of all beams and was the least ductile. The beam with the most amount of strengthening (CBCF2-d with five layers of CFRP) deflected the greatest amount out of all the beams and while not as ductile as the control beams, was the most ductile of the strengthened beams. Carbon FRP is a linear-elastic material and its inability to plastically deform ultimately resulted in all strengthened beams being less ductile than the control beams.

3.2 *CFRP and longitudinal steel strains*

The load versus CFRP strain results for each of the strengthened beams are shown in Figure 5. Figure 5a shows the strain result at the top face of the beam over the interior support (hogging moment region), while the larger of the strains on the bottom face of each mid-span (sagging moment region) are shown in Figure 5b. The peak strains over the interior support are larger than the midspan strains owing to the interior

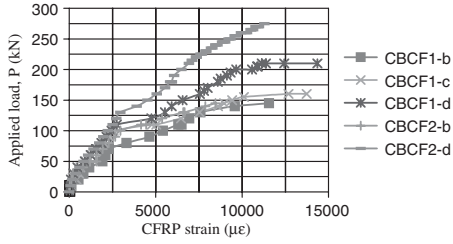

(a) Hogging moment region

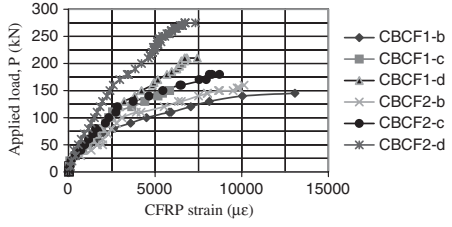

(b) Sagging moment region

Figure 5. Load-strain curves.

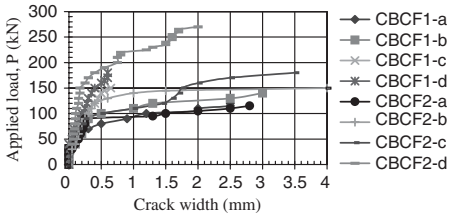

(a) Hogging moment region

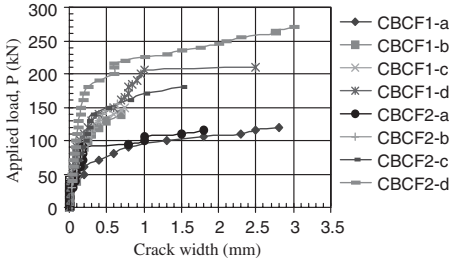

(b) Sagging moment region

Figure 6. Load-crack width curves.

support attracting more load. The high stress obtained in the CFRP is attributed to the effective anchorage system which eliminated any premature debonding of the CFRP at the plate ends. Inspection of strain gauge results revealed the longitudinal steel reinforcement yielded over the interior support prior to yielding in the mid-span region while no stirrups yielded in the interior support region for all tests.

3.3 *Crack pattern and propagation*

Crack widths at the interior support and mid-span region, at the longitudinal tensile steel level, were measured. The load versus maximum crack widths in the hogging and sagging moment region relationships are shown in Figures 6a and 6b respectively. The crack widths for the strengthened beams in most cases were less than the control beams due to restraint offered by the CFRP.

3.4 *Failure loads and modes*

Table 2 gives the ultimate load, P_u for each test. The failure mode is also given and, where relevant, the load that CFRP debonding, P_{db}, and rupture, P_{rup}, initiated. Both control beams failed by crushing of the compressive concrete. Various failure modes for the strengthened beams were observed, such as rupture of the CFRP followed by concrete crushing, and concrete crushing without CFRP rupture. In all tests the longitudinal tension steel was found to have yielded. Due

Table 2. Summary of test results.

Test	P_u (kN)	P_{db} (kN)	P_{rup} (kN)[#]	Failure mode[#] Mid-span	Interior support
CBCF1-a	120	–	–	C	C
CBCF1-b	145	130	140	R	R
CBCF1-c	155	120	155	R	R
CBCF1-d	210	140	205	R	R
CBCF2-a	120	–	–	C	C
CBCF2-b	160	130	150	PR	R
CBCF2-c	190	160	180	R	C
CBCF2-d	275	140	NR	C, NR	NR

[#] C = Concrete crushing, R = CFRP rupture, PR = partial rupture across the width of CFRP, NR = no rupture of CFRP.

to sufficient anchorage measures being taken, in all cases the CFRP did not debond at the ends but instead debonded along the interface between the CFRP, away from the anchorage hoops, at high load levels. Despite debonding, the beams were still able to resist additional load as the anchorage hoops enabled the load to be transferred between the concrete substrate and the CFRP. No significant degradation of any of the anchorage hoops (regardless of the number of layers of CFRP used to form the hoop) was observed and as a result all hoops were considered effective in eliminating plate end debonding in all tests. As the anchorage hoops are not the main focus of this paper, they will not be further discussed. Test CBCF2-d was strengthened with the most amount of CFRP and was in turn the only strengthened beam to fail by concrete crushing. The CFRP essentially over-reinforced the section enabling the compressive capacity of the concrete to be reached prior to the tensile capacity of the CFRP being reached.

3.5 *Ductility and deformability*

Energy methods have been found to be give a better measure of ductility in FRP-strengthened RC beams, as opposed to traditionally used deformation based methods for plain RC beams (e.g. Grace et al. 1999b).

In this paper the ductility of the beams is evaluated by a newly proposed ductility index β based on energy considerations. The ductility index β is defined as the ratio of the plastic energy stored in the specimen during the entire loading process area, A_{plt}, to the total absorbed energy, A_{all}. The quantity A_{plt} is calculated from the load versus mid-span deflection curves (Figure 4) and is defined as the area surrounded by the load-deflection curve, the horizontal axis and an unloading line. This unloading line commences from the end of the load-deflection curve, terminates where it bisects the horizontal axis, and its slope is equal to the

Table 3. Ductility class.

Test	A_{plt} (mm^2)	A_{all} (mm^2)	β	Ductility class
CBCF1-a	4323	5319	0.81	Ductile
CBCF1-b	380.2	1176	0.32	Brittle
CBCF1-c	3148	4441	0.71	Ductile
CBCF1-d	2804	4870	0.58	Semi-ductile
CBCF2-a	2758	3485	0.79	Ductile
CBCF2-b	3097	4350	0.71	Ductile
CBCF2-c	4107	6033	0.68	Semi-ductile
CBCF2-d	7792	11150	0.70	Ductile

slope of a line extending from the origin to a point on the load-deflection curve corresponding to first yield of the internal tension steel reinforcement. The quantity A_{all} represents the total energy absorbed by the beam. It is the total area under the load-deflection curve and considers elastic and plastic deformation. A summary of β as well as the quantities A_{plt} and A_{all} for each beam test are given in Table 3.

Based on the ductility index β for each beam, ductility is classified in three categories, namely ductile ($\beta \geq 0.70$), semi-ductile ($0.5 \geq \beta < 0.70$), and brittle ($\beta < 0.50$). Such classification concept was adopted by Grace et al. (1998) for concrete beams reinforced with FRP reinforcing bars although different limits were applied. A summary of the ductility classification for each test beam is given in Table 3. The control beams are the most ductile and the beam strengthened with the least amount of CFRP, CBCF1-b, is the least ductile as it failed by CFRP rupture before adequate ductility had been displayed.

4 THEORETICAL STUDY

Internal forces are easily determined in statically determinate structures (e.g. simply supported beams). Determination of internal forces in continuous beams are however more complicated. In both determinate and indeterminate beams the stiffness of the cross-section will affect the internal forces and the stiffness is dependent on factors such as concrete tensile strength, steel yield, and in the current study the amount of CFRP strengthening. An analysis of internal forces in both determinate and indeterminate beams must therefore consider the change of sectional stiffness, with respect to the load level, along the length of the member.

Redistribution of internal stresses in a continuous beam occurs providing enough rotational capacity exists at important regions of the beam such as at the interior support and the middle of the spans. In plain RC beams sufficient rotation normally exists, provided the reinforcing steel has adequate elongation capacity. When CFRP strengthening is applied the rotational capacity may be limited by the low elongation capacity and brittleness of the CFRP. The CFRP strengthening may well rupture before sufficient section rotation and redistribution of internal stresses has taken place. As a result, a pseudo plastic hinge concept is proposed herein. As opposed to plain RC beams, the load carrying capacity in FRP strengthened beams can still increase once the steel reinforcement has yielded. Limited internal stress redistribution can occur in FRP-strengthened RC beams despite their reduced ductility over that of plain RC beams without FRP strengthening (Zhang et al. 2004).

4.1 *Analytical model*

A key assumption in evaluating the flexural capacity of FRP-strengthened RC beams is that plane sections remain plane and a detailed description of the calculation procedure is given in Teng et al. (2002). Based on this assumption an analytical model to determine the moment distribution in statically indeterminate CFRP strengthened RC beams that incorporates FRP brittleness is now summarised.

The hogging moment, M_s, over the interior support is

$$M_s = \alpha_s P L_0 \tag{1}$$

where P is the total applied load on each span, and L_0 is the span between support points. The moment coefficient, α_s, is equal to

$$\alpha_s = \frac{\frac{98}{B_m} + \frac{30}{B_s}}{3\left(\frac{54}{B_m} + \frac{74}{B_s}\right)} \tag{2}$$

where B_m and B_s represent the stiffnesses in the sagging and hogging moment regions respectively. The stiffnesses represent either a cracked or uncracked section, are a function of the applied load (moment), and are constant along the entire sagging or hogging moment region of the beam respectively and that particular load level. The stiffness, B, (otherwise known as B_m and B_s) can be calculated as follows for an uncracked section (GB50010 2002)

$$B = 0.85 E_c I_0 \tag{3}$$

and a cracked section

$$B = \frac{E_s(A_s + A_{frp,e})d_e^2}{1.15\psi + 0.2 + \frac{6\alpha_E \rho}{1 + 3.5\alpha_E \rho'}} \tag{4}$$

where E_c and E_s are the elastic moduli of the concrete and steel reinforcement (MPa) respectively,

I_0 is the uncracked second moment of area transformed to concrete (mm^4), A_s the cross-sectional area of tension steel reinforcement (mm^2), $A_{frp,e}$ the equivalent cross-sectional area of CFRP (mm^2), ψ the stress deviation coefficient of steel bars, $\alpha_E = E_s/E_c$, and ρ and ρ' the ratio of the cross-sectional area of the tension steel reinforcement to CFRP, and the compression steel reinforcement to CFRP respectively. The equivalent cross-sectional area, $A_{frp,e}$, is calculated from $A_{frp}\sigma_{frp,u}/f_y$ where $\sigma_{frp,u}$ is the stress in the CFRP at ultimate load and can be computed from a sectional analysis described in Teng et al. (2002), A_{frp} is the cross-sectional area of the CFRP and f_y the yield strength of the steel reinforcement.

The reaction of the external support, R_1, is

$$R_1 = \frac{P}{2} + \frac{M_s}{L_0} \tag{5}$$

The moment m_1, located directly beneath the load point nearer to an external support, is given by

$$M_{m_1} = \frac{1+\alpha_s}{3} PL_0 \tag{6}$$

Since the stiffnesses B_m and B_s vary with the applied load, the internal moment M_s and M_{m_1} and the reaction R_1 at load P are determined by accumulation of increments of the corresponding moment ΔM_s, ΔM_{m_1} and ΔR_1 under various loading increments ΔP from the onset of loading to the computed load level P. For each increment of hogging moment ΔM_s, the quantities ΔM_{m_1} and ΔR_1 are determined by substituting an appropriate value of ΔP into Equations 1, 5 and 6. The mid-span deflection increment Δf_m of the specimens under a load increment ΔP can be found by the following expression

$$\Delta f_m = \int_0^{L_0/2} \frac{\Delta M \overline{M}}{B} x dx = \frac{1035}{124416 B_m} + \frac{25}{4068 B_s} \tag{7}$$

where ΔM is the incremental moment due to ΔP, and M the moment due to a unit load acting on the mid-span of the beam. The total deflection f_m at load P can be found by summing all Δf_m.

4.2 *Comparison between analytical and experimental results*

Due to space restrictions, only the analytical predictions of deflection as well as hogging and sagging moments are presented in Figures 7 and 8 respectively for the most heavily strengthened beam (test CBCF2-d). The analytical predictions and comparison with experimental results for the remainder of the tests are given in Zhang et al. (2004).

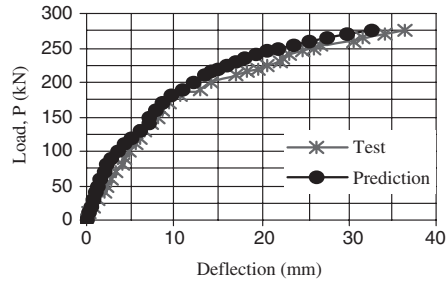

Figure 7. Load-deflection curves: test and prediction.

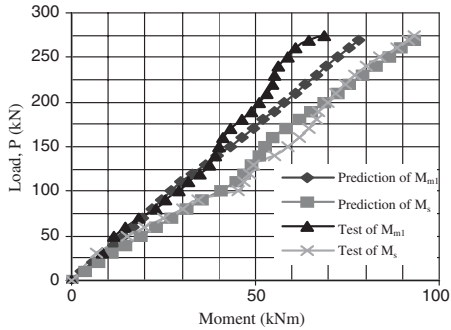

Figure 8. Load-moment curves: test and prediction.

Generally there is a very good correlation between the experimental and predicted load-deflection response in Figure 7. The correlation between experimental and predicted load-moment relationships in Figure 8 is generally reasonable but not as good as the load-deflection results. Predictions in Figure 8 are generally more conservative than the test result. On the whole the analytical model is accurate and can therefore be used with confidence.

5 CONCLUSIONS

Tests on eight two-span continuous CFRP strengthened RC beams have been reported. Substantial strength gains were found for CFRP strengthened beams compared to the unstrengthened control beams. The amount of strength enhancement increased with the amount of CFRP applied. To prevent premature failure by separation of the FRP from the beam face, strips of CFRP, known as anchorage hoops, were wrapped around the end regions of the CFRP. These anchorage hoops were effective and ensured the CFRP carried substantial stress. The longitudinal CFRP composites restrained the opening of cracks thus enhancing

serviceability. The strengthened beams also generally exhibited ductility, considering the brittleness of the failure mode which was by CFRP rupture or concrete crushing. A relatively simple analytical solution was proposed and the analytical predictions generally correlated well with the experimental results.

ACKNOWLEDGEMENTS

The authors are grateful for the financial support provided by the China Nature and Science Foundation (Project Number 50238030), China Ministry of Science and Technology (Project Number 2001AA336010), and Jiangsu Civil Defense Office (Project Number 2001-104). The authors are also grateful to the Structural Laboratory of Southeast University, China and the Laboratory of RC and PC structures of the China Ministry of Education. The Faculty of Engineering at the University of Technology, Sydney (UTS) is also thanked for supporting a visit to UTS by the first author of this paper in February 2004.

REFERENCES

El-Refaie, S.A., Ashour, A.F. & Garrity, S.W. 2003. Sagging and hogging strengthening of continuous reinforced concrete beams using carbon fiber-reinforced polymer sheets. *ACI Structural Journal* 100(4): 446–453.

GB50010. 2002. *Code for Design of Concrete Structures*, Ministry of Construction of PR China, New World Press, Beijing, China.

Grace, N.F., Soliman, A.K., Abdel-Sayed, G. & Saleh, K.R. 1998. Behavior and ductility of simple and continuous FRP reinforced beams. *Journal of Composites for Construction ASCE* 2(4): 186-194.

Grace, N.F., Soliman, A.K., Abdel-Sayed, G. & Saleh, K.R. 1999a. Strengthening of continuous beams using fiber reinforced polymer laminates. In C.W. Dolan, S.H. Rizkalla & A. Nanni (eds.) *Fourth International Symposium on Fiber Reinforced Polymer Reinforcement for Reinforced Concrete Structures, FRPRCS-4, Proc. inter. symp., November 1999, Baltimore, USA: 647–658*, American Concrete Institute.

Grace, N.F., Abdel-Sayed, G., Soliman, A.K. & Saleh, K.R. 1999b. Strengthening reinforced concrete beams using fiber reinforced polymer (FRP) laminates. *ACI Structural Journal* 96(5): 865–874.

Grace, N.F. 2001. Strengthening of negative moment region of reinforced concrete beams using carbon fiber-reinforced polymer strips. ACI *Structural Journal* 98(3): 347–358.

Teng, J.G., Chen, J.F., Smith, S.T. & Lam, L. 2002. *FRP-Strengthened RC Structures*. John-Wiley & Sons, UK.

Zhang, J.W., Smith, S.T., Zhang, T.T. & Lu, Z.T. 2004. Strengthening of continuous RC beams with FRP composites *in prep*.

FRP Composites in Civil Engineering – CICE 2004 – Seracino (ed)
© 2005 Taylor & Francis Group, London, ISBN 90 5809 638 6

Strengthening efficiency of RC beams with externally bonded carbon fibre and glass fibre sheets

G.J. Xiong, X. Jiang & J. Liu
Dept. of Civil Eng., Shantou Univ., Shantou, P.R. China

ABSTRACT: In order to increase strengthening efficiency, a method to strengthen reinforced concrete beams by combining unidirectional carbon fibre reinforced polymer (CFRP) sheet (to bond to the tension faces of the beams) and bi-directional glass fibre reinforced polymer (GFRP) sheet (to wrap 3 sides of the beams continuously) was put forward. A comparative test program including ten beams was carried out. The test results showed that under the premise of preventing the tension delamination of the bottom concrete cover, the hybrid CF/GF reinforced polymer (H-CF/GF-RP) strengthening led to a significant increase of deformation capacity of the strengthened beams at a very low cost compared to CFRP strengthening. The stiffness of H-CF/GF-RP strengthened beams is similar to that of CFRP strengthened ones.

1 INSTRUCTION

Carbon fibre reinforced polymer (CFRP) strengthened reinforced concrete (RC) beams may fail due to peeling off of the bottom concrete cover along the level of the longitudinal steel reinforcement. This kind of failure is considered undesirable because the full strength of the CFRP is not utilized. The cover tension delamination may be delayed, or prevented in some cases, by wrapping spaced CFRP transverse strips ("U-strips") around three sides of strengthened concrete beams (Brena et al. 2003, Spadea et al 1998). It was reported that full CFRP sheet wrap (3-side U-wrap) continuously along the beam span clearly provided a greater amount of anchorage and confinement action to eliminate the delamination (Shahawy et al. 2001). However, the displacement levels of CFRP strengthened beams failed in tension by rupture of the CFRP were still considerable lower than those of the control beams (Brena et al. 2003, Shahawy et al. 2001, Spadea et al. 1998), and the strengthening cost increased greatly. It should be noted that because the cover tension delamination may be prevented in most cases by adding spaced three-sided FRP strips at the ends of CFRP sheets and the span (Brena et al. 2003, Spadea et al. 1998), it can be inferred that the peeling stress value is not high. In the light of this the authors put forward a method to use bi-directional GFRP sheet/sheets to continuously wrap concrete beams. It is to be hoped that the relatively weak transverse direction of the GFRP may prevent bottom concrete cover from peeling off, and the relatively strong longitudinal direction may make a noticeable contribution for increasing deformation capacity of strengthened concrete beams because glass fibre (GF) has a much larger elongation (3∼5.4%) than CF (1∼1.5%) (ACI-440 2000).

According to the research results of FRP, when GF and CF hybridise together the GF with a higher elongation will bear the extra load due to the fracture of CF, retarding the progress of fracture of CFs, leading to a significant increase of average elongation, and in some cases, a bilinear "ductile" stress–strain behaviour of the FRP at a lower cost (Qiao 1997). Hybrid fibre-reinforced polymer (HFRP), therefore, is thought to be developing direction in the 21th century. The authors also take the view that because the durability of FRP mainly depends on polymer (similar to that concrete protects steel), H-CF/GF-RP may be as durable as CFRP.

2 EXPERIMENTAL PROGRAM

2.1 *Materials*

The composition of the concrete mixes was 0.44:1:1.50:2.41(water:ordinary portland cement:sand:stone). The 28-day concrete strength was 40.1 MPa. 10 mm and 12 mm diameter deformed steel bars were used as main reinforcement. The yield strength and elastic modulus of the 10 mm diameter bars were 411 MPa and 200 GPa respectively. The yield strength and elastic modulus for the 12 mm diameter bars were 606 MPa and 210 GPa respectively. 8 mm diameter steel bars

Table 1. Mechanical properties of different FRP laminates.

FRP name	Composites types	Tensile strength (MPa)	Elastic modulus (GPa)	Elongation (%)
2CF	Two layers of 100 mm wide CF	1823	180.5	1.01
1GFt	One layer of 100 mm GF(transverse direction)	104	7.22	1.44
1CF/2GF	One layer of 100 mm CF and two layers of 125 mm GF (longitudinal direction)	528	34.5	1.53

with a yield strength of 233 MPa and an elastic modulus of 210 GPa were used as stirrups and maintain bars.

The thickness and price of the CF sheet containing unidirectional fibres only were 0.11 mm and US$ 20/m^2 respectively. The thickness and price of the GF sheet containing bi-directional fibres were 0.53 mm and US$ 0.8/m^2 respectively. The volume ratio between longitudinal fibres and transverse fibres of the GF sheet was 4:1. The fibre characteristics were supplied by the manufacturer, the tensile strength, modulus and elongation of the CF were 3652 MPa, 252 GPa and 1.5% respectively; the tensile strength, modulus and elongation of the GF were 1280 MPa, 42.8 GPa and 3% respectively. Because the fibre characteristics are normally much higher than those of the final composite products (Brena et al. 2003, Okeil et al. 2001) the mechanical properties of FRP laminates designed and used in this research were tested by the authors and are listed in Table 1.

2.2 *Specimen preparation*

tiffEquation-II/SE98E.2 Ten rectangular beams were cast with dimensions of 125×200 mm in cross section and 2300 mm in length. As shown in Fig. 1 and Table 2, two 10 mm diameter deformed steel bars were used as bottom bars for Pa and all strengthened beams giving a reinforcement ratio of 0.74%. Two 12 mm diameter steel bars were used as bottom bars for Pb beam giving a reinforcement ratio of 1.07%. Stirrups of 8 mm diameter, at a spacing of 150 mm or 200 mm, were used throughout the length of the ten beams. All of beams were wet-cured by covering with wet burlap for 28days, and then, exposed in outdoor environment up to 6 months before testing.

The process of applying fibre sheet to concrete involved surface preparation, priming, resin undercoating, fibre sheet application, resin overcoating and curing with a reference to ACI-440 (2000).

Two types of strengthening, as shown in Fig. 1 and Table 2, were adopted. 2C, U2C and F2C employed CF sheet only, and U1C2G as well as F1C/2G employed both CF sheet and GF sheet simultaneously. Continuous GFRP L-wraps were used for strengthening F1C/2G beams. The use of L-wraps (instead of U-wrap) was for more convenient installation and better bond quality. Two F2C beams and two F1C/2G beams

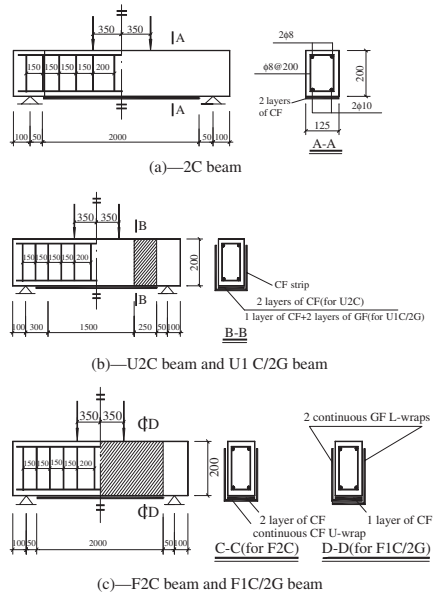

Figure 1. Layouts of FRP materials of strengthened beams.

were made in order to understand their behaviour better.

The authors take the view that if the ultimate moment capacities of strengthened beams were close to that of the control beam, the comparison of displacement ratios (fracture deflection / yield deflection) of the two kinds of beams would be more rational, and therefore, two un-strengthened beams (P_a and P_b) with different steel reinforcement ratios were made as control beams. All strengthened beams had the same steel reinforcement ratio as P_a beam. The estimated moment capacities of the most of strengthened beams were close to that of P_b beam.

2.3 *Loading methods and measurements*

All beams were tested as simply supported beams under four-point loading, over a effective span of

Table 2. Details of tested beams.

Beam name	Strengthening type	Strengthening cost ($)*
Pa	Control	–
2C	Two layers of 100 mm wide CF	12
U2C	Two layers of 100 mm wide CF with end U-strips	19.9
F2 C (1) F2 C (1)	Two layers of 100 mm wide CF with continuous CFRP U-wrap	43.5
U1C/2G(1) U1C/2G(2)	One layer of 100 mm wide CF+ two layers of 125 mm wide GF with end U-strips	19.3
F1C/2G(1) F1C/2G(2)	One layer of 100 mm wide CF+ two continuous GF L-wraps	20
Pb	Control	–

* Cost included materials, equipment and labor in China.

2100 mm, with the loads applied at 350 mm on either side of the midspan as shown in Fig. 1.

The following measurements were taken: (1) midspan deflection, using dial gauges of least count 0.01 mm; (2) concrete, steel bars and fibre sheet strains at midspan, using electrical-resistance strain gauges. The tests were performed by using load control before load reaching 40 kN, and followed by using displacement control in order to observe the later stage of the load-deflection curve better. The applied loads were monitored through a high-accuracy load cell with a load sensitivity of 0.1 kN. All of the measurements were automatically recorded through a data logger.

3 RESULTS AND DISCUSSION

3.1 *Failure mode*

The 2C beam failed in the end cover peeling off. Every specimen with end CFRP U-strips exhibited a strengthening failure mode of mid-span cover tension delamination. The strengthening-failure of every beam with three-sided continuous FRP wrap/wraps was marked by the fracture of the bottom FRP at midspan. At this stage, though the internal tension steel had yielded as well on every strengthened beam the strain in the compression portion of the concrete never reached the crushing stage for any strengthened beams. This failure mode was also observed by shahawy et al (2001). It should be noted that the cover delamination at beam ends did not occur either for F1C/2G beams. Because the possibility of the cover delamination at beam ends is much higher than that at mid-span, it can be concluded that bi-directional GFRP L-wraps are reliable to prevent mid-span delamination.

Table 3. Test and calculation results of beams.

Beam name	Tested FRP fracture load/ calculated FRP fracture load (kN)	Fracture deflection (mm)/ fracture FRP strain (%)	Relative load capacity*/ relative deformation capacity**/ displacement ratio***
Pa	29.38/29.57	46.40/–	1/1/14.2
2C	45.50/54.90	16.1/0.55	1.55/0.347/2.78
U2C	44.70/54.90	22.2/0.59	1.52/0.478/4.19
F2 C (1)	54.70/54.90	24.32/0.95	1.86/0.524/3.43
F2 C (2)	52.40/54.90	22.3/0.87	1.78/0.481/3.48
U1C/2G(1)	66.30/70.43	29.58/0.91	2.26/0.638/4.20
U1C/2G(2)	63.03/70.43	32.52/0.87	2.15/0.701/4.94
F1C/2G(1)	70.68/70.43	32.64/1.40	2.41/0.703/4.89
F1C/2G(2)	68.3/70.43	38.0/1.28	2.32/0.819/5.47
Pb	58.30/58.16	48.81/–	1.98/1.052/6.96

* Relative load capacity – (fracture load of each beam) ÷ (fracture load of beam Pa).
** Relative deformation capacity – (fracture deflection of each beam) ÷ (fracture deflection of beam Pa).
*** Displacement ratio – (fracture deflection) ÷ (yield deflection) for each beam.

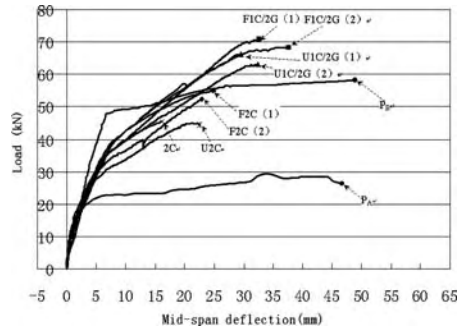

Figure 2. Load-midspan deflection curves for all specimens.

3.2 *Strengthening-failure-load and deflection capacity*

The load and deflection as well as FRP strain corresponding to strengthening-failure load for every specimen are listed in Table 3. The load-deflection curves of all specimens are shown in Fig. 2. The strengthening-failure-loads of F2C and F1C/2G beams were about 82% and 137% higher than the ultimate load of control beam P_a respectively.

The fracture deflections of F1C/2G beams were about 52% higher than those of F2C beams, and the corresponding composite fracture strains of the formers were about 47% higher than those of the latters. It

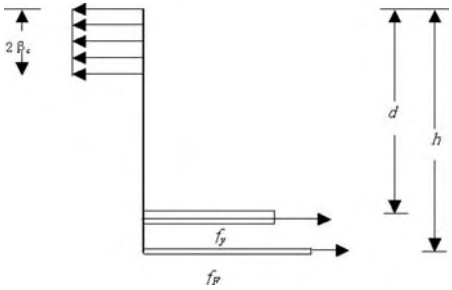

Figure 3. Sketch for calculating fibre-fracture moment.

should be noted that the fracture deflections of the H-CF/GF-RP and CFRP strengthening beams were about 28% and 52% lower than that of control beam P_b respectively; the displacement ratios of the two kinds of strengthened beams were about 26% and 50% lower than that of beam P_b respectively.

3.3 *Calculation of strengthening-failure moment*

The strain distribution of the all beams accorded with the plane deformation assumption before and after steel yielding. Though the strain in the compression portion of the concrete never reached the crushing stage for any strengthened beam the strengthening-failure moment can still be approximately calculated by the Equation 1 below (Ross et al. 1999):

$$M_u = f_y A_s \times (d - \beta_C) + f_F A_F \times (h - \beta_C) \quad (1)$$

As shown in Fig. 3, where M_u = strengthening failure (fibre sheet fracture) moment of beam; f_y = yield strength of steel bars; A_s = area of steel bars; $\beta_c = 1/2$ depth of compression zone of RC beam; f_F = strength of fibre sheet(s); A_F = area of fibre sheet(s); d = effective depth of RC beam; and h = depth of RC beam.

From Table 3 it can be seen that the calculation has a good agreement with test results.

3.4 *Comparison of strengthening efficiency*

As shown in Table 3 and Fig. 2, the fracture deflection and failure load of F1C/2G beams were about 48% and 30% higher than those of F2C beams. The stiffness of F1C/2G beams was similar to that of F2C beams. The strengthening cost of H-CF/GF-RP strengthened beams was 54% lower than that of CFRP strengthened beams (Table 2).

4 CONCLUSIONS

The cover tension delamination may be prevented in some cases by wrapping spaced CFRP U-strips on strengthened concrete beams. The delamination may be eliminated by using CFRP U-wrap continuously along the beam span. However, the displacement levels of CFRP strengthened beams failed in tension by rupture of the CFRP were still considerable lower than those of the control beams. Under the premise of eliminating cover tension delamination, H-CF/GF-RP strengthening can obtain both a significant increase of deformation capacity and a remarkable increase of load carrying capacity at a very low strengthening cost. The stiffness of H-CF/GF-RP strengthened beams is similar to that of CFRP strengthened beams. Within the indicated scope of this study, the particular conclusions may be summarized as follows:

1. The fracture load, deflection and strengthening cost of H-CF/GF-RP strengthening beams were about 30% higher, 48% higher and 54% lower than those of CFRP strengthening beams.
2. The deformation capacities of H-CF/GF-RP and CFRP strengthening beams were about 28% and 52% lower than that of control beam respectively.

REFERENCES

American Concrete Institute (ACI-440). 2000. *Guide for the design and construction of externally bonded FRP system for the strengthening concrete structures*. ACI-440-, Detroit: ACI.

Brena SF, Bramblett RM, Wood SL, Kreger ME. 2003. Increasing flexural capacity of reinforced concrete beams using carbon fibre-reinforced polymer composites. *ACI Structural Journal* 100(1): 36∼46.

Okeil AM, EI-Tawil S, Shahawy M. 2001. Short-term tensile strength of carbon fibre-reinforced polymer laminates for flexural strengthening of concrete girders. *ACI Structural Journal* 98(4): 470–478.

Qiao RS. 1997. *Micro Mechanical Properties of Composites*. Xian, China: Northwest University of Technology Press. p.117–123, in Chinese.

Ross CA, Jerome DM, Tedesco JW, Hughes ML. 1999. Strengthening of Reinforced Concrete Beams with Externally Bonded Composite Laminates. *ACI Structural Journal* 96(3): 212–220.

Shahawy M, Chaallal O, Beitelman TE, El-Saad A. 2001. Flexural strengthening with carbon fibre-reinforced polymer composite of preloaded full-scale girders. *ACI Structural Journal* 98(5): 735∼742.

Spadea G, Bencardino F, Swamy RN. 1998. Structural behavior of composite RC beams with externally bonded CFRP. *Journal of Composites for Construction* 2(8): 132∼137.

FRP research in Italy (special session)

FRP Composites in Civil Engineering – CICE 2004 – Seracino (ed)
© 2005 Taylor & Francis Group, London, ISBN 90 5809 638 6

FRP research in Italy – towards a new code for FRP strengthening

G. Monti
Dipartimento di Ingegneria Strutturale e Geotecnica, Università di Roma La Sapienza, Italy

ABSTRACT: An overview of some current developments in the FRP research in Italy is attempted, with the awareness that it can be neither exhaustive nor detailed. A deeper attention is devoted to one of the major recent achievements, that is, a pre-normative document regarding FRP strengthening, recently issued in Italy under the auspices of the National Research Council. This document stems from a nationwide effort that has brought together the competences and the experiences of almost all professors and researchers involved in this emerging and promising field, from 15 universities, of the technical managers of major production and application companies, and of the representatives of public and private companies that use FRP for strengthening artefacts. In a sense, it represents the synthesis of all researches carried out in Italy in the last ten years.

1 INTRODUCTION

The unique situation of Italy for as regards the preservation of existing constructions is the result of the combination of two aspects: the medium-high seismic hazard over a large portion of territory – as testified by the recent seismic zonation that set the highest expected PGA at 0.35 g for a 475 years return period – and the extreme complexity of a built environment that has no comparison in the world.

Construction typologies in Italy span from those reckoned as historical heritage – which in some cases dates back to some 2000 years ago – to those built in the last five centuries, during and after Renaissance, which are considered as cultural and architectural heritage of Italy (and the world's!), to finally those made in more recent times, notably during and after the economic boom of the 1960ies, and now rapidly obsolescing. The two former categories are largely composed of masonry buildings, while to the latter mainly belong reinforced concrete constructions.

This has motivated the growth of two clearly distinct fields of research and application for FRP: one for (old) masonry and one for (relatively recent) reinforced concrete constructions.

It goes without saying that for the historical, cultural and architectural heritage, the issue of structural safety is only a portion of the wider concepts of restoration, preservation and conservation. In this respect, it should be underlined that, in most cases, these concepts do not allow a systematic use of innovative materials, such as FRP, for strengthening purposes, unless it is demonstrated that they comply with somewhat strict requirements regarding formal and material compatibility.

These essential considerations have so complex and articulated implications that they deserve deeper considerations in the following section 2.6, where an attempt is made to describe the philosophical and methodological bases of preservation of historical construction in Italy and the constraints posed to the use of FRP in this field.

With the distinction in the two above described main fields of research on FRP, namely, masonry and reinforced concrete, the first studies have started towards the beginning of the 90ies by some pioneering groups that were striving at finding innovative solutions for increasing the safety of existing constructions, that could compete with the more developed and applied ones of concrete jacketing, steel plating, base isolation, and dissipative bracings.

In ten years the interest has spread so widely and rapidly that now FRP has become one of the most active and prolific research fields throughout the Country. In the last three years, ten interuniversity research projects have been funded on a 3-year basis by the Ministry of Scientific Research as deemed of national interest, gathering more than 20 different universities nationwide to collaborate on the most diverse FRP-related topics.

As a consequence to this intense commitment, a series of remarkable outcomes also resulted at the European level, thus confirming the European vocation of Italy, with at least ten universities constantly involved in European initiatives dealing with FRP, from both the research and the educational standpoint.

One such example is the recently started ENCORE joint program under the 6th Framework Program of the EU, where two major Italian universities participate

under the coordination of the University of Sheffield, with the objective of providing a bridge among the three sectors of material science, construction and academic research on FRP so to accelerate the industrial adoption of new materials, by means of training activities, dissemination of results and knowledge transfer throughout Europe.

Another notable recent achievement in Europe is the *fib* Bulletin no. 14, 'Design and Use of Externally Bonded FRP Reinforcement (FRP EBR) for Reinforced Concrete Structures', issued in 2001 as the result of the activity of the *fib* Task Group 9.3 'FRP Reinforcement for Concrete Structures', to which the Italian delegates have offered a valuable contribution, especially in the chapter devoted to confinement.

Finally, the most important testimony of the intense activity in Italy in the field of FRP is the recently issued pre-normative document CNR-DT 200/2004: 'Instructions for Design, Execution and Control of Strengthening Interventions by Means of Fibre-reinforced Composites' (2004), under the coordination of prof. Luigi Ascione and under the auspices of the Research National Council (CNR).

This document, described in more details in section 2, sets for the first time in Italy some standards for production, design and application of FRP in constructions that were dramatically needed in a continuously growing (and, sometimes, unruly) market. It is also conceived with an informative and educational spirit, which is crucial for the dissemination, in the professional sphere, of the mechanical and technological knowledge needed for an aware and competent use of such materials.

The document is the result of a remarkable joint effort of almost all professors and researchers involved in this emerging and promising field, from 15 universities, of the technical managers of major production and application companies, and of the representatives of public and private companies that use FRP for strengthening artefacts.

Thus, the resulting FRP code naturally encompasses all the experience and knowledge gained in ten years of countless studies, researches and applications of FRP in Italy.

2 THE NEW FRP CODE IN ITALY

The pre-normative document CNR-DT 200/2004: 'Instructions for Design, Execution and Control of Strengthening Interventions by Means of Fibre-reinforced Composites' (2004) is composed of the following chapters:

- Materials (with Annex),
- Basic concepts of FRP strengthening and special problems,
- Strengthening of reinforced concrete and pre-stressed concrete structures,
- Strengthening of masonry structures.

2.1 *Materials*

The chapter on Materials has a prevailing informative character and contains the fundamental information to obtain a basic knowledge on the composite materials, on their components (fibres, matrices, and adhesives) and of their physical and mechanical properties. It also includes an Annex describing the most usual production techniques and some basic notions on the mechanical behaviour of composites.

The most notable aspect is that a possible classification of composites usually adopted for structural strengthening is proposed, and some appropriate criteria for products qualification and acceptance are introduced.

This chapter was based on the studies carried out at the Polytechnics of Milan.

2.2 *Basic concepts*

It is stated that the design of the FRP strengthening intervention must meet with the requirements of strength, serviceability and durability. In case of fire, the strengthening resistance must be adequate to the prescribed exposure time.

The design working life of the strengthened structure is taken equal to that of new structures. This implies that the design actions to be considered are those of the current design codes for new constructions.

The safety verifications are performed for both the serviceability and the ultimate limit states. The format is that of the partial factor method. The design properties of both the materials and the products are obtained from the characteristic values, divided by the appropriate partial factor.

A rather innovative point (following the indications of Eurocode 0) is that the design properties X_d of the existing materials in the structure to be strengthened are obtained as function of the number of tests performed to acquire information on them:

$$X_d = \frac{\eta}{\gamma_m} m_X (1 - k_n V_X) \tag{1}$$

where η is a conversion factor, lower than 1, accounting for special design problems (related to environmental conditions and long duration phenomena), γ_m is the material partial factor, m_X is the mean value of the property X resulting from the number n of tests, the value k_n is given as function of the number n and the coefficient of variation V_X is supposed known. This latter can be assumed equal to 0.10 for steel, to 0.20

for concrete and to 0.30 for masonry and timber. The partial factor γ_m for FRP for the ultimate limit state verifications is taken as 1.20 under quality control and as 1.30 in other situations.

The design capacity is given as:

$$R_d = \frac{1}{\gamma_{Rd}} R\{X_{d,i}; a_{d,i}\} \quad (2)$$

where $R\{\cdot\}$ is the function describing the relevant mechanical model considered (e.g., flexure, shear, anchorage, etc.) and γ_{Rd} is a partial coefficient accounting for the uncertainties in the above capacity model (equal to 1.20 or 1.35 for anchorage, to 1.10 or 1.20 for shear, depending on whether quality is controlled or not); the function arguments are, in general, a set of mechanical and geometrical properties, of which $X_{d,i}$ and $a_{d,i}$ are, respectively, the design value and the nominal value of the i-th quantity.

An essential and innovative aspect is related to the safety verifications in the presence of fire. It is suggested that the load combination for exceptional situations, where E_d is the design value of the indirect thermal action due to fire, refer to the following situations:

- Exceptional event in the presence of strengthening (with E_d), in case the strengthening was designed for a predefined fire exposure time. In this case, the service actions of the frequent combination are to be considered. The elements capacity, appropriately reduced to account for the fire exposure time, should be computed with the partial coefficients relevant to the exceptional situations;
- After the exceptional event (without E_d), in the absence of strengthening. In this case, the service actions of the quasi-permanent combination are to be considered. The elements capacity, appropriately reduced to account for the fire exposure time, should be computed with the partial coefficients relevant to the service situations.

The Universities of Rome and Naples collaborated to writing this chapter.

2.3 *Reinforced concrete structures*

Anchorages. The optimal anchorage length is given as (units in mm):

$$L_e = \sqrt{\frac{E_f t_f}{2 f_{ctm}}} \quad (3)$$

where E_f and t_f are, respectively, the modulus and the thickness of FRP, and f_{ctm} is the concrete mean tensile strength. The design debonding strength is:

$$f_{fdd} = \frac{1}{\gamma_{Rd}} \frac{k_c k_{cr}}{4} \sqrt{\frac{k_b E_f}{\gamma_c t_f}} \sqrt{f_{ck} f_{ctm}} \quad (4)$$

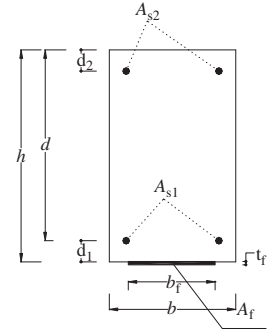

Figure 1. Notation for flexural strengthening.

where $k_c = 2/3$ for uneven surfaces, 1 otherwise, $k_{cr} = 5$ in cracked concrete zones, 1 otherwise, k_b is a scale/covering coefficient ≥ 1, γ_c is the concrete partial factor, and f_{ck} is the concrete characteristic strength.

The main contribution to this chapter came from the Universities of Bologna and Naples that are very active in the study of FRP anchorages behavior.

Flexure. The flexural capacity is attained when either the concrete compressive strain reaches its ultimate value or when the FRP tensile strain reaches its ultimate value $\varepsilon_{fd} = \min(\eta_a \varepsilon_{fu}/\gamma_f, f_{ffd}/E_f)$ where the first value corresponds to failure and the second to debonding as previously defined. The flexural capacity is then given as (notation in Figure 1):

$$M_u = \psi b x f_{cd}(d - \lambda x) + A_{s2}\sigma_{s2}(d - d_2) + A_f \sigma_f d_1 \quad (5)$$

where the neutral axis x is found by solving:

$$0 = \psi b x f_{cd} + A_{s2}\sigma_{s2} - A_{s1} f_{yd} - A_f \sigma_f \quad (6)$$

in which ψ and λ are non-dimensional coefficients representing, respectively, the intensity and the position of the compressive concrete resultant. However, the strengthened capacity cannot be considered as greater than twice the initial capacity.

This chapter resulted from the studies, both analytical and experimental, conducted at the Universities of Sannio and Chieti.

Shear and Torsion. Shear strengthening configurations can be in the form of side bonded, U-jacketed and wrapped FRP strips/sheets. The design shear strength of the strengthened element is given as:

$$V_{Rd} = \min\{\phi_c V_{Rd,ct} + \phi_s V_{Rd,s} + V_{Rd,f}, V_{Rd,\max}\} \quad (7)$$

where $V_{Rd,ct}$, $V_{Rd,s}$ and $V_{Rd,f}$ are the concrete, transverse steel and FRP contribution, respectively, while

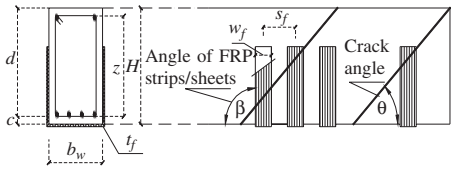

Figure 2. Notation for shear strengthening.

$V_{Rd,max}$ is the shear producing collapse in the compressed diagonal concrete strut. The two coefficients ϕ account for the reduced contributions of concrete and steel when FRP debonds and depend on both the strengthening configuration and the ratio between transverse steel and FRP.

The FRP contribution to the overall strength is given based on the chosen strengthening configuration. For side bonding (with notation in Figure 2):

$$V_{Rd,f} = 0.9d\frac{f_{fed}}{\gamma_{Rd}}2t_f\frac{\sin\beta}{\sin\theta}\frac{w_f}{s_f} \tag{8}$$

while for U-jacketing and wrapping:

$$V_{Rd,f} = 0.9d\frac{f_{fed}}{\gamma_{Rd}}2t_f\left(\frac{w_f}{s_f}\right)^2(\cot\theta+\cot\beta)\sin\beta \tag{9}$$

where f_{fed}, termed effective debonding strength, is given, in the case of side bonding, as:

$$f_{fed} = f_{fdd}\frac{z_{rid,eq}}{0.9d}\left(1-0.6\sqrt{\frac{L_{eq}}{z_{rid,eq}}}\right)^2 \tag{10}$$

with:

$$z_{rid,eq} = z_{rid} + L_{eq} \tag{11}$$

$$z_{rid} = 0.9d - L_e\sin\beta \tag{12}$$

$$L_{eq} = \frac{u_1}{f_{fdd}}E_f\sin\beta \tag{13}$$

while, in the case of U-jacketing and wrapping, respectively, it is given by:

$$f_{fed} = f_{fdd}\cdot\left[1-\frac{1}{3}\frac{L_e\sin\beta}{0.9d}\right] \tag{14}$$

$$f_{fed} = f_{fdd}\left[1-\frac{1}{6}\frac{L_e\sin\beta}{0.9d}\right] + \\ +\frac{1}{2}\left(\eta_R\cdot f_{fd}-f_{fdd}\right)\cdot\left[1-\frac{L_e\sin\beta}{0.9d}\right] \tag{15}$$

where f_{fd} is the FRP design strength, and:

$$\eta_R = 0.2+1.6\frac{R}{b_w} \qquad 0\le\frac{R}{b_w}\le 0.5 \tag{16}$$

is a coefficient depending on the rounding radius R with respect to the beam web width b_w.

For as regards strengthening in torsion, this is obtained through the application of wrapping strips/sheets at an angle of 90° to the element axis. The design torsional strength of the strengthened element is given as:

$$T_{Rd} = \min(\phi_s T_{Rd,s} + T_{Rd,f}, T_{Rd,\max}) \tag{17}$$

where $T_{Rd,s}$ and $T_{Rd,f}$ are the transverse steel and FRP contribution, respectively, while $T_{Rd,max}$ is the torque producing collapse in the compressed diagonal concrete strut. The coefficient ϕ accounts for the reduced contributions of steel when FRP debonds and depends on both the strengthening configuration and the ratio between transverse steel and FRP. The FRP contribution to the torsional strength is given as:

$$T_{Rd,f} = 2f_{fed}t_f bd\frac{w_f}{s_f}\cot\theta \tag{18}$$

where f_{fed} is given by (15).

Experimental and analytical studies conducted at the Universities of Rome and Cassino established the basis for this chapter.

Confinement. This aims both at increasing the ultimate strength in elements under axial load, and the ductility in FRP-confined elements under axial load and flexure. In case of elements with circular cross section of diameter D, the confined/unconfined concrete strength ratio is:

$$\frac{f_{cc}}{f_{cd}} = 1+2.6\left(\frac{f_l}{f_{cd}}\right)^{2/3} \tag{19}$$

while the ultimate concrete strain is:

$$\varepsilon_{ccu} = 0.0035+0.015\sqrt{\frac{f_l}{f_{cd}}} \tag{20}$$

where both depend on the confinement pressure exerted by the FRP sheet, given as:

$$f_l = 2\frac{E_f\varepsilon_{fd,rid}t_f}{D} \tag{21}$$

where $\varepsilon_{fd,rid} = 0.004$ is the FRP conventional ultimate strain, corresponding to an unacceptable degradation of concrete. However, the strengthened capacity cannot be considered as greater than twice the initial capacity.

For the case of rectangular sections with dimensions $b \times d$, with corners rounded with a radius $r_c \geq 20$ mm, the confining pressure exerted by an FRP wrapping can be computed by:

$$f_l = \frac{E_f k_s \varepsilon_{fd,rid} t_f}{\max(b,d)} \tag{22}$$

where k_s is an appropriate shape factor defined as:

$$k_s = 1 - \frac{(b-2r_c)^2 + (d-2r_c)^2}{3bd} \tag{23}$$

For as regards the ductility increase, the sectional ultimate curvature can be evaluated by adopting the classical parabola-rectangle law for concrete, with the ultimate concrete strain given by:

$$\varepsilon_{ccu} = 0.0035 + \frac{2.5\rho_f E_f k_s \varepsilon_{fd,rid}^2}{f_{cd}} \tag{24}$$

where the FRP/concrete ratio ρ_f is given by $4t_f/D$ for circular sections and by $2t_f/\max(b,d)$ for rectangular ones.

The chapter of confinement resulted form the joint collaboration between the Universities of Salerno and Roma.

2.4 *Masonry structures*

The application of FRP on masonry walls has the primary aim of increasing their strength and, secondarily, of increasing their collapse displacements. The objectives of FRP strengthening in masonry structures are: a) transmission of stresses either within the structural elements or between adjacent elements, b) connection between elements, c) inplane stiffening of slabs, d) limitation of cracks width, e) confinement of columns in order to increase their strength.

It is again underlined that the choice of the strengthening FRP material should avoid any incompatibility, both physical and chemical, with the existing masonry.

The strengthening intervention can include: a) increase of strength in walls, arches or vaults, b) confinement of columns, c) reducing the thrust of thrusting elements, d) transformation of non structural elements into structural elements, e) stiffening of horizontal slabs, f) application of chains in the building at the slabs and roof levels.

The masonry walls can be FRP-strengthened to prevent the out-of-plane collapse modes due to: overturning, vertical flexure, and horizontal flexure (Figure 3).

In these cases, the design of the FRP strengthening is performed through simple equilibrium between the acting forces and the resisting force of FRP strips located on top of the wall to restrain its rotation.

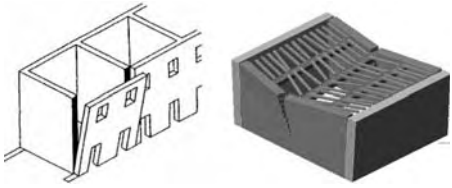

Figure 3. Collapse modes of masonry walls: overturning (left) and horizontal flexure (right).

Figure 4. FRP strengthening of a masonry barrel vault.

For as regards the in-plane collapse modes, these are due to: flexure, shear. The wall shear strength is given by the sum of the masonry and the FRP shear strengths:

$$V_{sh} = V_{sh,m} + V_{sh,f} \tag{25}$$

where $V_{sh,m} = d\, t f_{vk}/\gamma_m$ and:

$$V_{sh,f} = \frac{0.6 d\, A_{fw} f_{fd}}{s_f}(\cos\alpha + \sin\alpha) \tag{26}$$

where $d =$ steel depth (if any), $t =$ wall thickness, $f_{vk} =$ characteristic shear strength of masonry, $A_{fw} =$ FRP strip area, $s_f =$ FRP strip spacing, $f_{fd} =$ FRP design strength, $\alpha =$ FRP angle to the shear force direction.

When strengthening elements with either single (barrel vaults, in Figure 4) or double (groin and cross vaults, in Figure 5) curvature, the FRP strips should contrast the relative rotation at the hinge zones that develop where the limited tensile strength of masonry is attained. Thus, application of FRP strips over the outer (inner) surface of the vault thickness can prevent formation of hinges on the opposite inner (outer) surface.

The FRP-strengthening of arches includes two possible structural schemes: a) arch on fixed restraints,

Figure 5. FRP strengthening of a masonry cross vault.

Figure 6. FRP strengthening of a masonry dome.

b) arch supported by columns. The aim is to avoid formation of four hinges, which would imply collapse. The FRP-strengthening is applied on either (preferably) the outer or the inner surface, in the form of fabrics that adapt better to curved shape than prefab strips.

The FRP-strengthening of domes should increase the capacity of both the membrane and the flexural regimes. For the former, FRP strips should be applied circumferentially around the dome base (Figure 6), while for the latter, FRP strips should be applied along the meridians.

The load bearing capacity of masonry columns can be increased by confining them through FRP. The confined strength (which cannot be taken as greater than 1.5 the initial strength) can be computed as:

$$f_{mck} = f_{mk} + k_1 k_V k_H f_l \le 1.5 f_{mk} \tag{27}$$

where f_{mk} is the unconfined masonry compressive strength. The confining pressure f_l is evaluated as:

$$f_l = \rho_f E_f \varepsilon_{f,\lim} \tag{28}$$

where E_f = FRP modulus, $\varepsilon_{f,lim} = 0.004$, and:

$$\rho_f = \frac{2 t_f b_f}{\max(b,d) s_f} \tag{29}$$

is the FRP strengthening ratio, with t_f b_f being the area of each confining strip, b, d the masonry cross section dimensions, and s_f the strip spacing. The coefficients in the formula are:

$$k_1 = \frac{g_m}{1250} \tag{30}$$

with the masonry mass density g_m in kg/m^3, while:

$$k_V = \left(1 - \frac{s_f - b_f}{2\min(b,d)}\right)^2 \tag{31}$$

$$k_H = \begin{cases} 1 & \text{circular} \\ 1 - \dfrac{(b-2r_c)^2 + (d-2r_c)^2}{3\,b\,d} & \text{others} \end{cases} \tag{32}$$

where r_c is the corners rounding radius.

The universities involved in studies related to this topic are those of Bologna, Cassino, Florence, Naples, Padua, Pavia, Perugia, Salerno, and Venice.

2.5 *FRP strengthening in seismic zones*

The above described chapters on strengthening also contain specific indications regarding constructions in seismic zones. These follow the approach of the most recent Italian and International codes, for as regards: assessment techniques, safety requirements (limit states), seismic protection levels, analysis methods, verification criteria (distinction between ductile and brittle elements).

Reinforced concrete buildings. FRP strengthening is regarded as a selective intervention technique, aiming at: a) increasing the flexural and shear capacity of deficient members, b) increasing the ductility (or the chord rotation capacity) of critical zones through confinement, c) improving the performance of lap splice zones through confinement, d) prevent longitudinal steel bars buckling through confinement, e) increase the tensile strength in partially confined beam-column joints through application of diagonal strips.

A relevant innovation concerns the definition of the inspiring principles of the intervention strategies: a) all brittle collapse mechanism should be eliminated, b) all "soft story" collapse mechanism should be eliminated, and c) the global deformation capacity of the structure should be enhanced, either: c1) by increasing the ductility of the potential plastic hinge zones without changing their position, or c2) by relocating

the potential plastic hinge zones by applying capacity design criteria. In this latter case, the columns should be flexure-strengthened with the aim of transforming the frame structure into a high dissipation mechanism with strong columns and weak beams.

Failure of brittle mechanisms such as shear, lap splicing, bar buckling, joint shear, should be avoided. For shear, the same criteria apply as for the non-seismic case, with the exception that side bonding is not allowed and FRP strips/sheets should only be applied orthogonal to the element axis. For lap splices of length L_s, adequate FRP confinement should be provided, having thickness:

$$t_f = \frac{\max(b,d)}{2E_f}\left(1000\frac{f_l}{k_H} - E_s\right) \tag{33}$$

where E_s = transverse steel modulus, and f_l = confinement pressure:

$$f_l = \frac{A_s f_{yd}}{\left[\frac{u_e}{2n} + 2(d_b + c)\right]L_s} \tag{34}$$

where u_e = perimeter of the cross section inscribed in the longitudinal bars, of which n are spliced, and c = concrete cover. For bar buckling, adequate FRP confinement should be provided, having thickness:

$$t_f = \frac{10\,n\max(b,d)}{E_f} \tag{35}$$

where n = total number of longitudinal bars under potential buckling.

Contributions to this topic came essentially from the Universities of Rome and Naples, which are currently working on FRP strengthening of beam column joints.

Masonry buildings. Starting form the same principles as for RC buildings, when FRP-strengthening a masonry building one should also consider that: a) masonry walls inadequate to resist vertical and horizontal actions should be strengthened or rebuilt, b) orthogonal and corner walls should be adequately connected, c) slab/wall and roof/wall connections should be ensured, d) thrusts from roofs, arches and vaults should be counter-reacted by appropriate structural elements, e) slabs should be in-plane stiffened, f) vulnerable elements that cannot be strengthened should be eliminated, g) irregularity of buildings cannot be corrected by FRP applications, h) local ductility increase should be pursued whenever possible, i) the application of local FRP strengthening should not reduce the overall structural ductility.

The Universities of Pavia and Genoa, which are actively involved in the field of seismic protection of masonry constructions, have mainly contributed to this topic.

2.6 *Quality control*

A series of in-situ checks and operations are specified in order to validate the quality level of the applications of composite materials: check and preparation of the substrate, evaluation of the substrate degradation, removal and reconstruction of the substrate with possible treatment of steel bars.

A series of requirements for a correct application are also given for as regards: humidity conditions, environmental and substrate temperature, construction details and rules. The quality control of the application is then based on semi-destructive and non-destructive tests.

Indications on these issues came from the University of Naples, Calabria and Bologna.

3 PRESERVING THE HISTORICAL HERITAGE

As a further comment to the strengthening interventions with FRP on masonry buildings described above, an attempt is made herewith to shortly illustrate the philosophical and methodological bases of preservation of historical constructions in Italy. Being a matter of extreme complexity, the approach discussed herewith is still open to discussion and under continuous evolution and might as well hold a different view from other approaches accepted in some Italian universities.

The objective is clear: encourage (seismic) assessment studies of historical urban buildings and environments that could guide towards the identification and the design of a strengthening strategy – be it of conservation, of reconstruction, of amelioration, of retrofitting – that be in complete harmony with the existent.

In this respect, interventions using FRP should be carefully chosen, trying to minimise the invasiveness and the visual impact. However, there is a general consensus that FRP bonded to masonry structural elements complies with the principles of the chart of Athens, as opposed to conventional (steel and concrete) solutions, because of its reversibility and easy recognition of age difference.

Here, the relationship between *shape* and *matter* acquires a strong and meaningful value. When selecting an intervention strategy with FRP one should avoid relying on its remarkable strength to locally strengthen possibly cracked masonry members. One should rather remember that the knowledge of the material-related aspects (strength properties, masonry typology, …) of an artefact is, from the seismic

assessment standpoint, only subordinate to the knowledge of the shape-related aspects (global geometry, in-plan and elevation configurations, …).

The global seismic performance of a masonry artefact primarily depends on shape-related aspects: symmetry, walls relative and absolute in-plan location, height-wise thickness variations, presence of voids, holes, etc. It is perhaps superfluous to recall that the safety verification of walls against collapse by overturning is based solely on geometrical data, totally disregarding the characteristics of the constituent materials. Thus, the choice of FRP 'because it is a strong material' becomes meaningless; more important is rather to correctly place it according to equilibrium considerations.

Another important objective when strengthening a masonry building is to enhance the connections both between orthogonal walls and between corner walls. This can be attained, for example, by 'sewing' inadequate connections by means of FRP strips. In order to correctly design the intervention, one should clearly identify all inadequate connections throughout the structure. This traditionally requires in-situ verifications and inspections tests that are often in-vasive and destructive. In most case, this so-called 'cultural sacrifice' is deemed unacceptable.

Alternatively, this can be avoided by trying and 'read the building texture' and reconstructing the stratification, growth and aggregation modalities in the course of the centuries. The recognition of the prolongation, rotation, intersection, and sliding of walls helps at correctly defining the connection degree between adjacent walls. Also, walls identified as 'synchronic', that is, built at the same time, will be adequately connected and collaborating, whereas walls recognized as 'diachronic', that is, built at different times, will be considered as detached and not collaborating. This in turn affects, both, the outcome of the safety assessment of local and global collapse mechanisms, and the extent of the eventual FRP strengthening intervention.

4 CONCLUSIONS

The peculiarities of Italy, highly seismic and endowed with a built environment unique in the world, render every research in this field a continuous and challenging task. This nationwide effort has resulted in a pre-normative document (CNR-DT 200/2004) that, beyond regulating a rapidly growing professional and technical field, is also conceived with an informative and educational spirit, which is crucial for the dissemination, in the professional sphere, of the mechanical and technological knowledge needed for an aware and competent use of such materials.

SOME RECENT PAPERS

Aprile, A., and Benedetti, A. (2004). Coupled flexural-shear design of R/C beams strengthened with FRP. *Composites: Part B*, Elsevier, 35, 1–25.

Aprile, A., Spacone, E., and Limkatanyu, S. (2001). Role of Bond in Beams Strengthened with Steel and FRP Plates. *Journal of Structural Engineering*, ASCE, 127(12), pp. 1445–1452.

Arduini, M., Di Tommaso, A., and Nanni, A. (1997). Brittle failure in FRP plate and sheet bonded beams. *ACI Structural Journal*, 94(4), 363–369.

Arduini, M., and Nanni, A. (1997). Behavior of precracked RC beams strengthened with carbon FRP sheets. *Journal of Composites for Construction*, ASCE, 1(2), 63–70.

Ascione, L., and Feo, L. (2000). Modeling of composite/concrete interface of RC beams strengthened with composite laminates. *Composites: Part B*, Elsevier, 31(6/7), 535–540.

Ascione, L., and Feo, L. (2002). Strengthening of cracked RC beams with FRP sheets: an experimental investigation. *International Conference on Composites Engineering (ICCE/9)*, San Diego, USA.

Barboni, M., Bendetti, A., and Nanni, A. (1997). Carbon FRP Strengthening of Doubly Curved Precast PC Shell. *Journal of Composites for Construction*, ASCE, 1(4), 168–174.

Camata, G., Spacone, E., Al Mahaidi, R., and Saouma, V. (2004). Analysis of Test Specimens for Cohesive Near-Bond Failure of FRP-Plated Concrete. *Journal of Composites for Construction*, ASCE, in press.

Camata, G., Corotis, R., and Spacone, E. (2004). Simplified Stochastic Modeling and Simulation of Unidirectional Fiber Reinforced Composites. *Probabilistic Engineering Mechanics*, 19(1–2), 33–40.

Ceroni, F., Manfredi, G., and Pecce, M. (2001). Cracks width in RC beams strengthened with carbon fabrics. *Proc. of the Fifth Conference on Non-Metallic Reinforcement for Concrete Structures,FRPRCS5*, Thomas Telford, Cambridge, UK, 16–18 July, Vol. 2, 917–926.

Ceroni, F., Pecce, M., and Matthys, S. (2003). Tension Stiffening of RC Ties Strengthened with Externally Bonded FRP Sheets, *J. of Composites for Constructions*, ASCE, 8(1).

Ceroni, F., and Pecce, M. (2004). Modelling of Tension Stiffening behaviour of RC ties strengthened with FRP sheets, *J. of Composites for Constructions*, ASCE, submitted.

Ianniruberto, U., and Imbimbo, M. (2000). Shear resisting contribution of composite for RC beams strengthened with FRP sheets, *Proceedings International Conference Advancing with Composite 2000*, Milan, May, 233–241.

Ianniruberto, U. and Imbimbo, M. (2002). Experimental analysis on the shear behaviour of RC beams strenghtened with GFRP sheets. *Proc. Third International Conf. on Composites in Infrastructure, ICCI '02*, San Francisco, California, 10–12 June.

Manfredi, G., Marcari, G., and Pecce, M. (2004). In-plane shear performance of stone masonry panels strengthened with FRP. *Journal of Structural Engineering*, ASCE, (submitted).

Monti, G., Nisticò, N., and Santini, S. (2001). Design of FRP jackets for upgrade of circular bridge piers. *Journal of Composites for Construction*, ASCE, Vol. 5, No. 2.

Monti, G., and Santini, S. (2002). Reliability-based calibration of partial safety coefficients for FRP. *Journal of Composites for Construction*, ASCE, 6(3).

Monti, G., Renzelli, M., and Luciani, P. (2003). FRP Adhesion to Uncracked and Cracked Concrete Zones. *Proceedings of the 6th International Symposium on Fibre-Reinforced Polymer (FRP) Reinforcement for Concrete Structures (FRPRCS-6)*, Singapore, July, 183–192.

Pecce, M., Manfredi, G., and Cosenza, E. (2000). Experimental response and code models of GFRP RC beams in ultimate and serviceability conditions. *Journal of Composites for Construction*, ASCE, 4(4), November, 182–190.

Prota, A., Nanni, A., Manfredi, G., and Cosenza, E. (2003). Capacity Assessment of RC Subassemblages Upgraded with CFRP. *Journal of Reinforced Plastics and Composites*, Sage, 22(14), 1287–1304.

Realfonzo, R., Prota, A., Manfredi, G., and Pecce, M. (2002). Flexural Strength of FRP-confined RC Columns. *Proc. 1st fib Congress*, October, Osaka, Japan.

Spadea, G., Bencardino. F., and Swamy, R.N. (1998). Structural behaviour of composite RC beams with externally bonded CFRP. *Journal of Composite for Construction,* ASCE, 2(3), 132–137.

Spoelstra, M.R., and Monti, G. (1999). FRP-confined concrete model. *Journal of Composites for Construction, ASCE*, Vol. 3, No. 3.

Thomsen, H., Spacone, E., Limkatanyu, S., and Camata, G. (2003). Failure Mode Analyses of Reinforced Concrete Beams Strengthened in Flexure with Externally Bonded Fiber Reinforced Polymers. *Journal of Composites for Construction*, ASCE, 8(2), 123–131.

FRP Composites in Civil Engineering – CICE 2004 – Seracino (ed)
© 2005 Taylor & Francis Group, London, ISBN 90 5809 638 6

Bond tests on concrete elements with CFRP and anchorage systems

F. Ceroni & M. Pecce
University of Sannio, Engineering Dept., Benevento, Italy

ABSTRACT: Interface failures represent a typical issue of FRP laminates externally applied to reinforced concrete elements, due to high stress concentrations in the anchorage zone of most types of applications. Therefore anchorage systems and bond models are key issue of a reliable design. Experimental tests to evaluate the efficiency of anchorage systems to avoid the delamination failure at the end of FRP laminates have been performed on T-shaped elements that represent various structural situations. A first approach with a simply FEM analysis is introduced considering non-linear bond behaviour at the interface.

1 INTRODUCTION

The reliability in strengthening existing RC structures with FRP externally bonded is strongly related to bond behaviour at the interface and anchorage systems. Delamination is a typical failure for RC elements with FRP laminates or sheets; furthermore it often occurs at the anchorage where there is high concentration of stresses.

When the external reinforcement is used to upgrade structures in seismic areas (confinement of columns, strengthening of beam–column joints), the ductility is a key issue of the design. Thus, brittle failure due to the debonding has to be avoided and anchorage systems may be designed for both strength and ductility considerations.

Several types of anchorage have been studied and tested by researchers [1–7]. The efficiency of a bond anchorage (FRP bonded to concrete) can be due to adequate transfer length, as provided by formulations of various authors [3, 8, 9, 10].

The external reinforcement may peel off in the uncracked anchorage zone as result of bond shear fracture through the concrete or, due to high stress concentration, in correspondence of shear or flexural cracks; therefore localized debonding can be caused by unevenness of the concrete surface.

To avoid delamination at the end, an additional anchorage capacity may be obtained by gluing fibres transversal to the direction of the external reinforcement or by applying steel or FRP plates simply bonded or bolted. For using bolts to fix FRP laminates it is generally suggested to apply an additional layer of multidirectional fibres; because sections where bolts are placed on unidirectional sheets could be starting points for local debonding.

Fib bulletin 14 [3] suggests an anchorage system consisting in the realization of a hole filled with resin, then a glass tow is forced through in the hole and the ends are splayed outwards in a circle and are bonded on the FRP sheet. These types of anchorage can be very useful, eg. for T-beams strengthened in shear, and several configurations have been proposed and tested by [5], varying distance between fans, number of carbon layers and geometrical properties of the elements. Also steel U-shaped devices embedded in the concrete are suggested as anchorage [3]. Experimental tests [4, 11] on reinforced concrete ties externally bonded with FRP sheet with this system have shown that the anchorage allows not only to have an increase of the ultimate strength, but also an increment of the ductility of the strengthened member with higher displacements at ultimate conditions.

Considering the successful development of the new reinforcement technique represented by the methodology of the near-surface mounted FRP rods, a combined anchorage system for external laminates can be also realized using FRP bars. It consists into realizing a groove in the concrete transversally to the fibre direction at the end of the FRP reinforcement: the sheet is positioned in the groove, an FRP bar is put in the groove to fix the sheet and the hole is then filled by epoxy resin. This system was tested as anchorage for external FRP shear reinforcement [7], giving a very good efficiency.

To investigate different solutions of anchorages, bond shear tests have been executed in the Magnel Laboratory for Concrete Research on concrete specimens strengthened with carbon fibre FRP (CFRP). Fourteen tests have been executed investigating the bond behaviour between concrete and CFRP when dealing with a T-shaped section and for different strengthening

configurations, mainly with respect to additional mechanical fixings. Details about specimen's configuration and results have been reported in [12]; in the following some experimental results are summarized and first theoretical and numerical comparisons are worked out.

2 TEST PROGRAM

2.1 *Test set-up*

An experimental program of 14 specimens was designed to study the efficiency of different anchorage solutions at the end of external FRP reinforcement. The configuration of the specimen is a T-shape that simulates real geometrical conditions of beam–column connections, footing zone of columns and T-beams. Each specimen is made by two concrete blocks with a superior prismatic block and an inferior T-shaped block. The two blocks are connected during the phases of casting, manipulation, preparation and moving of the specimen in the tensile machine, by a stiff plastic tube and a wooden box, in order to sustain the superior block and to keep the alignment of the two blocks. To have confinement of the concrete, internal reinforcement is provided with steel stirrups.

On two opposite sides of the specimens (sides with the T-shaped section) CFRP laminates are applied with a width of 100 mm. In six specimens the CFRP is provided along the web. For the other eight specimens the anchorage systems are realized by extending the FRP on the flange of the T-section (90° angle). No bond is provided between the CFRP and the wooden box separating the two concrete blocks. In figure 1 the configuration of specimen with fibres extended to the web is reported.

The loading arrangement provides tension to the FRP laminate by compression on both the concrete blocks, pulling them apart. To achieve this loading condition by using a tensile loading machine, the specimen contains two central diwidag steel bars inserted in the plastic tube (the latter been put in the concrete blocks during casting). One end of each bar is fixed to the block by a bolted steel spreader plate, while the other end is clamped in the testing machine. In the central zone between the two blocks, the plastic tube is cut to insert the steel bars and spreader plates. Prior to testing the wooden box is dismantled, so that the only connection between the two concrete blocks is provided by the CFRP. For all tested specimens the FRP laminate is anchored to the concrete of the superior block by gluing a steel plate and applying a mechanical external anchorage system, in order to avoid a debonding failure in this part. For specimens having the FRP laminate on the vertical and horizontal plane, the 90° angle of the concrete block at the intersection of the two planes was rounded by an epoxy filling having a curvature radius of 25 mm.

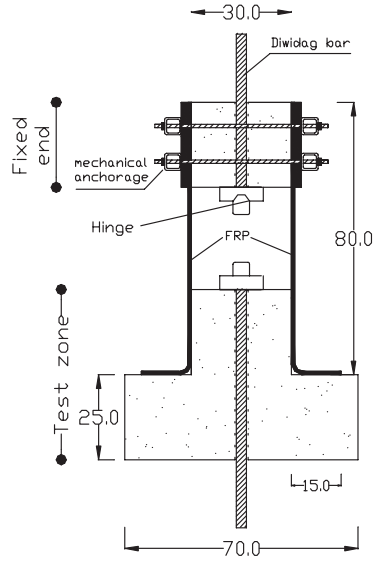

Figure 1. Specimen configuration.

The tests were carried out in displacement control way with a speed of 0.1 mm/min.

An overview and details of the different configurations are provided in table 1. Series TA1 and TA2 are reference ones because they have no extra anchorage for the FRP laminate. More details about the anchorage system configurations are reported in [12].

Several strain gauges were applied on the FRP laminates: one strain gauge was applied at the middle of the unbonded FRP and at least 2 times four strain gauges were glued along the bonded part on both sides of the specimen according to the scheme of figure 2. In addition, four LVDT transducers were positioned on both sides of the specimen at the beginning of the bonded zone, in order to measure the slip between concrete and FRP at the loaded end of the laminate.

2.2 *Materials*

The mean cubic compressive strength of concrete, obtained by experimental test on cubes (150 mm side) at the age of testing, is reported in table 2 for each batch. Therefore 3-point bending tests on 3 prisms (150 mm × 150 mm × 600 mm) were performed to have the tensile strength $f_{ct,b}$, and compression tests on cylinders (∅150 mm × 300 mm) to determine the secant E-modulus E_c (evaluated between 0.5 MPa and 1/3 of the compressive strength).

Table 1. Characteristics of specimens.

Specimen	Anchorage type
TA1-1	Laminate only on vertical plane: vertical bond
TA1-2	length = 250 mm
TA2-1	Laminate on vertical plane and extended to
TA2-2	horizontal one, vertical bond length = 250 mm
TA3-1	Laminate on vertical plane and extended to horizontal one, vertical bond length = 100 mm
TA3-2	Laminate on vertical plane and extended to horizontal one + steel plates bonded on FRP: vertical bond length = 250 mm, FRP length before steel plates: 150 mm
TA4-2	Laminate on vertical plane and extended to horizontal one + steel plates bonded on FRP and bolted on both sides of FRP: vertical bond length = 250 mm, FRP length before steel plates: 120 mm
TA4-1	Laminate on vertical plane and extended to horizontal one + FRP laminate plates bonded: vertical bond length = 250 mm, FRP length before steel plates: 120 mm
TA5-1	Laminate on vertical plane with an FRP bar cut-in at the end: vertical bond length = 100 mm, FRP length before FRP bars: 50 mm
TA5-2	Laminate on vertical plane with an FRP bar cut-in at the end: vertical bond length = 250 mm, FRP length before FRP bars: 150 mm
TA6-1	Laminate only on vertical plane with a bond length of 250 mm + FRP plates bonded at the end
TA6-2	Laminate only on vertical plane with a bond length of 250 mm + Steel plates bonded at the end
TA7-1	Laminate on vertical plane with a bond length of 250 mm + extension on horizontal plane with FRP bar in the corner
TA7-2	Laminate on vertical plane with a bond length of 100 mm + extension on horizontal plane with FRP bar in the corner

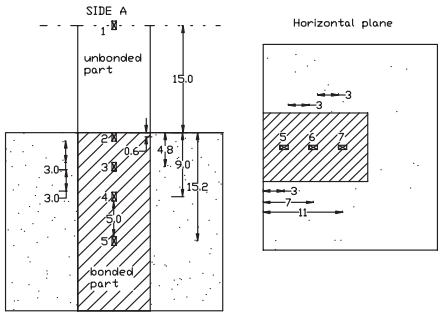

Figure 2. Location of strain gauges.

Table 2. Mechanical properties of the concrete.

Batch	TA1	TA2	TA3	TA4	TA5	TA6	TA7
$f_{c,cub}$ [MPa]	45.0	44.7	42.7	46.3	42.6	35.6	35.4
$f_{ct,b}$ [MPa]	3.95	4.01	4.01	5.18	4.8	4.19	3.91
E [GPa]	32.6	32.6	36.2	30.6	32.1	31.9	32.8

Table 3. Test results.

Specimen	F_{max} [kN]	Failure mode
TA1-1	33.41	Delamination
TA1-2	29.36	Delamination
TA2-1	20.95	Delamination + fracture of fibres at the beginning of the bonded side
TA2-2	20.94	Delamination on vertical plane with propagation on the horizontal plane
TA3-1	26.71	Delamination on vertical plane with propagation on the horizontal plane
TA3-2	29.00	Delamination on vertical plane with detachment of steel plate
TA4-1	45.00	Detachment of FRP plate with tensile rupture of fibres in the angle
TA4-2	28.77	Delamination of fibres and tensile failure in the corner, anchorage intact
TA5-1	46.60	Failure of fiber in tension at the groove after delamination
TA5-2	25.50	Failure of fiber in tension at the groove after delamination
TA6-1	48.80	Delamination with slip of fibres from anchorage
TA6-2	49.30	Delamination with slip of fibres from anchorage
TA7-1	47.50	Failure of fibre in tension at the end of the superior prismatic block
TA7-2	29.60	Failure of fibre in tension at the groove

The internal steel reinforcement is made by deformed steel bars S500 (characteristic yield strength 500 MPa). The external FRP is a wet–lay–up system; the thickness, s, the ultimate strength, f_u, and strain, ε_u, the Young's modulus, E_f, as declared by the manufacturer, are respectively 0.111 mm, 3400 MPa, 1.4%, 230 GPa. The tensile strength obtained by experimental tests on fibres is 2340 MPa.

3 TEST RESULTS

3.1 *Failure mode*

In table 3 the results of the tests are summarized in terms of maximum load and failure modes. The maximum theoretical ultimate load of the specimens, assuming sufficient anchorage capacity to obtain

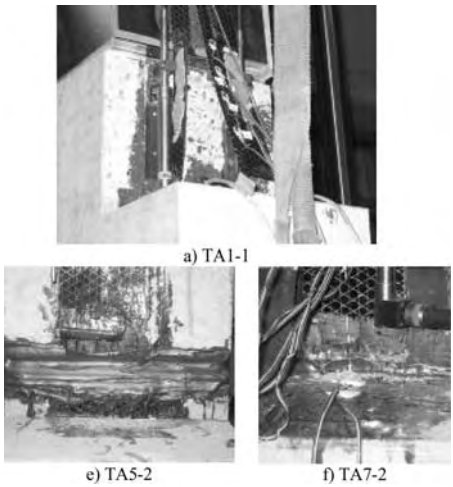

Figure 3. Experimental failure modes.

CFRP fracture in tension and considering the experimental tensile strength of fibres, is 52 kN, that is very near to the experimental ultimate load registered when fibre fracture happened. Examples of failure modes are reported in figure 3.

The delamination load N_{max} and transfer length $L_{t,max}$ of the bonded interface have been calculated according to the following formulation suggested by fib bulletin 14 [3]:

$$N_{f,max} = \alpha c_1 k_c k_b b_f \sqrt{f_{ctm} E_f t_f} \quad (1)$$

$$L_{t,max} = \sqrt{E_f t_f / (f_{ctm} \cdot c_2)} \quad (2)$$

$$k_b = 1.06 \sqrt{\frac{2 - b_f / b}{1 + b_f / b_o}} \geq 1.0 \quad (3)$$

where f_{ctm} is the mean tensile strength of concrete, t_f, b_f and E_f are thickness, width and Young's modulus of fibres, $\alpha = 0.9$, $k_c = 0.87$, $c_1 = 0.64$ are parameters experimentally calibrated, $b_o = 400$ mm is a refer width and b is the width of the concrete element. It results equal to 31.3 kN assuming a tensile strength of concrete equal to the average bending tensile strength (4.3 MPa) of all batches. The theoretical maximum load is very similar to the experimental strength of specimens of batch TA1, which have CFRP applied only on the vertical plane. The transfer length given by eqn.2 is 80 mm.

For the specimens without additional anchorage devices, when the CFRP is applied also on the horizontal plane (specimens TA2-1, TA2-2), a reduction

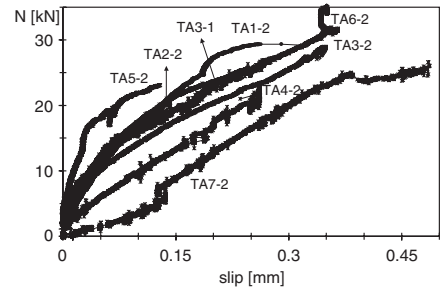

Figure 4. Load–displacement relationship.

of about 30% of the maximum load was observed with respect to series TA1 (with CFRP only along the vertical plane). This result is probably due to local effects in the corner. This observation is less pronounced when the bond length of laminate on the vertical plane is shorter (specimen TA3-1 has a bond length of 100 mm instead of 250 mm).

When applying additional anchorage systems, in some cases these are very effective, allowing the CFRP to reach its tensile strength. In other cases the anchorage can not be considered efficient because the ultimate load is less or equal to the failure load of the reference specimens. Detailing and application procedure strongly influence the effectiveness of the system. Application of bolts on steel plates produced concentrated stresses, realization of curved CFRP in a corner is difficult, and grooves for FRP bars produce points where local failure phenomena (local debonding, cutting of fibre, stress concentration) could develop.

When the CFRP is applied only vertically and additional anchorage is provided by a transverse plate (FRP or steel), the failure load can have an increment up to 57% (specimen TA6-2) with respect to the mean value of the reference specimens (TA1-1 and TA1-2). This configuration appears a favourable solution, considering also the easier modality of application.

In some cases where the anchorage had no effect on the strength of the specimen, greater displacements were registered by the LVDT transducers. In figure 4 a comparison between displacement measured by transducers is reported for different specimens; it is possible to observe that specimens TA4-2 and TA7-2, even if equipped of anchorage (with steel plates bolted and FRP bars in the corner respectively), had greater slips. The greater deformability of bond law for these two specimens, starting from the beginning of the test, was probably due to a non efficient gluing of the external reinforcement. The ultimate load was comparable with the ones of the reference specimens (TA1-1 & TA1-2) and failure mode was characterized by fibre fracture for stress much lower than the

tensile strength of fibres; therefore it was confirmed that local phenomena damaged the effectiveness of the anchorage.

3.2 *Strain behaviour*

The experimental results in terms of strain distribution along the FRP are reported in figure 5. The point zero of the x axis is assumed at the beginning of the bond length of the laminate.

Strain distributions along the FRP laminate evidenced that the effective transfer length is not greater than 100 mm, while the remaining part of the bond length is stressed only at failure condition. For this reason some specimens (TA3-1, TA5-2, and TA7-2) were realized considering a reduced bond length of 100 mm.

Since the system studied can be significant of anchorage problems in T-beam strengthened in shear, some considerations about the effective strain have been developed. According to the model of [8, 13 and 14], at the ultimate limit state in shear the FRP delamination occurs at an effective strain in the principal material direction that in general is less than the tensile failure strain of fibres. Fib bulletin [3] gives formulations for the effective strain fitted on the all published experimental results on shear strengthening of RC members; the expressions are:

– Fracture control:

$$\varepsilon_{f,e} = 0.17 \cdot \left(\frac{f_{cm}^{2/3}}{E_f \rho_f} \right)^{0.3} \varepsilon_{fu} = 0.00881 \qquad (4)$$

– Peeling-off:

$$\varepsilon_{f,e} = 0.65 \cdot \left(\frac{f_{cm}^{2/3}}{E_f \rho_f} \right)^{0.56} 10^{-3} = 0.00485 \qquad (5)$$

In table 4 the strain ε_1 in the free part of FRP laminate and the strain ε_2 at the first bonded point measured by strain gauges are reported at failure load. The experimental values are similar to the ones given by equations. 4 and 5 suggested by fib bulletin in hypothesis of fracture and peeling control.

Also the original formulation suggested by [14] and [8] have been calculated and reported in the following; the values of effective strain are similar to one given by eqn.4.

$$\varepsilon_{f,e} = 0.008712 \qquad (6)$$

$$\varepsilon_{f,e} = 0.008675 \qquad (7)$$

By the experimental measures of strain gauges, an experimental bond relationship $\tau_f - s_f$ can be obtained for a laminate with thickness t_f and Young's modulus of fibres E_f as follows:

$$\tau_f(x) = t_f \cdot E_f \cdot \frac{\varepsilon_k - \varepsilon_{k-1}}{x_k - x_{k-1}} \qquad (8)$$

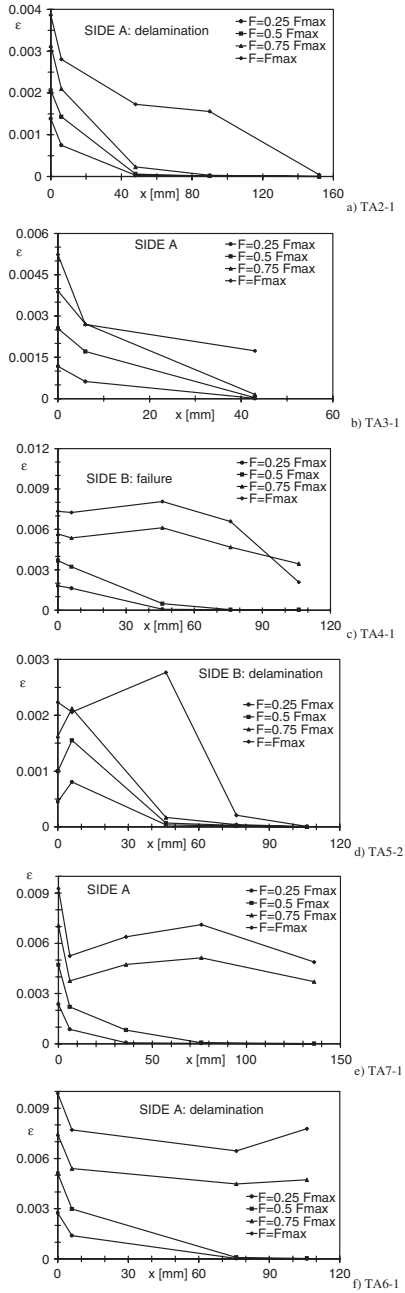

Figure 5. Strain distribution along the FRP.

Table 4. Strain values at failure conditions.

Specimens	F_{max} (kN)	Failure	ε_1	ε_2
TA1-1	33.4	delamination	0.00654	0.0059
TA1-2	29.4	delamination	0.00575	0.0044
TA2-1	21.0	delamination	0.00410	0.0028
TA2-2	20.9	delamination	0.00410	0.0032
TA3-1	26.7	delamination	0.00523	0.0027
TA3-2	29.0	delamination	0.00568	0.0035
TA4-1	45.0	Fiber fracture	0.00881	0.0073
TA4-2	28.8	delamination	0.00563	0.0031
TA5-1	46.6	Fiber fracture	0.00913	0.0059
TA5-2	25.5	delamination	0.00499	0.0024
TA6-1	48.8	Fiber fracture	0.00956	0.0077
TA6-2	49.3	Fiber fracture	0.00966	0.0049
TA7-1	47.5	Fiber fracture	0.00930	0.0057
TA7-2	29.6	delamination	0.00580	–

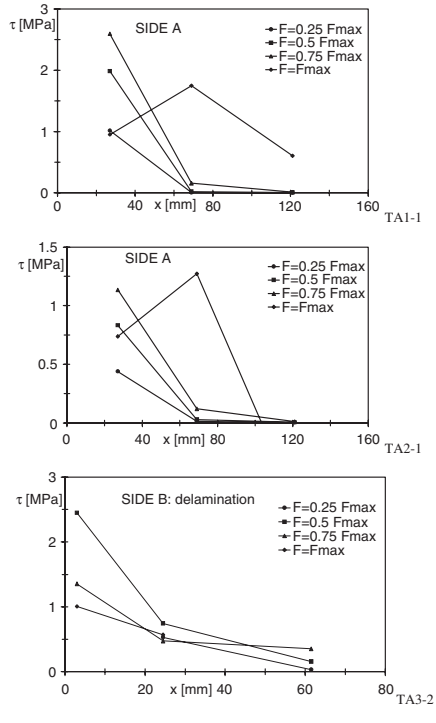

Figure 6. Experimental shear stress–slip relationship.

$$s_f(x) = \sum_{i=1}^{k} (\varepsilon_{i+1} - \varepsilon_i) \cdot (x_{i+1} - x_i) \quad (9)$$

where $x = (x_k + x_{k-1})/2$, being x_k and x_{k-1} the abscissas of two following strain gauges, ε_k and ε_{k-1} the corresponding measured strains. The strain gauges to evaluate the bond-slip law are chosen considering the measure points closest to the unbonded area of lamina. Referring to figure 2, where an example of strain gauges disposition is reported, measures of instruments 2 and 3 are used. In figure 6 the distribution of shear stress along the FRP laminate is reported for some specimens.

In table 5 the values of τ_{max} and the corresponding slip s_1, are reported for the reference specimens TA1-1- and TA1-2. For the same specimens the experimental τ_f–s_f relationships are depicted in figure 7. It is clear that the maximum shear stress depends on the maximum load and on the failure mode.

Table 5. Experimental bond parameters.

Specimen		TA1-1	TA1-2
Side A	τ_{max} (MPa)	2.7	2.5
	s_1 (mm)	0.20	0.18
Side B	τ_{max} (MPa)	–	2.2
	s_1 (mm)	–	0.16

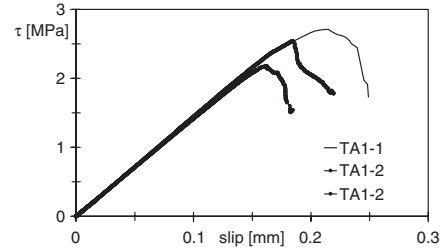

Figure 7. Experimental shear stress–slip relationship.

Table 6. Experimental slopes of shear stress–slip relationship.

Specimen	Side A k_0 (MPa/mm)	Side B k_0 (MPa/mm)
TA1-1	13.5	–
TA1-2	13.9	13.8
TA2-1	12.9	13.4
TA2-2	12.6	14.0
TA3-1	18.7	–
TA3-2	16.9	13.8
TA4-1	–	14.6
TA4-2	15.1	14.1
TA5-2	15.4	15.4
TA6-1	–	14.5
TA6-2	11.1	–
TA7-1	22.6	22.1
Mean	**15.3**	**15.1**

In table 6 for all specimens the values of the initial slope, k_0, of the experimental τ_f–s_f relationships are reported. It is interesting to notice that there is a very low scatter of this parameter.

4 FIRST APPROACH WITH FEM MODEL

A first approach with a finite element model has been developed with the software Lusas. It allows studying the propagation of the maximum shear stress along the concrete-FRP laminate interface; furthermore the distribution of tensile stress in concrete at the interface can be evaluated at ultimate condition, when delamination occurs in experimental specimens. The specimen geometry is modelled in hypothesis of plane stress.

The finite element used to model the geometry of the specimen is a plane stress element (QPM8) with 8 nodes to have a quadratic interpolation between nodes. Due to the symmetry of the specimen only an half part of the T-shaped block has been modelled; the tensile load is applied at the end of the FRP laminate introducing full restrain along the vertical symmetry axis and the horizontal base of the specimen (figure 8). The pulling force transferred to the concrete at the top of the specimen from the bolted steel spreader plate is simulated applying full restrains.

Concrete and FRP are assumed as linear elastic materials, while the adhesive layer is modelled by bidirectional springs with non-linear behaviour. The axial stiffness of spring is evaluated as the ratio of the Young's modulus to the adhesive thickness, for the shear behaviour a non-linear shear stress–slip, τ_f-s_f relationship is adopted. Particularly the bilinear law for τ_f-s_f suggested by fib bulletin 14 (fig. 9) is considered in order to set the significant parameters.

Numerical modelling has been applied with two sets of parameters:

- case 1: $\tau_{max} = 3$ MPa; $s_1 = 0.05$ mm; $s_{max} = 0.1$ mm; based on parametric analysis and comparisons with experimental results developed in [15];
- case 2: $\tau_{max} = 3$ MPa; $s_1 = 0.15$ mm; $s_{max} = 0.3$ mm; being the values of s_1 and s_{max} identified by the experimental results of the tests herein discussed.

  At the moment only the reference specimen has been modelled considering the configuration without any type of anchorage. The maximum load given by the model corresponds to reaching s_{max} at the loaded end.

For case 1 the maximum load results 22 kN; the maximum shear stress is reached at about 20–30 mm from the loaded end. In figure 10 the stress distribution of the maximum principal stress in concrete is reported. The maximum tensile stress in concrete is about 2.5 MPa that is much lower than the mean tensile strength of the concrete used. Distribution of tensile stresses in concrete exhausts in about 110 mm from the loaded end.

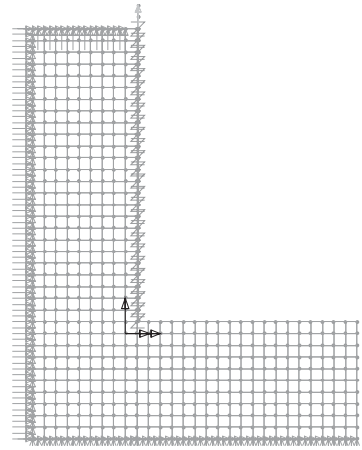

Figure 8. Specimen modelled by FEM.

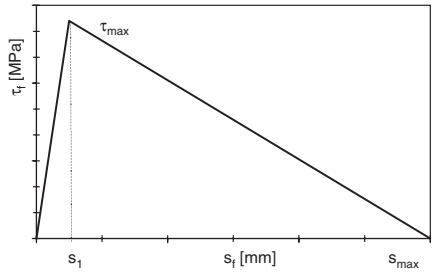

Figure 9. Shear stress–slip relationship of fib bulletin 14[3].

If parameters of case 2 are introduced in the bond law, the maximum tensile load increases to 37 kN. The maximum shear stress is reached at about 30–40 mm from the loaded end. The maximum tensile stress in concrete reaches 2.2 MPa. As shown in figure 11, the distribution of tensile stress in the concrete exhausts at 150 mm from the loaded end. The experimental value of the maximum load is lower than the numerical one (29 kN for specimen TA1-1, 33 kN for specimen TA1-2) and also tensile stress pointed out by the model is much lower than the concrete strength. However it is worth to notice that delamination occurred experimentally in a very thin layer of concrete, where surely the full tensile strength of material is not reached.

In conclusion the theoretical behaviour obtained with a simply FEM model is significant of the experimental results, introducing the effective bond law. However it is also confirmed the importance to define

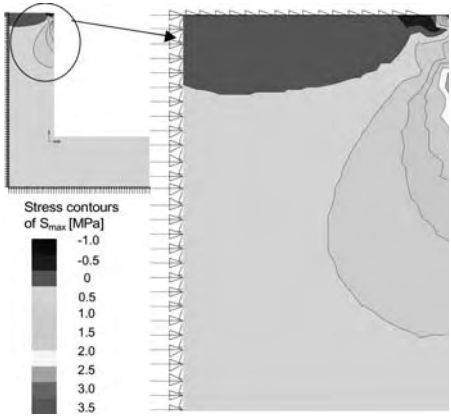

Figure 10. Maximum principal stress in concrete for case 1 at 22 kN.

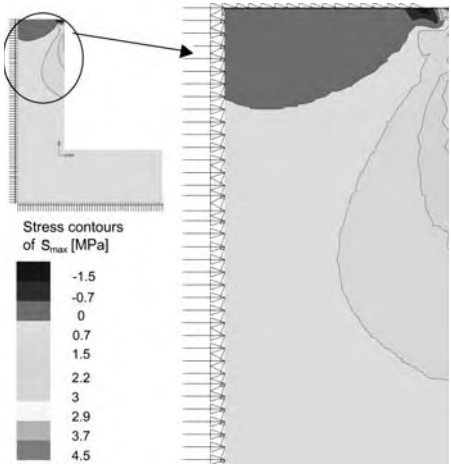

Figure 11. Maximum principal stress in concrete for case 2 at 37 kN.

and calibrate the bond law, either for the ascending or for the descending branch, since it governs the ultimate load when delamination occurs. The model has to be extended to the other types of specimens, introducing the various anchorage systems used by a suitable configuration of the finite elements.

5 CONCLUSIONS

From the experimental tests information has been obtained about strength, ductility and failure modes for different types of anchorage systems for FRP laminates externally bonded to concrete elements. Given the aforementioned anchorage configurations, the following is noted:

- the effective transfer length is not greater than 100 mm and the remaining part of the bond length is stressed only after debonding;
- detailing of the anchorage and application procedure can strongly influence the effectiveness of the system, also reducing the maximum load when delamination occurs;
- the effective strains given by fib bulletin [3] at the delamination or fibers failure conditions are in good agreement with the experimental values;
- the very simple FEM model used, where the non-linear behaviour of the bond law is introduced by springs connecting concrete and FRP, gives significant results, but underline the importance of a detailed definition of the significant parameters of the bond law.

In conclusion the test results confirm that bond behaviour of FRP laminates glued to concrete is quite well defined by available formulations in terms of linear elastic relationship and delamination strain. On the contrary is more uncertain the non-linear branch of the bond law and the effect of the anchorage systems on delamination strength.

This last point is particularly important since a new anchorage system, not enough and correctly tested, could reduce the delamination load due to local failures and damage.

The good results of this first numerical analysis points out the opportunity of developing the FEM model to introduce the other anchorage systems.

REFERENCES

1 J D Hall, H R Schuman, H R Hamilton III, 'Ductile anchorage for connecting FRP strengthening of under reinforced masonry building', *ASCE Journal of Composite for Construction*, January–February 2002, Vol. 6, No. 1.

2 K H Tan, 'Details of FRP reinforcement: an overview', *FRP Composite in Civil Engineering*, Vol. 2, pp. 1247–1254, Ed. J G Teng, Elsevier Science, 2001.

3 Fib, *FRP as Externally Bonded Reinforcement of RC Structures: Basis of design and safety concept*, fib Task Group 9.3, fib Bullettin 14, International federation for structural concrete, Lausanne, Switzerland, 2001.

4 M Blaschko, 'Anchorage device for FRP strips', Proceedings of the Fifth Conference on Non-Metallic Reinforcement for Concrete Structures, *Proc. of FRPRCS5 International symposium*, Cambridge, UK, pp. 1255–1264, Vol. 2, Tomas Telford Editor, July 2001.

5 Y Jinno, H Tsukagoshi, Y Yabe, 'RC Beams with Slabs strengthened by CF sheets and bundles of CF strands', *Proc. of FRPRCS5 International symposium*,

Cambridge, UK, pp. 981–987, Tomas Telford Editor, July 2001.
6 K Koayshi, S Fujii, Y Yabe, H Tukagoshi, T Sugiyama, 'Advanced wrapping system with CF-anchor: Stress Transfer mechanism of CF-anchor', *Proc. of FRPRCS5 International symposium*, Cambridge, UK, Tomas Telford Editor, July 2001.
7 A Khalifa, A Belarbi, A Nanni, 'Shear performance of RC members strengthened with externally bonded FRP wraps', *Proceedings of 12WCEE Conference*, 2000.
8 A Khalifa, W J Gold, A Nanni, A M I Aziz (1998), Contribution of externally bonded FRP to shear capacity of rc flexural members. ASCE Journal of Composites for Construction, 2(4), 195–202.
9 J G Teng, J F Chen, S T Smith, L Lam, *FRP Strengthened RC Structures*, John Wiley & Sons Ltd, 2002.
10 K Brosens, D Van Gemert, 'Anchorage design for externally bonded carbon fiber reinforced polymer laminates', *Proc. of FRPRCS4 International symposium*, Baltimore, November 1999.
11 P Mukhopadhyaya, N Swamy, C Lynsdale, 'Optimizing structural response of beams strengthened with GFRP plates', *Journal of composites for construction*, May 1998.
12 F Ceroni, S Matthys, M Pecce, L Taerwe, Bond test on concrete T-shaped sections strengthened with CFRP. Advanced Polymer Composites for Structural Applications in Construction -ACIC2004- Guildford, Surrey, UK, 20–22 April 2004, pp. 126–133.
13 B Taljsten, L Elfgren, Strengthening concrete beams for shear using CFRP-materials: evaluation of different application methods, Composites: Part B 31 (2000), Elsevier, pp. 87–96.
14 T C Triantafillou, (1998), Shear strengthening of reinforced concrete beams using epoxy bonded FRP composites. ACI Structural Journal, 95(2), 107–115.
15 F Ceroni, M Pecce, 2003. Experimental and Theoretical crack behavior of RC ties FRP EBR, Int. Conference CCC 2003, 16–19 Settembre 2003, Cosenza, Italy, pp. 319–324.

FRP Composites in Civil Engineering – CICE 2004 – Seracino (ed)
© 2005 Taylor & Francis Group, London, ISBN 90 5809 638 6

Flexural strengthening of RC beams using emerging materials: ultimate behavior

A. Prota, G. Manfredi, A. Nanni & E. Cosenza
Department of Structural Analysis and Design, University of Naples Federico II, Naples, Italy

M. Pecce
Department of Engineering, University of Sannio, Benevento, Italy

ABSTRACT: An experimental analysis has been conducted to assess the effectiveness of an innovative system based on Steel Reinforced Polymer (SRP) laminates for the flexural strengthening of Reinforced Concrete (RC) beams; such external reinforcement has been impregnated with either epoxy resin or cementitious mortar. Experimental performance of SRP strengthened members have been compared to those of beams externally bonded with comparable amounts of Carbon Fiber Reinforced Polymer (CFRP). A summary of laboratory outcomes is herein offered focusing on the ultimate behavior. Experimental results are used to assess the possibility of extending ACI 440.2R-02 recommendations to the case of SRP. A modified equation for the bond-dependent coefficient is proposed to account for the different bond behavior of the cementicious mortar.

1 INTRODUCTION

Over the last decade FRP composites have emerged in construction mainly for the strengthening and rehabilitation of RC structures. The flexural and shear strengthening of beams as well as the confinement of columns using FRP laminates have been extensively analyzed both in a laboratory and field environment. In addition to the high mechanical properties, the use of these materials has allowed exploiting other features like their high durability and their high resistance to aggressive and harsh environments, their easy and rapid installation, their light weight and low impact on the original geometry of strengthened members, and the possibility of targeting their density and texture to the requirements of the specific application.

Even though there is a wide consensus at both academic and industrial level that FRP composites represent a real and competitive alternative to traditional strengthening techniques, one of the barriers to their larger diffusion in construction is represented by their low fire resistance (Nanni et al. 2001). This is a problem that affects both Carbon (CFRP) and Glass (GFRP) laminates and it is related to the properties of epoxy resins generally used to impregnate the fibers. In addition, some other reasons of concern are raised by the linear-elastic behavior up to failure of the fibers and by the orthotropic behavior of FRP laminates.

The present paper deals with an innovative strengthening system based on SRP composites that could be an alternative technique for structural applications whose requirements could not be fulfilled by FRP materials. Similarly to FRP, SRP composites are obtained by impregnating steel fibers with either an epoxy or a cementitious matrix. The steel fibers are given by cords identical to those used as radial reinforcement of car tires; steel cords could vary between the highly twisted cords, for optimum ductility, and slightly twisted cords, which are more open to allow resin penetration (Hardwire 2002). The steel tape has very high strength and stiffness and is economical to produce; its density can be targeted to meet the requirement of reinforcement, viscosity of resin, and cosmetic application. No special resin is required for wetting the steel cord reinforcement, as it is required for GFRP and CFRP fibers where the sizing plays a critical role.

For applications where fire resistance is the parameter governing the strengthening job, the use of a low-density steel tape could allow overcoming such problem by installing an SRP composite impregnated with a cementitious matrix not sensitive to fire and high temperatures. It is also possible to improve the bond of such laminates using mechanical anchorages that are in general not compatible with the use of FRP. If this is done, the design of the anchorages could also count on the ductility of steel fibers that could be needed in order to redistribute high stresses at anchorage location and prevent local failures. In addition to fire resistance, the use of a traditional material such as a polymer modified cementitious matrix reduces the

uncertainties and the likelihood of defects related with the mixing of an epoxy resin which typical workers of the construction industry are not familiar with.

In general, even though an high-density steel tape impregnated with an epoxy resin is selected, the cost of steel fibers lower than carbon or glass fibers could make SRP laminates more cost effective than FRP; this could be the driving criterion in the choice of SRP rather than FRP especially if there is no requirement for high durability performance (i.e., interior applications in buildings). Finally, in cases where the composite reinforcement is required to withstand high stresses in the direction perpendicular to fiber axis (i.e., concentration of high shear stresses), the SRP laminates could perform much better than FRP whose transverse mechanical properties are not significant.

This paper focuses on the application of SRP materials as externally bonded flexural reinforcement for RC members. Experimental studies have been carried out on the use of FRP systems for flexural strengthening (Fanning et al. 2001, Brena et al. 2003, Shin & Lee 2003); Alaee & Karihaloo (2003) lately proposed a technique for the repair of flexural members using externally bonded high performance fiber reinforced concrete strips. No systematic test has been conducted yet on concrete elements strengthened using SRP laminates. In order to investigate the flexural behavior of RC beams strengthened with SRP composites, two different types of steel tape have been used at the University of Naples Federico II, Italy, to strengthen RC beams using cementitious grout and epoxy resin. Additional beams strengthened with comparable amount of unidirectional Carbon FRP (CFRP) laminates have been tested and compared with those strengthened with SRP composites.

2 EXPERIMENTAL PROGRAM

Detailed information about the test setup, specimen properties and strengthening schemes can be found in Prota et al. (2004) with a brief summary offered herein.

A total of ten RC shallow beams (400 mm wide, 200 mm high and 3.7 m long), were cast; the stirrups were D8 mm steel bars spaced at 100 mm center-to-center. For all specimens, five D10 steel bars were used as tensile reinforcement and two D8 steel bars as compression reinforcement. Seven of these beams were strengthened with two different types of steel tape, namely 3X2 cord (i.e., high-density) and 12X cord (i.e., low-density); the high-density tape was impregnated with epoxy resin (i.e., type A beams) and the low-density tape was bonded with cementitious grout (i.e., type B beams). The remaining two beams were strengthened with CFRP laminates impregnated with epoxy resin (i.e., type C beams).

In two type B beams, the steel tape impregnated with cementitious grout was mechanically anchored with nail anchors (i.e., B-3 and B-4). Table 1 reports the test matrix of the research program, summarizing the type (i.e., S-HD and S-LD standing for high-density and low-density SRP tape, respectively) and matrix (i.e., E and C standing for epoxy and cementitious, respectively) of the externally bonded reinforcement, and its amount in terms of width and number of plies.

Table 1. Test matrix.

Specimen	External reinforcement	Matrix	Total width (mm)	Plies
D	–	–	–	–
A-1	S-HD	E	150	1
A-2	S-HD	E	300	1
A-3	S-HD	E	300	2
B-1	S-LD	E	200	1
B-2	S-LD	C	200	1
B-3	S-LD	C	200	1
B-4	S-LD	C	400	2
C-1	Carbon	E	450	2
C-2	Carbon	E	900	3

The installation was performed according to typical procedures. No primer was used for bonding SRP tapes with either epoxy or cementitious grout, whereas a primer was used to install CFRP laminates on beams C-1 and C-2. When more than one ply was installed, the following ply was bonded with an offset of 100 mm from the cut-off point of the previous.

All the beams were tested as simply supported members, over a clear span of 3.4 m. They were loaded up to failure under a four-point bending configuration, with a constant moment region of 1.0 m across the mid-span; tests were carried out under displacement control. The instrumentation of all beams included two horizontal linear variable displacement transducers (LVDTs) placed on one side of the specimen to record displacements over a length of 350 mm across the mid-span at heights of the compressive concrete fiber and of the concrete fiber corresponding to tensile steel rebars, respectively. Strain gages were also used to measure strains on the externally bonded reinforcement at mid-span. Three strain gages were placed along the transverse direction of the mid-span cross-section if the laminate width was less than 200 mm, five were indeed mounted if the width was larger.

The control beam, D, showed a collapse due to concrete crushing in the constant moment region at a load equal to 49.30 kN. The installation of the high-density SRP tape bonded with an epoxy resin at the bottom of a type D beam allowed to increase the strength up to 86.30 kN for beam A-1, 121.10 kN for beam A-2 and 100.40 kN for beam A-3; it is important to underline that A-2 and A-3 had the same area of external reinforcement arranged on a single ply and double width, or on two plies and half width, respectively (Table 1).

Figure 1. Bottom View of A-2 Beam at Failure.

Figure 2. Bottom View of B-1 Beam at Failure.

The mode of failure was similar for these three beams; it was concrete cover separation (Fig. 1) which initiated at one of the loading points and caused the separation of the concrete cover up to the depth of the longitudinal steel bars (Teng et al. 2001).

The installation of the low-density SRP tape allowed investigating the performance of an epoxy versus a cementitious matrix by comparison between beams B-1 and B-2 that were identical in terms of amount and configuration of external steel reinforcement (Table 1). The epoxy resin allowed beam B-1 attaining its failure at ultimate load equal to 88.60 kN, whereas beam B-2 failed at 72.70 kN.

In addition, the possibility of delaying SRP delamination was explored by nailing the laminates of beam B-3, strengthened with same amount and configuration of steel reinforcement adopted for beam B-2. A comparison of the performance at ultimate highlights that beams B-2 and B-3 failed at loads of 72.70 kN and 71.50 kN, respectively; this points out that the nails were unable to increase the ultimate capacity of beam B-3. Finally, beam B-4 was strengthened with a double amount of SRP tape with respect to the other three type B beams and its external reinforcement was nailed similarly to beam B-3. The ultimate behavior showed that doubling the tape area enabled B-4 to reach an ultimate strength of 86.70 kN very close to that of the epoxy bonded beam with half area of SRP (i.e., beam B-1).

The failure of beams B-1 and B-2 was due to interfacial debonding which initiated at one of the loading points (Teng et al. 2001). The epoxy allowed beam B-1 a better engagement of the concrete substrate than that provided by the cementitious grout on beam B-2; this can be observed by comparing Figures 2–3. The failure of beams B-3 and B-4 was also due to interfacial debonding after nail bearing.

The use of CFRP laminates allowed for a strength increase that was more significant than that obtained with the equivalent amount of SRP tape bonded with epoxy; the ultimate loads for C-1 and C-2 beams were

Figure 3. Bottom View of B-2 Beam at Failure.

96.50 kN (about 12% more than A-1) and 134.80 kN (about 34% and 11% more than A-2 and A-3, respectively), respectively. The collapse of both C-1 and C-2 beams was similar to that of type A beams; it was due to FRP debonding initiated at one of the loading points with separation of the concrete cover more pronounced for C-2 than for C-1.

3 EXPERIMENTAL-THEORETICAL ANALYSIS

3.1 *Strength and failure modes*

The nominal flexural strength of tested beams was calculated according to the recommendations of the ACI 318-02 and ACI 440.2R-02 guidelines. Since the goal was to perform a comparison with experimental values, both C_E (i.e., environmental-reduction factor) and ψ_f (i.e., additional FRP strength reduction factor) were taken equal to 1.

The calculations were conducted considering a compressive strength of concrete, f'_c, equal to 29.7 MPa and a yield strength of internal steel rebars, f_y, equal

to 500 MPa; the design rupture strain, ε_{fu}, was taken as 0.015 and 0.012 for FRP and SRP laminates, respectively.

In order to determine the failure mode according to the ACI 440.2R-02 guidelines, the following equation should be considered:

$$\varepsilon_{fe} = \varepsilon_{cu}\left(\frac{h-c}{c}\right) - \varepsilon_{bi} \le k_m \varepsilon_{fu} \quad (1)$$

where $\varepsilon_{cu} = 0.003$ = maximum usable compressive strain of concrete, h = overall thickness of the member, c = neutral axis corresponding to concrete crushing, ε_{bi} = strain level in the same fiber at the time of the FRP installation (computed based on a uniformly distributed dead load and equal for tested beams to $w_{DL} = 2$ kN/m), and k_m is the bond-dependent coefficient. If (1) is verified, the failure mode is concrete crushing and the effective strain in the composite reinforcement is obtained from the linearity of the strain diagram as in (1). If (1) is not verified, the failure is due to FRP/SRP rupture and

$$\varepsilon_{fe} = k_m \varepsilon_{fu} \quad (2)$$

The ACI 440.2R-02 document provides two expressions for computing k_m depending on the value of the product:

$$nE_f t_f \quad (3)$$

where n = number of plies of FRP reinforcement, E_f = tensile modulus of elasticity of FRP, and t_f = nominal thickness of one ply of the FRP reinforcement. The threshold value is 180 MPa. For beams discussed in the present paper, the product (3) is always less than such value and then the following equation should be used to compute k_m:

$$k_m = \frac{1}{60\varepsilon_{fu}}\left(1 - \frac{nE_f t_f}{360000}\right) \le 0.90 \quad (4)$$

By means of k_m, the ACI 440.2R-02 reduces the maximum usable strain in the external reinforcement and thus SRP/FRP rupture represents a conventional way to account also for premature failures.

For all tested beams, the ultimate neutral axis position was computed by a trial and error procedure from the equilibrium equation imposing that the summation of horizontal compressive (i.e., concrete and compressive steel reinforcement) and tensile (i.e., tensile steel and FRP reinforcements) forces is equal to zero. Then, the strains in concrete, steel reinforcement and FRP were determined, and the nominal flexural moment was calculated from the moment equilibrium around the centroid of the tensile steel reinforcement. For beams A-2, B-4, C-1 and C-2, equation (1) was verified implying concrete crushing. For all the other five beams, equation (2) governed and the expected failure mode involved FRP/SRP rupture. The results of such theoretical analysis are reported in Table 2, where a comparison with experimental outcomes is also proposed.

The theoretical prediction (i.e., concrete crushing) was not confirmed by experiments for one beam of both series A and B (i.e., A-2 and B-4) and for the two beams of series C (Table 2). The same amount of external reinforcement arranged in different configurations determines that the ACI formulas are able to capture the failure mode of A-3 (i.e., two plies and width equal to 37.5% that of the beam), whereas they do not perform in the same way if the SRP is arranged on one ply, but on a width equal to 75% of that of the beam (i.e., A-2). Since the first term of (1) is almost equal for both (i.e., 0.090 versus 0.092 in Table 2), the difference is due to values of k_m that are equal to 0.90 (i.e., it would be 1.06, but the limit controls) and 0.71 for A-2 and A-3, respectively.

For beams B-1, B-2 and B-3 the k_m value would be 1.17, whereas it would be 0.95 for B-4; therefore, the limit of 0.90 controls all of them. This allows predicting the failure mode on B-1, B-2 and B-3 beams,

Table 2. Comparison between theoretical and experimental predictions in terms of strength and failure modes.

	Theoretical					Experimental	
Beam	$\varepsilon_{cu}\left(\frac{h-c}{c}\right) - \varepsilon_{bi}$	$k_m\varepsilon_{fu}$	ε_{fe}	Failure mode	Mn (kNm)	M (kNm)	Failure mode
D	–	–	–	Concrete crushing	26.13	29.58	Concrete crushing
A-1	0.0119	0.0108	0.0108	SRP rupture	51.16	51.78	SRP delamination
A-2	0.0090	0.0108	0.0090	Concrete crushing	66.31	72.66	SRP delamination
A-3	0.0092	0.0086	0.0086	SRP rupture	64.69	60.24	SRP delamination
B-1	0.0126	0.0108	0.0108	SRP rupture	48.22	53.16	SRP delamination
B-2	0.0126	0.0108	0.0108	SRP rupture	48.22	43.62	SRP delamination
B-3	0.0126	0.0108	0.0108	SRP rupture	48.22	42.90	SRP delamination
B-4	0.0095	0.0108	0.0095	Concrete crushing	63.44	52.02	SRP delamination
C-1	0.0105	0.0131	0.0105	Concrete crushing	57.65	57.90	FRP delamination
C-2	0.0080	0.0114	0.0080	Concrete crushing	72.58	80.88	FRP delamination

while the effective strain in the SRP reinforcement is overestimated when two plies are installed (i.e., B-4) and concrete crushing is expected. The same happens for the two CFRP strengthened beams. Finally, for the nine strengthened beams, the analysis according to ACI 440.2R-02 would provide ultimate strains in the tensile steel reinforcement, ε_s, much larger than 0.005 (i.e., ranging between 0.0061 of C-2 and 0.0084 of B-1) and then all largely fall into the region where the strength reduction factor, ϕ, is equal to 0.90. For this reason, no changes appear necessary to the formulas considering that a correction aiming at fitting all experimental failure modes would not affect the overall safety of the strengthening design.

The same analysis can be conducted in terms of nominal flexural moments. The ACI approach is conservative for both A-1 and A-2 beams and overestimates the strength of A-3 by 7.4% (Table 2). With respect to series B, it is conservative for the beam impregnated with epoxy (i.e., B-1), whereas overestimates the strength of those impregnated with cementitious by about 11.4% (i.e., B-2 and B-3) and 22% (i.e., B-4). It is always conservative for the CFRP strengthened beams (Table 2).

The main conclusion of such comparison is that the ACI 440.2R-02 approach overestimates by more than 10% the strength of the beams whose SRP reinforcement is bonded with cementitious (i.e., B-2, B-3 and B-4). If one were to back calculate the effective strain in the SRP that would provide a conservative strength estimate for those three beams, such value would be found equal to about 0.58% (i.e., B-2 and B-3) and 0.47% (i.e., B-4) of ε_{fu}. Based on the experimental results reported in this paper, equation (4) could be safely extended to external reinforcements bonded with cementitious as follows:

$$k_m = \frac{1}{120\varepsilon_{fu}}\left(1 - \frac{nE_f t_f}{360000}\right) \qquad (5)$$

The strength prediction that would be obtained for the three beams according to equation (5) are summarized in Table 3; it is recalled that beams B-2 and B-3 are identical from a strength point of view as the presence of nails is not accounted for in the adopted formulas. It is noted that the use of equation (5) reduces so much the effective strain in the SRP of B-4 beam that the strain in its tensile steel reinforcement at ultimate is lower than 0.005 (i.e., 0.0048). This would have an important repercussion from a design stand point because it would determine the use of a strength reduction factor lower than 0.90.

Table 3. Theoretical strength using a modified k_m.

Beam	ε_{fe}	Failure mode	Mn (kNm)
B-2/B-3	0.0070	SRP rupture	42.16
B-4	0.0057	SRP rupture	50.44

3.2 *Moment-curvature relationships*

The behavior of tested beams was also analyzed in terms of moment-curvature relationships. For the control beam, the experimental mean curvature was determined from readings of LVDT transducers mounted over a gage length of 350 mm across mid-span at the heights of both compressive concrete and internal steel reinforcement (Fig. 4a). For the strengthened beams, the experimental mean curvature was obtained from readings of the LVDT transducer mounted on the compressive concrete and of strain-gages installed at mid-span on the external reinforcement (Fig. 4b).

Experimental moment–curvature trends are depicted in Figures 5–8; for each curve, the code of the relevant beam is followed by the symbol EX in parenthesis. The analysis of the moment-curvature relationships points out that the control beam cracks at about 5 kNm and yields at about 25 kNm, with corresponding curvatures of 1.96×10^{-6} and 2×10^{-5} rad/mm, respectively. A-1 and A-2 beams show a cracking moment of about 13.5 kNm, which is higher than that provided by A-3 (i.e., about 9.7 kNm); up to the cracking moment A-1 and A-2 curves are very similar, even though A-2 is slightly stiffer than A-1 that is closer to D up to its cracking (Figure 5). Then, A-1 yields at about 35.4 kNm, whereas A-2 and A-3 yield at about 45 kNm. For these two beams, branches between cracking and steel yielding, and steel yielding and ultimate are very similar. Experimental ultimate moment values have been already discussed for all beams in the previous section and are summarized in Table 2.

Curves of all beams of series B show very similar trends up to the cracking moment of about 6 kNm and are all stiffer than the control beam (Figs. 6–7). No matter whether the SRP tape is bonded with epoxy, cementitious, or nailed, beams B-1, B-2 and B-3 show a similar yielding moment of about 35 kNm. However, B-1 and B-2 have similar branches between cracking and yielding, whereas the presence of the nails stiffen B-3 that attains the yielding with a curvature about 20% lower than the other two beams (Figure 7). The higher amount of external reinforcement causes

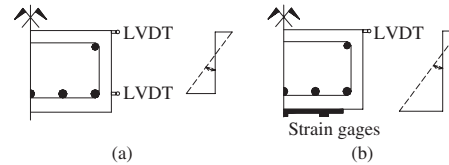

Figure 4. Experimental curvature of control (a) and strengthened beams (b).

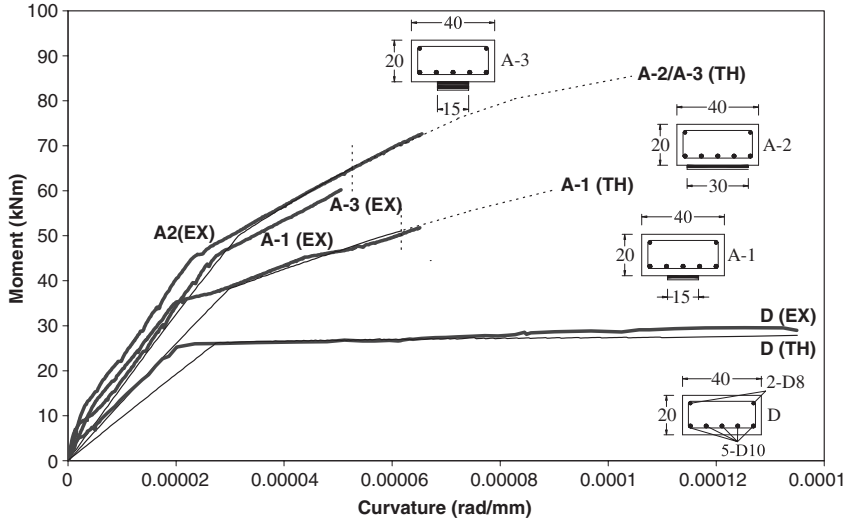

Figure 5. Comparison in terms of moment–curvature relationships between control and high-density SRP strengthened beams.

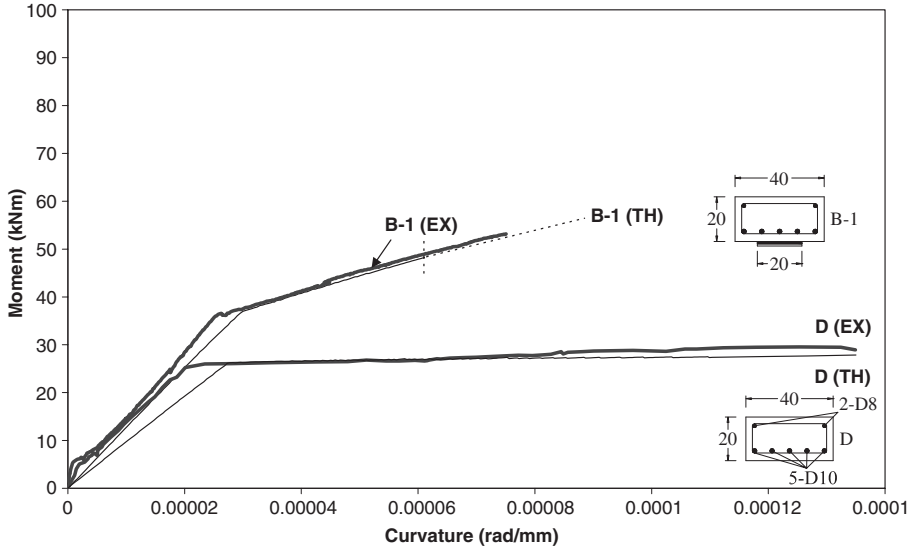

Figure 6. Comparison in terms of moment–curvature relationships between D and B-1 beams.

that B-4 yields at a moment of about 43 kNm; its curve is almost overlapped to that of B-2 until such beam yields. Both CFRP strengthened beams crack at about 10.5 kNm and their initial slope is stiffer than that of D; after the cracking point, the curves start diverging and reflect that the higher amount of external reinforcement makes C-2 cross-section stiffer (Figure 8).

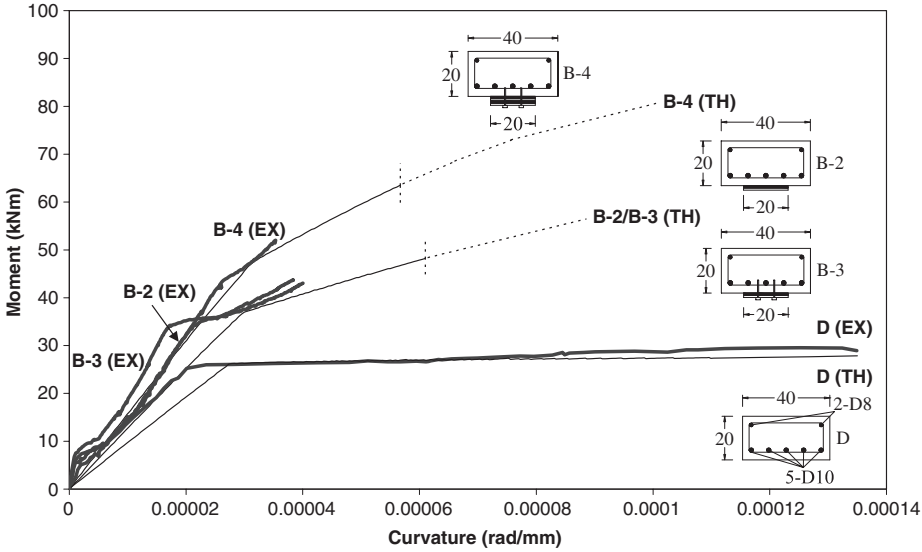

Figure 7. Comparison in terms of moment–curvature relationships between control and SRP cementitious bonded beams.

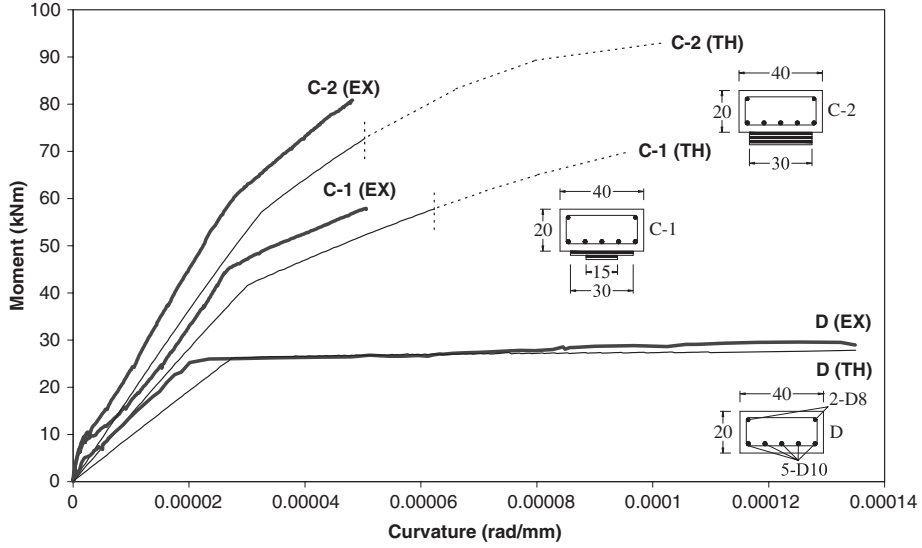

Figure 8. Comparison in terms of moment–curvature relationships between control and CFRP strengthened beams.

Theoretical moment–curvature relationships were computed for tested beams using the above mentioned material properties; they are compared to experimental curves in Figures 5–8 where they are denoted by TH in parenthesis after the code of each relevant beam. Theoretical curves are drawn considering, since the beginning, the moment of inertia of the cracked cross-section and they are drawn in Figures 5–8 as the sum

of a continuous line and a dashed line. The continuous branch represents the moment-curvature that is obtained by stopping the analysis of the cross section when the strain in the external reinforcement (i.e., SRP or FRP) of each beam attains the value of ε_{fe} computed according to ACI 440.2R-02 (Table 2). The dashed branch represents the portion of the moment-curvature that could be attained if premature failures are not considered and then the ultimate composite strain is not reduced via the coefficient k_m discussed in the previous sections. Therefore, the dashed branches allow understanding the reductions of strength (i.e., moment) and deformation (i.e., curvature) capacity that the cross-section undergoes if premature failures (i.e., delamination) are accounted in addition to conventional failure modes (i.e., concrete crushing and FRP/SRP rupture). As expected, the experimental curves are in general stiffer than those theoretical; this is because the experimental are mean curvatures (i.e., average over a length of 350 mm where in general only three cracks formed), whereas those theoretical represent curvatures of the cracked cross-section.

4 CONCLUSIONS

The results of a theoretical-experimental analysis are herein presented with respect to RC beams strengthened in flexure with emerging materials. The comparison focuses mainly on the ultimate behavior and allows assessing the strength gains provided by FRP and SRP systems; for the latter, the performance of epoxy resin and cementitious mortar are compared.

The paper confirms that the ACI 440.2R-02 approach provides conservative strength estimates for both FRP and SRP systems, if the external reinforcement is bonded with epoxy. The different bond behavior of a cementitious mortar is not predicted by the current ACI 440.2R-02 equations; a modified expression for the bond coefficient k_m has been herein proposed in order to extend them to systems impregnated with mortar. Further tests will need to be performed in order to confirm the reliability of the modified equation.

ACKNOWLEDGMENTS

The authors would like to thank Hardwire LLC, Pocomoke City, MD, Mapei Spa, Milan, Italy, and Sika Italia, Milan, Italy, for donating the steel tapes, the FRP system, and the epoxy resin/cementiciuous grout used to bond SRP, respectively.

REFERENCES

ACI Committee 318. 2002. *Building Code Requirements for Structural Concrete*, American Concrete Institute, Farmington Mills, MI, pp. 443.

ACI Committee 440. 2002. *Guide for the Design and Construction of Externally Bonded FRP Systems for Strengthening Concrete Structures*. American Concrete Institute, Farmington Hills, MI, USA, pp. 103.

Alaee, F.J., & Karihaloo, B.L. 2003. Retrofitting of Reinforced Concrete Beams with CARDIFRC. *ASCE Journal of Composites for Construction*, V.7, No.3, pp. 174–186.

Brena, S.F., Bramblett, R.M., Wood, S.L., & Kreger, M.E. 2003. Increasing Flexural Capacity of Reinforced Concrete Beams using Carbon Fiber-Reinforced Polymer Composites. *ACI Structural Journal*, V.100, No.1, pp. 36–46.

Fanning, P.J., & Kelly, O. 2001. Ultimate Response of RC Beams Strengthened with CFRP Plates. *ASCE Journal of Composites for Construction*, V.5, No.2, pp. 122–127.

Hardwire LLC. 2002. What is Hardwire, *www.hardwirellc.com*, Pocomoke City, Maryland, USA.

Prota, A., Tan, K., Nanni, A., Pecce, M., & Manfredi, G. 2004. Performance of RC Shallow Beams Externally Bonded with Steel Reinforced Polymer. *ACI Structural Journal* (under review).

Nanni, A., Cosenza, E., Manfredi, G., & Prota, A. 2001. Composites in Construction: Present Situation and Priorities for Future Research. In E. Cosenza, G. Manfredi, & A. Nanni (ed.), *Proceedings of the Workshop Composites in Construction: A Reality*, *Capri, Italy, 20–21 July, 2001*, ASCE ISBN 0-7844-0596-4, pp. 269–277.

Shin, Y., & Lee, C. 2003. Flexural Behaviour of Reinforced Concrete Beams Strengthened with Carbon Fiber-Reinforced Polymer Laminates at Different Levels of Sustaining Loads. *ACI Structural Journal*, V.100, No.2, pp. 231–239.

Teng, J.G., Chen, J.F., Smith, S.T., & Lam, L. 2001. *FRP Strengthened RC Structures*, John Wiley & Sons, Ltd, Chichester, England, pp. 245.

FRP Composites in Civil Engineering – CICE 2004 – Seracino (ed)

Flexural strengthening of RC beams using emerging materials: cracking behavior

F. Ceroni & M. Pecce
Engineering Dept., University of Sannio, Benevento, Italy

A. Prota & G. Manfredi
Dept. of Structural Analysis and Design, University of Naples, Italy

ABSTRACT: This paper presents some experimental results about cracking phenomena of reinforced concrete (RC) beams strengthened with externally bonded composite materials. Carbon Fiber Reinforced Polymers (CFRP) laminates or steel (SRP) tapes have been used. Some comparisons with analytical results in terms of cracks width and crack spacing are reported using an analytical models developed by the authors. The model allows taking into account the non linear behavior of materials and bond laws. Comparisons at service condition with code formulas are also reported. Interesting considerations about the different bond behavior of cementitious grout and epoxy resins are developed in order to have a calibration of the bond law.

1 INTRODUCTION

The use of externally bonded composite laminates is by now a diffuse technique to strengthen existing RC structures. However, some aspects of ultimate and serviceability conditions still need experimental and numerical analysis; furthermore, especially for serviceability checks, there is a lack of code provisions. In particular FRP laminates have been already applied in many cases to strengthen beams, but even if some experimental and numerical information are available, information about tension stiffening and cracking behaviour of such elements strengthened with FRP is necessary. These last aspects are complex and involve laminate and interface properties that influence the cracking of the concrete element. Recently, the application of steel reinforced polymer (SRP) has been also analyzed as a new concept in composite reinforcements for structural strengthening. In particular the steel cord of piano wire used as the reinforcement for radial tires have been considered for this application; this is one of the strongest industrial materials known, and also corrosion resistance is suitable enhanced (Tashito et al., 1999, Hardwire 2002).

It is very permeable and allows for high viscosity resins to be used, including cementitious mixtures and thermoset putties.

No information is yet available about the bond behaviour at concrete interface and cracking of the beams strengthened using these emerging materials.

For the external reinforcement with FRP and SRP laminates a key issue is the bond behaviour at the concrete-fibres interface, that governs the effectiveness of the system; about this subject many experimental and theoretical studies concern the phenomenon of peeling that often characterizes the failure mode and in general happens where a stress concentration occurs (Smith & Teng, 2002a; Smith & Teng, 2002b).

The cracking behaviour has not been well developed yet, due also to the lack of experimental tests on beams: more information need about the transfer of the stresses and about the interaction between the internal and the external reinforcement; tests and models available in literature have been carried out with reference to ties elements (Tripi et al., 2000; Ueda et al., 2002, Ceroni et al. 2004; Sato et al., 2002; Zhang et al., 2003).

The modeling of tension stiffening in RC elements is based on many experimental tests and on a consolidated knowledge of the steel-concrete bond; therefore, code formulas are reliable (CEB, 1985; Eurocode2, 1991). For RC elements strengthened with FRP laminates, there is no standard experimental procedure for bond tests: the experimental results focus on the definition of the transfer length and the delamination load (Smith & Teng, 2002a; Smith & Teng, 2002b) and some design provisions are given by the fib bulletin 14 (2001).

In this paper experimental results about the cracking of flexural RC beams reinforced with CFRP and SRP laminates are analyzed. A model developed by the authors (Ceroni et al., 2001; Ceroni & Pecce, 2002) to calculate crack widths in RC tensile elements externally strengthened with FRP is applied to perform an

experimental-theoretical comparison. The model has a mono-dimensional approach and allows introducing non-linear constitutive relationships for materials and bond laws; furthermore, the formation of the first crack and the crack propagation can be taken into account, even if in this case is not applied. The model assumes that the tension zone of the section can be considered similar to a tie, and the crack width distribution along the depth has to be established.

Also indications given by codes (Eurocode2, 1991, and ACI 318, 1999) to calculate mean strain and mean crack widths are examined and compared with the experimental results.

2 CRACKING AND CODE FORMULATIONS

The cracking behaviour of RC elements externally bonded with composite materials is very complex. In addition to the stress transfer between steel bar and concrete, the transfer between the external laminate and the concrete, depending on the bond law at the interface, has to be introduced. The development of cracks is progressive and the crack number increases as the load increases until a stabilised cracking condition is reached. At this stage no more crack will form, because the tensile stress transferred to the concrete between two cracks is smaller than the tensile strength of concrete. The concrete between two cracks is able to withstand these tensile stresses incorporating a stiffening effect (tension stiffening) on the deformability of the elements.

When an external reinforcement is applied, the development of cracking is modified because of the additional stresses transferred to the tensile concrete by the laminate. The number of cracks and crack spacing will change depending on the bond behaviour at the concrete-laminate interface. Typically the bond behaviour between concrete and laminate seems to be stiffer compared to that between steel and concrete, allowing the transfer of high stresses over a very short length (fib bulletin 14, 2001).

The average crack width, w_m, is usually evaluated neglecting contribution of concrete strain in tension and can be expressed as:

$$w_m = \varepsilon_{sm} \cdot s_{rm} \tag{1}$$

where ε_{sm} is the mean steel strain and s_{rm} the mean crack spacing.

Codes provide reliable formulations to calculate w_m for RC elements in service conditions (Eurocode2, 1991; ACI 318, 1999) that are based on numerical parameters validated through experimental tests.

Eurocode2 suggests the following formulation for the average strain in a generic RC element:

$$\varepsilon_{sm} = \varepsilon_s \left[1 - \beta_1 \beta_2 \left(\frac{\sigma_{cr}}{\sigma_s} \right)^2 \right] \tag{2}$$

where β_1 takes into account the bond characteristics of the internal reinforcement ($\beta_1 = 1$ for ribbed bars, $\beta_1 = 0.5$ for smooth bars) and β_2 considers the loading type ($\beta_2 = 1$ for short-term loading, $\beta_2 = 0.5$ for long-term loading); σ_{cr} = the tensile stress in the steel bar at the first cracking load; σ_s and ε_s = stress and strain in the steel bar at the load corresponding to the condition examined:

$$\varepsilon_s = \frac{M}{E_s \cdot I} y \tag{3}$$

for element subjected to a bending moment M, where I is the moment of inertia of the cracked section.

To evaluate crack distance in RC elements, EC2 provides the following formulation:

$$s_{rm} = 50 + 0.25 \cdot k_1 \cdot k_2 \cdot \frac{\phi}{\mu_s} \quad [\text{mm}] \tag{4}$$

where k_1 = bond coefficient equal to 0.8 for deformed steel bars, and 1.6 for plane steel bars; k_2 = coefficient to take in account type loading, equal to 0.5 for flexural load, and 1 for tensile load; ϕ = diameter of steel bar; $\mu_s = A_s/A_{ct,eff}$, where $A_{ct,eff}$ = the effective area of concrete in tension and A_s the area of steel reinforcement. For flexural elements EC2 suggests to calculate $A_{ct,eff}$ as the minimum value between $[2.5 \cdot B \cdot c]$ and $[B \cdot (H-x_c)/3]$, being B, H, c, x_c width, height, concrete cover and neutral axis of the section.

When an externally fibre reinforcement is applied, Eqn.4 could be modified to introduce the contribution of external reinforcement in μ_s (and keeping ϕ the diameter of the steel bar):

$$\mu_s = \frac{A_s + A_1 \cdot E_1 / E_s}{A_{ct,eff}} \tag{5}$$

where A_1 and E_1 = area and the Young's modulus of the external reinforcement, respectively.

The American Concrete Institute (ACI 318, 1999) proposes an empirical formula, where computation of crack widths is independent on the evaluation of crack spacing:

$$w_{max} = 0.0112 \cdot k \cdot \beta \cdot \sigma_f \cdot \sqrt[3]{c \cdot A} \cdot 10^{-3} \quad [\text{mm}] \tag{6}$$

where $\beta = (H-x_c)/(h-x_c)$, being H the total height of section, $h = (H-c)$, c the concrete cover in tension, x_c

the position of the neutral axis; σ_s = the stress in the steel bar in MPa; A = the effective area of concrete in tension surrounding each steel bar; k = 1.

A specific formulation for elements strengthened with FRP laminates is suggested in the fib bulletin 14 (2001) and by Matthys (2000). This formulation has been compared with experimental results of RC ties externally bonded with carbon and glass fibres in (Ceroni et al., 2004). Results indicates that the theoretical prediction underestimate the experimental values.

3 THE EXPERIMENTAL PROGRAM

The experimental program was aimed at evaluating the effect of various types of external flexural reinforcements on RC beams. A total of ten RC shallow beams, 400 × 200 × 3700 mm in size, were cast. The stirrups were Φ8 mm steel bars spaced at 100 mm center-to-center. For all specimens, five Φ10 and two Φ8 steel bars were used as tensile and compression internal reinforcement, respectively. One of these beams was not strengthened (specimen D), the other nine were externally reinforced using two different types of steel tape, namely 3x2 cord (i.e., type "A") and 12x cord (i.e., type "B"), and CFRP laminates (i.e., type "C").

Seven beams were strengthened with steel tapes impregnated with epoxy resin or cementitious grout (i.e., A and B beams); the remaining two beams (i.e., C-1 and C-2) were strengthened with CFRP laminates impregnated with epoxy resin. Two of the beams strengthened with steel tape using cementitious grout were mechanically anchored with nail anchors (i.e., B-3 and B-4). Table 1 reports the test matrix of the research program, summarizing the area of tensile steel, A_s, the type, the matrix, the bond width, b_l, and the number of plies, n_l, of the externally bonded reinforcement.

3.1 *Material properties*

The concrete mean cubic strength experimentally tested was 29.7 MPa. Based on experimental tests, the yield stress, the ultimate stress and the ultimate strain for Φ10 bars were 500 MPa, 600 MPa and 12%, respectively. In Figure 1, the stress-strain relationships for three tests on steel bar diameter Φ10 are reported.

The CFRP laminates have a unidirectional fiber texture with a density of 300 g/m^2 and an equivalent fiber thickness of 0.167 mm. Some experimental tests performed on carbon fiber specimens, according to indications of ASTM D3039/D3039M, gave a mean value of tensile strength of 2630 MPa (standard deviation 375 MPa), with a corresponding strain of 0.0103 (standard deviation 0.0014). These values are lower than ones usually declared by manufacturer (3450 MPa and 0.015), because failure was often not caused by tension of fibers, but by slipping phenomena at the anchorage, that did not allow using the total strength of fibers. The Young's modulus was 246 GPa (standard deviation 12 GPa).

Table 1. Test matrix.

Beam	A_s (mm^2)	Ext. reinf.	Matrix	b_l (mm)	n_l
D	392.5	–	–	–	–
A-1	392.5	3X2	E	150	1
A-2	392.5	3X2	E	300	1
A-3	392.5	3X2	E	150	2
B-1	392.5	12X	E	200	1
B-2	392.5	12X	C	200	1
B-3∗	392.5	12X	C	200	1
B-4∗	392.5	12X	C	200	2
C-1	392.5	CFRP	E	300/150	2
C-2	392.5	CFRP	E	300	3

∗ with nails, E = epoxy, C = cementitious.

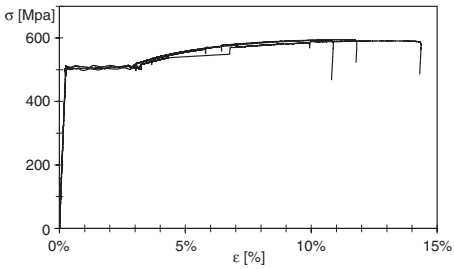

Figure 1. Experimental stress–strain relationship for ϕ10 steel bar.

The 3x2 steel cord (Hardwire 2002) is made by twisting 5 individual zinc coated wires together (3 straight filaments wrapped by 2 filaments at a high twist angle). The density of the 3x2 tape used in this research program consists of 8.7 cords per cm, which is considered high-density tape. According to the manufacturer the strength is 1.34 kN/mm.

The 12x steel cord (Hardwire 2002) is made by twisting two different individual brass coated wire diameters together in 12 strands and then over-twisting one wire around the bundle. The density of the 12x tape used to strengthen the beams consisted of 6.3 cords per cm, which is considered medium-density tape. According to the manufacturer, the strength is 0.79 kN/mm.

Several tensile tests on 3x2 and 12x steel cord were performed according to indications of ASTM D3039/D3039M. For 3x2 the mean value of tensile strength was 2440 MPa (standard deviation 450 MPa), the corresponding strain was 0.013 (standard deviation 0.00297), the Young's modulus was 183 MPa (standard deviation 32 MPa). For 12x the mean value of tensile strength was 2815 MPa (standard deviation

2a) steel tape 3x2

2b) steel tape 12x

Figure 2. Failure modes of steel tape.

Figure 3. Development of crack in correspondence of stirrups.

400 MPa), the corresponding strain was 0.012 (standard deviation 0.0059), the Young's modulus was 216 MPa (standard deviation 55 MPa). Experimental results indicated that dispersion of results of steel specimens was greater than carbon fibers: this was often due to the geometrical configuration of cords that induced slipping at the anchorage of specimens with distortions and premature failure modes. In Figure 2 examples of failure modes of cords 3x2 and 12x are reported.

3.2 *Experimental cracking behaviour*

The crack pattern was observed and documented for different load levels until steel yielding. The presence of steel stirrups spaced of 100 mm influenced the development of cracks during the load history (Fig. 3). Only at failure condition more cracks formed between stirrups.

In general no relevant difference in crack spacing was observed for the unstrengthened and all the strengthened beams; only at failure condition the beams externally reinforced were characterized by a smaller crack spacing with a crack pattern more irregular due to local debonding at the concrete-laminate interface (Fig. 4). Crack width in the constant moment region was measured by a mechanical deformometer considering displacements of seven gages having 50 mm length as benchmarks.

In Figure 5 the experimental mean crack widths, evaluated as the average of measures of gages where almost a crack formed, are reported for all the beams where the epoxy resin was used.

4a)

4b)

Figure 4. Cracking pattern: 4a) beam unstrengthened (D); 4b) beam strengthened (A1).

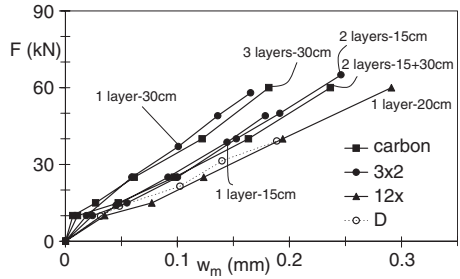

Figure 5. Experimental values of mean cracks width.

The graph of figure 5 shows that the maximum effect in terms of reduction in crack widths with respect to the reference beam D is obtained when carbon fibers and steel 3x2 cords are applied. This effect is greater when increasing the width of the external bonded reinforcement. For the 3x2 steel cords having the same area (125 mm^2), crack widths are smaller when 1 layer of 300 mm is used rather than 2 layers of 150 mm. Effects of carbon and 3x2 steel reinforcement having similar areas (3 layers and 1 layer having bond length of 300 mm) are comparable. For the same width of external reinforcement no relevant effect is produced when the total area increases (for the 3x2 steel cords no sensible reduction of crack widths there is using 1 or 2 layers). This phenomenon in the elastic range of steel was already evidenced by Ceroni & Pecce (2002). Before steel yielding the tension stiffening effect is relevant but seems to be independent on the amount of fibers if the bond length is the same because in this behavioral range the constitutive and bond laws are linear. After steel yielding, the tension stiffening is greater when the external reinforcement

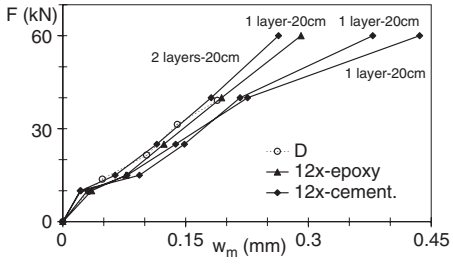

Figure 6. Experimental values of crack widths.

area increases, due to the non-linear interface bond relations.

For the beam strengthened with the 12x steel cords, crack widths are similar to the reference beam (D), evidencing that the external reinforcement had no sensible effect. The 3x2 steel tape has an high-density, respect to the low-density of the 12x steel tape.

In figure 6 the experimental values of crack widths are reported for all the beams reinforced with the 12x steel tape. The graph confirms that the 12x steel tape does not reduce crack widths with respect to the unstrengthened beam D. The use of epoxy resin compared to the cementitious grout produces a stiffer behavior. Different adhesives have different bond laws that are characterized by various shear moduli and thickness of the layer. In general, due to the greater thickness of the steel tape and to the higher density of the cementitious grout, the adhesive layers are thicker giving less stiff bond relationships. Increasing the number of layers of steel tape causes a small reduction of crack widths.

To the aim of comparing the experimental and model results in terms of cracking spacing and width, a service load is defined for the bare and strengthened beams as follows:

$$F_{serv} = \frac{F_{u,th}}{1.5} \tag{7}$$

where $F_{u,th}$ is the theoretical failure load obtained by calculating the ultimate moment of the section taking into account the nominal strength of materials reduced by their safety factors: $\gamma_s = 1.15$ for internal steel reinforcement, $\gamma_{cfrp} = 1.3$ for carbon fibers and $\gamma_{sfrp} = 1.3$ for steel cords.

It is important to underline that this service load definition is conventional; really the definition has to be reviewed evaluating the effective strength of the beam due also to the delamination crisis and not only to the section crisis.

In Table 2 the following data are reported:

- the ultimate experimental load, $F_{u,exp}$;
- the ultimate theoretical load, $F_{u,th}$;

Table 2. Experimental results at service load.

Beam	$F_{u,exp}$ (kN)	$F_{u,th}$ (kN)	F_{serv} (kN)	η	W_{exp} (mm)	$S_{rm,exp}$ (mm)	n
D	48.3	40	27	1.8	0.120	100	11
A-1	86.7	84	56	1.5	0.179	100	11
A-2	120	108	72	1.7	0.165	100	11
A-3	100	108	72	1.4	0.246	100	11
B-1	88.3	80	53	1.7	0.250	95	11
B-2	73.3	80	53	1.4	0.325	85	12
B-3∗	71.7	80	53	1.3	0.360	104	10
B-4∗	86.7	104	69	1.3	0.264	100	10
C-1	96.7	99	66	1.5	0.237	94	10
C-2	135	120	80	1.7	0.182	106	9

∗ With nails.

- the service load, F_{serv}, calculated according to Eqn.7;
- the ratio η between the experimental ultimate load and the service load;
- the mean experimental cracks width measured by mechanical deformometer, w_{exp}, at F_{serv};
- the number of cracks, n, at F_{serv};
- the mean crack spacing, $s_{rm,exp}$, at F_{serv}.

Considering the evolution of cracks during the loading history of beams, the crack pattern observed at the service load corresponds to a stabilized cracking situation, because no more cracks formed until the failure when cracking became irregular. It is clear that the service load is not the same for all the beams and that crack width is higher for higher service load values.

4 THE ANALYTICAL MODEL

A model of cracking behavior of RC ties strengthened with FRP laminates was dealt with by the authors and used to calculate crack widths and spacing (Ceroni et al., 2001; Ceroni & Pecce, 2003). The approach is one-dimensional and uses non-linear constitutive relationship for materials and bond laws. Furthermore, the formation of first crack and crack propagation could be taken into account. The analytical results given by the model were compared in terms of mean strain and mean crack width with experimental data (Ceroni et al., 2004) on RC ties externally bonded with FRP laminates (Ceroni & Pecce, 2003).

The model is extended to beams considering the part of beam in tension as a tie with a section equal to the effective area of concrete in tension surrounding the internal steel reinforcement. The tie element is reinforced with internal steel bars and external laminate (Fig. 7).

The slip at steel-concrete and concrete-laminate interfaces, s_s and s_l, can be defined as follows:

$$s_s(z) = u_s(z) - u_{ct}(z) \tag{8}$$

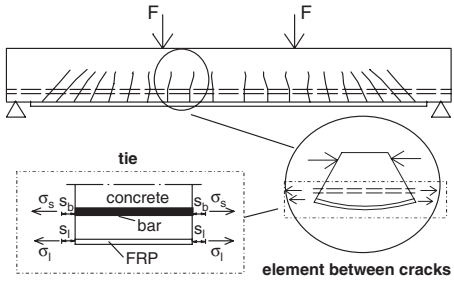

Figure 7. Model definition.

$$s_l(z) = u_l(z) - u_{ct}(z) \tag{9}$$

where u_{ct} = displacement in concrete, u_s and u_l = displacements of steel and FRP along the bar direction. The problem is based on the following equilibrium equations:

$$\frac{d\sigma_s}{dz} = \frac{4 \cdot \tau_s(z)}{\phi} \tag{10}$$

$$\frac{d\sigma_l}{dz} = \frac{\tau_l(s_l, z) \cdot b_l}{A_l} \tag{11}$$

$$\frac{d\sigma_c}{dz} = -\frac{\tau_s(s_s, z) \cdot \pi \cdot \phi}{A_{ct}} - \frac{\tau_l(s_l, z) \cdot b_l}{A_{ct}} \tag{12}$$

where $\sigma_s, \sigma_c, \sigma_l$ = tensile stresses in steel, concrete and FRP laminates, τ_s and τ_l = bond stress of steel bar and FRP at concrete interface, ϕ = bar diameter, b_l = width of laminate.

Finally the constitutive relationships of steel, FRP, concrete and the bond–slip relations have to be defined. To introduce any non-linear relationship, equations are solved numerically by a finite difference method using an iterative shooting procedure. The procedure is divided in two steps, assuming the hypothesis that bond-slip behaviour of steel and FRP are independent. The RC element is solved first, then assuming a constant crack width along the section, i.e. $s_l = s_s$, the FRP bond behaviour is analyzed.

The total tensile force at the cracked section is given by the sum of the contributions of steel bar and FRP laminate. For each load step the detailed distributions of strains, stresses and slips along the entire element are known. Therefore, the tensionstiffening behavior of the element is defined calculating the mean strain ε_{sm}, and the crack width is valuable as twice the slip at the cracked section.

This procedure needs to establish the cracks spacing that can be evaluated by the model introducing a cohesive behaviour of concrete in tension (Ceroni & Pecce, 2003). However, in this case the experimental mean crack spacing is assumed as initial value because an effect by stirrups position was observed.

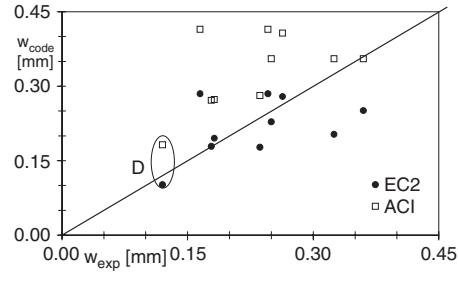

Figure 8. Comparison between experimental values and codes formulation for mean crack widths.

5 THEORETICAL-EXPERIMENTAL COMPARISON

5.1 *Comparison with code formulation*

The experimental mean cracks widths (w_{exp}) at the service load are compared in Figure 8 with the theoretical values given by Eurocode2 (Eqn. 1) and ACI 318-99 (Eqn. 6); in the Eqn. 1 the experimental crack spacing at the service load reported in Table 2 was used. Crack spacing calculated assuming $A_{ct,eff} = 2.5 \cdot B \cdot c$ overestimates the experimental value that was influenced by stirrups spacing.

In Eqn. 6, the effective concrete area in tension surrounding each bar was estimated to be equal to $A_{ct,eff} = 2.5 \cdot B \cdot c$ divided to the number of bars.

It is possible to notice that for the strengthened beams the ACI code formulation overestimates the experimental values.

5.2 *Comparison with model*

The numerical model is applied considering the experimental constitutive relationship of steel, a linear constitutive relationship for CFRP and SRP, the non linear law developed by (Eligehausen et al., 1983) for the bond behaviour of steel bar in concrete, and nonlinear bond behaviour of FRP without degradation near cracks.

The bond behavior of fibers externally bonded to concrete depends on the materials characteristics and its definition is still not well established; the fib bulletin 14 (2001) reports an example of bilinear bond model developed by Holzenkämpfer (1994); this bond law is characterized by significant points, τ_{max}, s_1, s_{max}.

A calibration of the FRP bond law was developed by comparing the theoretical and experimental

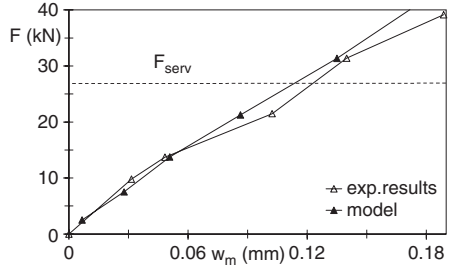

Figure 9. Crack widths for unstrengthened beam D.

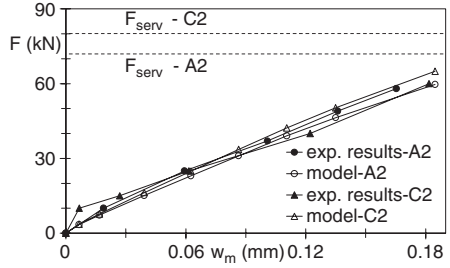

Figure 10. Crack widths for beams A2 and C2.

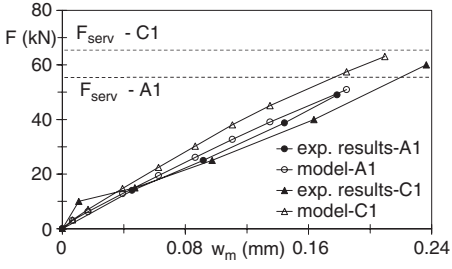

Figure 11. Crack widths for beam C1 and A1.

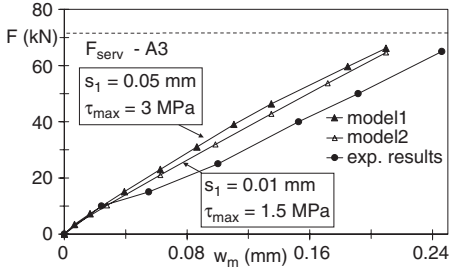

Figure 12. Crack widths for beam A3.

average strains, ε_m, of RC ties externally bonded with carbon and glass fibres (Ceroni & Pecce, 2002). It was evidenced that a reduction of τ_{max} causes a less stiff behaviour before steel yielding with a lower yielding load. A reduction of s_{max} gives a less stiff behaviour after yielding; an increasing of s_1 determines a greater deformability before yielding. By this parametric analysis, the following bilinear law was established:

$\tau_{max} = 3$ MPa; $s_1 = 0.05$ mm; $s_{max} = 0.1$ mm.

This bond law has probably to be re-calibrated for the SFRP to account for the effect of the cementitious matrix and the number of steel cords plies applied as external reinforcement. The effective area of concrete in tension is assumed equal to $A_{ct,eff} = 2.5 \cdot B \cdot c$.

Some comparisons between the experimental crack widths and the theoretical values given by the model are reported in the following Figures (9–12). In Figure 9 the comparison between model and experimental results is reported for the unstrengthened beam D.

In Figure 10 the comparison is reported for beam A2 and C2 having similar area of external reinforcement (125 mm^2 of 3x2 steel tape and 150 mm^2 of carbon fibers respectively) with the same width (300 mm) and adhesive (epoxy).

In Figure 11 the comparison is reported for beams A1 and C1 having similar area of external reinforcement (62 mm^2 of 3x2 steel tape and 75 mm^2 of carbon fibers respectively) with the same adhesive (epoxy). For beam C1 the effect of two layers of carbon fiber having different width (150 and 300 mm) is not well replicated by the model.

In Figure 12 it is evident that for beam A3 the model with the same bond law of carbon is not efficient. This is probably because of the effect of two layers of steel cords. Decreasing the maximum shear stress to 1.5 MPa and increasing the corresponding slip to 0.1mm, in order to take into account the greater thickness of adhesive layer, a better agreement with the experimental results is obtained.

For beams reinforced with 12x cords, because of the experimental crack widths are comparable or greater than the unstrengthened beam D, it is clear that the model need to be assessed with suitable bond law or considering transversal effects.

In Table 3 in correspondence of the service load the theoretical mean crack width given by the model, w_{theor}, and the percent difference to the experimental values, Δ, is reported for the unstrengthened beam and for the ones strengthened using carbon fibers and 3x2 steel cords.

Table 3. Experimental and theoretical crack widths at service load.

Beam	$F_{serv.}$ (kN)	w_{exp} (mm)	w_{theor} (mm)	Δ(%)
D	27	0.120	0.11	8.3
A-1	56	0.179	0.179	−0.3
A-2	72	0.165	0.18	−9.1
A-3	72	0.246	0.21	14.6
C-1	66	0.237	0.205	13.3
C-2	80	0.182	0.166	8.8

6 CONCLUSIONS

The experimental results for cracking behaviour of RC beams externally strengthened with composite materials made by carbon fibres or steel cords have led to the following conclusions:

- at similar serviceability load, cracks widths are smaller for increasing the width of laminate rather than the area;
- the high-density steel cords and carbon fibres, both impregnated with epoxy, give very similar results when the area of external reinforcement was the same;
- the low-density steel cords, bonded with cementitious grout, seems to give a low tension stiffening effect;
- nails distributed along the entire beam have no effect on cracking behaviour;
- code formulations for evaluation of average cracks width and spacing when an external composite reinforcement is applied need further study.

Regarding the model proposed by the authors, when assessed for RC ties externally strengthened with composite materials, the model seems in good agreement with experimental results also for beams. However, the bond law has to be re-calibrated, taking into account the type of material, number of layers applied and type of adhesive.

ACKNOWLEDGEMENT

The authors would like to thank Hardwire LLC, Pocomoke City, MD, Mapei Spa, Milan, Italy, and Sika Italia, Milan, Italy, for donating the steel tapes, the FRP system, and the epoxy resin/cementitious grout used to bond SRP, respectively.

REFERENCES

ACI, 1999, *Building code requirements for structural concrete*, ACI 318-99, American Concrete Institute, Detroit, Michigan, USA.

ASTM D3039/D3039M-00

CEB, 1985, Manual on Cracking Deformation, Bulletin d'Information n°158-E.

Ceroni F., Manfredi G. & Pecce M., 2001. Cracks width in RC beams strengthened with carbon fabrics, Proc. of the Fifth Conference on Non-Metallic Reinforcement for Concrete Structures, FRPRCS5, Cambridge, UK, 16–18 July 2001.

Ceroni F. & Pecce M. 2002. Bond behaviour of R.C. elements externally reinforced with FRP laminates, Proc. of the International Symposium "Bond in Concrete – from research to standards" 20–22 November 2002, Budapest, pp. 622–629.

Ceroni F. & Pecce M. 2003. Experimental and Theoretical crack behavior of RC ties FRP EBR, International Conference "Composites in construction", CCC 2003, 16–19 September 2003, Cosenza, Italy, pp. 319–324.

Ceroni F., Pecce M. & Matthys, S. 2004. Tension Stiffening of RC Ties Strengthened With Externally Bonded FRP Sheets, ASCE Journal of Composites for Constructions, Vol. 8, No. 1, January–February 2004.

Eligehausen R., Popov E.P. & Bertero V.V. 1983. Local Bond Stress-Slip Relationships of Deformed Bars Under Generalized Excitations, Report n°.83/23, EERC, University of California, Berkeley.

Eurocode2 1991. Common Unified Rules for Concrete Structures, ENV 1992-1-1.

Fib Bullettin 14, 2001. FRP as Externally Bonded Reinforcement of R.C. Structures: Basis of design and safety concept, TG9.3.

Hardwire LLC, 2002. "What is Hardwire," www.hardwirellc.com, Pocomoke City, Maryland.

Mapei, 2000. "World-wide Leader in Products for the Building Industry", http://www.mapei.it, Milan, Italy.

Matthys S., 2000. Structural behaviour and design of concrete members strengthened with externally bonded FRP reinforcement, Ph Doctoral thesis, Faculty of Engineering, Department of Structural Engineering, Ghent University, Ghent, Belgium.

Sato Y., Ueda T. & Shoji K., 2002. Tension stiffening effect of reinforced concrete member strengthened by carbon fiber sheet, Proc. of the International Symposium "Bond in concrete", Budapest, 20–22 November 2002, pp. 606–613.

Smith S.T. & Teng J.G., 2002a. FRP-strengthened RC beams. I: review of debonding strength models. Engineering Structures, Volume 24, Issue 4, April 2002, pp. 385–395.

Smith S.T. & Teng J.G., 2002b. FRP-strengthened RC beams. II: assessment of debonding strength models. Engineering Structures, Volume 24, Issue 4, April 2002, pp. 397–417.

Tashito, H., Tarui, T., Sasaki, S., Yoshie, A., Nishida, S., Ohashi, S., Nakamura, K. & Demachi, H., 1999, "Ultra High Tensile Strength Steel Cord," Nippon Steel Technical Report No. 80, Tokyo, Japan, pp. 38–43.

Tripi J.M., Bakis C.E., Boothby T.E. & Nanni A., 2000. Deformation in concrete with external CFRP sheet Reinforcement, Journal of Composites for Construction, Vol. 4, No. 2, pp. 85–94.

Ueda T., Yamaguchi R., Shoji K. & Sato Y., 2002. Study on Behavior in Tension of Reinforced Concrete Members Strengthened by Carbon Fiber Sheet, Journal of Composites for Construction, ASCE, August.

Zhang Y., Toutanji H. & Balagrou P., 2003. Crack widths in R.C. beams externally bonded with CFRP sheets, Proc. of FRPRCS-6, Singapore, 8–10 July 2003.

FRP Composites in Civil Engineering – CICE 2004 – Seracino (ed)

FRP confined concrete constitutive relationships

C. Faella, R. Realfonzo & N. Salerno
Dept. of Civil Engineering, University of Salerno, Italy

ABSTRACT: In this paper some preliminary results of compression tests performed on concrete specimens confined by fiber reinforced polymers (FRP) systems are presented. The test results are compared to some numerical expressions proposed in the technical literature for the evaluation of the confined concrete strength and ultimate strain. The comparison enables to evaluate the reliability of the analytical relationships.

Furthermore, the problem of the definition of a constitutive relationship able to simulate the behaviour of the FRP confined concrete under compression is faced, introducing a new constitutive law obtained by modifying the well known relationship proposed by Popovics. This law is extended to the case of FRP confined concrete by introducing a linear expression to define the relationship between lateral and axial strain. In this way the iterative procedure proposed by other authors to extend the abovementioned constitutive law to the case of FRP confined concrete is avoided.

1 INTRODUCTION

A procedure for the reinforced concrete elements strengthening which is characterised by the external application of *Fibre Reinforced Polymer* (FRP) materials is imposing itself and spreading in the last years. Often it consists of applying textiles made by glass fibre (GFPR – glass fibre reinforced polymers), by carbon (CFRP) or by aramid fibres (AFRP), sticking them to the concrete support by means of resins.

The FRP materials present a linear-elastic stress–strain behaviour; when they are used to confine the concrete elements, this peculiar behaviour determines an action of the confining system significantly different with respect to the one made by the traditional systems, which use steel devices.

Actually, for these last ones, it is possible to assume – as usually done for numerical modelling – the activation of a constant confining pressure proportional to the material yielding stress.

On the contrary, in the case of FRP the lateral pressure developed by the confining system is variable during the entire loading process and linearly increasing with the lateral strain of the element. This causes a substantial modification of the confined concrete behaviour under compression.

The differences at the stress–strain constitutive law level, with respect to the confinement offered by the steel stirrups, have been evidenced during numerous recently conducted experimental programs.

An advanced state of art on such topic is presented in a recent volume written by Teng et al. (2002).

Contemporaneously to the experimental studies, the development of analytical models implemented in order to reproduce the stress–strain relationship of the concrete confined by FRP has been recently observed. The reliability of such models depends on a correct definition of the strength (f_{cc}) and of the ultimate strain (ε_{cc}) of the confined concrete; these parameters depend on the confining pressure (f_l) and, consequently, on the typology, the geometry and the efficiency of the confining system.

The constitutive relationships currently proposed follow two different approaches:

- from one side relationships obtained by adapting the constitutive laws proposed for concrete confined by steel elements are formulated;
- on the other side "ad hoc" constitutive relationships, based on the experimental observation of the behaviour of concrete specimens wrapped by FRP systems, are proposed.

The first models, more accurate, generally require complex solutions based on iterative procedures, in order to introduce – in the case of FRP – an adequate variation law of the confining pressure with the element axial deformation. The second ones, simplest but less accurate, frequently allow an easy implementation in analytical models for the evaluation of the behaviour of FRP confined R/C sections under axial load and bending moment.

A constitutive relationship belonging to the first of the two classes previously evidenced is presented in the following; this relationship derives by the well known constitutive law proposed by Popovics (1973) for the ordinary reinforced concrete case.

The Popovics relationship was already successfully extended by other authors to the examined case

(Spoelstra & Monti, 1999), but for the aforesaid reasons, the adopted model currently requires the implementation of an iterative procedure.

In order to avoid subsequent iterations, a simple relationship between the lateral strain (which the confining pressure depends on) and the axial strain is here introduced.

2 CONSTITUTIVE RELATIONSHIPS FOR THE CONFINED CONCRETE

A preliminary definition of the constitutive stress–strain (f_c–ε_c) relationship of the confined concrete is needed in order to model the behaviour of confined R/C members under bending moment and axial load.

In case of concrete confined with steel stirrups or other metallic devices is frequently used the Popovics' constitutive law:

$$fc = \frac{fcc \cdot x \cdot r}{r - 1 + x^r} \tag{1}$$

where, f_{cc} is the compressive strength of the confined concrete; $x = \varepsilon_c/\varepsilon_{cc}$; ε_{cc} is the confined concrete ultimate strain; $r = E_c/(E_c - E_{c,sec})$; E_c is the tangent elastic modulus of unconfined concrete; $E_{c,sec}$ is the secant modulus ($E_{c,sec} = f_{cc}/\varepsilon_{cc}$).

In order to describe the f_c–ε_c law the evaluation of the confinement pressure f_l is needed since the compressive strength f_{cc} and the corresponding strain ε_{cc} are dependent on such parameter.

In the case of concrete confined by using steel systems, the confinement pressure f_l assumes a constant value which is proportional to the yielding strength of steel; in this case f_{cc} and ε_{cc} are frequently obtained by:

$$f_{cc} = f_{c0} \cdot \left(2.254 \cdot \sqrt{1 + 7.94\frac{f_l}{f_{c0}}} - 2\frac{f_l}{f_{c0}} - 1.254\right) \tag{2}$$

$$\varepsilon_{cc} = \varepsilon_{c0}\left[1 + 5\left(\frac{f_{cc}}{f_{c0}} - 1\right)\right] \tag{3}$$

proposed by Mander et al. (1988) and by Richart et al. (1929) respectively.

In Equations (2) and (3) f_{c0} and ε_{c0} are the unconfined concrete strength and the corresponding strain; the last one is generally assumed to be equal to 0.2%.

Equation (2) has also been applied successfully to the case of FRP confinement systems and it is adopted in the American Concrete Institute guide lines (ACI, 2002). However, since FRP materials have an elastic-linear behaviour up to failure, the lateral pressure f_l provided by FRP systems is not constant, being proportionally dependent on the lateral strain ε_l of the concrete element. In particular, in case of cylindrical elements wrapped by FRP materials the confinement action can be expressed by:

$$f_l = \frac{2 \cdot n_l \cdot t_j \cdot E_{frp} \cdot \varepsilon_l}{D} = C_j \cdot \varepsilon_l \tag{4}$$

where t_j is the nominal thickness of the single FRP layer, n_l is the number of layers, E_{frp} is the Young's modulus of the FRP sheets and D is the diameter of the cylindrical specimen. The parameter C_j then represents the stiffness of the confining system.

Equation (4) can be used also for the case of square specimens; however, in this case:

$$f_l = f_{lx} = f_{ly} = \frac{2 \cdot n_l \cdot t_j \cdot E_{frp} \cdot \varepsilon_l}{D}$$

and D is the dimension of the side of the specimens.

According to Equation 4 the maximum value of the confinement pressure is given by:

$$f_{lu} = \frac{2 \cdot n_l \cdot t_j \cdot E_{frp} \cdot \varepsilon_{j,u}}{D} \tag{5}$$

where $\varepsilon_{j,u}$ is the failure strain of the FRP system.

It is well known that the failure of the confined elements happens for lateral strain values lower than the ultimate strain values ($\varepsilon_{u,FRP}$) obtained by performing standard tensile tests on FRP sheets; generally the suggested value is:

$$\varepsilon_{ju} \approx (0.5 - 0.8) \cdot \varepsilon_{u,FRP}$$

The main reasons of this reduction are:

- the concrete collapse may happen when axial and lateral strains attain limit values before the ultimate strain in FRP sheets has been reached;
- the system may be subjected also to local stress concentration due to a non-homogeneous deformation of the concrete member;
- the fibers are generally misaligned for the presence of voids or an inadequate surface preparation;
- the curved shape of the concrete element, especially in case of square or rectangular cross sections at corners with a small radius.

In order to estimate some of these effects, in a recent paper Faella et al. (2004) proposed a coefficient less than 1 to multiply the confinement pressure given by Equation (5); such a coefficient (k_c) can be obtained by the following relation:

$$\varepsilon_{j,u} = \varepsilon_{frpu}\frac{\alpha \cdot d_j}{2 \cdot R} = \left(1 - \frac{\alpha \cdot d_j}{2 \cdot R \cdot \varepsilon_{frpu}}\right) \cdot \varepsilon_{frpu} = k_c \cdot \varepsilon_{frpu} \tag{6}$$

where d_j is the fiber diameter, R is the corner radius, α is a coefficient dependent on the quality of the execution.

According to Equation (6) the maximum value of f_l given by Equation (5) can be rewritten as follows:

$$f'_{lu} = k_c \cdot f_{lu} = k_c \cdot \frac{2 \cdot n_l \cdot t_j \cdot E_{frp} \cdot \varepsilon_{frp,u}}{D} \quad (7)$$

Obviously, in the case of cylindrical elements the radius R – reported in Equation 6 – is equal to R = D/2.

Coming back to the constitutive relationship, it is to be underlined that, on the base of what already said, in the case of FRP, due to the impossibility to consider as for the steel stirrups a constant lateral pressure, it is necessary to define a relationship which gives the confining pressure f_l as function of the axial strain ε_c of the system; indeed, varying the axial strain ε_c, the transversal strain ε_l and – consequently – the confining pressure also vary; this determines a "step by step" variation of the strength f_{cc} and of the corresponding strain ε_{cc} of the confined concrete. Therefore, rigorously, the stress–strain relationship of the concrete confined by FRP can be expressed as a function:

$$f_c = f_c[\varepsilon_c, f_l(\varepsilon_c)] \quad (8)$$

where it is necessary to define the relationship between the confining pressure and the axial strain, i.e.– according to Equation (4) – between the lateral and axial strain of the compressive element.

Elaborating the model proposed by Pantazopoulou and Mills (1995) for the unconfined concrete, Spoelstra and Monti obtained the following relationship:

$$\varepsilon_l(\varepsilon_c, f_l) = \frac{E_c \cdot \varepsilon_c - f_c(\varepsilon_c, f_l)}{2 \cdot \beta \cdot f_c(\varepsilon_c, f_l)} \quad (9)$$

where β is a constant depending on the concrete mechanical properties ($\beta = E_c/f_{c0} - 1/\varepsilon_{c0}$).

Introducing Equation (9) and using the Equations (2) and (3) for the determination of f_{cc} and ε_{cc} as function of the lateral pressure, the Spoelstra and Monti model allows to apply again the Popovics' constitutive law implementing an iterative procedure.

3 CONFINED CONCRETE STRENGTH

In the last years, in addition to the Equation 2, numerous relationships to estimate the strength f_{cc} of concrete elements confined by FRP systems were proposed by several researchers; all these laws need the evaluation of the confinement pressure f_l.

Some of such relationships have been derived by the well known one proposed by Richart et al. (1929) again for the case of concrete confined by steel stirrups:

$$f_{cc} = f_{c0} + k_1 \cdot f_l \quad (10)$$

where k_1 was set by the Authors equal to 4.1.

The proposals for the case of FRP confinement systems are obtained by Equation (10) by modifying the k_1 coefficient; some of them are the following:

- Karbhari and Gao (1997): $k_1 = 2.1\ (f_l/f_{c0})^{-0.13}$
- Samaan et al. (1998): $k_1 = 6.0\ (f_l)^{-0.3}$
- Saafi et al. (1999): $k_1 = 2.2\ (f_l/f_{c0})^{-0.16}$
- Toutanji (1999): $k_1 = 3.5\ (f_l/f_{c0})^{-0.15}$
- Lam and Teng (2002): $k_1 = 2.15$

A different type of expression has been recently proposed by Spoelstra and Monti (1999):

$$f_{cc} = f_{c0} \cdot \left(0.2 + 3\sqrt{\frac{f_l}{f_{c0}}}\right) \quad (11)$$

In all the abovementioned expressions the confinement pressure is evaluated by Equation (4).

All the relationships reported herein can be considered suitable only in the case of specimens having a circular section. In the case of prismatic elements the introduction of a further coefficient k_s, known as "shape coefficient", needs; such a coefficient allows to evaluate the efficiency of the confinement. In fact, in the case of concrete specimens with square or rectangular cross section the confined area of concrete $A_{c,eff}$ is a portion of the total area A_c since an "arc effect" may be observed (see Figure 1); the amount $A_{c,eff}$ depends on the radius R of the rounded corners.

Assuming that the arcs of parable shown in Figure 1 form – at both the ends – an angle of 45° with the sides of the specimen, the coefficient k_s can be obtained by the following expression:

$$k_s = \frac{A_{c,eff}}{A_c} = 1 - \frac{2 \cdot (D - 2R)^2 / 3}{D^2 - R^2 \cdot (4 - \pi)} \quad (12)$$

Therefore, the coefficient k_s depends on the ratio R/D between the radius R and the side dimension D of the concrete specimen; as expected for R/D = 0.50 (circular section) k_s is equal to 1.

According to the model shown in Figure 1, it is possible to estimate the value of strength of the confined

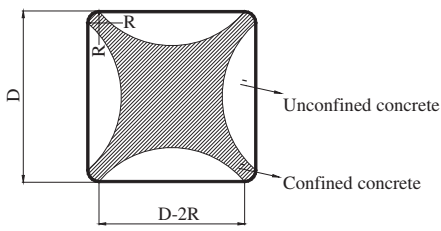

Figure 1. Prismatic specimen geometry.

concrete that can be obtained by performing tests on prisms, by using the following relationship.

$$f'_{cc} = f_{c0}(1 - k_s) + f_{cc} \cdot k_s \tag{13}$$

Furthermore, remembering Equation (10), frequently used to evaluate f_{cc}, Equation (13) can be rewritten as follows:

$$f'_{cc} = f_{c0} \cdot (1 - k_s) + f_{cc} \cdot k_s = f_{c0} + k_1 \cdot k_s \cdot f_l \tag{14}$$

The Eqs. (13) and (14) are obtained assuming that when the load increases the non confined portion ($A_c - A_{c,eff}$) keeps its strength f_{c0} (i.e. there is not degradation).

Furthermore, introducing in the (14) the abovementioned coefficient k_c, it follows:

$$f'_{cc} = f_{c0} + k_s \cdot k_1 \cdot f'_l = f_{c0} + k_c \cdot k_s \cdot k_1 \cdot f_l \tag{15}$$

A different expression of the shape coefficient was proposed by Mirmiran et al. (1998):

$$k_s = \frac{2 \cdot R}{D} \tag{16}$$

Such formulation was recently assumed by the new Italian seismic code. It is to be noted that for $R = D/2$ (circular section) the (16) gives $k_s = 1$ again.

4 CONFINED CONCRETE ULTIMATE STRAIN

Even for the determination of the maximum values of the axial strain, many proposals are in bibliography in addition to the already seen (Equation 3).

First of all it is necessary to clarify that, generally, it is to be distinguished the value ε_{cc} of the strain corresponding to the strength f_{cc}, and the value of the ultimate strain ε_{cu}. However, since the lateral pressure induced by the FRP confining systems increases with the axial strain, frequently the constitutive relationship of the confined by FRP concrete, obtained by experimental tests, does not present a "softening" branch, i.e. the maximum compressive strength is reached for a strain value ε_{cc} equal ε_{cu}.

Such two values are sometimes different ($\varepsilon_{cu} > \varepsilon_{cc}$) when experimental tests are made by prismatic specimens, in particular for low values of confinement action.

Frequently used analytical formulations for the ultimate strain estimation are:

– *the Fardis and Khalili* relationship (1982):

$$\varepsilon_{cc} = 0.002 + 0.0005 \cdot \frac{2 \cdot E_{frp} \cdot t_j}{D \cdot f_{c0}} \tag{17}$$

which, assuming $\varepsilon_{c0} = 0.002$ and indicating with $\varepsilon_{frp,u}$ the ultimate effective strain concerning the confining system, can be written as:

$$\varepsilon_{cc} = \varepsilon_{c0} \cdot \left(1 + \frac{0.25}{\varepsilon_{frp,u}} \cdot \frac{f_l}{f_{c0}}\right) \tag{18}$$

– *the Karbhari and Gao* model (1997):

$$\varepsilon_{cc} = \varepsilon_{c0} + 0.01 \cdot \frac{2 \cdot E_{frp} \cdot \varepsilon_{frpu} \cdot t_j}{D \cdot f_{c0}} = \varepsilon_{c0} \cdot \left(1 + 5 \cdot \frac{f_l}{f_{c0}}\right) \tag{19}$$

where the coefficient 5 which multiplies the f_l/f_{c0} ratio is obtained for $\varepsilon_{c0} = 0.002$.

– *the Sieble et al.* relationship (1997):

$$\varepsilon_{cu} = 0.004 + \frac{2.8 \cdot \rho_{frp} \cdot f_{frp} \cdot \varepsilon_{frp,u}}{f_{cc}} \tag{20}$$

where ρ_{frp} indicates the FRP volumetric ratio ($= 4t_j/D$, in the case of circular sections) and f_{frp} the tension in the confining system;

– *the Lam and Teng* law (2002), valid for CFRP:

$$\varepsilon_{cu} = \varepsilon_{c0} \cdot \left(2 + 15 \cdot \frac{f_l}{f_{c0}}\right) \tag{21}$$

5 ANALYTICAL MODELS VS EXPERIMENTAL RESULTS

In the following the above reported analytical expressions given by the technical literature for the evaluation of the strength and the ultimate strain of the concrete confined by FRP are compared to some experimental results.

The results concern an experimental test campaign recently carried on at the University of Salerno.

The experimental programme is characterised by 140 specimens: 20 cylindrical and 120 prismatic. The specimens are made of two different concrete typologies, having an average design cubic ($15 \cdot 15$ cm) strength equal to 20 and 35 MPa respectively and are confined by carbon fibres sheets (CFRP).

In order to evaluate the influence of the confining pressure, the wrapping is performed both by one and by two sheets of CFRP; the same tests are also carried out on unconfined elements.

The used carbon textile has unidirectional fibres; the technical characteristic (mean values) of the non impregnated sheet are the following:

– tensile strength: 4200 MPa;
– tension elastic modulus: 240 GPa;
– nominal thickness: 0.17 mm;
– ultimate strain: 1.75%.

The tests, performed controlling the displacements, are divided as following: 50 tests characterised by the

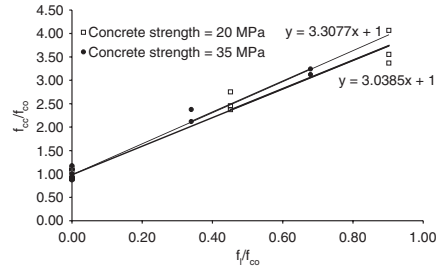

Figure 2. Compressive strengths of cylindrical specimens.

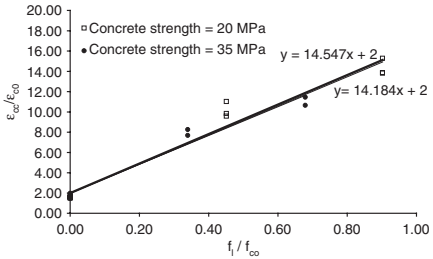

Figure 3. Ultimate strain of cylindrical specimens.

axial load applied in the centre of the cross section: 20 on cylindrical specimens ($15 \cdot 30$ cm) and 30 on prismatic ($15 \cdot 15 \cdot 25$ cm) ones.

In order to determine the influence of the specimen shape, the prismatic ones are divided in three typologies, having different rounding radii of the corners (R = 10, 20 and 30 mm).

The results obtained by the tests on confined and unconfined cylindrical specimens show that the concrete strength more than doubles using for confining only one CFRP sheet and becomes more than three times using two of them. The larger increments are found in the case of the "poorest" concrete.

In Figure 2 the confined concrete strength adimensionalised with respect to the unconfined one is reported as function of the ratio between the lateral confining pressure and unconfined concrete strength.

Furthermore, in the figure two lines with the following equations:

$$\frac{f_{cc}}{f_{c0}} = 1 + k_f \frac{f_l}{f_{c0}} \tag{22}$$

which better approximate the test data are shown.

The values of the angular coefficient k_f of the two lines, obtained for the two different concrete classes, are evidenced in the graph.

Considering the (15) and the (6), being for cylindrical specimens $k_s = 1$ and in our case:

$$k_c = 0.935 \tag{23}$$

it is possible to estimate, for both the cases, the value k_1 which is in all the equations derived by the (10):

$$k_1 = \frac{k_f}{k_c} \tag{24}$$

Assuming, for any concrete class, the precautionary value $k_f = 3$, it results:

$$k_1 = \frac{k_f}{k_c} = \frac{3}{0.935} \cong 3.20 \tag{25}$$

Such value allows an immediate comparison with the abovementioned k_1 expressions (see section 3).

In Figure 3 the obtained ultimate strains are reported, in addition to the trend lines with equation:

$$\frac{\varepsilon_{cu}}{\varepsilon_{c0}} = 2 + k_\varepsilon \cdot \frac{f_l}{f_{c0}} \tag{26}$$

The values of the angular coefficient k_ε of the two lines are evidenced in the graph.

Introducing even in this case the adjusted lateral confining pressure given by the (7), and consequently expressing the ultimate strain with the:

$$\frac{\varepsilon_{cu}}{\varepsilon_{c0}} = 2 + k_2 k_c \cdot \frac{f_l}{f_{c0}} \tag{27}$$

it can be deducted the k_2 value as function of k_ε.

Assuming, for any concrete class, $k_\varepsilon = 14$, it is:

$$k_2 = \frac{k_\varepsilon}{k_c} = \frac{14}{0.935} \cong 15 \tag{28}$$

which is equal to the coefficient proposed by Lam e Teng (2002).

After all, on the base of the shown test data, the two following expressions are derived for the evaluation of the strength and the ultimate strain, confirming other results in literature:

$$\frac{f_{cc}}{f_{c0}} = 1 + 3.2 \cdot k_c \frac{f_l}{f_{c0}} \tag{29}$$

$$\frac{\varepsilon_{cu}}{\varepsilon_{c0}} = 2 + 15 \cdot k_c \cdot \frac{f_l}{f_{c0}} \tag{30}$$

The reliability of such expressions should be evaluated considering the results of other tests.

Finally, in Figures 4 and 5 the comparison between the test data, the two proposed expressions and the above reported bibliography models, is presented.

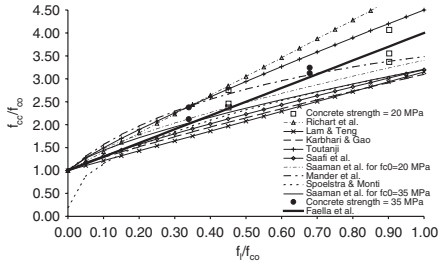

Figure 4. Modelling vs experimental results: concrete strengths.

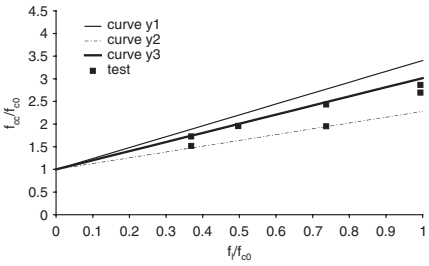

Figure 6. Modelling vs experimental results: concrete strengths.

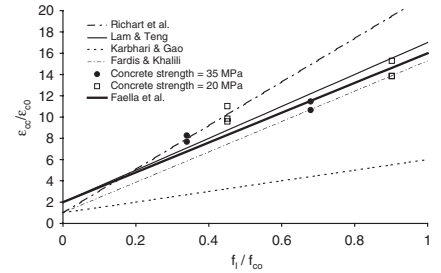

Figure 5. Modelling vs experimental results: concrete strains.

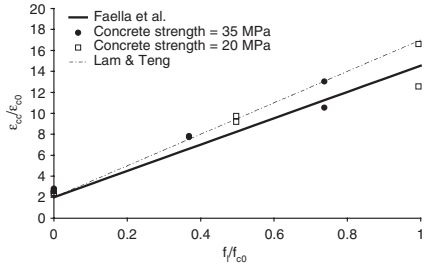

Figure 7. Modelling vs experimental results: concrete strains.

The results obtained by the tests on confined and unconfined prismatic elements show that the concrete strengths largely depend on the bend radius of the corners: in particular increasing R an evident increment of the f_{cc} values can be observed.

For the prismatic specimens, in the three examined cases (R = 10, 20 e 30 mm), the coefficient k_c is respectively equal to: $k_c = 0.514$; $k_c = 0.757$; $k_c = 0.838$.

In Figure 6, for the specimens having R = 30 mm, the comparison between the experimental strengths and three analytical curves, denominated as y_1, y_2 and y_3, is shown. The curve y_1 is obtained by:

$$y_1 = \frac{f_{cc}}{f_{c0}} = 1 + k_1 \cdot \left(1 - \frac{2\cdot(D-2R)^2/3}{D^2 - R^2\cdot(4-\pi)}\right)\cdot\frac{f_l}{f_{c0}} \quad (31)$$

i.e. using the shape coefficient given by Equation 12.

The curve y_2 is provided by:

$$y_2 = \frac{f_{cc}}{f_{c0}} = 1 + k_1 \cdot \left(\frac{2\cdot R}{D}\right)\cdot\frac{f_l}{f_{c0}} \quad (32)$$

i.e. adopting the coefficient given by Equation 16.

Finally, the curve y_3 is obtained by the (15), considering the coefficient k_s given by the (12):

$$y_3 = \frac{f_{cc}}{f_{c0}} = 1 + k_1 \cdot \left(1 - \frac{2\cdot(D-2R)^2/3}{D^2 - R^2\cdot(4-\pi)}\right)\cdot k_c \cdot \frac{f_l}{f_{c0}} \quad (33)$$

The analytical curves are evaluated assuming $k_1 = 3.2$, i.e. the value estimated by the Equation 25.

It is to be observed that the curves y_1 and y_2 respectively represent an upper and a lower threshold which contain the experimental points; instead, the curve y_3 gives the intermediate values which better catch the trend of the experimental data.

Finally, again for the case with R = 30 mm, Figure 7 shows the comparison between the ultimate strains experimentally obtained and two analytical curves: the Lam & Teng law and the one expressed by the Equation (30). The comparison shows that both the models quite well reproduce the experimental data.

6 AXIAL VS LATERAL STRAIN

As aforesaid, in order to model the confined R/C element behaviour under any load type, the preliminary

evaluation of the confined concrete constitutive relationship f–ε is necessary. This relationship allows to reproduce the compressive behaviour of the section portions where the passive confinement is effective.

The typical trend of the FRP confined concrete f–ε curve shows two different branches.

Initially, for low axial strain, the mechanical behaviour is essentially governed by the unconfined concrete properties: during such phase very low lateral strains can be observed and the confining system contribution is almost negligible. As evidenced by many researchers, when the axial strain is approximately equal to 0.2%, the confined concrete strength is only lightly larger than the unconfined one.

When the axial strain (and consequently the lateral one) increases, the confining effect becomes more evident; a progressive reduction of the curve slope is observed till such curve becomes almost linear.

In this phase the behaviour is essentially governed by the properties of the FRP confining system: the concrete which is inside the FRP system progressively loses its integrity because of the crack spreading and the energy introduced in the system – initially absorbed by the concrete specimens and by FRP system – is mostly transformed in the elastic strain energy of the FRP system.

The axial load carried by the specimen increases until the fiber failure; however, the system is transformed in a sort of container of a very cracked stony material able to absorb only modest transversal loads.

The above reported observations allow to understand why the ACI guidelines provide an upper threshold equal to 0.4% for the maximum lateral strain of a confined concrete element when transversal loads act.

Concerning the relationship between the lateral ε_l and the axial ε_c strain, the compression tests showed that such relationship significantly depends on the confining system stiffness (the parameter C_j introduced in Equation 4) and on the concrete strength.

In particular, for very low values of the axial strain the concrete shows an almost elastic behaviour and the relationship between the two strains can be described with a linear law:

$$\varepsilon_l \cong \nu_0 \cdot \varepsilon_c \tag{34}$$

Therefore, the ratio:

$$\lambda = \frac{d\varepsilon_l}{d\varepsilon_c} \tag{35}$$

is a constant about equal to the value ν_0 of the Poisson's modulus which characterises the elastic behaviour of the unconfined concrete.

After this quasi-elastic phase, when the axial strain increases, the parameter λ grows until a maximum value λ_{max}; subsequently it decreases towards an asymptotic value λ_u generally larger than ν_0.

Mirmiran & Shahawy (1997) formulated the following relationship for the estimation of the maximum λ value based on a regression analysis of experimental data:

$$\lambda_{max} = -0.7611 \cdot \ln \frac{C_j}{f_{c0}} + 4.0167 \tag{36}$$

They also provided a similar relationship for the evaluation of the asymptotic value, given by:

$$\lambda_u = -0.1375 \cdot \ln \frac{C_j}{f_{c0}} + 0.8646 \tag{37}$$

Therefore, for high values of the axial strain – generally larger than 0.5%÷1%–the relationship between lateral and axial strain can be described by the following linear formula (Xiao & Wu, 2000):

$$\varepsilon_l = \varepsilon_{l0} + \lambda_u \cdot \varepsilon_c \tag{38}$$

By experimental tests, Xiao and Wu (2001) estimated the ε_{l0} value (in such case it was $\varepsilon_{l0} = 0.047\%$).

Other formulae for the λ_u evaluation have been proposed; in particular, the followings may be remembered (Xiao & Wu 2001; Chun & Park 2002):

$$\lambda_u = 10 \cdot \left(\frac{C_j}{f_{c0}} \right)^{-0.9} \tag{39}$$

$$\lambda_u = -0.2305 \cdot \ln \frac{C_j \cdot \varepsilon_{ju}}{f_{c0}} + 0.087 \tag{40}$$

7 A NEW CONSTITUTIVE MODEL

The use of the Popovics' constitutive law in the case of FRP confined concrete needs the implementation of the Spoelstra & Monti iterative procedure.

In order to simplify such procedure the relationship between lateral and axial strain given by Equation (38) is adopted in the following; this means to assume a constant value of λ for all the loading process, neglecting its real variation; for a further simplification ε_{l0} is neglected. By such assumptions it is still possible to use the Popovics' law without the iterations proposed by Spoelstra and Monti.

The parameter λ to be introduced in the (38) has been evaluated by estimating the λ value which minimize the scatter between an experimental stress strain curve and the corresponding analytical curve obtained applying – by the above described procedure – the Popovics' model. Such optimal value evaluation procedure was repeated many times, examining the experimental f–ε law obtained by several authors.

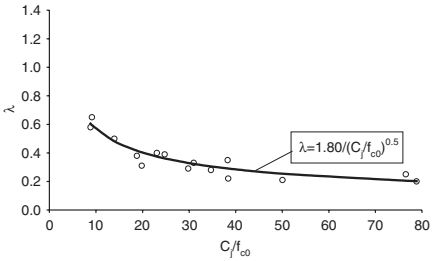

Figure 8. Equivalent Poisson modulus estimated values.

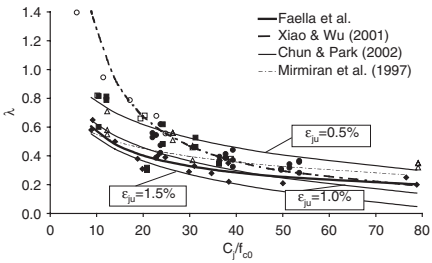

Figure 9. Bibliography relationship vs experimental data.

The obtained λ values and the curve which better interpolates the estimated points are shown in Figure 8 for different values of the ratio C_j/f_{c0}.

The trend curve assumes the equation:

$$\lambda_u = 1.8 \cdot \left(\frac{C_j}{f_{c0}} \right)^{-0.5} \tag{41}$$

In Figure 9 the comparison between such trend curve, the curves concerning the laws expressed by the (37), (39) and (40) and many experimental points gained by compression tests on cylindrical specimens, is reported; the test data are obtained as lateral-axial strain ratio at the specimen failure.

It is to be underlined that, due to the fact that the (40) – proposed by Chun and Park – also depends on the confining system ultimate strain, three different values of such parameter varying in a possible range are considered when this curve is plotted.

In Figure 10 a comparison between some stress-strain experimental curves and the curves obtained both by applying the iterative procedure by Spoelstra and Monti and by using the here proposed modified Popovics' model, is shown.

For the evaluation of the curves concerning the modified Popovics' model, the formulation presented

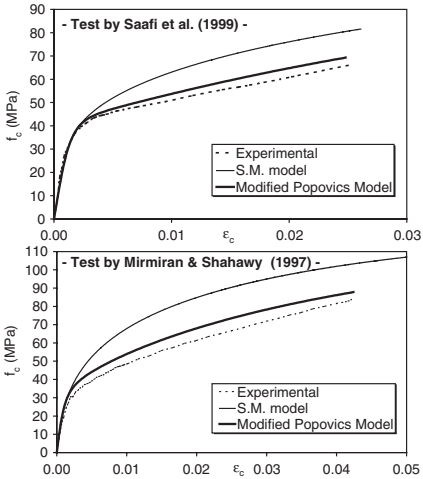

Figure 10. Analytical vs experimental constitutive relationship.

in the section 2 is adopted, substituting the Equation 9 with the following relationship:

$$\varepsilon_l = 1.8 \cdot \left(\frac{C_j}{f_{c0}} \right)^{-0.5} \cdot \varepsilon_c \tag{42}$$

The results obtained for the two reported cases, concerning tests performed by different authors, are evidently very good; however, it is to be said that the curves simulated by the Popovics modified relationship are part of the adopted data in the determination phase of the λ_u modulus.

After all, the obtained relationship needs a further validation by a comparison with new experimental data in order to test the actual reliability.

8 CONCLUSIONS

In this paper the problem of the definition of a constitutive law of the FRP confined concrete able to well simulate the experimental behaviour is studied.

In order to pursue this aim, the well known Popovics' relationship is considered and an application of this constitutive model which does not request any iteration is proposed. At this purpose a simple linear relationship between lateral and axial strain of the FRP confined element is formulated, and an equivalent Poisson modulus – which is the angular coefficient of the aforesaid linear relationship – is estimated. Such evaluation of the modulus has requested the examination of numerous experimental data found

in bibliography. The obtained constitutive law seems to be reliable; however, a further evaluation phase of the proposed model is necessary on the base of new experimental data.

REFERENCES

ACI 2002. ACI440.2R-02 "Guide for the design and construction of externally bonded FRP systems for strengthening concrete structures. *ACI Committee 440*.

Chun, S. & Park, H. 2002. Load carrying capacity and ductility of RC columns confined by carbon fiber reinforced polymers, *Proc. of the International Conference ICCI'02*.

Faella, C., Realfonzo, R. & Salerno, N. 2004. Sulla resistenza e deformazione di elementi in c.a. confinati con tessuti in FRP, *Proc. of the XI Conf. ANIDIS*, Genova, (in italian).

Fardis, M.N. & Khalili, H. 1982. FRP-encased concrete as a structural material, *Magazine of Concrete Research*, 34 (122), 191–202.

Karbhari, V.M. & Gao, Y. 1997. Composite jacketed concrete under uniaxial compression – verification of simple design equations, *J. of Materials in Civil Eng.*, ASCE, 9(4).

Lam, L. & Teng, J.G. 2002. Strength models for Fiber-Reinforced Plastic-confined concrete, *Journal of Structural Engineering*, ASCE, 128(5), 612–623.

Mander, J.B., Priestley, M.J.N. & Park, R. 1988. Theoretical stress-strain model for confined concrete, *Journal of Structural Engineering*, ASCE, 114(8),1824–1826.

Mirmiran, A. & Shahawy, M. 1997. Behavior of concrete columns confined by fiber composites, *Journal of Structural Engineering*, ASCE, 123(5), May, 583–590.

Mirmiran, A., Shahawy, M., Samaan, M., El Echary, H., Mastrapa, J.C. & Pico, O. 1998. Effect of column parameters on FRP-confined concrete, *J. of Comp. for Const.*, ASCE, 2(4).

Pantazopoulou, S.J. & Mills, R.H. 1995. Microstructural Aspects of the mechanical response of plain concrete, *ACI Materials Journal*, Vol. 92, November–December, 605–616.

Popovics, S. 1973. Numerical approach to the complete stressstrain relation for concrete, *Cement and Concrete Res.*, Vol. 3(5), 583–599.

Richart, F.E., Brandtzaeg, A. & Brown, R.L. 1929. The failure of plain and spirally reinforced concrete in compression, *Eng. Exp. Station*, Bull. 190, Univ. of Illinois, Urbana, III.

Saafi, M., Toutanji, H.A. & Li, Z. 1999. Behavior of concrete columns confined with fiber reinforced polimer tubes, *ACI Materials Journal*, Vol. 96, No 4, July–August, 500–509.

Samaan, M., Mirmiran, A. & Shahawy, M. 1998. Model of Concrete Confined by Fiber Composites, *Journal of Structural Engineering*, ASCE, Vol.124, No 9,1025–1031.

Seible, F., Priestley, M.J.N., Hegemier, G.A. & Innamorato, D. 1997. Seismic retrofit of RC columns with continuous carbon fiber jackets. *J. of Comp. for Const.*, ASCE, 1(2), 52–56.

Spoelstra, M.R. & Monti, G. 1999. FRP-confined concrete model, *J. of Comp. for Construction*, ASCE, 3(3), 143–150.

Teng, J.G., Chen, J.F., Smith, S.T. & Lam, L. 2002, FRP-strengthened RC structures. *Ed. by John Wiley & Sons, Ltd.*

Toutanji, H.A. 1999. Stress-strain characteristics of concrete columns externally confined with advanced fiber composite sheets. *ACI Materials Journal*, 96 (3), 397–404.

Xiao, Y. & Wu, H. 2000. Compressive behaviour of concrete confined by carbon fiber composite jackets, *J. of Materials in Civil Engineering*, ASCE, Vol. 12(2), May, 139–146.

Xiao, Y. & Wu, H. 2001. Concrete stub columns confined by various types of FRP jackets, *Proc. of the Conf. on "FRP Composites in Civil Engineering"*, CICE, Hong Kong.

FRP Composites in Civil Engineering – CICE 2004 – Seracino (ed)
© 2005 Taylor & Francis Group, London, ISBN 90 5809 638 6

Debonding in FRP strengthened RC beams: comparison between code provisions

C. Faella & E. Martinelli
Dept. of Civil Engineering, University of Salerno, Italy

E. Nigro
Dept. of Structural Analysis and Design, University of Naples "Federico II", Italy

ABSTRACT: Managing with existing structures is one of the most frequent tasks for today's structural engineers. One of the most effective way for improving the flexural strength of RC members consists in bonding FRP laminates at their soffit in order to upgrade the existing steel bars. For this reason, strengthening RC beams by Externally Bonded FRP laminates is getting more and more common and the following Code Provisions have been issued in various countries. One of the most important problems to be faced when managing FRP strengthened beams deals with the possible premature failure due to debonding between the adhesive layer and concrete. Various code provisions will be examined and compared in the present paper for obtaining some indications about the different safety levels achievable after complying them.

1 INTRODUCTION

In the last decade a lot of research efforts have been carried out for understanding the behavior of reinforced concrete beams strengthened by externally bonded FRP. The key subject of these studies is the mechanical characterization of the FRP-to-concrete adhesive interface. Different contributions about this topic have been summarized and compared by Chen & Teng (2001). Roberts (1988) provided a simplified model for evaluating interface stresses in FRP (or even steel) strengthened beams; simplified equations for evaluating shear and normal stresses throughout the FRP-to-concrete interface have been provided by assuming linear elastic behavior of the adhesive interface. Moreover, Saadatmanesh et al. (1998) provided similar relationships even obtained under simplified hypotheses for the interface behavior; both experimental and numerical comparisons pointed out that applying simplified analytical formulae results in a close approximation of the complex stress pattern developing throughout the interface.

After these studies and various relevant field applications, strengthening RC beams by Externally Bonded FRP laminates is getting more and more common and the following Code Provisions have been issued in various countries:

– *fib* bulletin 14 (2001) in Europe;
– ACI 440 (2002) in the United States;
– JSCE Recommendations (2001) in Japan.

One of the most important problems to be faced when managing FRP strengthened beams deals with the possible premature failure due to debonding between the FRP laminate and concrete. Indeed, that is one of the most widely studied phenomena in the scientific literature dealing with FRP strengthening of RC members, both under the experimental and theoretical standpoint (Faella et al., 2002). Codes of practice take the main conclusions of such studies to provide different recommendations for checking bond effectiveness under both serviceability and ultimate limit state.

In the present paper, the main provisions dealing with bond checks and given by the three documents listed above will be compared in order to point out the main parameters which they depend on. Moreover, the different level of severity of the various methods will be emphasized and the role played by the mechanical models and by the values assumed for the mechanical properties will be emphasized as well. In this way it will be possible to state why the check procedure suggested by a code could be more or less severe than the others and which are the relationships between the models on which they are based. The performances of the examined methods will be also verified on the basis of some experimental tests available in the technical literature or conducted by the authors.

2 OVERVIEW OF THE MAIN CODES

Before going in depth about the different methodologies provided by the various codes for checking

the safety of the FRP strengthened RC members, it is important to emphasize that the experimental evidence demonstrates that additional failure modes can be observed for a FRP strengthened RC beam with respect to the usual RC members in flexure. For example, JSCE Recommendations (2001) introduce the following failure modes for the Ultimate Limit State:

- crushing of concrete after yielding of steel reinforcement;
- concrete crushing;
- anchorage failure of the continuous fiber sheet;
- fiber-sheet-to-concrete interface failure due to the progress of flexural cracking and shear cracking;
- breakage of the continuous fiber sheet after yielding of steel reinforcement.

The first two modes deals with the flexural strength of the strengthened section and can be checked by considering the usual hypotheses for the section behavior, mainly consisting in assuming that plane sections remain plane after beam deformation: strain offset can be assumed for scaling the FRP strain with respect to the one of the beam suffit due to initial strain generally present in beam before strengthening (*fib* bulletin 14, 2001). On the contrary, the last three failure modes depends on the presence of the FRP as a strengthening element. Indeed, the last one consisting in FRP tearing is quite unlikely to occur, especially for carbon fibers, due to the significant strength of fibers. Premature failure due to loss of bonding is much more usual to occur instead of FRP rupture. For this reason the third and the fourth failure modes have to be checked as ultimate limit states for FRP strengthened beams; the three codes listed in the introductory chapter suggest different methodologies for checking this ULS condition.

Finally, it is interesting to underline that the presence of the externally bonded FRP strengthening results in further checks even for at the Serviceability Limit State. However, only the european document (*fib* bulletin 14, 2001) provides an explicit check for interface stresses with the aim of controlling the long term damage.

In the next sections, the various provisions will be shortly overviewed and compared one another in terms of their mechanical meaning and implications.

2.1 *ACI 440.2 R-02 (2002)*

The ACI 440 (2002) document provides a simple implicit way for verifying that premature failures due to loss of bonding could not occur neither in the anchorage zone nor throughout all the interface length. In other words, it assumes a limited strain development in the FRP plate when determining the ultimate bending moment of the strengthened section. The following relationship is suggested:

$$\varepsilon_{f,e} = \kappa_m \cdot \varepsilon_{f,u} \tag{1}$$

where the κ_m factor can be evaluated as follows (ACI440/02-Eq. 9.2):

$$\kappa_m = \begin{cases} \dfrac{1}{60\varepsilon_{f,u}} \cdot \left(1 - \dfrac{n_f E_f t_f}{360000}\right) & \text{if } n_f E_f t_f \le 180000 \\ \dfrac{1}{60\varepsilon_{f,u}} \cdot \left(\dfrac{90000}{n_f E_f t_f}\right) & \text{if } n_f E_f t_f > 180000 \end{cases} \tag{2}$$

In every cases κ_m must be lesser than 0.90. Equations (1) and (2) point out the key role played by the FRP axial stiffness represented by the product $E_f t_f$ between its Young's Modulus and thickness; indeed, the number n_f of plies utilized in the strengthening intervention magnifies the effect of the FRP axial stiffness in reducing the effective strain that can be utilized for developing the ultimate bending moment without debonding due to premature failure. The FRP contribution to the bending nominal bending moment defined by the ACI provision is generally reduced by multiplying the FRP tensile stress by the parameter $\Psi_f = 0.85$. Moreover a coefficient ϕ must be also considered for obtaining the ultimate bending moment, resulting in an equivalent reduction of the effective strain in FRP, named "design value" in the following. Both curves referred to nominal and design value (obtained for $\phi = 0.9$) of the effective strain are represented in Figure 1, but in the following only the strain design values will be considered.

No specific controls dealing with Serviceability Limit States are provided by ACI 440 (2002), other than the ones that apply for usual reinforced concrete members (stress limitation in service, deflection check etc.).

2.2 *JSCE recommendations*

The Japanese Code of Standards (JSCE Recommendations, 2001) introduces an explicit methodology for checking the FRP strengthened beams against the premature failure due to loss of bonding. A double check procedure is provided consisting in assessing that no loss of bonding occurs neither in the anchorage zone nor along the adhesive interface. Pull out tests and theoretical studies (see, for example, Faella et al., 2002) have pointed out that the ultimate strength of a FRP-to-concrete adhesive joint depends on the fracture energy G_f (mainly in mode II) of concrete and of the Young's Modulus and thickness of the FRP plate. Based on these experimental and theoretical findings, the following check can be carried out for verifying that the FRP plate subjected to a tensile stress σ_f in correspondence of the first bending crack of the beam does not fail due to anchorage failure (JSCE Rec./ 2001 – Eq.6.4.1):

$$\sigma_f \le \sqrt{\frac{2G_f E_f}{t_f}} \tag{3}$$

Indeed, the distance ranging between the end section of the FRP plate and the position of the first flexural crack should affect the ultimate strength of the FRP-to-concrete adhesive joint (see Faella et al., 2002). Nevertheless, no relationships have been suggested by the japanese code to account for this effect. Moreover, a quite similar relationship is proposed for checking the adhesive interface between two adjacent flexural cracks against the loss of bonding. Such a check can be carried out by verifying that the following inequality holds (JSCE Rec./2001 – Eq.6.4.2)

$$\Delta\sigma_f \le \Delta\sigma_{f,max,JSCE} = \sqrt{\frac{2G_f E_f}{t_f}} \qquad (4)$$

between the axial stress variation $\Delta\sigma_f$ throughout two subsequent cracks and the corresponding interface strength $\Delta\sigma_{f,max,JSCE}$. Consequently, no substantial difference exists between the verification formulae suggested for anchorage and interface check against loss of bonding (namely, equations (3) and (4)).

Finally, it is useful to remember that a value $G_f = 0.50$ N/mm can be assumed in lack of specific experimental pull-out tests. Moreover, a crack distance ranging between 150–250 mm is suggested to be assumed in evaluating the stress variation $\Delta\sigma_f$.

2.3 *Fib bulletin 14*

fib bulletin 14 (2001) is not just a code of standard in a strict sense, but is aimed to collect the most important contributions about verifying FRP-strengthened RC members. For this reason, it is possible to find more than one approach for facing the problem of the safety verification of strengthened members. That is the case of RC beams strengthened by externally bonded FRP whose verification of the adhesive interface against premature failure phenomena can be carried out by means of three quite different approaches. The second one will be presented in detail and utilized in the next sections of the present paper. The first and the third ones can be summarized as follows:

– according to approach #1 the anchorage verification can be carried out essentially by controlling that a relationship like equation (1) holds. Indeed, a reducing factor accounting for the distance between the end of the FRP plate and the first crack is also provided. Moreover, debonding failure throughout the adhesive interface is prevented by limiting FRP ultimate strain to an effective value ranging between 0.0065 and 0.0085. Such a latter provision is compared in Figure 1 to the strain limitation imposed by equations (1) and (2) according to ACI 440 (2002).
– Even according to approach #3 a verification of the end anchorage is provided just like the one provided in approach #1. On the contrary, premature failure throughout the interface is obtained in terms of shear stress evaluated in a simplified way by considering the case in which steel bar are elastic or yielded.

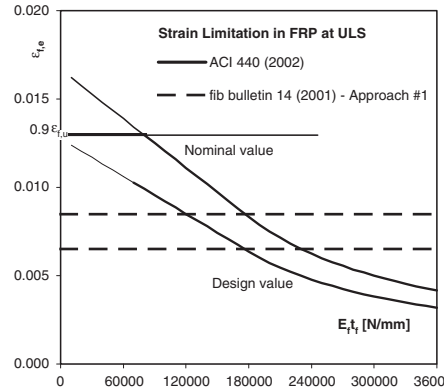

Figure 1. Effective FRP strain limitation for avoiding premature failure according to two different code provisions.

Beyond the great apparent difference characterizing the various approaches under the formal standpoint, Faella et al. (2003) pointed out that a substantial equivalence could be recognized between such methodologies by assuming suitable values for the mechanical properties utilized in calculations.

Finally, it is important to underline that an explicit stress limitation in service is provided by the european document based on the Roberts simplified model for evaluating interface shear stress throughout the FRP interface with particular attention to the FRP cut-off section.

2.3.1 *Ultimate Limit State according to Approach #2*

Approach #2 is surely the most original and organic for verifying Ultimate Limit State against FRP interface loss of bonding. It works in a way that is not so different by the JSCE methodology. First of all anchorage verification can be carried out utilizing equation (3). A possibly reduced strength due to an insufficient distance between FRP cut-off section and the first crack for developing the transferring length throughout the FRP-to-concrete joint can be considered.

Stress check against delamination between two adjacent cracks can be carried out by means of a relationship like the following one:

$$\Delta\sigma_f \le \Delta\sigma_{f,max,fib}\,. \qquad (5)$$

A quite complex relationship can be stated for evaluating $\Delta\sigma_{f,max,fib}$ accounting for both crack average distance s_{rm} and the initial stress σ_{min} between the

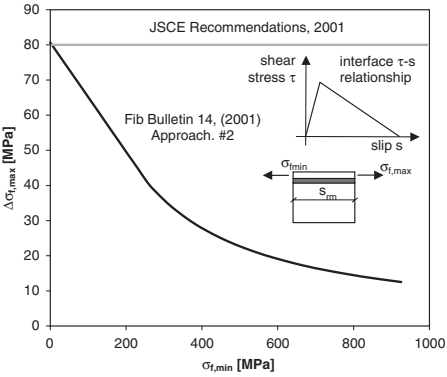

Figure 2. Relationship between the maximum stress variation in FRP between two cracks evaluated according to JSCE and *fib* provisions.

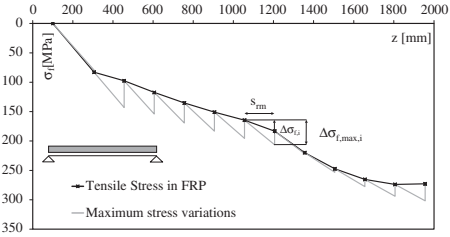

Figure 3. Interface verification according to *fib* bulletin 14 (2001) – Approach #2.

two cracks and the fracture energy G_f of the adhesive interface:

$$\Delta\sigma_{f,max,fib} = \Delta\sigma_{f,max,fib}(\sigma_{min}, G_f, s_{rm}). \quad (6)$$

Figure 2 shows the relationship between the interface strength between two adjacent cracks estimated according to JSCE and *fib* provisions (determined for a given value of s_{rm} and G_f).

fib bulletin also provides relationships for estimating the average distance to be assumed between flexural cracks; Figure 3 shows the evaluation of the stress variation $\Delta\sigma_{f,i}$ and the corresponding maximum value $\Delta\sigma_{f,max,i}$ (by omitting the subscript "fib" for the sake of brevity) according to the general relationship (6) ; such calculations have to be carried out for each segment between two adjacent cracks.

The possible definition of the global safety factor SF for the analyzed beam can be stated as follows:

$$SF = \min_i \left(\frac{\Delta\sigma_{f,max,i}}{\Delta\sigma_{f,i}} \right) \geq 1. \quad (7)$$

which gives the analytical condition because the stress verification against interface loss of bonding does not occur.

2.3.2 *Serviceability limit state*

Stress limitation under service loads is imposed to interface shear stress evaluated according to a linear elastic analysis; a simplified formula is suggested (Roberts, 1988):

$$\tau_{fl} = \left[V_{x=0} + \sqrt{\frac{G_a}{E_f t_f t_a}} \cdot M_{x=0} \right] \cdot \frac{t_f \cdot (h - x_c)}{I_c}. \quad (8)$$

where $V_{x=0}$ and $M_{x=0}$ are the shear force and the bending moment in the FRP cut-off section.

Shear stress evaluated by equation (8) can be compared with a suitable strength for the adhesive interface. Fib bulletin assumes f_{ctk} as a limit for interface shear stress, being f_{ctk} the characteristic value of the concrete tensile strength.

Two important remarks have to be pointed out before going to the next sections:

- no mention is done about interface normal stresses, arising as well as shear ones, and even affecting the FRP-to-concrete interface behavior;
- quasi-permanent load condition is considered in evaluating $V_{x=0}$ and $M_{x=0}$ to determine interface shear stress according to equation (8); the choice of such a load combination is likely due to the aim of controlling long terms behavior of the adhesive interface.

With reference to the last remark, it is important to observe that stress limitation during service life of beam must be also aimed to control interface deformations in order to verify that they remain within the elastic threshold; interface slips overcoming the elastic range of the ideal bi-linear relationship (also represented in Figure 2) would result in progressive interface damage under cyclic loads. For this reason it would appear more rational to refer the above check to rare load combination to strictly control the possible excursions of the interface slip beyond the elastic range.

3 CODE PROVISIONS AND EXPERIMENTAL RESULTS

The relationships reported and commented above for performing the ULS check against failure due to loss of bonding have pointed out the key role played by the axial stiffness of the FRP plate represented by the $E_f t_f$ parameter. Experimental evidence confirms the general trend resulting in a substantial reduction of the FRP effective strain as $E_f t_f$ parameter increases.

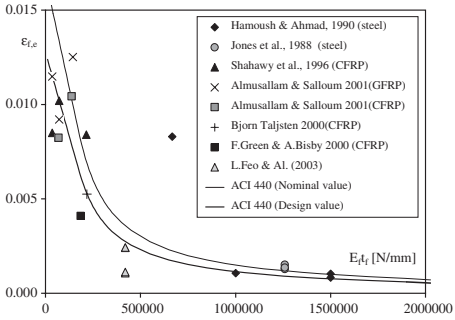

Figure 4. Experimentally observed values of the FRP strain at debonding.

Figure 4 shows the values measured in experimental tests on FRP-strengthened beams in flexure failing after FRP debonding. The general trend interpreted by equation (1) and (2) according to ACI 440 document is confirmed by the distribution of the experimental points on the plane.

Indeed, scatter affecting the experimental measures is not negligible, but the ACI curve generally fit very closely the points representing them. For this reason, such a curve will be often taken as a reference in the following figures.

4 PARAMETRIC ANALYSIS

The present section deals with presenting the main results of a wide parametric analysis carried out on a typical RC member strengthened by FRP; such an analysis is aimed to point out the key differences among the various verification methods under the quantitative standpoint. A simply supported ribbed slab typical of RC floors and roofs is considered (Figure 5).

Such a structural member is characterized by a typical tee shaped section (Figure 6) whose fixed dimensions are listed in Table 1.

The other parameters are assumed variable in the following ranges:

- the span length to slam depth L/H_t ranges between 20 and 30;
- the steel geometric percentage ranges between 0.2 and 0.4%;
- the sustained load g_k is a relevant parameter if we suppose that no propping systems would be present during the strengthening intervention; its value is chosen as a fraction of the ultimate load of the unstrengthened section. Let M_g and $M_{u,0}$ be the bending moment due to g_k and the ultimate flexural strength of the unstrengthened section, respectively: in the following parametric application the $M_g/M_{u,0}$ ratio ranges between 0.1 and 0.90;
- the distance *a* between the FRP-cut-off section and the slab support is assumed ranging between 0 and L/4.

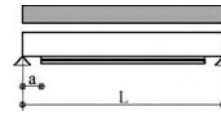

Figure 5. Structural scheme of the RC ribbed slab considered in the parametric analysis.

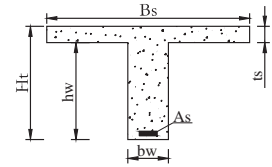

Figure 6. Transverse section of the slab.

Table 1. Fixed dimensions of the transverse section.

Dimension symbol	Length [mm]
B_s	500
b_w	100
t_s	40
H_t	200

The cases generated by combining the various numerical values of the parameters listed above have been analyzed according to the provisions of the main codes of standards in order to obtain the value of the maximum live load q_k resulting in debonding failure when combined with the sustained load g_k. According to *fib* bulletin – Approach #2 such a value can be found by imposing the equality condition in relationship (7). In such a manner, the ultimate value of the resisting bending moment M_u of the strengthened beam achieved before debonding occurs can be evaluated and the corresponding values $\varepsilon_{f,e}$ of the strain developed in FRP can be obtained. No details about the numerical procedure adopted in calculations will be provided here, other than it deals with the hypothesis of plane sections for beams and works with nonlinear constitutive loads for structural materials (fiber approach has been adopted for evaluating the force and the moment corresponding to normal stresses in concrete).

A similar procedure can be carried out for determining the effective values $\varepsilon_{f,e}$ of FRP strain according to JSCE Recommendations.

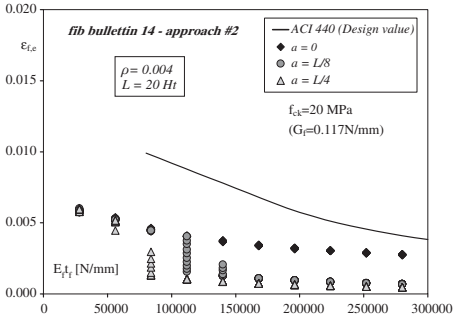

Figure 7. *fib* bulletin – Approach #2: FRP effective strain versus axial stiffness ($L/H_t = 20$ – $M_g/M_{u,0} = 0.1$–0.9).

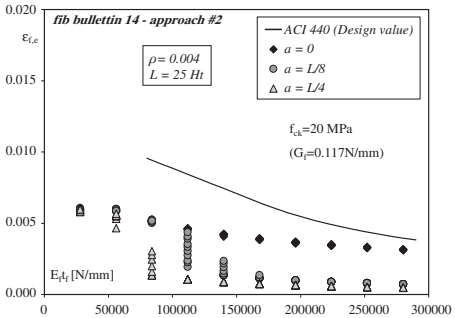

Figure 8. *fib* bulletin – Approach #2: FRP effective strain versus axial stiffness ($L/H_t = 25$ – $M_g/M_{u,0} = 0.1$–0.9).

The first series of figures (from Figure 7 to Figure 9) deals with quantifying the axial strain developed in the FRP plate in correspondence of the external load resulting in interface debonding according to *fib* bulletin provisions.

Even Figure 7, Figure 8 and Figure 9 show that the resulting effective values for FRP axial strain are generally much lower than the corresponding values provided by equation (1) and (2) according to ACI 440 provision.

By comparing the above referred figures it is possible to recognize a slight influence of the spanlength-to-beam-depth ratio on the FRP strain which tend to increase with thickness itself.

In each one of the same figures three different values of the distance *a* between the external support and the FRP cut-off section have been considered. The greater strain values develop when $a = 0$ is considered; in such case the beam failure is uniquely due to loss of bonding throughout the interface (generally in correspondence of the section where steel yields), while no anchorage crisis occurs. In the other cases ($a = L/8$ and $a = L/4$) both failure modes can be observed; for the smaller values of the $E_f t_f$ parameter, the effective strain developed in FRP plate is not significantly affected by distance *a*. On the contrary, the *a* parameter becomes significant when $E_f t_f$ increases; for example, with reference to the case $a = L/8$, a sudden change can be observed between the first points and the ones obtained for greater $E_f t_f$ values; this fact means the two different failure modes occur in the two cases depending on $E_f t_f$.

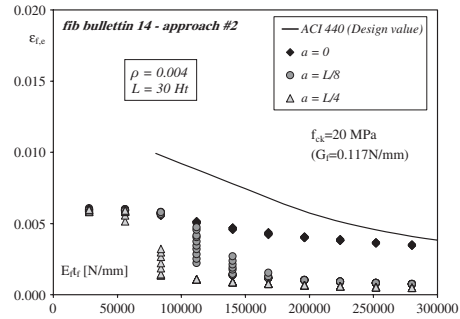

Figure 9. *fib* bulletin – Approach #2: FRP effective strain versus axial stiffness ($L/H_t = 30$ – $M_g/M_{u,0} = 0.1$–0.9).

The sudden switching between the two failure modes can be clearly observed in Figure 7, Figure 8 and Figure 9 where anchorage crisis (resulting in very low strains developed in FRP) prevent the bonding failure throughout the interface as $E_f t_f$ increases. Moreover, anchorage failure for $a = L/4$ is more frequent to occur than in the case of $a = L/8$, as one could easily foresee.

Calculation resulting in Figure 7, Figure 8 and Figure 9 have been conducted with reference to a fracture energy value determined according to *fib* document ($G_f = 0.117$ N/mm).

It is important to observe that experimental findings and theoretical models (Faella et al., 2002) show fracture energy values generally greater than the one assumed by the European document; effective strain, values closer to the ACI ones, could be obtained by adopting such values for G_f.

Figure 10 shows the difference between *fib* and JSCE methodologies under the quantitative standpoint. Due to the fact that $\Delta\sigma_{f,max,JSCE}$ is always greater than $\Delta\sigma_{f,max,fib}$ for a given value of fracture energy G_f and crack spacing s_{rm}. Black points in Figure 10 are generally characterized by larger effective strain values.

The effect of fracture energy on the effective axial strain developed in FRP when loss of bonding occur is showed in Figure 11 with reference to JSCE Recommendations for the cases of $a = L/8$. Two values have been considered for G_f: the first

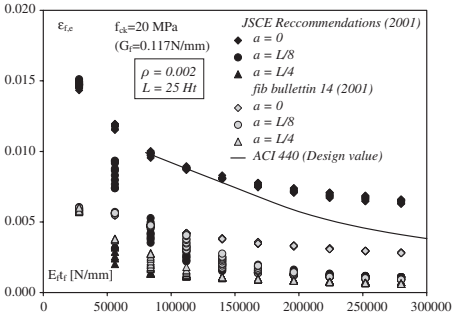

Figure 10. Comparison between codes in terms of FRP effective strain (G_f is always assumed according to the values provided by *fib* for $f_{ck} = 20$ MPa – $M_g/M_{u,0} = 0.1$–0.9).

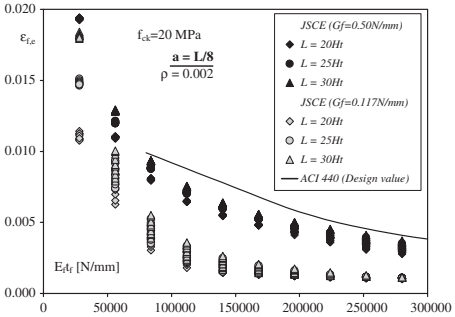

Figure 11. JSCE Recommendations: FRP effective strain depending on fracture energy value ($M_g/M_{u,0} = 0.1$–0.9).

one ($G_f = 0.117$ N/mm) is obtained according to *fib* document provisions for concrete, whose compressive strain is $f_{ck} = 20$ MPa; the second one ($G_f = 0.50$ N/mm) is suggested by JSCE in lack of experimental data about FRP-to-concrete adhesive joint. Figure 11 shows that effective strain obtained assuming the latter one is between twice and three times the corresponding one determined for the former value (as it would be possible to foresee because interface strength in equation (4) is proportional to the square root of G_f). Moreover, Figure 12 shows the influence of crack spacing assumed in equations (6): generally speaking, verification are as severe as crack spacing increases. For this reason, in Figure 12 points determined for closer cracks result higher than the corresponding ones obtained for the greater value of s_{rm}.

The next three figures deals with the $M_u/M_{u,0}$ ratio between the ultimate bending moment M_u of the FRP-strengthened section and the corresponding value $M_{u,0}$ characterizing the unstrengthened one.

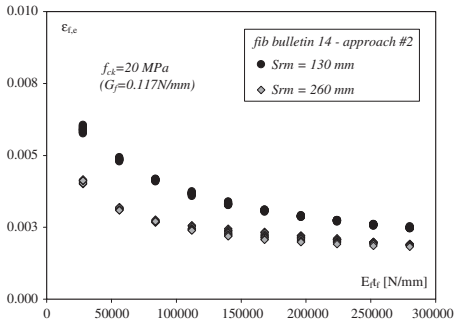

Figure 12. Influence of crack spacing on the resulting effective strain for FRP according to *fib* bulletin – Approach #2 ($M_g/M_{u,0} = 0.1$–0.9).

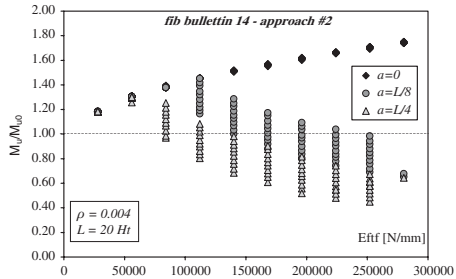

Figure 13. *fib* bulletin – Approach #2: ultimate bending strength ratio depending on FRP cut-off to support distance ($L/H_t = 20$ – $M_g/M_{u,0} = 0.1$–0.9).

The importance of the failure mechanism on the effectiveness of the strengthening intervention has been already pointed out in the previous figures where FRP strains developed when debonding are hugely affected by anchorage failure. Figure 13, Figure 14 and Figure 15 confirm such a trend emphasized in the previous ones. All the figures referred above show that $M_u/M_{u,0}$ ratio (and, consequently, the effectiveness of the strengthening intervention itself) increases with $E_f t_f$ parameter for $a = 0$. On the contrary, if $a > 0$ the anchorage failure can occur resulting in a progressive decrease of the $M_u/M_{u,0}$ ratio after a given value of the $E_f t_f$ parameter. Reduction in $M_u/M_{u,0}$ ratio when $a = L/4$ is generally greater than the case of $a = L/8$ because the greater the distance a, the more prone is the beam to fail in anchorage. Sometimes the $M_u/M_{u,0}$ ratio is lesser that one because anchorage crisis occurs for external loads lower than the ones corresponding to the ultimate bending moment of the unstrengthened member. Comparing Figure 13, Figure 14 and Figure 15, $M_u/M_{u,0}$ ratio seems to be not so affected by the L/H_t ratio.

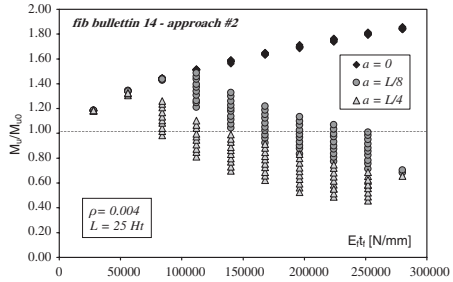

Figure 14. *fib* bulletin – Approach #2: ultimate bending strength ratio depending on FRP cut-off to support distance ($L/H_t = 25$ – $M_g/M_{u,0} = 0.1$–0.9).

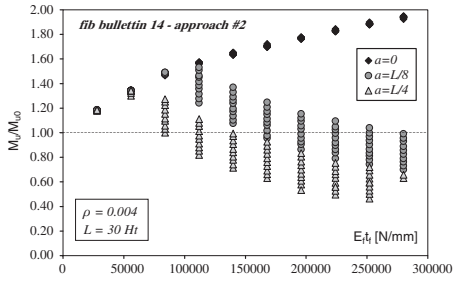

Figure 15. *fib* bulletin – Approach #2: ultimate bending strength ratio depending on FRP cut-off to support distance ($L/H_t = 30$ – $M_g/M_{u,0} = 0.1$–0.9).

Finally, it is interesting to observe the differences between Ultimate Limit State versus Serviceability Limit State in terms of the maximum value of the net load q_k complying with both the conditions mentioned above. Only the *fib* document provides an interface stress limitation. For this reason the following three different conditions, always dealing with fib bulletin 14 provisions, have been considered:

– ULS verification against loss of bonding;
– SLS verification under the quasi permanent combination (as suggested by fib bulletin);
– SLS verification under the rare load combination (as needed for limiting the interface deformations within the elastic range and, consequently, crisis due to progressive damage).

The resulting values of the net load obtained according to the three verifications listed above are represented in Figure 16 and Figure 17 with respect to $E_f t_f$ parameter. For the adhesive stiffness in equation (8) a value $K_h = G_a/t_a = 1000\ N/mm^3$ have been considered. Figure 16, obtained assuming $a = L/8$, shows that SLS verification against quasipermanent load

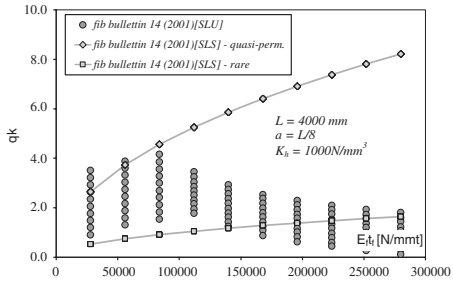

Figure 16. *fib* bulletin 14: comparison between the net live load against ultimate and serviceability check for loss of bonding ($a = L/8$ – $M_g/M_{u,0} = 0.1$–0.9).

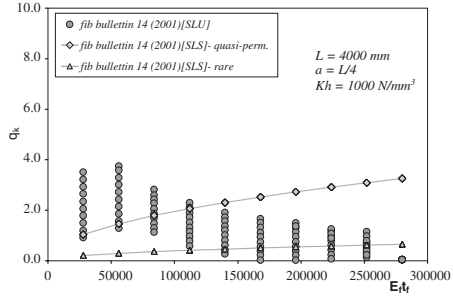

Figure 17. *fib* bulletin 14: comparison between the net live load against ultimate and serviceability check for loss of bonding ($a = L/4$ – $M_g/M_{u,0} = 0.1$–0.9).

combination never controls the net load value. On the contrary, SLS verification under the rare load combination is generally in the same range of the ULS check.

On the contrary, in Figure 17 ($a = L/4$) SLS condition, especially under rare load combination, often controls the value of the resulting net load.

5 CONCLUSIONS

The main codes provisions dealing with strengthening RC members by externally bonding FRP plates have been compared even under the conceptual and quantitative standpoint.

Analogies and differences among them have been emphasized and shortly commented. All the considered provision for the ULS consist in substantially similar assumptions dealing with the fact that stress variation between two flexural cracks has to be controlled for avoiding loss of bonding. In a substantially equivalent way, the FRP strain can be limited by a suitable effective value, possibly depending on the FRP

characteristics. A parametric analysis shown that a quantitative equivalence can be recognized by utilizing suitable values of the key parameters (namely, the fracture energy G_f). In fact, effective strains evaluated according to *fib* provisions are generally lower that the ones suggested by ACI document; however, experimental results pointed out that larger values should be assumed for G_f parameter.

Another key aspect has been finally focused by emphasizing the relationship between ULS and SLS conditions on the resulting value of the net load of the strengthened member.

REFERENCES

Chen J. F., Teng J. G. 2001: Anchorage Strength Models for FRP and Plates Bonded to Concrete, ASCE Journal of Structural Engineering, vol. 127, No. 7, July, 784–791.

Roberts T. M. 1988: Approximate analysis of shear and normal stress concentrations in the adhesive layer of plated RC beams, The Structural Engineer, Vol. 66, No. 5, 85–94.

Malek A. M., Saadatmanesh H., Ehsani M. R. 1998: Prediction of failure load of R/C beams strengthened with FRP plate due to stress concentration at the plate end, ACI Structural Journal, Vol. 95, No. 2, 142–152.

fib: Bulletin d'information n. 14 2001: Externally bonded FRP reinforcement for RC structures.

Faella C., Martinelli E., Nigro E. 2002: Aderenza tra calcestruzzo e fogli di FRP utilizzati come placcaggio di elementi inflessi. – Parte seconda: modelli teorici ed elaborazioni numeriche (in Italian), XIV Congresso C.T.E., Mantua (Italy).

ACI Committee 440.2 R-02 2002: Guide for the Design and Construction of Externally Bonded FRP Systems for Strengthening Concrete Structures, Revised 28.

JSCE 2001: Recommendations for upgrading of concrete structures with use of continuous fiber sheets, Concrete Engineering Series 41.

CEB 1985: Design Manual on "Cracking and Deformations", Prepared by Comité Euro-International du Béton.

Faella C., Martinelli E., Nigro E. 2003: Sulle verifiche di aderenza in travi inflesse in cemento armato placcate con materiali FRP (in Italian), Proceedings of the 32nd Conference of the Italian Society for Stress Analysis (AIAS), Salerno (Italy), Paper 195.

Almusallam Al-Salloum 2001: Ultimate strength prediction for RC beams externally strengthened by composite materials, Composites Structures – Part B, 32, pp. 609–619.

Shahawy, M. A., Arockiasamy, M. 1996; Beitelman, T.; Sowrirajan, Reinforced concrete rectangular beams strengthened with CFRP laminates Composites Structures – Part B, 27, pp. 225–233.

Di Nardo E., Feo L., Giordano A. 2003: Valutazione Numerico-Sperimentale Delle Tensioni Interlaminari In Strutture In C.A. Rinforzate Con Lamine Pultruse in CFRP (in Italian), Proceedings of the 32nd Conference of the Italian Society for Stress Analysis (AIAS), Salerno (Italy).

FRP research in the Middle East (special session)

FRP Composites in Civil Engineering – CICE 2004 – Seracino (ed)
© 2005 Taylor & Francis Group, London, ISBN 90 5809 638 6

Numerical modeling of RC beams strengthened with CFRP under dynamic loading

S. Mohammadi & A.A. Mousavi Khandan
Civil Department, Faculty of Engineering, University of Tehran, Tehran, Iran

ABSTRACT: In recent years, strengthening of tensile face of reinforced concrete beams with fiber reinforced polymer (FRP) sheets has been increased as a popular approach for flexural strengthening of reinforced concrete (RC) beams. This paper presents a combined finite/discrete element method based on 2D and 3D modeling of a strengthened RC beam subjected to dynamic loadings. Complexity of interaction of different contact elements in the form of discrete element method and taking to account all failure criteria including cracking in concrete or delamination of CFRP composite laminates from concrete substrate and etc. makes it necessary to do such an analysis for considering complex mechanism of failure. The proposed approach adopts a node to face contact based delamination control to simulate the inter-FRP-RC interactions. The validity of developed algorithm is verified by solving available standard and experimental tests from the literature.

1 INTRODUCTION

Different approaches have been developed to retrofit existing structures due to their damage by loads higher than the design service loads, or by chemical processes due to aggressive environmental conditions. Plate bonding for structural strengthening was utilized in the early 1960s and was used primarily in France and South Africa. Klaiber et al. (1987) & Lander et al. (1981) studied the use of epoxy-bonded steel plates to strengthen bridge girders in Europe, South Africa, and Japan. Later, in 1982 the technique of applying fiber reinforced polymer (FRP) sheets to the tensile face of reinforced concrete (RC) beams were developed for flexural strengthening by Meier (1978) in Switzerland. Because of unique advantages of FRP composites in comparison to the conventional steel bars and plates, such as high strength-to-weight ratio and considerably good resistance to corrosion, they have been widely applied to the strengthening and upgrading of structurally inadequate or damaged concrete structures. Later, the effectiveness of glass-FRP plates bonded to the tension face of the RC beams was experimentally investigated by Saadatmanesh & Ehsani (1991). Extensive research has been carried out on the numerical modeling of concrete beams strengthened by FRP composite. Although finite element analyses (FEA) have been carried out on plated RC beams (Zhang et al. 1997, Ziraba 1995, Arduini et al. 1995, Quantrill et al. 1995, He et al. 1997, Jerome et al. 1997, Rahimi et al. 2001), little success has been made in simulating debonding failures, especially for beams which are under dynamic loads. This is primarily because of the complexity of the problem and the interaction of different interfaces between concrete, steel, FRP plate and adhesive layer. The problem becomes extremely difficult when the RC beam is loaded dynamically, where different geometry, stiffness and interaction between the interfaces before and after debonding or cracking of the RC beam is expected in any new time step. Therefore, adopting a proper debonding model for the adhesive layer and a fracture criterion for concrete cracking is essential for an accurate simulation. In FEA, there are two major approaches representing cracking in concrete structures; discrete and smeared crack approaches. The smeared crack approach which defines a reduced equivalent continuum has some deficiencies such as mesh sensitivity, incapability for taking into account the new geometry and its trend to spread the crack formation over a region of the structure so unable to accurately predict the local fracture failures (Rahimi & Hutchinson 2001). The other essential part of the simulation is the bonding/ debonding behavior of the adhesive layer. In recent years, many efforts have been made to study the interfacial bonding/debonding behaviors. Taljstentheoretically derived a linear equation that calculates the load carrying capacity of FRP-bonded concrete prism under uniaxial tensile loading. More investigations of FRP-concrete interfacial bond models were reported by Yuan et al. (2001) and Nishida et al. (1999), in which several types of nonlinear shear

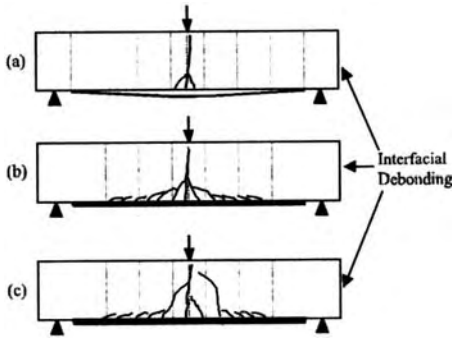

Figure 1. Interfacial debonding failure mode (Zhishen et al. 2003).

stress versus relative displacement (τ–δ_t) relationships were proposed.

By examining the results of a wide range of experimental tests, debonding failures in flexurally strengthened RC beams may be broadly classified into two types: plate end debonding (including cover separation failure and plate end interfacial debonding) in which failure starts from one of the plate ends due to local stress concentration, and intermediate crack induced debonding in which debonding starts from either a flexural crack or a flexural shear crack (Teng et al. 2002). In the cover separation failure microdiagonal cracks that occur in the interfacial concrete finally connect together and lead to the delamination of FRP sheets (Fig. 1b). In this case, it is assumed that the bond strength of adhesive layer is relatively high. The other type of debonding happens within epoxy adhesive layer, which is mainly due to weak or imperfect bond (Fig. 1a). In both of these cases one flexural crack locally occurs at mid span from which the debonding initiates and propagates, no matter if the interfacial debonding happens within adhesive layer or though interfacial concrete. The second major type of debonding is schematically shown in Figure 1c, in which a secondary diagonal shear or flexural crack occurs beside the first flexural concrete crack at mid span. Then, the debonding starts to propagate from the root of the secondary diagonally shear or flexural crack (Zhishen et al. 2003).

In this study, a new approach has been developed which utilizes a combined finite/discrete element method. The proposed algorithm consists of full material and geometry non-linearities. The Sprenger (Sprenger et al. 2000) criterion is adopted for modeling the bonding behavior of FRP-concrete interface. To verify the performance of the proposed algorithm an experimentally tested RC beam subjected to dynamic loading is simulated and the results will be discussed (Jerome et al. 1997).

2 PRINCIPLES OF MODELING

In this simulation, a combined finite/discrete element method is utilized. All types of non-linearity in material or geometry are considered in this study. Using an "explicit central difference time integration technique" reduces the time of computation, especially for large models. Cracking in the concrete material is considered using a non-linear fracture mechanic method on the basis of plasticity theory and utilizing discrete elements.

The discrete element method, utilizes the principles of penalty based contact mechanics enforcing virtual springs to tie degrees of freedom. Also for modeling bonding/debonding behavior of FRP-concrete interface a mixed mode model was used on the base of Hashin criterion with a bilinear strain softening model.

The use of discrete elements in problems with changing geometry in successive time steps, with its capability of remeshing and adaptivity, provides us with a powerful numerical tool for modeling complex problems. In fact, creation and propagation of crack in a structure can be geometrically followed by remeshing of the finite elements (Mohammadi 2003).

For 3D problems, mixed mode debonding model of FRP-concrete interface developed and Drucker-Prager material model was used in concrete. The overall failure of the model was investigated by monitoring the maximum principal stress.

3 MATERIAL MODELING

There are three major fracture and failure behavior in concrete structures strengthened with FRP composites. So, it's essential to assume proper material models and a suitable delamination criterion in order to conduct a successful simulation.

3.1 *Concrete material model*

The compressive behavior of concrete was modeled by Drucker-Prager material model and an associated flow rule. The Rankine fracture model is utilized to model the concrete behavior in tension while a bilinear strain softening relation is adopted for a smooth non-local release of energy.

3.2 *CFRP material model*

The behavior of CFRP is assumed to be linear elastic and orthotropic till unidirectional CFRP sheets reach their tensile strength as no rupture in CFRP sheets has been reported in experimental tests (Jerome et al. 1997).

3.3 *Material model for FRP-concrete interface*

Debonding in FRP-concrete interface is one of the major failure modes in strengthened RC beams. In the

proposed algorithm, a 3D Hashin model is adopted to predict initiation of interfacial debonding. Primary model has established on the base of softening time independent plasticity model.

Assuming large deformations (though small strains), the rate of the Green-Lagrangian strain tensor is decomposed into an elastic and an inelastic parts. The inelastic strain rate follows the associated flow rule:

$$\dot{\bar{E}} = \dot{\bar{E}}^{el} + \dot{\bar{E}}^{in} \tag{1}$$

$$\dot{\bar{E}}^{el} = \bar{C}\dot{\bar{S}} \tag{2}$$

$$\dot{\bar{E}}^{in} = \dot{\bar{E}}^{pl} = \dot{\lambda}\frac{\delta F}{\delta \bar{S}} \tag{3}$$

Here, $\bar{C}$ is the elasticity matrix for plane isotropic behavior of the material. $\bar{S}$ is the stress matrix, λ is the inelastic coefficient and F is the yield function.

The Hashin delamination criterion is a function of interlaminar stresses $\bar{S}^{33}, \bar{S}^{13}, \bar{S}^{23}$, tensile strength in direction of the thickness Z_0 and tangential strength of layer R_0.

$$\frac{\left(\bar{S}^{33}\right)^2}{Z_o^{\,2}} + \frac{\left(\bar{S}^{13}\right)^2 + \left(\bar{S}^{23}\right)^2}{R_o^{\,2}} \le 1 \tag{4}$$

A plot of the criterion is shown in Figure 2. The yield function $F(\bar{S}, \alpha)$ is obtained by reformulation of the delamination criterion:

$$F\left(\bar{S}, \alpha\right) = g\left(\bar{S}\right) - Z(\alpha) \le 0 \tag{5}$$

$$g\left(\bar{S}\right) = \sqrt{\bar{S}^T A \bar{S}} \tag{6}$$

$$A = \begin{bmatrix} 0 & 0 & 0 & 0 & 0 & 0 \\ 0 & 0 & 0 & 0 & 0 & 0 \\ 0 & 0 & 1 & 0 & 0 & 0 \\ 0 & 0 & 0 & 0 & 0 & 0 \\ 0 & 0 & 0 & 0 & \left(\frac{Z_o}{R_o}\right)^2 & 0 \\ 0 & 0 & 0 & 0 & 0 & \left(\frac{Z_o}{R_o}\right)^2 \end{bmatrix} \tag{7}$$

$Z(\alpha)$ is a linear softening function as follows:

$$Z\left(\alpha\right) = Z_o\left(1 - \mu\alpha\right) \tag{8}$$

And it is depicted in Figure 3. The variable α can be assumed as the equal inelastic strain. The parameter μ

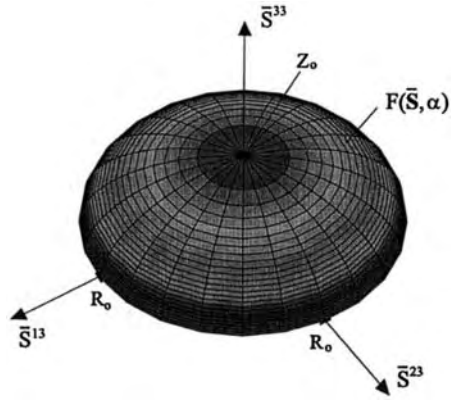

Figure 2. Delamination criterion of Hashin.

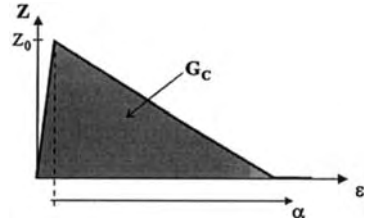

Figure 3. Softening function.

describes the slope of the softening function $Z(\alpha)$. It is a material parameter and can be determined from the critical energy release rate G_c, tensile strength Z_0 and the thickness of the intermediate layer h_T:

$$\mu = \frac{Z_o \times h_T}{2G_c} \tag{9}$$

The rate of the internal variable is defined with the evolution law:

$$\dot{\alpha} = -\dot{\lambda}\frac{\partial F}{\partial Z} \tag{10}$$

The gradient of the yield function is derived as follows:

$$\frac{\partial F}{\partial \bar{S}} = \frac{1}{g(\bar{s})} A\bar{S} = N, \quad \frac{\partial F}{\partial Z} = -1 \tag{11}$$

Substitution of Equation 11 into Equations 1–3 and introducing a backward Euler integration algorithm within a time step $t_{n+1} = t_n + \Delta t$ yields:

$$\bar{E}_{n+1} = \bar{C}^{-1}\bar{S}_{n+1} + \bar{E}_n^{\,pl} + \frac{\lambda}{g\left(\bar{S}_{n+1}\right)} A\bar{S}_{n+1} \tag{12}$$

$$\bar{S}_{n+1} = \left[\bar{C}^{-1} + \frac{\lambda}{Z(\alpha_{n+1})} A \right] \left[\bar{E}_{n+1} - \bar{E}_n^{pl} \right] \tag{13}$$

$$\bar{S}_{n+1} = P\bar{E}^{tr} \tag{14}$$

Where subscripts n and $n+1$ denote the quantities of the known converged configuration at time t_n and t_{n+1}, respectively. Updating the internal parameter α is performed using a backward Euler integration:

$$\alpha_{n+1} = \alpha_n + \lambda \tag{15}$$

Linearization of the stress tensor has to be derived for the finite element formulation. After some algebric manipulations we end up with the consistent tangent matrix:

$$\bar{D} = P - \frac{PN(PN)^T}{N^T PN + H} \tag{16}$$

With:

$$H = \frac{Z'}{1 - \lambda \dfrac{Z'}{Z}}, \text{ and } Z' = -\mu \tag{17}$$

4 NUMERICAL SIMULATION

Different classes of problems are simulated to assess the performance of the proposed algorithm. The first one examines the debonding phenomenon in a buckling analysis of a composite panel, and the second one simulates an experimental CFRP strengthened RC beam.

4.1 *Numerical simulation of a composite beam*

A pre-cracked unidirectional composite panel as depicted in Figure 4 is subjected to an incrementally increasing loading until the local and global buckling modes occur (Mohammadi & Forouzansepehr 2003).

Figures 5 and 6 show the predicted buckling modes, where the local and global buckling modes occurred at loads 1410 lbf/in. (246.93 N/mm) and 7310 lbf/in. (1280.18 N/mm), respectively. The results are comparable to the loads 1312 lbf/in. (229.77 N/mm) and 7821 lbf/in. (1396.67 N/mm), reported by Progini (Fig. 6).

4.2 *Example beam and material properties*

A strengthened RC beam, reportedly tested by Jerome & Ross (1997), was analyzed in this study. The dimensions of the simply supported beam were $3 \times 3 \times 30$ in. ($7.62 \times 7.62 \times 76.2$ cm). There was no tensile steel in the beam, while the beam was strengthened by CFRP panels.

The size of the CFRP panels was 3×30 in. and each was composed of three plies. The adhesive material

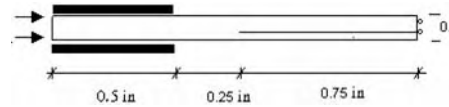

Figure 4. Geometry of a composite panel with an initial interlaminar crack.

Table 1. Material properties of composite panel.

	Value			Value	
Parameter	ksi	MPa	Parameter	lbf/in.	N/mm
E_{xx}	20200	139274.1	G_{IC}^{**}	0.5	0.0876
E_{zz}	1410	9721.6	G_{IIC}^{**}	0.5	0.0876
E_{yy}	1410	9721.6			
G_{xy}	810	5584.75		Unitless	
G_{yz}	546	3764.54	ν_{yz}	0.29	
X_T^*	220	1516.85	ν_{xy}	0.29	
Y_T^*	6.46	44.54	ν_{xz}	0.29	
X_C^*	231	1592.69			
Y_C^*	36.7	253.04			
S^*	15.5	106.87			

* Parameters of Hoffman yield criterion.
** Fracture energy release rate.

Figure 5. Local and global buckling modes.

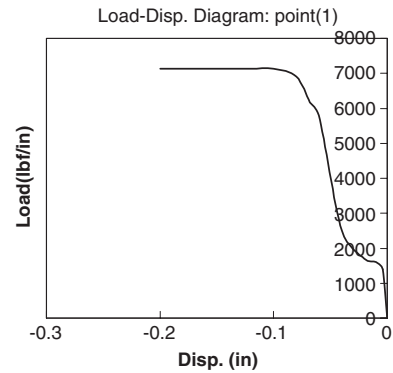

Figure 6. Displacement versus time in local and global buckling modes.

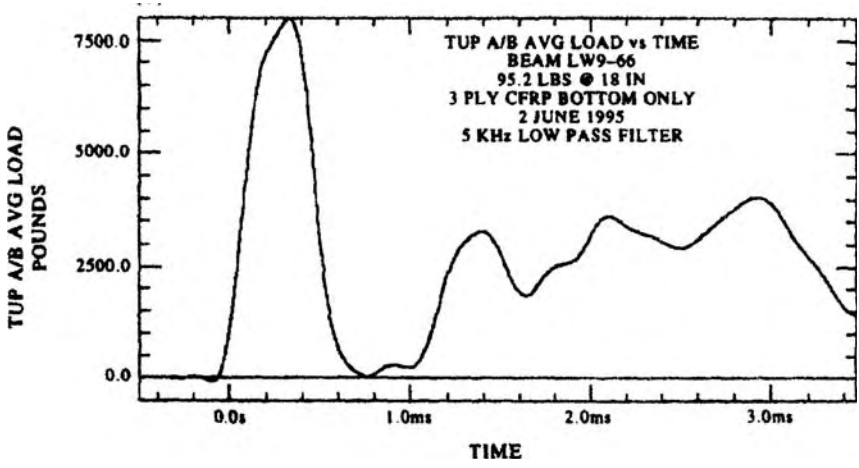

Figure 7. Tup load–time curve (Jerome et al. 1997).

Table 2. Concrete material model parameters.

Parameter	Value
E_0 (initial tangent modulus)	2.4×10^4 MPa
ν (Poisson's ratio)	0.2 (unitless)
f_t (Uniaxial cut-off tensile strength)	4.35 MPa
f_c (Uniaxial maximum compressive strength)	46.4 MPa
σ_t (Uniaxial ultimate compressive strength)	39.5 MPa
ρ (mass density)	1892.7 kg/m^3

Table 3. CFRP material model parameters.

Parameter	Value
0° Tensile strength	2206.9 MPa
0° Tensile strength	137.9 GPa
Fiber volume	60%
Cured three-ply thickness	0.4953 mm
ρ (mass density)	1577.25 kg/m^3

used to bond CFRP panels was a thixotropic, modified, two part epoxy.

In order to determine the dynamic behavior of beams externally reinforced with CFRP panels, a series of drop-weight center-point loading were conducted (Jerome et al. 1997). Dynamic loading curve versus time was achieved by converting voltage-vs-time signal of a series of electrical resistance strain-gages to load-vs-time signal as shown in Figure 7.

Properties of concrete and CFRP panels used in this test are given in Tables 2 & 3. Experimental

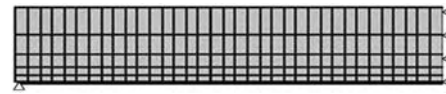

Figure 8. Finite element mesh and boundary conditions.

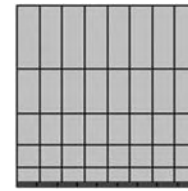

Figure 9. Cross section of the beam.

observations showed that final failure in strengthened concrete beams using CFRP tensile sheets was flexural cracking of concrete beams at nearly mid span and delamination of CFRP sheets afterwards. The following sections discuss 2D and 3D finite element simulations of the mentioned test.

4.3 *Numerical simulation and discussion for 3D*

Because of the symmetry of loading and geometry only half of the beam was modeled by assuming suitable boundary conditions as depicted in Figure 8. 8-noded cubic elements were used for modeling of the FRP sheet and concrete beam. In the concrete beam the size of elements were gradually increased due to their distance from bottom of the beam by an increasing ratio of 0.7^{-1} as shown in Figures 8 & 9. No contact

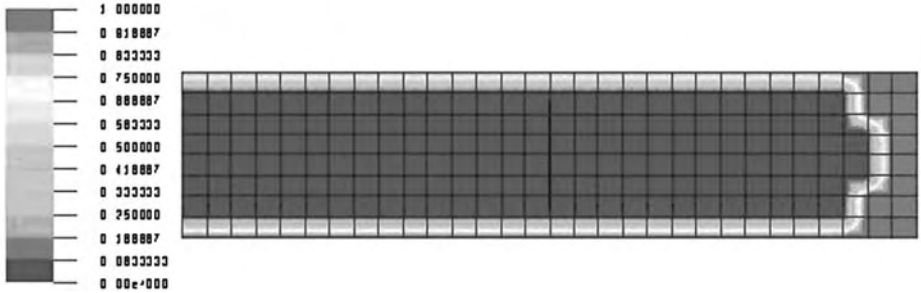

Figure 10. Delamination growth in CFRP plate at time step = .00047 s (0 = fully bonded, 1 = delaminated).

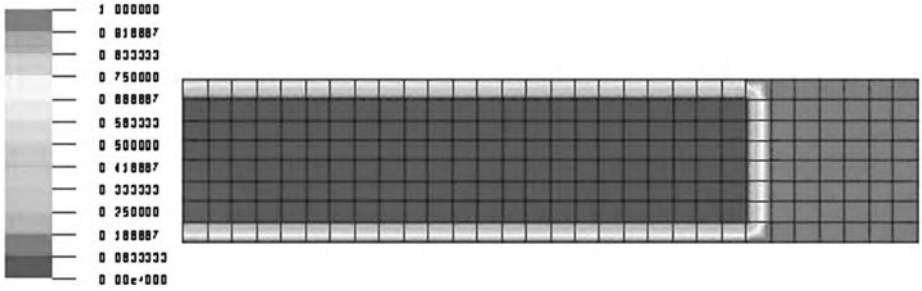

Figure 11. Delamination growth in CFRP plate at time step = .00075 s (0 = fully bonded, 1 = delaminated).

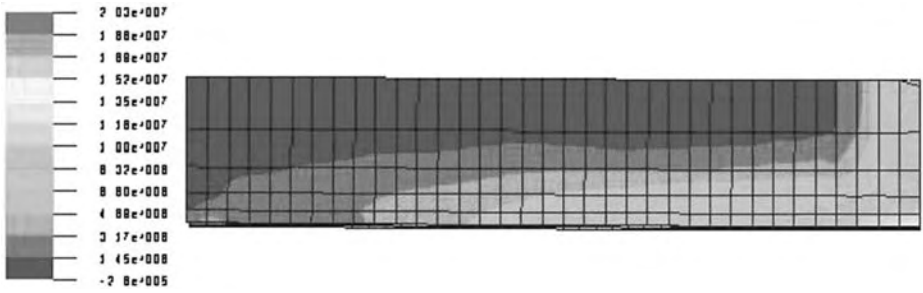

Figure 12. Contour of maximum principle stress in Pa at time step = .00075 s.

interface elements are used in adhesive layer and the contact of adjacent elements was conducted by a node to face contact method. For the concrete part 1200 elements were used and CFRP sheets were composed of 630 8-noded cubic elements.

There is a lack of information for adhesive material. Descriptive Properties of adhesive layer, like fracture energy release rate and bond strength are taken 0.5 N/mm and 4 MPa respectively.

Delamination of CFRP sheet from concrete beam was approximately started at 470 μs at middle of the beam and propagated toward the support. At 750 μs one fifth of the total length of FRP sheet has been debonded from bottom of the beam as shown in Figures 10 & 11.

As it is observed from Figure 12 the maximum principle stress has exceeded from the tensile strength of concrete in the middle part of the beam which

is an indication of occurrence of flexural cracking. The extent of delamination in interlaminar layer to one-fifth length of FRP sheets beside the excess of principle stress from the tensile strength of concrete occurs at 750 μs which is closely similar to the experimental observations by Jerome et al. (1997) where failure of the beam was reportedly occurred at 730 μs.

The displacement history at mid span of the beam, computed in the numerical analysis, was plotted against the time in Figure 16, marked by circular point compared to full line which shows the displacement resulted from the experimental tests.

The existing differences of resulted displacements in numerical simulation comparing to experimental results, can be attributed to the fact that the simulated beam has more stiffness than the tested beam which is a consequence of elastic behavior of concrete in tensile regime without any tensile fracture. Figures 10 & 11 show debonded region of CFRP sheet from mid span at 470 μs and 750 μs in which bright gray shows the debonded region. Also, Figure 12 shows the maximum principle stress contour at 750 μs.

4.4 *Numerical simulation and discussion for 2D modeling*

The same beam modeled in section 4.3 is considered. Properties of concrete, CFRP panels and adhesive layer were exactly the same as previous model. As cited in Jerome et al. (1997) it was observed that flexural cracks occurred between 400 μs till 500 μs and by 600 μs, the cracks ran to the upper surface of the beam, which is in a close agreement with results of the performed simulation.

Data, from an strain gage, located on the bottom center of the beam, indicated an abrupt change of slope in the strain-vs-time curve at about 430 μs, indicating crack initiation has occurred. Another strain gage, located on the original neutral axis of the beam also indicated failure at about 430 μs. Another strain gage, located at 2.75 in. (6.985 cm) from the bottom of the beam, showed a change of slope in strain vs. time at about 555 μs, indicating the crack(s) had reached the upper surface of the beam. A post-test damage assessment indicated a single flexural crack had formed at the beam's midpoint.

Analysis was conducted in a plane stress state. Triangular plane stress elements were used for concrete beam and CFRP sheet. The size of these elements varied due to their distance to CFRP sheet, so those elements adjacent to CFRP sheet had a size of 0.001 m and elements adjacent to top of the beam had a size of 0.01 m. The elements of CFRP sheet had a size of 0.00025 m which was decomposed of two layers of elements through the thickness. Details of the mesh are shown in Figure 13. The behavior of CFRP sheet was assumed to be elastic, due to its high strength and

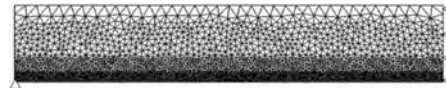

Figure 13. Finite element mesh and boundary conditions.

Figure 14. Cracking pattern at time step = .00046 s.

Figure 15. Cracking pattern at time step = .00075 s.

the experimental observations. Also, cracking behavior of the concrete beam in tensile regime was taken into account by assuming a Rankine bilinear strain softening model.

The results show that flexural cracks were propagated at the bottom part of mid span at 460 μs (Fig. 14). These flexural cracks started to propagate from two distinct origins; both of them were very close to mid span. Later, these cracks started to develop to upper surface of the beam in time interval of 460 μs to 750 μs. They reached to top of the beam at 750 μs (Fig. 15).

Then, at 0.00113 s those distinct cracks were attached to each other. Later, at 0.00127 s some signs of delamination were observed at bottom of the beam and at 0.00132 s delamination started to develop gradually.

At 0.00136, flexural cracks attached to each other at middle of the beam, while at 0.00145 s, more cracks were appeared and increased. At 0.00165 s microcracks started to develop from about mid height of the beam toward the left side (Fig. 17). Propagation of these cracks increased, so that at 0.00171 s they reached to bottom of the beam and it finally created a complete flexural cracking beside microcracks at bottom of the beam (Fig. 18). It is notable that the location where cracks stopped is exactly the same location where delamination of CFRP sheets stopped. It can be seen from the results that the creation and propagation of cracks have occurred at the peak point of the loading.

Also, the displacements computed from the simulations were plotted against experimental displacements at mid span in different time steps with rectangular points marking the displacements computed from the present analysis (Fig. 16). Acceptable agreement

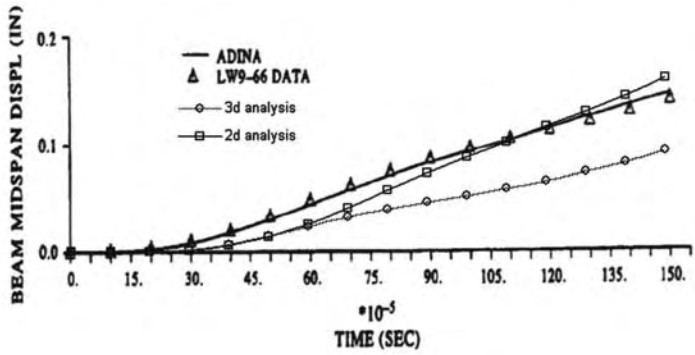

Figure 16. Comparision of mid point displacement vs. time for different solutions.

Figure 17. Cracking Pattern at time step = .000165 s.

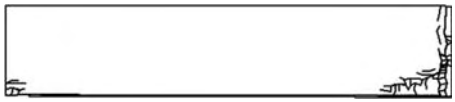

Figure 18. Cracking pattern at time step = .00174 s.

between the present modeling and tested results is an indicator of the validity of the algorithm.

5 CONCLUSION

This paper has presented a discrete crack model based on finite element analysis method for fiber reinforced polymer (FRP) plated reinforced concrete (RC) beams. A mixed coupling model for simulation of delamination of FRP sheet from concrete substrate was developed on the base of Hashin criterion. The proposed approach adopts a node to face contact based delamination control to simulate the linear-FRP-RC interactions. Conducting analyses in 2D and 3D and comparing the results with the test results showed that flexural cracking continued by delamination of FRP sheet from mid span is a major failure mode of the beam under dynamic loading induced by an impact hammer. In 3D analysis considerable difference in displacements show that assuming a suitable fracture model for concrete is indispensable for true prediction of overall behavior and failure mode. Close agreement between test results and performed analysis showed that the proposed algorithm for modeling this type of problems may effectively be used.

REFERENCES

Arduini M, Tommas AD & Manfroni O. 1995. Fracture mechanism of concrete beams bonded with composite plates. In Taerwe L (ed.), *Non-metalic (FRP) reinforcement for concrete structures*: 484–491. E&FN Spon: RILEM.

He JH, Pilakoutas K & Waldron P. 1997. Analysis of externally strengthening RC beams with steel and CFRP plates. *Proc. 7th int conf. on structural faults and repairs; Edinburgh*: 83–92.

Jerome DM & Ross CA. 1997. Simulation of the dynamic response of concrete beams externally reinforced with carbon-fiber reinforced plastic. *Comput struct* 64(5/6): 1129–1153.

Klaiber FW, Dunker KF, Wip TJ. & Sanders WW, Jr., Methods of strengthening existing highway bridges, *NCHRP research report No. 293, Transportation research board, Sep. 1987:11.*

Ladner M & Weder C. Geklebt Bewhrung im Stahlebetonbau, *Report No. 206, 1981*. EMPA Dubendorf.

Meier U. Bridge repair with high performance composite materials. *Material Tech, 1978*, Vol. 4: 125–128.

Mohammadi S. 2003. *Discontinuum mechanics by finite and discrete elements*. UK: WIT.

Mohammadi S & Forouzansepehr S. 2003. 3D adaptive multi fracture analysis of composites. *Materials Science Forum* 440–441: 145–152.

Nishida H, Kamiharako A, Shimomura T & Maruyama K. 1999. Bond mechanism between continuous fiber and concrete. *Proc JCI* 21(3): 1507–1512.

Quantrill RJ, Hollaway LC, Throne AM & Parke GAR. 1995. Preliminary research on the strengthening of reinforced concrete beams using GFRP. In Taerwe L (ed.), *Non-metalic (FRP) reinforcement for concrete structures*: 543–50. E&FN Spon: RILEM.

Progini P, Riccio A & Scaramuzzino F. 1999. Influence of Delamination Growth and Contact Phenomena on the Compressive Behavior of Composite Panels. *Journal of Composite Materials* 33(15): 1433–1465.

Rahimi R & Hutchinson A. 2001. Concrete beams strengthening with externally bonded FRP plates. *ASCE J Compos Constr* 5(1): 44–56.

Saadatmanesh H & Ehsani MR. 1991. RC beams strengthened with GFRP plates. I: experimental study. *J Struct Eng* 117(11): 3417–3433.

Sprenger W, Gruttmann F & Wagner W. 2000. Delamination growth analysis in laminated structures with continuum-based 3D-shell elements and a viscoplastic softening model. *Comput. Methods Appl. Mech. Engrg* 185: 123–139.

Taljsten B. 1996. Strengthening of concrete prisms using the plate-debonding technique. *Int J Fract* 81: 253–266.

Teng JG, Chen JF, Smith ST & Lam L. 2002. *FRP strengthened RC structures*. Chichester: John Wiley and Sons.

Zhang S, Raoof M & Wood LA. 1997. Prediction of peeling failure of reinforced concrete beams with externally bonded plates. *Proceedings of the Institution of Civil Engineers. Struct Build* 122: 493–496.

Zhishen Wu & Jun Yin. 2003. Fracturing behaviors of FRP-strengthened concrete structures. *Eng Fract Mech* 70: 1339–1355.

Ziraba YN. 1995. Computational model for reinforced concrete beams strengthened by epoxy bonded steel plates. *Finite Elem Anal Des* 12(4): 203–219.

Yuan H, Wu ZS & Yoshizawa H. 2001. Theoretical solution on interfacial stress transfer of externally bonded steel/composite laminates. *J Struct Mech Earthquake Eng JSCE* 4: 27–39.

FRP Composites in Civil Engineering – CICE 2004 – Seracino (ed)
© 2005 Taylor & Francis Group, London, ISBN 90 5809 638 6

Strengthening of RC columns with inadequate transverse reinforcement

A. Ilki, V. Koc, O. Peker, E. Karamuk & N. Kumbasar
Istanbul Technical University, Istanbul, Turkey

ABSTRACT: In this study, CFRP jacketed RC columns with low concrete strength and inadequate transverse reinforcement were tested under compression. The diameter of the longitudinal bars and the spacing of the transverse bars were designed to allow premature buckling of the longitudinal bars under axial stresses. The effects of the jacket thickness, cross-section shape, corner radius and the bonding pattern of CFRP sheets were investigated experimentally. The test results showed that CFRP jacketing of this type of columns was very effective in terms of deformability and strength enhancement. The buckling of the longitudinal bars was delayed significantly by the CFRP jackets. All the specimens with circular, square and rectangular cross-sections experienced a remarkable enhancement in strength and deformability. While the strength enhancement was more pronounced for the specimens with circular cross-section, specimens with square and rectangular cross-sections exhibited higher ultimate axial deformations. Specimens with greater corner radius reached relatively higher strengths. The compressive strengths and the corresponding axial deformations of the columns were also predicted by the empirical equations proposed by the authors before. It was seen that the predicted strength and ultimate axial deformations were in reasonable agreement with experimental data.

1 INTRODUCTION

In earthquake prone countries, many existing RC structures suffer from low quality of concrete and lack of adequate confinement reinforcement. In such cases, brittle behaviour and/or buckling of the longitudinal re-bars may cause premature strength degradation of the structural members. Wrapping these members by high strength carbon fibre reinforced polymer (CFRP) composite jackets can enhance both the axial strength and deformability of the members significantly and prevent the buckling of the longitudinal reinforcement.

Various studies proved that significant enhancement in compressive strength and deformability of concrete is possible by external confinement using high strength FRP composite sheets. The studies of Fardis and Khalili (1982) and Nanni and Bradford (1995) are among the initial research works on confinement of concrete members with FRP composites. Karbhari and Gao (1997), Toutanji (1999), Saafi et al. (1999), Fam and Rizkalla (2001) and Becque et al. (2003) developed extensive experimental data for cylinder specimens, for a variety of fibre types, orientations and jacket thickness, either for FRP jacketed concrete or concrete filled FRP tubes. Demers and Neale (1999) tested reinforced concrete columns of circular cross-section with FRP jackets. Rochette and Labossiere (2000), and Wang and Restrepo (2001), tested square and rectangular concrete columns confined by FRP composites. Wang and Restrepo (2001) adopted, Mander's model (1988) for the stress–strain behaviour of FRP wrapped concrete. Xiao and Wu (2000) investigated the effect of concrete compressive strength and thickness of CFRP jacket and proposed a simple bilinear stress–strain model for CFRP jacketed concrete. Tan (2002) tested half scale reinforced concrete rectangular columns with a section aspect ratio of 3.65 under axial loads and investigated the effects of fibre type and configuration and fibre anchors on the strength enhancement of the columns. Ilki and Kumbasar (2002) tested both damaged and undamaged cylinder specimens, which were externally confined with different thickness of CFRP jackets, under monotonic increasing and repeated compressive stresses. Based on experimental results they proposed simple expressions for ultimate strength and corresponding axial strain of CFRP jacketed concrete. Lam and Teng (2002) carried out an extensive survey of existing studies on FRP confined concrete and proposed a simple model based on a linear relationship between confined concrete strength and lateral confining pressure provided by FRP composites, which was quite similar to the model proposed by Ilki and Kumbasar (2002) before. Ilki and Kumbasar (2003), after testing CFRP jacketed concrete specimens with square and rectangular cross-sections modified the expressions that they have proposed before to cover non-circular cross-sections. Lam and Teng (2003a, 2003b) proposed design oriented stress–strain models for both uniformly and non-uniformly confined

concrete members. Ilki et al. (2004) tested FRP jacketed low strength concrete members with circular and rectangular cross-sections, and stated that when the unconfined concrete quality was lower, the efficiency of the FRP jackets was higher. De Lorenzis and Tepfers (2003), stated that none of the available models could predict the strain at peak stress with reasonable accuracy.

In this study, experimental results on the compressive behaviour of 13 low strength reinforced concrete column specimens strengthened by CFRP jackets are presented. The test parameters of this study were:

- CFRP jacket thickness (0.165, 0.495 and 0.825 mm)
- Cross-section (circular, D = 250 mm, square, 250 × 250 mm and rectangular, 150 × 300 mm)
- Corner radius (10, 20 and 40 mm)
- Wrapping pattern (continuous and as straps in the form of hoops and spirals).

Test specimens were produced with low strength concrete ($f'_c = 10.9$ MPa), plain reinforcement and inadequate transverse reinforcement for simulating many existing structures, particularly in developing countries. f'_c is the standard cylinder strength of concrete at 28 days of age.

Test results indicated that external lateral confinement by CFRP jackets improved the compressive strength and deformability of the specimens, as well as retarding the buckling of the longitudinal re-bars.

The empirical equations proposed by Ilki et al. (2004) for the compressive strength and ultimate axial deformation of CFRP jacketed concrete gave acceptable results.

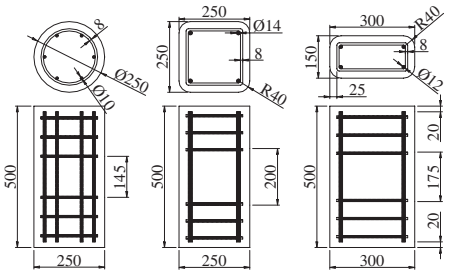

Figure 1. Cross-sections and reinforcement details (units: mm).

Table 1. Specimen details.

Specimen	f'_{co} (MPa)	Section shape	n	r (mm)	L.R.	T.R.
LS-C-1-a	12.8	C	1	–	6ϕ10	ϕ8/145
LS-C-3-a	12.8	C	3	–	6ϕ10	ϕ8/145
LS-C-5-a	12.8	C	5	–	6ϕ10	ϕ8/145
LS-R-1-1-40a	13.5	S	1	40	4ϕ14	ϕ8/200
LS-R-1-3-10a	13.5	S	3	10	4ϕ14	ϕ8/200
LS-R-1-3-20a	13.5	S	3	20	4ϕ14	ϕ8/200
LS-R-1-3-40a	13.5	S	3	40	4ϕ14	ϕ8/200
LS-R-1-5-40a	13.5	S	5	40	4ϕ14	ϕ8/200
LS-R-2-1-40a	13.5	R	1	40	4ϕ12	ϕ8/175
LS-R-2-3-40a	13.5	R	3	40	4ϕ12	ϕ8/175
LS-R-2-3-40a-H	13.5	R	3	40	4ϕ12	ϕ8/175
LS-R-2-3-40a-S	13.5	R	3	40	4ϕ12	ϕ8/175
LS-R-2-5-40a	13.5	R	5	40	4ϕ12	ϕ8/175

2 SPECIMENS

2.1 *Details*

Specimens were specially designed to reflect the existing vertical structural members in many developing countries. For this purpose low quality concrete and plain reinforcement were used during specimen production. 3 specimens with circular, 5 specimens with square and 5 specimens with rectangular cross-sections with the height of 500 mm were constructed. Longitudinal reinforcement ratios, ρ_l, were around 0.01 for all specimens, while the volumetric transverse reinforcement ratio, ρ_h, were 0.007, 0.005 and 0.008 for specimens with circular, square and rectangular cross-sections, respectively. Reinforcement arrangement was designed to obtain approximately equal s/d (s, transverse reinforcement spacing, d, longitudinal bar diameter) ratios for specimens with different cross-sections to investigate the effects of buckling of the longitudinal bars. Cross-sections and reinforcement details are given in Figure 1. General information about the specimens are given in Table 1.

In this table, f'_{co} is the concrete strength of the member on the test day, n is the number of CFRP plies and r is the corner radius of the cross-section. C, S, R, L.R. and T.R. represent circular, square, rectangular cross-sections and longitudinal and transverse reinforcements, respectively.

To prevent stress concentrations on the corners of the non-circular specimens, corners were rounded to 40 mm radius, while corners of 2 specimens were rounded to 10 and 20 mm to examine the effects of corner radius on the behaviour. Two specimens were wrapped with hoop and spiral type CFRP straps to investigate the effects of the different wrapping patterns. Note that, both for specimen LS-R-2-3-40a-H (with hoop type straps) and LS-R-2-3-40a-S (with spiral type straps), the straps were 50 mm wide and bonded on the specimens with 50 mm clear spacing.

Specimen names were given in the form of: LS (low strength) – R (cross-section type, either Rectangular or Circular) – 2 (cross-sectional aspect ratio) – 3 (number of CFRP plies) – 40a (corner radius) – H (wrapping pattern).

Table 2. Concrete mix proportion and compressive strength.

Property	Value	Unit
Cement	150	kg/m^3
Water	210	kg/m^3
Sand	638	kg/m^3
Gravel	982	kg/m^3
Stone powder	286	kg/m^3
Fly ash	40	kg/m^3
Admixture	1.14	kg/m^3
Slump	210	mm
FDAST	310 × 310	mm × mm
$f'_{c,28}$	10.9	MPa
$f'_{c,90}$	13.9	MPa
$f'_{c,180}$	15.9	MPa

FDAST: flow diameter after slump test.

Table 3. Reinforcement properties.

	Bar				
Property	ϕ8	ϕ10	ϕ12	ϕ14	Unit
d	8.0	10.1	12.2	13.8	mm
f_y	476	367	339	345	MPa
ε_y	0.0024	0.0018	0.0017	0.0017	mm/mm
f_{smax}	–	523	471	477	MPa
ε_{smax}	–	0.19	0.23	0.23	mm/mm
f_{su}	–	377	335	294	MPa
ε_{su}	–	0.27	0.30	0.31	mm/mm

2.2 *Materials*

Specially designed ready mixed concrete was used for all specimens for obtaining low concrete strength. Standard cylinder compression tests were carried out at the ages of 28, 90 and 180 days. The concrete mix-proportion and standard cylinder compressive strengths at different ages ($f'_{c,j}$) are presented in Table 2. In the mixture, ordinary Portland cement with the 28 days strength of 42.5 MPa and admixture (degussa YKS® MR25 S mid-range superplastisizer) were used.

The number and the diameter of the longitudinal bars were arranged to obtain approximately equal longitudinal reinforcement ratio. Transverse reinforcement spacing of circular, square and rectangular specimens were 145, 200 and 175 mm, respectively. A clear cover of 20 mm was formed for longitudinal reinforcement at the bottom and top faces of the specimens for preventing direct loading of reinforcing bars. Reinforcement properties are given in Table 3.

In Table 3, f_y, f_{su} and f_{smax} represent the yielding stress, ultimate stress and tensile stress of the reinforcement, respectively. ε_y, ε_{su} and ε_{smax} are tensile strains corresponding to f_y, f_{su} and f_{smax}, respectively.

Table 4. Mechanical and geometrical properties of CFRP.

Property	Value	Unit
Characteristic tensile strength	3430	MPa
Characteristic tensile modulus	230000	MPa
Maximum tensile strain	0.015	mm/mm
Effective area per unit width	0.165	mm^2/mm
Unit weight	1820	kg/m^3

Figure 2. Specimen production.

FRP materials behave linear elastic till rupture. The effective thickness of the CFRP sheets was 0.165 mm for one layer. The geometrical and mechanical properties of the CFRP sheets are given in Table 4. These properties are taken from the specifications of the manufacturer.

2.3 *Construction*

Specimens were produced in the Structural and Earthquake Engineering Laboratory and cured in the same conditions for 7 days, Figure 2.

The specimens were tested after strengthening with 1, 3 and 5 plies of CFRP sheets. All the specimens were jacketed externally by unidirectional CFRP sheets in transverse direction with 0-degree orientation. Before wrapping the specimens with CFRP jackets, surface preparation procedure was carried out, which included sanding, cleaning, forming one layer of epoxy-polyamine primer and one layer of epoxy putty, Figure 3.

Then epoxy adhesive was used for bonding CFRP sheets on the specimens. Additional layers of epoxy adhesive were applied between the CFRP jacket plies and on the outer ply of CFRP jacket when more than one ply was wrapped, Figure 4. The compressive and tensile strengths of the epoxy system were around 80 and 50 MPa, respectively. Tensile elasticity modulus

Figure 3. Primer and putty application.

Figure 4. CFRP wrapping.

and ultimate elongation of the epoxy system were around 3000 MPa and 0.025, respectively. The steps during jacketing were carried out with great care to prevent stress concentrations due to surface irregularities and to obtain the tight fitting of the CFRP jackets on the specimens. For obtaining satisfactory bonding, 150 mm overlap length was formed at the end of the wrap. In the cases of wrapped jacket to be more than one ply, the sheet was wrapped continuously and 150 mm overlap was formed at the end of the wrap.

3 TESTING PROCEDURE

The specimens were tested under monotonic uniaxial compressive loads by using an Amsler universal testing machine with the capacity of 5000 kN. Two different gauge lengths were used for measurement of average axial strains by displacement transducers. For this purpose, four transducers in the gauge length of 270 mm and four transducers in the gauge length of 500 mm were used, Figure 5. Axial and lateral strains were measured at mid-height by surface strain gauges

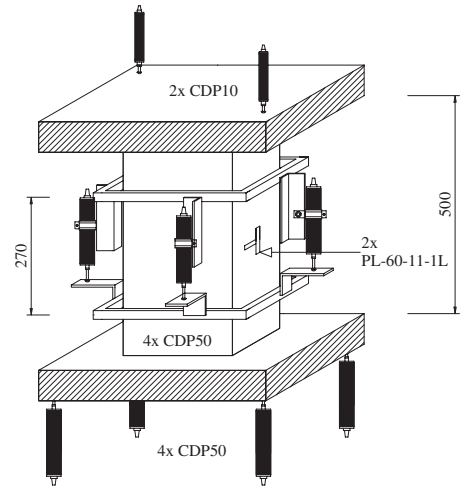

Figure 5. Test setup (units: mm).

with the gauge length of 60 mm for all of the specimens. For specimens with circular cross-section, two vertically and two horizontally bonded strain gauges were used with 180 degree intervals around perimeter, for non-circular specimens vertical strain gauges were bonded on two opposite sides. For specimens with square cross-sections two horizontal strain gauges were bonded on two opposite sides. For rectangular specimens two horizontal strain gauges were bonded on short and long sides. To obtain the deformations of the longitudinal and transverse reinforcement, strain gauges were used with the gauge lengths of 5 and 3 mm, respectively. For data acquisition a 50 channel TML-ASW-50C switch box and a TML-TDS-303 data logger were used. General appearance of the test setup is shown in Figure 5.

As also mentioned by Mirmiran and Shahawy (1997), the average axial strains measured by the displacement transducers were quite close to the measurements recorded by the strain gauges, consequently in this paper, the given axial strains were obtained by the measurements of the displacement transducers, unless otherwise is mentioned.

4 TEST RESULTS

All specimens failed due to rupture of CFRP sheets at high axial strain levels around mid-height. The rupture of CFRP sheets was only one vertical cut with the height of 200–250 mm for the jackets of 1 ply, 3–4 vertical cuts with the heights of 20–70 mm for the jackets of 3 plies and more vertical cuts of lower heights

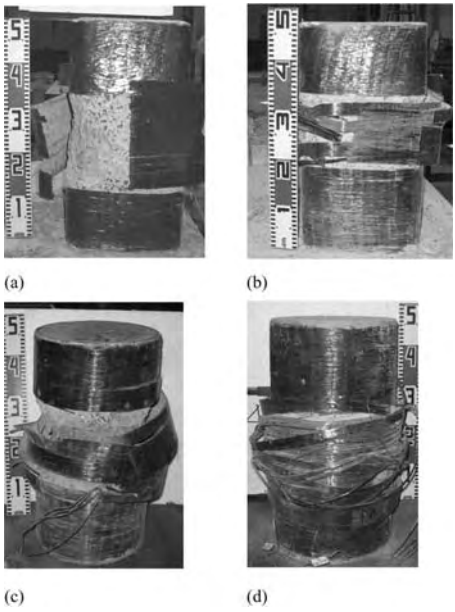

Figure 6. (a) LR-1-1-40a, (b) LS-R-1-3-40, (c) LS-C-3-a, (d) LS-C-5-a.

for the jackets of 5 plies. For square and rectangular specimens, rupture of the sheets was around the corners just after the rounded portion. Some of the tested specimens are shown in Figure 6.

The test results are given in Table 5. In this table, f'_{cc} and ε_{cc} are the confined concrete strength and corresponding axial strain, ε_{ch} is the maximum measured lateral strain and ε_{co} is the strain corresponding to unconfined concrete strength. ε_{co} was assumed as 0.002 in this study. As seen in this table, with respect to unconfined concrete, for specimens with circular cross-section compressive strengths increased about 130, 340 and 560% for CFRP jackets of 1, 3 and 5 plies, respectively. The strength increase for CFRP jacketed specimens with square cross-section were 50, 180 and 280% for 1, 3 and 5 plies, respectively. The strength enhancements for specimens with rectangular cross-section were 40, 160 and 270% for 1, 3 and 5 plies, respectively. Note that unconfined concrete strength of the member, f'_{co} was assumed to be 85% of the standard cylinder strength. The ultimate axial strains corresponding to confined concrete strengths were around 10.8, 21.5 and 33.0 times the unconfined concrete for 1, 3 and 5 plies of CFRP jackets for specimens with circular cross-section. For specimens with square cross-section the axial ultimate strains were 6.0, 19.6 and 24.3 times of the unconfined concrete for 1,

Table 5. Test results for externally confined columns.

Specimen	f'_{cc} (MPa)	ε_{cc} GL:500	ε_{cc} GL:270	ε_{ch} GL:60	$\frac{f'_{cc}}{f'_{co}}$	$\frac{\varepsilon_{cc}}{\varepsilon_{co}}$
LS-C-1-a	29.0	0.022	0.023	0.010	2.3	10.8
LS-C-3-a	56.1	0.043	0.043	0.007*	4.4	21.5
LS-C-5-a	84.9	0.066	0.068	0.015*	6.6	33.0
LS-R-1-1-40a	20.6	0.017	0.014	0.011	1.5	6.0
LS-R-1-3-10a	24.7	0.048	0.037	0.009	1.8	24.2
LS-R-1-3-20a	29.3	0.054	0.056	0.013	2.2	27.1
LS-R-1-3-40a	37.4	0.055	0.044	0.015	2.8	19.6
LS-R-1-5-40a	51.7	0.068	0.053	0.015	3.8	24.3
LS-R-2-1-40a	18.4	0.018	0.015	0.008	1.4	6.6
LS-R-2-3-40a	34.9	0.062	0.064	0.009*	2.6	22.1
LS-R-2-3-40a-H	19.6	0.031	0.034	0.011	1.5	10.9
LS-R-2-3-40a-S	18.5	0.022	0.023	0.010	1.4	7.9
LS-R-2-5-40a	50.2	0.086	0.099	0.016	3.7	35.9

* Out of order before reaching peak stress.
GL: gauge length (mm).

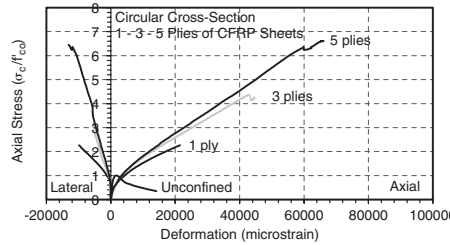

Figure 7. Axial stress–deformation relationships for specimens with circular cross-section in 500 mm gauge length.

3 and 5 plies of CFRP jackets, respectively. For specimens with rectangular cross-section the ultimate axial strains were 6.6, 22.1 and 35.9 for 1, 3 and 5 plies of CFRP jackets, respectively. The transverse strains of CFRP jackets at failure were between 0.008 and 0.016 independent of the thickness of the jacket, with an average value as 0.012. Note that only the strain gauges that worked until failure were taken into consideration while determining the average.

The axial stress–deformation relationships in the gauge length of 500 mm for the specimens with circular cross-section are given in Figure 7. For the specimens with square and rectangular cross-sections the axial stress–deformation relationships are given in Figures 8 and 9, respectively. Figure 10 represents a comparison of different cross-section types. Test results indicated that the cross-section shape had a significant effect on the behaviour; the strength enhancement was more pronounced for the specimens with circular cross-section, while the specimens with rectangular cross-section exhibited higher ultimate

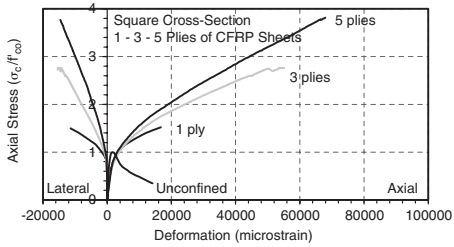

Figure 8. Axial stress–deformation relationships for specimens with square cross-section in 500 mm gauge length.

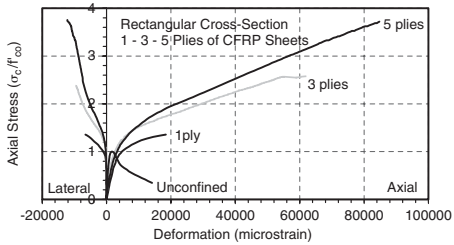

Figure 9. Axial stress–deformation relationships for specimens with rectangular cross-section in 500 mm gauge length.

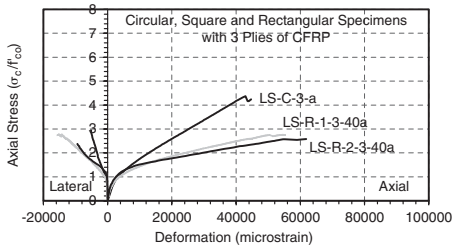

Figure 10. Axial stress–deformation relationships for specimens with circular, square and rectangular cross-sections in 500 mm gauge length.

axial deformations. For demonstrating the effect of corner radius for specimens with square cross-section, a comparison is given in Figure 11. Specimens with greater corner radius reached higher strengths while no significant difference between axial strains was observed. Specimens strengthened with CFRP sheet straps (either like individual hoops or continuous spirals) behaved similarly with the specimen strengthened with 1 continuous ply of CFRP jacket, Figure 12. Note that the amount of CFRP sheets for specimens LS-R-2-3-40a-H and LS-R-2-3-40a-S was half of the amount of CFRP sheets in the jacket of the specimen LS-R-2-3-40a and 1.5 times that of specimen LS-R-2-1-40a. In

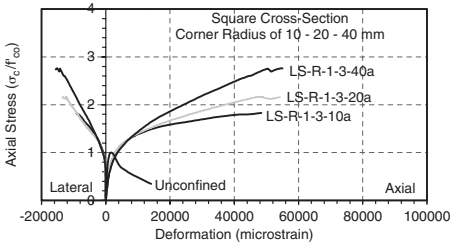

Figure 11. Axial stress–deformation relationships for specimens with different corner radius.

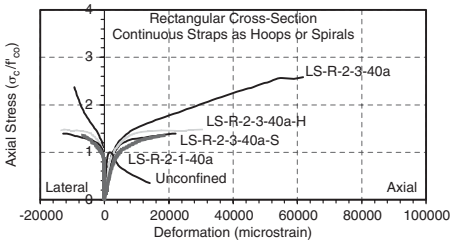

Figure 12. Axial stress–deformation relationships for continuous and strap type jackets.

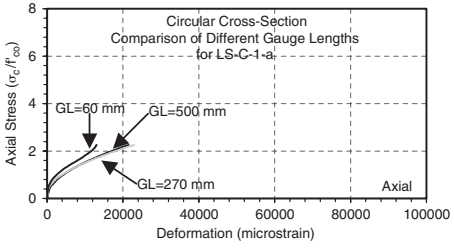

Figure 13. Axial stress–deformation relationships for different gauge lengths.

Figure 13, the average vertical deformations obtained by the displacement transducers in 270 and 500 mm gauge lengths and by strain gauges in 60 mm gauge length are compared.

In Figures 7–11, the gauge length for the vertical deformation measurements of unconfined standard cylinders was 150 mm. Note that all stress–strain relationships are given with the non-dimensional vertical axis, and while determining the stress–strain relationship of confined concrete, the contribution of longitudinal reinforcing bars was subtracted by considering the actual stress–strain relationships of these bars including the strain-hardening region. It should also be noted that although the major contribution of

the enhancement in strength and deformability was provided by the external CFRP jacket, the internal transverse reinforcement had also some influence. The contribution of internal transverse reinforcement is minimal for the specimens with square and rectangular cross-section.

5 PREDICTION OF CONFINED STRENGTH AND CORRESPONDING AXIAL STRAINS

For prediction of ultimate strengths and corresponding axial strains of CFRP jacketed specimens, the empirical equations proposed by Ilki et al. (2004) were used, Equations 1 and 2. These equations were proposed based on experimental results of the specimens with circular and rectangular cross-section.

$$\left[\frac{f'_{cc}}{f'_{co}}\right]_{CFRP} = \left[1+2.4\left(\frac{f'_{l\max}}{f'_{co}}\right)^{1.2}\right] \quad (1)$$

$$\left[\frac{\varepsilon_{cc}}{\varepsilon_{co}}\right]_{CFRP} = \left[1+20\left(\frac{h}{b}\right)\left(\frac{f'_{l\max}}{f'_{co}}\right)^{0.5}\right] \quad (2)$$

In Equations 1 and 2, f'_{lmax} is the maximum effective transverse confinement stress provided by CFRP jacket and can be calculated by Equation 3 based on the equilibrium between the resultant transverse compressive force applied on the concrete and the tensile force of the wrapping material.

$$f'_{l\max} = \frac{\kappa_a \rho_f \varepsilon_{h,rup} E_{frp}}{2} \quad (3)$$

In Equation 3, κ_a is the efficiency factor that is to be determined based on the section geometry as the ratio of effectively confined cross-sectional area to the gross cross-sectional area, E_{frp} and ρ_f are the tensile elasticity modulus and ratio of the cross-sectional area of FRP jacket to the cross-sectional area of concrete, respectively. Based on test results, ultimate tensile strength of CFRP wrapped around concrete members ($\varepsilon_{h,rup}$) is assumed to be 70% of the ultimate strain (ε_{frp}) corresponding to tensile strength of CFRP.

While predicting the confined concrete strength and corresponding axial strain, the contribution of internal transverse reinforcement (ITR) was also taken into account. For this purpose, the empirical equations proposed by Ilki et al. (2003) and Mander et al. (1988) were used for strength and corresponding strain, respectively, Equations 4 and 5. In Equation 4, f'_l is the effective confinement stress provided by internal transverse reinforcement.

$$\left[\frac{f'_{cc}}{f'_{co}}\right]_{ITR} = \left[1+4.54\frac{f'_l}{f'_{co}}\right] \quad (4)$$

Table 6. Comparison of experimental and analytical results.

		Exp.		Analy.		Comparison	
	f'_{co}	f'_{cc}	ε_{cc}	f'_{cc}	ε_{cc}	(2)	(3)
Specimen	(1)	(2)	(3)	(4)	(5)	(4)	(5)
LS-C-1-a	12.8	29.0	0.022	26.18	0.018	1.11	1.18
LS-C-3-a	12.8	56.1	0.043	46.37	0.036	1.21	1.20
LS-C-5-a	12.8	84.9	0.066	66.57	0.051	1.28	1.31
LS-R-1-1-40a	13.5	20.6	0.017	17.78	0.018	1.16	0.91
LS-R-1-3-10a	13.5	24.7	0.048	21.96	0.025	1.13	1.97
LS-R-1-3-20a	13.5	29.3	0.054	23.94	0.027	1.22	2.03
LS-R-1-3-40a	13.5	37.4	0.055	27.31	0.030	1.37	1.84
LS-R-1-5-40a	13.5	51.7	0.068	38.31	0.038	1.35	1.79
LS-R-2-1-40a	13.5	18.4	0.018	17.43	0.035	1.05	0.53
LS-R-2-3-40a	13.5	34.9	0.062	27.76	0.059	1.26	1.05
LS-R-2-3-40a-H	13.5	19.6	0.031	19.80	0.042	0.99	0.72
LS-R-2-3-40a-S	13.5	18.5	0.022	19.80	0.042	0.94	0.52
LS-R-2-5-40a	13.5	50.2	0.086	36.69	0.075	1.27	1.14
				Average		1.18	1.24
				S. deviation		0.13	0.52

$$\left[\frac{\varepsilon_{cc}}{\varepsilon_{co}}\right]_{ITR} = \left[1+5\left(\frac{f'_{cc}}{f'_{co}}-1\right)\right] \quad (5)$$

After the strength and deformability enhancements provided by external CFRP jacket and internal transverse reinforcement were determined separately, the total enhancement in strength and corresponding strain was calculated by using Equations 6 and 7.

$$\left[\frac{f'_{cc}-f'_{co}}{f'_{co}}\right]_{TOTAL} = \left[\frac{f'_{cc}}{f'_{co}}-1\right]_{CFRP} + \left[\frac{f'_{cc}}{f'_{co}}-1\right]_{ITR} \quad (6)$$

$$\left[\frac{\varepsilon_{cc}-\varepsilon_{co}}{\varepsilon_{co}}\right]_{TOTAL} = \left[\frac{\varepsilon_{cc}}{\varepsilon_{co}}-1\right]_{CFRP} + \left[\frac{\varepsilon_{cc}}{\varepsilon_{co}}-1\right]_{ITR} \quad (7)$$

For combined contribution of FRP jacket and internal transverse reinforcement, Wang and Restrepo (2001) have determined the effective lateral confinement stresses provided by FRP jacket and internal transverse reinforcement separately and then used the model proposed by Mander et al. (1988) for concrete confined by internal steel reinforcement by replacing the transverse confinement stress provided by internal reinforcement with the total transverse confinement stress provided by internal reinforcement and external FRP jacket.

In Table 6, the comparisons of experimental and analytical results are given.

6 CONCLUSIONS

In this study, experimental results for reinforced concrete columns produced with low strength concrete and

without adequate transverse reinforcement strengthened with CFRP sheets are presented.

The conclusions are as follows:

- The confinement of reinforced concrete columns with CFRP sheets, improved both axial load carrying capacity and ductility characteristics, remarkably.
- The strength enhancement was more effective for circular cross-sections, while ultimate axial strains were higher for rectangular cross-sections, due to insufficient flexural stiffness of the FRP sheets.
- The premature buckling of the longitudinal reinforcement was prevented and the contribution of the longitudinal reinforcing bars to the axial resistance and ductility was maintained until very large axial strains.
- The improvement provided with one ply of CFRP jacket was very remarkable, further increase in jacket thickness resulted with significantly higher strengths and axial deformation capabilities.
- Specimens with greater corner radius reached higher strengths while no significant difference between ultimate axial strains were observed.
- Specimens strengthened with CFRP sheet straps of 3 plies performed similar to the specimen with continuous CFRP jacket of one ply, in contrast to the higher amount of CFRP sheets used for these specimens. In addition, the bonding of straps was more difficult than continuous jackets.
- The empirical equations, proposed by the authors before, predicted the compressive strength and corresponding axial strains of the specimens tested in this study with a reasonable accuracy.

ACKNOWLEDGEMENTS

The authors wish to thank Yapkim-Degussa Construction Chemicals Company, Set Italcementi Group, Mr. Tayfun Pala, Mr. Bulent Turgut, Mr. Metin Tiryaki, for their contributions during the preparations of the specimens. Assistance of Mr. Cem Demir and Mr. Esen Yilmaz during experiments is also acknowledged.

REFERENCES

Becque, J., Patnaik, A.K., and Rizkalla, S.H. (2003), "Analytical models for concrete confined with FRP tubes", *J. Compos. Const*., 7(1), 31–38.

De Lorenzis, L., and Tepfers, R. (2003), "Comparative study of models on confinement of concrete cylinders with fiber-reinforced polymer composites", *J. Compos. Const*., 7(3), 219–237.

Demers, M., and Neale, K.W. (1999), "Confinement of reinforced concrete columns with fibre-reinforced composite sheets-an experimental study", *Can. J. Civ. Eng*., 26(2), 226–241.

Fam, A.Z., and Rizkalla, S.H. (2001), "Confinement model for axially loaded concrete confined by circular fiber-reinforced polymer tubes", *ACI Struct. Jour*., 98(4), 451–461.

Fardis, M.N., and Khalili, H. (1982), "FRP-encased concrete as a structural material", *Magazine of Concrete Research*, 34(121), 191–202.

Ilki, A., and Kumbasar, N. (2002), "Behavior of damaged and undamaged concrete strengthened by carbon fiber composite sheets", *Struct. Eng. and Mech*., 13(1), 75–90.

Ilki, A., and Kumbasar, N. (2003), "Compressive behaviour of carbon fibre composite jacketed concrete with circular and non-circular cross-sections", *Journal of Earthquake Engineering*, 7(3), 381–406.

Ilki, A., Fukuta, T., and Ozdemir, P. (2003), "Behaviour of confined concrete and a trilinear stress-strain model", *Technical Journal of Turkish Chamber of Civil Engineers*, 14(1), 2853–2871.

Ilki, A., Kumbasar, N., and Koc, V. (2004), "Low strength concrete members externally confined with FRP sheets", *Struct. Eng. and Mech*., (accepted for publication).

Karbhari, V.M., and Gao, Y. (1997), "Composite jacketed concrete under uniaxial compression-verification of simple design equations", *ASCE Journal of Materials in Civil Engineering*, 9(4), 185–193.

Lam, L., and Teng, J.G. (2002), "Strength models for fiber-reinforced plastic-confined concrete", *J. Struct. Eng*., 128(5), 612–623.

Lam, L., and Teng, J.G. (2003a), "Design-oriented stress-strain model for FRP-confined concrete", *Construction and Building Materials*, 17, 471–489.

Lam, L., and Teng, J.G. (2003b), "Design-oriented stress-strain model for FRP-confined concrete in rectangular columns", *Journal of Reinforced Plastics and Composites*, 22(13), 1149–1186.

Mander, J.B., Priestley, M.J.N., and Park, R. (1988), "Theoretical stress-strain model for confined concrete", *ASCE Journal of the Structural Division*, 114(8), 1804–1826.

Nanni, A., and Bradford, N.M. (1995), "FRP jacketed concrete under uniaxial compression", *Constr. Build. Mater*., 9(2), 115–124.

Rochette, P., and Labossiere, P. (2000), "Axial testing of rectangular column models confined with composites", *ASCE Jour. of Composites for Construction*, 4(3), 129–136.

Saafi, M., Toutanji, H., and Li, Z. (1999), "Behavior of concrete columns confined with fiber reinforced polymer tubes", *ACI Materials Journal*, 96(4), 500–509.

Tan, K.H. (2002), "Strength enhancement of rectangular reinforced concrete columns using fiber-reinforced polymer", *J. Compos. Const*., 6(3), 175–183.

Toutanji, H.A. (1999), "Stress-strain characteristics of concrete columns externally confined with advanced fiber composite sheets", *ACI Materials Journal*, 96(3), 397–404.

Wang, Y.C., and Restrepo, J.I. (2001), "Investigation of concentrically loaded reinforced concrete columns confined with glass fiber-reinforced polymer jackets", *ACI Structural Journal*, 98(3), 377–385.

Xiao, Y., and Wu, H. (2000), "Compressive behaviour of concrete confined by carbon fiber composite jackets", *ASCE Jour. of Materials in Civ. Eng*., 12(2), 139–146.

FRP Composites in Civil Engineering – CICE 2004 – Seracino (ed)
© 2005 Taylor & Francis Group, London, ISBN 90 5809 638 6

Innovative three-sides wrapping technique for rectangular RC columns using CFRP sheets

A.A. El-Ghandour[1] & A.A. Abdelrahman[2]
[1]*Assistant Professor,* [2]*Associate Professor*
Department of Structural Engineering, Ain Shams University, Cairo, Egypt

ABSTRACT: This paper experimentally investigates the efficiency of a new strengthening technique for edge rectangular RC columns using partial wrapping of CFRP sheets from three sides only. The reduced confining effect is compensated by the provision of CFRP anchors near the ends of the sheets. The clear vertical sheets' spacing, the number of layers as well as the positioning of anchors (anchorage length) are the main investigated parameters. Test results, including the sheets' strains, demonstrate activation of the anchors. Key test results also indicate a reasonable load carrying capacity (25%) and ductility enhancements when compared to similar columns with total CFRP wrapping (34% capacity enhancement). The former capacity enhancement is acceptably reduced with increasing clear vertical spacing and fewer number of CFRP layers to 21% and 18%, respectively. However, slightly shorter anchorage lengths are found to dramatically decrease the capacity enhancement to 11%.

1 INTRODUCTION

Recently, RC columns' wrapping using fiber-reinforced-polymers (FRPs) laminates has emerged as one of the most promising technologies for capacity enhancement, especially in seismic regions, where the vertical earthquake excitation produces an increase in the vertical loads. The corrosion resistance of such materials has made their use more attractive compared to the traditional steel jacketing technique. The unchanged stiffness of the upgraded columns, hence, preventing extra seismic loads to be attracted, is also very advantageous compared to the RC jacketing technique. Furthermore, the high tensile strength of FRPs, especially carbon ones (CFRP), results in a better column's confinement than traditional techniques, hence, leading to higher capacity and ductility increases.

Previous studies by Hosotani et al (1997) and Matthys et al (1999) have demonstrated a very high efficiency of the wrapping technique for circular RC columns using CFRP laminates, from both capacity and ductility points of views. Moving to square than rectangular columns, the lower confinement due to the out-of-plane displacements of the laminates induced by the axial loads as well as the laminates planes of weaknesses around sharp corners, resulted in progressively lower efficiencies of the technique, as concluded by Rochette et al (2000). In such situations, Neale et al (1997) has formerly demonstrated that rounding the corners of the columns before applying the composite wraps improved the previous low efficiency. In addition, it was recently demonstrated by Hosny et al (2001) that anchoring the laminates to prevent their out-of-plane deformations together with rounding the column's corners, resulted in very high improvements in the technique's efficiency, depending on the anchorage system used.

This paper investigates a further development in the wrapping technique of rectangular RC columns using CFRP laminates, emerging from a practical need to facilitate the upgrading process of the columns in terms of time, labor and cost savings. In fact, except for interior columns, which are not intersected by walls and partitions, the wrapping technique of all other columns of any existing building requires the destruction of the parts of the walls adjacent to the columns, followed by the rebuilding of the removed parts after completion of the work. The time, labor and cost consumptions in the latter construction jobs accompanying the wrapping process worsen in cases where the edge and corner columns are in question; since parts of the building's façade are to be demolished and reconstructed. A direct solution to this problem appears to exist in wrapping the edge and corner columns from three and two sides, respectively. However, since the wrapping is a technique whose efficiency is highly dependant on the degree of concrete confinement added to the upgraded column, hence, the previously suggested solution is in risk to turn partially or totally inefficient in enhancing the load carrying capacity and ductility of the wrapped column and, thus, needs experimental investigation, as presented in this paper.

The experimental study of this paper investigates the behavior of RC rectangular columns wrapped with horizontal unidirectional CFRP sheets from three sides only together with a CFRP mechanical anchorage system. The main test parameters include the clear vertical spacing between successive wraps, the number of CFRP layers as well as their horizontal extension on the free opposite sides of the columns (anchorage length). The test results in terms of capacity and failure mode, internal steel and external CFRP wraps' strains as well as concrete strains, are used to evaluate the efficiency of the three-sides wrapping in comparison with the traditional four-sides one and the influence of the test parameters.

2 EXPERIMENTAL WORK

2.1 *Columns details*

Six medium scale rectangular RC columns having an aspect ratio of 1:2.4 were prepared, cast, strengthened with CFRP sheets and tested to failure at the RC Laboratory of the Department of Structural Engineering of Ain Shams University. All columns had 125 × 300 mm cross-sectional dimensions and an overall height of 1250 mm, as shown in Figure 1.

Figure 1 also shows that two 175 mm height steel caps were prepared, partially filled with a layer of rich cement grout and fitted at both ends of the specimens, in order to prevent any stress concentration in the columns near the loading plates. The clear height of the specimens between the steel caps was equal to 900 mm, as shown in the same figure. Concerning the internal steel reinforcement, Figure 1 shows that each column was longitudinally reinforced with six 10 mm diameter bars equivalent to 1.25% reinforcement ratio, while the transverse reinforcement consisted of 6 mm diameter stirrups spaced at 125 mm equivalent to a volumetric percentage of 0.46%. The specimens' dimensions as well as the internal steel reinforcement details were kept the same for all tested columns, while the strengthening scheme was changed.

2.2 *Strengthening schemes*

One control specimen coded C was tested without strengthening, while the other five coded C1 to C5 were upgraded through the wrapping of horizontal unidirectional CFRP sheets according to the various schemes shown in Figure 2. The corners of the strengthened columns were rounded at a radius of 15 mm, in order to avoid fiber discontinuities around sharp corners, as shown in the same figure.

Figure 2 shows different four-sides (C1) and three-sides (C2 to C5) wrapping schemes, with the main test parameters being the clear vertical wraps' spacing, s,

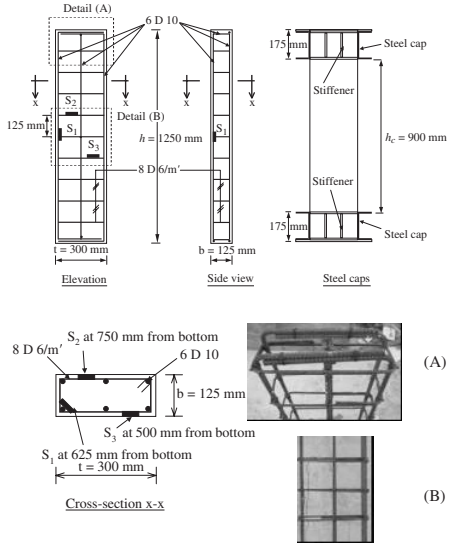

Figure 1. Columns' details and internal steel strain gauge locations.

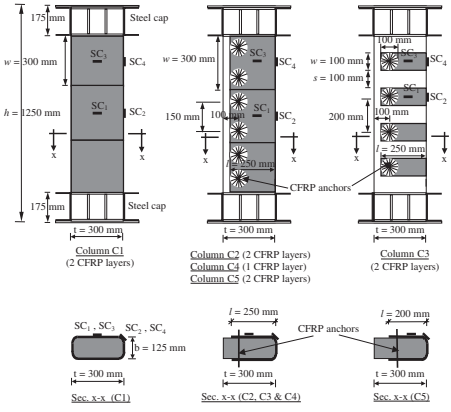

Figure 2. Schematic drawing for the wrapping schemes and CFRP strain gauge locations.

the number, n, as well as the anchorage length, l, of the CFRP layers, as detailed in the following:

- C1 was traditionally strengthened with four-sides wrapping using two layers of CFRP sheets, $n = 2$, over the whole column's clear height, h_c, hence, resulting in zero clear spacing, $s = 0$, between successive wraps of width, $w = 300$ mm each.

- C2 was similarly strengthened as C1 ($n = 2$ and $s = 0$), but with three-sides wrapping through stopping the horizontal CFRP sheets at a distance of 50 mm from the far edge of the cross-sectional longer sides, $l = 250$ mm. A mechanical anchorage system was provided at 50 mm from the ends of the sheets by using CFRP anchors through the column's width and vertically spaced at 150 mm.
- C3 was similarly strengthened as C2, but with clear spacing, $s = 100$ mm, between successive wraps of width, $w = 100$ mm each. A similar anchorage system to C2 was used through providing one CFRP anchor for each wrap, hence, resulting in a vertical anchor's spacing of 200 mm.
- C4 was similarly strengthened and anchored as C2, but using only one layer, $n = 1$, of horizontal CFRP sheets.
- C5 was similarly strengthened as C2, but with shorter horizontal sheets' extension, $l = 200$ mm, by stopping the sheets at a distance of 100 mm from the far edge of the cross-sectional longer sides. The CFRP anchors were also positioned at 50 mm from the ends of the sheets and vertically spaced at 150 mm.

The sheets were wrapped after the concrete reached an age of 28 days following the technical steps specified by the manufacturer and in the light of the ACI 440-02 (2002). Holes for the CFRP anchors were first drilled in columns C2 to C5 at the required vertical spacing. The columns' concrete surface was then prepared using a hammer and a blower, their corners rounded at a radius of 15 mm and the irregularities flattened with epoxy paste. Afterwards, the epoxy adhesive was manually spread over both the columns' surface as well as the surface of the CFRP sheets. This was followed by the manual application of the sheets on the columns, with the fibers oriented in the horizontal direction, in order to increase the confinement of the concrete section.

The CFRP anchors used to fix the horizontal sheets in C2 to C5 were then provided according to the technical steps of Figure 3. In fact, the CFRP wrapping sheets were actually used to form the anchors. They were cut to the required dimensions and guided by a steel bar through the holes drilled in the columns. The anchors penetrated the first wrapping layer by separation of parallel fibers to avoid discontinuities and maintained straight after removal of the guiding steel bar using two steel jaws, as shown in Figure 3a. This was followed by the impregnation of the holes containing the anchors with epoxy adhesive in order to fill any existing voids, as shown in Figure 3b. The ends of the anchors were then cut to the required length and radially spread over the top surface of the layer using epoxy adhesive, as shown in Figure 3c. The application of the second CFRP layer in C2, C3 and C5, took place afterwards.

(a) Insertion (b) Injection (c) Cutting

Figure 3. Application steps of the CFRP anchors in C2 to C5.

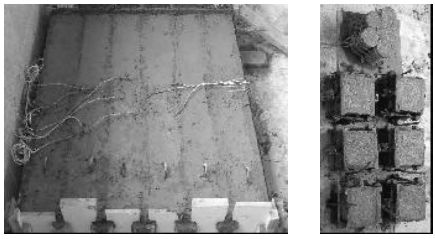

Figure 4. Casting of the columns and control specimens.

2.3 *Materials properties*

The internal longitudinal reinforcement of all columns were made of deformed steel bars (St. 360/520) of yield stress, $f_y = 360$ MPa, and ultimate tensile strength, $f_u = 520$ MPa. The internal transverse stirrups used for the columns were made of smooth steel bars (St. 240/350) of yield stress, $f_y = 240$ MPa, and ultimate tensile strength, $f_u = 350$ MPa. All the previous internal steel reinforcement had a constant modulus of elasticity, $E_s = 200$ GPa.

The concrete used was a normal weight concrete of 28-days average compressive strength, $f_{cu} = 39.4$ MPa, with mix proportions 3.5 kN/m^3 ordinary Portland cement, 7.1 kN/m^3 sand from natural resources, 12 kN/m^3 crushed limestone (25 mm maximum nominal size) and a water cement ratio of 0.53. All columns were cast horizontally in the same wooden form, at the same time and from the same batch of concrete, as shown in Figure 4. For all columns, concrete was compacted in the form using a poker vibrator, followed by water curing and covering with polythene sheeting for one week. For control purposes, two sets of six concrete cubes and six concrete split cylinders were cast along side the columns (Figure 4) and were tested on the same day as the columns, to provide values of the concrete characteristic strength, f_{cu}, and splitting tensile strength, f_{ctr}. Table 1 shows the results of these control specimens.

Finally, the mechanical properties of the CFRP sheets together with the epoxy paste and epoxy

Table 1. Test results of the control specimens.

Control specimen	1	2	3	4	5	6
Cubes f_{cu} (MPa)	40	40.1	40.8	39.6	38.45	37.2
Split cyl. f_{ctr} (MPa)	4.14	4.14	4.14	3.82	3.5	3.18

Table 2. Mechanical properties of the strengthening system.

Material property	Epoxy paste	Epoxy adhesive	CFRP sheets
Compressive strength, MPa	50–60	*	*
Tensile strength, MPa	15–20	30	3800
Young's modulus, GPa	4.3	3.8	240
Flexural strength, MPa	20–25	*	*
Bond strength (conc.), MPa	3–3.5	(1)	*

* = not available, (1) = failure occurs in concrete.

adhesive, are summarized in Table 2 as obtained from the manufacturer's data sheets.

2.4 *Instrumentations*

Extensive measurements were made of strains on key locations of the tested specimens. Strains in the internal longitudinal bars as well as the transverse stirrups were measured using three HPM electrical strain gauges of 10-mm length and 120-Ohm resistance, coded S_1 to S_3 for each specimen, as previously indicated in Figure 1. Another four electrical strain gauges coded SC_1 to SC_4 were mounted on key locations of the surface of the CFRP sheets, as previously indicated in Figure 2, in order to monitor the tensile strains of both the straight and bent portions of the sheets. The longitudinal compressive and transverse tensile concrete strains of the tested specimens were also measured using four Linear Variable Distance Transducers (LVDTs) coded D_1 to D_4, as shown in Figure 5. It should be noted that the pair of transducers used at both sides of the specimens for each strain's type, as shown in the figure, was used to monitor and correct the effect of any inclination in the specimens' verticality by averaging the strain readings.

2.5 *Test setup and loading procedure*

All specimens were tested under the effect of a uniaxial compressive static load, monotonically increasing from zero up to failure. Two hydraulic jacks, each of 2000-kN capacity, were used for this purpose. The two jacks were connected to the same pump fitted with an electronic gauge of 5-kN accuracy, so that each jack received the same pressure and applied the same load

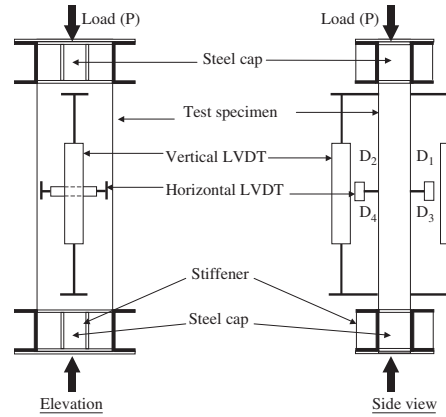

Figure 5. Positioning of vertical and horizontal LVDTs.

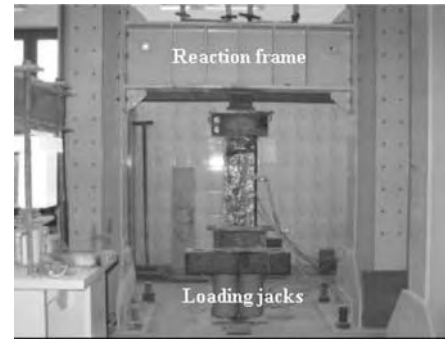

Figure 6. Test setup.

to the columns. The columns were vertically adjusted between the two adjacent jacks resting on the rigid floor of the test setup and the reaction frame, as shown in Figure 6.

At the early stages of loading, load increments of 25-kN were applied to the columns and were gradually reduced till 5-kN near failure, in order to get accurate values of strains and failure loads. Each load increment was applied during a period of about 2 minutes at the end of which the load was held constant for about 5 minutes, to allow measurements and observations. One loading cycle was applied in the previous manner from zero up to failure.

3 EXPERIMENTAL RESULTS

3.1 *Test observations and failure modes*

The control column, C, failed abruptly through the sudden formation of an inclined crack, as shown in

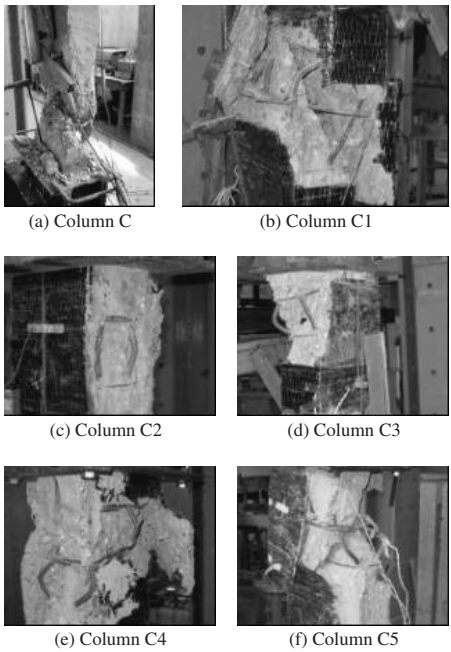

(a) Column C (b) Column C1

(c) Column C2 (d) Column C3

(e) Column C4 (f) Column C5

Figure 7. Failure patterns of the tested columns.

Figure 7a, where the concrete cover spalled off, the longitudinal steel bars buckled and the load suddenly dropped to zero. All the other strengthened columns, C1 to C5, failed at higher loads in a less brittle manner through either the rupture of the CFRP sheets at the corners (where a plane of weakness existed) alone or together with that of the CFRP anchors, hence, pulling both the sheets and the concrete cover out-of-plane, as shown in Figures 7b, c, d, e and f. In both previous cases, this was followed by the formation of a similar inclined crack as in C as well as the buckling of the longitudinal steel bars, as shown in the same latter figures. It should be noted that none of the strengthened columns experienced rupture of the CFRP anchors prior to that of the sheets' corners, hence, revealing full activation of the anchors prior to failure. It should also be noted that none of the strengthened columns experienced a sudden drop to zero load, hence, revealing the less brittle failure due to the extra-confinement added by the wrapping system when compared to the control column.

3.2 *Capacity and deformability*

Table 3 shows the axial capacity, P_u, of the tested columns together with the ultimate longitudinal compressive concrete strain, ε_{cu}. The capacity as well as the ultimate longitudinal compressive concrete strain enhancement ratios for the strengthened specimens relative to the control one, P_u/P_c and $\varepsilon_{cu}/\varepsilon_c$, respectively, are also shown in the table.

Table 3. Axial capacities and ultimate longitudinal compressive concrete strains.

Spc. no.	CFRP sheets s (mm)	n	l (mm)	P_u (kN) (1)	P_u/P_c (2)	ε_{cu} $\times 10^{-3}$ (3)	$\varepsilon_{cu}/\varepsilon_c$ (4)
C	None	None	None	1195	1.0	2.4	1.0
C1	0	2	4 sides	1600	1.34	5.4	2.25
C2	0	2	250	1490	1.25	4.8	2.0
C3	100	2	250	1440	1.21	4.5	1.87
C4	0	1	250	1410	1.18	4.3	1.79
C5	0	2	200	1330	1.11	3.8	1.58

(1) P_u = capacity of the strengthened column, (2) P_c = capacity of the control column, (3) ε_{cu} = ultimate longitudinal compressive concrete strain of the strengthened column, (4) ε_c = ultimate longitudinal compressive concrete strain of the control column.

Concerning the axial capacity, Table 3 shows a reasonable capacity enhancement of 25% for C2 with three-sides wrapping when compared to the 34% enhancement attained by the conventional four-sides wrapping in C1. The former reduction is normally attributed to the lower confinement induced by the three-sides wrapping technique when compared to the traditional one. Table 3 also shows further capacity enhancement's reductions to 21, 18 and 11%, for larger vertical wraps' clear spasing, s, lower number of wraps, n, and shorter anchorage length, l, in C3, C4 and C5, respectively. However, a closer comparative look at the former two reductions shows the low sensitivity of the capacity enhancement to both the s and n parameters, since large variations in those parameters resulted in only 4 and 7% further reductions for C3 and C4, respectively, when compared to C2, as shown in the table. Nonetheless, the extreme sensitivity of the capacity enhancement to the anchorage length, l, parameter can also be noted in Table 3 from the further 14% reduction for C5 when compared to C2, as a result of a relatively slight variation of the latter parameter. Accordingly, it can be concluded that, unlike for the s and n parameters, the induced confinement of the three-sides wrapping system is dramatically affected by the anchorage length parameter, l.

Concerning the ultimate longitudinal compressive concrete strains, Table 3 first shows deformability enhancement ratios for the strengthened columns relative to the control specimen of almost 1.6 times the respective capacity enhancement ratios attained. This reveals the higher efficiency of the extra confinement induced by the wrapping technique in increasing the columns' failure deformation when compared to

the corresponding axial capacity enhancement. The previous finding further justifies the well-established literature that the wrapping technique is more attractive for use where ductility enhancement is required, especially in seismic regions. Table 3 also confirms relative deformability reductions for columns C2 to C5 (wrapped from three sides) when compared to C1 (conventionally wrapped) that were in line with the respective relative capacity reductions. Thus, the reasonable deformability of C2, the low sensitivity of the deformability to the *s* and *n* parameters as well as its high sensitivity to the anchorage length, *l*, parameter, were further confirmed in the table. Again, it should be noted that the previous deformability reductions were around 1.6 times the respective capacity reductions, as shown in Table 3.

3.3 *Longitudinal compressive strains*

Figures 8 and 9 show the load versus the longitudinal compressive concrete and steel strain curves at positions D_1 and S_1, respectively, of the columns. The slightly higher concrete strain values when compared to the corresponding steel ones at equal load levels are experimentally accepted and attributed to minor traditional errors in the steel strain gauges' readings.

Figures 8 and 9 first show the linear longitudinal compressive strain responses of the control specimen till failure and all the other strengthened columns up to around 80% of their failure loads. These linear responses nearly followed similar trajectories for all tested specimens, as shown in both figures, hence, revealing the unchanged stiffness of the strengthened columns when compared to the control one; a finding which turns more attractive the use of the wrapping technique to strengthen RC columns in seismic regions, since no extra seismic loads will be attracted. The linear response of the control column, C, shown in both figures, till failure which occurred without yielding of the internal steel longitudinal bars (0.0014 failure strain), as demonstrated in Figure 9, gives a further proof of the highly brittle response and failure type of C. On the other hand, Figures 8 and 9 show the increasingly non-linear responses of all the other strengthened columns beyond 80% of their enhanced failure loads. The latter, together with the highly post-crushing and post-yielding compressive strain levels developed in the concrete (0.0054 in C1 to 0.0038 in C5) and longitudinal bars (0.005 in C1 to 0.0032 in C5) at failure of the strengthened columns, shown in Figures 8 and 9, respectively, give a clear indication of the satisfactory beneficial confining effect of the three-sides wrapping technique used for C2 to C5, when compared to the conventional wrapping of C1, from both capacity and ductility points of views. In this respect and similar to the findings of the previous section, the figures first show that the previous strain

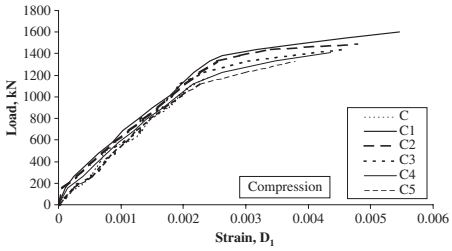

Figure 8. Load–longitudinal compressive concrete strain curves of the tested columns.

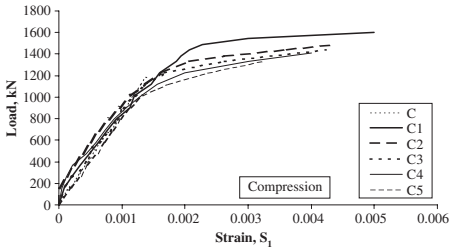

Figure 9. Load–longitudinal compressive steel strain curves of the tested columns.

enhancements were reasonably reduced for C2 when compared to C1. The slight strain reductions in C3 and C4 with much higher clear spacing, *s*, and half the number of CFRP layers, *n*, respectively, relative to C2, can also be noted in the figures. Finally, the relatively high strain reductions in C5, having slightly shorter anchorage length, *l*, when compared to C2, were similarly noted in both figures.

3.4 *Transverse tensile strains*

Figure 10 shows the load versus the transverse tensile steel stirrup's strain curves at position S_2 of the tested columns.

As expected, figure 10 first shows that the transverse tensile stirrup's strains were about 40 to 50% the longitudinal compressive bar's strains in all respective specimens up to failure. A comparative look at the figure again confirms all the previous findings of this study. This included the linear and similar stiffness responses of all tested columns up to around 80% of their failure loads, as well as the brittle behavior of C till failure, where its ultimate stirrup's strains only reached a value of 0.0005, far below yielding. It should be noted that the small non-linearity near failure of the control column's response in figure 10 was due to the non-linear characteristics of the transverse strain of

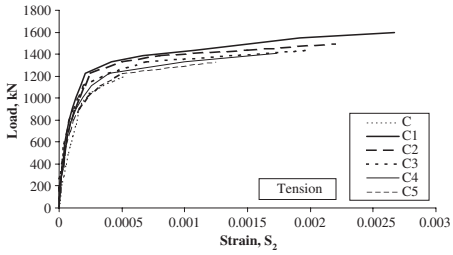

Figure 10. Load–transverse tensile steel strain curves of the tested columns.

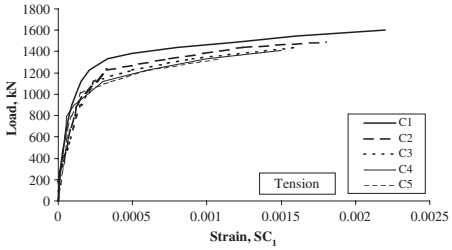

Figure 11. Load–CFRP tensile strain curves of the tested columns.

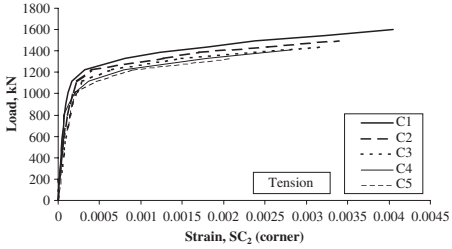

Figure 12. Load–CFRP tensile strain curves at corners of the tested columns.

concrete axially loaded in compression [Park & Paulay (1975)]. The increasingly non-linear trends of all the strengthened columns' responses beyond the previous load level, together with the high transverse stirrup's strains developed at enhanced failure loads, can also be detected in Figure 10. In addition, the satisfactory confining effect of the three-sides wrapping technique when compared to the conventional one is also noted in Figure 10, through the small reductions in the stirrup's strain at failure of C2 to a value of 0.0022 when compared to the 0.0027 value in C1, hence, revealing the yielding of the stirrups of both columns. The latter figure also proves the none-harmful effect of either highly increasing the wraps' clear spacing, *s*, in C3 or halving the number of layers, *n*, in C4, since either yielding (0.002) or nearly yielding (0.0017) stirrups' strains where developed in C3 and C4, respectively, at failure. Finally, the dramatic decrease in the stirrup's strain at failure of C5 to a value of 0.00125 (far below yielding), shown in Figure 10, provides further proof of the criticality of any small changes in the anchorage length, *l*, parameter.

3.5 *Tensile strains in the CFRP sheets*

Figures 11 and 12 show the load versus the tensile strain curves in the CFRP sheets at positions SC_1 and SC_2 (corners), respectively, of the strengthened columns.

Considering Figures 11 and 12, the non-linearity of all CFRP strain responses in both figures can first be noted and is again attributed to the non-linear characteristics of the transverse strain of concrete axially loaded in compression [Park & Paulay (1975)]. In addition, a comparative look at Figures 11 and 12 shows that the corner strains of each specimen till failure (Figure 12) were almost twice the straight portion's strains (Figure 11), due to the well-established stress concentration phenomena around sharp corners. Normally, Figure 11 also shows that the strains developed in the straight portion of the CFRP sheets of each column were approximately of the same order as the corresponding transverse tensile stirrups strains previously shown in Figure 10.

A closer look at Figures 11 and 12 shows that relatively high strains were developed for the conventionally wrapped (C1) as well as the three-sides wrapped (C2) columns, up to values of 0.0022 (straight) and 0.0041 (corner) and values of 0.0018 (straight) and 0.0034 (corner), respectively, at failure. The latter slight reductions for C2 give a final proof that its CFRP anchors were fully activated prior to failure and that the three-sides wrapping system tested in this study can be adopted successfully. The further slight reductions in Figures 11 and 12 at failure of C3 and C4 to values of 0.0016 (straight) and 0.0032 (corner) and values of 0.0015 (straight) and 0.0028 (corner), respectively, gives further confirmation of the low sensitivity of the gained confinement to even large variations in both the clear wraps' spacing, *s*, and number of layers, *n*, parameters. On the other hand, the high strain reductions witnessed in Figures 11 and 12 at failure of C5 to values of 0.0011 (straight) and 0.0021 (corner), respectively, also give a clearer confirmation for the very high sensitivity of the gained confinement to the anchorage length, *l*, parameter. Finally, it is worth mentioning that all the previous developed strains in the CFRP sheets at failure, shown in Figures 11 and 12, were highly lower than the 0.0155 maximum tensile strain reported by the manufacturer; in line with

the finding reported by Hosny et al (2001). This is due to the CFRP sheets' planes of weakness around sharp corners, where their rupture dictated the failure of all the strengthened columns of this program, as previously stated in section 3.1.

4 CONCLUSIONS

The innovative strengthening system of wrapping RC rectangular columns with CFRP sheets in three sides only together with the use of CFRP anchors, has experimentally demonstrated satisfactory confining effect and associated enhancements in all aspects of structural behavior, which were comparable to these resulting from the conventional four-sides wrapping, as follows:

- Less brittle failure modes, due to the gained concrete confinement. This was initiated by either the rupture of the CFRP sheets at corners alone or combined with that of the CFRP anchors, followed by the formation of an inclined crack as well as the buckling of the longitudinal steel bars.
- Reasonable axial capacity and ultimate deformability enhancements up to 25% and 200%, respectively, compared to the respective 34% and 225%, resulting from conventional wrapping.
- Unchanged column's stiffness up to around 80% of the axial capacity, hence adding the benefit of attractive usage in seismic regions; since no extra loads would be attracted by the strengthened columns.
- Reasonable non-linear longitudinal compressive concrete and steel strain responses prior to failure at values up to 0.0048 and 0.0043, respectively, compared to the respective values of 0.0054 and 0.005, resulting from conventional wrapping. Thus, the longitudinal steel yielded in both cases.
- Reasonable non-linear transverse tensile steel strain response prior to failure at stirrup's strain up to the post-yielding value of 0.0022, compared to the respective value of 0.0027 value in conventional wrapping.
- Full activation of the CFRP anchoring system, as deducted from the reasonable strain levels developed in the CFRP sheets at failure, up to values of 0.0018 and 0.0034 in the straight portions and at corners, respectively, compared to the respective values of 0.0022 and 0.0041, resulting from conventional wrapping.

The satisfactory confining effect and the associated structural enhancements resulting from the three-sides CFRP wrapping system introduced in this study were found low sensitive to the variations of both the vertical wraps' clear spacing, *s*, as well as the number of CFRP layers, *n*; since large variations of the two latter parameters resulted in relatively small variations in the previously achieved enhancements.

The anchorage length, *l*, of the CFRP sheets was found an extremely critical parameter affecting the efficiency of the three-sides wrapping technique investigated in this study; since only small reductions in this parameter resulted in relatively dramatic reductions in the confining effect and the associated structural enhancements.

ACKNOWLEDGMENT

The authors whish to acknowledge the financial support of Ain Shams University. The support provided by MBrace S & P and Liftslab-Egypt Companies as well as by Eng. Mostafa Saad during the experiments, is also acknowledged.

REFERENCES

ACI 440-2002. Guide for the Design and Construction of Externally Bonded FRP Systems for Strengthening Concrete Structures. American Concrete Institute Committee 440, Farmington Hills, Michigan, USA, October, 45 pp.

Hosny, A., Shahin, H., Abdelrahman, A. & El-Afandy, T. 2001. Strengthening of Rectangular RC Columns Using CFRP. Proceedings of the fifth International Conference on Fiber Reinforced Plastics for Reinforced Concrete Structures (FRPRCS-5), Cambridge, UK, July 16 to 18, Vol. 2, pp. 773–782.

Hosotani, M., Ka Washima, K. & Hoshikuma, J. 1997. A Study on Confinement Effect of Concrete Cylinders by Carbon Fiber Sheets. Proceedings of the Third International Symposium on Non-Metallic (FRP) Reinforcement for Concrete Structures (FRPRCS-3), Japan Concrete Institute, Sapporo, Japan, October 14 to 16, Vol. 1, pp. 217–224.

Matthys, S., Tearwe, L. & Audenaert, K. 1999. Tests on Axially Loaded Concrete Columns Confined by Fiber Reinforced Polymer Sheet Wrap. Proceedings of the Fourth International Symposium on Fiber Reinforced Polymer Reinforcement for Reinforced Concrete Structures (FRPRCS-4), SP-188, American Concrete Institute, Baltimore, Maryland, USA, October 31 to November 5, pp. 217–228.

Neale, K. & Labossiere, P. 1997. State-of-the-Art Report on Retrofitting and Strengthening by Continuous Fiber in Canada. Proceedings of the Third International Symposium on Non-Metallic (FRP) Reinforcement for Concrete Structures (FRPRCS-3), Japan Concrete Institute, Sapporo, Japan, October 14 to 16, Vol. 1, pp. 25–39.

Park, R. & Paulay, T. 1975. Reinforced Concrete Structures. John Wiley and Sons, New York, USA, 200 pp.

Rochette, P. & Labossiere, P. 2000. Axial Testing of Rectangular Column Models Confined with Composites. Journal of Structural Engineering, American Society of Civil Engineers (ASCE), Vol. 4, No. 3, pp. 129–136.

FRP Composites in Civil Engineering – CICE 2004 – Seracino (ed)

Moment redistribution in RC continuous beams strengthened in flexure by CFRP laminates

A.A. El-Ghandour[1], A.A. Abdelrahman[2], E.A. Nasr[3] & H.A. Aly[4]
[1]*Assistant Professor,* [2]*Associate. Professor,* [3]*Professor &* [4]*M.Sc. Student*
Department of Structural Engineering, Ain Shams University, Cairo, Egypt

ABSTRACT: An experimental investigation in the behavior of RC continuous beams strengthened in flexure with CFRP laminates was conducted. Six medium scale two-span beams were tested under static loading till failure. The test parameters included the internal flexural reinforcement ratio as well as the position and number of laminates. Key test results showed considerable capacity enhancement for all strengthened beams, at the price of brittle peeling failure and reduced ductility. General improvements in all aspects of flexural behavior were also monitored. In addition, the more uniform stiffness distribution along the strengthened beams' lengths resulted in reactions and internal forces' values closer to the elastic ones as well as lower moment redistribution ratios. All previous benefits were more pronounced for beams with lower internal reinforcement ratio. Finally, the sagging strengthening technique proved much higher efficiency than the hogging one, which also demonstrated negative results in some structural aspects.

1 INTRODUCTION

Upgrading of reinforced concrete (RC) structures has recently been a widespread application in the construction industry. This is usually done with an aim of enhancing the load carrying capacity of the different structural elements, in order to fulfill the increases of either the superimposed loads in the new building codes or these resulting from the change of use of the structure. Since beams are among the most important structural elements, their upgrading (strengthening) process has been the subject of several improvements, starting from the traditional techniques (concrete and steel jacketing as well as steel plate bonding) up to the most updated applications of using Fiber-Reinforced-Polymers (FRP) materials in the flexural and shear strengthening of these elements. However, most of the research work investigating the two latter applications has been focused on simply supported beams, while only little work dealt with continuous beams, although they represent the majority of beams existing in RC structures. Nonetheless, the little literature on FRP strengthening of continuous beams is found to provide enough key issues for further investigations, since it dealt with flexural strengthening (El-Refaie et al 2003) or shear strengthening (Arduini et al 1997, Khalifa et al 1999, Tann et al 2000) or both (Grace et al 1999).

This paper presents an experimental investigation in the structural behavior of RC two-span continuous beams strengthened in flexure using Carbon-Fiber-Reinforced-Polymers (CFRP) laminates, when tested statically from zero till failure. The flexural internal reinforcement ratio as well as the position and number of CFRP strengthening laminates were the main parameters investigated. The test results including crack patterns, deflections, tensile strains in the flexural reinforcement and CFRP laminates as well as failure loads are presented and discussed. Key experimentally derived structural aspects of behavior, including end support reactions, failure moments, sagging and hogging bending moments, sagging and hogging moment redistribution ratios as well as deflection ductility, are also discussed. Finally, design oriented conclusions are highlighted.

2 EXPERIMENTAL WORK

2.1 *Beams details*

A total of six medium scale two-span RC continuous beams were tested to failure under the effect of two equal mid-span concentrated static loads, as shown in figure 1. The figure also shows the beams' geometry, detailing of internal steel reinforcement as well as the internal steel strain gauges' locations. All beams had a 300 mm deep T-shaped cross-section and an overall length of 4500 mm over two equal clear spans of 2150 mm each, as shown in the figure. The beams were divided into two groups of three beams each,

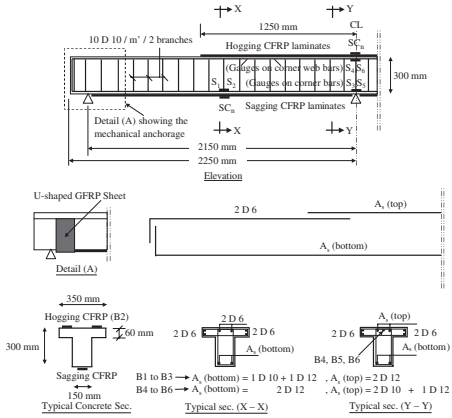

Figure 1. Beam details, steel and CFRP strain gauge locations.

according to the main sagging internal tension steel reinforcement ratio. Beams coded B1 to B3 of group (1) were provided with sagging tension steel of two bars of diameters 10 and 12 mm ($\rho = 0.42\%$), while B4 to B6 of group (2) had two bars of diameter 12 mm corresponding to a higher reinforcement ratio ($\rho = 0.5\%$), as shown in figure 1. For each group, the hogging internal tension steel was calculated to result in a hogging flexural capacity similar to the sagging one of the T-shaped cross-section; i.e., each beam would reach its hogging and sagging flexural capacities at the same time. Figure 1 also shows that shear reinforcement were provided in all beams in the form of closed stirrups of 10 mm diameter bars at 100 mm spacing, designed to prevent shear failures even in strengthened beams. Finally, figure 1 shows the typical positioning of the CFRP laminates bonded to either the hogging or sagging regions of the beams, together with their respective strain gauges' locations.

2.2 *Strengthening schemes*

The positioning as well as the number of CFRP strengthening laminates were the main test parameters, as detailed in table 1. The table shows that the first beam of each group, namely B1 and B4, was not strengthened and considered as a control specimen. The rest of the beams were strengthened in either their hogging or sagging moment regions, symmetrically about the beams' cross-sectional vertical axis, as indicated in figure 1 and table 1. In case of hogging strengthening of B2 in table 1, the laminates were symmetrically extended on both sides of the central support bypassing the mid-span concentrated loads, as shown in figure 1, in order to ensure enough anchorage length. On the other hand, the sagging strengthening of the

Table 1. Strengthening schemes.

Group no.	Beam no.	Hogging laminates No.	Hogging laminates Area (mm^2)	Sagging laminates No.	Sagging laminates Area (mm^2)
Group (1)	B1	None	None	None	None
	B2	2	120	None	None
	B3	None	None	2	120
Group (2)	B4	None	None	None	None
	B5	None	None	1	60
	B6	None	None	2	120

rest of the beams was accomplished through extending the CFRP laminates to cover the whole soffits of the beams, in addition to the provision of a mechanical anchorage at the ends of the laminates in the form of U-shaped GFRP sheets, as shown in detail (A) of figure 1. Each CFRP laminate was 50 mm wide and 1.2 mm thick with a total effective area of 60 mm^2. The total area of the laminates used for each beam is shown in table 1.

The application of the CFRP laminates to the beams was accomplished according to the manufacturer's specifications and in the light of the ACI 440-02 (2002). This included the surface preparation of the concrete substrate using a grinder and checking of surface deviation. This was followed by the application of the epoxy resin primer then the epoxy resin adhesive to the concrete substrate using a brush. Finally, the CFRP laminates were placed by hand and pressed onto the adhesive with a rubber roller.

2.3 *Materials properties*

The internal flexural reinforcement of all beams was made of deformed steel bars (St. 400/600) of yield stress, $f_y = 400$ MPa, and ultimate tensile strength, $f_u = 600$ MPa. The internal transverse stirrups (shear reinforcement) were made of deformed steel bars (St. 360/520) of yield stress, $f_y = 360$ MPa, and ultimate tensile strength, $f_u = 520$ MPa. The transverse internal reinforcement used for the flanges of the beams was made of smooth steel bars (St. 240/350) of yield stress, $f_y = 240$ MPa, and ultimate tensile strength, $f_u = 350$ MPa. All the previous reinforcement had a constant modulus of elasticity, $E_s = 200$ GPa.

The concrete used was a normal weight concrete of 28-days average compressive strength, $f_{cu} = 39.4$ MPa, with mix proportions 3.5 kN/m^3 ordinary Portland cement, 7.1 kN/m^3 sand from natural resources, 12 kN/m^3 crushed limestone (25 mm maximum nominal size) and a water cement ratio of 0.53. All beams were cast in the same wooden form, at the same time and from the same concrete batch. Concrete was

Table 2. Test results of the control specimens.

Control specimen	1	2	3	4	5	6
Cubes f_{cu} (MPa)	40	40.1	40.8	39.6	38.45	37.2
Split cyl. f_{ctr} (MPa)	4.14	4.14	4.14	3.82	3.5	3.18

Table 3. Mechanical properties of the strengthening system.

Material property	Epoxy primer	Epoxy adhesive	CFRP laminates
Compressive strength, MPa	65–75	>60	*
Tensile strength, MPa	10–15	*	≥2700
Young's modulus, GPa	9	*	≥165
Flexural strength, MPa	20–30	>30	*
Bond strength (conc.), MPa	(1)	>3.5	*

* = not available, (1) = failure occurs in concrete.

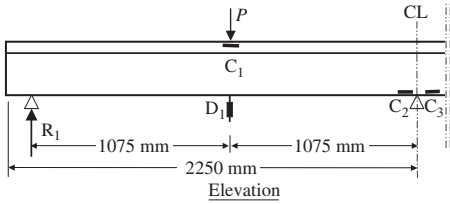

Figure 2. Deflection and concrete strain measurements.

compacted in the form using a poker vibrator, followed by water curing and covering with polythene sheeting for one week. For control purposes, two sets of six concrete cubes and six concrete split cylinders were cast along side the beams and were tested on the same day as the beams, in order to provide values of the concrete characteristic strength, f_{cu}, and splitting tensile strength, f_{ctr}, as shown in table 2.

Finally, the mechanical properties of the CFRP laminates together with the epoxy resin primer and adhesive, are summarized in table 3, as obtained from the manufacturer's data sheets.

2.4 *Instrumentations*

Extensive measurements were made at key locations of the tested beams, as previously shown in figure 1 as well as figure 2 below. The crack propagation was monitored during the tests until failure of the beams.

Two 0.01 mm accuracy Linear Variable Distance Transducers (LVDTs) coded D_1 and D_2 were used to measure the mid-spans deflections of each beam, as shown in figure 2. Eight HPM electrical strain gauges of 10 mm length and 120 Ohm resistance, coded S_1 to S_8, were mounted on the internal longitudinal steel bars of each beam to monitor the tensile and compressive strains, as previously indicated in figure 1. Figure 1 also shows that the maximum tensile strain at the middle of each CFRP strengthening laminate was measured using another two HPM electrical strain gauges similar to the steel ones and consecutively coded $SC_{n=1,2,etc}$. Finally, the compressive concrete strains at the mid-spans as well as at the central support sections were measured by means of another four HPM electrical strain gauges of 100 mm length and 120 Ohm resistance, coded C_1 to C_4, as shown in figure 2.

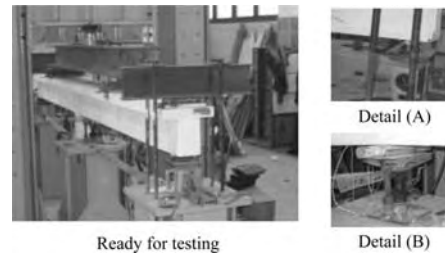

Figure 3. Test setup.

2.5 *Test setup and loading procedure*

The two-spanned beams were tested under the effect of a total static load, $2P$, increasing incrementally from zero up to failure and divided through the use of a rigid steel beam into two-equal loads, P (figure 2), each acting at the mid-span section of each span, as shown in figure 3. The end support reactions (R_1 in figure 2 and R_2) were monitored during the tests using two 50 kN capacity and 1 kN accuracy dynamometers placed under the beams between the bottom steel plate of the support and the steel base of the test machine, as shown in detail (A) of figure 3. The central support of the beams was provided with a vertical screw to ensure their horizontal alignment before loading, as shown in detail (B) of figure 3.

The loading was manually applied using a hydraulic jack of 500 kN capacity and 5 kN accuracy, placed between the reaction-frame of the test machine and the steel beam used to distribute the load in two, as shown in figure 3. Each load increment was applied during a period of about 2 minutes, at the end of which the load was held constant, to allow measurements and observations. One loading cycle was applied from zero up to failure.

3 EXPERIMENTAL RESULTS

3.1 *Test observations*

The crack propagation in all tested beams followed the similar traditional sagging and hogging patterns in continuous beams. However, it was noted that improved patterns were associated to the corresponding strengthened regions, in terms of crack distribution and widths. In fact, the provision of the CFRP laminates at the beams' soffits resulted in more uniform sagging crack distributions covering longer portions of the beams' spans and having smaller widths, when compared to the corresponding control beam of each group, as shown in figure 4 (a and b) for beams B3, B5 and B6 at failure. This was accompanied with a less uniform hogging crack distributions covering shorter portions of the respective beams' hogging regions and having bigger widths, as shown in the same figure. The previous is clearly attributed to the effect of the strengthening laminates in enhancing the beams' stiffness in the corresponding regions and, hence, attracting higher moments from the adjacent un-strengthened parts. Figure 4 (a) also shows the opposite trend followed by beam B2 strengthened in its hogging region.

The tested beams experienced two distinct modes of failure. Control beams B1 and B4 failed in a ductile flexural failure manner, through the yielding of the main tensile hogging and sagging internal bars at the same time (as-designed), followed by concrete crushing at the respective opposite sides. On the other hand, all the strengthened beams failed abruptly in an explosive manner at higher capacities, due to the peeling of the concrete cover along the steel reinforcement level adjacent to the external CFRP laminates, as shown figure 5. It should be noted that neither the extension of the hogging laminates to cover the whole hogging region over the central support in B2 nor the mechanical anchorage of the sagging laminates provided by the U-shaped GFRP sheets adjacent to the supports, prevented the peeling mode of failure. However, the previous precautions redirected the peeling away from the laminates' ends, as shown in figure 5. It was also noted that the mechanical anchorage resulted in the sagging strengthening system being able to sustain the ultimate load after the occurrence of the peeling failure. An extreme demonstration of this benefit was in B5, where de-bonding took place at one span at 84% of its failure load and the beam was still able to carry higher loads until de-bonding of the second span at failure. The modes of failure together with the tested beams capacities, P_u, are summarized in table 4.

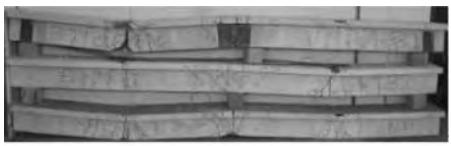

(a) Beams B1, B2 and B3 (upward direction)

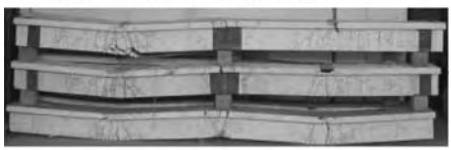

(b) Beams B4, B5 and B6 (upward direction)

Figure 4. Crack patterns of the tested beams at failure.

Figure 5. Typical peeling failure of the strengthened beams.

Table 4. Beams' capacities and modes of failure.

Group no.	Beam no.	CFRP laminates No.	CFRP laminates Area (mm^2)	Ultimate load P_u (kN)	Failure mode
Group (1)	B1	None	None	170	Flexure
	B2	2 (top)	120 (top)	235	Peeling
	B3	2 (bot.)	120 (bot.)	255	Peeling
Group (2)	B4	None	None	195	Flexure
	B5	1 (bot.)	60 (bot.)	250	Peeling
	B6	2 (bot.)	120 (bot.)	280	Peeling

3.2 *Deflections*

Figure 6 shows the total load, $2P$ (P is the mid-span point load) versus the mid-span deflection, D_1, curves of the tested beams.

Figure 6 shows that all beams exhibited similar pre-cracking stiffness and deflection responses. It can also be noted from the figure that all strengthened beams exhibited higher post-cracking stiffness and smaller deflection responses when compared to the respective control ones. The latter aspects were directly proportional to the number of CFRP laminates and were more pronounced in beams of group (1) with lower internal reinforcement ratio when compared to these of group (2), as shown in figure 6. This reveals the higher efficiency of the CFRP laminates in case of lower reinforcement ratio. The logical stiffer response of beams of group (2) with higher internal reinforcement ratio is also noted in figure 6, when compared to these of group (1). Finally, figure 6 shows that, for equal number of laminates and reinforcement ratio, the hogging strengthening of B2 resulted in a similar response obtained from the sagging strengthening of B3. However, a lower ultimate deflection was obtained at a slightly lower capacity for B2, hence, revealing the higher efficiency of the sagging strengthening near failure. This is attributed to the fact that the latter system resulted in stable simply supported mechanisms of the adjacent spans after occurrence of the hogging flexural failure.

3.3 *Internal tensile steel strains*

Figures 7 and 8 show the total load versus the internal tensile steel strain curves of the bottom bars at the mid-span section, S_2, and the top bars over the central support, S_4, respectively, for all tested beams.

Figures 7 and 8 show that all beams had similar pre-cracking responses. They also show that, as designed, the sagging and hogging bars yielded at the same load level for the control beams B1 and B4. In addition, the yielding load level of B4 was higher than that of B1, due to the higher reinforcement ratio of the former beam. For each group, the sagging and hogging bars of the strengthened beams yielded at higher loads than the corresponding control ones, as shown by the stiffer post-cracking responses of the former beams indicated in both figures. The figures also show that these stiffer responses were directly proportional to the number of laminates. However, it should be noted that the hogging strengthening of B2 resulted in a lower stiffness response for its sagging bars at 85% of its failure load, when compared to B3 (same group but strengthened in sagging with a similar number of laminates), as shown in figure 7. This confirms the higher efficiency of the sagging strengthening near failure. Finally, the general higher post-cracking stiffness responses of group (2) beams when compared to these of group (1), can also be noted in figures 7 and 8.

3.4 *Tensile strains in CFRP laminates*

Figure 9 shows the total load versus the tensile strain curves, SC_2, at the middle of the CFRP laminates for all strengthened beams.

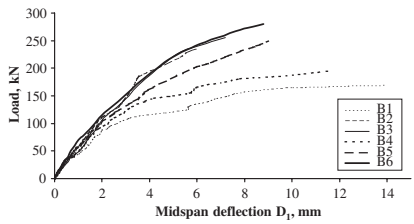

Figure 6. Total load–midspan deflection curves.

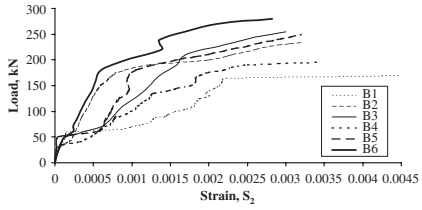

Figure 7. Total load–sagging tensile steel strain curves.

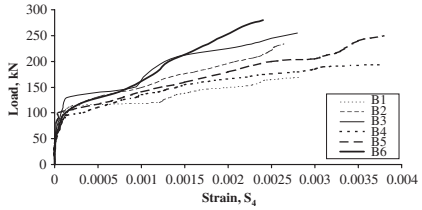

Figure 8. Total load–hogging tensile steel strain curves.

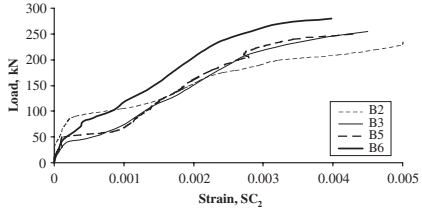

Figure 9. Total load–tensile strain curves at the middle of the CFRP laminates of the strengthened beams.

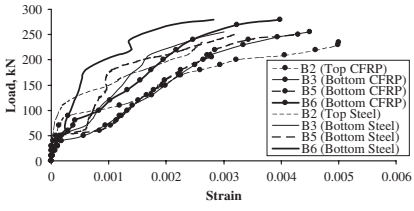

Figure 10. Comparison of laminates and adjacent bars' strains.

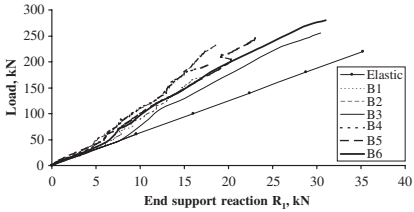

Figure 11. Total load–end support reaction curves.

Table 5. Ultimate load and moment enhancement ratios.

Group no.	Beam no.	CFRP laminates no.	Ult. load enhanc. ratio α	Ult. moment enhanc. ratio β
Group (1)	B1	None	1	1
	B2	2 (top)	1.38	1.55
	B3	2 (bot.)	1.5	1.81
Group (2)	B4	None	1	1
	B5	1 (bot.)	1.28	1.31
	B6	2 (bot.)	1.44	1.97

Figure 9 shows that, for all beams, the tensile strains in the laminates increased significantly after concrete cracking and yielding of the internal steel bars, until reaching an average level of 0.0045 at beams' failure. The similar pre-cracking stiffness responses of all strengthened beams and the higher post-cracking stiffness responses of group (2) beams are again witnessed in the figure. The stiffer post-cracking responses increasing with the number of laminates are also witnessed in figure 9. This is clearly indicated by the lower strains at equal load levels as well as the lower failure strains for the beams strengthened with a higher number of laminates. The previously established lower efficiency of the hogging strengthening near failure compared to the sagging one, is further confirmed by the lower stiffness response of B2 at approximately 80% of its failure load when compared to that of B3, as shown in figure 9.

Comparisons of the above laminates' tensile strain curves with these in the adjacent internal bars, S_2 or S_4, for all strengthened beams till failure, are shown in figure 10. The figure first shows the nearly similar pre-cracking strains developed in the laminates and the adjacent bars. Beyond cracking, the figure shows that the laminates developed higher strains than the adjacent bars at equal load levels, hence, revealing effective composite action between the laminates and the concrete substrate. The figure also shows that the previous strains' difference increased with increasing loads, until reaching its maximum gap at yielding of the bars. Beyond yielding, the gap decreased gradually, as shown in figure 10, since the stiffness of the internal bars' responses decreased dramatically. However, the figure shows that the strains of the laminates remained higher till failure.

3.5 *End support reactions*

Figure 11 shows the total load versus the end support reaction, R_1, curves for all tested beams. The elastic end support reaction response, assuming uniform flexural stiffness along the beam's span, is also plotted in the figure.

Figure 11 shows that the pre-cracking responses of all beams were nearly similar and close to the elastic one. With increasing loads after cracking, the end support reaction for each beam became increasingly lower than the elastic one till failure, as shown in the figure, as a result of the loss in the beam's flexural stiffness and the associated reduction in the portion of total load transferred to the end supports. Figure 11 also shows that the former reduction was partially compensated by the sagging strengthening of B3, B5 and B6, as depicted from their relatively closer reaction values to the elastic one at equal load levels, when compared to their respective control beams. The previous increases in the reactions were directly proportional to the number of sagging laminates provided, as shown in the figure. Figure 11 also shows that B2 followed an opposite trend than the previous beams, since its hogging strengthening attracted more load to the central support region, hence, resulting in the lowest amount of load transfer to the end supports. Hence, unlike the hogging strengthening, the sagging one was beneficial in getting the end support reaction values closer to the elastic one, as a result of the gained relatively uniform flexural stiffness along the beams' spans when compared to the control ones. Finally, the sharp decrease, shown in figure 11, in R_1 response of B5 at around 84% of its failure load is again attributed to the laminates' de-bonding at one span at this load level, prior to the de-bonding of the second span at failure.

3.6 *Ultimate load and moment enhancement ratios*

Table 5 shows the ultimate load and moment enhancement ratios for all strengthened beams. The ultimate

load enhancement ratio, α, for each strengthened beam was calculated as the ratio between its total failure load and that of its respective control beam. The ultimate moment enhancement ratio, β, of a strengthened section for each strengthened beam was calculated as the ratio between the ultimate moment of that section at beam's failure and that of the corresponding section of the respective control beam. It should be noted that the experimental moment of each beam at any load level was calculated from equilibrium considerations using the values of the end support reaction and mid-span applied load.

Considering the ultimate load enhancement ratios, α, of table 5, it can be noted that the sagging or hogging strengthening were effective, since they resulted in satisfactory capacity enhancements up to 1.5 that of the control beam. The higher efficiency of those techniques for lower reinforcement ratio is also noted from the higher ratio of B3 compared to B6 in the table. Table 5 also confirms the lower efficiency of the hogging strengthening compared to the sagging one, as noted from the lower ratio of B2 in comparison to B3. Finally, the direct proportionality between the number of laminates and the ultimate load enhancement ratio is further proven from the higher ratio of B6 when compared to that of B5 in table 5.

Considering the ultimate moment enhancement ratios, β, of table 5, it can be noted that all strengthened sections resisted higher moments than the corresponding ones in the respective control beams. Furthermore, unlike simply supported beams, table 5 shows that the moment enhancement ratio of a strengthened section in each strengthened beam was higher than the corresponding beam's load enhancement ratio, due to the moment redistribution induced by the increased stiffness of the strengthened section. Nonetheless, the two previous ratios are similar in strengthened simply supported beams.

3.7 *Load–moment relationships*

Figures 12 and 13 show the total applied load versus the sagging and hogging bending moment curves, respectively, of all tested beams. The sagging and hogging bending moment responses obtained from elastic analysis are also shown in the figures, respectively.

Figures 12 and 13 confirm the nearly similar pre-cracking responses of all tested beams, which were also very close to the elastic ones. With increasing loads till failure, the higher differences between each beam's sagging and hogging responses and the corresponding elastic ones, are also shown in the figures. This is normally attributed to the concrete cracking as well as the yielding of the internal steel and the resulting degradation in stiffness. The figures also show that the sagging moments were always lower and the hogging moments were always higher than the

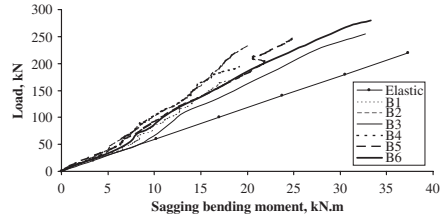

Figure 12. Total load–sagging bending moment curves.

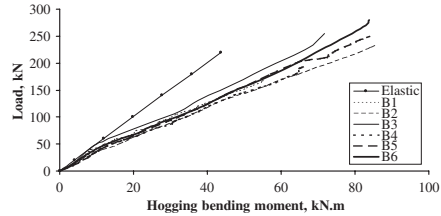

Figure 13. Total load–hogging bending moment curves.

corresponding elastic ones. However, figures 12 and 13 show that the sagging strengthening of the beams attracted higher sagging moments at the price of lower hogging ones when compared to the respective control beams, due to the resulting partial compensation of the reduced stiffness at their regions. Accordingly, it can be noted from the figures that the sagging strengthening brought both sagging and hogging responses of each strengthened beam closer to the corresponding elastic ones. The latter improvement was normally directly proportional to the number of sagging laminates, as depicted in the figures. The hogging strengthening of B2 logically resulted in opposite sagging and hogging responses' trends, as noted in the figures, hence, confirming the previously established disadvantage of the hogging system compared to the sagging one. The sharp decrease in the sagging moment and the corresponding sudden increase in the hogging moment of B5 at 84% of its failure load, shown in the figures, is again attributed to the laminates' de-bonding at one span at this load level, prior to the de-bonding of the second span at failure.

3.8 *Moment redistribution and beams ductility*

Table 6 shows the sagging and hogging moment redistribution ratios, γ (%), at failure of all tested beams, defined as follows:

$$\gamma = \left(\frac{M_a - M_e}{M_e} \right) \times 100 \qquad (1)$$

Table 6. Moment redistribution ratio and ductility index.

Group no.	Beam no.	CFRP laminates no.	Moment redist. ratio, γ (%)		Ductility index μ
			Sagg.	Hogg.	
Group (1)	B1	None	−37.36	63.92	1.62
	B2	2 (top)	−49.29	84.33	1.25
	B3	2 (bot.)	−24.44	41.81	1.36
Group (2)	B4	None	−41.98	71.82	1.47
	B5	1 (bot.)	−40.67	69.58	1.36
	B6	2 (bot.)	−29.83	51.03	1.13

where M_a = actual experimental failure moment and M_e = corresponding moment from elastic analysis. First, the moment redistribution ratios were directly proportional to the internal reinforcement ratio, as noted from the higher ratios of control beam B4 when compared to those of B1 in table 6. The table also shows that the sagging strengthening reduced the sagging and hogging moment redistribution ratios, as noted from the lower ratios in B3 compared to B1 as well as the lower ratios in B5 and B6 compared to B4. The previous reductions were directly proportional to the increase in the number of sagging laminates, as noted from the increasingly lower ratios of B5 to B6 when compared to their control beam B4 in table 6. The higher efficiency of the sagging strengthening in case of lower reinforcement ratio is further noted from the higher reductions in the moment redistribution ratios of B3 than B6 when compared to their respective control beams in table 6. The opposite trend followed by B2 due to its hogging strengthening can be noted in the table, from its higher moment redistribution ratios when compared to its control beam B1. Finally, the expected constant variations in the sagging and hogging moment redistribution ratios for each strengthened beam when compared to its respective control one should be noted in all previous results shown in table 6.

On the other hand, the deflection ductility index, μ, developed by Mukhopadhyaya et al (1998) for simply supported beams strengthened with GFRP plates, is adopted in this study and the results shown in table 6. The latter index was defined as follows:

$$\mu = \frac{\Delta_u}{\Delta_y} \tag{2}$$

where Δ_u = experimental mid-span failure deflection and Δ_y = experimental mid-span deflection at yielding of the tensile internal reinforcement. Table 6 shows that expected lower ductility was experienced for higher reinforcement ratio, as detected for B4 and B6 in comparison with B1 and B3, respectively. In addition, the table shows that all strengthened beams exhibited lower ductility than the respective control ones, due to the stiffening effect provided by the laminates. This ductility reduction is normally directly proportional to the increase in the number of sagging laminates, as noted from the increasingly reduced ductility in B5 to B6 when compared to their control beam B4 in table 6. For a similar number of sagging laminates, a beneficial lower ductility reduction is experienced for beams with lower reinforcement ratio, as for B3 when compared to B6 relative to their respective control beams in the table. Finally, the lower efficiency of the hogging strengthening when compared to the sagging one is further confirmed in table 6, from the lower ductility of the hogging strengthened beam B2 than the sagging one B3, in comparison with control beam B1, although similar number of laminates was provided in both former beams.

4 CONCLUSIONS

The CFRP strengthening resulted in higher efficiency for beams with lower reinforcement ratio, in terms of all aspects of structural behavior till failure.

The CFRP strengthening system was disadvantageous in changing the beams' failure mode from ductile flexural to abrupt peeling at reduced ductility.

The extension of the laminates to cover the whole hogging region as well as the mechanical anchorage of the sagging laminates, only redirected the peeling away from the laminates' ends.

The mechanical anchorage of the sagging laminates resulted in the strengthening system being able to sustain the failure loads after peeling's occurrence.

The CFRP strengthening system did not affect the beams' pre-cracking behavior, but resulted in general improvements in all aspects of post-cracking behavior (more uniform crack patterns, lower deflections and strains at increased capacities). Higher improvements were attained for larger number of laminates.

The sagging CFRP strengthening system proved higher structural efficiency than the hogging one, especially near failure, as well as lower ductility

reductions. This is attributed to the former system's resulting stable simply supported mechanisms of the adjacent spans at post-hogging failure.

Unlike the hogging system, the sagging strengthening resulted in a more uniform stiffness distribution along the beams' spans, hence, getting the experimental end support reactions and moments closer to the elastic ones. Accordingly, the latter system also resulted in lower moment redistribution ratios.

Unlike simply supported beams, the moment enhancement ratios of the strengthened continuous beams were higher than their load enhancement ratios, due to the moment redistribution induced by the increased stiffness of their strengthened regions.

REFERENCES

ACI 440-2002. Guide for the Design and Construction of Externally Bonded FRP Systems for Strengthening Concrete Structures. American Concrete Institute Committee 440, Farmington Hills, Michigan, USA, October, 45 pp.

Arduini, M., Nanni, A., Di Tommaso, A. & Focacci, F. 1997. Shear Response of Continuous RC Beams Strengthened with Carbon FRP Sheets. Proceedings of the 3rd International Symposium on Non-Metallic (FRP) Reinforcement for Concrete Structures (FRPRCS-3), Japan Concrete Institute, Sapporo, Japan, Vol. 1, October, pp. 459–466.

El-Refaie, S.A., Ashour, A.F. & Garrity, S.W. 2003. Sagging and Hogging Strengthening of Continuous Reinforced Concrete Beams Using Carbon Fiber-Reinforced Polymer Sheets. ACI Structural Journal, American Concrete Institute, Farmington Hills, Michigan, USA, July–August, pp. 446–453.

Grace, N.F., Soliman, A.K., Abdel-Sayed, G. & Saleh, K.R. 1999. Strengthening of Continuous Beams Using Fiber Reinforced Polymer Laminates. Proceedings of the 4th International Symposium on Fiber Reinforced Polymer Reinforcement for Reinforced Concrete Structures (FRPRCS-4), SP-188, American Concrete Institute, Baltimore, USA, October 31 to November 5, pp. 647–657.

Khalifa, A., Tumialan, G., Nanni, A. & Belarbi, A. 1999. Shear Strengthening of Continuous Reinforced Concrete Beams Using Externally Bonded Carbon Fiber Reinforced Polymer Sheets. Proceedings of the 4th International Symposium on Fiber Reinforced Polymer Reinforcement for Reinforced Concrete Structures (FRPRCS-4), SP-188, American Concrete Institute, Baltimore, USA, October 31 to November 5, pp. 995–1008.

Mukhopadhyaya, P., Swamy, R.N. & Lynsdale, C. 1998. Optimizing Structural Response of Beams Strengthened with GFRP Plates. Journal of Composites for Construction, American Society of Civil Engineers, Reston, USA, May, pp. 87–95.

Tann, D.B. & Delpak, R. 2000. Shear Strengthening of Continuous Reinforced Concrete Beams Using Externally Bonded Carbon Fiber Sheets. Proceedings of the 10th BCA Annual Conference on Higher Education and the Concrete Industry, Concrete Communication Conference 2000, Birmingham, UK, June 29–30, pp. 325–338.

FRP Composites in Civil Engineering – CICE 2004 – Seracino (ed)
© 2005 Taylor & Francis Group, London, ISBN 90 5809 638 6

FE modeling of FRP strengthened RC joints

D. Mostofinejad
Associate Professor, Civil Engineering Department, Isfahan University of Technology (IUT), Isfahan, Iran

S.B. TalaeiTaba
Ph.D. student, Civil Engineering Department, Isfahan University of Technology (IUT), Isfahan, Iran

ABSTRACT: Use of FRP composites for strengthening of beams and columns in RC structures has attracted great attention in recent decades. However, less attention has been paid to strengthening of RC connections with FRP laminates. In the current study, a FE modeling has been proposed for non-linear analysis of RC joints covered with FRP overlays. The model consists of the effects of anchorage slip and anchorage extension of the steel reinforcement in connection zone. As for the creditability of the method, some available experimental works were modeled and non-linearly analyzed using ANSYS. The results showed that the model can predict the experimental works with good accuracy. At the end and as a case study, a base joint specimen was strengthened with FRP laminates in 7 different cases and the specimens were analyzed using the aforementioned modeling. The results showed that good ductility and strength enhancement could be taken from some of the strengthening cases.

1 INTRODUCTION

Use of FRP composites in strengthening of reinforced concrete structures has been of great interest for civil engineers in recent years. Many researches have been directed to strengthening of different reinforced concrete members such as beams, columns and slabs with FRP laminates; nevertheless, less attention has been paid to FRP strengthening of reinforced concrete joints. Parvin & Granata (1998a, b, c, 2000, 2001), Mosallam (2000), and Gergely et al. (2000) conducted some experimental and numerical studies on the subject of strengthening of RC joints with FRP Laminates. They pointed out to the increase in the strength of joints and decrease in the ultimate rotation of the joints as the results of FRP strengthening of RC connections.

Due to complexity of behavior of reinforced concrete joints, presenting an appropriate finite element modeling for non-linear analysis of RC connections is of great importance. Such a model enables the researchers to assess the behavior of any reinforced concrete joint with different dimension and different configuration of strengthening laminates; while the similar assessment based on experimental tests in the laboratory is very difficult due to the limitation in dimension, cost, and practical aspects.

The main objective of the current study has been focused on the introduction of a comprehensive non-linear finite element modeling for the analysis of RC joints using available softwares. This model when verified could be utilized to predict the behavior of RC connections with different amount of longitudinal and transverse reinforcements in beam and column, and different configurations of FRP laminates in the joint region.

2 FINITE ELEMENT MODELING

For non-linear finite element analysis, ANSYS software was used. To model the characteristics of concrete, SOLID65 element was used. This element is capable to simulate the cracking and crushing of concrete, and to consider the reinforcement as volume fraction in 3 perpendicular directions, which could be accounted for the modeling of the transverse reinforcement in the members. Furthermore, to model the longitudinal reinforcement and the FRP composites, LINK8 and SOLID45 elements were used, respectively.

As for failure criterion, the 5-parameter William-Varnk model was used. The model is able to account for the cracking of concrete in tension and crushing of concrete in compression; and to take the cracks as smeared cracks into consideration. Some important parameters to perform the failure envelope in the model are the compressive strength of concrete, the modulus of rupture, and the shear transfer coefficients for open and closed cracks. The latter coefficients may be taken as 1.0 and 0.2 to 0.25 for closed and open cracks, respectively, as recommended by Kachlakev et al. (2001). Furthermore, based on the recommendation of

Kachlakev et al. (2001), since the crushing of concrete under pure compression rarely happens, the crushing could be eliminated from the concrete elements for better convergence in analysis.

As for the modeling of FRP composites in ANSYS, an anisotropic material with the name of ANISO was used. The material in both compression and tension and in any direction of x, y and z, uses a bi-linear stress–strain curve.

3 MODELING OF ANCHORAGE SLIP

The anchorage slip and anchorage extension of the longitudinal reinforcement considerably affect on the behavior of reinforced concrete joints. It may influence on the rotation of the joint and even lead to brittle and sudden failure of the flexural concrete members as mentioned by Alsiwat & Saatioglu (1992).

To account for the anchorage slip and anchorage extension of the reinforcement in the current study, the non-linear spring model recommended by Soroushian et al. (1988) was used. Two sets of models were considered to take into consideration the effects of hooked reinforcement and straight anchored reinforcement; the pull out–slip relationship for the first one from the study conducted by Soroushian et al. (1998), and the bond–slip relationship for the second one based on the study carried out by Ueda et al. (1987).

4 MODELING OF AN EXTERNAL RC JOINT

An external reinforced concrete joint was selected and non-linearly modeled in ANSYS using the aforementioned procedure. The dimension and the reinforcement in beam and column of the joint are shown in Figure 1. The compressive strength of concrete was taken as 30 MPa, and the yield strengths of longitudinal and transverse reinforcements were taken as 420 MPa and 280 MPa, respectively.

To model the anchorage slip of longitudinal reinforcement of the beam in the joint region, the bars were generated between separate nodes next to concrete nodes. Then, the bar nodes connected to concrete nodes with non-linear spring elements of COMBIN39 in the software. The end supports of the top and bottom columns were fixed and monotonic concentrated load applied to the tip of the beam. Finer meshes were chosen for the connection region due to probability of stress concentration and more cracking. The meshes in the beam and column are shown in Figure 1. To perform the non-linear analysis, the load applied step by step and the modified Newton–Raphson method used for the solution.

As for verification of the results, the connection theoretically analyzed separately, and the moment–rotation curve of the joint was drawn regarding the

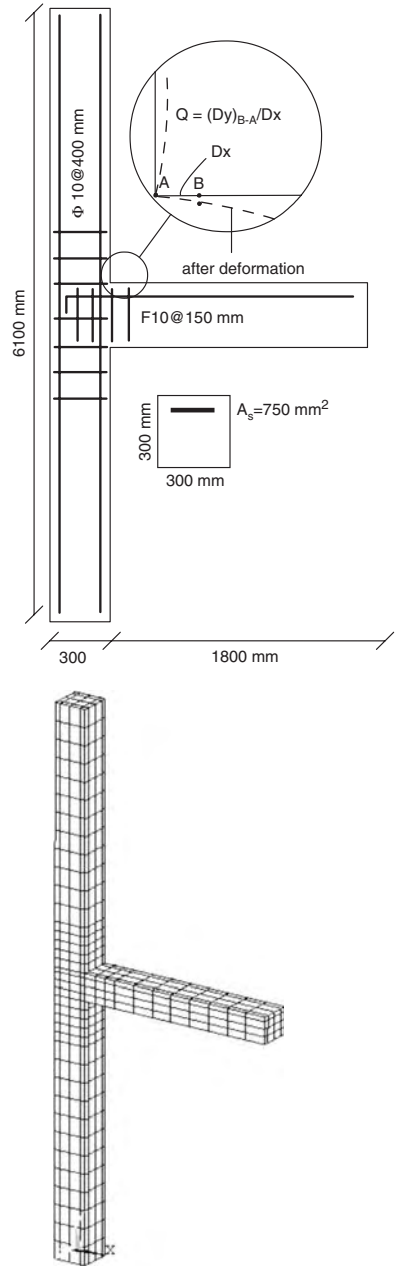

Figure 1. Specification of the selected RC joint and its FE meshes.

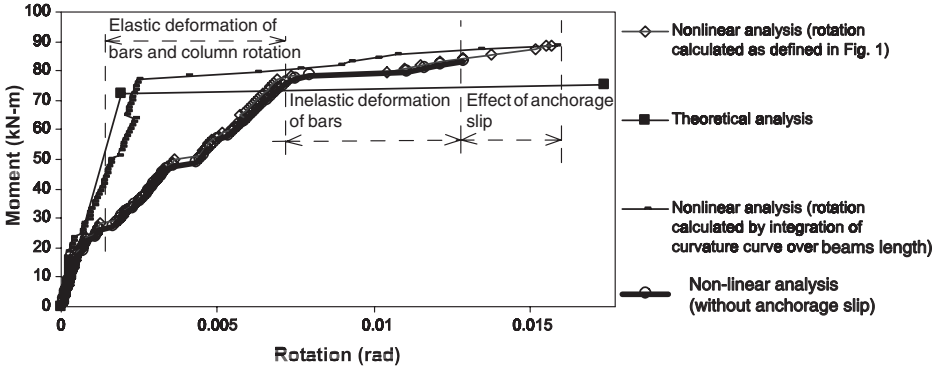

Figure 2. Moment–rotation curve for selected RC joint.

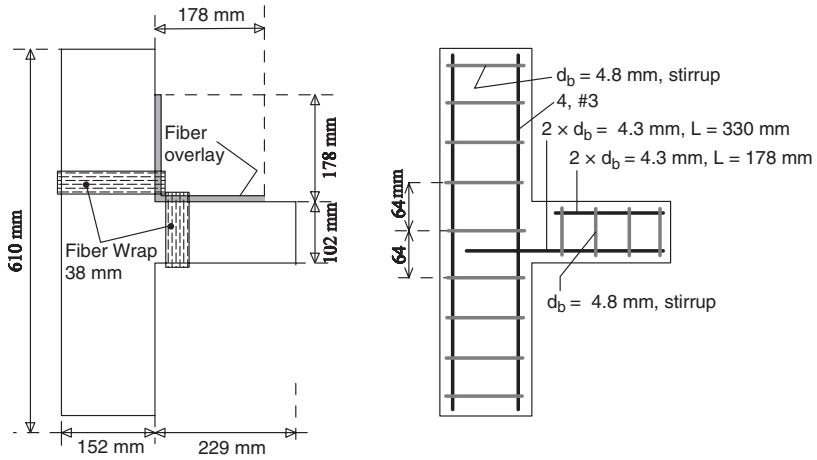

Figure 3. Reinforcement specification of the RC joint and FRP strengthening plan (Parvin & Granata 2001).

effects of anchorage slip. Figure 2 shows the moment-rotation curve of the joint extracted from the results of non-linear FE analysis and theoretical analysis. In Figure 2, there are two M–θ curves extracted from the FE analysis; in one of them the rotation (θ) is calculated as the ratio of the difference of vertical displacements of points A and B in Figure 1 to their horizontal distance; and in the other one the rotation is calculated as integration of the curvature over the length of the beam, as it is calculated in theoretical analysis.

In Figure 2, an acceptable agreement could be observed between the moment-rotation curves extracted from the theoretical analysis and the non-linear FE analysis with the same procedure of calculation of rotation as in the theoretical analysis. Furthermore, comparing the moment–rotation curves drawn from the results of FE analysis with and without the effect of anchorage slip in Figure 2, shows that disregarding the anchorage slip of the longitudinal reinforcement in the analysis, significantly underestimates the final rotation and the ductility of the joint.

5 MODELING OF AN FRP STRENGTHENED RC JOINT

As a verification of the modeling and the analysis for the RC joint strengthened with FRP composites, an experimental study conducted on FRP strengthened RC joint by Parvin & Granata (2001) was selected. Figure 3 shows the dimension and the reinforcement of

the specimen as well as arrangement of FRP laminates. Other characteristics of the materials could be found in the original paper (Parvin & Granata 2001).

The modeling of the different components of the specimen was performed as described in the previous sections. Since in the specimen there is not any tensile reinforcement at the end of the beam, the solution stopped right after the occurrence of cracking at the end of the beam. It is mostly due to instability caused by modulus of elasticity being equal to zero after cracking of the element. To overcome the problem, a series of dummy elements from LINK8 – 3D truss element – with very small area sections and from concrete with no cracking property modeled in 3 directions between the end region of the beam and the column.

The far ends of the columns fixed to the supports and the monotonic load applied to the tip of the beam. Figure 4 shows the moment–rotation curves extracted from the non-linear FE analysis and the experimental data. Since a very good agreement could be observed between the curves, it could be concluded that the presented FE modeling is reliable.

6 CASE STUDY ON SOME STRENGTHENED SPECIMENS

As a case study on a RC joint strengthened with FRP laminates, a base joint was selected and 7 different cases were chosen for its strengthening. A description of the base joint and the strengthened cases is as follows:

6.1 *Control specimen*

The control joint specimen known as "Base" is a connection composed of a column of total height of 6 m and a beam of 2 m connected to the middle of the column. Both beam and columns are with the section of 400×400 mm the longitudinal reinforcement of the beam (in tension zone) and column are $\rho_{beam} = 0.3\rho_{max}$; 0.8% and $\rho_{column} = 4\%$, respectively. The transverse reinforcement for both beam and column in connection region is ϕ10@100 mm; while in the other parts of the beam and column, it is respectively ϕ10@175 mm and ϕ10@400 mm. Note that connection region is a limited length of the beam and column where the transverse reinforcement should be closely spaced according to ACI 318 to provide ductile behavior against earthquake. In the base specimen, length of the connection region calculated as 800 mm for the beam and 500 mm for the column.

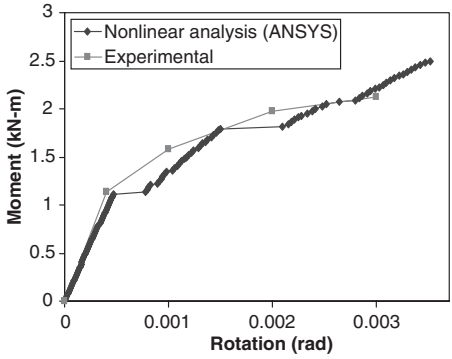

Figure 4. Calculated from FE analysis and experimental M–θ curves.

6.2 *Strengthened specimens*

Four general strategies considered for strengthening of the "Base" joint specimen with FRP sheets as follows:

1 L-shape overlays on the beam-column joint (Fig. 5.a);
2 U-shape overlays under the beam (Fig. 5.b);
3 FRP laminates on both sides of the beam (Fig. 5.c);
4 Column wrapping (Fig. 5.d).

Combining the four aforementioned strategies, 7 cases defined for strengthening of the "Base" specimen as given in Table 1. The thickness of FRP laminates was taken equal 3 mm for all cases. Other

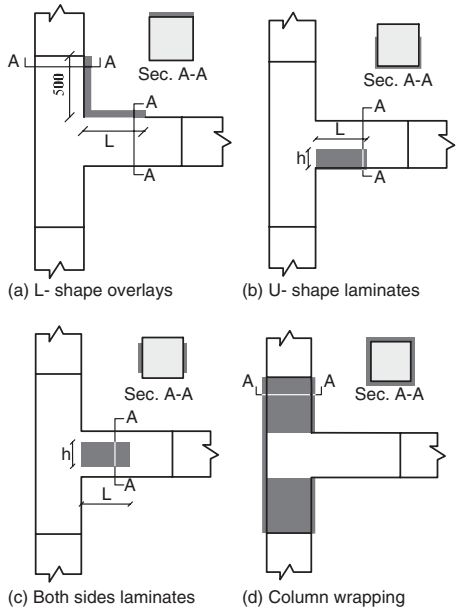

Figure 5. Strengthening cases with FRP overlays.

characteristics of CFRP laminates are given in Table 2. Note that the characteristics given in Table 2, satisfy the consistency conditions which are necessary for a non-isotropic material like ANISO in ANSYS as described in ANSYS user's manual (1996) and stated by Kachlakev et al. (2001).

6.3 *Results of the analysis*

Different results including the ultimate load, stresses in concrete and reinforcements, stresses in FRP laminates, the crack pattern at various stages and the ductility of each specimen were investigated.

Table 1. Characteristics of the strengthened specimens.

Joint name	L-shape overlays L (mm)	U-shape laminates L	U-shape laminates h	Both sides laminates L	Both sides laminates h	Column wrapping
S1	400					No
S2	400					Yes
S3		400	200			No
S4		400	200			Yes
S5				400	400	No
S6				400	400	Yes
S7						Yes

Figure 6 shows the moment–rotation curves for the base and the strengthened specimens. Some other results including the flexural capacity of the joint, the ductility factor and the ultimate rotation for all specimens are given in Table 3.

7 DISCUSSION ON THE RESULTS

7.1 *Flexural capacity*

The results show that the flexural capacities of the strengthened specimens have increased compared to

Table 2. Mechanical properties of CFRP laminates used for FE modeling.

Modulus of elasticity (GPa)	In fibers' direction		$E_x = 62$
	Perpendicular to fibers' direction		$E_y = 4.8$
			$E_z = 4.8$
Tensile strength (MPa)	In fibers' direction		$\sigma_x = 935$
	Perpendicular to fibers' direction		$\sigma_y = 26$
			$\sigma_z = 10$
Compressive strength (MPa)	In fibers' direction		$\sigma'_x = 10$
	Perpendicular to fibers' direction		$\sigma'_y = 152$
			$\sigma'_z = 232.94$
Shear modulus (MPa)	$G_{xy} = 3270$	Poison's ratio	$\nu_{xy} = 0.22$
	$G_{xz} = 3270$		$\nu_{xy} = 0.22$
	$G_{yz} = 1860$		$\nu_{yz} = 0.30$

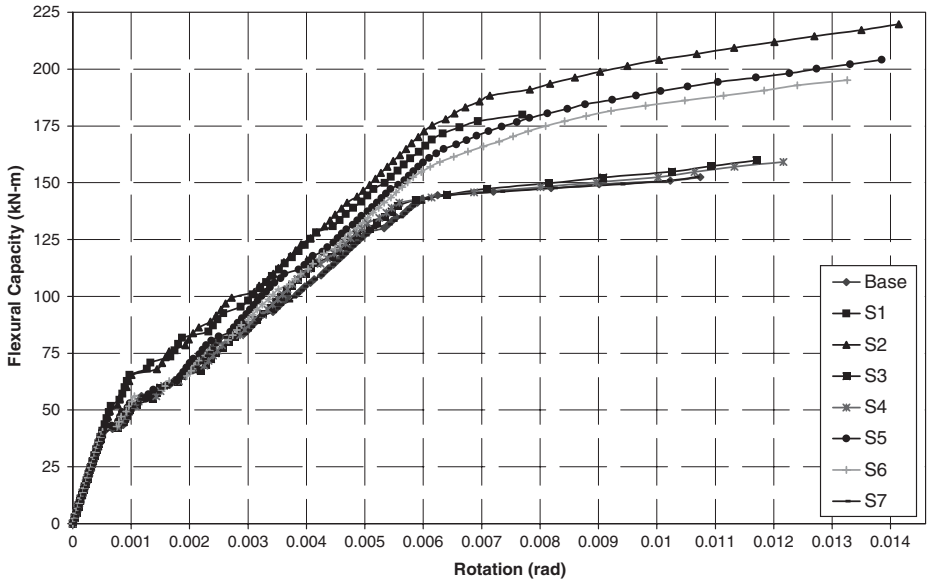

Figure 6. Moment–rotation curves of the base specimen and the strengthened specimens (extracted from non-linear analyses).

that of base specimen. The increase in flexural capacities of specimens S1 and S2 is due to tensile action of L shape laminates in tensile face of the beam; however, in specimens S3, S4, with U shape FRP laminates, it could be contributed to the preventing from crack propagation as well as the confinement of the concrete in compression zone of the beam.

7.2 *Ductility enhancement*

It could be observed from Table 3 that the highest ductility factor is related to strengthened specimen S2, and then to specimen S6. The high growth of ductile behavior in specimen S2, may be contributed to the simultaneous column wrapping and use of FRP overlays; which cause the end part conditions of the beam to be close to fix support. The latter provides the necessary conditions for the longitudinal reinforcement of the beam to yield right after the strengthened length, which may be interpreted as movement of the plastic hinge. The relative increase in ductility factors of the specimens S3 to S6 is basically due to confinement of the compression concrete of the beam caused by the FRP laminates over the compression region of the beam, which leads to the improvement of the ductility of the beam and the whole connection. It could be seen from Table 3 that the column wrapping with FRP composites increases the ductility of the joint compared to the similar specimens without column wrapping.

Table 3. Selected results of the non-linear analyses of strengthened specimens.

Joint name	Ductility factor	Flexural capacity (kN-m)	Ultimate rotation (rad.)
Base	1.8	153	0.0107
S1	1.25	179.9	0.0077
S2	2.35	219.74	0.0141
S3	2.15	159.81	0.0117
S4	2.23	159.2	0.0122
S5	2.22	204.05	0.0107
S6	2.27	195.1	0.0109
S7	1.83	153	0.0107

7.3 *Ultimate rotation*

The ultimate rotation in strengthened specimen S1 has decreased compared to that of base specimen, while it has increased or has not changed in the other strengthened specimens as shown in Table 3. In fact, the L shape overlays without column wrapping have diminished the rotation of the joint. However, the column wrapping with FRP laminates has provided a more ductile behavior for the whole connection with a higher ultimate roation.

7.4 *Mode of failure*

Mode of failure in connections is from the most important behavioral characteristics which is determinative for ductile behavior and energy absorption in the joint.

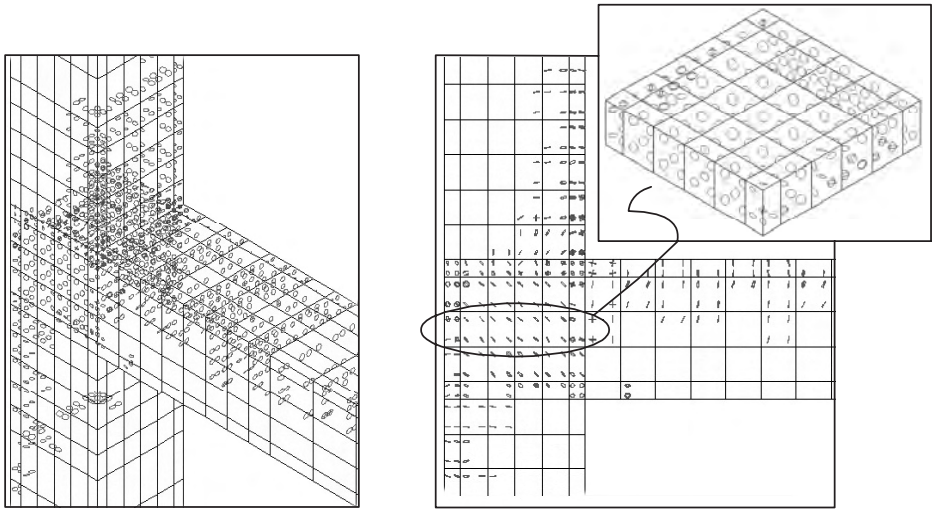

Figure 7. Shear failure of joint.

Scrutiny in the results of the analyses showed 3 types of failure in the connection specimens as follows:

1 Flexural failure at the end of beam at the face of column (full flexural cracks at the end of beam). This type of failure observed in specimens "Base", S3, S4, S6 and S7.
2 Flexural failure in the beam at a distance equal to length of strengthening overlays from the face of the column. This type of failure observed in specimens S1and S2.
3 Shear failure of joint as shown in Figure 7 (diagonal cracks in conjunction of beam and column). This type of failure observed in specimen S5.

8 SUMMARY AND CONCLUSIONS

In this paper, attempt was made to introduce a rational and comprehensive procedure for modeling of FRP strengthened RC connections for non-linear FE analysis. Appropriate elements from ANSYS were chosen to account for realistic behavior of each component in the connection, and the modeling and the analysis procedure were verified using some existing experimental data. A case study on a typical RC connection with some particular strengthening strategies with FRP laminates was performed. The results of this study could be summarized as follows:

1 Realistic non-linear analysis of RC connections with FRP overlays could be performed using ANSYS.
2 The modeling of anchorage slip in the embedded reinforcement is possible using non-linear spring models.
3 Ignoring the anchorage slip of the longitudinal reinforcement of the beam embedded in column in FE analysis, leads to underestimating of the ultimate rotation of the joint up to 25%.
4 L shape overlays from FRP composites at beam-column connection plus column wrapping with FRP laminates, and U shape overlays under the beam are very good strengthening strategies for strength and ductility enhancement in the RC joints.

REFERENCES

Alsiwat, J. M. & Saatcioglu, M. 1992. Reinforcement anchorage slip under monotonic loading. *Journal of structural engineering* 118(9): 2421–2438.

Gergely, J., Pantelides, C. P. & Reaveley, L. D. 2000. Shear strengthening of RC-joint using CFRP composites. *Journal of composites for construction, ASCE* 4(2): 56–64.

Kachlakev, D., Miller, T., Yim, S. & Chansawat, K. 2001. Finite element modeling of reinforced concrete structures strengthened with FRP laminates. Oregon State University: Final report for Oregon Department of Transportation Research Group, Salem, OR: *113 pp.*

Mosallam, A. S. 2000. Strength and ductility of reinforced concrete moment frame connections strengthened with quasi-isotropic laminates. *Composites: Part B* (31): 481–497.

Parvin, A. & Granata, P. 1998a. External fiber composites reinforcement of concrete structural members. *Proc. of the 8th Japan-U.S. conf. on composite materials*: 942–948.

Parvin, A. & Granata, P. 1998b. Numerical study of structural joints reinforced with composite fabrics. *Structures and materials*: 411–421.

Parvin, A. & Granata, P. 1998c. Use of FRP overlays at beam-column connections. *Proc. of the 2nd intern. conf. on composites in infrastructure,* 1: 213–220.

Parvin, A. & Granata, P. 2000. Investigation on the effects of fiber composites at concrete joints. *Composites: Part B* (31): 499–509.

Parvin, A. & Granata, P. 2001. An experimental study on kevlar strengthening of beam-column connections. *Composites: Part B* (53): 163–17.

Paulay, T. & Priestley, M. J. N. 1992. *Seismic design of reinforced concrete and masonary buildings*. New York: Wiley and Sons.

SAS IP, Inc. 1996. *ANSYS user's manual* (9th ed.).

Soroushian, P., Obaseki, K., Nagi, M. & Rojas Maximo, C. 1988. Pullout behavior of hooked bars in exterior beam-column connections. *ACI structural journal* 85(6): 269–279.

Ueda, T., Lin, I. & Hawkins, N. M. 1987. Beam bar anchorage in exterior column-beam connections. *ACI Journal*: 412–422.

FRP research in Southeast Asia (special session)

FRP Composites in Civil Engineering – CICE 2004 – Seracino (ed)
© 2005 Taylor & Francis Group, London, ISBN 90 5809 638 6

FRP research in Southeast Asia: durability and structural protection

K.H. Tan
National University of Singapore, Singapore

ABSTRACT: The Southeast Asian region has witnessed a rapid increase in the application of FRP reinforcement in beam, slab and column strengthening in recent years. However, due to its climatic, geographical and political characteristics, there are several unique research works which are highlighted herein. First, the performance of FRP-strengthened beams under tropical climate is discussed. It was found that without appropriate protection of the FRP reinforcement, the combined effect of UV radiation, wetting and heating could result in a reduction in flexural capacity of the strengthened beams of about 10% in six years. Under sustained service load, the reduction increased drastically, depending on the type of FRP system. Next, the structural response of FRP-strengthened RC shear walls under far-field earthquake effects is examined using both pushover and cyclic load tests. Compared to the un-strengthened wall, the strength and ultimate displacement of the walls were increased by about 30 and 20% respectively. Finally, the response of masonry walls against blast effects is discussed. Both laboratory and field tests indicated that masonry walls could be effectively strengthened with FRP systems to take blast loads.

1 INTRODUCTION

The Southeast Asian region comprises ten countries, Brunei, Cambodia, Indonesia, Laos, Malaysia, Myanmar, Philippines, Singapore, Thailand, and Vietnam. It has a population of about 500 million, a total area of 4.5 million square kilometers, and a combined gross domestic product of US$737 billion (ASEAN 2004). The author has earlier discussed the status, prospects and research needs related to FRP reinforcement for the region (Tan 1997). It was postulated that "FRP applications may be expected to increase, especially in view of the good economic growth of the region and the need to upgrade structures either due to the affluence of society or damage caused by environmental or human factors".

Since then, the region has witnessed an increasing application of FRP reinforcement in the construction industry, especially in recent years. Typical applications include beam, slab and column strengthening; and fundamental research in these areas had been carried out in several institutions in the region. Due to its geographical, social, economic and political characteristics, however, there are some unique issues for which research activities had been focused on and these are highlighted in this paper.

First, the performance of FRP-strengthened beams under tropical climate is discussed. GFRP-strengthened beams, some of which were subjected to sustained loads, were placed in simulated tropical weather chamber for periods of up to one year. The combined effect of ultra-violet (UV) radiation, wetting and heating on the flexural capacity of the strengthened beams is discussed.

Next, the structural response of FRP-strengthened RC shear walls under far-field earthquake effects is examined using both pushover and cyclic load tests on scaled specimens. Finally, the structural protection of masonry walls against blast effects is discussed using the results of field tests.

2 PERFORMANCE OF FRP-STRENGTHENED BEAMS UNDER TROPICAL CLIMATE

2.1 *Test program*

The high average annual temperature, high humidity and relatively constant UV dosage in tropical countries such as Singapore is believed to have detrimental effects on the mechanical performance of externally bonded FRP systems, which may thus affect the performance of FRP-strengthened structures.

A durability study has therefore been carried out at the National University of Singapore to investigate the effects of tropical climate on the engineering properties of glass FRP composites and FRP-strengthened beams. An accelerated test chamber was designed to simulate the tropical climate, as characterized by the meteorological data of Singapore for the period between 1987 and1997. The typical daily event was reproduced by a 4-hour test cycle, comprising 1.5 hours of heating using UV-A light source (representing sunshine hours), 1.5 hours of wetting (rain) and

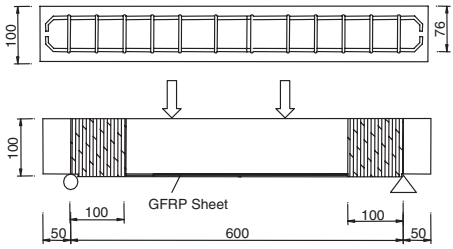

Figure 1. FRP-strengthened RC beams (Top: internal reinforcement; Bottom: external reinforcement).

Table 1. Properties of fiber fabrics and resins.

	G1	G2
Fiber type	E-Glass	E-Glass
Tow sheet form	Unidirectional roving	Bidirectional woven roving
Tensile strength (MPa)	1700	130
Elastic modulus (GPa)	71	11
Ultimate strain (%)	2.0	1.25
Resin type	2-part, 100% solid, low viscosity amine-cured epoxy	Orthophthalic unsaturated polyester
Tensile strength (MPa)	54	30
Elastic modulus (GPa)	3.00	0.67
Ultimate strain (%)	2.5	4.4

1 hour of dark period (night). While the proportions of light/dark and wet/dry periods, and relative humidity (RH) level were kept the same as that of the outdoor condition, the UV-A irradiance was increased by six times. At six test cycles per day, the test chamber provides weathering effects at an accelerated rate of six (Liew & Tan 2003).

Besides tensile and bond specimens, small reinforced concrete beams bonded with two types of GFRP composites, as shown in Fig. 1, were fabricated and exposed outdoor and in the weathering chamber, and tested after exposure periods of up to one year.

The properties of the fiber sheets and resins for the two GFRP systems, G1 and G2, according to the manufacturers' specifications, are shown in Table 1.

2.2 *Deterioration of FRP material properties and beam strength*

The appearance of the tensile specimens after one-year outdoor exposure or two-month accelerated test is shown in Fig. 2. For G1 composites, the original bluish color of epoxy faded and the surfaces lost their gloss, revealing the embedded whitish E-glass fibers. Similarly, the translucent polyester resin in G2 composites turned whitish and the surface texture

(a) G1 (b) G2

Figure 2. Appearance of FRP Composites (Left to right: under indoor ambient condition for 1 year, under outdoor condition for 1 year, under accelerated weathering for 2 months).

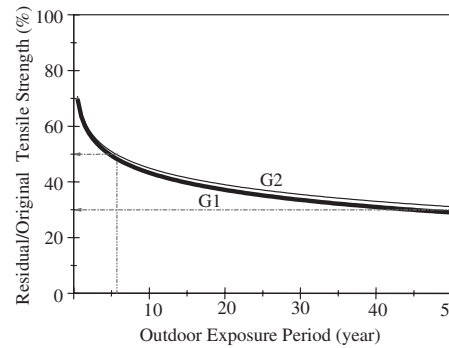

Figure 3. Reduction in tensile strength of GFRP Composites under tropical weathering.

became powdery, exposing the bi-directional E-glass fibers with time.

Figure 3 illustrates the reduction in tensile strength over time for specimens placed in the tropical environment. It can be seen that the reduction in tensile strength could be as large as 50 percent in six years or 70 percent in 50 years for both the GFRP systems investigated. Similar reduction in FRP-concrete interfacial bond strength has been observed (Tan 2004).

The FRP-strengthened beams could fail by concrete crushing, rupture of FRP composites or bond failure of the FRP-concrete interface. By incorporating the time-dependent material properties obtained from the weathering tests, the failure modes and flexural strength of the strengthened beams could be predicted using the strain compatibility approach for different periods of exposure to the tropical climate.

Table 2 shows that both the failure modes and ultimate flexural strength could be accurately predicted. Also, the ratios of the flexural strength of weathered to un-weathered beams indicated a 10% reduction in flexural strength for both G1 and G2 FRP-strengthened beams, after 72 months (or six years) of exposure under tropical climate.

Table 2. Ultimate strength of selected FRP-strengthened beams.

Specimen**	Outdoor age, t (mths)	Pred. Pu(t) (kN)	Pred. F.M.*	Test Pu(t) (kN)	Test F.M.*
OB-G1-6 m	6	44.8	FR	46.5	FR
CB-G1-1 m	6	44.8	FR	47.9	FR
OB-G1-1y	12	44.4	FR	47.5	FR
CB-G1-2 m	12	44.4	FR	44.8	FR
CB-G1-6 m	36	42.9	FR	44.2	FR
CB-G1-1y	72	41.8	FR	41.6	FR
OB-G2-6 m	6	37.0	CC/FR	43.2	CC
CB-G2-1 m	6	37.0	CC/FR	42.7	CC
OB-G2-1 y	12	36.5	FR	34.5	FR
CB-G2-2 m	12	36.5	FR	42.4	FR
CB-G2-6 m	36	35.8	FR	40.4	FR
CB-G2-1 y	72	35.2	FR	32.4	FR

* Failure Mode – CC: Concrete crushing; FR: GFRP rupture.
** OB: Outdoor Exposure; CB: Weathering Chamber.

Table 3. Effect of combined sustained loading and tropical weathering on ultimate strength of FRP-strengthened beams.

Specimen	Weathering Period (days)	Without sustained load		With sustained load	
		P_u (kN)	Failure mode*	P_u (kN)	Failure mode*
G1-0d	0	45.4	CC	45.2	CC
G1-5d	5	46.2	CC	33.5	CC
G1-15d	15	43.7	CC	31.8	CC
G1-1m	30	48.0	FR	36.1	CC
G2-0d	0	39.0	CC	39.4	CC
G2-5d	5	40.4	CC	27.6	CC
G2-15d	15	42.3	CC	27.3	CC
G2-1m	30	42.6	CC	26.7	CC

* CC: Concrete crushing; FR: GFRP rupture.

2.3 *Effect of sustained loads*

A limited number of G1 and G2 FRP-strengthened beams were subjected to sustained loads equal to about 50% of the ultimate load-carrying capacity of the un-strengthened beam. This was done by placing two 50 mm diameter rods in between the top faces of a pair of beams at third points, and subjecting the beams to forces applied through two prestressing bars placed adjacent to each 'support' end of the beams. The beams were then placed in the weathering chamber for periods of up to one month. Thereafter, they were subjected to loading as shown in Fig. 1 to failure.

As indicated in Table 3, there is an obvious reduction in load-carrying capacity, especially for beams strengthened with G2 composites, due to the combined effect of sustained loading and tropical weathering.

As the ultimate strength of the un-strengthened beam was about 27 kN, the contribution of the FRP composites was reduced by more than 50% for G1 FRP-strengthened beams and totally nullified in the case of G2 FRP-strengthened beams within a short time. Even though the number of specimens is too few for a more conclusive deduction, it is clear that some form of protection is required of the FRP reinforcement.

3 STRENGTHENING AGAINST FAR-FIELD EARTHQUAKE EFFECTS

3.1 *Characteristics and concerns*

Although some countries like Malaysia, Singapore, and some regions of Thailand are sited away from active earthquake belts, they share a common concern of the far-field effect on tall buildings constructed on soft ground due to major earthquakes some 350 to 700 km away. Such earthquakes produce waves that travel far along the rock bed and are amplified through soft ground, causing undesirable vibrations of buildings whose natural period of vibration is close to that of the ground motions.

High rise RC shear wall frame buildings in Singapore, typically seen in housing estates, are designed according to BS8110 (1985) which does not provide for any seismic actions. Studies were therefore carried out to evaluate their vulnerability to low seismic excitation (Li et al. 2004).

3.2 *Strengthening of shear core wall*

A 25-storey point block, the plan view of which is shown in Fig. 4, was considered as the prototype for study. The I-shaped shear core walls each consists of symmetrical left and right flanges joined by a web. The lower 2.59 story of the prototype was chosen for pushover and cyclic load tests.

Four scaled models of the shear wall, two without FRP retrofitting and the other two that were bonded with one-layer glass FRP system (consisting fabrics of 915 g/m^2 in unit weight and 0.352 mm in thickness, with Young's modulus of 69.7 GPa, ultimate tensile strength of 1668 MPa and corresponding strain of 0.02), were fabricated. The model wall was 1036 mm high, and 1314 mm after attaching the load transfer beams to the top of the wall. The length of the flange wall was 657 mm, and the length of the web wall was 955 mm. The thickness of the wall was 45 mm throughout.

For each pair of specimens, one was subjected to pushover test while the other to cyclic loading, as shown in Fig. 5. To simulate axial loadings from upper stories, a uniformly distributed load was applied on the top of the wall using post-tensioning tendons to

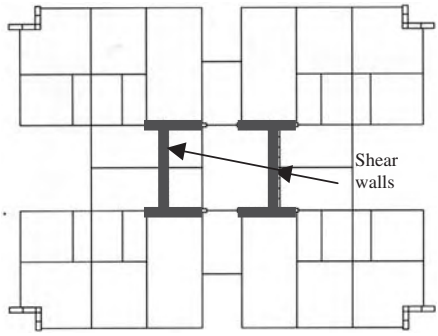

Figure 4. Plan view of prototype 25-story point block.

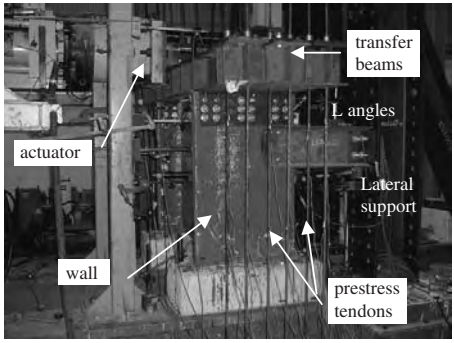

Figure 5. Load test on I-shaped wall retrofitted with glass FRP system.

produce an average axial compression ratio of 0.24. The lateral load from the actuator was applied to the top of the wall through the transfer beams.

The pushover test was carried out at a slow rate of 0.006 mm/s. For the cyclic loading, the rate was as follows: 0.006 mm/s in the first three cycles (with peak displacements of 3 mm, 6 mm and 9 mm); 0.01 mm/s in the fourth cycle (with a peak displacement of 12 mm), and 0.05 mm/s in the final cycles (with peak displacements of 15 mm twice and 30 mm twice).

3.3 *Effectiveness of FRP system*

Under both pushover tests (Kong et al. 2003) and cyclic load tests (Li et al. 2004), the control (unstrengthened) walls failed ultimately in a brittle manner due to diagonal cracks that originated from the compressive edge at the bottom of the side flange to the 'second story' level. The FRP-strengthened wall failed in a more ductile manner with FRP debonding and concrete crushing, followed by FRP rupture at the base of the side flange that was under compression. The ultimate loads for

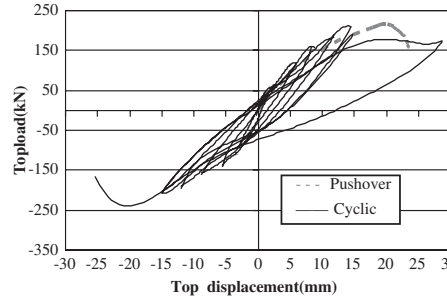

Figure 6. Load–displacement relation under pushover and cyclic loading tests.

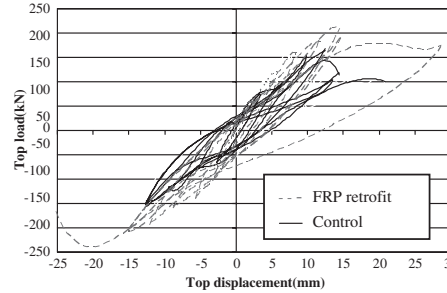

Figure 7. Load–displacement relations of control and FRP-strengthened walls under cyclic load tests.

the control and FRP-strengthened specimens under the pushover tests were 148 kN and 215 kN respectively.

Figure 6 compares the load–displacement relation of the walls under pushover and cyclic load tests. It is seen that the pushover load test is a simple and backbone representation of the cyclic load behavior. The load–displacement relation of the FRP-strengthened wall under cyclic load test is compared to that of the control specimen in Fig. 7. It is found that due to the installation of FRP reinforcement, the ultimate load capacity and displacement were increased by about 20% and 30% respectively.

4 STRUCTURAL PROTECTION AGAINST BLAST EFFECTS

4.1 *Domestic gas explosions and terrorist acts*

In recent years, explosion incidents due to accidents or terrorist acts have become a global concern, as is of the Southeast Asian region. A unique study was therefore carried out at the National University of Singapore to strengthen un-reinforced masonry brick walls against

blast effects. A scheme, using a primary externally bonded FRP system and a secondary steel anchorage and stiffener frame, was conceptualized, developed and tested in the laboratory and in the field (Patoary & Tan 2003, Tan & Patoary 2004).

The characteristic wall response under lateral loads was first determined from laboratory tests on isolated and in-built wall specimens. A simplified method to derive the blast resistance of strengthened masonry walls from static test results was then established. Based on parametric studies, charts to aid in strengthening design to mitigate blast effects were developed. Field tests were carried out in Australia and Singapore together with dynamic analysis using DIANA finite element software to confirm the viability of the developed scheme.

4.2 *Blast resistance and static strength*

To evaluate the blast resistance of the wall, first, the pressure-time history is obtained from the program CONWEP (TM5-855-1 1986) for an assumed TNT charge. The pressure-time history is simplified to an equivalent triangular pressure pulse with zero rise time defined by peak pressure P and the positive phase duration t_d.

For a given structure or structural member, the natural period T_n could be determined from its mass and equivalent elastic stiffness, either based on static test results or analytical modeling. Thus, knowing the value of t_d/T_n, the dynamic load factor *DLF*, which is the ratio of the maximum dynamic deflection to the deflection that would have resulted from the static application of the peak pressure, could be read from the chart of TM5-1300 (1990). The required static resistance of the wall is calculated as the peak pressure multiplied by *DLF*. If the required static resistance is equal to the actual static resistance of the wall, then the blast resistance is determined. Otherwise, a different TNT charge is assumed and the procedure repeated until convergence is obtained.

Figure 8 shows the blast resistance in terms of TNT charge at 10 m stand-off distance for 1 m by 1 m, 115 mm (half-brick) thick walls strengthened with FRP systems. It is interesting to note that the blast resistance is linearly proportional to the static strength enhancement, defined as the ratio of the ultimate load capacity P_u of the strengthened wall to that of the un-strengthened wall P_o. Also, the blast resistance depends on the failure mode, being highest for flexural compression, next for punching shear and least for flexural debonding.

4.3 *Field tests*

Four large-scale blast tests were carried out in Woomera, Australia, two between September and October, 2002, and the other two in May 2004. Of the

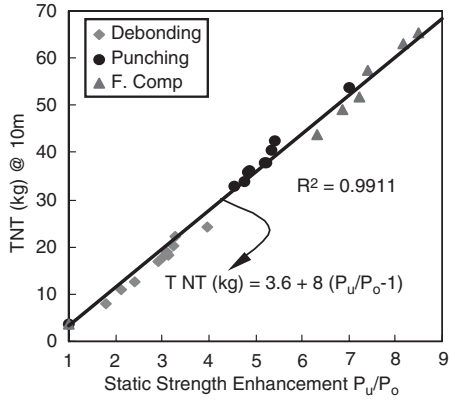

Figure 8. Relation of blast resistance to static strength enhancement.

first two tests, one test involved 27 tonnes of explosives while the other test 5 tonnes of explosives. For each test, three box structures were located at scaled distances (defined as $R/W^{1/3}$ where R is the distance from the center of the charge in meters and W is the mass of spherical TNT charge in kg) of 2, 3 and 4.2. Each box module had two 2.4 m wide by 2.1 m high side walls and one 1.7 m wide by 2.1 m high back wall, all constructed of masonry bricks of half- or full-brick thickness and reinforced with FRP systems with or without intermediate stiffeners. All the test walls survived the blasts without damage (Tan 2003).

The subsequent two tests were conducted on the same six walls that survived the first two tests. The walls were subjected to TNT charge of 5 tonnes, and were placed at scaled distances of 1.5, 2.5 and 3.5 for the third test. One of the walls in the third test was placed together with the other three walls in the fourth test, at scaled distances of 0.5, 2, 3 and 4.2. Despite the more severe and repetitive blasts, all walls survived with no visible damage.

The Australian tests involved specimens placed relatively far from the blast source. Two separate tests were carried out on an offshore island in Singapore to study the behavior of FRP-strengthened walls subject to close-distance blasts. As shown in Fig. 9, four wall specimens, W1, W2, W3a and W3b, were prepared and tested.

Each wall measured 1.8 m wide, 1.4 m high and 230 mm in thickness, and was bonded with two sheets of glass FRP fabrics of 915 g/m^2 (with thickenss of 0.352 mm per sheet, Young's modulus of 69.7 GPa, ultimate tensile strength of 1668 MPa and corresponding strain of 0.02), both on the front and back faces. Except for Wall W2, each wall was further anchored to the abutment frame using steel angles and anchor bolts.

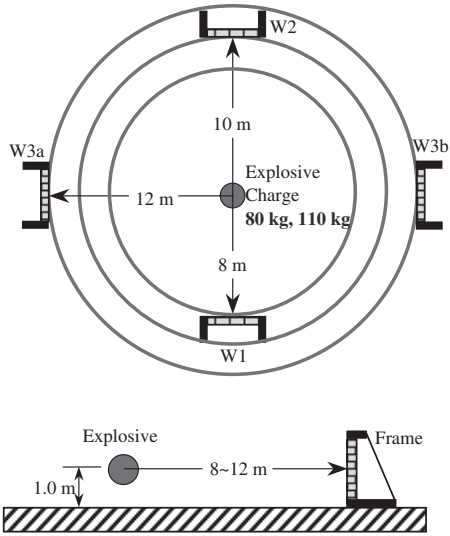

Figure 9. Field tests on strengthened walls subjected to close-distance blasts.

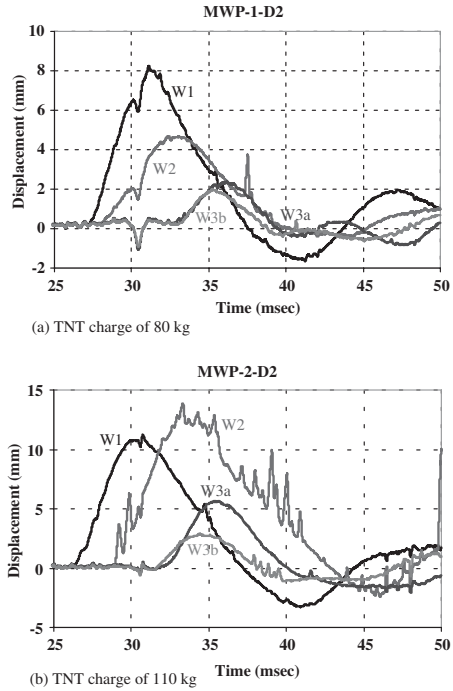

Figure 10. Distance-time history of FRP-strengthened masonry walls subject to TNT charge at 8-m stand-off.

Walls W1 and W2 were placed at 8 m and 10 m respectively from the blast source, which was set at 1 m above the ground, to be in line with the centers of the walls. Both Walls W3a and W3b were placed at 12 m from the blast source.

The walls were subjected to a 80-kg TNT charge in the first instance. Except for small pits due to the impounding soil particles and slight debonding of the FRP reinforcement at the top of the walls on the back face, there was hardly any damage.

Figure 10(a) shows the displacement-time history for the walls. It is seen that the maximum displacement sustained decreased with the distance from the blast source. The results of Walls W3a and W3b were quite similar, confirming the reliability of the field measurements.

The appearance of Wall W1, which was placed closest to the blast, after the second test using 110-kg TNT charge is shown in Fig. 11. A large portion of the FRP reinforcement, covering about one-third of the wall surface, has debonded from the front face of the wall. On the back face, the debonded area has extended downward from the top of the wall, although it was not as extensive as for the front face. This wall was observed to move backwards with respect to the abutment-frame, with a longitudinal separation gap between the bottom edge of the wall and the anchoring angle.

Wall W2, which was not anchored to the abutment-frame, suffered increased debonding of FRP reinforcement from the top of the wall on both the front and back faces. However, the extent is not as large as in Wall W1, probably due to the slightly further distance from the blast. The other two walls, W3a and W3b, however, did not show any serious damage or debonding of FRP reinforcement.

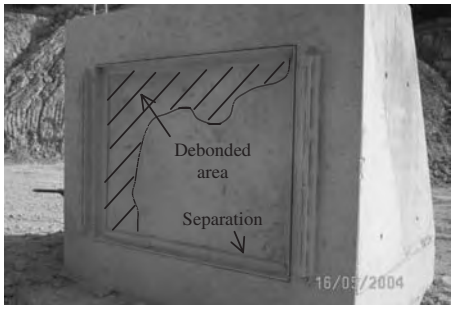

Figure 11. Appearance of FRP-strengthened wall W1 after subjecting to 80-kg and 110-kg TNT charge at 8-m stand-off.

The displacement-time history of the walls after the second blast is shown in Fig. 10(b). All walls were displaced more than they were during the first blast. The larger maximum displacement sustained by Wall W2 compared to Wall W1 was probably due to the absence of anchoring angles, which resulted in lesser restraint to rotation at the edges of the wall.

5 CONCLUDING REMARKS

The Southeast Asian region has seen a rapid increase in the use of FRP reinforcement in recent years, particularly in strengthening works. Besides fundamental research on typical beam, slab and column strengthening, some unique research pertaining to the climatic, geographical and political situations of the region have also been pursued. Three such research works were highlighted in this paper.

The study on glass FRP reinforcement under accelerated weathering indicated that without additional protection, glass FRP reinforcement that is frequently used due to economical reasons is liable to deteriorate under the combined effects of rain, shine and UV radiation that are characteristics of the tropical climate. This is particularly so when the structure is further subjected to sustained loads.

In structural protection, FRP reinforcement was found to contribute effectively to enhanced ultimate load capacity, and ultimate displacement and ductility of shear walls that were not originally designed for seismic actions, under lateral loads. Also, it was found to be an efficient material in strengthening masonry walls against blasts. Further works in FRP research are expected to increase in the Southeast Asian region, considering the increasing interests in the material among the community.

ACKNOWLEDGMENTS

The author is grateful for the financial support provided by the National University of Singapore and the Ministry of Defence, Singapore under research grants R-264-000-140-112 and R-264-000-096-232 respectively, in carrying out the studies described in his paper. In addition, he would like to thank Mr Y.S. Liew, Dr K.H. Kong, and Dr M.K.H. Patoary, in particular, for assisting in the projects.

REFERENCES

ASEAN Secretariat. 2004. Overview of Association of Southeast Asian Nations. http://www.aseansec.org/64.htm.

British Standards Institution; BS8110 1985: Structural use of concrete Parts 1, 2 and 3. British Standard. London.

Kong K.H., Tan K.H. & Balendra, T 2003. Retrofitting of shear walls designed to BS 8110 for seismic loads using FRP. In *Proceedings of the Sixth International Symposium on FRP Reinforcement for Concrete Structures (FRPRCS-6), Singapore, 8–10 July*. Vol. 2, 1127–1136.

Li, Z.J., Kong, K.H., Balendra, T. & Tan, K.H. 2004. Behaviour of FRP retrofitted shear walls designed according to BS8110. In *18th Australasian Conference on the Mechanics of Structures and Materials (ACMSM 18), Perth, Australia, 1–3 December.*

Liew, Y.S. & Tan, K.H. 2003. Durability of GFRP Composites under Tropical Climate. In *Proceedings of the Sixth International Symposium on FRP Reinforcement for Concrete Structures (FRPRCS-6), Singapore, 8–10 July*. Vol. 2, pp. 769–778.

Patoary, M.K.H. & Tan, K.H. 2003. "Blast Resistance of Prototype In-Built Masonry Walls Strengthened with FRP Systems", Best Paper Award (Honourable Mention), In *Proceedings of the Sixth International Symposium on FRP Reinforcement for Concrete Structures (FRPRCS-6), Singapore, 8–10 July*. Vol. 2, pp. 1189–1198.

Tan, K.H. 1997. State-of-the-Art Report on Retrofitting and Strengthening by Continuous Fibers: Southeast Asian Perspective – Status, Prospects and Research Needs (Keynote Lecture). In *Proceedings of the Third International Symposium on Non-metallic (FRP) Reinforcement for Concrete Structures, Sapporo, Japan, 14–16 October.* Vol. 1, 13–23.

Tan, K.H. 2003. Blast Mitigation using Fibre-Reinforced Polymer Systems (Invited Paper). In *2nd International Symposium on New Technologies for Urban Safety of Mega Cities in Asia, Tokyo, Japan, 30–31 October*. 239–246.

Tan, K.H. & Patoary, M.K.H. 2004. Strengthening of Masonry Walls against Out-of-Plane Loads using FRP Reinforcement. *ASCE Journal of Composites for Construction, USA*. Vol. 8, No. 1, pp. 79–87.

Tan, K.H. 2004. Corrosion of FRP under tropical climate (Invited Paper). In *Proceedings of JSCE Materials & Environment 2004, Tokyo, Japan, 26–28 April*. I-31–I-38.

TM5-855-1. 1986. Fundamentals of protective design for conventional weapons. *Headquarters, Department of the Army*, Washington, DC.

TM5-1300. 1990. Structures to resist the effects of the accidental explosions. *US Department of Army, Picatinny Arsenal*, New Jersey, Technical Manual.

FRP Composites in Civil Engineering – CICE 2004 – Seracino (ed)
© 2005 Taylor & Francis Group, London, ISBN 90 5809 638 6

Evaluation, selection and acceptance criteria for using FRP systems for strengthening reinforced concrete and masonry structures

R. Jamaji, J. Quek & S.K. Savardekar
FYFE Asia Pte Ltd, Singapore

ABSTRACT: Rapid growth in the structural rehabilitation industry in Southeast Asia has seen the advent of a variety of new materials and techniques for strengthening purposes. One such technique is the use of fibre reinforced polymers (FRP) or composite systems for structural strengthening and retrofitting of concrete and masonry structures. The perceived simplicity in using FRP for strengthening such structures has brought about a spate of composite material suppliers in the Southeast Asian region. It is of prime importance to realize that the incorporation of FRP systems for structural purposes is not merely limited to supply and sale of constituent materials and site application but encompasses a wide range of issues pertaining to their development such as testing, environmental durability, usage, material quality control and post-installation quality assurance. The absence of relevant regional standards should however not act as a deterrent to using composite systems for structural strengthening. Technical reports, papers published by various engineering organizations, FRP societies, technical committees, researchers and academics from universities regionally and worldwide are available to assist engineers in the evaluation, acceptance, selection and use of an appropriate FRP system for structural purposes. This paper aims to present various issues that need to be considered in evaluating, accepting and selecting a FRP system for structural use based on documented resources that are currently available.

1 INTRODUCTION

With the increased popularity and use of fibre reinforced polymers or composite systems in the structural repair and rehabilitation industry in Southeast Asia, the need to understand evaluation and acceptance criteria for specification of such systems is being felt more and more by engineers, specifiers, and agencies ordering structural retrofit using composites. The technique of using FRP systems for structural enhancement mitigates several disadvantages inherent in the conventional strengthening methods and hence it is gaining preference over traditional strengthening methods such as concrete jacketing, steel plate bonding and sprayed concrete. Furthermore, successful track records of the incumbent composite developers and applicators has also helped raise confidence levels of engineers in specifying use of composites for structural applications. To seize the opportunities created by the increased demand of FRP systems amid lack of regional standards pertaining to their specification and usage, many organisations that were traditionally involved in the business of conventional repairs or supply of construction materials and chemicals have jumped into the business of selling FRP systems with insufficient knowledge about their material characterisation, application, performance, and long-term durability. This has led many of these agencies to misrepresent an assortment of fibre fabrics and resins collected from disparate sources as valid structural composites. It is, therefore, important for engineers and specifiers to develop a clear understanding of the requirements for characterisation, evaluation and acceptance of a FRP system before its incorporation for structural purposes to ensure a sound and durable structural retrofit.

In the absence of relevant local standards and codes of practice, reliance is laid on reports and recommendations of technical committees set up by professional societies and engineering bodies of international stature for the purpose of standardising the use of FRP systems for structural applications. The following sections will cover some of the guidelines for selection of a suitable composite system for structural applications to ensure the intended structural performance as well as a durable retrofit.

2 CATEGORISATION AND CHOICE OF COMPOSITE SYSTEMS

Composite systems can be categorised either on the basis of their constituent materials or their methods of

production and application. Generally, a typical FRP system that is bonded to the external surface of the member being strengthened comprises of continuous high strength fibres composed of either of e-glass, carbon, aramid or a combination of these, embedded in an epoxy resin matrix. The resin matrix not only serves the function of fixing the reinforcing fibres in place but also provides a shear path to effectively transfer load between the fibres (ACI 2002). The fibrous constituent of a composite system may be produced in dry woven fabric form or as a unidirectional sheet of continuous parallel dry fibres or as a pre-cured pultruded section. On the basis of their methods of application, composite systems may be categorised as wet lay up (dry fibre fabrics or sheets saturated with resin at project site), pre-impregnated systems (factory-saturated but uncured fabrics or sheets) or pre-cured laminate systems (pultruded fibres and shapes pre-cured in a resin matrix). The choice of appropriate constituent materials for a composite system and its method of installation may be based on but not limited to the following factors:

- Level and type of strengthening required.
- Desired mechanical and physical properties.
- Profiles and dimensions of the structural elements that require strengthening.
- Anticipated service and environmental exposure conditions.
- Compatibility of the resin with and its adhesion to the fibres and concrete.

3 BASIS AND LEVEL OF STRENGTHENING

The feasibility of using a specific type of composite system for strengthening of structural elements should be based on the results of a thorough structural investigation to determine in-situ strengths of their constituent materials (concrete, reinforcing steel) and resulting load carrying capacities. An assessment report, tabulating deficiencies in the capacities of structural elements to resist existing loads or additional loads intended to be imposed, shall be prepared from the results of investigation and analysis and used as a basis for FRP strengthening.

As in the case of all externally applied strengthening systems, a judicious approach is to limit the extent of strengthening such that in the event of loss of the externally applied FRP system, the retrofitted element is capable of resisting at least unfactored dead plus live loads (ACI 2002). This limit on strengthening is imposed to guard against collapse of the structure should an accidental failure of the FRP system occur due to fire, vandalism, or other unforeseen causes. Overall structural adequacy of the element should be considered in the design process as strength enhancement against a particular mode of failure (e.g. bending) may increase the vulnerability of the element towards another failure mode (e.g. shear). Other factors such as acceptable levels of safety against serviceability requirements such as deflection and cracking, service temperatures, fire protection, ultimate fatigue strength etc. should also be given due consideration when deciding on the viability of using a composite system for structural strengthening.

4 COMPOSITE SYSTEM EVALUATION CRITERIA

Proprietary composite systems should have been developed through material characterisation and structural testing. A composite system considered for use should have sufficient test data demonstrating adequate performance of the system in similar applications, including its method of installation. Untested combinations of fibres and resins could yield an unexpected range of properties as well as potential material incompatibilities (ACI 2002).

The evaluation criteria should examine crucial parameters of a composite system concerning composite material properties, behaviour under various anticipated environmental exposures, actual performance under loads vis-à-vis the theoretical calculated strength enhancement and its installation procedure. The following approach may be used by structural engineers prior to selection of a suitable composite system to evaluate the efficacy of an FRP system, intended for use in a structural strengthening application.

4.1 *Material characterisation*

The properties of a FRP system should be characterised as a composite, recognizing not just the material properties of the individual fibres, but also the efficiency of the fibre-resin system and fabric architecture. Every system is unique in that fibres and resin components are designed to work together (Fib 2001). The specified material-qualification programs should require sufficient laboratory testing to measure the repeatability and reliability of critical properties. Testing of multiple batches of FRP materials is recommended for this purpose (ACI 2002).

The material characterisation exercise involves ascertaining mechanical and physical properties of the FRP system intended for use as an engineering material. Besides the standard mechanical properties such as ultimate tensile strength, tensile modulus, and elongation at break that are essentially required for design purposes, properties such as fatigue, creep, coefficient of thermal expansion, impact, and interlaminar shear strength should also form part of the test regime. Repeatability and reliability of the critical material properties should be validated by carrying out

Table 1. Material Characterisation Testing (ICC 2003).

System properties	Test method	Number of specimens*
Tensile strength	ASTM D 3039–95a	20
Elongation	ASTM D 3039–95a	20
Tensile modulus	ASTM D 3039–95a	20
Coefficient of thermal expansion	ASTM D 696–91 or E 1142-97	5
Creep	ASTM D 2990-95	5
Void content	ASTM D 2584-94 or D 3171-95	5
Glass transition (Tg) temperature	ASTM D 4065-95	20
Impact	ASTM D 3029-94, Method 1	5
Composite interlaminar shear strength	ASTM D 2344-84 (1995)	20

* Specimen sets shall exhibit a coefficient of variation (COV) of 6 percent or less. Outliers are subject to further investigation according to ASTM E 178. If the COV exceeds 6 percent, the number of specimens shall be doubled.

adequate number of laboratory tests ensuring that the composite system exhibits a uniform range of values for various application conditions. The constituents of the composite system should thus be engineered so as to attain a desired range of physical and mechanical properties of the system. The use of untested or off-the-shelf combinations of fibres and epoxy resins to form a composite for structural applications is prohibited as the resulting system could exhibit an unpredicted range of properties as well as potential material incompatibilities (ACI 2002). Some of the tests that a composite system should undergo as part of its stringent material characterisation regimen are listed in Table 1 above. Submission of the relevant test reports should form an essential part of the acceptance criteria. Figure 1 and Figure 2 show some of the material characterisation tests underway on a composite system.

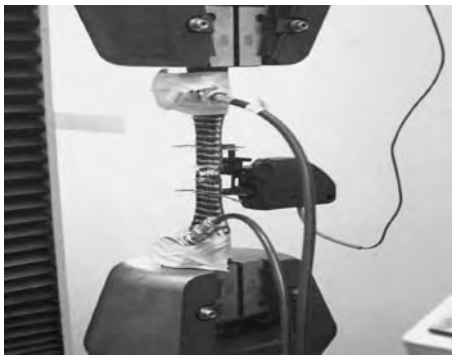

Figure 1. Testing to determine mechanical properties of a cured composite as part of material characterisation (Fyfe 2001).

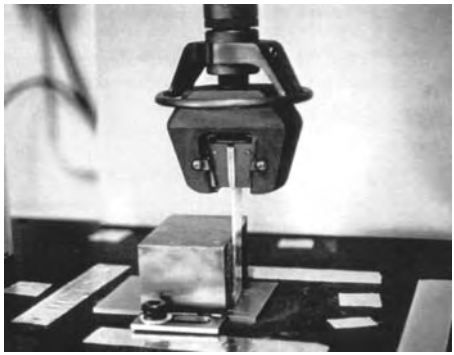

Figure 2. Testing to determine shear bond strength of cured composite with concrete as part of material characterisation (Fyfe 2001).

4.2 *Durability criteria*

Long term exposure to certain environmental conditions such as UV light, alkalinity, saltwater, high temperature, high humidity, freeze thaw cycles and some chemicals can adversely affect the constituents of a composite system, thereby leading to drop in its initially characterised mechanical properties and intended performance overtime (CSTR55 2000). Loss in the mechanical properties of an FRP system upon exposure to various environmental conditions overtime should be determined by carrying out accelerated laboratory tests that simulate anticipated long-term environmental exposure conditions. Resulting loss in mechanical properties should not exceed the limits prescribed by standards such as ASTM. Based on environmental exposure conditions, the guaranteed laboratory test values of the material properties need to be reduced appropriately for use in design equations. Various available documents on the use of composites prescribe environmental safety factor values and design approaches to handle different environmental exposure conditions. Table 2 below shows some of the accelerated environmental ageing tests and corresponding acceptance criteria for an FRP system. Only such FRP systems whose behaviour and performance under various adverse environmental exposure conditions have been assessed to conform to relevant standards should be recommended for structural use (ICC 2003).

Table 2. Environmental durability testing of the composite matrix (ICC 2003).

Environmental durability tests	Test specifications	Test cond'n	Test duration	% Retention of mechanical properties	
				1000 hrs	3000 hrs
Water resistance	ASTM D 2247-97 ASTM E 104-85 (96)	100% immersion at 38°C	1000, 3000 & 10000 hrs	90	85
Saltwater resistance	ASTM D 1141-91 ASTM C 581-94	100% immersion at 24°C	1000, 3000 & 10000 hrs	90	85
Alkali resistance	ASTM C 581-97	100% immersion in $CaCO_3$, pH 9.5	1000 & 3000 hrs	90	85
Dry heat resistance	ASTM D 3045-92	62°C	1000 & 3000 hrs	90	85
Freeze thaw cycle	ICC AC 125	−17°C (4 hrs)/100% humidity (12 hrs)	20 cycles	90	90
Fuel resistance	ASTM C 581-94	Exposure to diesel fuel	4 hrs. (min.)	90	90

Figure 3. Cyclic load test on full scale bridge pier. The control specimen shows extensive cracking of the RC pier (Fyfe 2001).

Figure 4. Cyclic load text on the same full scale bridge pier strengthened with FRP. Specimen shows no cracking of the RC pier (Fyfe 2001).

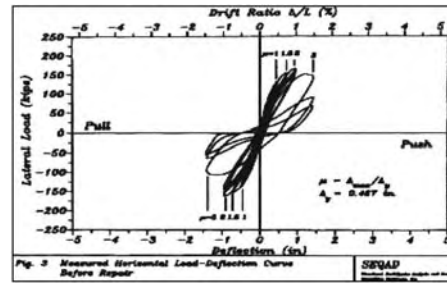

Figure 5. Cyclic load test on a full scale control circular column specimen. Lateral load vs. deflection chart shows a ductility of 3 (Fyfe 2001).

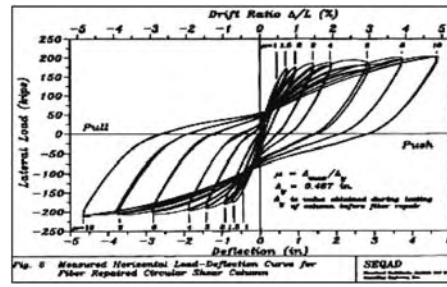

Figure 6. Cyclic load test on the same full scale FRP strengthened circular as-built column shows an increase in ductility to 10 (Fyfe 2001).

4.3 *Performance criteria*

Composite systems shall be selected based on their known behaviour in the anticipated service conditions. Independent structural testing is required to evaluate a composite system's performance for a specific application (ACI 2002). Theoretical strength enhancements obtained from design equations and engineering analysis should be verified by carrying out load tests on control and strengthened specimens of structural components. The test specimens should be representative of the as-built elements in terms of physical dimensions, constituent materials, reinforcement as well as FRP strengthening details. Such tests must simulate actual expected loading conditions, deflections, ductilities and support conditions. Figures 3–6 show examples of cyclic load tests on control and strengthened specimens of a bridge pier and an as-built circular column to validate the use of FRP for seismic applications. Excessively scaled down specimens should not be used unless results of load tests conducted

Figure 7. A bridge span strengthened for increase in live loads with a composite system being subjected to full service loads to evaluate its performance (Jamaji et al. 2003).

Figure 8. Data acquisition and monitoring post strengthening performance of the bridge span (Jamaji et al. 2003).

on full scale specimens earlier are already available and subsequent tests are required for verification of repeatability criteria only. Results obtained from tests on highly scaled down specimens may overestimate the actual level of strength enhancement attained by using an FRP system on as-built elements.

For critical or large scale applications, a structural test program on intended application may be specified as part of system qualification criteria prior to incorporation of composite system. If feasible, pre and post strengthening load tests may be conducted on the element/structure, to compare various structural parameters such as strains and deflections to validate the composite system's performance. These tests can be considered as proof load tests only as they would only indicate the ability of a structure to resist short-term service loads, rather than indicating its ultimate load carrying capacity or long-term performance. Thus, composite systems should be qualified for use on a project only on the basis of available documented structural test data for the intended application. Figure 7 and Figure 8 show an example full service load testing and monitoring of critical parameters for a bridge span strengthened with an FRP system.

4.4 *Prequalification from an installation perspective*

Composite system manufacturers generally specify their own proprietary installation procedures, which may vary among various manufacturers. However, the key parameters that are critical to the performance of the FRP system can be evaluated on common grounds. As such, evaluation of a composite system from installation perspective should be based on, but not limited to the following parameters.

4.4.1 *Installer competency*

The composite system installer, if different from the system developer, should get all his installation personnel trained and certified by the FRP system developer (CSTR55 2000). The installer should be able to produce evidence of training of its installation personnel as well as of having successfully completed projects using FRP in the past. In addition, the FRP system installer should essentially be competent to carry out general concrete repair and surface preparation works which normally precede the composite installation and are crucial to the overall success of the FRP strengthening technique. For uncommon or critical installations, a "mock-up" of surface preparation and composite application on a test area should be additionally specified.

4.4.2 *Fibre impregnation method*

In order that a wet lay-up FRP system can develop its specified properties, it should be ensured that the fibre-resin ratio is in accordance to the manufacturers specifications. High resin content can over saturate the fabric and may have an adverse effect on the composite material properties, whereas, low resin content can starve the fibres of the saturant thereby leading to ineffective load transfer and bonding of the fibres to the substrate. The use of mechanised equipment such as resin impregnators or fabric saturators that effectively control the fibre-resin ratio should be a standard requirement for all wet lay up type applications. Figure 9 shows a mechanical fabric impregnator/saturator in operation. However, for situations where manual saturation of the fibres is inevitable, the fibre resin ratio should be effectively controlled by saturating a known quantity of fibres with the required quantity of resin by manual means prior to application on the element. Manual saturation may be allowed considering the competency and experience of the composite installer.

4.4.3 *Fibre orientation*

The strength enhancement provided by a composite system depends on the alignment of its primary fibres in the direction of force on the element. Deviation of fibres from the desired orientation can adversely affect the actual strength enhancement gained by

Figure 9. A mechanical fabric saturator to control the fibre-resin ratio in operation (Fyfe 2001).

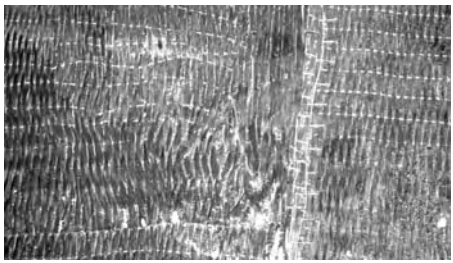

Figure 10. Fibres of non-engineered fabrics separate and misalign during cutting, saturation and installation reducing the intended strength of the FRP system (Jamaji et al. 2003).

Figure 11. Properly engineered fabrics retain their strength and integrity after saturation and during installation (Jamaji et al. 2003).

the element (Fyfe 2001). Therefore, the installation procedure proposed for a composite system should appropriately address the issue of fibre fraying and mis-alignment commonly caused by the inability of a fabric to retain its structure upon cutting, saturation and installation (see Figure 10). FRP systems that use specifically engineered fabrics that retain their structure on cutting, saturation and installation should only be recommended for structural strengthening use (see Figure 11). All fabrics intended to be specified for a structural strengthening applications should be subjected to a simple manual test to determine the ability of the fabric to resist fraying and separation of the fibres upon installation.

5 CONCLUSION

The use of FRP systems for strengthening reinforced concrete structures is a viable and attractive alternative to conventional strengthening techniques in the techno-commercial sense and thus has seen rapid proliferation and deployment worldwide. However, in order to achieve the overall objective of a long-term and durable structural retrofit, the composite system proposed should be thoroughly evaluated for its suitability before its acceptance for intended structural application. The evaluation criteria, based on available international documentation on the use of FRP systems, should encompass the issues pertaining to consistency of material properties, durability under anticipated environmental exposure conditions, performance under intended use and pre-requisites for installation. Hence, composite systems developed for structural strengthening applications should be viewed as much more than just fibre-resin combinations. Structural engineers and designers should only specify those FRP systems for use in structural strengthening applications that have qualified the evaluation criteria as set forth above.

REFERENCES

American Concrete Institute (ACI 440.2R-02) 2002. *Guide for the design and construction of externally bonded FRP systems for strengthening concrete structures*: Reported by ACI Committee 440: 3–15. USA.

Concrete Society Technical Report No.-55. 2000. *Design guidance for strengthening concrete structures using fibre composite materials*: Report of a Concrete Society Committee: 13–28: Berkshire: UK.

Fédération International du Béton (Bulletin No. 14) 2001, *Externally bonded FRP reinforcement for RC structures*: Task group 9.3 FRP reinforcement for concrete structures: 1–6: Lausanne: Switzerland.

FYFE Co. LLC. (rev. 5) 2001, *Design Manual for the TYFO® Fibrwrap® System*: 5–26, Appendix C: FYFE Co. LLC. California: USA.

ICC (ICBO) Evaluation Service (AC125) 2003, Interim criteria for concrete and reinforced and unreinforced masonry strengthening using fibre-reinforced polymer (FRP), composite system: 3–10: California: USA.

Jamaji, R., Savardekar, S.K. & Sim, M.W. 2003, *Composite technology for structural repair, strengthening and protection – A global showcase*: slides 64–126 : FYFE Asia Pte Ltd-Singapore, India Composites 2003: Hyderabad: India.

FRP Composites in Civil Engineering – CICE 2004 – Seracino (ed)
© 2005 Taylor & Francis Group, London, ISBN 90 5809 638 6

Long-term deflections of FRP-strengthened beams under sustained loads

M.K. Saha & K.H. Tan
National University of Singapore, Singapore

ABSTRACT: External bonding of FRP composites to the tension soffit of reinforced concrete beams has proven to be an effective method for flexural strengthening. However, the long-term serviceability of such FRP-strengthened beams is still a concern due to lack of long-term performance data. This study aims to investigate the long-term deflection characteristics of FRP-strengthened beams under sustained loads. Nine reinforced concrete beams, externally bonded with glass FRP reinforcement were subjected to sustained loads for six months. The test parameters were FRP reinforcement ratio and sustained load levels. The long-term deflections were found to reduce by 16 and 26 percent for beams with FRP reinforcement ratios of 0.64 and 1.92 percent, respectively. Also, the deflections were found to be lesser for lower level of sustained loads. The total beam deflections predicted using the Effective Modulus Method (EMM), were found to compare with the experimental results well, being conservative by about 20%.

1 INTRODUCTION

Deflections constitute one of the important serviceability criteria in the design of concrete structures. To keep the deflections of reinforced concrete (RC) members within allowable limits, some control mechanisms, such as appropriate design and construction procedures and the use of appropriate materials like short fiber reinforcements to provide higher beam stiffness and better crack control, have been recommended by ACI Committee 435 (1995).

The use of continuous fiber sheets impregnated in resin matrix or what is commonly termed as fiber reinforced polymer (FRP) composites can be another measure for deflection control as unidirectional FRP composite possesses high stiffness-weight ratio and has a high resistance to creep deformation (Phillips, L. N., ed. 1989). Therefore, when externally bonded to RC beams, it should offer improved resistance to deflections due to sustained loading which includes time-dependent deflections that are governed by creep and shrinkage of the constituent materials.

Although some works have been carried out on the instantaneous deflection control of RC beams using externally bonded FRP system (El-Mihilmy et al. 2000), no studies were performed with respect to long-term deflection control.

Along with ACI approach (ACI Committee 318 1989), some analytical methods (Ghali and Favre 1986, Gilbert 1999) are available to compute the long-term deflections in RC members. These are based on strain compatibility and equilibrium of forces with different models to account for the curvature due to creep and shrinkage. Gutiérrez et al. 1996, on the other hand, introduced a time-step method for the analysis of stress and strain incorporating the functions of creep and shrinkage of concrete. Once the curvature is known, deflections can be computed by double integration of the curvature or by using conjugate beam method.

For the case of steel fiber reinforced concrete (SFRC) beams, analytical methods to predict long-term deflections have been proposed by Tan et al. (1994) and Ezeldin et al. (1995). Tan et al. (1994) proposed the Effective Modulus Method (EMM) using ACI's recommended creep and shrinkage model to compute the long-term deflections.

This paper presents the experimental investigation on long-term deflection control of RC beams using externally bonded FRP system and compares the results with the analytical predictions based on the Effective Modulus Method.

2 ANALYTICAL PREDICTIONS

The instantaneous deflection of a simply supported elastic beam of span length l, subjected to uniformly distributed load w, can be expressed as:

$$\Delta_i = \frac{5}{384}\frac{wl^4}{E_c I_e} \tag{1}$$

where E_c is the modulus of elasticity of concrete and I_e is the effective moment of inertia of the concrete

section, which, based on Branson (1977)'s formula, is given by:

$$I_e = \left(\frac{M_{cr}}{M_a}\right)^3 I_g + \left[1-\left(\frac{M_{cr}}{M_a}\right)^3\right] I_{cr} \le I_g \qquad (2)$$

where M_{cr} = cracking moment; M_a = maximum applied moment; and I_g and I_{cr} = moment of inertia of a gross and a cracked section, respectively. The cracking moment can be calculated from elastic theory. For an uncracked transformed section of a FRP-bonded beam (Fig. 1), I_g can be expressed as:

$$I_g = \frac{bh^3}{12} + bh\left(\bar{y}-\frac{h}{2}\right)^2 + \frac{n_{co}bt_{co}^{\ 3}}{12} + n_{co}bt_{co}(d_{co}-\bar{y})^2 \qquad (3)$$

where b = width, h = height, $\bar{y}$ = distance of neutral axis from the top fiber, $n_{co} = E_{co}/E_c$ = ratio of modulus of elasticity of FRP composite to concrete, t_{co} = thickness of FRP composite layer, d_{co} = effective depth of composite layer from top concrete fiber.

For a cracked section:

$$I_{cr} = \frac{bx^3}{3} + nA_s(d-x)^2 + (n-1)A_s'(x-d')^2 + \frac{n_{co}bt_{co}^{\ 3}}{3} + n_{co}bt_{co}(h-x)^2 \qquad (4)$$

where d and d' = distances from extreme compressive surface to the centroids of tensile and compressive bars, respectively; A_s and A_s' = total area of tensile and compressive bars, respectively, $n = E_s/E_c$ = modular ratio of steel to concrete. The neutral axis, x for a cracked section can be determined considering strain compatibility and equilibrium of forces.

2.1 *Long-term deflections*

The creep coefficient for concrete can be expressed as (ACI 209R 1982):

$$\phi(t,t_0) = \frac{(t-t_0)^c b}{a+(t-t_0)^c} \qquad (5)$$

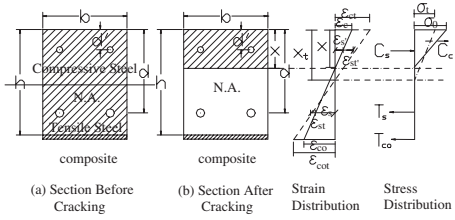

(a) Section Before Cracking (b) Section After Cracking

Figure 1. Concrete section before and after cracking.

where t is the time when deflection is to be computed, t_0 is the age of concrete at the time of application of loading, and a, b, c are experimental constants. Creep coefficient for FRP composites can be derived empirically following the idealized relationships between the logarithms of the fiber strain and the time for any particular stress level (Holmes and Just 1983), thus:

$$\phi_{co}(t,t_0) = \left(\frac{t}{t_0}\right)^n - 1 \qquad (6)$$

where t is the time in hour, $t_0 = 1$ hour. Here n is the gradient of the curve which has to be determined from experimental results.

Therefore, the effective modulus of elasticity for concrete can be expressed as [Neville et al. (1983)]:

$$E_e(t,t_0) = \frac{E_c(t_0)}{1+\phi(t,t_0)} \qquad (7)$$

and the effective modulus of elasticity for FRP composite can be expressed as:

$$E_{co}(t,t_0) = \frac{E_{co}(t_0)}{1+\phi_{co}(t,t_0)} \qquad (8)$$

By putting the values of $E_e(t,t_0)$ and $E_{co}(t,t_0)$ in place of E_c and E_{co} respectively, the neutral axis, x_t can be found after any time period. Using x_t, $I_{cr,t}$ and $I_{e,t}$ can be calculated after any time t by placing these parameters in Eqs. (4) and (2) respectively. Then using $E_e(t,t_0)$ and $I_{e,t}$ in Eq. (1), the "instantaneous plus creep" deflection can be found.

Curvatures due to shrinkage of concrete in an asymmetrically reinforced concrete member can be found by fictitious tensile force method (ACI Committee 435.2R 1966):

$$\varphi_{sh} = \frac{T_s e}{E_e I_{cr,t}} \qquad (9)$$

Here, T_s is the fictitious compressive force induced to the steel and FRP composite; e is the eccentricity of the steel and FRP composite from uncracked transformed concrete section centroid. For a FRP-bonded section:

$$T_s e = \left[\begin{matrix} A_s E_s(d-\bar{y}_t) + A_s' E_s(\bar{y}_t - d') + \\ btE_{co}(t,t_0)(d_{co}-\bar{y}_t) \end{matrix}\right] \varepsilon_{sh}(t,t') \qquad (10)$$

where $\bar{y}_t$ is the centroid of uncracked transformed concrete section from the top fiber and $\varepsilon_{sh}(t,t')$ is the shrinkage strain at time t, with drying commencing at time t'. The shrinkage strain can be expressed as:

$$\varepsilon_{sh}(t,t') = \frac{t}{\alpha+t}\varepsilon_{sh,u} \qquad (11)$$

where α is an experimental constant and $\varepsilon_{sh,u}$ is the ultimate shrinkage strain. Shrinkage of FRP composite can be ignored as the main component responsible for the shrinkage of composite that is the resin, is known to have shrinkage of the order of 2% by volume (Holmes and Just 1983).

The deflection due to shrinkage for a simply supported beam can be expressed as:

$$\Delta_{sh} = \frac{1}{8}\varphi_{sh} l^2 \quad (12)$$

This deflection will be added to the previously determined "instantaneous plus creep" deflection to get the total deflection.

3 TEST PROGRAM

A test program as shown in Table 1 was initiated to investigate the effect of glass FRP reinforcement on long term deflection and to verify the accuracy of the analytical predictions.

A total of nine beams were fabricated. Three beams (designated CB-∼) were not bonded with FRP, three beams (GB1-∼) were bonded with 1 layer (0.8 mm thickness) of glass FRP (FRP reinforcement ratio = 0.64%) and the remaining three (GB3-∼) were bonded with 3 layers (2.4 mm thickness in total) of glass FRP (FRP reinforcement ratio = 1.92%); the FRP reinforcement ratio being defined as FRP reinforcement area divided by gross area of concrete.

Three of the beams (one each of the beams with FRP reinforcement ratios of 0%, 0.64% and 1.92%) were loaded to the service load level (ultimate strength/1.7 or $0.59P_u$) computed for the beam without FRP. In the same way, the other six beams (three beams in each group) were loaded to the service load level computed for the glass FRP-bonded beams with FRP reinforcement ratios of 0.64% and 1.92% respectively.

3.1 *Material properties*

Concrete – To achieve a 28-day concrete cube compressive strength of 40 MPa, the mix proportion was set at 1:1.96:2.6:0.53 by the weight of Ordinary Portland Cement, natural sand, crushed granite of 10 mm nominal size and water. A total of six cubes (100 × 100 × 100 mm), six cylinders (150 mm diameter and 300 mm height) and six prisms (100 × 100 × 400 mm) were cast to measure the concrete cube strength, modulus of elasticity and modulus of rupture at 28 days respectively. The average values of the concrete properties are shown in Table 2. Data for concrete creep and shrinkage function were taken from the literature (Tan et al. 1994).

Steel Reinforcement – Tests were conducted to measure the yield strength and modulus of elasticity. Three types of reinforcements were used. Hot-rolled deformed high yield bars (T10 – 10 mm diameter as tensile reinforcement and T6 – 6 mm diameter as compressive reinforcement) as longitudinal reinforcement, and plain round hot rolled mid-steel bars (R6–6 mm diameter) as transverse reinforcement were used. The average values of yield strength and modulus of elasticity of reinforcement bars are shown in Table 3.

Glass Fiber Reinforced Polymer (GFRP) – The properties of fiber and resin, as supplied from the manufacturer, are shown in Table 4. Uni-directional roving E-glass fiber with a two-part, 100% solid, and low viscosity amine cured epoxy were used to form the GFRP composite of 0.8 mm thickness per layer. Primer was

Table 2. Concrete properties.

Concrete cube strength (MPa)	39.5
Modulus of elasticity (GPa)	27.2
Modulus of rupture (MPa)	4.67

Table 3. Steel reinforcement properties.

Reinforcement type	Yield strength (MPa)	Modulus of elasticity (GPa)
Tension, T10	520	194
Compression, T6	525	183
Shear, R6	212	200

Table 1. Test program.

Total sustained load (kN)	FRP reinforcement ratio (%)		
	0	0.64	1.92
15.8 ($0.59P_0^*$)	CB-59 = $0.59P_0$	GB1-49 = $0.49P_1$	GB3-40 = $0.40P_3$
18.8 ($0.59P_1^*$)	CB-70 = $0.70P_0$	GB1-59 = $0.59P_1$	GB3-49 = $0.49P_3$
22.8 ($0.59P_3^*$)	CB-85 = $0.85P_0$	GB1-70 = $0.70P_1$	GB3-59 = $0.59P_3$

*Flexural capacity of the un-strengthened beam = P_0
Flexural capacity of the 1-layer GFRP-strengthened beam = P_1
Flexural capacity of the 3-layer GFRP-strengthened beam = P_3

Table 4. Fiber and resin properties.

Fiber	Type	E-glass
	Sheet form	Uni-directional roving
	Tensile strength (MPa)	1700
	Modulus of elasticity (GPa)	71
	Ultimate strain (%)	2
Resin	Type	Two part, 100% solid, low viscosity, amine cured epoxy
	Tensile strength (MPa)	54
	Modulus of elasticity (GPa)	3
	Ultimate strain (%)	2.5

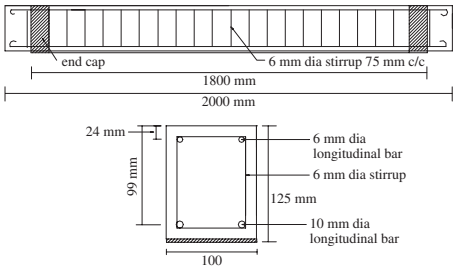

Figure 2. Glass FRP-bonded RC beams and section properties.

used, according to the manufacturer's instruction, to prepare the beam surface for proper bonding of GFRP.

3.2 *Specimen details*

The specimen configuration is shown in Fig. 2. All the beams are 100×125 mm in cross-section and 1800 mm in span length. They were longitudinally reinforced with two T10 bars (10 mm diameter) as tensile reinforcement and two T6 bars (6 mm diameter) as compressive reinforcement. R6 stirrups (6 mm diameter) were placed at a spacing of 75 mm throughout the entire length of beam so as to prevent the beams from failing in shear. The tensile reinforcements were placed at a depth of 99 mm while the compressive reinforcement depth was 24 mm from the top surface. At the GFRP cut-off points near the end span, carbon fiber sheet was attached transversely to prevent any type of premature debonding of the GFRP from the beam soffit.

3.3 *Test set-up and instrumentation*

The beams were simply supported over a 1800 mm span on the steel frame as shown in Fig. 3. Loads were applied using concrete blocks and steel plates at quarter points along the span to simulate uniform loading.

Figure 3. Test set-up for glass FRP-bonded RC beams.

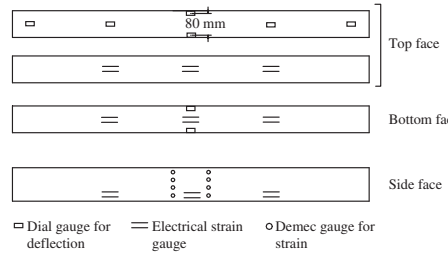

Figure 4. Instrumentation for glass FRP-bonded RC beams.

The instrumentation on the beams is depicted in Fig. 4. Strain gauges of 5 mm length were mounted on the tensile reinforcement bars at ¼th, mid and ¾th span before casting of beams. Strain gauges were also installed on the concrete top and bottom faces at ¼th, mid and ¾th span for each beam. Four pairs of demec pins of 200 mm gauge length were installed on the side face of each beam at mid-span.

Deflections were measured at mid-span, quarter spans and at end supports using a transferable dial beam. Also, two dial gauges were placed at mid span on front and back sides of the beam at 10 mm away from the beam edges to nullify any unintentional adverse effect due to loading. After adjusting for the end movement, the average of the two dial-gauges readings was taken as the mid- span deflection.

Readings were taken on the days of 1, 3, 5, 7, 10, 14, 21 days, weekly up to 3 months, and every 15 days thereafter till 6 months.

4 TEST RESULTS

Test results were collected up to 6 months after the sustained loading was imposed. In Fig. 5, the long-term deflections for beams are compared with respect

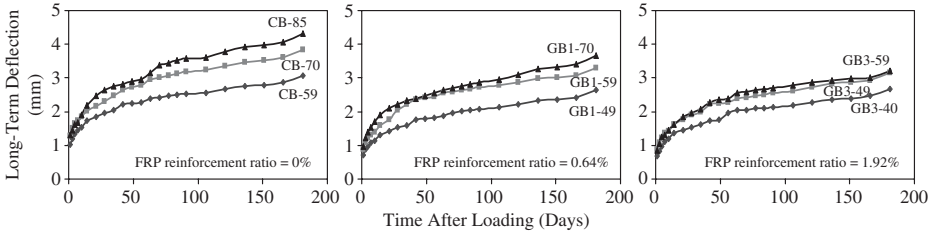

Figure 5. Long-term deflections for glass FRP-bonded RC beams subjected to different load levels.

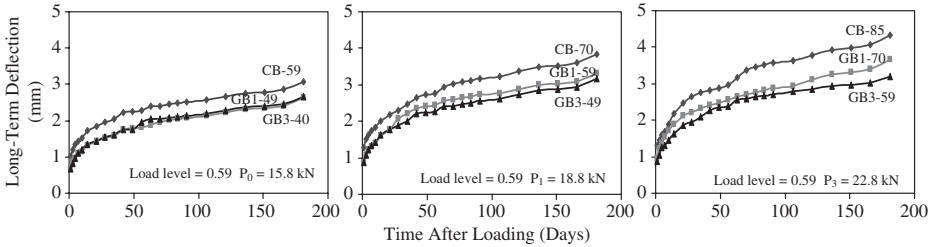

Figure 6. Long-term deflections for glass FRP-bonded RC beams with various amount of FRP subjected to same load levels.

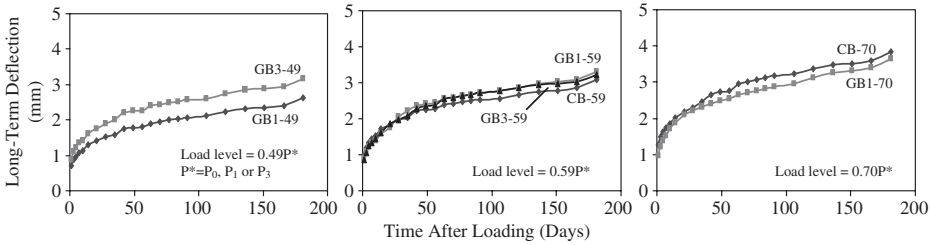

Figure 7. Long-term deflections for glass FRP-bonded RC beams subjected to same sustained load ratio.

to the sustained load levels. As expected, the higher the sustained load, the higher was the deflection.

In Fig. 6, the beams are grouped according to the magnitude of the sustained loads. Under the same magnitude of sustained loads, the larger the FRP reinforcement ratio, the smaller was the long-term deflection. Under the service load (0.59 P_0) of the control beam, the long-term deflection of GB1-49 is 14% lesser than the control beam (CB-59) after six months.

Under the service load for beam GB1 (0.59 P_1), the long-term deflection for beam GB1-59 and beam GB3-49 are 14% and 18% lesser than for beam CB-70, respectively.

For beams loaded at the service load of beam GB3-59 (0.59 P_3), beam GB3-59 showed 26% and beam GB1-70 showed 16% less deflection than for beam CB-85.

In Fig. 7, deflections are compared among the beams loaded to the same percentage of their respective flexural capacity. In general, there is very close correlation among the beams subjected to the same sustained load ratio. However, on closer examination, especially for beams GB3-49 and GB1-49 that were subjected to lower sustained load levels, the higher the FRP reinforcement ratio, the larger is the long-term deflection under a specific sustained load ratio. This implies that the contribution of externally bonded glass FRP to long-term deflection control is not exactly proportional to its contribution to the flexural strength of the beam.

A comparison between the prediction of the EMM and test results is shown in Fig. 8. The method is, in general, conservative; the average difference is 23% with respect to the values at the end of six months.

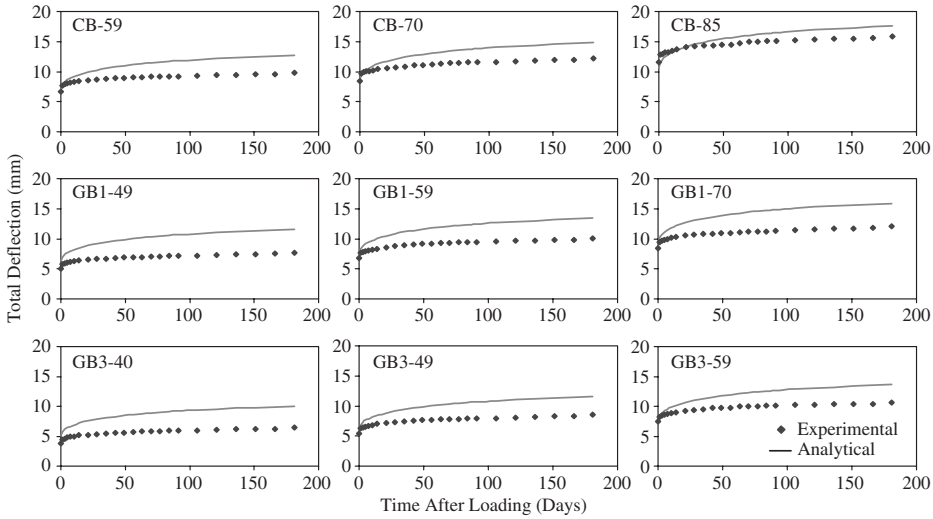

Figure 8. Comparison of test results with analytical prediction.

5 CONCLUSIONS

The following conclusions can be made from the results obtained so far:

(1) The contribution of externally bonded glass FRP to long-term deflection control is distinctly proven.
(2) The contribution of FRP in deflection control is not to the same extent as flexural strengthening, especially at lower sustained load levels.
(3) The higher the sustained load, the higher was the long-term deflection.
(4) Under the same sustained load, the larger the FRP reinforcement ratio, the smaller is the long-term deflection.
(5) The proposed Effective Modulus Method predicts the experimental results well and is conservative.

REFERENCES

ACI Committee 209R 1982. Prediction of Creep, Shrinkage, and Temperature Effects in Concrete Structures. *Manual of Concrete Practice*, American Concrete Institute, Detroit, Michigan: 92.

ACI Committee 318 1989. *Building Code Requirements for Reinforced Concrete and Commentary*. ACI, Detroit, Michigan: 353.

ACI Committee 435R 1995. *Control of Deflection in Concrete Structures.* American Concrete Institute, Redford Station, Detroit, Michigan: 66–71.

ACI Committee 435.2R 1966. Deflections of Reinforced Concrete Flexural Members. *Manual of Concrete Practice*, ACI, Detroit, Michigan: 1–29.

Branson, D.E. 1977. *Deformations of Concrete Structures*. McGraw-Hill Book Co., New York: 546.

El-Mihilmy, M.T. & Tedesco, J.W. 2000. Deflection of Reinforced Concrete Beams Strengthened with Fiber-Reinforced Polymer (FRP) Plates. *ACI Structural Journal*, Vol.97, No.5: 679–680.

Ezeldin, A.S. & Shiah, T.W. 1995. Analytical Immediate and Long-Term Deflections of Fiber-Reinforced Concrete Beams. *Journal of Structural Engineering*, ASCE, Vol. 121, No. 4: 727–738.

Ghali, A., & Favre, R. 1986. *Concrete Structures: Stresses and Deformations.* Chapman and Hall Ltd, London, UK: 9–10.

Gilbert, R.I. 1999. Deflection Calculation for Reinforced Concrete Structures-Why We Sometimes Get It Wrong. *ACI Structural Journal*, Vol.96, No.6: 1030.

Gutiérrez, S.E., Cudmani, R.O. & Danesi, R. F. 1996. Time-Dependent Analysis of Reinforced and Prestressed Concrete Members. *ACI Structural Journal*, Vol. 93, No. 4: 420–427.

Holmes, M. & Just, D.J. 1983. *GRP in Structural Engineering.* Applied Science Publishers Ltd, Essex, England: 20–23.

Neville, A.M., Dilger, W.H., & Brooks, J.J. 1983. *Creep of Plain and Structural Concrete.* Construction Press, Longman Inc., New York: 361.

Phillips, L.N., ed. 1989. *Design with Advanced Composite Materials.* Springer-verlag, London, England: 77–80.

Tan, K.H., Paramasivam, P., & Tan, K.C. 1994. Creep and Shrinkage Deflections of RC Beams with Steel Fibers. *Journal of Materials in Civil Engineering*, ASCE, Vol. 6, No. 4: 394–414.

FRP Composites in Civil Engineering – CICE 2004 – Seracino (ed)

Engineered cementitious composites for effective FRP-strengthening of RC beams

M. Maalej & K.S. Leong
Department of Civil Engineering, National University of Singapore, Singapore

ABSTRACT: This paper presents the results of an experimental program designed to evaluate the performance of FRP-strengthened RC beams incorporating ECC as a ductile layer around the main flexural reinforcement (ECC layered beams). The load-carrying and deflection capacities as well as the maximum FRP strain at failure are used as criteria to evaluate the performance. Further, 2-D numerical simulation is performed to verify the experimental results. The results have shown that ECC can indeed be used to delay debonding of the FRP resulting in effective use of the FRP material. The method of using ECC in combination with FRP can be adopted for repair and strengthening of deteriorating RC structures.

1 INTRODUCTION

The applications of Fibre Reinforced Polymer (FRP) Composites to concrete structures have been studied intensively over the past few years in view of the many advantages that FRPs possess (Teng et al. 2002, Täljsten 2003). While FRP has been shown to be effective in strengthening RC beams, strength increases have generally been associated with reductions in the beam deflection capacity due to premature debonding (Bonacci & Maalej 2002, Buyukozturk et al. 2004). Debonding failure modes occur mainly due to interfacial shear and normal stress concentrations at FRP-cut off points and at flexural cracks along the RC beam.

In the present study, it is suggested that if the quasi-brittle concrete material which surrounds the main flexural reinforcement is replaced with a ductile engineered cementitious composite (ECC), then it would be possible to delay the debonding failure mode and hence increase the deflection capacity of the strengthened beam. ECC is a cement-based material designed to exhibit tensile strain-hardening by adding to the cement-based matrix a specific amount of short randomly-distributed fibres of proper type and property (Li and Leung 1992, Li 2003). ECCs are characterized by their high tensile strain capacity, fracture energy and notch insensitivity (Maalej et al. 1995). Under uniaxial tension, sequentially developed parallel cracks contribute to the inelastic strain at increasing stress level. The ultimate tensile strength and strain capacity can be as high as 5 MPa and 4%, respectively. The latter is two orders of magnitude higher than that of normal or ordinary fibre reinforced concrete.

When ECC is introduced in a RC member, more but thinner cracks are expected to form on the beam tensile face rather than fewer but wider cracks in the case of an ordinary concrete beam (Maalej & Li 1995). More frequent but finer cracks are expected to reduce crack-induced stress concentration and result in a more efficient stress distribution in the FRP layer. The objective of the present paper is therefore to establish both experimentally and numerically the structural performance of FRP-strengthened RC beams incorporating a ductile ECC layer around the main flexural reinforcement. The load-carrying and deflection capacities as well as the maximum FRP strain at failure are used as criteria to evaluate the performance.

2 EXPERIMENTAL INVESTIGATION

2.1 *Experimental investigation*

Two series of RC beams were included in the experimental program. One series consisted of two ordinary RC beams (beam A1 and A2) and another series consisted of two ECC layered beams (ECC-1 and ECC-2). In each series, one specimen was strengthened using externally-bonded CFRP while the second was kept as a control in order to compare its load–deflection behaviour under third-point loading with the strengthened specimen. The ECC layer was about one third of the total depth of the beam as shown in Figure 1 and only one layer of CFRP sheet was used to strengthen the beam. The specimen dimensions and reinforcement details of the ECC layered beams were similar to those of the ordinary RC beams (A1 and A2), except that for beam ECC-2, the distance between the support and the CFRP cutoff point was increased from 25 mm to 100 mm to intentionally increase the peeling stresses in the region around the CFRP cutoff point.

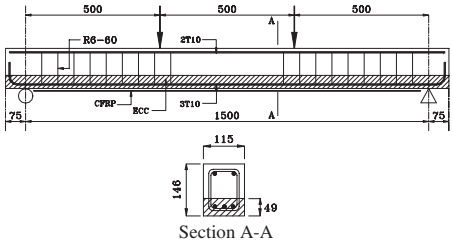

Figure 1. Specimen reinforcement details.

Table 1. Fibre properties.

Fibre type	Length (mm)	Diameter (μm)	Young's modulus (GPa)	Tensile strength (MPa)
Steel	13	160	200	2500
Polyethylene	12	39	66	2610

Table 2. ECC and concrete mix proportions (by weight).

Material	Cement	FA	CA	Silica fume	WRA	Water
ECC	1.00	–	–	0.1	0.02	0.28
Concrete	1.00	2.09	2.55	–	0.02	0.43

FA = fine aggregates; CA = 10 mm maximum-size coarse aggregates; WRA = water reducing admixture.

Table 3. CFRP properties provided by manufacturer.

Property	E_a (MPa)	G_a (MPa)	t_a (mm)	E_p (GPa)	f_{pu} (MPa)	ε_{pu} (%)
Value	1824	622	0.636	235	3550	1.5

The ECC material used in this investigation was reinforced with both high modulus (steel) and relatively low modulus (polyethylene) fibres with respective volume fractions of 0.5% and 1.5%. The properties of both fibres are given in Table 1. In addition, Type I portland cement, silica fume and superplasticizer were used to form the cement paste. Further details on the mix constituents of the ECC and the concrete are given in Table 2. The material properties for the CFRP and those for the ECC and concrete at 28 days are shown in Tables 3 and 4, respectively. A typical tensile stress–strain curve of ECC obtained from a laboratory test is shown in Figure 2.

To measure the tensile strain distribution in the CFRP, the CFRP sheet in each strengthened beam was instrumented with 27 electrical strain gauges distributed along the length of the beam. The detail positions of the strain gauges are shown in Table 5. A total of 10 strain gauges spaced at 20 mm were placed near the cutoff point to measure the steep variation of strain (see Figure 3).

Table 4. Material properties of ECC and concrete.

Material	Compressive strength (MPa)	Tensile strength (MPa)	Modulus of elasticity (GPA)
ECC	54.0	3.28[a]	18.0
Concrete (ECC-1 & ECC-2)	44.8	3.43[b]	29.0
Concrete (A1 & A2)	42.8	3.41[b]	27.3

[a] Direct tensile; [b] Split cylinder.

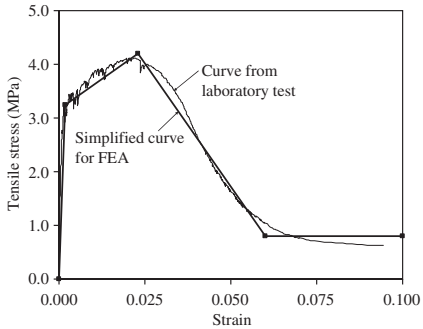

Figure 2. Tensile stress–strain curve of ECC.

Table 5. Location of strain gauges on the CFRP sheet along half the length of the beam.

	Distance from beam edge (mm)						
		FRP cutoff point	Gauge number				
Beam	Support		1–10	11	12	13	14
A2	75	100	120–300	340	420	580	825 (ctr.)
ECC-2	75	175	195–375	415	495	655	825 (ctr.)

2.2 *Test results*

The load–deflection curves of the control as well as the CFRP-strengthened ECC beams (beams ECC-1 and ECC-2, respectively) are presented in Figure 4 together

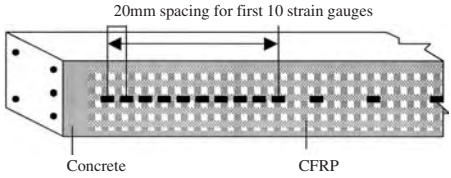

Figure 3. Instrumentation of CFRP sheet for measuring strain distribution.

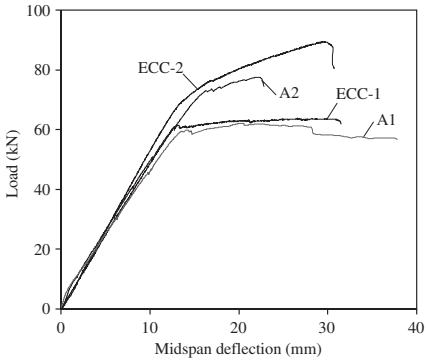

Figure 4. Load–deflection curves of beams A1, A2, ECC-1, and ECC-2.

Table 6. Summary of test results.

Beam	Load at failure P_{fail} (kN)	% of ctrl.	Deflection at failure Δ_{fail} (mm)	% of ctrl.	Max CFRP strain at failure	Failure mode
A1	60.4	–	38.6	–	–	CC*
A2	77.5	128	21.9	57	0.00991	ICID**
ECC-1	62.4	–	31.4	–	–	CC
ECC-2	89.5	143	29.6	94	0.01137	ICID

* CC = concrete crushing; ** ICID = intermediate crack-induced debonding.

with the load–deflection curves of beams A1 and A2. A summary of the test results is shown in Table 6.

The failure mode of both CFRP-strengthened beams was by intermediate flexural crack-induced interfacial debonding. For Beam ECC-2, however, about half of the CFRP sheet (along the longitudinal direction of the beam) was seen to debond followed by complete debonding of the CFRP sheet as shown in Figure 5.

It can be seen from Figure 4 that the ultimate load of beam ECC-1 was slightly higher (3% more) than

Figure 5. Debonding and separation of CFRP in beam ECC-2.

that of beam A1. The slight increased of strength may be attributed to the contribution of the ECC material to the moment capacity of the beam section because of its ability to carry tensile stresses. As for the strengthened beams, beam ECC-2 depicted higher load-carrying capacity compared to beam A2. If expressed in term of strengthening ratio, ECC-2 had a strengthening ratio of about 1.43, compared to 1.28 for beam A2. Also, it can be seen that beam ECC-2 showed a significantly higher deflection capacity (29.6 mm) at peak load compared to beam A2 (21.9 mm). If one looks at the ductility indices, beam ECC-2 had a deflection ductility (Spadea et al. 2001) and energy ductility (Naaman & Jeong 1995) of 2.30 and 1.70, respectively, which are about 39% and 22% higher than those for beam A2, respectively.

On the cracking behaviour, both ECC-1 and ECC-2 showed considerable number of fine cracks compared to the ordinary RC beams (beam A1 and A2) as revealed in Figures 6 and 7. The crack spacings were consequently much smaller in the former beams, particularly in ECC-2. These multiple but fine cracks play a major role in reducing crack-induced stress concentration resulting in more efficient stress distribution in the CFRP sheet and a better stress transfer between the FRP and the concrete beam. This delays intermediate crack-induced interfacial debonding and results in higher strengthening ratio and higher deflection capacity and, therefore, a more effective use of the FRP material.

The use of ECC layer is also expected to delay plate-end peeling of the concrete cover due to the high fracture energy of the ECC material (Maalej et al. 1995). In this experiment, despite the large distance between the support and the FRP cutoff point in beam ECC-2, plate-end debonding or concrete cover peeling were not observed. Based on the models by Saadatmanesh & Malek (1998) and Smith & Teng (2002), an ordinary RC beam with a cutoff distance

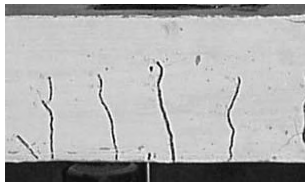

(a) A1 control beam

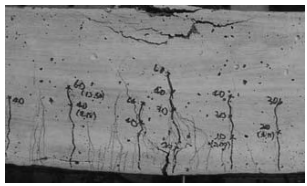

(b) ECC-1 control beam

Figure 6. Cracking behaviour at midspan of control beams A1 and ECC-1, respectively.

(a) Cracking patterns of beam A2

(b) Cracking patterns of beam ECC-2

Figure 7. Cracking patterns in beams A2 and ECC-2 around the loading point.

equal to that of ECC-2 would have failed by peeling of the concrete cover.

3 FINITE ELEMENT INVESTIGATION

A numerical simulation using the finite element analysis (FEA) package DIANA (de Witte & Feenstra 1998) was performed to verify the experimental results such as the load–deflection curves and the strain distribution in the CFRP reinforcing layer. The FEA model used for beam ECC-2 was similar to that of beam A2 except that the bottom one-third of the beam was modeled with ECC and the CFRP cutoff distance was increased from 25 mm to 100 mm.

As the ECC material is characterized by its tensile pseudo-strain hardening behaviour, the user-defined multi-linear tension-softening model in DIANA was used to model the ECC tensile behaviour (Figure 2). The plasticity of both ECC and concrete in compression was modeled using the Drucker-Prager plasticity model. The input values for concrete, ECC and steel reinforcement are shown in Tables 7 to 9.

Table 7. Input parameters for ECC.

Parameter	Values
Young modulus (GPa)	18.0
Poison's ratio	0.2
Drucke-Prager yield criteria	
• C, $Sin\,\Phi$, $Sin\,\Psi$	22.66, 0.1736, 0.1736
Tensile strength, f_{ct} (MPa)	3.28
Compressive strength, f_c' (MPa)	54.0
Multi-linear tension curve	0.00, 0
	3.28, 0.00018
	4.20, 0.023
	0.80, 0.06
	0.80, 0.1
Shear retention, Beta (β)	0.2

C = cohesion; Φ = friction angle; Ψ = dilatation angle.

Table 8. Input parameters for concrete.

Property\Specimens	A1 & A2	ECC-1 & ECC-2
Young modulus (GPa)	27.3	29
Poison's ratio	0.2	0.2
Drucke-Prager yield criteria		
• C,	17.98,	18.8,
$Sin\,\Phi$,	0.1736,	0.1736,
$Sin\,\Psi$	0.1736	0.1736
Tensile strength, f_{ct} (MPa)	3.41	3.43
Compressive strength, f_c' (MPa)	42.8	44.8
Tension stiffening		
• Maximum tensile strain ε_s	0.003	0.003
Shear retention, Beta (β)	0.2	0.2

Table 9. Input parameters for steel reinforcement.

Property	Value
Young modulus, E (GPa)	180
Yield strength, σ_y (MPa)	547

3.1 *Load–deflection curves*

Figures 8 and 9 show the load–deflection responses of the control beams (A1 and ECC-1) and the CFRP-strengthened beams (A2 and ECC-2), respectively.

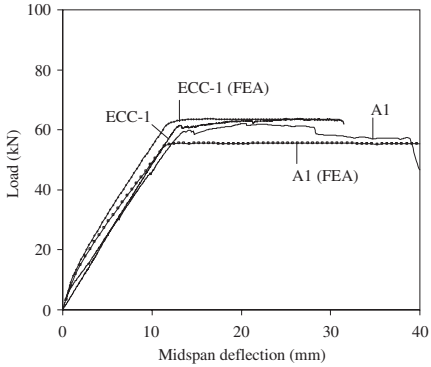

Figure 8. Load–deflection response of control beams.

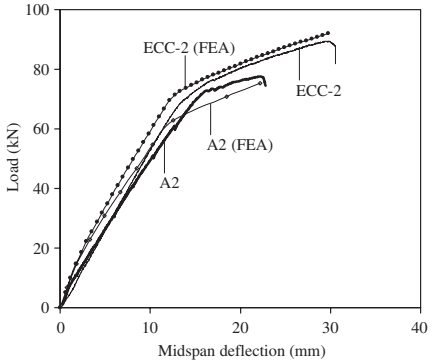

Figure 9. Load–deflection responses of strengthened beams.

Overall, it can be seen that the finite element model predicts the load–deflection responses reasonably well.

3.2 *CFRP strain distribution*

The peak-load strain distribution in the CFRP for beams A2 and ECC-2 is shown in Figure 10. It can be seen that the strain values are in reasonable agreement with the experimental values, except at the constant moment region where the predicted CFRP strains are somewhat higher than the experimentally-measured values. At high strain values ($>10{,}000\ \mu\varepsilon$), the integrity of the bond between the strain gauge and the CFRP could be seriously affected and hence may not be able to measure the true strain in the CFRP.

3.3 *CFRP stress distribution*

Figure 11 shows the shear stress distribution in the adhesive layer of beams A2 and ECC-2. For beam

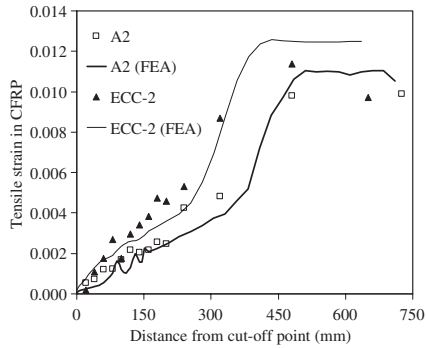

Figure 10. CFRP strain distribution of beam A2 and ECC-2 at peak load.

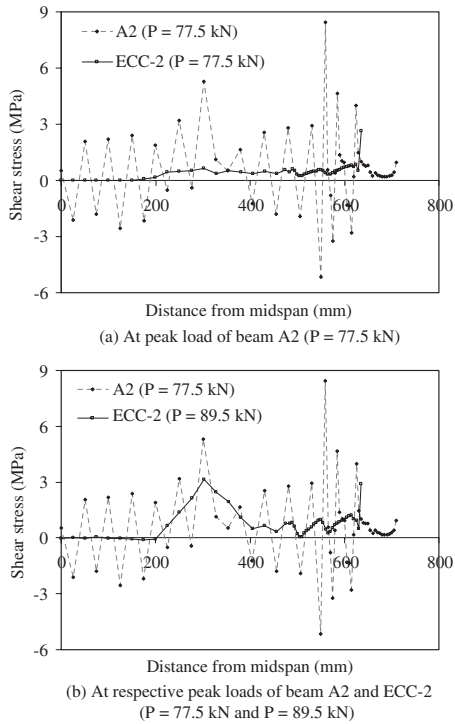

Figure 11. Shear stress distribution in the adhesive layer of beam A2 and ECC-2.

A2, the shear stress distribution is not smooth and oscillations are seen to form across the beam span. These oscillations are attributed to the formation of transverse cracks at the tensile face of the concrete

beam. In the case of beam ECC-2, however, no significant oscillation of shear stress is noticed. The shear stress distribution is considerably smoother due to the fine width of the crack in the ECC layer.

Beam A2 failed by intermediate crack-induced debonding at a peak load of 77.5 kN. It is assumed in this case the shear stress in the adhesive layer had reached a critical value. From Figure 11(a), it can be seen that all along the CFRP layer, the maximum shear stress in beam A2 is significantly lower than that in beam ECC-2. Therefore, it is expected that beam ECC-2 would fail at a critical load significantly higher than 77.5 kN (the failure load of beam A2). Indeed, beam ECC-2 failed at a peak load of 89.5 kN by intermediate crack-induced debonding. Figure 11(b) compares the shear stress distribution for both beams at their respective peak loads. It is seen that the shear stress in beam ECC-2 reaches a peak of 3.14 MPa at a distance of about 300 mm from midspan (or 50 mm away from loading point along shear span of the beam). It is interesting to note that this is the same location where the shear stress distribution in beam A2 has a local peak (the global peak occurs at a distance of 560 from midspan). It is also interesting to note that this is the same location around which intermediate crack-induced debonding is believed to have initiated in both beams.

At a load of 77.5 kN, the shear stress distribution in beam ECC-2 was not sufficiently critical to cause failure. This meant that the applied load in beam ECC-2 could be further increased without failure until a critical value is reached. This increase in the applied load is made possible by the ability of the linear elastic CFRP material to provide a higher contribution to the section moment capacity of beam ECC-2 in comparison to beam A2. The low interfacial shear stresses in beam ECC-2 allowed the CFRP material to carry higher tensile stresses, leading to a more effective use of the CFRP in beam ECC-2 compared to beam A2. Consequently, the CFRP failure strain in the former beam is significantly higher than that in the latter beam as indicated in Figure 10.

4 CONCLUSIONS

The application of an ECC material in a CFRP-strengthened beam was experimentally and numerically investigated. The results showed that ECC had indeed delayed debonding of the CFRP and resulted in effective use of the CFRP material. With the use of ECC as a ductile layer, RC beams can be effectively strengthened while minimizing loss in deflection capacity. The method of using ECC in combination with FRP can be adopted for repair and strengthening of deteriorating RC structures.

Further works can be done to investigate other possible types of failure modes in CFRP-strengthened beams as well as bond strength between FRP laminates and ECC.

REFERENCES

Bonacci, J.F. & Maalej, M. 2001. Behavioral trends of RC beams strengthened with externally bonded FRP. *Journal of Composites for Construction* 5(2): 102–113.

Buyukozturk, O., Gunes, O. & Karaca, E. 2004. Progress on understanding debonding problems in reinforced concrete and steel members strengthened using FRP composites. *Construction and Building Materials* 18(1): 9–19.

de Witte, F.C. & Feenstra, P.H. (ed) 1998. *DIANA User's Manual, Release 7. Netherland: TNO Building and Construction Research*.

Li, V.C. 2003. On engineered cementitious composites (ECC) a review of the material and its applications. *Journal of Advanced Concrete Technology* 1(3): 215–230.

Li, V.C. & Leung, C.K.Y. 1992. Theory of steady state and multiple cracking of random discontinuous fiber reinforced brittle matrix composites. *J. of Engng. Mechanics* 118(11): 2246–2264.

Maalej, M. & Li, V.C. 1995. Introduction of strain hardening engineered cementitious composites in design of reinforced concrete flexural members for improved durability. *ACI Structural Journal*. 92(2): 167–176.

Maalej, M., Hashida, T. & Li, V.C. 1995. Effect of fiber volume fraction on the off-crack-plane fracture energy in strain-hardening engineered cementitious composites. *Journal of the American Ceramic Society* 78(12): 3369–3375.

Naaman, A.E. & Jeong, S.M. 1995. Structural ductility of concrete prestressed beams with FRP tendons. *Proceeding of the Second International RILEM Symposium on Non-Metallic Reinforcement for Concrete Structures, Ghent, Belgium, RILEM Proceedings* 29, pp. 379–386.

Saadatmanesh, H. & Malek, A.M. 1998. Design guidelines for flexural strengthening of RC beams with FRP plates. *Journal of Composites for Construction (ASCE)* 2(4): 158–164.

Smith, S.T. & Teng, J.G. 2002. FRP-strengthened RC beams. II: assessment of debonding strength models. *Engineering Structures* 24(4): 397–417.

Spadea, G., Swamy, R.N. & Bencardino, F. 2001. Strength and ductility of RC beams repaired with bonded CFRP laminates. *Journal of Bridge Engineering* 6(5): 349–355.

Täljsten, B. 2003. *FRP strengthening of existing concrete structures design guidelines*, Second Edition, Luleå, Sweden: Luleå University Printing Office.

Teng, J.G., Chen, J.F., Smith, S.T. & Lam, L. 2002. *FRP Strengthened RC Structures*. West Sussex: John Wiley & Sons, Ltd.

Long-term monitoring (special session)

FRP Composites in Civil Engineering – CICE 2004 – Seracino (ed)
© 2005 Taylor & Francis Group, London, ISBN 90 5809 638 6

Field monitoring of concrete structures with internal or external FRP reinforcement

J.P. Newhook
Dalhousie University, Halifax, Nova Scotia, Canada

ABSTRACT: Field projects involving the use of fibre reinforced polymer reinforcement for concrete have often been implemented in advance of codes and design guidelines. Consequently, engineers have instrumented and tested these innovative structures to verify their performance and safety. This paper reviews a number of instrumented projects within the ISIS Canada program. Field data verifying the durability of glass fibre reinforced polymers is presented. Monitoring considerations and research needs for long-term monitoring of concrete structures with FRP are discussed.

1 INTRODUCTION

Since its inception in 1995, the Intelligent Sensing for Innovative Structures (ISIS Canada) Network of Centres of Excellent Program has participated in over 38 field projects in Canada demonstrating a variety of innovative civil engineering technologies. Many of these projects have involved the use of fibre reinforced polymer (FRP) reinforcement, either as external strengthening for existing concrete structures or internal reinforcement for new concrete structures. To aid in earlier acceptance of these technologies and to provide the infrastructure managers with increased confidence in the innovative materials, several projects were instrumented with a variety of sensors. Load testing and initial service load readings were then collected and compared against theoretical performance. This aspect of project monitoring was often referred to as design verification.

Where opportunities existed, field sensor readings were collected periodically for further verification of performance. As remote monitoring technologies were developed, a number of projects were monitored on a semi-continuous or continuous basis. This led to the second phase of monitoring which may be classified as long-term health monitoring.

This paper discusses several of the key field monitoring projects within the ISIS program which fall into either or both of the two monitoring categories. Typical results are presented along with early conclusions that have been developed related to the performance of FRP under field conditions. In all cases, the initial design verification results have been positive. While the continuous monitoring results have been consistent with these initial results, participation in these activities has led to closer of examination appropriate strategies for long-term monitoring. Isolation of vehicle induced strains from sensor noise, sensor drift and temperature effects are key considerations. Furthermore, identifying possible FRP damage or deterioration mechanisms and understanding their influence on structural response is necessary to adequately interpret long-term readings.

2 MONITORING FOR DESIGN VERIFICATION

Most projects involving FRP reinforcement in Canada where completed prior to the official adoption of national design codes. In fact, these projects were often key demonstration structures which led to the accelerated acceptance of FRP as a reinforcement and strengthening material by the civil engineering community. Even today, after the adoption of the first versions of the building code 'Design and Construction of Building Components with Fibre Reinforced Polymers (CSA S806, 2002) and the bridge code 'Canadian Highway Bridge Design Code' (CSA S6, 2000), many new projects are still ahead of the current provisions and are leading the way for the next advancements in code criteria. Despite the substantial amount of laboratory testing and analysis preceding implementation of FRP applications, these leading-edge projects required a means of verifying the actual performance and safety in the field. The most common method employed by ISIS Canada, as well as many other researchers around the world, is to instrument key elements of the structure and then assess their response during load testing. The load testing can be conducted

before the bridge is open to traffic or can even be an assessment of the structure's response under the initial service loading.

In the majority of projects the instrumentation is mainly strain gauges. ISIS Canada has made extensive use of fibre optic based strain gauges (ISIS Canada 2001) but many varieties of gauges are acceptable for this short-term objective. The general philosophy of short-term verification is to demonstrate that the strain response is within an acceptable range. This range may be defined by the empirical results from scale model tests or by prediction using the principles of mechanics of materials and numerical modelling. In addition to assessing the magnitudes of strains, the engineers also seek to demonstrate strain compatibility between the FRP reinforcement and the concrete component. This confirms that the FRP is properly bonded to the structure and participating in load resistance. This aspect is particularly important for projects where the FRP elements are used for external strengthening or rehabilitation. Several examples of short-term verification monitoring are presented below.

2.1 *Internal FRP reinforcement*

A number of slab on girder bridge projects have been completed in Canada in which glass or carbon FRP, or a combination of both, have been used as reinforcement for the concrete deck slab and in the curbs and barrier walls or as prestressed tendons in bridge girders.

The specific details of the projects can be found in the respective references. In each project, the deck reinforcement or tendons were instrumented and monitored as a heavy vehicle crossed the span. In some projects, FRP reinforcement was only used in part of the deck and the steel reinforcement in adjacent spans could also be monitored and the strain values compared. Typical strain monitoring results are presented in Table 1. Deck reinforcement strains are typically less than 15 micro-strain for a single truck pass, while the strains in the FRP prestressing tendons are less than 35 micro-strain. Where strain compatibility and girder/deck composite actions could also be checked, the FRP was found to be properly bonded and responding as predicted by simple linear elastic analysis.

2.2 *External FRP reinforcement*

The effectiveness of monitoring the response of external FRP for initial design verification is highly dependant on the nature of the strengthening application. ISIS Canada has used external FRP wraps and laminates in field projects for flexural strengthening, shear strengthening and column strengthening. A partial list of application is presented in Table 2.

While instrumentation was installed on a number of these projects, its effective in a long-term monitoring program is questionable. In the case of flexural laminates, the monitoring may be beneficial. For example, in the Ste. Emelie de l'Energie bridge strengthening project (Labossiere et al. 2000) a laminate strain of 80 to 100 micro-strain was recorded during load testing. The researchers were able to use these readings to verify the performance of the laminate. However, when the laminate is used to strengthen for shear or when the laminate is used to strengthen columns by confinement, the theoretical and recorded strain values in the FRP are very small unless a member failure occurs. The readings for the Portage Creek Bridge (Mufti et al. 1999), a FRP column wrap, and the Maryland Bridge (Hutchinson et al. 2003), FRP shear strengthening, were less than 5 micro-strain. The vehicle response was difficult to distinguish from signal noise. The load testing may be used more as a proof load to demonstrate that the strengthened structure can sustain a certain load without signs of distress but direct assessment of laminate integrity from low strain readings are often not meaningful.

Table 1. Typical internal FRP strain values for vehicle loads.

Structure	Reinforcement type	Strain range ($\times 10^{-6}$)
Wotton Bridge Deck (Benmok. et al. 2002)	GFRP top bars CFRP bottom bars	0−5 0−15
Salmon River Bridge (Mufti et al. 1999)	GFRP in curbs	0−12
Centre Street Bridge (Shrive et al. 2002)	GFRP in deck	0−15
Taylor Bridge (Mufti et al. 2003)	CFRP tendons	0−15
Beddington Bridge (Mufti et al. 2003)	CFRP tendons	0−35

Table 2. Typical external FRP strain values for vehicle loads.

Structure	Reinforcement type	Strain tange ($\times 10^{-6}$)
Ste. Emelie de l'Energie (Labossiere et al. 2000)	CFRP flexure	0–100
Portage Creek Bridge (Mufti et al. 1999)	CFRP column wrap	0–2
Maryland Bridge (Hutchinson et al. 2003)	CFRP shear	0–5

3 LONG-TERM MONITORING

Due to the large number and variety of field projects, ISIS Canada has been able to institute long-term monitoring of a number of its field projects. This has led to a re-examination of the objectives for

long-term monitoring of FRP. The initial verification testing conducted at the completion of construction is often sufficient to demonstrate the proper installation and function of the FRP. Long-term monitoring therefore must have additional objectives beyond simple verification of design assumptions. ISIS has identified the several objectives which may be realized by long-term monitoring. Some are unique to the use of FRP but others have more general applicability. These objectives are: establishing the long-term performance of structures with FRP, examining the durability of FRP in field environments, creating a statistical database of actual loads on structures to facilitate code calibration, facilitating evaluation after extreme loading, calibrating numerical modelling of field structures and advancing the field of structural health monitoring (SHM).

3.1 *Long-term performance*

One of the prime objectives is to address the issue of lack of long-term experience with the use of FRP in these types of civil engineering applications. In general, engineers are still expressing a lack of comfort with FRP as many believe that there is still a level of uncertainty about its performance over long periods of time in field applications. From a monitoring perspective, the objective is to demonstrate that the response, and hence performance, of the FRP is the same after a long period of field use as it was initially after construction. To accomplish this objective, a number of the field projects that were instrumented and tested after construction are targeted for periodic repeating of the load testing after several years of service life. Some the ISIS projects in this category include the Wotton Bridge (Benmokrane & El-Salakawy 2002), Joffre Bridge (Benmokrane et al. 2000) and Ste. Emelie de l'Energie Bridge (Labossierre et al. 2000). The strategy is to repeat the load testing as accurately as possible and compare the strain response to the initial load test values. Both the magnitude of the strain values and strain compatibility can be used as indicators. If the response is similar, then the FRP can be said to be functioning in a manner consistent with its initial condition. Visual inspection to confirm a lack of visible distress in the structure is used to support the findings of the instrumented tests.

3.2 *Durability of FRP*

The issue of long-term performance is also being investigated from a more detailed perspective. In the case of internal FRP reinforcement, a number of accelerated durability tests on glass FRP have suggested that there may be a durability problem due to the high alkalinity of concrete (Benmokrane et al. 2001). Researchers at ISIS are using long-term monitoring to examine this issue in several ways. The simplest

Figure 1. Plan view of concrete deck on Hall's Harbour Wharf.

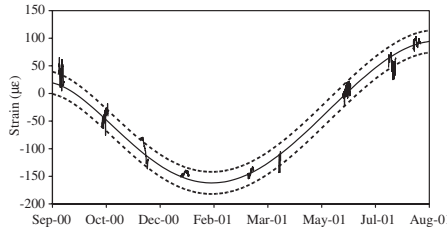

Figure 2. Representative GFRP strain results for full year at Hall's Harbour.

approach, which is being applied to all instrumented projects regardless of the duration of monitoring, is indirect assessment through demonstration of satisfactory field conditions. Based on the results of accelerated laboratory testing, design codes and guidelines indicate the service strain range of glass FRP should be kept below 20–30% of ultimate strain in order to reduce the possibility of alkaline based deterioration of the FRP during the service life of the structure. Strain monitoring results, such as those shown in Table 1, indicate that the live load service strain range is generally below 1% of the ultimate FRP strain from heavy vehicle loads.

In the Hall's Harbour Wharf Project (Newhook et al. 2000), a pile supported concrete wharf deck (see Figure 1) was constructed using GFRP reinforcement. With the aid of Fabry-Perot fibre optic sensors, the strain in selected GFRP rods was monitored over several years. The monitoring was conducted on a continuous basis with live load, temperature and storm loadings being recorded. Using the data records from one sensor for a full year of monitoring, a bandwidth of typical annual strain readings was constructed.

In Figure 2, the central solid line represents the mean values recorded while the dashed lines represent the 5th and 95th percentile of the readings. In addition, nine of the weekly data files are plotted in their entirety

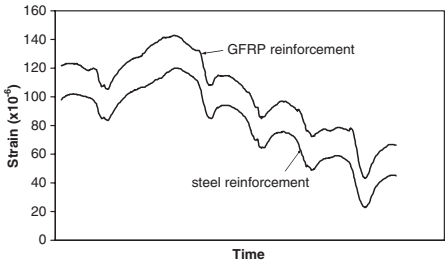

Figure 3. Typical strain profiles for a week at Hall's Harbour.

in the figure for perspective. The seasonal variations with temperature are seen to be much more significant than the smaller live load strains fluctuations. The complete strain range, including all environmental loadings, is still only 350 micro-strain which is still less than 3% of the total strain capacity for GFRP. The durability of the GFRP is indirectly established as the monitoring results indicate that the strain conditions most favourable for deterioration do not exist.

In several field projects, researchers have also developed a more direct means of assessing the durability of GFRP. In the Hall's Harbour Project and the Centre Street Bridge Project (Shrive et al. 2002) both steel and GFRP reinforcement were used in similar locations in the structure. In the case of Hall's Harbour, a hybrid reinforcing scheme was used where the flexural reinforcement for the pile caps beams included an upper layer of steel reinforcement and a lower layer of GFRP. The beam had an overall depth of 1000 mm and the two reinforcing layers were separated by only 45 mm. The monitoring program included strain gauges on both layers of reinforcement. The strain compatibility between the two could be observed. A typical strain plot over a one week period (in which the temperature fluctuates between 25 to 10 degrees Celcius) in the second year of monitoring is shown in Figure 3. It can be seen that both layers respond in a similar fashion to be small live load effects as well as the larger temperature effects. This demonstration of strain compatibility was representative of all results for a three year monitoring period.

In the Centre Street Bridge Project, a section of the deck used a glass FRP grid for top reinforcement while other sections used steel reinforcement (Figure 4). Strain gauges at each section allowed for the comparison of strain response of steel and GFRP under similar vehicle and temperature loads. The structure is being continuously monitored and a representative record for a one week period is shown in Figure 5. The response of the GFRP is very similar to that of the steel reinforcement. This comparison has been on going for three years with similar results. A detailed visual inspection also confirmed that no concrete cracking could

Figure 4. GFRP grid in Centre Street bridge deck.

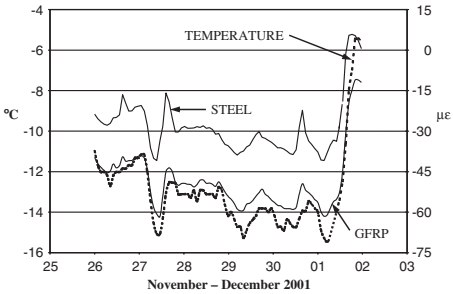

Figure 5. Comparison of GFRP versus steel reinforcement strains for Centre Street Bridge.

be observed in either the steel reinforced of GFRP reinforced sections of the deck.

Both projects are examples of a more direct assessment of GFRP durability in the field. The positive assessment however relies on the assumption that any deterioration in the GFRP would have a significant impact on either the magnitude of strain response or on strain compatibility (Newhook 2002).

To provide more conclusive assessment of the durability of FRP in field projects, ISIS is currently undertaking to program of extracting cores with GFRP from field projects and examining them for signs of alkaline deterioration. These cores will be taken from several projects where monitoring has been ongoing and the results of the physical examination can be correlated with monitoring results. In this manner both the durability of GFRP and the viability of the long-term strain monitoring technique can be established.

3.3 *Evaluation after extreme loads*

In the case of the Portage Creek Bridge (Mufti 2002), CFRP wraps were applied to the piers of the bridge to facilitate a seismic upgrade. Instrumentation was added to the structure to monitor the performance of

the laminates and response of the structure during and after a seismic event. As prediction of the time of both minor and major seismic events is not possible, the monitoring system is designed to be a long-term continuous monitoring system such that an event can be captured. It is hoped that readings during a minor tremor can be used to improve understanding of structure response and assess the contribution of the repair system. If a major seismic event occurs, the monitor system may not only provide valuable information about response but may also be used to help assess the condition and safety of the bridge for continued use.

3.4 *Universal objectives*

Statistical information on loads, improved modelling techniques and advancement of SHM techniques are all objectives that have universal benefits beyond just structures with FRP applications. The projects in which ISIS is undertaking continuous long-term monitoring can also be useful in providing statistical data on vehicle or environmental loads on bridges. In Canada for example, no statistical data exists on the annual distribution of axle loads on a bridge. This information is extremely important for understanding fatigue life of bridge components. While the ISIS monitoring systems have not been designed with weigh in motion data in mind, the simple statistical information on strain response can be used a basis for characterizing anticipated fatigue cycles during service life.

Other ISIS researchers are currently examining issues related to modelling the complex response of field structures using finite element techniques. The Saskatchewan River Bridge Project (Bolingbroke et al. 2002) is specifically calibrating theoretical models for prediction of dynamic response against measured field readings. To gain a fundamental understanding of structural response under service level live loads, a scale model of a slab on girder bridge system commonly used by ISIS is being extensively tested under controlled conditions in the lab. Identifying the response of the system to progressive damage and creating a calibrated numerical model are key tasks (Yang et al. 2004). The ability to model response to service loads and damage is essential in the designing of a SHM system and in the final interpretation of the monitoring data.

A companion paper in this conference also discusses the issue of creating a long-term monitoring scheme for the detection of debonding in externally applied CFRP flexural laminates (Sarazin & Newhook 2004). While the damage mechanism is specific to an FRP application, the concept of damage modelling and isolation of damaged response from other phenomena which occur during the service life of a structure is a fundamental issue for all long-term monitoring projects.

3.5 *Central monitoring and data management*

Due to the growing number of continuously monitored projects in the ISIS program, resources have also been devoted to the general issue of monitoring many projects from a central location. Currently, a strategy has been developed where local site computers are networked to a central server (Han et al. 2004). Using a data streaming version of the TCP/IP protocol data can be automatically transferred in real time from the sites to the central server. All sites can be viewed over the central server with only a five second delay between collecting of data from the sensors and processed viewing of the information. The sensor response can be correlated with live video from web cameras at site.

Concurrent with this effort, the issue of data reduction and management is being investigated. Continuous monitoring of even a few sensors quickly generates large quantities of data. To be effective, the SHM systems should process the data in real-time, compare the information against preset thresholds and save only that information which is deemed to be relevant or important. Simple algorithms can be used to accomplish this data reduction, but the setting of thresholds or establishing what is important requires significant planning and engineering judgment. The objectives of the monitoring activity, such as durability assessment of GFRP, detection of debonding or statistical record of loading must be clearly understood and used as a basis for designing the data management algorithms. Many other issues need to be considered such as isolation of live load from environmental load, establishing the natural 'aging' of the structure and the value of ambient load response versus controlled load response.

Improvements in data management through the use of neural network techniques (Card & McNeill 2004) are also being pursued. Currently a system has been developed which will learn the normal characteristics of the data and identify when a novel event in the data has occurred. In the case of the Portage Creek Bridge Project this novel event could be a seismic tremor or in other structures it could simply be a larger than normal vehicle load. A proposed data management scheme is to save only the information associated with novel events and then examine it in a more rigorous fashion but structural engineers to determine its significance. The system also has the ability to identify when the baseline normal characteristics of the sensor response is changing.

4 CONCLUSIONS

Long-term monitoring of FRP in field projects presents both opportunities and challenges. The opportunity exists to demonstrate the long-term performance, durability and benefits of FRP materials thereby accelerating their adoption and improving

codes and standards. Currently monitoring results from many projects have been used to indirectly establish the durability of glass FRP by both indirect and direct assessment.

The challenges are related to the design and implementation of long-term monitoring systems. In general, the issues are related to understanding and modeling the response of the structure or component under all field conditions and to predict whether damage or deterioration has occurred. Many practical issue of data processing and management need to be addressed. ISIS has been able to implement initial solutions to some of these problems but much more detailed work remains. While structures with either internal or external FRP are the prime focus of the ISIS Canada Program, the needs and concepts discussed in the paper are generally applicable to the broader field of structural health monitoring of any civil infrastructure.

REFERENCES

Benmokrane, B. & El-Salakawy, E. 2002. Design, construction and monitoring of a bridge deck reinforced with FRP bars: Wotton Bridge. In Aftab A. Mufti (ed.), *Proceedings of the First International Workshop on Structural Health Monitoring of Innovative Civil Engineering Structures, Winnipeg, Canada, 2002*. Winnipeg: ISIS Canada.

Benmokrane, B., Rahman, H., Mukhopadhaya, P., Masmoudi, R., Chekried, M., Nicole, J. & El-Safty, A. 2000. Use of fibre reinforced polymer reinforcement integrated with fibre optic sensors for concrete bridge deck slab construction. *Canadian Journal of Civil Engineering* 27: 928–940.

Benmokrane, B., Wang, P., Ton-that, M.T. & Laoubi, K. 2001. Durability of GFRP composites reinforcing rods in concrete environment. In C. Burgoyne (ed.) *Proceedings of the Fifth International Conference on Fibre-Reinforced Plastics for Reinforced Concrete, Cambridge, July 2001.* London: Thomas Telford.

Bolingbroke, B., Wegner, L. & Sparling, B. 2002. Measuring the dynamic properties of an overpass structure to assess structural health. In Aftab A. Mufti (ed.), *Proceedings of the First International Workshop on Structural Health Monitoring of Innovative Civil Engineering Structures, Winnipeg, Canada, 2002*. Winnipeg: ISIS Canada.

CSA. 2000. *Canadian Highway Bridge Design Code CSA-S6- 00*. Toronto: Canadian Standards Association.

CSA 2002. Design and Construction of Building Components with Fibre Reinforced Polymers CSA-S806-002. Toronto: Canadian Standards Association.

Card, L. & McNeill, D. 2004. Novel event identification for SHM systems using unsupervised neural computation. *Proceedings of the International Symposium on NDE for Health Monitoring and Diagnostics Vol. 5393, San Diego, March, 2004*. Washington: SPIE – The International Society for Optical Engineering.

Han, L., Newhook, J.P. & Mufti, A.A. 2004. Centralized remote structural monitoring and management of real-time data. *Proceedings of the International Symposium on NDE for Health Monitoring and Diagnostics Vol. 5393, San Diego, March, 2004*. Washington: SPIE – The International Society for Optical Engineering.

Hutchinson, R., Tadros, G., Kroman, J. & Rizkalla, S. 2003. Use of externally bonded FRP systems for rehabilitation of bridges in Western Canada. In S. Rizkalla and T. Nanni (eds.) *Field Applications of FRP Reinforcement: Case Studies SP-215*. Famington Hills: American Concrete Institute.

ISIS Canada. 2001. Design Manual No. 1 – Installation, Use and Repair of Fibre Optic Sensors. Winnipeg: ISIS Canada NCE Program.

Labossierre, P., Neale, K.W., Rochette, P., Demers, M., Lamothe, P., LaPierre, P. & Desgagne, G. 2000. Fibre reinforced polymer strengthening of the Sainte Emelie de l'Energie Bridge: design, instrumentation and field testing. *Canadian Journal of Civil Engineering* 27: 916–927.

Mufti, A.A. 2002. Structural health monitoring of innovative Canadian civil engineering structures. *Structural Health Monitoring*, 1(1): 89–103.

Mufti, A.A., Newhook, J.P. & Mahoney, M. 1999. Salmon River Bridge field assessment. In T. Viraraghavan and C. Borbely (eds.), *Proceedings of the Canadian Society for Civil Engineering Annual Conference Vol. I, Regina, 1999.* Montreal: Canadian Society for Civil Engineering.

Mufti, A.A., Tadros, G., Newhook, J.P. & Cheng, R. 2003. Structural Health Monitoring of Innovative Bridge Structures in Canada. *Proceedings of Fib Congress, Osaka, Japan, 2003*. Tokyo: Prestressed Concrete Engineering Association.

Newhook, J.P. 2002. Assessing the durability of glass FRP through continuous strain monitoring. In Aftab A. Mufti (ed.), Proceedings of the First International Workshop on Structural Health Monitoring of Innovative Civil Engineering Structures, Winnipeg, Canada, 2002. Winnipeg: ISIS Canada.

Newhook, J.P., Bakht, B., Tadros, G. & Mufti, A.A. 2000. Design and Construction of a Concrete Marine Structure Using Innovative Technologies. In J. Humar and G. Razaqpur (eds.) *Proceedings of Third International Conference on Advanced Composite Materials in Bridges and Structures, Ottawa, 2000*. Montreal: Canadian Society for Civil Engineering.

Sarazin, G. & Newhook, J.P. 2004. Strain monitoring techniques for FRP laminates. *Proceedings of the Second International Conference on FRP Composites in Civil Engineering, Adelaide, December, 2004*. Rotterdam: Balkema.

Shrive, P., Newhook, J.P., Brown, T., Shrive, N., Tadros, G. & Kroman, J. 2002. Centre Street Bridge innovative deck slab. *Proceeding of the Annual Conference of the Canadian Society for Civil Engineering, Montreal, 2002*. Montreal: Canadian Society for Civil Engineering.

Yang, C., Limaye, V. & Newhook, J.P. 2004. Experimental evaluation of load distribution in steel-free bridge decks. *Proceeding of the Annual Conference of the Canadian Society for Civil Engineering, Saskatoon, 2004*. Montreal: Canadian Society for Civil Engineering.

FRP Composites in Civil Engineering – CICE 2004 – Seracino (ed)
© 2005 Taylor & Francis Group, London, ISBN 90 5809 638 6

EIS-based sensors for NDE of FRP-strengthened concrete beams: experiments and finite element simulation

R. Harichandran, S. Hong, L. Udpa & Z. Zeng
Michigan State University, East Lansing, Michigan, USA

ABSTRACT: A nondestructive evaluation (NDE) technique based on electrochemical impedance spectroscopy (EIS) is developed for concrete beams strengthened with carbon fiber reinforced polymer (CFRP) sheets to detect the debonding of CFRP from concrete. Copper tape on the surface of the CFRP sheet, stainless steel wire embedded in the concrete, and reinforcing bars were used as sensing elements. In laboratory experiments, the CFRP was progressively debonded using a wedge and impedance measurements were taken using various pairs of electrodes. Changes in the impedance spectra, and the capacitance parameters obtained from equivalent circuit analysis, can be used to assess the global state of the bond between CFRP and concrete. Impedance measurements taken between embedded wire sensors can be used to locate debonded regions. Preliminary finite element simulations are performed to elucidate the experimental observations.

1 INTRODUCTION

Many structures built in the past need to be strengthened and retrofitted to overcome deficiencies caused by increased load demands, environmental deterioration and structural aging. Thirty-five percent of all bridges in the U.S. are estimated to be structurally deficient and require repair, strengthening, widening or replacement (Karbhari 2000). To overcome structural deficiencies, composite materials such as fiber reinforced polymers (FRP) are often used in strengthening and retrofitting. Enhancing the flexural performance of structures by bonding FRP plates or sheets is a simple and expedient technique for strengthening and retrofitting structures (Rahimi et al. 2001), and carbon fiber reinforced polymer (CFRP) is usually the preferred material.

Structural components strengthened or retrofitted with FRP behave as composite components, and their strengths are calculated by taking this into account. Interfacial bonding between the adherents is critical in achieving composite behavior and increased strength, especially in flexural members. Concrete structures strengthened or retrofitted with FRP plates can exhibit undesirable brittle failure if the interfacial bond between the adherents degrades. Delamination of the FRP plates and ripping of concrete are common failure modes (Nguyen et al. 2001) initiated by high localized stress concentrations in the interface layer (Buyukozturk 1998).

Visual inspection is not a reliable method of assessing the integrity of interfacial bond in composite components. "Tap" tests are time consuming and difficult to conduct in structural components that are difficult to access. Destructive tests are not feasible for in-service structures. Different NDE methods, including vibration, ultrasonic and microwave techniques, have been used to detect or monitor damage in FRP-strengthened structures. For bridges, evaluation without prolonged lane closures is difficult with these methods. Some of these NDE methods indicate only global measures of interfacial bond integrity and others are complicated to use in the field. An inexpensive technique suitable for monitoring concrete structures rehabilitated with CFRP is presented in this paper.

1.1 *Background concepts on EIS*

Traditionally, electrochemical impedance spectroscopy (EIS) has been used to detect coating deterioration and substrate corrosion, and the EIS technique is performed in an electrolyte with counter and reference electrodes (Scully et al. 1989). Use of an external electrolyte is cumbersome in the field. However, it is possible to use *in-situ* electrodes to measure the impedance in the ambient condition without submerging the electrochemical cell.

In-situ sensors have been adapted to detect moisture ingress and crack propagation in structural adhesive bonds (Davis et al. 1999, 2000, 2003). This sensor technology uses EIS to inspect the integrity of the bond. The impedance typically increases in magnitude as the crack propagates. In the simplest method for detecting debonding, the impedance spectra can

be compared directly. However, additional information can be obtained from the impedance spectra by using equivalent circuit analysis. Davis et al. found that the resistive components in the equivalent circuit they used were functions of moisture content and the capacitance parameter was a function of both moisture content and bonded area.

1.1.1 *Electrical Impedance*

Ohm's law defines resistance as the ratio between voltage, V, and current, I, in an electrical circuit. Electrochemical impedance is a generalized resistance to current flow through an electrochemical cell. It is generally measured by applying an alternating voltage across a pair of electrodes and measuring the alternating current.

At the steady-state, electrical resistance to a direct current is constant in time since current and voltage are at their constant steady state values. However, the steady-state electrical impedance, Z, is dependent on the frequency of the alternating (harmonic) excitation. When the excitation signal is harmonic, the response signal also is harmonic at the same frequency. Z is a complex-valued quantity defined as the ratio between the excitation voltage, $V(t)$, and the response current, $I(t)$:

$$Z = \frac{V(t)}{I(t)} \tag{1}$$

For harmonic excitation

$$V(t) = V_0 e^{j\omega t} \tag{2}$$

where ω is the circular frequency of the applied voltage (expressed in rad/second), V_0 is the amplitude and j is the unit imaginary number. The response signal $I(t)$ may be expressed as

$$I(t) = I_0 e^{j(\omega t - \phi)} \tag{3}$$

where I_0 is the amplitude of the response signal and ϕ is the phase shift. Eq. 1 then yields

$$Z = Z_0 e^{j\phi} \tag{4}$$

where Z_0 is the magnitude and ϕ is the phase angle of the impedance. The real part of Z ($Z_0 \cos\phi$) represents resistive behavior, while the imaginary part ($Z_0 \sin\phi$) represents capacitive behavior.

1.1.2 *EIS and equivalent circuit analysis*

In EIS, an AC voltage is applied between the sample and reference electrodes. The complex impedance spectrum is then measured as a function of frequency. Two methods of analyzing the impedance spectra are common. The first method is to simply compare the raw spectra. The impedance spectrum can be plotted in different ways. The conventional presentations are the Bode magnitude and phase plot (Figure 4), Nyquist plot (Figure 6), and real and imaginary impedance plots. The magnitude of impedance, phase angle, real impedance or imaginary impedance are compared over the entire frequency range or over specific frequency ranges. The second method is to analyze the impedance spectra by using a lumped parameter equivalent circuit model. In this method, the parameters of an electrical circuit which has a theoretical impedance similar to that of the measured impedance are estimated, and spectra are compared based on the differences in the estimated parameters. The equivalent circuit used in this research is shown in Figure 1. The circuit consists of a loop that is composed of a resistance, capacitance and a constant phase element (CPE), and two simple resistor/capacitor circuits in series. Different equivalent circuits can be used to approximate a measured impedance spectrum, and some experience is required to select an appropriate circuit.

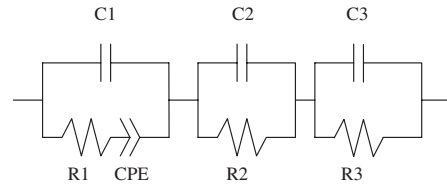

Figure 1. Equivalent circuit configuration.

The impedance of a resistor, R, is $Z_R = R$ and is real-valued. The impedance of a capacitor, C, is purely imaginary and is $Z_C = 1/(j\omega C)$. The constant phase element (CPE) is often used in equivalent circuits to represent distributed properties. The impedance of the CPE is given by

$$Z_{CPE} = A(j\omega)^{-\alpha} \tag{5}$$

when $\alpha = 1$ (maximum value), the CPE is equivalent to a capacitor with $A = 1/C$, and when $\alpha = 0$ (minimum value), the CPE is equivalent to a resistor with $A = R$.

Figure 2 shows the charge transfer process in a CFRP-strengthened reinforced concrete beam with the rebar and the CFRP used as electrodes. Ions in the electrolyte (concrete pore fluid) approach the electrodes up to the outer surface of the so-called electrical double layer. Charge transfer between ions and an electrode involves long-range electrostatic forces, so that their interaction is essentially independent of the chemical properties of ions. Charge transfer through the electrolyte occurs by the diffusion of ions. At low excitation frequencies, the impedance to current flow is controlled by the rate of diffusion, while at

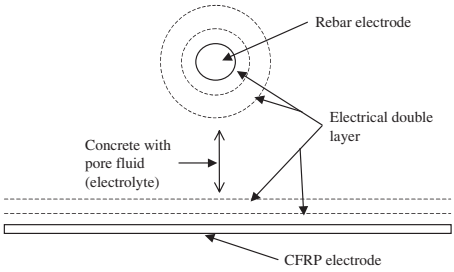

Figure 2. Charge transfer mechanism.

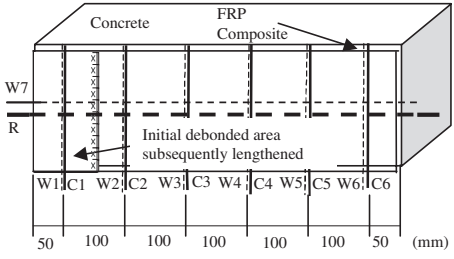

Figure 3. Sensor arrangement.

high frequencies, the impedance is controlled by the kinetics of the charge transfer processes at the electrode/electrolyte interface. It is hypothesized that the two loops containing a resistance and capacitance in the equivalent circuit represent the double layer effects and the loop with the CPE element represents the body of concrete (electrolyte).

2 EXPERIMENTAL SETUP AND PROCEDURES

The study on detection of CFRP debonding was conducted with 150 mm × 150 mm × 600 mm reinforced concrete specimens with chloride (11.0 kg NaCl per cubic meter of concrete). Each specimen was prepared with an initial 100 mm long crack by using a teflon insert. To propagate the interfacial crack between the CFRP layer and the concrete substrate, a wedge (sharpened saw blade) was driven with a hammer. The wedge test was conducted in a refrigerator and in the ambient condition. The refrigerator provided a stable temperature of about 6°C and a stable relative humidity of about 35%. The ambient condition represented a temperature of about 22°C and a relative humidity that varied from 30% to 60%. The sensor (electrode) arrangement is shown in Figure 3. The C_i sensors consisted of copper tape with conductive adhesive mounted directly on the outside surface of the CFRP.

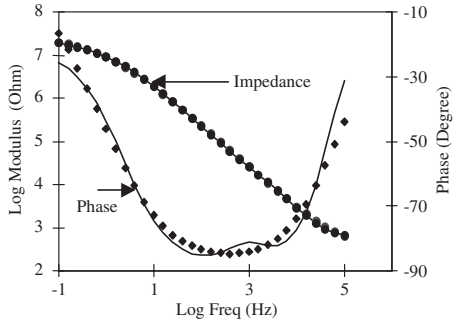

Figure 4. Measured (dots) and fitted (lines) impedance spectra–rebar to external sensor.

The W_i sensors consisted of stainless steel wire set into grooves on the concrete specimen before the CFRP was bonded. R represents a reinforcing bar (rebar).

Different sensor combinations were used to produce impedance spectra. Combinations of internal sensors (W_i) to external sensors (C_i), rebar (R) to external sensors, and rebar to internal sensors were used to produce the raw impedance spectra at different crack states. The impedance spectra were obtained using a commercial potentiostat and software manufactured by GAMRY Instruments, Inc. Thirty-one impedance measurements spanning the frequency range from 0.1 Hz to 100 kHz were taken to construct each spectrum. Once the raw impedance data was obtained, equivalent circuit analysis was performed. This analysis adjusts the parameters of the circuit shown in Figure 1 such that the impedance of the circuit closely matches the data. Equivalent circuit analysis was performed using computer software provided by GAMRY Instruments. Typical impedance measurements from the rebar to the external sensor and the impedance of the equivalent circuit are shown in Figure 4.

3 EXPERIMENTAL RESULTS

3.1 *Parameters of the equivalent circuit*

The elements of the equivalent circuit in Figure 1 control the behavior of the fitted impedance spectrum over different frequency ranges. The C1, R1 and CPE parameters control the fitted impedance spectrum in the low to mid-frequency region (0.1–100 Hz). The C2, C3, R2 and R3 parameters control the fitted impedance spectrum in the mid- to high-frequency region (100–100,000 Hz).

The impedance measurements shown in Figure 4 are characteristic of an electrochemical system governed by mixed kinetic and diffusion control. Moisture in the concrete specimen serves as an electrolytic medium

for transporting charges between sensors. At low excitation frequencies, the movement of ions (diffusion) dominates the current flow in the concrete specimen, and factors such as different moisture levels, temperature, chemical compositions, and crack networks within the concrete affect the rate of ion transport. Subsequently, the C1, R1 and CPE parameters in the equivalent circuit are sensitive to the humidity, temperature, chloride content, and cracking caused by freeze-thaw cycles, wet-dry cycles and corrosion at the time of measurement. At high frequencies the impedance is governed by the kinetics of the charge transfer processes at the electrode-electrolyte interface which is not very sensitive to the above factors. As a result, the C2 and C3 parameters are less sensitive to changes in environmental conditions because they reflect the behavior of the impedance spectrum in the mid- to high-frequency region.

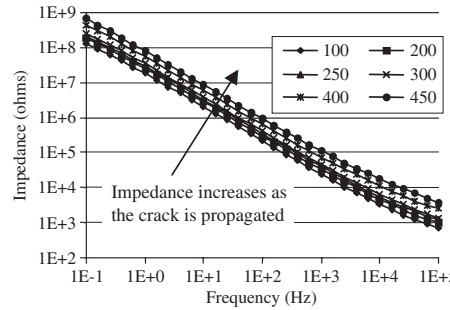

Figure 5. Bode magnitude plot of typical impedance spectra measured from the rebar to copper tape for wedge test in controlled environment (legend gives the debonded length in mm).

3.2 *Effect of CFRP debonding*

Investigation of the debonding of CFRP reinforcement from concrete was conducted in the controlled and ambient conditions. Impedance measurements were made from the internal sensors (stainless steel wire or reinforcing bar) to each of the copper tape sensors, and equivalent circuit analysis was performed for all impedance measurements. Impedance measurements taken from the reinforcing bar (R) and stainless steel wire sensors (W_i) to all of the copper tape sensors (C_i) were essentially identical. This observation implies that the highly conductive CFRP sheet serves as a single continuous electrode. As a result, each equivalent circuit parameter value corresponding to the impedance measurement from a given internal sensor to each external copper tape sensor was averaged at each crack state.

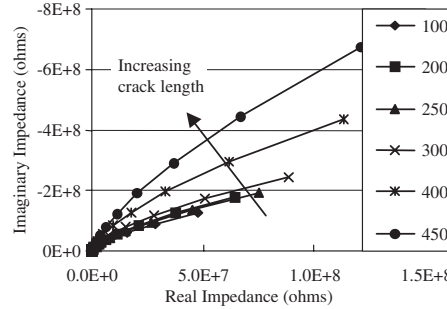

Figure 6. Nyquist plot of typical impedance spectra measured from the rebar to copper tape for wedge test in controlled environment (legend gives the debonded length in mm).

3.2.1 *Assessing the global state of the bond*

The effect of CFRP debonding was studied using impedance measurements from the rebar (R) to the copper tape sensors (C_i), and from the internal wire sensors (W_i) to the copper tape sensors. Impedances were measured for each concrete specimen at the initial crack state (100 mm crack length) and at extended crack states. Tests were performed both in a refrigerator as well as in the ambient condition. The debonding was best observed with impedance measurements from the rebar to the copper tape sensors. Typical impedance spectra for tests in the controlled environment are shown in Figure 5 (Bode magnitude plot) and Figure 6 (Nyquist plot). In the Nyquist plot, data points on the left correspond to measurements at high frequencies and those on the right correspond to measurements at low frequencies.

Figure 5 shows that the effect of debonding is reflected over the entire frequency range. The magnitude of impedance increases over the entire frequency range as the debonded length is increased. Figure 6 also shows that the radius of the arc in the Nyquist plot increases with increasing debonded length.

Figures 7 and 8 show Bode and Nyquist plots, respectively, of the impedance spectra corresponding to measurements made on a specimen in ambient conditions. For clarity, only the low- to mid-frequency range is shown in Figure 7. Note that compared to the impedances measured in the controlled environment (refrigerator), those measured in the ambient environment are higher because of the higher temperature and humidity levels. In the low-frequency range the impedance behaves somewhat erratically and increases when the debonded length was increased from 100 to 150 mm, but then decreases when the debonded length was increased further from 150 to 250 mm. This was due to increasing humidity in the

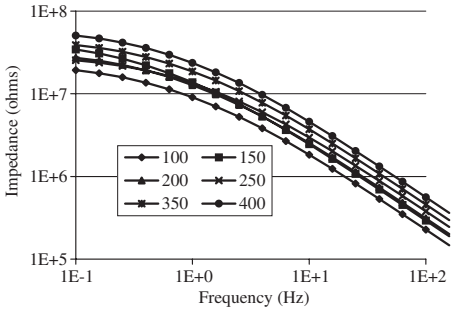

Figure 7. Bode magnitude plot of typical impedance spectra measured from the rebar to copper tape for wedge test in ambient condition (legend gives the debonded length in mm).

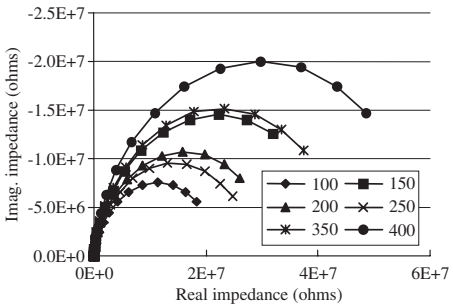

Figure 8. Nyquist plot of typical impedance spectra measured from the rebar to copper tape for wedge test in ambient condition (legend gives the debonded length in mm).

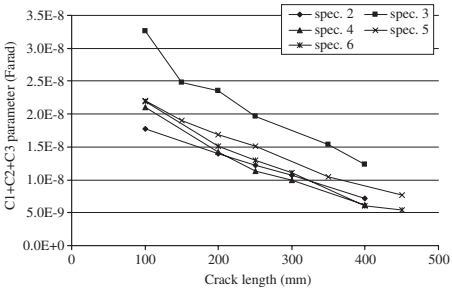

Figure 9. Variation of the C1 + C2 + C3 parameter from equivalent circuit analysis for wedge test from the rebar to external sensors.

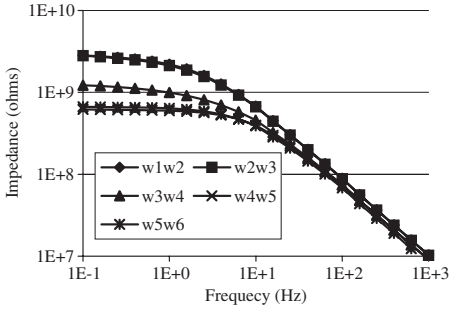

Figure 10. Bode magnitude plot of impedance spectra measured between pairs of internal sensors in ambient condition when crack tip was between W3 and W4 (legend shows the internal sensors used).

ambient environment. However, in the mid- to high-frequency range the measured impedance increased with increasing debonded length.

Some of the circuit parameters from the equivalent circuit analysis correlate well with the debonded length. Figure 9 shows that the sum of the C1, C2 and C3 parameters from the equivalent circuit analysis for five of the six specimens tested. Specimens 2, 4 and 6 were tested in the controlled environment and specimens 3 and 5 were tested in the ambient condition. Results for specimen 1 are not shown because it was damaged. The C1 + C2 + C3 value correlates especially well with the debonded length and was found to be relatively insensitive to temperature and humidity variations.

3.2.2 *Detecting the location of debonded regions*

While impedance measurements between the rebar and external sensors provide a global assessment of the debonded area, they are incapable of revealing the location of debonded regions. However, impedance measurements between pairs of internal wire sensors (W_i) can be used to detect debonded regions. Measurements were made between adjacent sensors (such as W1 and W2, W2 and W3 and so on). Measurement between sensors in the debonded region produce higher impedance magnitudes, while those between sensors in the bonded region produces lower impedance magnitudes.

Impedance spectra for measurements taken with pairs of internal sensors are shown in Figure 10 when the crack tip was located between the W3 and W4 sensors. The impedance magnitude is much lower when both sensors used are in the bonded region (W4W5 and W5W6), than when both sensors are in the debonded region (W1W2 and W2W3). When one sensor is in the bonded region and the other is in the debonded region (W3W4), the impedance magnitude is in between those for the other two cases. It is postulated that the reason for this distinctive difference in the magnitude of impedance is the path of current flow in each case. When the impedance measurement

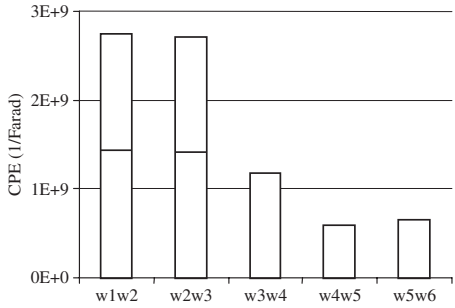

Figure 11. Variation of the CPE parameter from equivalent circuit analysis for pairs of internal sensors in ambient condition when crack tip was between W3 and W4 (legend shows the internal sensors used).

is made between sensors in the debonded area, current must flow through the concrete, and the impedance is high. On the other hand, when measurements are made between sensors in the bonded area, current probably flows predominantly through the highly conductive CFRP sheet, with charge transfer between the internal sensors and the CFRP sheet, resulting in lower impedances. This hypothesis is confirmed later using finite element simulations.

While raw impedance measurements are sufficient to detect debonded regions, equivalent circuit analysis also can be used. The effect of debonding on the impedances measured between internal sensors is best observed with the CPE parameter. The variation of the CPE parameter is shown in Figure 11 when the crack tip was between the W3 and W4 sensors. The magnitude of the CPE parameter when the two sensors used are in the debonded region is about two orders of magnitude higher than that when both sensors are in the bonded region.

3.2.3 *Environmental and size effects*

Concrete structures rehabilitated with CFRP can be subjected to a variety of short- and long-term environmental conditions. Short-term environmental conditions such as temperature, humidity, and chloride ion concentration from deicing agents that exist a few days before impedance measurements are taken change the environment within the concrete and influence the measured impedances. Long-term environmental conditions such as freeze-thaw cycles, wet-dry cycles, and corrosion also influence the impedance measurements because they change the ion diffusion within concrete by extending crack networks. The variability in measured impedance due to short- and long-term environmental effects must be understood if the measurements are to be used to detect debonding of CFRP from concrete. Size effects between laboratory-scale specimens and real structures also must be investigated.

Hong and Harichandran (2004) studied the effect of environmental conditions and size using small 150 mm × 150 mm × 300 mm concrete specimens and a large 457 mm × 610 mm × 2.44 m concrete beam. They found that the C1 + C2 + C3 value could be used to detect the global debonded area and pairs of internal sensors could be used to detect debonded locations irrespective of environmental conditions.

4 FINITE ELEMENT SIMULATION

For the optimal and effective use of EIS-based sensors it is important to have available a computational model for studying the underlying charge transfer processes. Such a model can be used to design the sensor system for different structural configurations, and be used as a tool to probe the diagnosis provided by measurements. The conductivity distribution of the specimen affects the current density distribution in the interior as well as potentials at the surface when current is injected through the electrodes. Given the surface potential measurements, the potential and current distribution within the specimen can be calculated by solving the associated Laplace's equation using finite element (FE) analysis.

For the static case where a DC current is injected into the electrodes, the governing equation can be derived starting from the property of divergence free current density $\boldsymbol{J}$, i.e.,

$$\nabla \cdot \boldsymbol{J} = 0 \tag{6}$$

where

$$\boldsymbol{J} = \sigma \boldsymbol{E} \tag{7}$$

$$\boldsymbol{E} = -\nabla V \tag{8}$$

σ = conductivity, $\boldsymbol{E}$ = electric field intensity, and V = electric scalar potential. Substituting (7) and (8) into (6), yields the governing Laplace's equation (Udpa 1986)

$$\nabla \cdot \sigma \nabla V = 0 \tag{9}$$

The Ritz variational method (Zienkiewicz 1977) is used to solve (9) for the potential. The energy functional is

$$F = \sum_{e=1}^{M} F^e \tag{10}$$

with the elemental energy functional F^e given by

$$F^e = \frac{1}{2} \int_{\Omega^e} V^e \nabla \cdot \sigma^e \nabla V^e \, d\Omega \tag{11}$$

For the two-dimensional case, (11) reduces to

$$F^e = \frac{1}{2}\int_{S^e} \sigma^e \left[\left(\frac{\partial V^e}{\partial x} \right)^2 + \left(\frac{\partial V^e}{\partial y} \right)^2 \right] dS \tag{12}$$

In this formulation, σ^e is assumed to be constant within each element. In (10)–(12), the superscript e denotes elemental variables, M is the total number of elements in the solution domain, Ω^e is the eth subdomain in 3-D, and S^e is the eth subdomain in 2-D. V^e is expanded in terms of the nodal values at the three vertices of the eth triangular finite element and the corresponding shape functions, i.e.,

$$V^e = \sum_{j=1}^{3} N_j^e(x,y) V_j^e \tag{13}$$

Substituting the expansion (13) into the elemental energy functional (12) and minimizing the functional with respect to the nodal potentials, yields the elemental system of equations:

$$[K^e]\{V^e\} = \{b^e\} \tag{14}$$

in which the entries of the matrix $[K^e]$ are given by

$$K_{ij}^e = \int_{S^e} \sigma^e \left(\frac{\partial N_i^e}{\partial x}\frac{\partial N_j^e}{\partial x} + \frac{\partial N_i^e}{\partial y}\frac{\partial N_j^e}{\partial y} \right) dS \tag{15}$$

$b_i^e = 0$, $i,j = 1, 2, 3$, and $\{V^e\}$ is the vector of unknowns. The elemental system of equations are assembled to create the global system of equations

$$[K]\{V\} = \{b\} \tag{16}$$

Equation (16) is solved for unique values of $\{V^e\}$ by imposing appropriate boundary conditions (Sharma et al. 1999).

The measured impedance Z can be calculated using energy considerations. The total energy in the electromagnetic field is the sum of dissipated energy (resistance) and stored energy (reactance) (Ida 1985):

$$\frac{U^2}{Z} = \int_{\Omega} \sigma E^2 d\Omega \tag{17}$$

where U is the voltage difference of the electrodes, Z is the impedance to be calculated, Ω is the solution domain, and E is the electric field. E can be computed using (8).

The above formulation can be readily modified for simulating EIS tests in which the excitation is harmonic.

Preliminary results from FE simulations are presented for DC current injection into the simple 2-D specimen shown in Figure 12. A CFRP sheet is adhered to the bottom of a concrete block that is 600-mm-long and 150-mm-high. The CFRP is debonded from the left side to its center. Internal electrodes are placed in the concrete above the CFRP as shown. In the simulation presented, the Dirichlet boundary conditions are imposed on the electrodes by assigning voltages of 1 V to the anode and −1 V to the cathode, respectively. The conductivity of the concrete and the CFRP are assumed to be 1 S/m and 100 S/m, respectively. In order to avoid a singular system matrix, a small value of conductivity rather than zero conductivity is assigned to the debonded area.

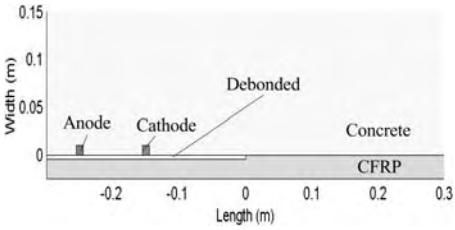

Figure 12. Geometry of concrete specimen with CFRP layer.

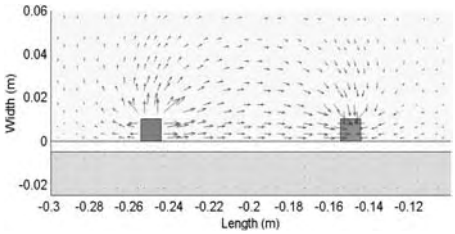

Figure 13. Current field with both sensors in the debonded region.

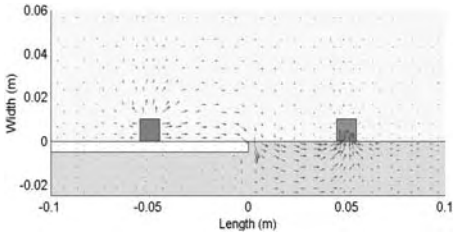

Figure 14. Current field with one sensor in the debonded region and the other in the bonded region.

The model was used to predicted current density distributions. Figures 13–15 show illustrations of the current field and its magnitude in the vicinity of the electrodes for three different cases. The size of

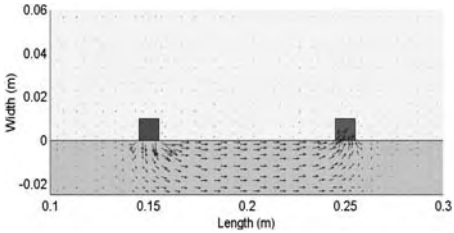

Figure 15. Current field with both sensors in the bonded region.

the arrows representing the field is proportional to the magnitude of the current in each illustration. However, the relative magnitudes are different from one illustration to another. The illustrations clearly indicate that:

1. Case 1, Figure 13: When both electrodes are in the debonded region, current flows primarily through the concrete.
2. Case 2, Figure 14: When one electrode is in the debonded region and the other is in the bonded region, the current flows first through the concrete and then through the CFRP.
3. Case 3, Figure 15: When both electrodes are in the bonded region, the current flows primarily through the CFRP.

The impedance would be the highest for Case 1, lowest for Case 3, and intermediate for Case 2. This confirms the experimental results shown in Figure 10 at the lowest frequency, where the excitation is closest to the DC case assumed in the simulations.

5 CONCLUSIONS

Electrochemical impedance spectroscopy (EIS) is used for nondestructive evaluation (NDE) of bond deterioration in concrete beams strengthened with carbon fiber reinforced polymer (CFRP) sheets. Sensor elements (electrodes) consisted of: (a) copper tape with a conductive adhesive applied to the outside of the CFRP; (b) stainless steel wire placed in grooves on the bottom face of the concrete; and (c) reinforcing bars. Impedance measurements were taken between pairs of sensors using a potentiostat. An equivalent circuit was fitted to each measured impedance spectrum and the circuit parameters were estimated. Variations in the measured impedance spectra and the equivalent circuit parameters due to debonding of the CFRP sheet was studied in a controlled environment (constant temperature and humidity) and in an ambient condition (constant temperature, but fluctuating humidity).

Impedance measurements taken between the rebar and the external copper tape sensors can be used to assess the total debonded area (global state). The sum of the capacitance parameters in the equivalent circuit correlates well with the debonded area and is not sensitive to environmental factors. Impedance measurements taken between pairs of internal wire sensors reveal the location of debonded regions.

The use of EIS-based sensors is an inexpensive technique for effective NDE of concrete structures strengthened with CFRP sheets.

ACKNOWLEDGEMENTS AND DISCLAIMER

This research was partially sponsored by the Michigan Department of Transportation (MDOT). The project manager was Roger D. Till.

MDOT assumes no liability for the contents of this paper and use thereof. The contents of this paper reflect the views and opinions of the authors who are responsible for the accuracy of the information presented herein. The contents do not necessarily reflect the views of MDOT and do not constitute a department standard, specification or regulation.

REFERENCES

Bard, A.J. & Faulkner, L.R. 1980. *Electrochemical methods: fundamentals and application*. New York: Wiley-Interscience Publication.

Buyukozturk, O. & Hearing, B. 1998. Failure behavior of precracked concrete beams retrofitted with FRP. *Journal of composites for construction*: 138–144.

Davis, G.D., Dacres, C.M. & Krebs, L.A. 1999. In-Situ sensor to detect moisture intrusion and degradation of coatings, composites, and adhesive bonds. *Proc. tri-services conf. on corrosion*, Myrtle Beach, South Carolina.

Davis, G.D., Krebs, L.A., Drzal, L.T., Rich, M.J. & Askeland, P. 2000. Electrochemical sensors for nondestructive evaluation of adhesive bonds, *J. Adhes*. 72: 335–358.

Davis, G.D., Rich, M.J., Harichandran, R.S., Drzal, L.T., Mase, T. & Al-Ostaz, A. 2003. Development of electrochemical impedance sensor to monitor delamination and moisture uptake in CFRP-reinforced concrete structures. *Proc. 81st annual meeting of the Transportation Research Board (CD-ROM)*. Washington, DC. Paper No. 03-2392.

Harichandran, R.S., Hong, S., Al-Ostaz, A. & Davis, G.D. 2003. EIS-based NDE of bond integrity in concrete bridges strengthened with CFRP. *Proc. 1st international conf. on structural health monitoring and intelligent infrastructure*. Tokyo, Japan, 1183–1190.

Hong, S. & Harichandran, R.S. 2004. Nondestructive evaluation of CFRP/concrete bond in beams using electrochemical impedance spectroscopy. *Proc. 82nd annual meeting of the Transportation Research Board (CD-ROM)*. Washington, DC. Paper No. 04-3123.

Ida, N. & Lord, W. 1985. A finite element model for three dimensional eddy current NDT calculations. *IEEE transactions on magnetics*. MAG-21, 6: 2635–2643.

Karbhari, V.M. & Zhao, L. 2000. Use of composites for 21st century civil infrastructure. *Computer method in applied mechanics and engineering*. 185: 433–454.

Macdonald, J.R. 1987. *Impedance spectroscopy: emphasizing solid materials and systems*. New York: Wiley-Interscience Publication.

Nguyen, D.M., Chan, T.K. & Cheong, H.K. 2001. Brittle failure and bond development length of CFRP-concrete beams. *J. composites for construction*. February: 12–17.

Rahimi, H. & Hutchinson, A. 2001. Concrete beams strengthened with externally bonded FRP plates. *J. composites for construction.* February: 44–56.

Scully, J. & Kendig, M. 1989. Basic aspects of the application of electrochemical impedance for the life prediction of organic coatings on metals. *Proc. Corrosion 89*, Paper 32, NACE.

Sharma, S., Sun, Y. & Udpa, L. 1999. Finite element modeling for simulating remote field flaw detection in aircraft frame. *IEEE transactions on magnetics*, May: 1750–1753.

Udpa, L. 1986. Imaging of electromagnetic NDE phenomena, PhD dissertation, Colorado State University.

Zienkiewicz, O.C. 1977. *The finite element method in engineering*. 3rd edition. London: McGraw-Hill Book Co.

FRP Composites in Civil Engineering – CICE 2004 – Seracino (ed)

Strain monitoring techniques for FRP laminates

G.A. Sarazin & J.P. Newhook
Dalhousie University, Halifax, Nova Scotia, Canada

ABSTRACT: Reinforced concrete beams that do not meet the required ultimate load carrying capacity are being strengthened using carbon fibre reinforced polymer (CFRP) laminates. Debonding of the laminate at or near the concrete/FRP interface has been identified as a possible flexural mode of failure and could be instigated by poor installation, poor adhesive durability, or the presence of concrete cracking. Therefore, debonding at service load levels is a concern for these systems. This paper presents several methods to detect debonding damage using strain monitoring techniques. Theoretical and experimental work was conducted and the strain results were found to be sensitive to the presence of induced debonded zones, although the presence of noise in the low level tests made positive damage identification difficult.

1 INTRODUCTION

The use of external fibre reinforced polymer (FRP) laminates to strengthen existing structures is steadily increasing around the globe. Substantial research and testing has been conducted on concrete beams strengthened in flexure with FRP laminates. The majority of this work, however, has focussed mainly on the issue of behaviour and failure at ultimate. This was necessary to ensure the development of proper design criteria and for safety in field projects.

The engineering community is now looking to early field applications using these strengthening techniques as test beds for demonstrating the feasibility and reliability of this approach. As such, many field strengthened beams have been instrumented for the purposes of verifying performance of individual laminates and repair schemes. A common approach is to apply a select number of strain gauges and monitor the strain levels in the laminates under specific load testing or under normal traffic loading. Normal levels of strain response are taken as verification of the proper functioning of the laminate.

This paper discusses the issue of strain based monitoring of FRP laminates under field conditions from the perspective of developing a performance or damage index. Specifically, the paper examines the service level performance of concrete beams strengthened for flexure with carbon FRP. The particular performance issue is partial debonding of the laminate from the concrete substrate. Laboratory beams were constructed and tested under low strain level, typical of those observed in field project monitoring. Each beam was strengthened by a carbon FRP laminate; but, specific debonding zones were introduced in some of the beams. A series of discrete electronic strain gauges were bonded to the laminates and monitored during testing. Finite element models of the beams were developed and calibrated against the experimental beams. The results were then used to examine ideas for a damage/performance index which could be used in field projects.

2 BACKGROUND

Several design guidelines and codes have been developed including: the American Concrete Institute's (ACI) "Externally bonded FRP systems for strengthening concrete structures" (2001), ISIS Canada's "Strengthening Reinforced Concrete Structures with Externally-Bonded Fibre Reinforced Polymers" (2001) and the Canadian Standards Association's "CSA Standard S806-02, Design and Construction of Building Components with Fibre-Reinforced Polymers" (2002). These documents describe methods to design strengthening for beams accounting for the four flexural modes of failure: concrete crushing, steel yielding followed by concrete crushing, steel yielding followed by FRP rupture, and debonding of the laminate at or near the FRP/concrete interface. Failure of the strengthened beam by debonding of the FRP reinforcement is considered in some codes (ISIS Canada) by assuming that it can be avoided by using sufficient anchorages or by allowing a sufficient development length. Other codes (CSA) specify that two separate modes of debonding failure must be considered: shear/tension failure of the concrete substrate at the FRP cutoff point (anchorage failure), and debonding of adhesive bond line due to vertical section translations

from cracking. There are no recommendations on how these debonding failures should be considered except to suggest that transverse anchorages using FRP sheets or other proven anchorages methods may be used.

Failure at the adhesive/concrete/FRP laminate interface has been examined by numerous authors and a few of the applicable papers are discussed here. Leung (2001) indicated that delamination is favoured by large member size, low adhesive thickness, low plate stiffness, and a small contact area between the plate and adhesive. Karbhari (2001) suggested that substantial research is required to examine the durability of FRP strengthening systems in terms of moisture-rich zones at the concreteadhesive/resin interface since previous research conducted by the author has shown that delamination or separation through freeze-thaw cycling or dramatic temperature cycling can occur. The influence of a Poisson ratio mismatch between the concrete and the FRP on the delamination behaviour was conducted by Taheri et al. (2002). It was found that the higher the Poisson ratio mismatch between the concrete and the FRP was, the earlier the likelihood of the onset of FRP delamination. Sebastian (2001) suggested that although much research effort to date has been invested on end peel, in practice midspan debond may be critical in many single span simply supported FRP-plated concrete bridges.

The purpose of the research reported in this paper was to develop a strain based monitoring scheme which can be implemented into a structural health monitoring system. The objective of such a system is to identify the existence, or preferably lack of existence, of debonding in the laminate. This requires a thorough understanding of the damaged response of the structure and a calibrated theoretical model.

3 EXPERIMENTAL PROGRAM

The experimental program developed for this purpose consisted of 12 CFRP strengthened concrete beams (Sarazin, 2004), 10 with induced debonded zones. The beams were based on a recent field project, the Sainte-Emelie-de-l'Energie Bridge (Labossiere et al. 2000). Only 3 types of beams (6 beams) will be discussed in this paper: the two control beams, and the four beams with debonded zones located at quarterspan (debonded length of 20% and 30% of the laminate length). The quarterspan beams are presented because it was found that the axial strain in the laminate was more sensistive to debonding damage when the debonded zones were located within high shear loading zones.

3.1 *Description of beams*

Typical beam details are shown in Figures 1 and 2. The control beams were designated Control 1 and 2;

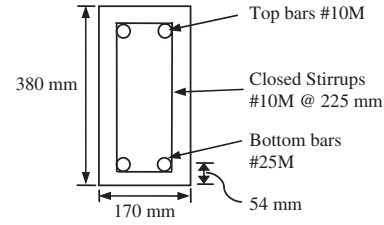

Figure 1. Cross section of test beams.

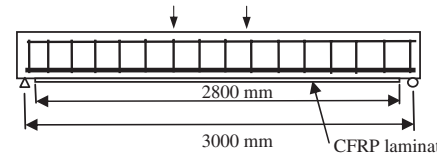

Figure 2. Elevation view of test beams.

Table 1. Material properties.

Material	E (MPa)	ν	G (MPa)	f* (MPa)
Concrete	30,000	0.2	12,500	60
Steel	200,000	0.3	77,000	420
CFRP	217,000	0.3	83,460	2300
Adhesive (bonded)	4500		2900	
Adhesive (unbonded)	0.05	0.032		

* ultimate strength for concrete and CFRP; yield strength for steel.

the beams with a 20% debonded zone of 560 mm length centered at the quarterspan were designated Q20; and the beams with a 30% debonded zone of 840 mm length centered at the quarterspan were designated Q30. After curing, the bottom soffit of each beam was sandblasted to create a proper surface for bonding.

The structural strengthening system consisted of a pultruded uniaxial CFRP laminate attached to the concrete surface using an epoxy adhesive. In order to create the debonded zones, a layer of polyurethane plastic was attached to the laminate and the adhesive was spread over top of this protective layer. This created a virtually frictionless surface between the laminate and the adhesive, preventing the transfer of shear forces from the concrete into the laminate. The material properties determined through testing are given in Table 1.

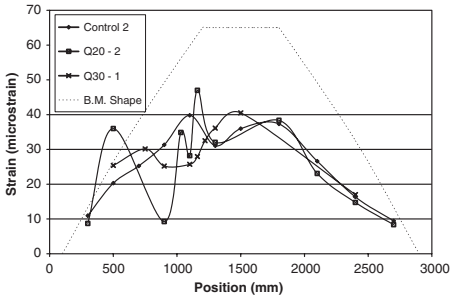

Figure 3. 10 kN strain distributions.

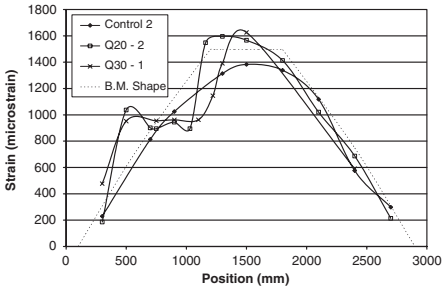

Figure 4. 150 kN strain distributions.

3.2 *Instrumentation*

For the assessment of the damage detection techniques, information was collected about the applied load, midspan deflection, and strain profile along the bottom of the CFRP laminate. To determine the strain profile along the length of the laminate, several strain gauges were bonded to the bottom of the laminate after it had been bonded to the beam. The gauges were distributed along the length of the laminate in order to assess strain response both within and outside of the induced debonded zone. Several gauges were placed in a close proximity to the edge of the debonded zone to examine the strain behaviour at these "transition" zones.

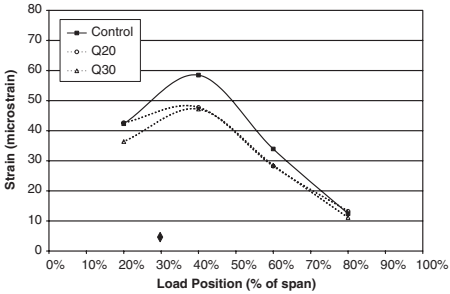

Figure 5. LPIP values at 900 mm.

3.3 *Testing*

Each beam was loaded in the four point load set-up shown in Figure 2 both before and after bonding of the laminate. The load level was initially limited to 10 kN to produce service level strain values consistent with those observed in field monitoring (Labossiere et al. 2000). The strain values in the control beams and debonded beams were compared prior to concrete cracking. The beam loads were cycled to 80 kN and then 160 kN and the strain profiles compared after concrete cracking. This was believed to be the upper limit of cracked service state response. The beams were then loaded to failure.

3.4 *Results of experimental tests*

Initially, the stiffness of the beams was examined as a possible damage indicator. This method was abandoned as the theoretical increase due to the presence of the laminate was small compared to the experimental variation from beam to beam. The strain distributions for beams Control 2, Q20-2, and Q30-1 at 10 kN and at 150 kN load levels are shown in Figures 3 and 4, respectively. The shape of the bending moment diagram (B.M. Shape) is also shown for reference.

The influence of noise in the system significantly affected the strain distributions at the low load levels (10 kN), while the distributions at 150 kN were not similarly affected. The location of the debonded zones, which is unclear in the 10 kN tests, is clearly visible as the flat portion of the Q20 and Q30 curves in the 150 kN tests.

A further set of tests were conducted to examine how the position of the load would influence the strain pattern. A load of 10 kN was applied at 1/5, 2/5, 3/5 and 4/5 of the span. These tests will be referred to as the Load Position Influence Pattern (LPIP) tests. The LPIP values for the strain gauge located at 900 mm are shown in Figure 5. The location of the strain gauge is marked by a black diamond.

The magnitude of the strain readings for the quarterspan debonded beams is lower than the control beam indicating the presence of damage. This will be further examined as a damage indicator.

4 FINITE ELEMENT MODEL

Strain is a local phenomena but it is affected by the global characteristics of the structure and load pattern.

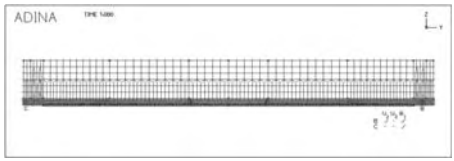

Figure 6. Finite element model of beam.

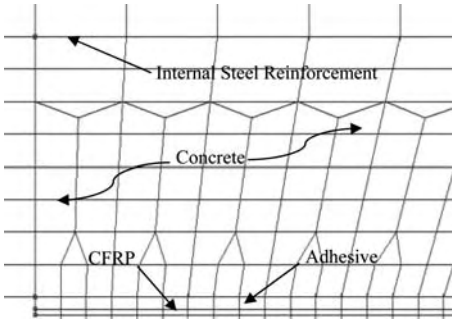

Figure 7. Close-up of finite element model mesh.

Any strain sensing damage detection technique will therefore have to be structure-specific and a theoretical modelling technique is required. The 2D finite element model shown in Figure 6 was created based on the laboratory test specimens using plane stress elements for the concrete, adhesive and CFRP, while the internal steel reinforcement was modelled as a truss element. A close-up of a section of the mesh showing all key elements of the model is given in Figure 7. The model was created using the material properties listed in Table 1.

4.1 *Verification of FEM predictions*

Figures 8 and 9 show both the experimental and theoretical model strain distributions of the control beam and the 30% quarterspan debond beam, respectively, for an applied load of 10 kN.

Although there is some fluctuation in the strain readings, the finite element model does predict the strain response of the control beams very well. As discussed above, the variation is mostly attributable to the effects of noise in the low values of experimental strain.

For beam Q30-1, the FEM again predicts the general pattern of strain response. The influence of the debonded zone on the shape of the strain distribution is clearly visible for both the FEM and the experimental results. A large amount of noise in the beam Q30-2 strain results prevented any meaningful comparison

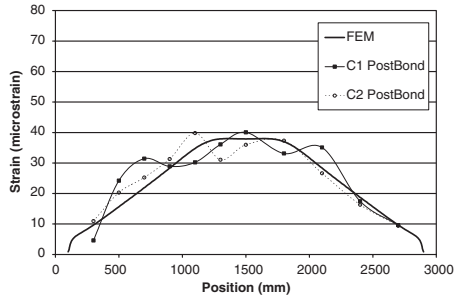

Figure 8. Control beam strain distributions.

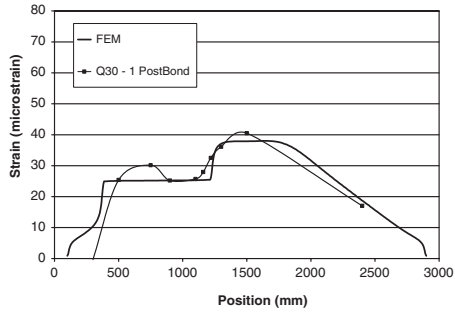

Figure 9. Q30 beam strain distributions.

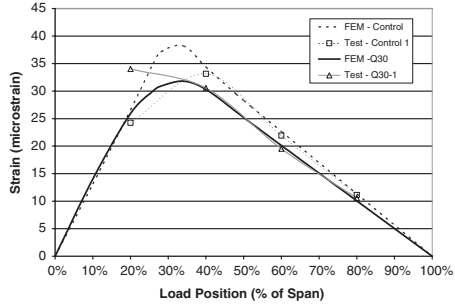

Figure 10. Test and F.E. values of LPIP at 900 mm.

and it is omitted from the figure. It is also noted that the shape of the experimental strain profile, shown at the 150 kN load level (Figure 4), which is less sensitive to the noise effects, agrees very well with the F.E.M. predicted shape.

Figure 10 shows the LPIP values for both the experimental and F.E. results of the control beam and the 30% quarterspan debond beam at 900 mm.

Except for the readings acquired when the load was located at 1/5 of the span, the experimental results closely match the finite element model results.

5 PROPOSED DAMAGE INDICATORS

Once the sensitivity of the strain profile to debonding was identified and the ability of the F.E.M. to predict this response verified, the F.E.M. was used to examine the issue of debonding damage indicators which may be used in a field monitoring program. Examples of several possible damage indicators that can be used for Structural Health Monitoring are presented. Generally SHM systems relying on strain readings require an exact repeat of the loading using periodic load tests; although the periodic running of a known control vehicle may be possible. Sophisticated weight-in-motion systems could also be utilized along with statistical analysis and neural networks to effect real time monitoring under operating conditions.

In either system, monitoring is usually based on the idea of tracking trends in behaviour for the same beam, rather than different beams as used in the experimental study. It is assumed that the laminate is fully bonded at its initial condition and that any change in strain response with time could be correlated against a proposed index. Each index idea is presented in terms of the methodology which would be followed. It is assumed that an appropriate F.E. model would be developed for each case.

5.1 *Method I – complete profile comparison*

Strain profiles of the initial condition of the structure are generated for the load in a specific position. A parametric study is then carried out using the finite element model to generate profiles for various damage situations for a predetermined "critical" debond length (e.g. 20% Quarter etc.). A large family of curves, such as the one shown in Figure 11, are produced for different debond locations and load positions. The load test would be conducted periodically and its results compared to the family of curves. An expert system could also be used to automate the identification of damage process. This method would be difficult to implement with random loading although the shape of the strain profile is not magnitude sensitive, only load position sensitive.

Alternatively, the system could look for a change in the strain profile and then produce the family of curves based on the change. In this circumstance, a comparison with theory would only need to examine a reduced family of debond damage curves.

5.2 *Method II – LPIP comparison*

The fully bonded structure would be tested to measure the Load Position Influence Pattern (LPIP) for each gauge location as a load truck crossed the bridge (An LPIP is similar to an influence line as it gives the strain value at a specific location as a fixed load moves across the span). This would create a point load at every place along the beam. The finite element model is then used to generate the damaged LPIP for each gauge. A plot is required for each different debond location and magnitude. The area beneath the curve is then related to the level of damage as shown in Figure 12 and Equation 1. Note that the x-axis scale in Figure 12 is not linear in order to highlight the difference in areas in and around the debond zone.

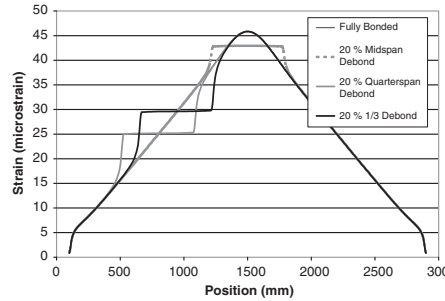

Figure 11. Strain debond profiles for point load located at midspan.

Figure 12. LPIP curves for strain gauge at 900 mm.

$$D.I. = \frac{A_u - A_d}{A_u} \quad (1)$$

This method requires separate damage indicators for each gauge location, but it does have the advantage that it uses several readings instead of one reading to detect damage. This method may be better suited for random load applications and statistical analysis.

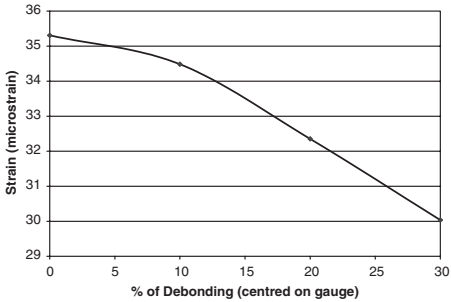

Figure 13. Typical strain vs. debonded length plot (800 mm).

5.3 *Method III – strain gauge magnitude tracking*

This method measures the initial strain magnitude for each gauge when the load is directly over the gauge position. The finite element model then generates a plot of strain magnitude versus debonded length for a debond centred on each gauge. A typical strain vs. debonded length plot is shown in Figure 13. A damage indicator based on the change in the strain at this location can be generated as shown in Equation 2. Periodic load tests could then track the trend in the magnitude of strain. This method is very sensitive to load repeatability. If random loads are being used, the yearly load patterns should have similar statistical distributions and the representative average of the peak values for a vehicle pass for a statistically significant period of time could be used instead of the individual strain reading.

$$D.I. = \frac{\varepsilon_u - \varepsilon_d}{\varepsilon_u} \qquad (2)$$

6 CONCLUSIONS

This paper was an initial step in the determination of suitable damage indicators for use in a structural health monitoring system to detect CFRP laminate debonding damage in the field using strain readings. In experimental tests, the axial strain distribution of the CFRP laminate was found to be sensitive to the presence of the induced debonded zones. However, the level of noise present in the low load level tests made the positive detection of the debonded zones very difficult. The debonded zones were easily detected at load levels of 1/4 and 1/2 of the ultimate load when they were located in a high shear, varying moment region of the beam. It was discovered that only strain gauges within or near to the debonded zone were sensitive to the debonding damage. The work clearly showed the necessity for many strain monitoring points along a laminate.

It was demonstrated that a finite element model could be developed to predict the strain response. This model was used to propose several methods for damage detection. The methods proposed in the paper are generic and would need structure-specific models before implementation. Further modelling would also be required to isolate strain changes due to debonding from other long-term phenomena.

ACKNOWLEDGEMENTS

The authors wish to acknowledge funding support provided by the Natural Sciences and Engineering Research Council of Canada and the ISIS Canada NCE program.

REFERENCES

American Concrete Institute. (2001). *ACI 440.2R Externall-Bonded FRP Systems for Strengthening Concrete Structures*. Farmington Hills, Michigan: American Concrete Institute.

CSA. (2002). *CSA Standard S806-02 Design and Construction of Building Components with Fibre-Reinforced Polymers*. Toronto, Canada: Canadian Standards Association.

ISIS Canada. (2001). *Strengthening Reinforced Concrete Structures with Externally-Bonded Fibre Reinforced Polymers, Design Manual No. 4*. Winnipeg, Canada: ISIS Canada.

Karbhari, V.M. (2001). Materials Considerations in FRP Rehabilitation of Concrete Structures. *ASCE Journal of Materials in Civil Engineering*, 13(2): 90–97.

Labossiere, P., Neale, K.W., Rochette, P., Demers, M., Lamothe, P., Lapierre, P., and Desgagne, G. (2000). Fibre reinforced polymer strengthening of the Sainte-Emelie-del'Energie bridge: design, instrumentation, and field testing. *Canadian Journal of Civil Engineering*, 27: 916–927.

Leung, C.K.Y. (2001). Delamination Failure in Concrete Beams Retrofitted with a Bonded Plate. *ASCE Journal of Materials in Civil Engineering*, 13(2): 106–113.

Sarazin, G.A. (2004). *Detection of Debonding Damage in CFRP Strengthened Concrete Beams*. Master of Applied Science Thesis, Halifax, Canada: Dalhousie University.

Sebastian, W.M. (2001). Significance of Midspan Debonding Failure in FRP-Plated Concrete Beams. *ASCE Journal of Structural Engineering*, 127(7): 792–798.

Taheri, F., Shahin, K., and Widiarsa, I. (2002). On the parameters influencing the performance of reinforced concrete beams strengthened with FRP plates. *Composite Structures*, 58: 217–226.

Materials and products

FRP Composites in Civil Engineering – CICE 2004 – Seracino (ed)
© 2005 Taylor & Francis Group, London, ISBN 90 5809 638 6

Test and analysis of the basic mechanical properties of CFRP sheets

Y.X. Yang, Q.R. Yue, J.S. Cao, Y. Zhao & P. Cai
National Diagnosis and Rehabilitation of Industrial Building Engineering Research Center, Beijing, China

ABSTRACT: Fiber reinforced polymer (FRP) material, which is a kind of advanced structural material, has been used in civil engineering more and more widely. However, there is not a normal checking method that suits for civil engineering now in China because of short period application. We all check the FRP material by the standard of composite materials. So it is essential for us to establish a normative checking method in research and application, which needs a large amount of test results to determine the influencing factors. A large amount of experimental studies were conducted focusing on the action factors that influence the test results of FRP materials in this paper. The influences of all the factors are discussed in details in this paper, which can provide essential results for us to establish a normative checking method.

1 INTRODUCTION

Fiber reinforced polymer (FRP) materials have been used in civil engineering more and more widely due to their excellent performance. They are not only used in new-built construction, but also used in structure strengthening and rehabilitation. Among all the FRP materials, carbon fiber reinforced polymer (CFRP) sheet is used prevailingly at present. However, the test standards of composite are referred to check the basic properties of the advanced materials, which can't meet the needs of the research and application in civil engineering [1]. In order to establish a normative checking method that reflects the real state in China and up to the international level, the National Diagnosis and Rehabilitation of Industrial Building Engineering Research Center takes on the compilation of the national code "Application and technique specification for advanced fiber reinforced polymer materials" and the "Technical specification for strengthening concrete structures with carbon fiber reinforced polymer laminate". One of the main tasks is to determine the checking method and standard that checks the properties of the FRP materials. In order to establish the normative checking method, a large amount of test results are needed to determine the influencing factors. A large amount of experimental studies were conducted focusing on the action factors that influence the test results of FRP materials in this paper, which can provide essential results for us to establish a normative checking method.

2 ANALYSIS OF THE INFLUENCING FACTORS

Test results showed that a lot of factors affect the test results of the specimen in the whole process of fabrication and test. The main factors are the fabrication process of the specimens and the test method.

2.1 *Fabrication process of the specimens*

When the dry carbon fiber sheets is coated with resins, redundant air exists in the resin and at the interface between the carbon fibers and the resin. So stress concentration exists at the defect and leads to failure of the specimen.

When cutting the CFRP sheets, it is very difficult to control the actuate dimensions of the specimen, especially the width. The dimensional error by manual fabrication is usually ± 0.3 mm.

The surfaces of the aluminum tab at both ends of the specimen are not absolutely even, so the force transferred in the specimen was not smooth, which causes the carbon fibers rupture gradually.

2.2 *Performance of the FRP materials*

CFRP sheet specimen consists of carbon fiber sheet and resin, so its strength is the action of both the carbon fibers and resin. Because the mechanical property of the resin is unstable and discrete, the test results fluctuate unpredictably. From the failure modes of the specimens, the most of the specimens ruptured after the carbon fiber tows disperse. Test results showed that at the initial loading, resin is very active for the carbon fibers. But after the carbon fiber tows disperse, due to the serious deformability difference between the resin and the carbon fibers, the lateral shear force of the resin is harmful to the carbon fibers.

2.3 *Test method*

When we calculate the mechanical property value of the CFRP sheets, the calculating width and nominal

Table 1. Test results summary of different width.

Mechanical properties			Width/mm				
			8	10	12	15	21
Brand I	Tensile strength	Mean value (MPa)	4099.6	4181.8	4608.6	4101.9	3949.3
		Standard deviation (%)	1123.4	632.4	298.8	423.875	407.474
		Coefficient of variation (%)	0.274	0.1512	0.0648	0.1033	0.1032
	Elongation	Mean value (MPa)	1.54	1.7313	1.75	1.7519	1.7333
		Standard deviation (%)	0.3056	0.1352	0.106	0.2174	0.2326
		Coefficient of variation (%)	0.1981	0.0781	0.0607	0.1241	0.1342
	Elastic modulus	Mean value (MPa)	236.4	228.77	249.67	235.163	229.247
		Standard deviation (%)	41.8	25.9688	13.31	9.6541	17.7185
		Coefficient of variation (%)	0.1769	0.1135	0.0533	0.0411	0.0773
Brand II	Tensile strength	Mean value (MPa)	4055.1	3919.7	3860.6	4197.1	3723.1
		Standard deviation (%)	415.4	632.11	706.15	1025.2	915.23
		Coefficient of variation (%)	0.1024	0.1613	0.1829	0.2443	0.2458
	Elongation	Mean value (MPa)	1.63	1.59	1.585	1.667	1.5667
		Standard deviation (%)	0.0884	0.2434	0.2796	0.3798	0.3109
		Coefficient of variation (%)	0.0543	0.1528	0.1764	0.2279	0.1985
	Elastic modulus	Mean value (MPa)	229.4	227	230.85	235.65	230.97
		Standard deviation (%)	12.83	10.31	9.47	14.59	16.87
		Coefficient of variation (%)	0.0559	0.0454	0.0410	0.0619	0.073
Brand III	Tensile strength	Mean value (MPa)	4154.3	4116.9	4303.5	3917.3	3969.3
		Standard deviation (%)	486.68	914.56	300.76	590.4	495.5
		Coefficient of variation (%)	0.1172	0.2221	0.0699	0.1507	0.1248
	Elongation	Mean value (MPa)	1.6867	1.71	1.61	1.66	1.633
		Standard deviation (%)	0.1767	0.3871	0.1407	0.264	0.1839
		Coefficient of variation (%)	0.1048	0.2259	0.0872	0.1591	0.1126
	Elastic modulus	Mean value (MPa)	233.9	236.5	253.9	239.4	248.8
		Standard deviation (%)	4.946	5.832	6.98	7.5	13.568
		Coefficient of variation (%)	0.0211	0.0247	0.0275	0.0314	0.0545

thickness are adopted. But due to the error of the fabrication of the specimens, the true widths are different from the calculating width, so the computed strengths are different from the true strength of the CFRP sheets. The measuring error and measuring range of the test machine, the environmental conditions of fabrication also influence the test results.

2.4 *Dimensions of the specimen*

The influence of specimen dimensions on the test results depends mainly on the probability of the dimensional defects occurrence. Commonly, the probability of defects occurrence increase with the increase of the width, length, thickness of the specimens. The proper dimension of the specimen is discussed in this experimental study.

3 TEST RESULTS

Some of the test results are listed in Table 1–Table 4.

4 ANALYSIS OF TEST RESULTS

4.1 *The width of specimen*

From the failure modes of the specimens, the carbon fiber tows ruptured gradually. Some of the fiber tows ruptured at first, then the load is sustained by the rest fiber tows and the stress in the rest carbon fibers increase sharply, which results in the final failure of the specimen. Defects, such as air pore, resin bulk and cutting damage, increase with the increase of the specimen width. The variation of strength versus specimen width and the coefficient of variation of strength versus specimen width are plotted in Figure 1.

In Figure 1, it can be seen that the strength and the coefficient of variation alter with different width. For two type of the CFRP sheets, when the width of the specimen is close to 12 mm, the strength of the CFRP sheets attains the maximum value. Meanwhile, the coefficient of variation is minimal. For the third type of CFRP sheets, the strength is maximal when the width is 15 mm and the coefficient of variation is minimal. The reason is that with the decrease of the width, the error

Table 2. Test results summary of different length.

Mechanical properties		Length/mm		
		230	280	330
Tensile strength	Mean value (MPa)	4289.3	3718.2	3324.8
	Standard deviation (MPa)	370.5247	318.4	435.78
	Coefficient of variation	0.0864	0.0856	0.1311
Elongation	Mean value (%)	1.6068	1.52	1.36
	Standard deviation (%)	0.1834	0.1353	0.2090
	Coefficient of variation	0.1142	0.0889	0.1531
Elastic modulus	Mean value (GPa)	268.5041	241	236.8
	Standard deviation (GPa)	20.9937	12.6	9.24
	Coefficient of variation	0.0782	0.0521	0.039

Table 3. Test results summary of different resin content.

Serial number	Weight before gelatinization (g)	Weight after gelatinization (g)	Weight of resin (g)	Tensile strength (MPa)	Elastic modulus (GPa)	Elongation (%)
1	4.1	6.7	2.6	1745	196	0.8
2	3.9	6.3	2.4	3457	215.5	1.5
3	4	6.4	2.4	3136	215.9	1.5
4	4.2	6.1	1.9	3628	227.4	1.6
5	4.2	8.4	4.2	4241	232.4	1.8
6	4.3	6.4	2.1	4236	219.7	1.8
7	4.2	6	1.8	3411	215.3	1.5
8	4	6.5	2.5	3446	224.4	1.5
9	3.9	9.5	5.6	2921	223.3	1.2
10	4.2	6.5	2.3	3222	213.1	1.4
11	4.2	6.4	2.2	3467	214.5	1.5
12	3.9	6.2	2.3	3589	221.7	1.6
13	3.9	5.9	2	3285	209.4	1.4
14	4.1	6.1	2	3889	227.6	1.6
15	4.2	7	2.8	3026	213.4	1.4

Table 4. Test results summary of different layer of CFRP sheets.

Mechanical properties		Layers	
		1	2
Tensile strength	Mean value (MPa)	4289.3	3816.5
	Standard deviation (MPa)	370.5247	388.3
	Coefficient of variation	0.0864	0.1017
Elongation	Mean value (%)	1.6068	1.68
	Standard deviation (%)	0.1834	0.1897
	Coefficient of variation	0.1142	0.1129
Elastic modulus	Mean value (GPa)	268.5041	228.3
	Standard deviation (GPa)	20.9937	12.2
	Coefficient of variation	0.0782	0.0535

caused during the fabrication increase. The probability of the defect occurrence increases with the increase of width. So the optimal width of the specimen is between 12 mm and 15 mm. Referring to the "Test method for tensile properties of oriented fiber reinforced plastics" and considering the present fabrication level, the suggested width of the specimen is 15 mm [2].

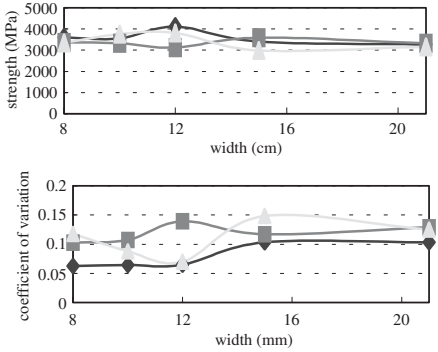

Figure 1. Strength and coefficient of variation versus width.

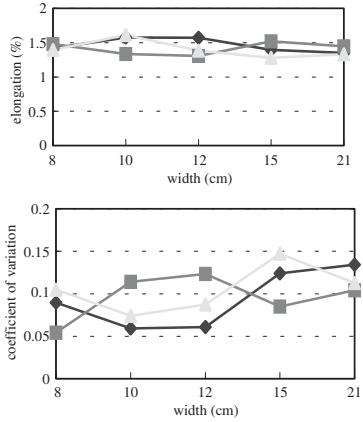

Figure 2. Elongation and coefficient of variation versus width.

The variation of elongation and coefficient of variation versus width are shown in Figure 2.

It can be seen in Figure 2 that the elongation and its coefficient of variation varied with different widths. Moreover, the coefficient of variation varied rapid and the maximum is high. So the elongation of CFRP sheets is unstable, a suggested fluctuating range is needed in practice.

Figure 3 shows that with the different width, the change of elastic modulus and its degree of discrete are small, so elastic modulus is stable and the value 210 GPa is suggested in practice.

4.2 *The length of specimens*

All the specimens are fabricated by the same CFRP and of the same width 15mm in the test and they are

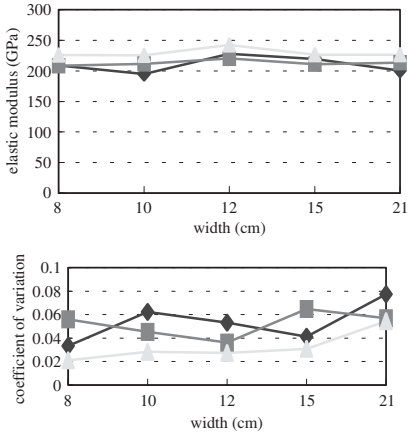

Figure 3. Elastic modulus and coefficient of variation versus width.

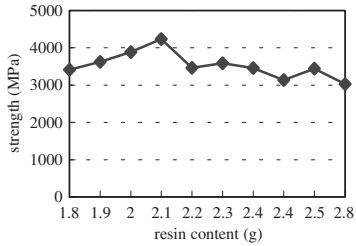

Figure 4. Strength versus resin content.

all made by one person. Therefore, the change of data is mainly influenced by the length of specimens. Table 2 shows the values of every index become small with the increasing of the length, because the probability of existence of defects also increases. Since the requirement of fabrication and test of specimens, the length cannot be too small. Thus the length of 230 mm is considered as the standard length of specimens.

4.3 *Resin content*

Specimens with the length 230 mm and with the width 15 mm were taken from 15 groups in the test. Without considering the influence of size, the influence of the resin content can be analyzed. From the data the relative curve between strength and the resin content is achieved.

Figure 4 shows that the specimens with the length of 230 mm and with the width of 15 mm have the best strength with the resin content about 2.0～2.1 g. More or less resin content is disadvantage to strength.

Table 5. Resin content and strength value.

Resin content (g)	1.8	1.9	2	2.1	2.2	2.3	2.4	2.4	2.5	2.8
Strength (MPa)	3411	3628	3889	4236	3467	3589	3457	3136	3446	3026

4.4 *The thickness of specimens*

30 specimens were tested with one layer of sheet and two layers of sheets separately. From Table 4, compared with each index, the strength and the elastic modulus of CFRP specimens with one layer of sheet is better than those with two layers of sheets evidently, but the elongation has no change. Since the probability of defects with two layers of sheets increases, the specimens with one layer of sheet have the more probability to damage and their strength will be low. In the same time, if the CFRP specimens are fabricated with two layers of sheets with different performance, the resin between CFRP sheets will have disadvantage to strength when in tension.

4.5 *Fabrication process*

The influence of fabrication process on the mechanical properties is small, so the suggested process is as follows. At room temperature the dry carbon fiber sheet is placed on a piece of isolating film and coated by the mixed resin on both surface. Then cover another isolating film on the CFRP sheets and roll it repeatedly from the center to the ends by a glass rod until the surface of the CFRP sheets is uniform and there is no white spot. After the resin precure, cut the CFRP sheets into proper dimensions.

4.6 *Test of specimens*

The test of specimens has small influence. Therefore the hydraulic actuator test machine with capacity of 20 kN is suggested, and the velocity of loading is 2 mm/min.

5 CONCLUSIONS

(1) The dimensions of specimens influence the mechanical properties significantly. So from the above analysis, the specimen with the length of 230 mm and width of 15 mm is suggested and the specimen is fabricated by only one layer of dry CFRP sheet. The proper resin content is about 2.0–2.1 g.
(2) The error of fabrication process and the method of test has small influence on the mechanical properties, but controlling the fabrication process and the method of test is suggested.
(3) The composite material consists of two different materials – fiber and resin, which will influence the mechanical properties. Thus the research of the matching between the two materials is needed.

ACKNOWLEDGEMENTS

The writers wish to acknowledge the funding of the National High Technology Research and Development Program of China (The 863 Plan, #2001AA336010), the National Natural Science Foundation of China (#50238030) and the Special Foundation for Institute of Science and Technology of China in 2003 (#2003EG213003).

REFERENCES

Yue, Q.R. 2002. Advances of the application of fiber reinforced polymers (FRP) in civil engineering, the 2nd national conference on FRP composites in civil engineering in China, Tsinghua university press: 18–22.

National code of China, 1999. Test method for tensile properties of oriented fiber reinforced plastics (GB/T 3354–1999).

FRP Composites in Civil Engineering – CICE 2004 – Seracino (ed)
© 2005 Taylor & Francis Group, London, ISBN 90 5809 638 6

Mineral based bonding of CFRP to strengthen concrete structures

B. Täljsten
Department of Civil Engineering, Luleå University of Technology, Luleå, Sweden
Skanska Teknik AB, Solna, Sweden

ABSTRACT: The advantages of FRP-strengthening have been shown time and again during the last decade. All over the world several thousand structures retrofitted with FRPs exist. There are various reasons why the retrofit is needed, but since buildings and civil structures usually have a very long life, it is not uncommon that the demands on the structure change with time. The structures may have to carry larger loads at a later date or fulfil new standards. In extreme cases, a structure may need repair due to an accident, or due to errors made during the design or construction phase, such that the structure needs to be strengthened before it can be used. This paper presents tests where the epoxy has been replaced with a cement based bonding agent for retrofitting with composites. Pilot tests show that full composite action can be achieved and that only minor changes in the design procedure needs to be taken. In comparison with traditionally CFRP strengthened concrete slabs the strengthening system with the cement based bonding agent showed as good or even better behaviour with regard to load bearing capacity and deflection at failure.

1 INTRODUCTION

1.1 *Background*

Over the past decade, the issue of deteriorating infrastructure has become a topic of critical importance in Europe, and to an equal extent in North America and Japan. FRP (Fibre Reinforced Polymers) are today used for various applications, such as reinforcement in RC and PC structures, stay cables and newly built structures. However, by far the most extensive application is in repair and strengthening of existing structures. This strengthening technique may be defined as one in which composite sheets or plates of relatively small thickness are bonded with an epoxy adhesive to, in most cases, a concrete structure to improve its structural behaviour and strength. The sheets or plates do not require much space and give a composite action between the adherents. The adhesive that is used to bond the fabric or the laminate to the concrete surface is normally a two-component epoxy adhesive. The old structure and the newly adhered material create a new structural element that has a higher strength and stiffness than the original.

The motivation for research and development into repairing, strengthening and restoration of existing structures, particularly concrete systems, is increasing. If consideration is given to the capital that has been invested in the existing infrastructure, it is not always economically viable to demolish and rebuild a deficient structure.

The challenge must be to develop relatively simple measures such as restoration, reparation and strengthening that can be used to prolong the life of structures. This challenge places a great demand on both consultants and contractors. Also, there could be difficulties in assessing the most suitable method for an actual repair; for example, two identical columns within the same structure can have totally different lifespan depending on their individual microclimate.

The use of epoxy as the bonding medium for the adherent has proven to give excellent force transfer. Not only does epoxy bond to concrete, steel and composites, it has also shown to be durable and resistant to most environments. However, when epoxy are used for plate bonding some drawbacks can be identified. Firstly, epoxy as a bonding agent may create problem in the work environment, secondly, epoxy should have a minimum application temperature, often 10°C, and thirdly, epoxy create sealed surfaces (diffusion closed) which may imply freeze/thaw problems for concrete structures. In addition to this, high temperatures might cause problems to the cold cured adhesives mostly used for CFRP strengthening. To avoid some of these problems it is suggested that cement based CFRP strengthening methods are used. Applications and research in this field is limited. Nevertheless, this paper presents a pilot study where concrete slabs have been strengthen with CFRP grids and a cementitious bonding agent.

1.2 *History*

At the end of the 1980s, Luleå University of Technology commenced research into the repair and strengthening of existing concrete structures utilizing the plate bonding technique. Initially steel plates were used to strengthen members. Currently, however, all research is focused on plate bonding using fibre reinforced polymer (FRP) composite materials in which, carbon fibre composite is the favoured material. The method of strengthening existing concrete structures with the use of epoxy adhesives originates in France in the 1960s (L'Hermite, 1967), (Bresson, 1971 a, b), where tests on concrete beams with epoxy bonded steel plates were conducted. There is also reported use of this strengthening method in South Africa in 1964, (Dussek, 1974). Since then, the application of epoxy bonded steel plates has been used to strengthen bridges and building in several countries over the world; Switzerland (Ladner & Flueler, 1974), (Fässler & Derendinger, 1980), the former Soviet Union (Steinberg, 1973), the United Kingdom (Swamy & Jones, 1980), Australia (Palmer, 1979), the United States (Klaiber et al., 1987), Japan (Raithby, 1980) and Sweden (Täljsten, 1990), just to mention a few.

Even though the method was used widely, it was not considered very successful. The drawbacks such as corrosion, the need of overlap joints, the heavy working loads during installation and the need for pressure on the adhesive during hardening could not be overcome. In 1995, one of the last applications to strengthen bridges with steel plates was carried out in Sweden, and this is shown in Figure 1 where the steel plates is mounted onto a bridge. This project was considered successful, but the disadvantage of the technique, viz. heavy plates, need of joints, bolting and pressure during curing of the adhesive, still remained. An inspection after 8 years shows no corrosion or degradation of the strengthening system.

In the last decade the plate bonding method has gone through a revival. The reason for this is mainly the increased need for retrofitting of our existing buildings and bridges. However, another very important factor is the introduction of advanced composites to the civil engineering arena. Fibre composites and reinforced plastics offer unique advantages in applications where conventional materials cannot supply a satisfactory service life (Agarwal & Broutman, 1990). The high strength to weight ratio and the excellent resistance to electrochemical corrosion of composites make them attractive materials for structural applications. In addition, composites are formable and can be shaped to almost any desired form and surface texture. One interesting application of currently available advanced composite materials is the retrofitting of damaged or structurally inadequate building and bridges. In Switzerland, (Meier, 1987), one of the first

Figure 1. Strengthening of a concrete bridge with steel plates. Carried out in Sweden during the mid 1990s.

applications with the use of carbon FRP (CFRP) was carried out at the end of the 1980s, and since then several thousand applications have been carried out worldwide.

Clearly there is a great potential for, and considerable economic advantages in, FRP strengthening. However, if the technique is to be used effectively, it requires a sound understanding of both the short-term and long-term behaviour of the bonding system. It also requires reliable information concerning the adhesion to concrete and composite. The execution of the bonding work is also of great importance in order to achieve a composite action between the adherents. Of the utmost importance is to know the practical limits of any proposed strengthening method.

1.3 *Research at Luleå University of Technology*

At Luleå University of Technology, Sweden, research has been carried out in the area of plate bonding. The research work started in 1988 with steel plate bonding and is now continuing with FRP materials. Both comprehensive experimental work and theoretical work have been carried out. The laboratory tests have included strengthening for bending as well as for shear (Täljsten, 2001) and torsion (Täljsten, 1998). Full-scale tests on strengthened bridges have also been performed (Täljsten , 1994), (Täljsten & Carolin, 1999) and (Täljsten, 2000). In particular, the theory behind the development of peeling stresses in the adhesive layer at the end of the strengthening plate has been studied, as has been the theory of fracture mechanics to explain the non-linear behaviour in the joint (Täljsten, 1994), (Täljsten, 1996) and (Täljsten, 1997).

In Sweden the FRP strengthening methods have been used in the field for almost 10 years now, and both laminates and wrap systems are used. Sweden is also one of the first countries in the world where a national code exists for FRP strengthening (Täljsten, 2003).

2 ADVANTAGES AND DISADVANTAGES USING FRP IN CONSTRUCTION

2.1 *Background*

There exist many technical solutions for structural problems and deficient concrete, and the final decision is always based on many factors. Some of these factors include: material cost, demand for mechanical strength and stiffness, impact resistance and resistance to vandalism, resistance against environmental effects, long-term properties such as relaxation and creep, application, and production methods. In addition, in some cases, the client may not be familiar with the purposed solution and, therefore, chooses a more conventional method. Even though advanced composites have been used for retrofitting over a decade now many clients are still not familiar with the technology. All technologies do contain advantages and disadvantages and so does CFRP retrofitting, below are some of the advantages and disadvantages are listed.

2.2 *Advantages*

FRP strengthening poses a number of potential advantages:

Handling and transportation: The composite materials used for strengthening are very light and easy to handle. In comparison to steel plate bonding where plates not longer than 2–3 metres can be handled, here almost infinitely long plates or sheets can be handled. In addition, no overlap plating is necessary. Also, compared to traditional concrete overlays or shotcrete, much less material has to be transported when FRP strengthening is used.

Durability and maintenance: Carbon fibre composites have especially good durability, longterm fatigue properties, and do not normally need to be maintained over time.

Thin strengthening layers: In many situations, thin strengthening layers can be advantageous. Thin layers will not change the dimension of the existing structure and can also be combined with thin concrete overlays or surface-protecting materials. Here low underpasses for road traffic can be an application where otherwise complicated methods of strengthening would be needed.

Construction time: Time is always a critical factor in the construction industry. If time can be reduced, money can be saved. FRP strengthening can often be done during short periods without stopping the traffic, and little time is needed for hardening of the bonding agents.

Pre-stressing possibilities: During the last few years, products have been introduced to the market that can be pre-stressed in combination with bonding. This gives a higher utilisation of the strengthening product, at the same time reducing existing cracks, and increasing the yield load of the existing steel reinforcement. It is also possible to use pre-stressing to increase the shear capacity of concrete structures.

Design: The possibility to optimise the FRP materials in the direction most needed is a benefit for design. In addition, compared to many other strengthening techniques, few methods have undergone such thorough investigation regarding testing, design and application as FRP strengthening. Therefore, the consultant can rely on existing design guidelines.

Cost: The cost of a strengthening work with composites compared to traditional methods is often lower, even though the material costs are higher.

2.3 *Disadvantages*

Potential disadvantages for CFRP retrofitting are:

Mechanical damage: Since the FRP materials themselves are brittle; they can be damaged by vandalism or by other types of attacks. If this is a concern, the FRP should be protected. Fortunately, if damage should occur, repairs can be easily undertaken.

Long-term properties: Carbon fibre composites with an epoxy matrix are said to have very good long-term properties. However, since the materials have only been used for approximately 10 years in the building industry, not enough data exists to verify this. However, the main concern is probably not the composite itself, but rather the adhesive layer. Nevertheless, the experience from older steel plate bonding projects shows that many of these structures are still in use with no visible deterioration of the bond layer. If the right type of material is used, and if the strengthening work is carried out carefully, 30 years of use can be guaranteed.

Working environment: Since epoxies are used for bonding the sheets or laminates to the structure, the working environment is very important. If these materials are not handled as prescribed, a risk for injuries to the labourers exist. However, with correct handling, the risk for injuries is very low.

Temperature and moisture dependence: The hardening process of thermosetting adhesives is moisture and temperature dependent. It can be necessary, therefore, in some environments to heat to the structure.

Lack of experience: Lack of experience is of course a large disadvantage. However, this can be overcome with education. Importantly, the knowledge must reach the consultants and the clients.

Conservatism: The well-known conservatism of the construction industry towards something new can be difficult to overcome. As above, the solution is education and the dissemination of knowledge.

Design: The lack of experienced building consultants that understand composites and how they should be used is a big drawback. Since it is the consultant that recommends a solution, if s/he does not know that

a certain method exists or how to handle it, s/he will of course suggest another method.

Cost: The carbon fibre sheets or laminates are much more expensive when compared to traditional building materials, at least per m^2 or per kg. In some contexts this is a factor and other methods will be used. Nevertheless, as mentioned earlier, the whole strengthening project needs to be considered to get a fair comparison.

Nevertheless, if one consider the relatively short time CFRP retrofitting has existed it has had a very important impact on the construction industry. Not only have we obtained a new repair and strengthening method, we have also introduced a total new material to be added to steel, concrete and wood. What impact this will have in the future no one knows, but probably larger than we expect today. To overcome some of the listed drawbacks with epoxy bonded CFRP products mineral based bonding systems might be a part of the solution. In the next section this will be discussed in more detail.

3 MINERAL BASED BONDING SYSTEMS

3.1 *Background*

It would be, from several points of view, very beneficial and interesting if the epoxy adhesive could be replaced with a mineral-based bonding agent, such as modified concrete. One of the drawbacks with epoxy is that it is considered toxic; on the skin, thermosetting components can cause irritations and eczema. Inhalation of epoxy resins should also be avoided. The hardeners have, as a rule, a pungent smell that can cause temporary irritation of the breathing passages.

Inhalation of amines does not normally cause any poisoning. The risk of swallowing thermosetting components is deemed minor. In order to avoid problems with epoxy work, the work should be well planned in advance, and personal protective equipment should be used. Another reason why it would be beneficial to replace epoxy is when retrofitting work is carried out on areas where the concrete needs to be diffusion open – i.e. wrapping of columns or similar applications. Low temperatures might also cause problems for thermosetting adhesives, where most formulas need at least 10°C to get the exothermic hardening process started. Here it would be possible to apply the cement-based bonding agent at temperatures as low as 0°C. That means that if the epoxy adhesive could be replaced with a mineral-based bonding agent a more environmental friendly, diffusion open and less temperature sensitive strengthening system could be obtained. However, these systems will most likely also have drawbacks. For example, laminates or dry fabrics will be complicated to bond, the laminate due to low adhesion to the composite and the fabric due to inferior wetting of the fibre. Research with the use of short FRP fibres have been going on for some time now, see for example (Kesner et al., 2003), (Li, 1998) and (Rossi, 1997). However, research with the use of long FRP fibres is limited. Research studying cement overlays with textiles of carbon fabrics embedded in cement based matrix to strengthen masonry walls has been carried out by (Kolsch, 1998). The strengthening system prevents partial or complete collapse of masonry walls in the critical out-of-plane direction during a seismic event. A study to improve the bond between carbon fibres and cementitious matrices has been carried out by (Badanoui, 2001), where dry fibre fabrics were used. It was found that a pre-treatment with silica fume and high amounts of polymers improved the bond behaviour of carbon fibre to the cement. However, it was also stressed that more research is needed in this field. A very interesting pioneering work has been carried out by (Wiberg, 2003). Large-scale tests of ordinary concrete beams strengthened with a cementitious fibre composite were reported. The composite used was made of polymer-modified mortar and a unidirectional sheet of continuous dry carbon fibres applied by hand. Both flexural and shear strengthening were tested. From the tests it was concluded that the method works, and that considerable strengthening effects can be achieved. In comparison with epoxy bonded carbon fibre sheets, the amount of carbon fibre needed to reach the same strengthening effect for the cementitious strengthening system was more than double. The reason for this is mainly due to problems with wetting the carbon fibre. This is also emphasised by (Badanoiu & Holmgren, 2003), where it was found that the load capacity of the cementitious carbon fibre composite is influenced by the amount of fibres in the tow. If the cementitious matrix can penetrate into the interior of the carbon fibre tow, a higher number of filaments will be active during loading, and this will lead to the increase in load carrying capacity.

3.2 *Pilot tests*

At Luleå University of Technology a research program is currently ongoing regarding the use of cementitious bonding agents in combination with carbon fibre composites. In this paper a brief description of pilot tests, (Becker, 2003), carried out on strengthen concrete slabs will be presented. The research at Luleå University of Technology is focused on the use of cementitious bonding agent as a replacement for epoxy adhesive. In comparison to tests performed by earlier researchers, for example by (Wiberg, 2003), a different path to overcome problems with wetting the fibres has been chosen. Instead of using dry fibres, a thin composite is chosen. This composite may be in the shape of a small rod (1D), grid (2D) or grid (3D).

Figure 2. CFRP grid used in slab 3, 4 and 6.

Table 1. Data for the reinforcement.

Reinforcement	E [GPa]	f_y [MPa]	ε [%]
Steel	209	483	–
Fabric	228	–	1.50
Grid	242		1.43

Table 2. Material data for the bonding agents.

Bonding agent	τ_a [MPa]	E_a [GPa]
Cementitious	>5.0	35.5
Epoxy	>5.0	4.8

In the pilot test, a two dimensional grid has been chosen as reinforcement.

In this particular case, matrix for the grid consists of epoxy, and the product is manufactured in factory-controlled environment. The composite grid used in the test is shown in Figure 2. In total, six slabs were tested, one reference slab, one with additional steel reinforcement and three with carbon fibre grids. Here, one of the grids was sanded to increase the bond to the cementitious bonding agent, and for one of the tests the amount of carbon fibre was doubled. In the last slab tested, traditional epoxy bonded carbon fibre fabric was used for strengthening. In Table 1 the material data of the carbon fibre grid and carbon fibre fabric are shown, together with the quality of the steel reinforcement. Here, E denotes the Young's modulus and f_y the yield stress for the steel, ε is the ultimate strain for the CFRPs. In Table 2 are the data, shear strength, τ_a, for the cementitious bonding agent and the epoxy adhesive recorded for together with the Young's modulus for respectively bonding agent. The shear strength was measured by a torque test and the obtained value for the epoxy adhesive is failure in the concrete substrate.

The square in the grid was 45×47 mm, with a cross sectional area corresponding to 59 mm^2/m in the loaded direction. The procedure for bonding the CFRP grid to the slab, No. 3, 4 and 6, was the following; first the slab was sand blasted and thoroughly cleaned, to simplify the application procedure the slab was placed upside down, and a thin layer of the cementitious mortar was then applied on the slab surface. The grid was then placed in position and the rest of cementitious mortar was applied. A thin plastic layer was placed over the slab, to avoid early shrinkage. The cementitious

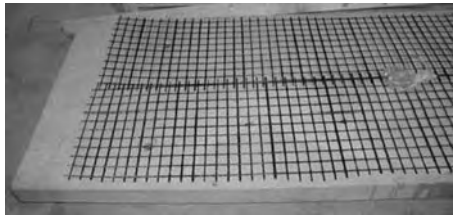

Figure 3. Concrete slab with the CFRP grid placed in position before applying the cementitious bonding agent.

Figure 4. Bonding the CFRP fabric to slab No. 5.

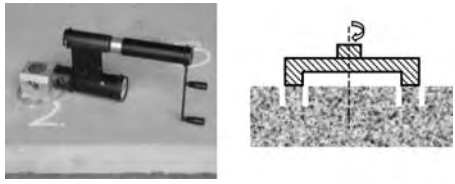

Figure 5. Torque test.

bonding agent was let harden in controlled environment, $+18 \pm 2$°C and 50% RH for 28 days before the slab was tested. The total thickness of the cementitious layer and the CFRP grid was approximately 8–10 mm. In Figure 3, the slab with the grid in position before applying the cementitious bonding agent is shown. It need to be mentioned that it would have been possible to apply the mortar upside down.

Slab No. 5 was strengthened with CFRP fabric and a normal bonding procedure was followed. First the slab was sand blasted, the surface cleaned properly and a primer applied. After the primer had hardened a thin layer of epoxy was applied and the CFRP fabric mounted in the adhesive and a new layer of adhesive applied. In Figure 4 bonding the bonding procedure is shown. Slab No. 5 was let harden 7 days in controlled environment, $+18 \pm 2$°C and 50% RH, prior testing. The concrete compressive and splitting strength together with the surface strength tested by a torque method was measured at time for testing. The principle for the torque test is shown in Figure 5.

Table 3. Data for tests with strengthened slabs.

Slab	Reinforcement	Bond	f_{cc} [MPa]	f_{ct} [MPa]	τ_a [MPa]	P_c [kN]	P_y [kN]	P_f [kN]
1	–	–	49.4	5.5	4,5	4	25	25
2	Extra steel 4 no ϕ 8	–	49.4	5.5	5,4	5	38	38
3	1 BPE® NSMG 43	Cement	49.4	5.5	5,4	4	32	35
4	1 BPE® NSMF 43	Cement	49.4	5.5	4,5	4	32	40
5	BPE® Composite 200S	Epoxy	50.8	5.9	5,3	5	35	41
6	2 BPE® NSMG 43	Cement	50.8	5.9	5,3	10	40	51

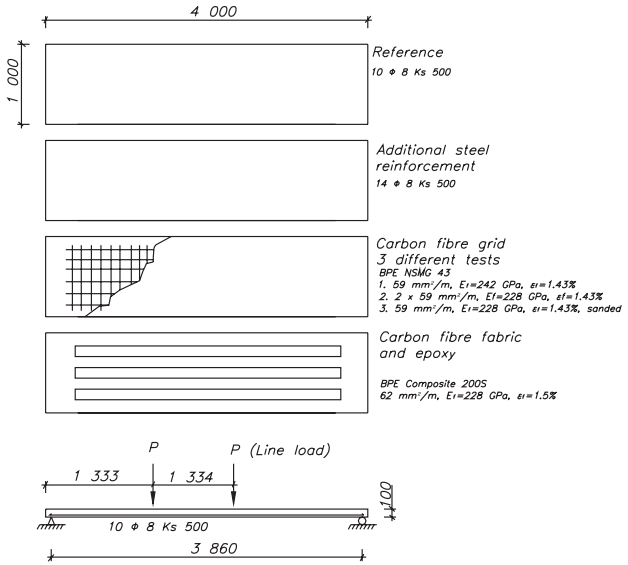


Test set-up for the slabs


Failure of slab No. 3, breakage of fibre and debonding of polymer concrete


Failure of slab No. 5, breakage of fibre and debonding of the fabric

Figure 6. Test set-up for the pilot test.

In Table 3 the material data and dimensions of the slabs are shown, and in Figure 6 is the load set-up for the slabs shown. In Table 3, f_{cc} and f_{ct} is the compressive and splitting strength of concrete, respectively. P_c is the cracking load for concrete and P_y the yield load for the slab. The failure load is denoted P_f. The result from the torque test is denoted τ_a. It can be noticed in Table 3 that the strength values from the torque and the splitting test are almost of the same magnitude.

The slabs in the pilot test are shown in Figure 6. It can be noticed that all the slabs have the same size, but that they have been strengthened by different methods. All slabs, except the reference slab and slab No. 6 with two CFRP grids, have been designed for the same failure load. Slab No. 2 is strengthened with 4 no of extra steel reinforcement, ϕ 8, slab No. 3 and No. 4 have been strengthened with one single layer of CFRP grid, for slab No. 3 the grid has been sanded prior bonding, this to increase the bond between the cementitious bonding agent and the grid. Slab No. 5 is strengthened by traditional epoxy bonded fabrics. The cross sectional area of the fabric is 62 mm^2/m. The last slab, slab No. 6, was strengthened with 2 layers of CFRP grid. The slabs were loaded with two line loads up to failure, the loading was deformation controlled with a load rate of 0,03 mm/s. This rate was doubled when the steel in the slab reached yielding. The load deflection curves from the test are recorded for in Figure 7, where the total load is plotted as a function of the mid-deflection.

It can be noticed in Figure 7 that the slab with the highest reinforcement content, i.e. No. 5 with two layers of carbon fibre grid, sustained the highest load at failure. Slabs 2, 3, 4 and 5 were all designed for approximately the same failure load. Slab No. 3 reached

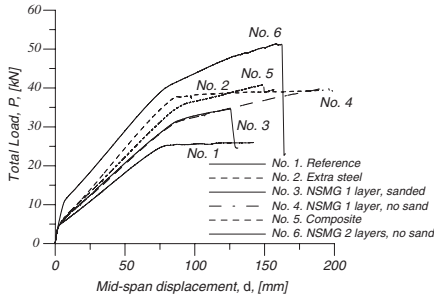

Figure 7. Load–deflection curves for the pilot test.

failure earlier than the other slabs due to breakage of the fibres. The reason for fibre breakage was that the bond between the grid and the cementitious bonding agent probably was too high, resulting in high stress concentrations. As a consequence a failure arose at a crack in the cementitious bonding material. In slab No. 4 a small slippage between the cementitious bonding material and the grid provided for a higher load. However, in comparison with slab No. 5, where fabrics had been bonded with epoxy to the slab, a less stiff behaviour could be noticed for the slabs with a single carbon fibre grid. The reason for this less stiff behaviour depends most likely on the fact that the epoxy bonded fabric prevent early cracking. The same effect cannot be obtained with the CFRP grid. Slabs No. 2, 4 and 5 reached approximately the same failure load. The slab with extra steel reinforcement, No. 2, showed stiffer behaviour than slabs No. 3, 4 and 5. In Figure 6, the right hand side is a photo of the test set-up shown together with the failure modes for slabs No. 3 and No. 5. For both of these slabs debonding occurred after fibre breakage. This was not the case for slabs No. 2, 4 and 6, where extensive cracking and large deflections preceded fibre breakage. This may also be noticed in Figure 7, where large deflections were obtained for all these slabs. In addition slab No. 6 obtained the highest failure load and was also the stiffest slab of the ones tested. Also the cracking and steel yielding loads were considerably higher for slab No. 6. compared to the other slabs. A FE-model was also developed – corresponding quite well to the laboratory tests; however due to space limitations, this model is not presented here, see (Becker, 2003).

4 SUMMARY AND CONCLUSIONS

In this paper the use of cementitious bonding agents in combination with advanced composite materials is discussed. A pilot test is presented, and it can be seen from the results that slabs strengthen with CFRP grids and bonded to concrete with a cementitious bonding agent are comparable to a slab strengthen with epoxy bonded carbon fibre fabrics and a slab with increased steel reinforcement. The failure mode for the slab strengthened with sanded CFRP grid and epoxy bonded fabric was quite brittle, whereas the failure mode for the other slabs was more ductile.

The test was considered promising, and the pilot tests presented are now being followed up with more comprehensive research at Luleå University of Technology.

ACKNOWLEDGEMENT

The research presented in this paper has been funded by several organisations. Here the Swedish National Road Administration, the Development fund of the Swedish Construction Industry and Skanska AB should be acknowledged.

REFERENCES

Agarwal B.D. and Broutman L.J., 1990, Analysis and Performance of Fibre Composites, John Wiley & Sons Inc. ISBN 0-471-51152-8, 1990, p. 449.

Badanoiu A. and Holmgren J., Cementitious composites reinforced with continuous carbon fibres for strengthening of concrete structures, Journal of Cement & Concrete Composites, vol. 25, 2003, pp 387–394.

Badanoui A., 2001, Improvement of the bond between carbon fibres and cementitious matrices, Technical report 2001:1, Concrete Structures, ISSN 1404-8450, Royal Institute of Technology, Department of Structural Engineering, 100 44 Stockholm, Sweden, p. 44.

Becker D., 2003, Betongplattor förstärkta med kolfiberkomposit – En experimentell och teoretisk analys (In Swedish). Master Thesis, Department of Civil and Mining Engineering, Division of Structural Engineering, Luleå University of Technology, SE-97187 Luleå, Sweden, 2003:130 CIV, p. 150.

Bresson J., 1971, Novelles resherches et applications concernant lútilisation des collages dans les structures. Betong plaque, Annales de l+institute technique, No. 278, 1971.

Bresson J., 1971, Realisation practique dún reinforcement par collage dármatures, Anneles de ITTBTP, Suppl. 278, Feb. 1971, pp 50–52.

Dussek I.J., 1974, Strengthening of bridge beams and similar structures by means of epoxy-resin bonded external reinforcement. Transport research record 785, Washington, USA, 1974, pp 21–24.

Fässler A. und Derendinger P., 1980, Die Sanierung der Gizenbrucke uber die Muota, Schweizer Ingenieur und Architekt, Sonderdruck aus heft 41/1980, p. 9.

Kesner K.E., Billington S.L and Douglas K.S., 2003, Cyclic Response of Highly Ductile Fibre-reinforced Cement-Based Composites, ACI Materials and Journals – Technical Paper, September–October 2003, pp 381–390.

Klaiber F.W., Dunker K.F., Wipf T.J. and Sanders JR W. W., 1987, Methods of strengthening existing highway bridges,

Transportation Research Board, Washington D.C., September 1987, p. 16.
Kolsch H., 1998, Carbon fibre cement matrix (CFCM) overlay system for masonry strengthening, Journal for composites for construction, Vol. 2, No. 2, May 1998, pp 105–109.
L'Hermite R., 1967, Lápplication des colles et resins dans la construction. La betong coffrage portant, Annales línstitut technique, No. 239, 1967.
Ladner M. and Flueler P., 1974, Versuche an Stahlbeonbauteilen mit geklebter Armierung, Schweiserische Bauzeitung, Heft 19, Mai 1974, pp 9–16.
Li V.C., 1998, Engineered Cementations Composites-Tailored Composites Through Micromechanical Modelling, Fibre Reinforced Concrete: Present and the future, N. Banthia, A. Bentur and A. Mufti, eds. Canadian Society for Civil Engineering, Montreal Quebec, Canada, pp 64–97.
Meier U., 1987, Repair of bridges with high performance composite materials, Material + Technik, Vol. 15, No. 4, 1987, pp 125–128.
Palmer P.M., 1979, Repair and Maintenance of concrete bridges with particular reference to the use of epoxies, tech. Report No. 14, Main Roads Dept., Perth, Western Australia, August 1979.
Raithby K.D., 1980, External strengthening of concrete bridges with bonded steel plates, Transport and Road Research Laboratory, report 612, Crowthorne, Beerkshire, 1980, p. 21.
Rossi P., 1997, High Performance Multimodal Fibre reinforced Cement Composites (HPMRERCC): The LCPC Experience, ACI Materials Journal, V94, No. 6, November–December, pp 478–483.
Steinberg M., 1973, Concrete polymer materials and its worldwide development. American Concrete Institute, 1973, pp 12.
Swamy R.N. and Jones R., 1980, Technical Notes – Behaviour of plated reinforced concrete beams subjected to cyclic loading during glue hardening, The International Journal of Cement Composites, Vol. 2, No. 4, November 1980, pp 233–234.
Täljsten B., 2001, "Design guidelines – a Scandinavian approach", International Conference on FRP Composites in Civil Engineering CICE 2001 Ed. J.G. Teng, Hong Kong, ISBN: 0-08-043945-4
Täljsten B., 1990, Förstärkning av betongkonstruktioner genom pålimning av stålplåtar (Strengthening of concrete structures by adhesively bonded steel plates, In Swedish), Tekniska Högskolan i Luleå, Avdelningen för konstruktionsteknik, Licentiatuppsats 1990:06L, p. 212.
Täljsten B., 1994, Plate Bonding, Strengthening of Existing Concrete Structures with Epoxy Bonded Plates of Steel or Fibre reinforced Plastics Doctoral Thesis 1994:152D, Div. of Structural Engineering, Luleå University of Technology, ISSN 0348-8373, 308 pp.
Täljsten B., 1996, Strengthening of concrete prisms using the plate-bonding technique, International Journal of Fracture 82: 253–266, 1996, 1996 Kluwer Academic Publishers, Printed in the Netherlands.
Täljsten B., 1997, Strengthening of Beams by Plate Bonding, Journal of Materials in Civil Engineering, November 1997, pp 206–212.
Täljsten B., 1998, Förstärkning av betongkonstruktioner med stålplåt och avancerade kompositmaterial utsatta för vridning, Forskningsrapport, Luleå tekniska universitet, Avdelningen för konstruktionsteknik, Institutionen för Vägoch vattenbyggnad, 1998:01, ISSN 1402-1528 (In Swedish).
Täljsten B., 2000, Förstärkning av befintliga betongkonstruktioner med kolfiberväv eller kolfiberlaminat, Dimensionering, material och utförande, Teknisk Rapport, Luleå tekniska universitet, Avdelningen för Konstruktionsteknik, 1999:12, ISSN 1402-1536, 1999, p. 122 (In Swedish).
Täljsten, B. 2003, FRP Strengthening of Existing Concrete Structures. Design Guideline Division of Structural Engineering, Luleå University of Technology, Luleå 2003, Second edition, 228 pp, ISBN 91-89580-03-6.
Täljsten, B. and Carolin, A., 1999, Strengthening of a concrete railway bridge in Luleå with carbon fibre reinforced polymers – CFRP: load bearing capacity before and after strengthening, Technical Report 1999:18, Luleå: Luleå University of Technology, Structural Engineering. 61 pp.
Wiberg A., 2003, Strengthening of concrete beams using cementitious carbon fibre composites, Doctoral Thesis, ISSN 1103-4270, Royal Institute of Technology, Structural Engineering, 100 44 Stockholm, Sweden, p. 140.

FRP Composites in Civil Engineering – CICE 2004 – Seracino (ed)

Coaxially reinforced composite rods

V.N. Kestelman
KVN International, King of Prussia, USA

G.E. Freger & D.G. Freger
East Ukrainian National University (EUNU), Lugansk, Ukraine

ABSTRACT: Unidirectionally reinforced composite rods have some drawbacks such as tendency to separation in compression along reinforcement, low resistance to shear and transversal stretching. The most promising way to control rod properties is application of spiral reinforcement where combination of hybridization and spatial reinforcement makes it possible to modify rod properties in a wide range. Technological process of rod production includes additional process of spiral winding of the main fiber material. Profile of necessary cross-section is formed from a spirally reinforced semi-finished product which is a hollow tube made up of one or several coaxial fiber layers spirally wound by a thread of auxiliary reinforcement. Analysis of rod loading condition permits to develop a method of calculation of stress–strain condition and effective longitudinal modulus of elasticity and shear modulus of a round rod.

Experimental study of dependence of separation threshold and strength of the rod on its structural and geometric parameters in compression has been carried out.

Results show that introduction of a spiral layer changes strain condition and type of failure in compression. The efficiency of the layer introduction is determined both by the layer properties and ratio of modulus of elasticity of the main and auxiliary reinforcement. Introduction of spiral winding permits to increase rod strength in compression by 20–40%, in shear – by 10–20%.

1 INTRODUCTION

Rod elements made of fibrous composites are a frequent component of spatial trussed design thanks to a set of specific advantageous properties, including low linear thermal expansion coefficient (LTEC), good radioparent features and some other. These advantages are however bounded by known drawbacks, most unfavorable among which is anisotropy of elastic and strength characteristics. High tensile properties of the material in reinforcement direction are in contradiction with poor transversal characteristics, low interlayer shear modulus, and etc. This, in its turn condition impaired strength of rods from unidirectional composites at a lengthwise compression and relatively low critical load values. Such rods start to break and loose their bearing capacity much earlier than the material strength and bearing capacity of its fibers are exhausted being dependent upon accumulation of microdamages in the bulk. Fracture of rods of unidirectional composites occurs as a result of delamination of their fibers arising from binder cracking and bulging of individual unstable fibers.

The critical force value under which the straight-line equilibrium state of the rod becomes unstable is determined as follows:

$$P_C = EJ\left(\frac{\pi}{L}\right)^2 \frac{1}{1+\frac{k}{GF}EJ\left(\frac{\pi}{L}\right)^2}, \qquad (1)$$

where E – the efficient elastic modulus of the rod material; L – its length; J – cross-sectional inertia moment; K – coefficient dependent on cross-section geometrical form; G – longitudinal shear modulus; F – cross-sectional area.

The analysis of above dependence evidences that the critical load can be raised under given geometrical parameters of the structure through enhancing elastic constants of the material. To increase the resistance to interlayer shear and transverse tearing it is worthwhile using hybrid spirally reinforced fillers and the spiral reinforcement procedure. Moreover, rather coarse structural units produced by spiral winding of one or a few types of fibrous reinforcements with fibers of some other type can be employed with this aim. As a result, a built-up cylinder is achieved in which coaxial longitudinal layers of the main reinforcement are

alternating with thin stiffening layers. Hence, the spirally reinforced rod represents a multilayered hybrid composite.

The operation of composite rods under temperature difference requires high enough strength along with rigidity, length stability of the rod element, etc. Investigation results of a number of authors indicate that the integral LTEC of a hybrid unidirectional composite can be regulated by combining fibers with the positive (glass-reinforced plastic) and negative (carbon plastic) LTEC. An essential drawback of the method is introduction of majority of the low-modular filler in direction of the main reinforcement that reduces article rigidity. In a number of cases it's proposed to regulate the LTEC value of a thin-walled carbon plastic rod by various spatial reinforcement schemes to ensure high bearing capacity of the rod element that, unfortunately doesn't take into account the material temperature sensitivity.

In contrast, spiral reinforcement allows for diversity in choosing main and auxiliary materials, their mutual disposition, different geometrical parameters of stiffening layers, probability of varying in fact any properties of the produced rod, including the integral LTEC of the material. Thus, there arises a problem of predicting elastic and thermoelastic properties of spirally reinforced rods and their optimum designing with allowance for their performances. The studied rods represent inhomogeneous multilayered structures. The fundamentals of the theory of designs of the type are set forth in [1] where relations for each element of the piecewise-homogeneous body are given and conditions of an ideal mechanical and thermomechanical contact between them are reported. Nevertheless, solutions of a number of practical problems by this method encounter perceptible analytical and computation difficulties and necessitate the development of new methods of solutions.

By combining different reinforcing fibers in a hybrid spirally reinforced rod and varying geometrical parameters of the main and stiffening layers one can change in fact any properties of rod elements. Here arises a problem of defining elastic and strength characteristics of such rod elements and the issue of the choice of an optimum material structure for a set operation regime.

2 MATHEMATICAL MODEL

As a design model of the hybrid spirally reinforced rod we choose a built-up cylinder of circular cross-section (Fig. 1) consisting of N thick main layers S_i rigidly connected to thin stiffening layers L_i $(i = 1, \ldots, N)$. One of the rod faces is considered as rigidly fastened. The coordinates are so that Z axis is parallel to the rod generatrix and its origin coincides with the gravity

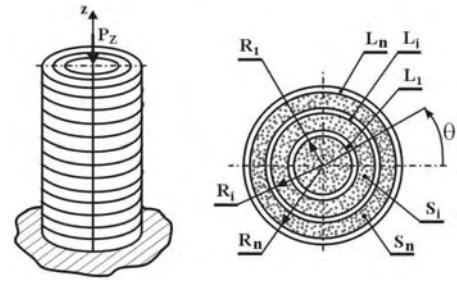

Figure 1. The design model of a hybrid spirally reinforced rod.

center of its idle face. In this case, plane $r\Theta$ is parallel to that of the cylinder cross-section.

It's been specified above that layers S_i, L_i $(i = 1, \ldots, N)$ are spirally anisotropic. The considered type of anisotropy relates to a case of a local orthotropic body [2]. This means that there are 13 S_i independent elastic constants in each point of the cylinder in the chosen coordinates $r\Theta z$.

Technical characteristics of layers S_i, L_i $(i = 1, \ldots, N)$ can be calculated on the basis of known formulas with account of the reinforcing fiber properties, that of the binder and filling degree of the layer. To compute elastic constants of layers S_i and L_i the local coordinates $r_1\Theta_1 z_1$ is chosen so that axis z_1 be aligned with the reinforcing layer direction, and axis r_1 be parallel to r axis. Transfer from the local coordinates $r_1\Theta_1 z_1$ to $r\Theta z$ is exercised by the pivot turn r by angle γ_i determined by twisting of layer S_i fibers under the action of the winding fiber, and by the packing angle β_i of layer $L_i (i = 1, \ldots, N)$.

2.1 *Calculation of loading conditions*

What concern rods under study, it's possible to avoid solution of Saint-Venant's problem for built-up spirally anisotropic bodies and the problem on a complex loading of a compound piecewise-homogeneous rod element by introduction of an assumption on smallness of the layer breadth as compared to contacting bulk bodies and the one that cross-sections of the rod remain plane at deformation. This will lead to the solution of 3 spatial problems of the theory of elasticity, namely on the rod loading by an axial force P_Z, rod twisting by torque M_{TR} and bending moments M_1 and M_2.

Loading conditions in this case are accounted for as integral face conditions

$$\int_S \sigma_z dS = P_z; \tag{2}$$

$$\int_S r\tau_{\theta z} dS = M_{TR}; \tag{3}$$

$$\int_S r\sin\Theta\sigma_z dS = M_1; \quad \int_S r\cos\Theta\sigma_z dS = M_2; \tag{4}$$

$$\text{where } S = [\underset{N}{U} S_i]U[\underset{N}{U} L_i]; \quad dS = rdrd\Theta; \tag{5}$$

Layers S_i in the rod model considered are inhomogeneous and local-orthotropic. As it follows from [3], the integral face conditions (2)–(4) are true for each layer. Like in the case when layers S_i are homogeneous the assumption on smallness of layer breadths L_i enables consideration of face loads of the built-up spirally anisotropic rod using the integral face conditions.

Hence, the problem on a complex loading of a built-up spirally anisotropic rod is reduced to solution of three spatial problems: the problem on longitudinal loading, the twisting problem and that on bending with torques. The loading conditions are taken into account in the integral face conditions (2)–(4).

Let's consider an axisymmetric loading of a spirally anisotropic rod S whose cross-section is a circular ring or circle. The elasto-equivalent directions of the rod material are disposed along the helical lines whose inclination to the generatrix is conditioned by fiber twisting under the action of the winding thread. Since the elastic constants of the rod are independent of variableΘ, then under the axisymmetric loading

$$\tau_{rz} = \tau_{r\theta} = 0. \tag{6}$$

For further transformations let's write coefficients a_{ij} of Hook's law as

$$\begin{aligned} &a_{ij} = a_{ij}^{(0)} + \gamma_0^2 r^2 C_{ij}; \quad i,j = 1,2,3; \quad i = j = 4,5,6 \\ &a_{i4} = \gamma_0 r C_{i4}; \quad i = 1,2,3; \quad a_{56} = \gamma_0 r C_{56}, \end{aligned} \tag{7}$$

where $a_{ij}^{(0)}$ are elastic properties of rod S in reinforcement direction.

The dependencies for determining constants C_{ij} through $a_{ij}^{(0)}$ are of the form

$$\begin{aligned} &C_{11} = 0; && C_{14} = 2\left(a_{13}^{(0)} - a_{12}^{(0)}\right); \\ &C_{12} = a_{13}^{(0)}; && C_{22} = 2a_{13}^{(0)} + a_{44}^{(0)}; \\ &C_{13} = a_{12}^{(0)}; && C_{23} = a_{11}^{(0)} + a_{33}^{(0)} - a_{44}^{(0)}; \\ &C_{24} = -2a_{11}^{(0)} + 2a_{13}^{(0)} + a_{44}^{(0)}; && C_{44} = 4a_{11}^{(0)} + 4a_{13}^{(0)} + 4a_{33}^{(0)} - 2a_{44}^{(0)}; \\ &C_{33} = 2a_{13}^{(0)} + a_{44}^{(0)}; && C_{55} = a_{66}^{(0)}; \quad C_{56} = a_{44}^{(0)} - a_{66}^{(0)}; \\ &C_{34} = -a_{13}^{(0)} + a_{33}^{(0)}; && C_{66} = a_{44}^{(0)}. \end{aligned}$$

Since coefficients a_{ij} of Hook's law depend on small angle γ_0, it's natural to apply the perturbation theory for the problem solution. With this aim the stresses and strain will be written as

$$f = f^{(0)} + \gamma_0 f^{(1)} + \gamma_0^2 f^{(2)}, \tag{8}$$

taking that $\gamma_n^0 \approx 0$ at $n \geq 3$.

Since the unstrained face of the rod is rigidly fixed, then

$$W = a\,z, \tag{9}$$

$$U_\theta = a_0 r\,z, \tag{10}$$

where unknown constants a, a_0 are found from face conditions (2) and (3).

The problem is solved in three stages. The solution corresponding to γ_0^0, i.e. to transversely isotropic material is found at the first stage. In this case the solution of the plane problem is of the form

$$\sigma_r^{(0)} = A_{-1} r^{-2} + A_1; \quad \sigma_\theta^{(0)} = -A_{-1} r^{-2} + A_1, \tag{11}$$

Stresses $\sigma_z^{(0)}, \tau_{\Theta Z}^{(0)}$ and displacements $U_r^{(0)}$ are easily found from Hook's law

$$\begin{aligned} &\sigma_z^{(0)} = \frac{1}{a_{33}^{(0)}} a - 2\frac{a_{13}^{(0)}}{a_{33}^{(0)}} A_1; \\ &\tau_{\Theta z}^{(0)} = \frac{1}{a_{44}} a_0 r; \\ &U_z^{(0)} = \frac{a}{a_{33}^{(0)}} r + A_{-1}\left(a_{12}^{(0)} - a_{11}^{(0)}\right) r^{-1} + A_1 b_1 r, \end{aligned} \tag{12}$$

At the second stage the solution corresponding to γ_0^0 and γ_0^1 is sought. By equating coefficients of similar exponents of the small perimeter γ_0 from Hook's law

$$\begin{aligned} \tau_{\theta z}^{(1)} &= -A_{-1}\frac{1}{a_{44}^{(0)}}(C_{14} - C_{24}) r^{-1} - \\ &- A_1 \frac{1}{a_{44}^{(0)}}\left(C_{14} + C_{24} - \frac{2a_{13}^{(0)} C_{34}}{a_{33}^{(0)}}\right) r - \frac{C_{34}}{a_{33}^{(0)} a_{44}^{(0)}} ar. \end{aligned} \tag{13}$$

$$\begin{aligned} &\sigma_r^{(1)} = B_{-1} r^{-2} + B_1 + a_0 B_3 r^2; \\ &\sigma_\theta^{(1)} = -B_{-1} r^{-2} + B_1 + 3a_0 B_3 r^2; \\ &\sigma_z^{(1)} = -2\frac{a_{13}^{(0)}}{a_{33}^{(0)}} B_1 + a_0 b_2 r^2; \\ &U_r^{(1)} = B_{-1}\left(a_{12}^{(0)} - a_{11}^{(0)}\right) r^{-1} + B_1 b_1 r + a_0 b_3 r, \end{aligned} \tag{14}$$

At the third stage the terms corresponding to $\gamma_0^0, \gamma_0^1, \gamma_0^3$ are defined.

$$\begin{aligned} &\sigma_r^{(2)} = C_{-1} r^{-2} + C_1 + C_0 A_1 \ln r + C_{31} A_1 r^2 + C_{32} ar^2; \\ &\sigma_\theta^{(2)} = C_{-1} r^{-2} + C_1 + C_0 A_1 (\ln r + 1) + 3r^2 (C_{31} A_1 + C_{32} a), \end{aligned} \tag{15}$$

Hence, SSS of the spirally anisotropic rod is determined during axisymmetric loading by dependencies (9), (10) and

$$\sigma_r = \left(A_{-1} + \gamma_0 B_{-1} + \gamma_0^2 C_{-1}\right) r^{-2} + \gamma_0 A_{-1} C_0 \ln r + \\ + A_1 + \gamma_0 B_1 + \gamma_0^2 C_1 + \left(\gamma_0 a_0 B_3 + \gamma_0^2 A_1 C_{31} + \gamma_0^2 a C_{32}\right) r^2;$$

$$\sigma_\theta = -\left(A_{-1} + \gamma_0 B_{-1} + \gamma_0^2 C_{-1}\right) r^{-2} + \gamma_0^2 A_{-1} C_0 \ln r + \gamma_0^2 C_0 A_{-1} + A_1 + \\ + \gamma_0 B_1 + \gamma_0^2 C_1 + \left(3\gamma_0 a_0 B_3 + 3\gamma_0^2 A_1 C_{31} + 3\gamma_0^2 a C_{32}\right) r^2;$$

$$\sigma_z = -2\frac{a_{13}^{(0)}}{a_{33}^{(0)}}\left(A_1 + \gamma_0 B_1 + \gamma_0^2 C_1 + \gamma_0^2 A_{-1} b_4 + \gamma_0^2 A_{-1} C_0 \ln r\right) + \frac{a}{a_{33}^{(0)}} + \\ + \left(\gamma_0 b_2 a_0 + \gamma_0^2 A_1 b_5 + a\gamma_0^2 b_6\right) r^2;$$

$$\tau_{\theta z} = \frac{C_{24} - C_{14}}{a_{44}^{(0)}} r^{-1}\left(\gamma_0 A_{-1} + \gamma_0^2 B_{-1}\right) + \\ + \left[a_0 + b_7\left(\gamma_0 A_1 + \gamma_0^2 B_1\right) - \gamma_0 \frac{C_{34}}{a_{33}^{(0)} a_{44}^{(0)}} a\right] r + b_8 a_0;$$

$$U_r = \left(a_{12}^{(0)} - a_{11}^{(0)}\right)\left(A_{-1} + \gamma_0 B_{-1} + \gamma_0^2 C_{-1}\right) r^{-1} + \\ + \left[b_1\left(A_1 + \gamma_0 B_1 + \gamma_0^2 C_{-1}\right) + \right. \\ \left. + a\frac{1}{a_{33}^{(0)}} + A_{-1} b_{11}\right] r + \left[\gamma_0 a_0 b_3 + \gamma_0^2 A_1 b_9 + \gamma_0^2 a b_{10}\right] r^3 + \\ + \gamma_0^2 A_{-1} C_0 \left(a_{11} + a_{12}\right) r \ln r, \qquad (16)$$

where unknown constants are found from the boundary and face conditions.

3 EXPERIMENTAL

The process of manufacturing spirally reinforced rods includes their molding from a fibrous material by pultrusion followed by packing of the spiral layers. The needed filling degree and dimensions of each intermediate layer and the article as a whole are reached at every stage of forming with the help of spinnerets of the required open flow area. The reinforcing layers are packed immediately after leaving the spinneret using special winders. Solid rod elements are produced 20 mm in diameter and tubular ones have 25 mm inner and 35 mm outer diameters, and their longitudinal to transversal layer relation is 1:0 till 2:3. There are 2 coaxial layers (main reinforcement) and 3 layers of the auxiliary reinforcement. Winding pitch of the spiral reinforcement is 1 mm. The initial materials were glass braids, carbon braids and organic fibers of 29.4 tex, boron fibers and epoxide compound-based binders. Properties of the rod element ingredients are given in Table 1.

The winding fiber tension force is chosen within 5–8 N/braid. The obtained braids are cured in a polymerizing oven following a standard time–temperature regime. As far as inner stresses might appear during cooling of the rod element a part of the samples were formed so as to exclude the effect of SSS during testing. With this aim each layer was cured immediately after molding and the reinforcing layer was laid on the cold-set binder after polymerization and cooling of the main layer.

Table 1. Properties of reinforcing fibers.

Parameters	Boron	Organic	Glass	Carbon
Breaking tensile stress, MPa, $\times 10^2$	25–38	22	35	20–22
Elastic modulus, MPa, 10^2				
Under tension	4000	1100	950	2700
Under shear	1600	15	40	75
Relative elongation at rupture, %	0.8	3	4	1.2
LTEC 10^6 K^{-1}	2.4	3	5	−0.5
Poisson's ratio	0.2	0.3	0.3	0.22

Table 2. The compressive strength dependence of rod elements on face closure type.

	Unidirectional		Wrapped	
Type of closure	σ_P, MPa	W, %	σ_P, MPa	W, %
Simple supported, polished	232	13.4	201	12.5
Inserted in metal shells	295	6.9	249	9.2
Filled up in metal shells	382	1.6	389	6.2
Filled up in metal shells and movable at loading along guides	396	4.3	416	5.4

The formed rod elements were cut into 50 mm long specimens and endured less than 20 ± 2°C and 65% humidity not less than for 16 h.

To obtain the real strength values of the rods under study under compression various types of face closure has been studied:

1. The faces are simply supported, polished, and assist conditions of free cross-deformation of face areas.
2. The faces are inserted in metal shells to simulate conditions of constrained cross-deformation of outer areas of the rod with some limitations of the inner ones.
3. Faces are inserted into metal shells and filled up with a cold-set compound to simulate conditions of constrained deformation of all face areas of the rod.

The unidirectional and spirally reinforced glass-plastic rods underwent testing. The test results are presented in Table 2.

Figure 2. Failure of samples.

Proceeding from the above, the closure type of rod faces effects noticeably their strength during compression testing. The samples containing spiral layers are more sensitive to this factor as compared to unidirectional ones. Further investigations have given evidences that the samples incorporating a spiral reinforcing layer doesn't exhaust their bearing capacity but breakdown as a result of stability loss of the sample. To eliminate the phenomenon a tubular guide has been mounted for the shells to move with filled-in faces aimed at preserving relative coaxiality. As a result, trustworthy values of strength characteristics of the spirally reinforced rods under compression have been obtained.

The view of the destroyed samples is shown on fig.2

4 CONCLUSION

The conducted theoretical and experimental investigations have proved that introduction of a spiral layer changes SSS and fracture behavior of the rods made of fibrous CM under compression. The effectiveness of the layer is governed by its geometrical parameters and the relationship of the elastic moduli of the main and auxiliary reinforcements. Proposed earlier calculation method enables accurate forecasting of the delamination threshold and fracture behavior of the rod element.

REFERENCES

1. Bolotin V. V. & Novichkov Yu. N. 1980. Mech. of multilayer constructions. Moscow: Mashinostroeniye.
2. Freger, G. E. 1984. Research of composite materials based on spirally reinforced fillers. Mech. of Compos. Mater. 3: 412–416.
3. Freger, G. E. 1983. Investigation of tense state of spirally reinforced composites with high degree of filling. Mech. of Reinforced Plastics. Riga: Polytechnic Institute, 61–68.

Confinement of concrete in compression

FRP Composites in Civil Engineering – CICE 2004 – Seracino (ed)
© 2005 Taylor & Francis Group, London, ISBN 90 5809 638 6

Behaviour of large-scale columns confined with FRP composites in compression

H. Toutanji
Department of Civil and Environmental Engineering, University of Alabama in Huntsville, Huntsville, AL, USA

S. Matthys, L. Taerwe & K. Audenaert
Magnel Laboratory for Concrete Research, Ghent University, Ghent, Belgium

ABSTRACT: The behaviour of fiber reinforced polymer (FRP)-confined concrete has been extensively studied. Most of the existing models have been concerned with small-size cylinders. This paper presents the experimental and analytical results of axially loaded large-scale columns confined with FRP wrapping reinforcement. The effective circumferential FRP failure strain and the effect of increasing confining action were investigated. The reliability of different models for the prediction of the ultimate strength of FRP-confined concrete has been verified when applied to real scale axially loaded columns. A revision of an existing model developed earlier by the first author was presented. The revised model addresses the effective FRP failure strain that is attributed to localized stress concentrations near failure due to non-homogenous deformations of the damaged concrete. A comparison between the experimental results and those predicted by the existing models was investigated. Based on the model verification, results show that only few of these models seem to predict the behaviour of the tested large-scale columns accurately.

1 INRODUCTION

Concrete columns have an important function in the structural concept of many structures. Often, these columns are vulnerable to exceptional loads (such as impact, explosion or seismic loads), load increase (increasing use or change of function of structures, etc.) and degradation (corrosion of steel reinforcement, alkali silica reaction, etc.). On the other hand, confinement of concrete is an efficient technique to increase the load carrying capacity and ductility of concrete members primarily subjected to compression. By providing lateral confining pressure, the concrete is subjected to a tri-axial state of stress, so that the compressive strength and deformability increase. Since the introduction of FRP as externally bonded reinforcement, confinement by means of FRP wrapping has been of considerable interest for upgrading columns, piers, chimneys, etc. and several research programs have been conducted internationally.

To verify the effectiveness of FRP confinement with respect to real-scale axially loaded columns and to investigate some specific aspects of the modeling of FRP confined concrete, compression tests on large-scale columns wrapped with FRP have been performed (Matthys 2000). The variables considered in this test program included FRP type, full or partial wrapping, and fibre orientation (circular or helicoidal). This research mainly focuses on the experimental and analytical work concerning large-scale axially loaded columns, confined with external FRP wrapping reinforcement. The study also looks into the strength modeling of FRP confined concrete, i.e. the effective circumferential FRP failure strain and the effect of increasing confining action.

2 EXPERIMENTAL PROCEDURE

Eight large-scale columns were manufactured. The confined-concrete columns were subjected to axial loading. The test parameters of the wrapped columns are given in Tables 1a, b. The columns had a total length of 2 m, a longitudinal steel reinforcement ratio of 0.9% and 8 mm diameter stirrups spaced every 140 mm. Extra stirrup reinforcement was provided at the column ends. All columns have a 400 mm circular cross-section. Except for columns K6 and K7, the FRP is applied over the total area (full wrapping) in a circular way, providing 200 mm overlap length in the circumferential direction (no overlap was provided in the longitudinal direction). For columns K6 and K7 partial wrapping is applied, either in a circular way with a clear spacing of 200 mm (K6) or in a helicoidal

way with a pitch of 400 mm and a clear spacing of 200 mm (K7).

Different types of FRP reinforcement consisting of CFRP sheets (C240 and C640), GFRP fabrics (TU600/25) and HFRP (hybrid FRP) fabric (TU360G160C/27G) have been used to confine the concrete columns. Tensile tests (according to ASTM D3039/D3039M) were performed on FRP sheet specimens with a width of 50 or 100 mm. Results of the tensile tests of the FRP sheets and the longitudinal steel rebars and stirrups are reported in terms of mean values in Tables 2a, b.

The concrete columns were subjected to an axial load test in a compression testing machine with a capacity of 10000 kN. The load was applied in a displacement controlled mode at 0.5 mm/min. Due to problems with the loading control unit, the displacement rate of column K2 decreased after reaching maximum load. Axial and circumferential deformations of the columns were measured both manually and electronically. Manual measurements comprised dial gauges with a gauge length of 1 m and mechanical deformeters with a gauge length of 200 mm or 50 mm. For the electronic measurements, both strain stirrups (gauge length 200 mm or 80 mm) and strain gauges have been used.

Table 1a. Test parameters of wrapped columns.

		Concrete	
Spec.	Column diameter [mm]	Age at test [days]	f_c' (28 days) [N/mm^2][(1)]
K1	Ø 400	29	31.8
K2	Ø 400	28	34.3
K3	Ø 400	29	34.3
K4	Ø 400	29	39.3
K5	Ø 400	32	39.3
K6	Ø 400	28	35.8
K7	Ø 400	28	35.8
K8	Ø 400	32	39.1

(1) N/mm^2 = MPa.

Table 2a. Mean tensile properties obtained by tensile testing.

Type	Nominal dimensions (mm)	Yield strength (N/mm^2)
Steel Rebar S500[(1)]	Ø 8	560
	Ø 12	620
C-sheet 240 - Multipox T	300 x 0.117[(2)]	–
C-sheet 640 - Multipox T	300 x 0.235[(2)]	–
TU600/25 - PC5800	200 x 0.300[(2)]	–
TU360G160C/27G- PC5800	50 x 0.123[(2)]	–

(1) Characteristic yield strength value equal to 500 N/mm^2.
(2) Equivalent dry-fibre thickness.

Table 2b. Mean tensile properties obtained by tensile testing.

Type	Tensile Strength (N/mm^2)	Ultimate strain (%)	E-modulus (N/mm^2)
Steel Rebar S500[(1)]	610	2.77	200000
	720	8.73	200000
C-sheet 240 - Multipox T	2600	1.19	198000
C-sheet 640 - Multipox T	1100	0.22	480000
TU600/25 - PC5800	780	1.30	60000
TU360G160C/27G-PC5800	1100	0.96	120000

Table 1b. Test parameters of wrapped columns.

	FRP confinement					
Spec.	FRP type [mm]	No. of layers	Width [mm]	Clear spacing [mm]	Pitch [mm]	Wrapping [mm]
K1	–	–	–	–	–	–
K2	C240	5	300	0	0	full
K3	C640	4	300	0	0	full
K4	TU600/25	6	200	0	0	full
K5	TU600/25	2	200	0	0	full
K6	TU600/25	4	200	200	0	partial
K7	TU600/25	4	200	200	400	partial
K8	TU360G160 C/27G	4	50	0	0	full

3 EXPERIMENTAL TEST RESULTS

3.1 *Behaviour at ultimate load*

The test results of the columns in terms of maximum load Q_{max}, axial stress (maximum load Q_{max}/gross column section A_g), strength increase, axial (ε_{c1} and ε_{cu}) and circumferential strains ($\varepsilon_{c\ell 1}$ and $\varepsilon_{c\ell u}$) at maximum and ultimate load respectively and ratio of the circumferential strain $\varepsilon_{c\ell u}$ over the FRP failure strain ε_{fu} are given in Tables 3a, b. The mentioned strains are the mean values of the strain gauge measurements.

The unconfined ultimate compressive strength of the control column (K1) was 37.3 MPa. A strength increase up to 1.62 is found for the different columns and strongly depends on the wrapping lay-out, and FRP type and amount. The confined concrete columns failed by fracture of the FRP reinforcement, as shown in Figure 1. For the fully wrapped circular columns at ultimate load, when confinement action was no longer provided due to FRP fracture, the internal steel started buckling and the crushed concrete fell down between the fractured FRP. For the partially wrapped columns it was noted that the unconfined zones started crushing when reaching the strength of the plain concrete. For these columns, buckling of the internal steel occurred in the unconfined zones, after FRP failure.

Figure 1a. Failure of HFRP fully wrapped column.

Figure 1b. Failure of GFRP partially wrapped column.

Figure 1. Failure aspect of the confined columns.

Table 3a. Test results of compression tests on columns.

Specimen	Q_{max} [kN]	Q_{max}/A_g [N/mm^2]	Q/Q_{ref} [–]
K1 (Ø/Ref.)	4685	37.3	1.00
K2 (Ø/C240/#5/full)	7460	59.4	1.59
K3 (Ø/C640/#4/full)	7490	59.6	1.60
K4 (Ø/G/#6/full)	7580	60.3	1.62
K5 (Ø/G/#2/full)	5325	42.4	1.14
K6 (Ø/G/#4/partial-circ.)	5000	39.8	1.07
K7 (Ø/G/#4/partial-helic.)	4810	38.3	1.03
K8 (Ø/H/#4/full)	6230	49.6	1.33

Table 3b. Test results of compression tests on columns.

Specimen	ε_{c1} [mm/m]	ε_{cu} [mm/m]	$\varepsilon_{c\ell 1}$ [mm/m]	$\varepsilon_{c\ell u}$ [mm/m]	$\varepsilon_{c\ell u}/\varepsilon_{fu}$ [–]
K1 (Ø/Ref.)	2.8	3.1(1)	1.7	1.8(1)	–
K2 (Ø/C240/#5/full)	11.1	(12.0)(2)	6.9	(7.3)(2)	(0.61)(2)
K3 (Ø/C640/#4/full)	4.3	4.3	2.5	2.5	1.14
K4 (Ø/G/#6/full)	6.9	6.9	7.5	7.5	0.58
K5 (Ø/G/#2/full)	3.8	3.8	6.8	8.0	0.62
K6 (Ø/G/#4/partial-circ.)	2.8	3.3	1.6	3.3	0.25
K7 (Ø/G/#4/partial-helic.)	2.2	2.2	3.1	3.3	0.25
K8 (Ø/H/#4/full)	5.9	6.0	5.3	5.3	0.55

(1) Test stopped at an axial strain of about 3.1 mm/m.
(2) Problems with the load control unit of the actuator in the post peak region.

Results show that the strength increase basically depends on the amount and tensile strength of the FRP wrapping. The higher the axial stiffness of the FRP wrapping, the lower the ultimate axial strain and hence the lower the increase in ductility. The ratio $\varepsilon_{\ell u}/\varepsilon_{fu}$ (circumferential ultimate strain/ultimate strain of the fiber) for fully wrapped circular columns (except for K3) was between 0.55 and 0.62 as shown in Table 3b. This may indicate that secondary effects near failure, such as stress concentrations in the FRP due to non-homogeneous deformations of the damaged concrete are significant. This may have led to a non-uniform distribution of the strain in the FRP wrapping. It should be noted that the ultimate tensile failure strain (ε_{fu}) reported by the manufacturer was much higher than the mean strain value obtained in this study. The ultimate failure strain reported by the manufacturer was 0.4%.

Comparing fully and partially wrapped columns with the same type and total amount of FRP (Table 3a, b), less efficiency is obtained in case of partial wrapping as part of the concrete is unconfined. Furthermore, helicoidal wrapping results in a lower strength increase and axial strain compared to circular wrapping. This is due to the fact that the fibres are no longer aligned in an optimum way to restrain the lateral expansion of the concrete. The ratio $\varepsilon_{\ell u}/\varepsilon_{fu}$ obtained for the partially wrapped columns (K6 and K7) equals 0.3, which is much lower than the fully wrapped circular columns.

3.2 *Effective FRP strain coefficient*

According to the obtained test results, the mean effective FRP failure strain (circumferential failure strain, $\varepsilon_{\ell u}$) when reaching the ultimate state of the wrapped members is lower than the ultimate FRP strain $\varepsilon_{fu} = f_f / E_f$. The ratio of the circumferential strain at failure to the ultimate tensile strain of the FRP is referred to, as the effective FRP strain coefficient ($\beta = \varepsilon_{\ell u}/\varepsilon_{fu}$). Thus, the maximum lateral confinement pressure $f_{\ell u}$ is given as:

$$f_{\ell u} = K_{conf} \frac{\beta . f_f}{E_f} \tag{1}$$

For fully wrapped circular cross-sections K_{conf} is given by

$$K_{conf} = \frac{2 t_f E_f}{D} \tag{2}$$

where E_f is the elastic modulus of the FRP composite, f_f is the ultimate strength of the FRP composite, t_f is the thickness of the fiber and D is the diameter of the unconfined concrete.

To quantify the effective FRP strain coefficient (β), using the results of this study and others (Picher 1996, Watanable 1997, Mirmiran 1998, Matthys 1999, Toutanji 1999, Xiao 2000, Pessiki 2001), the coefficient (β) was expressed as a function of the parameter K_{conf}, as shown in Figure 2. For the purpose of obtaining a simple design equation for the lateral confinement pressure, the value β is set to be equal to 0.6. As shown in Figure 2 the effective FRP strain coefficient β, decreases with increasing the stiffness of the fiber. This implies that the value of β for CFRP is lower than that for GFRP, since carbon fiber has higher stiffness than glass fiber. This is in agreement with a study conducted by Lam & Teng (2003), which showed that β equal to 0.583 for CFRP-confined concrete cylinders and 0.669 for GFRP-confined concrete cylinders.

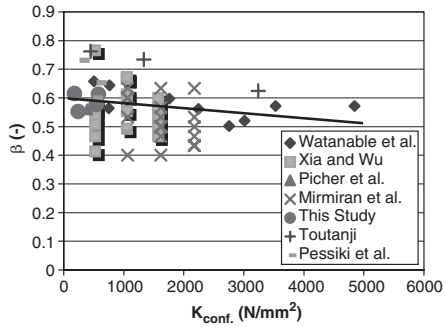

Figure 2. Effective FRP failure strain.

As β is related to f_f/E_f, the strength and stiffness of the FRP should be known. Because the characterization of the tensile properties of FRP is influenced by the way of testing, the tensile strength of the FRP should be determined in accordance with ASTM D3039/D3039M or similar method using flat coupons.

3.3 *Strength models of FRP-confined concrete*

Most of the existing strength models adopted the concept of Richart et al. (1929), in which the strength at failure for concrete confined by a hydrostatic fluid pressure takes the form:

$$f'_{cc} = f'_{co} + k_1 f_l \tag{3}$$

where f'_{cc} is the maximum strength of the confined concrete, f'_{co} is the maximum strength of the unconfined concrete, f_l is the lateral confining pressure, and k_1 is a confinement effectiveness coefficient.

A number of strength models have been proposed specifically for FRP-confined concrete. These models use Eq. (3) with a modified expression for k_1. Based on regression analysis, an equation for k_1 was obtained by Toutanji (1999). When k_1 is substituted in Eq. (3),

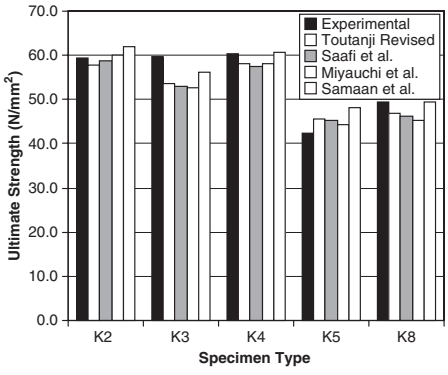

Figure 3. Comparison between the experimental values and those predicted by different models.

an expression to calculate the ultimate confining stress of FRP-confined concrete is obtained:

$$f_{cc}^{'} = f_{co}^{'}\left[1+3.5(\frac{f_l}{f_{co}^{'}})^{0.85}\right] \quad (4)$$

where f_l

$$f_l = \frac{2t_f E_f \varepsilon_l}{D} \quad (5)$$

Experimental data presented in this study and others (Lam & Teng 2003) have shown that the circumferential failure strain is mostly smaller than the ultimate strain obtained from standard tensile testing of the FRP reinforcement. As shown earlier, the effective FRP strain coefficient ($\beta = \varepsilon_{clu}/\varepsilon_{fu}$), was expressed as a constant and equal to 0.6.

Based on this finding, Toutanji's model (1999) was modified to account for the reduction in the lateral confinement stress. Thus, the lateral confining stress becomes:

$$f_l = \frac{2t_f E_f \varepsilon_{clu}}{D} \quad (6a)$$

$$\varepsilon_{clu} = \beta\varepsilon_{fu} \quad (6b)$$

Using a reduction factor β of 0.6 and substituting f_l into Eq. (1), the revised Toutanji's model to predict the ultimate axial compressive strength of FRP-confined concrete columns then can be given by the formula:

$$f_{cc}^{'} = f_{co}^{'}\left[1+2.3(\frac{\bar{f}_l}{f_{co}^{'}})^{0.85}\right] \quad (7a)$$

where

$$\bar{f}_l = \frac{2t_f E_f \varepsilon_{fu}}{D} \quad (7b)$$

where ε_{fu} is the ultimate tensile strength of the FRP.

A comparison between the ultimate strength predicted by various models and the experimental ultimate strength values is shown in Figure 3. Considerable similarities were found between the different models. However, the best predictions were found in models by Miyauchi et al. (1999), Saafi et al. (1999), Samaan et al. (1999), and Toutanji Revised. As expected, the model by Mander et al. (1988) tends to overestimate the ultimate strength. This model was developed for confining concrete under triaxial compression with equal lateral effective confining stress by steel spirals or circular hoops.

4 CONCLUSIONS

Confinement of concrete by means of FRP wrapping is an efficient technique to increase strength and ductility. The quality of execution and the wrapping configuration have a considerable influence on the effectiveness of the FRP wrapping. Beside the effectiveness (influence of partial wrapping and fibre orientation), the strength increase basically depends on the amount and tensile strength of the FRP wrapping. The increase in ductility (ultimate axial strain) is inversely proportional to the stiffness (E-modulus) of the FRP wrapping. Hence, for a given type of FRP, the higher the strength increase the lower the increase in ductility.

Due to several influencing factors, among which the local stress concentrations near failure, a reduced mean FRP failure strain is found for the wrapped specimens. To model this aspect, a reduction coefficient was introduced, referred to as the effective FRP strain coefficient ($\beta = \varepsilon_{lu}/\varepsilon_{fu}$), which is equal to 0.6. Because the characterization of the tensile properties of FRP is influenced by the way of testing, the tensile strength of the FRP should be determined in accordance with ASTM D3039/D3039M or similar method using flat coupons.

Four models, by Miyauchi et al. (1999), Saafi et al. (1999), Samaan et al. (1999), and Toutanji Revised, were found to predict the ultimate strength of FRP-confined concrete quite accurately. Results show that the predicted ultimate strengths compare well with those of experimental.

ACKNOWLEDGEMENT

The authors wish to acknowledge the financial support provided by the IWT (Institute for the Promotion

of Innovation by Science and Technology in Flanders). The financial support provided by Magnel Laboratory and Ghent University to support Professor Toutanji's sabbatical leave is also greatly acknowledged. In addition, the authors would like to thank Fortius, Syncoglas, ECC, Resiplast and S&P companies for their contributions of materials.

REFERENCES

ASTM D3039/D3039M 1995. Standard test method for tensile properties of polymer matrix composite materials. Annual book of ASTM Standards. *American Society for Testing and Materials (ASTM)* 15.03, Philadelphia, USA.

Lam, L. & Teng, J.G. 2003. Stress-strain for FRP-confined concrete for design application. In K. H. Tan (ed), *Proceedings of 6th International Symposium on Fiber Reinforced Polymer Reinforcement for Concrete Structures (FRPRCS-6)* 2: 601–612, Singapore.

Mander, J.B., Priestley, M.J.N. & Park, R. 1988. Theoretical stress-strain model for confined concrete. *Journal of ASCE Structural Engineering* 114(8): 1804–1826.

Matthys S., Taerwe L. & Audenaert K. 1999. Tests on axially loaded concrete columns confined by FRP sheet wrapping. In C.W. Dolan, S.H. Rizkalla, A. Nanni (eds), *Proceedings of 4th International Symposium on FRP for Reinforced Concrete Structures (FRPRCS-4)*: 217–228, Baltimore, USA.

Matthys, S. 2000. *Structural behavior and design of concrete members strengthened with externally bonded FRP reinforcement.* PhD Dissertation, University of Gent, Gent, Belgium.

Mirmiran, A., Shahawy, M., Samaan, M., El Echary, H., Mastrapa, J.C. & Pico, O. 1998. Effect of column parameters on FRP-confined concrete. *Journal of ASCE Composites for Construction* 2(4): 175–185.

Miyauchi, K., Inoue, S., Kuroda, T. & Kobayashi, A. 1999. Strengthening effects of concrete columns with carbon fiber sheet. *Transportation Japan Concrete Institute* 21: 143–150.

Pessiki, S., Harries K.A., Kestner, J.T, Sause, R. & Ricles, J.M. 2001. Axial behavior of reinforced concrete columns confined with FRP jackets. *Journal of ASCE Composites for Construction* 5(4): 237–245.

Picher, F., Rochette, P. & Labossiere, P. 1996. Confinement of Concrete Cylinders with CFRP. In H. Saadatmanesh & M. Ehsani (eds), *Proceedings of 1st International Symposium on Composites for Infrastructures*: 829–841, Tucson, Arizona.

Richart, F.E., Brandtzaeg, A. & Brown, R.L., 1929. The Failure of Plain and Spirally Reinforced Concrete in Compression. *Bulletin 190*, University of Illinois Engineering Experimental Station, Champaign, Illinois, USA.

Saafi, M., Toutanji, H.A. & Li, Z. 1999. Behavior of concrete columns confined with fiber reinforced polymer tubes. *ACI Materials Journal* 96(4): 500–509.

Samaan, M., Mirmiran, A. & Shahawy, M. 1999. Model of concrete confined by fiber composites. *Journal of ASCE Structural Engineering* 124(9): 1025–1031.

Toutanji, H.A. 1999. Stress-strain characteristics of concrete columns externally confined with advanced fiber composite sheets. ACI *Materials Journal* 96(3): 397–404.

Watanable, K., Nakamura, H., Honda, Y., Toyoshima, M., Iso, M., Fujimaki, T., Kaneto, M. & Shirai, N. 1997. Confinement effect of FRP sheet on strength and ductility of concrete cylinders under uniaxial compression. In *Proceedings of 3rd International Symposium on Non-Metallic (FRP) Reinforcement for Concrete Structures (FRPRCS-3)* 1: 233–240, Sapporo, Japan, JCI.

Xiao, Y. & Wu, H. 2000. Compressive behavior of concrete confined by carbon fiber composite jackets. *Journal of ASCE Materials Journal* 12(2): 139–146.

FRP Composites in Civil Engineering – CICE 2004 – Seracino (ed)
© 2005 Taylor & Francis Group, London, ISBN 90 5809 638 6

Theoretical model for concrete confined with FRP

Y.L. Huang
Department of Civil Engineering, Tsinghua University, Beijing, China

J.G. Teng & L. Lam
Department of Civil and Structural Engineering, The Hong Kong Polytechnic University, Hong Kong, China

L.P. Ye
Department of Civil Engineering, Tsinghua University, Beijing, China

ABSTRACT: Fiber reinforced polymer (FRP) composites have found increasingly wide applications in civil engineering due to their high strength-to-weight ratio and high corrosion resistance. One important application of FRP composites is as a confining material for concrete, particularly in the strengthening or seismic retrofit of existing reinforced concrete (RC) columns by the provision of an FRP jacket. FRP confinement can greatly enhance both the compressive strength and the ultimate strain of concrete. This paper presents a new stress–strain model for FRP-confined concrete in which the responses of the concrete and the FRP jacket as well as their interaction are explicitly considered. The key new feature of this model compared to existing models is a more accurate and more widely applicable lateral strain equation based on careful interpretations of test results of unconfined, actively confined and FRP-confined concrete. The model is shown to be accurate by comparing its predictions with results from tests on FRP-confined concrete. Furthermore, the model is also shown to give accurate predictions for steel tube-confined concrete, demonstrating the wide applicability of the model to concrete confined by different confining materials.

1 INTRODUCTION

Fiber reinforced polymer (FRP) composites have found increasingly wide applications in civil engineering due to their high strength-to-weight ratio and high corrosion resistance. One important application of FRP composites is as a confining material for concrete, particularly in the strengthening or seismic retrofit of existing reinforced concrete (RC) columns by the provision of an FRP jacket. FRP confinement can greatly enhance both the compressive strength and the ultimate strain of concrete.

A large number of studies have been carried out on the compressive behavior of FRP-confined concrete, leading to various stress–strain models. These models fall into two categories: (1) design-oriented models presented in closed-form expressions; and (2) analysis-oriented models which predict stress–strain curves using an incremental procedure. For a comprehensive and critical review of existing stress–strain models for FRP-confined concrete, the reader is referred to Teng & Lam (2004). While design-oriented models are given in closed-form expressions derived directly from test results, analysis-oriented models consider the responses of the concrete and the FRP jacket as well as their interaction in an explicit manner.

The majority of analysis-oriented models are based on the assumption that the axial stress and axial strain of concrete confined by a jacket at a given lateral strain are the same to those of the same concrete actively confined with a constant confining pressure which is equal to that supplied by the jacket. Such models include those developed by Mirmiran & Shahawy (1996), Spoelstra & Monti (1999), Fam & Rizkalla (2001), Chun & Park (2002), and Harries & Kharel (2002). As a result of this assumption, for a given axial strain, the axial stress of FRP-confined concrete can be evaluated using an active confinement model for concrete, provided the confining pressure at this moment (i.e. the current confining pressure) is known. The current confining pressure can be determined without difficulty if the lateral strain for the given axial strain is known. Therefore, the lateral strain–axial strain relationship, which is in general neither required nor available in an active confinement model, is the key to an accurate confinement model for FRP-confined concrete. It should be noted that as the confining pressure in FRP-confined concrete varies continuously with axial

strain while an active confinement model provides a family of stress–strain curves with each being for a given constant confining pressure, the evaluation of the stress–strain response of FRP-confined concrete using an active confinement model is a step-by-step incremental process.

In all five FRP confinement models mentioned above, the model by Mander et al. (1988) for steel-confined concrete is adopted as the active confinement model with no or slight modification. It may be noted that the behavior of concrete confined by steel transverse reinforcement with a yield plateau is very similar to that of actively confined concrete after the yielding of steel. These models however employ rather different lateral strain-axial strain relationships. Mirmiran & Shahawy (1996), Spoelstra & Monti (1999), Fam & Rizkalla (2001) and Chun & Park (2002) based their lateral strain equations on test results of actively confined or unconfined concrete. The validity of these equations for FRP-confined concrete has not been appropriately justified. Harries & Kharel (2002) based their two lateral strain equations (one for GFRP confinement and the other for CFRP confinement) on their own test results of FRP-confined concrete, but the accuracy is questionable due to the limitation of their test data (Teng & Lam 2004).

This paper presents a brief summary of a new analysis-oriented stress–strain model for FRP-confined concrete. Additional information on this model can be found elsewhere (Huang et al. 2004). The key new feature of this model is a more accurate and more widely applicable lateral strain equation based on careful interpretations of test results of unconfined, actively confined and FRP-confined concrete (Huang et al. 2004). The model is shown to be accurate by comparing its predictions with test results of FRP-confined concrete as well as steel tube-confined concrete.

2 LATERAL STRAIN-AXIAL STRAIN RELATIONSHIP

Based on test observations, the following expression is proposed to describe the lateral strain–axial strain relationship for unconfined concrete (Huang et al. 2004):

$$\frac{\varepsilon_c}{\varepsilon_{co}} = \Phi\left(\frac{-\varepsilon_l}{\varepsilon_{co}}\right) = A\left\{\left[1+B\left(\frac{-\varepsilon_l}{\varepsilon_{co}}\right)\right]^C - \exp\left[D\left(\frac{-\varepsilon_l}{\varepsilon_{co}}\right)\right]\right\} \quad (1)$$

where ε_c and ε_l are the axial strain and the lateral strain of concrete respectively; ε_{co} is the axial strain at the unconfined concrete strength; and A, B, C, and D are constants to be determined. The sign convention adopted in this paper is as follows: compressive stresses and strains in the concrete are positive but in the FRP, tensile stresses and strains are positive. For confined concrete, the effect of confining pressure σ_l on lateral strains is important and can be captured by the following equation (Huang et al. 2004):

$$\frac{\varepsilon_c}{\varepsilon_{co}} = \Phi\left(\frac{-\varepsilon_l}{\varepsilon_{co}}\right)\cdot\left(\alpha+\beta\frac{\sigma_l}{f_{co}'}\right) \quad (2)$$

where f_{co}' is the compressive strength of unconfined concrete, and α and β are constants to be determined. For actively confined concrete, σ_l is a constant value throughout the loading history, but for FRP-confined concrete, σ_l increases with the hoop strain ε_h and is given by

$$\sigma_l = \frac{E_{frp}t\varepsilon_h}{R} \quad (3)$$

where E_{frp} is the elastic modulus of the FRP jacket in the hoop direction, t is the thickness of the FRP jacket, R is the radius of the confined concrete core, and $\varepsilon_h = -\varepsilon_l$. The ratio between σ_l and f_{co}' is defined as the current confinement ratio.

For Eq. 3 to be applicable to unconfined concrete, it is obvious that $\alpha = 1$. A trial and error process showed that the available test data are best approximated with $\beta = 8$ (Huang et al. 2004). Furthermore, the constants A, B, C and D in Eq. 1 were determined using the available test data, with the final expression of the lateral strain–axial strain relationship being

$$\Phi\left(\frac{-\varepsilon_l}{\varepsilon_{co}}\right) = \frac{\varepsilon_c}{\varepsilon_{co}}\Big/\left(1+8\frac{\sigma_l}{f_{co}'}\right) = 0.85\left\{\left[1+0.75\left(\frac{-\varepsilon_l}{\varepsilon_{co}}\right)\right]^{0.7} - \exp\left[-7\left(\frac{-\varepsilon_l}{\varepsilon_{co}}\right)\right]\right\} \quad (4)$$

In Fig. 1, the normalized axial strain $\varepsilon_c/\varepsilon_{co}$. with further normalization to account for the effect of confining pressure (referred to as the equivalent normalized axial strain) is plotted against the normalized lateral strain $\varepsilon_l/\varepsilon_{co}$. In Fig. 1a, the test results of six unconfined concrete cylinders (152 mm × 305 mm) from Lam et al. (2004) with a strength of around 40 MPa are compared with the predictions of Eq. 4. In Fig. 1b, a similar comparison is presented for the results of 16 tests conducted by Candappa et al. (2001) on 100 mm × 200 mm cylinders with the unconfined concrete strength ranging from 40 MPa to 100 MPa, and 6 tests by Sfer et al. (2002) on 150 mm × 300 mm cylinders with unconfined concrete strengths of 32.8 MPa and 38.8 MPa. These specimens were tested with active

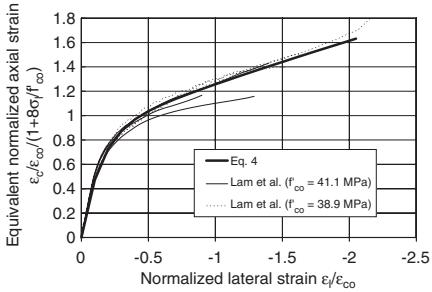

(a) Unconfined concrete

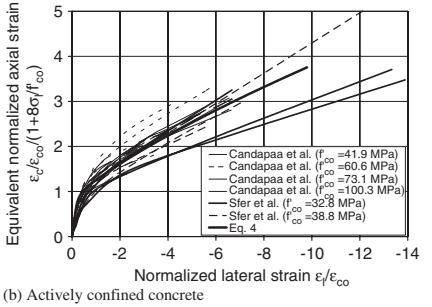

(b) Actively confined concrete

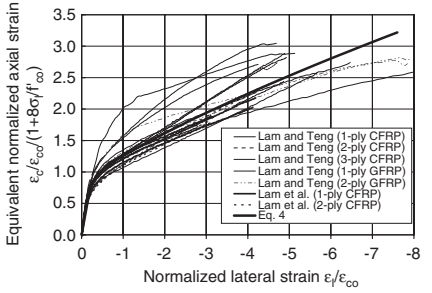

(c) FRP-confined concrete

Figure 1. Performance of the proposed lateral strain equation.

confinement at lateral pressures ranging from 1.5 MPa to 12 MPa. In Fig. 1c, the comparison is for the results of 16 tests on 152 mm × 305 mm concrete cylinders confined with FRP from Lam et al. (2004) and Lam & Teng (2004) with an unconfined concrete strength being around 40 MPa. These specimens were confined with FRP jackets comprising one to three plies of carbon FRP (CFRP) or one or two plies of glass FRP (GFRP). It is important to note that while the lateral strain–axial strain responses of these unconfined, actively confined and FRP-confined specimens are very different (Huang et al. 2004), the equivalent lateral strain–axial strain responses are reasonably close to each other. A few curves for FRP-confined concrete fall significantly above the predictions of Eq. 4 (e.g. the three specimens with three plies of CFRP). These results are from load-controlled tests by Lam & Teng (2004) so the different loading method may be a reason for the deviation, although other results from the same batch of load-controlled tests match Eq. 4 better. Most of the test results shown in Fig. 1 were obtained from displacement-controlled tests, including those by Lam et al. (2004), Candappa et al. (2001) and Sfer et al. (2002). Based on the comparisons shown in Fig. 1, it may be concluded that Eq. 4 provides a reasonably accurate lateral strain–axial strain relationship applicable to confined and unconfined concrete.

It is of considerable interest to note that the equivalent lateral strain–axial strain responses of high strength concrete (Fig. 1b) can be considered to be similar to those of normal strength concrete. Indeed, for the three tests on concrete with an unconfined strength of 32.8 MPa, the response of one specimen deviates from those of the other two of the same concrete strength in a range that encompasses the difference caused by a much higher concrete strength. This large variability in concrete lateral strain for a given axial strain is not surprising and has been discussed by van Mier et al. (1986). This fact should be borne in mind when discussing the accuracy of a model for FRP-confined concrete in which the lateral strain–axial strain equation is the key link between the responses of the concrete and the FRP.

3 STRESS–STRAIN RESPONSE

Once the lateral strain–axial strain relationship is available, the axial stress–strain response of FRP-confined concrete can be predicted without difficulty using the same approach as adopted in existing analysis-oriented models based on an active confinement model. The following axial stress–axial strain equation is used in all five existing models based on an active confinement model, which was originally proposed by Popovics (1973) and used in Mander et al.'s model (1988) for steel-confined concrete:

$$\frac{\sigma_c}{f'^{*}_{cc}} = \frac{\left(\varepsilon_c/\varepsilon^{*}_{cc}\right)r}{r-1+\left(\varepsilon_c/\varepsilon^{*}_{cc}\right)^{r}} \tag{5}$$

where σ_c is the axial stress of concrete, f'^{*}_{cc} and ε^{*}_{cc} are the peak axial stress and the corresponding axial strain of concrete under a specific constant confining pressure, respectively. The constant r in Eq. 5, approximately accounting for the brittleness of the concrete, is defined in Carreira & Chu (1985) as

$$r = \frac{E_c}{E_c - f'^{*}_{cc}/\varepsilon^{*}_{cc}} \tag{6}$$

where E_c is the elastic modulus of concrete. To determine f'^*_{cc}, the well-known equation proposed by Mander et al. (1988) for the axial compressive strength of concrete with active confinement is used in other analysis-oriented models (Mirmiran & Shahawy 1996, Spoelstra & Monti 1999, Fam & Rizkalla 2001, Chun & Park 2002). Mander et al.'s equation was found to be unsuitable for use with Eqs. 5 and 6 for accurate predictions of the stress–strain behavior of FRP-confined concrete (Huang et al. 2004), so in the present model, the following equations are used for f'^*_{cc} and ε^*_{cc}

$$\frac{f'^*_{cc}}{f'_{co}} = 1 + k_1 \frac{\sigma_l}{f'_{co}} \tag{7}$$

$$\frac{\varepsilon^*_{cc}}{\varepsilon_{co}} = 1 + k_2 \frac{\sigma_l}{f'_{co}} = 1 + 5k_1 \frac{\sigma_l}{f'_{co}} \tag{8}$$

where k_1 is the confinement effectiveness coefficient. These equations with $k_1 = 4.1$ were originally proposed by Richart et al. (1928, 1929) for actively confined and steel confined concrete. For use in the present model, the test results from FRP-confined concrete can be accurately predicted using $k_1 = 3.5$ (Huang et al. 2004). That is,

$$\frac{f'^*_{cc}}{f'_{co}} = 1 + 3.5 \frac{\sigma_l}{f'_{co}} \tag{9}$$

$$\frac{\varepsilon^*_{cc}}{\varepsilon_{co}} = 1 + 17.5 \frac{\sigma_l}{f'_{co}} \tag{10}$$

It should be noted that Eq. 9, defining the failure surface of actively confined concrete for use in the proposed stress–strain model, does not give the compressive strength of FRP-confined concrete f'_{cc}, as the compressive strength of FRP-confined concrete generally occurs on the descending branch of a corresponding stress–strain curve of actively confined concrete (Fig. 2) and is thus generally lower than the compressive strength of actively confined concrete with a constant confining pressure equal to the maximum confining pressure reached in an FRP jacket. The difference between f'^*_{cc} and f'_{cc} is shown in Fig. 2. Indeed, the compressive strength of concrete f'_{cc} with sufficient FRP confinement, which is reached when the FRP jacket ruptures, has been given by Lam & Teng (2003) as

$$\frac{f'_{cc}}{f'_{co}} = 1 + 3.3 \frac{f_l}{f'_{co}} \tag{11}$$

where f_l is the maximum confining pressure provided by the FRP jacket at hoop rupture, which is given by

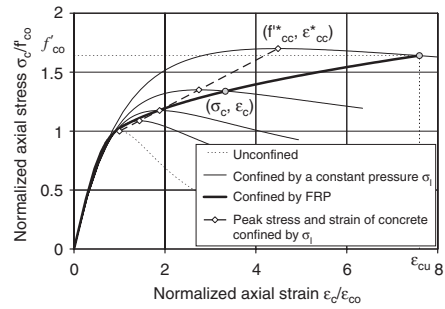

Figure 2. Generation of a stress–strain curve of FRP-confined concrete.

Eq. 3 with the hoop strain ε_h being that at hoop rupture $\varepsilon_{h,rup}$. Eq. 11 is thus consistent with Eq. 9.

Using Eqs. 4–6, 9 and 10, the axial stress–axial strain and the axial stress–lateral strain curves of FRP-confined concrete can be easily generated. The process is incremental, and becomes iterative if the axial strain is first specified. With the specified axial strain, the corresponding lateral strain ε_l and confining pressure σ_l for a given axial strain have to be found from Eqs. 3 and 4 through an iterative process. The prediction of a stress–strain curve of FRP-confined concrete using this procedure can be understood by examining Fig. 2. On the other hand, if the lateral strain of confined concrete is specified first, the corresponding confining pressure σ_l can be found from Eq. 3 and the corresponding axial strain ε_c can be directly obtained from Eq. 4.

For the application of the present model, it is suggested that the elastic modulus of unconfined concrete $E_c = 4730\sqrt{f'_{co}}$, and the axial strain at the peak stress of unconfined concrete $\varepsilon_{co} = 0.0022$, unless these values are available from tests. The latter is suggested by Eurocode 2 (ENV 1992 1991) for use in analysis.

4 COMPARISON WITH TEST DATA

Figure 3 shows a comparison between the predictions of the proposed model and the results obtained by Xiao & Wu (2000) from tests on 152 mm × 305 mm concrete cylinders. The concrete had an unconfined compressive strength of 33.7 MPa at an axial strain of 0.0026. The nine cylinders were confined by one to three plies of CFRP. The tensile strength and the elastic modulus of the CFRP were 1,577 MPa and 105,000 MPa respectively based on a nominal thickness of 0.38 mm per ply. In obtaining the predictions using the present model, the elastic modulus of unconfined concrete was taken to be $E_c = 4730\sqrt{f'_{co}}$ (MPa) which was also used in obtaining other results given

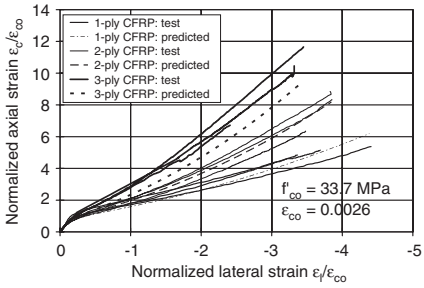

(a) Axial strain vs. lateral strain

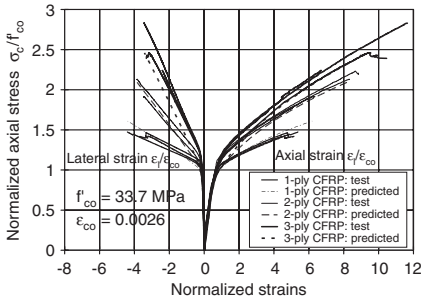

(b) Axial strain vs. axial and lateral strains

Figure 3. Comparison with Xiao and Wu's tests on CFRP-confined specimens.

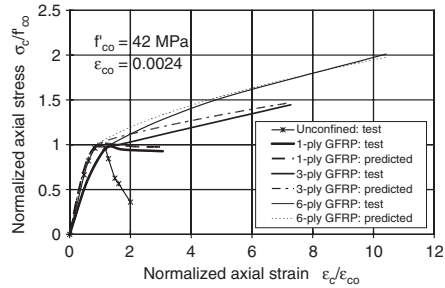

Figure 4. Comparison with Aire et al.'s tests on GFRP-confined specimens.

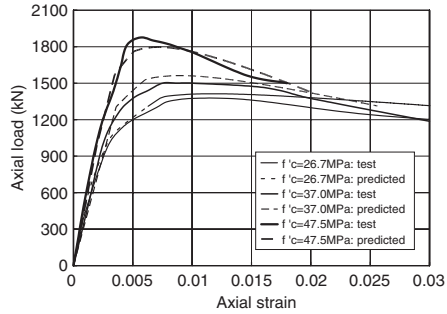

Figure 5. Comparison with Xiao et al.'s tests on steel-confined specimens.

in this paper. A good agreement between the predictions and the test data is observed for the stress–strain curves. Additional comparisons with the test data of Xiao & Wu (2000) are given in Huang et al. (2004) where it can be seen that the proposed model does not always predict the test results as closely as seen in Fig. 3. Nevertheless, the overall agreement between the predictions of the model and their test results is satisfactory, given the known variability of concrete behavior.

Figure 4 shows a comparison between the predictions of the proposed model and the test results obtained by Aire et al. (2001) on 150 mm × 300 mm concrete cylinders with an unconfined concrete strength of 42 MPa at an axial strain of 0.0024. These cylinders were confined with one, three, and six plies of GFRP. The elastic modulus and tensile strength of the GFRP were 65 GPa and 3,000 MPa respectively, based on a nominal thickness of 0.149 mm per ply. The lateral strains reported by Aire et al. (2001) are not used for comparison here as they appear to be unreliable, so the axial stresses are predicted using the proposed model from the available axial strains. It can be seen from Figure 4 that the specimen confined by 1 ply of GFRP has a stress–strain curve with a descending branch while the other specimens have bilinear ascending stress–strain curves. The proposed model provides reasonably close predictions for the responses of all these three specimens. The differences between the test data and the predictions for the initial responses is believed to be due to the use of $\varepsilon_{co} = 0.0024$ obtained from the unconfined specimen which is also shown in Figure 4. Apparent differences between the test stress–strain curves of unconfined and confined specimens can be seen at the initial stage of loading.

Since the present confinement model employs a lateral–axial strain equation of confined concrete that is independent of the type of confining material, the model can be expected to be applicable to concrete confined by materials other than FRP. In this sense, the present model is a unified model for concrete confined by different materials provided the stress–strain response of the confining device is appropriately modeled instead of using Eq. 3. Figure 5 shows a comparison between the predictions of the proposed model and the test results obtained by Xiao et al. (1991) on 170 mm × 350 mm concrete cylinders with unconfined concrete strength of 26.7 MPa at an axial

strain of 0.0024. These cylinders were confined with a steel tube with a thickness of 2.28 mm. The elastic modulus, yield stress and tensile strength of the steel were 220 GPa, 294 MPa, and 372 MPa, respectively. An iterative procedure is necessary when calculating the response of the steel tube subjected to biaxial stresses and this was realized using ABAQUS (2003) in this study. This is due to the incremental form of the flow theory of plasticity. The proposed model provides reasonably close predictions of the responses of all these three specimens, especially the positions of the yield point and the failure point, as well as the slope of the descending branch.

5 COMPARISON WITH OTHER MODELS

Teng & Lam (2004) compared the accuracy of different analysis-oriented models in predicting the results of selected tests on CFRP- and GFRP-confined cylinders conducted by Lam & Teng (2004). Figure 6 shows the comparisons between the predictions of available analysis-oriented models including the present model with test results. Details of the specimens are also shown in these figures. The elastic moduli and material ultimate tensile strains of the FRPs were obtained from flat coupon tests according to ASTM D3039 (1995) and calculated based on the nominal thicknesses, which were 0.165 mm per ply for the CFRP and 1.27 mm per ply for the GFRP. In predicting the stress–strain curves, the elastic modulus E_c and initial Poisson's ratio ν_c of unconfined concrete were either those specified in an individual model or taken to be $E_c = 4730\sqrt{f'_{co}}$ (MPa) and $\nu_c = 0.18$ if they are not specified in the model. The axial strain at the compressive strength of unconfined concrete ε_{co} was assumed a constant value of 0.002 for all models for a fair comparison for the other models as most of these models were developed based on this value, despite that $\varepsilon_{co} = 0.0022$ is normally suggested for use with the present model as stated earlier. The predicted stress–strain curves terminate at the point where the average FRP hoop rupture strains from the tests are reached. For the CFRP-confined concrete cylinders (Fig. 6a), the models of Spoelstra & Monti (1999), Fam & Rizkalla (2001), Chun & Park (2002) and the present model perform well and are superior to other models. However, for the GFRP-confined concrete cylinders (Fig. 6b), only the present model provides close predictions.

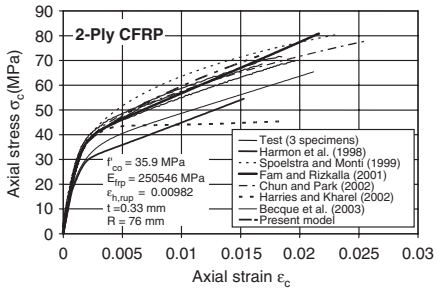

(a) Specimens confined with 2 plies of CFRP

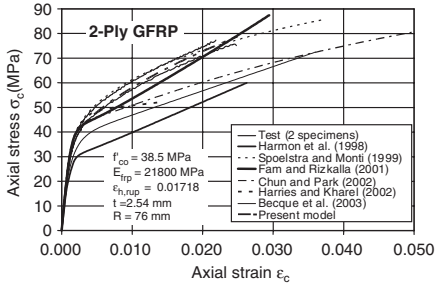

(b) Specimens confined with 2 plies of GFRP

Figure 6. Comparisons with other analysis-oriented models.

6 CONCLUSIONS

This paper has presented a new analysis-oriented stress–strain model for FRP-confined concrete in which the responses of the concrete and the FRP jacket as well as their interaction are explicitly considered. The key new feature of this model is a more accurate and widely applicable lateral strain equation based on careful interpretations of test results of unconfined, actively confined and FRP-confined concrete. In addition, a new failure surface is defined for use in the active confinement model employed in the proposed model based on test results of FRP-confined concrete. Independent test data were compared with predictions of the proposed model to demonstrate its accuracy. The advantages of the present model over existing analysis-oriented models include both simplicity and accuracy. It should be noted that although the focus of the paper has been on the stress–strain behavior of normal strength concrete confined with FRP, the proposed lateral strain equation is likely to be applicable to concrete of different strengths including high strength concrete. This equation therefore provides a starting point for the modeling of FRP-confined high-strength concrete. Furthermore, as the present confinement model employs a lateral-axial strain equation of confined concrete that is independent of the type of confining material, the model can be expected to be applicable to concrete confined by materials other than FRP. In this sense, the present model is a unified model for concrete confined by different materials (e.g. a material with a nonlinear stress–strain curve) provided

the stress–strain response of the confining device is appropriately accounted for. The success of the model in predicting steel tube-confined concrete has been demonstrated in the paper.

ACKNOWLEDGEMENTS

The authors are grateful for the financial support received from the Research Grants Council of the Hong Kong SAR (Project No: PolyU 5064/01E), the Natural Science Foundation of China (National Key Project No. 50238030), and The Hong Kong Polytechnic University provided through its Area of Strategic Development (ASD) Scheme for the ASD in Urban Hazard Mitigation.

REFERENCES

ABAQUS. 2003. *ABAQUS/Standard Theory and User's Manuals*, ABAQUS, Inc.

Ahmad, S.H. & Shah, S.P. 1982. Stress-strain curves of concrete confined by spiral reinforcement. *ACI Journal* 79(6): 484–490.

Aire, C., Gettu, R. & Casas, J.R. 2001. Study of the compressive behavior of concrete confined by fiber reinforced composites", In J. Figueiras, L. Juvandes, R. Faria, A.T. Marques, A. Ferreira, J. Barros, & J. Appleton (eds), *Composites in Constructions, Proceedings of the International Conference*. 239-243. A.A. Balkema Publishers, Lisse, The Netherlands.

ASTM D3039/D3039M – 95. 1995. Standard test method for tensile properties of polymer matrix composites materials. *Annual Book of ASTM Standards* 14.02.

Becque, J., Patnaik, A.K. & Rizkalla, S.H. 2003. Analytical models for concrete confined with FRP tubes. *Journal of Composites for Construction*. ASCE. 7(1): 31–38.

Candappa, D.C., Sanjayan, J.G. & Setunge, S. 2001. Complete triaxial stress-strain curves of high-strength concrete. *Journal of Materials in Civil Engineering*. ASCE. 13(3): 209–215.

Carreira, D.J. & Chu, K.-H. 1985. Stress-strain relationship for plain concrete in compression. *ACI Journal* 82(6): 797–804.

Chun, S.S. & Park, H.C. 2002. Load carrying capacity and ductility of RC columns confined by carbon fiber reinforced polymer. *Proceedings. Third International Conference on Composites in Infrastructure*. in CD-Rom format.

Fam, A.Z. & Rizkalla, S.H. 2001. Confinement model for axially loaded concrete confined by circular fiber-reinforced polymer tubes. *ACI Structural Journal* 98(4): 451–461.

Harmon, T.G., Ramakrishnan, S. & Wang, E.H. 1998. Confined concrete subjected to uniaxial monotonic loading. *Journal of Engineering Mechanics*. ASCE. 124(12): 1303–1308.

Harries, K.A. & Kharel, G. 2002. Behavior and modeling of concrete subject to variable confining pressure. *ACI Materials Journal* 99(2): 180–189.

Huang, Y.L., Teng, J.G., Lam, L. & Ye, L.P. 2004. Analysis-oriented stress-strain model for FRP-confined concrete. to be published.

Lam, L. & Teng, J.G. 2003. Design-oriented model for FRP-confined concrete. *Construction and Building Materials* 17(6–7): 471–489.

Lam, L. & Teng, J.G. 2004. Ultimate condition of FRP-confined concrete. *Journal of Composites for Construction.*ASCE. 8(6).

Lam, L. Teng. J.G., Cheung, C.H. & Xiao, Y. 2004. Behavior of FRP-confined concrete under cyclic axial compression, *Proceedings, International Symposium on Confined Concrete*, Changsha, China, 12–14 June.

Madas, P. & Elnashai, A.S. 1992. A new passive confinement model for the analysis of concrete structures subjected to cyclic and transient dynamic loading. *Earthquake Engineering and Structural Dynamics* 21: 409–431.

Mander, J.B., Priestley, J.N. & Park, R. 1988. Theoretical stress-strain model for confined concrete. *Journal of Structural Engineering.* ASCE. 114(8): 1804–1826.

Mirmiran, A. & Shahawy, M. 1996. A new concrete-filled hollow FRP composite column. *Composites Part B: Engineering* 27B(3–4): 263–268.

Popovics, S. 1973. A numerical approach to the complete stress-strain curve of concrete. *Cement and Concrete Research* 3(5): 583–599.

Richart, F.E., Brandtzaeg, A. & Brown, R.L. 1928. A Study of the failure of concrete under combined compressive stresses. *Bulletin No. 185.* University of Illinois. Engineering Experimental Station. Urbana. Ill.

Richart, F.E., Brandtzaeg, A. & Brown, R.L. 1929. The failure of plain and spirally reinforced concrete in compression. *Bulletin No. 190.* University of Illinois. Engineering Experimental Station. Urbana. Ill. 1929.

Sfer, D., Carol, I., Gettu, R. & Etse, G. 2002. Study of the behavior of concrete under triaxial compression. *Journal of Engineering Mechanics.*ASCE. 128(2): 156–163.

Spoelstra, M.R. & Monti, G. 1999. FRP-confined concrete model. *Journal of Composites for Construction.* ASCE. 3(3): 143–150.

Teng, J.G. & Lam, L. 2004. Behaviour and modelling of FRP-confined concrete. *Journal of Structural Engineering.* ASCE. 130(11).

van Mier, J. G. M. 1986. Multiaxial strain-softening of concrete Part 1: fracture. *Materials and Structures* 19(111): 179–190.

Xiao, Y. & Wu, H. 2000. Compressive behavior of concrete confined by carbon fiber composite jackets. *Journal of Materials in Civil Engineering.* ASCE. 12(2): 139–146.

Xiao, Y., Masahide, T. & Kenji, S. 1991. Triaxial compressive behavior of confined concrete. *Journal of Concrete Research and Technology*. JCI. 2(1): 1–14.

FRP Composites in Civil Engineering – CICE 2004 – Seracino (ed)
© 2005 Taylor & Francis Group, London, ISBN 90 5809 638 6

Strengthening of RC elements using CFRP: the French studies and the main results

J.-L. Clément
Laboratoire central des Ponts et Chaussées, Paris, France

ABSTRACT: A French institutional research program began in 2000 about the reinforcement and the strengthening of RC elements using CFRP. Today, at the end of this program, the main topics and the main results lead us to some conclusions, which will be presented here. The main topics are first the retrofitting of cylindrical concrete samples, under static and creep loading, then the fatigue behavior of small pre cracked RC beams with or without CFRP, RC prism subjected to localized loading, and finally the strengthening of RC columns loaded in composed flexion. Some of these results are now in French recommendations, which will be published in the beginning of 2004. Furthermore, we try now to answer to some questions, as for example the bond length between concrete and CFRP, using comparative tests and modeling. These different sections will be briefly presented in this paper.

1 RESEARCH PROGRAM

1.1 *Presentation*

At the LCPC. (Laboratoire Central des Ponts et Chaussées, France), which depends directly of the French Research Minister and the French Transportation Minister, the research is defined as projects of 4 or 5 years. In 2000, we had to write a general research program about the repairing and the strengthening of RC structures using CFRP. Today, it is the end of this first program and the main topics, results, and interrogations will be presented here.

1.2 *Main topics*

Some international rules or recommendations are existing, but nothing in France at the beginning of these studies even if some studies was soon performed (Varastehpour et al, 1997 & Ferrier et al, 1999). The main objective was to publish some recommendations, in collaboration with a task group of the AFGC, the French Association of Civil Engineering (AFGC 2003), which is directed by Pr. Hamelin.

So we decided to work on the retrofitting of concrete samples, under static and long term loading, in order to define a confinement model in simple cases.

We studied the fatigue behavior of pre cracked RC beams too, in order to be able to qualify the mechanical durability of CFRP when it is not possible to inject some resin into cracks and to define a design value of strength in the FRP.

We performed also some static tests on RC prism, strengthened or not, submitted to localized loading. The objective is to test some CFRP strengthened element in particular case as the end of bridge piles.

And we have just finish at the end of 2003 an experimental test campaign of buckling RC columns, with an initial eccentricity. In that case, two reinforcements and two concretes were chosen, with composites plates and/or carbon fabrics. The objective is to defined some design rules and a lot of time is now necessary to define these rules. Furthermore, some particular results will be presented.

2 RETROFITTING

2.1 *Retrofitting of concrete cylinder*

A lot of international studies and results are existing soon. In our case, we have performed some compressive tests of concrete cylinders of 16 cm of diameter and 32 cm height. The FRP used is the TFC of Freyssinet international, which is a 2D dry fabric. An example of sample during a test is shown on the Figure 1.

We obtain classical results in term of axial compressive stress versus longitudinal strain and transversal strain, which are shown on the Figure 2.

The particularity of this study is that we have performed some tests on aged concrete specimen. In fact, some 16×100 specimen were realized then

strengthened in order to applied some long term loading. After two years of creep loading, these samples were cut then tested using our MFL press of 5000 kN of capacity.

Figure 1. 16 × 32 retrofitted concrete sample during test.

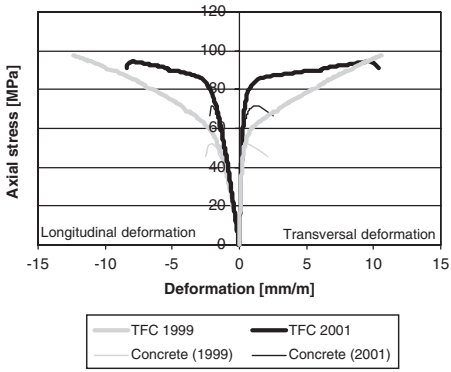

Figure 2. Axial compressive stress versus longitudinal and transversal strains in the case of 28 days loading and two years loading.

So we have now some results on samples after two years of aging, when the concrete and the FRP were at 20°C and 50% of relative humidity.

The results are shown on the Figure 2, too.

In the case of 28 days loading, the increasing of strength is about 80%.

For the old samples, the increasing is reduced to 20%.

In both cases, the tensile failure is obtained for the CFRP in tension.

These results show us that we have to be very careful on the models which can be developed in laboratory after 28 days tests: in reality, we have to strength some elements which can be aged, and the increasing of strength seems to be reduced. Of course, we are writing a model based of the Mirmiran approach, and it seems necessary to take into account the age of concrete during the design of FRP reinforcement. Of course, this study has to be completed (Verok et al, 2002).

2.2 *Creep loading of retrofitted cylinders*

In parallel with these retrofitting tests, we loaded during two years some 16 × 100 concrete samples with or

Figure 3. Strengthened concrete samples and reference concrete sample under creep loading (20°C, 50% RH).

without CFRP with constants loads (see Figure 3). All the concrete samples were tested in one of our climatic room: the temperature is equal to 20°C ± 1°C and the relative humidity is of 50% ± 5%.

The capacity of our creep frames, of 800 kN, enables us to load concrete sample up to 40 MPa, which is corresponding to 30% of VHPC concrete C120.

The creep loading value was chosen in order to verify that the axial compressive stress was equal first to 30% of the characteristic compressive stress of the concrete, what is classically used for creep tests on concrete.

When we do not see any difference between the specimens, we decided to increase the load up to 60% of the characteristic stress of the concrete.

The results we have obtained are shown on the Figure 4, in term of total creep compliance. In all cases, the creep compliance functions are the same. The explanation is that the transversal strain due to the applied compressive stress is not sufficient to induce tension in the FRP, for both the levels of stress. In that case, these results are related to the retrofitting ones, when the confinement effect is begin only when the axial stress leads approximately to the plain concrete ultimate stress.

The consequence in term of retrofitting of real RC columns is, as the concrete in place has soon be subjected to dead loads, that the long term creep strain will be very small. So it is not possible to use FRP to strength RC columns against creep effects.

The other consequence is that we cannot take into account a confinement effect in the case of services loading.

But what is to be noted is that we have no risk of creep strain and/or failure of the resin because of the lower level of transverse loading. Some studies have shown that the behavior of resin changes with the stress when it is greater than 20 MPa for our resins.

These two studies have so some consequences in term of mechanical durability, and in term of design too.

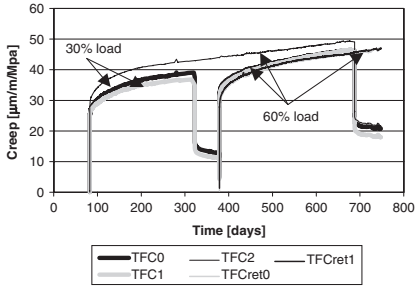

Figure 4. Comparison of the different creep compliances for all the performed tests.

3 FATIGUE

3.1 *Tests campaign*

Some tests was soon performed by Shahawy (Shahawy et al, 1998) and by Barnes (Barnes, 1999) in order to study the mechanical behaviour of RC strengthened beams subjected to fatigue loading, but without initial cracking before strengthening.

In the present study, 12 RC beams (15 × 20 × 70 cm) reinforced with HA8 are used. Only 6 beams reinforced with steel bar HA8, which have been realized under the fatigue test, are presented in this paper. We stuck one gauge on one reinforcement bar at the middle of each beam. The test was realized under 3 points bending experiment (Figure 5). Before fatigue test, all specimens were loaded until the summation of two cracks, which were located at two positions of stirrups near the middle of beams, arrived at 0.7 mm. This loading is called $F_{0.7}$. At this moment, the Max tensile stress arrived at about 350 Mpa (service state). During the fatigue test, we measured the force, the deflection, the strain in the reinforcement bar at the middle of beams and the widths of the two cracks for specimens without carbon cloth. For those strengthened by carbon cloth, besides preceding 5 values, we measured 3 strains on the lower carbon cloth, located at the positions of two cracks and at the middle of beam respectively.

Some RC beams were strengthened by TFC fabrics longitudinally and laterally (Wu et al, 2002).

The procedure of fatigue test is the following: first of all, a ramp until the average of F_{max} and F_{min}; and then, the fatigue load was applied until the rupture of specimens or until the end of certain cycles, for example one million cycles. During the procedure of ramp, of the first cycle and the last cycle of fatigue load, we measured the preceding 5 or 8 values all of 0.5 kN; for the middle procedure, we measured only the values at peaks and at valleys at

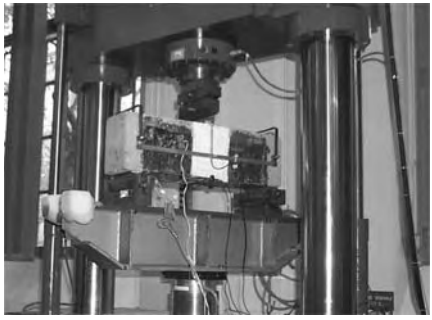

Figure 5. Three points bending fatigue test (reinforced with carbon cloth).

certain interval of cycles. The fatigue test was piloted with load.

3.2 *Tests results*

The main results for the RC pre cracked beams are written in Table 1, and those for the FRP strengthened RC beams in Table 2.

The main objective of this study is reached: the comparison between the case No 12, 13 and 8 permit us to conclude that in the case in service loading, the use of CFRP enables to prevent fatigue failure of steel. In that case, even if there is no resin in the crack, we have no problem of localized failure at the junction crack-fabrics. The external bonding of carbon cloth to initially crack-damaged RC structures is an effective method to restore the structural strength and ultimate fatigue life. Some of load transits by the FRP and the steel stress is lower. The fatigue failure of beams reinforced with carbon cloth is not a brutal failure: the steel bars are broken, but the specimen do not fail. The failure of strengthened beams is always a shear failure, with the de bonding of lateral FRP and the crushing of concrete between the longitudinal FPR and longitudinal steel bars.

The level of load in the CFRP do not be greater to 45 to 50% of his ultimate load capacity, in order to prevent fatigue failure.

But some questions are now to be solve: when the strengthening of a bridge is decided, is it necessary to stop the traffic? To solve this problem, we are thinking now to perform some tests of fatigue with FRP glued on the beams during fatigue loading.

Table 1. Results of tests for samples without carbon cloth.

No	$F_{0.7}$ (kN)	F_{min} (kN)	F_{max} (kN)	Cycles number at failure
12	54	40% $F_{0.7} = 21.6$	100% $F_{0.7} = 54$	511000
13	52	40% $F_{0.7} = 20.8$	100% $F_{0.7} = 52$	528000
21	57	5% $F_{0.7} = 2.85$	100% $F_{0.7} = 57$	128997

Table 2. Results of tests for samples with carbon cloth.

No	$F_{0.7}$ (kN)	F_{min} (kN)	F_{max} (kN)	Cycles number at failure
8	53	40% $F_{0.7} = 21.2$	100% $F_{0.7} = 53$	>2000000
16	54	60% $F_{0.7} = 32.7$	150% $F_{0.7} = 81.6$	266037
23	58	20% $F_{0.7} = 13$	112% $F_{0.7} = 65$	1040582 (stop)
24	58	12% $F_{0.7} = 7$	120% $F_{0.7} = 70$	371571

4 COLUMNS

4.1 *Test campaign and objectives*

Some studies on RC columns have shown that it is very difficult to be sure of the boundary conditions when compressive tests are carried out. Then, because of the reality, some columns of different levels of a building are not exactly superposed, because of the precision of implantation. Some columns belong to frame, and the loading is not always a central compression. For all these reasons, we have decided to realize some tests on RC columns 20×20, in combined flexure-compression-loading (Figure 6) In that case, we are sure of the deflection direction and it is

Figure 6. Strengthened RC column test equipment.

possible to limit the data acquisition by placing some strain gauges and transducers exactly where they are necessary.

The objective is to use some products, carbon fabrics and carbon plates, in order to define the principles of design rules. We are only at the end of the experimental study, where all tests were realized two times, with two concretes, two steel longitudinal and transversal reinforcements, and four industrial processes (Freyssinet International, Vinci-Construction, SIKA and VSL-Intrafor).

4.2 *Some partial results*

The test campaign was ended at the beginning of 2004. So we have only the experimental results without a complete interpretation (Quiertant et al, 2004).

Furthermore, some conclusions can be discussed now. First of all, the RC columns reinforced by 4 steel bars of diameter 16 mm and steel stirrups of diameter 8 mm, with a spacing lower than 200 mm, and which are reinforced using CFRP, show an increasing of the ultimate load and a great ductility. These conclusions depends of course of the type of FRP used. But in that case, the ultimate load is more or less of the order of value. It seems possible to take into account the longitudinal reinforcement in order to describe correctly the service behavior of the columns.

The results are quite different in the case of normal concrete strengthened RC columns. The longitudinal reinforcement is composed of 4 steel bars of diameter 12 mm, and the diameter of the stirrups is of 6 mm. In this case, the spacing is about 350 mm. The results for the RC columns of reference, without CFRP, are quite disperses. It means that probably the non homogeneity of the concrete is in that case predominant. For the first series of test, because of the high level of the reinforcement ratio, this effect is not important and the reference results are quite closed. The failure is always tensile failure of the CFRP, and appears by local buckling of a longitudinal steel bar between two stirrups. Consequently, it is the ultimate strain of the CFRP which leads to the registered failure values.

4.3 *Design consequences*

The principle of these tests are very clear, but the calculation is quite difficult. Because of the initial eccentricity of the load, the section is in flexion and all the concrete fibers are in compression. When the deflection becomes important, a part of the section is in tension. So it is not correct to take into account all the surface of the column to the calculation of the confinement. This problem is complex too because of the shape of this section.

5 CONCLUSION

This first French research program is now closed. The main results are taken into account in the French recommendations for the use of CFRP strengthening products:

- the study about retrofitting enables us to show the great influence of the inside strength of concrete, tested after 28 days or after a few months. All the existing models are based on 28 days tests, and some of them need to be adapted to old concrete,
- the main result of the creep study is that it is not available to take into account the CFRP to increase the stiffness of concrete specimen under service loading,
- in the case of fatigue loading applied to cracked beams strengthened using CFRP, the fatigue behaviour is really increased under service loading, and there is, in our cases, any risk of brutal failure if the stress level in the CFRP is lower than 40 to 50 percent of the ultimate strength of the composite. The security coefficient applied in the French recommendations are so justified.
- If CFRP is used to strength reinforced concrete columns, subjected to combined flexure-compression loading, the first results show the great accuracy of the CFRP, when the longitudinal and transversal metallic reinforcements soon exist. When the spacing of the stirrups are important, by buckling of bars leads to CFRP local failure in tension: the rules are now to be developed.

A second research program will begin in 2005, in order to study the bond behaviour of CFRP glued on concrete surface, with different tests, the effects of age and environment on the mechanical properties of strengthened elements, and the reinforcement of pre-cracked elements when the loading is applied when the strengthening is realized. These studies will permit us to complete and/or develop rules.

REFERENCES

AFGC, 2003. Réparation et renforcement des structures en béton au moyen des matériaux composites (in French), Scientific and technical document, AFGC ed., December 2003.

Barnes, R.-A. & Mays, G.-C. 1999. Fatigue performance of concrete beams strengthened with CFRP plates. *Journal of composite for construction*, May, pp. 63–72.

Ferrier, E., Naseri, H. & Hamelin, P. 1999. Fatigue Behavior of Composite Reinforcement for Concrete Structure. *Fourth International Symposium Fiber Reinforced Polymer Reinforcement for Reinforced Concrete Structures*. ACI special publication SP-188, pp. 535–545.

Quiertant, M., Toutlemonde, F. & Clément, J.-L. 2004. Combined flexure-compresion loading for RC-columns externally strengthened with longitudinal and transverse CFRP retrofitting. *Proc. of FIB symposium 2004*, April 26–28, Avignon, France.

Shahawy, M. & Beitelman, T.E. 1998. Fatigue Performance of RC Beams Strengthened by CFRP Laminates. *CDCC 98*, pp. 169–178, 1998.

Varastehpour, H. & Hamelin, P. 1997. Strengthening of concrete beams using fiber-reinforced plastics, *Matériaux et Constructions*, Vol. 30, April, pp. 160–166.

Verók, K., Clément, J.-L., Le Maou, F. & Boulay, C. 2002. Monotonically increasing compressive and creep tests on concrete cylinders retrofitted by carbon cloth. *Proceedings International conference on High performance structures and composites HPSC 2002*, March 11–13, Seville, Spain.

Wu, Z. Y., Clément, J.-L., Tailhan, J.-L., Boulay, C. & Fakhri, P. 2002. Fatigue test on damaged reinforced concrete specimens strengthened by carbon cloth. *Proceedings of HPSC 2002*, pp. 347–345, Seville, Spain.

Bond and interfacial stresses between FRP and concrete

FRP Composites in Civil Engineering – CICE 2004 – Seracino (ed)
© 2005 Taylor & Francis Group, London, ISBN 90 5809 638 6

Tests for the evaluation of bond properties of FRP bars in concrete

M. Guadagnini, K. Pilakoutas & P. Waldron
Department of Civil and Structural Engineering, The University of Sheffield, Sheffield, UK

Z. Achillides
Public Work Department, Cyprus

ABSTRACT: This paper reports on an experimental investigation that was carried out at the University of Sheffield to investigate the bond properties of FRP bars in concrete. Ten different types of rebars were tested. The rebars were supplied by six different manufacturers and varied in type of fibre, type of resin, diameter and surface treatment. Three specimens of each type of bar were tested in pull-out and splitting. As reference samples, tests on standard hi-grade deformed steel bars were also performed. The findings of this investigation are presented and discussed with a focus on assessing the merits of simple tests for material characterization.

1 INTRODUCTION

In recent years, various types of Fiber Reinforced Polymer (FRP) reinforcements have been developed for use as embedded or external reinforcement for concrete, and their use in the construction industry is still growing at an exponential rate. The adoption of these new types of reinforcements, however, requires the development of product specifications, testing standards and codes of practice that can not be derived by simply modifying and adapting existing parameters for the design and use of steel RC structures. The current know-how needs to be reevaluated and verified against the new materials.

While standards for the determination of the mechanical characteristics of advanced composites exist in the aerospace field, these standards do not cover their use for concrete, an issue that must be addressed in order to clarify the advantages as well as the economics of the use of these advanced materials as an alternative to conventional steel reinforcement.

Bond between concrete and FRP reinforcing bars is a fundamental aspect of the composite action of FRP reinforced concrete, and accordingly, needs to be adequately understood before FRP materials can be accepted widely in the construction industry.

As a step in the direction of increasing current knowledge of the bond properties of FRP bars and bond performance in concrete elements, an international round robin test (*i*RRT 2002) programme was designed with the following objectives:

1. To assist the various international committees working in the field of standardization to assess the merits of simple tests for material characterization and comparisons.
2. To enable the comparisons of results between different laboratories.
3. To enable simple comparisons between the properties of the different materials that have been tested.

Other indirect benefits that will result from this exercise are an increased familiarization with the range of FRP products available in the global market and a heightened awareness of the international efforts aimed towards the development of design guidelines and standardized tests to ensure reliable and replicable research.

The general organization of the *i*RRT was undertaken by the "ConFibreCrete" research network (1997) working together with the *fib* TG 9.3 (International Federation of Concrete 1995) and ISIS Canada (Intelligent Sensing for Innovative Structures 1998).

This paper describes the methodology that was used to carry out this series of tests and discusses the merits of simple tests for material characterization. The results of the experimental programme that was carried out at the University of Sheffield are also presented and commented upon.

2 EXPERIMENTAL PROGRAMME

Two simple tests were carried out on ten different types of FRP rebars with the objective of examining their properties in bond pull-out and splitting. Three specimens of each type of bar were tested in pull-out and three additional specimens in splitting (only

two specimens of Re-bar Chile S.A. were tested). For the purpose of comparison, the same tests were also performed on standard hi-grade deformed steel bars (British Standard Institution 1997).

In the case of the pull-out test, it was intended that no concrete splitting would occur and this test was considered to simulate the bond strength in confined conditions. The splitting test was designed to give a representative measure of the bond strength that could be obtained in bars near the surface of a concrete element.

2.1 *Concrete properties*

The strength of the concrete used to prepare the specimens for both the pull-out and splitting tests needed to be high enough not to affect the bond strength significantly. For this reason, a target concrete cylinder strength of 40 MPa was selected. A ready mixed concrete, which was obtained from a local supplier, was used for the experiments. The specifications of the mix were: 14 mm maximum aggregate size and cement type OPC/PFA with a slump of less than 50 mm. The compressive strength of the concrete was evaluated by testing 12 control cylinders (150 × 300 mm), which were cast at the same time and cured under the same conditions as the test specimens. An average cylinder compressive strength of 39.3 MPa was recorded for the control cylinders during the actual days of pull-out and splitting testing. The size of the concrete specimens (see §3.1 below) was selected in order to avoid splitting of the concrete in the case of bars with large diameters, based on the findings of similar experimental programmes (Achillides et al. 2004, International Federation of Concrete 2000).

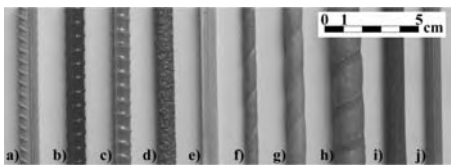

Figure 1. FRP bars tested in the *i*RRT. From left to right: (a) GFRP rebar (Chile S.A.); (b) #3 C-BAR Carbon and (c) #3 C-BAR Glass (Marshall Industries Composites Inc.); (d) ISOROD-Glass (Pultrall, Inc.); (e) GFRP rebar (Eurocrete Ltd.); (f) #2 GFRP, (g) #3 GFRP and (h) #5 GFRP bars (Hughes Brothers); (i) Carbopree and (j) Arapree (Sireg Spa).

2.2 *FRP bars*

The different types of bars that were tested during this research project were supplied by six different manufacturers, and varied in terms of their diameter, surface treatment and the type of fibre and resin that formed the composite. The types of surface treatment examined were of various natures including surface deformations resembling conventional deformed steel bars, sand coated finishes, spirally wound fibre tows to impress deformations, and combinations of thereof. All three principal fibre groups most widely used for the manufacture of commercial products (carbon, aramid and glass fibres) were represented within the sample specimens. The tested bars are shown in Figure 1, and their mechanical and physical properties are presented in Table 1.

3 PULL-OUT TEST

3.1 *Specimen preparation and test set-up*

Specimens for the pull-out tests were manufactured according to Figure 2. The 200 mm concrete cubes were cast with a 400 mm long FRP bar placed vertically along the central axis. An embedment length of 5 ϕ (five diameters) was chosen so that: (1) the embedment length would be short enough to avoid the development of high stresses in the bars, thereby

Table 1. Mechanical characteristics of FRP bars.

Bar	Manufacturer	Type	ϕ (mm)	f_u (MPa)	E (GPa)	Surface finish
SIR-A	Sireg Spa	Aramid	10	1350	60	PP
SIR-C	Sireg Spa	Carbon	10	2800	130	SC (fine)
HB-G2	Hughes Brothers	Glass	6.35	760	40.8	SC + HW
HB-G3	Hughes Brothers	Glass	9.53	690	40.8	SC + HW
HB-G5	Hughes Brothers	Glass	15.8	620	40.8	SC + HW
PUL-G	Pultrall Inc	Glass	9.5	689	42	SC (coarse)
CBAR-C	Marshall Industries	Carbon	10.3	1724	114	R (smooth)
CBAR-G	Marshall Industries	Glass	9.8	758	41	R (smooth)
EUR-G	Eurocrete Ltd	Glass	8 × 8*	900	45	PP
ReB-G	Re-Bars Chile S.A.	Glass	10	517–1207	41–55	R
S-12		Steel	12			R

PP = Peel ply; SC = Sand coated; HW = Helical wrap; R = Ribbed; * = square cross section.

eliminating the need for special devices to grip the bar during testing, and (2) the embedment length would be long enough to be representative of the bar surface deformations. Several layers of plastic sheet treated with de-moulding agent were wrapped around a portion of the bar to create the required non-contact area between bar and concrete. The bar was positioned within the concrete cube so not to project outward from the face of the concrete cube to avoid the wedging effect of un-bonded FRP entering the concrete (Achillides et al. 2004).

Figure 3 illustrates schematically the configuration used for the tests carried out in this experimental programme. The specimens were placed in a steel frame that was specifically made to fit a standard tensile testing machine. The steel rig comprised two 25 mm thick plates connected by four 20 mm diameter bolts. The bottom plate had a 30 mm diameter hole in its centre to allow for the FRP bar to run through, and three additional holes were positioned in a triangular configuration around the central hole to allow for displacement measurements of the loaded end of the bar relative to the concrete cube surface (Figures 3 and 4).

The slip of the unloaded end of the bar was also measured during the tests. The stiffness of the reaction plate was designed in order to eliminate any undesired deformation. In addition, a 5 mm thick wooden sheet was placed between the reaction area of the concrete and the test rig to ensure the development of a uniform contact pressure.

The load was applied to the bar in deflection control to capture the full development of the post peak behaviour. The tests were halted when displacement measurements greater than 8 mm were recorded for the loaded end.

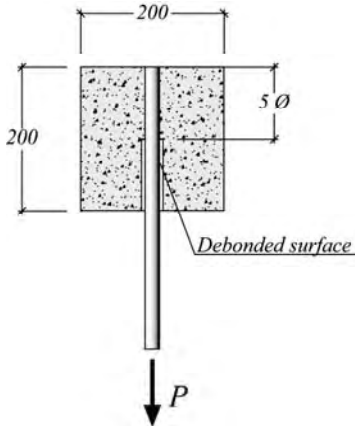

Figure 2. Details of the positioning of the bar in the concrete cube.

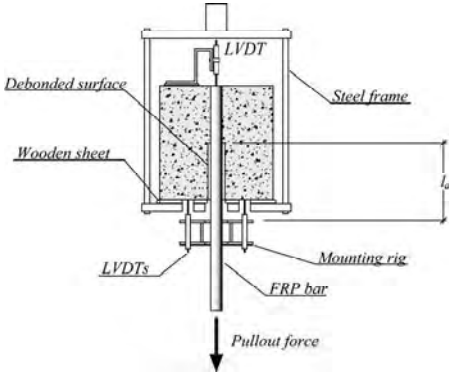

Figure 3. Loading frame for pull-out and splitting test.

3.2 *Data collection and representation*

Displacement transducers were used to monitor the development of the loaded-end slip and the unloaded-end slip. The unloaded-end slip was measured by a single transducer, whereas the loaded-end slip was measured via three displacement transducers, positioned at 120-degree intervals at a distance of 50 mm from the centre of the rebar, to account for bending (Figure 4).

The distance between the frame supporting the LVDTs and the beginning of the embedded part of the bar (l_a in Figure 3) was measured at the beginning of each test in order to determine the elastic extension of the bar that needed to be subtracted from the measurements of the loaded-end slip.

For this purpose, the elastic characteristics of the bar, as supplied by the various manufacturers, were adopted (Table 1).

Based on the data obtained during testing, average bond stress, τ_{av}, and average slip, δ_{av}, were calculated according to Eqs. (1) and (2) respectively.

$$\tau_{av} = \frac{P}{\pi \phi l_{bl}} \quad (1)$$

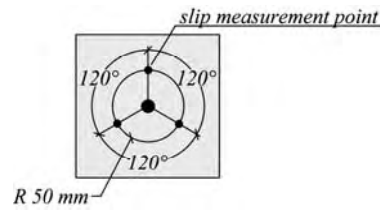

Figure 4. Positioning of LVDTs at the top face of the cube.

where P is the applied pull-out load (kN); l_{bt} is the true bonded length calculated at each increment of load (mm) – i.e. the initial bonded length minus the end slip – and ϕ is the nominal diameter of the bar (mm).

$$\delta_{av} = \frac{\sum_{i=1}^{n} \delta_i}{n} - \Delta l \quad (2)$$

where n is the number of LVDTs used to measure the slip of the loaded-end (3); δ_i (mm) is the displacement measured by the ith LVDT and Δl (mm) is the elongation of the bar between the frame supporting the LVDTs and the beginning of the embedded part of the bar (l_a in Figure 3).

3.3 *Experimental results*

The results obtained from the pull-out tests are shown in Table 2 in terms of average maximum pullout load, P_u; average maximum slip of the loaded-end at peak load, δ_{Lpeak}; and average maximum bond stress, $\tau_{pull\text{-}out\ max}$.

Figure 5 illustrates the average maximum pull-out bond stress for the tested bars. The dashed line shown in the figure represents the average value of the pull-out bond stress recorded for the steel bar specimens. A pull-through mode of bond failure was observed for all of the tested specimens. As expected, due to the selected geometry of the specimens and concrete strength, no splitting cracks developed throughout the tests.

Bond failure of all of the tested bars occurred on the bar surface, and hence, its development was substantially controlled by the shear strength between the resin and the fibres (see for example Figure 6).

Typical average bond stress versus slip relationships for some of the tested bars are shown in Figure 7 and Figure 8. In all of the experiments, slip of the loaded-end started at a very early stage of loading. This can be attributed to the loss of chemical bond between the surface of the bar and the concrete in the area surrounding the loaded-end. The bond resisting mechanism in this first stage of loading is the result of a combination of chemical adhesion and the mechanical interlocking of the bar deformations within the concrete (International Federation of Concrete 2000). With the progressive

Table 2. Summary of the results of the pull-out tests.

Bar	P_u (kN)	δ_{Lpeak} (mm)	$\tau_{pull\text{-}out\ max}$ (MPa)
SIR-A	15.73 ± 2.42	0.64 ± 0.04	10.01 ± 1.54
SIR-C	21.23 ± 0.75	0.30 ± 0.05	13.70 ± 0.48
HB-G2	10.15 ± 1.55	1.13 ± 0.13	16.03 ± 2.45
HB-G3	23.45 ± 1.01	0.87 ± 0.10	16.44 ± 0.71
HB-G5	55.74 ± 7.23	3.29 ± 0.96	14.04 ± 1.82
PUL-G	59.16 ± 1.37	0.84 ± 1.09	9.24 ± 0.66
CBAR-C	16.53 ± 1.12	1.17 ± 0.24	16.93 ± 0.67
CBAR-G	33.52 ± 1.31	1.19 ± 0.07	21.30 ± 0.87
EUR-G	28.21 ± 4.22	0.70 ± 0.11	9.24 ± 0.66
ReB-G	32.13 ± 1.50	2.29 ± 1.46	10.53 ± 0.95
S-12	34.27 ± 2.95	1.23 ± 0.28	15.15 ± 1.31

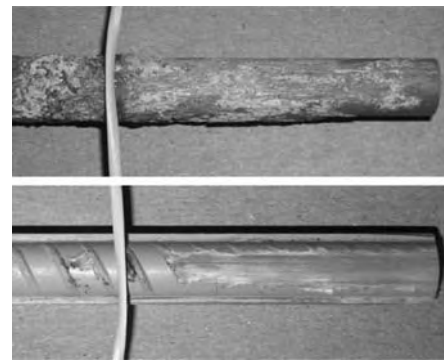

Figure 6. Specimens PUL-G (top) and ReB-G (bottom) after pull-out.

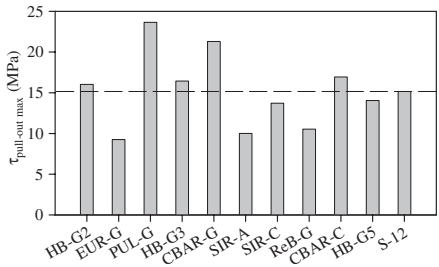

Figure 5. Maximum average pull-out bond stress.

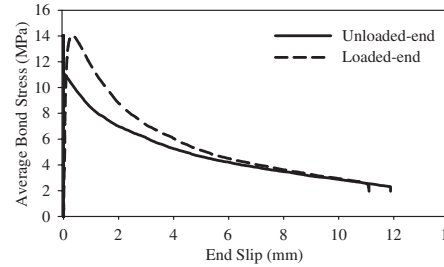

Figure 7. Pull-out test of a Carbopree (SIR-C) specimen.

failure of the chemical bond along the length of the embedded portion of the bar, and the degradation of the mechanical interlock, slip of the loaded-end increases more rapidly.

Conversely, slip of the unloaded-end appears to be negligible up to the point when the damage between the concrete and the surface of the bar has affected the whole embedment length (see for example Figure 7). This phenomenon always occurs soon after the maximum average bond stress is attained.

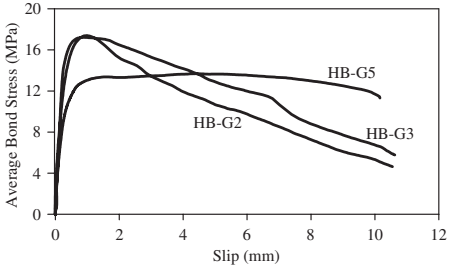

Figure 8. Average bond vs. slip of the loaded-end behaviour for Hughes Brothers GFRP bars.

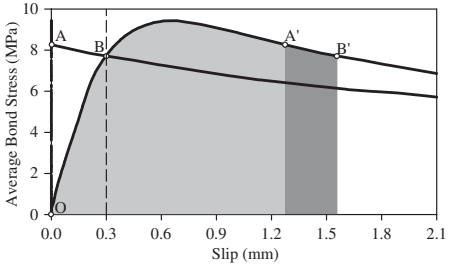

Figure 9. Example of the evaluation of the energy per unit of bonded surface performed on one of the Arapree (SIR-A) specimens.

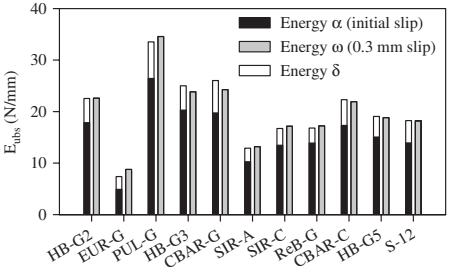

Figure 10. Energy per unit of bonded surface.

In an attempt to establish an objective way of determining the quality of the bond developed by the different bars, the energy that needs to be applied to the system to develop a displacement of the loaded-end (A′) corresponding to the initial slipping of the unloaded-end (A) (Energy α – area under the curve OA′ in Figure 9) was determined along with that necessary to develop a displacement of the loadedend (B′) corresponding to a slip of 0.3 mm at the unloaded-end (B) (Energy ω – area under the curve OA′B′ in Figure 9). A slip value of 0.3 mm for the the unloaded-end was arbitrarily chosen as a limit value that can be related to serviceability limit states at the structural level. Figure 10 shows the average values of energy per unit of bonded surface, E_{ubs}, calculated as described above. The energy that was dissipated to generate a 0.3 mm displacement of the unloaded end (Energy δ – area under the curve OAB in Figure 9) is also shown. As it can be observed, in the majority of the specimens, the additional energy that was needed to generate a displacement of the loaded-end from A′ to B′ (ω–α) was greater than the energy that was dissipated during the progression of the failure (δ).

This is an indication that residual frictional forces are still acting along the remaining embedded length of the bar.

4 SPLITTING TEST

4.1 *Specimen preparation and test set-up*

Specimens for the splitting test were prepared according to the specifications illustrated in Figure 11. The concrete prisms measured 200 mm in length, 100 mm in width and their depth, which was determined as a function of the diameter, ϕ, of the rod, measured 5ϕ.

In this series of tests, the FRP bars were placed vertically with a cover of 2ϕ and embedded for the entire depth of the concrete prisms.

In addition to the measurements taken for the pull-out test, the crack that developed on the outer surface of the concrete due to splitting stresses was monitored (Figure 12).

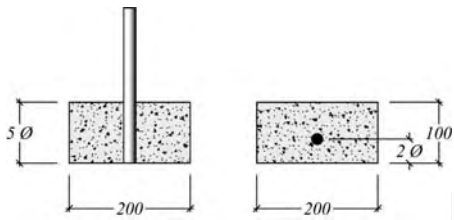

Figure 11. Positioning of the FRP bar for the split test.

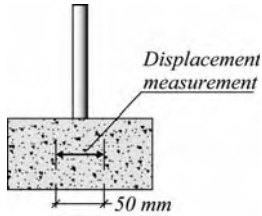

Figure 12. Positioning of gauge for the measuring of the splitting strain.

Table 3. Summary of the results of the splitting tests.

Bar	P_u (kN)	$\tau_{splitting\ max}$ (MPa)	Failure mode
SIR-A	7.67 ± 1.72	4.87 ± 1.12	TCCD
SIR-C	8.63 ± 1.42	5.50 ± 0.87	TCCD
HB-G2	2.07 ± 0.55	3.27 ± 0.81	TCF
HB-G3	6.37 ± 2.58	4.47 ± 1.86	TCF
HB-G5	17.37 ± 2.00	4.40 ± 0.50	TCF
PUL-G	7.23 ± 1.40	5.10 ± 0.95	TCF
CBAR-C	5.80 ± 1.61	3.50 ± 0.95	PCF
CBAR-G	6.47 ± 2.81	4.30 ± 1.91	PCF
EUR-G	4.20 ± 0.82	3.30 ± 0.66	TCCD
ReB-G	8.05 ± 0.07	5.15 ± 0.07	TCF
S-12	9.40 ± 2.70	4.17 ± 1.16	PCF

TCCD = Tiny concrete crack development; TCF = total concrete failure; PCF = partial concrete failure.

4.2 *Experimental results*

The results obtained from the splitting tests are shown in Table 3 in terms of average maximum splitting load, P_u; and average maximum bond stress, τ_{max}. The typical mode of failure that was observed for the tested specimens is also reported.

Since the data recorded for the slip of the loaded-end and the maximum crack width were highly variable, these measurements are not reported in the table summarizing the results. The high coefficient of variation within the measurements of the loaded-end slip can be attributed mainly to the particular configuration of LVDTs that was used for the splitting tests. Due to the geometry of the specimen and of the LVDT mounting rig, only two transducers, placed symmetrically about the axis of the bar, were used in this phase of the experimental programme to measure the loaded-end slip. The effect of bending due to the eccentric placement of the bar within the concrete specimen, however, was found to be more influential than expected.

The variability within the crack width measurements can be partly attributed to the variability of the concrete itself, as well as the complexity of adequately monitoring the crack development with the adopted instrumentation set-up.

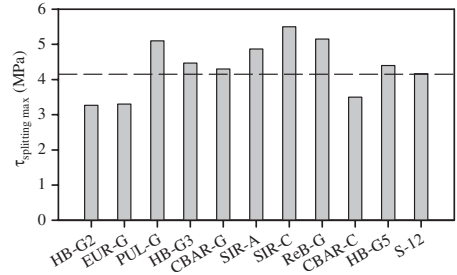

Figure 13. Average bond splitting strength for the tested bars.

Figure 14. Crack patterns for some of the tested specimens.

Figure 13 shows the average maximum splitting bond stress for the tested bars. The dashed line represents the average maximum value of the bond stress developed by the steel rebars.

Failure of all of the split tested specimens occurred within the concrete volume, and hence, was mainly governed by the tensile strength of the concrete.

The crack patterns observed varied considerably within the whole set of tested specimens as well as within each group of bars (Figure 14). A more detailed examination of the crack growth (Figures 15 to 17), however, enabled the identification of three main types of crack development: (*i*) instant cracks; (*ii*) sliding cracks; and (*iii*) multiple cracks. Instant cracks (Figure 15) generally developed when high bond stresses were generated along the embedded part of the bar. Slip of the unloaded-end took place as a result of the opening of the crack and the specimen failed in a brittle manner. Sliding cracks (Figure 16) were observed in specimens in which the average bond stresses generated along the embedded length of the bar were of medium intensity. In these cases, the crack started developing just before the maximum average bond stress was attained. The slip of the unloaded-end only

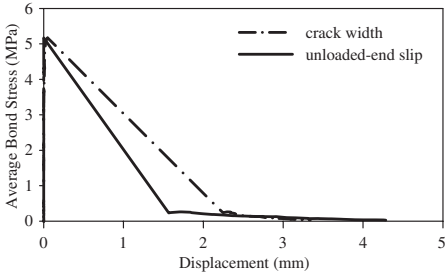

Figure 15. Splitting test of one of the ReB-G specimens with the development of an instant crack.

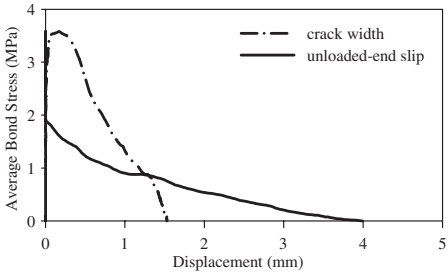

Figure 16. Splitting test for one of the CBAR-C specimens with the development of a sliding crack.

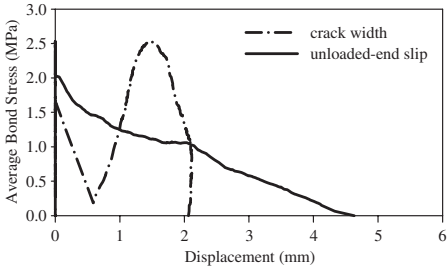

Figure 17. Splitting test of one of the CBAR-G specimens with the development of a multiple crack.

occurred at a later stage, together with a conspicuous increase in the width of the splitting crack. The multiple crack type (Figure 17) refers to specimens in which more than one crack developed before failure. In these cases, initiation of the first crack was accompanied by a drop in the average bond stress, but did not induce slipping of the bar. After this initial drop in the load applied to the system, bond stresses increased further, but generally only up to a level that was lower than that developed for instant and sliding crack types.

5 DISCUSSION AND CONCLUSIONS

Two types of tests were undertaken to investigate the bond properties of FRP bars embedded in concrete in both confined and un-confined conditions. Pull-out and splitting tests were conducted to gain a better understanding of FRP-concrete interaction and with the aim of assessing the merits of simple tests for material characterization. In light of the results obtained from the experimental work presented here, some issues on the reliability of small scale testing are presented and commented upon.

The pull-out tests conducted in the first phase of the programme seemed to yield consistent results both in terms of pull-out bond stress versus slip behaviour and the type of failure. The average coefficient of variation (CV) for the recorded maximum pull-out load values was of about 8%, with maximum CV values slightly over 15%. The higher average CV for the displacement measurements (25%) appears to be the result of various problems that were encountered during testing (e.g. malfunctioning of instrumentation). If questionable tests results were disregarded, the typical CV for displacement measurements would be under 15%.

The data obtained from the splitting tests, however, were markedly variable and it is unlikely that similar results could be obtained through subsequent testing using the same approach and specifications. The average CV for the recorded maximum pull-out load values was about 23%, with maximum values over 40%. The reasons for the high variability within the experimental results seemed to lie not only in the particular test arrangement that was selected but also in the high variability of the tensile behaviour of concrete. Whilst the natural variability of concrete is a factor that is difficult to account for, and is one of the fundamental aspects underlying the splitting behaviour of embedded bars, the arrangement of the instrumentation can be adjusted to eliminate measurement problems caused by the non-symmetrical geometry of the specimens. For example, an arrangement of LVDTs similar to that used in the pullout tests (e.g. 3 LVDTs evenly spaced around the bar) would be preferable to measure the displacement of the loaded-end.

A longer gauge length for the measurement of splitting cracks should also be adopted to enable adequate monitoring of the various types of crack patterns that can develop due to splitting stresses.

Despite the problems encountered during testing, the test results can still be interpreted at a structural level, providing important insights into the overall bond behaviour of composite rebars.

The results obtained for both the pull-out and splitting tests confirm the complex nature of the interaction between concrete and FRP bars. Unlike conventional steel bars, which are highly standardised in terms of their material properties and surface finishes, FRP bars

can differ not only in the type of constitutive materials but also in the type of surface finish and manufacturing process. All of these parameters are known to affect the bond behaviour of FRP rebars embedded in concrete (International Federation of Concrete 2000). The individual influence of each of these parameters, however, is not easily discernable from the experimental tests carried out as part of the research programme presented here. Targeted studies looking at the variation of bond behaviour in relation to a more restricted set of variables would perhaps yield results that could be more easily interpreted.

Nonetheless, the following conclusions can still be drawn:

- Provided that a good confinement of the bar is ensured, pull through type of failure of FRP bars is always achieved and no apparent cracking develops on the outer surface of the concrete specimens.
- Bars with smaller diameter develop higher average maximum bond stresses than similar bars with larger diameters.
- The bond strength developed by the bars appears to be greatly influenced by the type of surface treatment on the embedded bars. Sand coated bars exhibited higher average maximum bond strength than rebars with peel ply or ribbed finishes. On average the pull-out strength of FRP bars is similar to that of steel bars with some bars being better and other worse.
- Due to the eccentric arrangement of the bar within the concrete specimen, and the resulting small concrete cover, the development of stresses perpendicular to the surface of the bar becomes critical to the development of the crack pattern as well as the overall distribution of bond stresses. The distribution of radial stresses, or splitting stresses, depends upon bar size, surface treatment and concrete cover (i.e. confinement effect). These attributes are expected to affect mainly the behaviour of bars with protruded deformations, owing to the development of interlocking mechanisms between the bar deformations and surrounding concrete. Figure 18 shows a comparison between the different bars in terms of maximum average bond stress in unconfined (splitting) conditions. As can be seen from the figure, in un-confined situations, the recorded values of maximum average bond stresses were up to 80% lower than those recorded for the same bars in confined conditions.

Other phenomena such as small concrete cover in comparison to the maximum aggregate size of the concrete (HB-G2) and stiffness of bar deformations also affect the overall bond and cracking behaviour.

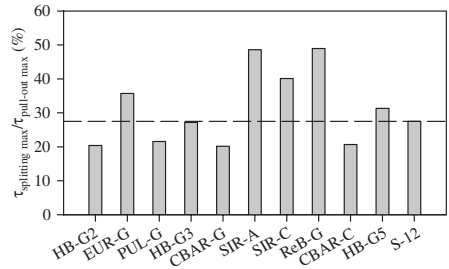

Figure 18. Splitting to pull-out bond ratio.

ACKNOWLEDGMENTS

This work would not have been possible without the generous support of the suppliers of FRP bars and the commitment of the participating laboratories. The authors wish to acknowledge the financial assistance of the European Union for the TMR Network "ConFibreCrete", and the support of the Intelligent Sensing for Innovative Structures (ISIS) Network and the International Federation of Concrete (*fib*) Task Group 9.3.

REFERENCES

Achillides Z. & Pilakoutas, K. 2004. Bond Behaviour of Fiber Reinforced Polymer Bars Under Direct Pullout Conditions, *Journal of Composites for Construction 8 (2)*: 173–181

British Standard Institution 1997. BS 4449 – Specification for Carbon Steel Bars for the Reinforcement of Concrete, BSI, London

ConFibreCrete, Development of Guidelines for the Design of Concrete Structures, Reinforced, Prestressed or Strengthened with Advanced Composites, Training and Mobility of Researchers, Research Network TMR "ConFibreCrete", http://www.shef.ac.uk/∼tmrnet, 18/10/2002

International Federation of Concrete 2000. Bond of Reinforcement in Concrete, State-of-art Report, Bulletin 10, Lausanne, pp. 434

International Federation of Concrete, fib Task Group 9.3, FRP Reinforcement for Concrete Structures, International Federation for Structural Concrete, http://allserv.rug.ac.be/∼smatthys/fibTG9.3, 18/10/2002

iRRT, International Round Robin Test for FRP Reinforcement, http://www.shef.ac.uk/∼tmrnet/rrt, 18/10/2002

ISIS Canada, Intelligent Sensing for Innovative Structures, http://www.isiscanada.com, 18/10/2002

FRP Composites in Civil Engineering – CICE 2004 – Seracino (ed)
© 2005 Taylor & Francis Group, London, ISBN 90 5809 638 6

On the interfacial mechanics of FRP-strengthened concrete structures

U.A. Ebead & K.W. Neale
The University of Sherbrooke, Sherbrooke, Quebec, Canada

L. Bizindavyi
Queen's University, Kingston, Ontario, Canada

ABSTRACT: The strengthening of concrete structures by means of externally-bonded fibre reinforced polymers (FRPs) is now routinely considered as a viable alternative to the rather costly replacement of these structures. Previous laboratory investigations of this strengthening technique for concrete beams in flexure and shear have shown that, despite its capability of considerably enhancing the strength capacities of the beams, premature failures by debonding can often limit the effectiveness of this method. In order to prevent this type of premature failure, several anchorage schemes have been suggested. However, at present, our basic understanding of the interfacial mechanics between the concrete and the bonded FRP for such reinforcements is rather limited. In this paper, we present results from an in-house finite element (FE) code, numerical model, and experimental investigation on carbon FRP (CFRP) and glass FRP (GFRP)-concrete joints subjected to direct shear. We first present the experimental set-up designed and constructed in our laboratory for this loading configuration. With the test set-up we investigate the shear conditions between the FRP and the concrete, to determine the strain distribution profiles in the FRP. The finite element code is developed to address the interfacial behaviour of FRP-concrete joints. This code is in its preliminary stage and is based on a linear elastic analysis. Further on-going developments include the use of more sophisticated material modelling such as the microplane model. The FE results discussed in the paper include the stress and strain distributions in the FRP, adhesive layer and concrete. A special emphasis is placed on the strain distribution in the FRP, the peeling-off stresses in the adhesive, and the shear stresses in the concrete layer adjacent to the interface. In addition, a simple elastic-based numerical analysis is presented and applied to this loading condition. Comparisons between experimental, FE, and numerical results are presented.

1 INTRODUCTION

With the flexural strengthening technique of bonding steel plates or FRP laminates to reinforced concrete beams, there is a persisting problem of premature failure due to delamination and peeling-off of the plates. This phenomenon has been investigated both experimentally and analytically by a number of authors. However, there is a lack of comprehensive studies on the FRP-concrete interface.

From flexural tests and modified beam tests on steel-to-concrete joints as well as composite-to-concrete joints, it was concluded that plate separation was due to high local interfacial bond stresses and peeling forces at the ends of the plates (Jones et al., 1980; Van Gemert, 1980; Quantrill et al., 1996a). These stresses were found to depend on the tensile strength of the concrete (Jones et al., 1980; Triantafillou and Plevris, 1992; Quantrill et al., 1996b), the flexural rigidity of the cracked plated section (Triantafillou and Plevris, 1992), the concrete surface preparation (Jones et al., 1980; Van Gemert, 1980; Ziraba et al., 1995), the strength and thickness of the adhesive (Jones et al., 1980; Quantrill et al., 1996b) and, to a lesser extent, on the plate aspect ratio b/t where b is the width of the bonded plate and t its thickness (Jones et al., 1980; Quantrill et al., 1996b).

Plate curtailment led to a considerable reduction of the strains in the inner plate without completely alleviating the delamination problem (Jones et al., 1980). On the other hand, the use of end anchorage plates (Jones et al., 1980; Quantrill et al., 1996a) was shown to be an effective way to prevent premature failure, allowing the full flexural strength potential to be achieved. The addition of side plates alone at the soffits (Quantrill et al., 1996b) was able to delay premature failure, but it could not prevent this from eventually occurring. As far as the bond strength is concerned, average values ranging from 1.5 MPa (Van Gemert, 1980) to 15 MPa (Quantrill et al., 1996b) have been reported.

Several local bond slip models have been developed for representing the interfacial behaviour when FRPs

are externally bonded to concrete surfaces as well as for predicting the bond strengths. Some of the most recent research on the interfacial behaviour of FRP sheets externally bonded to RC structures have been summarized (Teng et al., 2004). Based on the fracture energy criterion, analytical models were developed to predict the debonding failure load due to flexural cracks (Niu and Wu, 2000; Wu and Niu, 2001). As a result of the availability of numerous experimental data, neural network methods were used as an alternative for the prediction of debonding in FRP-plated beams (Smith et al., 2003).

The current literature suggests that there is a rather general agreement on many aspects of failure modes for bonded joints, despite the diversity of reinforcing materials used (i.e., steel, carbon fibre and glass fibre composites), the different concrete compressive strengths investigated, and the different specimen geometries employed. With few exceptions, practically all researchers conclude that the bond strength of externally bonded plates depends mainly on the quality of the surface preparation and the quality of the concrete itself. However, wide ranges of values have been reported for the maximum shear stresses in the joints at failure (2.5 MPa–15.32 MPa) and the maximum normal stresses (1 MPa–12.97 MPa).

Recent developments in FRP material technologies, with numerous new fibres and resin systems emerging in the construction industry, require not only a basic knowledge of the mechanical properties of each new product, but also their interfacial behaviour when applied as external reinforcement. To investigate this behaviour, a specially tailored test apparatus has been designed and constructed in our laboratory. It offers the advantages of being simple, removable, and being easily reshaped or resized according to various needs. With this test set-up, four independent tests can be performed using one single concrete block. This is made possible by the fact that each bond test involved only one lateral face of the block. Furthermore, the FRP-epoxy-concrete interface behaviour is essentially a surface phenomenon, as has been observed by Ziraba et al., (1996). Since the failure of an FRP/concrete joint does not induce any visible damage to both the remaining lateral surfaces and the bearing surface of the concrete block, the remaining lateral surfaces of the concrete block can therefore be reused for other bond tests.

The apparatus is versatile in the sense that not only FRP/concrete joints can be investigated, but other combinations of materials can be tested as well. Furthermore, static or cyclic loading can be applied. From the test results and a corresponding linear-elastic in-house FE code analytical model, the strain and resulting shear stress distributions along the bonded joints can be obtained. A combination of such results with those obtained from corresponding beam tests should be useful to establish appropriate guidelines for the analysis and design of composite-to-concrete joints.

2 EXPERIMENTAL PROGRAM

2.1 *Materials*

For the experimental program, two batches of concrete blocks of dimensions 150 × 150 × 400 mm were fabricated from a normal density concrete mix with a maximum aggregate size of 14 mm. The mean compressive strength for all the batches was 42.5 MPa, and the mean tensile strength from the standard three-point flexure tests was 3.5 MPa. The Young's modulus of the concrete, estimated from the concrete compressive strength, was 33.5 GPa.

Two types of fibre reinforced composite laminate were used in this investigation: GFRP (glass fibre reinforced polymer) and CFRP (carbon fibre reinforced polymer). The GFRP composite was prepared from the TYFO® SEH 51 fabric and the TYFO® S epoxy resin, while the CFRP composite was prepared from the Replarktm unidirectional sheet and the L 700S epotherm resin. These epoxy-FRP laminate systems were prepared in accordance with the manufacturers' specifications. Unidirectional laminates of both GFRP and CFRP with 1, 2, 3 and 6 plies were prepared in specially designed steel moulds so as to give a uniform laminate thickness. The CFRP and GFRP laminates of 1 and 2 plies were each cut into strips of 25.4 mm and 50.8 mm width, while the 3-ply laminates of both CFRP and GFRP were cut into strips of 25.4 mm. These strips were bonded on the concrete blocks for preliminary bond tests. Specimens from the 3-ply and 6-ply CFRP and GFRP laminates were tested in tension in order to determine their tensile strengths and elastic moduli. The thickness of one ply of CFRP and GFRP laminates is 0.33 and 1.00 mm, respectively.

For GFRP laminates, the values of mean strength and mean Young's modulus were found to be 472 MPa and 29.2 GPa, respectively. These values fall above the minimum values specified by the manufacturer: 448 MPa and 22.4 GPa respectively for minimum tensile strength and minimum tensile modulus. Specimens of the Tyfo® s epoxy resin were prepared and tested in tension according to standard ASTM-D 638. From these tests the values for Poisson's ratio, ν_a, and shear modulus, G_a, were found to be respectively 0.4 and 1.18 GPa.

For CFRP laminates, the tensile strength and tensile modulus were found to be 1014 MPa and 75.7 GPa respectively. No epoxy adhesive specimens were tested for the CFRP systems. However, values of Poisson's ratio for epoxy resins used with similar CFRP systems reported in the literature vary from $\upsilon_a = 0.38$–0.4 (Kazuaki et al., 1996; Hull and Clyne, 1996). The value $\upsilon_a = 0.38$ was used in this study.

Table 1. GFRP-concrete detailed bond tests.

Number of plies (1)	Bonded length [mm] (3)	Bonded width [mm] (4)	Failure load [kN]
1	135	25.4	9.04
1	145	25.4	9.67
1	150	25.4	9.30
1	155	25.4	7.57
1	160	25.4	10.42
1	180	25.4	11.41
1	240	25.4	8.75
1	240	25.4	10.14
1	280	25.4	11.65
2	120	25.4	13.82
2	210	25.4	14.90
2	220	25.4	15.50
2	240	25.4	16.42
2	240	25.4	15.50
2	240	25.4	16.51
2	260	25.4	19.00
2	260	25.4	18.82
2	280	25.4	17.80
2	305	25.4	20.90
2	320	25.4	21.40

Table 2. CFRP-concrete detailed bond tests.

Number of plies (1)	Bonded length [mm] (3)	Bonded width [mm] (4)	Failure load [kN]
1	50	25.4	7.30
1	80	25.4	8.73
1	135	25.4	9.00
1	145	25.4	8.90
1	160	25.4	10.42
2	100	25.4	11.40
2	120	25.4	12.80
2	160	25.4	14.30
2	220	25.4	14.50
2	240	25.4	15.10
2	260	25.4	15.39
2	320	25.4	15.68

2.2 *Bonding FRP laminates to the concrete blocks*

Two methods were used to bond the composite laminates to the concrete blocks: (i) bonding prefabricated cured GFRP and CFRP laminates on the concrete blocks, as opposed to (ii) the in-place bonding and curing of the GFRP fabric and the CFRP laminates directly on the concrete. The concrete surface was first sandblasted and then cleaned by air-blasting. The surfaces of the prefabricated laminates were roughened by sand paper and then cleaned and wiped with acetone to remove contaminants.

For the preliminary bond tests described in Section 2.5 the first preparation method, consisting of bonding prefabricated laminates to the concrete block, was adopted. This bonding procedure with CFRP laminates requires the prior application of a primer. This primer was applied evenly over the entire surface according to the manufacturers' specifications. The second method, which consisted of bonding and curing the GFRP fabric and unidirectional CFRP sheets directly on the concrete block, was used for the second and more detailed set of tests. For these tests, the same surface preparation procedure for the concrete blocks and primer application were employed for the CFRP-bonded joints. However, only 25.4 mm wide GFRP fabric and CFRP sheets with 1 and 2 plies were used for these tests.

During the preparation of the specimens, a relatively uniform thickness of 1–1.2 mm of the adhesive layer was assured by using aluminum guides. The bonded joints were allowed to cure for 14 days before the bond tests were performed. The various test parameters are listed in Tables 1 and 2 including the recorded failure load.

3 THE TEST APPARATUS

The test apparatus is shown schematically in Figs. 1(a) and 1(b), and a photograph of the assembly is given in Fig. 2(a) and Fig. 2(b). The assembly is mounted in a 100 kN MTS loading frame, and is composed of: 1 – the frame, 2 – the load cell, 3 – the servo-hydraulic grips, 4 – the FRP test laminate, 5 – an aluminum attachment for the Linear Variable Displacement Transducers (LVDTs), 6 – steel bolts, 7 – shear connectors, 8 – a roller (spherical) bearing attached to the shear connectors and designed so as to correctly align the specimen, 9 – two U-shaped longitudinal steel supports, of 150 kN load capacity, 10 – an aluminum ring for fixing the Linear Variable Displacement Transducers (LVDTs), 11 – two LVDTs, 12 – four steel rods to tightly secure the test specimen, 13 – the concrete block to which is bonded the FRP laminate, 14 – a threaded steel rod designed for a minimum tensile force of 150 kN, 15 – a counter-twisting attachment to prevent any rotation of either the test specimen or the test rig, 16- the lower platform of the frame, and 17 – the piston of the MTS load system.

By pulling on the FRP laminate, the face of the upper concrete section comes into contact with the bearing plate. The resulting bearing pressure is transmitted to the two U-shaped steel supports via the upper shear connector plate. The longitudinal steel supports transmit the applied load to the lower part of the frame via the lower shear connector plate and the threaded steel rod.

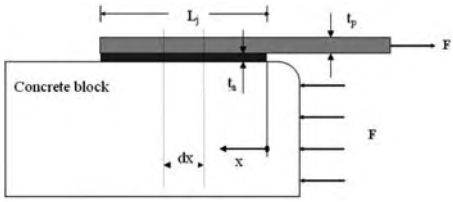

Figure 1a. Specimen configuration.

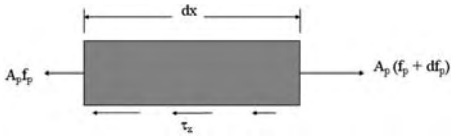

Figure 1b. Equilibrium of element of bonded laminate.

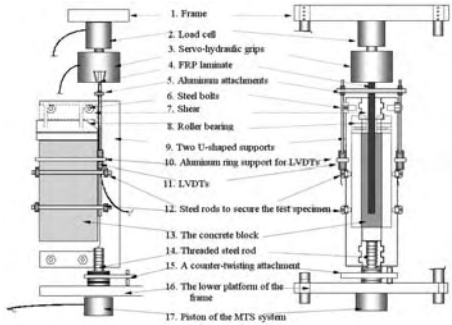

Figure 2. Test setup.

The alignment of the test rig was insured in two steps. First, after fixing the test rig on the lower platform of the frame via the threaded steel rod (14), the alignment of the whole assembly relative to the servo-hydraulic grips was insured by: (i) positioning a steel plate with a thickness of 6 mm in the grips, (ii) measuring the steel plate misalignment relative to the assembly by means of two displacement transducers fixed to both the U-shaped longitudinal steel supports and the steel plate, and (iii) minimizing the readings of the two transducers. Afterwards, the test rig was prevented from twisting by fixing it to the lower platform of the loading frame by the counter-twisting attachment (15) which allowed only vertical movements. The steel plate was then removed from the grips and the FRP-concrete joint specimen was placed in the test rig. A proper alignment of the specimen itself was made possible by having elliptical holes in the upper and lower parts of the U-shaped supports which

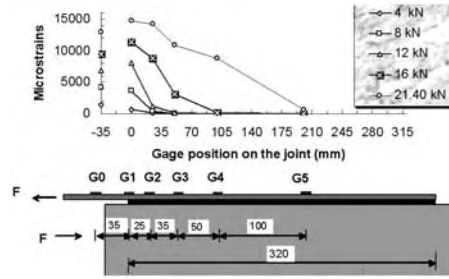

Figure 3. Strain distribution along a 2-ply GFRP-concrete joint.

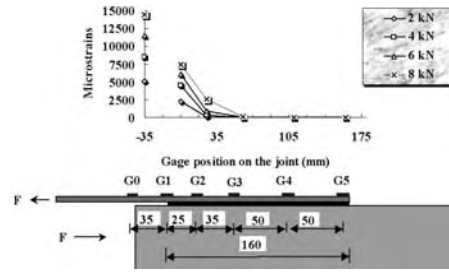

Figure 4. Strain distribution along a 1-ply CFRP-concrete joint.

permitted the necessary movement of the U-shaped supports relative to the shear connectors.

3.1 *Strain profiles along the bonded joints*

Figures 3 and 4 show the strain gage readings at various two load levels for the 1-ply CFRP-to-concrete and 2-ply GFRP-to-concrete. Gage G0 refers to the strain in the composite specimen alone, while the readings beginning with gage G1 represent the strains in the bonded joints. From these strain distribution profiles, three distinct profile trends corresponding to three different regions of the joint, which depend on the levels of loading, may be identified. The first trend corresponds to exponentially decreasing strain distributions as the load is initially applied. This exponential trend extends over the region between gages G1 and G3. The distance required for the strain to reach zero defines the so-called initial transfer length. The maximum load level associated with this strain distribution trend is that needed to initiate a crack in the concrete block at the bearing end. In the case of GFRP bonded joints, cracking at the most highly stressed end began at 55% to 63% of the ultimate tensile capacity of the GFRP laminate, while for the CFRP bonded joints cracking

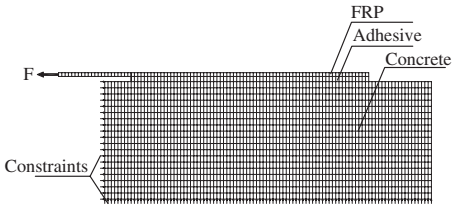

Figure 5. Finite element model.

began between 62% and 68% of the ultimate tensile capacity of the CFRP laminate.

Once a crack is initiated, further loading gradually displaces the transfer region towards the unloaded end, and the resulting strain profiles show a more or less bilinear decreasing trend, with a transition point occurring at the limit of the initial transfer region. This transition point coincides with either gage G3 or G4 as can be seen from Figs 3, 4 and 6. During the final stages of loading Figs 3 and 4 (for GFRP-to-concrete joints) show a more or less linearly decreasing strain profile trend, while Fig. 6 (2-ply CFRP bonded joint) depicts a somewhat non-linear trend. The corresponding transfer region extends from gage G4 to the end of the joint. It should be noted that for the 1-ply CFRP bonded joint (Fig. 5), only an exponential-type strain distribution profile was observed.

4 ANALYTICAL MODEL

4.1 *Analysis of bonded joint*

An analytical model for determining the shear stress distribution on a bonded composite-to-concrete joint, based on shear lag theory and valid only in the elastic range is developed in this section. For a detailed analysis, the reader is referred to the theoretical investigations carried out by Malek et al. (1996) and Maeda et al. (1997).

Figures 1(a) and 1(b) show the joint configuration and a typical segment of a bonded joint with the appropriate system of forces used in this analysis. From the equilibrium of an element Δx of the FRP laminate, one can write:

$$\frac{A_p}{A_c} = -\frac{df_p(x)}{df_c(x)} \quad ; \quad \tau(x) = t_p \frac{df_p(x)}{dx} \qquad (1a,1b)$$

where $A_p, A_c, f_p(x), f_c(x)$ and $\tau(x)$ are, respectively, the FRP laminate cross-section, the concrete block cross-section, the axial tensile stress applied on the FRP laminate, the axial compressive stress in the concrete block and the shear stress at a position x of the joint.

The shear stress in the adhesive can be expressed as

$$\tau_x = G_a \gamma(x) \qquad (2)$$

where G_a and $\gamma(x)$ are, respectively, the shear modulus and shear strain of the adhesive. From strain compatibility, we have:

$$t_a \frac{d\gamma(x)}{dx} = \frac{du(x)}{dx} = \varepsilon_p(x) - \varepsilon_c(x) \qquad (3)$$

where, t_a, $u(x)$, $\varepsilon_p(x)$ and $\varepsilon_c(x)$ are, respectively, the thickness of the adhesive, the longitudinal displacement, the strain in the FRP laminate and the strain in the adjacent concrete layer. Combining equations 2 and 3 and assuming a linear behaviour of the FRP laminate and the concrete in tension, one can write:

$$\frac{f_p(x)}{E_p} - \frac{f_c(x)}{E_c} = \frac{t_a}{G_a} \frac{d\tau(x)}{dx} \qquad (4)$$

Combining 1a, 1b and 4, one can write:

$$\frac{d^2\tau(x)}{dx^2} - \lambda^2 \tau(x) = 0 \qquad (5)$$

with

$$\lambda = \left[\frac{G_a}{E_p t_p t_a} (1 + \eta\rho) \right]^{\frac{1}{2}}$$

$$\eta = \frac{E_p}{E_c} \text{ and } \rho = \frac{A_p}{A_c} = -\frac{df_c(x)}{df_p(x)}$$

The solution to equation 6 takes the form:

$$\tau(x) = B\cosh(\lambda x) + C\sinh(\lambda x) \qquad (6)$$

The constants B and C are obtained by employing the following boundary conditions:

$$\text{at x} = 0,\ \varepsilon_p = -\frac{F}{A_p E_p},\ \varepsilon_c = \frac{F}{A_c E_c}$$

$$\text{at x} = L_j,\ \varepsilon_p = \varepsilon_c = 0.$$

Combining these boundary conditions with equations 4 and 6, the constants B and C are found to be:

$$B = \tau_m \frac{\lambda L_j}{\tanh(\lambda L_j)},\quad C = -\lambda L_j \tau_m \qquad (7)$$

where $\tau_m = F / b_p L_j$ represents the mean shear stress

on the bonded joint. Once the shear stress distribution along the joint is found, the axial stress in the FRP laminate can be computed from an integration of equation 6b, and takes the form:

$$f_p(x) = \frac{\tau_m L_j}{t_p \sinh(\lambda L_j)} \left[\sinh \lambda\left(x - L_j\right)\right] \quad (8)$$

The resulting strain in the FRP laminate is obtained from Hooke's law as:

$$\varepsilon_p(x) = \frac{1}{E_p} \frac{\tau_m L_j}{t_p \sinh(\lambda L_j)} \left[\sinh \lambda\left(x - L_j\right)\right] \quad (9)$$

5 FINITE ELEMENT ANALYSIS

A plane-stress linear elastic finite element analysis of the FRP-concrete joints is presented. The finite element model of the corresponding experimental test is build in an in-house code that is developed for the purpose of investigating the interfacial behaviour of FRP composites when bonded to concrete. The constitutive models of concrete, adhesive and FRP laminates are elastic. The material parameters required to define the constitutive models of different materials are obtained experimentally and used in the analysis. Since the problem modelled using the code is a simple shear test, then the stresses generated in concrete at the interface is mainly shear stresses. The shear stresses in concrete are directly proportioned to the diagonal tension. One can assume the concrete behaviour in tension until cracking occur is elastic. The implementations of the code lie in the range of pre-cracking stage in concrete. The in-house code is in its preliminary stage. Next stage in this code includes defining failure criteria and then developing a more accurate constitutive material model for the materials.

5.1 *Finite element model*

Figure 5 shows the mesh configuration, boundary conditions and load application of the finite element application. The model consists of layers of concrete, adhesive and FRP composite. The notations of the dimensions and the coordinates can be taken from Figure 1. The model allows full transfer of load between concrete and adhesive and between adhesive and FRP composite by adopting the full bond assumption. However, it accurately represents the experimental testing by considering the presence of the adhesive layer as an intermediate layer. To simulate the actual testing, a gap along the interface is modelled at the edge of the concrete block. This gap was modeled in this analysis and in the experimental program to eliminate the concentrated shear stresses and peeling-off stresses at the

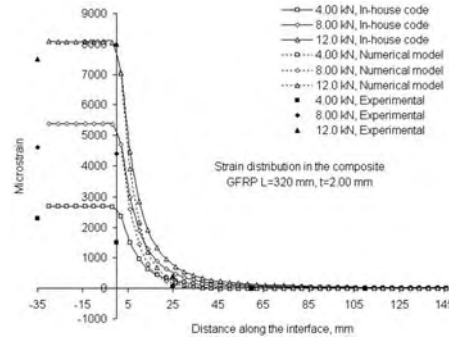

Figure 6. Strain distribution in the adhesive for a CFRP-concrete joint.

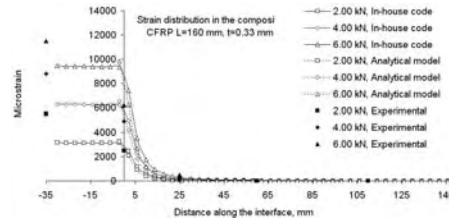

Figure 7. Strain distribution in the adhesive for a GFRP-concrete joint.

concrete edge. It was observed during the experimental testing that a local failure occurred when there is no gap at the edge of concrete at the interface. Models for the cases without a gap are also introduced for the sake of comparison.

5.2 *Case studies*

Finite element models are studied for selected cases corresponding to the experimental tests. The selected cases are two GFRP-concrete joints and two CFRP-concrete joints. For the GFRP-concrete joints, the bonded lengths and the FRP thicknesses are 160 and 1.00 mm (1-ply); and 320 mm and 2.00 mm (2-ply), respectively. For the CFRP-concrete joints, the bonded lengths and the FRP thicknesses are 180 and 0.33 mm; and 320 mm and 0.66 mm, respectively.

6 NUMERICAL RESULTS

Samples of experimental as well as numerical strain distribution profiles for GFRP-to-concrete and CFRP-to-concrete joints are shown in Figures 6 and 7. Both the numerical model and the in-house finite element

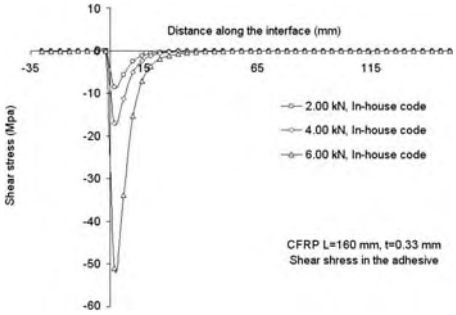

Figure 8. Shear stress distribution in the adhesive for a CFRP-concrete joint.

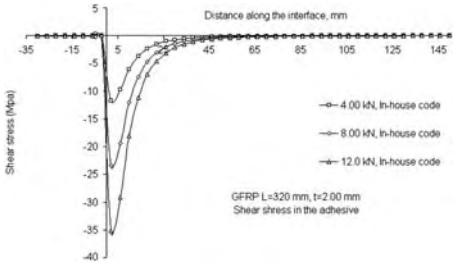

Figure 9. Shear stress distribution in the adhesive for a GFRP-concrete joint.

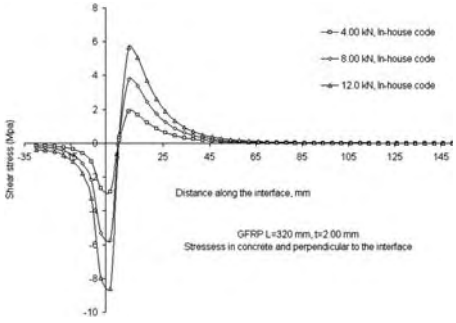

Figure 10. Stresses in concrete perpendicular to interface for a CFRP-concrete joint.

code predict fairly well the strain distribution in the FRP composite.

The advantage of the in-house finite element code over the experimental testing is the ability to estimate the interfacial behaviour of the FRP-joint in terms of the shear stress distributions in the concrete adjacent

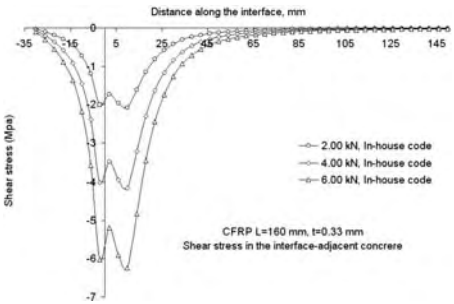

Figure 11. Shear stress distribution in the interface-adjacent concrete layer for a GFRP-concrete joint.

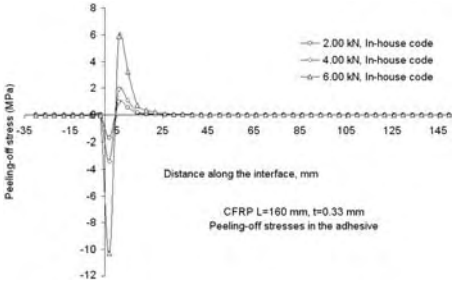

Figure 12. Peeling-off stress distribution in the adhesive layer for a CFRP-concrete.

to the interface and in the adhesive layer as well as the peeling-off stresses in the adhesive. These quantities could not be measured experimentally. Considering the concordance in the estimation of the shear strain distribution between the experimental and the in-house code results, one can expect that the other quantities are estimated fairly accurately. Figures 8 and 9 show the shear stress distribution in the adhesive for a 1-ply CFRP-concrete joint and for a 2-ply GFRP-concrete joint. In addition, Figure 10 shows the stresses in concrete perpendicular to the interface for a 1-ply CFRP-concrete joint. Figure 11 shows the shear stress distribution in the concrete adjacent to the interface for a 2-ply GFRP-concrete joint. Finally, the peeling-off stress distribution along the interface in the adhesive layer for a 1-ply CFRP-concrete joint and for a 2-ply GFRP-concrete joint are shown in Figures 12 and 13.

7 CONCLUSION

An experimental and analytical investigation has been carried out with the objective of improving our understanding of the transfer mechanisms involved when

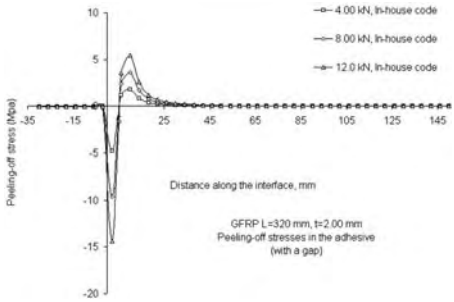

Figure 13. Peeling-off stress distribution in the adhesive layer for a GFRP-concrete joint.

composite laminates are bonded to concrete. From the experimental standpoint, a new and fairly simple test apparatus was designed. The test rig could be a useful tool for testing not only concrete-to-composite joints, but also other combinations of materials. Furthermore, it offers the possibility of performing four pull-out bond tests on the same concrete block, thus allowing materials savings and eliminating potential problems with variability of the concrete surface quality. The test apparatus can also be resized according to the study at hand. The tests results obtained from this test apparatus (strain distributions along the joint) are very reproducible and complement the findings of others.

From the tests, it was possible to develop the full tensile capacity of the bonded composite plates for both 1 and 2-ply GFRP and CFRP plates. It was seen that, for 1-ply and 25 mm wide GFRP-to-concrete joints, bond lengths of 160 mm were sufficient to develop the full tensile capacity of the composite. For 2-ply and 25 mm wide GFRP-to-concrete joints, bond lengths of 260 mm were sufficient to develop the full tensile capacity of the composite. In the case of 1 and 2-ply 25 mm wide CFRP-to-concrete joints, bond lengths of 80 mm and 220 mm, respectively, were sufficient to develop the full capacity of the composites.

From the analytical standpoint, a fairly simple analysis based on shear lag theory was developed and results were compared with the experimental data. For the linear elastic range the analytical results were shown to be in good agreement with the experimental data.

A plane stress linear finite element analysis is used to model the problem of FRP/concrete interface. A fairly good agreement was achieved with both the experimental results and the aforementioned numerical model in terms of the strain distribution along the composite. A main advantage of this in-house code is its ability to estimate the interfacial stresses and strains in the joint. The code in its present state is a linear elastic code. Future plans of enhancing the code will consider the nonlinearity in both the analysis and the material behaviour. For the limited purpose of the test, such a linear elastic finite element code can predict fairly well the interfacial behaviour of the FRP/concrete in the elastic range.

REFERENCES

Chajes, M.J., Januszka, T.F., Mertz, D.R., Thomson, T.A., Jr., and Finch, W.W. 1995. Shear Strengthening of Reinforced Concrete Beams Using Externally Applied Composite Fabrics. ACI Structural Journal, 92(3): 295–303.

Chajes, M.J., Finch, W.W., Jr., Januszka, T.F., and Thomson, T.A., Jr. 1996. Bond and Force Transfer of Composite Material Plates Bonded to Concrete. ACI Structural Journal, 93(2): 295–303.

Hull, D., and Clyne, T.W. 1996. An Introduction to Composite Materials. 2nd Edition, Cambridge University Press, Cambridge, UK.

Jones, R., Swamy, R.N., Bloxham, J., and Bouderbalah, A. 1980. Composite Behavior of Concrete Beams with Epoxy Bonded External Reinforcement. International Journal of Cement Composites, 2(2): 91–107.

Kazuaki, N., Atsushi, Y., and Hiroyiki, H. 1996. Numerical Approach for Evaluation of Stress Transmissibility of Composite Interface. Design and Manufacturing of Composites, Proceedings of the Joint Canada-Japan Workshop on Composites, Kyoto, Japan, Hoa, S.V., and Hamada, H., Editors: 183–186.

Kobatake, Y., Kimura, K., and Katsumata, H. 1993. A Retrofitting Method for Reinforced Concrete Structures Using Carbon Fiber. Fiber Reinforced Plastic (FRP) Reinforcement for Concrete Structures: Properties and Applications, Nanni, A., Editor, Elsevier Science Publishers, Oxford, UK: 435–450.

Maeda, T., Asano, Y., Sato, Y., Ueda, T., and Kakuta, Y. 1997. A Study on Bond Mechanism of Carbon Fiber Sheet. Non-Metallic (FRP) Reinforcement for Concrete Structures, Proceedings of the Third International Symposium (FRPRCS-3), Japan Concrete Institute, Sapporo, Japan, 1: 279–286.

Malek, A.M., Saadatmanesh, H., and Ehsani, M.R. 1996. Shear and Normal Stress Concentrations in RC Beams Strengthened with FRP Plates. Advanced Composite Materials in Bridges and Structures, El-Badry, M., Editor, Canadian Society for Civil Engineering, Montreal, Quebec, Canada: 629–637.

Neubauer, U., and Rostasy, F.S. 1997. Design Aspects of Concrete Structures Strengthened with Externally Bonded CFRP Plates. Proceedings of the 7th International Conference on Structural Faults and Repair, UK, 2: 109–118.

Niu, H. and Wu, Z. 2001. Interfacial Debonding Mechanism Influenced by Flexural Cracks in FRP-Strengthened Beams. Journal of Structural Engineering, 47A: 1277–1287.

Quantrill, R.J., Hollaway, L.C., and Thorne, A.M. 1996. Experimental and Analytical Investigation of FRP Strengthened Beam Response: Part I. Magazine of Concrete Research, 48(177): 331–342.

Quantrill, R.J., Hollaway, L.C., and Thorne, A.M. 1996. Prediction of the Maximum Plate End Stresses of FRP Strengthened Beams: Part II. Magazine of Concrete Research, 48(177): 343–351.

Smith, S.T., Teng, J.G., and Lu, M. 2003. Neural Network Prediction of Plate end Debonding in FRP-Plated RC Beams. Fibre Reinforced Polymer Reinforcement for Concrete Structures, FRPRCS-6. Edited by Kiang Hwee Tan. Published by World Scientific Publishing Company. Singapore, 2: 193–204.

Teng, J.-G., Lu, X.Z., Ye, L.P., and Jiang, J.J. 2004. Recent Research on Intermediate Crack-Induced Debonding in FRP-Strengthened RC Beams. Advanced Composite Materials in Bridges and Structures, ACMBS-IV, Edited by Mamdouh El-Badry and Laszlo Dunaszegi. Published by CSCE. On CD-ROM. Calgary, Alberta, Canada. 12 pages.

Triantafillou, T.C. and Plevris, N. 1992. Strengthening of RC Beams with Epoxy-Bonded Fiber-Composite Materials. Materials and Structures, 25: 201–211.

Van Gemert, D.-A. 1980. Repairing of Concrete Structures by Externally Bonded Steel Plates. International Journal of Adhesion, 2: 67–72.

Wu, Z. and Niu, H. 2000. Study on Debonding Failure Load of RC Beams Strengthened with FRP Sheets. Journal of Structural Engineering, 46A: 1431–1441.

Ziraba, Y.N., Baluch, M.H., Basunbul, I.A., Azad, A.K., Al-Sulaimani, G.J., and Sharif, A.M. 1995. Combined Experimental-Numerical Approach to the Characterization of the Steel-Glue-Concrete Interface. Materials and Structures, 28: pp. 518–525.

FRP Composites in Civil Engineering – CICE 2004 – Seracino (ed)
© 2005 Taylor & Francis Group, London, ISBN 90 5809 638 6

Bond behavior of CFRP rods in RC beam with hanging region

Rendy Thamrin, Tran Thang Ngoc, Samnang Hir, Naoki Yoshikawa & Tetsuzo Kaku
Toyohashi University of Technology, Toyohashi, Aichi, Japan

ABSTRACT: Due to the higher tensile strength, non-plastic (having no yield point) behavior and a little lower bond strength, carbon fiber reinforced polymer (CFRP) rods are favorable materials to investigate the development or anchorage length of reinforced concrete members compared with the conventional mild steel bars. This paper presents an experimental study on bond behavior of longitudinal bars in hanging region of the reinforced concrete beams. In order to realize the bond splitting failure, CFRP rods were used as longitudinal bars. The main test variables are (a) transverse reinforcement ratio and bond length in hanging region, and (b) transverse reinforcement ratio in shear span. Based on the test results, the provision of the Architectural Institute of Japan (AIJ) code on the development length of the hanging region was evaluated, and a model for predicting additional deflection due to the tension shift force was also presented.

1 INTRODUCTION

When shear inclined cracking develops in the shear span on reinforced concrete beam, the tension shift of the longitudinal tensile force occurs and a certain quantity of the tensile force exists at the support as shown in Fig. 1. This additional tensile force must be anchored in the hanging region beyond the support.

AIJ Code provides the development length greater than effective depth of the beam past the support, and ACI Code does not explicitly treat the effect of shear on tensile force and provides the minimum distance which ever is greater of the effective depth or 12 bar diameters past the theoretical cutoff point for flexure. The objective of the paper is to confirm the existence of the tension shift experimentally and to evaluate the code provisions for hanging region.

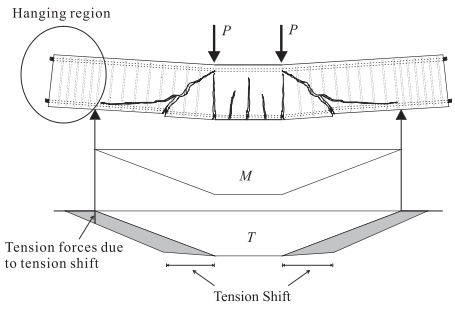

Figure 1. The phenomenon of tension shift in reinforced concrete beam with hanging region.

Due to the higher tensile strength, non-plastic (having no yield point) behavior and a little lower bond strength, carbon fiber reinforced polymer (CFRP) rods are favorable materials to investigate the development length or anchorage length of reinforced concrete members and to realize the bond splitting failure of the beam consciously.

Hence, the CFRP deformed rods were used in this experiment as the longitudinal tension bars instead of the conventional steel bars. Totally sixteen reinforced concrete beams were monotonically loaded to failure. Four of them were not comprised of any development length in the hanging region to observe the failure mode and the improper behavior due to lack of development length. The main variables were (a) transverse reinforcement ratio and development length in the hanging region, and (b) transverse reinforcement ratio in the shear span.

This paper considered not only the shear capacity but also the deformation of the beam after shear inclined cracking. A model predicting the additional curvature due to tension shift after shear inclined cracking was presented, and the deflection at the midspan was calculated.

2 EXPERIMENTAL SETUP

In this study, sixteen reinforced concrete beams have been tested. Specimens were divided into two groups G1 and G2. Details of specimen and test variables are

Table 1. Detail of specimens and test variables.

Specimens	fc' (MPa)	Longitudinal Reinforcement (Tension)			Transverse Reinforcement in Shear Span		Transverse Reinforcement in Hanging Region		
		Number	d_b (mm)	ρ %	d_b (mm)	ρ_{ws} %	Bond Length L_b (mm)	d_b (mm)	ρ_{wh} %
G1-1	38.25	2	10	0.575	6	0.669	160	6	0.725
G1-2									0.544
G1-3									0.272
G1-4							220		0.725
G1-5									0.544
G1-6									0.272
G1-7							280		0.544
G1-8									0.272
G2-1	40.2	4		1.151		0.967	0	0	
G2-2						0.870			
G2-3						0.777			
G2-4						0.680			
G2-5	48.5					0.967	100		
G2-6						0.870			
G2-7						0.777			
G2-8						0.680			

Table 2. Properties of reinforcement material.

	Longitudinal reinforcement		Transverse reinforcement steel ($d_b = 6$ mm)
	Tension CFRP rods ($d_b = 10$ mm)	Compression steel ($d_b = 10$ mm)	
Tensile strength (MPa)	1906	–	–
Young modulus (GPa)	164	168	168
Yield strength (MPa)	–	403	550
Fibre content	60%	–	–
Specific gravity	1.52	–	–

shown in Table 1 and Table 2 presents the information of reinforcement materials.

All of the specimens were 130 mm wide and 230 mm deep. The specimen was simply supported and subjected to two-point loads. The distance between loading and supporting point was 450 mm. To observe bond stress in the shear span, strain gages were attached on the longitudinal reinforcement at the support and the loading point. Specimen detail and loading position are shown in Fig. 2.

In the case of beam group 1 (G1), the effect of development length in hanging region to the bond characteristic on the specimens were investigated using three different hanging lengths: 160, 220, 280 mm (see Table 1). The influences of transverse reinforcement in hanging region were also investigated by using three different reinforcement ratios, ρ_{wh} (0.27, 0.54, and 0.72%).

Furthermore, in the case of G2, the influence of transverse reinforcement in shear span was observed by using four different reinforcement ratios, ρ_{ws} in shear span (0.68, 0.77, 0.87, and 0.97%). The effect of bond length, L_b (0 and 100 mm) was also investigated as illustrated in Fig. 2(b).

Figure 3 shows the experimental result conducted by Kaku et al. (Kaku et al. 1992) related to the bond characteristic of CFRP rods used in this study. It is shown that even though CFRP rod has lower bond strength comparing to the conventional steel bar, this value is still higher than the required bond strength calculated using Fujii-Morita equation (Fujii-Morita 1982).

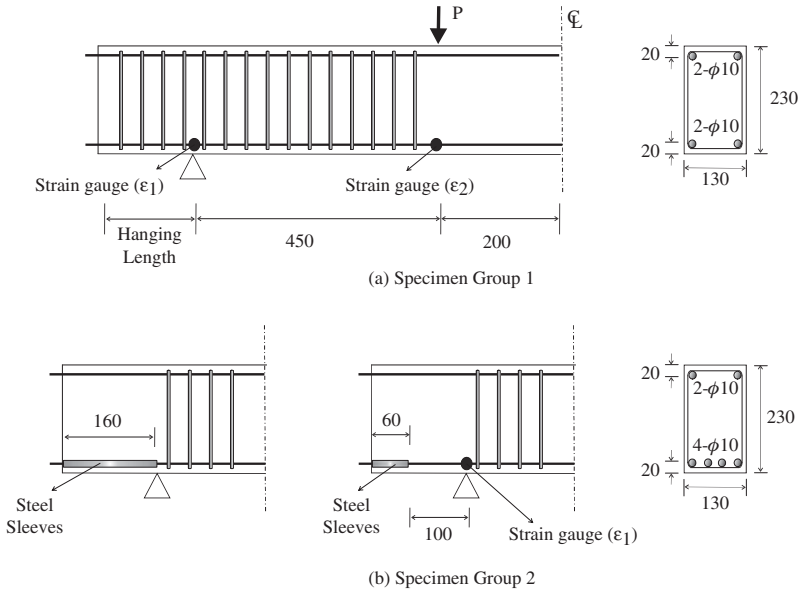

Figure 2. Specimen detail and loading position.

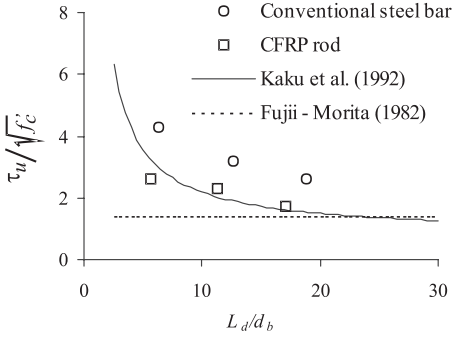

Figure 3. Bond behavior of CFRP rods.

3 BOND STRESS AND TENSION FORCE

3.1 *Bond stress*

Experimental bond stress, τ, in the shear span can be calculated by measured strains at the support, ε_1, and at the loading point, ε_2, as follows:

$$\tau_s = \frac{E_f d_b}{4L_{bs}}(\varepsilon_2 - \varepsilon_1) \quad (1)$$

while bond stresses in the hanging region were determined by:

$$\tau_h = \frac{E_f d_b}{4L_b}\varepsilon_1 \quad (2)$$

where E_f is the elastic modulus of FRP, d_b is the diameter of longitudinal reinforcement, L_{bs} is the shear span length, and L_b is the embedded length in hanging region.

Since the bond provision of AIJ is based on the Fujii-Morita proposal, the test results were compared with Fujii-Morita equation (Fujii-Morita 1982). The equation can be written as follows:

$$\tau_u = \tau_{co} + \tau_{st} \quad (3)$$

$$\tau_{co} = (0.117 b_i + 0.163)\sqrt{f_c'}\,(MPa) \quad (4)$$

$$\tau_{st} = (9.51\frac{kA_{st}}{sNd_b})\sqrt{f_c'}\,(MPa) \quad (5)$$

where τ_u is the bond strength, τ_{co} is the bond strength carried by concrete, τ_{st} is the bond strength carried by stirrups, b_i is the parameter for evaluating the geometrical arrangement of longitudinal bars, f_c' is concrete compression strength, k is the coefficient representing the efficiency of stirrups, A_{st} is the total area of stirrup

legs, s is the spacing of stirrups, N is number of longitudinal bars, and d_b is the diameter of longitudinal reinforcement.

Furthermore, a basic development length (L_d) for FRP rod, provided by ACI Committee 440, was also used as a comparable one with Fujii-Morita equation. The equation is given as follows:

$$L_d = K_2 \frac{d_b^{\,2} f_{fu}(MPa)}{\sqrt{f_c'}(MPa)} \tag{6}$$

Equation (6) can be written in term of bond strength as follows:

$$\tau_{ACI} = \frac{T}{L_d \phi} = \frac{A_f f_{fu}}{L_d \phi} = \frac{\sqrt{f_c'}(MPa)}{4K_2 d_b} \tag{7}$$

where T is the tension force of longitudinal reinforcement, ϕ is the perimeter of longitudinal reinforcement, A_f is area of longitudinal reinforcement, f_{fu} is the ultimate tensile strength of the FRP rod, K_2 is a constant taken 1/40 (Ehsani & Saadatmanesh 1996), and d_b is the diameter of longitudinal reinforcement.

3.2 *Tension force at the support*

The AIJ or ACI-318 codes require only the effective depth or 12 d_b for the development length in hanging region. But, if the tension force at the support after shear inclined cracking were known, a more precise provision could be presented. Based on statistical analysis a model for predicting the tension force at support as the function of shear force was proposed. Using this model not only the development length but also the additional deflection due to additional curvature can be determined. The detail of the proposed model will be described in section 4.3.

4 TEST RESULTS AND DISCUSSION

Summary of test results and observed failure modes are shown in Table 3. Based on experimental results, three main points will be discussed: the effect of transverse reinforcement ratio and bond length in hanging region, the influence of hanging region and transverse reinforcement ratio in shear span, and deflection behavior of the beams.

4.1 *Discussion on beam group 1*

In order to investigate the effect of transverse reinforcement ratio in hanging region, shear forces are plotted against bond stresses in hanging region as shown in Fig. 4. Figure 4(a) and (c) show that with increasing of transverse reinforcement ratio in hanging region from $\rho_{wh} = 0.27\%$ to 0.73%, there is no significant difference of bond stresses in hanging

Table 3. Bond strength and type of failure for each specimens.

	Experimental			Calculated						
				Fujii-Morita			ACI			
Specimens	V_{max} (kN)	τ_s (MPa)	τ_h (MPa)	τ_{co} (MPa)	τ_{st} (MPa)	τ_u (MPa)	τ_{ACI} (MPa)	τ_s/τ_u	τ_s/τ_{ACI}	Type of failure
G1-1	95.90	2.55	4.23	4.38	3.62	8.00	6.18	–	–	Flexural
G1-2	83.90	2.51	3.81	4.38	3.62	8.00	6.18	0.31	0.41	Bond
G1-3	76.70	2.69	4.04	4.38	3.62	8.00	6.18	–	–	Shear
G1-4	88.70	1.97	3.21	4.38	3.62	8.00	6.18	–	–	Flexural
G1-5	91.60	2.18	3.10	4.38	3.62	8.00	6.18	0.27	0.35	Bond
G1-6	85.00	3.14	5.05	4.38	3.62	8.00	6.18	0.39	0.51	Bond
G1-7	90.80	2.42	1.91	4.38	3.62	8.00	6.18	–	–	Shear
G1-8	95.70	3.66	2.33	4.38	3.62	8.00	6.18	–	–	Flexural
G2-1	73.20	1.54	–	2.70	1.89	4.60	6.34	0.34	0.24	Bond
G2-2	86.90	1.82	–	2.70	1.70	4.41	6.34	0.41	0.29	Bond
G2-3	72.60	2.04	–	2.70	1.52	4.22	6.34	0.48	0.32	Bond
G2-4	59.80	1.80	–	2.70	1.33	4.03	6.34	0.45	0.28	Bond
G2-5	97.70	2.18	2.31	2.97	2.08	5.05	6.96	–	–	Shear
G2-6	78.20	1.19	2.56	2.97	1.87	4.84	6.96	–	–	Shear
G2-7	78.20	1.18	3.09	2.97	1.67	4.64	6.96	–	–	Shear
G2-8	71.10	1.22	4.15	2.97	1.46	4.43	6.96	–	–	Shear

Note: V_{max} = maximum experimental shear force; τ_s = maximum bond stress in shear span, Eq. (1); τ_h = maximum bond stress in hanging region, Eq. (2); τ_u = total bond strength calculated using Eq. (3); τ_{co} = bond strength carried by concrete, Eq. (4); τ_{st} = bond strength carried by stirrups, Eq. (5); τ_{ACI} = bond strength calculated using Eq. (7).

region. Although Fig. 4(b) shows a little difference, the variation is not proportional to ρ_{wh}. Therefore, there is no influence of ρ_{wh} on bond stress in hanging region.

In Fig. 5, bond stresses in shear span are plotted versus shear forces to observe the influence of bond length in hanging region on bond stress in shear span. With increasing of bond length in hanging region from 160 mm to 280 mm, there is no significant decrease of bond stresses in shear span. Hence, bond length greater than 160 mm, which is still shorter than effective depth of the beam ($d = 210$ mm), has no further effect on the beam. As a result, the recommendation in AIJ and ACI codes, which suggested that the development length at hanging region should be equal or greater than the effective depth of the beam, is conservative.

4.2 *Discussion on beam group 2*

From test results of beams G2-5 to G2-8, shear forces are plotted against bond stresses in hanging region and bond stresses in shear span, as shown in Fig. 6(a) and (b), respectively.

These figures point out that as transverse reinforcement ratio in shear span (ρ_{ws}) increases, bond stresses in both hanging region and shear span decrease. Thus, bond stresses are significantly affected by ρ_{ws}.

To observe the relationship between bond stresses in shear span and that in hanging region, a typical curve, beam G2-7, from Fig. 6(a) and (b) are plotted on the same graph as shown in Fig. 7. Initially, the beam is uncracked where it exhibited linear behavior. This is attributed to the linear elastic characteristics of CFRP bars and concrete, and the perfect bond between CFRP bars and concrete. With additional loading, cracking occurs at the constant moment zone. Furthermore, when applied moment exceeds the cracking moment, a considerable increase in bond stresses show in shear span. Bond stress in shear span increases linearly as the load increases.

Until this stage of loading, bond stresses in hanging region (strain measured in tension longitudinal reinforcement at support, ε_1) are still zero. With further loading, inclined cracking occurs at shear span resulting in transfer of supplementary bond stresses from shear span to the hanging region (tension shift occurs).

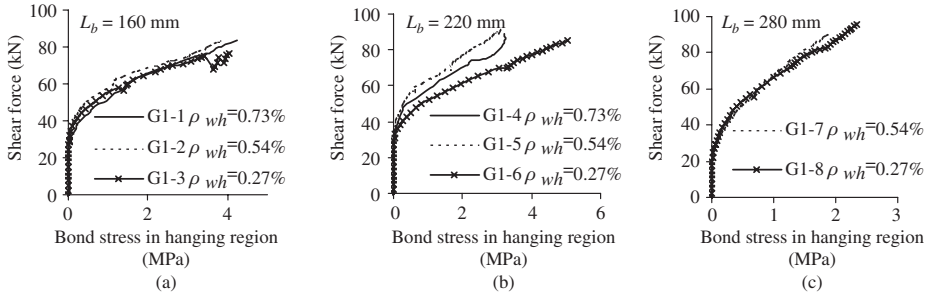

Figure 4. The effect of transverse reinforcement in hanging region on bond stress in hanging region.

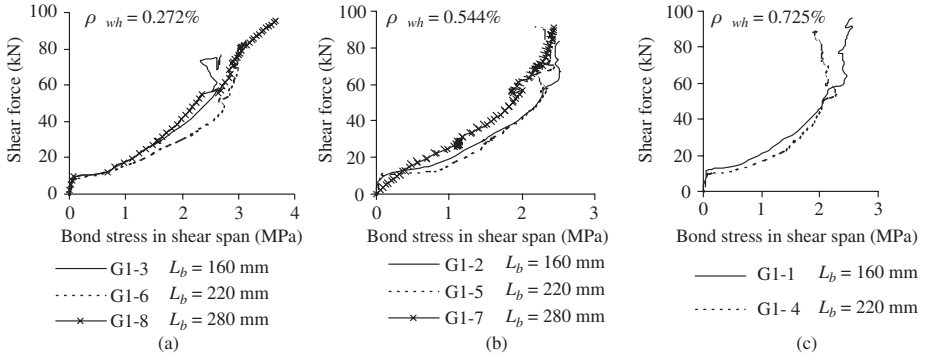

Figure 5. The effect of bond length in hanging region on bond stress in shear span.

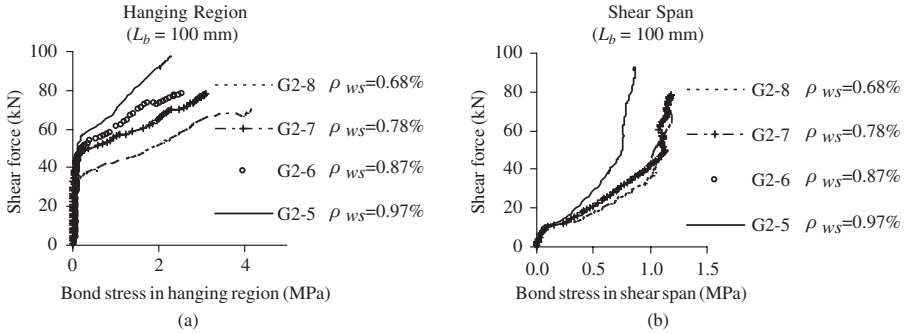

Figure 6. The effect of transverse reinforcement in shear span.

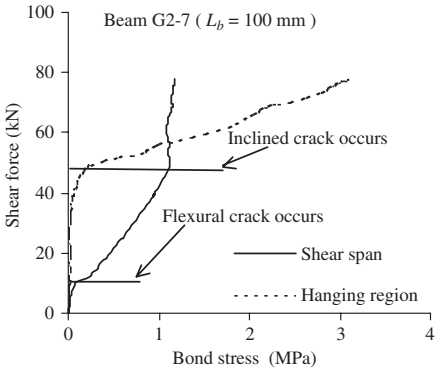

Figure 7. A typical relationship between bond stresses in shear span and hanging region.

Consequently, bond stress in hanging region start to increase. From this stage, bond stress in hanging region increases linearly, whereas bond stress in shear span remains constant with additional loading until failure.

To compare bond stress behavior in shear span without hanging region to that with hanging region, bond stresses in shear span are plotted versus shear forces in Fig. 8. As can be seen, these figures show significant influence of hanging region on bond stresses in shear span. Bond stresses in shear span without hanging region are higher than those with hanging region of 100 mm. With additional loading after shear inclined cracking, bond stress in shear span continues to increase for the beams without hanging region, but it almost remains constant for the beam with hanging region. This is due to the fact that there is a transfer of additional tension force in tension reinforcement to the hanging region after shear inclined cracking, as explained in Fig. 7. It is noted that the beams without hanging region (G2-1 to G2-4) failed in bond splitting failure mode, while beams with hanging region (G2-5 to G2-8) failed in shear. Moreover, the ultimate load carrying capacity of the beams with hanging region is higher than that of the beams without hanging region. This is because of the contribution of hanging region to the bond splitting capacity of the beams. It should be also noted that, in practical case, simply supported beam generally incorporates hanging region to prevent bond splitting failure mode, which is brittle and dangerous. As shown in Table 3, bond strengths predicted by ACI-440 equation (τ_{ACI}) are higher than those of experimental results for beams without hanging region. Thus, ACI-440 overestimates the bond strength of CFRP bars. Similarly, bond strengths predicted by Fujii-Morita equation (τ_u) are bigger than test results as well. Therefore, it would be not safe to use equation either suggested by ACI-440 or Fujii-Morita for predicting bond strength of CFRP rods in reinforced concrete beams without hanging region in which the failure mode is governed by bond splitting.

4.3 *Deflection behavior*

Statistical analysis has been conducted using strain data of each specimen (ε_1). Only the representative specimens G1-2 and G2-5 were presented in this paper (see Fig. 9). Based on the results of linear regression, an equation $T = AV - B$ was obtained where $A = 0.46$ and $B = 10.23$, then the coefficient A can be simplified to 0.5.

Furthermore, according to ACI-318 Sec. 11.3.1.1, shear force carried by concrete, V_c, is given by:

$$V_c(N) = \frac{\sqrt{f_c'}(MPa)}{6} b_w d \qquad (8)$$

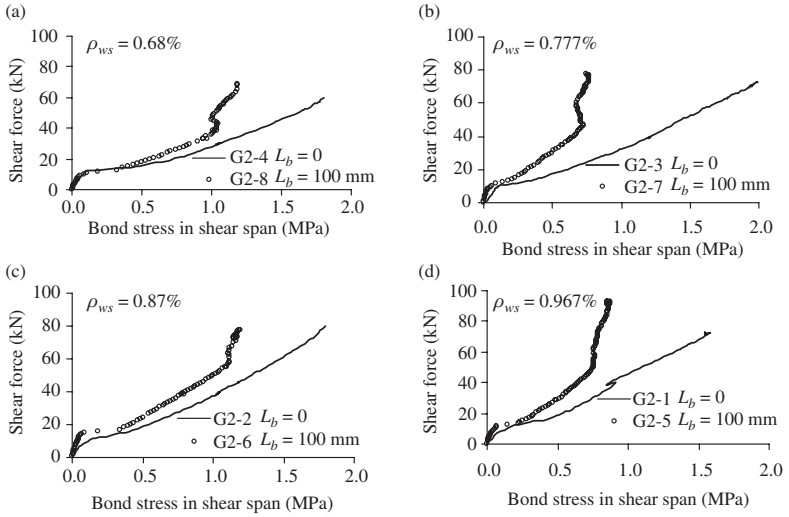

Figure 8. Influence of hanging region on bond stresses in shear span.

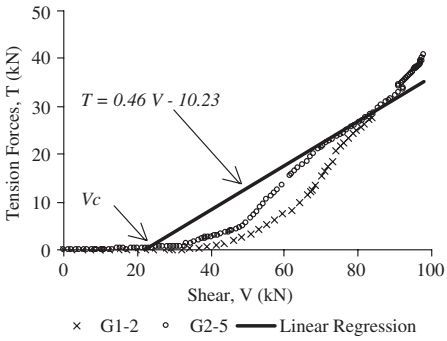

Figure 9. Relationship between shear force and tension force in longitudinal reinforcement at support.

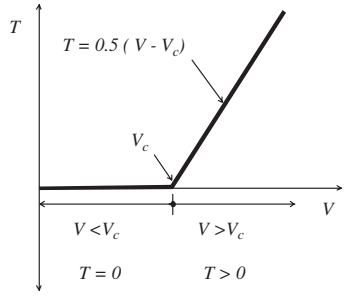

Figure 10. Suggested model to calculate additional tension forces at support due to tension shift.

where b_w is the web width, and d is the effective depth.

In the case of beam with FRP reinforcement V_c should be multiplied by E_f/E_s due to low modulus elasticity of FRP, as suggested in ACI-440 sec. 9.2, where E_f is the elastic modulus of FRP reinforcement, and E_s is that of steel. All of specimens were calculated with Equation (8) and E_f/E_s factor. It was found that V_c ranging from 15 kN to 20 kN. Based on this fact it is reasonable to replace the coefficient B to 0.5 V_c. Then a model to illustrate the additional tension force in the longitudinal reinforcement at support due to tension shift can be proposed. Figure 10 describes the model more clearly and can be explained as follows:

If $V < V_c$

$$T = 0 \tag{9}$$

and if $V > V_c$

$$T = 0.5(V - V_c) \tag{10}$$

where T is the tension force and V is the shear force.

In this study the proposed model was applied to calculate the additional curvature after the shear inclined cracking. The additional deflection due to additional curvature was calculated and added to analytical

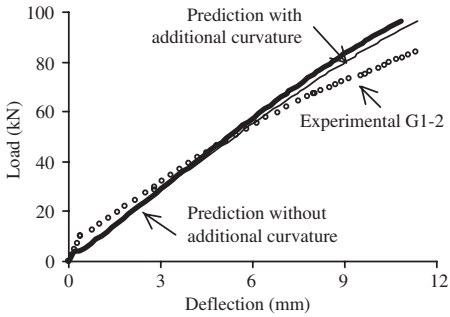

Figure 11. Analytical load-deflection curve compare with experimental results.

deflection, which was calculated based on theoretical moment-curvature (Park & Paulay 1975).

Subsequently, the additional curvature can be calculated as:

$$\varphi_a = \frac{\varepsilon_a}{z} \tag{11}$$

where ϕ_a is the additional curvature after shear inclined cracking, ε_a is the additional strain, z is the lever arm of internal forces.

It is shown from Fig. 11 that the load–deflection curve calculated with additional curvature shows a little improvement comparing to the one without additional curvature. It is noted that other effects should be also considered to calculate the deformation of RC beam failed in shear, such as the effect of dowel action, slippage of longitudinal bars, and so on.

5 CONCLUSIONS

Totally 16 beams have been tested to investigate the bond behavior of RC beams with hanging region using CFRP rods. The results of analytical and experimental investigation described above, led to the following conclusions:

1. AIJ and ACI codes conservatively provide development length at hanging region.
2. ACI-440 and Fujii-Morita equations overestimate the bond strength of CFRP bars in the beams without hanging region.
3. Hanging region has significant influence on improving bond splitting capacity of the beams.
4. Transverse reinforcement ratio in hanging region has no influence on bond stress in hanging region.
5. Transverse reinforcement ratio in shear span significantly affects bond stress in both hanging region and shear span.
6. Analytical load–deflection curve calculated by additional curvature shows a little improvement comparing with that neglecting additional curvature.

NOTATION

A_f = total area of longitudinal reinforcement (mm^2)
A_{st} = total area of stirrups legs (mm^2)
b_i = parameter for evaluating the geometrical arrangement of longitudinal bars
b_w = beam width (mm)
d = effective depth (mm)
d_b = diameter of longitudinal reinforcement (mm^2)
E_f = elastic modulus of FRP (MPa)
f'_c = concrete compression strength (MPa)
f_{fu} = ultimate tensile strength of the FRP rods (MPa)
k = coefficient representing the efficiency of stirrups
K_2 = constant
L_b = embedded length in hanging region (mm)
L_{bs} = shear span length (mm)
L_d = development length (mm)
N = number of longitudinal bars
s = spacing of stirrups (mm)
T = tension force in the longitudinal reinforcement (N)
V = shear force (N)
V_c = shear force carried by concrete (N)
z = lever arm of internal force (mm)
ε_1 = measured strain at the support
ε_2 = measured strain at the loading point
ε_a = additional strain after inclined cracking
ϕ = perimeter of longitudinal reinforcement (mm)
φ_a = additional curvature after inclined cracking
ρ = longitudinal reinforcement ratio
ρ_{wh} = transverse reinforcement ratio in hanging region
ρ_{ws} = transverse reinforcement ratio in shear span
τ_{ACI} = bond stress calculated from ACI development length equation (MPa)
τ_{co} = bond strength carried by concrete (MPa)
τ_h = bond stress in the hanging region (MPa)
τ_s = bond stress in the shear span (MPa)
τ_{st} = bond strength carried by stirrups (MPa)
τ_u = bond strength (MPa)

REFERENCES

ACI 318-95, 1995, Building Code Requirements for Structural Concrete, American Concrete Institute.

ACI Committee 440, 2000, Guide for the Design and Construction of Concrete Reinforced with FRP Bars, American Concrete Institute.

AIJ, 1999, Standard for Structural Calculation of reinforced Concret Structures – Based on Allowable Stress Concept, Japan, (in Japanese).

Ehsani. M. R., and Saadatmanesh, H., 1996, *Design Recommendations for Bond of GFRP Rebars to Concrete*, Journal of Structural Engineering, Vol. 122, No. 3, pp. 247–254.

Hansapinyo, C., Pimanmas, A., Maekawa, K., and Chaisomphob, T., 2003, *Proposed Model of Shear Deformation of Reinforced Concrete Beam After Diagonal Cracking*, Journal of Materials, Concrete Structure, Pavements, JSCE, Vol. 58, No. 75, pp. 305–319.

Kaku, T., Zhang, J., Iizuka, S., and Yamada, M., 1992, *A Proposal of Equation for Bond Splitting Strength of Reinforced Members Including High Strength Concrete Level*, Concrete Research and Technology, Japan Concrete Institute, Vol. 3, No. 1, Issue 5, pp. 97–108, (in Japanese).

Morita, S. and Fujii, S., 1982, *Bond Capacity of Deformed Bars Due to Splitting of Surrounding Concrete, Bond in Concrete*, edited by Bartos. P., Applied Science Publisher, pp. 331–341.

Park, R., and Paulay T., 1975, *Reinforced Concrete Structures, John Wiley*, New York, 769 pp.

Thamrin, R., Kaku, T., and Komiya, I., 2003, *Study of Flexural and Bond Behavior of RC Beam with FRP rods*, Proceedings of The Ninth East Asia-Pacific Conference on Structural Engineering and Construction, Bali, Indonesia, pp. RCS-256–RCS-261.

FRP Composites in Civil Engineering – CICE 2004 – Seracino (ed)
© 2005 Taylor & Francis Group, London, ISBN 90 5809 638 6

Dowel resistances of bond interfaces between FRP sheets and concrete

Jianguo Dai, Tamon Ueda, Yasuhiko Sato & Hadiyono Jaqin
Hokkaido University, Sapporo, Japan

ABSTRACT: Bonding FRP sheets externally to existing concrete structures to prevent the spalling of concrete is becoming a popular application of FRP technology in Japan. In the paper, a series of experimental studies are performed to observe the failure mechanisms at different peeling stages of FRP sheet–concrete interfaces under dowel action, and also, to calibrate the interface spalling fracture energy, which can be used for spalling prevention design of concrete structures by using externally bonded FRP sheets. Experimental parameters are concrete strength, stiffness of FRP, properties of adhesives, methods for concrete surface treatment as well as the preset initial crack length between FRP sheets and concrete. Analytical models clarifying relationships among peeling angle, interface spalling energy and dowel force capacity are built up. The effects of FRP stiffness, adhesive types, and concrete strength on the interface-peeling angles, interface spalling energy as well as the interface dowel resistance are discussed. Finally, suggestions for optimal spalling prevention design of FRP sheet–concrete interfaces are given.

1 INTRODUCTION

Technology of bonding FRP sheets to the surface of existing concrete structures for the purpose of preventing spalling of concrete from tunnel lining or elevated bridges has obtained popularity in Japan. Various FRP materials with different stiffness have been applied in engineering applications. It has the necessity of developing guidelines, which include both test method and analytical model to calibrate design parameters of FRP sheet-concrete interface under the spalling action.

Wu et al. (2000) did substantive work related to the spalling resistance of FRP sheet–concrete interfaces. They performed punching shear tests for concrete slabs with externally bonded one and two directional FRP sheets. The center of each strengthened slab had a hole for exerting punching shear force. Based on experimental results, they tried to use interface-spalling energy to predict the spalling resistance of FRP sheet–concrete interfaces under shear punching. But the interface peeling mechanisms at different peeling stages have not been sufficiently clarified, and also the model for deriving interface spalling fracture energy from their experimental results was rather complex. By following Wu et al. (2000)'s work, Yoshikawa et al. (2002) proposed another solution for predicting the spalling resistance of FRP sheet–concrete interfaces. They considered that the interface spalling resistance is contributed by tension softening area of concrete. They treated FRP sheets as tension elements in concrete tension softening area by neglecting their bending stiffness (see Figure 1). By knowing the tension softening diagram of concrete, the interface tensile stresses distributed in that area can be determined from the interface crack open displacements, which are linearly proportional to the peeling angle (see Figure 1). However, FRP sheets in tension softening area of concrete look like beams more than tension elements. Therefore, their model always gave much lower prediction on interface spalling resistances than test results although they could link their model to concrete properties. And also, they can not consider the effects of adhesives.

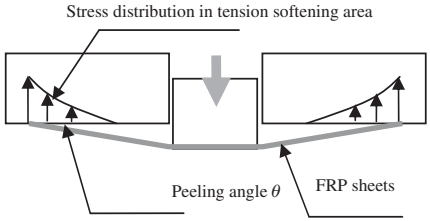

Figure 1. Force equilibrium between the spalling force and tensile stresses in concrete.

It should be mentioned that peeling of FRP sheets from concrete under spalling force is a mix-mode process including Mode I and Mode II failure simultaneously. Mode I failure is mainly affected by concrete properties and Mode II failure is significantly affected by adhesives besides the concrete properties (Dai et al. 2003 & 2004). Models based on fracture mechanics

have proved to be more suitably used for describing the FRP sheet–concrete interfaces' failure under different stress conditions. However, issues on how to use suitable test method to calibrate interface fracture energies under different conditions as well as how to use them for engineering design need to be further studied. The objectives of this paper are to clarify the failure mechanisms and to calibrate the interface fracture energy of FRP sheet–concrete interface under dowel action, which can be useful for spalling prevention design of concrete by using externally boned FRP sheets.

2 EXPERIMENTAL PHASE

2.1 *Experimental setup*

To study the failure of FRP sheet–concrete interfaces under dowel force action, test setup with an accurate displacement controlling system as shown in Figure 2 was developed based on a universal testing machine. A high strength bar was connected with the loading system. The high strength bar can impose the dowel force onto FRP sheets vertically by going through a notched concrete beam, of which the bottom was attached with one directional FRP sheets. A steel block was adhered on the top of FRP sheets at the notched location of the concrete beam and a ball hinge was set between the steel bar and steel block.

During the testing procedure, dowel forces and the corresponding vertical displacements of the steel block and concrete beam at the notched locations were recorded continuously. The open displacement of FRP sheet–concrete interface (CMOD), which is defined as the relative displacement between the steel block and concrete beam at the location where dowel force is imposed, can be calculated consequently. Strain gages were put on the surface of FRP sheets with the interval of 20 mm.

2.2 *Experimental materials*

Properties of Carbon Fiber Sheets (FTS-C1-20) used in this study are shown in Table 1. Two types of adhesives FR-E3P and CN-100 were used in the study. But a same primer FP-NS was used for all specimens. The adhesives' properties are also shown in Table 1. Adhesive CN-100 has higher elongation but lower elastic modulus in comparison with FR-E3P. Two types of concrete with the compressive strength of 23.4 MPa and 42.1 MPa respectively are prepared.

2.3 *Details of specimens*

In total, 11 one directional FRP sheets externally bonded concrete beams were prepared. Those beams have different concrete strength, adhesive bond layers, FRP stiffness (layers of FRP sheets) and initial un-bonded length between FRP sheets and concrete (refer to Table 2).

Each rectangular concrete beam has a 150 mm × 150 mm section area and a 900 mm span. As shown in Figure 3, a 50 mm wide × 50 mm high notch was made in the mid of each beam to accommodate steel

Figure 2. Photograph of dowel test setup.

Table 1. Properties of CFRP sheets and adhesives.

Material type	f_t (MPa)	E_f (E_a) (GPa)	ε_u (%)	ρ (g/m^3)	t_f (mm)
FTS-C1-20	3550	230	1.5	200	0.11
FR-E3P	44.7	2.41	1.5	–	–
CN-100	11.8	0.39	60	–	–
FP-NS	48.1	2.41	1.5	–	–

Note: f_t = tensile strength; E_f, E_a = elastic modulus of FRP and adhesive respectively; ε_u = fracturing strain; ρ = fiber density; t_f = thickness of FRP sheets.

Table 2. Details of specimens and experimental results.

No.	f_c' (MPa)	E_a (GPa)	$E_f t_f$ (kN/mm)	a (mm)	$\tan\theta$	P_d (kN)	G_{fs} (N/mm)
1[s]	23.4	2.41	50.6	22.5	0.071	0.93	0.57
2[s]	42.1	2.41	50.6	22.5	0.081	1.19	0.84
3[s]	42.1	0.35	50.6	22.5	0.083	1.79	1.07
4[s]	42.1	2.41	111.2	22.5	0.046	0.91	0.35
5[s]	42.1	2.41	50.6	2.5	0.076	1.14	0.67
6[s]	42.1	2.41	50.6	12.5	0.075	1.16	0.62
7[s]	42.1	2.41	50.6	42.5	0.081	1.14	0.80
8[s]	42.1	2.41	50.6	62.5	0.081	1.51	0.82
9[c]	42.1	2.41	25.3	2.5	0.102	1.58	1.04
10[c]	42.1	2.41	50.6	2.5	0.082	1.57	0.88
11[c]	42.1	2.41	111.2	2.5	0.061	1.70	0.80

Note[1]: f_c' = compressive strength of concrete; $E_f t_f$ = FRP stiffness, a = initial set un-bonded length between FRP sheets and concrete; θ = peeling angle; P_d = dowel force capacity at the stable peeling stage; G_{fs} = spalling fracture energy.
Note[2]: "s" means that concrete surface is treated with sand disk; "c" means that concrete surface is treated with sand cutter, which can make the coarse aggregates more exposed.

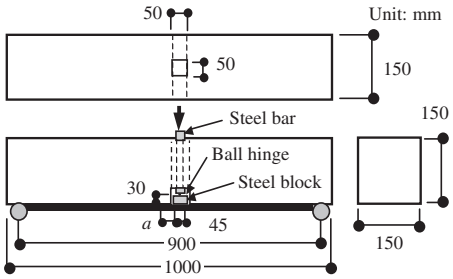

Figure 3. Size of testing concrete beams.

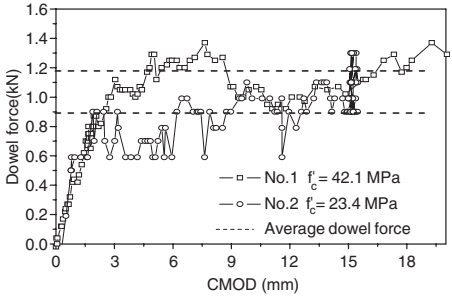

Figure 4. Effects of concrete strength on dowel resistance.

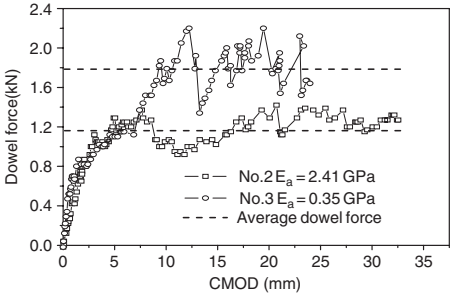

Figure 5. Effects of adhesives on dowel resistance.

block bonded on the upper surface of FRP sheets and ball hinge. A hollow column with section area of 50 mm × 50 mm was preset throughout each beam to permit steel bar to go it through then exert dowel force onto FRP sheets. 60 mm wide FRP sheets were bonded to concrete beams till the beams' supporting points. Steel block bonded on FRP sheets has the size of 45 × 60 × 30 mm. Steel bar has a diameter of 30 mm.

3 EXPERIMENTAL RESULTS

3.1 *Dowel force-CMOD curves*

All experimentally observed dowel force-CMOD curves are shown in Figures 4 to 7. Figure 4 indicates effects of concrete strength on the interface dowel force resistance. As expected, higher concrete strength brings higher interface dowel resistance. When concrete strength increases from 23.4 MPa to 42.1 MPa, the average dowel force (see horizontal dashed lines in Figure 4) of FRP sheet–concrete interfaces during peeling increases by about 30% (see No. 1 and No. 2 specimens in Table 2). Figure 4 shows effects of bonding adhesives. It can be seen that low elastic modulus brings higher interface dowel resistance. The reason is that the spalling failure of FRP sheet–concrete interface is a mix-mode one. As shown in later analytical part, the interface spalling fracture energy is usually bigger than Mode I but smaller than Mode II interface fracture energy. The later one is greatly affected by the adhesive properties (Dai et al. 2004). Therefore, to use soft adhesive is an efficient solution for the FRP sheet–concrete interface to improve not only its shear bond but also its dowel force capacity.

Figures 6.1 and 6.2 show the effects of FRP stiffness on the interface dowel force resistances. It can be seen that the dowel force at the initial interface peeling (see circled points in Figures 6.1 and 6.2) increases with FRP stiffness. The increase is very significant when there is a 2.5 mm preset un-bonded length a between FRP sheets and concrete (see Figure 6.2) but becomes much less significant when the a becomes 22.5 mm (see Figure 6.1). At the later peeling stage shown in Figures 6.1 and 6.2, FRP stiffness ranging from 25.3 to 111.2 kN/mm has almost no effects on the interface dowel resistance (see Figure 6.2 and specimens No. 9∼11 in Table 2). By comparing two load-CMOD curves shown in Figure 6.1, it is even found that dowel resistance during later peeling stage is a bit lower when the FRP stiffness is higher. That is probably due to the deviations of concrete surface treatment. On the whole, for an FRP sheet–concrete interface without initial un-bonded length, higher FRP stiffness can bring higher initial peeling dowel force. However, after a several-centimeter peeled length is induced, the FRP stiffness hardly affects the interface dowel resistance any more.

Figures 7.1 and 7.2 indicate the effects of preset initial un-bonded length a on the dowel force resistance. The FRP stiffness are 50.6 kN/mm and 111.2 kN/mm for specimens in Figure 7.1 and Figure 7.2 respectively. In Figure 7.1, the dowel forces at the first peeling (see those circled points in Figure 7.1) decreases when a increases from 2.5 mm to 12.5 mm, but then turns to increase till a nearly constant value when a continuously increases to 62.5 mm (see the dashed tendency line in Figure 7.1). The FRP's stiffness of the specimens in Figure 7.2 is two times of those in

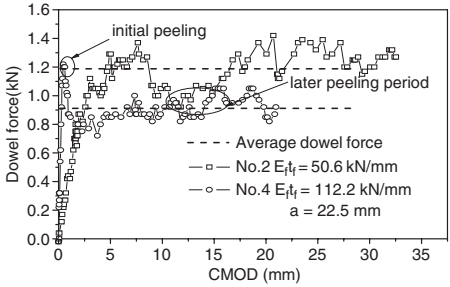

Figure 6.1. Effects of FRP stiffness on dowel resistance.

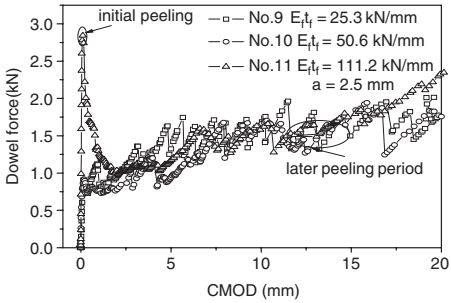

Figure 6.2. Effects of FRP stiffness on dowel resistance.

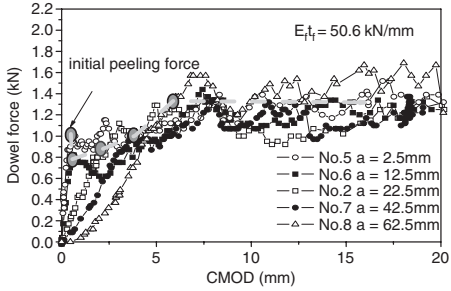

Figure 7.1. Effects of initial un-bonded length.

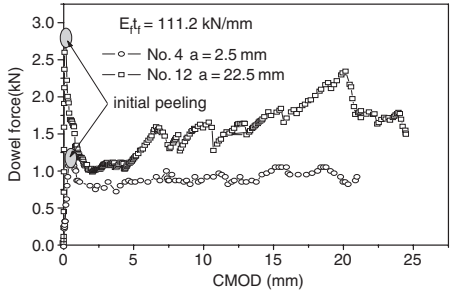

Figure 7.2. Effects of initial un-bonded length.

Figure 7.1. It is indicated in Figure 7.2 that the interface dowel force resistance decreases significantly at first interface peeling when *a* increases from 2.5 mm to 22.5 mm, implying the dowel force at initial peeling is more sensitive to *a* in case of using higher FRP stiffness. But if *a* further increases (refer to section 3.4 about the detection of *a* during test), for example, in the later interface peeling stage, the dowel force resistance becomes almost independent of *a* in cases of using both high and low stiffness FRP sheets.

3.2 *Observation on the failure*

Figure 8 shows all peeled FRP sheets after dowel tests. It can be seen that the peeling occurs most often in the concrete layer just underneath adhesive layer. Occasionally, the peeling penetrates into the interface between adhesive and FRP sheets (see Specimen No. 8 in Figure 8). However, that interface failure is accompanied with higher dowel resistance in comparison with those specimens with concrete failure (see No. 8 in Figure 7.1). The damage of concrete substrate with the strength of 23.4 MPa is more severe than that of concrete substrate with strength of 42.1 MPa (see No. 1 and No. 2 in Figure 8). Moreover, when softer

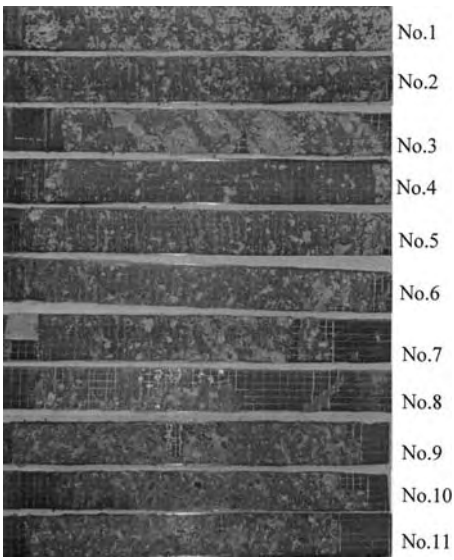

Figure 8. FRP sheets after peeling.

adhesive is used (No. 3 in Figure 8), volume of concrete attached to FRP sheets is more than that of No. 2, in which normal adhesive is used. Cracks can also be seen inside the softer adhesive layer. The corresponding interface dowel resistance is higher as it has been shown in Figure 5. On the other side, specimen No. 4 that has lightest damage of concrete brings lower interface dowel resistance as indicated in Figure 7.2. This lightest damage of concrete may be due to insufficient exposures of concrete coarse aggregates, because specimens No. 9, No. 10 and No. 11, for which concrete cutter rather than sand disk was used for surface treatment, have more severe concrete damage. And also, the heavier damage of concrete is accompanied with higher interface dowel resistance (refer to the column dowel resistance P_d in Table 2). So to make coarse aggregates heavily exposed can improve the dowel resistances of FRP sheet–concrete interfaces.

3.3 *Peeling mechanisms at different stages*

Based on the experimental results discussed in section 3.1, a typical dowel force-CMOD curve for an FRP sheet-concrete interface can be drawn in Figure 9 by assuming there is a very short initial peeling length a. In fact, a is impossible to be set zero during experiments. Accordingly, the whole curve can be divided into four stages. During stage 1, the interface open displacement (CMOD) is mainly related to the deformation of adhesive layer, which is also greatly affected by the bending stiffness of FRP sheets. The work done by exerted dowel force is mainly consumed for separating the FRP sheets vertically from concrete surface rather than increasing the strain energy in FRP sheets. Correspondingly, the initial interface peeling can be approximately regarded as a Mode I failure. When the dowel force reaches the first peak point, the initial interface peeling happens and following that the interface dowel resistance, which is bending force in the peeled FRP sheets, decreases sharply. Peeling in stage 2 is rather unstable. The interface peeling can still be related to Mode I failure approximately. Behaviors of FRP sheets in stage 1 and 2 can be simulated by modeling them as beams on elastic foundation (Dai et al. 2003). Due to the further increase of CMOD, the bending stiffness and bending deformation of FRP sheets becomes less influential and the work done by the dowel force is transferred to increase the strain energy in FRP sheets. So the interface dowel force resistance starts to increase again. Meanwhile the interface crack length a stops increasing and the interface lies in a stable stage (stage 3 in Figure 9). After the tensile force in FRP sheets reaches a critical value, the interface peeling enters into the peeling stage 4, during which the peeling can self-propagate even without further increase of the dowel force. In this study, displacement controlling loading system is applied, so that the interface peeling is rather stationary. As shown in next section, the strains in peeled FRP sheets do not change any longer during this stage, meaning the work done by dowel force is consumed in cohesive part of interface only. The interface lies in mix-mode loading condition.

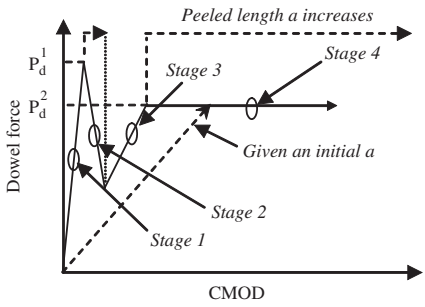

Figure 9. Typical dowel force-CMOD relationships for FRP sheet–concrete interface.

Therefore, a typical dowel force-CMOD curve as shown in Figure 9 can be composed of the following four stages: linear stage, unstable stage, stable stage, and self-propagation stage. And also, the interface peeling shifts from stage 1 into stage 4 soon after the peeling develops only several centimeters. It is not suitable to take the peak load achieved in stage 1 (P_d^1 in Figure 9) for the interface dowel resistance design because it is very sensitive to interface flaws, for examples, even several centimeter initial un-bonded lengths. Instead, rather constant dowel resistance P_d^2 (see Figure 9), whose prediction method will be discussed in later analytical part, can be taken for interface spalling prevention design. Values of P_d in Table 2 are obtained by averaging the dowel resistances of each specimen during the peeling stage 4. The unstable peeling stage 2 can be avoided by setting an initial un-bonded length a between FRP sheets and concrete during dowel test (see the dashed line in Figure 9). Then the P_d^2 can be obtained more directly. In the case that FRP stiffness is 50.6 kN/mm, $a = 60$ mm has proved to be long enough.

3.4 *Strain on the outer surface of FRP sheets*

To keep tracing the peeled length between FRP sheets and concrete, a line of strain gages were put on the surface of FRP sheets at one side of each concrete beam. Figure 10 shows the change of strains of FRP sheets with the increase of CMOD at different locations. It is shown that the local strain on the outer surface of FRP sheets reaches a peak minus value first and then changes to plus and increases, and finally stops at an almost constant peak value till the ultimate failure of interface. When FRP sheets keep good contact with concrete substrate, the FRP sheets lie in local bending

condition, which makes strains of the outer surface of FRP sheets minus. However, in the cohesive bonding part, work done by dowel force stretches the FRP sheets till a critical plus value at the same time when it completely separates the FRP sheets from concrete. As a result, the peak minus value of strain can be related to the initial peeling of the FRP sheets from the concrete.

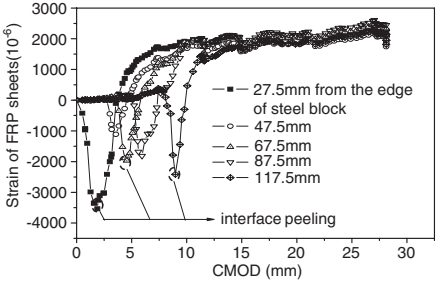

Figure 10. Relationship between strain of FRP sheets and CMOD.

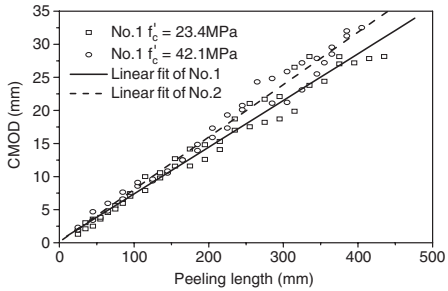

Figure 11.1. Effects of concrete strength on peeling angle.

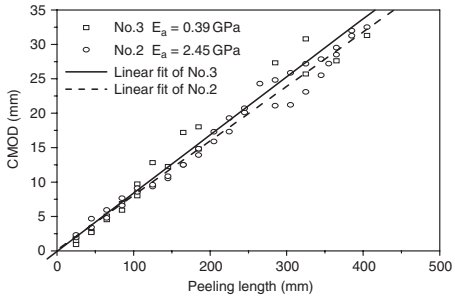

Figure 11.2. Effects of concrete strength on peeling angle.

After the FRP sheets have peeled from concrete completely, it can be seen in Figure 10 that strains of peeled FRP sheets at different locations almost have a same value even with the further increase of CMOD, which implies that the bending stiffness can be neglected and the peeled FRP sheets can be considered as an element under tension only.

3.5 *Peeling angle*

As mentioned in the last section, corresponding to a given CMOD the peeled location of FRP sheets from concrete can be determined from reading strain gages attached on the outer surface of FRP sheets. Therefore, it is not difficult to get relationships between the recorded CMOD and the corresponding interface peeled length L_p for all specimens. Consequently, values of tan θ, where θ is the interface peeling angle as shown in later Figure 12, for all specimens can be obtained (see Table 2) trough regressing all experimental data shown in Figures 11.1 to 11.4. From Figures 11.1 to 11.4, which show the observed relationships between CMOD and the peeling length for

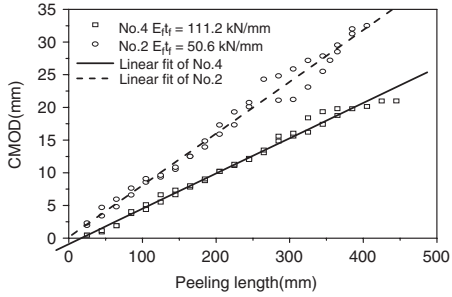

Figure 11.3. Effects of FRP stiffness on peeling angle.

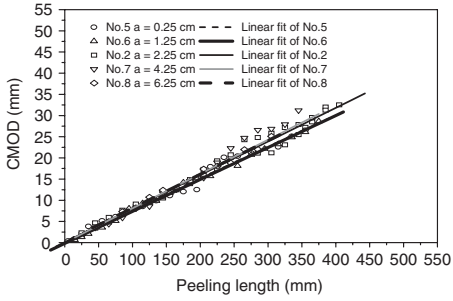

Figure 11.4. Effects of initial un-bonded length on peeling angle.

specimens with different concrete strength, adhesive properties, different initial un-bonded lengths and different FRP stiffness, the following phenomenon can be observed:

(1) The peeling angle θ almost keeps constant during the whole peeling procedure (see experimental data and regressed lines in all figures) because:

$$\tan\theta = \frac{CMOD}{L_p} = const. \quad (1)$$

(2) Bigger peeling angle can be achieved in the cases of using higher strength concrete (see Figure 11.1) and a softer adhesive (see Figure 11.2). Both cases bring higher interface dowel resistance as discussed in Section 3.1. Therefore, the peeling angle can be linked to the interface dowel resistance.
(3) Peeling angle is smaller in the case of using higher FRP stiffness (see Figure 11.3).
(4) The set initial un-bonded length between FRP sheets and concrete does not affect the peeling angle (see Figure 11.4). It should be mentioned that here is mainly discussing the peeling angle after the peeled length exceeds 20 mm. When the peeled length is shorter than that, it is impossible to know the exact peeling length corresponding to a given CMOD.

4 ANALYTICAL MODEL

During the procedure of interface peeling, the work done by dowel force is approximately consumed in two ways. One is to increase the strain energy stored in peeled FRP sheets and another is to compensate the energy consumed in cohesive area during interface peeling. The concrete can be assumed as rigid or the energy stored in concrete beams can be regarded as constant due to the rather constant dowel force. Therefore, the following equation can be satisfied during the interface peeling of FRP sheets strengthened concrete beams under dowel action:

$$P_d \cdot dCMOD = dU + 2G_{fs} \cdot b \cdot dL_p \quad (2)$$

where: P_d is the maximum interface dowel resistance achieved in peeling; $dCMOD$ is the increment of the open displacement between FRP sheets and concrete at the location where the dowel force is added; dU is the strain energy increment of FRP sheets at both sides; G_{fs} is the interface spalling energy; b is FRP sheets' width; dL_p is increment of peeled length at one side.

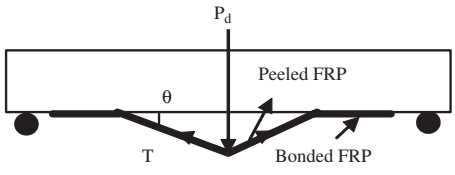

Figure 12. Sketch of dowel test during stable peeling stage.

As discussed in section 3.4, the peeled FRP sheets can be simulated as an element under tension as shown in Figure 12, by neglecting the open displacement and slip at the tip of crack, the tensile strain ε_f in FRP sheets can be calculated by the following equation:

$$\varepsilon_f = \frac{1}{\cos\theta} - 1 \quad (3)$$

θ is a constant value during peeling as described in Section 3.5 in Equation 3. So the strain in peeled FRP sheets ε_f is also a constant value during peeling. The fact is in accordance with the experimental observation that the strains of peeled FRP sheets at different locations does not increase any longer after it reaches a peak value (refer to Section 3.4).

Therefore,

$$dU = 2 \cdot \frac{1}{2} E_f \varepsilon_f^{\,2} \cdot b \cdot t_f \cdot \Delta L_p \quad (4)$$

Because tan θ is a constant value, it can be obtained from Equation 1 that:

$$\frac{dCMOD}{dL_p} = \tan\theta \quad (5)$$

With the substitution of Equations 4 and 5, Equation 2 can be rewritten as follows:

$$G_{fs} = \frac{P_d \cdot \tan\theta - E_f t_f \varepsilon_f^{\,2} b}{2b} \quad (6)$$

It can be seen from Figure 12 that the following equation is correct according to force equilibrium:

$$P_d = 2T \cdot \sin\theta = 2E_f t_f b \cdot (\frac{1}{\cos\theta} - 1) \cdot \sin\theta \quad (7)$$

By combining Equations 3, 6 and 7, the relationship between the interface spalling fracture energy and the peeling angle can be obtained as follows:

$$G_{fs} = E_f t_f \left[\tan\theta \cdot (\tan\theta - \sin\theta) - (\frac{1}{\cos\theta} - 1)^2 / 2 \right] \quad (8)$$

In the experiments, both the dowel force and the peeling angle can be obtained as discussed above. Therefore, strain in FRP sheets during peeling can be obtained directly from Figure 12 as follows:

$$\varepsilon_f = \frac{P_d}{2E_f t_f b \sin\theta} \quad (9)$$

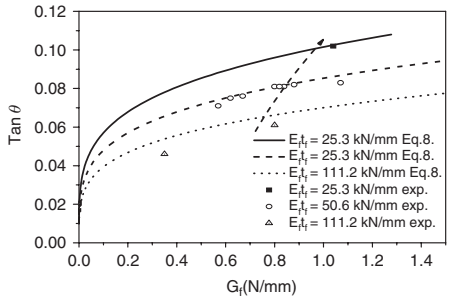

Figure 13. Relationships between peeling angle and the interface spalling energy.

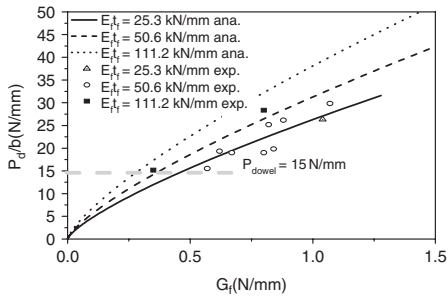

Figure 14. Relationship between G_{fs} and dowel resistance.

Consequently, the interface spalling energy can be calculated directly from experimental test results as well by substituting Equation 9 into Equation 6.

Figure 13 shows the comparisons of experimental and analytical relationships between peeling angle and the interface spalling energy for all specimens. It can be seen that Equation 8 can fit the experimental results quite well. The agreement indicates that the interface spalling fracture energy can be calculated from observed peeling angles directly based on Equation 8. On the other hand, if we eliminate θ from Equations 7 and 8, the interface spalling energy can be calibrated through investigating the interface dowel resistance only whereas without the necessity of observing the peeling angle during test.

Moreover, it is indicated in Figure 13 that even the stiffness of FRP sheets is same, the observed interface spalling fracture energy distributes in a rather big range. For example, the spalling fracture energy G_{fs} lies between 0.57 N/mm and 1.07 N/mm when the FRP stiffness is 50.6 kN/mm. The rather big range distribution of the interface spalling fracture energy is caused by different concrete and adhesive properties. Besides that, effect of surface treatment is very clear when the FRP stiffness is 111.2 kN/mm. Two specimens have same material properties. However, the G_{fs} of one specimen is 0.35 N/mm and another is 0.80 N/mm. The interface spalling energy is usually smaller than Mode II but higher than Mode I fracture energy, because the Mode I fracture energy of FRP sheet–concrete interface is about 0.1∼0.2 N/mm (Authors, 2003) and Mode II fracture energy is above 1.0 kN/mm (Authors, 2004). In addition, it is found that observed interface-spalling energy in this study tends to be high when the FRP stiffness is small whereas be lower when the FRP stiffness is high (see the arrowed dash line in Figure 13).

Figure 14 shows the relationship between interface spalling energy G_{fs} and interface dowel resistance P_d. It can be seen that relationship between P_d and G_{fs} is correctly predicted in Figure 13 although the analytical results give a bit overestimation, which is due to neglecting the interface slip during analysis. The value of P_d increases with the G_{fs}, which can be improved by using comparatively soft but ductile adhesives or making coarse aggregates more exposed on concrete surface. However, no clear evidence indicates that greater FRP stiffness brings higher dowel resistance although higher FRP stiffness can bring smaller dowel deformation. Due to the rather similarly scattering of observed dowel resistances in the cases of using different FRP stiffness, a simple value of 15 N/mm can be given as the dowel resistance that FRP sheet–concrete interface can undertake from a viewpoint of safe design.

5 CONCLUSIONS

The following conclusions can be drawn up based on the experiments and analysis in this study.

(1) Based on a series dowel tests, it has been clarified that peeling of an FRP sheet–concrete interface under dowel force can be divided into four stages so called linear, unstable, stable, and self-propagation stage.
(2) It is found that the interface peeling angle keeps constant during self-propagation peeling stage of any FRP sheet–concrete interface under dowel action regardless of its material components. Based on that, analytical model showing the relationships among dowel force, peeling angle and spalling fracture energy can be formulated.
(3) The proposed analytical model gives a solution on calibrating the spalling fracture energy of an FRP sheet–concrete interface from the obtained dowel force resistance. On the other hand, the calibrated spalling fracture energy can be used for predicting the dowel force resistances of FRP sheet–concrete interfaces.

(4) Experimental evidences show that the interface spalling fracture energy increases with concrete strength, but decreases with increasing the FRP stiffness and adhesive elastic modulus.
(5) The present study shows that exposing the coarse aggregate heavily and using low elastic modulus but highly ductile adhesive are efficient solutions to improve the interface dowel force resistances. But there is no clear evidence showing that increasing FRP stiffness can improve the interface dowel resistance based on the present database, although it can increase dowel capacity at first peeling point, which is rather sensitive to the interface flaws near the loading point and can not become a parameter for design purpose. Of course, increasing the FRP stiffness can bring smaller peeling angle and consequently can help decrease the dowel deformation.

REFERENCES

Dai Jianguo, Tamon Ueda, Yasuhiko Sato and Muttaqin Hassan. 2003. Mode I Fracture Behaviors of FRP-Concrete Interfaces. *Proceedings of the Japan Concrete Institute*, Vol. 25, 1577–1582.

Dai Jianguo, Tamon Ueda, Yasuhiko Sato and Hiroki Ozaki, 2003. Experimental Study on Mix-Mode Fracture of FRP Sheet-Concrete Interfaces, *Proceedings of JCI International Symposium: Latest Achievement in Technology and Research on Retrofitting Concrete Structures*, July, Kyoto, 113–120.

Dai Jianguo, Tamon Ueda and Yasuhiko Sato, 2004. Development of Nonlinear Bond Stress-Slip Model of FRP sheet-concrete Interfaces with a simple method. *Journal of Composites for Constructions, ASCE* (accepted for publication).

Wu Z. S., Asakura T., Yoshizawa H., Yuan H., Kobayashi A., and Takahashi T., 2000. Experimental and analytical studies on peeling behaviors and spalling resistance effect of externally bonded continuous fiber sheets. *Proceedings of Japan Society of Civil Engineering*, Vol. 49, No. 662, 45–58.

Yoshikawa K. 2002. Design method for tunnel lining retrofitting with externally bonded FRP sheets. *Technical presentation of Japan Railway Technical Research Institute*, No. 153.

FRP Composites in Civil Engineering – CICE 2004 – Seracino (ed)
© 2005 Taylor & Francis Group, London, ISBN 90 5809 638 6

Experimental and numerical investigations of bond between CFRP and concrete

Karsten Schilde & Werner Seim
Department of Structural Engineering, University of Kassel, Germany

ABSTRACT: For experimental studies a test set-up has been developed, in order to simulate geometrical and mechanical conditions between two cracks of a post-strengthened concrete slab. Five test series with 37 tests have been carried out. These tests were bonding tests without a relative crack-surface displacement. A 3-dimensional finite element model with solid and shell elements has been used for numerical calculations. This paper undertakes to describe the results of three of these test series as well as portraying the results of a finite element calculation.

1 INTRODUCTION

Post-strengthening concrete structures with steel-plates has been in use since the end of the 1960s. Extensive theoretical and experimental studies have led to suitable guidelines for the post-strengthening of slabs and beams; e.g. (Jansze 1997). These theories assume that stress peaks at the plate end cause bond failure. The stress peaks are induced by the eccentricity of tension forces at the end of the steel–plate.

CFRP-strips have been used since the 1990s to increase the load-bearing capacity of concrete structures. CFRP-strips are much thinner than steel-plates. Therefore, the stresses resulting from the distance between tension force in the laminate and the adhesive respectively the concrete surface are negligibly small.

Although these facts are well known and various tests (Kaiser 1989, Deuring 1993, Seim et al. 1999, Sebastian 2001, Seim et al. 2003) have shown that failure of concrete slabs strengthened by the use of externally bonded CFRP-strips always starts in a section where high shear forces and high bending-moments exist (see Figure 1 area B), experimental investigations on bond and anchoring were restricted to the situation at the end of the laminate (see Figure 2 area A); see e.g. (Neubauer 2000), (Niedermeier 2001) and (Chen & Teng 2001). Reasons for debonding are stress peaks at flexural cracks and shear cracks respectively. Additionally to the crack opening, a relative displacement resulting from shear forces seems to be of relevance, because supplementary normal stresses between laminate and concrete surface are induced. To simulate a section of high shear forces and high bending moments, a new test set-up had to be developed. With the results of 5 test series (ZRE 1, ZRE 2, ZRE 3, ZRE 4 and ZRE 5) the test set-up was upgraded to apply a relative displacement and three test series (ZRE 6, ZRE 7 and ZRE 8) with relative

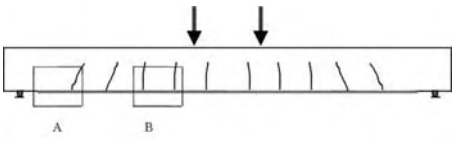

Figure 1. Bending member strengthened with CFRP-strip.

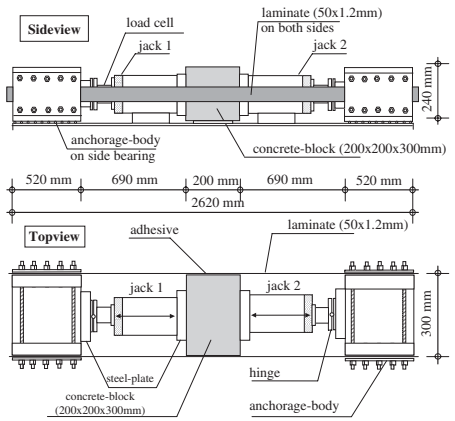

Figure 2. Test set-up.

displacement will follow. Next to the experimental investigations, finite element calculations were carried out to recalculate the test results.

2 TEST SET-UP

2.1 *Anchorage bodies*

The test set-up consists of the test specimen (a concrete block with two bonded CFRP-laminates), two anchorage-bodies and two jacks. In order to use the anchorage-bodies repeatedly, they were made of steel instead of concrete. This kind of anchorage-body saves time and alleviates the installation of the test-setup. The laminates are clamped to the anchorage-bodies by contact. Tests to check the suitability of the anchorage-bodies have shown that the contact pressure is sufficient to hold the laminate without any slip of the CFRP-laminate effecting the test results.

2.2 *Dimensions*

In 1998, 14 full-scale slabs post strengthened by use of CFRP-strips were tested at the University of California, San Diego (Seim et al. 1999). These slabs were uniaxially spanned. Crack distances for the tests lay between 75 mm and 330 mm. Results of calculations based on equations for admitting crack widths (Neubauer 2000) showed similar values.

For the test series 200 mm were chosen for the length of the concrete-block to represent the crack distance. The dimensions of the concrete blocks were 200 mm × 300 mm × 200 mm.

2.3 *Material parameters*

The compression strength of the concrete lay between 22.8 (series ZRE 5) and 41.6 (series ZRE 3) N/mm^2.

Material values of the adhesive, Ispo concretin SK 41 and stoPox SK 41 (StoPox SK 41, 2003), were taken from producer's designation. The compression strength was denounced with more than 100 N/mm^2, the bending tensile strength with more than 30 N/mm^2 and the Young's modulus with about 11,000 N/mm^2.

The ultimate tensile strength of the uni-directional laminate, S&P Laminates CFK 150/2000 (width: 50.0 mm; thickness: 1.2 mm) constituted 2850 N/mm^2 and the Young's Modulus 188,800 N/mm^2.

3 THEORETICAL PRINCIPLES

Figure 3 shows a section between two cracks (A and B). Compression forces in the concrete zone (F_c and $F_c + \Delta F_c$) are at work, the tension forces of the steel reinforcement (F_s and $F_s + \Delta F_s$) and the tension forces of the CFRP-strip (F_L and $F_L + \Delta F_L$). Figure 4

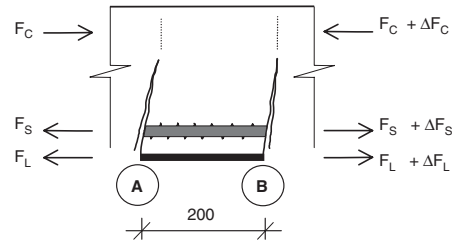

Figure 3. Forces at two crack surfaces A and B.

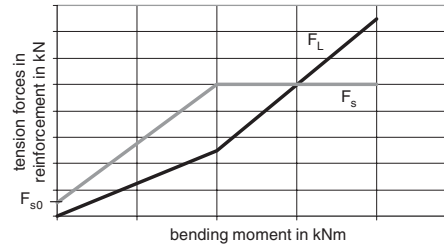

Figure 4. Development of the tension forces F_L and F_s for increasing bending moment.

shows the development of the tension forces F_L and F_s resulting from the bending moment.

The force F in the equations (2) and (3) is the tension force calculated from the bending moment M (generated by live and dead loads acting after post-strengthening) and the average value of the inner lever arms of the laminate z_L and the steel reinforcement z_s:

$$F = \frac{M}{(z_L + z_s)/2 \cdot} \tag{1}$$

Before the steel-reinforcement yields, the split of the increasing tension force F depends on the stiffness, the inner lever arm and the proportion of the areas of the laminate and the steel reinforcement:

$$F_L = F \cdot \frac{E_L \cdot A_L \cdot z_L}{E_s \cdot A_s \cdot z_s + E_L \cdot A_L \cdot z_L} \tag{2}$$

and

$$F_s = F \cdot \frac{E_s \cdot A_s \cdot z_s}{E_s \cdot A_s \cdot z_s + E_L \cdot A_L \cdot z_L} + F_{s0} \tag{3}$$

with

$$F_{s0} = \varepsilon_{s0} \cdot A_s \tag{4}$$

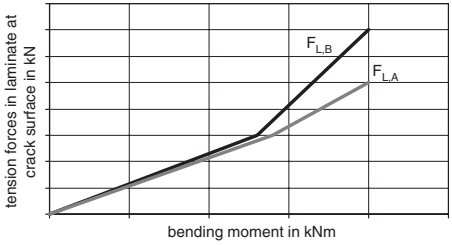

Figure 5. Development of tension forces $F_{L,A}$ and $F_{L,B}$.

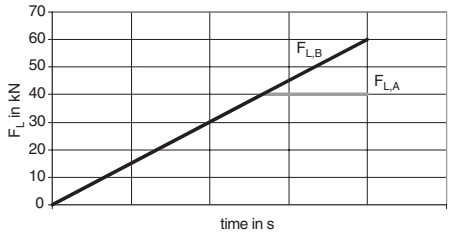

Figure 6. Simplified loading procedure at test.

where ε_{s0} is the pre-strain in the steel reinforcement resulting from the dead load before post-strengthening.

After steel yielding the steel is not able to take any more tension forces (acceptance: ideal elastic–plastic behavior of the steel reinforcement without any plastic hardening). So the tensile force for the steel reinforcement is calculated to

$$F_s = f_{sy} \cdot A_s \qquad (5)$$

where f_{sy} is the yielding stress of the steel.

Figure 5 shows the tension forces of the laminate at the two crack surfaces A and B. The difference of the laminate forces ΔF_L is small up to the yielding of the steel reinforcement. After the yielding of the steel reinforcement the laminate has to take the whole increase of the tension force and consequently the difference of the force ΔF_L increases, too.

For the tests the small difference ΔF_L before yielding of the steel reinforcement was neglected. With both jacks, for example for test ZRE 2-6 (see as well the Figures 9, 10, 11, 12 and 13) the forces were brought up to 40 kN for each CFRP-laminate. Then the load of jack 2 was increased until failure of the bond between the laminate and the concrete, whereas the load of jack 1 was held constant (see Figure 6). Four strain gauges glued on the CFRP-strips in a distance of 0.3 m from the concrete block made it possible to control the load path.

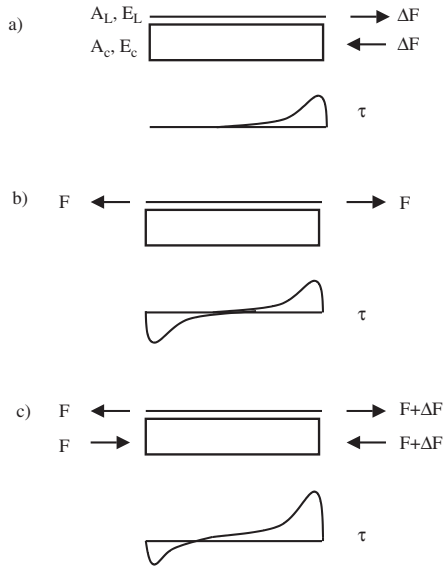

Figure 7. a) Equilibration bond, b) Compatibility bond, c) Combination of equilibration and compatibility bond.

The force F_L which was brought up in both jacks, before the additional force ΔF_L was added, ranged from 30 kN up to 80 kN per laminate.

The combination of two materials (e.g. laminate and concrete) results in two types of bond for symmetric respectively asymmetric loading conditions (see Figure 7). Equilibration bond means that a force difference ΔF is transmitted by shear forces from one material to the other material (see Figure 7a). If only one layer is exposed to symmetric load conditions, nevertheless the other material will take a part of the force in the section of the bonding length, transmitted by shear stresses (see Figure 7b). Figure 7c shows a possible combination of equilibration and compatibility bond.

4 TEST RESULTS

Figures 8 and 9 show the test failure loads of the test series ZRE 4 and ZRE 5. The compression strength of concrete amounted for the test series ZRE 4 to 25.0 N/mm^2 and for the test series ZRE 5 to 22.8 N/mm^2 after 28 days. The two test series contained 11 tests, six in the fourth and five in the fifth test series. As expected, the maximum additional force ΔF_L decreases with an increase of F_L. Values for ΔF_L lay between 8 kN and 18 kN.

Two tests of series ZRE 4 and one test of series ZRE 5 failed preliminary due to a small incline of the laminate to the center line of the test set-up. These results have not been included in Figure 8 and Figure 9.

Figures 10, 11, 12 and 13 show the distribution of composite strains ε_L and shear stresses τ_L at the interface between composite and concrete for test ZRE 2-6. Strains were measured by strain gauges. Shear stresses had been calculated from strain gradients. The values in the legends notify the forces in the left laminate generated by jack 2 ($F_{L,B}$) and jack 1 ($F_{L,A}$); see Figure 2. As the forces of both jacks are raised equally, the strain gradient forms symmetrically (see Figure 10). The maximum values of shear stresses τ_L between two strain gauges have been calculated with 6.5 N/mm^2 (see figure 11). As was to be expected, the

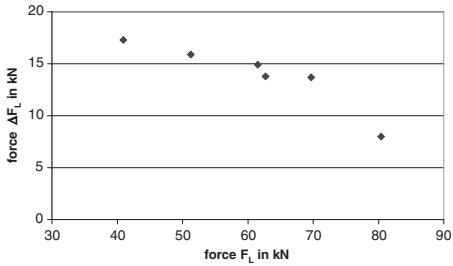

Figure 8. Failure loads of test series ZRE 4.

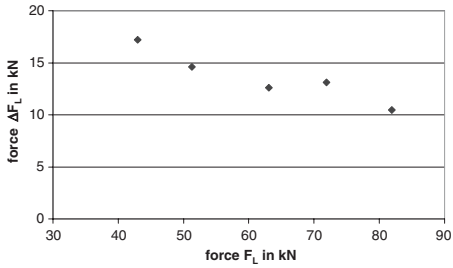

Figure 9. Failure loads of test series ZRE 5.

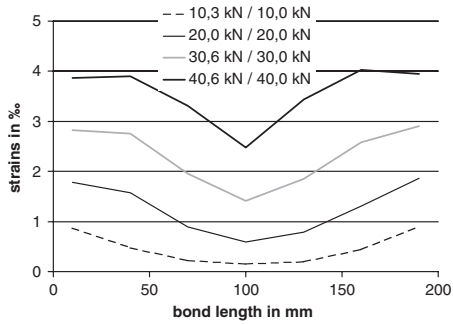

Figure 10. Test ZRE 2-6 (left laminate), composite strains for symmetric load conditions.

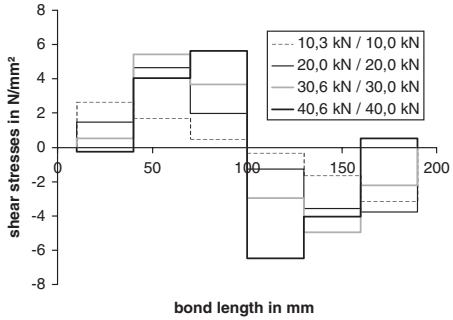

Figure 11. Test ZRE 2-6 (left laminate), shear stress distribution for symmetric load conditions.

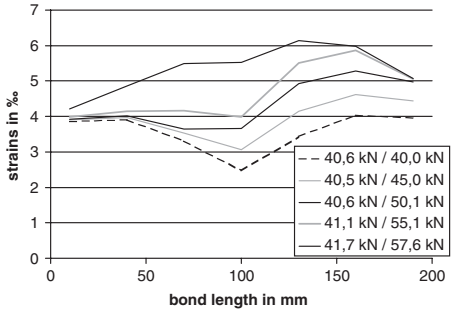

Figure 12. Test ZRE 2-6 (left laminate), composite strains; asymmetric load conditions.

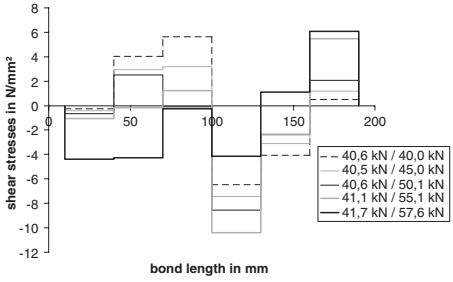

Figure 13. Test ZRE 2-6 (left laminate), composite strains; asymmetric load conditions.

zero-crossing of shear stresses τ_L lies in the middle of the bond length. Furthermore, it is remarkable that with increasing load the maximum of the shear stresses moved from the edge to the center of the bond length (see Figure 11). This was caused by shear deformation of the adhesive and by successive destruction of the interface between laminate and concrete. As long as the forces of both jacks raise equally, there is a combination of equilibration bond and compatibility bond acting in the interface between concrete and laminate.

Changing to asymmetric loads with $F_{L,A}$ at 40 kN, the strain gradients changed significantly (see Figure 12). The strains ε_L in the laminate increased at the left side at a force of 57.6 kN from 3.9‰ up to 5.1‰. At the middle of the left side the maximum strains ε_L reached a value of 6.1‰. As expected, the strains ε_L in the laminate at the right end of the interface remained nearly constant.

It can be assumed that at a load of 57.6 kN the substantial increase of the strains ε_L over the whole interface length is caused by preceding destruction of interface between laminate and concrete (debonding). The aggregate interlock effect causes deflection in the laminate and so accessorily shear stresses. The maximum shear stresses τ_L amounted to 11.3 N/mm^2. Figure 13 shows that the zero-crossing of shear stresses shifted from the center of bond length to the area of the interface end with the lower load. That means that with increasing additional force ΔF_L the proportion of the compatibility bond to the equilibration bond decreases and at least at a load at 57.6 kN, the additional force ΔF_L is transmitted only by equilibration bond (see Figure 13) although a zero-crossing exists.

Figure 14 shows the displacement of the left (point A) and right end (point B) of the interface depending on the force $F_L + \Delta F_L$ measured with displacement transducers for test ZRE 2-6. For symmetric load conditions, the gradients of displacement of the interface ends are equal, too.

Between a force from 26.5 kN up to 29.4 kN the left interface end (point A) indicates no displacement and at a force of 1.5 kN the right interface end (point B) indicates a displacement of 0.3 mm. Both were probably caused by a slip of the displacement transducers. The calculatively corrected curves are drawn in Figure 14, too. The displacements of both interface ends are nearly equal up to a force of 40 kN with values of 0.35 mm and 0.37 mm.

Failure of the bond over the whole bonding length occurs at a maximum force $F_L + \Delta F_L$ of 57.6 kN. At that time the displacements account for the interface ends 0.03 mm, 0.95 mm respectively.

It may be assumed that greater parts of the interface are debonded and that the displacement of the laminate occurs only in the direction of the higher load at failure. This means that at the limit state only equilibration bond acts at the interface of concrete and the CFRP-strip.

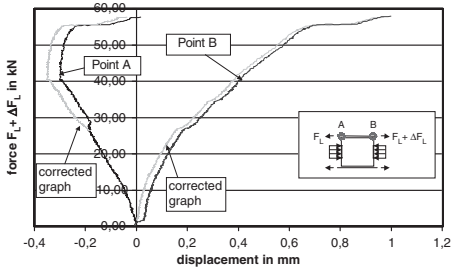

Figure 14. Displacements of left and right end of interface depending on the force $F_L + \Delta F_L$.

5 FINITE ELEMENT MODEL

To verify the test results, finite element calculations have been carried out with ANSYS 7.0 (ANSYS 2003). Figure 15 shows the element mesh of the test specimen, considering vertical symmetry (Engelhard 2001). Shell elements were used for the CFRP strips, solid elements for the concrete and the adhesive. A three-dimensional model was used, because this makes it possible to consider the volume propagation of the strains and forces respectively in the concrete.

First, calculations were carried out with a linear elastic material model to get a suitable mesh convergence. The maximum and minimum dimensions of the solid elements representing the concrete block were chosen between 12.5 mm and 6.25 mm. The width of the shell element representing the CFRP-strip had to be at least 12 mm and at most 25 mm. The thickness of the adhesive layer basically amounted to 2.0 mm. Some calculations were carried out with an adhesive

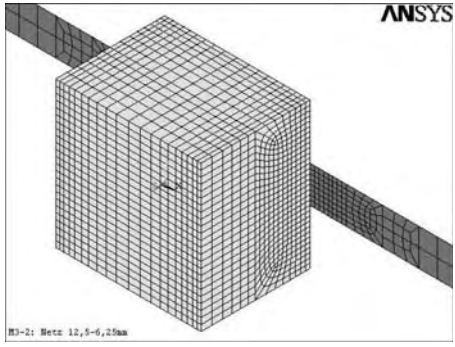

Figure 15. Finite-element model of specimen utilizing symmetry.

Table 1. Material parameters for finite element calculation.

	Young's modulus N/mm²	Compression strength N/mm²	Tensile strength N/mm²
Concrete*	28,600	33.0	3.1
Adhesive	11,000	100.0	30.0
Laminate	188,000	–	–

* poission's ratio is assumed to 0.2.

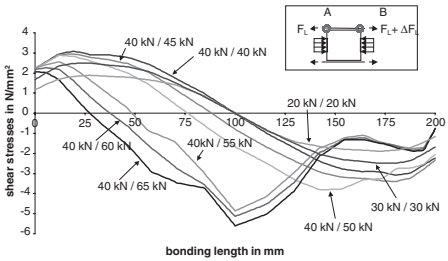

Figure 16. Shear stresses over bond length; results from calculation.

thickness of about 3.5 mm and 5.0 mm. To avoid numerical problems at the calculations, a virtual steel reinforcement (content: 5‰) was smeared over all elements of the concrete block.

The material parameters introduced for the finite element calculations are documented in Table 1. The shell elements for the laminate had a linear elastic behavior and the solid elements for the adhesive a bilinear elastic-plastic behavior. For the concrete failure the Willam/Warnke-criterion was applied; see e.g. (Chen 1994). The stress–strain-relation of the compression zone of the concrete is described by the polygonal compression stress–strain diagram from Eurocode 2, (Eurocode 2, 1992).

Debonding of laminate from concrete is demonstrated by the collapse of the concrete elements after tensile strength has been achieved.

Figure 16 shows the shear stresses over bond length and Figure 17 shows the comparison of the displacement of interface ends between the finite element calculation and test ZRE 2-6.

As established by testing, the shear stresses – taken from the surface layer of the concrete elements – arrange themselves symmetrically under symmetric load conditions. With increasing loads at one end on the CFRP-strip, the zero crossing of the shear stresses moves from the center to the less loaded margin. The maximum stresses move with increasing loads from the edges to the center (see Figure 16). For the finite element calculations the aggregate interlock effect has been considered. Therefore the shear stresses do not

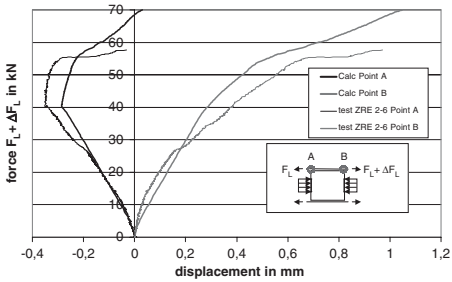

Figure 17. Comparison of the of the displacement interface end between FE-calculation and test ZRE 2–6.

decrease down to zero after collapse of the concrete elements.

The comparison of the deflection of the interface ends have an equal gradient (see Figure 17). The values of the deflections from the numerical calculation are smaller compared with the deflections measured at the test ZRE 2-6. This means that the deflection behavior of the finite element model is stiffer than the real material behavior of test specimen ZRE 2-6.

6 CONCLUSION

Results from 3 test series on bonding behavior between concrete surface and laminate have been documented. Strains, shear stresses and displacements have been portrayed and it could be shown, that the new developed test set-up is well suited for the investigations of bonding between laminate and concrete.

Additionally numerical investigations have been presented. Correspondence between measured displacements and numerical results could be demonstrated.

The test set-up was amplified in order to investigate the influence of a relative displacement at a crack surface. The aim of the experimental and numerical investigations of bond between CFRP and concrete is to develop a mechanical model of the debonding phenomenon.

The help of S&P Clever Reinforcement Company and of StoCretec GmbH which provided laminates and epoxy as well as of the Deutsche Forschungsgemeinschaft (German Research Foundation) which is founding this research project is acknowledged.

REFERENCES

ANSYS 7.2 2003. ANSYS Inc. Canonsburg

Chen, J.F. & Teng, J.G. 2001. Anchorage strength models for FRP and steel plates bonded to concrete, Journal of Structural Engineering, Vol.127(7): 784–791

Chen, Wai-Fah 1994. Constitutive Equations for Engineering Materials: Plasticity and modeling, Amsterdam – London – New York – Tokyo: Elsevier

Deuring, Martin 1993. Verstärken von Stahlbetonbauteilen mit gespannten Faserverbundwerkstoffen; Zürich: ETH-Bericht Nr. 224

Engelhard, Heiko 2001. Nachträgliche Verstärkung mit CFK-Lamellen – Numerische Untersuchungen zum Verbund zwischen Lamelle und Beton. Kassel: Fachgebiet Baukonstruktion und Bauwerkserhaltung

Eurocode 2 1992. DIN V ENV 1992-1-1, Ausgabe: 1992-06 Eurocode 2: Planung von Stahlbeton- und Spannbetontragwerken – Teil 1: Grundlagen und Anwendungregeln für den Hochbau; Deutsche Fassung ENV 1992-1-1: 1991

Jansze, Willem 1997. Strengthening of Reinforced Concrete Members in Bending by Externally Bonded Steel Plates – Design for Beam Shear and Plate Anchorage. Delft: Delft University of Technology

Kaiser, Hans-Peter 1989. Bewehren von Stahlbeton mit kohlenstoffaserverstärkten Epoxidharzen, Zürich: ETH-Bericht Nr. 8918

Neubauer, Uwe 2000. Verbundtragverhalten geklebter Lamellen aus Kohlenstoffaser-Verbundwerkstoff zur Verstärkung von Betonbauteilen. Braunschweig: TU Braunschweig Heft 150

Niedermeier, Roland 2001. Zugkraftdeckung bei klebearmierten Bauteilen. München: Technische Univertsität, Berichte aus dem konstruktivemn Ingenieurbau; 2001/11

Schilde, Karsten & Seim, Werner & Engelhard, Heiko 2002. Experimental determination of interface shear stresses simulation the midspan area of concrete slabs post-strengthened with CFRP strips. In The third international conference on composites in infrastructure, San Francisco, 10–12 June 2002

Sebastian, Wendel M. 2001. Significance of Midspan Debonding Failure in FRP-Plated Concrete Beams. Journal of Structural Engineering 127(7): 792–798

Seim, Werner & Karbhari, Vistap & Seible, Frieder 1999. Nachträgliches Verstärken von Stahlbetonplatten mit Faserverstärkten Kunststoffen. Beton- und Stahlbetonbau 94(11): 440–456

Seim, Werner & Schilde, Karsten 2002. Experimentelle und theoretische Untersuchungen zum Verbund zwischen Betonbauteilen und nachträglich aufgeklebten hochfesten Kohlefaserlamellen. Zwischenbericht zum DFG-Forschungsvorhaben SE 741/3-1. Kassel

Seim, Werner & Vasques, Alvaro & Karbhari, Vistap & Seible, Frieder 2003. Poststrengthening of Concrete Slabs: Full-Scale Testing and Design Recommendations. Journal of Structural Engineering 129(6): 743–752

StoPox SK 41 2003. Technisches Merkblatt: StoPox SK 41. Krifftel: StoCretec GmbH, www.stocretec.de

FRP Composites in Civil Engineering – CICE 2004 – Seracino (ed)
© 2005 Taylor & Francis Group, London, ISBN 90 5809 638 6

Recent researches on interfacial behavior of FRP sheets externally bonded to RC structures

X.Z. Lu & L.P. Ye
Department of Civil Engineering, Tsinghua University, Beijing, China

J.G. Teng
Department of Civil and Structural Engineering, Hong Kong Polytechnic University, Hong Kong, China

Y.L. Huang, Z. Tan & Z.X. Zhang
Department of Civil Engineering, Tsinghua University, Beijing, China

ABSTRACT: The interfacial behavior between FRP sheets and concrete is very important and often controls the behavior of FRP-strengthened RC structures. A series of studies on this problem recently undertaken at Tsinghua University in collaboration with The Hong Kong Polytechnic University in China are summarized in this paper. The research includes: bond tests, local bond–slip relationships, and the debonding behavior and strength of flexurally-strengthened and shear-strengthened RC beams based on tests and finite element analysis. In particular, new finite element models were developed to gain a deeper understanding of debonding failure mechanisms, and finite element and test results were combined in the establishment of design methods.

1 INTRODUCTION

Strengthening RC structures with externally bonded FRP sheets and plates has become very popular over the past decade. For shear and flexural strengthening of RC beams, debonding failure modes at the FRP-to-concrete interface often govern the ultimate load. Broadly speaking, the debonding problem requires research in two aspects: (a) the local bond–slip behavior, including the bond strength and the local bond–slip constitutive relationship; and (b) the ultimate debonding strength of FRP-strengthened RC elements, including flexurally- and shear-strengthened RC beams.

Recent research has led to many progresses in both aspects. A number of bond strength models and bond–slip models, as well as design models to predict the debonding strengths of beams have been proposed. Some valuable work has also been conducted in which the two aspects are integrated so that the debonding strengths of RC beams can be explained/predicted using local bond–slip models (Chen & Teng 2003, Teng et al. 2003). The FRP research group at Tsinghua University, in collaboration with The Hong Kong Polytechnic University, has completed a series studies on interfacial behavior in the past two years. These studies have included bond tests, numerical simulations, the exploration of debonding mechanisms, and the development of design models. The outcomes from these studies include unified interfacial models for local bond–slip relationships and bond strengths, and ultimate flexural and shear debonding strengths of RC beams. This paper provides a summary of the main results of this research program.

2 LOCAL BOND–SLIP BEHAVIOR

2.1 *Experimental research*

The direct-shear test is the most common method for studying the local bond–slip behavior of FRP-to-concrete interfaces. Twelve double-shear specimens were tested by Tan (2002). The tests were carefully conducted, leading to reliable results. The strain distributions in the FRP sheet in a typical specimen are shown in Figure 1.

2.2 *Finite element models for the direct-shear test*

2.2.1 *General*

In order to better understand the debonding mechanism and develop bond–slip models, finite element (FE) models were developed. In the proposed FE models, the elements modeling the FRP plate are connected to the elements modeling the concrete directly without

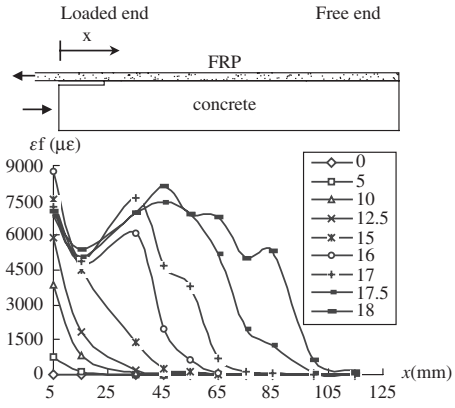

Figure 1. Strain distributions in FRP plate.

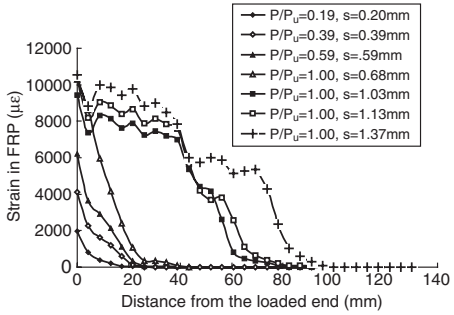

Figure 2. Strain distributions in FRP plate from macro-scale FE model.

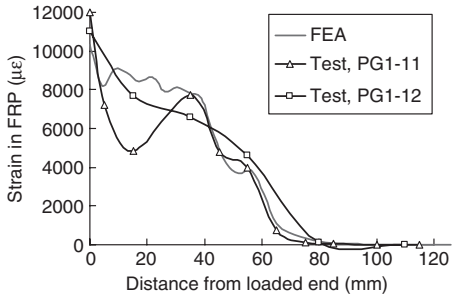

Figure 3. Comparison of strains in FRP between test and macro-scale FE model.

any interface elements. Hence, debonding is modeled as the fracture of the concrete under the FRP plate. However, because of the shear locking problem in the concrete constitutive law with a conventional smeared crack model, the debonding process cannot be correctly simulated with the commonly used orthogonal fixed angle crack model (FACM) or coaxial rotating angle crack model (RACM) (Lu et al. 2004a). As a result, two novel FE models were proposed to solve the problem, which are referred to as the macro-scale model and the meso-scale model, respectively. In the macro-scale model, the element size is relatively large (larger than 2 mm, similar to the thickness of the concrete layer pulled off by the FRP sheet), and a specially-developed non-coaxial RACM is adopted for the concrete. By contrast, in the meso-scale model, the concrete is still modeled with the FACM, but the concrete element size is kept very small (0.25 or 0.5 mm).

2.2.2 *Macro-scale finite element model*

In the macro-scale FE model, the crack propagation in the concrete beneath the FRP sheet has to be described with only one or two layers of concrete elements, so the concrete constitutive law needs to be capable of representing the rotating cracks and the interlocking effect of cracked concrete. Hence, a non-coaxial RACM model was developed. The crack orientation is kept perpendicular to the principal tensile stress, and tensile softening and the shear retention factor representing the effect of shear interlocking are described respectively by the following equations:

$$\sigma_{nn} = f_t e^{-\alpha_1(\varepsilon_{nn}-\varepsilon_{cr})} \quad (1a)$$

$$\beta = (\beta_1 - \beta_2)e^{-\alpha_2(\varepsilon_{nn}-\varepsilon_{cr})} + \beta_2 \quad (1b)$$

where σ_{nn} and ε_{nn} are the direct stress and strain normal to the crack; $\varepsilon_{cr} = f_t/E_c$, here f_t is the tensile strength and E_c is the elastic modulus of concrete.

In this crack model, the principal stresses and the principal strains of cracked concrete are not in the same directions. This is why it is referred to as the non-coaxial RACM. Based on an analysis of the constitutive parameters in comparison with selected test results, it is proposed that $\alpha_1 = 3724$, $\alpha_2 = 800$, $\beta_1 = 0.5$ and $\beta_2 = 0.001$, respectively.

The strain development obtained from the FE model for the specimen shown in Figure 1 is given in Figure 2. The comparison between the FE results and the test results is shown in Figure 3.

2.2.3 *Meso-scale finite element model*

Although the macro-scale FE model can correctly simulate the debonding behavior, the physical interpretations of the parameters in Eqs 1a & 1b are not easy. Hence, a meso-scale FE model was subsequently proposed in which the concrete is modeled with very fine elements with their sizes being one order smaller than the thickness of the fracture zone of concrete (0.25 or 0.5 mm). Thus, there are enough elements in the FE

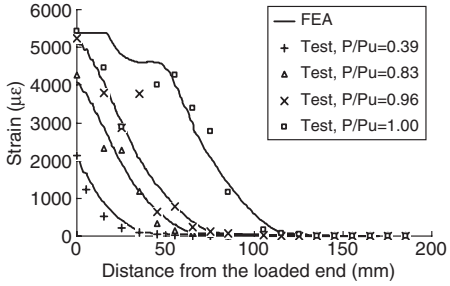

Figure 4. Comparison of strains in FRP between test and meso-scale FE model.

model to represent crack propagations in the concrete. The tensile softening of cracked concrete is controlled through the fracture energy of concrete, and by a comparison with selected direct-shear test results, it was found that the following proposal by Kang (1996) is the best among available relationships for representing the shear resistance of cracked concrete through interlocking:

$$\tau_{cr} = (0.543w^{-0.585} + 0.1999)\sqrt{f_c}\Delta^{0.72} \quad (2)$$

where w is the crack width and Δ is the relative slip between the crack faces, both in mm; f_c (MPa) is the compressive strength of concrete; and τ_{cr} (MPa) is the shear stress resisted by the cracked concrete.

A typical comparison of strains in the FRP sheet is shown in Figure 4. The development of crack patterns in the concrete from the meso-scale FE model is shown in Figure 5. The predicted debonding process is almost the same as that observed in the test. With these numerical results, the failure mechanism of debonding can be explained as follows. The shear force in the interface causes cracking in the concrete, and these cracks separate the concrete into a series of meso-scale cantilever columns. With further increases in the load, these cantilever columns fail in flexure one by one, which results in interfacial debonding (Figure 6). A more detailed discussion of this debonding process can be found in Lu et al. (2004b & 2004c).

2.3 *Bond–slip models*

Based on meso-scale FE analysis and test results, three bond–slip models have been proposed (Lu et al. 2004c–e). The three models are referred to as the precise model, the simplified model and the bilinear model, respectively.

The precise model can take explicit account of the effect of the adhesive layer, which is important when the adhesive is much softer than those currently in common use. The precise model is composed of an

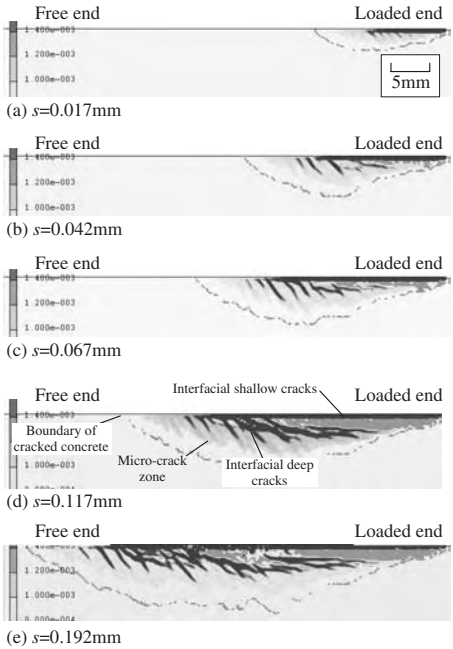

Figure 5. Propagation of cracks in concrete.

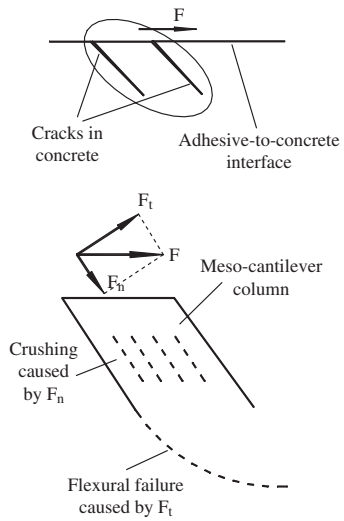

Figure 6. Meso-cantilever column and its failure modes.

ascending branch and a descending branch, and they are described separately using the following equations:

$$\tau = \tau_{\max}\left(\sqrt{s/(s_0 A)+B^2}-B\right) \quad \text{if } s \le s_0 \tag{3a}$$

$$\tau = \tau_{\max}\exp\left[-\alpha(s/s_0-1)\right] \quad \text{if } s > s_0, \tag{3b}$$

where τ (MPa) is the bond stress, s (mm) is the interfacial slip, $A=(s_0 - s_e)/s_0$, and $B=s_e/[2(s_0 - s_e)]$.

The local bond strength $\tau_{\max}$ and the corresponding slip s_0 are given by

$$\tau_{\max} = 1.5\beta_w f_t \tag{3c}$$

$$s_0 = 0.0195\beta_w f_t + s_e, \quad s_e = \tau_{\max}/K_0 \tag{3d}$$

The FRP-to-concrete width ratio β_w is expressed as

$$\beta_w = \sqrt{(2.25 - b_f/b_c)/(1.25 + b_f/b_c)} \tag{3e}$$

where b_c (mm) and b_f (mm) are the widths of the concrete prism and the FRP sheet respectively. The initial stiffness of the bond–slip model is defined by:

$$K_0 = K_a K_c/(K_a + K_c) \tag{3f}$$

where $K_a = G_a/t_a$, $K_c = G_c/t_c$. G_c (MPa) is the elastic shear modulus of concrete and t_c (mm) is the effective thickness of concrete whose deformation forms part of the interfacial slip and may be taken as 5 mm. G_a (MPa) and t_a (mm) are the shear modulus and thickness of the adhesive layer.

The parameter α controls the shape of the descending branch and is given by

$$\alpha = \tau_{\max} s_0/\left(G_f - G_f^{\,a}\right) \tag{3g}$$

where the total interfacial fracture energy G_f can be expressed as:

$$G_f = 0.308\beta_w^{\,2}\sqrt{f_t}\left(\frac{K_a}{2500}\right)^{-0.449} \text{if } K_a < 2500\text{MPa/mm} \tag{3h}$$

$$G_f = 0.308\beta_w^{\,2}\sqrt{f_t} \quad \text{if } K_a \ge 2500\text{MPa/mm} \tag{3i}$$

The fracture energy of the ascending branch of the bond–slip curve G_f^a can be calculated as:

$$G_f^{\,a} = \int_0^{s_0}\tau ds = \tau_{\max} s_0\left[\frac{2A}{3}\left(\frac{1+B^2A}{A}\right)^{3/2} - B - \frac{2}{3}B^3A\right] \tag{3j}$$

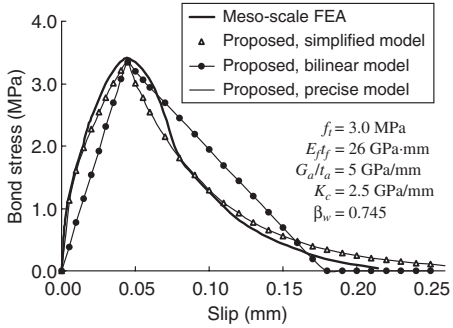

Figure 7. Proposed bond–slip models.

Table 1. Comparison of ultimate load between test results and proposed models

Model	Precise model	Simplified model	Bilinear model
Average error (%)	0.1	0.1	0.1
Standard deviation	0.155	0.155	0.156
Correlation coefficient	0.910	0.910	0.908

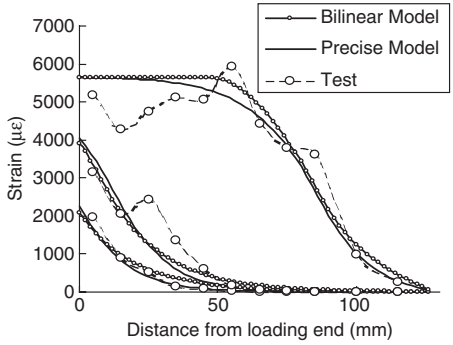

Figure 8. Comparison of strain distributions in the FRP plate for Specimen PG1-2 tested by Tan (2002)

For normal adhesives layers, whose K_a is usually larger than 2.5 GPa/mm, the precise model can be simplified by having $A=1$, $B=0$ and $s_e=0$, which is then referred to as the simplified model. The bilinear model has the same total fracture energy and the same coordinates of the peak point of the bond–slip curve as the simplified model. The shape of the proposed bond–slip curves are shown in Figure 7.

Table 1 provides the statistics of comparisons of the ultimate load between the three proposed models

and 254 direct-shear test results found from the existing literature. Very close agreements are seen. The strain distributions in the FRP sheet numerically predicted with the proposed bond–slip models are also in close agreement with the test results (Figure 8). Further extensive comparisons are available in Lu et al. (2004d, 2004e), where it is demonstrated that the proposed models are much more accurate than all existing bond–slip models.

3 FLEXURAL IC DEBONDING IN FRP-STRENGTHENED RC BEAMS

3.1 *General*

The failure mode of intermediate crack (IC) debonding in RC beams bonded with tension face FRP sheets was observed in many tests (Teng et al. 2003). At Tsinghua University, 14 specimens were tested by Fang (2002) to study the flexural debonding behavior. Some design proposals were derived from these test results (Fang 2002, Huang & Ye 2004).

To gain a better understanding of flexural debonding due to intermediate cracks, the bond–slip models presented above were used in FE simulations of RC test beams. It was found that a direct use of these bond–slip models did not lead to satisfactory results (Lu et al. 2004f). Subsequently, a dual debonding criterion with the common smeared crack approach was proposed. Furthermore, design models were established.

3.2 *Experimental study*

The 14 specimens of 4-point bending beams tested by Fang (2002) were strengthened with CFRP sheets bonded to the soffit. The dimensions of the beams are 1700 mm × 150 mm × 200 mm, with a clear span of 1500 mm. The key parameters studied are the length of the FRP sheet, and the spacing, width and height of the U-jackets. A typical load–deflection curve of a specimen without U-jackets is shown in Figure 9, while curves of specimens with different U-jackets are shown in Figure 10, in which CB0 is the control specimen. It can be seen that the debonding failure of specimens without U-jackets is much more brittle than that of beams with U-jackets.

3.3 *Dual debonding criterion and bond–slip models*

A problem with the smeared crack approach in modeling IC debonding is that it cannot precisely capture slip concentration near a flexural crack, so a modification of the method was proposed.

As shown in Figure 11, if there is no flexural crack in an element of concrete connected with the interface element, the slip in the interface element can be well

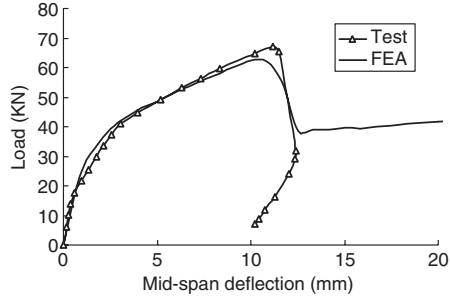

Figure 9. Load–deflection curves of specimen B2 without U-jackets tested by Fang (2002).

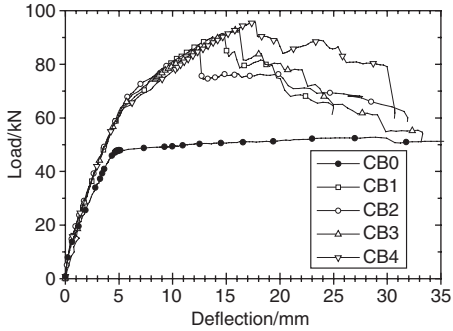

Figure 10. Load–deflection curves of specimens with different U-jackets tested by Fang (2002).

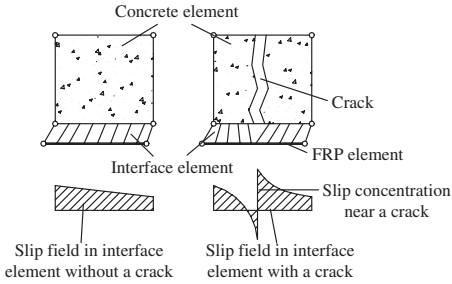

Figure 11. Slip fields within an interface element.

described by the shape function of the interface element, and the proposed bond–slip models can be used to predict interfacial debonding directly. However, if there is a flexural crack in the concrete element, the slip concentration near the crack cannot be properly described by the shape function of the interface element. Interfacial slips now occur on both sides of the

crack, and the total amount of interfacial slip within the element should be equal to the width of the flexural crack. Based on this observation, local debonding can also be assumed to occur if the total slip within an element exceeds $2s_0$. The adoption of this debonding check to gether with the direct use of a bond–slip model leads to what is referred to as a dual debonding criterion (Lu et al. 2004f, Teng et al. 2004).

Based on the results of a meso-scale FE simulation of an FRP-strengthened beam, the bond–slip behavior between FRP sheet and concrete can be divided into two types, depending on the distance of a location on the interface to the nearest flexural crack. If the location is far away from the flexural crack, the bond–slip behavior can be well described by one of the bond–slip models proposed in Section 2.3. However, if the location is close to the flexural crack, the bond–slip behavior is significantly different. The descending branches of the bond–slip models in Figure 7 should be replaced by a sudden drop. Based on this observation, a FE model was developed, in which the modified bond–slip model without a descending branch is used if an interface element fails as a result of a flexural crack but otherwise, the original bond–slip model with a descending branch is used.

3.4 *Comparison between FE and test results*

45 RC beam specimens, including those tested at Tsinghua University, failing by IC debonding, were simulated with the FE model described above. In all these beams, no additional anchorage measures such as U-jacket were used. A comparison of the ultimate flexural debonding strengths in terms of the total applied load is shown in Figure 12. The FE results are in close agreement with the test results. Comparisons of the load–deflection curve and the FRP strains for a typical specimen B2 tested by Fang (2002) are shown in Figure 9 & 13. Good agreements are also seen.

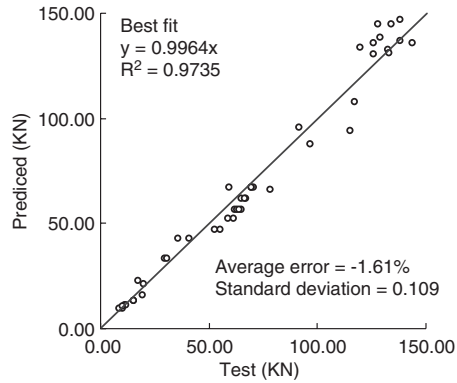

Figure 12. Comparison of IC debonding strengths between test and FE results.

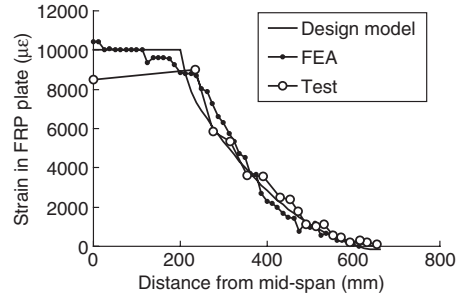

Figure 13. Strains in FRP when debonding initiates in specimen B2 tested by Fang (2002).

3.5 *Design models*

3.5.1 *Design model I*

With the numerical results from the above FE model, the flexural debonding process and mechanism were examined in detail, and a design model was proposed for the IC debonding strength (Lu et al. 2004g, Teng et al. 2004). The interfacial bond stresses are mainly caused by the shear force in the beam and the opening-up of flexural cracks, and they are represented by τ_s and τ_c respectively. Most existing flexurally-strengthened beams were tested under concentrated loads, and for this loading condition, the maximum shear force and the widest flexural crack are expected to appear at the section under the concentrated load. Thus, the extreme values of τ_s and τ_c appear at the same section, too. Debonding starts at this section if the sum of τ_s and τ_c equals to the local bond strength $\tau_{\max}$. Furthermore, by appropriate numerical smoothing, it was found that the distribution of interfacial bond stress when debonding starts can be approximated with two triangular blocks, representing τ_s and τ_c respectively, as shown in Figure 14. The length of the stress block representing τ_c is close to L_{ee} given in Yuan et al. (2004), which is the effective bond length under elastic deformation. The expression of L_{ee}, incorporating the bilinear bond–slip model, is given by Yuan et al. 2004:

$$L_{ee} = \sqrt{\frac{4E_f t_f}{\tau_{\max}/s_0}} = 0.228\sqrt{E_f t_f} \tag{4a}$$

The length of the stress block representing τ_s, which is denoted by L_d, is equal to the distance from the loaded section to the end of the cracked region or the

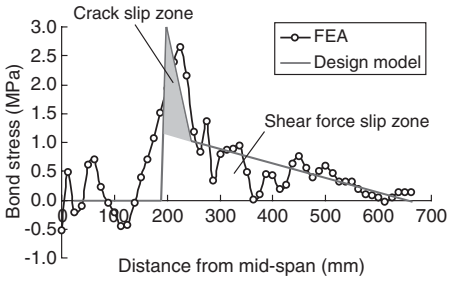

Figure 14. Interfacial bond stress: FE results and design model.

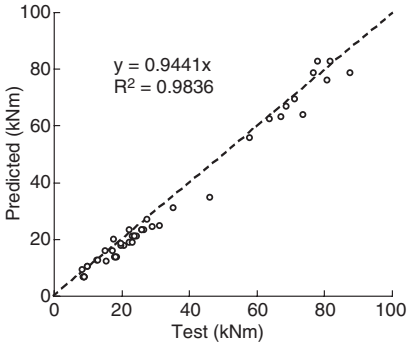

Figure 15. IC debonding moments at the critical section: tests versus design model I.

plate end if the plate is terminated within the cracked region. Therefore, the total force in the FRP plate is:

$$T = \left(\frac{\tau_{c,\max} L_{ee}}{2} + \frac{\tau_{s,\max} L_d}{2} \right) b_f \tag{4b}$$

When $\tau_{s,\max} + \tau_{c,\max} = \tau_{\max}$, debonding occurs, where $\tau_{\max}$ can be obtained from Eq. 3c. A factor α_c is introduced here to represent the ratio between $\tau_{c,\max}$ and $\tau_{\max}$, i.e,

$$\tau_{c,\max} = \alpha_c \tau_{\max} \tag{4c}$$

$$\tau_{s,\max} = (1-\alpha_c)\tau_{\max} \tag{4d}$$

The strain ε_{fd} in the FRP sheet at the critical section when debonding occurs can be obtained as:

$$\varepsilon_{fd} = \frac{T}{E_f t_f b_f} = \frac{\alpha_c \tau_{\max} L_{ee} + (1-\alpha_c)\tau_{\max} L_d}{2E_f t_f} \tag{4e}$$

Based on a regression of FE results, it is suggested that:

$$\alpha_c = 3.32 L_{ee} / L_d \tag{4f}$$

With the debonding strain ε_{fd} and the plane section assumption, the ultimate flexural debonding strength of a beam can be calculated. The test results of 73 RC beams are compared in Figure 15 with results given by the proposed design model, demonstrating a close agreement. These beams include the 45 specimens mentioned in Section 3.4, were all bonded with a soffit FRP plate without additional anchorage measures, and all failed by IC debonding. The performance of the proposed design model is much better than all existing models (Lu et al. 2004g).

3.5.2 *Design model II*

A simpler design model for IC debonding was proposed by Huang & Ye (2004). In this model, the bond stress distribution along the interface when the debonding is fully developed is simplified to be a trapezoidal block. The maximum bond stress $\tau_{\max}$ was taken to be 1 MPa if no U-jacket is used and to be 1.2 MPa if U-jackets or other additional anchorage measures are adopted. Then, ε_{fd} is given by

$$\varepsilon_{fd} = \frac{\tau_{\max}(L_d + 150)}{2E_f t_f} \tag{5}$$

This model is simpler than the more accurate model presented above (Eq. 4e), and considers the benefit of additional anchorage measures such as U-jackets. This model was found to compare well with Fang's (2002) tests. When compared with test results from other sources, the model is conservative (Lu et al. 2004g).

4 SHEAR DEBONDING IN RC BEAMS STRENGTHENED WITH FRP U-JACKETS

4.1 *Experimental research*

RC beams strengthened with FRP U-jackets generally fail by shear debonding (Chen & Teng 2003). Fourteen beams were tested by Tan (2002) and eleven of them were strengthened with FRP U-jackets, including carbon and glass FRP sheets. Based on these test results and FE analysis, a shear strengthening design model has been proposed.

4.2 *Finite element simulation*

In order to better understand the shear debonding mechanism of RC beams strengthened with FRP

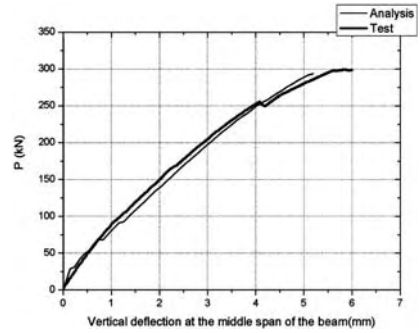

Figure 16. Load–deflection curves of a shear-strengthened beam.

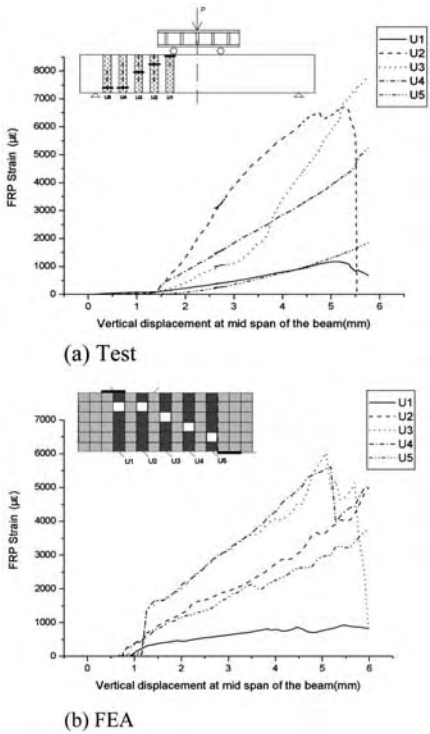

Figure 17. Comparison of strains in the FRP across the diagonal shear crack.

U-jackets, a FE model was set up to simulate such debonding behavior. A bond–slip model similar to that given in Section 2.3 was adopted in the FE analysis. The shear behavior of the RC beam model is governed by the shear retention factor in the smeared crack concrete model (Zhang & Ye 2004). A shear retention factor of 0.06 was found to give predictions in best agreement with Tan's (2002) test results. Typical comparisons between FE results and test results are shown in Figure 16 and Figure 17. In Figure 16, the load–deflection curve from the FE model lies very close to that from the test. In Figure 17, the strains in the FRP across the diagonal shear crack from FE analysis and the test are compared and the curves are again close to each other. Hence, the FE model successfully simulated the shear debonding phenomenon.

Based on the test and FE results, a design proposal for the contribution of the FRP sheets to the shear strength was developed, which is given as:

$$V_f = 2k_f \tau_{\max} A_{fb} \tag{6}$$

where A_{fb} (mm) is the area of the FRP sheet above the diagonal shear crack. If $\tau_{\max}$ is given by Eq. 3c, then $k_f = 0.25$, which leads to accurate but slightly conservative predictions for Tan's (2002) tests. It was found that k_f is related to the shear span ratio. This proposal will be improved in future research.

5 CONCLUSIONS

Intensive recent research at Tsingua University in collaboration with The Hong Kong Polytechnic University has examined different aspects of the interfacial behavior between FRP sheets and concrete. Both experimental and numerical investigations have been carried out. Based on this recent research, the following conclusions may be drawn:

(1) Through the use of an appropriate concrete constitutive law, the debonding process observed in the direct-shear test can be correctly simulated without the use of interface elements. Furthermore, local bond–slip models can be derived from numerical results, in conjunction with test results. The local bond–slip model should be composed of an ascending branch and a descending branch. The tensile strength of concrete is the main factor that governs the shape and the area (i.e. interfacial fracture energy) of the bond–slip curve unless a very soft adhesive layer is adopted.

(2) A bond–slip model established on the basis of direct-shear tests can be applied to simulate debond-ing in RC beams shear- or flexurally-strengthened with FRP. However, two aspects should be paid particular attention if the conventional smeared crack model is used to model concrete. First, slip concentration near a flexural crack cannot be correctly described by the shape function of an interface element. Hence, an additional debonding criterion is needed to take this

slip concentration into account. Second, the bond–slip behavior of a point on the interface near a flexural/shear crack is different from that established from direct-shear tests. At such locations, the interfacial behavior can be correctly modeled by dropping the descending branch.

(3) Details of a debonding failure cannot be easily observed in tests. With appropriate FE models, debonding mechanisms can be clearly understood. In addition, accurate design models can be proposed based on the FE and test results. Several such models have been introduced in this paper.

ACKNOWLEDGEMENT

The authors gratefully acknowledge the financial support provided by the Natural Science Foundation of China (National Key Project No. 50238030), the National High Technology Research and Development Program of China (863 Program) (No. 2001AA336010) and The Hong Kong Polytechnic University through the Area of Strategic Development (ASD) Scheme for the ASD in Mitigation of Urban Hazards.

REFERENCES

Chen, J.F. and Teng, J.G. 2003. Shear capacity of FRP-strengthened RC beams: FRP debonding. *Construction and Building Materials*, 17 (1): 27–41.

Fang, T.Q. 2002. *Study on U-shaped sheet behavior of anti-debonding in the concrete beam reinforced flexurally with FRP.* Master Thesis. Tsinghua University. China.

Huang, Y.L. and Ye, L.P. 2004. Nonlinear FE analysis for bond stress of RC beams flexural strengthened with CFRP sheet. *Engineering Mechanics*, accepted.

Kang, Q.L. 1996. *Finite element analysis for reinforced concrete.* Beijing: China Water Power Press: 120–126.

Lu, X.Z., Tan, Z., Ye, L.P. and Jiang, J.J. 2004a. Finite element analysis for debonding in the interface between FRP sheet and concrete. *Engineering Mechanics*, accepted.

Lu, X.Z., Ye, L.P., Teng, J.G. and Jiang, J.J. 2004b. Meso-scale finite element model for FRP sheets/plates externally boned to concrete, to be published.

Lu, X.Z., Teng, J.G., Ye, L.P. and Jiang, J.J. 2004c. bond–slip models for FRP plate/sheet-to-concrete interfaces. *Proceedings, International Conference on Advanced Polymer Composites for Structural Applications in Construction*, University of Surrey, 20–22 April, 2004, accepted.

Lu, X.Z., Teng, J.G., Ye, L.P. and Jiang, J.J. 2004d. bond–slip models for FRP sheets/plates externally bonded to concrete, to be published.

Lu, X.Z., Teng, J.G., Ye, L.P. and Jiang, J.J. 2004e. Effect of a very soft adhesive on the interfacial behavior between FRP sheets and concrete, to be published.

Lu, X.Z., Teng, J.G., Ye, L.P. and Jiang, J.J. 2004f. Finite element model for intermediate crack debonding in FRP-strengthened RC beams, to be published.

Lu, X.Z., Teng, J.G., Ye, L.P. and Jiang, J.J. 2004g. Design model for intermediate crack debonding in FRP-strengthened RC beams, to be published.

Tan, Z. 2002. *Experimental Research for RC Beam Strengthened with GFRP*. Master Thesis. Tsinghua University. China.

Teng, J.G., Smith, S.T., Yao, J. and Chen, J.F. 2003. Intermediate crack-induced debonding in RC beams and slabs. *Construction and Building Materials*, 17 (6–7): 447–462.

Teng, J.G., Lu, X.Z., Ye, L.P. and Jiang, J.J. 2004. Debonding in FRP-strengthened RC beams due to intermediate flexural cracks. *Proceedings, The Second International Conference on Structural Engineering, Mechanics and Computation*, Cape Town, South Africa, 5–7 July, 2004, accepted.

Yuan, H., Teng, J.G., Seracino, R., Wu, Z.S. and Yao. J. 2003. Full range behavior of FRP-to-concrete bonded joints. *Engineering Structures*, 26 (5): 553–564.

Zhang, Z.X. and Ye, L.P. 2004. Numerical research on shear behaviors of RC beams strengthened with U-type FRP sheets. *Engineering Mechanics*, accepted.

FRP Composites in Civil Engineering – CICE 2004 – Seracino (ed)
© 2005 Taylor & Francis Group, London, ISBN 90 5809 638 6

Taper ended FRP strips bonded to RC beams: experiments and FEM analysis

B. Gao & J.K. Kim
Department of Mechanical Engineering, Hong Kong University of Science & Technology, Clear Water Bay, Kowloon, Hong Kong, China

C.K.Y. Leung
Department of Civil Engineering, Hong Kong University of Science & Technology, Clear Water Bay, Kowloon, Hong Kong, China

ABSTRACT: External bonding of fiber reinforced plastic (FRP) strips to reinforced concrete (RC) beams has been widely accepted as an effective method for strengthening. The ultimate flexural strength of strengthened RC beams can be significantly improved, but often at the expense of ductility of the beam. This paper reports a recent study regarding the influence of FRP strips with tapered ends on structural performance of strengthened RC beams. The tapered FRP strips studied here consisted of FRP layers with continuously varying thickness at the ends. The four point bending experiments indicate that the use of taper ended FRP strips enhanced both the load capacity and the corresponding deflection, compared to the beams bonded with normal FRP strips. The numerical study based on the finite element method (FEM) suggests that these improvements arose from the reduced stress concentrations at the ends of FRP strip, which in turn resulted in delayed crack initiation from them.

1 INTRODUCTION

On account of deterioration caused by aging and environment and poor routine maintenance, as well as the requirements to increase the load carrying capacity and to change the use of structures, the needs for rehabilitation and upgrading of reinforced concrete (RC) structures are becoming increasingly apparent. Various methods for strengthening and rehabilitation of RC structures have been developed in the past several decades. Amongst these methods, external bonding of fiber reinforced plastic (FRP) strips to the beam tensile face has been widely accepted as an effective and convenient method, because FRPs possess a number of beneficial characteristics including high strength and stiffness, high resistance to corrosion and chemicals, light weight due to low density, as well as reduced maintenance of strengthening system and mechanical fixing (Buyukozturk & Hearing 1998, Saadatmanesh & Malek 1998, Teng et al. 2002).

These studies found that the FRP strips increased the strength and stiffness of the beam, but reduced its ductility. The improved ultimate loading capacity was often impaired by premature failure modes in bending, such as concrete cover separation initiated from the cut off point of FRP strips and further fracture with cracks propagating along the steel rebar on the tension side (Gao et al. 2004). In an effort to delay these local failure modes, many measures have been suggested, such as the use of end anchors to wrap around the FRP strip ends (Garden & Hollaway 1998), and the termination of FRP strips near the supports (El-Mihilmy & Tedesco 2001, Gao et al. 2004). Another alternative method is the application of tapered end in FRP strips. In the design of adhesive bond repairs, tapering has been widely applied to avoid premature failure by reducing the adhesive peel stresses (Baker & Jones 1998, Chalkley & Baker 1999). When the taper ended FRP strips are applied to strengthen RC beams, the FRP strip thickness can be varied gradually at cut off points by arranging appropriate length in each layer. Very few studies have so far been conducted to investigate the effectiveness of taper ended strips and to optimize important tapering parameters for maximum benefits of FRP reinforcement (Takeda et al. 1996).

The two major local failure mechanisms of strengthened RC beams, such as delamination of FRP strip and concrete cover separation, often originate from the interfacial cracks at FRP strip ends due to stress concentrations. These stress concentrations have been studied using analytical models and the finite element method (Gao et al. 2002, Malek et al. 1998). As a continuation of our previous studies (Gao et al. 2004), this paper investigates the effect of taper ended FRP

strips on the structural performance of strengthened RC beams, in terms of loading capacity and ductility, based on four point bending experiment. The stress profiles along the FRP-concrete interface, including the principal, normal and shear stresses, were specifically studied based on the finite element analysis to correlate the findings on local failure mechanisms affected by the taper ended strips. Special emphasis was placed on the changes in stress concentrations at the FRP strip ends for different conditions of taper ended FRP strip.

2 EXPERIMENTAL PROGRAM

2.1 *Materials*

The RC beams were prepared using concrete (supplied by Kin Hing Concrete Company Ltd), which consisted of coarse aggregate, sand, cement and water. The strength of concrete was measured from the compression test of a series of cylindrical specimens of 100 mm in diameter and 200 mm in height. The compressive strengths of the concrete were 47.8 MPa and 62.1 MPa; and the elastic moduli were 32.5 GPa and 37.1 GPa in terms of ACI Building Code 318-83, respectively, for the first and second group specimens. Two kinds of steels were applied, including hot rolled, high yield steel and mild steel. The stirrups and the compressive longitudinal steel rebars were made of mild steel of 8 mm in diameter. The tensile longitudinal rebars were made of hot rolled, high yield steel of 10 mm in diameter. The modulus and tensile yield strength of the steel were 200 GPa and 460 MPa, respectively, as measured from the tensile test. The carbon fiber reinforced plastic (CFRP) strips used in this work were basically the same as that used in our previous studies (Gao et al. 2001, Gao et al. 2003), namely MRL-T7-200 (supplied by Reno Carbon Fiber), a unidirectional carbon fiber reinforced epoxy prepreg with a nominal tensile strength of 4.2 GPa and a modulus of 225 GPa. The adhesive used to bond the CFRP onto the concrete consisted of an epoxy resin (MRL-A3), a primer (MRL-A2) and a hardener (MRL-B2). The primer was used to enhance the bonding, which was a mixture of epoxy primer and hardener in the ratio of 100:35 by mass. The resin was a mixture of epoxy resin and hardener in the ratio of 100:35 by mass. The cured resin has a nominal tensile strength of 29.8 MPa and a modulus of 1 GPa.

2.2 *Specimen fabrication and flexural test*

A total of ten RC beams were fabricated to characterize the structural performance of the beams with FRP strips in four point bending test, and the details of external FRP strip reinforcements and taper conditions are summarized in Table 1.

Table 1. Summary of specimens for four point bending test.

Beam designation	Taper condition	Taper distance (mm)*	Maximum load (kN)	Deflection at failure (mm)
(1st group) 1T0	No FRP	–	68.6	19.0
(1st) 1T6LN	No taper	–	116.2	7.5
(1st) 1T6L1a	Taper in 1	50	138.6	9.7
(1st) 1T6L2a	Taper in 2	50	130.2	8.8
(2nd group) 2T0	No FRP	–	71.3	27.8
(2nd) 2T6LN	No taper	–	135.9	8.0
(2nd) 2T6L1a	Taper in 1	50	139.6	8.7
(2nd) 2T6L2b	Taper in 2	100	146.6	9.9
(2nd) 2T4LN	No taper	–	133.3	10.6
(2nd) 2T4L1a	Taper in 1	50	137.7	11.4

*The taper distance representing the length difference between both close taper layers at each side.

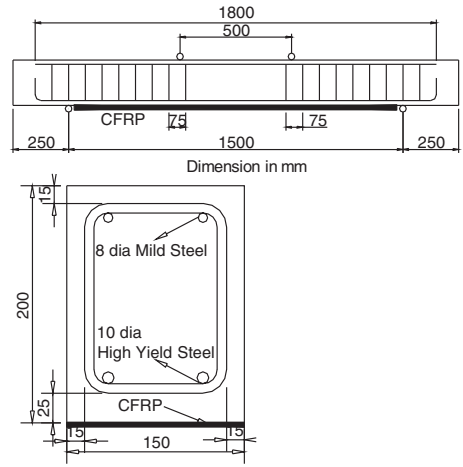

Figure 1. Dimensions of the FRP strengthened reinforced concrete beam.

All RC beams had the same overall cross sectional dimensions, internal longitudinal reinforcement and stirrup arrangements. They were 200 mm high × 150 mm wide × 2000 mm long, with 25 mm in concrete cover depth. The beams were reinforced with 10 mm steel rebars on the tension side and 8 mm steel rebars on the compression side. 8 mm stirrups were added at a 75 mm center-to-center spacing as shown in Figure 1. The steel reinforcement ratio was about 0.86%. All beams were overdesigned in shear to avoid conventional shear failure. Before bonding the FRP strips, the concrete surface on the soffit of the beams

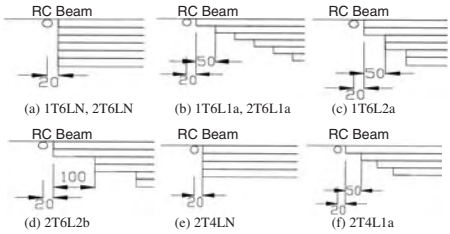

Figure 2. Configurations of various tapered ends of FRP.

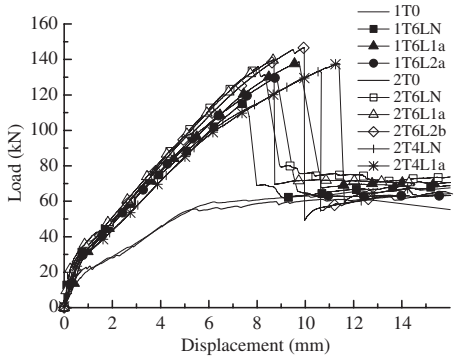

Figure 3. Load vs midpoint displacement records of four point bending tests.

was roughened using a jet chisel to remove all laitance and to expose the aggregates. The rough surface was then cleaned with water and compressed air. A primer, consisting of primer (A2) and hardener (B2), was applied to cover the roughened surface. The CFRP sheets were bonded to the concrete surface using the adhesive consisting of epoxy resin (A3) and hardener (B2). Finally, a resin overcoat was applied on top of the CFRP sheets, followed by curing at room temperature for a week.

The FRP strips used were 150 mm wide, 1460 mm long, and 0.44 mm or 0.66 mm thick (with 4 or 6 layers of FRP sheet). Six different taper end configurations are shown in Figure 2, consisting of taper in each layer and every two layers with different taper distances.

The four point flexural tests of strengthened RC beams were performed on an MTS810 universal testing machine with a maximum load capacity of 500 kN under the displacement control mode. The load-displacement data were automatically recorded using a data logger. The specimen supports consisted of a pin support and a roller support at two ends. The inner and outer loading spans were 500 mm and 1500 mm, respectively. Three linear variable displacement transducers (LVDTs) were used to measure the deflection of the beam at the positions of mid span and two loading points.

2.3 *Results and discussion*

The load vs midpoint-displacement responses of the strengthened RC beams are shown in Figure 3, and the summary of ultimate failure loads and the corresponding deflections are presented in Table 1. As a result of strengthening with CFRP strips, there were significant increases in ultimate failure load and reductions in deflection capacity. The four or six layers of CFRP reinforcement in the second group gave rise to remarkable strength gains of 87% and 90.6% over the control beam 2T0 without CFRP, respectively. This result was at the expense of reduced deflection capacity to 38.1% and 28.8%, respectively, of that of the control beam due to the premature concrete cover separation. The beams 1T0 and 2T0 without CFRP showed typically ductile flexural responses. After yielding of tensile steel reinforcement, concrete crushing occurred at the inner loading span of the beam's upper part due to the high compressive stress concentration. All samples, except the beams 1T0 and 2T0, exhibited concrete cover separation as the principle failure mode. After crack initiation in concrete near the end of CFRP strip, debonding of the CFRP strip occurred gradually with lumps of concrete detached from the longitudinal steel rebar. This observation further confirms that the externally bonded CFRP strips could increase the strength and stiffness of RC beams, but would reduce the ductility.

To study the effects of taper ended FRP strips, different taper configurations were investigated and the experimental results are discussed in the following. Figure 3 suggests that the FRP strips with tapered ends improved the strengthening performance in terms of increased loading capacity and deflection at failure. The larger the number of tapers used, the more improvement in strengthening performance. The beams 1T6LN, 2T6LN and 2T4LN without tapers in FRP strips showed ultimate loads of 116.2 kN, 135.9 kN and 133.3 kN and the deflections at failure of 7.5 mm, 8.0 mm and 10.6 mm, respectively. When the FRP strip ends were tapered at a distance of 50 mm in each layer (i.e. beams 1T6L1a, 2T6L1a and 2T4L1a), the enhancements of the ultimate load were 19.3%, 2.2% and 3.0%, respectively. The corresponding increases of deflection at failure were 29.3%, 8.8% and 7.6%, respectively. If the number of tapers was decreased from taper in 1 to taper in 2 (say beam 1T6L2a), the improvements over the beam without taper decreased, namely 12.1% and 17.3% in loading capacity and deflection (compared to 19.3% and 29.5% for beam 1T6L1a, respectively). The taper distance was also an important parameter that affected the strengthening performance. When FRP strips with

tapered ends were used, there were negligible changes in beam stiffness and in major failure mode.

Nevertheless, marginally more shear/flexural cracks occurred in the vicinity of FRP tapered ends, along with concrete cover separation from the FRP end. The efficiency of tapered ends in improving the strengthening performance of FRP strips was further confirmed by the reduced stress concentrations at the end of the FRP, as predicted in a finite element analysis discussed below.

Since the concrete strengths in two groups were different, their influences on the performance of RC beams need to be clarified. The increase in concrete strength from 47.8 MPa to 62.1 MPa resulted in the improvements in ultimate strength and displacement from 68.6 kN and 19.0 mm (for virgin RC beam 1T0) to 71.3 kN and 27.8 mm (for beam 2T0), respectively. With the FRP strips bonded, the effect of concrete strength on RC beam strength became less sensitive. Enhancements of 17% in maximum load and 6.7% in midpoint displacement were noted for the beam 2T6LN over the beam 1T6LN due to the higher concrete strength. When the taper ended FRP strips were bonded, the benefits of stronger concrete material completely vanished, or even resulted in negative influence: the beam 2T6L1a with a higher concrete strength showed an increase of only 1% in maximum load with a concomitant reduction of 10% in deflection than the beam 1T6L1a. In summary, the higher the concrete strength, the higher the loading capacity and ductility of RC beams without FRP strip reinforcement. With the FRP strips bonded, the benefits of high concrete strength on maximum load and displacement of RC beam decreased significantly, in particular those with taper ended FRP strips. Decreased stress concentrations at the FRP end due to higher concrete strength was mainly responsible for these observations, which will be further proven by the FEM analysis.

3 NUMERICAL ANALYSIS

3.1 *Finite element method*

An FE code ANSYS 5.7 was used in the finite element analysis. The strengthened RC beam model consisted of an FRP strip bonded with an adhesive layer to the RC beam, which was loaded in four point bending. The reinforcing steel bar was modelled as one-dimensional link elements, while quadrilateral eight-node plane stress elements were used for all other components. The symmetric loading geometry of the test allowed a 2D analysis of a half-beam. At the symmetric axis of the beam, the nodes were tied to the boundary, allowing displacements only in the vertical direction. To ensure sufficient accuracy of the results the elements in the vicinity of CFRP strip ends were refined, where stresses were highly concentrated. Figure 4 shows the

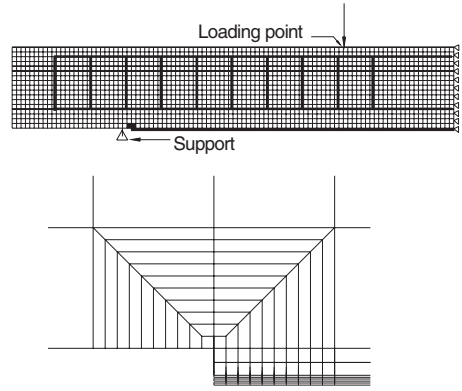

Figure 4. 2D FE model with a mesh refined at CFRP strip end.

model and the mesh near the CFRP strip end. The total number of elements and nodes in the baseline model were varied in terms of the simulated object, e.g. 6096 and 17902 for the case of 1T6L2a, respectively. All components used in the model were assumed to be isotropic and linear elastic, and the FRP-concrete interface was perfectly bonded. The Poisson's ratio was assumed to be 0.2 for concrete, 0.3 for steel and 0.35 for adhesive and CFRP. The mechanical properties of the components are described in Section 2.1.

3.2 *Results and discussion*

3.2.1 *Effect of tapered end*

To study the influence of taper ended FRP strips, three cases with/without tapered ends for the specimens in the first group were simulated, including the beams 1T6LN (no taper), 1T6L1a (taper in each layer, with 50 mm in taper distance) and 1T6L2a (taper in every two layers, with 50 mm in taper distance). The changes in stress distribution along the concrete-FRP interface and stress concentrations at the FRP ends due to taper are specifically discussed in the following.

Typical stress profiles as a function of position from the CFRP plate end for different taper configurations are shown in Figures 5, 6 and 7, respectively for the principal, normal and shear stresses. The maximum stress values at the end of FRP strips are summarized in Table 2, along with percentage reductions in these stresses compared with those for the beams bonded with normal FRP strips without taper.

The principal stress showed a concentration at the end of FRP and a reduction in a short distance, followed by a linear surge toward the plateau value in the majority of the outer span of the loading jig. Within the inner span of the loading jig, the principal stress was constant due to the constant bending moment.

The stress concentrations of the normal (Figure 6) and shear (Figure 7) stresses components were more pronounced than the principal stress component within 15 mm from the FRP plate ends.

There was negligible normal stress component for the FRP strip without taper for the majority of beam length, except the FRP end. However, the normal stresses for those containing tapers exhibited characteristic rapid ups and downs at the taper corners due to the abrupt changes in local stiffness associated with the FRP thickness (Figure 6). Similar characteristic rapid increases and decreases of shear stress components were seen for those with tapers (Figure 7).

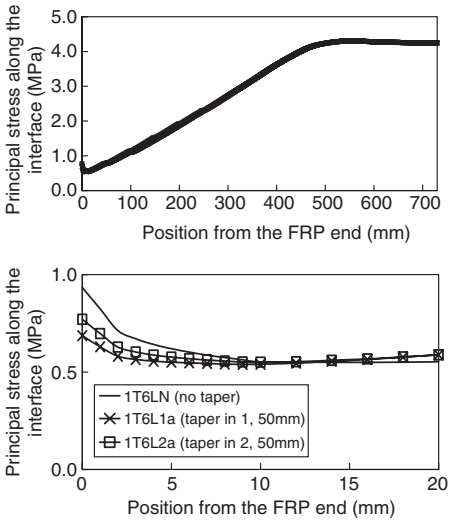

Figure 5. Influence of taper ended FRP on principal stress distribution along the concrete-FRP interface.

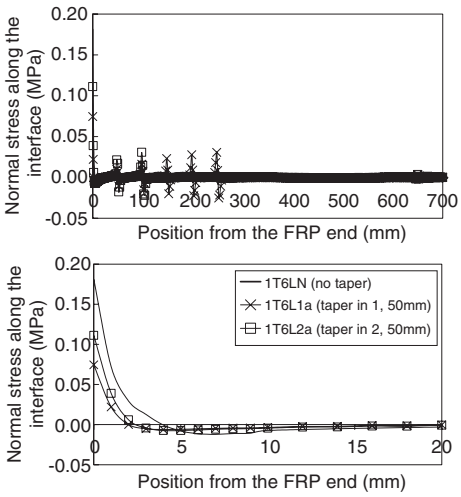

Figure 6. Influence of taper ended FRP on normal stress distribution along the concrete-FRP interface.

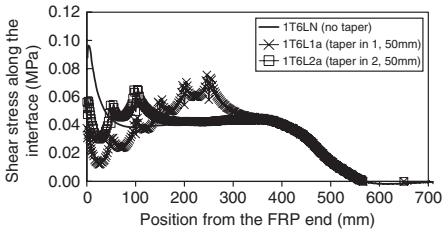

Figure 7. Influence of taper ended FRP on shear stress distribution along the concrete-FRP interface.

Table 2. Summary of stress concentrations at the end of FRP for all cases.

Beam	Taper condition	Taper distance (mm)	Principal stress (decrease) (MPa, %)	Normal stress (decrease) (MPa, %)	Shear stress (decrease) (MPa, %)
1T6LN	No taper	–	0.934 (0)	0.181 (0)	0.096 (0)
1T6L1a	Taper in 1	50	0.687 (26)	0.075 (59)	0.038 (60)
1T6L2a	Taper in 2	50	0.771 (18)	0.111 (39)	0.057 (41)
2T6LN	No taper	–	0.892 (0)	0.161 (0)	0.086 (0)
2T6L1a	Taper in 1	50	0.672 (25)	0.066 (59)	0.033 (62)
2T6L2b	Taper in 2	100	0.747 (16)	0.091 (44)	0.046 (47)
2T4LN	No taper	–	0.814 (0)	0.129 (0)	0.067 (0)
2T4L1a	Taper in 1	50	0.672 (18)	0.066 (49)	0.033 (51)

* Decrease representing the reduction of stress due to individual taper over the stress for the corresponding beam without taper.

Another interesting observation is that the concentrations of all stress components studied at the FRP strip end were reduced significantly by applying tapers: the more the tapered strip the larger the reduction in stress concentration (compare 1T6L1a vs 1T6L2a, Table 2). Among the second group of specimens with six FRP layers, the beam 2T6L1a with taper showed 25%, 59% and 62% reductions of principal, normal and shear stresses, respectively, against the beams without taper (2T6LN); and for those strengthened with four layers of FRP, the beam 2T4L1a with taper showed 18%, 49% and 51% stress reductions compared to the beams without taper (2T4LN).

These stress reductions can delay the crack initiation from FRP ends, which in turn contributed to increasing the load capacity of RC beams. The local changes in FRP strip thickness at its ends due to the tapering showed little negative influence on the stiffness of the whole beam stiffness. This means that the improved maximum load can impart a higher ductility of the beam. This hypothesis was in part proven by the experimental result in that the application of taper ended FRP increased both the load capacity and the corresponding deflection at failure.

The RC beams with more tapered steps resulted in larger stress reductions than those with the same FRP thickness and less number of tapered steps, which agreed well with experiment. For example, the beam 1T6L1a with six tapered steps showed 26%, 59% and 60% reductions, respectively, for the principal, normal and shear stress components, compared to the control beam without taper; whereas the beam 1T6L2a with three tapered steps showed 18%, 39% and 41% reductions.

3.2.2 *Effect of concrete strength*

The experiments have shown that the higher concrete strength could give rise to a higher load capacity regardless of FRP arrangement, and a higher bending deflection in most cases. These observations can also be confirmed by the FEM analysis presented above. In general, a higher compressive concrete strength showed a higher elastic modulus. The effect of concrete strength can be shown by varying the corresponding elastic modulus in the FEM models. With an increase of concrete strength and elastic modulus as well, the beam 2T6LN obtained smaller stress concentrations than the beam 1T6LN under the same loading conditions. The reductions in stress concentration were 4.5%, 11.1% and 10.4%, respectively for the principal, normal and shear stresses. Furthermore, the stress concentrations at the end of FRP for the beam 2T6L1a with a higher concrete strength were 2.2%, 12% and 13.2% lower than that for the beam 1T6L1a, respectively.

Since all strengthened RC beams tested in this study failed by concrete cover separation, the principal stress at the end of FRP was considered as the most dominant stress component that initiated the failure. It is interesting to note that the sensitivity of principle stress on concrete strength was reduced when taper ended FRP strips were used. For example, for the beams with normal FRP, a higher concrete strength gave rise to a principal stress reduction of 4.5% (2T6LN compared to 1T6LN); in comparison, for the beams with taper ended FRP strips, only 2.2% reduction was obtained due to higher concrete strength (2T6L1a compared to 1T6L1a). As a result, only a negligible (1%) increase in load capacity was obtained in experiment when taper was applied, which was well below the enhancement of 17% for the FRP strips without taper. This suggests that the effect of concrete strength on structural performance of RC beams diminished gradually when the beams were strengthened with FRP strips, especially with those with tapers. In other words, the tapered end of FRP improved significantly the effectiveness of applying FRP strips, and maximized the efficiency of FRP. Therefore, if one attempts to optimize the efficiency of FRP to strengthen RC beams, applying tapered ends in FRP strips is a very useful point to be considered. In addition, the tapered end concept is also very attractive from the viewpoint of material cost reduction because of the expensive CFRP prepreg. For example, the beam 1T6L1a with six steps of taper can reduce the total consumption of FRP prepregs by about 17% compared to the control beam 1T6LN without taper.

4 CONCLUSIONS

External bonding of FRP strips to RC beam has been widely accepted as an efficient and convenient method for strengthening the beams. The FRP strips increase the strength and stiffness of the concrete structure, but reduce the ductility. The high ultimate loading capacity is often impaired by premature failure modes, such as concrete cover separation. In this paper, to improve the flexural performance of FRP strengthened RC beams, the FRP strips thickness was gradually varied at cut off point providing tapered ends. The flexural test indicates that the beams with FRP strips with tapered ends improved the strengthening performance, in terms of loading capacity and deflection at failure. The larger the number of tapered end in FRP sheets, the more improvement in strengthening performance compared to those without.

The finite element method was used to analyze the stress distributions along the FRP strip-concrete interface, including principal, normal and shear stresses components. The numerical study indicates that there were significant concentrations of all three stress components at the FRP strip ends, and these stress concentrations were reduced with the use of tapered end. The larger the number of tapered FRP sheets, the

lower the stress concentrations. The lower stress concentrations delayed the initiation of the failure, and thus enhancing the load capacity and corresponding ductility, which was further confirmed by experiment findings. It is suggested that the concept of tapered FRP ends is worthy of further study, because it does not only increase the strengthening performance of FRP, but also potentially reduce the expensive material costs.

ACKNOWLEDGEMENT

The Research Grants Council of the Hong Kong SAR (Project No. HKUST 6050/99E), provided the financial support of this work. The authors wish to thank the Construction Materials Laboratory and Central Facilities, such as AEMF and DMSF, in HKUST for their technical supports.

REFERENCES

Baker, A.A. & Jones, R. 1998. *Bonded Repair of Aircraft Structures*. Dordrecht: M. Nijhoff.

Buyukozturk, O. & Hearing, B. 1998. Failure behaviour of pre-cracked concrete beams retrofitted with FRP. *Journal of Composites for Construction* 2: 138–144.

Chalkley, P. & Baker, A. 1999. Development of a generic repair joint for certification of bonded composite repairs. *International Journal of Adhesion & Adhesives* 19: 121–132.

El-Mihilmy, M.T. & Tedesco, J.W. 2001. Prediction of anchorage failure for reinforced concrete beams strengthened with fiber-reinforced polymer plates. *ACI Structural Journal* 98: 301–314.

Gao, B., Kim, J.K. & Leung, C.K.Y. 2002. Numerical analysis of reinforced concrete beams strengthened with FRP strips: effects of adhesive properties. *Proceeding of the 9th International Conference on Fibre Reinforced Composites*. New-castle: 175–182.

Gao, B., Kim, J.K. & Leung, C.K.Y. 2003. Effect of rubber modifier on interlaminar fracture toughness of CFRP-concrete interface. *Composite Science and Technology* 63: 883–892.

Gao, B., Kim, J.K. & Leung, C.K.Y. 2004. Experimental investigation of taper ended FRP strips in FRP strengthened RC beams. *Proceeding of the 4th International Conference on Advanced Composites Materials in Bridges and Structures*. Alberta.

Gao, B., Leung, C.K.Y. & Kim, J.K. 2004. Prediction for failure mode of strengthened RC beams with failure diagram. *Composites Science and Technology*, submitted.

Gao, B., Leung, W.H., Cheung, C.M., Kim, J.K. & Leung, C.K.Y. 2001. Effects of adhesive properties on strengthening of concrete beams with composite strips. *Proceedings of the International Conference on FRP Composites in Civil Engineering*. Hong Kong: Elsevier. 423–432.

Garden, H.N. & Hollaway, L.C. 1998. An experimental study of the influence of plate end anchorage of carbon fibre composite plates used to strengthen reinforced concrete beams. *Composite Structures* 42: 175–188.

Malek, A.M., Saadatmanesh, H. & Ehsani, M.R. 1998. Prediction of failure load of R/C beams strengthened with FRP plate due to stress concentration at the plate end. *ACI Structural Journal* 95(1): 142–152.

Saadatmanesh, H. & Malek, A.M. 1998. Design guidelines for strengthening of RC beam with FRP plates. *Journal of Composites for Construction* 2(4): 158–164.

Takeda, K., Mitsui, Y. & Murakami, K. 1996. Flexural behaviour of reinforced concrete beams strengthened with carbon fibre sheets. *Composites Part A* 27: 981–987.

Teng, J.G., Chen, J.F., Smith, S.T. & Lam, L. 2002. *FRP-Strengthened RC Structures*. Chichester: John Wiley & Sons.

FRP Composites in Civil Engineering – CICE 2004 – Seracino (ed)
© 2005 Taylor & Francis Group, London, ISBN 90 5809 638 6

Bond characteristics of CFRP fabrics bonded to concrete members using wet lay-up method

H. Pham & R. Al-Mahaidi
Monash University, Melbourne, Victoria, Australia

ABSTRACT: Wet lay-up method offers a great flexibility for field applications and is generally the cheapest alternative among other methods to bond fibre reinforced polymer composites to concrete. Understanding the characteristics of the bond formed by this method is essential for its strengthening applications. In this study, twenty-two single shear-lap tests are carried out. The parameters varied are FRP bond length, FRP thickness and support block height. Two main failure types were observed; interfacial failure in the concrete layer just below the bond surface and shear tension failure propagated inside the concrete block. The test results are used to verify an analytical model, in which interfacial behaviour is idealised using a bond-slip relationship and the cracking inside concrete is modeled with smeared cracks. This model proved to be able to represent the behaviour of the shear-lap blocks quite adequately.

1 INTRODUCTION

Strengthening reinforced concrete members using fibre reinforced polymers (FRP) has emerged as a potential method to address their strength deficiency problems. The most widely used method is to bond FRP on to concrete using wet lay-up method. In this method, the composite and bonding are formed at the same time. Epoxy resin functions as the medium to transfer shear stress both between fibres and between fibres and concrete. Wet lay-up method offers a great flexibility for field application and is generally the cheapest alternative among other methods of bonding.

The mechanical performance and durability of FRP in strengthening application depends primarily on the bonding with the structure. The current quality of the epoxy adhesives has proved to be efficient to transfer the stresses between FRP and concrete. However, FRP still tends to delaminate or debond from concrete. The reason is that the bond stress is transferred only in a limited area due to the existence of effective bond zone. This lead to local shear stress concentration. Stress concentration may also result from the discontinuity near the end of FRP. The problem is compounded by the fact that concrete has relatively low shear strength. Therefore, premature failure tends to occur in the concrete adjacent to the bonding interface. As a consequence, when the amount of FRP material is increased, the strength of FRP available for design can decrease significantly.

Consequently, to be able to design FRP for strengthening, understanding of bonding and debonding mechanisms is essential. The bond behaviour is dependant on numerous factors including but not limited to adhesive properties, FRP properties, concrete substrate, concrete surface preparation, concrete strength, adhesive thickness, FRP thickness and FRP bonded area. In the present study, only FRP thickness and FRP bonded area were investigated using a simple shear-lap test set-up. A non-linear finite element model is also implemented to simulate the test.

2 PREVIOUS RESEARCH

2.1 *Experiments*

Substantial experimental work exists on shear-lap testing. There is a great variation in test configurations, laminate types, adhesive types and specimen dimensions. There are also a variety of failure modes reported. Therefore, a summary of test set-ups and failure types is presented first. It is followed by description on a general trend in the behaviour observed in those tests.

Figure 1 shows three most commonly used set-ups: double pull-pull test, single pull-push test and bending test. Double pull-pull test is the most frequently reported. The main advantage is that FRP does not need to be anchored. Single pull-push test is also used widely. The main advantage is the reduced use of FRP and concrete materials. The third type of shear-lap testing is by bending a concrete beam. FRP is bonded across a saw cut in the middle.

Figure 2 shows five observed failure modes reported in literature (Neubauer and Rostasy, 1997; Chen and Teng, 2001; Yao et al., 2002). The first mode is *shear tension failure*, which occurs when cracks start at the unloading end of FRP and propagate deep into the concrete block. This tends to happen when the laminate stiffness is significant. The second type is *FRP tensile rupture*, which may occur if FRP area is small enough. *Cohesion failure* through adhesive, has also been reported. *Delamination* can also occur within FRP layers. These modes are not common especially for normal strength concrete which has a low shear strength compared to that of adhesives and FRP. The fifth mode is the most commonly observed. Concrete fails a few millimetres beneath the concrete-adhesive interface. A concrete prism can also be pulled out near the loading end. This is called *interfacial bond failure*.

Despite a wide range of materials and configurations used, a general trend exists in terms of the force transfer behaviour and failure mechanisms of a composite-concrete joint. Tension is transferred to the concrete mainly via the shear stress in a short length nearest to the applied load. This length is called the effective bond length. As the load increases and cracking on the concrete propagates, there is a shift of the active bond zone toward the other end. As a result, there exists an effective bond length L_e beyond which anchorage strength does not increased, irrespective of the bond length (Chajes et al., 1996; Maeda et al., 1997; Lee, 2003).

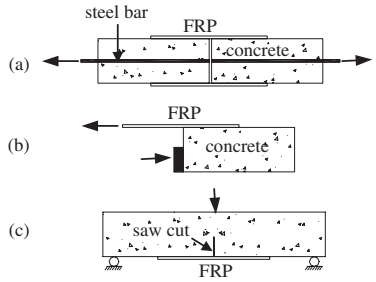

Figure 1. Different set-ups for shear tests: (a) Double pull-pull test; (b) Single pull-push test; (c) Bending test.

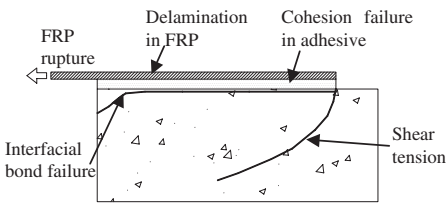

Figure 2. Possible failure locations.

3 EXPERIMENTAL PROGRAM

3.1 *Test method and material properties*

Single pull-push tests were used in this experimental program. The concrete block sizes were 140 × 140 × 300 mm. The blocks were held down by a steel cage as shown in Fig. 3. Two steel plates are bonded to the other end of CFRP using epoxy for gripping.

The process of applying CFRP to concrete involved two main steps: surface preparation and bonding. The concrete surface was prepared using high-pressure water jet (4000 psi or 28 MPa) to remove the paste and expose the coarse aggregates. This method proved to be efficient and lead to a relatively rough surface suitable for bonding. Before bonding CFRP, the surface was vacuumed and a primer layer was applied. Bonding operation included resin under-coating, carbon fibre sheet application and resin over-coating. The curing period was 1 week at room temperature.

The blocks were loaded using a Baldwin universal testing machine with a load range of 100 kN. They were loaded at a rate of 0.2 mm per min for most of the time. The blocks were instrumented with strain gauges and LVDTs (Fig. 4).

The concrete cylinder strength was 55.6 MPa (172 days). The carbon fibre fabric used had a mean elastic modulus of 209000 MPa and a nominal thickness of 0.176 mm. The adhesive used was MBT Saturant with a reported elastic modulus greater than 3500 MPa.

The variables considered were the bond length L, the number of CFRP plies and the support block clearance H. Two identical specimens were prepared for each configuration (denoted a and b).

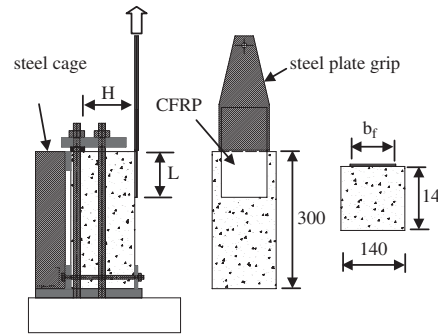

Figure 3. Test set-up.

3.2 *Test results*

3.2.1 *Failure modes*

The specimens bonded with two plies of CFRP failed by interfacial bond failure. Concrete just below the bond line ruptured in shear with a thin layer of concrete substrate still bonded to the laminate. Close examination of the failure surface revealed the type of failure mechanism. During bonding, epoxy infiltrated into the rough surface of concrete. The interface shear strength was mainly due to the interlocking between the epoxy and the concrete surface irregularities. When the shear stress increased to a high value, those irregularities started to rupture with cracks propagating both through the paste and the aggregate. Since there were many irregularities on the surface, the cracking happened gradually starting from the loading end transferring the stress to the next bond area (Figs. 5, 6).

For most specimens failing in this mode, a triangular concrete prism was also pulled off near the loading end.

The specimens bonded with 6 plies of 100 mm bond length failed by shear tension failure; whereas the ones with longer bond length failed either due to shear tension failure or interfacial debonding. This was due to the fact that the thicker the CFRP layer is, the better the stress is transferred to the CFRP unloaded end.

Table 1. Variables in the experimental program and test results.

Designation	L (mm)	No. of plies	H (mm)	bf (mm)	Max. load (kN)	Max. average bond stress (MPa)	Max. FRP tensile stress (MPa)
T1a	60	2	110	100	20.0	3.3	568
T1b	60	2	110	100	18.8	3.1	534
T2a	80	2	110	100	25.8	3.2	733
T2b	80	2	110	100	25.2	3.2	716
T3a	100	2	110	100	25.8	2.6	733
T3b	100	2	110	100	27.3	2.7	776
T4a	140	2	110	100	26.7	1.9	759
T4b	140	2	110	100	25.9	1.9	736
T5a	180	2	110	100	27.8	1.5	790
T5b	180	2	110	100	31.7	1.8	901
T6a	220	2	110	100	31.7	1.4	901
T6b	220	2	110	100	28.6	1.3	813
T7a	100	2	5	100	33.0	3.3	938
T7b	100	2	5	100	26.9	2.7	764
T8a	100	2	70	100	28.5	2.9	810
T8b	100	2	70	100	29.8	3.0	847
T9a	100	6	110	100	28.4	2.8	269
T9b	100	6	110	100	29.8	3.0	282
T10a	140	6	110	100	37.4	2.7	354
T10b	140	6	110	100	33.3	2.4	315
T11a	180	6	110	100	42.8	2.4	405
T11b	180	6	110	100	39.0	2.2	369

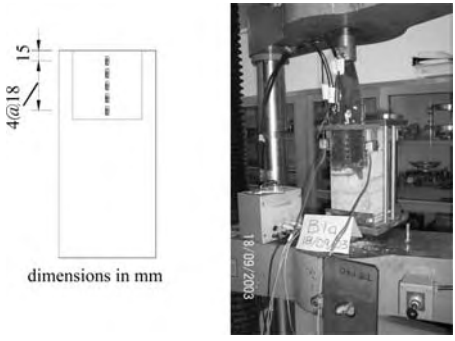

Figure 4. Strain gauge locations and test set-up.

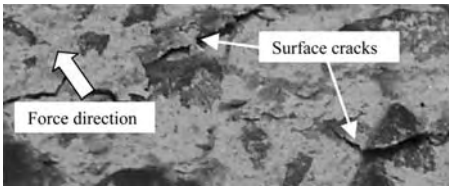

Figure 5. Typical surface cracking.

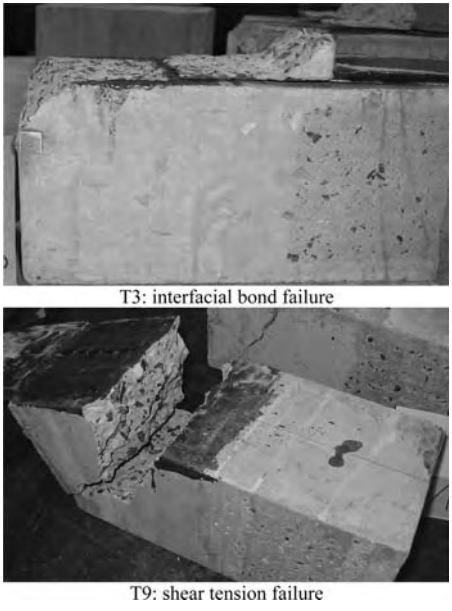

Figure 6. Two failure modes.

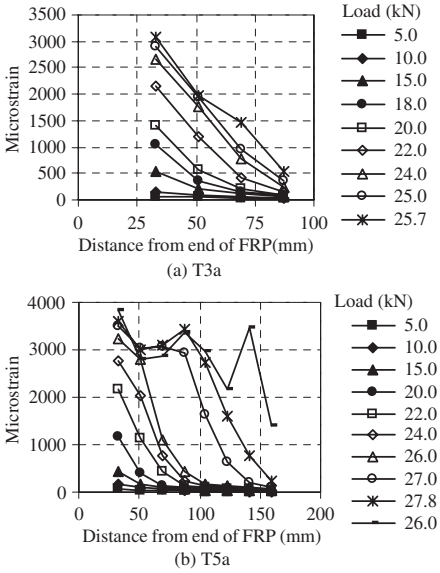

Figure 7. FRP strain distributions in T3a and T5a.

A major crack, therefore, tended to open up propagating deep into concrete and finally terminating near the support block location. When the bond length was longer, the stresses near both ends of FRP were high, resulting in inconsistency in failure modes. Another possible reason for the inconsistency was because of the difficulties in keeping the CFRP perfectly aligned with the concrete block. This problem was more significant when the CFRP layer was relatively thick due to bending of the composites while straightening out. This could be exacerbated due to some rotation of the concrete block under high loads.

3.2.2 *Strain, stress and slip distributions*

Figure 7 shows two examples of the strain distributions of T1a and T5a. The distributions indicated gradual delamination from the loading end to the other end with an effective bond length of around 100 mm.

The average bond stress between two adjacent strain gauges has been calculated using the following equation:

$$\tau = \frac{E_f\left(\varepsilon_{f,i+1} - \varepsilon_{f,i}\right)t_f}{\Delta L} \qquad (1)$$

where E_f and t_f are FRP elastic modulus and thickness; $\varepsilon_{f,\,i+1}$ and $\varepsilon_{f,\,i}$ are FRP strains and ΔL is the distance between strain gauges.

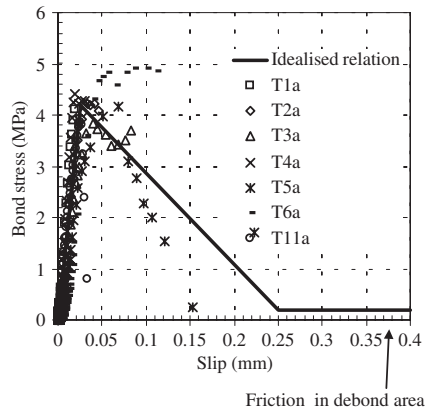

Figure 8. Bond stress–slip relationships.

The average slip is the incremental sum of the FRP extension.

$$s_i = \frac{\varepsilon_{f,i+1} + \varepsilon_{f,i}}{2}\Delta L + s_{i-1} \qquad (2)$$

It is worth noting that in Equation 2, since the concrete block stiffness is much higher than the CFRP stiffness, concrete elongation is ignored.

Figure 8 shows the relationship between the bond stress and the slip for several specimens. The curve shows a maximum stress of around 4.2 MPa at a slip of 0.025 mm. This is adopted in our models as described in section 4.

4 NLFEA MODELLING

4.1 *Model idealisation*

From the above experimental observations, a tensile softening relationship can be adopted for the bond stress–slip relationship. The idealised relationship, as shown in Fig. 8, was adopted for the interface elements between FRP and concrete in the 2D nonlinear finite element simulation (NLFEA) using DIANA. The horizontal portion of the curve is due to the fact that friction in the debonding area can still provide some shear resistance. The shear stress was taken to be constant at 0.2 MPa in this study.

Plane stress elements with 20 × 20 mm mesh were used to represent concrete. Eight-noded quadrilateral isoparametric elements were used. A smeared crack model based on total crack strain was utilised for concrete cracking. Tensile behaviour was described with a linear softening curve. The FRP was modeled using beam elements.

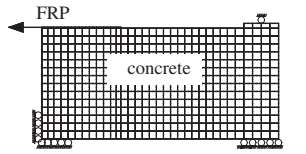

a. Finite element mesh

b. Interface element displacements and tractions (de Witte and Kikstra, 2003)

Figure 9. Nonlinear FEA model.

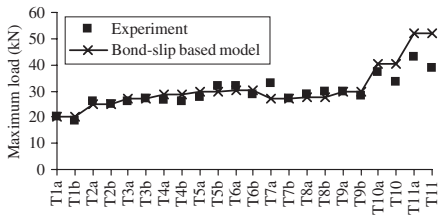

Figure 10. Correlation between bond-slip based model and experimental measurement.

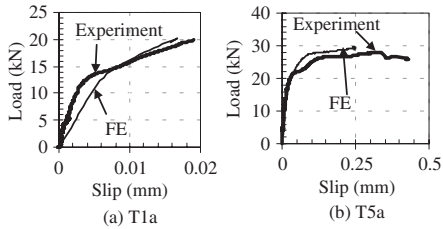

Figure 11. Load versus slip (at 42 mm from loading end) curves.

4.2 *Correlation*

Figure 10 compares the maximum pulling force as calculated by NLFEA and as measured in the experiments for all specimens. The predictions are reasonably accurate for most specimens except for T10 and T11 where the model gives higher failure loads. This may be due to the discrepancy in the failure mode of these specimens where the combination of both interfacial cracks and end crack lead to a lower failure, which is not captured by the FE model. The load-slip curves in Fig. 11 show an agreement between the experimental and FE results.

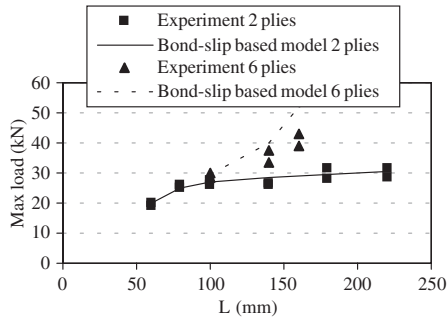

Figure 12. Effect of bond length.

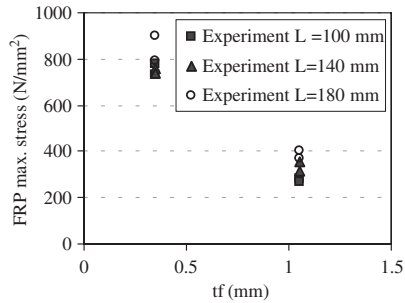

Figure 13. Effect of FRP thickness.

5 PARAMETRIC STUDY

5.1 *Effect of FRP bond length*

Figure 12 plots the maximum loads as measured and predicted versus the bond lengths for two series of specimens. For the specimens with 2 plies, the experimental results and the predictions from the proposed bond-slip model are very close. The curves show a development length of about 100 mm. The maximum loads still increase slightly for specimens with longer bond length as the friction in debonding area becomes more significant. The predicted curves for the series with 6 plies show similar trend as the experiments. However, the discrepancy becomes more significant as the bond length increases.

5.2 *Effect of FRP thickness*

Thicker FRP means better stress transfer along the bond area. However, the improvement usually does not outweigh the waste in FRP materials. Fig. 13 illustrates this point showing that the effective FRP stress is reduced significantly as the nominal fibre thickness is increased from 0.35 to 1.06 mm.

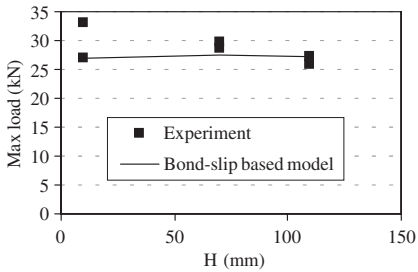

Figure 14. Effect of support block clearance.

5.2.1 *Effect of support block clearance*

Figure 14 indicates that the specimens with little clearance failed at a slightly higher load. This may be due to concrete confinement in the vicinity of the support block.

6 CONCLUSION

An investigation into the bonding between CFRP and concrete has been presented. The study shows two failure mechanisms of the bond: shear tension failure and interfacial bond failure. These failures are the result of high interfacial shear stresses near both ends of the composite. To simulate the bonding behaviour, a simple relationship with linear softening path and a permanent frictional resistance is proposed. This is incorporated in a NLFEA model. The model gives the ultimate load reasonably close to experimental values.

ACKNOWLEDGEMENT

The research reported in this paper is part of a study financed by Monash University Engineering Grant. All CFRP fabrics and adhesives were partly sponsored by MBT (Australia) Pty Ltd.

REFERENCES

Chajes, M. J., Finch, W. W., Jr., Januszka, T. F. and Thomson, T. A., Jr. (1996). Bond and force transfer of composite material plates bonded to concrete, *ACI Struc. J.,* 93(2), pp. 208–217.

Chen, J. F. and Teng, J. G. (2001). Anchorage Strength Models for FRP and Steel Plates Bonded to Concrete, *J. Struc. Eng. ASCE,* 127(7), pp. 784–791.

de Witte, F. C. and Kikstra, W. P. (2003). *DIANA User's Manual,*TNO DIANA BV, Delft, The Netherlands.

Lee, K. (2003). Shear strength of concrete T-beams repaired using carbon fibre reinforced polymer, Thesis, *Department of Civil Engineering,* Monash University.

Maeda, T., Asano, Y., Sato, Y., Ueda, T. and Kakuta, Y. (1997). A Study on Bond Mechanism of Carbon Fiber Sheet, *Proc., 3rd Symp. – Non-Metallic (FRP) Reinforcement for Concrete Struct.,* Japan, 1, 279–286.

Neubauer, U. and Rostasy, F. S. (1997). Design aspects of concrete structures strengthened with externally bonded CFRP-plates, *Proceeding of the 7th International Conference on Structural Faults and Repairs,* 109–118.

Yao, J., Teng, J. G. and Chen, J. F. (2002). FRP-to-concrete bond strength: an experimental study, *ACUN – 4,* Bandyopadhyay, S., Sydney, Australia.

FRP Composites in Civil Engineering – CICE 2004 – Seracino (ed)
© 2005 Taylor & Francis Group, London, ISBN 90 5809 638 6

A new approach for interfacial stress analysis of beams bonded with a thin plate

J. Yang
School of the Civil Engineering, The University of Leeds, UK

J.F. Chen
Institute for Infrastructure and Environment, The University of Edinburgh, UK

J.G. Teng
Department of Civil and Structural Engineering, The Hong Kong Polytechnic University, China

ABSTRACT: Extensive research has shown that bonding a fiber-reinforced polymer (FRP) plate to the tension face of a reinforced concrete (RC) or steel beam can effectively enhance its serviceability and ultimate strength. The controlling failure mode of such a strengthened beam often involves the premature debonding of the FRP plate from the original beam in a brittle manner. A solid understanding of the cause and mechanism of this debonding failure mode is important for the development of an accurate strength model so that this strengthening technique can be used more effectively and economically. This paper presents a new analytical solution for the interfacial stresses in simply supported beams bonded with a thin plate and subjected to arbitrary symmetric loads. While the bonding of FRP plates to RC beams represents the most common application of this strengthening technique, the present solution is generic in terms of the materials used to construct the beam and the thin plate. The solution is represented by Fourier series and is based on the minimisation of the complementary energy. The new solution not only takes into consideration the non-uniform stress distribution in the adhesive layer and the stress-free boundary condition at the ends of the plate, but also correctly predicts the drastic difference in the interfacial normal stress between the plate-to-adhesive interface and adhesive-to-concrete interface as revealed by finite element analysis. The solution methodology is general in nature and may be applied to the analysis of other types of composite structures.

1 INTRODUCTION

Extensive research has shown that bonding a fiber-reinforced polymer (FRP) plate to the tension face (or the soffit in the context of a simply supported beam) of a reinforced concrete (RC) beam can effectively enhance its serviceability and ultimate strength (Teng *et al.* 2002a). More recently, FRP plate bonding has also been used to strengthen steel beams. Central to the success of this technique is the effective stress transfer from the existing beam to the externally bonded FRP reinforcement. Research has shown that the controlling failure mode of such a strengthened beam often involves the premature debonding of the FRP plate from the beam in a brittle manner. As this debonding failure mode is closely related to the interfacial stresses between the FRP plate and the existing beam, extensive studies have been carried out during the last decade on the prediction of interfacial stresses, generally within the context of RC beams strengthened with an FRP plate, although a substantial amount of work on interfacial stresses in steel plated RC beams had been carried out before FRP plate bonding became popular. These include experimental studies (e.g. Garden *et al.* 1998, Ahmed *et al.* 2001 and Bonacci & Maalej 2001); numerical studies using the linear finite element method (e.g. Täljsten 1997, Malek *et al.* 1998, Rabinovich & Frostig 2000 and Teng *et al.* 2002b) and the nonlinear finite element method (e.g. Ascione & Feo 2000, Rahimi & Hutchinson 2001, Aprile *et al.* 2001), discrete section analysis (e.g. Arduini & Nanni 1997) and analytical solutions (e.g. Smith & Teng 2001). This paper presents a new analytical solution for interfacial stresses in an existing beam strengthened with a bonded FRP or steel soffit plate.

For simply supported FRP or steel plated beams, approximate analytical solutions for interfacial stresses have been developed using several methods. These include the staged analysis approach (Roberts 1989, Roberts & Haji-Kazemi 1989), the deformation

compatibility-based approach (Vilnay 1988, Täljsten 1997, Malek *et al.* 1998) and the shear-lag approach with or without considering the nonlinearity of concrete (e.g. Trantafillou & Deskovic 1991, Ye 2001 and Leung *et al.* 2001). A thorough review and comparison of the majority of these solutions can be found in Smith and Teng (2001) where a more general solution based on the compatibility-based approach is also given. All these solutions are based on the assumption that the shear and normal stresses are uniform across the thickness of the adhesive layer; they also violate the stress-free boundary condition at the ends of the adhesive layer.

The first solution that satisfies the stress-free boundary condition at the ends of the adhesive layer was developed by Rabinovich and Frostig (2000) who treated the adhesive layer as an elastic medium with a negligible longitudinal stiffness. This leads to a uniform shear stress distribution and a linearly varying transverse normal stress distribution across the thickness of the adhesive layer. This solution does not lead to explicit expressions for the interfacial stresses. Shen *et al.* (2001) proposed an alternative complementary energy approach, which resulted in closed-form expressions for interfacial stresses in a simply supported beam under uniformly distributed loads and symmetrical end moments. In their solution, Shen *et al.* (2001) also removed the assumption that the longitudinal stiffness of the adhesive layer is negligible as used by Rabinovich and Frostig (2000). Instead, they assumed that the longitudinal normal stress varies linearly across the thickness of the adhesive layer, leading to a parabolic shear stress distribution across the adhesive thickness. Yang *et al.* (2004) extended Shen *et al.*'s (2001) work to allow for arbitrary loadings.

Although the stress distribution assumed for the adhesive layer in Shen *et al.* (2001) and Yang *et al.* (2004) has a higher order form than those of other solutions, there is still one important limitation. At one stage of their solution process, the concrete-adhesive-FRP composite section was transformed into an equivalent FRP section and the geometrical properties (e.g. area, second moment of area) of the transformed section were used. Whilst this process helped to establish relationships between and thus reduce the number of unknown coefficients so that a closed-form solution was obtainable, this implies the partial use of the plane section assumption for the composite section (e.g. when the second moment of area is used) in the solution. Clearly, this assumption cannot be satisfied in the close vicinities of the plate ends.

This paper presents an improvement to Shen *et al.*'s (2001) approach so that the use of the plane section assumption for the composite beam is completely avoided. Simply supported beams bonded with a thin plate made of FRP, steel or another suitable material and subjected to arbitrary symmetric loads are considered in the present work. The interfacial stresses are represented by Fourier series and the solution is derived by minimising the complementary energy. Singular loads (e.g. point loads) and loads with discontinuities (e.g. patch loads) are treated as equivalent distributed loads using the distribution theory (e.g. Schwarz 1966, Yavari *et al.* 2000). The solution is compared with finite element predictions for selected examples.

It may be noted that the solution is generic in terms of the materials used to construct the beam and the thin plate. For example, it is equally applicable to RC beams strengthened with steel plates or metallic beams strengthened with FRP plates.

2 METHOD OF SOLUTION

2.1 *Geometry and loading*

Consider a simply supported RC beam with a span of $2L$. The bonded plate has a length of $2l$ (Fig. 1). The beam is subjected to an axial force N_0, a pair of end moments M_0 and a symmetrically distributed arbitrary transverse load $q(x)$. It may be noted that any thermal loading due to the difference in thermal properties between the materials for the beam and the plate

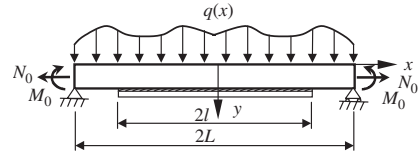

Figure 1. A plated beam under symmetric loads.

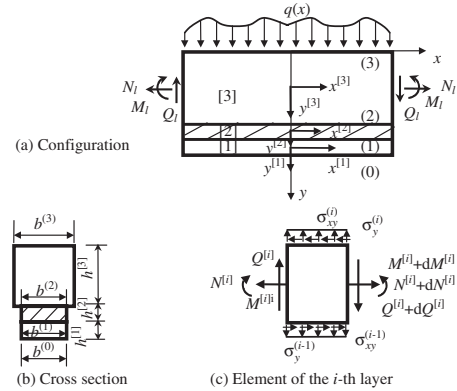

Figure 2. Notations.

(e.g. FRP, concrete, cast iron) can be easily included in N_0. The applied loading results in internal forces N_l, Q_l and M_l at the beam sections at the ends of the plate (Fig. 2a).

A global Cartesian co-ordinate system $x-y$ is used with its origin being at the middle of the top surface of the beam (Fig. 1). The strengthened portion of the beam consists of three layers: the concrete beam, the adhesive and the plate. A local coordinate system $x^{[i]}-y^{[i]}$ is adopted for each of the three layers, with the origin being at the geometrical centre of each layer (Fig. 2a). For ease of reference, these three layers are denoted by superscripts [1], [2] and [3] respectively (e.g. the thicknesses of the three layers are denoted by $h^{[1]}$, $h^{[2]}$ and $h^{[3]}$ respectively). Similarly, superscripts (0), (1), (2) and (3) are used to denote the surfaces and interfaces (e.g. the widths the surfaces/interfaces are $b^{(0)}$, $b^{(1)}$, $b^{(2)}$ and $b^{(3)}$ respectively) (Fig. 2b). Note $b^{(0)} = b^{(1)} = b^{(2)}$.

2.2 *Assumptions*

The present analysis takes into consideration the transverse shear stress and strain in the RC beam and the FRP plate but ignores the transverse normal stress in them. Additionally, the following four assumptions are adopted:

(1) each individual layer is elastic, homogeneous and orthotropic. Note that the assumption of orthotropic behaviour has implications only for the shear moduli of the materials for the RC beam and the bonded plate;
(2) the three layers are perfectly bonded (no slips or opening-up at the interfaces);
(3) the Euler-Bernoulli beam theory is adopted for the beam and the plate, whereas the adhesive layer is considered to be in a plane stress state; *and*
(4) the longitudinal stress in the adhesive is assumed to vary linearly across its thickness.

It may be noted that these same assumptions were listed in Shen *et al.* (2001) and Yang *et al.* (2004), but the plane section assumption was partially made use of in their solution process as noted earlier.

2.3 *Equilibrium equations of beam and plate*

For the beam and plate (*ith* layer, $i = 1, 3$, see Fig. 2c), equilibrium considerations lead to the following relations

$$\frac{dN^{[i]}(x)}{dx} = b^{(i)}\sigma_{xy}^{(i)}(x) - b^{(i-1)}\sigma_{xy}^{(i-1)}(x) \tag{1a}$$

$$\frac{dQ^{[i]}(x)}{dx} = b^{(i)}\sigma_{y}^{(i)}(x) - b^{(i-1)}\sigma_{y}^{(i-1)}(x) - \begin{cases} 0 & (i \neq 3) \\ q(x) & (i = 3) \end{cases} \tag{1b}$$

$$\frac{dM^{[i]}(x)}{dx} = Q^{[i]}(x) - \frac{h^{[i]}}{2}\left[b^{(i-1)}\sigma_{xy}^{(i-1)}(x) + b^{(i)}\sigma_{xy}^{(i)}(x)\right] \tag{1c}$$

where $N^{[i]}(x)$, $Q^{[i]}(x)$ and $M^{[i]}(x)$ are the axial force, shear force and bending moment respectively in the *ith* layer and $\sigma_{xy}^{(i)}(x)$ and $\sigma_{y}^{(i)}(x)$ are the shear and transverse normal stresses respectively at the *ith* interface. In Equation 1 and the rest of this paper, the superscript in $x^{[i]}$ is omitted because the global and the three local co-ordinate systems share the same horizontal axis.

2.4 *Boundary conditions at ends of plate*

The boundary conditions at the ends of the plate are

$$N^{[i]}(\pm l) = \begin{cases} 0 & (i \neq 3) \\ N_l & (i = 3) \end{cases}; \qquad Q^{[i]}(\pm l) = \begin{cases} 0 & (i \neq 3) \\ Q_l & (i = 3) \end{cases};$$

$$M^{[i]}(\pm l) = \begin{cases} 0 & (i \neq 3) \\ M_l & (i = 3) \end{cases} \tag{2a-c}$$

2.5 *Representation of stress fields*

2.5.1 *Stress field in the adhesive layer*

The adhesive layer is treated as an elastic continuum without any body force. The equilibrium equations in its local coordinate system are

$$\frac{\partial \sigma_x^{[2]}}{\partial x} + \frac{\partial \sigma_{xy}^{[2]}}{\partial y^{[2]}} = 0, \qquad \frac{\partial \sigma_{xy}^{[2]}}{\partial x} + \frac{\partial \sigma_y^{[2]}}{\partial y^{[2]}} = 0 \tag{3a,b}$$

where $\sigma_x^{[2]}$, $\sigma_{xy}^{[2]}$ and $\sigma_y^{[2]}$ denote the longitudinal, shear and transverse stresses respectively.

The longitudinal stress in the adhesive layer is assumed to be a linear function of $y^{[2]}$ and it then follows from Equation 3a that the shear stress distribution is parabolic. Equating the shear and normal stresses at lower and upper faces to the appropriate interfacial stresses, $\sigma_{xy}^{(i)}(x)$ and $\sigma_{y}^{(i)}(x)$ $(i = 1, 2)$ and adopting the equilibrium conditions of Equations 3a and b lead to

$$\sigma_x^{[2]} = \int_0^x \left[\frac{\sigma_{xy}^{(1)} - \sigma_{xy}^{(2)}}{h^{[2]}} + \frac{4y^{[2]}}{\left(h^{[2]}\right)^2} \left[\sigma_{xy}^{(1)} + \sigma_{xy}^{(2)} + \int_0^x \left[\frac{3\left(\sigma_y^{(1)} - \sigma_y^{(2)}\right)}{h^{[2]}} + \frac{\left(\sigma_{xy}^{(1)'} + \sigma_{xy}^{(2)'}\right)}{2} \right] dx \right] \right] dx \tag{4a}$$

$$\sigma_{xy}^{[2]} = \int \left[\frac{3\left(\sigma_y^{(2)} - \sigma_y^{(1)}\right)}{2h^{[2]}} - \frac{\left(\sigma_{xy}^{(1)'} + \sigma_{xy}^{(2)'}\right)}{4} \right] dx + \frac{y^{[2]}\left(\sigma_{xy}^{(1)} - \sigma_{xy}^{(2)}\right)}{h^{[2]}}$$
$$+ \frac{\left(y^{[2]}\right)^2}{\left(h^{[2]}\right)^2} \left\{ 2\left(\sigma_{xy}^{(1)} + \sigma_{xy}^{(2)}\right) + \int \left[\frac{6\left(\sigma_y^{(1)} - \sigma_y^{(2)}\right)}{h^{[2]}} + h^{[2]}\left(\sigma_{xy}^{(1)'} + \sigma_{xy}^{(2)'}\right) \right] dx \right\} \tag{4b}$$

$$\sigma_y^{[2]}=\frac{\sigma_y^{(1)}+\sigma_y^{(2)}}{2}+\frac{h^{[2]}\left(\sigma_{xy}^{(1)}-\sigma_{xy}^{(2)}\right)}{8}+y^{[2]}\left[\frac{\left(\sigma_{xy}^{(1)\prime}+\sigma_{xy}^{(2)\prime}\right)}{4}+\frac{3\left(\sigma_y^{(1)}-\sigma_y^{(2)}\right)}{2h^{[2]}}\right.$$
$$\left.+\frac{\left(y^{[2]}\right)^2}{2h^{[2]}}\left(\sigma_{xy}^{(2)\prime}-\sigma_{xy}^{(1)\prime}\right)+\frac{\left(y^{[2]}\right)^2}{\left(h^{[2]}\right)^2}\left[\frac{2\left(\sigma_y^{(2)}-\sigma_y^{(1)}\right)}{h^{[2]}}-\left(\sigma_{xy}^{(1)\prime}+\sigma_{xy}^{(2)\prime}\right)\right] \quad (4c)$$

in which a prime denotes differentiation with respect to x.

2.5.2 *Stress fields in the plate and the RC beam*

Using assumption 3, the longitudinal and shear stresses in the plate and the beam can be expressed as

$$\sigma_x^{[i]}=\frac{N^{[i]}(x)}{b^{(i)}h^{[i]}}+\frac{12M^{[i]}(x)y^{[i]}}{b^{(i)}\left(h^{[i]}\right)^3} \qquad (i=1,\ 3) \quad (5a)$$

$$\sigma_{xy}^{[i]}=-\frac{6Q^{[i]}(x)}{b^{(i)}\left(h^{[i]}\right)^3}\left[\left(y^{[i]}\right)^2-\frac{\left(h^{[i]}\right)^2}{4}\right]+\frac{1}{b^{(i)}h^{[i]}}\begin{cases}\sigma_{xy}^{(1)}\left(\dfrac{h^{[1]}}{2}-y^{[1]}\right) & i=1\\ \sigma_{xy}^{(2)}\left(\dfrac{h^{[3]}}{2}+y^{[3]}\right) & i=3\end{cases} \quad (5b)$$

As assumed, $\sigma_y^{[i]}$ $(i=1,\ 3)$ is neglected in both the RC beam and the plate.

2.6 *Solution procedure*

The interfacial normal and shear stresses may be expressed as Fourier series

$$\sigma_y^{(i)}(x)=\sum_m a_m^{(i)}\cos\frac{m\pi x}{l};\qquad \sigma_{xy}^{(i)}(x)=\sum_m b_m^{(i)}\sin\frac{m\pi x}{l} \quad (6a,b)$$

where $i=1,\ 2$; $a_m^{(i)}$ and $b_m^{(i)}$ are unknown Fourier coefficients; and $m=1,\ 2,\ldots\infty$. The constant term in Equation 6a has been set to zero to satisfy the equilibrium requirement that the integration of the interfacial normal stress over the entire length of the interface must be equal to zero. It may be noted that $\sigma_y^{(0)}=\sigma_y^{(3)}=\sigma_{xy}^{(0)}=\sigma_{xy}^{(3)}=0$ because no interfacial stresses exist on the top and bottom surfaces of the strengthened beam.

Substituting Equations 6a and b into Equation 1 yields

$$N^{[i]}(x)=\sum_m\left(\frac{l}{m\pi}\right)\left[b^{(i)}b_m^{(i)}-b^{(i-1)}b_m^{(i-1)}\right]\left[(-1)^m-\cos\frac{m\pi x}{l}\right]+\begin{cases}0 & i=1\\ N_t & i=3\end{cases} \quad (7a)$$

$$Q^{[i]}(x)=\sum_m\left(\frac{l}{m\pi}\right)\left[b^{(i)}a_m^{(i)}-b^{(i-1)}b_m^{(i-1)}\right]\sin\frac{m\pi x}{l}+\begin{cases}0 & i=1\\ Q^a(x) & i=3\end{cases} \quad (7b)$$

$$M^{[i]}(x)=\sum_m\left(\frac{l}{m\pi}\right)\left\{\left(\frac{l}{m\pi}\right)\left[b^{(i)}a_m^{(i)}-b^{(i-1)}a_m^{(i-1)}\right]-\frac{h'}{2}\left[b^{(i)}b_m^{(i)}+b^{(i-1)}b_m^{(i-1)}\right]\right\}$$
$$\times\left[(-1)^m-\cos\frac{m\pi x}{l}\right]+\begin{cases}0 & i=1\\ M^a(x) & i=3\end{cases} \quad (7c)$$

where $Q^a(x)$ and $M^a(x)$ are stress resultants in the corresponding un-strengthened beam caused by the same applied loads:

$$Q^a(x)=-\int q(x)dx \quad (8a)$$

$$M^a(x)=L\int_0^L q(x)dx-\int_x^L xq(x)dx-x\int_0^x q(x)dx+M_0 \quad (8b)$$

Substituting Equations 7 and 8 into Equation 5 and substituting Equations 6a and 8 into Equation 4 lead to the following stress components expressed in terms of the unknown coefficients $a_m^{(1)}$, $b_m^{(1)}$, $a_m^{(2)}$ and $b_m^{(2)}$:

$$\sigma_x^{[i]}=-\sum_m\frac{l}{m\pi}\left\{\frac{\left(b_m^{(i-1)}-b_m^{(i)}\right)}{h^{[i]}}+\frac{12ly^{[i]}}{\left(h^{[i]}\right)^3}\left[\frac{a_m^{(i-1)}-a_m^{(i)}}{m\pi}+\frac{h^{[i]}\left(b_m^{(i-1)}+b_m^{(i)}\right)}{2l}\right]\right\}$$
$$\times\left[(-1)^m-\cos\frac{m\pi x}{l}\right]+\begin{cases}0 & (i=1,2)\\ \sigma_x^a & (i=3)\end{cases} \quad (9)$$

$$\sigma_{xy}^{[i]}=-\sum_m\left\{\frac{3l\left(a_m^{(i-1)}-a_m^{(i)}\right)}{2m\pi h^{[i]}}+\frac{\left(b_m^{(i-1)}+b_m^{(i)}\right)}{4}-\frac{y^{[i]}\left(b_m^{(i-1)}-b_m^{(i)}\right)}{h^{[i]}}\right.$$
$$\left.-\frac{6l\left(y^{[i]}\right)^2}{\left(h^{[i]}\right)^3}\left[\frac{a_m^{(i-1)}-a_m^{(i)}}{m\pi}+\frac{h^{[i]}\left(b_m^{(i-1)}+b_m^{(i)}\right)}{2l}\right]\right\}\sin\frac{m\pi x}{l}+\begin{cases}0 & (i=1,2)\\ \sigma_{xy}^a & (i=3)\end{cases} \quad (10)$$

$$\sigma_y^{[i]}=\begin{cases}0 & (i=1,3)\\ \displaystyle\sum_m\zeta_m\left(y^{[2]}\right)\cos\frac{m\pi x}{l} & (i=2)\end{cases} \quad (11)$$

in which

$$\zeta_m\left(y^{[2]}\right)=\left\{\frac{\left(a_m^{(1)}+a_m^{(2)}\right)}{2}-\frac{h^{[2]}m\pi\left(b_m^{(1)}-b_m^{(2)}\right)}{8l}\right.$$
$$+\frac{3y^{[2]}}{2h^{[2]}}\left[\left(a_m^{(1)}-a_m^{(2)}\right)+\frac{m\pi\left(b_m^{(1)}+b_m^{(2)}\right)}{6l}\right]+\frac{\left(y^{[2]}\right)^2m\pi\left(b_m^{(1)}-b_m^{(2)}\right)}{2lh^{[2]}}$$
$$\left.-\frac{3\left(y^{[2]}\right)^2}{\left(h^{[2]}\right)^3}\left[\left(a_m^{(1)}-a_m^{(2)}\right)+\frac{h^{[2]}m\pi\left(b_m^{(1)}+b_m^{(2)}\right)}{2l}\right]\right\} \quad (12)$$

and σ_x^a and σ_{xy}^a are longitudinal and shear stresses in the un-strengthened beam caused by the same applied loads:

$$\sigma_x^a=\frac{N_t}{b^{(3)}h^{[3]}}+\frac{12y^{[3]}}{b^{(3)}\left(h^{[3]}\right)^3}M^a(x) \quad (13)$$

$$\sigma_{xy}^a=\frac{3y^{[3]}}{2b^{(3)}\left(h^{[3]}\right)^3}\left[\left(h^{[3]}\right)^2-4\left(y^{[3]}\right)^2\right]Q^a(x) \quad (14)$$

The unknown coefficients may now be determined by minimising the total complementary energy of the composite beam in the strengthened range. Only one

half of the beam is considered here owing to symmetry. The total complementary energy in half of the strengthened portion is

$$U=\frac{1}{2}\sum_{i=1}^{3}b^{(i)}\int_{H^{[i]}/2}^{H^{[i]}/2}\int_{0}^{l}\left[\frac{1}{E_x^{[i]}}\left(\sigma_x^{[i]}\right)^2+\frac{1}{E_y^{[i]}}\left(\sigma_y^{[i]}\right)^2 -\frac{2\nu_{xy}^{[i]}}{E_x^{[i]}}\sigma_x^{[i]}\sigma_y^{[i]}+\frac{1}{G_{xy}^{[i]}}\left(\sigma_{xy}^{[i]}\right)^2\right]dxdy^{[i]} \quad (15)$$

where $E_x^{[i]}$ and $E_y^{[i]}$ are the Young's moduli in x- and y-directions respectively; and $G_{xy}^{[i]}$ and $\nu_{xy}^{[i]}$ are the shear modulus and Poisson's ratio in the $x-y$ plane of the *ith* layer.

Minimising U by setting $\partial U/\partial c_{m,i}=0$, where $c_{m,i}$ is an element of the sub-vector $\mathbf{c_m}=\left[a_m^{(1)},\ b_m^{(1)},\ a_m^{(2)},\ b_m^{(2)}\right]^T$, leads to

$$\mathbf{C}\ \mathbf{c}\ =\mathbf{P} \quad (16)$$

where

$$\mathbf{C}=\begin{bmatrix}\mathbf{C_{11}} & \cdots & \cdots & \cdots & \cdots & \cdots\\ & \ddots & \vdots & \vdots & \vdots & \vdots\\ & & \mathbf{C_{mm}} & \cdots & \mathbf{C_{mn}} & \cdots\\ & & & \ddots & \vdots & \vdots\\ & sym. & & & \ddots & \vdots\\ & & & & & \mathbf{C_{MM}}\end{bmatrix} \quad (17)$$

$$\mathbf{c}=\left[\mathbf{c_1}\ \cdots\ \mathbf{c_m}\ \cdots\ \mathbf{c_M}\right]^T \quad (18)$$

$$\mathbf{P}=\left[\mathbf{P_1}\ \cdots\ \mathbf{P_m}\ \cdots\ \mathbf{P_M}\right]^T \quad (19)$$

in which M is the order of the Fourier series; $\mathbf{C_{mm}}$ and $\mathbf{C_{mn}}$ are sub-matrices of $\mathbf{C}$; and $\mathbf{P_m}$ is the sub-vector of $\mathbf{P}$. The elements of $\mathbf{C_{mm}}$, $\mathbf{C_{mn}}$ and $\mathbf{P_m}$ are given in Appendix A.

The interfacial stresses are obtained by solving Equation 16 and substituting the resulting coefficients into Equations 6a and b. All symmetrical loading cases can be considered by properly including various forms of the transverse load $q(x)$**,** axial force N_0 and end bending moment M_0 in the loading vector $\mathbf{P}$.

3 NUMERICAL EXAMPLES

3.1 *Uniformly distributed load (UDL)*

For a uniformly distributed load (UDL), the components of the applied loading are $N_0=0$, $M_0=0$, $q(x)=q$ and $M_l=(L-l)^2/2$.

An RC beam bonded with a steel plate subjected to a UDL $q=15$N/mm as given in Roberts and Haji-Kazemi (1989) is used here as the first example problem. The geometrical and material properties of the beam are: $L=1200$ mm, $l=900$ mm, $h^{[1]}=h^{[2]}=4$ mm, $h^{[3]}=150$ mm; $b^{(1)}=b^{(2)}=b^{(3)}=100$ mm; $E_x^{[1]}=E_y^{[1]}=200$ GPa, $E_x^{[2]}=E_y^{[2]}=2$ GPa, $E_x^{[3]}=E_y^{[3]}=20$ GPa, and $\nu_{xy}^{[2]}=0.25$. In their FE analysis, Teng *et al.* (2002b) used Poisson's ratios of $\nu_{xy}^{[3]}=0.17$ and $\nu_{xy}^{[1]}=0.3$ respectively for concrete and steel which were not specified by Roberts and Haji-Kazemi (1989).

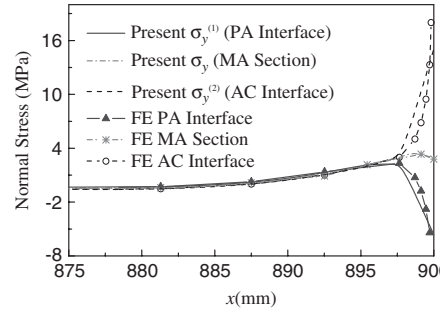

(a) Interfacial normal stresses

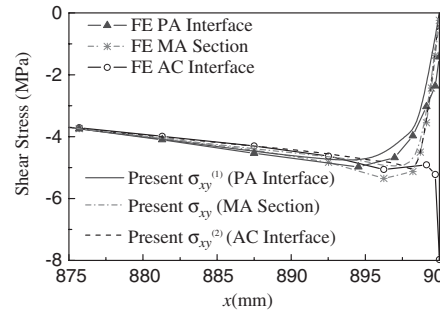

(b) Interfacial shear stresses

Figure 3. Steel plated beam under UDL.

Figure 3 compares the present predictions with Teng *et al.*'s (2002b) FE results for the interfacial stresses. The interfacial normal stresses at the plate-to-adhesive (PA) interface, the mid-adhesive (MA) section and the adhesive-to-concrete (AC) interface are small and almost identical to each other away from the vicinities of the plate ends. Near the plate ends, the interfacial normal stress at the MA section is larger than that away from the plate ends but the value is still limited. This stress at the PA and AC interfaces diverges dramatically towards the plate end and large compressive stresses are experienced at the PA interface. Clearly, the present predictions agree very closely with the FE results (Fig. 3a). It may be noted that this is the first analytical solution which correctly predicts the drastic

difference in the interfacial normal stress between the PA and AC interfaces, as demonstrated by its close agreement with FE predictions (Fig. 3a).

The interfacial shear stress (Fig. 3b) increases towards the plate end and then reduces rapidly to zero at the free edge, complying with the stress-free boundary condition there. Both the peak value and its corresponding location are slightly different at PA interface, the MA section and the AC interface. The present solution is again in close agreement with the FE results, except for the interfacial shear stress at the AC interface near the very end of the plate (within 1 mm), where the FE analysis encounters the problem of stress singularity (Teng *et al.* 2002b).

3.2 *Mid-span point load (MPL)*

For a beam under a point load at the mid-span, the components of the applied loading are: $N_0 = 0$, $M_0 = 0$, $q(x) = p\delta(x)$ and $M_l = p(L - l)/4$. Here $\delta(x)$ is the Dirac delta function used to represent the MPL in the context of Schwarz's distributed theory (Schwarz 1966, Yavari *et al.* 2000).

An RC beam bonded with a CFRP plate and subjected to a mid point load P = 150 kN is used here as the second example. The RC beam has a span $L = 3000$ mm, a width $b^{(3)} = 200$ mm, a depth $h^{[3]} = 300$ mm, Young's moduli $E_x^{[3]} = E_y^{[3]} = 30$ GPa and a Poisson's ratio $\nu_{xy}^{[3]} = 0.17$. The orthotropic FRP plate has a length $l = 2400$ mm, a width $b^{(1)} = 200$ mm, a thickness $h^{[3]} = 4.0$ mm, a Young's modulus in the x-direction $E_x^{[1]} = 100$ GPa and a shear modulus in $x-y$ plane $G_{xy}^{[1]} = 5$ GPa. The isotropic adhesive layer has a width $b^{(2)} = 200$ mm, a thickness $h^{[2]} = 2$ mm, Young's moduli $E_x^{[2]} = E_y^{[2]} = 2$ GPa, and a Poisson's ratio $\nu_{xy}^{[2]} = 0.35$. All these geometric and material properties, except the Poisson's ratios for the RC beam and the adhesive layer and the shear modulus for FRP plate, which are assumed common values here, were given by Smith and Teng (2001).

Figure 4 shows the present predictions of interfacial normal and shear stresses. Approximate analytical results from Smith and Teng (2001) and Täljsten (1997) are also shown for comparison. Both Smith and Teng (2001) and Täljsten (1997) assumed invariable normal and shear stresses across the thickness of the adhesive layer. The interfacial normal stresses from the two approximate analytical solutions agree well with the present solution away from the plate ends and in the vicinity of the point load (Fig. 4a). At the plate end, the present solution predicts a much higher stress (approximately 3 times) at the AC interface than the two approximate solutions. This is an inevitable result of the assumption of uniform shear and transverse normal stresses in the adhesive layer adopted by these approximate solutions. The present

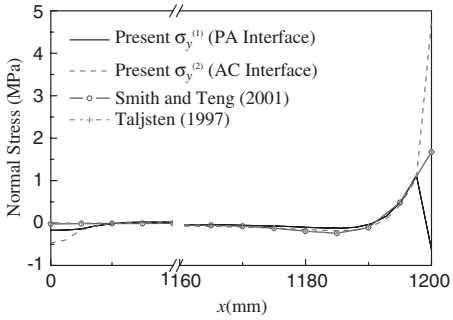

(a) Interfacial normal stresses

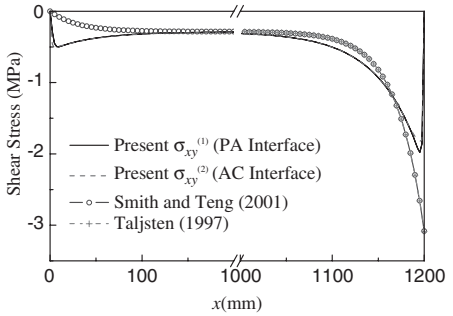

(b) Interfacial shear stresses

Figure 4. CFRP plated beam under middle point loads.

solution also predicts significant compressive interfacial stresses at the PA interface in the vicinity of the point load.

For the interfacial shear stress (Fig. 4b), very significant differences exist between the present solution and the two approximate solutions. The approximate solutions predict monotonically increasing shear stresses towards the plate end, which does not satisfy the stress-free boundary condition there. This stress-free boundary condition is satisfied by the present solution. Consequently, the peak shear stress predicted by the present solution is only about half of those predicted by the two approximate solutions. The approximate solutions are also unable to predict the significant interfacial shear stresses in the vicinity of the concentrated load.

3.3 *Two-point load (TPL)*

For a beam under two symmetrical point loads, the components of the applied loading are as follows: $q(x) = p[\delta(x - l_0) + \delta(x - l_0)]$, $N_0 = 0$, $M_0 = 0$

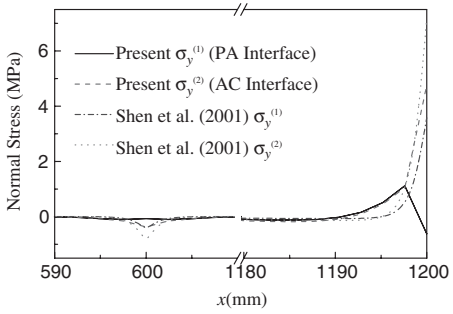

(a) Interfacial normal stress

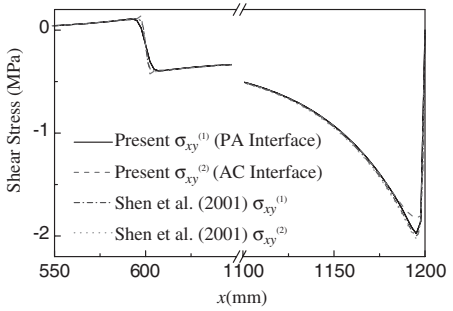

(b) Interfacial shear stress

Figure 5. CFRP plated beam under two point loads.

and $M_l = p(L - l)$. Here l_0 is the distance from the mid-span of the beam to either of the two point loads.

The same example CFRP plated RC beam as discussed above is examined here. It is subjected to a TPL with $p = 75$ KN at $l_0 = 600$ mm. The same example was used by Shen *et al.* (2001).

Figure 5 compares the present solution with Shen *et al.*'s (2001) high-order solution. The interfacial shear stresses from Shen *et al.*'s (2001) high-order solution are in close agreement with those of the present solution (Fig. 5b). However, significant differences exist between the two solutions for the interfacial normal stress. Near the plate end, Shen *et al.*'s (2001) solution predicts tensile stresses at both the PA and AC interfaces, in contrast to tensile stresses at the AC interface and compressive stresses at the PA interface as predicted by the present solution (Fig. 5a). Shen *et al.*'s (2001) solution also yields considerably different predictions for the peak values at both the plate end and directly below the concentrated load. This is believed to be due to the partial use of the plane section assumption in their solution process as discussed earlier.

4 CONCLUSIONS

This paper has presented a new interfacial stress analysis for simply supported beams strengthened with a soffit plate and subject to general symmetric loading. In this new analysis, the partial use of the plane section assumption in Shen *et al.* (2001) and Yang *et al.* (2003) is avoided. The resulting solution not only takes into consideration the non-uniform stress distribution in the adhesive layer and the stress-free boundary condition at the ends of the plate, but also correctly predicts the drastic difference in the interfacial normal stress between the PA and AC interfaces revealed by finite element analysis for the first time. The solution methodology is general in nature and may be applied to the analysis of other types of composite structures.

ACKNOWLEDGMENTS

The authors would like to acknowledge the financial supports provided by The Hong Kong Polytechnic University through its Area of Strategic Development (ASD) Scheme for the ASD in Urban Hazard Mitigation and the University of Edinburgh. They would also like to thank the British Government for an ORS award made to the first author.

REFERENCES

Ahmed, O., Van Gemert, D. & Vandewalle, L. 2001. Improved model for plate-end shear of CFRP strengthened RC beams, *Cement and Concrete Composites* 23: 3–19.

Aprile, A., Spacone, E. & Limkatanyu, S. 2001. Role of bond in RC beams strengthened with steel and FRP plates, *Journal of Structural Engineering, ASCE* 127(12): 1445–1452.

Arduini, M. & Nanni, A. 1997. Parametric study of beams with externally bonded FRP reinforcement, *ACI Structural Journal* 94(5): 493–501.

Ascione, L. & Feo, L. 2000. Modeling of composite/concrete interface of RC beams strengthened with composite laminates, *Composites: Part B* 31: 535–540.

Bonacci, J.F. & Maalej, M. 2001. Behavioural trends of RC beams strengthened with externally bonded FRP, *Journal of Composites for Construction, ASCE* 5(2): 102–113.

Garden, H.N., Quantrill, R.J., Hollaway, L.C., Thorne, A.M. & Parke, G.A.R. 1998. An experimental study of the anchorage length of carbon fiber composite plates used to strengthen reinforced concrete beams, *Construction and Building Materials* 12: 203–219.

Hobson, E.W. 1926. *The theory of function of a real variable and the theory of Fourier's series*, 2nd edn, Vol. 2: Cambridge.

Leung, C.K.Y. 2001. Delamination failure in concrete beams retrofitted with a bonded plate, *Journal of Materials in Civil Engineering, ASCE* 13(2): 106–113.

Malek, A.M., Saadatmanesh, H. & Ehsani, M.R. 1998. Prediction of failure load of R/C beams strengthened with FRP plate due to stress concentration at the plate end, *ACI Structural Journal* 95(1): 142–152.
Rabinvich, O. & Frostig, Y. 2000. Closed-form high-order analysis of RC beams strengthened with FRP strips, *Journal of Composites for Construction, ASCE* 4: 65–74.
Rahimi, H. & Hutchinson A. 2001. Concrete beams strengthened with externally bonded FRP plates, *Journal of Composites for Construction, ASCE* 5(1): 44–56.
Roberts, T.M. 1989. Approximate analysis of shear and normal stress concentrations in the adhesive layer of plated RC beams. *The Structural Engineer* 67(12): 229-233.
Roberts, T.M. & Haji-Kazemi, H. 1989. Theoretical study of the behavior of reinforced concrete beams strengthened by externally bonded steel plates, *Proceedings of the Institution of Civil Engineers, Part 2*, 87: 39–55.
Schwarz, L. 1966. *Thorie des Distributions*, Hermann: Paris.
Shen, H.S., Teng, J.G. & Yang, J. 2001. Interfacial stresses in beams and slabs bonded with thin plate, *Journal of Engineering Mechanics, ASCE* 127: 399–406.
Smith, S.T. & Teng, J.G. 2001. Interfacial stresses in plated beams, *Engineering Structures* 23: 857–871.
Täljsten, B. 1997. Strengthening of beams by plate bonding. *Journal of Materials in Civil Engineering, ASCE* 9(4): 206–212.
Tantafillou, T.C. & Deskovic, N. 1991. Innovative prestressing with FRP sheets: Mechanics of short-term behavior, *Journal of Engineering Mechanics, ASCE* 117(7): 1652–1672.
Teng, J.G., Chen, J.F., Smith, S.T. & Lam, L. 2002a, *FRP strengthened RC Structures*, Wiley, Chichester, U.K.
Teng, J.G., Zhang, J.W. & Smith, S.T. 2002b. Interfacial stress in RC beams bonded with a soffit plate: a finite element study, *Construction and Building Materials* 16(1): 1–14.
Vilnay, O. 1988. The analysis of reinforced concrete beams strengthened by epoxy bonded steel plates, *The international Journal of Cement Composites and lightweight Concrete* 10(2): 73–78.
Yavari, A., Sarkani, S. & Moyer, E.T. 2000. On applications of generalized functions to beam bending problems, *International Journal of Solids and Structures* 37: 5675–5705.
Ye, J.Q. 2001. Interfacial shear transfer of RC beams strengthened by bonded composite plates, *Cement and Concrete Composite* 23: 411–417.
Yang J., Teng, J.G. & Chen, J.F. 2004. A high order closed-form solution for interfacial stresses in soffit plated RC beams under arbitrary loads, *Proceedings of the Institution of Civil Engineers – Structures and Buildings* 157(SB1): 77–89.

APPENDIX A

The sub-matrices in Equation 17 are given in Equations A1 to A3.

$$\mathbf{C}_{mm} = \begin{bmatrix} (C_{mm})_{11} & (C_{mm})_{12} & (C_{mm})_{13} & (C_{mm})_{14} \\ & (C_{mm})_{22} & (C_{mm})_{23} & (C_{mm})_{24} \\ & & (C_{mm})_{33} & (C_{mm})_{34} \\ & sym. & & (C_{mm})_{44} \end{bmatrix} \quad \text{(A1)}$$

in which

$$(C_{mm})_{11} = b^{(1)} l \left\{ \frac{18l^4}{m^4\pi^4} \left[\frac{1}{E_x^{[1]}\left(h^{[1]}\right)^3} + \frac{1}{E_x^{[2]}\left(h^{[2]}\right)^3} \right] + \frac{3l^2}{5m^2\pi^2} \left[\frac{1}{G_{xy}^{[1]}h^{[1]}} + \frac{1}{G_{xy}^{[2]}h^{[2]}} - \frac{2\nu_{xy}^{[2]}}{E_x^{[2]}h^{[2]}} \right] + \frac{13h^{[2]}}{70E_y^{[2]}} \right\} \quad \text{(A2a)}$$

$$(C_{mm})_{12} = b^{(1)} \left\{ \frac{9l^4}{m^3\pi^3} \left[\frac{1}{E_x^{[2]}\left(h^{[2]}\right)^2} - \frac{1}{E_x^{[1]}\left(h^{[1]}\right)^2} \right] + \frac{l^2}{20m\pi} \left[\frac{1}{G_{xy}^{[2]}} - \frac{1}{G_{xy}^{[1]}} - \frac{12\nu_{xy}^{[2]}}{E_x^{[2]}} \right] + \frac{11m\pi\left(h^{[2]}\right)^2}{40E_y^{[2]}} \right\} \quad \text{(A2b)}$$

$$(C_{mm})_{13} = b^{(1)} l \left[-\frac{18l^4}{m^4\pi^4} \frac{1}{E_x^{[2]}\left(h^{[2]}\right)^3} - \frac{3l^2}{5m^2\pi^2} \left(\frac{1}{G_{xy}^{[2]}h^{[2]}} - \frac{2\nu_{xy}^{[2]}}{E_x^{[2]}h^{[2]}} \right) + \frac{9h^{[2]}}{140E_y^{[2]}} \right] \quad \text{(A2c)}$$

$$(C_{mm})_{14} = b^{(1)} \left[\frac{9l^4}{m^3\pi^3} \frac{1}{E_x^{[2]}\left(h^{[2]}\right)^2} + \frac{l^2}{20m\pi} \left(\frac{1}{G_{xy}^{[2]}} - \frac{2\nu_{xy}^{[2]}}{E_x^{[2]}} \right) - \frac{13m\pi\left(h^{[2]}\right)^2}{840E_y^{[2]}} \right] \quad \text{(A2d)}$$

$$(C_{mm})_{22} = b^{(1)} \left[\frac{6l^3}{m^2\pi^2} \left(\frac{1}{E_x^{[1]}h^{[1]}} + \frac{1}{E_x^{[2]}h^{[2]}} \right) + \frac{l}{15} \left(\frac{h^{[1]}}{G_{xy}^{[1]}} + \frac{h^{[2]}}{G_{xy}^{[2]}} - \frac{2\nu_{xy}^{[2]}h^{[2]}}{E_x^{[2]}} \right) + \frac{m^2\pi^2\left(h^{[2]}\right)^3}{210lE_y^{[2]}} \right] \quad \text{(A2e)}$$

$$(C_{mm})_{23} = -(C_{mm})_{14} \quad \text{(A2f)}$$

$$(C_{mm})_{24} = b^{(1)} \left[\frac{3l^3}{m^2\pi^2} \frac{1}{E_x^{[2]}h^{[2]}} - \frac{h^{[2]}}{60} \left(\frac{1}{G_{xy}^{[2]}} - \frac{2\nu_{xy}^{[2]}}{E_x^{[2]}} \right) - \frac{m^2\pi^2\left(h^{[2]}\right)^3}{280lE_y^{[2]}} \right] \quad \text{(A2g)}$$

$$(C_{mm})_{33} = b^{(1)} l \left\{ \frac{18l^4}{m^4\pi^4} \left[\frac{1}{E_x^{[2]}\left(h^{[2]}\right)^3} + \frac{1}{\beta E_x^{[3]}\left(h^{[3]}\right)^3} \right] + \frac{3l^2}{5m^2\pi^2} \left[\frac{1}{G_{xy}^{[2]}h^{[2]}} + \frac{1}{\beta G_{xy}^{[3]}h^{[3]}} - \frac{2\nu_{xy}^{[2]}}{E_x^{[2]}h^{[2]}} \right] + \frac{13h^{[2]}}{70E_y^{[2]}} \right\} \quad \text{(A2h)}$$

$$(C_{mm})_{34} = b^{(1)} \left\{ -\frac{9l^4}{m^3\pi^3} \left[\frac{1}{E_x^{[2]}\left(h^{[2]}\right)^2} - \frac{1}{\beta E_x^{[3]}\left(h^{[3]}\right)^2} \right] - \frac{l^2}{20m\pi} \left[\frac{1}{G_{xy}^{[2]}} - \frac{1}{\beta G_{xy}^{[3]}} - \frac{12\nu_{xy}^{[2]}}{E_x^{[2]}} \right] - \frac{11m\pi\left(h^{[2]}\right)^2}{40E_y^{[2]}} \right\} \quad \text{(A2i)}$$

$$(C_{mm})_{44} = b^{(1)} \left[\frac{6l^3}{m^2\pi^2} \left(\frac{1}{E_x^{[2]}h^{[2]}} + \frac{1}{\beta E_x^{[3]}h^{[3]}} \right) + \frac{l}{15} \left(\frac{h^{[2]}}{G_{xy}^{[2]}} + \frac{h^{[3]}}{\beta G_{xy}^{[3]}} - \frac{2\nu_{xy}^{[2]}h^{[2]}}{E_x^{[2]}} \right) + \frac{m^2\pi^2\left(h^{[2]}\right)^3}{210lE_y^{[2]}} \right] \quad \text{(A2j)}$$

where $\beta = b^{(3)}/b^{(1)}$ is the ratio of the beam to plate width.

$$\mathbf{C_{mn}} = \begin{bmatrix} (C_{mn})_{11} & (C_{mn})_{12} & (C_{mn})_{13} & (C_{mn})_{14} \\ (C_{mn})_{21} & (C_{mn})_{22} & (C_{mn})_{23} & (C_{mn})_{24} \\ (C_{mn})_{31} & (C_{mn})_{32} & (C_{mn})_{33} & (C_{mn})_{34} \\ (C_{mn})_{41} & (C_{mn})_{42} & (C_{mn})_{43} & (C_{mn})_{44} \end{bmatrix} \quad \text{(A3)}$$

in which

$$(C_{mn})_{11} = \frac{12b^{(1)}l^5(-1)^{m+n}}{m^2n^2\pi^4}\left[\frac{1}{E_x^{[1]}(h^{[1]})^3} + \frac{1}{E_x^{[2]}(h^{[2]})^3}\right] \quad \text{(A4a)}$$

$$(C_{mn})_{12} = \frac{6b^{(1)}l^4(-1)^{m+n}}{m^2n\pi^3}\left[\frac{1}{E_x^{[2]}(h^{[2]})^2} - \frac{1}{E_x^{[1]}(h^{[1]})^2}\right] \quad \text{(A4b)}$$

$$(C_{mn})_{13} = \frac{12b^{(1)}l^5(-1)^{m+n+1}}{m^2n^2\pi^4}\frac{1}{E_x^{[2]}(h^{[2]})^3} \quad \text{(A4c)}$$

$$(C_{mn})_{14} = \frac{6b^{(1)}l^4(-1)^{m+n}}{m^2n\pi^3}\frac{1}{E_x^{[2]}(h^{[2]})^2} \quad \text{(A4d)}$$

$$(C_{mn})_{22} = \frac{4b^{(1)}l^3(-1)^{m+n}}{mn\pi^2}\left(\frac{1}{E_x^{[1]}h^{[1]}} + \frac{1}{E_x^{[2]}h^{[2]}}\right) \quad \text{(A4e)}$$

$$(C_{mn})_{23} = \frac{6b^{(1)}l^4(-1)^{m+n}}{mn^2\pi^3}\frac{1}{E_x^{[2]}(h^{[2]})^2} \quad \text{(A4f)}$$

$$(C_{mn})_{24} = \frac{2b^{(1)}l^3(-1)^{m+n}}{mn\pi^2}\frac{1}{E_x^{[2]}h^{[2]}} \quad \text{(A4g)}$$

$$(C_{mn})_{33} = \frac{12b^{(1)}l^5(-1)^{m+n}}{m^2n^2\pi^4}\left[\frac{1}{E_x^{[2]}(h^{[2]})^3} + \frac{1}{\beta E_x^{[3]}(h^{[3]})^3}\right] \quad \text{(A4h)}$$

$$(C_{mn})_{34} = \frac{6b^{(1)}l^4(-1)^{m+n+1}}{m^3\pi^3}\left[\frac{1}{E_x^{[2]}(h^{[2]})^2} - \frac{1}{\beta E_x^{[3]}(h^{[3]})^2}\right] \quad \text{(A4i)}$$

$$(C_{mn})_{44} = \frac{4b^{(1)}l^3(-1)^{m+n}}{mn\pi^2}\left(\frac{1}{E_x^{[2]}h^{[2]}} + \frac{1}{\beta E_x^{[3]}h^{[3]}}\right) \quad \text{(A4j)}$$

and $(C_{mn})_{ij}(i = 1, \cdots, 4; \quad j < i)$ could be easily obtained by swapping m and n in $(C_{mn})_{ji}$.

In Eq. 19, the sub-vector is

$$\mathbf{P_m} = \left[(P_m)_1, (P_m)_2, (P_m)_3, (P_m)_4\right]^T \quad \text{(A5)}$$

where

$$(P_m)_1 = 0 \quad \text{(A6a)}$$

$$(P_m)_2 = 0 \quad \text{(A6b)}$$

$$(P_m)_3 = \frac{12l^2(-1)^m}{m^2\pi^2\beta E_x^{[3]}(h^{[3]})^3}\left[l(M_0 + M_{0l}) + L\int_0^L\int_0^x q(x)dxdx - \int_0^L x^2q(x)dx - \frac{l^2}{2}\int_0^L q(x)dx + \frac{1}{2}\int_0^L x^2q(x)dx\right] - \frac{6l^2}{5m^2\pi^2\beta G_{xy}^{[3]}h^{[3]}}\left[(-1)^{m+1}\int_0^L q(x)dx + \int_0^L q(x)\cos\frac{m\pi x}{l}dx\right] - \frac{12l^4}{m^4\pi^4\beta E_x^{[3]}h^{[3]}}\left[\int_0^L q(x)\cos\frac{m\pi x}{l}dx - (-1)^m\int_0^L q(x)dx\right] \quad \text{(A6c)}$$

$$(P_m)_4 = \frac{12l^2(-1)^m}{m\pi\beta E_x^{[3]}(h^{[3]})^2}\left[l(N_0h^{[3]} + 6M_0 + 6M_{0l}) + 6L\int_0^L\int_0^x q(x)dxdx - 6\int_0^L x^2q(x)dx - 3l^2\int_0^L q(x)dx + 3\int_0^L x^2q(x)dx\right] - \frac{l}{10m\pi\beta G_{xy}^{[3]}}\left[(-1)^{m+1}\int_0^L q(x)dx + \int_0^L q(x)\cos\frac{m\pi x}{l}dx\right] - \frac{l^3}{m^3\pi^3\beta E_x^{[3]}(h^{[3]})^2}\left[\int_0^L q(x)\cos\frac{m\pi x}{l}dx - (-1)^m\int_0^L q(x)dx\right] \quad \text{(A6d)}$$

where M_{0l} is the bending moment at the plate ends due to the applied transverse loads carried by the strengthened part of the beam:

$$M_{0l} = \int_0^L q(x)(L - x)dx \quad \text{(A7)}$$

FRP Composites in Civil Engineering – CICE 2004 – Seracino (ed)
© 2005 Taylor & Francis Group, London, ISBN 90 5809 638 6

Experimental study on bond stress-slip behaviour of FRP–concrete interface using electronic speckle pattern interferometry technique

S.Y. Cao
College of Civil Engineering, Southeast University, Nanjing, P.R. China

J.F. Chen
Institute for Infrastructure and Environment, The University of Edinburgh, UK

J.W. Pan
College of Civil Engineering, Southeast University, Nanjing, P.R. China

ABSTRACT: Fibre reinforced polymer (FRP) composites are widely used for strengthening reinforced concrete (RC) structures because of their superior properties. The effectiveness of this strengthening technique relies on effective stress transfer between FRP and concrete. Therefore, the bond behaviour between FRP and concrete plays a key role in maintaining the composite action between the external FRP and the RC member. This bond behaviour is generally measured using simple shear tests. However, it is often difficult to obtain accurate full field deformation in the bond area using common measurement techniques. This paper presents an experimental study on displacement field measurement in a CFRP-to-concrete double shear test using the non-destructive and non-contiguous Electronic Speckle Pattern Interferometry (ESPI) technique. Full-field in-plane displacements were measured in 33 test specimens. Both CFRP sheet and plate were used. The specimens had concrete strength varying from 20 to 60 MPa. The measured displacement field was then used to infer the bond stress-slip behaviour between FRP and concrete. An empirical bond-slip constitutive model is proposed based on the experimental results.

1 INTRODUCTION

Since first being researched in 1980s, externally bonding CFRP composites to strengthen and retrofit existing RC structures has become an efficient strengthening technique and is being successfully used worldwide. Clearly, effective stress transfer between FRP and concrete is essential to ensure the success of the technique. Extensive research has shown that most experimental RC members strengthened with externally bonded FRP composites failed due to debonding of FRP from concrete (Teng *et al*. 2002). Therefore, the bond behaviour between FRP and concrete plays a key role in maintaining the integrity of such strengthened RC members.

Several different set-ups have been used to test the FRP-to-concrete bond behaviour, but simple shear tests have been the most commonly used (Chen *et al.* 2001a).

Extensive research has been conducted in the last few years to investigate the bond behaviour between FRP and concrete. Most of the existing experimental studies (e.g. Chajes *et al.* 1996, Mukhopadhyaya *et al*. 1998, Bizindavyi *et al.* 1999, Nakaba *et al.* 2001, Toutanji & Ortiz 2001, Bizindavyi *et al.* 2003, Nehdi *et al.* 2003) have been concerned with the strain (stress) distribution in FRP along the bond length, the effective stress transfer length and the bond strength.

A realistic bond stress-slip constitutive model is essential to advance a theoretical FRP-to-concrete bond strength model and to investigate the load-displacement behaviour of such a bonded joint either through analytical or numerical analysis (e.g. Yuan *et al.* 2001, Wu *et al.* 2002, Yuan *et al.* 2004). Most existing FRP-to-concrete bond strength models are either empirical (e.g. Maeda *et al.* 1997) based on regression of test data or semi-empirical analysis (Chen & Teng 2001b) where a simple bond stress-slip constitutive model is assumed and the resulting solution is calibrated and modified based on test results.

However, very few experimental studies (e.g. Nakaba *et al.* 2001) have been concerned with the local bond stress-slip behaviour. Nakaba *et al*. (2001) measured the strain distribution using electrical resistance strain gauges along the bond length in a double shear test. The local slip and bond shear stress at a given location were obtained by integrating and differentiating

the discrete strain observations respectively, giving the local bond stress-slip relationship.

The chief reason for the lack of robust bond stress-slip constitutive models properly validated with quality experimental data may be the difficulties involved in accurately measuring both the local shear (bond) stress and slip using conventional devices such as strain gauges, micrometer gauges and various contact displacement sensors. Although the strain distribution along the FRP within the bond area is often measured in experimental studies, it is not a direct measurement of the shear (bond) stress. It is also evident that considerable effort is needed to measure the full-field displacement pattern in the bond area which may be used to deduce local slips.

In this study, the Electronic Speckle Pattern Interferometry (ESPI) technique is used to investigate the FRP-to-concrete bond stress-slip behaviour in a simple double shear test. The ESPI technique is an optical method of measuring structural deformations. It has the advantage of measuring the full-field displacements non-destructively and non-contiguously. The ESPI technique has wide applications in such areas as detecting either surface or internal flaws of integrated circuit boards, pressure containers and wielding objects, but has been rarely used in tests of concrete and masonry structures. Binda *et al*. (1998) measured deformation of solid masonry units under mechanical loading and concluded that the ESPI technique could be used effectively for small specimens with low-stiffness materials. More recently, Pan *et al*. (2003) showed that the ESPI technique could also be applied for accurately measuring the full-field in-plane deformations in an FRP-to-concrete shear test. It may be noted that a similar optical technique known as the Moiré interferomery method was used by Tripi *et al*. (2000) to observe detailed local deformations and strain on the surface of cracked rectangular concrete prisms externally reinforced with CFRP sheets.

A total of 33 double shear specimens were tested in this study. Both CFRP sheets and plates were used. The ESPI technique was used to measure the full-field in-plane displacements during the loading process. Based on the test results, a bond stress-slip constitutive model is proposed.

2 TEST PROGRAMME

2.1 *Specimen design*

The 33 specimens were designed in 11 groups, of which 6 groups were tested with CFRP plate and the rest 5 groups were tested with CFRP sheet. The CFRP plate had a width of 50 mm and thickness of 1.2 mm. Its ultimate tensile strength and Young's modulus were measured to be 3050 MPa and 165 GPa respectively. The CFRP sheet was 80 mm wide and had a nominal thickness of 0.111 mm. The ultimate strength and Young's modulus were 3408 MPa and 235 GPa respectively.

Table 1. Specimen details and chief test results.

Specimen designation	Concrete strength (MPa)	FRP bond length (mm)	Total no. of fringes	Ultimate end slip (mm)
C20AP	23.7	80	69	0.031
C20BP	23.7	120	159	0.071
C20CP	23.7	150	319	0.143
C25AP	28.6	80	134	0.060
C25BP	28.6	120	156	0.070
C25CP	28.6	150	422	0.189
C30AP	35.9	80	134	0.060
C30BP	35.9	120	279	0.125
C30CP	35.9	150	313	0.140
C40AP	46.1	80	161	0.072
C40BP	46.1	120	203	0.091
C40CP	46.1	150	221	0.099
C50AP	55.9	80	152	0.068
C50BP	55.9	120	302	0.135
C50CP	55.9	150	232	0.104
C60AP	61.2	80	154	0.069
C60BP	61.2	120	208	0.093
C60CP	61.2	150	288	0.129
C20AS	23.2	80	63	0.028
C20BS	23.2	120	232	0.104
C20CS	23.2	150	355	0.159
C30AS	33.3	80	286	0.128
C30BS	33.3	120	246	0.110
C30CS	33.3	150	270	0.121
C40AS	42.9	80	201	0.090
C40BS	42.9	120	261	0.117
C40CS	42.9	150	369	0.165
C50AS	56.0	80	–	–
C50BS	56.0	120	366	0.164
C50CS	56.0	150	418	0.187
C60AS	68.6	80	170	0.076
C60BS	68.6	120	270	0.121
C60CS	68.6	150	500	0.224

Apart from the form of CFRP composites, other major variables of the specimens included FRP bond length and concrete strength. The bond length of FRP varied from 80 mm to 150 mm. The design concrete cube strength varied from 20 to 60 MPa. The actual test 28-day cube strength ranged from 23.2 to 68.8 MPa. The concrete cube strength and FRP bond length for each specimen are listed in Table 1.

It may be noted that each specimen is represented by a specimen designation which consists of five letters and numbers. The first three numbers represent the concrete strength in the form of C followed by the design cube strength. The fourth letter represents the bond length, with letters A, B and C representing bond length of 80, 120 and 150 mm respectively. The last letter represents the type of CFRP, with P denoting plate and S sheet.

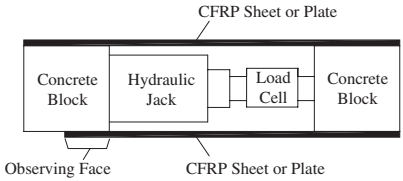

(a) Bond length less than 150 mm

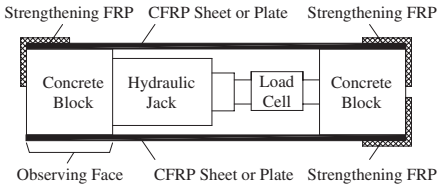

(b) Bond length equal to 150 mm

Figure 1. Test set-up.

Epoxy resins supplied by the CFRP plate and sheet manufacturers were used to bond the FRP to the concrete specimens. Both resins were tested. The shear strength, tensile strength and Young's modulus for the resin used for bonding CFRP sheets were 36.2 MPa 45.3 MPa and 3.2 GPa respectively. The corresponding values for the resin used for bonding CFRP plates were 40.6 MPa, 43.4 MPa and 2.0 GPa respectively.

2.2 *Test set-up and test procedure*

Each specimen consisted of two 150 mm concrete cubes with two CFRP plates or sheets bonded onto their two opposite faces, giving four bond areas. In these four bond areas, one was used as the test zone with a test FRP bond length for the specimen. For the other three bond zones, either a longer FRP bond length was used or they were strengthened to ensure that failure would occur in the test zone (Fig. 1).

The test set-up is shown in Figure 1. All tests were carried out on a holographic vibration isolation table under loading control. The load increment was about 2–5% of the ultimate load. During the whole loading process, the full-field fringe image of the test zone was recorded at each load increment.

2.3 *ESPI measurement*

The ESPI method was used in this study to measure the in-plane displacement on the FRP surface. A brief description of the method is given here. More details can be found in Pan *et al.* (2003). The method involves irradiating two symmetrical beams of coherent laser with wavelength λ onto the observation zone with an entry angle θ. A CCD camera is placed in the direction normal to the observation surface to take photographs. If the object at a location is deformed with an in-plane displacement $u(t)$ at time t, it results in a difference of $2u(t)\sin\theta$ between the two light paths. This leads to a phase difference between the two beams of

$$\varphi(t) = \frac{4\pi}{\lambda} \cdot \sin\theta \cdot u(t) \tag{1}$$

It can be proven that dark fringes appear in the CCD images when $\varphi(t) = 2n\pi$ for $n = 0, \pm1, \pm2, \ldots$ From Equation 1, the relationship between the in-plane displacement $u(t)$ and the fringe number n is

$$u(t) = \frac{n\lambda}{2\sin\theta} \tag{2}$$

This enables the evaluation of relative displacement between two points at any given time from the number of fringes in the corresponding image. In this study, two beams of coherence laser with a wavelength of $\lambda = 633 \times 10^{-6}$ mm were used to illuminate the object surface with an entry angle $\theta = 45°$. From Equation 2, this means that every fringe recorded represents a displacement of 447.6×10^{-6} mm. The direction of displacement is normal to the fringes.

3 FAILURE PROCESS AND MODES

3.1 *Displacement development*

Figures 2 and 3 show representative fringe images for two typical specimens at different stages during the loading process. It may be noted that each image represents the increment of deformation within a loading step. The start and finish loads relative to the ultimate failure load P_u for the increment is indicated for each of the pictures in Figures 2 and 3. The total deformation at a given loading level can be found from the summation of all the deformation increments from beginning to the given loading level.

Generally, there are two typical patterns of deformation development (thus bond stress transfer patterns). Figure 2 shows typical fringe images for specimens with CFRP sheet and 150 mm bond length. When the load is less than about 70% of the ultimate load P_u, the area covered by fringes (where deformation increases) increases continuously with the applied load (Figs 2b–e). This indicates that the main bond stress transfer region increases gradually as the load increases. When the load is about 70% of P_u, about half of the bond length (75 mm) is covered by fringes (Fig. 2e). This stress transfer zone remains almost unchanged as the applied load further increases until just before the final failure (Figs 2e–h). The length of this stable stress transfer zone is found to be correlated well to the effective stress transfer length L_e predicted from Chen and Teng's (2001) model. The measured stable zone for CFRP sheet specimens varies from 60 to 90 mm. The

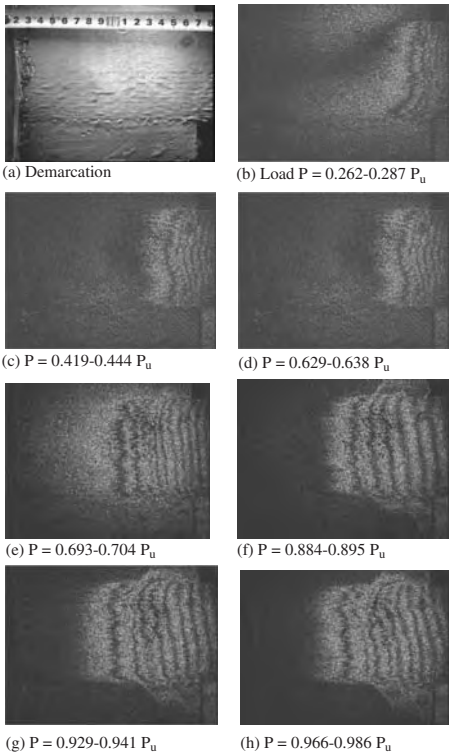

(a) Demarcation (b) Load P = 0.262-0.287 P_u

(c) P = 0.419-0.444 P_u (d) P = 0.629-0.638 P_u

(e) P = 0.693-0.704 P_u (f) P = 0.884-0.895 P_u

(g) P = 0.929-0.941 P_u (h) P = 0.966-0.986 P_u

Figure 2. Fringe images for Specimen C40CS (bond length = 150 mm).

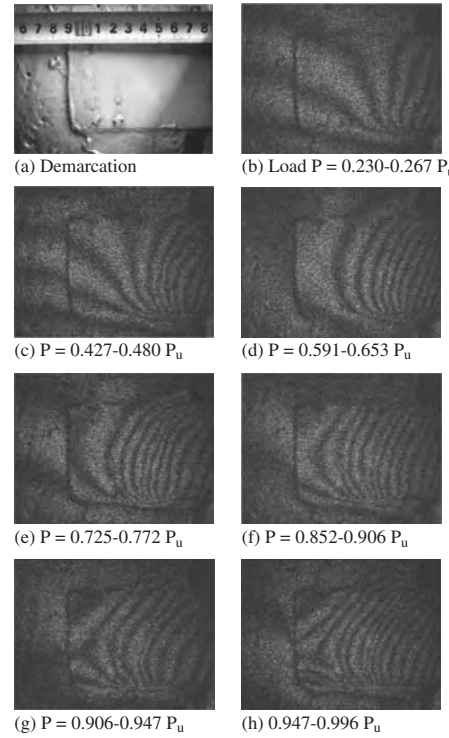

(a) Demarcation (b) Load P = 0.230-0.267 P_u

(c) P = 0.427-0.480 P_u (d) P = 0.591-0.653 P_u

(e) P = 0.725-0.772 P_u (f) P = 0.852-0.906 P_u

(g) P = 0.906-0.947 P_u (h) 0.947-0.996 P_u

Figure 3. Fringe images for Specimen C60AP (bond length = 80 mm).

predicted values of effective length vary from 60 to 78 mm.

It is seen that the fringes are not exactly straight in Figure 2. This indicates that the deformation and deformation gradient (thus stress) distribution in the FRP is non-uniform across the width. Furthermore, the fringes are curved with denser fringes at the edges of the FRP sheet than the middle. Therefore, the gradient of deformation (e.g. FRP strain and thus the stress) at the edges is larger than that in the middle. These are consistent with the results from a recent numerical study (Chen & Pan 2004).

When the bond length is relatively short compared with the effective bond length (i.e. for all specimens except those CFRP sheets with 120 and 150 mm bond length), the stable stress transfer zone cannot be seen. Figure 3 shows a set of fringe images for a typical CFRP plate specimen C60AP which had a bond length of 80 mm. The stress transfer zone increases with load and covers the full bond length when the load is about 70% of the ultimate failure load P_u.

In Figure 3, all fringes during the whole loading process are curved as in the early loading stages in Figure 2. This supports the conclusion drawn above that the deformation and stress distributions in the FRP is non-uniform across its width. Moreover, the fringes from this specimen are slightly non-symmetrical. This can be caused by many factors such as eccentricity of loading, geometrical asymmetry of sample, and potential non-uniformity of materials.

3.2 *Failure process*

For all the specimens except those FRP sheets with 150 mm bond length, the failure was sudden and accompanied with loud noises. There was no visible sign of local debonding. For those CFRP sheet specimens with 150 mm bond length, some noises were emitted when the load reached to about 90% of the ultimate failure load. This indicates that some local damage might have started. It may be noted that FRP debonding has not started yet at the time as seen from Figure 2 that the deformation zone is still very stable

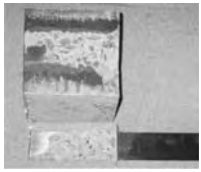

(a) Debonding within concrete (CFRP plate)

(b) Debonding within concrete (CFRP sheet)

(c) Debonding within adhesive (CFRP sheet)

(d) Rupture of CFRP sheet

Figure 4. Typical failure modes.

up to a loading of 0.986 P_u. Final failure was again sudden with loud noise. Because the tests were conducted under load control, the actual debonding process could not be detected.

3.3 *Failure mode*

All but one of the 33 specimens failed due to debonding. Of the 32 debonding failures, 30 failed within concrete with a thin layer of concrete attached to the FRP after failure (Figs 4a and b). The rest two (C20AS and C50AS) failed within the adhesive layer (Fig. 4c).

Only one specimen (C30BS) failed due to the rupture of FRP sheet outside the bond area at a relatively low stress level (about 2000 MPa) compared with the tensile strength of the FRP (Fig. 4d). This might be caused by the unevenness of adhesive on CFRP sheet out of the bond area, leading to uneven stress distribution in the CFRP fibres.

4 BOND STRESS–SLIP RELATIONSHIP

4.1 *Interpretation of measured data*

As discussed above, the relative deformation of FRP within a load increment can be determined from Equation (2) by counting the number of fringes in the fringe image. The relative displacement field at a given load level P can be obtained by summing all the incremental displacement fields from the start of loading up to the given loading level. The accumulative total number of fringes in the bond area near failure for each test is listed in Table 1. These numbers can be used to deduce the relative displacement from the loaded end to the free end of FRP at failure (i.e. the total elongation of

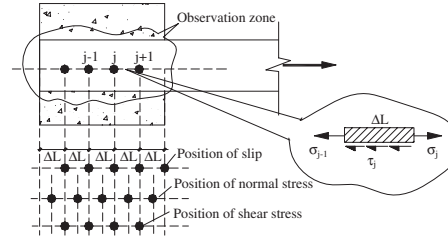

Figure 5. Data interpretation positions.

the bonded FRP). If the bond length is sufficiently large (i.e. when the slip at the far end of the FRP strip is negligible), this relative displacement can be treated as the displacement at the loaded end of FRP. Furthermore, if the compressive deformation of the concrete block is neglected (which is indeed negligible from the test results), the displacement field may be treated as the slip between FRP and concrete.

The measured displacement field can be used to deduce the strain field in FRP by differentiating once. Assuming that the longitudinal normal stress in the FRP is uniform through its thickness, its value at a given location can be obtained by multiplying the strain at the location by the Young's modulus of the FRP. The normal stress distribution in FRP may be further differentiated once to give the interfacial shear stress distribution between the FRP and adhesive. Therefore, the whole displacement, normal (longitudinal) stress and interfacial shear stress fields can be deduced.

In this study, the whole bond area was divided into small segments giving a series of nodes (Fig. 5). Within the *m*th load increment, the increment of relative deformation from node j − 1 to j is related to the number of fringes n_{mj}. The accumulative relative displacement from node j − 1 to j, d_j, at the *m*th loading level can be found from

$$d_j = \sum_{i=1}^{m} n_{ij} \cdot \frac{\lambda}{2\sin\theta} \tag{3}$$

Dividing d_j by the segment width ΔL gives the average normal strain in FRP between note j − 1 to j. The average normal stress and average local bond stress at locations shown in Figure 5 are then obtained as discussed above.

Several positions within the bond area were selected to investigate the local bond stress-slip relationship. Figure 6 shows typical results deduced from the experimental data. Despite under monotonic loading, it is significant that part of the descending branch of the bond stress-slip is obtained. It may be noted that the descending branch can only be obtained at positions near the loading end for specimens with sufficient

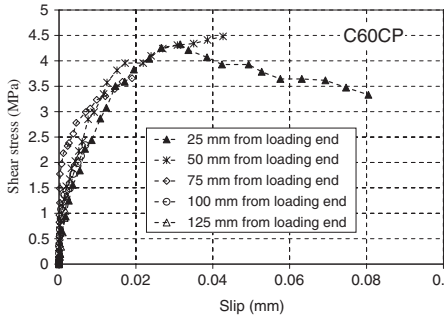

Figure 6. Typical tested shear stress-slip curve.

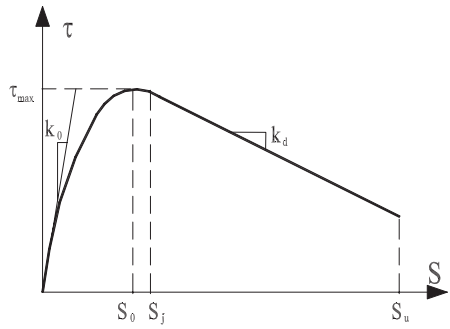

Figure 7. Idealised bond stress-slip curve.

bond length, where the local peak bond stress is reached before ultimate failure.

4.2 *Characteristics of bond stress-slip curve*

As seen in Figure 6, the bond stress-slip curve is clearly nonlinear. It rises very fast initially with a large initial stiffness. After the bond stress reaches about 20% to 30% of the peak value, the stiffness continuously reduces with the increase of bond stress and reaches zero at the peak bond stress. After the peak stress, the curve descends slowly with a close to linear trend.

The bond stress-slip curve may be characterised by three key parameters. They include the peak bond stress τ_{max}, the slip corresponding to the peak bond stress S_0 and the ultimate slip S_u. The deduced bond stress-slip curves in this study show that S_0 is within the range of 0.02 mm to 0.04 mm for most specimens, with an average of 0.029 mm and standard deviation of 0.010 for all the specimens.

The peak bond stress τ_{max} is found to be related to the cube strength of concrete f_{cu} and can be approximately expressed as $1.64\sqrt[4]{f_{cu}}$. However, this may have been underestimated because the deduced τ_{max} value here is the average stress in a small segment (Fig. 5) instead of the peak stress.

It is unfortunate that the ultimate slip S_u cannot be directly obtained from the deduced bond stress-slip curves in this study because the tests were conducted under load control so that the obtained descending branch is not sufficient to indicate this value. However, as discussed earlier this may be estimated from the displacement at the loading end of the FRP at the beginning of debonding when the bond length is sufficiently large. From the specimens with CFRP sheet, this value is estimated to be around 0.14 mm.

4.3 *A bond stress-slip model*

A mathematical model is developed here to describe the above bond stress-slip curve. The bond stress-slip curve ($\tau - S$) may be idealised as in Figure 7 which consists of two segments. The first segment increases nonlinearly with an initial stiffness k_0 and peaks at the slip of S_0. It then reduces to join the second segment. The second segment is assumed to be linear with a descending rate of k_d. The two segments are assumed to join at a point S_j after the peak with smooth connection (i.e. continuity in slope).

For convenience, the bond stress τ is normalised against τ_{max} and the slip S is normalised against S_0. Figure 8 shows an example of normalised bond stiffness obtained by differentiating the deduced bond stress-slip curves for two typical CFRP plate and CFRP sheet specimens. It is seen that the normalised stiffness-slip relationship is close to a hyperbola in the form of $d(\tau/\tau_{max})/d(S/S_0) = a/1 + bS/S_0 - c$ before the peak and remains close to a constant after it. Integrating the stiffness-slip curve gives the normalised bond stress in the following form:

$$\frac{\tau}{\tau_{max}} = a_1 \ln(a_2 + a_3\frac{S}{S_0}) + a_4\frac{S}{S_0} \quad (0 < S < S_j) \tag{4a}$$

$$\frac{\tau}{\tau_{max}} = \bar{\tau}_j - \bar{k}_d(\frac{S}{S_0} - \frac{S_j}{S_0}) > 0 \quad (S_j < S < S_u) \tag{4b}$$

where $a_1 - a_4$ are coefficients; $\bar{\tau}_j$ is the normalised bond stress at $S = S_j$; and $\bar{k}_d$ is the normalised descending stiffness.

Equation 4a must satisfy the following conditions at slip $S = 0$ and S_0:

$$\left.\frac{d(\tau/\tau_{max})}{d(S/S_0)}\right|_{S=0} = \bar{k}_0 \tag{5a}$$

$$\left.\frac{\tau}{\tau_{max}}\right|_{S=0} = 0 \tag{5b}$$

$$\left.\frac{d(\tau/\tau_{max})}{d(S/S_0)}\right|_{S=S_0} = 0 \tag{5c}$$

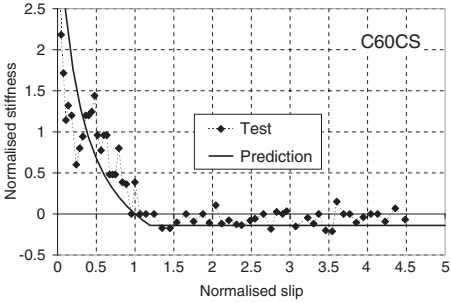

(a) Typical specimen with CFRP sheet

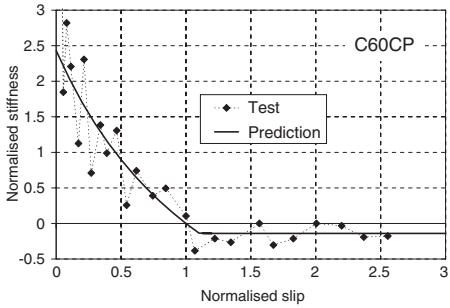

(b) Typical specimen with CFRP plate

Figure 8. Normalised bond stiffness.

$$\left.\frac{\tau}{\tau_{\max}}\right|_{S=S_u} = 1 \qquad (5d)$$

where $\bar{k}_0 = k_0 S_0/\tau_{\max}$ is the normalised initial stiffness. The initial stiffness k_0 may be estimated from the shear stiffness of the adhesive layer $k_0 = G_a/t_a$. Here G_a is the shear modulus and t_a is the thickness of adhesive layer.

Substituting Equation 4 into 5 gives the parameters a_1, a_2, a_3 and a_4. Substituting the resulting parameters into Equation 4 gives

$$\frac{\tau}{\tau_{\max}} = \left[\frac{1+\alpha_k}{\alpha_k}\ln\left(1+\alpha_k\frac{S}{S_0}\right)-\frac{S}{S_0}\right]\frac{\bar{k}_0}{\alpha_k} \quad (0<S<S_j) \qquad (6a)$$

$$\frac{\tau}{\tau_{\max}} = \bar{\tau}_j - \bar{k}_d\left(\frac{S}{S_0}-\frac{S_j}{S_0}\right) > 0 \quad (S_j<S<S_u) \qquad (6b)$$

in which α_k is a coefficient related to the normalised initial stiffness $\bar{k}_0$. Explicit expression of α_k is difficult to obtain but it can be expressed approximately as $\alpha_k = 0.1\bar{k}_0^2 + 1.63\bar{k}_0 - 3.7 > 0$.

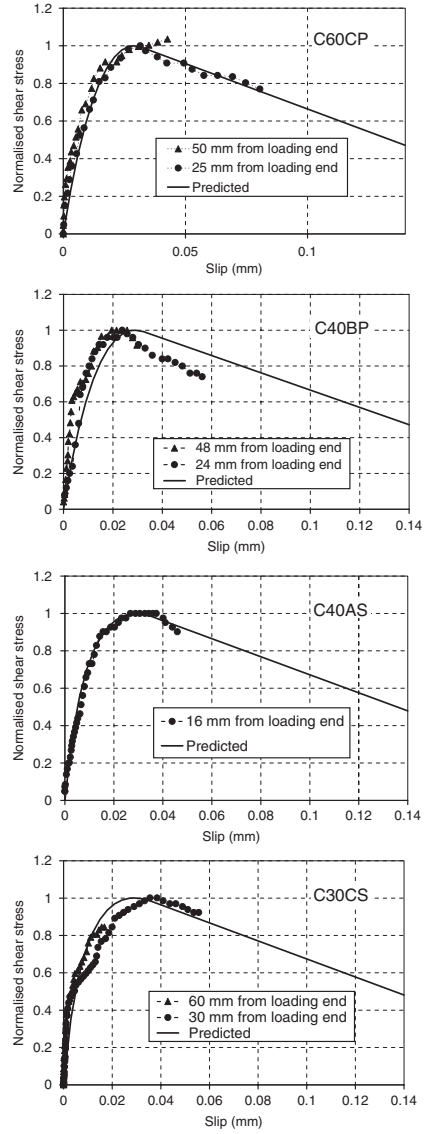

Figure 9. Measured vs predicted bond stress-slip curves.

The two parameters S_j and $\bar{\tau}_j$ in Equation 6 can be determined from the assumption of smooth connection between the two segments of the curve

$$S_j = \left[1+\frac{(1+\alpha_k)\bar{k}_d}{\bar{k}_0-\alpha_k\bar{k}_d}\right]S_0 \qquad (7a)$$

$$\bar{\tau}_j = \left[\frac{1+\alpha_k}{\alpha_k}\ln\left(1+\alpha_k\frac{S_j}{S_0}\right)-\frac{S_j}{S_0}\right]\frac{\bar{k}_0}{\alpha_k} \qquad (7b)$$

4.4 *Comparison with test data*

The complete bond stress-slip curve can be determined from Equation 6 if S_0, $\bar{k}_0 = k_0 S_0/\tau_{\max}$ and $\bar{k}_d$ are known. Assuming that the adhesive layer had a thickness of 2 mm and Poisson's ratio of 0.3, its shear modulus G_a can be obtained from the measured Young modulus E_a assuming homogeneity of the material. The initial shear stiffness is thus determined from $k_0 = G_a/t_a$.

Figure 9 shows the comparison of Equation 6 with test data for a number of typical specimens. The following values were used in the prediction: peak stress $\tau_{\max} = 1.64\sqrt[4]{f_{cu}}$, $S_0 = 0.029$ mm and $k_d = 0.14$. It is seen that the model is in close agreement with test results. However, further studies are required to determine the values of S_0, $\tau_{\max}$ and k_d for practical applications.

5 CONCLUSIONS

This paper has presented an experimental study on the bond behaviour between FRP and concrete in a double shear test. The Electronic Speckle Pattern Interferometry (ESPI) technique was used to measure the deformation field in the bond area. The measured deformation field was used to infer the local bond stress and slip relationship.

A total of 33 CFRP plate and CFRP sheet specimens were tested. Through analysing the test results of these specimens, an empirical bond stress-slip model has been proposed.

ACKNOWLEDGMENT

This work presented forms part of collaborative research between Southeast University, China and the University of Edinburgh, UK. The authors would like to acknowledge the financial support provided by the Foundation for University Key Teacher through the Ministry of Education of China. They would also like to thank Hwa-Ying Foundation for Education and Culture for sponsoring the first author's visiting scholarship at the University of Edinburgh.

REFERENCES

Binda, L., Facchini, M., Roberti, G.M. & Tiraboschi, C. 1998. Electronic speckle interferometry for the deformation measurement in masonry testing, *Construction and Building Materials* 12(5), 269–281.

Bizindavyi, L. & Neale, K.W. 1999. Transfer length and strength for composites bonded to concrete, *Journal of Composite for Construction, ASCE* 3(4), 153–160.

Bizindavyi, L., Neale, K.W. & Erki, M.A. 2003. Experimental investigation of bonded fiber reinforced polymer-concrete joints under cyclic load, *Journal of Composite for Construction, ASCE* 7(2), 127–134.

Chajes, M.J., Finch, W.W., Januszka, T.F. & Thomson, T. A. 1996. Bond and force transfer of composite material plate bonded to concrete, *ACI Structural Journal* 93(2), 208–217.

Chen, J.F. & Pan, W.K. 2004. Stresses in simple shear test specimens for steel or FRP-to-concrete bond strength: a 3D finite element study, *Advanced Composites for Structural Applications in Construction*, *Proc., ACIC2004*, 20–22 April, Surrey, 473–482.

Chen, J.F., Yang, Z.J. & Holt, G.D. 2001. FRP or steel plate-to concrete bonded joints: Effect of test methods on experimental bond strength, *Steel and Composite Structures*, 1(2), 231–244.

Chen, J.F. & Teng, J.G. 2001. Anchorage strength models for FRP and steel plates bonded to concrete, *Journal of Structural Engineering, ASCE* 127(7), 784–791.

Mukhopadhyaya, P., Swamy, R.N. & Lynsdale, C.J. 1998. Influence of aggressive exposure conditions on the behaviour of adhesive bonded concrete-GFRP joints, *Construction and Building Materials* 12(8), 427–446.

Nakaba, K., Kanakubo, T., Furuta, T. & Yoshizawa, H. 2001. Bond behavior between fiber-reinforced polymer laminates and concrete, *ACI Structural Journal* 98(3), 359–367.

Nehdi, M., El Damatty, A. & Rahimi,R. 2003. Investigation on lap-joint behaviour of GFRP plates bonded to silica fume and rice husk ash concrete, *International Journal of Adhesion and Adhesives* 23(4), 323–333.

Pan, J.W., Cao, S.Y., He, X.Y., Yang, F.J. & Liu, L. 2003. Application of electronic speckle pattern interferometry in measuring bond behaviour at FRP-concrete interface, *The Transaction of Southeast University* 22(3), 347–350 (in Chinese).

Teng, J.G., Chen, J.F., Smith, S.T. & Lam, L. 2002. *FRP Strengthened RC Structures*, Chichester, John Wiley & Sons.

Toutanji, H. & Ortiz, G. 2001. The effect of surface preparation on the bond interface between FRP sheets and concrete members, *Composite Structures* 53(4), 457–462.

Tripi, J.M., Bakis, C.E., Boothby, T.E. & Nanni, A. 2000. Deformation in concrete with external CFRP sheet reinforcement, *Journal of Composite for Construction, ASCE* 4(2), 85–94.

Wu, Z.S., Yuan, H. & Niu, H.D. 2002. Stress transfer and fracture propagation in different kinds of adhesive joints, *Journal of Engineering Mechanics* 128(5), 562–573.

Yuan, H., Wu, Z.S. & Yoshizawa, H. 2001. Theoretical solutions on interfacial stress transfer of externally bonded steel/composite laminates, *Journal of Structural Mechanics and Earthquake Engineering,* 18(1). 27–39.

Yuan, H., Teng, J.G., Seracino, R., Wu, Z.S. & Yao, J. (2004) "Full-range behavior of FRP-to-concrete bonded joints", *Engineering Structures,* Vol. 26, No. 5, pp. 553–564.

Maeda, T., Asano, Y. Sato, Y. Ueda, T. & Kakuta, Y. 1997. A study on bond mechanism of carbon fiber sheet, Proceeding of Third International Symposium of Non-Metallic (FRP) Reinfoecement for Concrete Structures, 1.279–286.

Flexural strengthening of concrete beams and slabs

FRP Composites in Civil Engineering – CICE 2004 – Seracino (ed)
© 2005 Taylor & Francis Group, London, ISBN 90 5809 638 6

Fatigue and post-fatigue quasi-static performance of RC-beams externally strengthened with CFRPs

C. Gheorghiu, P. Labossière & J. Proulx
Génie Civil, Université de Sherbrooke, Sherbrooke, Canada

ABSTRACT: The overall deterioration of transportation infrastructure due to ageing and increasing traffic loads motivated researchers to look for new ways of repairing and monitoring the existing structures. Numerous studies were conducted and proved the efficiency of bonding fibre-reinforced polymers (FRP) systems on structural elements such as reinforced concrete (RC) beams and columns. Although there is a huge potential for the use of FRP materials, their large-scale implementation is often impeded by the lack of data on their durability when subjected to extreme loading conditions. This paper presents an experimental project undertaken in order to assess the durability of RC beams strengthened with carbon-fibre-reinforced polymers (CFRPs). The 15 small-scale beams were loaded in fatigue for various numbers of cycles and load conditions and then tested monotonically to failure. Test results provide an insight on the potential performance of CFRP-strengthened beams subjected to severe fatigue loading conditions.

1 INTRODUCTION

In many countries, most of the transportation infrastructure was constructed in the middle of the twentieth century and is approaching the end of its expected life. In addition, there were significant increases in load requirements over that period. These facts illustrate the need for fast, efficient and durable strengthening methods. A technique now gaining popularity is the bonding of carbon-fibre-reinforced polymers (CFRPs) on structural elements. CFRPs are used extensively to strengthen reinforced concrete beams and columns in existing structures.

Although major applications of CFRPs are reported in the literature, design engineers are still concerned by the durability of these products under severe loading and climatic conditions. Results have been published on the durability of FRP for internal reinforcement [1] and the fatigue behaviour of woven composite laminates [2]. Some work has been conducted to evaluate the durability of CFRP-strengthened beams subjected to wet-dry cycles [3], or continuous immersion [4], and also under freeze-thaw cycles [5]. These researchers also published results from monotonic loading of RC beams strengthened with CFRPs. Few studies reported fatigue behaviour of strengthened beams [6], their response to a combination of fatigue loading and low temperature [7], or to a combination of fatigue loading and water exposure [8]. In addition, there are still no extensive data dealing with the fatigue response of beams subjected to different fatigue load levels and number of cycles.

The objective of the project reported here is to investigate the fatigue behaviour and the influence of the fatigue loading on the strength of CFRP-strengthened beams. The emphasis was placed on studying the load-defection behaviour of the CFRP-strengthened beam throughout fatigue and subsequent monotonic testing.

2 DESCRIPTION OF THE TEST PROGRAM

This section describes the main characteristics of the tested specimens, the properties of their constituent materials, the experimental loading apparatus, and the instrumentation.

2.1 *Specimen*

The typical geometry and reinforcement of the tested beams are shown in Figure 1. The specimens were fabricated from normal-strength ready-mixed concrete. The concrete strength was measured at three different times along the testing program and had a mean value of 50 MPa. The internal reinforcement is made of smooth and undeformed bars 6.35 mm in diameter and is providing the minimum steel quantity required by the Canadian Standard CSA-A23.3 for reinforced concrete. Steel rebars exhibit a yield strength of 600 MPa and a Young's modulus of 200 GPa.

All the beams were externally reinforced or strengthened with a unidirectional CFRP strip. The main properties of this CFRP plate are shown in Table 1. The 50 mm-wide plates were bonded to the

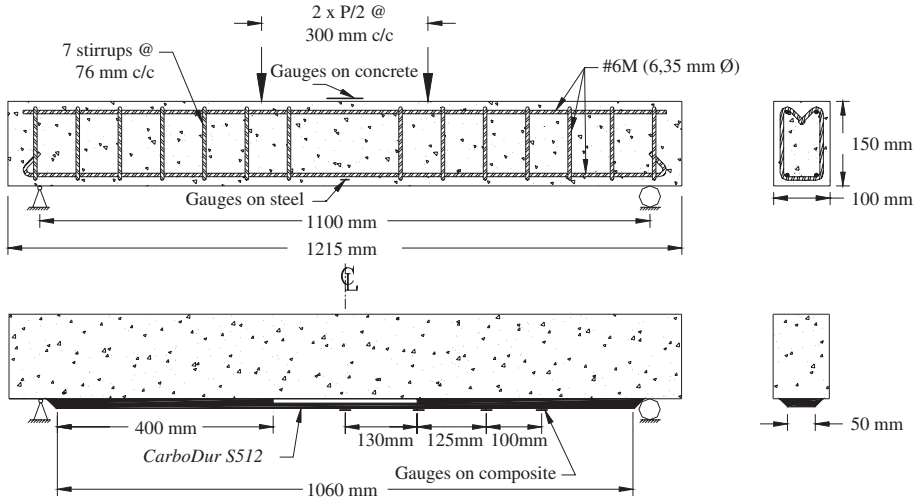

Figure 1. Specimen – geometry, loading and instrumentation.

Table 1. Properties of CFRP.

Product	E_{frp} (GPa)	ε_{frp} (%)	f_{frp} (GPa)	t (mm)
CFRP plate	155	1.6	2.4	1.2

Table 2. Fatigue loads.

Series	P_{min}/P_y (%)	P_{min} (kN)	P_{max}/P_y (%)	P_{max} (kN)
L	15	6.8	35	15.9
H	35	15.9	75	34.1

tension face of the beams with the proprietary mortar of the system on a 400 mm length at both ends, thus leaving a 260 mm unbonded portion in the middle. This configuration was selected to avoid concrete crushing and to trigger failure by delamination of the CFRP, eventually allowing the investigation of the concrete-CFRP interface.

2.2 *Testing procedure*

Prior to testing, all specimens were instrumented with strain gauges. One gauge was placed on the concrete surface, and two on the rebars, as shown in Figure 1. Four more gauges were installed on the CFRP, in order to measure the onset of delamination along the CFRP-concrete interface. A detailed analysis of these strain data has been published elsewhere [8]. The load cell was a part of the actuator, and one LVDT measured the midspan deflection of the beams.

All beams were subjected first to flexural cyclic loading, and then to monotonic, both under four-point bending configuration. The only exceptions were the two reference beams tested only monotonically. The location of the two loading points is shown in Figure 1. The fatigue test consisted of 400,000, 800,000 and 2,000,000 cycles at a load level producing 15-35 to 75% of the yielding moment M_y [8]. Table 2 indicates the minimum and maximum loads, P_{min} and P_{max}, applied to the beams.

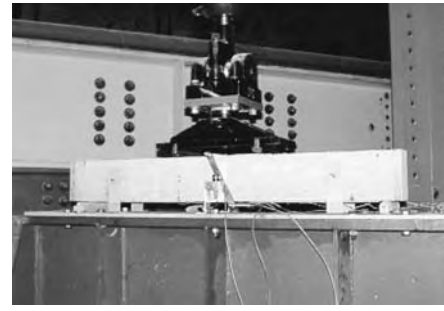

Figure 2. Test set-up for fatigue loading.

The fatigue load was applied with a MTS hydraulic actuator of 100 kN capacity controlled by a TestStar-II software. The test set-up for the fatigue loading is shown in Figure 2. The specimens were first

Figure 3. Test set-up for monotonic loading.

Table 3. Fatigue loading conditions.

Loading condition		
% of P_y	Cycles	Specimen
0	0	NA, NB
15–35	400 000	L400A, L400B
	800 000	L800A, L800B, L800C
	2 000 000	L2000A, L2000B
35–75	400 000	H400A, H400B
	800 000	H800A, H800B
	2 000 000	H2000A, H2000B
Total specimens = 15		

loaded monotonically up to the minimum value of the cyclic load identified in Table 2, and then the fatigue load was applied up to the maximum value. Between these extreme values, the CFRP plate remained in tension. At 2 cycles per second, 13 days were spent to test a beam for 2,001,000 cycles, including preparatory work. The sinusoidal loading was force-controlled using the TestWare-SX process module. Readings at minimum and maximum loads were taken at every 2000th cycle until cycle 801,000, and then they were spaced at every 10,000th cycle to the end of the test. Full cycle readings during the test were taken according to the following sequence: at 1st cycle and every 10th cycle to 200; at every 200th cycle to 1001; at every 20,000th cycle up to 801,000. Then, the space between two consecutive readings was increased to 100,000 up to the 2,001,000th cycle. For these preset times, the frequency was reduced to 0.05 Hz in order to obtain more data points for these cycles.

The beams were then loaded monotonically up to failure under four-point bending. The monotonic load, applied at the same location as for the cyclic loading on a Baldwin press of 267 kN capacity, had a rate of approximately 0.1 kN/s. Data were recorded at every 0.1 kN load increment. The test setup for the monotonic loading is shown in Figure 3.

The 15 specimens and their loading conditions are summarized in Table 3. The table lists two control specimens NA and NB that were tested only monotonically to failure. The other specimens were first tested in fatigue with low-level or high-level loads, identified in Table 2 as L-series and H-series, respectively. Beams 400A and B were loaded for a number of 400,000 cycles; for 800,000 cycles for 800A, B and C; and for 2,000,000 cycles for 2000A and B. Letters A, B and C actually indicate replica specimens that underwent identical loading conditions.

3 RESULTS

All the results obtained from testing the 15 beams are analysed in the following. The presentation of the results obtained during fatigue testing will be followed by a discussion on the post-fatigue monotonic loading.

3.1 *Fatigue behaviour*

Thirteen beams were tested in fatigue in order to investigate the influence of cycling on their strength and load-deflection response. Initially, all the specimens were loaded monotonically up to the minimum fatigue level before starting the application of the fatigue cycling. First are discussed the specimens that were tested with low-level cycling, that is a load producing 15–35% of the yielding moment. Then, the beams subjected to high-level fatigue, with a load producing 35 to 75% of the yielding moment, are presented.

3.1.1 *Low-level cycling*

Of the seven beams of the L-series, specimen L2000B, which was subjected to two-million-cycle fatigue load, was chosen for a detailed discussion. Figure 4 shows the load-deflection response of L2000B during the fatigue test. Only seven curves representing typical behaviour of the beam and corresponding to each order of magnitude from the first to the last cycle are illustrated. It can be observed that, apart from the first cycle, the hysteresis curves are very similar along the two-million-cycle test. For any cycle the load-deflection curve exhibits an ascending slope and a descending slope that practically closes the hysteresis loop. It is interesting to note that these curves show an almost linear-elastic behaviour with the loop area practically constant. This indicates that the change in stiffness between two consecutive cycles is negligible. In the case of the first cycle, the ascending slope is very different from the other curves. The step observed at about 10 kN in this ascending slope is due to the fact that the beam cracked at this instant in the loading sequence. It is interesting to note that, as a result of cracking and micro cracking, the area confined by the hysteresis loop in the first cycle is significantly larger than for the subsequent cycles. This fact shows that the

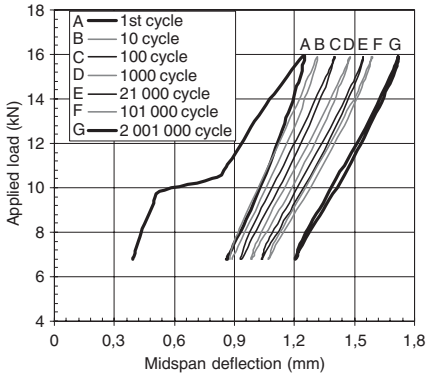

Figure 4. Load–deflection curves for beam L2000B.

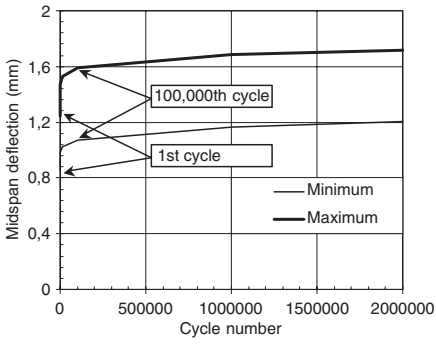

Figure 5. Deflection versus number of cycles for beam L2000B.

energy dissipated in the first cycle is more important then that dissipated in any other cycle during the test.

Another important parameter is the evolution of the deflection during cycling. As shown in Figure 4 for beam L2000B, there is a continuous increase in midspan deflection throughout the fatigue test. The evolution of this deflection can be alternatively represented with respect to the number of cycles. Figure 5 actually depicts the change in midspan deflection at the upper and lower limits of the fatigue cycle. Initially, a significant increase of the midspan deflection can be observed. This region extends up to about 100,000 cycles. At first cycle the deflection goes from 0.86 to 1.25 mm, and at 100,000 cycles from 1.07 to 1.59 mm. Then it is followed by a more stable region with deflection gradually increasing through cycles until the end of the test where it oscillates between 1.21 and 1.72 mm. This clearly indicates the continuous degradation of the stiffness during load cycling,

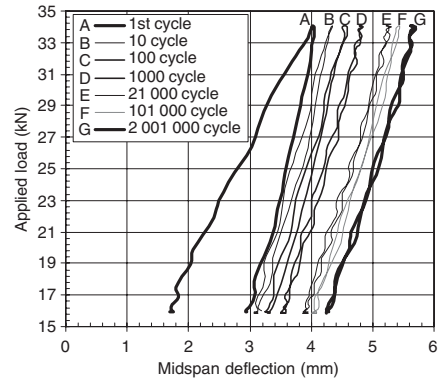

Figure 6. Load–deflection curves for beam H2000B.

though at a lower rate after the cycle 100,000. Similar results were obtained for the other beams in L-series.

3.1.2 *High-level cycling*

Three beams out of six withstood the load cycles of a magnitude producing 75% of the yielding moment. They are beams H400A, H800A, and H2000B. The others failed before reaching the proposed number of fatigue cycles due to premature degradation of the interface concrete-CFRP. Graphical results for the beam H2000B that withstood 2,000,000 cycles are analysed in the following.

Figure 6 shows the load-deflection hysteresis curves for beam H2000B that underwent the two-million-cycle test. It can be observed that there is no cracking in the first cycle, as opposed to the case that was presented in Figure 4 for beam L2000B. This is due to the fact that the current beam was monotonically loaded up to 15.9 kN, the minimum load applied during fatigue cycles, and this value largely exceeds the cracking load. Consequently, the beam had cracked before any cycling began. Although there is no sign of major cracking taking place in the first cycle, the area confined by the hysteresis loop is much larger than the area for any subsequent cycle. This demonstrates that during the first cycle the energy dissipation is the largest and the extent of micro cracking, that could not be detected visually, is very important. The fact that the slope remains the same for all curves further confirms that the stiffness has remained virtually unchanged until the last cycle. However, the residual deflection at midspan continues to increase with cycling.

The evolution of deflection with respect to number of cycles is plotted in Figure 7 for both maximum and minimum loads applied during the fatigue test of H2000B. The shape of the curves is similar to that observed for the beam L2000B. Initially, a significant increase of the deflection is observed up to about

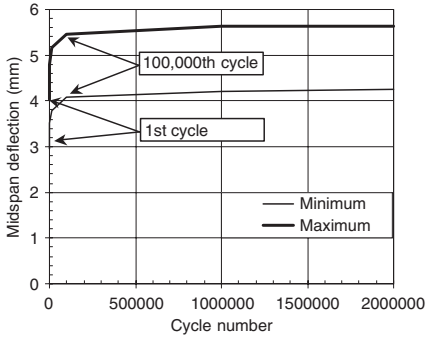

Figure 7. Deflection versus number of cycles for beam H2000B.

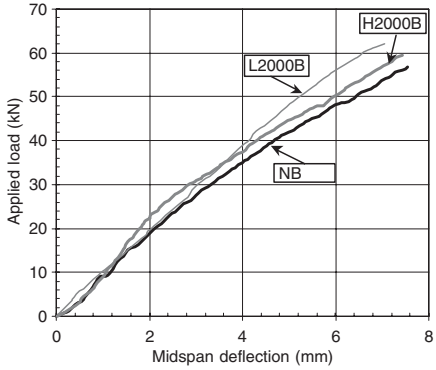

Figure 8. Load–deflection curves during monotonic test.

100,000 cycles. At first cycle it goes from 2.96 to 4.03 mm, and at 100,000 cycles from 4.09 to 5.46 mm. This is followed by a stable region where deflection is relatively constant until the end of the test where it oscillates between 4.26 and 5.64 mm. This region in the deflection curve is more stable than that of beam L2000B shown in Figure 5. This can be explained by the fact that H2000B was subjected to higher load amplitudes causing cracking stabilization. Therefore, the deflection remained almost constant after the very first cycles. For L2000B, subjected to lower load amplitudes, the cracking continues until the end of the test, and this translates into a gradual increase in midspan deflection, as can be observed in Figure 5.

3.2 *Monotonic behaviour*

Following the fatigue cycling, the beams were loaded monotonically to failure. Figure 8 compares the load-deflection response of beams L2000B and H2000B with that of NB. The reference specimen NB is a CFRP-strengthened RC beam identical to the other specimens in L and H series. The only difference is that NB was tested monotonically to failure alone, without any previous loading. The dark curve represents the midspan deflection against load for beam NB. As the applied load increases, its relationship to the deflection remains almost linear until about 9 kN. This value represents the cracking load and is consistent with the observation made in section 3.1.1 for the beam L2000B. At this point a short load plateau is observed, after which the load-deflection curve exhibits a new linear relationship until failure of the beam. The failure mode observed for all beams is delamination of the CFRP plate from the beam, as can be seen in Figure 3.

It can be observed that for the two beams that were subjected to fatigue cycles, there is no load plateau.

Table 4. Monotonic test results.

Beam	P_{min}–P_{max} (%)	$P_{u,exp}$ (kN)	Δ_u (mm)
NA	–	55.6	8.00
NB	–	56.7	7.54
L400A	15–35	56.6	7.74
L400B	15–35	54.7	6.74
L800A	15–35	56.5	6.92
L800B	15–35	55.0	7.42
L800C	15–35	57.2	6.78
L2000A	15–35	58.7	6.80
L2000B	15–35	59.4	7.43
H400A	35–75	62.2	6.68
H400B*	35–75	–	–
H800A	35–75	59.4	6.22
H800B**	35–75	–	–
H2000A***	35–75	–	–
H2000B	35–75	62.1	7.05

Failed at *203 000, **709 000 and ***243 000 cycles.

This can be explained by the fact that these beams were cycled in fatigue, and as a consequence, they were cracked before the failure test. However, the slope of the load-strain curves is similar to the one observed for the case of NB. It is interesting to note that the bilinear load-deflection response observed in previous studies [9] for RC beams strengthened with CFRP is also observed in the case of the reference beam NB.

Table 4 lists some of the results from the monotonic failure tests on both reference and fatigued beams. For the fatigued specimens, the ultimate load $P_{u,exp}$ varies from 54.7 to 62.2 kN. For the parameters used in this study, there is no clear influence of the fatigue loading on the monotonic post-fatigue behaviour in terms of residual strength. The ultimate deflection measured during failure test, Δ_u, varies from 6.22 to 7.74 mm. If one takes into account the residual deflection due to the fatigue cycles, then the total deflection of fatigued

specimens is very similar to that obtained for the control specimens. Again, no trend is observed between the change in ultimate deflection and the number of fatigue cycling.

4 CONCLUSION

An experimental program was conducted on the fatigue response of small-scale beams externally strengthened with CFRPs. The results provide an insight on the long-term behaviour of a repair system that is gaining widespread use. The effect of severe fatigue loading on the flexural behaviour of such system was addressed. During the fatigue tests the beams showed a consistent response independently of the number of fatigue cycles. The specimens maintained most of their initial stiffness until end of test. Initially, the beams showed an important deflection increase until 100,000 cycles. Then, the response stabilized with deflections being asymptotic to the maximum values corresponding to the load amplitudes. Following the cyclic tests, the beams were subjected to monotonic loading up to failure. Results from these tests showed that the number of fatigue cycles had no significant effect on the load-deflection response of the beams. The total deflection, including the residual deflection due to cycling, is not significantly different from that of the control specimens. In addition, the ultimate load reached by the beams does not appear to be influenced by fatigue cycling. Further work needs to be done in order to develop analytical and numerical models for the CFRP-strengthened RC beams.

ACKNOWLEDGEMENTS

The financing of this research project provided by the Network of Centres of Excellence ISIS Canada and by the Natural Sciences and Engineering Research Council of Canada (NSERC) is gratefully acknowledged. The authors also thank Mr. Marc Demers and Mr. Claude Aubé for their assistance in the laboratory.

REFERENCES

[1] Uomoto, T., "Durability of FRP reinforcement as concrete reinforcement", *Proceedings of the International Conference on FRP Composites in Civil Engineering*, J.G. Teng, Editor, Elsevier, Hong Kong, 85–96, 2001.

[2] Kelkar, A.D., "Behavior of low cost manufactured thick FRP woven composite laminates under cyclic loading", *Proceedings of the International Conference on FRP Composites in Civil Engineering*, J.G. Teng, Editor, Elsevier, Hong Kong, 235–243, 2001.

[3] Beaudoin, Y., Labossière, P. and Neale, K.W., "Wet-dry action on the bond between composite materials and reinforced concrete beams", *1st International Conference on Durability of Fibre Reinforced Polymer (FRP) Composites for Construction*, Benmokrane B. and Rahman H., eds., Sherbrooke, Canada, 537–546, 1998.

[4] Raîche, A., Beaudoin, Y. and Labossière, P., "Durability of composite materials used as external reinforcement for RC beams", *Proceedings of the Annual Conference of the Canadian Society for Civil Engineering*, Regina, Canada, 155–164, 1999.

[5] Green, M.F., Bisby, L.A., Beaudoin, Y. and Labossière, P., "Effect of freeze-thaw cycles on the bond durability between fibre reinforced polymer plate reinforcement and concrete", *Canadian Journal of Civil Engineering*, **27**(5), 949–959, 2000.

[6] Heffernan, P.J. and Erki, M.A., "Fatigue behavior of reinforced concrete beams strengthened with carbon fibre reinforce plastic laminates", *Journal of Composites for Construction,* ASCE, **8**(2), 132–140, 2004.

[7] Lopez, M.D.M., Naanan, A.E., Pikerton, L. and Till, R.D., "Behavior of RC beams strengthened with laminates and tested under cyclic loading at low temperatures", *Proceedings of the International Conference on FRP Composites in Civil Engineering*, J.G. Teng, Editor, Elsevier, Hong Kong, 415–422, 2001.

[8] Gheorghiu, C., Labossière, P. and Raîche, A., "Environmental fatigue and static behaviour of RC beams strengthened with CFRP", *Journal of Composites for Construction,* ASCE, 2003 (in print).

[9] Shahawy, M. and Beitelman, T.E., "Static and fatigue performance of RC beams strengthened with CFRP laminates", *Journal of Structural Engineering*, ASCE, **125**(6), 613–621, 1999.

FRP Composites in Civil Engineering – CICE 2004 – Seracino (ed)
© 2005 Taylor & Francis Group, London, ISBN 90 5809 638 6

A generic design approach for all adhesively-bonded longitudinally-plated RC beams

Deric John Oehlers
Department of Civil and Environmental Engineering, The University of Adelaide, Australia

ABSTRACT: The fundamental debonding mechanisms for longitudinally plated beams and slabs is now well understood and recognised in guidelines. Furthermore, research is well advanced in quantifying these debonding mechanisms and has reached a stage where plating can be applied in practice and with confidence. A generic design procedure is presented for adhesive bonding longitudinal plates to RC beams and slabs that can be applied to prestressed and unprestressed beams, that covers all plate materials, plate configurations and plate adhesion to any surface, covers all four major debonding mechanisms at serviceability or ultimate limit states, and quantifies the flexural and shear strengths as well as the ductility associated with moment redistribution.

1 INTRODUCTION

There are now several good guidelines[1–4] available for adhesive bonding longitudinal FRP plates to the tension faces of unprestressed RC beams and slabs in order to increase their strength and stiffness; these guidelines usually prohibit moment redistribution due to the brittle nature of an FRP plated section.

In this paper, we will be looking at a generic design approach[5] that can be applied to bonding longitudinal plates to any surface of prestressed or unprestressed RC beams or slabs, Figs. 1(b) to (d), and to any combination of plates as in Fig. 1(e). These generic design rules apply to any type of plate material such as brittle FRP pultruded plates or those formed by the wet lay up procedure or metal plates such as steel or aluminium that can yield prior to debonding. Furthermore, this generic design approach allows for and quantifies moment redistribution in both FRP and metal plated beams, Fig. 1(a), quantifies the flexural and shear capacities of longitudinally plated beams, is developed in a form that can accommodate new forms of plating such as near surface mounted plates and applies to both serviceability and ultimate limit states.

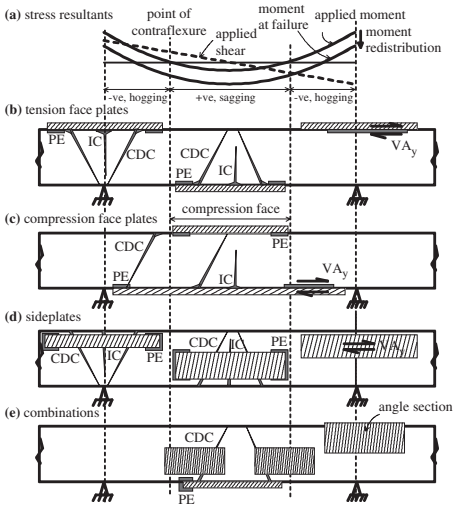

Figure 1. Longitudinally plated beams.

2 DESIGN GUIDELINES

The debonding mechanisms described in current design guidelines[1–5] are compared in Fig. 2 for the case of a tension face plated beam of which all the guidelines apply. The guidelines themselves either refer directly to a debonding mechanism in which case the jargon used to describe the mechanism is given in Fig. 2(b) or they refer to a publication which is shown as *referenced*. It can be seen, Fig. 2, that there is now general recognition of the three major debonding mechanisms which are shown as IC, CDC and PE debonding. However, a fourth debonding mechanism, VAy, is shown based on the elementary structural mechanics VAy/Ib or VQ/Ib equations.

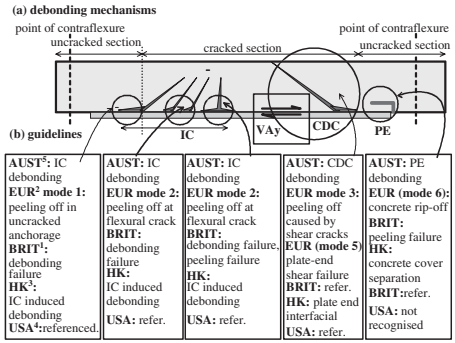

Figure 2. Guideline debonding mechanisms.

3 MAJOR DEBONDING MECHANISMS

3.1 *Intermediate crack (IC) debonding due to flexure*

Whenever a crack intercepts a plate, Fig. 3, the high strain concentrations at the intercept are relieved by the IC interface cracks shown. These IC interface cracks continue to propagate as the intermediate crack width s_{cr} increases under flexure until they spread uncontrollably causing IC debonding. IC debonding is generally associated with high moment regions of a beam where the flexural cracks are at their widest and the plate strains are at their maximum. They are characterized by crack propagation away from the high moment region, by partial interaction τ/δ (shear-stress/interface-slip) at the interface, and a lower bound to the strain at which IC debonding occurs ε_{IC} can be obtained directly from pull tests.

3.2 *Critical diagonal crack (CDC) debonding due to vertical shear*

Reinforced concrete beams fail under vertical shear when a critical diagonal crack forms and slides. This is associated with the concrete component of the shear capacity V_c. It needs to be stressed that a CDC is not a flexural crack nor a flexural-shear crack but it is associated with the single diagonal crack that eventually slides and which governs the shear capacity V_c. As the width of the CDC s_{cr}, Fig. 4, increases due to shear, the plate resists the widening of s_{cr} through its IC debonding resistance along the axis of the plate and the force the plate exerts across the CDC increases V_c. Eventually the IC debonding resistance ε_{IC} is achieved causing the plate to debond through IC debonding and V_c reduces. It can be seen that the CDC debonding resistance depends on the IC debonding resistance of the plate. However, CDC debonding is associated with the shear capacity or failure of an RC beam and it

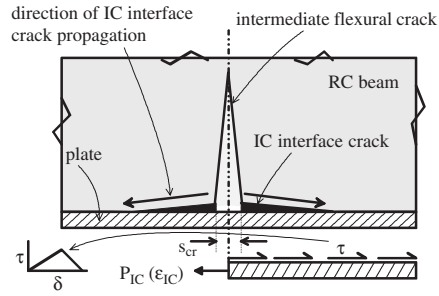

Figure 3. IC debonding mechanism.

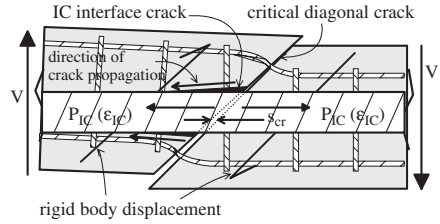

Figure 4. CDC debonding mechanism.

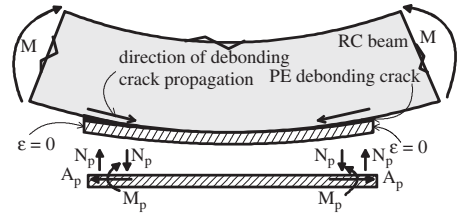

Figure 5. PE debonding mechanism.

is the rigid body shear deformation across the CDC that increases the crack width s_{cr} and not the flexural deformations as in IC debonding in flexural regions.

3.3 *Plate end (PE) debonding due to curvature*

Plate end debonding, Fig. 5, is due to the stress concentrations at the plate end due to the discontinuity of the plate and are induced by the curvature in the RC beam. The curvature induces the axial force in the plate A_p and moment in the plate M_p which induce the normal forces N_p across the plate interface which induce cracking and eventually debonding. Unlike IC debonding where the debonding cracks start where the plate strains are at their maximum and propagate to lower moment regions, PE debonding cracks start where the plate strains are zero and the debonding cracks

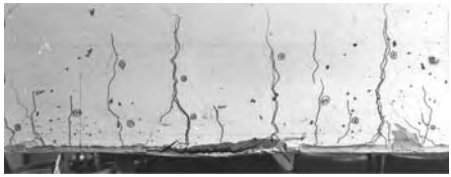

Figure 6. IC debonding in constant moment region.

Figure 7. PE debonding in constant moment region.

propagate towards the position of maximum moment. PE debonding can be easily prevented by terminating the plate at a point of contraflexure.

3.4 *Interface shear stress (VAy) debonding*

VAy debonding is due to the elementary interface shear stresses VAy/Ib or VQ/Ib which occur away from stress concentrations due to either the discontinuity of the plate (PE debonding) or stress concentrations due to flexural cracks (IC debonding) or due to critical diagonal cracks (CDC debonding). This form of cracking or debonding rarely occurs in research as the stress concentrations that occur in practice and mentioned above are much larger. However, it is felt that this debonding mechanism may govern in prestressed beams or at serviceability prior to cracking. It needs to be stressed that the VAy approach cannot be used to prevent IC or PE debonding, as these can occur in constant moment regions as in Figs. 6 and 7, nor prevent CDC debonding.

4 DESIGN PHILOSOPHIES FOR STRENGTH

The debonding mechanisms affect both the strength and ductility. At present, there would appear to be two distinct design philosophies for strength which are based on the IC debonding resistance.

4.1 *Hinge design philosophy*

Tests and numerical simulations have shown that the IC debonding resistance from pull-tests is generally a lower bound to the IC debonding resistance in beams. The hinge approach[3,5] restricts the IC debonding resistance used in beams to that obtained from pull-tests, Fig. 8. Hence the IC interface debonding cracks are

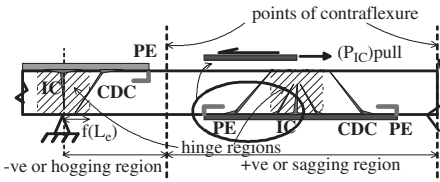

Figure 8. Hinge design philosophy.

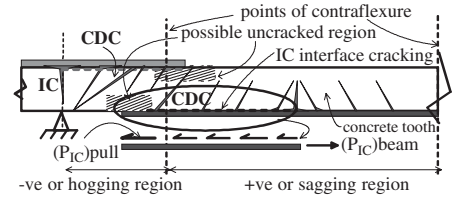

Figure 9. Anchorage design philosophy.

limited to a small hinge region which is of the same order as the effective length of the plate L_e, that is the anchorage length required to achieve the maximum stress in the plate in a pull test. The extent of the plate is then governed by either CDC or PE debonding. Restricting the IC debonding cracks to within the hinge region ensures that there is no interaction between IC and PE debonding as at present this interaction has not been quantified. Furthermore, restricting the IC debonding resistance to that obtained from pull-tests allows the plate to be terminated short of the point of contraflexure and allows this design philosophy to be applied to plates on any surface, Fig. 1.

4.2 *Anchorage design philosophy*

The anchorage approach[2] requires that the plate is anchored in an uncracked region which invariable will be close to the point of contraflexure, Fig. 9, so that the concrete teeth can act as shear connectors increasing the IC debonding resistance above that obtained from pull tests. Research[2] has only quantified this increase for FRP tension face plates for which this approach should be restricted. Terminating the plate close to a point of contraflexure ensures that PE debonding will not occur and, hence, this approach also prevents any interaction between IC and PE debonding.

In summary, the hinge approach requires a larger cross-sectional area of plate but a shorter length of plate than the anchorage approach. The IC debonding resistance in the hinge approach can be determined directly from pull-tests whereas that in the anchorage approach is a property of the cross-section and beam[2] but allows larger strains and, thereby, larger curvatures and ductility.

5 DESIGN PHILOSOPHIES FOR DUCTILITY

The debonding mechanisms in many ways have a greater effect on the ductility than on the strength and because of this can severely hamper or restrict the use of plating. The affect of plating on the beam ductility is illustrated below in terms of the ability to redistribute moment. However the same principles govern the ability to design ductile plated structures whether it be for static or seismic loads. It is felt that this is now a major issue in the advancement of plating.

5.1 *Moment redistribution requirement*

To illustrate the importance of ductility, let us consider the plated beam in Fig. 10. Let us assume that the hogging regions are already plated and have a plated capacity of $(M_h)_p$ and the sagging region is unplated with a sagging capacity of $(M_s)_u$. Curve A is the distribution of moment at failure if both sections can reach their moment capacity and which has a static moment capacity of $(M_h)_p + (M_s)_u$. If the hogging plated region is brittle, that is having attained its moment capacity it is unable to maintain its moment capacity with further rotation, then the distribution of moment at failure is given by curve B where the static moment is $1.5(M_h)_p$, this could be less than the static capacity $(M_h)_p + (M_s)_u$ so there is no point in plating the sagging region. In contrast, if the hogging region is ductile and can redistribute 30% of its moment as shown, then the static moment increases to $1.5(M_h)_p/0.7$ in curve C which is a 43% increase over the brittle scenario. Hence the sagging region can be plated to increase its strength from $(M_s)_u$ to $1.5(M_h)_p/0.7 - (M_h)_p$. It is also worth noting in this example that as moment redistribution does not occur in the sagging plated region then brittle plated sections, such as FRP surface plates can be used here. In contrast, in the hogging region the plated sections must be ductile to accommodate the 30% redistribution which would probably require the use of metal surface plates or FRP near surface mounted plates.

5.2 *Moment redistribution concept*

The concept of moment redistribution is illustrated in Fig. 11 for the case of a continuous beam with the same moment/curvature (M/χ) response in the hogging and sagging region, Fig. 11(a). In this example, the hogging region has to maintain its moment capacity at M_u whilst the sagging capacity increases from $M_u/2$ to M_u, Fig. 11(a) and (b). Hence in the hogging region, the secant flexural rigidity reduces from EI to $(EI)_{sec}$, Fig. 11(a). There are two approaches that allow for this moment redistribution. It can either be assumed that the rotation required occurs in a small plastic hinge, Fig. 11(c) which accommodates the discontinuity in the slope at the support, Fig. 11(e), which is the neutral axis depth (k_u) approach. Alternatively, it can be assumed that there is no discontinuity in the slope, Fig. 11(e), so that the moment redistribution is accommodated by variations in the flexural rigidities in the regions, Fig. 11(d).

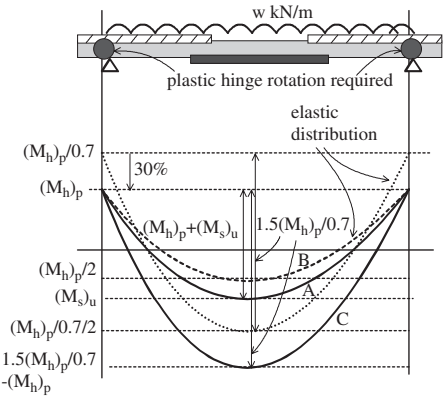

Figure 10. Moment redistribution in plated beam.

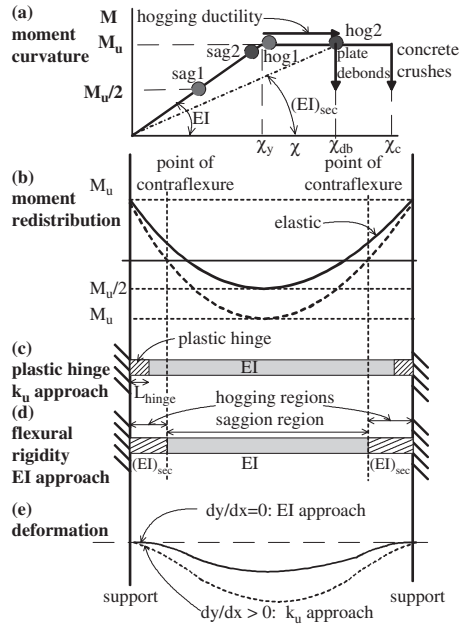

Figure 11. Moment redistribution concept.

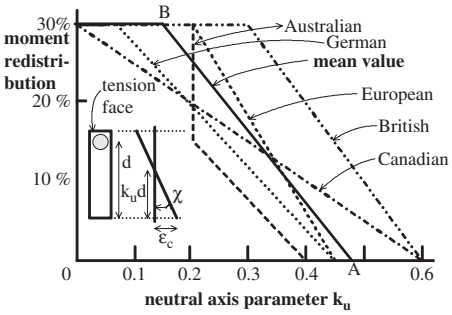

Figure 12. k_u parameter.

5.3 *Neutral axis depth (k_u) approach*

The amount of moment redistribution allowed by various RC codes is shown in Fig. 12. The k_u approach works because the rotation θ of a plastic hinge of length L_{hinge} is given by

$$\theta = \chi L_{hinge} = \frac{\varepsilon_c}{k_u d} d = \frac{\varepsilon_c}{k_u} \qquad (1)$$

where χ is the mean curvature over the plastic hinge and is equal to $\varepsilon_c/k_u d$ where ε_c is the concrete crushing strain and d is the effective depth. If it is assumed that $L_{hinge} = d$ and ε_c is constant, then θ is directly proportional to $1/k_u$. Hence this approach only works when concrete crushing governs failure which is usually not the case for plated structures.

The mean values of k_u in Fig. 12 are used in Fig.13 to show the interaction between the neutral axis depth factor k_u and the plate debonding strains ε_{db}. To make this comparison it is assumed that the concrete crushes at ε_c and, hence, this is the pivotal point in the strain profile even though it is realised that plate debonding is likely to occur before concrete crushing which will push the pivotal point to the left. Ranges of debonding strains for CFRP surfaces plates, near surface mounted CFRP plates and steel surface plates are shown. It can be seen that the very low debonding strains associated with surface CFRP plates warrant 0% moment redistribution, whereas near surface mounted CFRP plates can accommodate about 20% redistribution and steel surface plates can accommodate up to 30% redistribution as they can be designed to yield prior to debonding. However, unless the plate can be designed not to debond before concrete crushing at ε_c then the k_u approach cannot be used.

5.4 *Flexural rigidity approach*

The flexural rigidity approach assumes that there is no discontinuity at the support, Fig. 11(e), so that

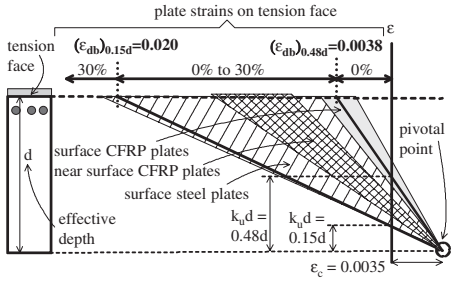

Figure 13. Moment redistribution in plated structures.

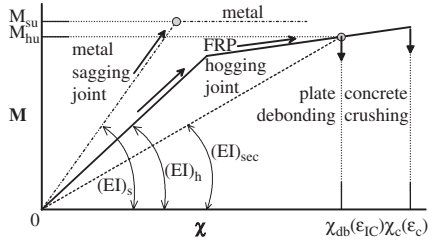

Figure 14. Variation in flexural rigidities.

moment redistribution is accommodated by variations in the flexural rigidities between the hogging and sagging regions, Fig. 11(d). The flexural rigidities can be obtained directly from the M/χ behaviour of the plated section, Fig. 14. In the example in Fig.11, the sagging joint has only to attain its moment capacity such as M_{su} in Fig. 14 so that the flexural rigidity remains fixed at $(EI)_s$. Whereas, the hogging region has to reduce in stiffness, to accommodate the moment being redistributed from the hogging region, from $(EI)_h$ to $(EI)_{sec}$ at the debonding curvature, that is the curvature at which the plate strains reach ε_{IC}.

In summary, the k_u approach should only be used for unplated sections or for plated sections in which concrete crushing at ε_c precedes plate debonding; this limits the use to plates with very high debonding strains such as thin steel plates where yield occurs prior to debonding. The flexural rigidity approach can be applied to any debonding strain ε_{IC} and can even be applied to plated beams in which debonding occurs whilst the section remains pseudo elastic.

6 ANALYSIS OF FLEXURAL CAPACITY AND DUCTILITY

The sectional analysis for the flexural capacity of a plated beam is shown in Fig. 15. The section can fail,

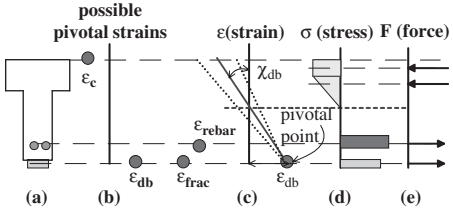

Figure 15. Flexural analysis.

Fig. 15(b), by either concrete crushing ε_c, fracture of the reinforcing bars ε_{rebar}, fracture of the plate ε_{frac} or debonding of the plate ε_{db}; it is a question of finding which of these failure modes occurs first. For the case of plate debonding, Fig. 15(c), the strain profile is pivoted about the debonding strain until longitudinal equilibrium, Fig. 15(e), is found. From which, the moment capacity can be obtained as well as the curvature χ_{db} and hence flexural rigidity $(EI)_{sec}$ for the moment redistribution analysis. It is essential in this analysis to allow the concrete to remain in part elastic as in Fig. 15(d).

7 ANALYSIS OF SHEAR CAPACITY

It is now recognised that longitudinal plates debond at the formation of a critical diagonal crack which is totally independent of the presence of stirrups. It is, therefore, a question of finding the increase in the concrete component ΔV_c due to plating of the shear capacity V_c. There would appear to be two approaches. Those which determine ΔV_c as well as its position and orientation θ within a region as shown in the hogging region in Fig. 16, in which case only part of the region needs to be plated. The other approach determines ΔV_c but not the position nor orientation of the critical diagonal crack and, hence, all of the region needs to be plated and fully anchored, L_e, as in the sagging region.

It needs to be stressed that the purpose of these analyses is to determine the shear load at which CDC debonding occurs. In a slab without stirrups, this happens to also be the shear capacity. However in a beam with stirrups it is the shear to cause plate debonding after which the beam behaves as unplated and its shear capacity may be greater due to the contribution from the stirrups.

8 SUMMARY

The design philosophies are illustrated in Fig. 17 for an encastre beam with a uniformly distributed load.

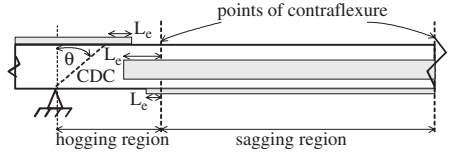

Figure 16. CDC debonding approaches.

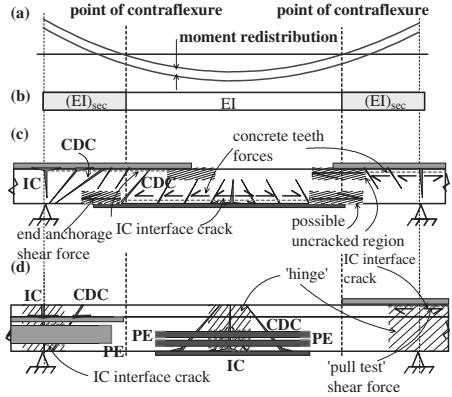

Figure 17. Summary of design philosophies.

1. Moment redistribution, Fig. 17(a), can be accommodated using the flexural rigidity approach, Fig. 17(b), where the flexural rigidity of the region redistributing moment can be obtained from the curvature at which debonding occurs.
2. Moment redistribution code approaches based on the neutral axis depth factor k_u can only be used in unplated regions or where the plate debonding strain is very large so that concrete crushing precedes plate debonding.
3. The anchorage approach, Fig. 17(c), requires the plate to be terminated close to a point of contraflexure in order to achieve the maximum plate strains and, hence, beam ductilities. The IC debonding resistance now depends on both the IC pull-test resistance but also on the beam properties that is the distribution of the applied load and flexural cracks, and also on the sectional properties. The beam must still be checked for CDC debonding but not for PE debonding.
4. The hinge approach, Fig. 17(d), restricts the IC debonding resistance to that obtained from a pull-test and hence the IC debonding resistance is independent of the beam and sectional properties, so that this approach can be applied to plates on any surface of the beam. CDC and PE debonding have to be checked.

REFERENCES

1. Concrete Society Technical Report No. 55 (2000). *Design guidance for strengthening concrete structures using fibre composite materials.* The Concrete Society. Century House, Telford Avenue, Crowthorne, Berkshire, UK.
2. fib bulletin 14 (2001). *Externally bonded FRP reinforcement for RC structures. Design and use of externally bonded fibre reinforced polymer reinforcement (FRP EBR) for reinforced concrete structures.* Task Group 9.3 FRP reinforcement for concrete structures. Lausanne, Switzerland.
3. Teng, J.G., Chen, J.F,. Smith, S.T. and Lam, L. (2002). "FRP Strengthened RC Structures." *John Wiley and Sons.* Ltd. Chichester, England.
4. ACI 440.2R-02 (2002). Emerging Technology Series. *Guide for the Design and Construction of Externally Bonded FRP Systems for Strengthening Concrete Structures*. Reported by ACI Committee 440. American Concrete Institute, Farmington Hills, Michigan, USA.
5. Oehlers, D.J. and Seracino, R. (2004). "Design of FRP and steel plated RC structures: retrofitting of beams and slabs for strength, stiffness and ductility." Elsevier, September.

FRP Composites in Civil Engineering – CICE 2004 – Seracino (ed)
© 2005 Taylor & Francis Group, London, ISBN 90 5809 638 6

Prestressed near surface mounted reinforcement (NSMR) for strengthening concrete beams

H. Nordin[1] & B. Täljsten[1,2]
[1] *Department of Civil and Environmental Engineering, Luleå University of Technology, Luleå, Sweden*
[2] *Skanska Teknik AB, Solna, Sweden*

ABSTRACT: Strengthening concrete structures with fibre reinforced polymer materials have today grown to be a widely used method over many parts of the world. To utilize the FRP (Fibre Reinforced Polymers) more efficiently, prestressing may be used. Most of the research carried out with prestressed Carbon Fibre Reinforced Polymers (CFRP) for strengthening has been with surface bonded laminates. However, in this paper tests with prestressed CFRP quadratic rods placed in the concrete cover in sawed grooves are discussed. This have proven to be an advantageous way of bonding CFRP in the concrete structure, and the transfer of the shear forces between the CFRP and the concrete become more efficient. This compared to surface bonded laminates. In the presented tests no mechanical device has been used to keep the prestress during testing, which then means that the adhesive has to transfer all shear stresses to the concrete. Furthermore the tests show that the prestressed beams exhibit a higher first crack-load as well as a higher steel-yielding load compared to non-prestressed strengthened beams. The ultimate load at failure is also higher, compared to nonprestressed beams, but in relation not as large as for the cracking and yielding loads.

1 INTRODUCTION

All over the world there are structures intended for living and transportation. The structures are of varying quality and function, but they are all ageing and deteriorating over time. Of the structures needed in 20 years from now about 85–90% of these are probably already built. Some of these structures will need to be replaced since they are in such bad condition. It is not only deterioration processes that make replacement necessary, errors can have been made during the design or construction phase so that the structure needs to be strengthened before it can be fully used. New and increased demands from the transportation sector may furthermore be reason for strengthening. If any of these situations should arise it needs to be determined whether it is more economical to strengthen a structure or to replace it. A strengthening method that has been increasingly used the last decade is plate bonding with Fibre Reinforced Polymers (FRP) materials. Extensive research and laboratory testing has been carried out all over the world and at many different locations. These investigations show that the method is very effective and a considerable strengthening effect can be achieved (Meier, 1995).

At Luleå University of Technology, Sweden, research is carried out in the area of plate bonding. The research work started in 1988 with steel plate bonding and is still continuing, now with FRP materials. Both comprehensive experimental work and theoretical work have been accomplished (Täljsten, 1994). The laboratory tests have included strengthening for bending as well as for shear (Carolin, 2003) and torsion (Täljsten, 1998). Full-scale tests on strengthened bridges have also been performed (Täljsten, 1994, Täljsten and Carolin, 1999). In the area of theory, the peeling stresses in the bond zone at the end of the strengthening plate have been studied in particular; in addition the theory of fracture mechanics introducing non-linear behavior in the bond has also been investigated (Täljsten, 1994, 1996, 1997).

In Sweden FRP strengthening have been used in the field for almost 10 years now and both laminates and wrap systems have been and are used. Sweden is also one of the countries where a national code exists for external FRP strengthening of concrete structures (Täljsten, 2003).

2 PRESTRESSING WITH NSMR

The purpose with NSMR (Near Surface Mounted Reinforcement) is to insert additional reinforcement into sawed grooves in the concrete cover. The idea of placing extra reinforcement in the concrete cover

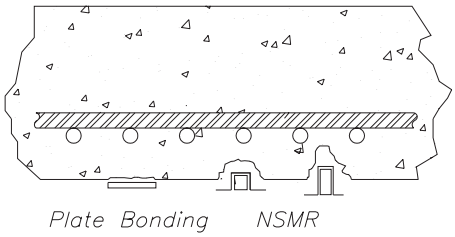

Figure 1. Schematic sketch of NSMR.

for strengthening is not new. The first known documented application was made in northern Sweden in 1940's where a bridge slab had to be strengthened in the negative moment zone (Asplund, 1949). Steel bars where placed in the concrete cover and bonded with a cement grout. Before the actual strengthening was carried out, four test slabs were loaded until failure, strengthened with the same technique. The results proved that the method could work and by March 1948 more then 600 meters of steel bars were bonded in the concrete cover of a bridge. However, in these type of applications it might be difficult to obtain good bond to the original structure, and in some cases, it is not always easy to cast the concrete around the steel reinforcing bar.

Researchers have tested NSMR with CFRP circular rods (De Lorenzis et al, 2000, Hassan and Rizkalla, 2001). A pilot study with rectangular rods has earlier been undertaken at Luleå University of Technology with the first tests done in 1996 (Täljsten and Carolin, 2001) and prestressed NSMR (Nordin, 2003). The sawing of grooves is only possible on structures with sufficient concrete cover to the steel reinforcement. One should remember that the thickness of the concrete cover is primarily depending of the workmanship when the structure was built rather than the code that design was based upon.

Opposite to external strengthening techniques the use of NSMR will, in a better way, protect the strengthening material from external damage. Another advantage is that the concrete surface will not be completely covered as in some cases with CFRP wraps, which can lead to built-in moisture in the structure with possible future freeze-thaw problems. In Figure 1, the principle for NSMR is shown. It can be noticed in Figure 1 that it is possible to achieve an increased bond surface with NSMR compared to traditional laminate plate bonding. This implies that more energy is needed to introduce failure in the concrete. This assumes sufficient bond between the CFRP and the concrete.

The insertion of the strengthening material in the concrete cover should vouch for a more efficient force transfer between the concrete and the composite. The bonded area will change and be dependent of the geometry of the inserted reinforcement. If the rods are placed too close to each other, the failure may occur from interaction between the two rods and maybe also by interaction from the existing steel reinforcement.

Full-scale tests and field applications have shown that the pre-treatment when using plate bonding can be work intense and therefore often expensive. In traditional plate bonding the concrete laitance layer must be removed and the aggregates must be exposed before adhesive and the composite can be applied, this to ensure good bond between the constituents. In the most cases this may be carried out by sandblasting and is neither complicated nor expensive. However, if the surface has larger irregularities, from formwork for instance, then a more powerful surface treatment is often needed. Often grinding in combination with sandblasting is used, this work is often time consuming and costly.

When placing the strengthening material in presawed slots in the concrete cover no surface treatments are needed, except cleaning with medium pressurised water, approximately 150 bars, immediately after sawing. In addition, if a stiff "rail" is used as support for the saw then the grooves will become straight and are possible to make also on rough surfaces. This is probably also a more advantageous method for the workers to do the pre-treatment compared to grinding, at least from a work environmental point of view.

Another issue regarding the execution work is the use of thermosetting polymers as epoxy. Epoxy, if it is handled in a wrong way, may be allergenic and harmful to man. Therefore the possibilities to replace the epoxy by cement grout would be preferable. This will also give possibilities to use NSMR under conditions with high humidity and even in submerged conditions. Another possible way to carry out the bonding works is to use injection or infusion techniques (Täljsten and Elfgren, 2000).

Probably, the biggest advantage of NSMR can be found in increased force transfer compared to laminates, but also increased durability and impact resistance are advantages with the technique. Traffic running underneath a bridge with low clearance may, sooner or later, result in damages on the bridge. For a concrete bridge this is not critical but can cause severe damages to an unprotected and badly designed reinforcement, for example traditional plate bonding as well as external post tensioning are very sensitive for vehicle impact.

In addition fire, vandalism and environmental loads may also harm the composite. A damage of the reinforcement can give severe problems and eventually failure of the structure. With NSMR the fragile composite will be more protected from outer damage then traditional plate bonding and external post tensioning systems.

3 THEORY

CFRP composites may be prestressed to achieve a more effective utilization of the material. There are also several other reasons why a prestressing force should be applied to a concrete structure. One reason to prestress is that the applied axial load induces a bending moment that opposes the self-weight of a concrete structure, (Garden and Hollaway, 1998). Another reason is that the first crack load is considerably increased compared to non prestressed strengthened beams and beams without strengthening, this can increase the durability of the concrete structure. However, the ultimate load is approximately the same as non prestressed strengthened concrete structures (Wight et al, 1995). Tests on concrete beams prestressed with CFRP sheets at room and low temperatures have also been carried out (El-Hacha et al, 2001).

One of the most important advantages when strengthening a structure with prestressing members is the reduction of stress in existing tensile steel reinforcement. This should indicate an increase of the fatigue behaviour of the members in the structure (Garden and Hollaway, 1998) and (Wight and Erki, 2001).

In design for strengthening in bending with NSMR, the same design equations as for traditional FRP strengthening may be used, see equation (1). Equations for anchorage and peeling failure need to be somewhat modified, see for example (De Lorenzis et al, 2002, De Lorenzis and Nanni, 2002 and Harmon et al, 2003).

$$M_d = A_s'\sigma_s'\left(\beta x - d_s'\right) + A_s f_y\left(d_s - \beta x\right) + \\ + \varepsilon_f E_f A_f\left(h - \beta x\right) \tag{1}$$

Here M_d is the designed bending moment, A_s', A_s and A_f are the cross sectional areas of compressive reinforcement, tensile reinforcement and composite, respectively. E_f is the Young's modulus of the composite and ε_f the strain in the composite. σ_s' is the stress in compressive reinforcement and f_y the yield stress in the tensile reinforcement, d_s and d_s' are the level arm to the tensile and compressive reinforcement, respectively.

The distance to the neutral axis is denoted x, β is a factor considering the simplification of the compressive stress block of concrete, and here β is set to 0.4.

The theoretical stress and strain distribution of a rectangular prestressed beam with NSMR is shown in Figure 2. Here Figure 2b shows the strain distribution where it has been assumed that plain sections remain plain during loading. In Figure 2c and 2d the stress distribution due to the bending moment and the prestressing force is shown.

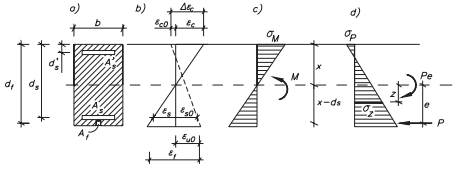

Figure 2. Stresses and strains acting on a prestressed cross-section.

Study Figure 2c, the stress at level z from the bending moment is:

$$\sigma_M = \frac{M}{I} z \tag{2}$$

Correspondingly the stress from the compressive force at level z is:

$$\sigma_P = -\frac{P}{A} - \frac{P \cdot e}{I} z \tag{3}$$

The combination of these stresses gives the total stress at level z:

$$\sigma_z = \left(\sigma_P + \sigma_M\right)_z = \frac{M}{I} z + \left(-\frac{P}{A} - \frac{P \cdot e}{I} z\right) \tag{4}$$

where the bending moment, M, acts on a cross section together with a prestress force P. Here, e is the level arm from the centre of gravity to the prestress force; z is the distance from the centre of gravity to studied lamella. A and I are the cross sectional area and moment of inertia for an un-cracked section respectively.

4 LABORATORY SET-UP

In this study a total of 15 concrete beams have been tested. The beams tested were four meters long with a cross-section of 200 × 300 mm. The longitudinal steel reinforcement was 2 Ø16 Ks 500 at the upper and lower part of the beam. The steel stirrups was placed at a spacing of 75 mm and consisted of Ø10 steel bars with the same steel quality as for the longitudinal steel. A 15 × 15 mm groove was sawn up in the concrete cover in the bottom of the beams, see Figure 3. One beam acted as a reference and was not strengthened, four beams were strengthened without prestressing and the remaining 10 were strengthened with prestressed quadratic CFRP rods. During the tests three variables were changed for the NSMR rods; bond length, modulus of elasticity and the prestressing force.

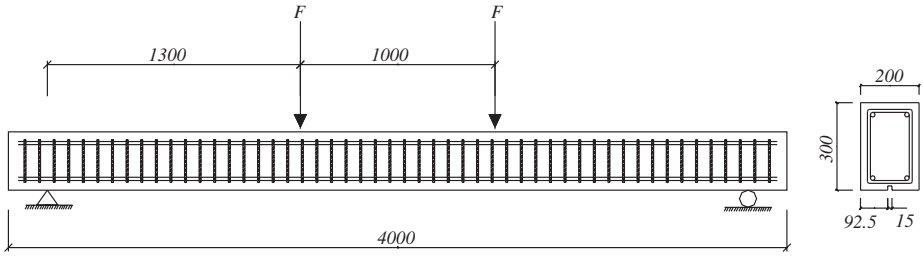

Figure 3. Test set-up.

Table 1. Data of the CFRP used.

	E_f [GPa]	ε_{fu} [‰]	f_f [MPa]
BPE® NMSR 101S	160	17.5	2800
BPE® NMSR 101M	250	8	2000

Two bond lengths were tested, 3200 mm and 4000 mm, in most field applications it is not possible to place the CFRP rod over the whole beam length due to the supports and therefore a 3200 mm rod that not goes beyond the supports was tested.

Two types of NSMR quadratic rods was used; BPE® NMSR 101S and BPE® NMSR 101M. The S rod has a modulus of elasticity of 160 GPa and the M rod 250 GPa. The cross-section for both types of rods used is 10×10 mm. In Table 1 the material data for the rods are recorded.

In the tests two levels of prestressing force were aimed to be used, 32 kN and 56 kN, those loads corresponding a stress in the rods of 320 MPa and 560 MPa respectively.

In Table 2 the different types of beams tested can be seen. In the Table S and M are the two qualities of CFRP rod and P stands for prestressed. The concrete used had an average compressive strength $f_{cc} = 65$ MPa and an average tensile strength $f_{ct} = 3.7$ MPa, for each beam three tests were made for both compressive and tensile strength.

During the tests the midpoint displacement, the strain in the CFRP (four gauges), tensile steel reinforcement (three gauges) and the upper part of the concrete (two gauges) was measured.

In all the tests BPE® Lim 465/464 epoxy adhesive was used. The properties for the adhesive are recorded in Table 3, where f_{ac} and f_{at} is the compressive respectively tensile strength of the adhesive. E_a denotes the Young's modulus of the adhesive used.

The prestressing was made with the beams placed on the floor with the bottom face up. The pre-sawed slots were cleaned from all contaminations such as dust and small particles and were the filled with sufficiently amount of adhesive at time for bonding/prestressing. The rods were then positioned in the adhesive filled slots. The quadratic rods were then subjected to a prestressing force until the sufficient strain was reached. The epoxy adhesive was then left to cure for 5 days in ambient conditions (20°C and 50% RH) before releasing the prestressing force. There was no mechanical anchorage used and consequently at releasing the prestress the adhesive had to transfer all the shear stress in to the concrete. In Figure 4 the beams during prestressing are shown.

Table 2. Beams tested.

	CFRP		Prestress	
Beam	Length [mm]	E [GPa]	Load [kN]	Strain [μstr]
Ref	–	–	–	–
BS1	3200	160	–	–
BS2	4000	160	–	–
BM1	3200	250	–	–
BM2	4000	250	–	–
BPS1	4000	160	29	1800
BPS2	4000	160	30	1870
BPS3	3200	160	33	2060
BPS4	4000	160	35	2160
BPS5	3200	160	56	3500
BPS6	4000	160	56	3500
BPM1	3200	250	32	1280
BPM2	4000	250	32	1280
BPM3	3200	250	54	2140
BPM4	4000	250	38	1500

Table 3. Material properties of the epoxy adhesive.

	f_{ac} [MPa]	f_{at} [MPa]	E_a [GPa]	Viscosity
BPE® Lim 465/464	103	31	7	Tix

Figure 4. Prestressing set-up.

Table 4. The tensile strain on the CFRP, at the middle and the end, before and after release of prestress force.

	Middle		
Beam	Initial [μstr]	After [μstr]	Loss [%]
BPS1	1802	1708	5.2
BPS2	1869	1816	2.8
BPS3	2095	2003	4.4
BPS4	2189	2101	4.0
BPS5	3386	3273	3.3
BPS6	3496	3166	9.4
BPM1	1234	1180	4.4
BPM2	1261	1184	6.1
BPM3	2060	1761	14.5
BPM4	1481	1368	7.6

5 RESULTS FROM TESTS

5.1 *Prestressing*

After the adhesive in the slots had cured for five days the prestressing force was released and taken as shear forces in the bond zone. A compressive force was then introduced to the lower part of the beam and a tensile force to the upper part. The strain at the ends of the rods (bonded area) was mostly lost when the prestressing force was released. But after less then 200 mm along the rod the loss of prestressing strain was only about 10–20% (depending on prestressing force), this loss should be able to be avoided with a mechanical anchor system. At the middle of the beam the strain loss was between 5 to 10%, see Table 4.

For the ends of the rods it became clear that the workmanship of the strengthening was very important.

The beams with the smallest loss of strain at the ends were the beams where the strengthening had been carried out with least problems.

Table 5. The significant values for loads and midpoint displacement.

	Cracking		Yielding		Ultimate	
Beam	Load [kN]	Displ. [mm]	Load [kN]	Displ. [mm]	Load [kN]	Displ. [mm]
Ref	10	1.2	70	33	75	61
BS1	14	2.0	90	22	123	50
BS2	13	1.9	87	23	117	55
BM1	11	1,8	105	28	122	41
BM2	11	1,8	106	27	122	37
BPS1	20	2.4	97	25	121	46
BPS2	21	2.0	95	23	121	44
BPS3	23	2.3	105	26	120	38
BPS4	23	2.3	108	26	123	39
BPS5	26	2.2	119	28	122	33
BPS6	N/A	N/A	117	28	148	107
BPM1	25	2.5	121	28	128	32
BPM2	25	2.8	122	28	132	33
BPM3	32	3.7	129	28	131	30
BPM4	23	2.3	121	28	123	29

When studying Table 4 it can be seen that there is no difference in loss between the rods with different modulus of elasticity, the percentage loss is about the same for both. It is the prestressing force that has an effect on the strain loss at the end.

5.2 *Bending tests*

The tests in bending have shown interesting and promising results. In Table 5 are the significant loads with midpoint displacement presented (cracking, yielding of steel reinforcement and ultimate loads). The results show that both an increased cracking load and steel yielding load can be achieved by strengthening with prestressed CFRP rods in the concrete cover of a beam. All the strengthened beams failed by fibre rupture.

The results from the tests that can be seen in Table 5 indicate that there is no difference between beams strengthened with 3.2 m rods and 4 m rods when testing bending. It was however noticed that there was cracks from the end of the rods when using 3.2 m rods, the cracks is most likely due to the high peeling stresses at the end of the rod.

There is a significant difference between cracking and yielding loads when comparing the effects of different prestressing forces. For concrete cracking loads the percentage difference is largest. The force that have been introduced to the lower part of the beam when prestressing the CFRP rod increases the loads needed to create cracks in the concrete. Since higher prestressing forces created higher stresses in the concrete and steel higher loads are needed to counteract those forces. When it comes to steel yielding the higher compressive

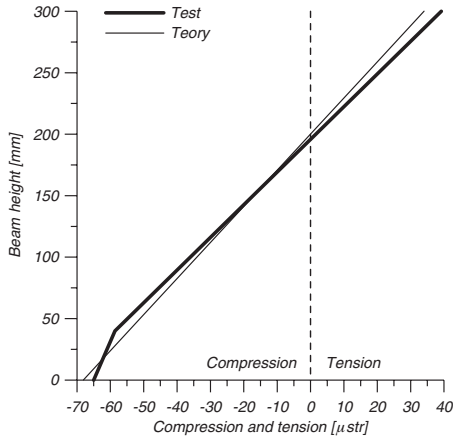

Figure 5. The strain over the height of the beam after release of prestressing force.

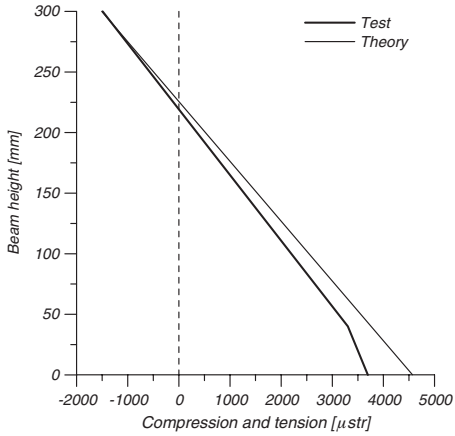

Figure 6. The strain over the height of the beam at the load 100 kN.

forces in the lower part of the beam helps delaying the steel yielding to higher loads.

5.3 *Comparison theory and test*

Using equation (4) the theoretical strain for beam BSP4 has been compared to the measured strain at the midpoint of the beam. The comparisons have been done directly after the release of the prestressing force, Figure 5, and at 100 kN load during bending, Figure 6. The strain from the tests have been measured from three points on the beam, at concrete on the top, on the steel reinforcement on the lower part of the beam and on the CFRP rod. When studying Figure 5 and 6 the theory correspond well to the tests.

6 CONCLUSIONS

Fifteen concrete beams have been tested; fourteen of these were strengthened with rectangular NSMR rods. The results from the tests show that strengthening technique using CFRP bonded in the concrete cover is a efficient method to transfer the stresses between CFRP and concrete, both for nonprestressed and prestressed CFRP. The problems with end peeling of the strengthening material that have been a problem when prestressing surface bonded CFRP laminates are minimized with the use of NSMR rods.

The tests show a large increase in crack and steel yielding loads. The increase in load for steel yielding can be very important for a constructions life, the fatigue behaviour will improve and as a consequence the crack widths will be smaller which then can result in a more advantageous behaviour in the service limit state (SLS) with increased durability.

Furthermore, it is showed in the tests that the force transfer between the prestressed rectangular CFRP rod and concrete works very well, even without mechanical anchorage devices.

It is the authors' belief that it in the near future will be possible to use this prestressing technique in field applications. It would, though, be preferable to use mechanical anchorages at the end to minimise the strain loss due to prestressing and to avoid future creep in the bond zone.

7 CURRENT WORK

During the spring and summer of 2004 a series of tests is being done comparing different strengthening techniques. A total of 7 beams have been tested including external prestressing with steel and CFRP tendons, the NSMR technique is also being used, both with and without prestress. The beams tested are T-beams with a length of 6 meters; the cross section and the test set-up of the beams can be seen in Figure 7.

The beams tested are only described briefly since evaluation of the tests is still ongoing. First a reference beam was tested (Reference), then two beams with external prestressed steel tendons (Steel A and Steel B), the first where the tendon follow the bending moment curve and the second where straight tendons were used. The next tested beam was reinforced with an internal post-stressed steel tendon (Steel C). For the beam denoted CFRP in Table 6 prestressed circular CFRP tendons were used. Then two beams were tested

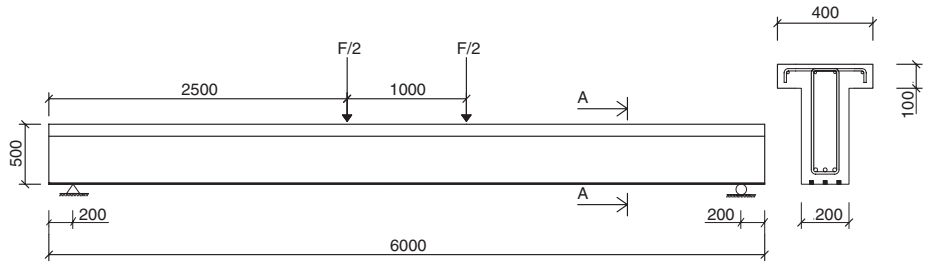

Figure 7. Test set-up for large-scale beams, here a sketch of the strengthened NSMR beam is shown together with a photo of the test set-up.

Table 6. The preliminary results from the tests.

Beam	Cracking [kN]	Yielding [kN]	Ultimate [kN]
Ref	25	105	105
Steel A	75	205	303
Steel B	75	203	243
Steel C	74	208	274
CFRP	50	145	159
NSMR NP	27	180	288
NSMR PS	N/A	220	324

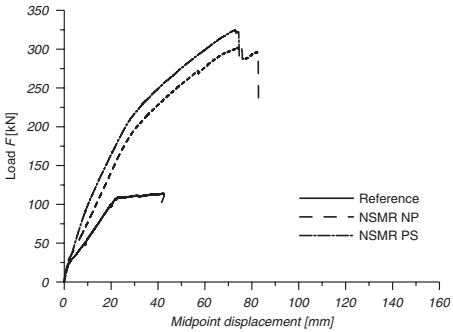

Figure 8. Load–deflection curves of the reference and the NSMR beams tested.

with NSMR, one with non prestressed NSMR (NSMR NP) and one with prestressed NSMR (NSMR PS). In Figure 8 the load–deflection curve from the tested NSMR beams and the reference beam are shown. It can clearly be seen in Figure 6 that the prestressed beam had a higher internal steel-yielding load compared to the non-prestressed beam.

As the tests still are being evaluated only the cracking, yielding and ultimate load are presented and in Table 6 these preliminary results are shown. The beam with external prestressed CFRP tendons had problems with slippage in the anchorage device and therefore the load results are lower then it probably would be if the anchorage would had worked properly. However, this test will be repeated.

Nevertheless, an early conclusion that can be drawn from these tests is that both external prestressed steel cables and the NSMR strengthening technique (with or without prestress) gives a good strengthening effect on the tested beams.

Externally prestressed CFRP cables may also be a profitable technique, but here improvement with anchorage is needed.

8 FUTURE WORK

As the results from the tests presented has shown that the prestressing NSMR technique can be an efficient strengthening method, the next step is to investigate more parameters that may affect the strengthening result. This might be multiple prestressed rods, anchor device for the ends, strengthening of different structural elements, to mention a few.

Of utmost importance is to develop a strengthening system that will be practical applicable in the field. Such a system will include a semi-mechanical anchorage system which will be critical for prestressing the rods but also will help maintain the prestressing force, i.e. decreasing the strain loss at the ends. The long-term behaviour has to be studied. What happens over time with the prestress? For example, how will creep affect the strengthening?

The very next step is to improve the anchorage for both external CFRP tendons as well as for the prestressed NSMR rods.

To investigate the normal and shear stress in the CFRP rods, tests are going on, where an optical fibre is integrated in the composite. Opposite to strain gauges, with the fibre optics it might be possible to see what happens in the entire strengthening material and not only at discrete points. This technique will first be used

in the laboratory to optimise the anchorage device, but if it works as intended it will also be used in field, where it then would be possible to follow a structure over time.

ACKNOWLEDGEMENT

The research presented in this paper have been funded by several organizations, here the Swedish National Road Administration, the Development fund of the Swedish Construction Industry and Skanska AB should be acknowledged.

REFERENCES

Asplund, S.O. (1949), "Strengthening Bridge Slabs with Grouted Reinforcement", Journal of the American Concrete Institute, Vol. 20, No. 6, January, pp. 397–406.

Carolin A. (2003) "Carbon Fibre Reinforced Polymers for Strengthening of Structural Elements", Luleå Univeristy of Technology, Division of Structural Engineering, Doctoral Thesis 2003:18 ISBN 91-89580-04-4.

De Lorenzis L., Nanni A. and La Tegola, A., (2000), "Flexural and Shear Strengthening of Reinforced Concrete Structures with Near Surface Mounted FRP Rods" Advanced Composite Materials in Bridges and Structures, Proc. of 3rd Int. Conf., Ed. Humar, J.L and Razaqpur, A.G. Ottowa, ISBN: 0-7709-0447-5, pp. 521–528.

De Lorenzis L., Rizzo A. and La Tegola, A., (2002), "A modified pull-out test for bond of near-surface mounted FRP rods in concrete, Journal of Composites, Part B: engineering, Vol. 33, 2002, pp 589–603.

De Lorenszis L. and Nanni A., 2002, Bond between near-surface mounted FRP rods and concrete in structural strengthening, ACI Structural Journal, Vol. 99, No. 2, March–April, 2002, pp 123–133.

El-Hacha R., Wight G. and Green M., (2001), "Long-term behaviour of concrete beams strengthened with pre-stressed CFRP sheets at room and low temperatures", Conf. Proceedings: Concrete Under Severe Conditions – Environment and Loading, University of British Columbia, Vancouver June 18–20, 2001, Edt. Banthia N., Sakai K. and Gjörv O.E., ISBN 0-88865-782-X, pp 1817–1826.

Garden H.N. and Hollaway L.C., 1998, "An experimental study of the failure modes of reinforced concrete beams strengthened with pre-stressed carbon composite plates" Composites Part B, 411–424.

Hassan T. and Rizkalla S. (2001), "Strengthening of bridge-slabs with FRP systems" Conf. Proceedings: Structural Faults & Repair, London, June 2001.

Harmon T.G., Kim J.Y, Kadros J., Johnson T. and Stark A., 2003, Bond of Surface-Mounted Fibre-Reinforced Polymer Reinforcement for Concrete Structures, ACI Structural Journal, Sep.–Oct., V.100, No.5, pp 557–564.

Meier U., (1995), "Strengthening of structures using carbon fibre/epoxy composites" Construction and Building Materials, Volume 9, Issue 6, December 1995, pp 341–351.

Nordin H., (2003) "Fibre Reinforced Polymers in Civil Engineering – Flexural Strengthening of Concrete Structures with Prestressed Near Surface Mounted CFRP Rods" Luleå, Luleå Univeristy of Technology, Division of Structural Engineering, Licentiate thesis 2003:25 ISBN 91-89580-08-7.

Täljsten B., (1994), "Plate Bonding, Strengthening of Existing Concrete Structures with Epoxy Bonded Plates of Steel or Fibre reinforced Plastics" Doctoral Thesis 1994:152D, Div. of Structural Engineering, Luleå University of Technology, ISSN 0348-8373, 308 pp.

Täljsten B., (1996), "Strengthening of concrete prisms using the plate-bonding technique", International Journal of Fracture 82: 253–266, 1996, 1996 Kluwer Academic Publishers, Printed in the Netherlands.

Täljsten B., (1997), "Strengthening of Beams by Plate Bonding", Journal of Materials in Civil Engineering, November 1997, pp 206–212.

Täljsten B., (1998), Förstärkning av betongkonstruktioner med stålplåt och avancerade kompositmaterial utsatta för vridning, Forskningsrapport, Luleå tekniska universitet, Avdelningen för konstruktionsteknik, Institutionen för Vägoch vattenbyggnad, 1998:01, ISSN 1402-1528 (In Swedish).

Täljsten B. and Carolin A, (1999), "Strengthening of a concrete railway bridge in Luleå with carbon fibre reinforced polymers – CFRP: load bearing capacity before and after strengthening", Technical Report 1999:18, Luleå: Luleå University of Technology, Structural Engineering. 61 pp.

Täljsten B. (2003): "Strengthening of existing concrete structures with externally bonded Fibre Reinforced Polymers – design and execution". Technical report. Luleå University of Technology, Division of structural engineering.

Täljsten B. and Carolin A., (2001), "CFRP strengthening, Concrete beams strengthened with Near surface mounted CFRP laminates", FRPRC-5 in Cambridge UK, July 2001, ISBN: 0 7277 3029 0, 2001, pp 107–116.

Täljsten B. and Elfgren L, (2000) " Strengthening concrete beams for shear using CFRP-materials: evaluation of different application methods" Composites Part B: Engineering, Vol. 31, No. 2, March 2000, pp 87–96.

Wight R.G., Green M.F. and Erki M.A., 1995, "Post-strengthening concrete beams with pre-stressed FRP sheets". Non-metallic (FRP) Reinforcement for Concrete Structures 1995, ISBN 0 419 20540.

Wight G. and Erki M.A., 2001, "Pre-stressed CFRP for strengthening concrete slabs in fatigue", International Conference on FRP Composites in Civil Engineering CICE 2001 Ed. J.G. Teng, Hong Kong, ISBN: 0-08-043945-4.

FRP Composites in Civil Engineering – CICE 2004 – Seracino (ed)

Static behavior of 40 year-old prestressed concrete bridge girders strengthened with various FRP systems

O.A. Rosenboom, R.O. Carneiro, T.K. Hassan, A. Mirmiran & S.H. Rizkalla
North Carolina State University, Raleigh, NC, USA

ABSTRACT: This paper presents preliminary experimental results of a research program aimed at investigating the static behavior of 40 year-old prestressed concrete bridge girders strengthened with various Carbon Fiber Reinforced Polymer (CFRP) systems. Five 40 year old, 9.14 m long, prestressed bridge girders have been tested: one control and four specimens strengthened with various CFRP systems. Test results showed that there is virtually no difference in behavior between the control and the strengthened specimens up to yielding of the prestressing strands, which occurred well after the expected service loading level of the bridge. The measured ultimate strength was increased according to the design value based on finite element analysis. The behavior of the tested specimens was predicted using non-linear finite element analysis. Excellent agreement was observed between the measured and the predicted behavior up to failure. Cost-effective analysis was also performed for various CFRP strengthening techniques. Comparing the percent increase in ultimate strength to the cost of the strengthening procedure, near surface mounted (NSM) technique has proven to be the most cost-effective system.

1 INTRODUCTION

1.1 *Research objectives*

The primary objective of the research described in this paper is to provide the prestressed concrete industry as well as the departments of transportation with a value engineering and cost-effectiveness analysis of prestressed concrete bridge girders strengthened with various CFRP systems. The feasibility of using CFRP strengthening systems to upgrade the load carrying capacity of prestressed concrete bridges is investigated. Although there is an ever-expanding research database of reinforced concrete strengthened with different CFRP systems, the benefits of various strengthening techniques to prestressed concrete is limited (Hassan & Rizkalla 2002).

1.2 *Background*

The characterization of NSM strengthening systems with regards to performance has been well researched for reinforced concrete members (Hassan & Rizkalla 2002, De Lorenzis & Nanni 2001, De Lorenzis et al. 2000). It has been proven to be a viable, if not superior, alternative to externally bonded strengthening systems. With regards to prestressed concrete, externally bonded (EB) systems have been applied to aged prestressed girders (Takács & Kanstad 2000). NSM strengthening was carried out on prestressed slabs (Hassan & Rizkalla 2002). In both cases, performance gains were made with respect to ultimate load capacity. Debonding failure of externally bonded FRP systems were observed by many researchers most often at the termination point of the FRP strip/sheet for strengthened systems with a short span, and at the mid-span section for long span members. Many rational models predicting the failure loads of reinforced concrete members strengthened with FRP due to plate end debonding have been proposed (Smith and Teng 2001). Nevertheless, very little research work has been reported on the mid-span debonding mechanism (Wu & Niu 2000). Although of less concern in NSM systems, debonding models have been characterized from earlier plate-based work (Hassan & Rizkalla 2003).

2 EXPERIMENTAL PROGRAM

2.1 *Test specimens*

As part of the extensive research program sponsored by North Carolina Department of Transportation, five 40 year old 9.14 m long prestressed concrete bridge girders were tested at the Constructed Facilities Laboratory (CFL) at North Carolina State University (NCSU).

One specimen was tested as a control specimen, while the remaining four specimens were strengthened with NSM CFRP bars, strips and externally bonded CFRP strips and sheets. All five specimens were C-Channel type prestressed concrete bridge girders as

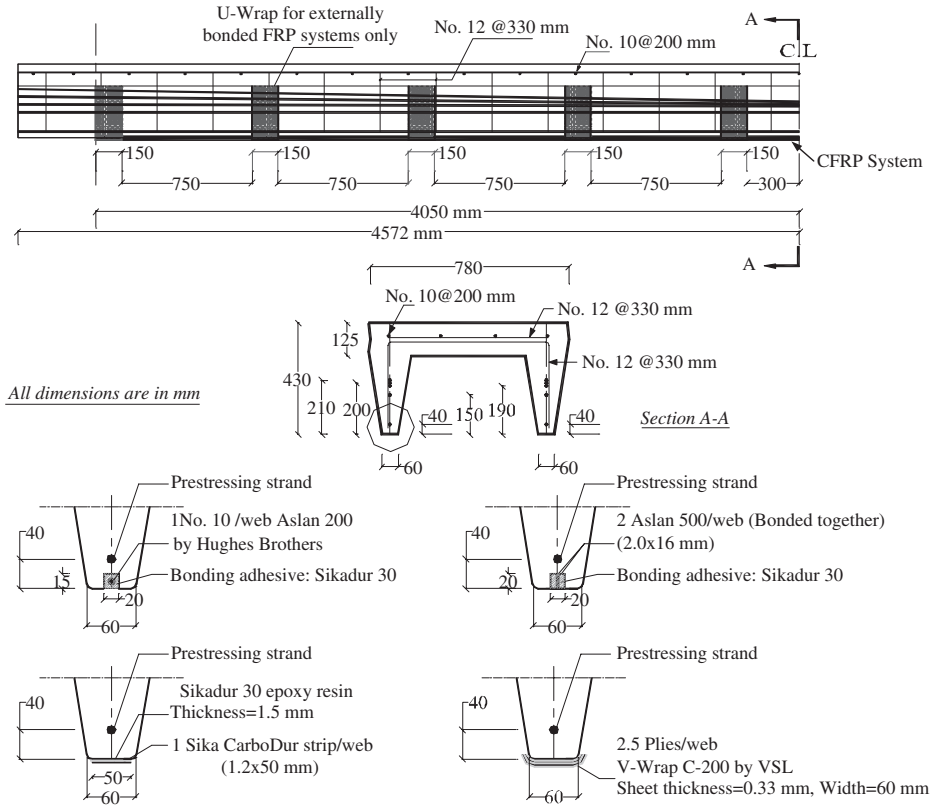

Figure 1. Plan and cross-section of C-channel girders.

shown in Figure 1. The girders were taken from the same bridge in Cartaret County, NC, USA, which was erected in 1961. The girders were in fair to good condition upon delivery. According to core samples tested per ASTM C42, the average compression strength of the concrete ranged from 48 MPa to 74 MPa. Each girder had ten 1725 MPa seven-wire stress relieved prestressing strands (five in each web) and a 125 mm deck with minimal reinforcing as shown in Figure 1. The wearing surface had been removed prior to delivery. The camber of the girders at mid-span due to prestressing and self weight was 40 mm.

Four different types of CFRP systems were applied to the two webs in each strengthened specimen: two were Externally Bonded (EB) and two were Near-Surface Mounted (NSM). Within the limits of the geometry of the supplied materials and specimen dimensions, they were all designed to achieve 30 percent increase in strength. The first EB system used one 50 mm wide Sika CarboDur strip per web, bonded using SikaDur 30 adhesive. The second EB system used two and a half 50 mm wide plies of VSL V-Wrap C-200 sheets per web bonded using VSL saturant. The first NSM system used one 10 mm Aslan 200 CFRP bar per web. The bars were provided by Hughes Brothers and were bonded using SikaDur 30 adhesive. The second NSM system used two 2 mm × 16 mm Aslan 500 strips per web provided by Hughes Brothers. The strips were bonded together prior to strengthening using SikaDur 30 adhesive. The strips were bonded to concrete using the same adhesive.

For the two EB systems, 150 mm wide U-wraps were provided at 900 mm spacing along the length of the girder to control the debonding mechanism. Figure 1 shows the reinforcement details and Table 1 provides the material properties of the CFRP systems along with the groove dimensions.

Table 1. Material properties of CFRP strengthening systems.

System	A_{FRP} (mm^2)	E_{FRP} (GPa)	f_{uFRP} (MPa)	w_G^* (mm)	d_G^* (mm)
NSM bars	130	124	2070	19	19
NSM strips	130	131	2070	19	19
EB strips	119	165	2800	–	–
EB sheets	84	228	3790	–	–

*w_G and d_G are the width and depth of the NSM groove, respectively.

2.2 *Design of strengthened specimens*

The design of the strengthened specimens proceeded after the testing of the control specimen. The objective of the strengthening was to achieve a 30 percent increase in the ultimate load carrying capacity in comparison to the control specimen. Each strengthened specimen was designed using a cracked section analysis program (Response 2000). The manufacturer's properties were used to model the FRP materials. The prestressing and mild steel reinforcing properties were taken from the provided specifications. The concrete strength was obtained from core samples. It was recognized that the EB systems are more prone to delamination compared to NSM systems. According to Malek et al. 1998, the shear stresses at the cut-off points of the CFRP sheets/strips were significantly less than the shear strength of the concrete. Therefore, plate-end debonding should not be a concern. To delay delamination-type failures along the length of the girder, 150 mm wide U-wraps were provided at 900 mm spacing. This arrangement of the U-wraps was selected to simulate typical anchorage details commonly used for reinforced concrete members.

2.3 *Test setup/instrumentation/loading*

The girders were tested using a 490 kN MTS hydraulic actuator mounted to a steel frame placed at the midspan of the girder. To simulate loading on an actual bridge, a set of truck tires filled with silicon rubber filler were used to apply the load from the actuator. The footprint of the two tires was approximately 250 mm × 500 mm per the AASHTO specified loading area (AASHTO 2003). The supports for the girders on either side included a 64 mm thick neoprene pad, a 25 mm thick steel plate and hydrostone used for leveling purposes. The width of the neoprene pads was 216 mm, which yielded a clear span for the girder of 8710 mm.

The behavior of the girders during testing was monitored using a set of string potentiometers placed at midspan, quarter span and at the ends to measure the deformation in the neoprene pads. The compressive strain in the top concrete surface was measured using a combination of PI gauges and strain gauges placed around and between the loading tires. PI gauges were placed at the level of the lowest prestressing strands to measure the crack width. Six strain gauges were applied to the CFRP reinforcement. The specimens were loaded up to a load level of 20 kN and unloaded and then reloaded again up to failure with a rate of 2.5 mm/min. This loading scenario was used to determine the effective prestressing force in the girders by observing the reopening of the flexural cracks (Zia & Kowalsky 2002). Based on test results, the effective prestressing per strand ranged between 67 to 80 kN. After yielding of the prestressing strands, the loading rate was increased to 5 mm/min.

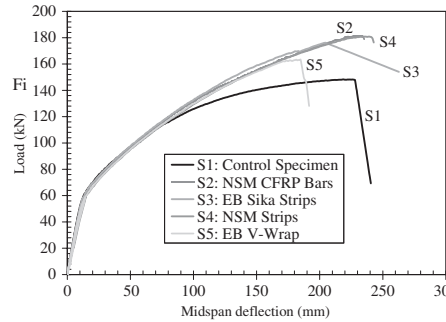

Figure 2. Load–deflection behavior of the test specimens.

2.4 *Test results – control specimen*

All the tested girders were uncracked prior to testing. Cracking of the control specimen occurred at a load level of 61.5 kN. Flexural cracks were evenly distributed along the length of the girder. It was observed that steel stirrups acted as crack initiators even for the strengthened specimens. Yielding of the prestressing strands took place at a load level of 115 kN based on the PI gauge readings. The specimen failed due to concrete crushing at a load 148 kN with an ultimate displacement of 228 mm. The average crack width at failure was 1.9 mm according to the PI gauge readings on the tension face. Due to confinement effects at the loading zone, crushing occurred first at the edge of the girder at midspan slightly before it occurred underneath the loading tires. The load–deflection behavior as well as the load-concrete compressive strain behavior are shown in Figures 2 and 3, respectively. Both of these plots do not include the camber of the girder. The concrete compressive strain at failure, ε_{cu}, was 0.0029. Test results are summarized in Table 2.

2.5 *Test results – strengthened specimens*

Test results for the strengthened systems are summarized in Table 2 and shown in Figures 2–4. Brief descriptions of each test are provided below.

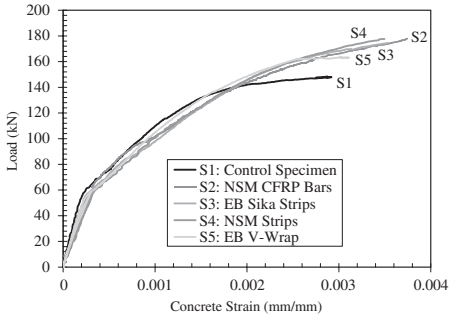

Figure 3. Load-concrete strain behavior of the test specimens.

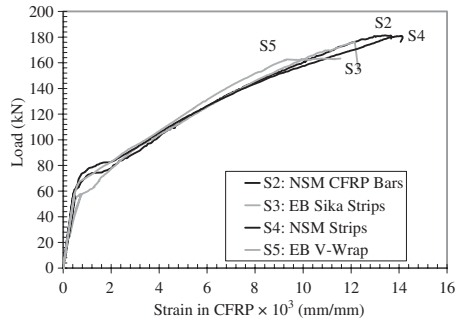

Figure 4. Load versus tensile strain in CFRP for strengthened specimens.

Table 2. Summarized test results.

System	f'_c (MPa)	P_e (kN)	P_{ult} (kN)	P_{cr} (kN)	ε_{FRP} (mm/mm)	ε_{cu} (mm/mm)	I (%)
Control	74	72	148	61.5	–	.0029	–
NSM bars	66	80	181	55.0	.0137	.0036	22
NSM strips	60	69	182	55.0	.0146	.0035	23
EB strips	48	72	176	57.0	.0122	.0034	19
EB sheets	51	67	163	57.0	.0117	.0026	10

where f'_c is average compressive strength of the concrete based on core tests; P_e is the measured effective prestressing force per strand; P_{ult} is the ultimate load carrying capacity of the test specimen; P_{cr} is the cracking load; ε_{FRP} is the maximum measured tensile strain in the FRP reinforcement at ultimate; ε_{cu} is the maximum measured compressive strain in the concrete at ultimate and I is the percentage increase in ultimate capacity compared to the control specimen.

Figure 5. Typical failure due to concrete crushing of the specimens strengthened with NSM CFRP systems.

2.5.1 *NSM CFRP systems*

Both NSM Strengthened systems performed similarly during testing. Both specimens experienced flexural cracking at a load level of 55 kN. The initial stiffness of the strengthened systems was identical to that of the control specimen, as was the postcracking stiffness. After yielding of the prestressing strands, presence of the CFRP reinforcement constrains opening of the cracks and consequently reduced the deflection compared to the control specimen. The flexural cracks were spaced closer together than the control specimen. The failure of both girders strengthened with NSM CFRP reinforcement was due to concrete crushing followed by debonding of the NSM CFRP reinforcement at a load of 180 kN for the NSM bars and 181 kN for the NSM strips as shown in Figure 5. Since the ultimate strain in the concrete controlled the failure mode of both specimens, the curvature and consequently, the deflection at ultimate were very similar.

Test results showed that strengthening of the prestressed girders using NSM CFRP bars and strips increased the ultimate load carrying capacity by 22 and 23 percent, respectively. The maximum measured tensile strain in the NSM CFRP bars and strips at failure was 81 and 86 percent of the manufactured rupture strain, respectively.

2.5.2 *EB CFRP systems*

The performance of both prestressed concrete girders strengthened with externally bonded CFRP strips and sheets matched those strengthened with NSM systems and the control specimen before and after cracking. Flexural cracking at mid-span was observed at a load level of 57 kN for both specimens. The flexural crack spacing was similar to that of the NSM systems up to failure. For the EB CFRP strips, failure occurred due to midspan debonding of the strips between the provided U-wraps at a load level of 176 kN. The debonded length extended 3700 mm from midspan as shown in Figure 6.

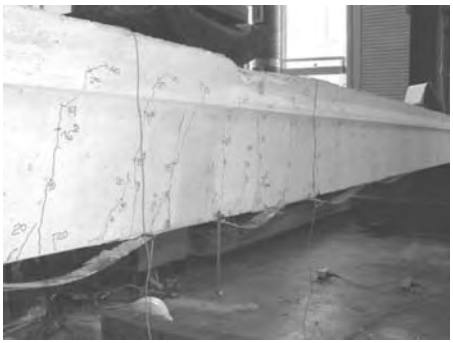

Figure 6. Debonding of externally bonded CFRP strips.

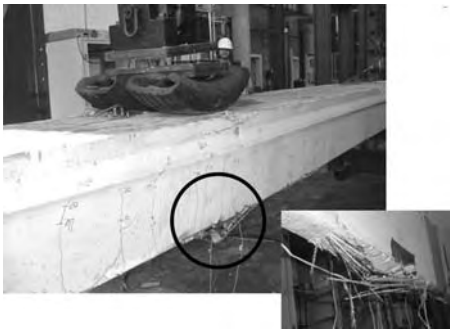

Figure 7. Rupture of externally bonded CFRP sheets.

Delamination occurred at the concrete substrate. However, in some areas debonding at the FRP-adhesive interface was observed possibly due to a poor bond during installation. For the EB CFRP sheets, failure was due to rupture of the sheets at midspan at a load of 163 kN as shown in Figure 7. After failure it was also noted that the sheets had debonded over a distance of approximately 500 mm from midspan. The maximum measured tensile strain in the CFRP sheets at failure was 1.17 percent, which is 70 percent of the manufacturer's guaranteed rupture strain. Compared to the control specimen, the EB CFRP strips and EB CFRP sheets achieved an increase in the ultimate load carrying capacity of 19 percent and 10 percent, respectively.

Figure 8 shows the applied load versus crack width relationships for the tested specimens. Comparable crack widths were observed for all the strengthened specimens. Strengthening of prestressed concrete members using FRP systems decreased the crack width at ultimate by 20–40 percent in comparison to the control specimen.

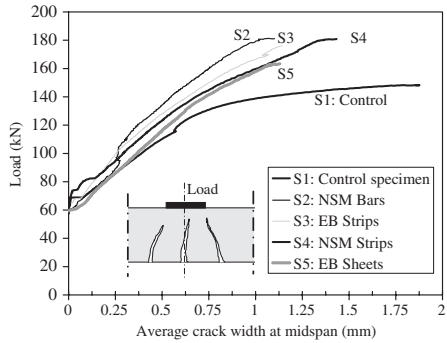

Figure 8. Average crack width for the prestressed concrete girders.

3 ANALYTICAL MODELING

3.1 *Non-linear finite element model*

The control specimen as well as the specimen strengthened with NSM CFRP bars (S1 and S2) were analyzed using non-linear finite element program. The finite element modeling described in this paper was conducted using the ANACAP program (Version 2.1). ANACAP software employs the classical incremental theory of plasticity that relates the increment of plastic strain to the state of stresses and stress increment (James 1997). The concrete material is modeled by the smeared cracking methodology in which progressive cracking is assumed to be distributed over an entire element (Gerstle 1981). The reinforcement is assumed to be distributed throughout the concrete element. The analysis is conducted using an incremental-iterative solution procedure, in which the load is incrementally increased. Within each increment equilibrium is iteratively achieved. At the end of each step, the ANACAP program adjusts the stiffness matrix to reflect the nonlinear changes in the stiffness. Verification of the ANACAP program using independent experimental results can be found elsewhere (Hassan et al. 2000).

3.2 *Modeling of the C-channels*

Figure 9 shows the mesh dimensions used in the finite element model. Due to symmetry, one quarter of the girder was modeled as shown in Figure 9. The concrete was modeled using 20-node isoparametric brick elements. Each node has three translational degrees of freedom. The compressive strength of the concrete as well as the effective prestressing in the strands were set identical to the measured values, given in Table 2. The wheel load was applied as uniform pressure acting on the top of the girder. The load was applied gradually using step-by-step analysis up to failure.

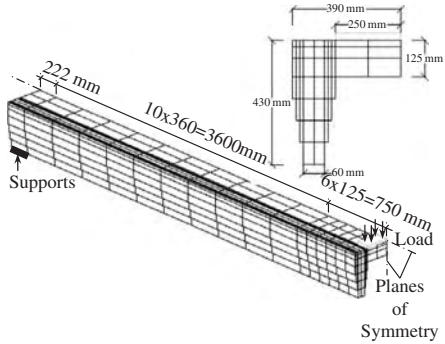

Figure 9. Mesh dimensions used in the finite element model.

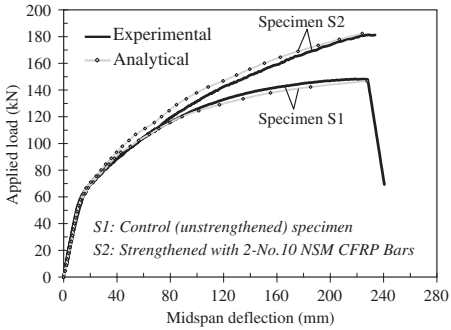

Figure 10. Predicted and measured load–deflection behavior of the C-channels.

The predicted load-deflection behavior for specimens S1 and S2 compared to the experimental results is shown in Figure 10. The predicted values matched the experimental results with a sufficient accuracy. Failure occurred due to crushing of the concrete at the mid-span section. The predicted failure loads were within one percent of the measured values for both specimens. The tensile strain in NSM CFRP bars at a distance of 600 mm from the mid-span section was predicted using non-linear finite element analysis. The results were compared to the measured values as shown in Figure 11.

The predicted values compared well with the experimental results up to a load level of 150 kN, beyond which the experimental results were slightly less than the predicted values. This could be attributed to possible slippage of the NSM CFRP bars from the surrounding adhesive. Such a phenomenon was not considered in the analysis as a perfect bond was always assumed between the concrete and the reinforcement.

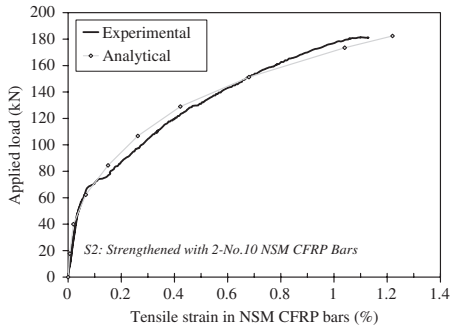

Figure 11. Predicted and measured load-tensile strain behavior of NSM CFRP bars.

4 COST-EFFECTIVENESS ANALYSIS

The benefits of NSM CFRP reinforcement for strengthening were clearly highlighted in the previous sections. The advantage of using this system in comparison to the EB system is obvious. Nevertheless, it may not be the most cost-effective solution due to the time consumed in cutting of the grooves and other installation requirements.

To closely resemble field conditions, the strengthening was conducted while the girders were placed side by side as they would be on a bridge, supported by a steel substructure provided by the NCDOT. The strengthening started in February when night-time temperatures were below those recommended for curing of adhesive by its manufacturer. Therefore a plastic enclosure was provided as well as propane heaters. This cost was assumed to be similar for all types of bridges repaired under these conditions and was not included in the analysis.

To determine the cost-effectiveness of each strengthening technique the following items were considered: (1) labor cost of the professional FRP applicators, (2) time taken to complete all tasks, (3) material costs and (4) equipment used for strengthening. The material costs include all primers, adhesives and CFRP that may be required in a field application. Equipment items included in Table 4 are the rental of the sandblasting pot, compressor and the purchase of two 180 mm diamond saw blades used to cut the grooves. All other equipment (such as grinders, mixers, safety equipment, etc) is either assumed to be provided by the contractor or used equally in each of the strengthening systems. These values in Tables 3 & 4 should be used for comparison purposes only.

The cost analysis indicated that the most cost-effective systems (when comparing the variables described above and the percent increase in ultimate strength of the specimen) were the NSM systems.

Table 3. Strengthening cost – labor.

Task	NSM bars (hrs)	NSM strips (hrs)	EB strips (hrs)	EB sheets (hrs)
Groove cutting	11	11	–	–
Surface preparation	1.25	1.25	3.88	3.88
Lay-up	5.63	6.13	10	9.75
Total/beam	17.9	18.4	13.9	13.6
Total/meter*	2.17	2.23	1.69	1.66
$/meter**	97.65	100.35	76.05	74.70

* Based on a strengthened length of 8.23 m.
** Based on an assumed labor cost of $45/hour.

Table 4. Strengthening cost – materials/equipment/ summary.

Task	NSM bars ($/m)	NSM strips ($/m)	EB strips ($/m)	EB sheets ($/m)
Adhesive, primer, etc	21.44	21.44	16.48	8.54
CFRP	24.4	18.55	198.72	19.53
Equipment*	5.47	5.47	0.00	0.00
Sandblaster rental	2.40	2.40	7.44	7.44
Total/meter (mat&equip)	53.72	47.87	222.65	35.51
Total cost/meter*	151.37	148.22	298.70	110.21
Cost effectiveness**	14.5	15.5	6.4	9

* Including labor costs above.
** Based on (% increase in ultimate strength)/(Cost per meter) $\times 100$.

Although being more labor-intensive to install, the CFRP and adhesive are cheaper per meter than the EB systems and the percent increase in ultimate strength is greater. Of the EB systems, the CFRP sheets showed the least increase in ultimate capacity. However, the inexpensive material costs made it more cost-effective compared to the externally bonded CFRP strips.

5 CONCLUSIONS

Five 40 year old 9.14 m long prestressed girders have been tested under static loading: one control and four strengthened with different CFRP systems. Based on the results, the following conclusions can be drawn:

1. The ultimate strength of prestressed concrete members can be substantially increased using FRP strengthening systems. The ultimate load carrying capacity of aged prestressed girders tested in this research program increased by as much as 23 percent in comparison to the control specimen according to the design value.
2. Serviceability could not be used as a criterion to compare the efficiency of various FRP strengthening techniques for prestressed concrete members, since negligible differences were observed among the various techniques at the service load level.
3. The selected configuration of U-wraps enhanced the behavior of the strengthened prestressed girders and delayed delamintaion of externally bonded CFRP strips and sheets.
4. Using NSM or EB FRP systems reduced the crack width at ultimate by 20–40 percent compared to the unstrengthened specimen.
5. Defining cost-effectiveness as the percent increase in ultimate capacity divided by the cost of the strengthening, the most cost-effective systems are those which utilize NSM strengthening. Externally bonded CFRP strips is the least cost-effective system compared to the other techniques.
6. The behavior of the aged unstrengthened as well as strengthened prestressed concrete girders can be well predicted using a non-linear finite element analysis.

ACKNOWLEDGEMENTS

The authors would like to acknowledge the support of the North Carolina Department of Transportation through Project 2004-15, National Science and Engineering Research Council of Canada and the National Council of Scientific and Technological Development, CNPq, Brazil. Several industry members made appreciated material donations: David White of the Sika Corporation and Doug Gremel of Hughes Brothers. In addition, Structural Preservation Systems carried out the strengthening work and provided the VSL materials. The authors would also like to thank Jerry Atkinson, the technician at the Constructed Facilities Laboratory, whose help was invaluable.

REFERENCES

American Society for Testing and Materials, 2003. Standard Test Method for Obtaining and Testing Drilled Cores and Sawed Beams of Concrete. *ASTM C42-03.*

De Lorenzis, L.A., Nanni, A. & La Tegola, A. 2000. Flexural and Shear Strengthening of Reinforced Concrete Structures with Near Surface Mounted FRP Rods. In J. Humar and A.G. Razaqpur (eds), *Proc., 3rd International Conference on Advanced Composite Materials in Bridges and Structures, Ottawa, Canada, 15–18 August 2000*.

De Lorenzis & Nanni, A. 2001. Characterization of FRP Rods as Near-Surface Mounted Reinforcement. *Journal of Composites for Construction* 5(2): 114–121.

Gerstle, K.H. 1981. Material modeling of Reinforced Concrete. IABSE Colloquium on Advanced Mechanics

of Reinforced Concrete, Introductory Report, Delft, Netherlands, 1981.

Hassan, T., Abdelrahman, A., Tadros, G., and Rizkalla, S. 2000. FRP Reinforcing Bars For Bridge Decks, Canadian Journal for Civil Engineering 27(5): 839–849.

Hassan, Tarek & Rizkalla, Sami, 2003. Investigation of Bond in Concrete Structures Strengthened with Near Surface Mounted Carbon Fiber Reinforced Polymer Strips. Journal of Composites for Construction 7(3): 248–257.

Hassan, Tarek & Rizkalla, Sami, 2002. Flexural Strengthening of Prestressed Bridge Slabs with FRP Systems. PCI Journal, Jan 2003: 76–93.

James, R.G. 1997. ANACAP Concrete Analysis Program Theory Manual Version 2.1. Anatech Corp., San Diego, CA, 1997.

Malek, A.M., Saadatmanesh, H. & Ehsani, M.R. 1998. Prediction of Failure Load of RC Beams Strengthened with FRP Plate Due to Stress Concentration a the Plate End. ACI Structural Journal. 95(1): 142–152.

Smith, S.T. & Teng, J.G. 2002. FRP Strengthened RC Beam I – Review of Debonding Strength Models. *Engineering Structures* 24(4): 385–395.

Smith, S.T. & Teng, J.G. 2002. FRP Strengthened RC Beam II – Assessment of Debonding Strength Models. *Engineering Structures* 24(4): 397–417.

Takács, P.F. & Kanstad, T. 2000. Strengthening prestressed concrete beams with Carbon Fiber Reinforced Polymer plates, *NTNU Report R-9-00*, Trondheim, Norway, 2000

Wu, Zhishen & Niu, Hedong 2000. Study on Debonding Failure Load of RC Beams Strengthened with FRP Sheets. *Journal of Structural Engineering*. 46(3).

Zia, P. & Kowalsky, M.J. 2002. Fatigue Performance of Large-Sized Long-Span Prestressed Concrete Girders Impaired by Transverse Cracks. *Federal Highway Administration Report*, FHWA/NC/2002–024.

FRP Composites in Civil Engineering – CICE 2004 – Seracino (ed)

Bridge strengthening with prestressed CFRP plate systems

D. Millar & P. Scott
Sika Australia Pty. Ltd., Sydney, Australia

R. Clénin
Sika Services AG, Zurich, Switzerland

ABSTRACT: Thanks to intensive research and development projects at the Swiss Federal Laboratories for Material Testing and Research (EMPA) in Dübendorf, Switzerland and at Sika, a composite strengthening system with externally bonded CFRP plates were developed and successfully applied to strengthen the Ibach bridge in 1991 in Switzerland. This paper presents a new technique to strengthen reinforced concrete structures with prestressed bonded and/or non-bonded CFRP plate systems with worldwide applications especially for bridge strengthening.

1 INTRODUCTION

Flexural strengthening of concrete structures with CFRP plate systems are state-of-the-art nowadays. Design regulations, recommendations and national standards (ACI-440, fib, CSA S806, JBDPA, etc.) have been established, and the use of non-prestressed CFRP plate systems is already common in the construction industry. Numerous tests world-wide have shown that 60% maximum of the tensile strength of CFRP plates can be mobilised in ultimate limit state (ULS) because the bond strength which depends primarily on the tensile strength of the concrete cover is insufficient to develop the tensile strength of CFRP plates.

2 PRESTRESSED CFRP PLATES

In 1993, Deuring [1] was the first to succeed in prestressing CFRP plate at EMPA Laboratories. The system is based on the principle of a stationary "violin bow". However this tensioning system is not suitable for site application.

Appropriate anchoring of prestressed CFRP plates into concrete is the way to exploit the full range of its high strain capacity in the ultimate limit state. Prestressing of plates allows you to:

- reduce stresses in re-bars in Service Limit State
- increase of the stiffness of structures
- increase flexural strength sensibly
- balance dead and permanent loads
- compress cracked concrete sections
- open new opportunities for CFRP systems

These were the reasons why, together with its consultants and industrial partners, Sika developed & tested systems for prestressing CFRP plates.

3 LEOBA CARBODUR SYSTEM

Table 1. System information.

CarboDur CFRP plate	V914	E-Modulus, min.	165 GPa
Dimension	90 × 1.4 mm	Pre-tensioning strain	0.95%
Cross-section	126 mm^2	Tensioning force	200 kN
Tensile strength, min.	2800 Mpa	First application	2001

3.1 *Anchorage systems*

The conception of anchorage consists of temporary anchors during prestressing of plates and the final permanent anchors. The temporary anchor is a friction anchor where the CarboDur plate is clamped between bolted steel plates and the prestressing force is transmitted with sufficient margin of safety by simple friction. Only permanent anchor needs to develop in ULS the full strength, therefore it is a combination with clamping and bonding [2]. The operation procedure of prestressing on site is:

- Provide recesses in concrete, place anchor plates on epoxy mortar, install tilt-up bolts
- Install temporary fix and moving anchors

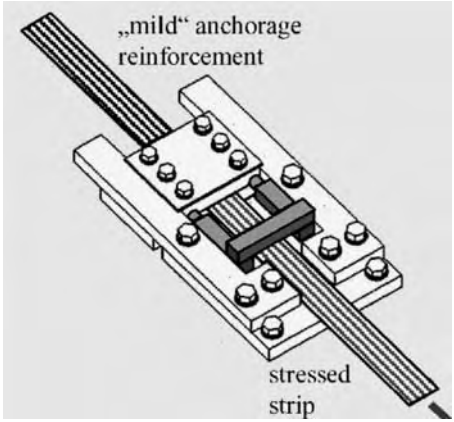

Figure 1. Live anchor, stressing jack.

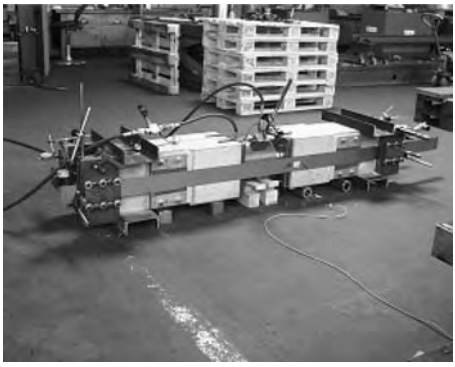

Figure 2. Testing of anchorage.

- Prestress and install permanent anchors
- Remove temporary spacer after curing of epoxy adhesive

3.2 *Anchorage tests*

Tests for temporary and permanent anchors were performed at the Institute of Structural Concrete and Building Materials at the University of Leipzig with a “push-apart” test set up consisting of two concrete blocks in line with an intermediate jack. The concrete blocks are symmetrically connected at two opposite faces with CFRP plates. In this way it was possible to test 4 anchorages simultaneously. CFRP plates were stressed by pushing apart the concrete blocks with the intermediate jack and the permanent anchor is installed by bonding and clamping after the prestressing force has been applied.

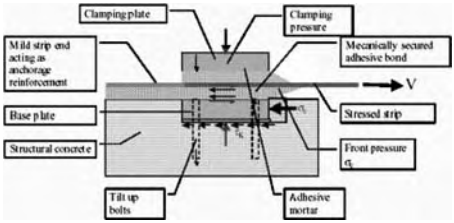

Figure 3. Load transfer – principle.

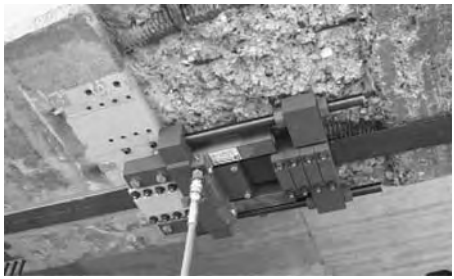

Figure 4. Jack with temporary & permanent anchors.

Figure 5. The Koerschtal bridge.

Test results showed an excellent behavior of anchorages because the failure always happened in CFRP plates, i.e. the system meets the same qualification standards as any other system using steel bars, strands or wires.

3.3 *Introduction of prestressing*

The prestressing force is transmitted into concrete by both, bond of the epoxy adhesive mortar underneath

Figure 6. Prestressing in progress.

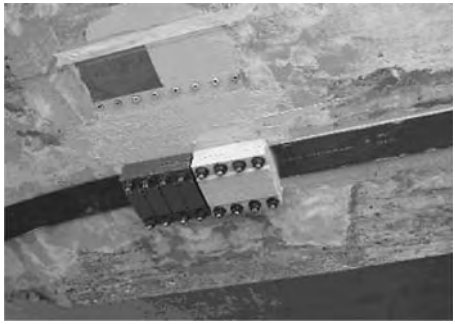

Figure 7. Temporary & permanent anchors.

the steel base plate, and the front face of the plate. The tilt up moments are borne by bolts which are also used to fix the base plate during curing of the epoxy adhesive.

3.4 *Hydraulic jack*

A horseshoe jack with a stress capacity of 225 kN was developed comprising two pistons connected by a transverse steel bar which is easy to use and handle when access is difficult.

After jacking, the temporary anchor is fixed by means of a cross beam supported by two threaded bars during the curing of the epoxy adhesive of the permanent anchor so that the jack can be removed immediately.

3.5 *Case studies*

Rehabilitation of Koerschtal Bridge Stuttgart, Germany

A seven span prestressed concrete bridge built in 1964 was cast in three segments so that the longitudinal cables were coupled in construction joints [3]. Cracks

Figure 8. Applied CarboDur CFRP plates.

Table 2. System information.

CarboDur CFRP plate	S624
Dimensions	60 × 24 mm
Cross-section	144 sqmm
Tensile strength, min.	2800 Mpa
E-modulus, min.	165 GPa
Pre-tensioning strain	0.95%
Tensioning force	220 kN
Anchor dimensions	60/80 × 110 mm

have been observed in all these bridge sections. Structural analysis showed that with actual traffic loads and temperature effects the fatigue resistance of the cable coupler became critical. For the rehabilitation of the Koerschtal bridge, 5 tendons with a length of 8 m were applied to each main girder. Local cracks were closed due to this prestressing force of appr. 900 kN per girder.

4 STRESSHEAD SYSTEM

The Sika-StressHead in an non-bonded or bonded prestressing system for CFRP plates. The tendon consists of a CFRP plate connected to two CFRP made end anchors, called StressHead as shown in Fig. 9.

4.1 *Anchorage system*

The conception of fixed and movable anchorages is guided by the idea of having a simple and flexible system adaptable for each project. They are made of structural steel [4,5]. The prestressing force is introduced into a concrete structure by a circular steel profile acting as a dowel with a diameter of 116 mm and 200 mm length placed into a drilled hole.

4.2 *Laboratory testing*

The objective of all tests is to assure that the system will perform its function when applied to the structure.

Figure 9. StressHead with CarboDur plate.

Figure 10. Fixed anchorage.

Figure 11. Special designed movable anchorage for redirection.

4.2.1 *Short-term tests*

Tendons are tested in a universal machine as follows:

Overall displacement, force, strain in the CFRP plate and slip between anchor and CFRP plate are

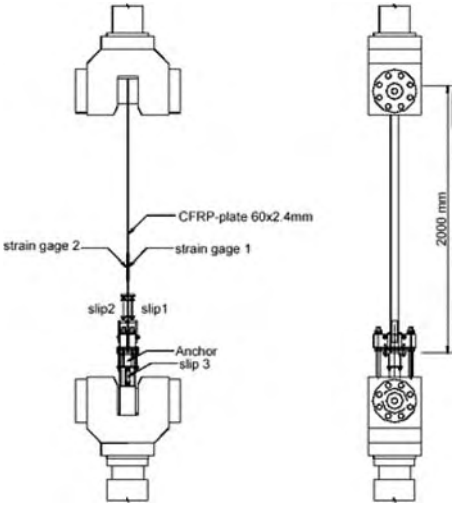

Figure 12. Test layout for short-term test.

Figure 13. The Huettenbridge.

measured continuously. The ultimate tensile strength, specified to be at least 75% of the tensile strength of plate, was reached in all test specimens.

4.2.2 *Cyclic load tests*

The objective of these tests is to test whether the anchor is able to withstand cyclic loading [6]. The load parameters were:

- Working stress = stress at prestressing
- Stress amplitude: f = 200 N/sqmm
- Number of cycles: 200'000
- Frequency: appr. 1 Hz

Tests showed that there is no displacement-slip between CarboDur plate and StressHead anchor.

Figure 14. View under the bridge.

Figure 15. 30 m of prestressed CFRP plate.

Figure 16. Anchorage on the tension side.

Figure 17. Connection through cross the girders.

4.2.3 *Long-term tests*

As for the cyclic load tests, it's the anchor that is of interest and not the plate itself. Creep of the CFRP can be ignored compared to possible slippage between the anchor and the CFRP plate. As the anchor is not of glue-filled pot type but uses wedges made of CFRP, creep does not cause serious problems. The first test results show that immediately after stressing some slippage between anchor and CFRP plate occurs. But after a short time, increase in slippage can be ignored.

4.3 *Case studies*

Huetten – Bridge Wertehnstein near Luzern, Switzerland

Narrow access road to an industrial area, crossing a river.

The only way for trucks to get into the industrial forest region near Werthenstein leads over a small bridge, built in the 1950's. This bridge was designed for a maximum load of 16 tons. Due to the traffic load increase in Switzerland, the bridge had to be upgraded to 40 tons. Further options were either to replace the bridge or restrict it to larger trucks. The bridge owner and project engineer decided to upgrade the bridge with pre-stressed CFRP material based on a cost – lifecycle analysis.

The decisive factors were easy installation, no corrosion problems with the tendon, its thin geometry and the possibility of making a prestressing on an existing structure with the compound effect of the CFRP plate bonded to the substrate compared to the other alternatives. With the StressHead prestressing system, all the requirements could be fulfilled. The possibility of connecting tendons through cross girders was used successfully for the first time (see also drawing Fig. 16). The bridge was prestressed with a total force of 800 kN over the total length of 30 m.

In addition to the flexural upgrading, the existing shear reinforcement, which consisted of 45° offset reinforcement, was not sufficient for the increased load. Shear reinforcement with up to 12 layers of heavy

Figure 18. Anchorage on the fix side.

Figure 19. Cutting of the slits for shear reinforcements.

carbon fabric have been used, wrapped totally around the girders for proper anchorage.

Number of prestressed tendons: 6
Length of prestressed tendon: 30 m, 15 m

Sung San Bridge, Seoul, Korea
Situated in City of Seoul this bridge is a reinforced concrete continuous frame and a two-way bridge deck with inclined haunch, which has 8 spans with 15,00 m of length and a width of 17,00 m. On a distance of approx. 1.50 m from the support axis #5 it was stated a

Figure 20. Impregnation of fabric (shear reinforcement).

Figure 21. Fabric wrapped around the girders.

Figure 22. Applied Sika-StressHead tendons.

large, through-crack in the bridge deck. With an appropriate disposition of prestressed CFRP plates on the whole width and length of the span, the necessary flexural strength of the critical section was re-established. Due to the prestressing the cracks were compressed.

In order to simplify and to accelerate the intervention on job site, unbonded prestressed tendons were applied.

Number of prestressed tendons: 11
Length of prestressed tendons : 11,80 m

5 CONCLUSIONS

Two systems with bonded and/or non-bonded CFRP plates were presented including a short overview of system testing in laboratories before proceeding with strengthening application of reinforced concrete structures, especially bridges. These systems exploit the full tensile strength of the very high strength of CFRP plates and because of their efficient anchorage, they open new opportunities of CFRP in competition with steel tendons. To prove that, the case studies which were presented are the best evidences.

ACKNOWLEDGMENT

The authors acknowledge the assistance of Mr. Hans-Peter Andrä, PhD. CEO Leonhardt, Andrä & Partner of Stuttgart, Germany and Mr. Gregor Schwegler, PhD, CEO StressHead Ltd. of Lucerne, Switzerland, in preparation of this paper and providing photos, diagrams etc.

REFERENCES

[1] M.Deuring: Verstärken von Stahlbeton mit gespannten Faserverbundwerkstoffen, Diss.ETH Nr.10199, Zürich 1993
[2] H-P.Andrä, M.Maier: Post-strengthening with Externally Bonded Prestressed CFRP Strips. IABSE Congress Lucerne, 2000, pp. 382–383
[3] H-P.Andrä, G.König, M.Maier: First Application of CFRP Tendons in Germany. IABSE Symposium, Melbourne 2002, pp. 370–371
[4] G.Schwegler, T.Berset: The use od prestressed CFRP-Laminates as post-strengthening. IABSE Congress Lucerne, 2000, pp. 370–371
[5] G.Schwegler, T.Berset: Methods for strengthening reinforced concrete structures, IABSE Symposium, Melbourne 2002, pp. 318–319
[6] ASTRA Development Project No.83/99/A “Spannverankerung für CFK-Lamellen”

FRP Composites in Civil Engineering – CICE 2004 – Seracino (ed)
© 2005 Taylor & Francis Group, London, ISBN 90 5809 638 6

CFRP strengthened openings in two-way concrete slabs

O. Enochsson[1], T. Olofsson[1] & B. Täljsten[1,2]
[1] *Division of Structural Engineering, Luleå University of Technology, Luleå, Sweden*
[2] *Skanska Teknik AB, Solna, Sweden*

ABSTRACT: Strengthening with FRP composites has existed for over a decade, and the most common way to strengthen structures is in bending where the design is more or less straightforward. Another common application for FRP strengthening is to strengthen slabs or walls before holes are made. In these situations, FRP fabrics are very suitable. After coating the wall or slab, the hole is made where after the strengthening material takes up the additional loads. However, there have not been many studies reported on slabs with holes strengthened with CFRP and especially, not when a distributed load has been applied.

In this project, laboratory tests are carried out. Two-way full-scale concrete slabs have been tested with a made hole that have been strengthen or repaired with CFRP fabrics and loaded with a uniform load. The strengthened slabs are compared to an as-built homogeneous slab, slabs as built with a hole and slabs weakened by a made hole. The study shows that it is fully possible and quite effective to strengthen or repair openings in slabs with CFRP fabrics.

1 INTRODUCTION

Advanced composites have been applied in a number of repair and strengthening projects (Täljsten 1997), (Täljsten & Elfgren 2000), (Nordin et al 2002) and (Carolin et al 2002). The area of composites in construction, and in particular for strengthening, has been one of the fastest growing new areas within civil engineering during the last 10 years. Much focus and effort has been placed on understanding the behavior of Fiber Reinforced Polymers (FRP) strengthen concrete structures. The question then is why advanced composites are suitable for civil engineering applications. FRP composite materials have a number of advantages when compared to traditional construction materials such as steel, wood and concrete. FRPs offer excellent corrosion resistance to environmental agents as well as the advantages of high stiffness-to-weight and strength-to-weight ratios when compared to conventional construction materials. Perhaps the biggest advantage of FRPs is tailorability. Reinforcement can be arranged according to the loading conditions so that a FRP structure or a component can be optimised for performance. Even though strengthening with FRP composites has existed for over a decade, still the most common way to strengthen structures is in bending where the design is more or less straightforward, however structures are also strengthened due to confinements and to some extent for shear.

One common application is to strengthen slabs and walls before holes are made. In these situations, FRP fabrics are very suitable and after coating the wall or slab, the hole is made, see Figure 1. However, there has not been many studies reported on slabs with holes strengthen with Carbon Fiber Reinforced Polymers (CFRPs), (Vasques & Karbhari 2002), and especially, not when a distributed load has been applied, (Mosallam & Mosalam 2002).

Figure 1. Strengthening before holing of a ventilation shaft in an existing structure due to a changed area of use. Stabilator AB.

2 AIM AND SCOPE

The scope of this research project is to examine CFRP strengthening of holes in walls or slabs. The main aim

of the presented work is to widen the knowledge about CFRP composites as a material for strengthening or repair of made holes particularly in two-way concrete slabs, but the results can be translated in some extent to one-way concrete slabs and concrete walls, too.

The analytical and the experimental work are focused to analyze the safety and ability of CFRP composites to take up the additional section forces caused by the hole in the concrete slab. Especially, the aims are to:

1 Clarify if the design method to calculate the amount of CFRP laminates for strengthen a made hole in an existing concrete slab, used today in Sweden, gives a load-capacity equivalent to an as-built homogeneous slab.
2 Indicate if deficient or deteriorated structures can be restored to its original load-capacity by a repair with CFRP composites.
3 Investigate the strengthened or repaired slabs ductility in order to generate ample visual warnings before ultimate collapse i.e. if the safety can be secured by a ductile behaviour.

3 EXPERIMENTAL PROGRAM

The experimental program consisted of full-scale concrete slab specimens loaded to failure using a uniform load. The objective was to compare the result from experiments on corresponding slabs:

1 With no hole.
2 With as built holes strengthened with traditional reinforcement according to Swedish design rules.
3 With sawed up holes strengthened with CFRP designed to reach the same effect as traditional reinforcement.

The experimental program was limited to quadratic slabs with a side length of 2.6 m, a thickness of 100 mm and with two different sizes of holes, 0.85 × 0.85 m and 1.2 × 1.2 m.

3.1 *Test setup*

To receive a uniform load distributed on the slab surface a new unique test-rig was designed where the loading was applied through an airbag system.

Three different airbags were manufactured, one for the tests with no holes and the other two were used in testing slabs with holes. The underlying air-bag was embedded by an exterior and interior structure to concentrate the load on the slab surface, see Figure 2.

The test slabs were simply supported along its four edges. The loading surface of 2.4 × 2.4 m extended from the edge of the hole out to the supported edges. Four load cells measuring the reaction forces coming from the line support in each corner measured the uniform load. The support construction was designed for a load greater than three times the original design load for the homogeneous slab, to take up the pressure from the airbag. Since the slab was loaded "upside-down", springs was mounted on each corner to eliminate the weight of the heavy support construction from the load reading. However, the loading method with an airbag system is well tested at Luleå University of Technology in Sweden, and has previously been used quite extensively on tests of roof sheeting profiles.

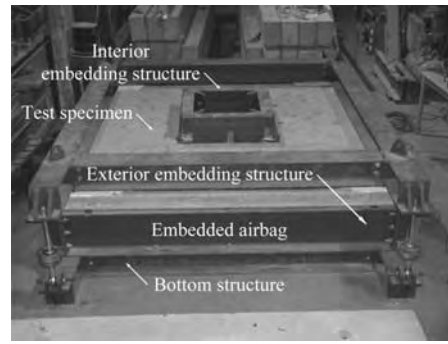

Figure 2. Test setup with the line support structure applied on top of the slab. The line support structure is connected to the bottom exterior embedding structure with a load cell in each corner.

Both deflections and strains were measured according to a grid defined over the surface of the slab. Deflections were measured with Strain Gauge based Displacement Transducers (SGDTs). Strains were measured with Strain Gauges (SGs), in the concrete (50 mm glued SGs), in the reinforcement (10 mm welded SGs), and on the CFRP strips (10 mm glued SGs). Figure 3 shows the location of the measuring points along observation lines for different types of slabs. Figure 4 shows a typical setup of gauges for slabs with an opening.

3.2 *Test specimens*

A total number of 10 slabs were manufactured with designated 28 days strength of $f_{cc} = 40$ MPa, in four batches, one for each type of slab. Six cubes 150 × 150 × 150 mm were manufactured for each batch to measure the actual concrete strengths at the time of testing.

All slabs was reinforced with a base of welded fabric Nps 50 ϕ 5 − s 150, with a concrete cover of 15 mm. Additional reinforcement bars of the same type were added in the slabs with casted holes. The bars were tied to the welded mesh and placed near the hole over a distance of 120 mm, starting 30 mm from the edge. The corners were additionally strengthened with two bars

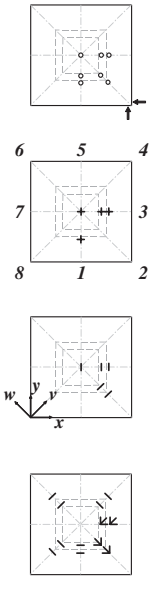

Figure 3. Instrumentation in the slabs depending on the size of any openings and used strengthening material. The numbers designate the location- or observation lines.

Figure 4. Typical setup of gauges in slabs with an opening.

placed in 45-degrees angle as shown in Figure 5. The concrete surfaces of all slabs that were strengthened or repaired with CFRP were sand-blasted to give a good bond.

The homogenous reference slab was designed for a uniform load of 15 kN/m^2 (in total 86.4 kN), according to the Swedish norm, BBK 94 (1995). The designs of the other nine test specimens are based on the same

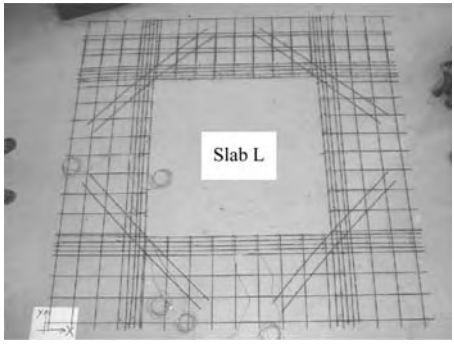

Figure 5. Welded fabrics with tied additional reinforcement bars and welded strain gauges for a large opening.

Table 1. Test program and description of specimens.

Designation	Description
H	*Homogeneous slab as-built without a hole*: Reference slab as-built without a hole, reinforced traditionally.
Swe	*Weakened slab by a small sawed up hole*: Reference slab weakened with a small sawed up hole (0.85 × 0.85 m).
Sre	*CFRP repaired pre-cracked slab with a small sawed up hole*: Simulates a CFRP repaired slab,cracked due to a weakening consisting of a small sawed up hole.
Sst	*CFRP strengthen slab with a small sawed up hole*: Simulates a slab strengthened with CFRP laminates before a small hole is made.
S	*Slab as built with a small hole*: Reference slab as built with a small hole.
Lwe	*Weakened slab by a large sawed up hole*: Reference slab weakened by a large sawed up hole (1.20 × 1.20 m).
Lre	*CFRP repaired pre-cracked slab with a large sawed up hole*: Simulates a CFRP repaired slab, cracked due to a weakening consisting of a large sawed up hole.
Lst	*CFRP strengthen slab with a large sawed up hole*: Simulates a slab strengthened with CFRP laminates before a large hole is made.
L	*Slab as built with a large hole*: Reference slab as built with a large hole.

design load as for the homogeneous slab. The test program is given in Table 1.

The concrete splitting- and compression strength, shown in Table 2, is the average value of six tests.

Table 2. Average concrete strengths from splitting- and compression strength tests of six cubes, and shear strength from at least one torque test of respective CFRP strengthened slab.

Slab	Cast batch	Splitting strength, [kN]	Tensile strength, [MPa]	Compression strength, [MPa]	Shear strength, [Mpa]
H	3	111	2.50	46	–
Swe	1	150	3.36	54	–
Sre	1	150	3.36	54	2.69*
Sst	1	150	3.36	54	3.52*
S	4	120	2.69	44	–
Lwe	2	131	2.95	50	–
Lre	2	131	2.95	50	2.97*
Lst	2	131	2.95	50	3.81*
L	4	120	2.69	44	–

* Torque test carried out on a cracked surface i.e. on a tested slab from the experimental program.

Table 3. Nominal material properties of primer and adhesive.

Product	Adhesitivity to concrete, [MPa]	Youngs modulus, [GPa]	Tensile-/ shear strength, [MPa]	Failure strain, [%]
Primer	17	–	–	3.0
Adhesive	–	2	50/17.6	3.0

Table 4. Nominal material properties of CFRP laminate.

Product	Lamina thickness, [MPa]	Youngs modulus, [GPa]	Tensile strength, [MPa]	Failure strain, [%]
300S*	0.17	234	3600	1.5
200S*	0.11	234	3600	1.5

* Number denotes the unit weight [g/m^2] and S qualifies high strength.

The tensile strength value is evaluated from the splitting strength. Torque tests were conducted on the CFRP repaired or strengthened specimens to evaluate the shear strength of the concrete surface near the bonded area.

The slabs were strengthened using BPE® Composite high strength laminates with two different weights 200 g/m^2 and 300 g/m^2, respectively. The nominal material properties of the CFRP laminates are shown in Table 3. To get the amount of the CFRP fabrics to correspond to the additional reinforcement bars in the slabs casted with a hole the widths of the CFRP laminates were calculated by translating the section area of the steel bars according to Equation 6, into a corresponding area of the CFRPs. Table 4 shows the material properties of the used primer and adhesive.

Table 5. Location, width and length of applied CFRP laminates in respective slab.

Slab	Edge length, [m]	Laminate type	Location in relation to hole edges	Width [mm]	Length [m]
Lre, Lst	1.2	300S	Along	282	1.80
Lre, Lst	1.2	200S	Corners 45°	220	0.60
Sre, Sst	0.85	300S	Along	212	1.45
Sre, Sst	0.85	200S	Corners 45°	220	0.80

Figure 6. Configuration of CFRP laminates applied around a sawed up opening. Marks of the location lines can be seen on the interior embedding structures.

The length and the width of the applied strips are shown in Table 5, note the differences between the lengths of the strips applied at corners in 45-degrees angle. Figure 6 shows the typical configuration of the CFRP composites applied around the openings.

3.3 *Test procedure*

Great care was taken to arrange the airbag to give a well-distributed uniform load and allow it to expand upwards simultaneously as the slab's deflection was increased. A thin protective layer was placed between the airbag and the concrete surface to protect the airbag at failures. In addition, the contact surface at the support was checked and aligned to get evenly distribution of the reaction forces along the supports. The airbag was filled with a compressor at an approximate loading rate of totally 40 N/sec, which corresponds approximately to 417 Pa/min for the homogeneous reference slab. The load, displacement and strain were measured

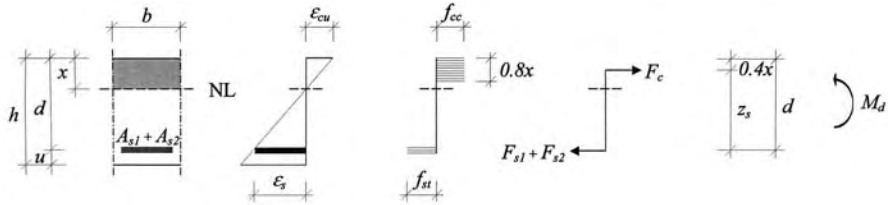

a) Cross section of a slab manufactured with welded fabrics and tied reinforcement bars.

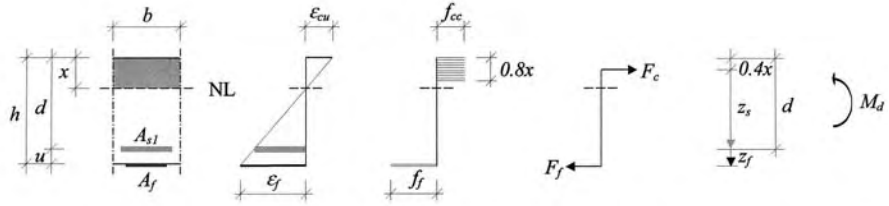

b) Cross section of a slab manufactured with welded fabrics and strengthened or repaired with CFRP composite laminates.

Figure 7. Relationships in a cross section near an opening strengthened with either steel reinforcement or CFRP composite laminates.

and collected with a computerized acquisition system, continuously until failure. The crack propagation and distribution was carefully observed and registered throughout the test.

4 THEORY

4.1 *Simple calculation method of required amount of CFRP laminates*

A conventional way to calculate the required section area of CFRP laminates for strengthening e.g. a made hole in a concrete slab, is to convert the sectional area of required additional steel reinforcement in a slab designed as-built with a holes, into to a corresponding section area of CFRP laminates. However, usually concern is only taken to differences of the Youngs modulus. To improve the calculation, an expression is derived that takes differences between the effective heights of the steel strengthened cross-section and the CFRP strengthened cross-section according to Figure 7, into account.

When the strengthening effect shall be equal between the two cross-sections, the moment capacity must also be equal, i.e.

$$M_f = M_s \tag{1}$$

where M_f is the moment capacity for the FRP reinforcement and M_s is the moment capacity for the steel reinforcement.

To calculate the necessary section area of CFRP A_f, Equation 1 is expressed as the section force F times the inner lever arm z, see Figure 7

$$F_{s2} z_s = F_f z_f \tag{2}$$

where the subscript *s2* stands for the part of steel reinforcement bars that shall be replaced with the CFRP reinforcement, subscript *f*.

Expressing Equation 2 in stress form using the areas A of the steel reinforcement and fiber yields

$$\sigma_{s2} A_{s2} z_s = \sigma_f A_f z_f \tag{3}$$

which by using Hookes law gives the section area as

$$A_f = \frac{E_{s2}\varepsilon_s z_s}{E_f \varepsilon_f z_f} A_{s2} \tag{4}$$

The strain in the CFRP, ε_f can be expressed according to relations in Figure 7, as

$$\varepsilon_f = \frac{z_f}{z_s}\varepsilon_s \tag{5}$$

which together with the inner level arm for a normal reinforced cross-section z_s and a CFRP reinforced cross-section z_f, gives the simplified expression

$$A_f = \frac{E_s}{E_f}\left(\frac{1}{1+\frac{u}{z_s}}\right)^2 A_s \qquad (6)$$

which gives the necessary CRFP reinforcement area.

4.2 *Yield line theory*

The yield line theory is *an upper bound method* that overestimates the failure capacity if wrong yield lines are selected, see further e.g. (Hillerborg 1996) or (Jones & Woods 1967). The method can be used to quickly estimate the failure capacity of reinforced concrete slabs. The theory is based on that the failure is concentrated to distinct crack patterns, so called yield lines. This implies that the slab behaves in a perfectly plastic manner and that the segments between the yield lines are flat and rigid. Normally, several yield line patterns must be controlled and the pattern giving the lowest failure load gives the design value.

5 RESULT

5.1 *Observations*

Some test was aborted prematurely due to failure in the airbag (Swe) or because the design limit of the test-rig was reached (S and L). Most tests showed a ductile failure except when the bond failed or when laminate failure occurred. Inspections of slab (Lre) and (Lst) showed that the laminates had bonded poorly to the concrete surface probably due to poor preparations. However, prior to collapse large deformations and cracking had occurred.

5.2 *Deflections*

Figure 8 shows the behavior of the homogenous slab (H) and the slabs with small holes (Sst, Sre and Swe) in accordance to there intended use, see Table 1.

The two as-built slabs with a hole are considerable stiffer than the homogeneous slab, especially before the theoretically calculated failure load for the homogeneous slab (H) is reached. Note that the load is given in unit kN/m^2, which means that the total load in unit kN is greater for the slab with no hole due to the difference in area. This is especially noticeable for the weakened slab in Figure 9 where the displacement is shown as a function of the total load. The ultimate load for slab (S) could not be recorded since the test

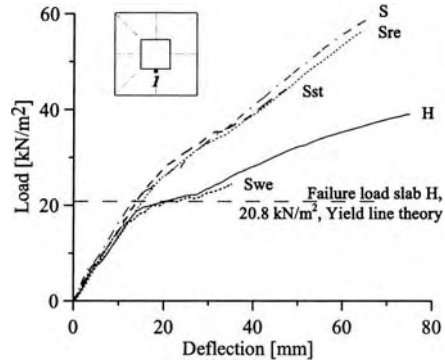

Figure 8. Comparison between (distributed) load-deflection relationships at the edge of the opening in location line 1 for a slab without a hole and slabs with a made hole.

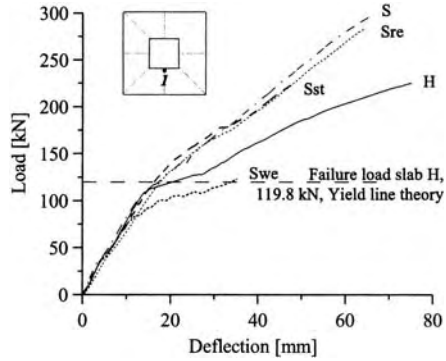

Figure 9. Comparison between (total) load-deflection relationships at the edge of the opening in location line 1 for a slab without a hole and slabs with a made hole.

Figure 10. Crack formation at ultimate load along line 2 of the weakened slab with a large hole, Lwe.

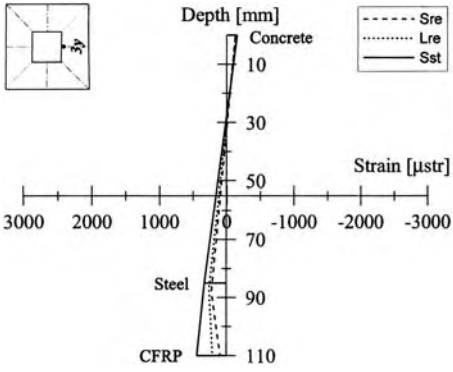

Figure 11. Comparison of strain distributed over the depth of the cross section from slab Sre, Lre and Sst at linear behaviour (i.e. at load 10 kN/m^2).

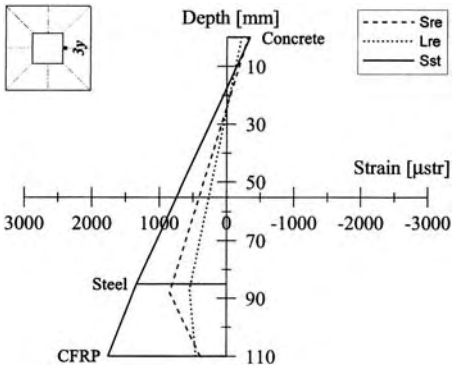

Figure 12. Comparison of strain distributed over the depth of the cross section from slab Sre, Lre and Sst at the beginning of nonlinear behaviour (i.e. at load 30 kN/m^2). Note a noticeable difference between concrete cover.

was stopped when the load limit for the test-rig was reached.

The slab weakened by a sawed up hole and without additional reinforcement (Swe), follows the homogeneous curve (H) and reaches the ultimate limit sooner, as expected. The repaired slab, (Sre) and strengthened (Sst), shows the same trail as the slabs as-built with a hole (S).

The behavior of the slabs with large holes was similar to the slabs with small holes.

Diagonal cracks first forms in the corners regardless of the geometry of the slab. These cracks propagate and gets wider as the load increases, see Figure 10.

5.3 *Strain distribution*

Figure 11 & 12 show the strain distribution over the cross section at two different load levels. Figure 11 shows the distribution when the slab is still in the linear elastic range, whereas Figure 12 shows the distribution when the slab has started to crack.

The behavior is according to the theory shown in Figure 7. The strain distribution is linear in the Sst test as expected. In the repaired test slabs (Sre, Lre) some inelastic strains have already developed in the concrete and the steel reinforcement due to the pre-cracking procedure. Upon reloading the strain in the rebar is localized to the cracked zones, whereas the strain in the CFRP laminates is distributed over a larger area.

5.4 *Failure loads*

Two types of load levels has been defined:

– *Design load*, defining the level where the plate stiffness radically decreases. This point usually coincides with the formation of yield lines in the slab.

Table 6. Summary of theoretical- and experimental loads with the corresponding deflection.

	Deflection [mm]		Load [kN/m^2]		
Slab	At design load	At final load	Design load	Final load	Yield line theory
H	13.3	57.5	19.1	39.0	20.8
Swe	15.0	35.2	18.3	24.4	18.9
Sre	19.7	67.2	25.9	56.9	–
Sst	19.2	47.8	26.8	44.5	–
S	17.0	66.5	23.5	59.3	–
Lwe	14.8	53.0	20.7	32.9	20.8
Lre	17.5	47.8	31.0	44.2	–
Lst	14.4	52.9	24.5	54.6	–
L	14.7	61.0	23.3	66.9	–

– *Final load*, defining the ultimate load capacity or for some tested slabs the load at which the test was aborted.

Table 6 shows the measured deflections at the above defined load levels, together with a comparison with the calculated load according to yield line theory. The CFRP reinforcement slab shows a stiffer behavior compared to the reference slabs (H, L and S). All slabs with CFRP laminates have a higher design and final load compared to the homogeneous one.

This is more clearly seen in Table 7 where the load ratios between the tested slabs with a small hole and the reference slabs (H and S), have been compared.

The test results for the repair applications, repaired pre-cracked slabs, indicates that the CFRP system restores and even increases the final load-capacity when compared to both the weakened slabs and the

Table 7. Experimental load ratios of considered slab with a small opening in relation to reference slab H and S, respectively.

	Ratios of design load		Ratios of final loads	
	Slab	Slab	Slab	Slab
Slab	Slab H	Slab S	Slab H	Slab S
H	*Ref.*	0.81	*Ref.*	0.66
Swe	0.96	0.78	0.63	0.41
Sre	1.36	1.10	1.46*	0.96*
Sst	1.40	1.14	1.14*	0.75*
S	1.23	*Ref.*	1.52	*Ref.*

* No failure, test interrupted when the design load for the test fixture was reached.

homogeneous slab. For repaired slab with a small hole, the final load-capacity was increased with approximately 133% (Sre-Swe/Swe), and 34% for the repaired slab with a large hole (Lre-Lwe/Lwe). In relation to the homogeneous as-built slab (H), the final load-capacity was increased with 46% for the small hole (Sre-H/H), and with 13% for the large hole (Lre-H/H).

For strengthening applications of slabs in which a hole were made, the use of CFRP system resulted in almost equal final load as the slab as-built with a small hole (Sst/S). However, the ultimate failure load could not be recorded since both tests were aborted prematurely. The result for the large hole (Lst/L) was significantly lower due to bond failure caused by poor workmanship during coating. In relation to the homogeneous as-built slab (H), the final load-capacity increased with 14% and 40% for the slab with a small hole (Sst-H/H) and a large hole (Lst-H/H), respectively.

6 DISCUSSION

The general result of the experimental investigation is that the repaired slabs, (Sre or Lre) and the strengthened slabs, (Sst or Lst), showed a similar load-deflection in comparison to the corresponding as-built slab with traditional reinforcement. This is the intention of the design method, to convert the amount of additional tied steel reinforcement in the as-built slab into corresponding amount of CFRP laminates in the repaired- or the strengthened slab. In addition, the CFRP strengthened slabs showed an appreciably stiffer response in comparison with the homogeneous slab (H) and the weakened slabs (Swe, Lwe) especially beyond the design load point.

The design method used works as intended. However, a more advanced design methods may lead to a more efficient use of the CFRP laminates, especially if the goal is to give a repaired slab equal strength as a homogeneous slab.

The result of CFRP strengthening and repair is dependent on good workmanship when applying the laminates to the concrete surface. Bond failure leads to a sudden failure with lower strength as one consequence. Therefore, applying CFRP needs good workmanship, elaborated work plans and follow-up schemas to assure a good quality of the strengthening work. In addition, the simplified design method should be supplemented with a design of the bond between the laminates and the concrete surface. The design should be made to avoid bond failure.

7 CONCLUSIONS

The work presented in this paper shows that CFRP composites can be used to maintain or even increase the original load-capacity of the tested two-way concrete slab specimens. Especially, the experiments showed that:

- The simple design method used to calculate the amount of CFRP laminates for strengthening of a made hole in an existing concrete slab, gives a load-capacity *higher* than the as-built homogeneous slab.
- Deficient or deteriorated structures can be restored to its original load-capacity by a repair with CFRP composites.
- The ductility of strengthened or repaired slabs is good enough if bond failure can be avoided. Special attention should be made on the bond design and the work plan to assure a good quality of the strengthening work.

Finally, more advanced design methods should lead to a more efficient use of the CFRP laminates in strengthening design, especially if the goal is to give a repaired slab equal strength as a homogeneous slab.

ACKNOWLEDGMENTS

The European Union regional funds and BPE System AB sponsored this pilot study. The work done by Anders Ericsson and Tobias Larsson is greatly acknowledged. The work by Lars Åström in preparation of the loading and monitoring equipment is also appreciated.

REFERENCES

BBK 94 (1995). *Boverkets handbok om betongkonstruktioner*, (The Swedish Building Administrations Handbook of Concrete Structures). Part 1 – Design. Stockholm,

Sweden: The Swedish Building Administration, Division of Buildings. ISBN 91-7147-253-5. (In Swedish).

Carolin, A. Täljsten, B. & Hejll A. (2002). *Behaviour of Concrete Beams Strengthened with CFRP and Dynamic Loads Acting During the Strengthening Application*. Int. Conf. in San Francisco, ICCI 02.

Hillerborg, Arne. (1996). *Strip Method Design Handbook*. First edition. London, UK: Chapman & Hall. ISBN 0-419-18740-5.

Johansson, K.W. (1943). *Brudlinieteorier*, (Yield Line Theories). Copenhagen, Denmark: Akademisk Förlag (1963). (In Danish).

Jones, L.L. & Wood, R.H. (1967). *Yield-line Analyses of Slabs*. First edition 1967. London, UK: Thames & Hudson Ltd and Chatto & Windus Ltd.

Nordin, H. Täljsten, B. & Carolin, A. (2002). *CFRP Near Surface Mounted Reinforcement (NSMR) for pre-stressing concrete beams*. Int. Conf. in San Francisco, ICCI 02.

Mosallam, A.S. and Mosalam, K.M. (2002). *Strengthening of two-way concrete slabs with FRP composite laminates*. Construction and Building Materials 17, Elsevier, pp 43–54.

Täljsten, B. (1997). *Strengthening of Beams by Plate Bonding.* Journal of Materials in Civil Engineering, November 1997, p. 206–212.

Täljsten, B. & Elfgren, L. (2000). *Strengthening of concrete beams for shear using CFRP-materials: evaluation of different application methods*. Composites: Part B: Engineering, No 31, Elsevier, p. 87–96.

Vasques, A. & Karbhari, V.M. (2002). *Fiber-Reinforced Polymer Composite Strengthening of Concrete Slabs with Cutouts*. ACI Structural Journal, Vol 100, No 5, September–October 2003.

FRP Composites in Civil Engineering – CICE 2004 – Seracino (ed)

Effect of CFRP sheets on the concrete–steel fatigue bond strength

A.A. Rteil, K.A. Soudki & T.H. Topper
University of Waterloo, Waterloo, ON, Canada

ABSTRACT: This paper presents the results of a study of the effect of transverse carbon fiber reinforced polymer (CFRP) sheets on the fatigue bond strength of steel reinforcing bars in concrete beams. Reinforced concrete bond-beams 150 × 250 × 2000 mm were tested. The variables were the area of the CFRP sheets (none or 1 U-wrap sheet), the reinforcing bar diameter (20 or 25 mm) and the load range applied. The results showed that increasing the bar diameter increased the fatigue bond strength for the unwrapped beams. The CFRP sheets increased the bond strength of the bond-beams with 20 mm bars. However, for the beams with 25 mm steel bars the failure mode changed from a bond splitting failure for the unwrapped beams to a diagonal shear failure for the CFRP wrapped beams, and there was little increase in strength.

1 INTRODUCTION

Civil engineering structures such as bridges and marine structures are subjected to repeated loading that can cause a fatigue failure even when the applied loads are less than the static capacity of the structure (ACI 215, 1974). Little research has been conducted to study the bond behavior of reinforcing steel bars in concrete beams under repeated loading (ACI 408, 1999).

The effect of confinement by fiber reinforced polymers (FRP) on the bond strength under static loading was recently studied (Hamad et al, 2004). It was found that the use of FRP sheets increased the bond strength by up to 33%. However, no research was found in a search of the literature that assessed the effect of FRP sheets on bond strength under repeated loading.

This paper presents the results of a research program designed to study the effect of repeated loading and the confinement provided by carbon FRP (CFRP) sheets on the behavior of the bond between the concrete and steel reinforcement in reinforced concrete beams.

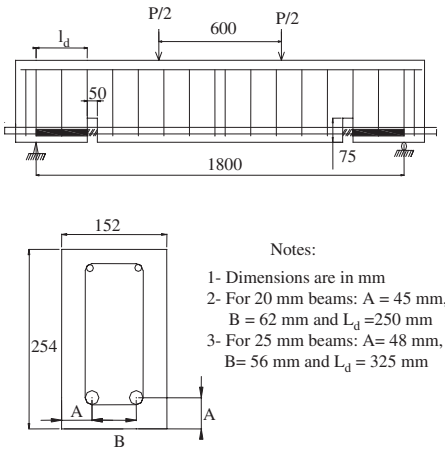

Figure 1. Longitudinal and cross-sectional details of a bond-beam specimen.

2 EXPERIMENTAL PROGRAM

Several kinds of test specimens have been reported in the literature for testing the behavior of the bond between concrete and steel reinforcement. In this study bond-beam specimens were used in order to obtain realistic bond behavior. The specimen was 250 × 150 × 2000 mm (Fig. 1). Each beam was reinforced by 2 steel bars either 20 or 25 mm in diameter. Smooth stirrups, 8 mm in diameter, were provided along the entire length of the beam at a spacing of 125 mm. Compression reinforcement consisting of two 8 mm smooth bars was provided in all the beams. All steel reinforcement was Grade 400 with a specified yield strength of 414 MPa.

In order to get the required anchorage length at the ends of the beam, low-density polyethylene tube covered the reinforcing bars to create the un-bonded zones. Two anchorage lengths were used, 250 mm for the beams reinforced with 20 mm diameter bars and 325 mm for beams reinforced with 25 mm diameter bars. These lengths were selected to insure that a bond splitting failure would occur and that the ratio of the

Table 1. Test matrix.

Set	Beam notation	Testing method	CFRP wrapped	Load range (%)	Bar diameter (mm)
	M-20		No	–	20
	M-R-20	Static	Yes	–	
	M-25		No	–	25
	M-R-25		Yes	–	
1	F75-20			75	
	F65-20			65	
	F60-20			60	
	F55-20	Fatigue	No	55	20
	F53-20			53	
	F50-20			50	
	F40-20			40	
2	F75-R-20			75	
	F65-R-20	Fatigue	Yes	65	20
	F55-R-20			55	
3	F70-25			70	
	F65-25			65	
	F60-25	Fatigue	No	60	25
	F55-25			55	
	F53-25			53	
	F50-25			50	
4	F70-R-25			70	
	F60-R-25	Fatigue	Yes	60	25
	F53-R-25			53	

anchorage length to bar diameter (l_d/d_b) was the same in the two types of specimens. Two empty pockets at the end of the un-bonded length were provided to allow for easy access to instrument tension steel. Blocks of high-density foam were installed around the tension reinforcement to create these pockets.

The specimens were divided into four sets. Sets 1 and 3 consisted of the unwrapped beams, while sets 2 and 4 consisted of CFRP wrapped specimens. Four beams (one from each set) were tested under static loading to determine the static strength of the beams. For the wrapped beams one layer of a U-shaped CFRP flexible sheet was placed transversely in the bonded region so that the fiber orientation was perpendicular to the steel reinforcement. The properties of the sheets as provided by the manufacturer are as follows: thickness 0.381 mm, elongation at break 1% and tensile strength 715 MPa.

A total of 19 tests were performed under repeated loading. Table 1 shows the test matrix and the test results. The load ranges applied are expressed as percentages of the static load capacity of the beam. The minimum load during a load cycle was kept constant at 10% of the static load capacity of the beam and the maximum loads were chosen to give bond failures at fatigue lives between 10^3 and 10^6 cycles. Beams that did not fail after 10^6 cycles were tested again at a higher load range.

Four LVDTs placed within the pockets measured the slip of the reinforcing bars at the loaded end relative to the concrete, while another four LVDTs placed on the bars outside the beam measured the free end slip. All the readings were saved on a computer through a SCXI data acquisition system.

The specimens were tested in four point bending under load control. Load was applied manually until the desired maximum load was reached. It was then decreased to the mean load. Thereafter a sine wave load cycle was applied about the mean load with a frequency of 1.5 Hz.

3 TEST RESULTS

3.1 *General behavior*

While loading for the first time, three flexural cracks in the constant moment region opened at about 20 kN for all beams. In the first few hundred cycles these cracks propagated until they reached a length equal to about 75% of the beam depth. Further cycling did not cause a further increase in the length or the width of these cracks.

For sets 1 and 3 (unwrapped beams) longitudinal cracks initiated from the pocket along the reinforcing bars during the first few hundred cycles. For beams that did not fail, these cracks then stopped growing. However, for beams that failed in fatigue longitudinal cracks continued to grow in width and length until failure. The rate of growth of the longitudinal cracks increased with increasing applied load range. Nevertheless, a single pattern of crack growth was observed for all unwrapped beams. For the first 20% of the beam's life longitudinal cracks propagated at a continually decreasing rate until they stopped. Then for the next 50% of the beam's life the cracks neither propagated nor widened. At about 80% of the beam's life the longitudinal cracks started propagating again at a continually increasing rate until failure (Fig. 2). The failure of all unwrapped beams occurred by bond splitting of the concrete cover in the bonded region (Fig. 2).

Because of the presence of the CFRP sheets it was not possible to see the crack patterns and crack propagation during cycling for sets 2 and 4. However, after the failure of the specimens the CFRP sheets were removed and inspection of the cracks under the CFRP sheets showed that for set 2 the cracks were longitudinal but finer than those in the unwrapped beams indicating that failure was also accompanied by a bond splitting (Fig. 3). Beams in set 2 (wrapped beams) had longer lives at each load range applied compared to their companion beams of set 1 (unwrapped beams). For set 4, a diagonal shear crack propagated from the support to the middle of the bonded region and there were no longitudinal cracks (Fig. 4) indicating that beams of set 4 failed in shear rather than bond. The

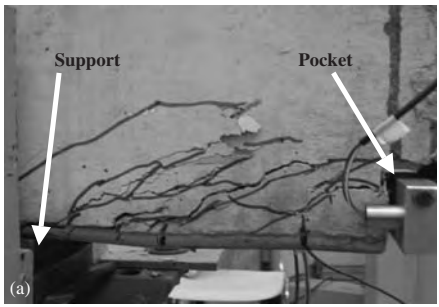

Figure 2. Typical longitudinal cracks for specimens in sets 1 and 3; (a) side cracks, (b) bottom cracks.

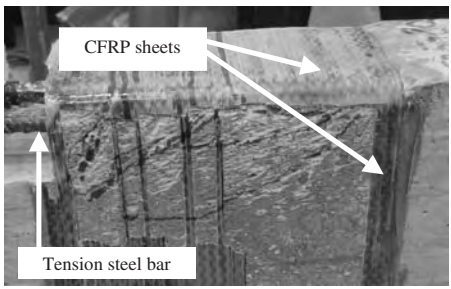

Figure 3. Longitudinal cracks under CFRP sheets in set 2 (beam upside down).

addition of CFRP sheets in set 4 resulted in a change in the mode of failure but little increase in the beam's life.

3.2 *Fatigue life behavior*

As the load range decreases, the fatigue life of the specimens increases linearly on a log-log scale (Fig. 5). In sets 1, 3 and 4 the fatigue limit, taken as the fatigue strength at one million cycles, was about 50% of the

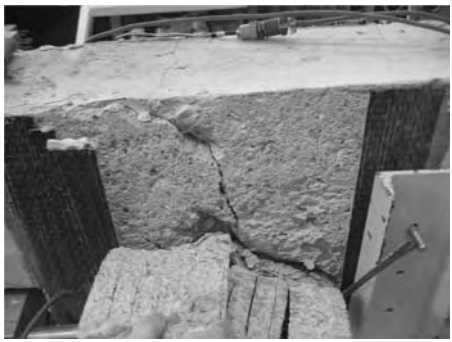

Figure 4. Shear crack in beams of set 4.

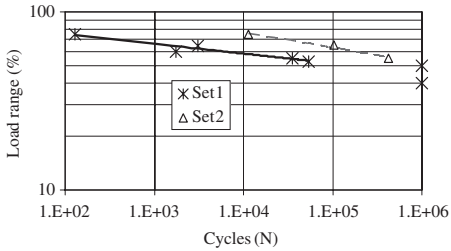

Figure 5. Variation of load range with number of cycles for sets 1 and 2.

static load capacity. The results for all the tests are presented in Table 2.

When CFRP was added for the beams with 20 mm reinforcing bars (set 2), the fatigue bond strength increased above that of the unwrapped beams (set 1) by 41% at 1000 cycles and by 22% at 100,000 cycles. For the 20 mm reinforcing bar, the confinement provided by CFRP sheets had a more pronounced effect at high load ranges (short life) than at low load ranges (long life) but the mode of failure did not change.

On the other hand, for the wrapped beams with 25 mm reinforcing bars (set 4) the failure mode changed from a bond to a shear failure and there was very little increase in fatigue strength (Fig. 6). This indicates that for the larger bar diameter, the confinement provided by the CFRP sheets increased the fatigue bond strength to a value higher than the fatigue shear strength, so that the beams failed in shear rather than in bond.

For the unwrapped beams increasing the bar diameter by from 20 to 25 mm increased the fatigue bond strength by only 14%. The increase is attributed to the larger diameter which provided more surface area for the bond stresses to transfer, which in turn decreased

Table 2. Test results.

Set	Beam notation	Load capacity (kN)	Number of cycle (N)
	M-20	100	–
	M-R-20	138	–
	M-25	120	–
	M-R-25	166	–
1	F75-20	–	130
	F65-20	–	3,080
	F60-20	–	1,750
	F55-20	–	35,000
	F53-20	–	53,969
	F50-20	–	1,000,000
	F40-20	–	1,000,000
2	F75-R-20	–	11,348
	F65-R-20	–	102,224
	F55-R-20	–	418,662
3	F70-25	–	820
	F65-25	–	27,688
	F60-25	–	41,102
	F55-25	–	606,847
	F53-25	–	278,173
	F50-25	–	1,000,000
4	F70-R-25	–	5,707
	F60-R-25	–	100,000
	F53-R-25	–	1,000,000

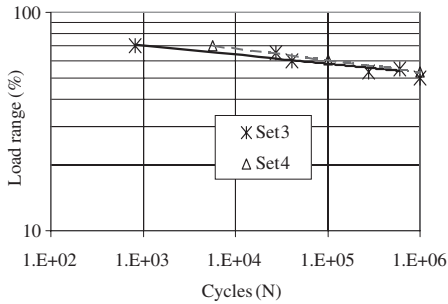

Figure 6. Variation of load range with number of cycles for sets 3 and 4.

the bond stress of beams in set 3 compared to those of set 1. It may also be noted that the increase was the same at all fatigue lives.

3.3 *Load-slip variation*

For the beams which did not fail and for those which failed in shear (set 4), no bond slip was recorded. Hence, the following discussion is limited to the beams in sets 1, 2 and 3 that failed in fatigue. For these beams, the slip increased with increasing cycles as shown in

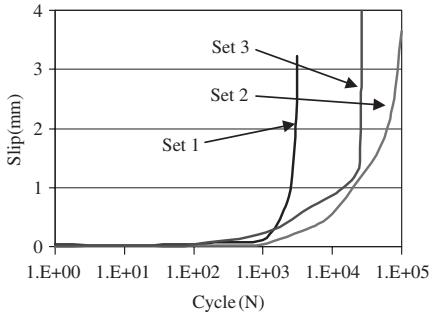

Figure 7. Typical variations of the bar slip with number of cycles.

Figure 7. However, the rate of the slip varied throughout the life. At the beginning of the test the rate of slip increase decreased and then for a period remained constant until near failure when it increased exponentially (Fig. 7). The exponential increase for the unwrapped beams occurred at a slip of about 0.5 mm for beams of set 1 and at a slip of about 1.25 mm for beams of set 3 (Fig. 7). When CFRP was added (set 2), the trend of the slip versus cycle was the same as for the unwrapped beams (Fig. 7); but, the slip in set 2 increased more gradually than in set 1. This is because the CFRP sheets were able to arrest the cracks and confine the steel bar, thus extending the failure process.

4 CONCLUSIONS

The effect of CFRP on fatigue bond strength in reinforced concrete beams was studied. Based on the results presented in this paper the following conclusions can be drawn:

1. For load ranges above the fatigue limit the bond between concrete and steel fails by a brittle splitting mode under repeated loading.
2. A fatigue limit of about 50% of the static load capacity of the beams was found for the two bar diameters used.
3. Increasing the bar diameter from 20 mm to 25 mm increased the fatigue bond strength for unwrapped beams by 14%. The increase was the same at all fatigue lives.
4. Adding CFRP increased the fatigue bond strength. For beams with 20 mm reinforcing steel bars the increase in strength decreased with decreasing load range and increasing fatigue life. For beams with 25 mm bars, CFRP sheets increased the fatigue bond strength to a level above the fatigue shear strength, and the beams failed in shear.

5. For beams that failed by fatigue of the bond, the slip of the reinforcing steel bar increased with increasing cycles.
6. For the unwrapped beams, the slip increased exponentially after reaching of 0.5 mm and 1.25 mm for beams reinforced with 20 mm and 25 mm reinforcing bars respectively. For the CFRP wrapped specimens, the slip increased gradually until failure.

ACKNOWLEDGEMENTS

The authors would like to acknowledge the help of the structures laboratory technicians at the University of Waterloo. The donation of the FRP sheets by SIKA Canada is greatly appreciated.

REFERENCES

ACI Committee 215, 1974. *Considerations for Design of Concrete Structures Subjected to Fatigue Loading (ACI 215–74)*. American Concrete Institute, Farmington Hills, MI.

ACI Committee 408, 1999. *State-of-the-Art Report on Bond under Cyclic Loads (ACI 408–99*). American Concrete Institute. Farmington Hills, MI.

Hamad, B.S., Rteil, A.A., and Soudki, K.A. 2004. Bond Strength of Tension Lap Splices in High-Strength Concrete Beams Strengthened with GFRP Wraps. *ASCE Journal of Composites for Construction* 8(1): 14–21.

FRP Composites in Civil Engineering – CICE 2004 – Seracino (ed)

Study of sewers strengthened by composite plates: numerical optimisation and experimental study

S. Kesteloot & C. Djelal
L.A.M.T.I., Faculty of applied sciences, Technoparc Futura, Béthune, France

S. Baraka & I. Benslimane
Structure & Réhabilitation, Bagnolet France

P. Domange
SIKA, Le Bourget France

ABSTRACT: Man-entry sewers in France are formed by several tens of thousands of structures, 10% of which require structural repair. Many repair techniques are now available, but are costly because applicable throughout the sewer interior. The construction and public works industry is now expert in selective strengthening methods using composite materials. The purpose of our study was to apply this technique to sewerage structures through an extensive programme of numerical experiments.

1 INTRODUCTION

Sewer management is increasingly problematic for local authorities. Their role is to maintain the networks of (man-entry and other) networks. Because of sewer networks' size and essential role in public health, they are considered a major asset. For this reason they must be maintained, through the repairs and replacements required to keep them in good working order.

Sewer networks are "drains" formed by pipes of different sizes. They convey rainwater and wastewater to treatment plants.

They age in different ways, according to the type of water they carry (domestic, rain or industrial) and the type of soil in which they are laid. They undergo numerous changes. [1]

Sewer renovation is generally more beneficial than reconstruction; hence network owners' growing interest in renovation techniques. These techniques must restore the capability of damaged networks to collect and convey wastewater, and must guarantee performance comparable to that of a new structure.

1.1 *Renovation techniques*

These techniques [2] fall into two main categories:

Structuring techniques
- Tubing with injection;
- Mortar or concrete, with or without fibre reinforcement;
- Prefabricated sections.

These techniques are used when the network structure requires repair by restoring mechanical strength sufficient to withstand its loadings: soil pressure, the weight of the sewer and the water it conveys, etc.

Non-structuring techniques
- Selective injection of sealant;
- Tubing without injection or filling of the annular void;
- Sealing liner;
- Anti-corrosion coating;
- Non-reinforced mortars (in some cases).

These techniques are used to improve or restore good water-flow conditions, or to restore leak tightness or protection against abrasion and corrosion.

These repair and strengthening techniques are both costly and applicable throughout the sewer interior. This has prompted the development of innovative methods, including the addition by gluing of composite strengthening plates. These provide a quick, economic and durable solution to the growing need to renovate damaged and ageing sewers.

1.2 *Presentation of the study*

Our study focused mainly on man-entry, ovoid, reinforced-concrete sewers. Figure 1 shows a standard T180 ovoid section.

Pultruded composite plates are used to strengthen the structure.

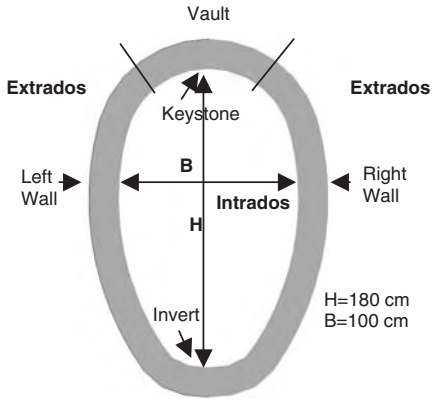

Figure 1. Constituents of a T180 ovoid section.

In order to transpose this construction-industry process to a water-saturated environment, a series of tests [3] was required to assess the feasibility of gluing composite plates to a moist, trickle-free substrate.

A digital simulation using the URUS finite-element computation code [4] was conducted on an unstrengthened ovoid reference to ascertain the structural functioning of a loaded ovoid section and to determine its collapse mechanism.

Once the latter was obtained, the area in need of strengthening was determined and then optimised.

A series of experiments on life-size structures was conducted to validate the results obtained by numerical computation.

2 NON LINEAR FINITE ELEMENT ANALYSIS

Several analytical methods [5], [6] have been developed to predict the bending behaviour of elements reinforced with glued-on composites. In view of the limits imposed by these numerical methods, and particularly on account of the complex distribution of stresses in the film of glue, it seemed necessary to use a more precise method.

2.1 *Fracture mechanics: general considerations – Theory of cracking*

The theory of cracking [7] presents macroscopic geometric discontinuities at the structural level, linear discontinuities in environments considered to be two-dimensional (plates, shells) and surface discontinuities in three-dimensional environments. It is used to predict the development of cracks until complete failure of the structure occurs.

The notion of fracture mechanics [8] is based on the fact that there is an increase in stresses at the crack tip.

This study falls within the field of non-linear fracture mechanics. Plasticity is involved from two aspects:

– In a plastic zone ahead of the fracture front,
– In the mechanism whereby the crack progresses by superimposition of the ductile fracture mechanism.

Elastic-type calculations indeed do not take into account the redistribution of stresses caused by localised damage.

The overall approach via thermodynamics, which generalises the energy release rate, is more effective.

2.2 *Description of the software used*

Numerous studies of numerical methods [9], [10] have already been carried out in recent years in the field of concrete. With the software currently available, it is possible to represent the state of the structures under loading.

It is proposed that the question should be studied again in the framework of fracture mechanics as the classical approaches in the form of stress intensity factors k [11] and contour integrals J [12] have not been fruitful. New software has recently been developed using energy release rate methods [13], whereby it is possible to perform the calculations for concrete. The finite-element software URUS Version 9 [4] will be used in the context of this study.

The finite elements used are triangular or quadrangular plate elements. Only the membrane effects will be taken into account (in plane stress conditions). During the simulations, solution in non-linear elastic conditions will be used.

The non-linear problem arises because of the constitutive law of the concrete. They are also limited in relation to strain. The URUS software possesses a library of predefined laws. By way of example, there is the "poly-line" constitutive law that corresponds to portions of linear segments linked to one another, or the "exponential" type law. The limits are prescribed in terms of strain.

The feature of the "exponential" type law is that it can be derived at any point. When this law is used, the exponential-type expression for this software is therefore as follows:

$$\partial\sigma = E_0 \, e^{\frac{\alpha\sigma}{\sigma-\bar{\sigma}}} \, \partial\varepsilon \qquad (1)$$

The strain limit is taken into account during compression and the energy release rate during traction.

The condition of brittle elastic media fracture due to instability, as formulated by Griffith [14] is expressed by the relation linking the energy release rate G to the area under the curve γ.

$$G \geq 2\,\gamma \qquad (2)$$

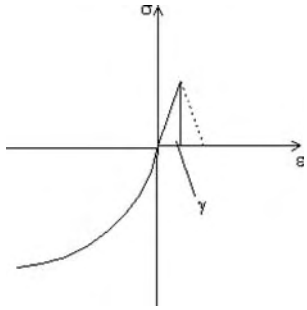

Figure 2. Energy release rate.

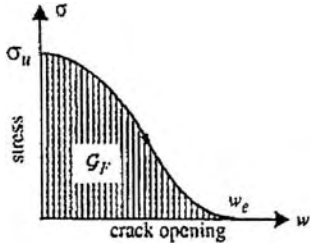

Figure 3. Cohesive crack model.

The software uses this condition, which is represented graphically in figure 2.

When $G = 2\gamma$, fracture is said to be "controlled", as the kinetic energy no longer increases. From a phenomenological standpoint, the energy release rate G defines the stable or unstable character of the crack. G is also the thermodynamic variable associated with the crack area, which justifies a phenomenological relation between G and the crack area.

The stress–strain law on the tension side is defined in the software only by the ascending branch. Physically, the descending (softening) branch is rather similar. Moreover, for common concrete, the tensile behaviour is not stable. Due to this uncertainty, it is possible to assume that the stress–strain is an isosceles triangle.

In the software, the crack opening is supposed to appear after the pic and not from the beginning of the tensile behaviour. The opening is calculated on the base of the principal tensile strain obtained in the cell (which may contain a steel bar) after the pic. Alternatively, this may be expressed by a form of fracture energy of that cell. This fracture is the energy dissipated when the tensile strain is exhausted.

$$G = \int_0^{w_e} \sigma(w)dw \qquad (3)$$

where w is the crack opening.

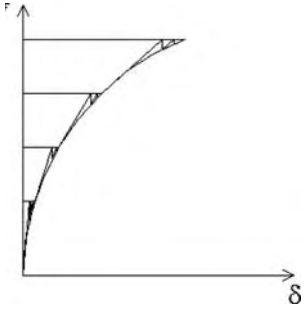

Figure 4. Incremented Newton-Raphson method.

When processing structures, the software uses a variant algorithm of the incremented modified Newton-Raphson method. A "numerical tangent" matrix is built and each load increment. The tangent is not updated in the same increment (equilibrated and iterations only). Figure 4 shows the method used.

Numerically speaking, the theorem of virtual work applies to all bodies (domain Ω of boundary S) can be written generally by the non-linear equation:

$$\int_\Omega \underline{B}^T \underline{\sigma} \cdot d\Omega + \underline{\sum} = 0 \qquad (4)$$

Where B is the strain matrix: $B = LN$, were N is the interpolate functions and N is the differential operation, $\delta\underline{\varepsilon} = \underline{B} \cdot \delta\underline{u}_n$ with the vector u_n (non constant) representing nodal displacements in the domain Ω [15]; $\underline{\sum}$ is the sum of all the forces. Non-linearity comes from the stress–strain constitutive operations (Mechanically non linear and geometrically linear), which is only known by increment (broken line behaviour or equation (1)).

In the context of the incremental method, equation (4) is therefore re-written incrementally in a symbolic manner:

$$\int_\Omega \underline{B}^T \Delta\underline{\sigma} \cdot d\Omega + \Delta\Sigma = 0 \qquad (5)$$

$\Delta\sigma$ representing the term of equation (1) and the other terms of the formula being taken from the previous step or previous iteration.

This is the equation that is solved in each increment, iteratively and numerically, with the integration on each element being performed numerically.

3 MODELLING ASSUMPTIONS

3.1 *Model used*

The chosen model was uniformly meshed with non-linear physically triangular plates. The mesh pitch

Figure 5. Face model mesh.

Figure 6. 3D model mesh.

was refined during the simulations. The chosen pitch was 0.1 m. The materials of the strengthened ovoid sections were assembled by bonding the elements with nodes whose degrees of freedom remained unrestricted. Boundary conditions were defined by locking the invert on the extrados side to form a 60° angle. To represent the structure symmetry, nil horizontal displacement was applied to the nodes on the axis of symmetry.

Figure 5 and 6 shows the chosen model.

The computation was then run until the iterative process no longer converged.

Table 1. Characteristics of the concrete.

Characteristics	Concrete substrate
Poisson's ratio	0.2
Young's modulus	15,400 MPa
Compressive strength	30 MPa
Tensile strength	2.4 MPa

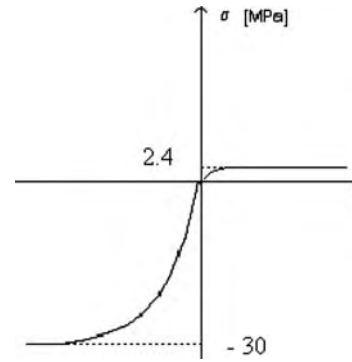

Figure 7. Constitutive law of concrete.

3.2 *Laws of behaviour*

3.2.1 *Concrete*

The characteristics of the concrete of ovoid sections were obtained from laboratory tests. Holes were drilled in an un-strengthened ovoid section, and then single compression tests and Young's modulus measurement tests were conducted. Table 1 gives the characteristics of the concrete.

The general form [16] of uni-axial laws of behaviour, used for the continuous media applicable to concrete, is given in Figure 7.

3.2.2 *Strengthening: carbon plates*

Because the final characteristics of composite materials depend on those of the fibres, Meier [17] chose various criteria for a comparative study. This study found that carbon fibre is best suited to structural strengthening.

Carbon fibre-based materials have a very low mass and are very strong. Instead of using large sheets, the composite comes in the form of 1.2 mm thick plates (Sika Carbodur). [18] The plates we used are made of one-directional composite materials, in the direction of the carbon fibres (longitudinal), which are embedded in an epoxydic matrix. We used 50 mm wide plates, given the substantial curve in the structure.

Table 2 gives the mechanical characteristics of the carbon plates.

Table 2. Characteristics of the strengthening plates.

Characteristics	Carbon plates
Poisson's ratio	0.2
Young's modulus	178,950 MPa
Compressive strength	280 MPa
Tensile strength	2750 MPa

Table 3. Characteristics of the glue.

Characteristics	Glue
Poisson's ratio	0.2
Young's modulus	12,800 MPa
Compressive strength	55 MPa
Tensile strength	2.4 MPa

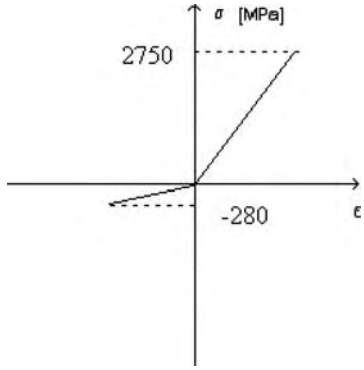

Figure 8. Constitutive law of the composite.

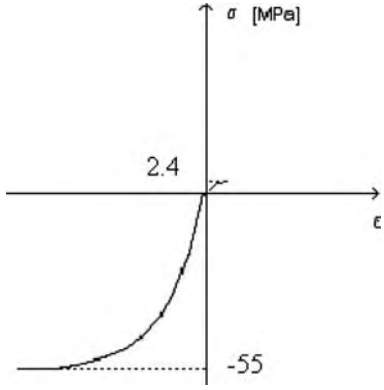

Figure 9. Constitutive law of the glue.

The law of behaviour chosen for the carbon plates is given in Figure 8.

3.2.3 *Bonding material: glue*

Glue plays a very important role in structural strengthening using composite plates. Deuring [19] found that the behaviour of a glue film decomposes in two areas: one elastic and nearly linear, the other plastic.

The laws of behaviour adopted for the glue are exponential. This type of law makes it possible to reproduce the linear elastic area, then the plastic area (Fig. 9). Table 3 gives the mechanical characteristics of the glue.

The law of behaviour of the glue is outlined in Figure 9.

4 RESULTS OF THE NUMERICAL COMPUTATIONS

An un-strengthened ovoid section was numerically computed to obtain its collapse mechanisms and define the areas in need of strengthening. The carbon plates were positioned transversally and continuously on the vault. After several numerical simulations, [20] the chosen transversal surface corresponded to a width of 0.75 metres. The results of this strengthening method are described in the next paragraph. Once the transversal strengthening area was determined, a longitudinal optimisation was performed in order to limit the number of plates (inter-plate spacing).

4.1 *Comparison between un-strengthened and strengthened ovoid sections*

The un-strengthened ovoid section was subjected to a loading equating to silty soil backfill 2 metres in height. During modelling, a series of load increments was applied to obtain its full collapse. The manufacturer of the ovoid sections certified their strength to be 138 kN. We obtained a rupture load of 157.5 kN, giving a safety coefficient of 1.15 compared to the manufacturer's value. The behaviour of the un-strengthened ovoid section is given in Figure 12. During the numerical simulation, the damaged areas were verified in relation to the line of the bending-moment diagram. [13]

With the strengthened ovoid section, collapse occurred at the fifth loading step, 262.5 kN. A 60% load gain over the un-strengthened ovoid section was thus observed. In addition, cracking was retarded. In the reference ovoid section, the first crack appeared at 95 kN in the vault, whereas it appeared at 160 kN in the invert of the ovoid section continuously strengthened by the positioning of the plates.

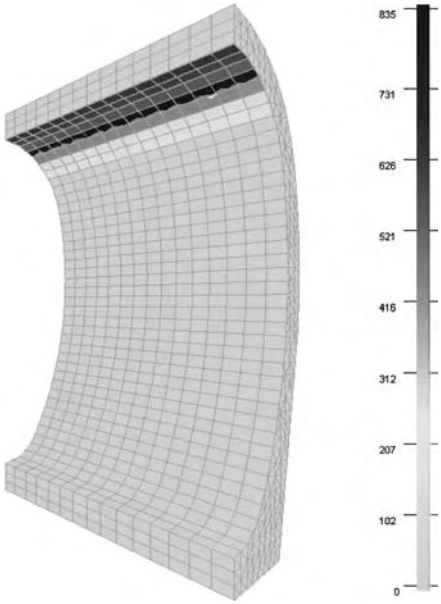

Figure 10. Collapse mechanism – mapping of the main stresses of the continuously strengthened ovoid section.

Figure 10 shows the stresses present at collapse of the continuously strengthened T180 ovoid section. The stresses in the concrete were low, because the glue transmitted the forces into the plates.

The behaviour of the strengthened ovoid section is identical to that of the un-strengthened section in terms of concrete elasticity, i.e. until the appearance of the first crack, in the un-strengthened ovoid section. The load-sag curve in Figure 12 shows the behaviour of a continuously strengthened ovoid section.

Our findings show that this type of strengthening is well suited to ovoid sewers, despite the considerable curve in the vault.

Having obtained these first results, we optimised the area in need of strengthening in order to limit the cost of in-situ application.

4.2 *Optimisation of the strengthening plates*

Different numerical strengthening cases were tested to determine the smallest possible area in need of strengthening.

First, one out of two plates was applied. The numerical results showed that it was possible to reduce the area in need of strengthening. The area finally chosen was one-third of the initial area. The chosen arrangement was 150 mm wide plates separated by a 300 mm gap.

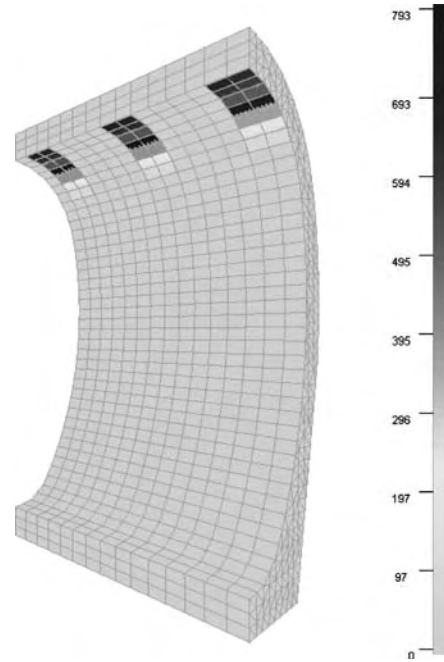

Figure 11. Collapse mechanism – mapping of the main stresses of the strengthened ovoid section with spacing.

The parameters determining the minimal strengthening area were as follows:

- Retardation of the first crack until 138 kN, the permissible load of a T180 ovoid section supplied by the manufacturer;
- Load gain greater than 30% of the reference ovoid-section load.

Figure 11 gives the mapping of the main stresses for the strengthened ovoid section with inter-plate spacing.

The load-sag curve of the strengthened ovoid with spacing (Fig. 12) indicates a slight change in elasticity around 105 kN. However, the significant change in rigidity occurs at 157.5 kN, the load at which the first crack appears in the vault between the carbon plates. The rupture load is 210 kN, a 35% gain over the un-strengthened ovoid section.

4.3 *Comparison and conclusion*

The differences in behaviour between the various models are shown in Figure 12.

The three load-sag curves are identical until 95 kN, when the first crack is observed in the un-strengthened

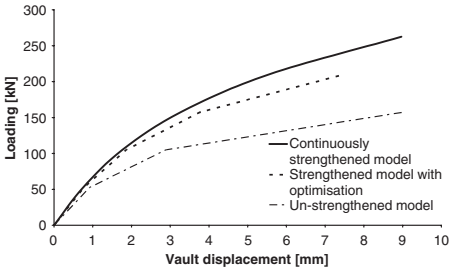

Figure 12. Comparison of the numerical curves.

ovoid section. The comparison between the behaviours of the two types of strengthened area shows a reduction in the rigidity of the strengthened ovoid section with spacing at about 105 kN. However, the two sections behave similarly until 157.5 kN. Above this loading there is a greater difference in rigidity, due to the appearance of the cracks between the plates. As for the reference ovoid section, the load-sag curve shows two main domains: the elastic domain up to 95 kN, then the plastic domain with appearance of cracks through to structural collapse.

Following these numerical computations, an extensive series of experiments was conducted to compared the obtained results to the numerical computations. Two un-strengthened ovoid sections were tested to verify the law of behaviour applied to concrete and to determine the collapse mechanism. Then two ovoid sections continuously strengthened in the vault were loaded to collapse. Application of composite plates on the vault achieves a 60% load gain and retards cracking.

For this paper, only the tests on strengthened ovoid sections with inter-plate spacing were compared to the numerical simulations.

5 COMPARISON OF TEST AND COMPUTATIONS

5.1 *Testing of a strengthened ovoid section with inter-plate spacing*

The ovoid sections were vertically loaded. The load was applied to the vault, and equated to the weight of backfill soil above the sewers. The jack load was transmitted to the structure by means of a wooden shuttering filled with sand, to uniformly distribute the load on the vault. (Fig. 13) The resultant horizontal thrust of the soil was not considered, in order to highlight the area under greatest stress, i.e. the vault.

We used an INSTRON press, which has a hydraulic jack with numerically controlled travel. The load

Figure 13. Loading.

Figure 14. Structural collapse.

was measured using a force sensor of 250 kN static capacity.

During the test, we measured sagging of the vault and displacement of the abutment walls in order to verify structural symmetry. Wall and vault displacements were measured using LVDT sensors connected to a data-acquisition unit.

Two T180 ovoid sections with inter-plate spacing were tested. The results were similar, so only one of the tests was used for this paper.

Cracks appeared at 168 kN, and first developed between the carbon plates. Cracks also appeared in the invert intrados and at the midpoint of the walls on the extrados side. Gradual opening of the cracks from the intrados towards the extrados was observed. These cracks caused the structure to collapse. (Fig. 14) Collapse occurred between the extreme point of loading and the edge of the strengthened area. We obtained the same collapse mechanism for the un-strengthened and continuously-strengthened sections.

The maximum recorded loading was 192 kN. During testing, the plates detached from the substrate.

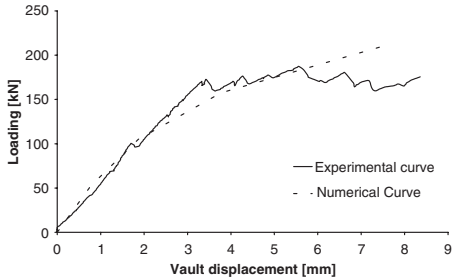

Figure 15. Comparison on the experimental and numerical curves.

However, detachment was caused by decohesion in the substrate and not by rupture of the glue bond.

Comparison of numerical simulation and experiment series Figure 15 gives the curves obtained by modelling and the experiment series.

In the elastic domain, behaviours were similar. The behaviour of the tested ovoid section showed quasi-elastic behaviour up to 160 kN. Cracks then appeared between the plates, showing the plastic behaviour of the section.

The numerical curve showed greater structural rigidity in the plastic domain. The difference in behaviour was caused by the difficulty of applying the plates to the curved surface. During testing, spaces were noted between the plates and the substrate. These spaces caused a loss of structural rigidity.

6 CONCLUSION

The application of carbon plates to sewer vaults achieves a 60% gain in rupture loads, and retards the appearance of the first cracks. The gaps in our understanding of ovoid-section behaviour were filled by finite element modelling. However, because our computations were based on perfect adhesion, we obtained slightly different behaviours when cracks appeared. For the application of carbon plates in the next stage of our experiment series, the strengthening plates will be placed by inflating a balloon.

Use of this strengthening method for sewer renovation reduces job cost by 60%. In addition, the section of the sewer is not reduced.

During loading, inter-plate spacing makes it possible to visualise the concrete cracking in the vault.

A series of tests was carried out on concrete sample reinforced by FRP in various environments. During joining in saturated environment, the results of the tests showed that it was necessary to apply a safety coefficient related to the problem of adherence to wet facing [21].

Long term effects are questionable. A research is under cause for answers the questions.

ACKNOWLEDGEMENTS

The authors wish to thanks the companies SIKA France, STRUCTURE & REHABILITATION and VALENTIN Environnement et Travaux Publics for their partnerships and financial support in the execution of this project.

BIBLIOGRAPHY

[1] Projet National RERAU, 'Restructuration des collecteurs visitables, *Guide technique*, Editions Lavoisier, (2002) (1) 1–2.

[2] 'Recommandations pour la réhabilitation des réseaux d'assainissement', AGHTM, Vol. 1 (1998).

[3] Kesteloot S., 'Synthèses des essais de collages', Rapport de recherche n°2, LAMH/Structure & Réhabilitation, (2003).

[4] URUS Version 9, 'Logiciel de calcul de structures par éléments finis', @bd soft.

[5] Täljsten B., 'Plate bonding, strengthening of concrete structures with epoxy bonded plates of steel or fiber reinforced plastics, *Doctoral thesis*, Lulea University of Technology, (1994).

[6] Triantafillou T.C., 'Shear strengthening of reinforced concrete beams using epoxy bonded FRP composite', *ACI Structural Journal*, (2) (1995) 107–115.

[7] Labbens R., 'Introduction à la mécanique de la rupture', *Ed. Pluralis* (1980).

[8] Carpinteri A., Chiaia Bernardino, Nemati K.M., 'Complex fracture energy dissipation in concrete under different loading conditions', *Mechanics of Materials*, 26 (1997) 93–108.

[9] Arduini M., Di Tommaso A., Manfroni O., 'Fracture mechanics of concrete beams bonded with composite plates', *Non-metallic (FRP) Reinforcement for concrete structures*, Edited by Taerwe, Rilem (1995) 485–491.

[10] Triantafillou T.C., Deskovic N., Deuring M., 'Strengthening of concrete structures with prestressed fiber reinforced plastic sheets', *ACI Structural Journal*, 89 (3) 235–244.

[11] Irwin G.R., 'Analysis of stresses and strains near the end of a crack traversing a plate', *Trans. ASME*, *Journal Applied Mechanics*, Vol. E24 (1957) 361.

[12] Rice J.R., 'A path independent integral and approximate analysis of strain concentration by notches and cracks', *Journal Applied Mechanics*, Vol. 35 (1968) 379–386.

[13] Lemaître J., Chaboche J.L., 'Mécanique des matériaux solides', *Editions Dunod*, Paris, (1985).

[14] Griffith A.A., 'The theory of rupture', Proceeding first intern, Cong. on applied Mechanics, (1924).

[15] Zienkiewick O.C., Taylor R.L., 'The finite-element method, Vol. 2, *Fourth Edition McGraw-Hill Book Company*, (1991) 211–277.

[16] Mazars J., 'Mécanismes physiques de rupture et modèles de comportement du béton hydraulique in

«Le béton hydraulique'», *Presse de l'Ecole Nationale des Ponts et Chaussées*, Paris (1982).
[17] Meier U., 'Strengthening of structures using carbon fibre/epoxy composites', *Constructions and Building Materials*, Vol. 9 (1995) 341–351.
[18] SIKA – Procédés de renforcement des structures par collage d'armatures à base de fibres de carbones, Cahier des clauses techniques CCT 37, August 2000.
[19] Deuring M., 'Verstärken von Stahlbeton mit gespannten Faserverbundwerkstoffen', *Doctoral thesis*, Eidgenössischen Technischen Hochschule, Zürich (1993).
[20] Kesteloot S., 'Simulation numérique pour l'optimisation du dimensionnement de la réhabilitation par fibres de carbones', Rapport de recherche n° 1, LAMH/Structure & Réhabilitation, (2002).
[21] Kesteloot S., Djelal C., Baraka S., Benslimane I., 'Finite-element modeling of concrete prisms reinforced with composites plates – Theory of cracking', *Materials and Structures*, Vol. 37, (2004).

Debonding failure in FRP strengthened beams

FRP Composites in Civil Engineering – CICE 2004 – Seracino (ed)
© 2005 Taylor & Francis Group, London, ISBN 90 5809 638 6

Verifications of some design equations of beams externally strengthened with FRP composites

L. Zhao & H. Toutanji
Department of Civil and Environmental Engineering, University of Alabama in Huntsville, Huntsville, AL, USA

ABSTRACT: Based on the available test information provided in literatures since 1990, a comprehensive database is assembled for an extensive survey of existing studies on the flexural behavior of reinforced concrete (RC) beams externally reinforced with fiber reinforced polymer (FRP) composites. Beam dimensions, material properties (concrete, steel reinforcement and FRP composites etc.), and corresponding flexural responses such as failure modes, moment capacities, etc. are collected in this database. The purpose of this database is to verify the design formulas presented in ACI 440.2R-02, Guide for the Design and Construction of Externally Bonded FRP Systems for Strengthening Concrete Structures (ACI 440). The performance of another two simple strength design models is investigated based on the same database and compared with that of ACI model. Finally, a simple modified design method is recommended. The modified design method is verified with the database.

1 INTRODUCTION

Flexural strengthening of reinforced concrete (RC) beams with fiber reinforced polymer (FRP) plate externally bonded to the tension face is one of the techniques developed during the last decade. With the addition of FRP reinforcement, beams exhibit several unique failure modes under flexural loading: (a) rupture of FRP plate, (b) concrete cover separation, (c) interfacial debonding of FRP plate, as shown in Figure 1 (Arrows indicating crack propagation directions). These failure modes are reported in many literatures along with the conventional failure modes such as crushing of concrete and concrete shear failure.

The interfacial debonding of FRP plate can be either induced by interfacial normal and shear stress concentration reaching a critical value or propagation of an intermediate crack towards plate end, as shown in Figure 1c, d. The current research does not discriminate between these two types of interfacial debonding failures. All failures in the interface between FRP and concrete substrate are classified as "interfacial debonding" in this paper. Interfacial debonding and concrete cover separation are generally defined as premature failures because neither the FRP nor the concrete reaches its full strength capacity under ultimate load. From experimental observation, over 63% of test beams failed in a premature manner (Bonacci 2001). For the significance of premature failure in FRP strengthening, many analytical and empirical models have been proposed to predict the premature failure strength. Smith & Teng (2002a, b) reviewed 12

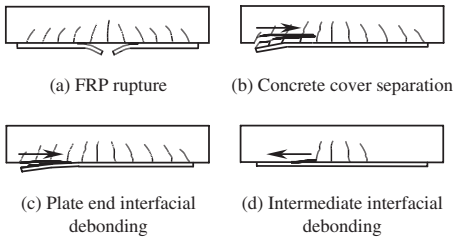

Figure 1. FRP-related failure modes of RC beams strengthened by FRP plate.

debonding strength models and evaluated them in a database of 59 test beams. Their study shows that most of these models do not provide a sufficiently safe prediction of ultimate strength for design use.

To standardize the use of FRP strengthening technique, American Concrete Institute (ACI) published a Guide for the Design and Construction of Externally Bonded FRP Systems for Strengthening Concrete Structures, ACI Committee 440.2R-02 (ACI 440). A design method for predicting the premature debonding strength of a RC beam with FRP reinforcement is presented. This ACI design method is of great importance in producing safe design for the application of FRP strengthening technique. However, it was recently found that the current ACI 440 design recommendations are unreliable and potentially unsafe for structures strengthened with FRP plate (Reed et al.

2004). So this paper is aimed at verifying the suitability of this method by applying different experimental data. A database is carefully assembled based on 115 test beams from an extensive survey of existing studies on flexural behavior of RC beams externally reinforced with FRP plates (Triantafillou & Plevris 1992, Nakamura et al. 1996, Takeda et al. 1996, Spadea et al. 1997, Spadea et al. 1998, Rahimi & Hutchinson 2001, Deng 2002, Grace et al. 2002, Smith & Teng 2002b, Zhang 2002, Brĕna et al. 2003, Pornpongsaroj et al. 2003, Valcuende et al. 2003 and Zhang et al. 2003). The database is used to verify the accuracy of the ACI 440 strength design equations.

2 OVERVIEW OF STRENGTH DESIGN MODELS

Three debonding strength design models established by different concepts are selected and overviewed. ACI 440 strength model is based on the maximum usable FRP strain; shear capacity based model relates the beam strength to ultimate shear capacity at plate end; and for maximum steel reinforcement ratio model, beam strength is determined by the unstrengthened beam with a maximum steel reinforcement ratio.

2.1 *ACI 440 model*

ACI Committee 440 proposed a design equation to predict the maximum usable FRP strain. This implies that the ultimate rupture strain of FRP plate either reported from the manufacturers or obtained in the laboratory can not be directly used in finding the ultimate moment capacity. An empirical reduction factor k_m, given by Eq (1), which is a function of the stiffness $nE_f t_f$ (N/mm) and the rupture strain of FRP ε_{fu}, has to be imposed on ε_{fu} to give maximum usable FRP strain; thus, limiting the tension force developed in FRP in calculating the debonding strength of FRP bonded RC beams. Then by applying strain compatibility method and equilibrium equations to the reinforced section, the ultimate strength could be found (ACI Committee 440 2002). By substituting the maximum usable strain with the rupture strain of FRP ε_{fu} and assuming a proper constitutive model for concrete, theoretical strength M_t, regardless of concrete cover separation or interfacial debonding, can be also obtained. This theoretical strength M_t will be later utilized as a measurement to evaluate ACI and other design models.

$$k_m = \begin{cases} \dfrac{1}{60\varepsilon_{fu}}\left(1-\dfrac{nE_f t_f}{360000}\right) \le 0.90 & nE_f t_f \le 180000 \\ \text{for} & \\ \dfrac{1}{60\varepsilon_{fu}}\left(\dfrac{90000}{nE_f t_f}\right) \le 0.90 & nE_f t_f > 180000 \end{cases} \quad (1)$$

where n is number of plies; E_f is the tensile modulus of FRP; t_f is the thickness for each ply.

2.2 *Shear capacity-based model*

The rationale of shear capacity-based model is that the premature failure strength is related to the shear strength of the concrete with no contribution of the steel shear reinforcement. The debonding strength is generally given in terms of the shear force at the plate end. One advantage of this model is the interfacial stresses between the plate and the beam does not need to be evaluated and little calculation is required to predict the strength.

Smith & Teng (2002b) proposed a simple design-oriented shear capacity-based model. The debonding strength is given by Eq. (2),

$$V_{u,end} = \eta V_c \quad (2)$$

where $V_{u,end}$ is the ultimate shear capacity at plate end. V_c is the shear capacity of the concrete in the RC beam alone, without the contribution from the shear reinforcement. $\eta = 1.5$. According to ACI Committee 318 (ACI 318-99), V_c can be calculated using Eq. (3),

$$V_c = 1.9bd\sqrt{f_c'} + 2500\rho_s bd \le 3.5bd\sqrt{f_c'} \quad (3)$$

where b and d are the width and depth of the beam section, respectively; f_c' is the compressive strength of concrete; and ρ_s is the tension steel reinforcement ratio.

Application of this model is limited with respect to the magnitude of moment at the plate end $M_{u,end}$. When $M_{u,end} < 0.67M_t$, this model yields conservative prediction of strength for beams included in Smith & Teng's database, although there is no data available to evaluate its performance when $M_{u,end} > 0.67M_t$.

2.3 *Maximum steel reinforcement ratio model*

The maximum steel reinforcement ratio model is suggested by Naaman (2003). He estimated that, compared to the unstrengthened RC beam, it is reasonable to design the strength increments for the same RC beam bonded with FRP as approximately 20% of the ultimate strength of the same RC beam calculated assuming a steel reinforcement ratio equal to ρ_{max}, which could be expressed as follows,

$$M_{u,\rho\max} = M_{uns} + 0.2M_{\rho\max} \quad (4)$$

$M_{u,\rho max}$ and M_{uns} are the ultimate moment capacity of strengthened and unstrengthened beam, respectively; $M_{\rho max}$ is the bending strength of the same RC beam calculated assuming a maximum steel reinforcement

ratio without FRP reinforcement. Both M_{uns} and M_{pmax} could be calculated based on ACI 318 considering the section is singly reinforced. Like the shear capacity-based model, a lot of calculation work could be saved compared to ACI method since apparently Eq. (4) does not include any information about FRP reinforcement.

3 DATABASE

To assess the above three design methods, a comprehensive database is constructed for flexural tests on RC beams externally strengthened by FRP composites. The criteria enforced in collecting the database are: (1) all beams have rectangular sections and are under-reinforced regardless of FRP plate; (2) all beams are simply supported under three or four-point loading; (3) all beams failed in a manner of either FRP debonding or cover separation; (4) all beams were statically loaded until failure and none were pre-loaded; (5) no anchorage on FRP plate has been used on any beam, such as bolted end of FRP or extension under support. Smith & Teng's database meets all the above requirements and 58 beams from it are included in the current database, with only one over-reinforced beam eliminated (Smith & Teng 2002b). The data is categorized according to failure modes (plate debonding or cover separation), FRP curing methods (wet lay-up or pultruded plate) and FRP types (carbon, glass or aramid).

4 RESULTS AND DISCUSSIONS

Statistical tools are used in analyzing the performance of the three strength models. The ratio of experimental nominal strength to predicted results is adopted to access each model. Tables 1–6 show the statistical values of the experimental-to-predicted strength ratio. Average, standard deviation, coefficient of variation and percentage of exceedence are calculated. The percentage of exceedence is defined as the percentage of number of tests with an experimental-to-predicted ratio less than 1. The greater this ratio is, the less conservative the model is. Tables 1–3 and 4–6 are for beams failed by plate debonding and cover separation, respectively. Tables 1 and 4 are for both types of FRP plate, wet lay-up and pultruded plate. Tables 2 and 5 are for wet lay-up plate beams only and Tables 3 and 6 are for pultruded plate beams only. From Tables 1 and 4, ACI model yields the most accurate and least scattered prediction for both types of premature failures. But more than half of its predictions are unconservative with percentage of exceedence of 55%. This conclusion was confirmed by Reed et al. (2004). Shear capacity-based model gives slightly unconservative average predictions for debonding failure but

Table 1. Experimental-to-predicted debonding strength ratio for beams failed by debonding (wet lay-up + pultruded).

Model	μ^*	S^*	V^*	E^*	n_t^*
ACI	1.00	0.15	0.15	55%	64
Smith	0.94	0.32	0.34	66%	64
Naaman	1.35	0.38	0.28	17%	64

$^*\mu$: Average; S: Standard deviation; V: Coefficient of variation; E: Percentage of exceedence; n_t: Number of tests.

Table 2. Experimental-to-predicted debonding strength ratio for beams failed by debonding (wet lay-up).

Model	μ	S	V	E	n
ACI	0.97	0.17	0.18	64%	33
Smith	1.15	0.34	0.30	39%	33
Naaman	1.32	0.33	0.25	15%	33

Table 3. Experimental-to-predicted debonding strength ratio for beams failed by debonding (pultruded).

Model	μ	S	V	E	n
ACI	1.03	0.12	0.12	45%	31
Smith	0.81	0.21	0.26	81%	31
Naaman	1.38	0.43	0.31	19%	31

Table 4. Experimental-to-predicted debonding strength ratio for beams failed by cover separation (wet lay-up + pultruded).

Model	μ	S	V	E	n
ACI	0.97	0.12	0.12	55%	51
Smith	1.09	0.25	0.23	33%	51
Naaman	1.30	0.26	0.20	10%	51

Table 5. Experimental-to-predicted debonding strength ratio for beams failed by cover separation (wet lay-up).

Model	μ	S	V	E	n
ACI	1.03	0.09	0.09	27%	21
Smith	1.26	0.22	0.17	14%	21
Naaman	1.30	0.36	0.28	24%	21

Table 6. Experimental-to-predicted debonding strength ratio for beams failed by cover separation (pultruded).

Model	μ	S	V	E	n
ACI	0.92	0.11	0.12	73%	30
Smith	0.97	0.20	0.21	47%	30
Naaman	1.31	0.16	0.12	0%	30

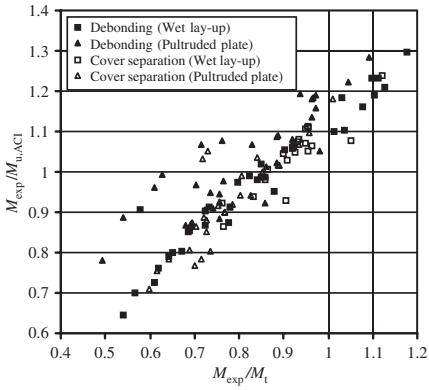

Figure 2. Experimental results vs prediction of ACI 440 model.

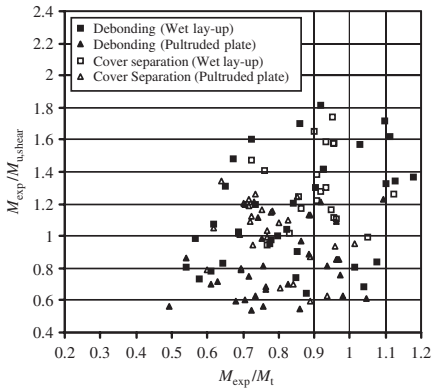

Figure 3. Experimental results vs prediction of shear capacity-based strength model by Smith & Teng (2002b).

conservative average for cover separation. The maximum reinforcement ratio model also produces safe average prediction and about 80–90% of them are conservative. For wet lay-up plate beams only, ACI prediction is still most accurate and least scattered and maximum reinforcement ratio method predicts most conservatively. For pultruded plate beams only, the same trends maintain as that for wet lay-up plate beams. From Tables 3 and 6, shear capacity-based model performs very unconservatively for pultruded plate beams. It is worth to note that maximum reinforcement ratio method is totally conservative for pultruded plate beams failed by cover separation.

Figures 2–4 show the different comparisons of debonding strength models. For 88% of beams in the database, the theoretical strength M_t without considering debonding is greater than its corresponding experimental debonding moment M_{exp}, justifying the use of M_t as the upper limit of beam strength. $M_{u,ACI}$, $M_{u,shear}$ and $M_{u,\rho max}$ are the debonding strength predicted by ACI 440 model, shear capacity-based model and maximum steel reinforcement ratio model, respectively. Although maximum reinforcement ratio method performs conservatively for most of beams as shown in Figures 2–4, it can be concluded that those three models could not be directly used for design and necessary modification is needed. If ACI model is to be used, a reduction factor of 0.7 is proposed to be applied on its prediction of debonding strength to ensure 99% safe design for RC beams.

Because cover separation or plate debonding may be triggered by the occurrence and development of flexural or diagonal crack in the vicinity of the plate end (ACI Committee 440 2002), those models might be improved by restricting the plate end shear force $V_{u,end}$ or bending moment $M_{u,end}$ obtained from preliminary

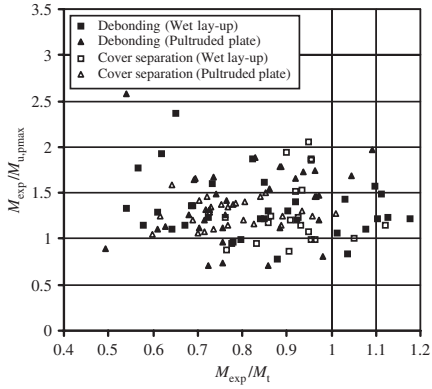

Figure 4. Experimental results vs prediction of maximum steel reinforcement ratio model by Naaman (2003).

strength prediction. Since the method proposed by Naaman (2003) seems most promising to be a design based one, the following modifications are suggested for it as Eq. (5) and (6):

$$V_{u,end} < 1.5V_c \tag{5}$$

$$M_{u,end} < 2.8M_{cr} \tag{6}$$

whichever smaller controls. M_{cr} is the cracking moment of the unreinforced section. $V_{u,end}$ and $M_{u,end}$ can be calculated from the strength model proposed by Naaman (2003). The performance of the modified

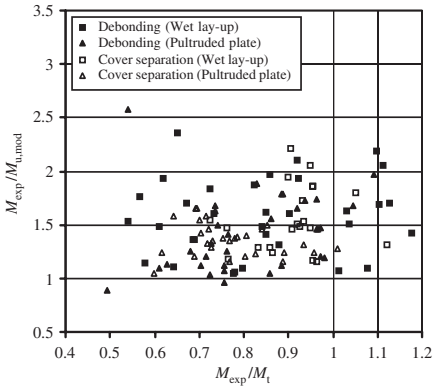

Figure 5. Experimental results vs prediction of modified strength model by Naaman (2003).

model is shown in Figure 5. It yields conservative design strength for 98% beams in the current database. The modified experimental-to-predicted strength ratios have an average of 1.47 and a standard deviation of 0.32. It is suggested that maximum steel reinforcement model be used for preliminary design since less calculation is involved.

5 CONCLUSIONS

This paper presents three strength models for design purpose, considering premature failure in FRP strengthened simply-supported RC beams. A large database of 115 beam tests is collected to verify those strength models.

The strength prediction by ACI is most accurate and least scattered than shear capacity-based model and maximum reinforcement ratio method. The maximum reinforcement ratio model is most conservative of the three.

However, none of the three models is conservative enough for a design purpose. Of the three models, maximum reinforcement ratio model is most promising to be used for preliminary design because it is simple to calculate and conservative. By necessary modification, it gives 98% safe prediction. If ACI model is to be used, a reduction factor of 0.7 is recommended to ensure 99% safe design for beams in the database.

ACKNOWLEDGEMENT

The authors would like to acknowledge the financial support of the National Science Foundation Grant CMS-9900431. The help of Mr. Eugene Anselm in collecting the database is also acknowledged.

REFERENCES

ACI Committee 318, 2000. *Building code requirements for structural concrete, ACI standard 318-99 and the commentary*, Farmington Hills, MI, USA.

ACI Committee 440 2002. *Guide for the design and construction of externally bonded FRP systems for strengthening concrete structures* (*ACI 440.2R-02*), Farmington Hills, MI, USA.

Bonacci, J.F. & Maalej, M. 2001. Behavioral trends of RC beams strengthened with externally bonded FRP. *Journal of Composites for Construction* 5(2): 102–113.

Brĕna, S.F., Bramblett, R.M., Wood, S.L. & Kreger, M.E. 2003. Increasing flexural capacity of reinforced concrete beams using carbon fiber-reinforced polymer composites. *ACI Structural Journal* 100(1): 36–46.

Deng, Y. 2002. *Static and fatigue behaviors of RC beams strengthened with carbon fiber sheets bonded by organic and inorganic matrices.* Ph.D. dissertation, University of Alabama in Huntsville, AL, U.S.A.

Grace, N.F., Abdel-Sayed, G. & Ragheb, W.F. 2002. Strengthening of concrete beams using innovative ductile fiber-reinforced polymer fabric. *ACI Structural Journal* 99(5): 692–700.

Naaman, A.E. 2003. Parameters influencing the flexural and shear response of RC beams strengthened with CFRP laminates. *Proceedings of the 2nd International Workshop on Structural Composites for Infrastructure Applications*, Cairo, Egypt.

Nakamura, M., Sakai, H., Yagi, K. & Tanaka, T. 1996. Experimental studies on the flexural reinforcing effect of carbon fiber sheet bonded to reinforced concrete beam, *Proceedings of 1st International Conference on Composites in Infrastructure, ICCI'96*, *Arizona, USA*: 760–773.

Pornpongsaroj, P. & Pimanmas, A. 2003. Effect of end wrapping on peeling behavior of FRP-strengthened beams. *Proceedings of 6th International Conference on Fibre Reinforced Plastics for Reinforced Concrete Structures*. Singapore: World Science Publishing Company.

Rahimi, H. & Hutchinson, A. 2001. Concrete beams strengthened with externally bonded FRP plates. *Journal of Composites for Construction*, ASCE 5(1): 44–56.

Reed, M.W., Barnes, R.W., Schindler, A.K. & Lee, H.W. 2004. Effects of traffic loads during FRP bridge strengthening. *Transportation Research Board, 83rd Annual Meeting*, Washington DC.

Smith, S.T. & Teng, J.G. 2002a. FRP-strengthened RC beams. I: review of debonding strength models. *Engineering Structures* 24(4): 385–395.

Smith, S.T. & Teng, J.G. 2002b. FRP-strengthened RC beams. II: assessment of debonding strength models. *Engineering Structures* 24(4): 397–417.

Spadea, G., Bencardino, F. & Swamy, N. 1997. Strengthening and upgrading structures with bonded CFRP sheets design aspects for structural integrity. *Proceedings of 3rd International Symposium on Non-Metallic (FRP) Reinforcement for Concrete Structures*, 1: 629–636.

Spadea, G., Bencardino, F. & Swamy, R.N. 1998. Structural behavior of composite RC beams with externally bonded

CFRP. *Journal of Composites for Construction* 2(3): 132–137.

Takeda, K., Mitsui, Y., Murakami, K., Sakai, H. & Nakamura M. 1996. Flexural behavior of reinforced concrete beams strengthened with carbon fiber sheets. *Composites Part A* 27A: 981–987.

Triantafillou, T.C. & Plevris, N. 1992. Strengthening of RC beams with epoxy-bonded fiber-composite materials. *Materials and Structures* 25: 201–211.

Valcuende, M., Benlloch, J. & Parra, C.J. 2003. Ductility of reinforced concrete beams strengthened with CFRP strips and fabric. *Proceedings of 6th International Conference on Fibre Reinforced Plastics for Reinforced Concrete Structures*. Singapore: World Science Publishing Company.

Zhang, Y. 2002. *Flexural behavior of reinforced concrete beams externally bonded with CFRP sheets*. Master thesis, University of Alabama in Huntsville, AL, U.S.A.

Zhang, G.F., Kishi, N. & Mikami, H. 2003. Influence of material properties of FRPS on strength of flexural strengthened RC beams. *Proceedings of 6th International Conference on Fibre Reinforced Plastics for Reinforced Concrete Structures*. Singapore: World Science Publishing Company.

FRP Composites in Civil Engineering – CICE 2004 – Seracino (ed)
© 2005 Taylor & Francis Group, London, ISBN 90 5809 638 6

Debonding failure in CFRP strengthened concrete beams

N. Khomwan & S.J. Foster
School of Civil and Environmental Engineering, The University of New South Wales, Sydney, Australia

S.T. Smith
Infrastructure and the Environment Group, Faculty of Engineering, University of Technology, Sydney, Australia

ABSTRACT: In this study, the results of tests on a series of six large-scale (6 metre long by 700 mm deep) CFRP reinforced beams are reported. The experimental parameters include the level of pre-damage at the time of repair and the concrete strength. Bond-slip measurements were taken between the concrete and the CFRP together with extensive strain measurements on the CFRP and concrete surfaces. The CFRP-concrete soffit bond-slip data collected together with other control data forms a valuable data set for verification of numerical models.

1 INTRODUCTION

Due to the significant level of investment that developed countries have placed in their public and private infrastructure, and the aging of this infrastructure, rehabilitation and strengthening of existing reinforced concrete structures has become a research focus. Further, with the advent of fibre reinforced plastics (FRPs) new strengthening approaches have come to the fore using external bonding technologies. This approach has shown significant advantages compared to traditional methods, mainly due to the outstanding mechanical properties of the composite materials, its light weight and the simple application to structural members.

In the last decade, extensive experimental investigations on externally bonded FRP structures have demonstrated the significant improvement in overall behaviour of these structures under both service and ultimate conditions (Ritchie et al., 1991, Arduini & Nanni, 1997, and Norris et al., 1997). Investigations on the failure behaviour of structures reinforced with FRPs have revealed new (often brittle) failure modes due to mechanisms such as debonding at the interface between the FRPs and the parent structure (Saadamanesh & Ehsani, 1991, Garden & Hollaway, 1998 and Arduini et al., 1997).

Although debonding failures have been experimentally investigated in earlier studies, the majority of tests have been on relative small-scale specimens and in many cases key test data for the development of a rational model have not been collected. For example, in no test series reported has the relative displacement between the bonded CFRP plate, or fabric, and the parent structure been measured. Rather, smaller control-size debonding samples such as those of Chajes et al. (1996) have been relied on for this measurement.

Experimental results have, generally, been poorly reported throughout the history of research on flexurally strengthened RC beams. For example, in 17 of the 59 tests said to be reliable by Smith & Teng (2002) for debonding type failures, the depth of the cover concrete was not reported. In 48 of the tests no control measurements were undertaken to determine the concrete tensile strength; in 33 tests no control tests were undertaken to determine the elastic modulus of the concrete; in 27 tests the elastic modulus of the steel reinforcing was not measured; in 30 tests the elastic modulus of the adhesive was not measured or was estimated from previous tests by the same research group and; the thickness of the adhesive layer was not measured in 21 of the 59 tests. In fact in only 10 of the 59 specimens in the database, all from one study (Garden et al., 1997), had control tests been undertaken on all key parameters likely to appear in a rational bond model. However, in these tests the beams were of small scale, just 100 mm square in section by one metre long. In addition to the relatively poor quality of the reporting of control data, of the tests reported in the Smith & Teng database one specimen had a span between supports of 4.6 metres with the remainder of the specimens with spans of 3.6 metres or less. Over one half of the specimens reported had a span of less than two metres!

This paper reports the results of six (of a planned series of eight) large-scale CFRP reinforced beams. The main experimental parameters are the levels of damage at the time of repair and the concrete strength. Bond-slip measurements between the concrete and the

CFRP together with extensive strain measurements on the CFRP and concrete surfaces are taken. The CFRP-concrete soffit bond-slip data collected together with other control data forms a valuable data set for verification of numerical models.

2 EXPERIMENTAL PROGRAM

2.1 *Test specimens*

The overall dimension and details of the reinforcement arrangements for the six beams tested are shown in Figure 1. The beams were 350 mm wide, 700 mm deep and 6500 mm long. All specimens were identical in dimensions and reinforcement arrangements. The test variables are the concrete strength and the extent of pre-damage. The details of the tests are given in Table 1. In the two remaining tests of this series, fatigue of the repaired beams are to be investigated.

For beam B2, the CFRP repair was affected at zero load. The beam was then loaded slowly to 250 kN and measurements taken. At 250 kN the test was paused and the specimen unloaded. Two major cracks in the constant moment region were identified and strain gauges attached to the CFRP adjacent to the cracks, as described below. The load was then gradually increased until failure. For beam B6 the repair was at zero load and the loading gradually increased to failure.

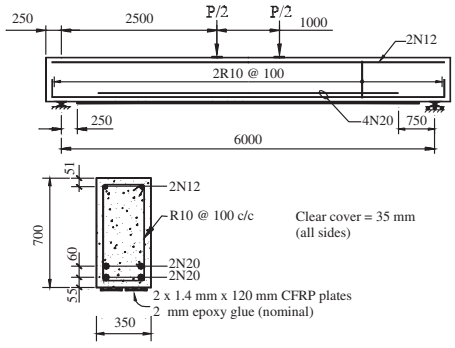

Figure 1. Details of CFRP strengthened beams.

Table 1. Test variables.

Beam	f_{cm} (MPa)	Pre-damage	Repair details
B1	37	NIL	NIL
B2	37	NIL	CFRP
B3	37	80%	CFRP
B5	53	NIL	NIL
B6	53	NIL	CFRP
B7	53	80%	CFRP

The loading history both prior to and after repair for beams B3 and B7 is given in Figure 2. At the first loading loop, the specimens were loaded to 240 kN, about 80% of the ultimate load of the control specimen before unloading to zero load. The load was again taken to 240 kN before unloading to 150 kN (≈50% of the strength of the control specimens) and held constant while the repair was affected. The load was held constant for 7 days while the epoxy cured and then increased gradually to failure.

2.2 *Materials*

The reinforcement used for the longitudinal steel consisted of nominally 500 MPa grade, hot rolled, deformed bars of 20 mm diameter for the bottom reinforcement and 12 mm diameter for the top reinforcement. The shear reinforcement was fabricated from nominally 250 MPa grade 10 mm diameter bars. Details of the material properties for the reinforcing steel are given in Figure 3.

The concrete was supplied by a local ready-mix supplier. The maximum aggregate size was 10 mm and was nominally 25 MPa for specimens B1 to B3 and 40 MPa for beams B5 to B7. The actual mean compressive strength (f_{cm}) results were obtained from the average of three 300 mm by 150 mm diameter cylinders tested in conjunction with the test beams (at

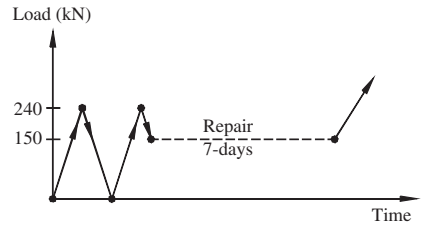

Figure 2. Loading procedure for specimens B3 and B7.

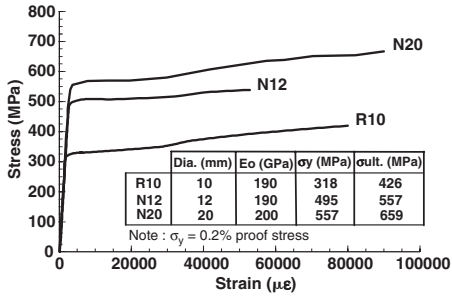

Figure 3. Material properties for steel reinforcement.

a rate of 20 MPa/min) with the results given in Table 1 and Figure 4.

The CFRP used in this project was CFK laminate 150/2000 as supplied by MBrace®. The thickness of this laminate was specified by the manufacturer as 1.40 mm and measurements taken with a micrometer confirmed an average thickness of 1.40 mm. This laminate was chosen due to its well defined material properties as opposed to using a wet lay-up system where the properties of the laminates are more variable. The resin used for the bonding of CFRP was a two-part epoxy adhesive (MBrace® laminate adhesive) that consisted of components A and B. The nominal mechanical properties of the CFRP and epoxy as given by the manufacturer are presented in Table 2.

The CFRP was tested to obtain the ultimate strength and elastic modulus using 12.5 mm wide by 300 mm long strips with the strain measured over a gauge length of 200 mm. Three specimens were prepared and tested at a rate of 2 mm/min with the results of the tests given in Figure 5. The mean ultimate strength of the three specimens was 2150 MPa, the ultimate tensile strain was 1.34% and the elastic modulus was 160 GPa.

The bond stress versus slip between the CFRP laminate and the concrete was obtained using double- shear bond tests. Two specimens were prepared, one specimen for each mix, using 100 mm square by 600 mm long prisms cast together with the beam specimens. The specimens were pre-cracked and FRP laminates applied to two sides using the same method as that for the beams. Before casting, steel bars were placed within the specimens with the bars discontinuous at the middle of the specimen. Thus, the two halves of the prism forming the test specimens were connected only through the FRP laminates. One side of the specimen was clamped with an applied force of 30 kN forcing delamination on the opposite side of the test specimen. The specimens are denoted as BS37 and BS53 corresponding to the mean cylinder strengths of 37 and 53 MPa, respectively.

The specimens were tested at a rate of 1 mm/min and were subjected to a tensile force applied to the embedded reinforcing bars. The test setup is shown in Figure 6 and the results of bond stress versus slip are given in Figure 7.

In addition to the bond strength-slip tests, a further two specimens were tested for each concrete mix for bond strength only. The average bond strengths were 4.2 MPa and 3.8 MPa for BS37 and BS53, respectively.

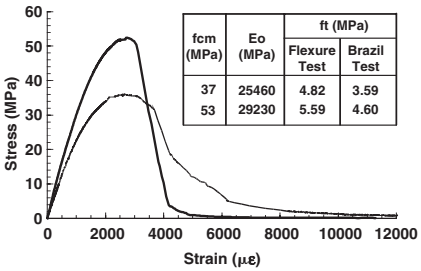

fcm (MPa)	Eo (MPa)	ft (MPa)	
		Flexure Test	Brazil Test
37	25460	4.82	3.59
53	29230	5.59	4.60

Figure 4. Material properties for concrete.

Table 2. Nominal CFRP material properties.

CFRP 150/2000	
Ultimate tensile strength	2700 MPa Min
Modulus of Elasticity	165 GPa Min
Ultimate strain	1.4%
Adhesive	
Compressive strength	>60 MPa
Flexural strength	>30 MPa
Specific Gravity@23°C	1.5
Full Cure@23°C	7 days

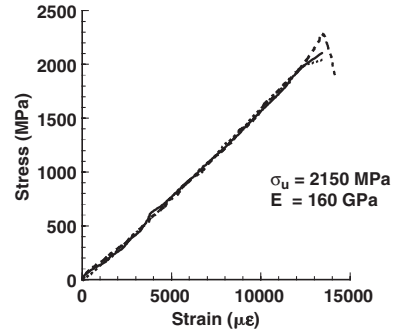

Figure 5. Actual tensile stress versus strain for the CFRP.

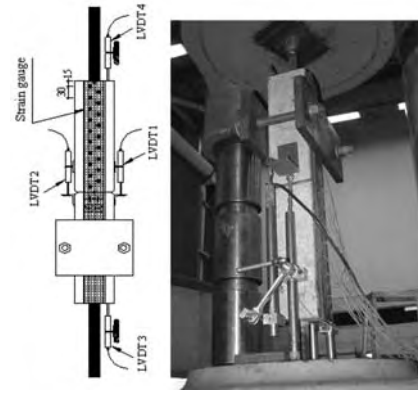

Figure 6. CFRP Bond test setup.

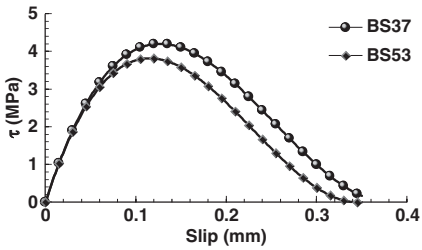

Figure 7. Measured bond stress versus slip.

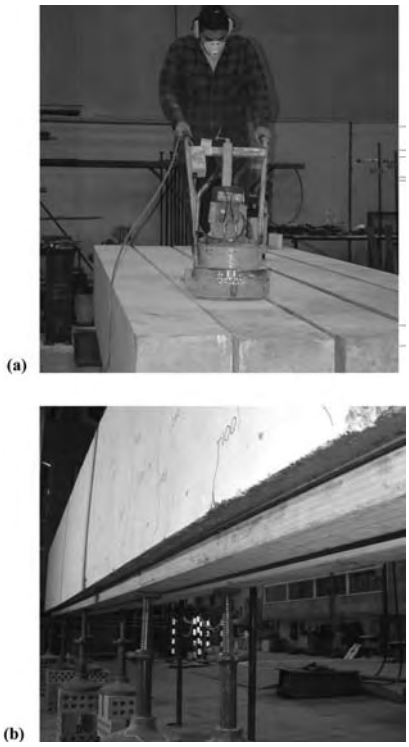

Figure 8. Preparation of strengthened specimens: (a) concrete surface preparation; (b) timber packing and props to hold the CFRP in place during curing.

All concrete test beam surfaces were ground to remove smooth cement paste to expose the aggregates (Figure 8a). Next, the roll of 120 mm wide CFRP was cut into lengths of 5500 mm. Surface preparation of the CFRP followed with sanding of the surface and cleaning to remove grease, oils, carbon dust or other contaminants prior to installation. After the CFRP and concrete surfaces were prepared, the primer was mixed as per the suppliers instructions and applied to the concrete surface. The epoxy adhesive was then mixed and applied to both CFRP and concrete surface to a nominal thickness of 2 mm. The CFRP was subsequently applied to the soffit of the beam specimen using light pressure and held in place using timber packing and props (Figure 8b).

Table 3. Average adhesive thickness.

Specimen	Adhesive thickness (mm)
B2	3.33
B3	3.39
B6	2.15
B7	3.48

On completion of the CFRP installation, the beam was cured at ambient temperature for at least 7 days before testing. Following each test, examining the failed specimens, the adhesive thicknesses were measured using a micrometer (Table 3).

2.3 *Test setup*

All specimens were tested in four-point bending using a 1000 kN capacity jack. Mechanical and electrical gauging and monitoring equipment was set up to measure loads, displacements, tensile steel strains, concrete strains and CFRP strains.

Electronic resistance strain gauges were attached to the main tensile reinforcement and external surfaces of CFRP plates. For the control beams, 12 strain gauges (S1 to S12 in Figure 9a.) were attached to the main tensile reinforcement at the mid span and beneath the load points. The strain gauges were installed on both layers of the main tensile reinforcement. For the strengthened beam specimens, six strain gauges (S1, S5, S6, S7, S8 and S10) were attached to the main tensile reinforcement. Four were attached at mid span and one at each load point. For specimen B2, 17 strain gauges were attached to the CFRP plates at the locations shown in Figure 9b. For specimens B3, B6 and B7 strains were measured in the CFRP plate at 16 locations along one half of the span (Figure 9c).

One of two modes of failure was anticipated, interfacial debonding or intermediate crack interfacial debonding. For specimen B2, strain gauges F8 to F17 were located adjacent to two large cracks within constant moment region. Strain gauges F1 to F7 were glued into position and the beam then loaded to 250 kN to induce cracking. The beam was then unloaded and strain gauges F8 to F17 glued to the CFRP adjacent to the cracks (Figure 9b).

Average surface strains were measured at the level of the reinforcement along the beam using Demec strain gauges (Figure 10a). Demec targets were also

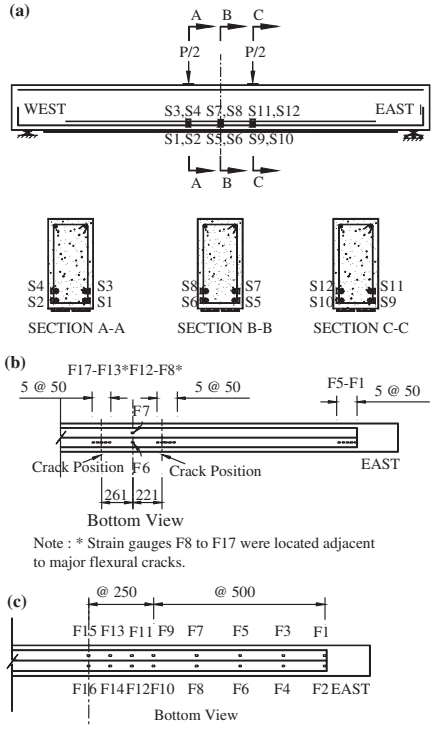

Figure 9. Strain gauge locations: (a) tensile reinforcement, (b) CFRP laminate of specimen B2; (c) CFRP laminate for specimen B3, B6 and B7.

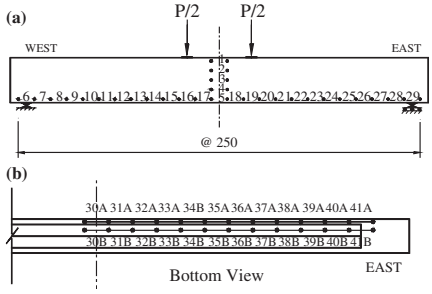

Figure 10. Details of Demec targets: (a) surface strains for all specimens; (b) soffit strains for specimen B3, B6, and B7.

located at the mid-section of the specimen to measure curvatures.

To measure the relative displacement (or slip) between the concrete and the CFRP plates at the soffit of the specimens, Demec targets were attached as

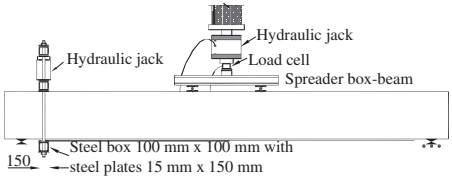

Figure 11. Test setup for strengthened beams (control beams similar).

Figure 12. Beam B2 after debonding failure.

shown in Figure 10b for beams B3, B6 and B7. Gauges 30A to 41A were attached to concrete adjacent to the CFRP and gauges 30B to 41B were attached to the CFRP at the time of the installation of the plates. For beams B3 and B7 this was with the load maintained at 150 kN.

For the strengthened beam specimens, one end of the CFRP plates was clamped, to induce failure at the other end, using a hydraulic jack and steel plate arrangement. The jack was pressured to apply a load of 240 kN which was held constant for the duration of the test. The test setup is shown in Figures 11 and 12 for beam B2.

3 RESULTS AND OBSERVATIONS

The failure loads and modes of failure are presented in Table 4. For the CFRP specimens two failure loads are given, before and after debonding. For the strengthened beams, P_u corresponds to the debonding failure and P_r is the post debonding capacity.

Failure of all strengthened specimens was by intermediate crack interfacial debonding with the debonding mechanism initiated by cracks in the vicinity of the constant moment region. For example, in beam B6, shown in Figure 13, debonding was initiated adjacent to a crack at approximately 700 mm east of midspan.

Table 4. Experimental failure loads and modes of failure.

Beam	Failure load (kN) P_u	P_r	P_u/P_r	Failure mode
B1	310	–	–	Flexure
B2	447	306	1.46	Debonding
B3	420	312	1.35	Debonding
B5	324	–	–	Flexure
B6	477	322	1.48	Debonding
B7	482	331	1.46	Debonding

Figure 13. Initiation of intermediate debonding failure (B6 at P = 450 kN).

Figure 14. Debonding failure in beam B3.

The debonding crack then continued along the specimen towards the supports until the force in the CFRP could not be sustained by the anchorage length. At this time a sudden debonding failure occurred (Figure 14).

The loads versus midspan deflections are given in Figure 15 and 16. The results show that the CFRP

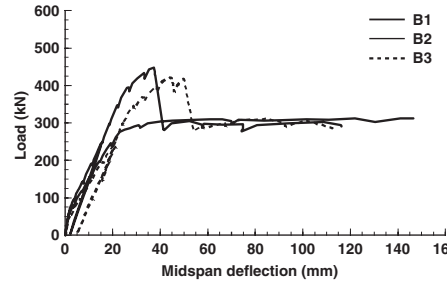

Figure 15. Load versus midspan displacement for B1, B2 and B3.

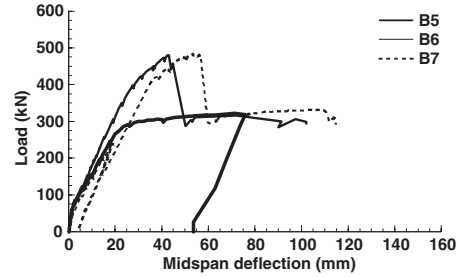

Figure 16. Load versus midspan displacement for B5, B6 and B7.

strengthening system increased the strength of the beams by approximately 35 to 50% compared to the control beams but failed in a less ductile manner. Comparing the results of beams B2 and B6 and beams B3 and B7 shows that the pre-damage affected only slightly the ultimate strengths of the beams. Comparing the results of beams B2 and B3 and of B6 and B7 shows that the strength of the strengthened beams increased with an increase in the concrete strength, however, the increase in strength was similar to the proportional increase between the control specimens B1 and B5.

In Figure 17 and 18 the steel strains at the midspan are plotted. The figures show that the steel strains at midspan are influenced by the applied load at the time of the attachment of the CFRP plates. For the control beams (B1 and B5) and repaired beams (B3 and B7), the steel strain reached the yield strain at 240 kN while the steel strains in the undamaged- strengthened beams B2 and B6 yielded strain at 320 to 350 kN.

The strains at the end of the CFRP plates for specimen B2 are given in Figure 19 and the strains in the vicinity of two monitored cracks of specimen B2 are given in Figure 20. The strains were similar and indicate that the discontinuity in the concrete at the crack did not change, significantly, the local stresses in the

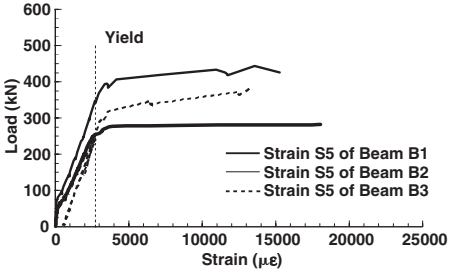

Figure 17. Load versus steel strains at midspan for beams B1, B2 and B3.

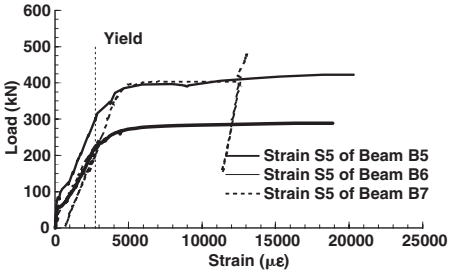

Figure 18. Load versus steel strains at midspan for beams B5, B6 and B7.

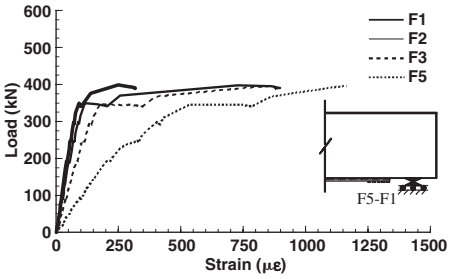

Figure 19. Beam B2 end-plate CFRP strains (gauge F1 to F5).

CFRP plate. Thus, the epoxy allowed for sufficient slip to produce near uniform distribution of strains in the CFRP between cracks in the constant moment region.

The strains along the beams are given in Figure 21 for beam B3 and B7 where each data point is taken as the average strain of adjacent strain gauges on the CFRP plates. The figures show that as the load increased beyond the capacity of the unstrengthened control beams, the strains in the CFRP increased rapidly. At 420 kN in beam B3 an approximately

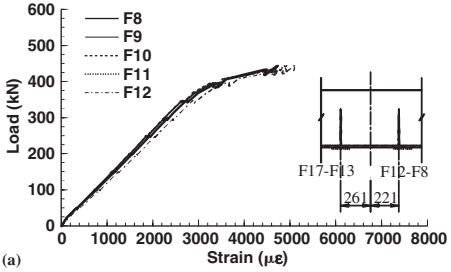

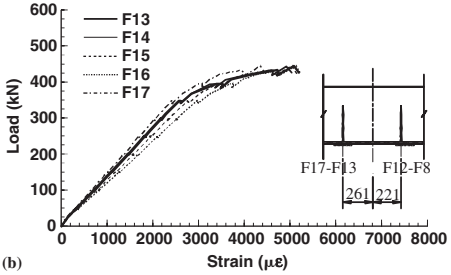

Figure 20. Specimen B2: CFRP strain data for strain gauges F8 to F17.

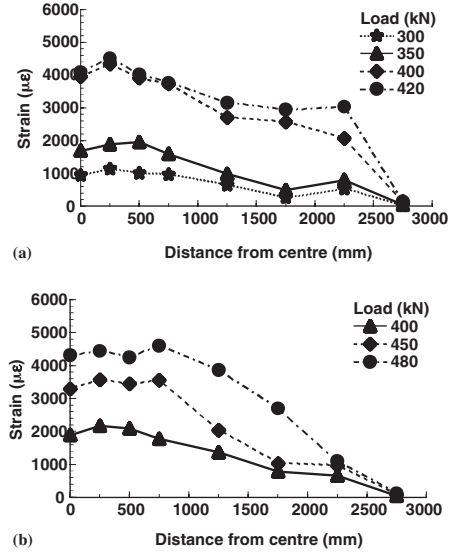

Figure 21. CFRP strains (gauge F2, F4, to F16) for beam: (a) B3; (b) B7.

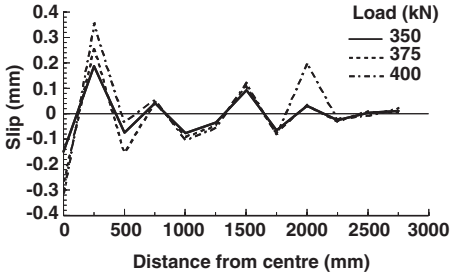

Figure 22. Slip between CFRP plate and concrete for beam B3.

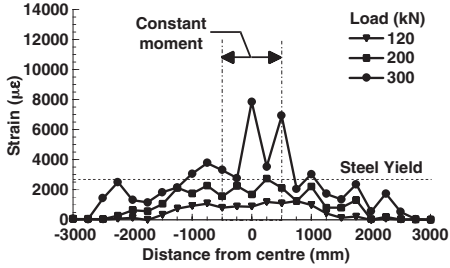

Figure 23. CFRP strain data of Demec gauge 6 to 29 along B1 specimen.

uniform strain is seen between 0 and 2300 mm from the centre of the specimen. For specimen B7 high, near uniform, strains were measured well beyond the constant moment region.

The slip between the CFRP and concrete of beam B3 is presented in Figure 22. The slip was calculated by the elongation difference between CFRP plate and concrete surface at the soffit of the beam. The elongations of CFRP and concrete are obtained by multiplying the strain results from Demec target measurements by the gauge length (250 mm). While care must be taken with the interpretation of these results as they only indicate average slip over the gauge length, some comments can be made. The figure shows that the slip was small at the distance from the centre of 2250 mm to the end of the CFRP plate which implies that there was little demand on bond at this location. On the other hand, the bond demands were highest within the constant moment region of the beam (between cracks). These observations are consistent with the measured strains in the CFRP (Figure 21a).

In Figure 23 and 24, the Demec strains measured at the level of the reinforcing steel are plotted for beams B1 and B3, respectively. Figure 23 shows that the yielding of the steel extended well beyond the constant moment region for the strengthened specimens.

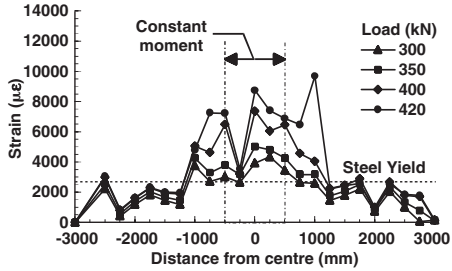

Figure 24. CFRP strain data of Demec gauge 6 to 29 along B3 specimen.

4 CONCLUSIONS

In this study, six large-scale beams were tested with a clear span of 6.0 m. All beams were identical in dimensions and steel reinforcement detailing with the test variables being the concrete strength and the degree of pre-damage. The beams were loaded in four-point bending and extensively gauged.

The experiments showed a significant increase in strength over that of the control beams for both the undamaged and pre-damaged specimens. A small increase in stiffness was also evident for the strengthened undamaged specimens but no significant increase in the pre-peak stiffness was evident for the pre-damaged and repaired specimens over that of the control beams. The increase in strength, however, is at a sacrifice of ductility. The debonding of the CFRP led to a sudden drop in load with the response of the beams reverting back to that of the control specimens.

The significance of this research is not, however, in its particular findings on strength and behaviour but that it provides a valuable and complete data set for the verification of numerical and improved design models.

ACKNOWLEDGEMENTS

The authors wish to thank MBT (Aust) Pty Ltd for the supply of the CFRP laminates and resins and their support towards the project. The advice on the test program of Andrew Sarkady is also gratefully acknowledged and appreciated.

REFERENCES

Arduini, M. & Nanni,A. 1997. Behaviour of Precracked RC Beams Strength with Carbon FRP Sheets. *Journal of Composites for Construction*, ASCE, 1(2): 63–70.

Arduini, M., Tommaso, A.D., & Nanni, A. 1997. Brittle failure in FRP Plate and Sheet Bonded Beams. *ACI Structural Journal*, 94(4): 363–370.

Chajes, M.J., Finch, W.W. Jr., Januszka, T.F., & Thomson T.A. Jr., 1996, Bond and force transfer of composite material plates bonded to concrete, *ACI Structural Journal*, 93(2): 208–217.

Garden, H.N., Hollaway, L.C., & Thorne, A.M. 1997, A preliminary evaluation of carbon fibre reinforced polymer plates for strengthening reinforced concrete members, Proc. Inst Civil Engineers Struct. Build., 127: 127–142.

Garden, H.N., & Hollaway, L.C. 1998. An Experimental Study of the Influence of Plate End Anchorage of Carbon Fibre Composite Plates used to Strengthen Reinforced Concrete Beams, *Composite Structures*, 42: 175–188.

Norris, T., Saadatmanesh, H., & Ehsani, M. 1997. Shear and Flexural Strengthening of R/C Beams with Carbon Fiber Sheets, *Journal of Structural Engineering*, ASCE, 123(7): 903–911.

Ritchie, P.A., Thomas, D.A., & Lu L.W. 1991, External Reinforcement of Concrete Beams using Fiber Reinforced Plastics. ACI Structural Journal, 88(4): 490–500.

Saadatmanesh, H., & Ehsani, M. 1991. RC beams strengthened with GFRP plates I: Experimental study, *Journal of StructuralEngineering*, ASCE, 123(7): 903–911.

Smith, S.T., & Teng, J.G. 2002. FRP-Strengthened RC Beams II: Assessment of Debonding Strength Models, *Engineering Structure*, 24(4): 397–417.

FRP Composites in Civil Engineering – CICE 2004 – Seracino (ed)
© 2005 Taylor & Francis Group, London, ISBN 90 5809 638 6

Parametric study of intermediate crack (IC) debonding on adhesively plated beams

I. Liu, D.J. Oehlers & R. Seracino
The University of Adelaide, Adelaide, South Australia, Australia

ABSTRACT: Reinforced concrete members retrofitted by adhesively bonding steel or fibre reinforced polymer (FRP) plates to the external surface is often subjected to premature debonding or peeling of the plate from the existing structure before reaching the desired strength or ductility. One of the main mechanisms of debonding failure is intermediate crack (IC) debonding. In this research, a generic model has been developed for IC debonding of plated RC beams based on partial interaction theory. Using this model, parametric studies on variation in crack spacing and rate of change of moment was carried out and it was found that both of these factors as well as the number of cracks in the beam can have large effects on the local behaviour and the resultant strains in the plated member.

1 INTRODUCTION

Retrofitting reinforced concrete members by adhesively bonding steel or fibre reinforced polymer (FRP) plates to the external surface is a simple technique which is rapid to apply, inexpensive, unobtrusive, and can be applied while the structure is in use. The main problem associated with adhesively bonding plates to RC members is premature debonding or peeling of the plate from the existing structure before reaching the desired strength or ductility. This form of failure is unique to plated structures. The debonding failure can be classified into 3 main categories (Oehlers 2000, Mohamed Ali 2000): (1) plate end PE debonding, caused by the existence of high interfacial shear and normal stresses at the plate end due to abrupt termination of the plate (Fig. 1); (2) critical diagonal crack CDC debonding due to vertical shear deformations of the beam (Fig. 2); and (3) intermediate crack IC debonding which is associated with the formation of flexural or flexural-shear cracks in the vicinity of the plate (Fig. 3). IC debonding is considered to be a more dominant failure mode compared to PE debonding, especially for thin FRP plates, however there is very limited literature regarding to this failure mechanism (Wu & Niu, to be published). Unlike PE debonding and CDC debonding, IC debonding is difficult to prevent, and since it is a much more ductile failure compared to PE and CDC debonding, it should be the failure that engineers design for when retrofitting beams using this technique.

In order to accommodate the intercepting flexure cracks in IC debonding, the plate requires infinite strains across the cracks, which is not possible, hence

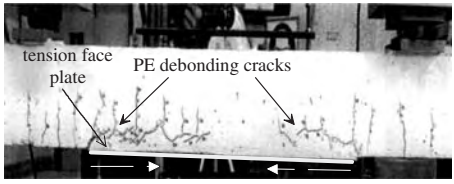

Figure 1. Plate end debonding.

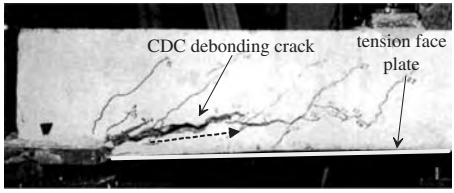

Figure 2. Critical diagonal debonding.

horizontal cracks occur at the plate/concrete interface. IC debonding cracks usually first occur at positions of maximum moment, where strains in the plate are largest (Oehlers & Seracino, to be published). From the roots of the intersecting cracks they propagate gradually towards the plate ends as illustrated in Figure 4. Because concrete has a much lower strength than the adhesive, these debonding cracks generally occur in the concrete adjacent to the adhesive-concrete interface. For IC debonding induced by flexural cracks, crack widening causes debonding propagation. For IC

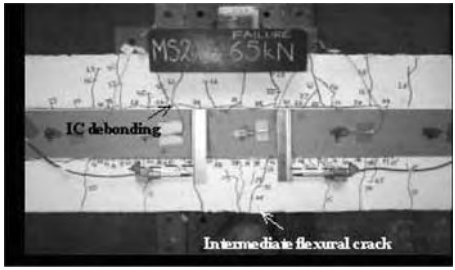

Figure 3. Intermediate crack debonding.

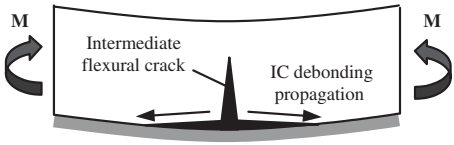

Figure 4. Intermediate crack debonding mechanism.

debonding induced by flexural-shear cracks, the relative vertical displacement between the two faces of the crack also produces peeling stresses at the interface, however this effect is less significant hence it is considered that the propagation of debonding is predominately caused by widening of crack (Teng et al. 2002).

In this research, a generic model has been developed for intermediate crack debonding of plated RC beams based on partial interaction theory (Oehlers & Bradford 1995). This model will allow us to have a better understanding of the behaviour of IC debonding, and hence predict when IC debonding will occur. Parametric studies have been carried out to study how the variation in crack spacing and rate of change of moment dM/dx affects the behaviour of IC debonding in plated members.

2 COMPUTER MODEL

The behaviour of composite beams, and plated and unplated reinforced concrete beams are similar in that for all 3 systems, the force in the concrete is transferred to the reinforcement or plate via the bond provided at the interface. Therefore, the partial interaction theory that was originally developed for composite beams (Johnson 1994) can also be applied to plated and unplated RC beams.

Before flexural cracking of concrete, there is no slip at the concrete/plate interface and so the strain is linearly distributed along the cross-section such as that illustrated in Figure 5a for a plated beam. Therefore the assumption of plane sections remaining plane holds and there is a *full interaction* between the plate and

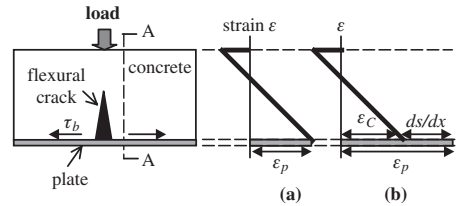

Figure 5. (a) Full interaction (b) partial interaction of plated beam.

the concrete i.e. plate strain at the interface is equal to the strain in the concrete adjacent to it. However, when cracking occurs, this causes high bondstress to develop near the crack, and as a result, sliding occurs between the concrete and the plate. That is there is slip at the interface given by Equation 1, where u_p and u_c is the displacement of the plate and the concrete respectively. Therefore the strain in the plate ε_p is no longer equal to the strain in the adjacent concrete ε_c such as shown in Figure 5b. This means that full interaction analysis can no longer apply to the structure. The difference between the plate and adjacent concrete strain is defined as slip strain ds/dx (Equation 2), and this is now a *partial interaction* problem.

$$s = u_p - u_c \tag{1}$$

$$\frac{ds}{dx} = \frac{du_p}{dx} - \frac{du_c}{dx} = \varepsilon_p - \varepsilon_c \tag{2}$$

To perform partial interaction analysis on plated beams, the "shooting technique" (Oehlers & Bradford 1995) is used. This involves performing segmental analysis along the member at fixed increments x to a point where the boundary conditions are known. Iterative procedures are carried out by changing the guessed slip at a crack s_{cr} until the boundary conditions are satisfied. Before performing the analysis, the location of the first crack needs to be chosen; for example for a beam subjected to a concentrated load, the first flexural crack is assumed to occur immediately under the applied load. For beams under flexure, the flexural cracks will occur at region of high moment and due to these cracks, there will be slip s and hence slip-strain ds/dx between the plate and the adjacent concrete. Therefore this cracked region is a partial interaction region such as that illustrated in Figure 6 and our partial interaction model applies here.

For a beam subjected to a point load, maximum slip s_{max} occurs beneath the load. For a beam with a single crack, as we move towards the support, the slip at the concrete/plate interface decreases until we reach a point where there is no further slip s, and the strain in the plate and the adjacent concrete is identical such as point A in Figure 6. From this point to the

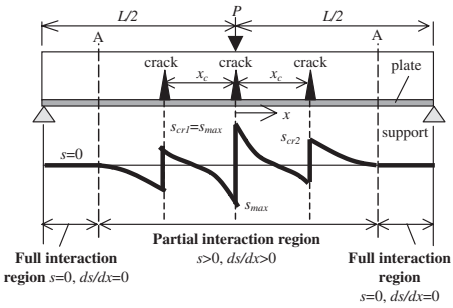

Figure 6. Partial interaction model for plated beams.

support we have full interaction, where $s = ds/dx = 0$ and this forms the boundary conditions for analysis with single crack.

If another crack forms in the partial interaction region as in Figure 6, this will change the stress and slip distribution along the beam. However, the beam needs to be reanalyzed based not only on the boundary conditions above, but also the boundary condition that the concrete tensile strain ε_{ct} at the concrete/plate interface equals zero at sections immediately adjacent to the crack. The model developed can be applied to tensile specimens as well as plated and unplated reinforced concrete beams. Using the model, the location of the flexural cracks can be found and the local stress and slip behaviour between cracks can be obtained.

The parametric study carried out in this context is on a simply supported plated RC beam, where a point load is applied at midspan $L/2$ and it is assumed that 3 flexural cracks forms at fixed crack spacing x_c as shown in Figure 6. As the aim of this parametric study is to examine the IC debonding behaviour at the plate-concrete interface, the reinforcing bars are hence neglected in the analysis. The beam is 375 mm wide (b) by 120 mm high (h), with a concrete strength f_c of 40 MPa. CFRP plate is adhesively bonded along the tension face over the entire length of the beam with a width b_p and thickness t_p of 50 mm and 1.2 mm respectively. The plate has a Young's modulus E_p of 144 GPa and a fracture strength f_{frac} of 3050 MPa. Analysis was carried out based on the non-linear bondstress-slip (τ_b-s) model shown in Figure 7, where $\tau_{b\cdot max} = 6$ MPa at $s_m = 0.02$ mm, and $s_f = 0.2$ mm. Debonding at the plate/concrete interface occurs when slip is greater than s_m.

3 VARIATION OF CRACK SPACING

Analysis was carried out on the simply supported beam illustrated in Figure 6 where the length of the beam L is kept at 2000 mm and the spacing between cracks

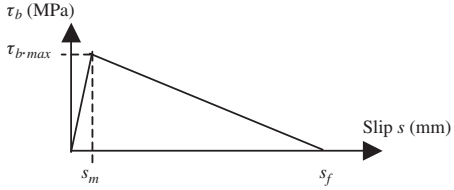

Figure 7. Bondstress-slip model (Teng et al. 2002).

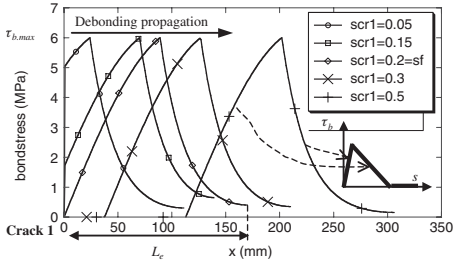

Figure 8. Bondstress τ_b vs x (single crack, $L = 2000$ mm) for various s_{cr1} (in mm).

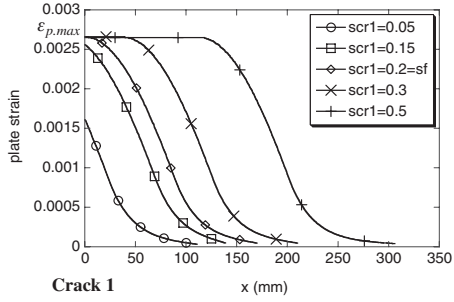

Figure 9. Plate-strain ε_p vs x (single crack, $L = 2000$ mm) for various s_{cr1} (in mm).

x_c is varied to observe the effects of crack spacing on the local behaviour of plated members. As the beam is symmetrical, analysis was carried out from the applied load P to the support.

For a beam with only a single crack beneath the load i.e. crack 1 in Figure 6, it was found that as the slip at crack 1 s_{cr1} increases, the resultant bond force P_b and hence the strain in the plate ε_p increases until s_{cr1} reaches s_f as shown in Figure 8 and Figure 9 respectively, where x is the distance from crack 1. At $s_{cr1} = s_f$, the bond force, given by the area under bondstress graph Figure 8, is at its maximum with a maximum plate strain $\varepsilon_{p\cdot max}$ of 0.00266 being reached at crack 1. As the slip at crack 1 further increases, the debonding

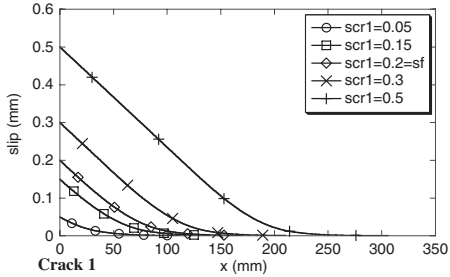

Figure 10. Slip s vs x (single crack, $L = 2000$ mm) for various s_{cr1} (in mm).

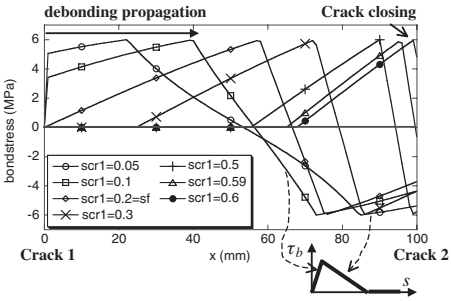

Figure 11. Bondstress τ_b vs x ($x_c = 100$ mm, $L = 2000$ mm) for various s_{cr1} (in mm).

crack propagates along the beam while the plate strain at crack 1 remains constant at $\varepsilon_{p\cdot max}$ (Fig. 9).

Note how as the slip at the crack increases, the point of full interaction ($ds/dx = s = 0$) moves closer to the support as shown by Figure 10, which means that the region of partial interaction is increasing due to debonding and eventually debonding failure will occur at the maximum plate strain $\varepsilon_{p\cdot max}$ of 0.00266. It should be noted that based on Teng's bond model (Teng 2002), the effective bond length Le for the beam analysed is 167 mm, which agrees with that found from our analysis as shown in Figure 8.

To study beams with different crack spacings, analysis was performed assuming 2 cracks, crack 1 and 2, had formed along the shear span $L/2 = 1000$ mm (Fig. 6) where a crack spacing x_c of 50 mm, 100 mm, 200 mm, and 400 mm was considered. Figures 11–13 show respectively the bondstress, slip, and plate strain distribution of a beam with $x_c = 100$ mm. It can be seen that the occurrence of a new crack largely affects the local behaviour of the beam. Due to the existence of a subsequent crack, there is a change in slip direction, i.e. negative slip, in between the cracks as shown in Figure 12. As a result, there is a change in direction in the bondstress between cracks in order to

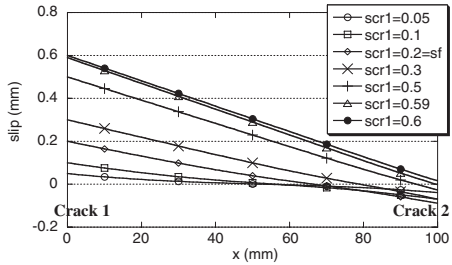

Figure 12. Slip s vs x ($x_c = 100$ mm, $L = 2000$ mm) for various s_{cr1} (in mm).

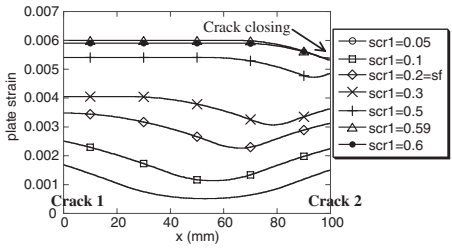

Figure 13. Plate-strain ε_p vs x ($x_c = 100$ mm, $L = 2000$ mm) for various s_{cr1} (in mm).

maintain equilibrium as illustrated in Figure 11. When the slip at crack 1 is small i.e. $s_{cr1} < s_f$ (=0.2 mm), the slip near crack 2 increases (in opposite direction) with increase in s_{cr1} which causes debonding cracks to occur at crack 1 propagating towards support as well as at crack 2 moving towards applied load. However as s_{cr1} increases to greater than s_f, the debonding cracks that were propagating from crack 2 towards applied load do not propagate any further i.e. slip near crack 2 decreases with increase in s_{cr1}, and the debonding cracks are now propagating in one direction towards the support.

From Figure 12, it can be seen that the point of zero slip between cracks shifts towards the subsequent crack, crack 2, as slip increases. Eventually the slip between the cracks will become so large that there will be no change in slip direction between the cracks i.e. at $s_{cr1} = 0.6$ mm, which indicates that the whole segment between the two cracks is moving towards the support, hence resulting in the closing up of crack 2. This is also demonstrated in Figure 13 where the plate strain increases as we approach a crack, however at $s_{cr1} = 0.6$ mm, the plate strain does not increase near crack 2, which indicates that the crack is closing up. The plate strains increase as slip increases and the maximum plate strain occurs just prior to closing up of crack 2, when zero slip occurs at crack 2.

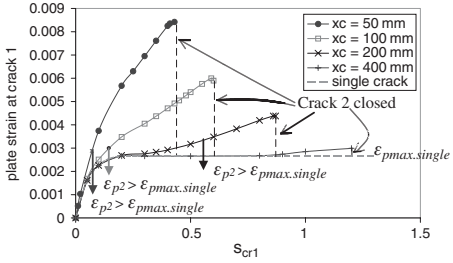

Figure 14. $\varepsilon_{p\cdot cr1}$ vs s_{cr1} for various crack spacings ($L = 2000$ mm).

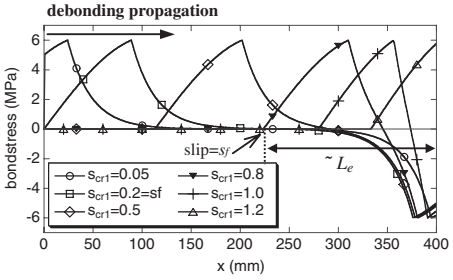

Figure 15. Bondstress τ_b vs x ($x_c = 400$ mm, $L = 2000$ mm) for various s_{cr1} (in mm).

Figure 14 is a comparison of the plate strains obtained at crack 1 $\varepsilon_{p\cdot cr1}$ at the corresponding slips for various crack spacing x_c considered. It can be seen that at small slip prior to debonding (i.e. at $s_{cr1} < s_m$), difference in crack spacing does not affect $\varepsilon_{p\cdot cr1}$ obtained. For a beam with single cracks, maximum plate strain $\varepsilon_{pmax\cdot single}$ is reached at $s_{cr1} = 0.2$ mm ($=s_f$) and remains constant as slip increases. However when there are multiple cracks in the beam, the smaller the crack spacing, the larger the plate strain at crack 1. Note that for crack spacings greater than the effective bond length ($Le = 167$ mm), due to the cracks being far apart, initially $\varepsilon_{p\cdot cr1}$ obtained is similar to that for a single crack beam. However as the slip becomes large and the debonding cracks begin to approach crack 2 such that the distance between the point where slip $= s_f$ and crack 2 is less than the effective bond length (Fig. 15), then $\varepsilon_{p\cdot cr1}$ obtained is larger than that for a single crack beam.

Note that in Figure 14, the analysis was carried out up to closing of crack 2. If there were cracks throughout the span, after crack 2 closes, the crack spacing from crack 1 to the next crack is doubled, hence the strain in the plate decreases. For example, for a crack spacing of 50 mm, at $s_{cr1} = 0.43$ mm and $\varepsilon_{p\cdot cr1} = 0.0084$, crack closes so that the distance between crack 1 and

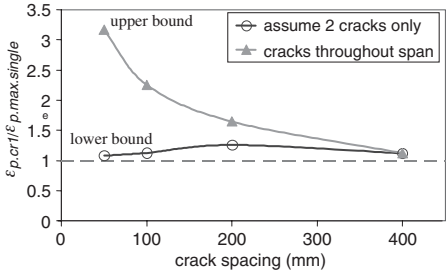

Figure 16. Ratio of $\varepsilon_{pmax\cdot cr1}$ and $\varepsilon_{pmax\cdot single}$ vs crack spacing.

the next crack is now 100 mm. Therefore for the same slip, $\varepsilon_{p\cdot cr1}$ drops to 0.005 due to increase in crack spacing. If there were only 2 cracks in the shear span such as the beam in Figure 6, as there is no further cracking after crack 2, the strain in the plate at crack 2 $\varepsilon_{p\cdot cr2}$ cannot exceed the maximum plate strain obtained for a single crack $\varepsilon_{pmax\cdot single}$. For example, for $x_c = 200$ mm shown in Figure 14, when the plate strain at crack 1 is 0.0034, $\varepsilon_{p\cdot cr2} = \varepsilon_{pmax\cdot single}$ and since there is no further cracking after crack 2, debonding cracks will propagate immediately from crack 2 to the support causing failure. For all the crack spacing x_c considered, failure occurred prior to crack 2 closing due to $\varepsilon_{p\cdot cr2} > \varepsilon_{pmax\cdot single}$, except for $x_c = 400$ mm where $\varepsilon_{p\cdot cr2} < \varepsilon_{pmax\cdot single}$, hence crack 2 closes at $s_{cr1} = 1.2$ and the plate strain reduces to that of single crack ($\varepsilon_{pmax\cdot single}$).

Figure 16 shows the ratio of maximum plate strain obtained at crack 1 $\varepsilon_{pmax\cdot cr1}$ and $\varepsilon_{pmax\cdot single}$ for different crack spacings. It can be seen that for fully cracked beams with cracks throughout the span, $\varepsilon_{pmax\cdot cr1}$ increases exponentially with decrease in crack spacing. This is the upper bound to the maximum strain that can be achieved in a plate for the crack spacing considered. However if the beams only have 2 cracks, at small crack spacing the maximum plate strain is close to that given by beam with a single crack. This case with 2 cracks forms the lower bound to $\varepsilon_{pmax\cdot cr1}$ for beams with multiple cracks. This shows that crack spacing and the amount of cracks along the beam largely influences the local stress and strain in a beam.

4 VARIATION OF RATE OF CHANGE OF MOMENT

The effects of rate of change of moment dM/dx on the local behaviour of plated beams is studied by analyzing the simply supported beam illustrated in Figure 6, firstly looking at a single crack, crack 1, then assuming 2 cracks in the beam, crack 1 and 2 at a fixed crack

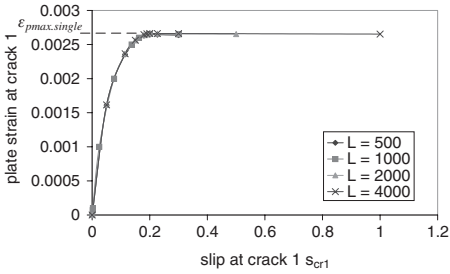

Figure 17. Effects of dM/dx on beam with single crack.

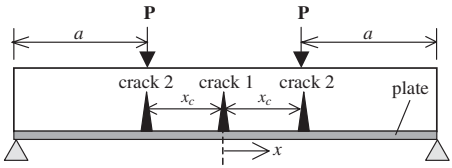

Figure 18. Beam under constant moment.

spacing x_c of 200 mm. The rate of change of moment is varied by changing the length of the beam L.

It can be seen from Figure 17 that varying L and hence the rate of change of moment does not affect the maximum plate strain in beams with single crack.

Analysis was carried out on a beam under constant moment (i.e. $L \to \infty$) with a fixed crack spacing x_c of 200 mm as illustrated in Figure 18. The bondstress distribution between 2 cracks is given in Figure 19. To maintain equilibrium, the point of zero slip always occurs at midpoint between 2 cracks, as opposed to varying moment region where the point of zero slip moves towards the next crack as slip increases. Therefore the debonding cracks in constant moment region will propagate in both directions and will not close up like those in varying moment regions. As the sum of bond force between cracks in constant moment region is equal to zero, the force in the plate is given by the resultant bond force in the varying moment region along the beam. If the beam is uncracked in the varying moment region i.e. region a in Figure 18, then the maximum plate strain that can be obtained is the same as that for a beam with single crack i.e. $\varepsilon_{pmax} = \varepsilon_{pmax\cdot single}$.

The comparison of plate strain at crack 1 $\varepsilon_{p\cdot cr1}$ at the corresponding slip s_{cr1} for different beam length L, hence different rate of change of moment considered is illustrated in Figure 20 where a crack spacing of 200 mm is considered. Analysis was carried out on beam length ranging from 500 mm to 8000 mm, assuming there are cracks throughout the beam at constant crack spacing. Like the analysis carried out for

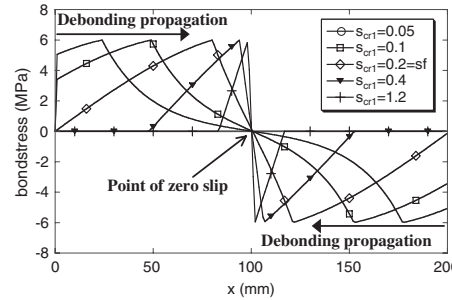

Figure 19. Bondstress τ_b vs x (constant moment, $xc = 200$ mm).

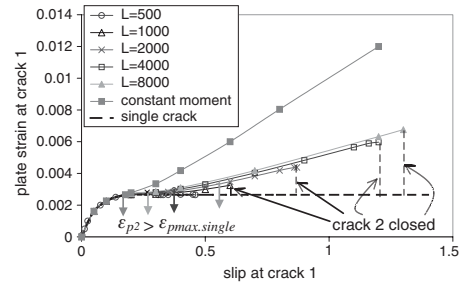

Figure 20. $\varepsilon_{p\cdot cr1}$ vs s_{cr1} for different beam length L ($x_c = 200$ mm).

varying crack spacing, $\varepsilon_{p\cdot cr1}$ increases with increase in slip at crack 1 until the maximum plate strain is reached just prior to crack 2 closing, after which there is a sudden drop in $\varepsilon_{p\cdot cr1}$ due to increase in crack spacing as a result of crack 2 closing. It can be seen from Figure 20 that when the beam is short i.e. $L = 500$ mm such that the rate of change of moment dM/dx is very high, the plate strain obtained at crack 1 $\varepsilon_{p\cdot cr1}$ for the relative s_{cr1} is similar to that found for a beam with single crack. As we increase L, which reduces dM/dx, initially at a small slip $\varepsilon_{p\cdot cr1}$ obtained is similar to that for single crack beam due to the large crack spacing ($x_c > Le$). However as slip increases, $\varepsilon_{p\cdot cr1}$ achieved becomes greater than that obtained from a single crack beam.

If we consider a beam with only 2 cracks in the shear span such as that illustrated in Figure 6, it was found that at $L > 1000$ mm due to the small rate of change of moment, the plate strain in crack 2 $\varepsilon_{p\cdot cr2}$ is relatively high. Since there is no further cracking after crack 2, therefore $\varepsilon_{p\cdot cr2}$ cannot exceed the maximum plate strain obtained for a single crack $\varepsilon_{pmax\cdot single}$. For beams with length greater than 1000 mm, it was found that plate strain at crack 2 reached $\varepsilon_{pmax\cdot single}$ before crack 2 closes up, hence causing debonding failure to occur at

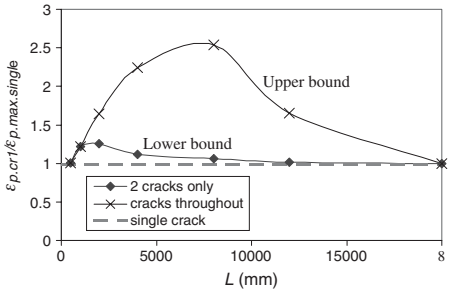

Figure 21. Ratio of $\varepsilon_{pmax\cdot cr1}$ and $\varepsilon_{pmax\cdot single}$ vs L ($x_c = 200$ mm).

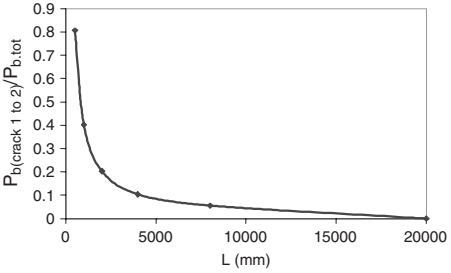

Figure 22. Ratio of bond force between crack 1&2 and total bond force vs L.

an earlier $\varepsilon_{p\cdot cr1}$ as shown by the arrows in Figure 20. For example, for $L = 2000$ mm shown in Figure 20, when the plate strain at crack 1 is 0.0034, $\varepsilon_{p\cdot cr2} = \varepsilon_{pmax\cdot single}$ and since there is no further cracking after crack 2, debonding cracks will propagate immediately from crack 2 to the support causing failure.

Figure 21 shows the ratio of maximum plate strain obtained at crack 1 $\varepsilon_{pmax\cdot cr1}$ and maximum plate strain obtained for a single crack $\varepsilon_{pmax\cdot single}$ for various beam length with fixed crack spacing of 200 mm. The upper bound of $\varepsilon_{pmax\cdot cr1}$ is determined by considering beams with cracks throughout the beam, and the lower bound is given by the beams with only 2 cracks in the span. When L is very small such that the rate of change of moment dM/dx is very high, the maximum plate strain obtained is similar to that of a beam with single crack. As L tends to infinity i.e. constant moment $dM/dx = 0$, $\varepsilon_{pmax\cdot cr1}$ tends to $\varepsilon_{pmax\cdot single}$. There is an optimum beam length at which a maximum strain in the plate can be achieved and this optimum length is dependent on the number of cracks along the beam as well as the crack spacing, which are in turn dependent on the rate of change of moment.

Figure 22 illustrates how the ratio of the resultant bond force between crack 1 and 2 $P_{b(crack1-2)}$ and the total bond force in the beam $P_{b\cdot tot}$ (i.e. resultant force in the plate) varies for different beam length, that is different dM/dx. It is found that the amount of force in the plate contributed by the segment between cracks increases exponentially with decrease in beam length (that is with increase in rate of change of moment).

5 CONCLUSION

- Crack spacing and the number of cracks along the beam largely affect the local stress and strain in beams, whereby smaller crack spacing results in larger plate strains.
- Amount of force in the plate that is contributed by the uncracked segment between adjacent cracks is linearly proportional to the crack spacing.
- There is an optimum beam length at which a maximum strain in the plate can be achieved and this optimum length is dependent on the number of cracks along the beam as well as the crack spacing, which are in turn dependent on the rate of change of moment.
- The amount of force in the plate contributed by the segment between cracks increases exponentially with decrease in beam length, that is with increase in rate of change of moment.

REFERENCES

Johnson, R.P. 1994. *Composite Structures of Steel and Concrete*. England: Blackwell Scientific Publications.

Mohamed Ali, M.S. 2000. *Peeling of plates adhesively bonded to reinforced concrete beams*, Ph.D. thesis, Adelaide: University of Adelaide.

Oehlers, D.J. & Bradford, M.A. 1995. Composite Steel And Concrete Structural Members: Fundamental Behaviour. New York: Pergamon.

Oehlers, D.J. & Seracino, R. To be published in Sept 2004. *Design of FRP and Steel Plated RC Structures: retrofitting beams and slabs for strength, stiffness and ductility*. Adelaide: Elsevier Science Ltd.

Oehlers, D.J. 2000. The choice of plating techniques for retrofitting of reinforced concrete bridge beams and slabs, *Austroads 4th Bridge Conference, Bridges for the new millennium*, Australia.

Teng, J.G., Chen, J.F., Smith, S.T. & Lam, L. 2002. *FRP Strengthened RC Structures*. England: John Wiley & Sons.

Wu, Z. & Niu, H. To be published. Load-carrying capacity on debonding failure of R/C beams externally strengthened with FRP sheets. *Journal of Composites for Construction, ASCE.*

FRP Composites in Civil Engineering – CICE 2004 – Seracino (ed)
© 2005 Taylor & Francis Group, London, ISBN 90 5809 638 6

Investigation of debonding failure in FRP plated beams

S.K. Sharma & M.S. Mohamed Ali
Bridge Engineering and Management, Central Road Research Institute, New Delhi, India

P.K. Sikdar
Director, Central Road Research Institute, New Delhi, India

ABSTRACT: Adhesively bonded FRP plates in strengthened structures are susceptible to debonding prematurely before reaching the designed strength due to many factors. One of the major factors that affecting the behaviour of the strengthened beams is the bond strength (interfacial shear strength) between the reinforcing plate and the concrete substrate, other than, the plate end debonding, critical diagonal crack debonding and intermediate crack debonding. The paper deals with the bond strength tests conducted using metallic and FRP plates and test results of the beams strengthened with different types of FRP plates to study the parameters that control the critical diagonal crack (CDC) and intermediate crack (IC) debonding modes. Useful guidelines are presented to quantify the plate-concrete interface bond strength, ultimate capacity of the tension face plated and side plated beams susceptible to axial peeling and shear peeling.

1 INTRODUCTION

Bonding of steel or fibre reinforced polymer (FRP) plates by adhesive to the surface of concrete structural elements have become increasingly popular for improving their strength and stiffness. However, these plates are susceptible to debonding prematurely before reaching the designed strength. The premature debonding of the plates are mainly caused by the formation of the critical diagonal shear crack (CDC) (Swamy *et al*. 1987), intermediate crack (IC) and plate end (PE) debonding (Oehlers and Moran 1990). The degree of strengthening is affected by many factors, of which, one major factor is the plate-concrete interface bond strength (interfacial shear strength). Therefore, a thorough knowledge of bond behaviour of plate-concrete interface is a prerequisite along with the other failure mechanisms such as CDC, IC and PE debonding. The paper describes in brief the plate-concrete interface bond strength tests conducted using metallic and FRP plates and the test results of the beams strengthened with different types of FRP plates to study the parameters that controls the intermediate crack and critical diagonal crack debonding modes.

2 BOND MECHANISM

To determined the plate-concrete interface bond strength different test schemes have been tried world over and are classified as: a) double shear pulling (double pull) test; b) double shear pushing (double push) test; c) single shear pulling (single pull) test; and d) single shear pushing (single push) test as shown in Fig. 1 (Chen *et al.* 2001). There is no uniformity in the tests schemes adopted. The bond strength could be significantly affected by the test method adopted (Chen *et al.* 2001). In general, the bending tests over estimates the bond strength while the shear pushing test gives the least values. There could be little difference between the double and single shear pushing tests, and between the double and single shear pulling tests.

2.1 *Development of design guidelines*

The important critical parameters that control the plate-concrete interface bond strength are; elastic modulus, tensile strength, width and thickness of the plate, and tensile strength of concrete. The another important parameter is the critical bond length ($L_{b,crit}$) which is defined as the maximum length of the bonded plate beyond which there is no further increase in the failure load (P_u). From the fundamental single shear pushing tests (Fig. 1d) that were conducted on different types of metallic and FRP plates observed that the tensile strength of the plate (f_p) has an effect on both the ultimate bond strength as well as on the critical bond length.

The relationship for the critical bond length $L_{b,crit}$ and the ultimate bond strength P_b for a given bond length L_b are developed (Sharma *et al.* 2002).

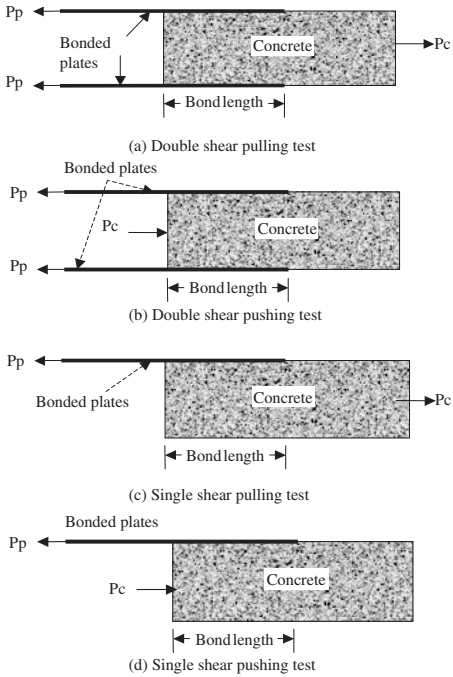

Figure 1. Shear test schemes.

$$L_{b,crit}/t_p = 0.0089x^3 - 0.439x^2 + 7.8645x \quad (1)$$

where x is a non dimensional parameter, and is given as

$$x = \frac{E_p^{0.25} f_p^{0.125}}{t_p^{0.5} f_b^{0.25}} \quad (2)$$

The corresponding bond strength $P_{b,crit}$ for a given $L_{b,crit}$ can be deduced from

$$P_{b,crit} = 1.277 L_b f_b b_p \quad \text{if } L_b/t_p < L_{b,crit}/t_p \quad (3)$$

$$= 1.277 L_{b,crit} \cdot f_b \cdot b_p \quad \text{if } L_b/t_p \geq L_{b,crit}/t_p$$

P_b is always $\leq A_p \cdot f_p$, where f_p = ultimate tensile strength in case of linear elastic plates like FRP and yield strength in case of metallic plates and f_b is Brazilian tensile strength of concrete, b_p is the width of the FRP plate.

These developed design guidelines are capable of predicting both the ultimate bond strength (P_b) and critical bond length ($L_{b,crit}$) of beams bonded with any type of plate with very good accuracy.

3 PEELING MODES

The debonding of the plated beams occur due to the stress concentrations at the plate ends and those in the vicinity of flexural and shear cracks in the RC member that intercept the plate (Mohamed Ali *et al.* 2001). The structural engineering mechanisms behind the various peeling modes, i.e., critical diagonal crack, intermediate crack and plate end debonding are discussed by Oehlers *et al.* (2003). The failure of the plated beams due to the axial peeling and the shear peeling of the external plates are the main concern of this study.

3.1 *Axial peeling*

In brief the axial peeling of the plates emanates in the vicinity of the maximum flexure/flexure shear region and propagates outwards and merges with the already existing cracks (flexure or flexure and shear or even diagonal shear cracks) to accommodate the excessive stresses (strains), which lead to complete debonding of the plate. The plate debonding cracks propagates towards the plate ends. The axial peeling controls both the strength and ductility of the FRP plated beam.

3.2 *Shear peeling*

The shear peeling mechanism is caused by the rigid body displacement across the critical diagonal shear crack due to the applied vertical shear force. The plate debonding becomes very rapid phenomena due to the rapid propagation of the debonding crack from the root of the diagonal shear crack to the end of the plate. The shear debonding can not be avoided but can be delayed provided the critical bond length of the plate is available, from the root of the critical diagonal crack. It is preferable to terminate the plate near the support or in the vicinity of the point of contraflexure.

3.3 *Test specimens*

The basic cross sections of the tension face plated and side plated RC beams (size 175 mm × 280 mm × 3400 mm) used in both the studies are shown in Fig. 2a. Carbon and glass FRP plates of thickness 1.2 mm and 10 mm were used in the tension face plated beams (Fig. 2b & c), 12 mm thick glass FRP plates in side plated specimens (Fig. 2d) and 4 mm thick for inclined strips (Fig. 2e).

The ultimate tensile strength and the elastic modulus of the carbon FRP plate were 2800 MPa and 165 GPa respectively. Whereas, the glass FRP plates (10 mm, 12 mm) and 4 mm thickness have ultimate tensile strength of 300 MPa and 330 MPa respectively and the elastic moduli were, 28 GPa and 41 GPa respectively. The uniaxial cylinder compressive strength (f_c) and Brazilian tensile strength (f_b) (cylinder of 150 mm dia. and 300 mm length), of the

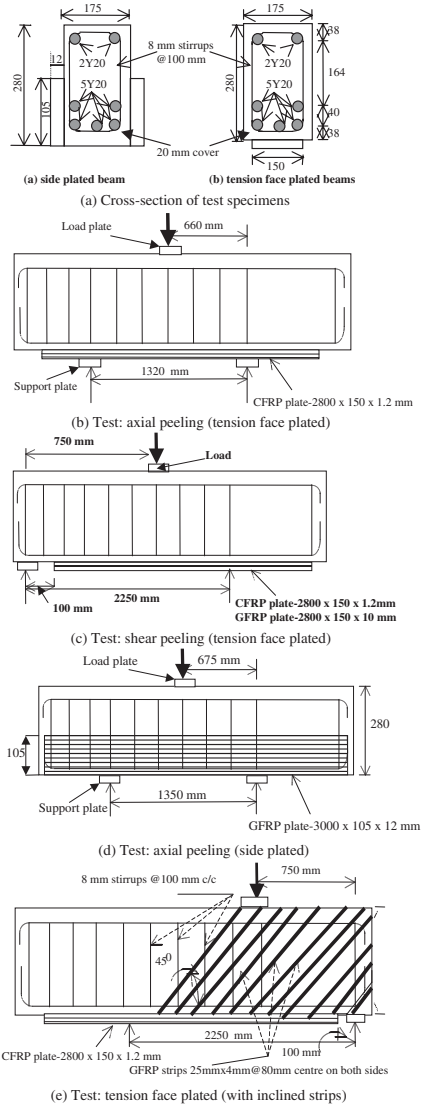

Figure 2. Plating schemes.

concrete are shown in Table 1. The specimens were tested under three point loading. Testing each beam individually, a total of four tests were performed in the axial peeling case and ten tests in the shear peeling case. The shear span to depth ratio (a/d) was kept as 3 in the shear peeling tests.

Table 1. Test results.

Item	AP-C-1	AP-G	APSG	APR
Plate dimensions {breadth (mm) × thickness (mm)}	150 × 1.2	150 × 10	–	Nil
Plate dimensions {depth (mm) × thickness (mm)}	–	–	105 × 12	–
Compressive strength of concrete (MPa)	51.6	42	42.4	42.8
Tensile strength of concrete (MPa)	3.72	4.04	4.40	3.72
Maximum moment at the onset of plate debonding (M_{max} kNm)	158.4	173.9	154.0	117.5
Maximum moment at plate debonding (kNm)	107.9	103.6	126.5	104.7
Maximum shear load (kN)	240	235	225	173.4
Maximum strain in plate at maximum moment (microstrains)	4300	4650	SW-2500 NW-2270	–
Maximum strain in plate at debonding (microstrains)	4500	4800	SW-1030 NW-950	–
Deflection (mm)				
(1) at maximum applied moment	10.83	11.00	11.0	12.40
(2) at debonding of plate/failure	18.30	21.25	16.0	17.14

The axial peeling tests were designated as AP-C-1, AP-G, APSG and APR while SPC-1-1, SPC-1-2, SPC-2-1/S, SPC-2-2, SPG-1/S, SPG-1-2 , SPSG-1, SPSG-2 and SPR-1, SPR-2 denote the shear peeling tests. The first two alphabets AP and SP denotes the axial peeling and shear peeling, the third alphabets C and G after hyphen stand for carbon and glass FRP materials plates respectively, SG stands for side plated beam with glass FRP plates and the numerical values 1 and 2 after hyphen indicate the category of carbon FRP plates of elastic moduli 165 GPa and 300 GPa respectively. The numerical values 1-1 and 1-2 in shear peeing tests indicate without and with shear stirrups whereas, 1/S denotes the inclined shear strips. A test on unplated reference beam in each category (APR&SPR-1, 2) was also carried out to determine the flexural strength and the shear strength of the beam with shear stirrups $V = V_{us} + V_{uc}$ and without stirrups V_{uc}.

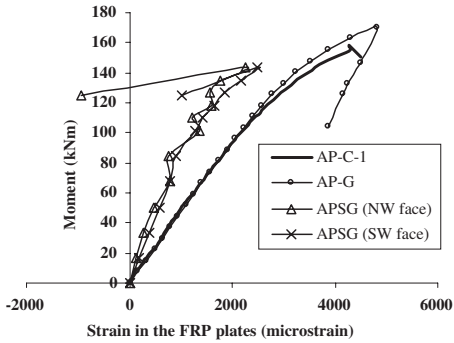

Figure 3. Strains in plated specimens.

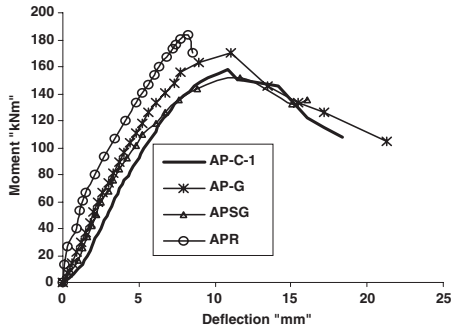

Figure 4. Moment vs deflection of specimens.

Figure 5(a). Final crack pattern of test AP-C-1.

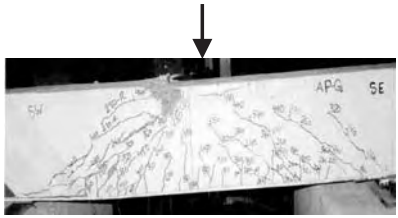

Figure 5(b). Final crack pattern of test AP-G.

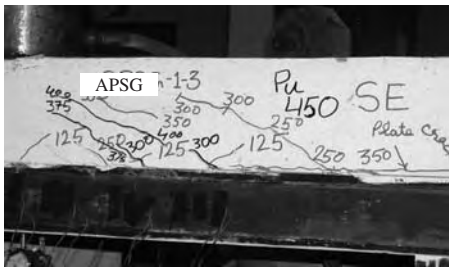

Figure 5(c). Final crack pattern of test APSG.

3.4 *Tests: axial peeling*

The axial peeling test results are shown in Table 1. The flexural capacity of the tension face plated beams AP-C-1 and AP-G enhanced by about 34.8% and 48% over the unplated reference specimen (APR) while in the case of side plated (APSG) specimen (Fig. 2d), the moment capacity enhanced in the range of 31%.

The magnitude of the deflection at the maximum applied moment was decreased by about 11% than the reference specimen (APR) in all the three tests. However, at the instance of debonding of the plates, the deflection in specimens AP-C-1 and AP-G increased by 6% and 24% than the deflection of the reference specimen (Table 1).

The magnitude of the maximum-recorded longitudinal strain in the FRP plate varied from 4300 to 4800 microstrains in tension face plated specimens while in side the plated specimens, it varied from 950 microstrains to 2500 microstrains. From the recorded magnitude of the longitudinal strains in the plates, it can be inferred that the FRP plates did not fracture as the strain magnitudes were less than the ultimate strain (16970 and 10714 microstrain). The plates debonded due to gradual propagation of the debonding cracks which is exhibited by the gradual drop in the magnitudes of the strains and moments in the case of tension face plated specimens whereas, the rapid fall in the strain magnitude (Fig. 3) demonstrated the rapid propagation of the debonding cracks. The performance of the glass FRP plated specimen (AP-G) was experienced comparable with the carbon plated beams as well as better pseudo-ductile beam behaviour was observed (Fig. 4). The crack pattern and the failure mode of the specimens tested in this study are shown in Fig. 5.

3.4.1 *Analytical Procedure*

The ductility is important because it permits large deflections which gives warning of failure and more importantly, permits the redistribution of moments which is the basic ability of the RC plated beams to attain design flexural capacity. The assumption

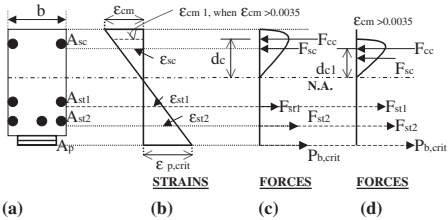

Figure 5. Stress–strain distribution in different components.

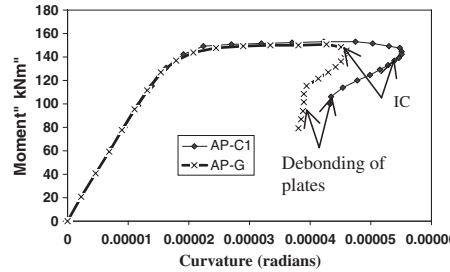

Figure 7(a). Moment–curvature relationship of tension face plated beams.

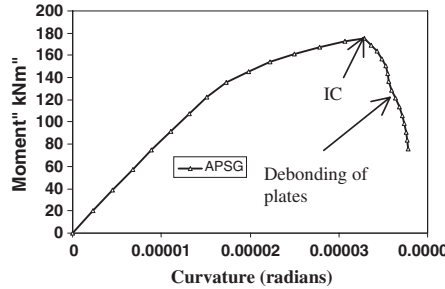

Figure 7(b). Moment–curvature relationship of the side plated beams.

made in the analysis are: (i) strain distribution in the rectangular RC beam section through-depth remains linear; (ii) The concrete in the tension zone is assumed to be ineffective in resisting the internal forces on a cracked cross-section, (iii) plane section remains plain after the deformation, and (iv) strains in the concrete and steel are compatible. However, the force in the plate F_p is restricted to critical that corresponds to critical bond strength $P_{b,crit}$. Figure 6 shows the strains and stresses in the plated concrete section.

The strains in the compression concrete (ε_{cc}) at any distance from the neutral axis, compression steel (ε_{sc}), tension steel (ε_{st1}, ε_{st2}) and strain in plate (ε_p) can be determined from the strain compatibility in terms of the strains in the extreme compression fibre (ε_{cm}). Crushing of concrete is assumed to occur at compressive strain of 0.0035.

From the corresponding stress–strain relationship, the forces F_{cc} in compression concrete can be determined from the expression proposed by Sebastian (2002) given as

$$F_{cc} = \frac{d_c b_w E_c \varepsilon_{cm}}{2}\left(1 - \frac{E_c \varepsilon_{cm}}{6 f_{cu}}\right) \quad (4)$$

where d_c is the depth of the compression concrete, b_w is the width of web, ε_{cm} is the strain in the extreme compression fibre, E_c and f_{cu} are the, Young's modulus and cube compressive strength of the concrete. The magnitude of the forces in the steel reinforcement at different levels (F_{sc}, F_{st1} and F_{st2}) were obtained from the product of the corresponding stress and cross sectional area of the reinforcement (Fig. 6c), and the magnitude of bond strength $P_{b,crit}$ was computed from Eq. (3). Now from the equilibrium condition, one can arrive at the depth of the neutral axis by trial and error using a simple Excel spreadsheet. The above procedure can be adopted for the side plated beams also. From the magnitudes of the forces in the various components and the magnitude of the corresponding lever arm, the moments (M_{cc}, M_{sc}, M_{st1}, M_{st2} and M_p) can be determined from the equilibrium of forces to arrive at the axial peeling strength M_{peel} or the ultimate moment capacity of the plated section. The magnitude of M_{cc} was deduced from the expression given as (Sebastian 2002).

$$M_{cc} = d_c^2 b_w E_c \varepsilon_{cm}\left(\frac{1}{3} - \frac{E_c \varepsilon_{cm}}{16 f_{cu}}\right) \quad (5)$$

The moment–curvature relationship for the tension face plated and side plated beams is shown in Figs. 7 (a)–(b). A large plateau in the case of the tension face plated beams as shown in Fig. 7(a) indicating the ductile behaviour. The drop in magnitude with the increased curvature indicates the onset of the axial peeling crack followed by further drop in the magnitude of the moment and the corresponding curvature denotes the propagation of the debonding crack. The steep fall in the magnitude of the moment at constant curvature exhibited the final debonding of the plates. The moment–curvature relationship for the side plated beam as shown in Fig. 7(b) reveals the similar behaviour but the plateau is not as large as it is in the case of the tension face plated beams.

The same behaviour is nearly revealed by the moment-deflection relationship (Fig. 4). The maximum moment capacity (M_{peel}) from the present procedure, i.e., theoretical (M_{theory}) and from the tests are

Table 2. Comparison of axial peeling results.

Specimen	f_c MPa	f_b MPa	Moment (M_{theory}) kNm	Moment (M_{test}) kNm
APR	42.8	4.04	N.A	117.5
AP-C-1	51.6	3.72	153.4	158.4
AP-G	42	4.04	150.6	173.9
APSG	42.4	4.4	175.3	151.87

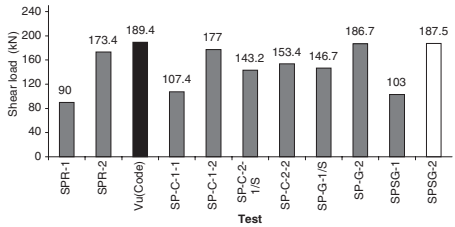

Figure 8. Shear peeling test results.
C-1-carbon FRP-$f_p = 2800$ MPa, $Ep = 165$ GPa
C-2-carbon FRP- $f_p = 1300$ MPa, $Ep = 300$ GPa
G-glass FRP- $f_p = 300$ MPa, $Ep = 28$ GPa (10-12 mm)
G-glass FRP- $f_p = 330$ MPa, $Ep = 41$ GPa (4 mm)

presented in Table 2 and they are well comparable with the test results (M_{test}).

3.5 *Tests: shear peeling*

In this study, the parameters varied were the type of the plates and the presence or the absence of the shear stirrups in a tested shear span; this was facilitated by providing shear stirrups in 3/4th of the beam. The test results of the beams that were provided with internal shear stirrups, without internal shear stirrups and those bonded with external strips are shown in Fig. 8. The failure of the tension face plated beams without shear stirrups, occurred due to the formation of a diagonal shear crack in the vicinity of the tension face plate end. This crack propagated towards the outer edge of the load plate and caused the instantaneous peeling off the external tension face plate along the concrete cover (Fig. 9a).

Whereas, in the case of beams that were provided with shear stirrups, the root of the diagonal shear crack occurred at a distance of about 250–280 mm from the support (short shear span) which propagated backward towards the support, i.e., plate end (Fig. 9b). The shear peeling of the plate was induced by the formation of the diagonal shear crack along with series of the diagonal shear cracks.

In case of side plated specimen (Fig. 9c & d), the plates debonded due to the formation of the diagonal shear cracks that propagated along the top edge of the plate parallel to the length of plate towards the plate

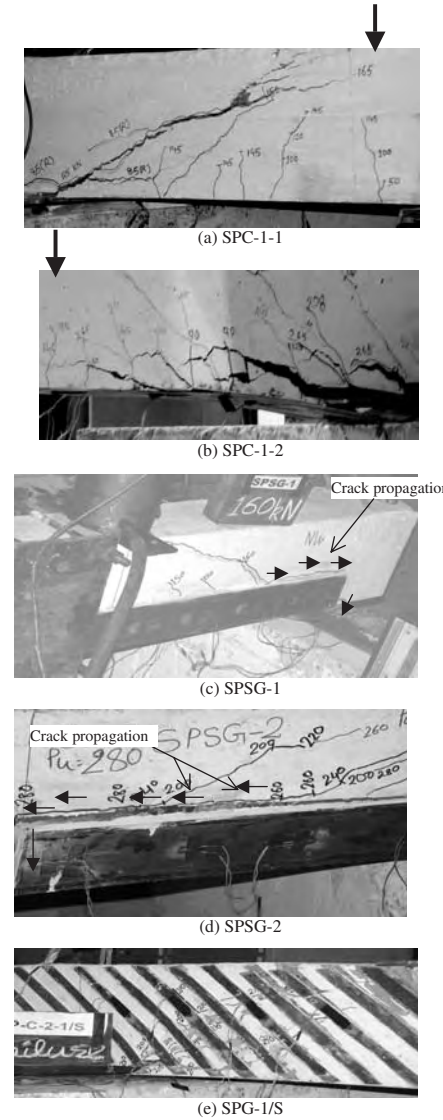

Figure 9. Failure mode of specimens.

end. In the case of the beams (SPG-1/S and SP-C-2-1/S) that were bonded with inclined glass FRP strips (of size 50 mm wide, 4 mm thick spaced 100 mm centers) Fig. 9e, the failure was delayed due to the presence of the side strips. The side strips debonded one after the other followed by the tension face plate; it was a rapid failure.

The test shear peeling strength V_{peel} of the specimens that had shear stirrups (SP-C-1-2, SP-G-2 and SPSG-2) was almost equal to the ultimate shear capacity V_u code ($V_u = V_{uc} + V_{us}$, 189.4 kN, Euro draft code-2001) except SP-C-2-2, which is 80% of the ultimate shear capacity (V_u code) as shown in Fig. 8. In the case of test SP-C-1-1, the shear peeling strength increased to 107.4 kN, which is about 19% more than that of the reference beam (SPR-1). However, in the case of the tests SP-C-2-1/S and SP-G-1/S, the shear peeling strength V_{peel} improved by about 59% and 63% over the reference beam (SPR-1). It is worth noting that the shear peeling strength of both the specimens SP-C-2-1/S and SP-G-1/S, is almost same irrespective of the different types of tension face material used (Fig. 8) and the shear peeling strength increased in the range of 33–37% over the tension face plated specimen (SP-C-1-1).

The shear peeling capacity of the side plated beam SPSG-1 enhanced by 14% over the reference beam (SPR-1), which is almost equal to the specimen SP-C-1-1. On the other hand, the shear peeling strength of the specimen SPSG-1 is 30% lower than that of the specimens SP-C-2-1/S and SP-G-1/S that had additional inclined GFRP strips.

The magnitude of the maximum recorded strain in the tension face plate ($\epsilon_{p,max}$) varied between 10% to 25% of the ultimate strain of the FRP plates except carbon plated beam SP-C-2-1/S ($E_p = 300$ GPa).

3.5.1 *CDC debonding strength of plated beams (A theoretical approach)*

3.5.1.1 Beams without internal shear reinforcement

In the case of the beams that are not provided with internal shear stirrups or where the spacing of the stirrups are larger than the maximum spacing as stipulated by the codes of practice (usually three-fourth of the effective depth), the plate debonding is induced by the formation of the critical diagonal crack (CDC) from the end of the support plate to the outer edge of the load plate (Fig. 10a). The rigid body displacement due to the vertical shear across the diagonal crack causes the plate to detach by a debonding crack that propagate from the root of the diagonal crack to the plate end, as illustrated in Fig. 10a. The formation of the critical diagonal crack and the shear debonding crack occur at the same load level without any visual warning. Therefore, the shear load required to cause the shear debonding V_{peel} for this case is the shear load at which the end critical diagonal crack occurs and it is given by Mohamed Ali *et al.* (2001) as

$$V_{peel} = \left(\frac{x_{crit}^{\ 2} + h^2}{a}\right)\left(\frac{f_{tef}\, b}{2}\right) \tag{6}$$

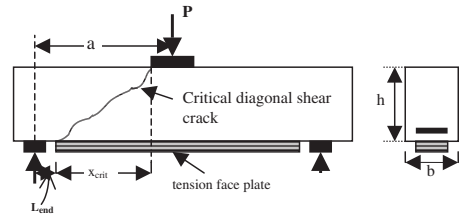

Figure 10(a). Beam without internal shear stirrups.

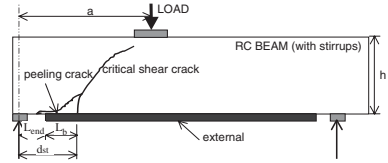

Figure 10(b). Beam with internal shear stirrups.

where a is the shear span, x_{crit} is the horizontal projection of the diagonal crack, b and h are the width and height of the beam, and f_{tef} is the effective tensile strength of the concrete which is given by

$$f_{tef} = 0.156 f_c^{2/3} \left(\frac{h}{100}\right)^{-0.3} \tag{7}$$

where the units are in N and mm, while f_c is the compressive strength of the concrete.

However, in the case of the side plated beams, the expression proposed by Mohamed Ali *et al.* (2001) to compute the shear peeling strength of the plated beams can be used.

The shear peeling strength of the beam SPC-1-1 tested in the present study was 93 kN which was computed from the above equations and compares well with the test strength of 107.4 kN (Fig. 8). The shear peeling strength of the side plated beam SPSG-1, obtained from Mohamed Ali *et al.* (2001) is 106 kN which is very well comparable with the test value 103 kN.

3.5.1.2 Beams with internal shear reinforcement

The RC beams with shear stirrups are normally designed to resist a shear load of $V_u = V_{uc} + V_{us}$ where V_{us} is the shear resistance offered by the stirrups. However, tests have shown that the CDC debonding can occur before V_u is realized due to the formation of shear cracks and the stirrups could not be stretched fully. This is due to the formation of the critical shear crack and subsequent development of the peeling crack at the root of the CD crack. As the strains in the composite plated section increase due to

the stress concentrations at the crack tips, the debonding crack gradually propagate outwards towards the support in the case of simply supported beams or the point of contra-flexure in the case of continuous beams Fig. 10(b). The increased strains in the plates and the associated increased crack width cause the plate to debond eventually. Therefore, the problem can be visualized as that of the formation of critical shear crack at a distance of d_{st} (effective depth of the outermost tension reinforcement) as it is the critical section for shear, considered in most of the codes of practice. Hence, the debonding layer of the plated section can be considered to be of length L_b as indicated in Fig.10(b) and the corresponding bond strength P_b can be computed from Eq.(3). Further, the strain in the plate $\acute{\varepsilon}_{plate}$ at which the debonding occurs can be computed from $\varepsilon_{plate} = P_b / b_p t_p E_p$, where b_p, t_p and E_p are the width, thickness and elastic modulus, of the plate respectively. The magnitudes of ε_{plate} and bond strength P_b can be used in standard flexural analysis procedures to determine the moment and hence the shear load at which the shear debonding occurs.

The shear peeling strength of the beam specimen SPC-1-2 tested in the present study as computed by the above procedure is 189.6 kN which is well comparable with the test debonding strength of 177 kN (Fig. 8). Whereas, in the case of specimens SP-G-2 and SPSG-2, the shear peeling strengths were 193 kN and 197.4 kN respectively which are also well comparable with the test values 186.7 kN and 187.5 kN.

4 CONCLUDING REMARKS

The shear peeling debonding mechanism in the RC plated beams without internal shear reinforcement is an instantaneous process which occurs due to the formation of the critical diagonal shear crack in the vicinity of the plate ends while, in the case of the beams with shear reinforcement, the process is similar but accompanied by a series of diagonal cracks. However, the axial peeling of the external plate is a gradual process and provides sufficient warning period prior to failure. The external FRP strips delayed the shear peeling of the plate in comparison to beams that were not provided with internal shear reinforcement. Equations have been proposed to compute the shear peeling strength and the maximum moment capacity in the axial peeling of the strengthened beams by external plating. The maximum moment that can be sustained by a plated beam can be estimated from the numerical analysis by considering the strain compatibility with respect to the strain in the extreme compression fibre and restricting the plate stress to $\sigma_{p,crit}$.

ACKNOWLEDGEMENT

Mr. Rajveer Singh's assistance during the testing work is gratefully acknowledged.

REFERENCES

Chen, J.F., Yang, Z.J., and Holt, G.D. (2001) "FRP or steel plate-to-concrete bonded joints: effect of test methods on experimental bond strength" *Steel & Composite Structures – An International Journal*, Vol. 1, No. 2, 231–244.

Eurocode 2: Design of concrete structures; Part-1 (Final draft) October-2001

Mohamed Ali, M.S., Oehlers, D.J. and Bradford, M.A. (2001). "Shear peeling of steel plates bonded to tension faces of RC beams," *Journal of Structural Engineering (ASCE)*, Vol. 127, No. 12, December, 1453–1459.

Oehlers, D.J., and Moran, J.P. (1990)."Premature failure of externally plated reinforced concrete beams." J. of *Struct. Engr. ASCE*, 116(4), 978–995.

Oehlers, D.J., Park, S.M., and Mohamed Ali, M.S. (2003) "A structural engineering approach to adhesively bonding longitudinal plates to RC beams and slabs" *Composites Part: A 34, Elsevier applied science and manufacturing*, 887–897.

Roberts, T.M. (1989) "Approximate analysis of shear and normal stress concentrations in the adhesive layer of plated R.C. beams. *Struct. Eng*., 67(12/20), 229–233.

Sebastian, W.M. (2002). "Sensitivities of strength and ductility of plated reinforced concrete sections to preexisting strains" *J. Struct. Eng*., 128(5), 624–636.

Sharma, S.K., Mohamed Ali, M.S., Goldar, D., and Sikdar, P.K. (2002). "Bond Strength Models of FRP and Metallic Plates Bonded to Concrete Surfaces," *Paper under review in ASCE Journal of Composite for Construction*.

Swamy, R.N., Jones, R. and Bloxham, J.W. (1987). "Structural Behaviour of Reinforced Concrete Beams Strengthened by Epoxy-Bonded Steel Plates," The *Structural Engineer* 1987: Vol. 65A, No.2, February, 59–68.

FRP Composites in Civil Engineering – CICE 2004 – Seracino (ed)
© 2005 Taylor & Francis Group, London, ISBN 90 5809 638 6

Prediction models for debonding failure loads of CFRP retrofitted RC beams

H. Pham & R. Al-Mahaidi
Monash University, Melbourne, Victoria, Australia

ABSTRACT: This study focuses on debonding failure in RC beams with CFRP bonded on the soffit using wet lay-up method. An experimental study, which involved 26 tests, was carried out. The experiments showed two failure modes: midspan debond and end debond. The first failure is the result of high bond stress near the tip of flexure-shear cracks; whereas the second type of failure is due to high shear stress developed in the weakest concrete layer at tension reinforcement level. The experiment indicates that U-straps can be effective in preventing midspan debond by limiting opening of flexure-shear cracks. When a U-strap is used as end anchorage, end debond can also be prevented since concrete shear resistance at tension reinforcement level is increased significantly. Based on observation from the experiments, two theoretical models are developed and verified with the experimental data together with a large database of other existing tests.

1 INTRODUCTION

Recently, fibre reinforced polymers (FRP) have been used to strengthen RC structures. The composites are bonded externally on the structures to take tensile stress. This method provides a fast and economical way of rehabilitation or repair of beams, columns and slabs. However, FRP tends to debond, which often leads to a brittle failure. Predicting debond failure loads is therefore essential before FRP can be safely used.

One of the main applications of FRP is to strengthen beams in flexure by bonding fibres on the soffit. Tension in the FRP often results in peeling of the strengthening material. This debonding phenomenon is complicated since it is affected by various parameters such as beam cracking and stress concentrations. There are two main types of debonding commonly observed in exiting experimental work: midspan debond and end debond. In the first type of failure, the FRP is separated first near the middle of the beam, where flexural or flexure-shear cracks are present. The second type of failure is when the FRP and concrete cover are peeled off from the end. Although, there has been significant amount of research on this topic, a simple reliable design method which is derived from the real failure mechanisms and verified with a large number of tests is still not available.

In this study, the authors attempt to address this issue. Testing of RC beams is carried out to study the failure mechanisms and the effect of several important parameters. Two simplified methods to predict end and midspan debond failure loads are proposed. Verification of the accuracy of those two models are then carried out using data from the present experiments together with a database of existing tests.

2 EXPERIMENTS

2.1 *Beam testing overview*

The experimental study comprises of two test set-ups.

In experimental program No. 1, a total of eighteen RC beams were constructed and tested under 4-point bending (Fig. 2a). Two were control beams and sixteen were retrofitted with carbon fibre reinforced fabrics using wet lay-up method. A typical beam cross-sectional dimensions are shown in Fig. 1. Variables in the test included the CFRP bond length, the area of tension reinforcement, the concrete cover, the number of fibre plies and the amount of shear reinforcement. Two identical beams were manufactured for each configuration (denoted a and b). The variables are listed in

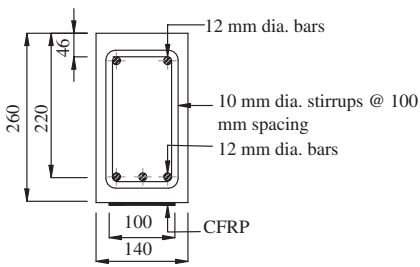

Figure 1. Beam E1 cross section.

Table 1. The beams were divided into two main groups. The E group had 10 beams retrofitted with a relatively thick layer of CFRP (6 layers or more). The S group had 6 beams retrofitted with 2 layers of CFRP. A steel clamp was used on all beams on one side to force end debond to the other side.

In experimental program No. 2, the beams were tested under 3-point bending. A total of 8 tests were carried out (Table 2). Out of those, four tests were done on the undamaged side of the beams tested in the first experiment. Four additional tests were also performed on newly manufactured beams of similar dimensions as beam E1. In one test, the beam was not anchored. In the other seven tests, the beams were anchored with non-prestressed or prestressed CFRP U-straps. In the first system, the CFRP strip of 50 mm wide was simply wrapped and bonded around the sides and the bottom of the concrete beam near the end of the longitudinal CFRP (Fig. 3b,c). In the second system, prestressing was introduced into the sides of the CFRP strap by inserting a wedge into the gap between the concrete and CFRP (Fig. 3b,c). The straps were stressed to around 500 microstrains. The wedge was bonded to the longitudinal CFRP but not to the vertical CFRP. This provided a mechanism in which the debond crack and sliding of the longitudinal CFRP can be minimized. These vertical CFRP straps were either placed at the CFRP end only or at a spacing of 180 mm in the shear span.

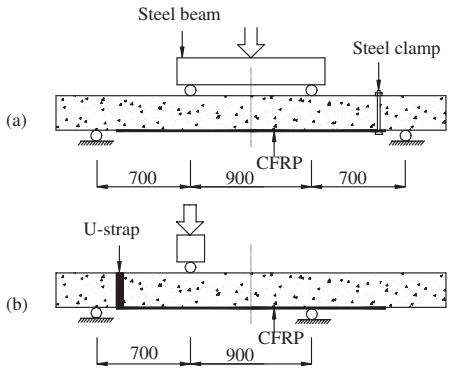

Figure 2. Loading set-up for 4-point bending (a) and 3-point bending (b).

The concrete was poured in two batches. The first batch was for six beams S1 to S3. The second batch was for the rest. The concrete cylinder strength for the first and second batch on the day of the first test of the series was 47.7 MPa (82 days) and 53.7 MPa (67 days), respectively. The properties of steel and CFRP reinforcement were also measured and listed in Table 3.

The process of applying CFRP to concrete involved two main steps: surface preparation and bonding. The concrete surface was prepared using high-pressure water jet to remove a thin layer of the paste to expose the coarse aggregates. The water jet operated at 4000 psi or 28 MPa. To ensure maximum bond, MBrace Primer was applied on the surface thoroughly with a brush. Bonding operation included resin under-coating, carbon fibre sheet application and resin over-coating.

2.2 *Test results*

The failure loads for all beams are listed in Table 4. The typical failure modes are shown in Fig. 7 and 8. In experimental program No. 1, the two control beams failed by typical steel yielding followed by concrete crushing.

Table 1. Variables in the experimental program No.1.

Beam designation	A_s ($n_s \times dia_s$)	($dia_{sv} - s$)	Concrete cover (mm)	A_f ($n_f \times t_f$)	L_0 (mm)	U-strap
C1	3 × 12	10−125	20	N/A	N/A	No
E1	3 × 12	10−125	20	6 × 0.176	150	No
E2	3 × 12	10−125	20	6 × 0.176	350	No
E3	2 × 12	10−125	20	6 × 0.176	150	No
E4	3 × 12	10−125	40	6 × 0.176	150	No
E5	3 × 12	10−125	20	9 × 0.176	150	No
S1	3 × 12	06−125	20	2 × 0.176	150	No
S2	3 × 12	06−90	20	2 × 0.176	150	No
S3	2 × 12	06−125	20	2 × 0.176	150	No

$n_s \times dia_s$: number of tension steel bars × bar diameter (mm).
$dia_{sv} - s$: stirrup diameters (mm) – spacing (mm).
$n_f \times t_f$: number of plies × ply thickness (mm).
L_0: distance from end of FRP to nearest support (mm).

Table 2. Variables in the experimental program No.2.

Beam designation	A_s ($n_s \times dia_s$)	($dia_{sv} - s$)	Concrete cover (mm)	A_f ($n_f \times t_f$)	L_0 (mm)	U-strap
E3b2	2 × 12	10−125	25	6−0.176	150	None
E3a2	2 × 12	10−125	25	6−0.176	150	1-N
E1b2	3 × 12	10−125	25	6−0.176	150	1-P*
E5a2	3 × 12	10−125	25	9−0.176	150	3-P
A1a	3 × 12	10−125	25	6−0.176	150	1-N
A1b	3 × 12	10−125	25	6−0.176	150	3-N
A2a	3 × 12	10−125	25	6−0.176	150	1-P
A2b	3 × 12	10−125	25	6−0.176	150	3-P

1-N one end non-prestressed U-strap.
3-N three non-prestressed U-straps @ 180 mm spacing.
1-P one end prestressed U-strap.
3-P three prestressed U-straps @ 180 mm spacing.
*the end strap was moved to the right by 60 mm due to unsuccessful prestressing of the first end strap.

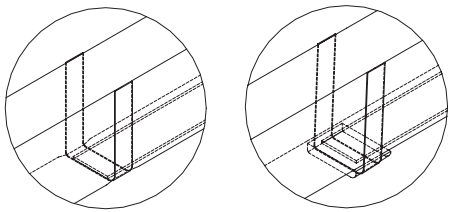

a) Non-prestressed strap b) Prestress-strap

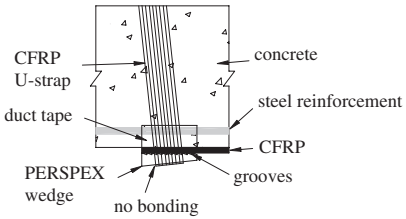

c) Prestressing system details

Figure 3. Two anchorage systems used.

Table 3. Mechanical properties of materials used.

Material	E (MPa)	F_Y (MPA)	F_T (MPA)
Steel (Y12)	192000	504	599
Steel (Y10)	204000	334	483
Steel (Y6)	238000	423	576
CFRP fabrics	209000	–	3900*
Adhesive	>3500*	–	>120*

*given by the manufacturer.

Beams in S series failed either by midspan debond or combination of both midspan and end debond. S1a and S1b failed by a combination of midspan debond and end debond. After steel yielded at a shear load of around 63 kN, flexure-shear cracks and shear cracks appeared clearly in shear spans. These cracks widened up as the load was increased. Concrete fractured simultaneously from the unclamped end of CFRP and from tip of a wide flexure-shear crack near middle of shear span. Stress was transferred along and cracking propagated toward the middle along the tension reinforcement level. S2a and S2b failed by midspan debond. A wide flexural shear crack under the load point initiated the delamination of CFRP from concrete. In S2a, that happened on the clamped side. In S2b, delamination occurred on the unclamped side. S3a failed by midspan debond, which first occurred on the clamped side. S3b failed due to a combination of midspan and end debond on the unclamped side.

All the beams in E series failed by end debond. All debonding happened on the unclamped side. The typical crack development is described here for beam E1a. Flexural vertical cracks appeared first in the pure bending region. As the load increased, shear cracks became visible in the shear span. The end shear crack originating from the FRP end became visible at 39 kN shear load level. The shear cracks widened more as the load increased. The portion of the end shear crack in the concrete cover layer became more inclined and finally joined the adjacent shear crack. At 59 kN, this crack opened further and about 100 mm of FRP was separated from the concrete. Similar stress redistribution described above occurred but since the steel reinforcement had not yielded yet, the response tended to be more gradual. The debonding crack propagated until the load reached a peak of 71 kN.

Table 4. Summary of failure modes and loads.

Designation	Failure modes	Exp. max. shear load	Predicted max. shear load
Ca	Concrete crushing	54.4	50.7
Cb	Concrete crushing	53.9	51.7
E1a	End debond	70.7	75.6
E1b	End debond	74.6	76.7
E2a	End debond	51.4	55.7
E2b	End debond	53.4	56.2
E3a	End debond	66.0	66.2
E3b	End debond	65.2	66.0
E4a	End debond	79.0	80.0
E4b	End debond	61.2	79.5
E5a	End debond	63.3	66.4
E5b	End debond	63.2	67.6
S1a	Midspan & end debond	73.8	70.4
S1b	Midspan & end debond	74.5	71.4
S2a	Midspan debond	80.4	72.2
S2b	Midspan debond	74.5	70.7
S3a	Midspan debond	60.3	55.4
S3b	Midspan & end debond	60.2	55.5
E3b2	End debond	60.0	66.0
E3a2	Midspan debond & rupture of end strap	75.9	70.5
E1b2	Midspan debond & debond of end strap	98.1	83.6
E5a2	Debond of straps & midspan debond	113.1	
A1a	Midspan debond & rupture of end strap	94.5	83.6
A1b	Debond and rupture of straps & midspan debond	108.7	
A2a	Midspan debond & debond of end strap	101.7	83.6
A2b	Debond of straps & midspan debond	114.5	

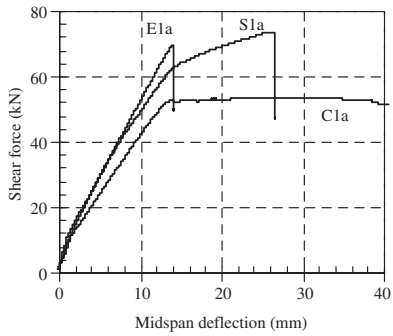

Figure 4. Loading curves of three beams.

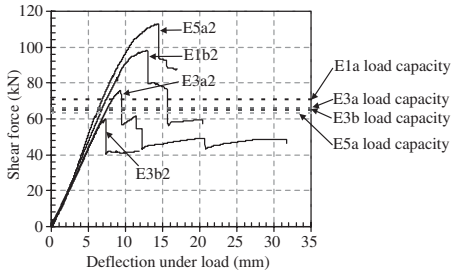

Figure 5. Loading curves of anchored retested beams.

In experimental program No. 2, the end U-strap proved to be effective in limiting end debonding but not midspan debonding. The strap increased concrete shear resistance at tension reinforcement level even after cracks were formed there. Beams E1a2 and E3a2 failed first by sliding of the main FRP underneath the U-strap followed by midspan debonding. The increases in the ultimate capacity as compared to E1a and E3a are 39 and 15%, respectively.

Midspan debonding can however be prevented by placing U-straps in the shear span at certain spacing. These straps limited the opening of flexure-shear cracks. E5a2 failed by debonding of the two U-straps near the load point from the one side of the beam followed by midspan debonding.

For beams with non-prestressed straps, sliding underneath the U-trap also occurred. That sliding

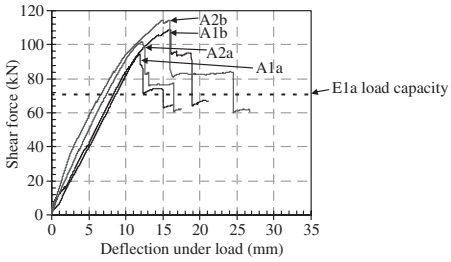

Figure 6. Loading curves of A beams.

End debond in E1a

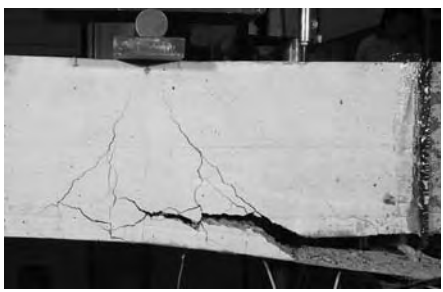

Midspan debond in E1a2

Figure 7. End debond and midspan debond.

Figure 8. Failure of beam A1b.

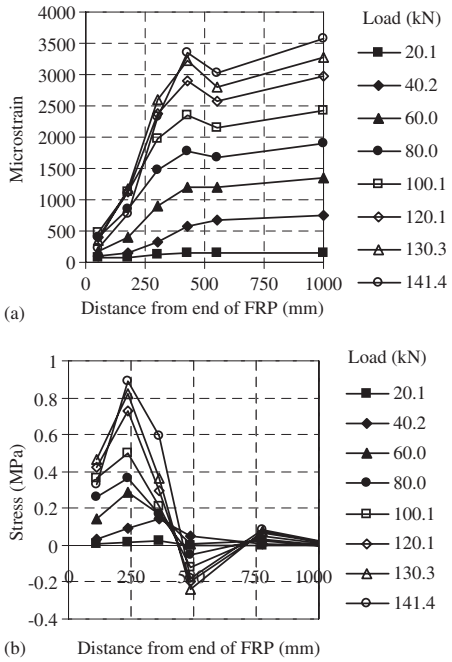

Figure 9. FRP strain distributions (a) and interfacial shear stress distributions (b) in beam E1a.

action lead to twisting of the CFRP strap. This was the reason the strap broke before the longitudinal CFRP was completely separated from the beam. For beams with prestressed straps, sliding was prevented. That led to a slight increase of 5% in the ultimate load (Fig. 6). The tension in the longitudinal composite was transferred directly to the two legs of the strap. The legs were eventually delaminated from concrete surface.

The variations in CFRP longitudinal strain and interfacial bond stress at different load levels for S1a and E1a are plotted in Fig. 9 and 10. The strain drops from the maximum value under the load point to a zero at the end of the plate. As expected, the maximum strain level in S beams is much higher than that in E beams. The bond stress is derived from the FRP strain distribution using the following equation:

$$\tau = \frac{E_f\left(\varepsilon_{f,i+1} - \varepsilon_{f,i}\right)t_f}{\Delta L} \qquad (1)$$

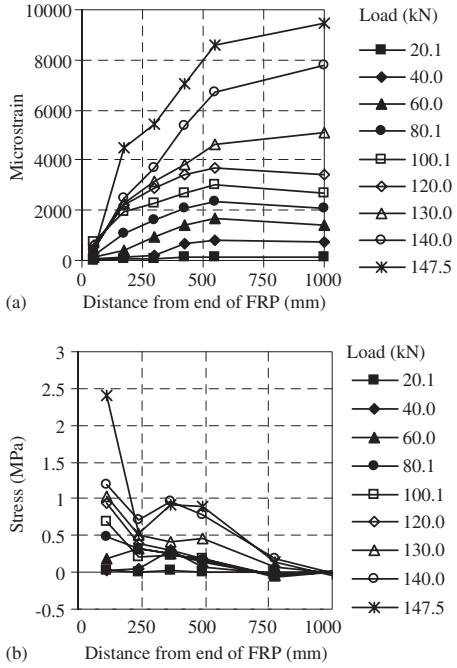

Figure 10. FRP strain distributions (a) and interfacial shear stress distributions (b) in beam S1a.

Table 5. Experimental studies on FRP retrofitting for flexural strengthening.

Reference	No. of test(s)	Reference	No. of test(s)
This study (Pham and Al-Mahaidi)	21	Garden et al. (1997)	10
Pham and Al-Mahaidi (2003)	2	Ahmed and Van Gemert (1999)	8
Arduini et al. (1997)	4	Beber et al. (1999)	8
Gao et al. (2001)	3	David et al. (1999)	4
Fanning and Kelly (2001)	4	Hau (1999)	3
Zarnic and Bosiljkov (2001)	1	Tumialan et al. (1999)	7
Rahimi and Hutchinson (2001)	12	Pornpongsaroj and Pimanmas (2003)	3
Ritchie et al. (1991)	8	Kishi et al. (2001)	8
Nguyen et al. (2001)	5	Takahashi and Sato (2003)	2
Quantrill et al. (1996)	3	Valcuende and Benlloch (2003)	4
He et al. (1997)	2	Chajes et al. (1994)	8
Mukhopadhyaya et al. (1998)	1	Sharif et al. (1994)	1
Triantafillou and Plevris (1992)	2		

where E_f and t_f are FRP elastic modulus and thickness; $\varepsilon_{f,i+1}$ and $\varepsilon_{f,i}$ are FRP strains and ΔL is the distance between strain gauges. The distributions for E1a show a clear peak near the FRP end whereas those for S1a do not have a clear peak in the shear span. This agrees with the failure modes observed as clear end debond in E1a and mixed end and midspan debond in S1a.

3 EXISTING EXPERIMENTAL AND THEORETICAL MODELS

Similar tests were found in literature and listed in Table 5 (including tests reported here). These beams failed either by end debond or midspan debond in a similar fashion as E1a and E1a2.

There have also been numerous models developed to predict debonding failure load. Summary and verification of those models have been described in Pham and Al-Mahaidi (2004). This study has found that the method recommended by Shehata et al. (2001) is relatively simple and gives conservative prediction for end debond. This method proposes a limit on the interfacial bond stress between FRP and concrete to the concrete shear stress, which can be taken as $0.3f_{ctm}$, where f_{ctm} is the concrete tensile strength. For midspan debond, a more detailed method, as explained in A.2 of fib Bulletin 14 (2001), is recommended. Envelop lines of the applied and resisting tensile forces are needed to be drawn along the beam.

4 PROPOSED MODELS

4.1 *Verification of beam theory*

To analyse the strains and stresses in a retrofitted section subjected to an applied moment, beam theory can be utilised based on the basic assumption that the strain varies linearly along the section from the top to the bottom fibre. The stress–strain response of FRP was taken to be elastic-perfectly brittle. The stress–strain curve for steel was perfectly elastic–plastic with no strain hardening. Concrete behaviour in compression was described by a nonlinear stress–strain curve by Hognestad (1951). Maximum concrete strain was taken as 0.003. Concrete peak stress was assumed to occur at a strain of 0.0025. The strain level in steel and FRP were calculated with the assumption that if the

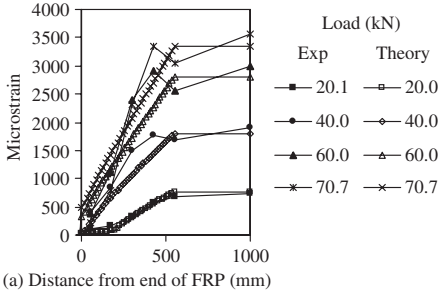

(a) Distance from end of FRP (mm)

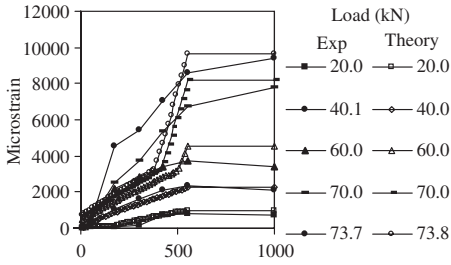

(b) Distance from end of FRP (mm)

Figure 11. Comparison of FRP strain distributions between experiments and beam theory predictions in E1a (a) and S1a (b).

applied moment M is greater than cracking moment M_r, the section is cracked and concrete is effective only in compression. This is only true at the crack locations. A better indication of the strain distribution in the reinforcement along a RC beam is the average strain, which can be calculated using the method described in CEB (1985).

Verification of the ultimate load for beams failing by concrete crushing or FRP rupture has been described previously in Pham and Al-Mahaidi (2004). The aim of this study is to verify the application of beam theory to compute reinforcement strain level at any applied moment, which is essential for the models for debonding failure proposed in the next section. The verification study is based on the measured strain values from the experiment.

Comparisons of FRP strain distributions for the tested beams are plotted in Fig. 11. The plots prove that the method described above can predict the peak FRP strain level with good accuracy. However, the predicted FRP strains in the shear span deviate significantly from the measured values at high loads. This is due to the presence of shear and flexure-shear cracks. Deviation occurs most clearly when the steel reinforcement undergoes yielding. For those cases, a more gradual decrease of the FRP strain is observed (Fig. 11b).

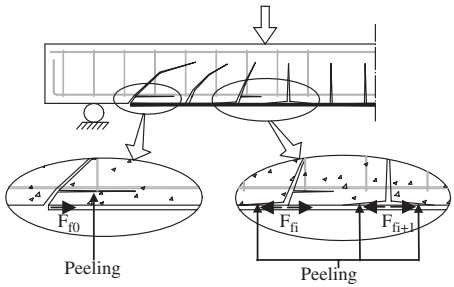

Figure 12. Failure mechanisms.

4.2 *Model derivation and verification for debonding*

The failure mechanisms are illustrated in Fig. 12 for a RC with sufficient shear strength. It is proposed that the debond capacity of retrofitted beams are controlled by two failure criteria. End debond occurs when the shear stress at the concrete layer near the tension reinforcement exceeds the concrete shear strength, which can be taken as 0.4 f_{ctm}, where f_{ctm} is direct concrete tensile strength. Midspan debond occurs when the force $F_{f,i}$ is large enough to cause peeling of FRP from concrete. The situation is similar to a simple shear test, in which FRP is bonded on a concrete block and pulled on one end until failure. Even though the situation is slightly different for a flexure-shear crack and a pure flexural crack, the main cause of debonding is the same, i.e. due to high interfacial bond stress near the crack. The maximum pulling force for that test can be calculated using the formula by Chen and Teng (2001) as follows:

$$P = \alpha \beta_f \beta_L \sqrt{f_{cm}}\, b_f L_e \qquad (2)$$

where $L_e = \sqrt{\frac{E_f t_f}{\sqrt{f_{cm}}}}$; $\beta_f = \sqrt{\frac{2 - b_f / b_c}{1 + b_f / b_c}}$;

$$\beta_L = \begin{cases} 1 & \text{if } L \geq L_e \\ \sin(\pi L / 2L_e) & \text{if } L < L_e \end{cases}$$

and b_c is the concrete web width; b_f, t_f and E_f are CFRP width, thickness and elastic modulus; L is the bond length and f_{cm} is the concrete compressive strength. α is a calibration factor to account for any difference between the behaviour of a beam failed by midspan debond and a shear-lap specimen failed by interfacial debond. Despite many similarities, the situation in a retrofitted beam is much more complex due to the presence of several factors such as bending deformation, shear deformation, the presence of tensile steel reinforcement and the assumption of plane

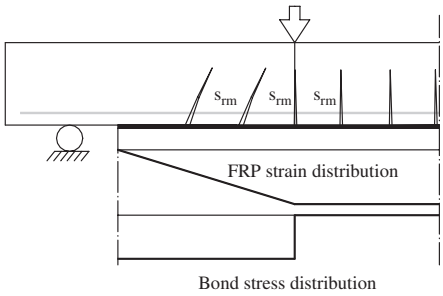

Figure 13. Assumption made in the calculation.

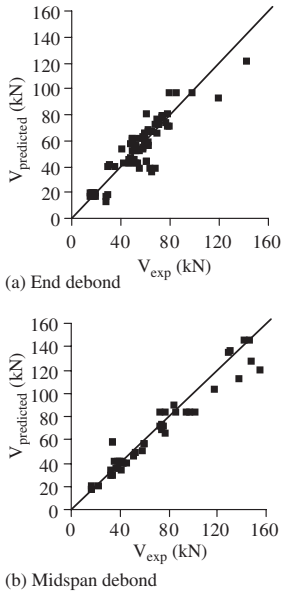

Figure 14. Comparison between the theoretical models and experimental results.

section at major cracks. This factor was first used by Teng et al. (2001). They carried out calibration with 8 beams and 9 slabs and suggested a value of 0.4. However, calibration with 48 beams in this study shows that α can be taken as 1.0.

Based on the findings from section 4.1, the CFRP strain (and therefore the bond stress) distribution along a simply supported beam can be simplified as in Fig. 13. It is worth pointing out that the assumption is only needed to calculate end debond loads. For the beams tending to fail by this mode, yielding of steel does not change the slope of the strain distribution significantly and the assumption is generally valid.

The database described above was used to validate the models with results shown in Fig. 14 indicating good agreement. The average of the ratio of the experimental results to the predicted failure loads is 1.06 and 1.09 for midspan and end debond, respectively. The standard deviations are 16.4% and 18.5%, respectively. Compared with the verification results of other models, the two proposed models are much simpler and much more accurate.

5 CONCLUSIONS

Two brittle failure modes in beams retrofitted with CFRP strips bonded to their soffits were observed. These are debonding at the end of FRP and debonding at a flexure-shear crack. These failures occurred due to high shear stress levels developed either at the end of CFRP or at a tip of a flexure-shear crack. Two theoretical models are developed based on the actual experimental observation and some available expressions. They have been validated and proved to be reliable.

One effective way of limiting debonding is to provide CFRP U-straps. These straps can limit end debond by improving concrete shear resistance at tension steel level. When placed at certain spacing in the shear span, midspan debond can also be limited as the opening of flexure-shear cracks is restricted and the bond between CFRP and concrete is improved. Prestressed U-straps tend to perform slightly better than non-prestressed ones.

ACKNOWLEDGEMENT

The research reported in this paper is part of a study financed by Monash University Engineering Grant. All CFRP fabrics and adhesives were partly sponsored by MBT (Australia) Pty Ltd.

REFERENCES

Ahmed, O. and Van Gemert, D. (1999). Effect of longitudinal carbon fiber reinforced plastic laminates on shear capacity of reinforced concrete beams, *Proceedings of the Fourth International Symposium on Fiber Reinforced Polymer Reinforcement for Reinforced Concrete Structures,* Maryland, USA, 1, 933–943.

Arduini, M., Di Tommaso, A. and Nanni, A. (1997). Brittle failure in FRP plate and sheet bonded beams, *ACI Struc. J.*, 94(4), pp. 363–370.

Beber, A. J., Filho, A. C. and Campagnolo, J. L. (1999). Flexural strengthening of R/C beams with CFRP sheets, *Proceedings of the Eighth International Conference on*

Advanced Composites for Concrete Repair, Forde, M. C., London, UK.

CEB (1985). *Cracking and deformation*, Ecole Polytechnique federale de lausanne.

Chajes, M. J., Thomson, T. A. J., Januszka, T. F. and Finch, W. W. J. (1994). Flexural strengthening of concrete beams using externally bonded composite materials, *Construction & Building Materials*, 8(3), pp. 191–201.

Chen, J. F. and Teng, J. G. (2001). Anchorage Strength Models for FRP and Steel Plates Bonded to Concrete, *J. Struc. Eng. ASCE,* 127(7), pp. 784–791.

David, E., Djelal, C., Ragneau, E. and Bodin, F. B. (1999). Use of FRP to strengthen and repair RC beams: experimental study and numerical simulations, *Proceedings of the Eighth International Conference on Advanced Composites for Concrete Repair*, Forde, M. C., London, UK.

Fanning, P. J. and Kelly, O. (2001). Ultimate Response of RC Beams Strengthened with CFRP Plates, *J. Composites for Construction*, 5(2), pp. 122–127.

fib Bulletin 14 (2001), *Design and use of externally bonded FRP reinforcement for RC structures*,

Gao, B., Leung, W.-H., Cheung, C.-M., Kim, J.-K. and Leung, C. K. Y. (2001). Effects of adhesive properties on strengthening of concrete beams with composite strips, *FRP composites in civil engineering*, Teng, J. G., Hong Kong, I, 423–432.

Garden, H. N., Hollaway, L. C. and Thorne, A. M. (1997). A preliminary evaluation of carbon fibre reinforced polymer plates for strengthening reinforced concrete members, *Proc. Instn Civ. Engrs Structs & Bldgs*, 127–142.

Hau, K. M. (1999). Experiments on concrete beams strengthened by bonding fibre reinforced plastic sheets, PhD Thesis, The Hong Kong Polytechnic University, Hong Kong, China.

He, J. H., Pilakoutas, K. and Waldron, P. (1997). Strengthening of reinforced concrete beams with CFRP plates, *Non-Metallic (FRP) Reinforcement for Concrete Struct. Proc., 3rd Symp.*, Japan, 1, 343–350.

Hognestad, E. (1951). In *Eng Expt Station Bull*, Vol. No. 399 Univ of Illinois.

Kishi, N., Mikami, H., Matsuoka, K. G. and KUrihashi, Y. (2001). Failure behavior of flexural strengthened RC beams with AFRP sheet, *FRPRCS-5 – Fibre-reinforced plastics for reinforced concrete structures*, Burgoyne, C., UK, 1, 85–95.

Mukhopadhyaya, P., Swamy, R. N. and Lynsdale, C. J. (1998). Optimizing Structural Response of Beams Strengthened with GFRP Plates, *J. Composites for Construction*, 2(2), pp. 87.

Nguyen, D. M., Chan, T. K. and Cheong, H. K. (2001). Brittle Failure and Bond Development Length of CFRP-Concrete Beams, *J. Composites for Construction*, 5(1), pp. 12–17.

Pham, H. B. and Al-Mahaidi, R. (2003). An Investigation into Debonding of FRP in Flexural Strengthening, *21st ARRB & 11th REAAA Conference*, Cairns, Queensland, Australia.

Pham, H. B. and Al-Mahaidi, R. (2004). Assessment of Available Prediction Models for the Strength of FRP Retrofitted RC Beams, *Comp. Struc.*, 66(1–4), pp. 601–610.

Pornpongsaroj, P. and Pimanmas, A. (2003). Effect of end wrapping on peeling behavior of FRP-strengthened beams, *FRPRCS-6 – Fibre-reinforced polymer reinforcement for concrete structures,* Tan, K. H., Singapore, 1, 277–286.

Quantrill, R. J., Hollaway, L. C. and Thorne, A. M. (1996). Experimental and analytical investigation of FRP strengthened beam response: Part I, *Mag. Conc. Research*, 48(177), pp. 331–342.

Rahimi, H. and Hutchinson, A. (2001). Concrete Beams Strengthened with Externally Bonded FRP Plates, *J. Composites for Construction*, 5(1), pp. 44–56.

Ritchie, P. A., Thomas, D. A., Lu, L.-W. and Connelly, G. M. (1991). External reinforcement of concrete beams using fiber reinforced plastics, *ACI Struc. J.*, 88(4), pp. 490–500.

Sharif, A., Al-Sulaimani, G. J., Basunbul, I. A., Baluch, M. H. and Ghaleb, B. N. (1994). Strengthening of initially loaded reinforced concrete beams using FRP plates, *ACI Struc. J.*, 91(2), pp. 160–168.

Shehata, I. A. E. M., Cerqueira, E. C., Pinto, C. T. M. and Shehata, L. C. D. (2001). Strengthening of R. C. beams in flexure and shear using CFRP laminate, *FRPRCS-5 – Fibre-reinforced plastics for reinforced concrete structures*, Burgoyne, C., UK, 1, 97-.

Takahashi, Y. and Sato, Y. (2003). Flexural behavior of RC beams externally reinforced with carbon fiber sheet, *FRPRCS-6 – Fibre-reinforced polymer reinforcement for concrete structures*, Tan, K. H., Singapore, 1, 237–246.

Teng, J. G., Smith, G., Yao, J. and Chen, J. F. (2001). Strength model for intermediate flexural crack induced debonding in RC beams and slabs, *FRP composites in civil engineering*, Teng, J. G., Hong Kong, I, 579–587.

Triantafillou, T. C. and Plevris, N. (1992). Strengthening of RC beams with epoxy-bonded fibre-composite materials, *Mat. & Struc.*, 25201–211.

Tumialan, G., Serra, P., Nanni, A. and Belarbi, A. (1999). Concrete cover delamination in reinforced concrete beams strengthened with carbon fiber reinforced polymer sheets, *Proceedings of the Fourth International Symposium on Fiber Reinforced Polymer Reinforcement for Reinforced Concrete Structures*, Maryland, USA, 725–735.

Valcuende, M. and Benlloch, J. (2003). Ductility of reinforced concrete beams strengthened with CFRP strips and fabric, *FRPRCS-6 – Fibre-reinforced polymer reinforcement for concrete structures*, Tan, K. H., Singapore, 1, 337–346.

Zarnic, R. and Bosiljkov, V. (2001). Behaviour of Beams Strengthened with FRP and Steel Plates, *The 2001 Structural Congress and Exposition*, Chang, P., Washington, D.C.

FRP Composites in Civil Engineering – CICE 2004 – Seracino (ed)
© 2005 Taylor & Francis Group, London, ISBN 90 5809 638 6

Prediction of debonding failure in FRP flexurally strengthened RC members using a local deformation model

S.T. Smith
Centre for Built Infrastructure Research, Faculty of Engineering, University of Technology, Sydney, Australia

R.J. Gravina
School of Civil & Chemical Engineering, RMIT University, Australia

ABSTRACT: Reinforced concrete (RC) beams and slabs can be strengthened by bonding fibre reinforced polymer (FRP) composites to their tension face. The performance of such flexurally strengthened members can be compromised by debonding of the FRP, with debonding initiating near the FRP end or at an intermediate crack (IC) in the member away from the end of the FRP. Despite considerable research over the last decade, reliable debonding strength models still do not exist. This paper presents a local deformation model for the prediction of the latter debonding mode, namely IC debonding. The progressive formation of flexural cracks, and the associated crack spacings and crack widths are modelled from initial cracking up to debonding. The bond characteristics between the longitudinal steel reinforcement and concrete, and the FRP and concrete, as well as the tension stiffening effect of the reinforcement and FRP to the concrete, are considered. The FRP-to-concrete bond-slip relation is used to determine the onset of debonding and the sensitivity of results to the bond-slip parameters is investigated. The analytical predictions compare well with experimental results of FRP-strengthened RC slabs.

1 INTRODUCTION

The flexural strength of reinforced concrete (RC) members can be increased by bonding fibre reinforced polymer (FRP) plates to their tension face. This method of strengthening has numerous advantages such as offering minimal increase in size and weight of existing structural members, ease of site handling and excellent corrosion resistance. Considerable research on this strengthening technique, in particular application to simply supported beams, has been conducted in the last decade and a comprehensive review is given in Teng et al. (2002).

Seven main failure modes have been identified from existing test observations (Teng et al. 2002, 2003; Smith and Teng 2002a,b) and they are summarised as (a) flexural failure by FRP rupture, (b) flexural failure by crushing of compressive concrete, (c) shear failure, (d) concrete cover separation, (e) plate end interfacial debonding, (f) intermediate flexural crack-induced interfacial debonding, and (g) intermediate flexural shear crack-induced interfacial debonding. The first three failure modes identified above are similar to those in conventional RC beams. Of the above failure modes, (d) to (g) are unique to plated beams and are referred to as debonding failures which generally occur before the ultimate moment capacity or shear capacity of the plated beam section is reached. Debonding that initiates near the plate end is referred to as plate end debonding and this includes the failure by concrete cover separation and plate end interfacial debonding. Debonding that initiates at an intermediate crack (IC) in the beam and then continues to one of the plate ends is referred to as intermediate flexural crack-induced interfacial debonding (Figure 1a) or intermediate flexural shear crack-induced interfacial

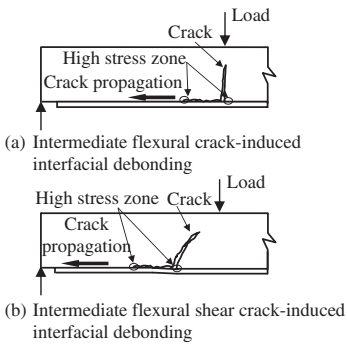

Figure 1. Debonding failure modes.

debonding (Figure 1b). Intermediate flexural crack induced debonding, which is the failure mode being investigated in the current study, is believed to be particularly important for relatively slender members, such as slabs, and members strengthened with a relatively thin FRP plate.

Teng et al.'s (2003) study revealed the limited progress that has been made to date on IC debonding strength models. Urgent work is therefore required to develop reliable and safe IC debonding strength models. A new method for predicting debonding failures, namely via a local deformation model, is introduced herein.

Existing local deformation based models have been used to investigate the behaviour of FRP strengthened RC members in tension (Ferretti and Savoia 2003) and bending (Ceroni et al. 2001, Aiello and Ombres 2003). Ceroni et al. (2001), Aiello and Ombres (2003), and Ferretti and Savoia (2003) have proposed non-linear models based on cracking which take into account the slip and bond stresses to form a series of non-linear governing equations that are solved via the finite difference method. These studies have been confined to the serviceability range. To date none of these models have considered failure by debonding and in particular IC debonding

A local deformation model was developed by Gravina and Smith (2004) that simulates the flexural behaviour of FRP flexurally-strengthened RC members failing by FRP rupture or concrete crushing. The current paper reports a modification to Gravina and Smith's (2004) model in order to predict IC debonding. A more complete account of the modified local deformation model is given in Smith and Gravina (2004). Strains in the FRP and steel reinforcement, slip between the FRP and concrete substrate as well as the steel reinforcement and surrounding concrete, and deflection of the strengthened member are produced from the local deformation model. Cantilevered RC slabs strengthened with FRP composites and reported to have failed by IC debonding, are used to confirm the accuracy of the local deformation model. Debonding is based on the FRP-to-concrete bond-slip model. As generic FRP-to-concrete bond-slip models currently do not exist, the sensitivity of debonding predictions to the assumed parameters of the bond-slip relation are assessed.

2 LOCAL DEFORMATION MODEL

A local deformation model was originally presented by Gravina and Warner (2003) for predicting the serviceability and ultimate limit state behaviour of RC beams. The model was later modified to incorporate externally bonded FRP composites for flexural strengthening (Gravina and Smith 2004). A summary of the analytical method for FRP strengthened flexural members is given below and a more comprehensive treatment, as well as simplifying assumptions and governing equations are given in Gravina and Smith (2004). The local deformation model has been found to be in good agreement with test results of FRP flexurally strengthened beams failing by either concrete crushing or FRP rupture (Gravina and Smith 2004).

2.1 *Method of analysis*

The method predicts the local flexural deformations in a determinate structural member at all stages of loading, from progressive formation of individual cracks up to ultimate failure either by FRP fracture, concrete crushing, or IC debonding. The strains in the tensile steel reinforcement, FRP strengthening, as well as the slip between the tensile steel and surrounding concrete, and FRP and concrete, are evaluated. The approach allows for global deformations such as rotation capacity and deflections to be determined based on a non-linear analysis. The model is also suitable for slabs but from herein beams will only be referred to as representing flexural members in general.

The analysis proceeds numerically by incrementing the local tensile steel strain, FRP strain, or concrete compressive strain at a driver section, chosen to be the section of maximum moment M_{sp} in the span. At a particular increment of deformation the moment at the driver section, M_{sp}, is evaluated using sectional equilibrium and compatibility requirements. It is assumed at this section of maximum moment the first flexural crack will form when the concrete tensile stress at the steel layer reaches the tensile strength of concrete f_{ct}. Since the beam is statically determinate the moment distribution along the length of the beam is known, and the sequence of calculations are as follows:

i. The beam is represented as a number of discrete blocks bounded by flexural cracks in the cracked region (Figure 2). In the uncracked region at each end of the beam the block edges are arbitrarily chosen. The crack positions (i.e. the number of cracked blocks), are initially assumed to be those from the previous converged load step.
ii. The distribution of local deformations over the length of the cracked blocks are evaluated by considering the behaviour of the tensile steel bar

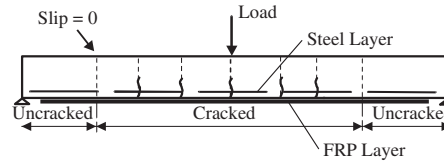

Figure 2. Beam discretisation.

surrounded by concrete and the FRP plate bonded to the concrete substrate. For infinite portions of the block, longitudinal stress equilibrium and slip compatibility equations for the steel layer and FRP layer, coupled together with the material relations and bond interface laws, are applied. A check is made to determine whether new cracks have formed, both at the minimum steel strain position between each pair of adjacent cracks and at the point of zero slip at the extremity of the cracked region. If a new crack has formed the cracked blocks are re-configured for the new crack and the procedure is repeated.

iii. The block rotations are calculated by integrating the tensile steel strain and the concrete compressive strain over the length of the block.

iv. The global deflections and rotations for the beam are determined by applying the moment-area theorem.

This procedure is continued until failure of the beam by fracture of the FRP, concrete crushing, or IC debonding. Concrete crushing occurs when the strain in the concrete exceeds 0.003 while FRP rupture occurs when the tensile capacity of the FRP is reached. Intermediate crack induced debonding occurs when the slip between the FRP and concrete reaches a critical value. Debonding is therefore dependent on the behaviour of the interface between the FRP and concrete and will be further discussed below.

2.2 *Bond-slip relationships*

In order to model local deformations, the bond-slip relations between the steel reinforcement and the surrounding concrete (otherwise known as *steel-to-concrete*), and the FRP plating and adjacent concrete substrate (otherwise known as *FRP-to-concrete*) are required. The following is a summary of the bond-slip relations for the steel-to-concrete and FRP-to-concrete interface adopted in this study.

2.2.1 *Steel-to-concrete bond-slip relation*

The bond behaviour between the reinforcing steel and concrete is modeled using the bond-slip relationship proposed in CEB-FIP (1993) (Figure 3). This relation caters for varying degrees of confinement of the concrete, and a reduction in bond stress near the transverse crack implicitly taking into account the effect of steel yielding.

This bond-slip relation is well established and will therefore not be discussed further.

2.2.2 *FRP-to-concrete bond-slip relation*

FRP-to-concrete bond-slip relations are not as developed as those of steel-to-concrete bond-slip relations. As a result, considerable research has been undertaken on developing FRP-to-concrete interface laws over the past decade or so and a comprehensive review of such research is given in Yuan et al. (2004). To date linear, bi-linear and non-linear relations have been proposed which are typically calibrated from the results of lap-shear tests performed on prismatic concrete specimens. These relations are however generally unique to the concrete and FRP material and geometric properties, and concrete surface preparation technique. No relations developed to date are of such a generic nature as that of the CEB-FIP (1993) bond-slip relation for steel-to-concrete.

For the present analysis, the non-linear FRP-to-concrete bond-slip relation of Savoia et al. (2003) is used (Figure 4) primarily because the local deformation model is numerically more stable when using a continuous bond-slip model. The relationship is given as:

$$\tau = \tau_{max} \frac{s}{s_{max}} \frac{n}{(n-1)+(s/s_{max})^n} \quad (1)$$

where τ is the shear stress, s the slip, τ_{max} the peak shear stress, s_{max} the reference slip (close to the slip corresponding to τ_{max}) and n a free parameter. The values of the parameters specified by Savoia et al. (2003) are: $\tau_{max} = 3.5 f_c'^{0.19}$ with f_c' denoting the concrete cylinder compressive strength, $s_{max} = 0.051$ mm and $n = 2.860$. These values are based on lap-shear test results of specific concrete strengths and FRP types. Different values for the reference slip s_{max} will be investigated in this study (refer to Section 3.2).

2.2.2.1 *Debonding*

The FRP-to-concrete bond-slip relation is used to dictate the onset of debonding. Debonding occurs when a critical slip is reached (Figure 4).

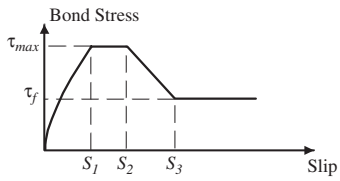

Figure 3. Steel-to-concrete bond-slip model (CEB-FIP 1993).

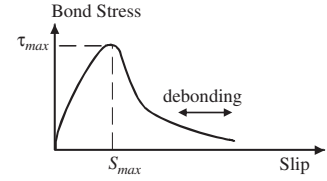

Figure 4. FRP-to-concrete interface law (Savoia et al. 2003).

According to Figure 4, just after initial loading chemical breakdown occurs between the concrete and FRP with increased interfacial slip and as a result bond stress increases. Once the peak stress is reached, interfacial softening (or micro-cracking) then starts and the shear (bond) stress reduces with increasing interfacial slip. For the continuous nonlinear bond-slip relation adopted in this study (Figure 4) a generic debonding slip is not known (unless specific lap-shear tests are undertaken) so debonding is deemed to occur when a large enough slip is reached such that minimal bond stress is present. Simulated slips at debonding, based on assumed values of s_{max} and comparison with test data, are given in Section 3.2.

Yuan et al. (2004) proposed a bi-linear ascending-descending bond-slip relation with complete debonding occurring where the descending (softening) portion of the relation bisected the horizontal axis. The slip to cause debonding is therefore well defined, however, this slip is not of a general nature.

Prior to debonding, and considering the same peak bond stress and peak bond stress slip, the bilinear bond-slip model of Yuan et al. (2004) and the continuous model of Savoia et al. (2003), offer little difference in results when incorporated into the local deformation model (Smith and Gravina 2004).

The peak bond stress τ_{max}, corresponding slip s_{max}, and slip at debonding s_{db} are three important variables that are required to define the shape of the bond-slip relation and the point of debonding. An important objective of the current study is to assess the sensitivity of the local deformation model results to the above mentioned variables. The values of the variables specified by Savoia et al. (2003), and given in Section 2.2.2, serve as a useful basis with which to choose values to vary.

2.3 *Constitutive relations for concrete, steel and FRP*

Figure 5 shows the constitutive material relations adopted in this study for the steel and FRP. The bilinear relation for steel allows for the strain hardening slope to be modelled. For steel, f_{su} is the ultimate tensile strength, f_{sy} is the yield strength and ε_{su} and ε_{sy} are the corresponding steel strains. For the FRP, f_{frp} is the rupture stress and ε_{frp} is the corresponding rupture strain. For concrete in compression the Warner (1969) law is used and for concrete in tension a linear–elastic relation is adopted. A more comprehensive account of all constitutive relations is given in Gravina and Smith (2004).

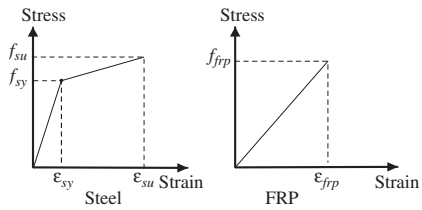

Figure 5. Constitutive material relations.

3 COMPARISON OF ANALYTICAL AND EXPERIMENTAL RESULTS

Comparisons are made between published test data and the predictions of the local deformation model for FRP-strengthened RC cantilever slabs failing by IC debonding. The details of the test slab are given below followed by a sensitivity study of the FRP-to-concrete bond-slip relation parameters in predicting debonding. Comparisons of the load-deflection response to experimental results as well as predictions of strain and slip distribution in the FRP and tensile steel at first cracking and debonding are finally given.

3.1 *Experimental data*

Tests CP1, CP2, CP3 and CP5 of Yao et al.'s (2002) study are used in the current study to verify the local deformation model. Yao et al. (2002) reported the results of an experimental program on RC cantilever slabs, strengthened on their tension face with externally bonded carbon FRP (CFRP) pultruded plates, and loaded at their free end. The plates were anchored into the fixed support and all slabs failed by IC debonding that initiated at a flexural crack in the peak moment position (support region). Once initiated, debonding rapidly extended to the free end of the slab. All debonding at the FRP-to-concrete interface took place in the concrete and this was confirmed by a thin layer of concrete remaining attached to the FRP upon debonding.

Geometric and material property details of the test slabs are given in Figure 6 and Table 1. In Table 1, b_c and D refer to the width and total depth of the slab respectively, f_c' the concrete cylinder compressive strength, d_s and A_s the depth to the internal tension steel reinforcement from the compressive face and the

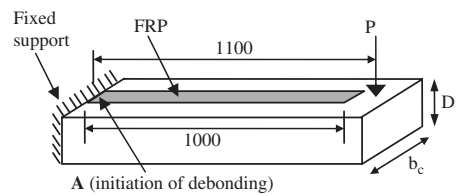

Figure 6. Details of test slabs.

corresponding steel cross-sectional area, and f_{sy} and E_s the yield strength and modulus of elasticity of the steel reinforcement respectively. The thickness and width of the FRP is denoted by t_{frp} and b_{frp} respectively, while the rupture strength and modulus of elasticity of the FRP are denoted by f_{frp} and E_{frp} respectively. Also contained in Table 1 are the load to produce debonding $P_{db,exp}$ and the debonding strain in the FRP $\varepsilon_{db,exp}$ at point A (Figure 6). From Table 1 it is evident the main variables tested in Yao et al.'s (2002) study are the concrete strength and area of steel reinforcement.

3.2 *Sensitivity of FRP-to-concrete bond-slip relation*

A positive feature of Savoia et al.'s (2003) continuous bond-slip model presented in Section 2.2.2 is specification of a generic expression for the peak bond stress. Here the bond strength is expressed in terms of the concrete strength and is easily determined from $\tau_{max} = 3.5 f_c'^{0.19}$, however, bearing in mind this expression was determined from tests with specific concrete strengths. As a result, this expression will be used to account for the change in concrete strength, for want of a better relationship, although the slip corresponding to the peak bond stress s_{max} as well as the slip corresponding to debonding s_{db} will be varied.

A sensitivity study is therefore undertaken on s_{max} and s_{db}. After specifying a value for $s_{\max}$ the local deformation model analysis is undertaken and stopped when the predicted strain in the FRP equals (approximately) the experimental debonding strain, $\varepsilon_{db,exp}$ measured at point A (Figure 6). The corresponding simulated slip when the analysis is terminated $s_{db,sim}$ is obtained from the local deformation model's results and this slip corresponds to the simulated point of debonding. Table 2 gives a summary of experimental debonding strain and load (as repeated from Table 1) and associated simulated debonding strain $\varepsilon_{db,sim}$ load $P_{db,sim}$ and slip $s_{db,sim}$.

Based on the results presented in Table 2, the maximum slip value at debonding $s_{db,sim}$ decreased with an increase in the concrete compressive strength. This is a reflection of the relation between maximum bond stress and concrete strength (i.e. $\tau_{max} = 3.5 f_c'^{0.19}$). The experimental strain could not be matched in the simulation for $s_{max} = 0.03$ mm in slab CP1 since insufficient bond strength was mobilised. In addition, when

Table 1. Cantilever slab geometric and material properties (Yao et al. 2002).

	Concrete				Steel			FRP				Measurements	
Slab	b_c (mm)	D (mm)	d_s (mm)	f_c' (MPa)[a]	A_s (mm^2)	f_{sy} (MPa)	E_s (GPa)	t_{frp} (mm)	b_{frp} (mm)	f_{frp} (MPa)	E_{frp} (GPa)	ε_{dbexp} ($\mu\varepsilon$)	$P_{db,exp}$ (kN)
CP1	301.5	150.5	117.4	27.0	314	343	208	1.2	50	2800	165	5420	19.95
CP2	303.6	151.9	111.3	37.7	314	343	208	1.2	50	2800	165	4298	17.58
CP3	302.7	150.0	108.2	12.6	157	343	208	1.2	50	2800	165	5240	13.31
CP5	304.0	149.0	117.4	24.6	157	355	210	1.2	50	2800	165	3761	10.11

[a] Converted from tested cube strength using $f_c' = 0.8 f_{cu}$

Table 2. Summary of experimental and analytical results.

	Experimental		Peak bond stress slip, s_{max} (mm)	Simulation		
Slab	$\varepsilon_{db,exp}$ ($\mu\varepsilon$)	$P_{db,exp}$ (kN)		$\varepsilon_{db,sim}$ ($\mu\varepsilon$)	$P_{db,sim}$ (kN)	$s_{frp,sim}$ (mm)
CP1	5110	19.95	0.03	4430	20.9	0.132
			0.065	5110	20.9	0.858
			0.09	5110	20.9	0.74
CP2	4298	17.58	0.03	4330	19.2	0.628
			0.065	4330	19.2	0.494
			0.09	4330	19.2	0.328
CP3	5240	13.31	0.03	5150	13.5	–
			0.065	5150	13.5	1.45
			0.09	5150	13.5	1.38
CP5	3761	10.00	0.03	3700	12.4	0.69
			0.065	3700	12.4	0.6
			0.09	3700	12.4	0.3

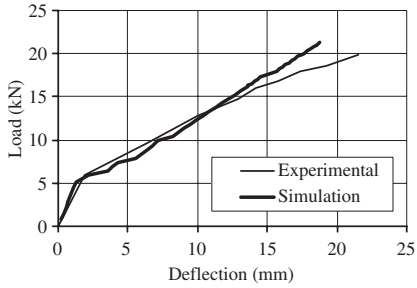

Figure 7. Load-deflection.

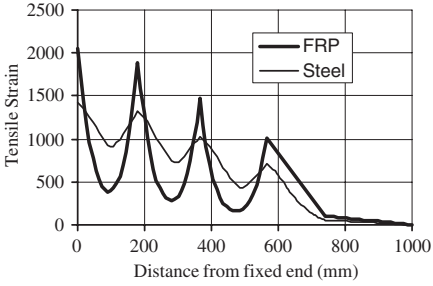

Figure 8. Tensile strain distribution (first cracking).

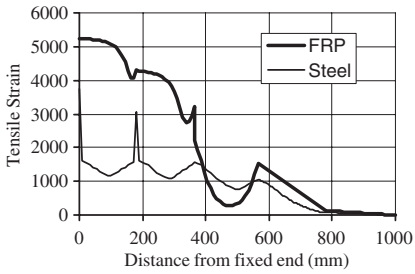

Figure 9. Tensile strain distribution (debonding).

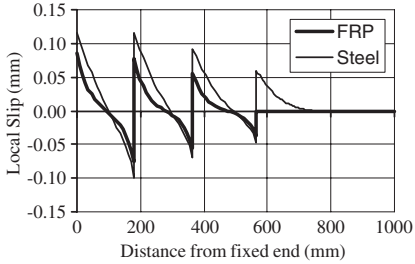

Figure 10. Slip distribution (first cracking).

considering the slabs independently, an increase in the peak slip at peak bond stress produced a reduction of the maximum slip value at debonding suggesting that a bond-slip relation for the FRP-to-concrete interface with a larger area under the ascending branch will produce less slip at debonding.

Based on the results presented in Table 2 for Slab CP1, $s_{max} = 0.065$ mm and $s_{db} = 0.8$ mm will be used to produce plots of the load-deflection response as well as distribution of strain and slip in the FRP and steel along the length of the slab.

3.3 *Load – deflection*

Figure 7 compares the simulated and measured load versus deflection beneath the applied load point response for the test cantilever slab CP1. For the simulation, the theoretical cracking load used in the analysis was matched to the experimental value of approximately 6 kN and a more detailed explanation of the treatment of the first cracking point in the analysis is given in Gravina and Smith (2004). According to the experimental results the peak load was reached at 20.0 kN with a maximum deflection of 21.5 mm in comparison to simulation results of 21.2 kN peak load and maximum deflection of 18.8 mm. Good correlation generally exists between theory and experiments although some deviation occurs prior to debonding with a smaller predicted deflection at debonding.

3.4 *FRP and steel strain – distance from plate end*

Figures 8 and 9 show the distribution of strain in the steel and FRP along the length of the slab based on the load to cause first cracking and the debonding load respectively for slab CP1. The horizontal axis denotes the distance from fixed end of the slab.

The position of the cracks can be seen in Figure 8 and these positions are identified by the four peaks. The strain in the FRP is maximum at the crack position. Here the tensile strain in the slab is resisted solely by the FRP. The strain in the FRP between the cracks decreases as both the FRP and concrete resist the tensile strains (otherwise known as *tension stiffening*).

Figure 9 shows a region of high localized strain in the FRP within a distance of 400 mm from the fixed support to be considerably larger than the steel signifying bond breakdown of the FRP-to-concrete.

3.5 *FRP and steel slip – distance from plate end*

The slip between the FRP and concrete at a load corresponding to first cracking and debonding is shown in Figures 10 and 11 respectively for slab CP1. At the

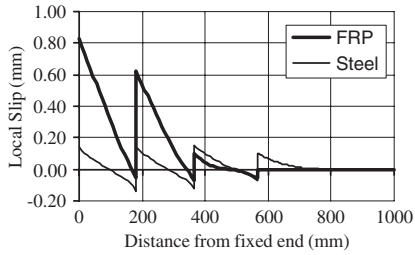

Figure 11. Slip distribution (debonding).

crack locations the slip between the FRP and concrete is a maximum. The slip varies from a maximum at the crack to zero, away from the crack. The direction of slip changes direction either side of a crack as expected. At debonding the slip in the FRP is predominantly in the same direction as opposed to that of the steel suggesting significant breakdown of bond between the FRP and concrete.

4 CONCLUSIONS

A local deformation model has been presented in this paper. The model considers local flexural deformations in a determinate structural flexural member at all stages of loading, from progressive formation of individual cracks up to debonding failure. The model predicts the strains in the tensile steel reinforcement, FRP strengthening, as well as the slip between the tensile steel and surrounding concrete and FRP and concrete substrate. The approach also allows for global deformations such as rotation capacity and deflections to be determined. The model correlated reasonably well with test data.

Debonding is governed by the bond-slip behaviour of the FRP-concrete interface. Despite considerable research undertaken on the development of bond-slip models to date, further work is still needed to develop a generic model.

ACKNOWLEDGEMENTS

The authors wish to thank the University of Technology, Sydney and RMIT University for the financial support provided through 2003/2004 ATN Research Staff Exchange Scheme Grants awarded to each author.

REFERENCES

Aiello, M.A. & Ombres, L. 2003. A model to predict the structural behaviour of reinforced concrete beams strengthened with externally bonded composite sheets. In M.C. Forde (ed.), *Tenth International Conference and Exhibition on Structural Faults and Repair-2001; Proc. (CR Rom) intern. symp., London, UK, 1–3 July 2003.*

CEB-FIP. 1993. Model Code for Concrete Structures, CEB Bulletin d'Information, Comitè Euro International du Bèton, Lausanne.

Ceroni, F., Manfedi, G. & Pecce, M. 2001. Crack widths in RC beams strengthened with carbon fabrics. In C.J. Buygoyne (ed.), *Fifth International Conference on Fibre-Reinforced Plastics for Reinforced Concrete Structures, FRPRCS-5; Proc. intern. conf., Cambridge, UK, 16–18 July 2001*: *917–926*. Thomas Telford.

Ferretti, D. & Savoia, M. 2003. Non-linear model for R/C tensile members strengthened by FRP-plates. *Engineering Fracture Mechanics* 70: 1069–1083.

Gravina R.J. & Warner, R.F. 2003. Local deformation model for reinforced concrete members in flexure. *Australian Journal of Structural Engineering* 5(1): 29–36.

Gravina, R.J. & Smith, S.T. 2004. Prediction of FRP-strengthened RC beam behaviour using a local deformation model. *in prep*.

Savoia, M., Ferracuti, B. & Mazzotti, C. 2003. Non-linear bond-slip law for FRP-concrete interface. In K.H. Tan (ed.), *Sixth International Symposium on FRP Reinforcement for Concrete Structures, FRPRCS-6; Proc. intern. symp., Singapore, 8–10 July 2003: 164–172*. World Scientific Publishing Company.

Smith, S.T. & Teng, J.G. 2002a. FRP-strengthened RC structures. I: Review of debonding strength models. *Engineering Structures* 24(4): 385–395.

Smith, S.T. & Teng, J.G. 2002b. FRP-strengthened RC structures. II: Assessment of debonding strength models. *Engineering Structures* 24(4): 397–417.

Smith, S.T. & Gravina, R.J. 2004. Prediction of debonding in FRP-strengthened RC beams using a local deformation model. *in prep*.

Teng, J.G., Chen, J.F., Smith, S.T. & Lam, L. 2002. *FRP-Strengthened RC Structures*. John Wiley & Sons. Chichester, West Sussex, UK.

Teng, J.G., Smith, S.T., Yao, J. & Chen, J.F. 2003. Intermediate crack-induced debonding in RC beams and slabs. *Construction and Building Materials* 17(6–7): 447–462.

Warner R.F. 1969. Biaxial moment thrust relations. *Journal Structural Division, ASCE* 85(St5): 923–940.

Yao, J., Teng, J.G. & Lam, L. 2002. Debonding in RC cantilever slabs strengthened with FRP strips. In R.A. Shenoi, S.S.J. Moi and L.C. Hollaway (eds.) *Advanced polymer composites for structural applications in construction; Proc. intern. conf., Southampton University, UK 15–17 April 2002*. Thomas Telford.

Yuan, H., Teng, J.G., Seracino, R., Wu, Z.S. & Yao, J. 2004. Full-range behaviour of FRP-to-concrete bonded joints: A closed form analytical solution. *Engineering Structures* 26: 553–565.

Shear and torsional strengthening of concrete beams

FRP Composites in Civil Engineering – CICE 2004 – Seracino (ed)
© 2005 Taylor & Francis Group, London, ISBN 90 5809 638 6

Torsional strengthening of reinforced concrete beams using CFRP composites

A.K.Y. Hii & R. Al-Mahaidi
Department of Civil Engineering, Monash University, Victoria, Australia

ABSTRACT: The construction boom over the last century has resulted in a mature infrastructure network in developed countries. Lately, the issue of maintenance and repair/upgrading of existing structures has become a major issue, particularly in the area of bridges. Fiber Reinforced Polymer (FRP) has shown great promise as a state-of-the-art material in flexural and shear strengthening as external reinforcement, but information on its applicability in torsional strengthening is limited. No numerical modelling work currently exists in literature. The need for torsional strengthening in bridge box girders is highlighted by the Westgate Bridge, currently the largest bridge in the world to be strengthened through the use of externally-bonded FRP laminates. This paper provides details on preliminary work investigating the torsional strengthening of solid reinforced concrete beams with externally-bonded CFRP laminates, through experiments and finite element modelling.

1 INTRODUCTION

The maturing of Australia's and other countries' bridging infrastructure has accelerated rapidly in the last century. However, times have changed, resulting in increased service loading and traffic volumes, diminished capacity through aging and environmental degradation, more stringent updates in design code regulations, and the need for seismic retrofit in some parts of the world. Other possible deficiencies in a bridge structure could be improper design, construction or maintenance. One new class of structural material known as Fiber Reinforced Polymer (FRP) has come up for its high tensile strength and in-plane stiffness, excellent corrosion resistance, linear behaviour to failure and light-weight (about one-quarter of steel's density) characteristics, all advantages over steel in traditional rehabilitation methods.

Use of FRP has shown promise in the area of strengthening and rehabilitation of structures, and has been used successfully in many applications around the world. Research into the use of FRP has shown great promise in flexural and shear strengthening as externally-bonded reinforcement, but information on its applicability in torsional strengthening is limited (Hii and Al-Mahaidi, 2004). Many buildings and bridge elements are subjected to significant torsional movements that affect the design. Such examples include spandrel beams in buildings, beams in eccentrically loaded frames of multi-deck bridges and box-girder bridges. The need for strengthening for increased torsional capacity may be required in these areas. A good example of this is the Westgate Bridge in Melbourne, Australia, currently the largest bridge in the world to be strengthened by FRP (Gosbell and Meggs, 2002); where due to lack of supporting guidelines the effective FRP strain at ultimate limit state for torsion was taken to be identical to shear. No numerical modelling work in the area of torsional strengthening with FRP currently exists in literature. The paper discusses the preliminary work carried out so far in an overall investigation of torsional strengthening of solid and box-section reinforced concrete beams with CFRP.

2 EXPERIMENTAL STUDIES

2.1 *Experimental program*

2.1.1 *Specimen geometry & design*

Three identical 2700 mm long reinforced-concrete beams of 140 × 260 mm deep cross-section were constructed. In the test, torsion was applied to the middle 1500 mm section of the beam. All three specimens were cast from the same batch of concrete. The average compressive strength of concrete on the day of testing (63 days) was 51.3 MPa. The internal steel reinforcement layout was identical for all three beam specimens. Two 12 mm diameter bars were used for the top compression steel, while the bottom tensile steel comprised of three 12 mm diameter bars. All stirrups were 6 mm in diameter. The spacing of stirrups in the test zone was 120 mm, while the spacing was narrowed to 60 mm to avoid unwanted failure outside

Table 1. Steel reinforcement properties.

Reinforcement properties	Stirrups ϕ6 mm	Longitudinal ϕ12 mm
Area (mm^2)	28.3	113.1
Young's modulus (MPa)	222000	216000
Yield strength (MPa)	450	600
Ultimate strength (MPa)	514	733

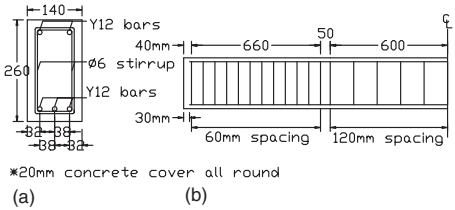

Figure 1. (a) Cross-section dimensions of beam specimens. (b) Side elevation of half of concrete beam.

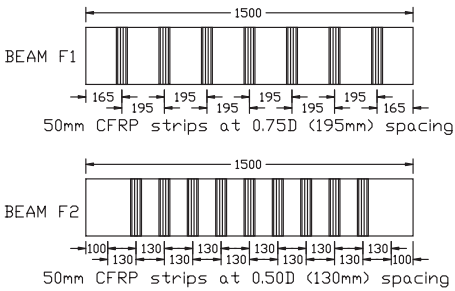

Figure 2. CFRP layout of strengthened Beams F1 and F2.

the test zone. Details of the steel reinforcement properties tested can be found in Table 1. The concrete cover was 20 mm thick all around. The dimensions of the beams and the reinforcement details are shown in Fig. 1. All three beams were designed according to AS3600-2001 (SAI, 2001) to be deficient in torsion under new loading requirements.

The first beam, C1, was designated as the control beam, where no CFRP strengthening scheme was provided. The second beam (F1) was strengthened with 50 mm wide CFRP single layer hoop strips spaced at 195 mm (0.75D) (D – full depth of beam) centres. 50 mm wide CFRP single layer hoop strips spaced at 130 mm (0.5D) centres were used to increase the torsional capacity of the third beam F2. The wrapping patterns and CFRP layout details are summarized in Fig. 2.

For this experiment, the CFRP sheets and epoxy resins were supplied by Master Builder's Technologies

Table 2. Specification of CFRP sheet used.

MBrace CF 130 (S&P C-sheet 240, high tensile CF)	
Fibre reinforcement	Carbon – high tensile
Fibre density	1.7 g/cm^3
Fibre modulus	240 GPa
Fibre weight (CF)	300 g/m^2
Thickness	0.176 mm
Tensile strength	3800 MPa
Tensile elongation, ultimate	1.55%

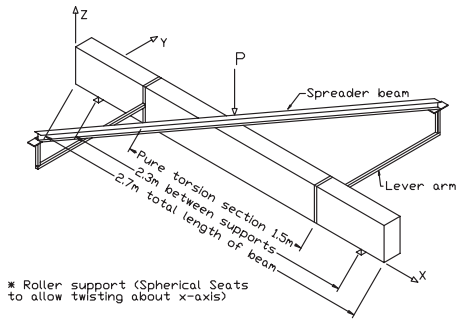

Figure 3. Schematic of test setup.

(MBT, 2002), as shown in Table 2. The wet lay-up method was used to apply the CFRP sheets onto the beam, following procedures recommended by MBrace Application Guidelines (MBT, 2003). Because the CFRP strips were required to run in a transverse direction, the beam edges were chamfered with an angle grinder to a radius of at least 15 mm. This was to prevent any sharp corners that would contribute to the reduction of fiber strength. A 150 mm overlapping length of strip was applied in the longitudinal fiber direction on top of the beam to prevent debonding. To ensure the quality of epoxy bond of the fibers to the concrete surface, a pullout test was carried out on each specimen, which was satisfied. Failure occurred in the concrete adjacent to the adhesive-to-concrete interface, with an average tensile strength of 4.3 MPa.

2.1.2 *Test rig*

The test rig is as shown in Figs. 3 and 4, which is very similar to the test setup employed by Ghobarah et al. (2002). Two SHS (Square Hollow Section) beams, which act as lever arms to apply the torsional moments, were attached to the concrete beams at a distance of 1.5 m from each other. A steel I-beam was laid down diagonally resting on hinged end supports (750 mm eccentricity from centreline of beam) on top of the lever arms. The I-beam was loaded at mid-span by a 250 kN capacity Instron hydraulic jack with 250 mm

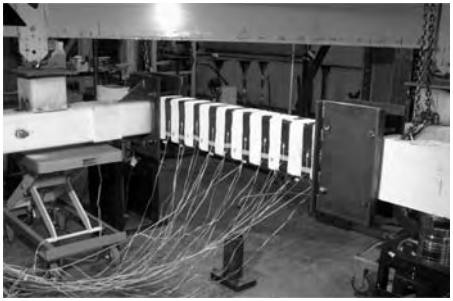

Figure 4. Side view of Beam F2 positioned in the test rig.

stroke capacity. Two spherical seats were fashioned for the end supports for the beam specimen. Both were free to move longitudinally to allow for beam elongation and allow the beam to twist freely under torque.

2.1.3 *Instrumentation*

An Instron load cell was used to measure the applied forces in the Instron hydraulic actuator. Load cells were placed at the end supports to measure the vertical reaction forces. The measurements also provided an easy way to verify the assumption of symmetry about the midspan of the beam. Later experimentation showed that the variation between both load cells was within 4% for all three specimens, which was deemed to be acceptable. For ease of attachment, inclinometers were placed on the ends of beam specimens to measure the rotation of each lever arm, in addition providing a quick check for symmetry, which was found to give very similar readings. In all three beam specimens, electrical resistance strain gauges were placed at specific locations on the stirrups and longitudinal bars, and in the middle of the CFRP strips along the fiber direction to obtain strain distributions to be compared with numerical modelling results. All measurements were recorded with a computer controlled data acquisition system at three second intervals. Before beginning the test, a noise test was carried out to ensure all the instrumentation was working with no significant fluctuations in readings. Loading was displacement controlled. Finally, the crack width at the surface was measured using a micrometer with an accuracy of ± 0.01 mm.

2.2 *Experimental results*

2.2.1 *Cracking and ultimate strength*

The strengthening effects of CFRP hoop strips are evident from the torque-rotation graphs for Beams C1, F1 and F2 in Fig. 5 and Table 3. Increases in cracking strength of up to 21.4% were achieved with the strengthened specimens. The spacing of strips was found to play a significant role in cracking torque.

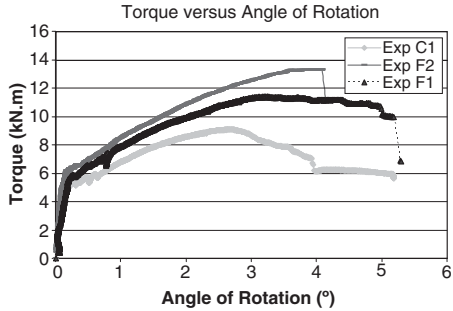

Figure 5. Comparison of torque–rotation graph (C1, F1, F2).

Table 3. Summary of cracking and ultimate strength.

	Beam C1	Beam F1	Beam F2
Cracking strength (kN.m)	5.1	5.6	6.2
Percentage increase (%)	–	9.2	21.4
Twist at cracking Load (°)	0.12	0.18	0.17
Ultimate strength (kN.m)	9.1	11.4	13.4
Percentage increase (%)	–	25.2	46.6
Twist angle at ultimate load (°)	2.69	3.19	3.97
Maximum twist (°)	5.18	5.31	4.15

This can be attributed to the effect of confinement from the CFRP strips. Beam C1 reached an ultimate torque of 9.1 kN.m and exhibited ductile behaviour. Beam F1 achieved a greater ultimate torque of 11.4 kN.m. Beam F2 had the largest ultimate torque of 13.4 kN.m with less ductile behaviour. It can be seen from Fig. 5 that an increase in post-cracking stiffness was achieved with the reduction in spacing of CFRP strips, leading to greater ultimate torsional strength. It was observed that the post-cracking stiffness was more linear until failure with the addition of CFRP strips, reflecting the linear elastic properties of CFRP. The smaller spacing in Beam F2 almost doubled the percentage increase in strength compared to F1 (46.6% versus 25.2%). As the spacing of the strips becomes smaller, the propagation and widening of cracks intersecting the CFRP strips are inhibited, and the increase in effective confinement provided by full strips will result in greater post-cracking stiffness. Also the externally bonded FRP laminates prevented cover spalling, thus utilizing the entire concrete cross-section in enhancing torsional strength.

2.2.2 *Failure mode*

Beam C1 failed through concrete spalling as shown in Fig. 6. This was the expected failure mode according

Figure 6. Concrete cover spalling in Beam C1.

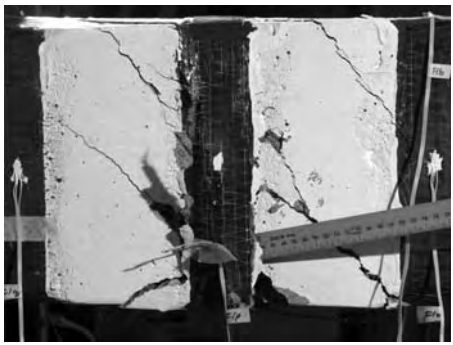

Figure 7. CFRP rupture in Beam F1.

Figure 8. CFRP rupture in Beam F2.

to Rahal's (2000) work. In Beams F1 and F2, failure occurred through rupture of the CFRP strips as shown in Figs. 7 and 8 respectively. The extra overlapping of fibers in the full strip wrap prevented the debonding mechanism from developing. Also, the specimens were designed to limit the amount of CFRP used to prevent crushing of inclined compressive concrete struts. By using only one layer of CFRP, the tensile stress in the fibers reaches a sufficiently high level for rupture to occur.

2.2.3 *Crack pattern*

Approximately 1.5 full spiral cracks formed during failure in Beam C1, with the majority of cracks forming near the area of concrete spalling. Substantial cracking occurred in the unwrapped space between

Table 4. Inclination angle and widths of spiral cracks.

	C1	F1	F2
Crack width at area of failure (mm)	2.3	1.8	1.5
Average crack width (mm)	1.5	1.0	0.6
Average inclination angle of cracks (°)	43	46	55
Inclination angle of failure crack (°)	43	46	60

Table 5. Comparison of CFRP strains.

CFRP strain value (microstrains)	F1	F2
Experimental maximum strain	12300	7800
Manufacturer's maximum strain	15500	15500
Percentage difference (%)	20.6	49.7

strips in Beams F1 and F2, with the larger cracks forming near the area of CFRP rupture. It was found that the addition of CFRP strips has resulted in more uniformly distributed and closely spaced torsional cracks. Further details can be found in Hii and Al-Mahaidi (2004). As the spacing of the strips narrowed, the widening of cracks intersecting the strips was reduced as shown in Table 4, where the crack widths were found to steadily decrease with smaller strip spacings. With smaller crack widths, greater aggregate interlock and post-cracking shear stiffness will be achieved in the concrete material, resulting in higher ultimate strengths due to greater concrete contribution. Of interest to note is that the inclination angle of spiral cracks increases with the smaller spacing of CFRP strips, as shown in Table 4. This could be attributed to the addition of CFRP strips, increasing the ratio of transverse to longitudinal reinforcement.

2.2.4 *Maximum CFRP strain*

The maximum strains in CFRP strips for specimens F1 and F2 can be found in Table 5. In Beam F1, the maximum local strain measured in the CFRP strip along the fiber direction was 12300 microstrains, close to the ultimate strain of 15500 microstrains. It was noted that the strain gauge was very close to where rupture of CFRP occurred (Fig. 7). For Beam F2, the maximum local strain measured in CFRP strip was 7800 microstrains, lower than in Beam F1. The reason for this is because none of the cracks formed happened to pass exactly through any of the CFRP gauges' location. This reflects the linear elastic property of FRP where the FRP strain is closely related to the crack width.

The much lower strain reading recorded in F2 compared to F1 reflects the lack of ductility in FRP composites. As discussed by Chen and Teng (2003), the inability for FRP composites to redistribute stresses

means that not all the strips intersecting the failure crack will develop ultimate strain at failure, hence the much lower strain values recommended by design guidelines such as FIB-14 (FIB, 2001). The slightly lower values recorded in F1 may be due to the ultimate strain developing at the side of the strip at rupture, while the strain gauge is located in the middle. This makes physical sense, as crack propagation will be halted at the side of the strip, resulting in a non-uniform stress distribution across the CFRP strip. This non-uniformity of stress distribution and lack of ductility means that the failure process will start once the most highly stressed point in the CFRP reaches ultimate tensile strength. This brittleness of FRP composites is a fundamental behavioural difference between steel and FRP reinforcement.

3 NUMERICAL STUDIES

DIANA v8.1 FE software (Witte and Kikstra, 2002a), was used to model the experimental specimens in the aforementioned section.

3.1 *Finite element analysis*

A general methodology was developed to systematically model the experimental specimens. In the first stage, three different base models with a given set of material properties for C1, F1 and F2 were developed to verify if the experimental behaviour of the control beam C1 could be simulated accurately. The different base models were needed due to the slightly differing geometric requirements from the location of CFRP strips. In the next stage of modelling, external CFRP reinforcement was added to the base models to verify if simulation of experimental behaviour of Beams F1 and F2 was possible, and to identify the limitations involved due to the assumptions made during modelling. Finally, parametric studies were carried out on Beams F1 and F2.

3.1.1 *Conceptual stage*

Due to the nature of the torsional problem, the model was generated with mainly three-dimensional elements, as there were out-of-plane as well as in-plane forces. Only one half of the whole beam specimen about the centreline at mid-span was modelled since the cross-sectional geometry, boundary conditions and loading were assumed to be symmetrical, which was verified in the experiments. This significantly reduced the computational time and resources in numerical analyses. Fig. 9 illustrates the generated FE model, where eight-node isoparametric solid brick elements (HX24L) were used for concrete. 10 by 6 over the depth and width, and approximately 40 brick elements along the length were used in the model. A refined mesh was used in the zone under torsion.

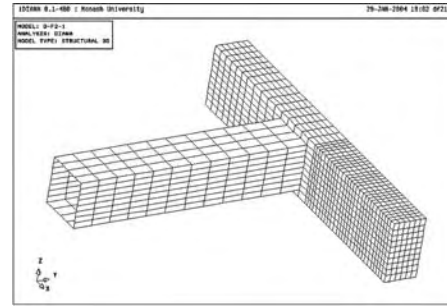

Figure 9. FE mesh of base models for F2 (hidden view).

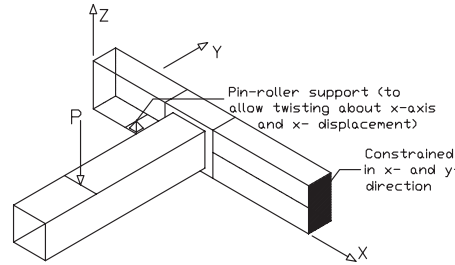

Figure 10. Boundary conditions imposed on FE model.

CFRP sheet strips were modelled using four-node quadrilateral isoparametric plane stress elements (Q8MEM). Due to the minimal thickness of the single layer used, it was safe to conclude the strips have a very low bending stiffness. It was also assumed that out-of-plane forces were negligible, as loading and forces carried by the strips were mainly in-plane. For the reasons above, the aforementioned plane stress element was suitable for the model. Perfect bond between the CFRP strips and concrete layer was assumed.

The SHS lever arm and loading plates were modelled with four-node quadrilateral isoparametric flat shell elements (Q20SF). The high width/depth ratio of the loading plates and lever arm make the flat shell elements particularly well suited for the task. Steel bars were modelled individually as embedded reinforcements in the concrete elements.

3.1.2 *Boundary conditions*

For the end support a pivot point was placed at mid-point (Fig. 10), which is fixed in the lateral and vertical directions, but unrestrained in the longitudinal direction to allow elongation/shortening of the beam under applied torque. To counter localized concrete crushing at the pivot point (which did not appear in experiments), the concrete brick elements around the support were given linear elastic properties. At mid-span, the

Table 6. Basic properties of the concrete material model.

Properties	Values
Mean compressive strength, f_{cm} (MPa)	51.3
Young's modulus, E_c (MPa)	36211
Tensile strength, f_t' (MPa)	2.15
Poisson's ratio, ν	0.2

beam cross-section's surface was constrained so there is no movement in the longitudinal and lateral direction to reflect the plane of symmetry at mid-span. Loading on the specimen was achieved by displacement of the point load on the lever arm.

3.1.3 *Material models*

Concrete cracking was based on the smeared crack approach. The "Fixed Total Strain Crack model" (Witte and Kikstra, 2002b) was selected as the constitutive model for concrete, which describes the tensile and compressive behaviour of a material with one stress-strain relationship. Young's modulus was determined in accordance with the Australian Standard AS3600-2002 (SAI, 2001). Further discussion on the concrete tensile strength can be found in Section 3.2.1. Poisson's ratio was taken to be 0.2. The basic material properties are summarized in Table 6.

The hardening and softening of concrete in compression was chosen to be modelled using the Thorenfeldt function. The influence of lateral cracking & lateral confinement on compressive strength was determined using the model according to Selby and Vecchio (1993). In tension, the behaviour is based on a bilinear stress–strain relationship. The remaining shear stiffness of cracked concrete due to aggregate interlock is approximated with the shear retention factor, which is the proportion of the elastic shear modulus. For the total strain orthogonal crack models, only the constant shear stiffness can be modelled.

The CFRP sheet was modelled as an orthotropic linear elastic material. Limitations in the software package do not allow us to model cracking in orthotropic materials. This was overcome by examining the strain level in the CFRP strips, where failure by FRP rupture would be deemed to have occurred when the ultimate strain (15500 microstrains) is reached. The CFRP properties used can be found in Tables 2 and 7. The Young's modulus in the lateral direction was assumed to be 10 percent and shear modulus assumed at 5 percent of the Young's modulus in the longitudinal direction, due to the unidirectional property of the CFRP strip. These figures were adapted for numerical stability in numerical modelling. With a small width to length ratio, the effect on the beam will be confined to localised regions where the strips were bonded, limiting their effect on the overall behaviour of the beam. Also, because the CFRP strips are mainly loaded in the longitudinal direction, the contribution in lateral and shear stiffness of the CFRP strips can be assumed to be negligible.

Table 7. Comparison of ultimate strengths for varying shear retention factors in Set B – NLFEA (base model C1).

Set B	Shear retention factor	Ultimate torque (kN.m)	Percentage of experiment (%)
B-C1-1	0.125	9.56	104.9
B-C1-2	**0.100**	**9.23**	**101.3**
B-C1-3	0.075	8.65	95.0
Exp C1	–	9.1	–

The steel reinforcement in the numerical models was taken to be a linear elastic isotropic material up until the yield point (Table 1). Yielding of the reinforcement was based on the Von Mises yield criterion with strain hardening. Both the lever arms and loading plates were assigned linear elastic properties to speed up the computation time. Non-linear properties were deemed unnecessary as it was designed to reach 50% of yield strength under maximum loading.

3.2 *Results of non-linear finite element analyses*

Five different sets of non-linear FE models were run, namely set A, B, C, D and E. The material models mentioned in previous sections were used throughout all the sets. Each run was named in a systematic manner, for example in C-F1-1, the first letter C stands for the set number, F1 for the specimen the model is simulating, and 1 for the number run within the set.

3.2.1 *Beam C1 – unstrengthened base model*

In Sets A and B, the objective was to determine the optimum concrete material properties to be used in the base models for C1, F1 and F2. In Set A, the objective was to simulate the experimental cracking strength in Beam C1 as accurately as possible. This was achieved by varying the tensile strength of the concrete material between the ranges of $0.3\sqrt{f_c'}$ and $0.7\sqrt{f_c'}$, a range generally found in most design codes. A tensile strength of $0.3\sqrt{f_c'}$ was chosen as the most appropriate, and is the recommended value for web-shear cracking by AS3600-2001 (SAI, 2001). However, the cracking strength was not modelled very well, with a difference of 46% with the lowest tensile strength (A-C1-4). This may be due to shrinkage effects in the specimens.

The purpose of Set B was to determine the optimal shear retention factor for the FE model to simulate the experimental ultimate strength in Beam C1 as accurately as possible. The results are as shown in Table 7 below. Based on the results, it was clear that the shear retention value of 0.100 (1.3% difference

Table 8. Comparison of cracking and ultimate strengths in Set E – NLFEA (beam model F1 and F2).

Set E	CFRP spacing	Strips	Ultimate torque (kN.m)	% of exp	Cracking strength	% of exp
E-F1-1	0.75D	Y	10.05	88.1	7.27	129.5
C-F1-1	0.75D	N	9.22	101.2	7.20	141.5
E-F2-1	0.50D	Y	10.11	75.7	7.52	121.7
D-F2-1	0.50D	N	9.41	103.3	7.43	146.0

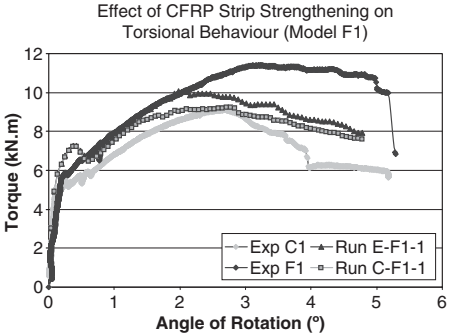

Figure 11. Effect of adding of CFRP strips (E-F1-1) over base model (C-F1-1).

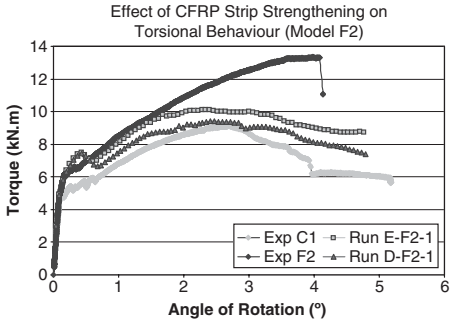

Figure 12. Effect of adding CFRP strips (E-F2-1) over base model (D-F2-1).

with experimental value) gave the closest approximation to the experimental ultimate strength. Therefore, the material values in B-C1-2 were used for the base models in C1, F1 and F2.

3.2.2 *Beam models F1 and F2*

Three sets were run to investigate Beams F1 and F2. In Set E, CFRP strips were added to base models C-F1-1 and D-F2-1 to determine the effect of strip spacing at 0.75D and 0.5D respectively. In Sets C and D, parametric studies of shear retention factors were carried out on F1 and F2 respectively.

The aim of Set E was to determine the effects of the addition of CFRP strips in Beams F1 and F2. It can be seen from Table 8, Figs. 11 and 12 that the addition of CFRP strips in E-F1-1 and E-F2-1 resulted in an increase in cracking and ultimate strength. Although the trend was correct, the predicted values were short of the experimental results, with the differences more apparent in E-F2-1. It was also found that the FE models do not fully take into account the effects of CFRP spacing on torsional behaviour on strengthened beams. The predicted cracking and ultimate load capacity of E-F2-1 was only marginally higher than E-F1-1.

The purpose of Sets C and D was to investigate the shear retention factor to account for the increase in concrete contribution with CFRP strengthening in Beams F1 and F2 respectively. The shear retention values used were from the range recommended by Al-Mahaidi and Nilson's (1979) model for smeared cracking. In this respect, the optimal shear retention factor was found to be 0.25 (0.18%), which was run C-F1-3. Due to the narrower CFRP strip intervals in F2, a higher shear retention factor range of 0.25 to 0.40 was used to account for the greater increase in strength. The optimal shear retention factor was found to be 0.40 (6.1%), which was run D-F1-4 as shown in Table 9. The ultimate strength of the models steadily increases with an increase in shear retention factor, as shown in Fig. 14.

3.3 *Discussion*

3.3.1 *Ultimate CFRP strain, failure mode*

It was observed that there was a significant difference between the CFRP strains recorded in FE models and experimental values, as shown in Table 10. As stated before concrete crack modelling was based on the smeared crack approach, where cracks are spread over a band of elements. In reality, discrete cracks form in small regions over the specimen under torsional loading. As the strain in the CFRP is closely related to the width of the crack, the CFRP strips are more highly stressed in the experimental discrete cracks than in numerical modelling. This would explain why CFRP rupture did not occur in the FE models. It was noted the higher shear retention factors in Sets C and D

Table 9. Comparison of cracking and ultimate strengths for varying shear retention factors in Sets C (F1) and D (F2).

Set E	Shear retention factor	Ultimate torque (kN.m)	% of exp	Cracking strength (kN.m)	% of exp
C-F1-2	0.15	10.66	93.4	7.60	136.7
C-F1-3	0.20	10.85	95.1	7.88	141.7
C-F1-4	0.25	11.39	99.8	8.10	145.7
Exp F1	–	11.4	–	5.6	–
D-F2-2	0.25	11.67	87.4	8.38	135.6
D-F2-3	0.35	12.19	91.2	8.75	141.6
D-F2-4	0.40	12.54	93.9	8.87	143.5
Exp F2	–	13.4	–	6.2	–

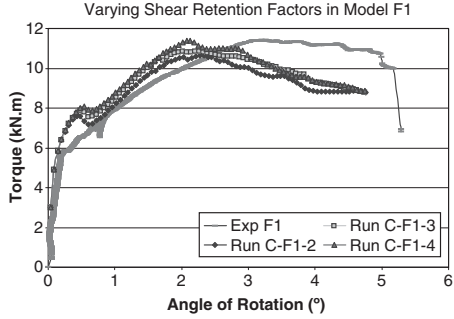

Figure 13. Comparison of torque–rotation behaviour in Set C with experimental results (Beam F1).

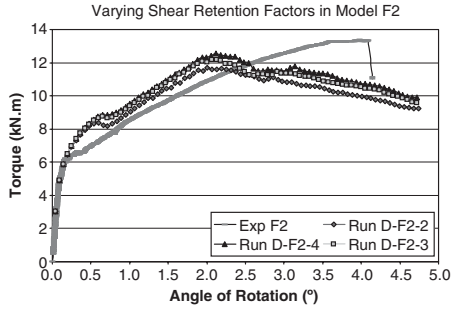

Figure 14. Comparison of torque–rotation behaviour in Set D with experimental results (Beam F2).

compared to Set E resulted in the FRP strips being slightly more stressed.

3.3.2 *Shear retention factor*

As discussed in Section 3.1.3, the remaining shear stiffness of cracked concrete due to aggregate interlock is approximated with the shear retention factor. The results from Sets C and D had shown that by increasing the shear retention factor, the numerical model emulates the torsional behaviour of strengthened specimens more accurately. This increase in shear retention factor can be justified as it was shown experimentally in Section 2.2.3 that the cracks widths were significantly smaller in the strengthened specimens, resulting in greater aggregate interlock and post-cracking shear stiffness in the concrete material. A summary of the relationship between the average crack widths measured in the specimens and the shear retention factors in the numerical models can be found in Table 11 above.

Table 10. Comparison of manufacturer and FE CFRP strains.

CFRP strain value (microstrains)	Set E		Set C	Set D
	E-F1-1	E-F2-1	C-F1-3	D-F2-4
Finite element max strain	5200	6300	7500	6800
Manufacturer's max strain	15500	15500	15500	15500
Percentage difference (%)	67	59	52	56

Table 11. Inclination angle and widths of spiral cracks.

	C1	F1	F2
Average crack width (mm)	1.5	1.0	0.6
Shear retention factor	0.10 (B-C1-2)	0.25 (C-F1-3)	0.40 (D-F1-4)

4 CONCLUSION

Based on the preliminary experimental work, the use of externally-bonded CFRP appears to be viable for torsional strengthening of reinforced concrete beams.

Further investigation is warranted in determining the actual strength contribution of the CFRP. The need for improved understanding of the failure modes and effect FRP materials have on the performance of retrofitted systems must be emphasised.

It appears that the total strain fixed crack model works well for modelling reinforced concrete beams. When extended to specimens strengthened with CFRP, the models do not simulate post-cracking behaviour as well. This was observed to be due to the cracks being "smeared" over a band of elements, thus the CFRP is not as highly stressed as it would in discrete cracks in experiments. Further investigation is needed in this area, possibly with discrete crack models. The modification of the shear retention factor of concrete in strengthened models is justified by the observation of smaller crack widths in the experiments. Further work is needed to correlate the shear retention value to the crack widths.

REFERENCES

Al-Mahaidi, R. A., and Nilson, A. H. (1979). "Non-linear Finite Element Analysis of Reinforced Concrete Deep Members." Cornell Univ., N.Y, Report No. 79–1.

Chen, J. F., and Teng, J. G. (2003). "Shear Capacity of Fiber-Reinforced Polymer Strengthened Reinforced Concrete Beams: Fiber Reinforced Polymer Rupture." Journal of Structural Engineering, 129(5), 615–625.

FIB. (2001). "Externally bonded FRP reinforcement for RC structures – FIB Bulletin 14." FIB, Lausanne.

Gosbell, T., and Meggs, R. (2002) "West Gate Bridge Approach Spans FRP Strengthening Melbourne, Australia." IABSE Symposium Melbourne, Melbourne.

Hii, A. K. Y., and Al-Mahaidi, R. A. (2004). "Torsional Strengthening of Reinforced Concrete Beams Using CFRP Composites." Department of Civil Engineering, Monash University, Melbourne, pp. 102.

MBT. (2002). "MBrace Brochure [online] [http://www.mbtaus.com.au]."

MBT. (2003). MBrace Application Guidelines, MBT.

Rahal, K. N. (2000). "Torsional strength of reinforced concrete beams." Canadian Journal of Civil Engineering, 27, 445–453.

SAI. (2001). AS3600-2001 – Concrete Structures, Standards Australia International Ltd.

Selby, R. G., and Vecchio, F. J. (1993). "Three-dimensional Constitutive Relations for Reinforced Concrete." University of Toronto, Department of Civil Engineering, Toronto.

Witte, F. C. d., and Kikstra, W. P. (2002a). Analysis Procedures, TNO Building and Construction Research.

Witte, F. C. d., and Kikstra, W. P. (2002b). Material Library, TNO Building and Construction Research.

FRP Composites in Civil Engineering – CICE 2004 – Seracino (ed)
© 2005 Taylor & Francis Group, London, ISBN 90 5809 638 6

Concrete shear-transfer strengthening with externally applied FRP composites

N. Saenz, C.P. Pantelides & L.D. Reaveley
Department of Civil Engineering, University of Utah, Salt Lake City, Utah, USA

ABSTRACT: This investigation is concerned with the determination of the contribution of fiber-reinforced polymer (FRP) composites to concrete shear transfer. The FRP composites were applied externally to plain concrete test units designed to fail at a known shear plane, which are generally known as push-off specimens. The FRP composite material used was a unidirectional carbon fiber fabric with epoxy resin, and was applied perpendicular to the failure plane. Test units with three different shear-to-transverse stress ratios were constructed to encompass many shear transfer applications. The experiments included test units with various FRP reinforcement ratios. It was determined that the shear strength contributed by the concrete-FRP shear friction interaction is a function of the concrete-to-concrete shear friction coefficient and the effective FRP composite tensile strain. Design procedures were developed based on a strut-and-tie model for strengthening concrete in shear transfer with externally applied FRP composites.

1 INTRODUCTION

Shear transfer tests were first used for steel reinforced concrete. The results of shear transfer tests were used to develop the "shear friction" hypothesis (Birkeland & Birkeland 1966). Mattock et al. (1969) studied initially cracked and uncracked concrete shear transfer specimens for steel reinforced concrete. Mattock & Hawkins (1972) in a study of uncracked and cracked shear transfer specimens found that the shear friction provisions of ACI 318 (1971) gave a conservative estimate of the shear transfer strength in cracked or uncracked shear planes. Walraven (1981) studied shear transfer specimens using concretes with compressive strength up to 62 MPa. The mechanism of aggregate interlock was presented where size of concrete aggregate, shear displacement, crack width, normal stress, and shear stress are considered. Hsu et al. (1987) developed a theory of shear transfer in initially uncracked concrete; the theory is based on the truss model and incorporates a softened compression stress-strain relation along the concrete struts. Hwang et al. (2000) introduced a softened strut-andtie model to determine the interface shear capacity of push-off and pull-off specimens for uncracked and cracked shear planes. The theory predicts that ultimate failure is caused by the crushing of concrete in the compression struts formed after cracking of the concrete, contrary to the shear friction concept. Mattock (2001) proposed simple shear friction design equations for all strengths of concrete, eliminating the 5.5 MPa shear stress limit, which is used in the ACI 318 (2002) Code. Kahn & Mitchell (2002) found that the ACI shear friction concept can be extended to high-strength concrete; they recommend the upper shear stress limit of $0.2 f_c'$ be retained but the 5.5 MPa shear stress limit be eliminated.

Dolan et al. (1998) adopted the Iosipescu test from ASTM D5379 (1998) to determine the shear transfer strength of reinforced concrete members externally reinforced with carbon reinforced polymer (CFRP) composites; a design equation was proposed which follows the shear friction theory; it was found that the shear strength is a function of the shear plane area, concrete shear capacity, coefficient of friction, area of bonded CFRP laminate, and bond strength of CFRP laminate. Shear transfer strength for internally reinforced glass fiber reinforced plastic (GFRP) composite stirrups was carried out by Burgoyne & Ibell (1999); an analysis based on Walraven's (1981) theory was used to predict the maximum shear stress.

2 STRUT-AND-TIE ANALYTICAL MODEL

A design relationship from the results of thirty shear transfer tests is developed. The strut-and-tie model has been studied for steel reinforced concrete and appears in the ACI 318 (2002) Code. The shear transfer unit used in the present tests, shown in Figure 1, was designed to fail in shear at a known plane. The units satisfy the conditions of a D-region, where there is a

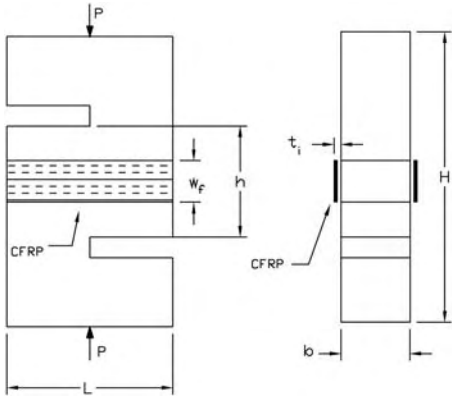

Figure 1. Typical CFRP reinforced shear transfer unit.

zone near concentrated loads, and an abrupt change in geometry near the shear failure plane.

Three types of test units were tested based on the shear-to-transverse stress ratio defined as:

$$k = \frac{P/bh}{P/bL} = \frac{L}{h} \tag{1}$$

where P = concentric applied load, h = shear plane height, b = width of rectangular cross section (127 mm), and L = unit length (305 mm) as shown in Figure 1. The width and length of the units were kept constant; for Type I, $h = 165$ mm and $H = 495$ mm; for Type II, $h = 203$ mm and $H = 533$ mm; and for Type III, $h = 241$ mm and $H = 572$ mm. The CFRP reinforcement ratio is defined as:

$$\rho_f = \frac{\sum_{i=1}^{N} t_i\, w_f}{b\, h} = \frac{n_f\, t_i\, w_f}{b\, h} \tag{2}$$

where n_f = number of CFRP composite layers, t_i = ply thickness, w_f = ply width, as shown in Figure 1. The CFRP composite was applied only on the two faces of the unit with dimension L.

The following assumptions were made to apply the strut-and-tie model in the as-built and CFRP reinforced units: (1) from the experimental measurements it was found that the shear strength of the unit is composed of two parts: (a) concrete shear friction strength, and (b) additional imposed shear stress resisted by the CFRP composite acting as a clamping force, which induces additional aggregate interlock/shear friction, until the bond between laminate and concrete fails.

The ultimate shear strength resisted by the unit can thus be evaluated as:

$$v_u = v_f + v_c \tag{3}$$

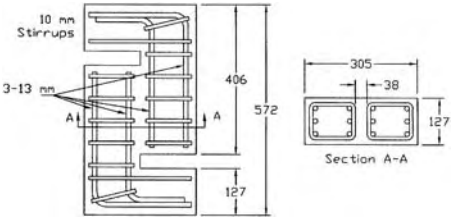

Figure 2. Internal steel reinforcement for Type III units.

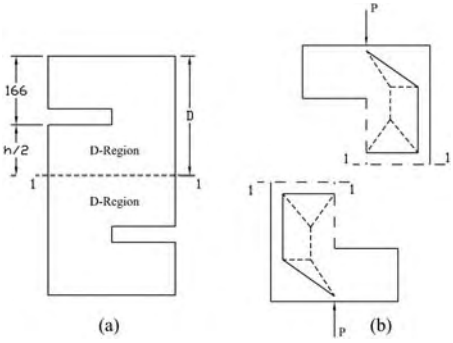

Figure 3. Typical strut-and-tie model: (a) D-regions; (b) model loaded at a single point.

where v_c = concrete shear friction strength; v_f = shear friction strength contributed by concrete-CFRP interaction; (2) the strut-and-tie model must be in equilibrium with the applied loads and reactions; (3) the angle of any strut and tie in a single node should not be less than 25 degrees; (4) if two D-regions overlap or meet in a plane, they can be considered as a single D-region for design purposes, if the maximum length-to-depth (L/D) ratio is less than two (ACI 318 2002).

2.1 *Strut-and-tie model for as-built test units*

Figure 2 shows the dimensions and steel reinforcement details of Type III units ($k = 1.26$); to ensure failure of the concrete unit in the shear plane, steel reinforcement was placed away from the shear plane to prevent undesirable failure modes such as flexural, compression, or bearing capacity failures.

Figure 3 shows a typical shear transfer unit and the location of the two different D-regions following ACI 318 (2002). For Type I units the length-to-depth (L/D) ratio is 1.23, for Type II units 1.14, and for Type III units 1.07, where L = unit length (305 mm) and D = one-half of the overall unit height, H, as shown in Figures 1, 3. Therefore, the two D-regions shown in Figure 3b can be considered as a single D-region.

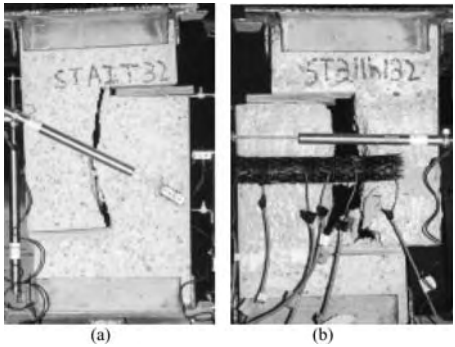

Figure 4. Typical failure modes: (a) Type III as-built unit; (b) CFRP reinforced unit.

Figure 3b shows a typical shear transfer unit with a concentric load applied at the shear plane, simulating the experimental setup of Figure 1. Symmetry about the shear failure plane and section 1-1 in Figure 3 is used to simplify the strut-and-tie model. The typical failure mode for the as-built and CFRP strengthened units is shown in Figure 4.

A Type III as-built unit is analyzed to compare the strut-and-tie model with the experimental shear transfer tests. The applied ultimate load, $P = 127.1$ kN, is the ultimate load of unit C3. Figure 5a shows the typical strut-and-tie model dimensions, and Figure 5b shows the structural analysis results. The shear friction theory proposed by Birkeland & Birkeland (1966) is used; it is assumed that the externally applied force, P_c, is resisted by a shear force, V_c, equal to the developed tie force at the shear plane, T_c, times the shear friction coefficient, μ, as shown in Figure 6. The shear friction coefficient is defined in the ACI 318 (2002) code and the PCI Handbook (1999) for monolithic concrete connections as $\mu = 1.4$.

For design purposes, the ultimate load is always known and the concrete shear strength can be found using experimental or rational equations, or through testing. The concrete will develop a tensile force if it does not fail in tension prematurely; the maximum shear force, V_c, that can be developed can be expressed as:

$$V_c = \mu f_t' b h = \mu T_c \quad (4)$$

where f_t' = concrete tensile strength which increases as the square root of the compressive strength, and T_c = concrete tie developed at the shear plane. Applying the experimental failure load, P_c, for as-built units in the strut-and-tie model the tie force, T_c, at the shear plane is calculated and the concrete tensile strength determined from Equation 4.

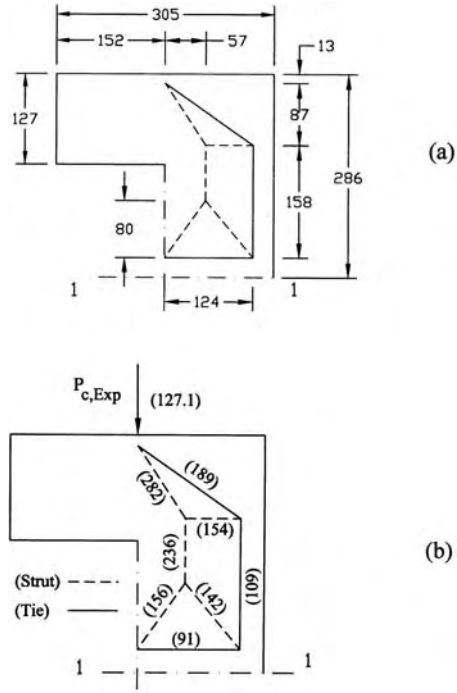

Figure 5. Strut-and-tie model for Type III as-built units: (a) model description, units in mm; (b) structural analysis results, units in kN.

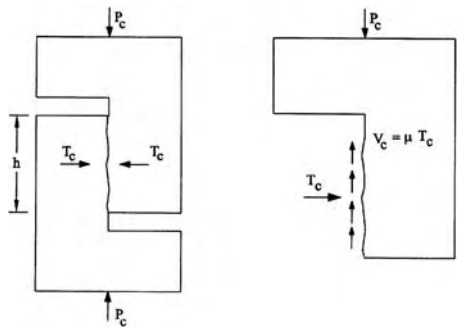

Figure 6. Shear friction principle for as-built units.

The strut-and-tie analysis results for the as-built units are summarized in Table 1; the concrete shear capacity can be calculated accurately using Equation 4 by experimentally determining or assuming the concrete tensile strength, or by performing a structural analysis using the strut-and-tie model.

Table 1. Experimental and strut-and-tie model results for as-built test units.

Test unit type	Shear transfer unit	Concrete compressive strength f_c' (MPa)	Experimental ultimate load P_u (kN)	Shear failure area $b{\cdot}h$ (mm^2)	Strut-and-tie concrete tensile	
					Force T_c (kN)	Strength f_t' (MPa)
I	C1	36.6	59.3	20968	44.0	2.10
II	C2	33.8	109.2	25806	81.8	3.17
III	C3	36.9	127.1	30645	90.8	2.96

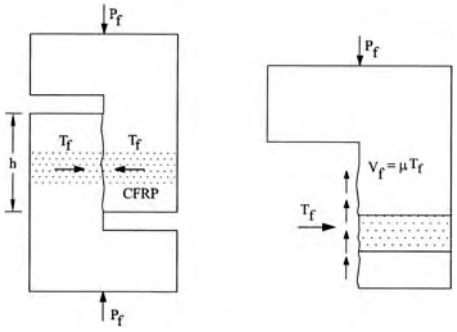

Figure 7. Shear friction principle for FRP-reinforced units.

2.2 *Strut-and-tie model for CFRP reinforced test units*

Using the same shear friction principle as for plane concrete, it is assumed that the externally applied force, P_f, is resisted by a shear force V_f, which is equal to the developed tie force at the shear failure plane due to the tension developed in the CFRP reinforcement, T_f, times the shear-friction coefficient, μ, as shown in Figure 7.

Once the CFRP reinforcement tensile force is developed, it results in a vertical force given as:

$$V_f = \mu T_f \tag{5}$$

The shear force contributed by the concrete-CFRP shear friction interaction is calculated using the experimental data, as:

$$P_f = P_u - P_c \tag{6}$$

where P_u = ultimate load; P_c = ultimate load resisted by concrete shear friction alone; P_f = remaining portion of ultimate load resisted by concrete-CFRP shear friction interaction.

For the as-built concrete units, the average experimental ultimate load, $P_{u,Exp}$, was applied in the strut-and-tie model so that, for Type I $P_{u,Exp} = 59.3$ kN, for Type II 109.2 kN, and for Type III units 127.1 kN. For the CFRP reinforced units, the experimental concrete-CFRP contribution, $P_{f,Exp}$, was calculated using Equation 6. The applied load for the CFRP reinforced units is the average of the two units with the same type and CFRP reinforcement ratio, ρ_f.

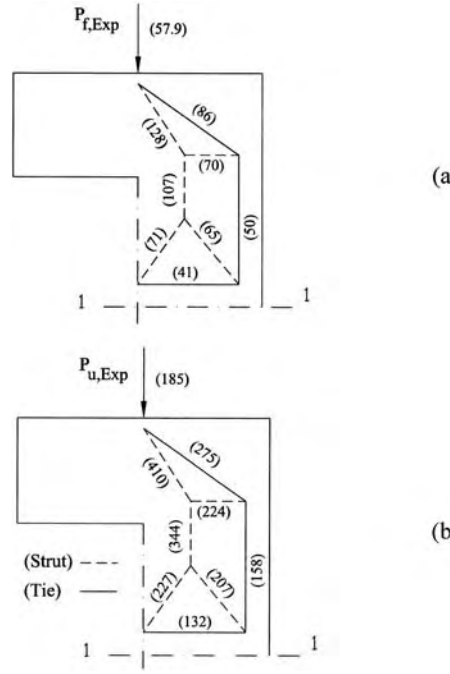

Figure 8. Strut-and-tie model analysis for CFRP reinforced Type III units with $\rho_f = 0.3\%$: (a) CFRP contribution results; (b) Ultimate calculated load results.

A Type III CFRP reinforced unit with $\rho_f = 0.3\%$ is analyzed. Figure 8a shows the structural analysis for the CFRP composite contribution and Figure 8b shows the superposition of the as-built unit forces, shown in Figure 5b, plus the CFRP reinforced unit forces. The calculated results are within ±5% of the experimental results, as shown in Figure 9.

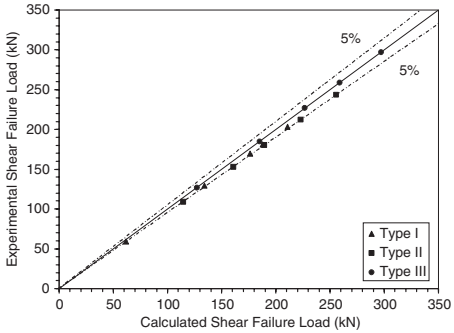

Figure 9. Experimental versus calculated ultimate load using strut-and-tie model.

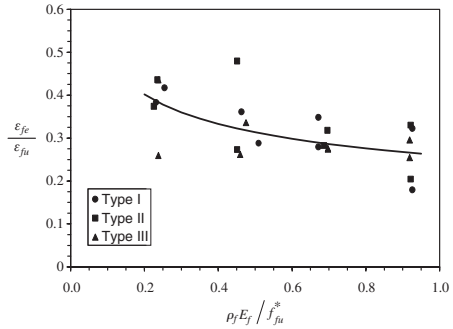

Figure 10. CFRP tensile strain efficiency.

It is clear that the ultimate load of the as-built and CFRP reinforced test units can be determined by using the strut-and-tie model. The strut-and-tie model can be used to analyze concrete members reinforced with CFRP composites subjected to shear stresses, where discontinuity regions are present.

3 DESIGN METHODS

Two design methods are presented: (a) simplified design method based on experimental results; and (b) strut-and-tie design method based on experimental and analytical results.

3.1 *Simplified design method*

The ultimate shear strength of the initially uncracked connections was found experimentally as:

$$v_u = 0.505\,\rho_f f^*_{fu} + 0.117\,f'_c \tag{7}$$

where f'_c = concrete compressive strength, f^*_{fu} = CFRP composite ultimate tensile stress, and ρ_f = CFRP composite reinforcement ratio, defined in Equation 2.

3.2 *Strut-and-tie design method*

The ultimate shear strength of the CFRP reinforced concrete connection is defined in Equation 2 in terms of the concrete shear friction strength, v_c, plus the shear friction strength contributed by the concrete-CFRP interaction, v_f, as:

$$v_u = \mu\left(T_c + T_f\right)/bh \tag{8}$$

Equation 8 can be used for design when the ultimate shear stress and material properties are known, so the number of CFRP composite layers can be obtained.

3.2.1 *Concrete shear friction strength*

The concrete shear friction strength is defined as:

$$v_c = \mu\,\gamma\,\sqrt{f'_c} \tag{9}$$

where γ = concrete tensile strength coefficient. All CFRP reinforced units had the same type of failure mode, because the CFRP reinforcement "locked up" the crack and the concrete-CFRP interaction behaved similarly for all three-unit types.

This failure mode is controlled by loss of bond between the CFRP laminate and the concrete as shown in Figure 4b. For design purposes, the concrete tensile strength coefficient is adopted from the ACI 318 Building Code (2002) as $\gamma = 0.50$.

3.2.2 *CFRP composite laminate efficiency*

The CFRP tensile strain efficiency is plotted in Figure 10, and was determined from the tests using a least squares fit, which represents the mean value as:

$$\xi_f = \frac{\varepsilon_{fe}}{\varepsilon_{fu}} = 0.26\left(\frac{\rho_f E_f}{f^*_{fu}}\right)^{-0.27} \tag{10a}$$

$$0.90 \geq \left(\frac{\rho_f E_f}{f^*_{fu}}\right) \geq 0.20 \tag{10b}$$

where ξ_f = CFRP composite efficiency, ε_{fe} = effective CFRP composite tensile strain, ε_{fu} = ultimate CFRP composite tensile strain, ρ_f = CFRP ratio, as defined in Equation 2, E_f = CFRP composite tensile modulus, and f^*_{fu} = CFRP composite ultimate tensile stress.

3.2.3 *Shear friction strength contributed by the concrete-CFRP interaction*

The shear strength contributed by the shear friction from concrete-CFRP interaction is found from Figure 7 as:

$$v_f = \frac{\mu T_f}{b h} \tag{11}$$

The effective tensile capacity of the FRP composite laminate is given as:

$$T_f = \xi_f \rho_f f_{fu}^* b h = \xi_f \varepsilon_{fu} E_f w_f \left(n_f t_i\right) \tag{12}$$

4 COMPARISON BETWEEN THE SIMPLIFIED AND THE STRUT-AND-TIE DESIGN MODELS

The simplified model of Equation 7 was derived using the method of least squares from experimental results. The first term in the equation is the shear friction strength contributed by the concrete-CFRP interaction, and the second term is the concrete shear friction strength. Therefore, from Equations 3 and 7 the shear friction strength contributed by the concrete-CFRP interaction is expressed as:

$$v_f = 0.505\, \rho_f f_{fu}^* \tag{13}$$

Comparing Equations 11–12 for the proposed strut-and-tie model to Equation 13, the coefficient of friction (0.505) can be expressed as a function of the effective CFRP composite tensile strain, ξ_f, and the shear friction coefficient, μ, as:

$$\mu\, \xi_f = 0.505 \tag{14}$$

The average value of the effective CFRP composite tensile strain, ξ_f, of Equation 10, was found from the experimental results as $\xi_f = 0.36$; using a shear friction coefficient for monolithic concrete connections, according to ACI 318 (2002) of $\mu = 1.4$, the product of the two is the same number, i.e. $1.4 \times 0.36 = 0.505$. Thus, the shear friction strength contributed by the concrete-CFRP interaction is a function of the concrete-to-concrete shear friction coefficient, μ, and the effective CFRP composite tensile strain, ξ_f.

Analyzing the second term of Equations 3, 7, the concrete shear friction strength can be expressed as:

$$v_c = 0.117\, f_c' \tag{15}$$

The CFRP reinforced test units had an average concrete compressive strength of 36.5 MPa. Substituting the concrete compressive strength in Equation 15, the average concrete shear friction strength is $0.117 \times 36.5 = 4.27$ MPa. Using Equation 9 and a shear friction coefficient of $\mu = 1.4$, the average concrete shear friction strength is found as $1.4 \times 0.5 \times (36.5)^{0.5} = 4.23$ MPa, which is almost identical to the result of Equation 15. In summary, both the simplified model and the strut-and-tie model can be used to calculate within the same accuracy the required CFRP reinforcement or the capacity of a CFRP reinforced connection.

The strut-and-tie model depends on the effective CFRP tensile strain, which is a function of the normalized CFRP stiffness, while the simplified design model represents the average ultimate shear strength of the total number of units tested. The strut-and-tie model can capture the shear friction contribution due to the prestressing effect of the CFRP composite. The simplified method represents the average coefficient of friction for the total population of the test units.

It can be shown that the simplified method can be unconservative since it represents the average experimental trend of the available data, while the strut-and-tie design method gives more rational and conservative results.

5 DESIGN EXAMPLE

The simplified design method and the strut-and-tie design method are used in this example. The number of CFRP composite layers for a shear transfer unit required to resist an ultimate load $P_u = 243.2$ kN is determined. The material and geometrical properties of the test unit are: $E_f = 68$ GPa; $f_{fu}^* = 903$ MPa; $f_c' = 36.1$ MPa; $b = 127$ mm; $h = 203$ mm; $w_f = 156$ mm; and $t_i = 1$ mm.

5.1 *Simplified design method*

The ultimate shear stress is:

$$v_u = \frac{P_u}{b h} = \frac{243.2\ x\ 1000}{127 \times 203} = 9.43\ MPa \tag{16}$$

Using the initial conditions and substituting Equation 16 into Equation 7, the required CFRP reinforcement ratio is:

$$\rho_f = \frac{\left(9.43 - 0.117\ x\ 36.1\right)}{0.505\ x\ 903} = 0.0114 \tag{17}$$

Substituting Equation 17 into Equation 2 the number of CFRP layers is:

$$n_f = \frac{0.0114\ x\ 127\ x\ 203}{1\ x\ 156} = 1.88 \tag{18}$$

This is only 6% different from the number of layers used in the test unit, of $n_f = 2.0$, which had an actual experimental failure load of $P_u = 243.2$ kN.

5.2 *Strut-and-tie design method*

From Equation 16 the ultimate shear stress is $v_u = 9.43$ MPa. The concrete shear friction strength from Equation 9 with $\gamma = 0.5$ is:

$$v_c = 1.4\ x\ 0.5\sqrt{36.1} = 4.20\ MPa \quad (19)$$

Substituting Equation 19 in Equation 3, the required shear strength contributed by the concrete-CFRP shear friction interaction is:

$$v_f = 9.43 - 4.20 = 5.23 \quad MPa \quad (20)$$

Substituting Equation 20 in Equation 11, the required effective tensile capacity of the CFRP laminate is:

$$T_f = \frac{5.23\ x\ 127\ x\ 203}{1.4\ x\ 1000} = 96.3 \quad kN \quad (21)$$

Substituting T_f from Equation 21, and ξ_f from Equation 10 in Equation 12, the CFRP reinforcement ratio satisfies:

$$96300 = \left[0.26\left(\frac{\rho_f \cdot 68000}{903}\right)^{-0.27}\right]\rho_f \cdot 903 \cdot 25781 \quad (22)$$

which gives the required $\rho_f = 0.0170$; this value is substituted in Equation 2, to determine the number of CFRP layers required as:

$$n_f = \frac{0.0170\ x\ 127\ x\ 203}{1.0\ x\ 156} = 2.80 \quad (23)$$

This result is 40% greater than the number of layers used in test unit, $n_f = 2.0$, which is conservative for design.

The simplified method and the strut-and-tie design method give results with some deviation. The strut-and-tie model depends on the effective CFRP tensile strain, which is a function of the normalized CFRP stiffness, while the simplified design model represents the average ultimate shear strength of the total number of units tested. The strut-and-tie model can capture the shear friction contribution due to the prestressing effect of the CFRP composite. The simplified method represents the average coefficient of friction for the total population of the units tested.

6 CONCLUSIONS

The shear strength contributed by the concrete-CFRP shear friction interaction is a function of the concrete-to-concrete shear friction coefficient and the effective CFRP composite tensile strain. The concrete shear strength is a function of the concrete tensile strength and the shear friction coefficient. The strut-and-tie model depends on the effective CFRP tensile strain, which is a function of the normalized CFRP stiffness, and can adequately capture the tensioning effect of the CFRP composite. The simplified method represents the average coefficient of friction for the total units.

The application of the strut-and-tie model in externally applied CFRP composites for reinforced concrete under shear transfer is successful in representing the true behavior, it is based on experimental evidence and could be used in design.

Analytical models for representing shear transfer of plain concrete and CFRP reinforced units were derived based on experimental results. Two design approaches are proposed: (1) a simplified design method; (2) a strut-and-tie design method; the two methods give results with some deviation. The simplified method can be unconservative because it represents the average trend of the available experimental data, while the strut-and-tie method gives conservative results.

ACKNOWLEDGEMENTS

The writers acknowledge the financial support of the National Science Foundation under Grant No. CMS 0099792. The writers acknowledge Sika Corporation and Eagle Precast Inc. for in-kind support; they also acknowledge the assistance of several graduate students at the University of Utah.

REFERENCES

ACI Committee 318. 1971. *Building Code Requirements for Reinforced Concrete*. Detroit: American Concrete Institute.

Committee 318. 2002. *318-02/318R-02: Building Code Requirements for Structural Concrete and Commentary*. Farmington Hills: American Concrete Institute.

ASTM International. 1998. D5379/D5379M-98 Standard Test Method for Shear Properties of Composites Materials by the V-Notched Beam Method. *Annual Book of ASTM Standards 1998* 15(3).

Birkeland, P.W. & Birkeland, H.W. 1966. Connections in Precast Concrete Construction. *ACI J. Proceedings* 63(3): 345–368.

Burgoyne, C. & Ibell, T. 1999. Use of Fiber-Reinforced Plastics Versus Steel for Shear Reinforcement of Concrete. *ACI Structural J.* 96(6): 997–1002.

Dolan, B.E., Hamilton III, H.R. & Dolan, W. 1998. Strengthening with Bonded FRP Laminate. *ACI Concrete Inter.* 20(6): 51–55.

Hsu, T.T.C., Mau, S.T. & Chen, B. 1987. Theory of Shear Transfer Strength of Reinforced Concrete. *ACI Structural J.* 84(2): 149–160.

Hwang, S.J., Yu, H.W. & Lee, H.J. 2000. Theory of Interface Shear Capacity of Reinforced Concrete. *J. of Structural Eng.* 126(6): 700–707.

Kahn, F.L. & Mitchell, A.D. 2002. Shear Friction Tests with High-Strength Concrete. *ACI Structural J.* 99(1): 98–103.

Mattock, A.H., Hofbeck, J.A. & Ibrahim, I.O. 1969. Shear Transfer in Reinforced Concrete. *ACI J. Proceedings* 66(2): 119–128.

Mattock, A.H. 2001. Shear Friction and High-Strength Concrete. *ACI Structural J.* 98(1): 50–59.

Mattock, A.H. & Hawkins, N.M. 1972. Shear Transfer in Reinforced Concrete-Recent Research. *PCI J.* 17(2): 55–75.

PCI. 1999. *PCI Design Handbook–Precast and Prestressed Concrete*. Fifth (ed), Chicago: PCI Precast/Prestessed Concrete Institute.

Walraven, J.C. 1981. Fundamental Analysis of Aggregate Interlock. *J. of Structural Division* 11: 2245–2270.

FRP Composites in Civil Engineering – CICE 2004 – Seracino (ed)

Shear strengthening of beams with composite materials

G. Monti, F. Santinelli & M.A. Liotta
Dipartimento di Ingegneria Strutturale e Geotecnica, Università di Roma La Sapienza, Italy

ABSTRACT: Design equations for shear strengthening with fibre reinforced polymers (FRP) of reinforced concrete beams are presented as derived from an experimental/analytical study. The proposed equations allow to compute the FRP strengthening contribution to the shear capacity at the ultimate limit state, in dependence on the chosen strengthening configuration. The FRP contribution is then added to those of concrete and steel, adequately weighed. These equations contain closed-form analytical expressions of the effective strength of the FRP sheet/strips crossing the shear cracks, as function of both the adopted strengthening configuration and some basic geometric and mechanical parameters. The equations' accuracy has been verified through correlation studies with experimental results obtained from the literature and from laboratory tests on 13 purposely under-designed real-scale beam specimens, strengthened with different FRP configurations.

1 INTRODUCTION

The development of practical and reliable design equations for shear strengthening of reinforced concrete elements with FRP composite materials is still hindered by significant uncertainties related to three aspects still not perfectly understood. The first regards the shear resisting mechanism that develops when FRP strips/sheets are side bonded, rather than U-jacketed or wrapped, to the element; in this case, a different mechanism than the Moersch truss activates, that is, a "crack-bridging" mechanism, similar in nature to those of aggregate interlock, dowel effect and concrete tooth. The second aspect regards the evaluation of the contribution of the FRP transverse strengthening to the shear capacity; as opposed to the case of steel transverse reinforcement, which is always considered as yielded, FRP is instead subjected to a variable tensile stress along the crack profile, which is usually expressed as an effective stress. The third aspect regards the evaluation of the relative contributions to the shear capacity of concrete, steel and FRP at ultimate; it is not guaranteed that both concrete and stirrups can exploit their maximum strength when in the presence of FRP strengthening.

These aspects are the object of the present work, where they are treated from both the experimental and the analytical standpoint.

2 EXPERIMENTAL TESTS

Experimental tests were carried out in the laboratory of the Department of Structural Engineering and Geotechnics of the University of Rome "La Sapienza" on 13 beam specimens purposely designed as under-reinforced in shear.

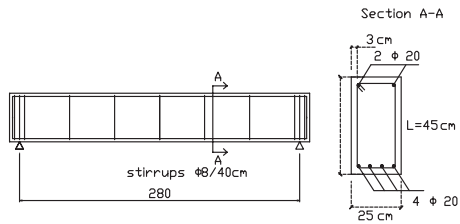

Figure 1. Reference specimen dimensions.

2.1 *Geometry and materials*

The beam specimens were made with concrete with mean compressive cubic strength $R_{cm} = 13.3$ MPa and FeB44k steel bars with mean yield strength $f_{ym} = 500$ MPa. The geometric dimensions of the beams were (Figure 1): span 3.0 m, cross-section width 250 mm and depth 450 mm. The longitudinal reinforcement was made of $4\phi20$ bottom and of $2\phi20$ top, while shear stirrups $\phi8/400$ mm were used. In view of the external strengthening application the bottom corners of the beam were rounded with 30 mm radius.

2.2 *Strengthening typology*

Thirteen reinforced concrete beams were prepared: two of them were bare concrete beams, without external strengthening, 11 were strengthened in shear

Table 1. Typology and nomenclature of beams.

STRENGTHENING APPLICATION	STRENGTHENING TYPE	FIBRES ANGLE	NAME	STRENGTHENING CONFIGURATION
	UNSTRENGTH-ENED	-	REF1	
		-	REF2	
SIDE BONDING	STRIPS	90°	SS90	
		45°	SS45	
		60°, 45°, 30°	SSVA	
	SHEETS	90°	SF90	
U-JACKETING	STRIPS	90°	US90	
		60°	US60	
		60°, 45°, 30°	USVA	
		60°, 45°, 30°	USVA+	
		45°	US45+	
		90°	US90 (2)	
	SHEETS	90°	UF90	

with different configurations: Side-Bonding (S) and U-Jacketing (U). Complete wrapping (W) was not considered due to its difficulty of practical application in real retrofit cases (due to the necessity of drilling the slab). Configurations with strips (S) and with sheets (F) were tested. Strips were oriented with different angles β with respect to the beam axis: 90° (vertical fibres), 60°, 45° or applied with variable inclination along the axis: from the midspan to the end 30°, 45° and 60°. Sheets were applied with fibres in the vertical direction. All strips/sheets were in a single layer of CFRP, having thickness 0.22 mm and elastic modulus $E_f = 390$ GPa.

The nomenclature used for each typology was (Table 1):

- The first letter denotes either side bonding (S) or U-jacketing (U),
- The second letter denotes either strips (S) or fabrics (F),
- The two following numbers denote the angle of inclination (in degrees) of the fibres with respect to the beam axis (45, 60, 90); in case of variable inclination, they are replaced by "VA",
- The final "+" symbol denotes a horizontal strip covering the U-jacketed strips at the bottom edge,
- The unstrengthened reference beams are named "REF".

Figure 2. Representative picture of a test.

2.3 *Test scheme*

The beams were loaded with a 3-point bending scheme. The span was 2.80 m. In Figure 2 a representative picture of a test is shown.

The tests were carried out under displacement control in order to follow the beam response also on the descending branch of the load–deflection curve, pushing the observation to a very advanced cracking state, far beyond the conventional ultimate limit state, until either stirrup rupture or hooks opening or FRP debonding, was observed.

2.4 *Tests description and results*

REF1: Reference specimen, unstrengthened. Formation of the first cracks at 100 kN load. Progressive

opening and formation of further cracks until failure. The failure was reached due to rupture of the second stirrup, at 550 mm from the left beam end, at 210 kN.

REF2: Reference specimen, unstrengthened. Formation of the first cracks at 110 kN load. Failure reached due to rupture of the third stirrup, at 900 mm from the left beam end, at 187 kN.

SS90: Beam with S-strengthening, with CFRP strips 150 mm wide at $\beta = 90°$, with 300 mm spacing. The first cracks were observed at the load of 120–130 kN. The beam failure was reached at 200 kN. The reinforcement seemed to strengthen the beam very little, because the principal crack crossed the strips close to their end.

SS45: Beam with S-strengthening, with CFRP strips 150 mm wide at $\beta = 45°$, with 300 mm spacing, measured along the beam axis. The first cracks were observed at the load of 120/130 kN. At 170 kN the strip at right of midspan started to debond at the bottom. The beam failure was reached at 202 kN for complete delamination of the lower part of the second and third strip at the left of the beam.

SSVA: Beam with S-strengthening, with CFRP strips 150 mm wide with variable inclination (30°–45°–60°) and with spacing as in Figure 3. At 90 kN of load the first flexural cracks were noted. Around 140 kN debonding of the third strip from left of the

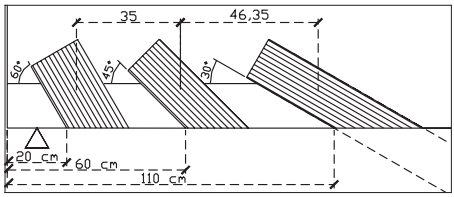

Figure 3. Configuration of SSVA strengthening.

beam started. Beam failure at 210 kN due to failure with complete debonding from the top of the 30°-strip.

SF90: Beam with S-strengthening, with CFRP sheets at $\beta = 90°$. At 208 kN debonding occurs at the beam midspan. At 213 kN first shear cracks observed. At 225 kN beam failure with rupture of the stirrup at 900 mm from the beam end.

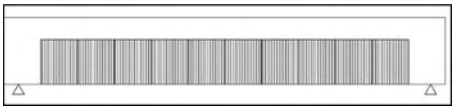

US90: Beam with U-strengthening, with CFRP strips 150 mm wide at $\beta = 90°$, with 300 mm spacing. Failure was due to the rupture of the third stirrup, after debonding of the second strip from left occurred. The failure load of 190 kN was close to the unstrengthened beam because the strips were not activated.

US60: Beam with U-strengthening, with CFRP strips 150 mm wide at $\beta = 45°$, with 300 mm spacing, measured orthogonally to the strips. Formation of the first shear cracks at 135 kN. The third strip from left started to debond from the top at 165 kN. Debonding also started from the bottom at 199 kN, probably because of a crack at the beam soffit. Specimen failure at 222 kN, apparently without stirrup rupture.

USVA: Beam with U-strengthening, with CFRP strips 150 mm wide with variable inclination (30°–45°–60°) as in SSVA. Vertical flexural cracks at midspan around 100 kN of load. Slightly inclined cracks at midspan around 110 kN. Formation of shear

Table 2. Maximum applied force for different strengthening schemes.

NAME	STRENGTHENING SCHEME	MAX APPLIED FORCE
REF1		210
REF2		187
SS90		200
SS45		202
SSVA		210
SF90		225
US90		190
US60		222
USVA		240
USV+		270
US45+		252
US90 (2)		179
UF90		250

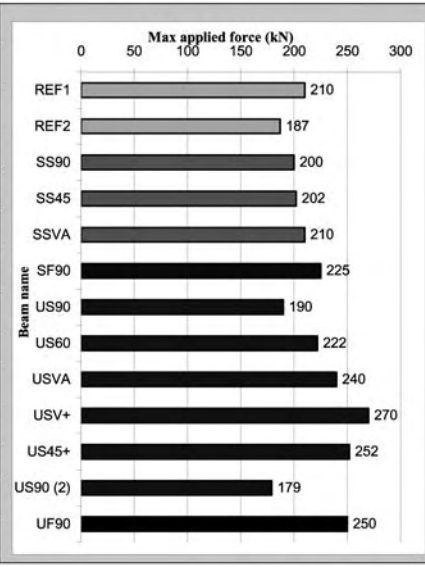

cracks located between the strips at 30° and 45°. Specimen failure at 240 kN for debonding from the top of the 30° strip.

USV+: Beam with U-strengthening, with CFRP strips 150 mm wide with variable inclination (30°–45°–60°) as in USVA with a further bottom collaboration strip on the beam sides. Shear cracks around 170 kN. Debonding of the mid-span strip at the beam bottom. Specimen failure at 270 kN without stirrup rupture.

US45+: Beam with U-strengthening, with CFRP strips 150 mm wide at $\beta = 45°$, with 300 mm spacing, measured along the beam axis. At 100 kN first flexural cracks were observed. At 167 kN first shear cracks were observed. At 223 kN debonding of the second strip from left started. At 232 kN debonding of the second strip from left started. Beam failure at 251 kN with complete debonding of the second strip.

US90(2): Beam with U-strengthening, with CFRP strips 150 mm wide at $\beta = 90°$, with 300 mm spacing. At 90 kN first flexural cracks were observed. At 127 kN first shear cracks were observed. At 135 kN the third strip from left started to debond. At 166 kN debonding of the second strip from left. Failure at 179 kN, accompanied by opening of the stirrups hooks.

UF90: Beam with U-strengthening, with CFRP sheets at $\beta = 90°$. First crack at 178 kN. Debonding starts at 206 kN. At 215 kN reinforcement buckling at the beam top, probably due to the upper concrete compression. Fabric failure around 250 kN and specimen failure at 260 kN with stirrups rupture.

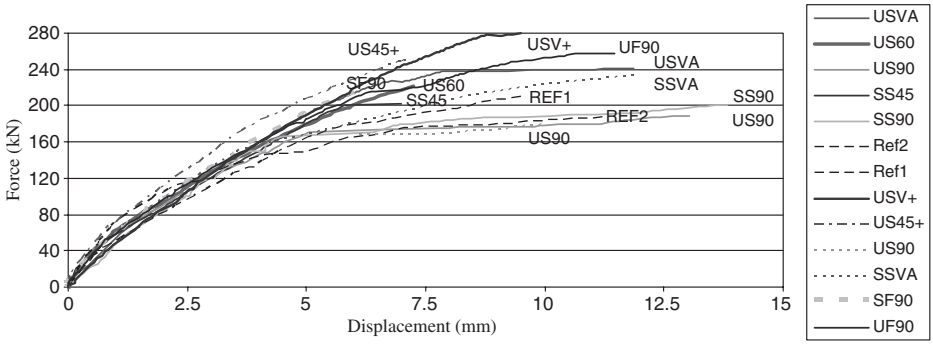

Figure 4. Comparative force–displacement diagrams for different strengthening schemes.

2.5 *Comments to the test results*

Tests have shown a load capacity increase in all the strengthened beams. Both Side-bonded and U-Jacketed strengthening configurations with 90° strips were inefficient with the adopted spacing because the cracks passed in between the strips. The strengthening effectiveness was sensibly increased with lower angles, in that cracks most likely crossed the inclined strips. Side-bonding configurations have shown low efficiency because the strips/sheets started to debond at the beam bottom as the first cracks occurred. Sheets configurations showed satisfactory results, but not the best in terms of efficiency of the quantity of material used: under this standpoint, configurations with inclined strips worked better. Configurations with the bottom collaboration strip gave the best results in terms of shear capacity increase (+35%). In Table 2 a test comparison chart is shown in terms of maximum force, and in Figure 4 in terms of force–displacement curves.

3 DESIGN EQUATIONS FOR FRP SHEAR STRENGTHENING

This section tries to provide a coherent analytical framework to describe the behaviour of RC elements FRP-strengthened in shear, following previous efforts made by other authors (Täljsten 1997, Triantafillou 1998, Khalifa et al. 1998, Chen & Teng 2003a, 2003b). The developed theory aims at producing closed-form mechanics-based expressions to describe the FRP stress distribution $\sigma_{f,cr}(x)$ along a shear crack (as qualitatively sketched in Figure 5), as opposed to regression-based formulas (Triantafillou & Antonopoulos 2000). Once this is correctly defined, the FRP resultant across the crack can be computed and the FRP contribution to the resisting shear be found. The analytical developments arrive at defining three predictive equations for: Side-Bonding (S), U-jacketing (U) and Wrapping (W).

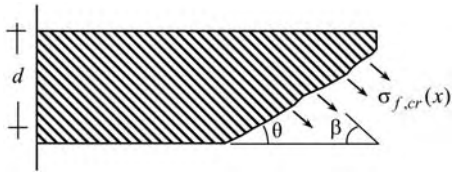

Figure 5. Stress distribution along an FRP sheet crossing a shear crack.

These equations define the maximum effective strength (or strain) of the FRP strip/sheet along the crack in analytical terms, as opposed to previous different approaches, based on regression analyses of experimental data. The obtained expression of the strength is given in terms of readily available geometrical and mechanical quantities of both the FRP strengthening and the RC beam and is then used to compute the FRP contribution to the overall shear strength, together with that of concrete and transverse reinforcement.

In the developments presented hereafter, the following hypotheses are made:

- Shear cracks are evenly spaced along the beam axis, and spacing is that due to flexure,
- At the ULS the cracks depth is equal to the internal lever arm $z = 0.9d$,
- The resisting shear mechanism is based on the Moersch truss, with compression struts, and shear cracks inclined with angle θ,
- In the case of side-bonding (S), because the Moersch truss cannot form as the tensile diagonal strut is missing, a different resisting mechanism of "crack-bridging" is considered to develop.

The notation used is shown in Figure 6.

In order to fully characterize the physical phenomenon, the following aspects must be analytically defined: the failure criterion of an FRP strip/sheet bonded to concrete, the stress-slip constitutive law, the compatibility equations (*i.e.*, the crack opening), and the boundary conditions (*i.e.*, the available bonded lengths on both sides of the crack depending of the different configurations).

3.1 *FRP strengthening design*

Through analytical developments (presented in detail in Monti et al. 2004) the effective strength in the case of Side-bonding (S), U-jacketing (U) and Wrapping (W) is defined.

In all cases the debonding strength must be defined (Monti et al. 2003):

$$f_{fdd} = \frac{1}{\gamma_{fd}} \sqrt{0.6 \frac{E_f f_{ctm} k_b}{t_f}} \quad \text{(units: N, mm)} \tag{1}$$

and the effective bond length (beyond which there is no increase of f_{fdd}):

$$L_e = \gamma_{fd} \cdot 0.6 \sqrt{\frac{E_f \cdot t_f}{\sqrt{f_{ctm} \cdot k_b}}} \quad \text{(units: N, mm)} \tag{2}$$

where E_f = FRP elastic modulus, t_f = strip/sheet thickness, $f_{ctm} = 0.27 \cdot R_{ck}^{2/3}$ = concrete mean tensile strength (with R_{ck} = concrete characteristic cubic strength). γ_{fd} is a partial coefficient for debonding.

In both previous equations k_b is:

$$k_b = \begin{cases} \sqrt{\dfrac{1.5}{1 + w_f / 100 \text{ mm}}} & \text{for sheets} \\ \sqrt{\dfrac{1.5 \cdot (2 - w_f / s_f)}{1 + w_f / 100 \text{ mm}}} & \text{for strips} \end{cases} \tag{3}$$

where, for strips: w_f = width measured orthogonally to the fibres, s_f = spacing measured orthogonally to β; for sheets $w_f = \min(0.9d, h_w) \cdot \sin(\theta + \beta) / \sin\theta$, with d = beam effective depth, h_w = beam web depth, β = angle of strip/sheet to the beam axis, θ = crack angle to the beam axis. In case $\theta = 45°$ and $\beta = 90°$, for sheets one has: $w_f = \min(0.9d, h_w)$.

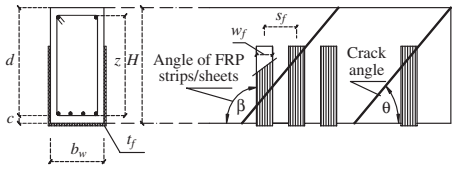

Figure 6. Geometry notation.

The effective strength of the FRP shear strengthening crossing the shear crack is then found by means of the theory presented in Monti et al. 2004.

In the case of side-bonding:

$$f_{fed,S} = f_{fdd} \cdot \frac{z_{rid,eq}}{0.9d} \cdot \left(1 - 0.6 \sqrt{\frac{L_{eq}}{z_{rid,eq}}}\right)^2 \tag{4}$$

where:

$$z_{rid,eq} = z_{rid} + L_{eq} \tag{5}$$

$$z_{rid} = 0.9d - L_e \cdot \sin\beta \tag{6}$$

$$L_{eq} = \frac{u_1}{\varepsilon_{fdd}} \cdot \sin\beta \tag{7}$$

where: $u_1 = k_b/3$, and it is observed that: z_{rid} is equal to the internal lever arm minus the bottom part with insufficient bond length, L_{eq} is the bond length projected vertically that would be necessary if the fabric strain $\varepsilon_{fdd} = f_{fdd}/E_f$ were uniform.

In the case of U-jacketing:

$$f_{fed,U} = f_{fdd} \cdot \left[1 - \frac{1}{3} \frac{L_e \sin\beta}{0.9d}\right] \tag{8}$$

In the case of wrapping:

$$f_{fed,W} = f_{fdd} \left[1 - \frac{1}{6} \frac{L_e \sin\beta}{0.9d}\right] + \\ + \frac{1}{2} \left(\eta_R \cdot f_{fd} - f_{fdd}\right) \cdot \left[1 - \frac{L_e \sin\beta}{0.9d}\right] \tag{9}$$

where f_{fd} is the design strength of FRP, and:

$$\eta_R = 0.2 + 1.6 \frac{R}{b_w} \qquad 0 \le \frac{R}{b_w} \le 0.5 \tag{10}$$

is a coefficient (Campione & Miraglia 2003) depending on the rounding radius R with respect to the beam web width b_w.

Note that, when using mechanical devices for blocking the free extremities of the U-jackets, in case one can experimentally ensure their good performance, the FRP contribution to shear strength can be computed from (9) as well.

3.2 *Shear capacity*

In case the reinforcement type is W or U, the Moersch resisting mechanism can be activated and the shear carried by FRP is expressed as:

$$V_{Rd,f} = 0.9\,d \cdot f_{fed} \cdot 2 \cdot t_f \cdot \left(\frac{w_f}{s_f}\right)^2 \cdot (\cot\theta + \cot\beta) \cdot \sin\beta \quad (11)$$

while for side-bonding (S) the FRP role is that of "bridging" the shear crack, so that:

$$V_{Rd,f} = 0.9\,d \cdot f_{fed} \cdot 2 \cdot t_f \cdot \frac{\sin\beta}{\sin\theta} \cdot \frac{w_f}{s_f} \quad (12)$$

with d = beam effective depth, f_{fed} = design effective strength of the FRP shear strengthening, given either by (4) for S-bonding or by (8) for U-jacketing or from (9) for Wrapping, t_f = thickness of FRP strip/sheet (on one side only), θ = crack angle.

Assuming cracks inclined of an angle $\theta = 45°$ with respect to the vertical and strips/sheets vertically aligned at $\beta = 90°$, the two previous equations become:

$$V_{Rd,f} = 0.9\,d \cdot f_{fed} \cdot 2 \cdot t_f \cdot \left(\frac{w_f}{s_f}\right)^2 \quad (13)$$

$$V_{Rd,f} = 0.9\,d \cdot f_{fed} \cdot 2\sqrt{2} \cdot t_f \cdot \frac{w_f}{s_f} \quad (14)$$

The shear verification should be performed by comparing the design acting shear with the shear capacity, given by:

$$V_{Rd} = \min\left\{\phi V_{Rd,ct} + V_{Rd,s} + V_{Rd,f}, V_{Rd,\max}\right\} \quad (15)$$

where $V_{Rd,ct}$ is the concrete contribution, given by (Italian Code (M.LL.PP. 1996) and EC2 (CEN 1991), respectively):

$$V_{Rd,ct} = 0.60 \cdot f_{ctd} \cdot b_w \cdot d \quad (16)$$

$$V_{Rd,ct} = \frac{0.18}{\gamma_c} b_w \cdot d \cdot \min\left\{1 + \sqrt{\frac{200\text{ mm}}{d}}, 2\right\} \cdot \sqrt[3]{100 \cdot \min\{0.02, \rho_{sl}\} \cdot f_{ck}} \quad (17)$$

and $V_{Rd,s}$ is the steel contribution, given by:

$$V_{Rd,s} = 0.9\,d \cdot f_{yd} \frac{n_{st} \cdot A_{st}}{s_{st}} (\cot\theta + \cot\beta_{st}) \sin\beta_{st} \quad (18)$$

where $f_{ctd} = 0.7 f_{ctm}/\gamma_c$ = concrete tensile strength, $\gamma_c = 1.5$ = concrete partial coefficient, b_w = web section width, ρ_{sl} = longitudinal geometric ratio, f_{ck} = concrete characteristic cylindrical strength, f_{yd} = design steel yield strength, n_{st} = transverse reinforcement arm number, A_{st}, s_{st} = area (one arm) and spacing of traverse reinforcement, and β_{st} = stirrups angle.

In (15), $V_{Rd,\max}$ is the strength of the concrete strut, given by (Italian Code and EC2, respectively):

$$V_{Rd,\max} = 0.30 \cdot f_{cd} \cdot b_w \cdot d \quad (19)$$

$$V_{Rd,\max} = 0.9\,d \cdot b_w \cdot \nu \cdot f_{cd} \cdot (\cot\theta + \cot\beta_{st})/(1 + \cot^2\theta) \quad (20)$$

with $\nu = 0.6[1 - (f_{ck}/250)]$ (in MPa).

Finally, in (15) $\phi = 1$ in the absence of FRP strengthening, while $\phi = 0.5$ in the presence of FRP strengthening, meaning that, when FRP reaches debonding, the concrete exploits only a fraction of its maximum strength.

Note that in EC2 the contribution of concrete to the resisting shear capacity (17) is not considered ($\phi = 0$), even in the absence of strengthening.

4 VALIDATION OF DESIGN EQUATIONS

The results obtained with the above presented equations applied to the case of the specimen beams tested in the lab are shown in Figure 7 and Figure 8. As the EC2 formulae systematically tend to overestimate the concrete contribution to the shear capacity, the Italian Code formula was only used.

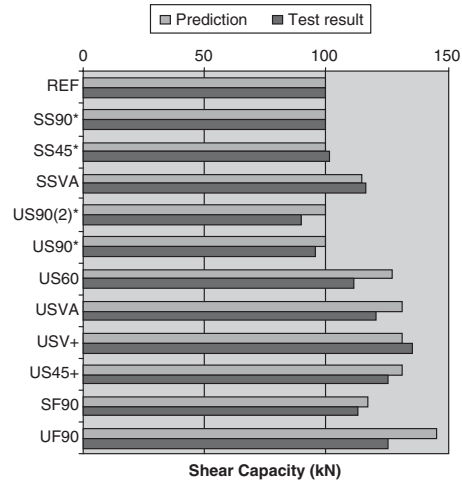

Figure 7. Prediction–test results comparison.

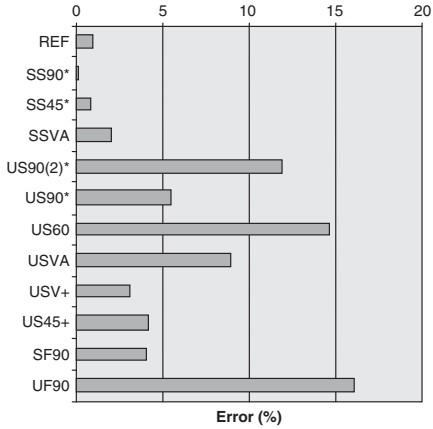

Figure 8. Prediction–test results error.

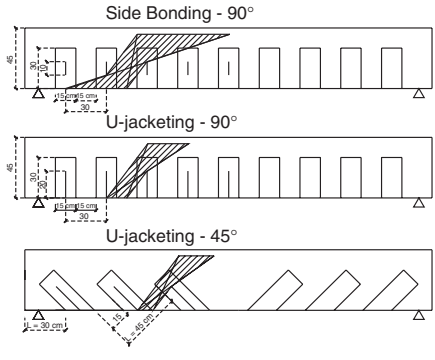

Figure 9. Crack formation fields with inadequate strip spacing.

Partial coefficients were set to 1 for the prediction of experimental results, and mean values of material properties were considered. The shear capacity of the reference beam was computed as the mean between the two tested unstrengthened specimens. Note that in the specimen SS90, SS45, and US90, the contribution of FRP strengthening was not considered, as it was recognised that the diagonal shear cracks did not cross the strips.

It can be observed that the mean error on the predictions where FRP strengthening was active is 7%, with a peak of 15% for the configurations US60 and UF90. Such an error is considered acceptable. Further tests are being carried out to validate the proposed equations on different reinforcing schemes.

A further information emerged from the tests regarding the limitation of the strips spacing, which should be sufficiently small to prevent cracks from not crossing at least one strip. From Figure 9 it can be seen that, thinking to "condense" the strips in an "equivalent stirrup" on the strip axis, having the same height of the strip minus the effective bond length L_e from both ends in case of S-bonding and only from one end in case of U-Jacketing, shear cracks can develop that do not cross excessively spaced strips in the effective zone. In fact, in case of S-bonding there is a field (represented in shaded region in Figure 9) where cracks can freely pass in between strips, without crossing them.

From the figure, it can be seen that such field reduces from S-bonding to U-jacketing and increasing the fibres angle. This suggests to adopt the following limitations: in strengthening measures made with strips, these should have a width w_f, measured orthogonally to the fibres direction β, not lower than 50 mm and not larger than 250 mm, and a spacing, measured orthogonally to the fibres direction β, $s_f \leq \min[0.5d, 3w_f, w_f + 200\,\text{mm}]$.

5 CONCLUSIONS

The above presented equations for the shear strengthening of beams with composite materials (FRP) showed good correlation with purposely carried out experimental tests. The equations matched the shear capacity increase with a more than acceptable error. The work carried out went through some of the unsolved aspects in previous analytical treatments of the phenomenon. In particular, closed-form analytical expressions for the effective stress of the FRP strips/sheets crossing the shear crack were found, which could be implemented in finite element formulations for FRP-strengthened elements (Monti & Barbato 2003). It has also been clarified in which cases relation (11), based on the formation of Moersch truss can be used (for W and U configurations), and when instead relation (12), considering only the bridging of cracks, must be used (for S configurations). In both cases it has been verified that the concrete cannot exploit its full contribution to the shear resistance of the beam, so that, in this first phase before more accurate evaluations will be made, it is considered with a weight $\phi = 0.5$ in equation (15). Finally, it is worth mentioning that the approach presented here has been incorporated in the recently issued Italian Instructions for strengthening RC structures with FRP (CNR 2004).

ACKNOWLEDGEMENTS

The authors wish to thank the Interbau srl company of Milan, Italy, for the specimens preparation and the CFRP application.

REFERENCES

Campione, G., & Miraglia, N. (2003). "Strength and strain capacities of concrete compression members reinforced with FRP". *Cement & Concrete Comp.*, Elsevier, 25, 31–41.

CEN (1991). Eurocode 2: Design of concrete structures – Part 1-1: General rules and rules for buildings. ENV 1992-1-1, Comité Européen de Normalisation, Brussels, Belgium.

CNR (2004). Instructions for Design, Execution and Control of Structural Strengthening by means of Fibre Reinforced Composites. Reinforced concrete and masonry structures. CNR-DT 200/2004, July (in Italian).

Chen, J.F., & Teng, J.G. (2003a). "Shear capacity of FRP-strengthened RC beams: FRP debonding". *Construction and Building Materials*, Vol. 17, No. 1, Feb., 27–41.

Chen, J.F., & Teng, J.G. (2003b). "Shear capacity of FRP-strengthened RC beams: FRP rupture". *J. of Structural Engineering*, ASCE, Vol. 129, No. 5, May, 615–625.

M.LL.PP. (1996). Norme tecniche per il calcolo, l'esecuzione ed il collaudo delle strutture in cemento armato, normale e precompresso e per le strutture metalliche. *DM 9.1.1996, Ministry of Public Works*, Roma, Italy.

Khalifa, A., Gold, W.J., Nanni, A., & Aziz, A.M.I. (1998). Contribution of externally bonded FRP to shear capacity of rc flexural members. *ASCE J. of Composites for Construction*, **2**(4), 195–202.

Monti, G., Renzelli, M., & Luciani, P. (2003). FRP-Adhesion to Uncracked and Cracked Concrete Zones. *FRPRCS-6*, Singapore.

Monti, G., & Barbato, M. (2003). Fiber-Section FE of FRP-Strengthened RC Beam in Flexure, Shear and Confinement. *FRPRCS-6*, Singapore.

Monti, G., Santinelli, F., & Liotta, M.A. (2004). Mechanics of shear FRP-strengthening of RC beams. *ECCM 11*, Rhodes, Greece.

Täljsten, B. (1997). Strengthening of concrete structures for shear with bonded CFRP-fabrics. *Recent advances in bridge engineering*. Eds. U. Meier and R. Betti, Dübendorf, 57–64.

Triantafillou, T.C. (1998). Shear strengthening of reinforced concrete beams using epoxy-bonded FRP composites. *ACI Structural Journal*, **95**(2), March–April, 107–115.

Triantafillou, T.C. & Antonopoulos, C.P. (2000). Design of concrete flexural members strengthened in shear with FRP. *ASCE J. of Composites for Construction*, **4**(4), 198–205.

FRP Composites in Civil Engineering – CICE 2004 – Seracino (ed)

Numerical predictions for the ultimate torque capacity of FRP strengthened reinforced concrete beams

M. Ameli & H.R. Ronagh
School of Engineering, The University of Queensland, Brisbane, Australia

M.A. Bradford & B. Uy
School of Civil & Environmental Engineering, The University of New South Wales, Sydney, Australia

ABSTRACT: Despite years of theoretical work on the ultimate torque capacity of reinforced concrete beams, the current models do not produce convincingly accurate results. The prediction of ultimate torque by the current code recommendations is rather conservative and there is no model that accurately predicts the ultimate torque capacity of strengthened beams. The study here is looking at these models in a comparative scenario measuring them against ANSYS and experimental results. For the numerical solution with ANSYS, a three-dimensional model is created in which the concrete is modeled by an eight-node solid element specifically designed for concrete material. This element is capable of handling plasticity, cracking in tension and crushing in compression and requires an iterative solution. Experimental benchmarking contains the results of a series of experiments on plain and FRP strengthened reinforced concrete beams subjected to torsion for which the torque-twist curves are extracted. The results of the study provide a good insight to the weaknesses and strengths of the torsion models and the accuracy of the numerical model.

1 INTRODUCTION

Ultimate torque capacity of reinforced concrete beams is usually predicted in the codes of practice by the Truss model either in its original form with a constant 45° crack angle or with a variable angle, neither of which are capable of predicting the ultimate torque adequately. There are a variety of other models available which have not found their roots in the codes as yet, including the Compression Field Theory and the Softened Truss Model, which offers higher accuracies in comparison to the Truss Model.

When it comes to predicting the ultimate capacity of FRP strengthened beams, the methods are even scarcer with methods used by Taljsten (1998) and Zhang et al. (2001) known to the authors. In a situation like this, recourse to numerical solutions is an obvious choice. Due to the highly nonlinear behaviour of concrete, however, this may prove not to be so easy. Concrete behaves differently in different stress fields; in tension, in compression or when confined. Steel rebars also move from elastic behaviour to plastic when yielding occurs.

In the current paper, an attempt is made to perform a nonlinear numerical analysis by ANSYS 7.1 in order to evaluate the ultimate torque capacity of plain and FRP strengthened reinforced concrete beams. The results are then benchmarked against some experimental results. In addition, a number of theoretical methods are also evaluated as to their effectiveness in predicting the torsional capacity of plain unstrengthened beams.

2 CHOSEN BENCHMARK

Numerical models are to be benchmarked against experiments. The experiments, which are reported in detail in a separate paper presented at this conference were performed at the University of Queensland.

The tests were on twelve rectangular reinforced concrete beams with dimensions 150 mm × 350 mm × 1900 mm that were cast in two batches of 6 beams each. The first batch used for CFRP (carbon fiber reinforced polymer) and the second for GFRP (glass fiber reinforced polymer) strengthening. Test span of beams was measured at 1600 mm. Longitudinal reinforcement bars were four N16 bars, one at each corner of the cross-section and stirrups were R6 with a spacing of 80 mm. Rebars and stirrups yield strength were 500 MPa and 250 MPa respectively. A concrete cover of 25 mm was considered in all beams. The compressive 28-day strength of concrete batches were measured at 39 MPa and 36 MPa for the first and second batches respectively. One beam of each batch, called

Table 1. Properties of fibres.

Type of fibre	Thickness (mm)	Modulus of elasticity (MPa)	Tensile strength (MPa)
CF130	0.165	240,000	3900
EG900	0.154	73,000	3400

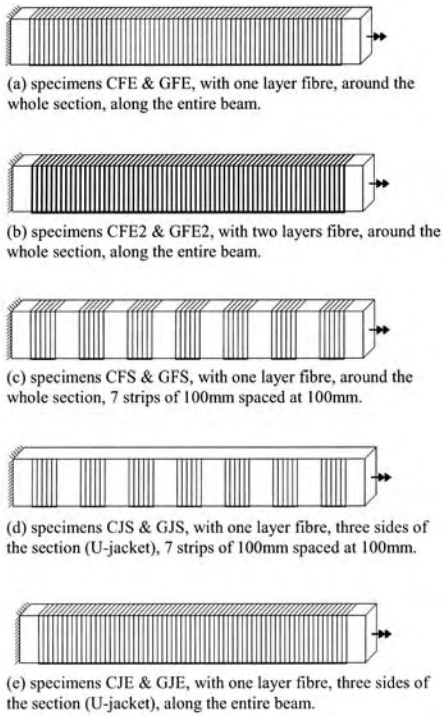

Figure 1. Schematic configuration of strengthened beams.

RC and RG, were tested without FRP as reference beams. The rest of the beams were then strengthened by carbon fibre (Mbrace CF130) and glass fibre (Mbrace EG900) in different configurations. Properties of the used fibres are shown in Table 1. Different configurations of FRPs were tried as shown schematically in Figure 1. These configurations were used for both CFRP and GFRP. In all rehabilitated beams, CFRP and GFRP sheets were employed vertically with respect to the longitudinal beam axis. Beams CFE and GFE were wrapped by one layer of CFRP and GFRP sheets respectively, around the perimeter of the section and along the entire beam.

Figure 2. The testing rig.

Beams CFE2 and GFE2 were the same but with two layers of FRP. Beams CJE and GJE were wrapped by CFRP and GFRP sheets respectively, on two sides and the bottom of the cross section as a U-jacket, along the entire beam. Beams CJS and GJS were wrapped by CFRP and GFRP sheets respectively, in U-jacket by 100 mm wide FRP strips at 100 mm spacing along the member. Beams CFS and GFS were wrapped by 100 mm strips of CFRP and GFRP sheets respectively, around the perimeter of the section at 100 mm spacing. The test set-up is shown in Figure 2. All beams were tested under pure torsion. The load was applied by two hydraulic jacks of 100 kN capacity. Jacks were located at 500 mm distances from the centre of the beam. Torsion was introduced by applying equal amounts of force to the free end of the beam through the jacks, one operating in tension and the other in compression. Jacks were connected to the loading frame through pinned joints. The end of the specimen was fixed in the rigid frame. It was fixed against twist while was free to have other displacements. The twist angle of the free end, (point of applying torque) was measured by a clinometer. It was also calculated from the displacements of the end cross-section measured by linear variable displacement transformers (LVDT).

3 FINITE ELEMENTS

ANSYS models concrete with its element SOLID 65. SOLID65 is a cubic element with eight nodes at each of it's corners each having three translational degrees of freedom (Fig. 3). SOLID65 is capable of cracking in tension, crushing in compression, and plastic deformation. It also comes with a rebar capability in which rebars can be defined within the element itself.

Reinforcement bars can also be modelled separately from SOLID65 using an element called LINK8. This element is a 3-dimentional spar and a uniaxial

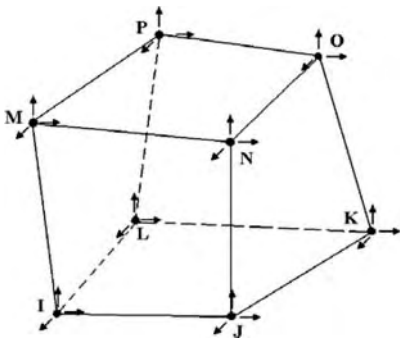

Figure 3. Element SOLID 65 and its degrees of freedom.

Figure 4. Element LINK8.

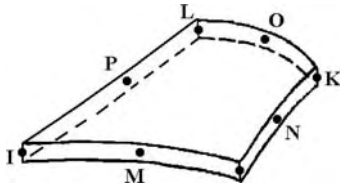

Figure 5. Element SHELL99.

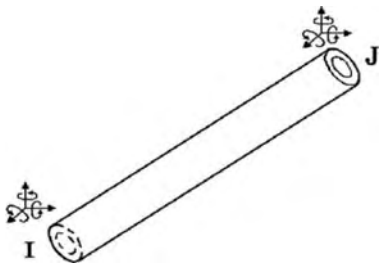

Figure 6. Element PIPE16.

tension-compression element with three degrees of freedom at each node (Fig. 4).

FRP wraps can be modeled in ANSYS by the element SHELL99. This element has six degrees of freedom at each node and is defined by eight nodes,

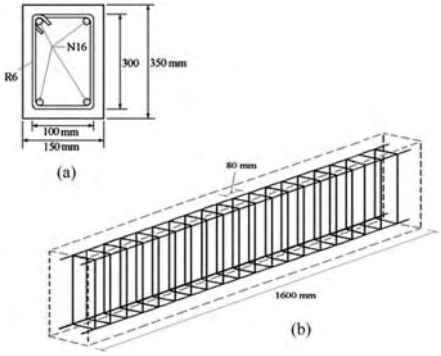

Figure 7. Assumed: (a) cross section, (b) layout of the reinforcements.

average or corner layer thicknesses, layer material direction angles, and orthotropic material properties (Fig. 5). The element SHELL99 may be used for layered applications of a structural shell model. Element SHELL99 does not have nonlinear capabilities and that fits well with FRPs which exhibit a linear elastic behaviour to failure.

One problem familiar to everyone using ANSYS for concrete is that ANSYS may not converge to a nonlinear solution when a crack extends completely through a concrete element. This is because the element will have no stiffness and its nodal displacements will not be restrained.

In order to overcome this problem, a series of dummy elements can be created at the free end of the beam model. These dummy elements could be used to constrain the concrete elements that are fully cracked. A usual dummy element is PIPE16. This element is a uniaxial element with tension-compression, torsion, and bending capabilities. Element PIPE 16 has six degrees of freedom at end node (Fig. 6).

4 NUMERICAL MODELS

Layout of the reinforcement and the cross-section used for modeling is shown in Figure 7. The dimensions are exactly the same as dimensions used in the experimental study. This layout is then meshed using the aforementioned elements. A couple of meshes are shown in Figure 8. The rest are very similar to these. Beams are named similar to their experimental counterpart with the only difference being that they now have an A in front of the abbreviation used. For example, beam RG, which was the plain beam used as a reference for all GFRP wrapped beams is now called ARG, emphasizing that it is the “A”nalytical RG.

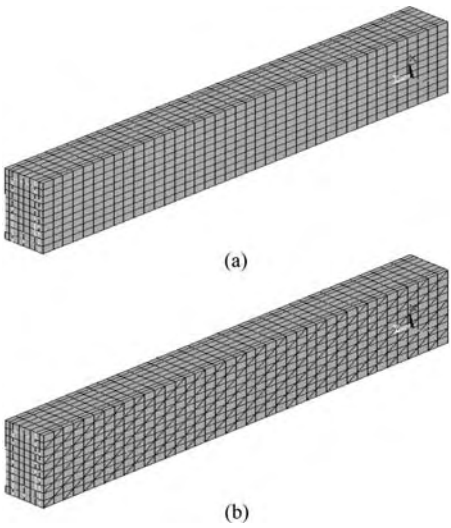

Figure 8. Mesh for beams, (a) ARC (ARG), (b) ACJE (AGJE).

Table 2. Characteristics of FRP materials used in numerical solution, MPa.

	Modulus of elasticity		Ultimate tensile strength	
	CFRP	GFRP	CFRP	GFRP
One layer	33,000	10,220	536	476
Two layers	37,714	11,242	613	524

In the modelling, one may note that the thickness of wraps is much higher than the thickness of the fibres. In the experimental studies, it was found that the thicknesses for one and two layers of CFRP were 1.2 mm and 2.1 mm respectively while for GFRP, they amounted to 1.1 mm and 2 mm. In using these thicknesses for SHELL99, a correction to the Elastic modulus and the material's strength needs to be implemented. Here, the use is made of the results of FIB (2001), which shows that a reduction based on the thickness ratio (measured thickness/fibre thickness) is sufficient as the saturant strength and stiffness are very small comparing to the fibres. The modulus and strengths used are shown in Table 2.

5 RESULTS AND DISCUSSION

The ultimate torsional strength of the beams ARC & ARG obtained from numerical solution are compared with some available theoretical models, codes of practice, and experiments in Table 3.

Table 3. Ultimate torque of the plain reinforced concrete specimens obtained from different sources, kNm.

	Beam ARC/RC	Beam ARG/RG
Numerical solution	14.78	14.09
Compression field theory	16.36	15.79
Softened truss model	16.08	15.43
AS3600	3.46	3.46
ACI	4.88	4.88
EC2	5.12	5.12
Experiment	15	14.8

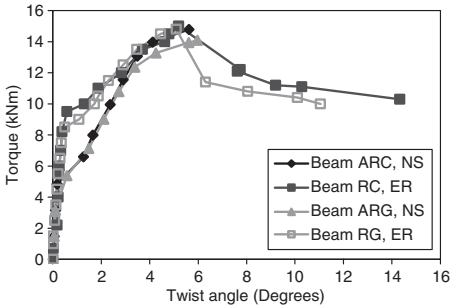

Figure 9. $T-\varphi$ relation for beams ARC/RC & ARG/RG obtained from numerical solution (NS) and experimental results (ER).

As is seen in Table 3, the results of the numerical solution, theoretical models and experiments are close together, whereas codes' predictions are conservative. It should be mentioned that according to the codes, the ultimate strength is independent of the concrete strength. The other analytical methods, like the Compression Field Theory of Mitchell & Collins (1974) or the Softened Truss Model of Hsu (1988), however, recognize its dependence.

Numerical solutions by ANSYS are reasonably close and a lower bound to the experimental observations. The $T-\varphi$ graphs shown in Figure 9 contain the ANSYS solution and the experimental results. As is seen, ANSYS is incapable of predicting the post-peak response, and its pre-peak response deviates from the experiments a little too soon. It however catches up reasonably well reaching the crest at almost the same twist as the experiments and around the same torque.

The deviation of ANSYS torques from the experimental torques occur at around 5 kNm which is close to the cracking torque according to AS3600 (2001)

Table 4. Maximum strain values at the ultimate torque.

	Strain, %			
	Beam ARC		Beam ARG	
Model	Rebar	Stirrup	Rebar	Stirrup
Comp. field theory	0.160	1.47	0.150	1.33
Softened truss model	0.146	0.270	0.138	0.26
ANSYS	0.184	0.126	0.185	0.126

(5.9 kNm and 5.7 kNm for beams RC and RG respectively). As is seen, the experimental results show considerable stiffness after cracking by continuing the almost linear elastic path while ANSYS torques diverge to the higher twists. This may be explained by the fact that in real experiments, shear stresses can still be transmitted across the cracks while in numerical analysis, as soon as the concrete cracks, the loads will be transferred to the reinforcement bars. The analytical solution becomes closer to the experimental results again as the level of shear transfer becomes lower due to crack gaps becoming larger and as such transferring lower stresses.

One important issue to evaluate the torsional strength of reinforced concrete beams is to define the strain in rebars and stirrups at the ultimate torque. In most codes of practice such as AS3600, the procedure for evaluating the ultimate toque is based on yielding of both longitudinal rebars and stirrups (Warner et al. 1998). This is not the case in Compression Field Theory and Softened Truss Model in which the strains in the bars at the ultimate torques can be calculated. These strains are compared here with ANSYS strains obtained at the ultimate. Yield strain of the stirrups and rebars are 0.125% and 0.25% respectively. The two analytical models of Table 4 then show that stirrups are at yield while rebars remain elastic even at the ultimate. This is confirmed by ANSYS. The strains predicted by ANSYS, however, are very different from analytical methods particularly for stirrups while the discrepancy between the two analytical methods is also very large.

Figures 10 & 11 also show the $T - \varphi$ relations of the FRP strengthened beams obtained from numerical solution and experiments. According to these figures, in all cases, the observed trend in the experiments at the early stages of the curves is the same as the numerical results. However, at the ultimate torques, the slope of the numerical curves are slightly smoother than the experiments. As is seen the only curves obtained from numerical solution that are above the experimental result are for beams ACJE and ACJS, but the differences, are not substantial. $T - \varphi$ relations for beams ACJS & CJS (AGJS & GJS) have the best agreement at ultimate strength compared to the others. These beams

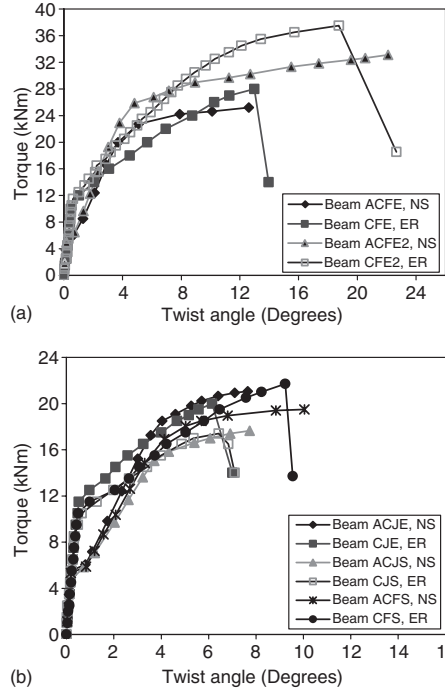

Figure 10. $T - \varphi$ relation for, (a) beams ACFE/CFE & ACFE2/CFE2, (b) beams ACJE/CJE, ACJS/CJS & ACFS/CFS, obtained from numerical solution (NS) and experimental results (ER).

have the least quantity of FRP materials in U-jacket strips.

Focusing on the ultimate torsional strength and the corresponding twist angle for all beams can give interesting results. These values for all strengthened beams obtained from numerical solution and the experiments are presented in Tables 5 & 6. According to Table 5, in all GFRP strengthened beams the ultimate torque obtained from numerical results, T_{un}, are less than the experimental values, T_{ue}. This pattern can also be seen in most of the CFRP strengthened beams.

In terms of the twist angle at ultimate torques (Table 6), values obtained from numerical solution, φ_{un}, are greater than the experimental results in all cases, φ_{ue}. The differences however are small and the numerical predictions seem acceptable.

6 CONCLUSION

In this investigation, ANSYS software was utilised in the nonlinear torsion analysis of plain and torsionally

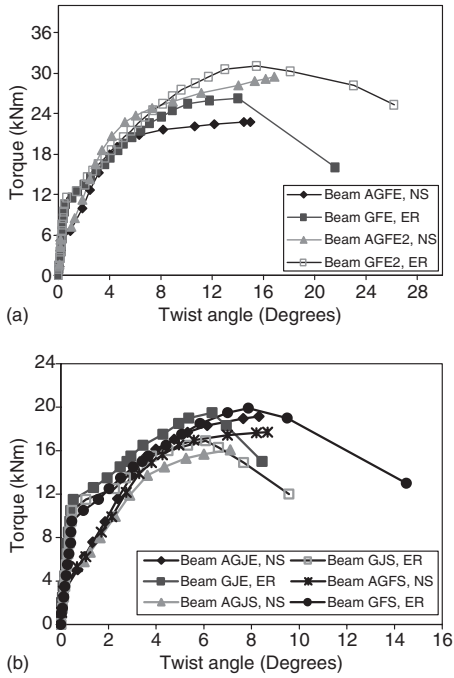

Figure 11. $T - \varphi$ relation for, (a) beams AGFE/GFE & AGFE2/GFE2, (b) beams AGJE/GJE, AGJS/GJS, & AGFS/GFS, obtained from numerical solution (NS) and experimental results (ER).

Table 5. Ultimate torques obtained from experiments (T_{ue}) and numerical solution (T_{un}), kNm.

Beam	T_{ue}	T_{un}	Beam	T_{ue}	T_{un}
CFE/ACFE	28	25.8	GFE/AGFE	26.3	22.71
CFE2/ ACFE2	36.5	33.12	GFE2/ AGFE2	31.1	29.37
CJE/ACJE	20	21.07	GJE/AGJE	19.5	19.15
CFS/ACFS	21.7	19.49	GFS/AGFS	19.9	17.7
CJS/ACJS	17.4	17.64	GJS/AGJS	16.9	16.07

strengthened reinforced concrete beams. The results of ANSYS were then compared with the theoretical models and experiments. The results show that:

a) For plain reinforced concrete beams:
The predictions of ANSYS, Compression Filed Theory and Softened Truss Model were close to the experimental results while the codes' predictions were vastly different. In addition, it shows that the code assumption about the yielding of both rebars and stirrups at failure may not be valid. Numerical analysis showed that rebars do not yield behaving elastically to failure.

b) For FRP strengthened beams:
Numerical results as well as experiments showed that, generally using FRP materials caused an increase in the ultimate torsional strength and the corresponding angle of twist. In most cases, however, the ultimate torques obtained from the numerical analysis were lower than the experimental values while the angle of twist at ultimate torque obtained from numerical analysis was greater than the experiments.

Table 6. Angles of twist at ultimate torques obtained from experiments (φ_{ue}) and numerical solution (φ_{un}), in degrees.

Beam	φ_{ue}	φ_{un}	Beam	φ_{ue}	φ_{un}
CFE/ACFE	12.98	14.16	GFE/AGFE	14.02	15.01
CFE2/ ACFE2	18.7	22.09	GFE2/ AGFE2	15.53	16.91
CJE/ACJE	6.2	7.65	GJE/AGJE	6.35	8.31
CFS/ACFS	9.23	10.04	GFS/AGFS	7.78	8.68
CJS/ACJS	6.4	7.73	GJS/AGJS	6.08	7.11

Numerical $T - \varphi$ curves had a good agreement with the experiments for loading up to the cracking torque. They then diverged from experimental values showing higher twists at similar loads until finally joined back in at torques close to the ultimate.

ACKNOWLEDGMENT

This study is supported by an ARC discovery grant, which is hereby gratefully acknowledged. The tests were carried out at the Structural Laboratories of the University of Queensland. Ahmad Khuzaini Sani and Cher Ng, undergraduate students of UQ were involved in the preparation and testing of the beams as part of their undergraduate theses. All Workshop and Structures lab staff should be thanked in particular Robert Stephan, Shane Walker and Paul Pezzopane who made every effort to make the job a pleasant experience.

REFERENCES

ACI 318-02. 2002. Building code requirements for structural concrete (318-02) and commentary (318R-02). American Concrete Institute, Farmington Hills, Michigan.

AS 3600. 2001. Australian Standard for Concrete Structures. Collins, M.P., Mitchell, D., Adebar, P., and Vecchio, F.J. 1996. A General Shear Design Method. *ACI Structural Journal*, Jan.-Feb 1996: 36–45.

European Standard. 2002. *Design of concrete structures*.

FIB (CIB-FIP), 2001. *Externally bonded FRP reinforcement for RC structures*. Stuttgart: Spring-Digital-Druck.

Hsu TC. 1988. Softened truss model theory for shear and torsion. *ACI Structural Journal*, 85(6): 624–635.

Mitchell, D. & Collins, M.P. 1974. Diagonal compression field theory a rational model for structural concrete in pure torsion. *ACI Journal proceeding*. 71(8): 396–408.

Rausch, E. 1929. *Berechnung des eisenbetons gegen vedrehung (torsion) und abscheren*. Berlin: Julius Springer- Verlag.

Warner, R.F., Rangan, B.V., Hall, A.S. & Faulkes, K.A. 1998. *Concretes structures*. Longman.

Zhang, J.W., Lu, Z.T. & Zhu, H. 2001. Experimental study on the behaviour of RC torsional members externally bonded with CFRP. *Proceedings of the CICE*, Hong Kong, I: 713–722, 2001.

FRP Composites in Civil Engineering – CICE 2004 – Seracino (ed)
© 2005 Taylor & Francis Group, London, ISBN 90 5809 638 6

Experimental investigations on FRP strengthening of beams in torsion

M. Ameli, H.R. Ronagh & P.F. Dux
School of Engineering, The University of Queensland, Brisbane, Australia

ABSTRACT: Many studies have been performed in recent years on strengthening beams in shear and bending using FRP wraps and laminates. Torsional strengthening however has not attracted as much attention. The current study on the torsional strengthening of reinforced concrete beams was performed on 12 reinforced concrete beams wrapped by carbon and glass fibres. Several different configurations were used for the FRPs and the torque-twist angle paths of the beams were recorded to failure. The failure modes, ductility levels and the increase in the torsional strengths are presented in this paper. Moreover, advantages and disadvantages of the two types of fibres used are compared and discussed. Attempts are also made to predict the torsional strength of the strengthened beams by modifying the available torsion models of plain RC beams.

1 INTRODUCTION

In the 90s, steel plating was considered as an effective strengthening technique for reinforced concrete structures. Gradually, however as FRPs became available at lower prices, a tendency toward using them as a substitute to steel plating is gaining momentum. The advantages are obvious, as these materials are lightweight, do not corrode, are easy to apply, and are fatigue resistant.

Despite them gaining popularity, there is yet more research to be done to fully understand their behaviour in particular applications. One can find a significant amount of research output in the literature in areas of shear and flexural strengthening but some areas like torsional strengthening and the effect of FRPs on beam-column joints are yet to be fully addressed.

In the area of torsional strengthening to which the current study is dedicated, there seems to be a shortage of convincing experimental and theoretical studies. The current paper presents the results of some experiments performed on torsionally strengthened beams, critically evaluates the accuracy of available analytical methods and elaborates on the influence of important parameters that can affect the behaviour of strengthened members. Two main strengthening materials, carbon and glass fibre are studied and compared as to their effects.

2 PREVIOUS STUDIES

As mentioned earlier, most of the investigations on externally bonded FRP sheets were focused on flexural and shear strengthening of reinforced concrete members, reference to which can be found in Khalifa et al. (1998) and Triantafillou (1997). Unlike that, there are not as many investigations on torsional strengthening of beams. The few that exist are explained in the following.

Ghobarah (2001) performed some torsional tests on reinforced concrete beams that were strengthened with CFRP (carbon fibre reinforced polymer) and GFRP (glass fibre reinforced polymer) in different configurations. His results showed that the strength increased considerably as well as the ductility levels. The findings were to some extent different from the findings of Ronagh & Dux (2003) who obtained lower angles of twist at failure in contrast to the levels reported by Ghobarah (2001). Panchacharam & Belarbi (2002) also performed some tests on FRP strengthened beams subjected to torsion. They used GFRP in different configuration to strengthen beams. They also performed an analytical study and calculated the ultimate torque using a parameter called "effective FRP strain" (FIB 2001). This parameter has basically emerged from the studies of Taljsten (1998). He suggests that the failure modes in shear and torsion for the strengthened beams are more or less the same and design equation for torsional contribution of fully wrapped beams can be obtained by:

$$T_{u,f} = \frac{2bht_f b_b \varepsilon_{fe} E_f}{s_f} (\cot\alpha + \cot\beta) \sin\beta \qquad (1)$$

where α is the angle of torsion crack and β is the orientation of fibres, both measured from the member's longitudinal axis, ε_{fe} is the effective strain in the fibres, b and h are the cross sectional dimensions of the beam, b_f is the minimum width of the cross section over the

Table 1. Properties of fibres.

Type of fibre	Thickness (mm)	Modulus of elasticity (MPa)	Tensile strength (MPa)
CF130	0.165	240,000	3900
EG900	0.154	73,000	3400

effective depth of the cross section, E_f is the modulus of elasticity of FRP, and s_f is the spacing of the FRP strips.

These very few studies are on beams that are different in dimension, levels of reinforcement, method of loading, etc, and as such do not lead to comfortable conclusions about the behaviour. A program of research has therefore been set up at the University of Queensland to address these issues and to arrive at more convincing conclusions.

3 EXPERIMENTAL PROGRAM

3.1 *Test beams*

Twelve rectangular reinforced concrete beams with dimensions 150 mm × 350 mm × 1900 mm were cast in two batches of 6 beams each. The first batch used CFRP and the second GFRP strengthening. Test span of beams was measured at 1600 mm. Longitudinal reinforcement bars were four N16 bars, one at each corner of the cross-section and stirrups were R6 with a spacing of 80 mm. Rebar and stirrup yield strength were 500 MPa and 250 MPa respectively. Concrete cover was 25 mm. The compressive 28-day strength of concrete batches was 39 MPa and 36 MPa for the first and second batches respectively. One beam of each batch, called RC and RG, were tested without FRP as reference beams. The remained were then strengthened by carbon fibre (Mbrace CF130) and glass fibre (Mbrace EG900) in different configurations. Properties of the used fibres are shown in Table 1. Different configurations of FRPs were tried as shown schematically in Figure 1. These configurations were used for both CFRP and GFRP. In all strengthened beams, CFRP and GFRP were employed vertically with respect to the longitudinal beam axis. Beams CFE and GFE were wrapped by one layer of CFRP and GFRP respectively, around the perimeter of the section and along the entire beam. Beams CFE2 and GFE2 were the same but with two layers of FRP. Beams CJE and GJE were wrapped by CFRP and GFRP respectively, on two sides and the bottom of the cross section as a U-jacket, along the entire beam. Beams CJS and GJS were wrapped by CFRP and GFRP sheets respectively, in U-jacket by 100 mm wide FRP strips at 100 mm spacing along the member.

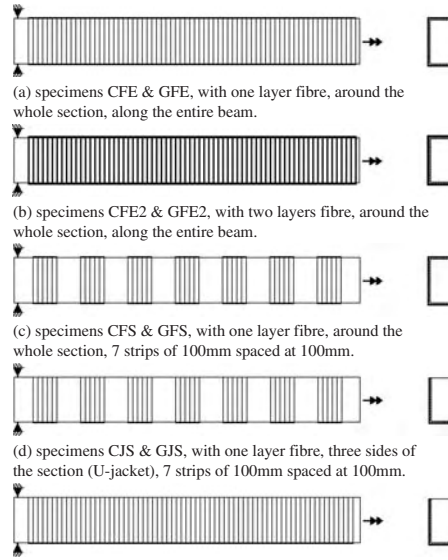

(a) specimens CFE & GFE, with one layer fibre, around the whole section, along the entire beam.

(b) specimens CFE2 & GFE2, with two layers fibre, around the whole section, along the entire beam.

(c) specimens CFS & GFS, with one layer fibre, around the whole section, 7 strips of 100mm spaced at 100mm.

(d) specimens CJS & GJS, with one layer fibre, three sides of the section (U-jacket), 7 strips of 100mm spaced at 100mm.

(e) specimens CJE & GJE, with one layer fibre, three sides of the section (U-jacket), along the entire beam.

Figure 1. Schematic configuration of strengthened beams.

Figure 2. Test set-up.

Beams CFS and GFS were wrapped by 100 mm strips of CFRP and GFRP respectively, around the perimeter of the section at 100 mm spacing.

3.2 *Test set-up*

The test set-up is shown in Figure 2. All beams were tested under pure torsion. The load was applied by two hydraulic jacks of 100 kN capacity. Jacks were located 500 mm from the centre of the beam. Torsion was introduced by applying equal amounts of force to the free end of the beam through the jacks, one operating

Table 2. Ultimate torque values (T_u) obtained form experiments and the corresponding percentage increase.

Beam	T_u	% increase*	Beam	T_u	% increase**
RC	15	–	RG	14.8	–
CFE	28	87	GFE	26.3	78
CFE2	36.5	143	GFE2	31.1	110
CJE	20	33	GJE	19.5	32
CFS	21.7	45	GFS	19.9	34
CJS	17.4	16	GJS	16.9	14

* Compared to the beam RC.
** Compared to the beam RG.

in tension and the other in compression. Jacks were connected to the loading frame through pinned joints. The other end of the specimen was fixed against twist while free to have other displacements. The twist angle of the free end (point of applying torque) was measured by a clinometer.

It was also calculated from the displacements of the end cross-section measured by linear variable displacement transformers (LVDT).

4 RESULTS AND DISCUSSION

Table 2 shows the results of tests in terms of ultimate torque for all 12 specimens. This table also indicates the percentage increase in the ultimate torque in comparison with the ultimate torque of the specimens without FRP sheets (beams RC and RG). It can be seen that using FRP sheets around the perimeter of the section and along the entire length caused a significant increase of the ultimate torque. The maximum increases, 143% and 110%, are for beams CFE2 and GFE2, which had two layers of CFRP and two layers of GFRP respectively. Beams strengthened with full strips (CFS and GFS) and U-jackets strips (CJS and GJS) do not exhibit the same amount of increase as those fully wrapped. It is also seen that the amount of increase in the ultimate torque for beam CJE (that is a U-jacket CFRP along the entire beam) is between those of CJS and CFS. This is also true for GJE whose ultimate resistance is between those of GJS and GFS. These experimental results can be compared to available methods. AS3600 predicts the ultimate torsional strength of a beam, T_{us}, as

$$T_{us} = f_{sy.f}\,(A_{sw}/s)\,2\,A_t\cot\theta_t \qquad (2)$$

where $f_{sy,f}$ and A_{sw} are the yield strength and the cross-sectional area of the stirrups respectively, A_t is the area enclosed by longitudinal bars at the corners, and θ_t is the crack angle of concrete that can be taken as 45°. The code method is basically a truss model (Rausch 1929). Using this, the torsional capacity of the reference beams RC and RG can be calculated as 4.9 kNm.

Another analytical method that can be used is the Compression Field Theory of Collins & Mitchell (1980). Unlike the Truss model, which is an equilibrium based model, the Compression Field Theory incorporates both equilibrium and compatibility conditions. CFT assumes that concrete carries no tension after cracking and the inclination angle of the diagonal compressive stress is the same as the inclination angle of the principal compressive strain. This assumption provides a means to relate the angle of cracks and the strains together as:

$$\tan^2\theta = \frac{\varepsilon_l - \varepsilon_{ds}}{\varepsilon_t + \varepsilon_{ds}} \qquad (3)$$

where θ is the angle of cracks measured from the horizontal beam axis, ε_l and ε_t are the strains in the longitudinal and transverse steel bars, respectively, and ε_{ds} is the maximum diagonal compressive strain in concrete. The analysis procedure by this method involves trial and error on the value of ε_{ds} until both equilibrium and compatibility conditions are satisfied. Compression Field Theory predicts values of 16.4 kNm and 15.8 kNm for the ultimate torque of beams RC and RG respectively.

Considering that the experimental results for the ultimate torque of beams RC and RG were 15 kNm and 14.8 kNm respectively, it is seen that the Compression Field Theory predicts the behaviour better than that of the AS3600.

There are not many analytical methods for calculating the ultimate torque of FRP strengthened beams. Panchacharam & Belarbi (2002) have proposed a method using Equation 1. They basically calculate the contribution of FRP sheets to the overall strength and then add it to the ultimate torque of unwrapped beams derived using other models (usually truss models). In that, they require a value for the effective strain and a method to distinguish the U-jacket wrapping from full wrapping. For the effective strain, they make use of FIB (2001) model and for U-jacket wrapping, they multiply the calculated torque by 0.5.

The results of analytical predictions for tested beams compared with the experimental results are shown in Table 3. Overall, it can be seen that the analytical ultimate torques predicted based on Compression Field Theory are much closer to the experimental results with the exception of specimen CFE2. Furthermore, the experimental ultimate torques T1, for the first seven beams of Table 3, are between the two analytical ultimate torques, T3 and T4, while being higher than the analytical torques for the last five beams. The percentage of differences between analytical torques (calculated in Table 3) and experimental results are presented in Table 4. As for Compression Field Theory, the closest prediction in CFRP wrapped beams is for CJE

Table 3. Analytical and experimental results compared, kNm.

Test-beam	Experimental torque, T1	Contribution of FRP, T2*	Analytical torque, T3**	Analytical torque, T4***
RC	15.0	–	4.9	16.4
CFE	28.0	17.1	22.0	33.5
CFE2	36.5	27.4	32.3	43.9
CJE	20.0	4.6	9.5	21.0
CFS	21.7	10.4	15.3	27.0
CJS	17.4	3.4	8.3	19.8
RG	14.8	–	4.9	15.8
GFE	26.3	7.1	12.0	22.9
GFE2	31.1	14.2	19.1	30.0
GJE	19.5	2.6	7.5	18.4
GFS	19.9	3.5	8.4	19.3
GJS	16.9	1.8	6.7	17.6

* According to the Equation 1 and FIB (2001).
** $T1 + T_{us}$ (according to AS3600, 2001).
*** $T1 + T_{us}$ (according to Compression Field Theory).

Table 4. Percentage of differences between analytical torques and experimental results.

Test specimens	Percentage of difference between T3 & T1*	Percentage of difference between T4 & T1*
RC	67	9
CFE	22	19
CFE2	11	20
CJE	53	5
CFS	29	24
CJS	52	14
RG	67	7
GFE	54	14
GFE2	39	4
GJE	62	6
GFS	58	3
GJS	61	4

* Calculated in Table 3.

with only 5% difference while others exhibit discrepancies of between 14% and 24%. Predictions using AS3600 are very different with an average error of 33%. The results of analytical method based on Compression Field Theory for GFRP strengthened beams were even more successful in predicting the ultimate torsional capacity. As is shown in Table 3, the percentage errors for three out of the five tests performed are less than 5%.

One problem associated with the current approach in calculating the strength of FRP wrapped beams is that the method is based on FRP rupture. FRP rupture is not the only failure mechanism as the beams may also collapse under diagonal crushing of concrete or debonding of the FRP sheets. In the current

(a) debonding (beam CJE).

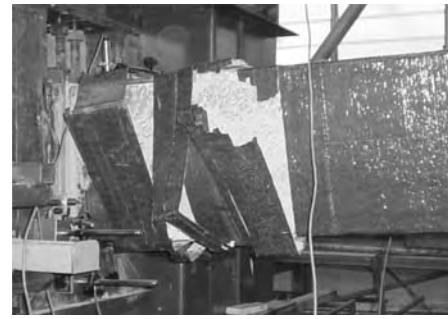

(b) fibre failure (beam CFE).

Figure 3. Different failure modes observed.

Figure 4. Crack angles (beam RC).

experiments, it was seen that all fully wrapped beams failed under FRP rupture while those with a shape of a U-jacket failed through debonding (Figure 3). It seems that multiplying a universal factor of 0.5 would not reasonably define the change in the failure mechanism.

Another observation relates to the angle of cracks. Major crack angles in the unwrapped beams were

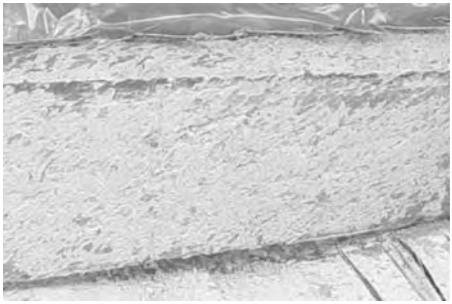

Figure 5. Cracks on beam GFE.

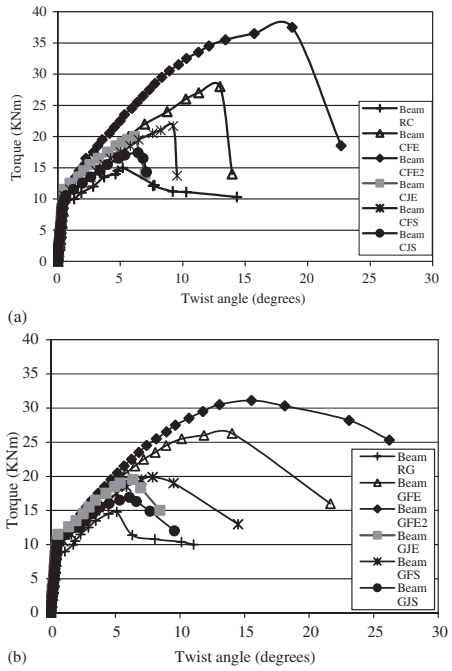

Figure 6. Torque–twist angle curves of all beams, (a) CFRP used for strengthening, (b) GFRP used for strengthening.

usually around 45° while minor crack angles varied between 43° and 47° (Figure 4). The range for crack angles in the FRP strengthened beams was wider, varying between 40° and 49°. It was also observed that for fully wrapped beams, the cracks were more evenly distributed along the entire length, unlike the unwrapped beams for which a local helical pattern of cracks was the usual observation. In addition, there existed a

(a)

(b)

Figure 7. Beam GFE2 with more than 26° twist angle.

significant number of micro cracks in the fully wrapped beams. It seems that FRPs help distributing the stresses to the whole body of concrete and as such the increase in the strength is partially due to the better utilisation of the concrete strength on top of what FRP provides itself. Figure 5 shows the crack pattern for beam GFE2 (full wrap using two layers of GFRP) after the wraps were peeled off. The cracks are small and so close that they may not be quite visible. Basically wherever the color is whiter a crack has been formed. It may be interesting to compare this crack pattern with that in Figure 4 for unwrapped beam RC.

Twist angles at the free end of the beams were also measured during the tests. Values of the twist angles versus load are presented in Figures 6a and 6b for CFRP and GFRP wrapped beams respectively. As is seen in Figure 6, the ultimate torque (the maximum torque at the crest of the curve) is higher in all FRP wrapped beams in comparison to the unstrengthened ones. The increase in the ultimate load is highest when beams are fully wrapped and is more with carbon fibres. This increase can be more than 100% in some cases while is not significant when strips or

U-jackets are used. As expected, the worst performing strengthening method is using strips in a U-jacket form.

In addition, it can be seen that after using FRP sheets, the twist angle at the ultimate torque for all beams has increased. For instance, this angle for beam RC (reference beam for CFRP strengthened beams) was about 5.2° and for beam CFE2, which had two layers of fully wrapped CFRP along the entire beam, an amazing 18.7°. The corresponding value for beam GFE2 was 15.53° compared to 5.1° for the reference beam RG. The behaviour clearly indicates a considerable increase in the energy absorbing capacity of the FRP wrapped beams and the ductility.

One interesting point that was observed during the experiments and is exhibited in the graphs is that all beams wrapped with CFRP fail fairly suddenly after reaching their peak torque while their post peak response is very much short-lived. The GFRP wrapped beams, however, have a longer post peak response and develop larger twist angles. This is interesting that, as the failure of both CFRP and GFRP wrapped beams have a similar initiation of failure at the peak. The GFRP ones, can then accommodate the failure in a much more relaxed way deforming significantly as they unload. The 26° twist of the GFE2 beam at failure is remarkable as is shown in Figure 7.

5 CONCLUSION

The results of this research can be summarised as follows.

Firstly, wrapping beams with CFRP and GFRP sheets can increase the torsional strength of reinforced concrete beams considerably. For different configurations increases from 16% to 143% were experienced for CFRP and from 14% to 110% for GFRP wrapping. The highest amount of increase belonged to full wrapping with two layers and the least amount to U-jacket wrapping in strips. Regarding to the little influence of U-jacket wrapping in strips on torsional strengthening, this method is not recommended to use.

The two analytical methods employed to evaluate the torsional contribution of reinforced concrete beams showed very different results. The results from Compression Field Theory, however, were much closer to the experimental results than those from the AS3600 method, which is based on a truss model. Two main failure types were observed. The first type of failure initiated by debonding of the FRP sheets from the surface of the concrete which in some cases included a portion of the concrete and occurred in U-jacket type wrapping. The second type of failure initiated by the rupture of FRP and occurred in fully wrapped cases either being in strips or around the whole perimeter of the cross-section.

ACKNOWLEDGMENT

This study was performed using Mbrace glass and carbon fibers. MBT supported the project by selling the materials to us at the cost price. Ahmad Khuzaini Sani and Cher Ng, undergraduate students of UQ were involved in the preparation and testing of the beams as part of their undergraduate theses. All Workshop and Structures lab staff should be thanked in particular Robert Stephan, Shane Walker and Paul Pezzopane who helped the students during setup and testing.

REFERENCES

AS 3600. 2001. Australian Standard for Concrete Structures. Collins MP & Mitchell D. Shear and torsion design of prestressed and non-prestressed concrete beams. *PCI Journal*, Sep.–Oct. 1980: 32–100.

FIB (CEB-FIB). 2001. Externally bonded FRP reinforcement for RC structures. *Technical report, Bulletin No. 14*.

Ghobarah, A. 2001. FRP composites in civil engineering. *Proceedings of the CICE*, Hong Kong, I: 701–712, 2001.

Khalifa A, Gold WJ, Nanni A & Aziz AMI. 1998. Contribution of Externally bonded FRP to shear capacity of flexural Members. *ASCE Journal of composites for construction*, 2(4): 195–203.

Panchacharam S & Belarbi A. 2002. Torsion behaviour of reinforced concrete beams strengthened with FRP composites. *First FIB Congress*, Osaka, Japan, October.

Rausch E. 1929. *Berechnung des eisenbetons gegen vedrehung (torsion) und abscheren*. Berlin: Julius Springer-Verlag.

Ronagh HR & Dux PF. 2003. Full-Scale torsion testing of concrete beams strengthened with CFRP, *Proceedings of the first international conference on the performance of construction materials in the New Millennium*, February 2003. Cairo: 735–743.

Taljsten B. 1998. *Forstarkning av betongkonstruktioner med stalplat och avancerade kompositmaerial utsatta for vridning*, Forskningsrapport, Lulea tekniska universitet, Avdelningen for konstruktionsteknik, Institutionen for Vagoch vattenbyggnad, 1998:01, ISSN 1402-1528 (In Swedish).

Triantafillou TC. 1997. Shear strengthening of concrete members. Using composites. Non-Metallic (FRP) Reinforcement for concrete structures. *Proceedings of the third symposium*, Japan, 1: 523–530, 1997.

FRP Composites in Civil Engineering – CICE 2004 – Seracino (ed)
© 2005 Taylor & Francis Group, London, ISBN 90 5809 638 6

Photographic strain monitoring for civil engineering

A. Carolin & T. Olofsson
Luleå University of Technology, Luleå, Sweden

B. Täljsten
Luleå University of Technology, Luleå, Sweden and Skanska Teknik AB, Solna, Sweden

ABSTRACT: The need for concrete strengthening and retrofitting is well known and a great amount of research is going on in this field. When strengthening for increased shear capacity the use of CFRP plate bonding has shown to be a competitive method both regarding structural performance and economical aspects. For design of shear strengthening, it has been found that the widely used truss model has limitations that are not completely investigated. The truss model needs to be modified to consider the linear elastic behaviour and anisotropic nature of the composite, especially when shear-moment interaction is studied. To evaluate the strain field in the shear span electrical strain gauges are normally used. However, this implies that the strain measurements are undertaken in discrete points and that it is very difficult to obtain a clear picture of the overall strain distribution in the shear span. In this paper a non-touching strain measurement method that covers a pre-defined area is presented. The method provides strains with high accuracy over a shear span and the measurements are effectively undertaken. Tests have been conducted on 4.5 m long strengthened concrete beams, where the strain measurements have been undertaken on a shear span 1.25 m times 0.5 m. Strains measured by the presented method is compared with strains measured by traditional electrical strain gauges. The presented monitoring method shows promising results and will also be possible to use for measuring of strains for evaluation of shear stresses in the bond line between CFRP composites and concrete.

1 INTRODUCTION

1.1 *Background*

All around the world, there are problems with deterioration and lack of load bearing capacity of many structures around us. These structures are built and used for several different purposes; bridges for transportation, houses for living, and telecom towers for communication just to mention a few. Lack of bearing capacity may be addressed by changed use of a structure, increased traffic flow, or even mistakes during design or construction phases. Deterioration will decrease the load bearing capacity and decreased load bearing capacity may also increase the rate of deterioration. Several structures will probably need to be replaced since they are in such bad condition or they cannot be upgraded to desired performance levels. The value of all built structures is enormous and it will not be possible to erect new structures for all new purposes or situations that will arise. Instead, existing structures must be strengthened or repaired to meet society's demands.

Today, several strengthening methods for improvement of the load bearing capacity exist. One of them, not necessarily always the most suitable one, is strengthening of structures by bonding carbon fibre reinforced polymers to the structure to add stiffness, tensile reinforcement or shear reinforcement, Burgoyne (1999), Carolin (2001) and Meier (1999). This method is very interesting for a huge range of applications and a great amount of research is undertaken in this field not only regarding equations describing behaviour but also experimental tests from small scale to full-scale tests in the field. The high number of already undertaken projects confirms that the method is competitive, both from a practical and economical point of view. Most research has been undertaken on flexural strengthening of concrete members and equations have been derived, equations that most researchers agree upon and now are used in design codes.

Although not the only problem facing structures today, shear deficiencies are becoming more and more prevalent Micelli et al. (2002). Shear strengthening is actualized by more or less the reasons already mentioned but also due to flexural strengthening. When increasing the flexure capacity by strengthening, the structure will be loaded closer to its maximum shear capacity, Täljsten (1994). A structure must have a certain safety margin against shear failure since it

is more dangerous and less predictable than flexural failure, Täljsten (2002).

When it comes to codes for shear strengthening, there still is a discussion on how design shall be taken care of. One suggestion will briefly be presented in this paper to increase the understanding of the problem. Previously research Carolin (2001) have shown that the composite is not uniformly stresses when bonded to the sides of a beam and that this strain field must be further studied to understand the behaviour of a member strengthened in shear. It has been discussed how the strain field actually looks like in shear span of beams simultaneously subjected to shear and bending. The non-uniform strain field is an issue both in service limit state and ultimate limit state. To be able to understand CFRP shear strengthen structures behaviour, theoretical as well as experimental studies are needed. This is also important if the CFRP strengthening method shall reach full acceptance for shear strengthening worldwide.

In this paper a method to measure strain fields with high accuracy over a large area is presented. A limited number of large specimens have been tested and the strain fields in the critical shear spans have been captured. The results from the measurements are a contribution to the derivation of design equations for shear strengthening.

1.2 *Theories for shear strengthening*

One way to express the shear capacity of a concrete beam, V_d, is as in Equation 1 where V_c, V_s and V_f are the contributions from the concrete, steel stirrups and externally bonded CFRP respectively.

$$V_d = V_c + V_s + V_f \tag{1}$$

For this equation the superposition principle is used which can be done up to a certain level of deformation. In design, because of limitations on allowable strain in fibres to prevent rupture and anchorage problems it is probable that the superposition principle is valid. This will not be further discussed in this paper but it is believed that the presented measuring technique can be an effective instrument to solve this uncertainty as well. In combination with Equation 1 the truss model is the most well-known and widely used theory for describing shear behaviour of a concrete member. The modified compression field theory, Vecchio & Collins (1986), is believed by some to be more accurate but it is much more complicated to use. Finite element models may also be used to describe shear behaviour of structures. But they are rather time consuming, considerably dependent of the users knowledge, and not suitable for codes. The truss model has wide acceptance, is easy to use and several researchers are already familiar with the model for predicting the contribution from externally bonded reinforcement. Therefore, the truss model will be shortly described here. Equation 2 is one suggestion on how the contribution from externally bonded fibres can be calculated.

$$V_f = \eta \varepsilon_{cr} E_f t_f r_f z \frac{\cos\theta}{\sin\alpha} \tag{2}$$

where, η, consider non-uniform strain distribution described later on, ε_{cr}, is maximum allowable strain, E_f, module of elasticity of composite, composite thickness, r, considers fibre arrangement (strips or sheets), z, beam height, α, crack inclination, and θ, angle between principal strain and fibre direction. There are several researchers that have suggested different approach and different solutions to express V_f based on truss model. Different derivations will not be repeated here but some can instead be found presented in detail in Triantafillou (1998); Täljsten (2002); Carolin (2003) and Chen & Teng (2003). In addition to obvious aspects such as; geometry; fibre amount; fibre arrangement; different failure modes; mechanical properties of the materials; etc, consideration must also be taken to strain distribution over a shear span. The main reason for this is that CFRP is linear elastic, which implies that different strains will cause different stresses, contradictory to steel that yields and redistribute stresses. Pure shear in a structural member is very unusual; most members are simultaneously subjected to both shear and flexural loading, which must be kept in mind when studying strain distribution.

The issue of non-uniform strain distribution has been known a long time and it has been addressed that a reduction factor is needed Sato et al. (1996). From a small amount of tests an empirically determined reduction factor including bond was identified. Based on a larger number of tests, a similar reduction factor but only considering bond failure was suggested by Triantafillou (1998). There exist several other models based on bond or more correct insufficient bond, Al-Sulaimani et al. (1994) and Maeda et al. (1997). Non-uniform strain distributions have been found in tests by others, Adey et al. (1998) but have not been further analyzed. In empirically based equations for the bearing capacity such as Izumo et al. (1998), a reduction factor is included. However, it is important to isolate the strain distribution in service limit state when a possible bond failure might be far away. A reduction factor, η, must be used if the truss model is used for design. This reduction factor has been analytically derived and to a limited extent verified experimentally, Carolin (2003). In theory, the factor is 0.45–0.67 depending on fibre alignment, fibre arrangement, and shear-moment relation. With a normalized beam height, the strain profile for 45° and 90° fibre alignments with end support loading condition may be found in Figure 1. Observe that a part of the fibres

are subjected to compression when applied in 45°. The normalized strains are integrated over height of the beam and the area is divided with the area for uniform fibre strains. An average fibre utilization, η, is defined where only positive fibre strains are considered. The average fibre utilization expresses the average strain in the fibres over the height compared to the most stressed fibre in the cross-section. To be able to verify the strain distribution it is necessary to measure the strains in the shear span. In previous research, Carolin (2001), this has been done with strain gauges. As will be shown in this paper, strain gauges is not the optimal for monitoring strain fields.

2 METHOD

2.1 *Test beams*

Large-scale tests have been undertaken on 23 rectangular reinforced concrete beams, which all are presented in detail in Carolin (2003). All beams are heavily reinforced in bending to ensure a shear failure. The thickness of the fibres as well as the fibre direction has been varied. Some of the beams were loaded until a shear crack formed and the beams were unloaded before the strengthening was applied.

Some beams have been strengthened with fibres on the sides only and others were wrapped with fibres around the entire beam. Several other parameters were varied as well. However, all beams were finally tested to failure by a deformation controlled loading. In this paper a limited number of the tested beams will be brought up for discussion with respect to strain measurements and strain distribution. These beams have been heavily reinforced with steel stirrups in one shear span to cause failure in the other span and therefore make it possible to focus the measurements on the failing shear span. In Figure 2 the test set up for the undertaken four point bending test and the test beams are shown. The beams have dimensions $4500 \times 500 \times 180$ mm with one shear span of 1250 mm without stirrups. The longitudinal reinforcement consists of twelve 16 mm bars in tension and two 16 mm bars in compression; all with yield strength of 515 MPa. The concrete compressive strength as an average was 55 MPa. For strengthening the unidirectional hand lay-up CFRP system StoBPE Composite S has been used. This system consists of primer, a low-viscosity epoxy resin and fibres with a stiffness of 234 GPa and a strain to failure at 1.5%. For the beams that will be used in the evaluation presented here, fibres have been applied in 45° and 90° direction both wrapped and on the vertical sides only in various combinations, including pre-cracking.

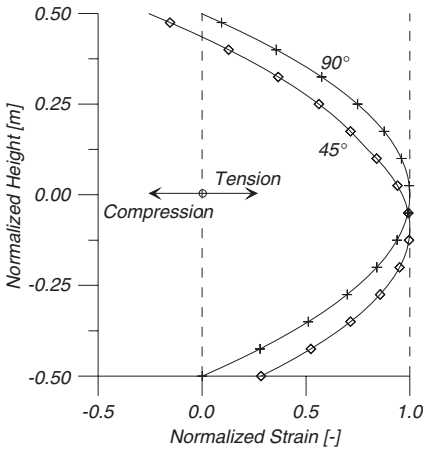

Figure 1. Longitudinal fibre strains over a shear span.

3 STRAIN MEASUREMENTS

3.1 *Photographic strain measurements*

When using photographic measurement the area is photographed before and after loading, i.e. photos are taken at different stages during loading. The photos are analysed with the help of computer software. Parts of pictures are identified and the centre of gravity is

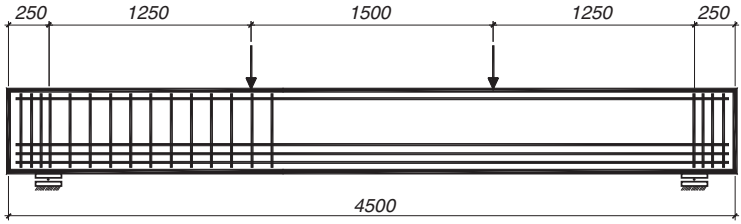

Figure 2. Test beam.

calculated. Difference in strain can be calculated for two stages by comparing the difference in distance between the studied parts. There exist different methods for performing these measurements and they are sometimes presented under different names. In this study has a random pattern and speckle pattern correlation been used and will be described. Another photographic method is the so-called grid-method that will also be described but not further discussed.

3.2 *Speckle pattern correlation*

For the speckle pattern correlation method a random pattern on a surface is used. In this case black and white sand was mixed and bonded to the surface as shown in Figure 3 where one shear span of a test beams is shown. The wires, seen in the back in Figure 3, are connected to ordinary strain gauges placed on the opposite side for later comparison of the results between the two methods. Every 30 kN during loading up to failure, the loading was paused and a photo were taken. For this purpose a professional camera with mid-size (69 × 56 mm) black and white film was used. After processing of the film the positives were scanned with a high quality film scanner, the picture was trimmed so that only the interesting area remained. Every trimmed photo then ended up in black and white containing about 37 Megapixels. A magnified part of the shear span is shown in Figure 4. The picture shows also a schematic division of the pattern into sub-pictures. One of the sub-pictures is shown in Figure 5. This sub-picture is then subjected to a threshold value making dark colours black and light colours white as shown in Figure 6. The centre of gravity for the sub-picture is calculated. The larger sub-picture that is chosen the better the accuracy becomes. On the other hand the centre of gravity is calculated for the whole sub-picture, which then will give the average position for the sub-picture even if there is non uniform strain distribution within it. Because of the large number of pixels within the sub-picture, the accuracy of positioning becomes high. With use of speckle correlation the same sub-picture is found in the second loading condition even if it has deformed, moved or been slightly damaged. For the evaluation the size

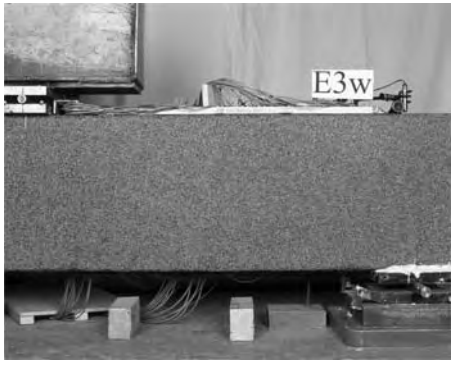

Figure 3. Studied shear span with applied pattern.

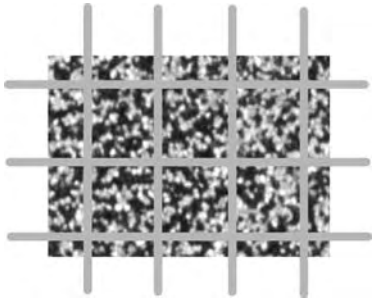

Figure 4. Magnification of shear span with applied pattern.

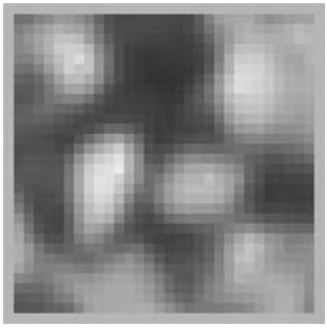

Figure 5. Magnification of sub-picture.

Figure 6. Sub-picture after threshold.

of the sub pictures is chosen as desired. The distance between sub-pictures may also be chosen as desired. Sub-pictures can be overlapping or have a certain distance between. For these test it was found satisfactory with sub-pictures of 128 × 128 pixels with 128 pixels between centres.

3.3 *Grid method*

This method implies that a uniform net in a divergent colour is painted or bonded to the studied area. The net may be in form of points bonded in a defined pattern or lines can form a uniform mesh. The method to calculate the strains is the same as for a speckle pattern. The big difference is that with the grid method, the grid must be defined before the tests are made. The gauge length can to a certain amount be chosen after the tests by eliminating some points in the evaluation. Another difference is that the accuracy is lower for this method since the centre of gravity cannot be determined as good as for the speckle pattern. This method has been used for monitoring of shear before. Because of the lower capacity of the grid method and use of less good cameras it has only been used for crack location, not for strain measurements. This may be found in Jeppsson (2000), Wiberg (2003) and Avril et al. (2004).

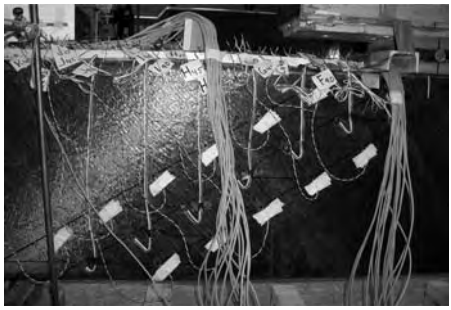

Figure 7. Strain gauges along expected crack.

3.4 *Strain gauge measurements*

The tested beams were monitored with strain gauges on the opposite side of the beam but in the same shear span. Previous test have shown approximately where the final shear crack forms and based on this information strain gauges were placed in three rows along this expected shear crack.

The mid row contained rosette strain gauges. Two of the individual gauges of the rosette were placed in the beam's longitudinal, and transverse direction. The third was placed in the 45-degree angle. The placements of the gauges are shown in Figure 7. In total 35 gauges were placed for measuring of strains in the shear span. When studying one of the precracked beams, the rosette gauges were placed along the crack.

4 RESULTS

4.1 *Measuring techniques*

The obtained results from the speckle pattern correlation method are very comprehensive. One can plot shear strains, principal strains, or strains in any arbitrary direction. Here is only one plot presented. The results from these area strain measurements is suitable to compare with finite element analysis since it is in the same format and is possible to import to the post processor. In Figure 8 a plot of the measured largest principal strains is shown where only the most interesting area is presented. The light coloured areas

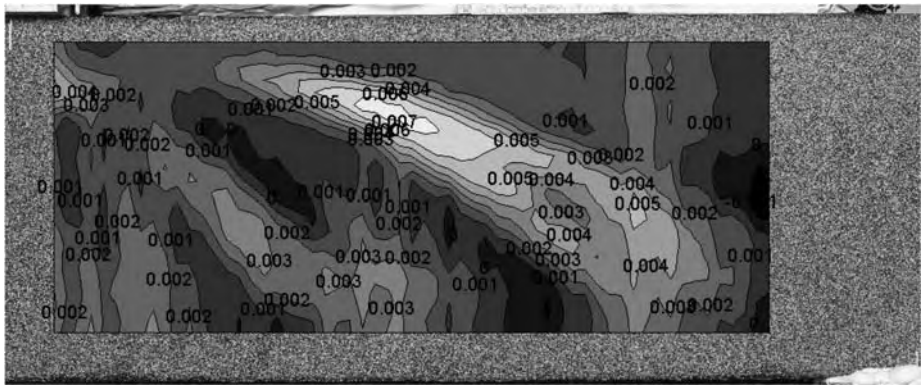

Figure 8. Largest principal strains.

are showing high tensile strains and darker areas are showing lower principal strains.

From Figure 8 it is obvious that placement of gauges, only measuring in a local point, is highly affecting the readings. Small movements within the studied area will give large differences in strain readings. However, strain readings from gauges correspond well with corresponding strains obtained by speckle pattern analyses.

4.2 *Strain distribution*

First, there is a fairly good agreement between strain distributions measured from tests and theoretically calculated strain distribution. It is clearly shown that the highest strain is in the centre of the beam. When studying strains in the upper (compressed) part of the beam, it is interesting to notice that fibres actually are compressed for fibres applied in a 45° direction Figure 8 is plotted for a rather low load within the service limit state. It can clearly be found that the strains are not uniformly distributed over the shear span. The plot also shows that two possible shear cracks can be identified. With higher loads the region becomes more cracked which verifies that the shear span is not subjected to one crack separated by rigid body motion, as may be believed after failure, but is more a cracked zone without any rigid body motion.

One beam was not loaded to failure but was unloaded just prior failure and the fibres were removed. From this beam it was possible to detect the cracked zone that was found from the strain measurements with the speckle method. For beams that were wrapped, a redistribution of strains was detected when the fibres debonded. Because of wrapping the fibres still contributed to the bearing capacity and the strain distribution was more uniform. The debonding started from the crack and propagated outwards. For the tested beams the average strain distribution factor, η, for not debonded fibres were in the range of 0.6 to 0.7 for all cases.

4.3 *Conclusions*

4.3.1 *Measuring technique*

The speckle pattern correlation method is an effective way of measuring strain fields. Strains can be monitored over an area in a cost-effective way, and the use of wires and amplifiers can be reduced. The only equipment needed are a good camera, ordinary studio flashes or other source of light, and a pattern on the surface. Measurement of strains with strain gauges in distinct points is not a suitable recording technique for studying behaviour of beams in shear. Strains are highly affected of distance to nearby cracks and gauges in distinct points may not only give uncertain values but also sometimes be misleading.

Photographic strain measurements offer a wider range of strain to be measured compared to traditional foil gauges. Sometimes an adjustable gauge length is preferable; with the presented method the gauge length and size of sub-pictures can be adjusted and combined to optimise accuracy. The redundancy of the measuring system is very good, even after damage of the used pattern the analysis gave valuable information. Further, if a sub-picture is not recognised between the two stages there are still several others to base the analysis on.

There are not only advantages with the presented method but also some drawbacks. One issue is the lack of experience in civil engineering using this kind of measuring technique. This is further discussed in the next paragraph together with suggestions for research areas. The equipment used is covetous for thieves compared to foil gauges that mean that its cameras cannot be left on a site without supervision. The method will not give continuous measurements and the results are not present at time of testing. This might be changed in the future but at this time the amount of data processed is so large that it cannot be done in real-time during testing. Because of this, photographic strain measurements should be used together with a limited number of strain gauges.

The method is not only suitable for measuring of strain fields in shear spans but may also be used for monitoring behaviour of two-way slabs, neutral axis in bending just to mention a few possible areas.

4.3.2 *Strain distribution*

The strains are not uniformly distributed over the cross-section of a rectangular beam. If using the truss model, a reduction factor for the strain distribution over a cross-section must be considered because of the linear elastic behaviour of the fibres. This is the case not only in ultimate limit state but also in service limit state regardless of debonding and the so-called rigid body motion. With satisfactory anchorage such as wrapping, strains can be redistributed which gives a higher load bearing capacity. However, for this to happen it is important that the fibres debond prior fibre rupture. The limits for validity of the addition formula must first be completely understood if the debonding redistribution is to be calculated for.

The presented strain measurements are in accordance with theoretical models. For rectangular beams the value 0.6 is recommended for engineering design, covering a wide range of possible load cases.

5 DISCUSSION

In conclusions, founded advantages and drawbacks with the presented method have already been stated. There are also some uncertainties that should be investigated further before researcher and society will have

the same confidence in using photographic strain measurement methods as for strain gauges. However, speckle pattern analysis has been used extensively in other areas and the research has gone further but has also to some extent become more complicated. Today, laser is sometimes used and with several cameras the method can measure three-dimensional strains and deformations. For civil engineering problems it is most likely that white light measurements is the most convenient with size of specimens and nature of tests in mind.

The most obvious issue to be studied is the limitations of the method. Depending of desired accuracy and area studied, the resolution of the camera equipment is critical. Every photo used in analysis contains a tremendous amount of information collected in one exposure. Critical for the quality of the photo are the speed of the studied object and the shutter speed of the camera. This means that it is important to find out the limits for the load rate and possibility to measure dynamic loading. The pattern is also very important. However, it is not completely understood how the pattern can be made to give reliable results with practical aspects in mind. The used pattern and the sustainability of the colours are important for the "gauge" lifetime. With adjustments of threshold values in the analysis it is possible that larger colour changes of the studied area to some extent can be acceptable and treated but to what extent is very uncertain.

One problem area in strengthening concrete structures with FRP is anchorage and peeling stresses. This has always been discussed but has been very difficult to measure. It is believed that the presented method can be used for very small areas and that, for instance, the peeling strains can be measured along the bond length. On the other end, in civil engineering it may in some cases be interesting to study large structures like whole bridges. With a larger object the resolution of the measurements will decrease but other issues, if measuring outside laboratory, such as convection in the air must also be kept in mind.

Until today, traditional cameras combined with scanners have been superior compared to digital cameras in respect of resolution. Since digital cameras are improving and somewhat giving different information on pixel level, it is probable that these cameras will be competitive for several applications. The use of digital cameras would be a great step towards automatization. Measurements that then may be used in combination with numerical models and structural health diagnostics.

ACKNOWLEDGEMENTS

The authors acknowledge the financial supports that have been provided by SKANSKA AB and The Development Fund of the Swedish Construction Industry, SBUF. Lukas Vesterlund at "luke.se" took photos and also performed scanning of film. Mikael Sjödahl at experimental mechanics should be thanked for his help with evaluation of the scanned photos. For help with the laboratory tests special attention should be given to Håkan Johansson, Lars Åström and Georg Danielsson at Testlab, Luleå University of Technology. Last but not least the student Andy Hägglund should be thanked for their enthusiasm and hard work when performing his Master Thesis.

REFERENCES

Adey, B., de Castro San Román, J. and Brühwiler, E. 1998. "*Carbon fibre shear strengthening of rectangular concrete beams*". Technical Report, Lausanne: École Polytechnique, 28 pp.

Al-Sulaimani, G. J., Sharif, A., Basunbul, I. A., Baluch, M. H. and Ghaleb, B. N. 1994. Shear Repair for Reinforced Concrete by Fiberglass Plate Bonding. *ACI Structural Journal*, July–August, pp. 458–464.

Avrila, S., Ferrier, E., Vautrin, A., Hamelin, P., and Surrel, Y. 2004. A full-field optical method for the experimental analysis of reinforced concrete beams repaired with composites. *Composites: Part A*, Vol. 35, pp. 873–884. Elsevier.

Burgoyne, C. J. 1999. Advanced Composites in Civil Engineering in Europe. "*Structural Engineering International*", Journal of the IABSE, V. 9, No. 4, November, pp. 267–273.

Carolin, A. 2001. "*Strengthening of concrete structures with CFRP. Shear strengthening and full-scale applications*". Licentiate thesis. Luleå: Luleå University of Technology.

Carolin, A. 2001. "*Strengthening of concrete structures with CFRP. Shear strengthening and full-scale applications*". Licentiate thesis. Luleå University of Technology, Division of Structural Engineering, 118 pp.

Carolin, A. 2003. *Carbon Fibre Reinforced Polymers for Strengthening of structural Elements*. Doctoral Thesis 2003:18, Luleå: Luleå University of Technology. Full-text at: http://epubl.luth.se/1402-1544/2003/18/LTU-DT-0318-SE.pdf

Chen and Teng, 2003. "*Shear capacity of strengthened RC beams: FRP debonding*". Construction and building Material, No. 17, Elsevier. pp. 27–41.

Izumo, K., Saeki, N., Horiguchi, T. and Shimura, K. 1998. "Study on shear strengthening of RC beams by prestressed fiber sheets", *Transactions of the Japan concrete institute*, V. 20, pp. 279–286.

Jeppsson, J. 2000. *Assessment of residual load carrying capacity of damaged concrete structures*. Licentiate Thesis, Lund: Lund University.

Maeda, T., Asano, Y., Sato, Y., Ueda, T. and Kakuta, Y. 1997. A study on bond mechanism of carbon fibre sheet. *Non-Metallic (FRP) Reinforcement for Concrete Structures, Proc. 3rd Symp*., Vol. 1, Japan, pp. 279–286.

Meier, U. 1999. "Structural Tensile Elements made of Advanced Composite Materials". *Structural Engineering International, Journal of the IABSE*, V. 9, No. 4, November, pp. 281–285.

Micelli, F., Annaiah, R. and Nanni, A. 2002. Strengthening of Short Shear Span Reinforced Concrete T Joists with Fiber-Reinforced Plastic Composites. *Journal of composites for construction*, Nov, pp. 264–271.

Triantafillou, T. C. 1998. "Shear Strengthening of Reinforced Concrete Beams Using Epoxy-Bonded FRP Composites". *ACI Structural Journal*, V. 95, No. 2, March–April, pp. 107–115.

Täljsten, B. 1994. *Plate bonding, Strengthening of existing concrete structures with epoxy bonded plates of steel or fibre reinforced plastics*. Doctoral Thesis, Luleå University of Technology, August 1994. 2nd Edition. 308 pp.

Täljsten, B. 2002. *FRP Strengthening of Existing Concrete Structures. Design Guidelines* Division of Structural Engineering, Luleå University of Technology, Luleå 2002, 228 pp.

Sato, Y., Ueda, T., Kakuta, Y. and Tanaka, T. 1996. "Shear Reinforcing Effect of Carbon Fiber Sheet Attached to Side of Reinforced Concrete Beams". *Advanced Composite Materials in Bridges and Structures*, El-Badry, M. M., Ed., pp. 621–628.

Svanbro, A. 2004. *Speckle Interferometry and Correlation Applied to Large-Displacement Fields*. Doctoral Thesis 2004:05, Luleå: Luleå University of Technology.

Vecchio, F. J. and Collins, M. P. 1986. The modified compression Field Theory for Reinforced Concrete Element Subjected to Shear. *ACI Structural Journal*, V. 83, No. 2, 1986, pp. 219–231.

Wiberg, A. 2003. *Strengthening of Concrete Beams Using Cementitious Carbon Fibre Composites*. Doctoral Thesis, Stockholm: KTH.

Strengthening of concrete columns and walls

FRP Composites in Civil Engineering – CICE 2004 – Seracino (ed)

Carbon FRP strengthened RC columns under combined flexure–compression loading

M. Quiertant & F. Toutlemonde
Laboratoire Central des Ponts et Chaussées, Paris, France

ABSTRACT: This paper describes an experimental investigation on the behavior of reinforced concrete columns externally strengthened with carbon fiber-reinforced polymer (CFRP) material. Studied columns were designed to be representative of buildings structural component. Four types of commercially available techniques of reinforcement, using plates, unidirectional or bidirectional composite fabrics, were tested. It was considered as necessary to get information on a wide spectrum of carbon fiber-reinforcement technique in order to provide a satisfactory set of experimental data for validating future suitable retrofitting design methods. The ten representative-scale square columns were tested under eccentric loading. Presented experimental results show that a significant improvement of the strength capacity and ductility of columns can result of the CFRP application. However, the observed gain strongly depends on the reinforcement techniques.

1 INTRODUCTION

The strengthening of flexural members by FRP plates or fabrics externally bonded to their tension face has been well studied and documented (ACI Committee 440 2000, fib-Bulletin 14 2001, Hamelin 2001) and is a commonly accepted and widespread technique. A typical application deals with the rehabilitation of damaged reinforced concrete beams.

More recently, experimental investigations have demonstrated the efficiency of external confinement of columns by the wrapping of FRP sheets. Usually, the jacketing is achieved by saturating fiber wrap in special epoxy formulation that allows them to be easily wrapped around columns. This technique provides a passive confinement that has been proven to increase the compressive strength of concrete.

As a combination of these two techniques, engineering departments of FRP planners and applicators usually propose to associate a flexural strengthening with a confinement by wrapping for column's retrofitting. The flexural strengthening can be carried out by prefabricated laminates or FRP sheets. Its main advantage is to moderate effect of eccentric loads that might lead to columns buckling.

Studies conducted so far on external strengthening of concrete columns have mainly concentrated on concentric loading and on retrofit systems designed for confinement only (no flexural strengthening) (Saadatmanesh et al. 1994, Lau & Zhou 2001).

However, in practice, structural concrete columns perfectly axially compressed rarely occur. Therefore, due to existing strain gradient in the confining wrap, a non-uniform confining pressure is applied and the stress–strain relationship for the concrete varied on the column cross section. Then an accurate analysis can only be carried out by numerical simulation considering complex stress–strain model for confined concrete (Mirmiran et al. 2000). Moreover, it was experimentally demonstrated that the flexural deformation of the column reduces the efficiency of the FRP jacket (Nanni & Norris 1995, Chaallal & Shahawy 2000, Parvin & Wang 2001).

This research thus proposes to investigate the behavior of RC columns externally strengthened with longitudinal and transverse CFRP retrofitting under combined flexure–compression.

The prior experimental investigation of Chaallal & Shahawy (2000) demonstrated that the strength capacity of beam-columns improved significantly as a result of the coupled action of the longitudinal and the transverse weaves of the bidirectional composite fabric. To study this concept of coupled reinforcement, Quiertant et al. (2004) have tested different types of commercially available techniques for (longitudinal) flexural reinforcement and (lateral) confinement. Various combinations of plates, unidirectional and bi-directional composite fabrics were investigated. Tested columns were design to be representatives of bridges structural applications, and were eccentrically loaded up to failure. The main conclusion of this preliminary study was that the strength capacity and ductility of columns improved significantly thanks to CFRP application but a large difference in ductility was observed between reinforcement techniques.

As a continuity of this previous work, the presented experimental study investigates the reinforcement effectiveness of the same combination of retrofitting techniques (longitudinal and lateral reinforcement) applied to columns with inferior quality of concrete and insufficient amount of transverse reinforcement which might be found in old buildings. The considered loading is the eccentric compression.

2 EXPERIMENTAL PROGRAM

2.1 *Program*

The experimental program consisted of the testing of ten square columns loaded under combined axial-flexural loading up to failure. The program comprised five groups of two identical specimens; a first group of two control columns (CC-a and CC-b) and four groups of similar columns but externally strengthened with 4 kinds of CFRP combining longitudinal and transverse reinforcement. The specimens were labeled as ESX-a and ESX-b for the two columns externally strengthened using the technique labeled X. In a same group, the external reinforcement was the same for each specimen. Repeating twice experiments was an experimental choice to increase the confidence level in the obtained results.

2.2 *Test set-up*

In order to test representative full-scale columns, it was necessary to create a loading frame capable of bringing stout specimens to failure. Assumptions based on previous experience in testing confined cylinder (Clement et al. 2000) were made on the concrete strength when reinforced with two layers of CFRP materials. Then, the design of the testing frame was based on a global vertical load capacity of 4.4 MN applied by four annular hydraulic jacks (filled in parallel within the same servo-controlled closed loop) inserted in a closed frame made of struts and ties and fixed to the strong floor (Fig. 1).

Basically, a vertical load is applied by hydraulic jacks between the lower and middle plates. While the middle plate is fixed on the strong floor, a vertical displacement of the lower plate is resulting from the jacks thrust. Lower and upper plates are linked by ties. Then consecutively to the displacement of the lower plate, a displacement of the upper plate is generated, also directed downwards.

Steel diffusion elements (called caps, Fig. 2) were designed to receive the load applied by plates and to transmit that loading 20 mm eccentrically to the column, thus generating the combined flexure–compression load. It corresponds to a nominal deviation accounted for in French design rules for columns. This magnitude of eccentricity was chosen in order to place the entire column under compression during the first part of the test. This is a particularly inadequate loading for the external reinforcement that can lead to local debonding of composite material and/or to local axial buckling of fibers. However, when bending becomes to be sufficiently pronounced, one side of the column is in tension.

The bearing zone of caps on plates is realized with partially spherical shapes of the cap thus forming a ball

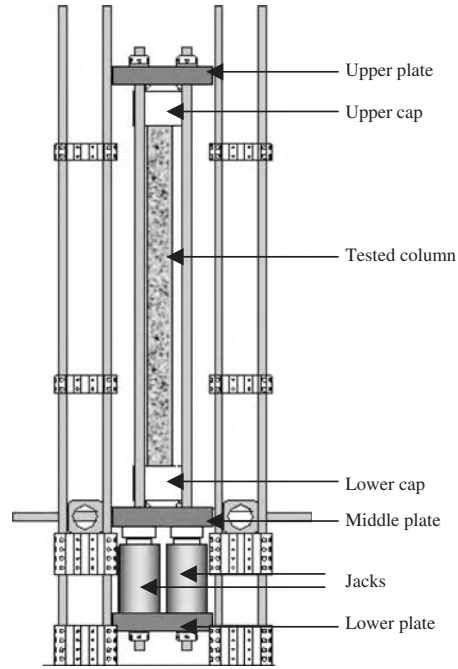

Figure 1. Test set-up for combined flexure–compression.

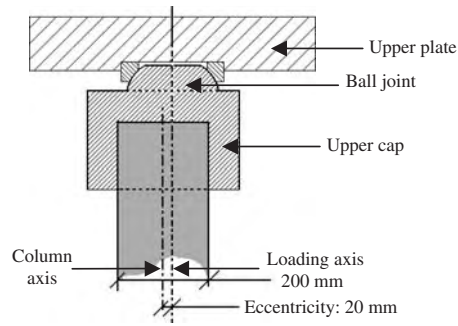

Figure 2. Principle of load application device (cap).

joint (Fig. 2). This kind of bearing ensures a free rotation of the column. Symmetrical bearing conditions are provided by the lower cap and upper cap. Particular care was taken of the experimental boundary conditions (lubrication of the ball joint, connection between the column and the cap ensured by a high strength grout) and the effectiveness of the mechanical scheme was checked during the tests.

2.3 *Tested specimens*

2.3.1 *Details of tested columns*

Tested columns had a 200 × 200 mm^2 square cross section and an overall height of 2,500 mm. For all the specimens, a unique batch of self-compacting concrete was delivered by a local supplier. The specimens were cast in moulds with chamfered corners in order to avoid the premature fracture of the CFRP fabric due to kinking, and to enhance the confining effect of the wrap.

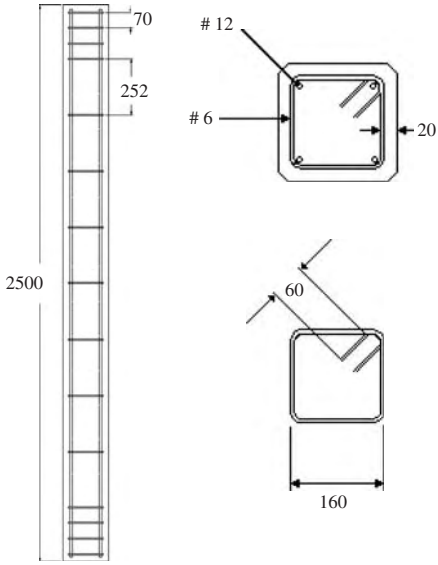

Figure 3. Reinforcement details of tested columns (dimensions in mm).

The dimensions and details of internal reinforcement are shown in Figure 3. A low amount of internal reinforcement was planed to be representative of ancient building application when retrofitting should be necessary.

2.3.2 *External strengthening*

Except for the two reference specimens, two layers of CFRP were bonded on columns. A flexural reinforcement was first achieved by a unidirectional composite (plate or sheet) bonded in the axial direction. Then each column was externally confined by transverse composite straps wrapped in a continuous spiral or in discontinuous rings (Table 1). Such methods, widely recognized, permit to exert a lateral pressure that increases strength and ductility of concrete in the axial direction (Saadatmanesh et al. 1994).

Structural analysis and resultant design was carried out by the authors while the strengthening of columns was accomplished by technical professional teams using their own procedures and products to ensure the representativeness of experimental results. It must be emphasized that the intent of the column's strengthening design was to cover a wide range of strengthening rates and techniques. Based on this consideration, it is easy to understand that no mechanical or cost equivalence was targeted for the studied strengthening

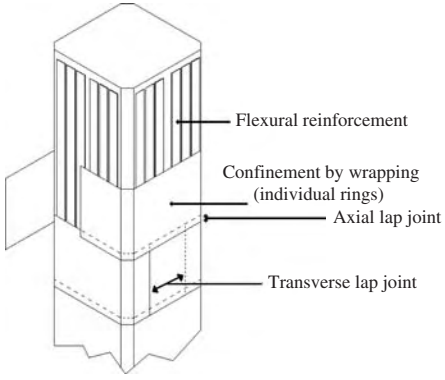

Figure 4. Principle of column's reinforcement.

Table 1. CFRP strengthening configuration of columns.

Specimen series	Flexural reinforcement	CFRP wrapping material	Wrapping configuration
CC	None	None	None
ES1	Six type x plates on each side	One layer of type 1 woven sheet	Continuous spiral
ES2	One layer of type 2 stretched sheet	One layer of type 2 stretched sheet	Discontinuous rings
ES3	Two type y plates on each side	One layer of type 3 stretched sheet	Discontinuous rings
ES4	One layer of type 4 stretched sheet	One layer of type 4 stretched sheet	Discontinuous rings

Table 2. Manufacturers reported CFRP system properties.

Carbon fiber product	Thickness (mm)	Tensile modulus (GPa)	Tensile strength (MPa)
Type 1 woven sheet	–	of fibers: 240-221	of fibers 4,900-4,510
	of one layer of CFRP: 0.43	of CFRP: 105	of the CFRP layer: 1,400
Type 2 stretched sheet	of the dry sheet: 0.117	of fibers: 240	
	of one layer of CFRP: 0.334	of CFRP: 84	of the CFRP >1,050
Type 3 stretched sheet	of the dry sheet: 0.13	of fibers: 230	of fibers >3,500
Type 4 stretched sheet	of the dry sheet: 1	of fibers: 235	of fibers 3,450
	of one layer of CFRP: 1	of CFRP: 62-70	of the CFRP: 620-700
Type x plate	of a plate: 1.2	of plate: 180	of plate: 3,000
Type y plate	of a plate: 1.2	of plate >165	of plate >2,800

Table 3. Average mechanical properties of concrete.

Modulus of elasticity	27.2 GPa
Poisson's ratio	0.19
Tensile strength	3.0 MPa
Compressive strength	40.1 MPa

techniques. The type 4 dry stretched sheets were saturated in special epoxy formulation before being laid to the columns. For other strengthening using dry sheet, CFRP was fabricated by the "wet lay-up" technique; that is, the dry sheets were placed on the surface of the column and then impregnated with epoxy resins. Prior to such laying of the sheets, adhesive was applied to column surfaces. The type 1 dry sheet was hand-laid with a winding angle (between transverse direction of column and fill direction of the fabric) of 20 degrees. In all cases, a unique epoxy formulation was used for saturant and adhesive.

The CFRP system manufacturer's reported material properties are shown in Table 2. The type 1 woven sheet is a bidirectional fabric (70% of fibers are in wrap direction).

2.3.3 *Mechanical properties of concrete*

In order to evaluate the effectiveness of external reinforcement by a comparison with reference columns, it was necessary, firstly to cast a set of 10 similar RC columns, and secondly to check that mechanical properties of the columns concrete remain stable all through the experimental program. This material analysis was necessary due to the long duration of the experimental study as compared to the age of columns (the first column was tested at the age of 309 days, 138 days before the last column).

A total of 30 concrete cylinders were cast at different steps of the casting of columns. These cylinders were tested at different age. According to the obtained results, the mechanical properties listed in Table 3 can be satisfactory used to conduct future structural analysis for all the columns tests.

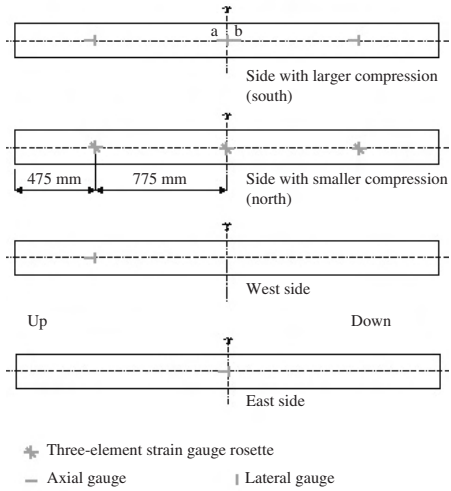

Figure 5. Details of the external instrumentation by strain gauges.

2.4 *Structural monitoring*

All specimens were instrumented using surface strain gauges both on the longitudinal and transverse direction on each face of the specimens (Fig. 5). Strain gauges were glued on concrete surface for control columns and on CFRP outer layer for other specimens. The strains on the internal steel reinforcement were also monitored. The deflections were recorded at 7 locations and the axial displacement was measured by 2 sensors. The applied load was recorded with four load cells. On the whole, 56 measurement channels helped describing the structural behavior of the columns. This extensive measurement program will be useful for calibration of future FE modeling and definition of serviceability and ultimate limit states

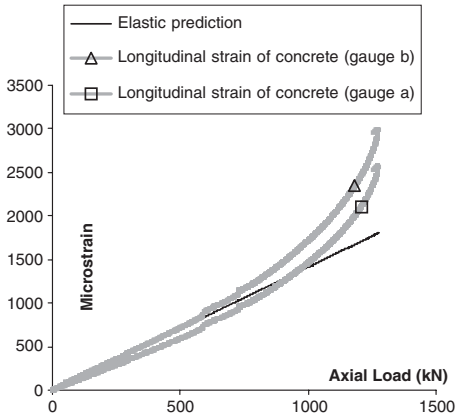

Figure 6. Load–axial strain curves on side with larger compression (CC-b).

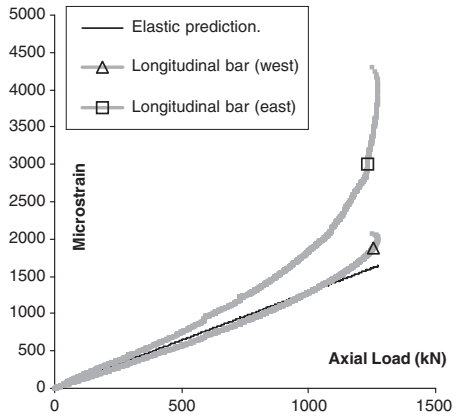

Figure 7. Load–axial strain curves on bars near the side with larger compression (CC-b).

for design recommendations. Only main results are presented in the following.

2.5 *Loading procedure*

The load was increased monotonically up to 70% of the expected failure load, with a constant 1 kN/s loading rate. Then the jack displacement was used as the servo-control parameter (∼0.08 mm/s) that helps recording post-peak behavior, provided the failure is ductile enough. Due to an operator error, loading was the only control parameter during the test of specimen ES3-b.

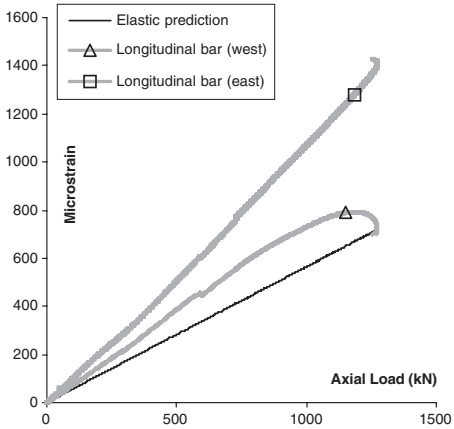

Figure 8. Load–axial strain curves of bars near the side with lower compression (CC-b).

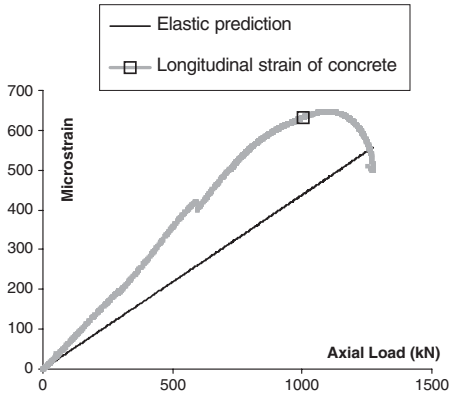

Figure 9. Load–axial strain curves on side with lower compression (CC-b).

3 MAJOR RESULTS

3.1 *Validation of testing process and analysis of hypotheses*

Within the hypotheses of the strength of materials theory and considering a homogenized inertia for the RC column, it is possible to predict the axial strain, at mid-height on the surface of the sides with respectively larger and smaller compression. With the same hypotheses, strains of the longitudinal reinforcement can be determined at mid-height. Compared with experimental data in the elastic part of the column behavior, results of this calculation permit to establish the validity of the loading set-up (Figs. 6–9). In

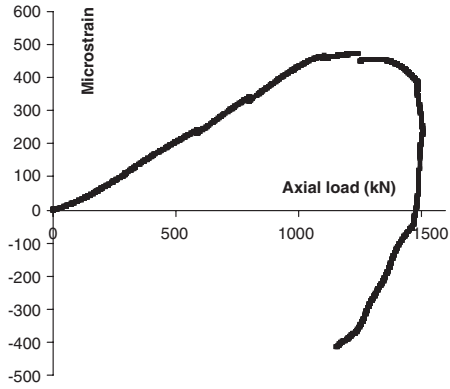

Figure 10. Example of transition from compressive loading to tension (load–axial strain curves on north side of ES1-a).

addition, the failure of most of the specimens near the mid-height confirms the dominant role of elastic second order moment.

The validity of the choice of magnitude of eccentricity, to obtain on one side the transition from compressive loading to tension, was checked. This evolution of the axial strain recorded on the side here called "side with lower compression" (see Fig. 5) is illustrated in the Figure 10. Such transition is due to a second order moment growing with the deflection of the column.

3.2 *Bearing capacity and failure mode*

A comparison of load–deflection curves between externally strengthened columns and the reference specimens is presented in Figure 11 for each series of test. As a first remark, it can be emphasized that strength and deformability enhancement

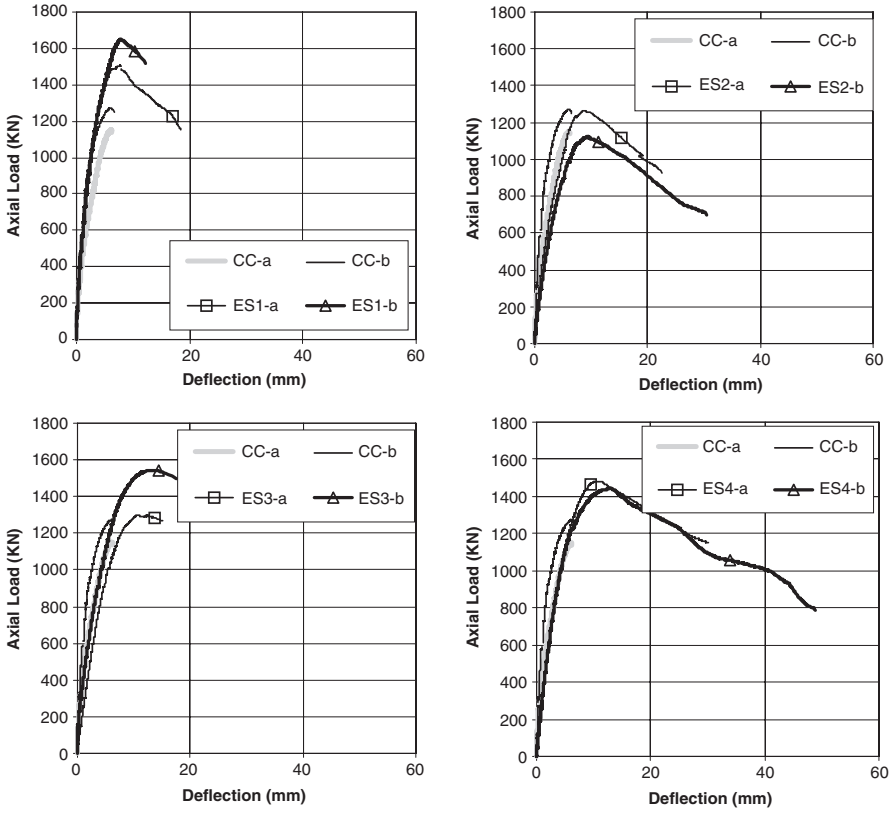

Figure 11. Load–mid-height deflection curves of all specimens.

Table 4. Experimental results for strength and mid-height deflection.

Specimen label	Load (kN)		Rate of strength enhancement*	Mid-height deflection (mm)		Rate of deformability enhancement*
	Max.	Average		Max.	Average	
ES1-a	1507			18.40		
ES1-b	1649			13.56		
		1578	1.30		15.98	2.48
ES2-a	1262			22.65		
ES2-b	1125			30.49		
		1194	0.98		26.57	4.13
ES3-a	1300			15.02		
ES3-b	1544			17.52		
		1422	1.17		16.27	2.53
ES4-a	1482			30.11		
ES4-b	1442			48.78		
		1462	1.21		39.44	6.13

* Average ESx/average CC.

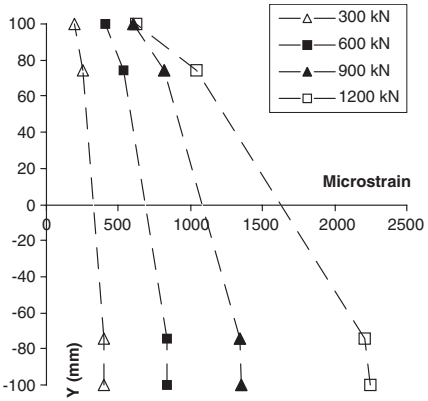

Figure 12. Typical longitudinal strain distribution on mid-height section of RC column (CC-b).

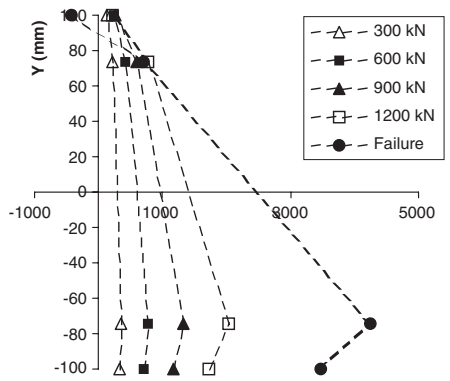

Figure 13. Typical longitudinal strain distribution on mid-height section of externally strengthened column (ES4-b).

strongly depends on the reinforcement technique. Note that the word "technique" is used here with a general meaning involving the choice of materials for the making of the composite and the way to lay it on the columns. Depending on the technique, the strength enhancement varied from 0.98 to 1.30. At present time, no definitive explanation is proposed by authors to justify the ineffectiveness of the retrofitting technique 2 (see Fig. 11 and Table 4).

Both externally strengthened columns and reference specimens (except CC-a) failed by crushing of the concrete and buckling of longitudinal bars on the side with larger compression near the column mid-height, as designed. The same mode of failure was observed for column CC-a but on an upper section (about 80 cm from the end of the column).

Rates of strength enhancement (basically calculated here as the ratio of the average value of the two maximum capacity of strengthened columns to the average value of maximum load of the reference specimens) and deformability enhancement (defined with the ratio of the maximum deflection until loss of stability) are presented in Table 4.

For CFRP strengthened specimens, one could see the hoop fracture of fibers during the last loading stage. The failure of specimens by rupture of the CFRP jacket due to hoop tension is the most common mode of failure for FRP-confined concrete (Lam & Teng 2003). In this study, the CFRP jacket failure was always initiated at a corner of the column at the most compressed face and appears latter on the tensile face, during post-peak behavior, when flexure of the column was increased. Sound of snapping of the fibers could be heard near

the failure load. The failure mode of presently reported CFRP strengthened columns is much less brittle than those described by Li & Hadi (2003) for high-strength concrete columns.

3.3 *Test data base for future design methods*

Using data recorded by longitudinal strain gauge, makes it possible to establish the longitudinal strain distribution on mid-height section for RC columns and for externally strengthened columns (Figs. 12–13). These data are helpful to understand the flexural behavior of the columns.

Table 5. Lateral strain on the side with larger compression.

Specimen label	Lateral strain (microstrain)	Loading (kN)	Failure of gauge
ES1-a	−4275	1489	Yes
	x	x	Yes
ES1-b	−1531	1649	No
	−1666	1457	No
ES2-a	−2566	1230	No
	−3926	1262	No
ES2-b	−1902	1125	No
	−2967	697	No
ES3-a	−1411	1300	No
	−1711	1269	No
ES3-b	−5840	1543	No
	x	x	No
ES4-a	−1982	1482	No
	−3990	1148	No
ES4-b	−3409	1442	No
	−5660	1353	No

Nevertheless, the observed failure of specimens is the rupture of the CFRP jacket due to hoop tension. The maximum hoop strain in FRP recorded during test can be then considered as mostly significant for design consideration. The experimental values of lateral deformation for a loading near failure of columns are reported on Table 5. On the last section of this table, it is specified if the gauge was broken after the failure of the specimen. For CFRP columns it never happened, due to the location of gauges that were not on the corner of columns where the fracture of the external strengthening jacket was always initiated. Note that the lateral strain of CFRP at failure of specimens is much lower than the CFRP material ultimate tensile strain reported on Table 2. This was ever underlined by Lam & Teng (2003).

3.4 *Flexural stiffness*

Deflections recorded for two loading steps are reported in Table 6. It can then be concluded that the composite material has not contributed to significantly enhance the flexural stiffness of columns during this part of the loading. Moreover it is surprising that for the two loading considered, average deflection of reference columns is smaller than three of the four average deflections of strengthened columns. In design consideration, the longitudinal external strengthening is applied to reduce the curvature of the column and consecutive secondary moment, hence limiting the induced compression and the concrete cracking on the tensile face. This kind of reinforcement mode was not here clearly demonstrated.

Table 6. Mid-height deflection for loading steps of 500 and 1100 kN.

	500 kN			1100 kN		
Specimen	Deflection (mm)	Average	Rate*	Deflection (mm)	Average	Rate*
CC-a	1.21			5.11		
CC-b	0.65			3.24		
		0.93	1.00		4.18	1.00
ES1-a	0.73			2.94		
ES1-b	0.88			2.99		
		0.81	0.87		2.97	0.71
ES2-a	1.68			5.59		
ES2-b	2.12			8.24		
		1.90	2.04		6.92	1.66
ES3-a	2.27			6.50		
ES3-b	1.46			4.93		
		1.86	2.00		5.72	1.37
ES4-a	1.71			4.84		
ES4-b	1.74			4.97		
		1.72	1.85		4.91	1.17

* Average ESx/average CC.

4 CONCLUSION

Depending on the CFRP strengthening technique (type of material and bonding process), significant increase in deformability and strength can be achieved for columns under combined flexural–compressive loading. The maximum strength enhancement was characterized by a ratio of 1.3. A ratio of 6.13 was obtained for deformability enhancement. Nevertheless, the external strengthening efficiency was shown, in the condition of our study, to be strongly dependant of the chosen technique. But considering the acceptable dispersion of results for the columns strengthened using the same technique and the fact that the inspections of specimens before and after the tests have not revealed significant default, authors conclude that the large difference observed on bearing capacity is representative of efficiency of the different techniques.

For the coupled strengthening methods tested, the expected strength enhancement was a result of the combined action of the longitudinal and transverse strengthening. Presented results show that when the transverse jacketing is strong enough, it enhances the compressive capacity of concrete through confinement action. Moreover, it is evident that the lateral pressure exerted by the straps also provides additional support against buckling of longitudinal bars. However, contribution of flexural reinforcement to strength enhancement was not clearly established in the tested strengthening configuration.

Experimental results presented in this paper and the related considerable database can be used as templates for future validation of CFRP strengthening design methods. Moreover, evidence was obtained that a unified model for concrete confined by different types of CFRP must consider the actual hoop rupture strain of CFRP rather than the ultimate material tensile strain.

REFERENCES

ACI Committee 440.2R02. 2002, Guide for the Design and Construction of Externally Bonded Systems for Strengthening Concrete Structures, ACI, Michigan, U.S.A.

Chaallal, O. & Shahawy, M. 2000. Performance of Fiber-Reinforced Polymer-Wrapped Reinforced Concrete Column under Combined Axial–Flexural Loading. *ACI Structural J*. 97(4): 659–668.

Clement, J.-L., Verok, K., Boulay, C. & Le Maou, F. 2000. Retrofitting of reinforced concrete columns with composites: static compressive tests and modeling–creep behaviour. *Proc. Computer Methods in Composite Materials and Structures CADCOMP, 13–15 September, Bologne, Italy*, 53–61.

Demers, M. & Neale, K.W. 1999. Confinement of reinforced concrete columns with fibre-reinforced composite sheets – an experimental study. *Canadian Journal of Civil Engineering* 26(2): 226–241.

fib-Bulletin 14. 2001. Externally bonded FRP reinforcement for RC structures, Lausanne, Switzerland.

Hamelin, P. 2001. AFGC: Recommendations concerning Repairing and Strengthening of Concrete Structures by Composite Materials. *FRP Composites in Civil Engineering*, Vol. 1, J.-G. Teng (Ed.), 165–175.

Lam, L. & Teng, J.G. 2003. Design-oriented stress–strain model for FRP-confined concrete. *Construction and Building Materials* 17: 471–489.

Lau, K.-t. & Zhou, L.-M. 2001. The mechanical behaviour of composite-wrapped concrete cylinders subjected to uniaxial compression load. *Composites Structures* 52: 189–198.

Li, J. & Hadi, M.N.S. 2003. Behaviour of externally confined high-strength concrete columns under eccentric loading. *Composite Structures* 62: 145–153.

Mirmiran, A., Zagers, K., & Yuan, W. 2000. Nonlinear finite element modeling of concrete confined by fiber composite. *Finite Element Anal Des* 35: 79–96.

Nanni, A. & Norris, M.S. 1995. FRP jacketed concrete under flexure and combined flexure-compression. *Construction and Building materials* 9(5): 273–281.

Parvin, A. & Wang, W. 2001. Behavior of FRP Jacketed Concrete Columns under Eccentric Loading. *ASCE Journal of Composites For Construction* 5(3): 146–152.

Quiertant, M., Toutlemonde, F. & Clement, J.-L. 2004. Combined flexure–compression loading for RC columns externally strengthened with longitudinal and transverse CFRP retrofitting. To be published In *Concrete Structures: The challenge of Creativity. Proc. fib. symp, Avignon*, *France 26–28 April 2004*.

Rochette, P. & Labossiere, P. 2000. Axial testing of rectangular column models confined with composites. *ASCE Journal of Composites For Construction* 4(3): 129–136.

Saadatmanesh, H., Ehsani, M.R. & Li, M.W. 1994. Strength and Ductility of Concrete Columns Externally Reinforced with Fiber Composite Straps. *ACI Structural J*. 91(4): 434–447.

FRP Composites in Civil Engineering – CICE 2004 – Seracino (ed)
© 2005 Taylor & Francis Group, London, ISBN 90 5809 638 6

Retrofit of two-column bridge piers with diamond-shaped columns for earthquake loading using CFRP

M. Saiidi, A. Itani, K. Sureshkumar & S. Ladkany
University of Nevada, Reno, Nevada, USA

ABSTRACT: This paper presents the seismic performance of two-column bents with diamond shape columns and suggests retrofit methods. The bents are from the main structure of a freeway bridge in Las Vegas, Nevada. The diamond shape of the columns is unique to this bridge. This bridge was built in the late 1960s. Two identical quarter-scale specimens were built. One two-column bent was tested as built and the other was retrofitted and tested using one of the shake tables at University of Nevada, Reno. The bents were tested in the strong direction of the columns, subjected to the 1994 Northridge earthquake until failure. The as-built specimen failed due to shear failure of a column. The columns of the second specimen were wrapped with carbon fiber reinforced plastic (CFRP). The performances of the retrofitted and as-built specimens were compared.

1 INRODUCTION

Most of the bridges in California and Nevada were built before the 1970s. These bridges lack the necessary details to provide sufficient ductility capacity for dynamic loading caused by earthquakes. The 1971 San Fernando earthquake caused extensive structural damage to this type of structures. The deficiencies for concrete bridges include insufficient shear strength, confinement, and structural detailing. These deficiencies usually cause non-ductile and unexpected modes of failure. Structural design codes have evolved to include the effect of seismic forces and are updated periodically to incorporate new information obtained from earthquakes and research. The current seismic philosophy is based on large inelastic deformations and energy dissipation during strong earthquakes and these seismic guidelines are applicable to new constructions.

Bridges built prior to 1971 required to be upgraded and retrofitted to resist strong seismic forces. Numerous studies have been conducted on the seismic behavior of bridge bents to understand the seismic enhancement by steel and FRP jackets (MacRae et al. 1994, Sexsmith et al. 1997, Pantiledes et al. 1999, Pulido et al. 2001). Retrofitted bridges have generally performed well in recent earthquakes in Northridge, California (1994) and in Kobe, Japan (1995).

The Nevada Department of Transportation has an ongoing program to evaluate and retrofit existing bridges in Nevada. Under this program it was decided to study the vulnerability of a multi-span freeway bridge in downtown Las Vegas to seismic forces and develop retrofit methods to improve the seismic performance of the bridge. The Viaduct can be divided in two parts. One is the main structure and the other was the ramp structures. The main structure has 24 spans and the piers are two, three, or four column bents. The columns are diamond shape. The shape of the columns is unique to this Viaduct. The seismic retrofit study of the main structure is presented in this paper. The study on the ramp structure is reported by Johnson et al. 2003.

The objective of this study was to evaluate the performance of two-column bents with diamond shape columns and suggest methods to retrofit them to withstand strong seismic forces.

The critical pier, the prototype, was selected based on the highest plastic shear demand (Dong et al. 2003). The main structure consisted of two, three, and four column bents. The two-column bent was found to be the most critical. Two identical two-column bents were built to ¼ scale. One specimen was tested as built using one of the shake tables at University of Nevada at Reno. Based on the results of the as built test, the columns of the second specimen were retrofitted using carbon fiber reinforced plastic (CFRP) jackets and tested. This paper presents the experimental results from both specimens.

2 AS-BUILT AND RETROFITTED SPECIMENS

2.1 *As-built specimen*

The as-built specimen (B2DA) was a quarter-scale model of the prototype. The test specimens utilized real

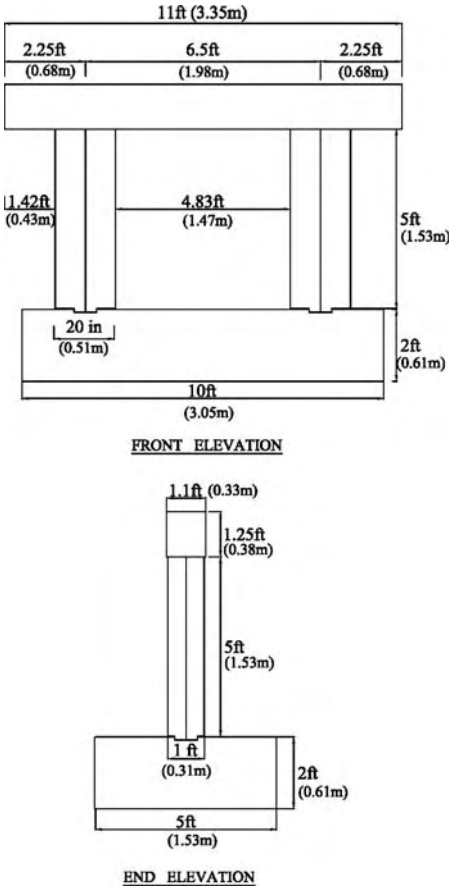

Figure 1. Test specimen dimensions.

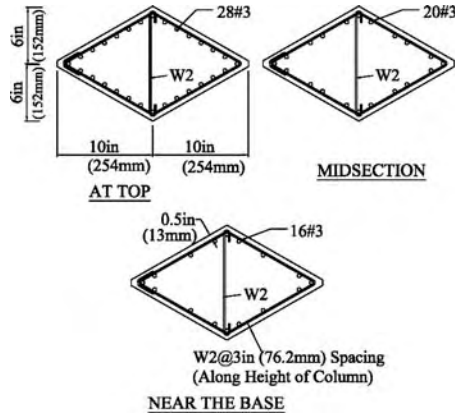

Figure 2. Column cross-sections.

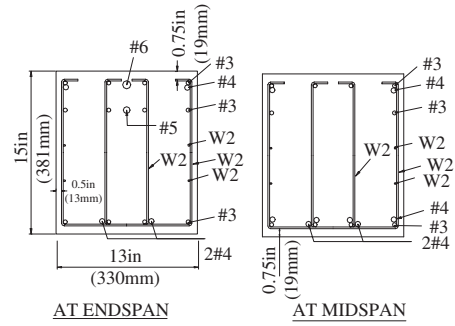

Figure 3. Beam cross-sections.

concrete and real reinforcing bars as opposed to model concrete and bars. Given the large size of the elements in the model, it was believed that size effect would not be an issue. The beam bars had been designed for gravity. The shear reinforcement in all elements was insufficient and the stirrups did not have proper hooks. The beam-column joints had no shear reinforcement. The column bases were detailed as a two-way hinge.

The longitudinal reinforcement of the columns was 2.6 percent in the plastic hinge region at the top of the columns. The confinement reinforcement ratio of the columns was 0.1% with spacing of the ties of 3 in (76 mm) along the height of the column. The beam had a maximum top reinforcement ratio of 1.0% at the face of the columns and a maximum bottom reinforcement of 0.84% at the midspan.

The confinement reinforcement ratio of the cap beam was 0.5% near the beam ends. These values were obtained from field data. On the day of testing, average concrete compressive strength of the beam was 6250 psi (43.1 MPa) and the column was 8100 psi (55.8 MPa) for the as-built and retrofitted specimens. The overall dimensions of the bent are shown in (Fig. 1). The column and beam sections at different locations along the members are shown in (Figs. 2 and 3).

2.2 *Retrofitted specimen*

The retrofitted specimen (B2DC) was identical to the as-built specimen except for the column jackets. The concrete and steel material properties were also the same.

Carbon fiber reinforced plastic (CFRP) jackets were used to retrofit instead of steel jackets in order to retain the diamond shape of the cross section. Fiber

reinforced plastic (FRP) jackets are easier to install compared to steel jackets. Only the columns were retrofitted as the failure of the as-built specimen was due to the shear failure of the south column, which is discussed later in this paper.

2.3 *CFRP retrofit design*

The primary purpose of the retrofit was to prevent the brittle shear failure of the columns. The confinement provided by the column ties was very small. Therefore the number of layers of CFRP required in providing the required minimum confinement stress was also calculated. The CFRP jackets were designed following the California Department of Transportation (Caltrans) design guidelines. Uni-directional CFRP jackets were used since these allow the designer to increase the shear capacity without significant increase in flexural capacity or stiffness. FRP jackets (SCH-41) supplied by Fyfe Co. Ltd. The design ultimate tensile strength in the fiber direction is 108 ksi (744 MPa), with a tensile modulus of 8900 ksi (61321 MPa), and the design fiber strain used was 0.6%. The laminate thickness is 0.04 in (1 mm).

Minimum jacket thickness that is required to satisfy the minimum confinement requirements was calculated based on Caltrans specification.

- Minimum confinement stress of 300 psi (2.1 MPa) in the lap-splice and/or plastic hinge zone with maximum material elongation of 0.001 in/in in the lap-splice zone and 0.004 in/in in the plastic hinge zone.
- A minimum confinement stress of 150 psi (1.0 MPa) and maximum material strain of 0.004 in/in must be maintained elsewhere in the column, with appropriate transition.

The jacket thickness is calculated for the average confinement pressure required in both the short and long directions of the column section. Expression for calculating the jacket thickness is as follows

$$t_j = \frac{f_l * B}{2 * E_j * \varepsilon_j * k_e * \cos\theta}$$

Where

f_l = confining pressure
ε_j = strain in the jacket
E_j = elastic modulus of jacket material
k_e = confinement efficiency factor, taken as 0.75 for the diamond shape section
B = dimension of the column in the direction considered.

In order to satisfy the minimum confinement requirement 4 layers of CFRP must be wrapped in the plastic hinge region and 2 layers in the rest of the column.

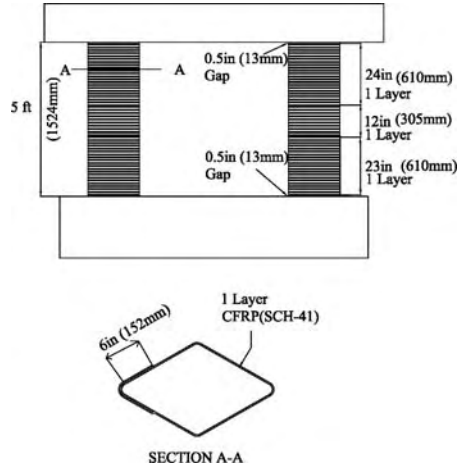

Figure 4. CFRP layout on the retrofitted specimen.

CFRP jacket was designed for shear using a conservative approach. The shear demand was obtained from pushover analysis using Drain 3-DX (Seyed Mahan 1999) at a 5% lateral drift. This is a drift level causing extensive non-linearity. A factor of safety of 1.7 (Saiidi et al. 2000) was added to the shear demand. The concrete shear capacity was neglected due to the net axial tension that could be generated in the columns as the lateral force increases. The axial load assumed to have no contribution to the total shear capacity due to the possibility of the column being in tension. Furthermore, only one-half the shear capacity of the transverse reinforcement was taken into account. This was because the tie hooks were not bent into the column core and that there was a possibility of bond slip. The thickness of the CFRP jacket around the columns was calculated using the following expression

$$t_j = \frac{V_{sj}}{2 * E_j * \varepsilon_j * h}$$

V_{sj} is the design shear, h is taken as 80% of the total section depth of the column in the strong direction, and ε_j is the design fiber strain of the CFRP.

One layer of CFRP was required across the entire length of the column. It was seen that the layers required in the specimen to satisfy the minimum confinement was high and is four times more in actual columns. Therefore the column was retrofitted for maximum shear demand using CFRP hoping that with the shear retrofit the ductility capacity of the bent will be increased to an acceptable level. Figure 4 shows the retrofit layout on the columns.

Figure 5. Test setup for the as-built specimen.

3 EXPERIMENTAL PROGRAM

The specimens were instrumented using strain gages on the longitudinal and transverse reinforcement to measured strains. Novotechnik displacement transducers were used to measure the curvatures and the bent displacements were measured using Temposonic displacement transducers. Load cells were used to measure the vertical and horizontal loads. Both specimens had the same instrumentation with strain gages at the same location to compare performances but the retrofitted specimen had extra strain gages on the CFRP jacket.

The test setup is shown in Fig. 5 and this was the same for both the specimens. The vertical and lateral loads were transmitted to the substructure through steel transfer beam fixed to the bent cap. The vertical load was applied to the bent through ties bars prestressed using hydraulic jacks.

The lateral load was transmitted through an inertial mass system. The as-built and the retrofitted specimen were subjected to the same loading protocol. The earthquake record used was the 1994 Northridge Sylmar acceleration, and was simulated with gradually increasing amplitudes in multiple runs. The initial run was at ten percent of the actual record (0.10 × Sylmar), but the multiplier was increased until failure. The time scale was modified by a factor of 0.48 to account for the quarter-scale of the model and the difference in vertical load on the bent and the inertial mass on the mass rig.

4 TEST OBSERVATIONS

4.1 *As-built specimen*

Shear crack at the beam ends started forming at 0.24 × Sylmar and significant flexural and shear cracks were observed by 1.07 × Sylmar. But after this the cracks at the beam ends stabilized while new cracks were observed at the beam-column joints

Figure 6. Shear failure in the south column of the as-built specimen.

Flexural cracks were observed on the columns after 0.36 × Sylmar. The main shear crack first formed at the south column top at 1.75 × Sylmar. Finally the as built bent failed due to shear failure of the south column at 2.25 × Sylmar. Figure 6 shows the bent after failure. No major shear cracks were observed at the top of the north column. The bent cap had extensive shear and flexural cracks.

The first crushing of concrete was observed at the south column base at 1.07 × Sylmar. North column base started crushing during 1.25 × Sylmar. Crushing at the south column top was at 1.5 × Sylmar but no crushing was observed at the north column top.

4.2 *Retrofitted specimen*

At 1.0 × Sylmar long but thin shear crack formed at the south beam end. Also several small shear and flexural cracks were observed at the beams ends. In the subsequent events after 1.5 × Sylmar, new shear and flexural cracks were seen in the joint region and adjacent to the joints on both ends of the bent cap.

In the retrofitted specimen the cracks moved from the beam ends to the joints as the intensity of earthquake loadings was increased. This phenomenon was observed in the as-built specimen. Deterioration on the columns could not be observed due to the CFRP jackets. No ruptured fibers were observed in the CFRP jacket on both columns.

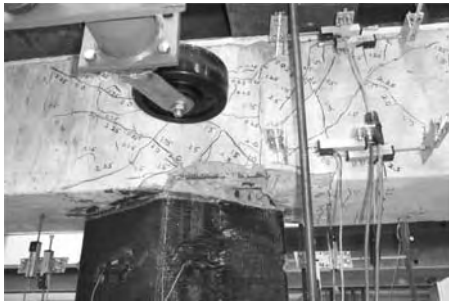

Figure 7. Beam-column failure of the retrofitted specimen.

Flexural cracks were seen at the bottom of the beam. Spalling of concrete at the beam bottom first occurred during 2.75 × Sylmar. The specimen failed at the beam-column joints at 2.87 × Sylmar (Fig. 7). Failure was assumed as the lateral load carrying capacity of the bent dropped by 20% of the peak load.

5 RESULTS AND DISCUSSION

5.1 *Overall performance of the bents*

The retrofit was effective in increasing the seismic performance of the bent. Force-displacement hysteresis plots are presented in Figs. 8 and 9 for the as-built and retrofitted specimens respectively. The displacement ductility capacity of the as-built bent was 5.5 and the displacement capacity of the retrofitted specimen was 9.6. This is a 75% improvement in the displacement ductility. Figures 10 and 11 show the force-displacement hysteresis envelopes for the as-built and retrofitted specimens, respectively. The displacement is measured at the top of the bent, relative to the fixed footing. Measured force-displacement envelopes were idealized to elasto-plastic curves to calculate the displacement ductility of the specimen. The elastic portion of the curve starts at the origin and passes through the event at which the first column reinforcement yielded. Then the yield level was established by equalizing the area between the measured and idealized curves.

It is also noted that the peak lateral loads of both specimens were approximately equal. This indicates that there is no significant increase in the flexural capacity of the bent due to the column retrofit and thus no increase in shear demand on the columns compared to the as-built specimen.

5.2 *Measured strains*

The longitudinal and transverse strains of the reinforcement in the critical sections of both specimens

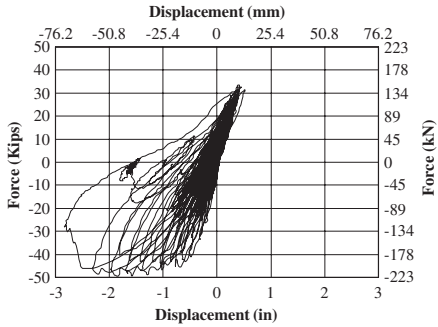

Figure 8. Accumulated force-displacement plot for B2DA.

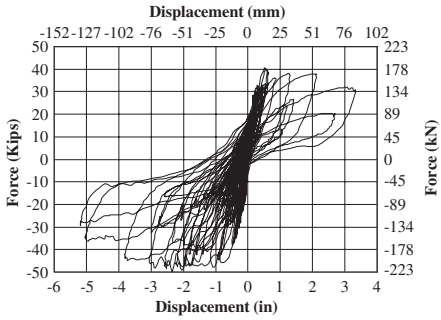

Figure 9. Accumulated force-displacement plot for B2DC.

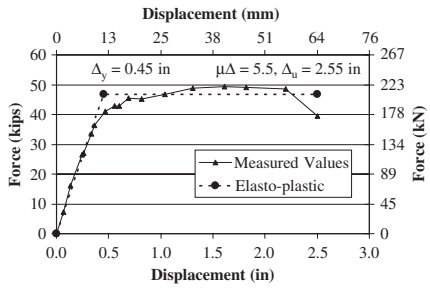

Figure 10. Force-displacement hysteresis envelope for B2DA.

are compared by using plots of strains versus peak displacement. The peak displacements measured from each run and its corresponding strains are plotted. The peak displacement was the maximum displacement of the specimen in the predominant direction of the earthquake.

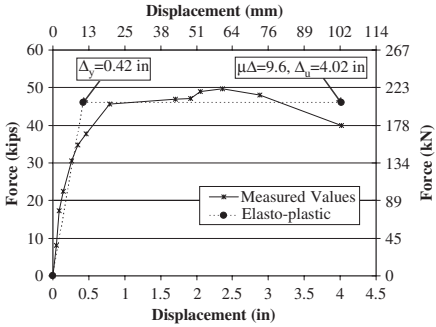

Figure 11. Force-displacement hysteresis envelope for B2DC.

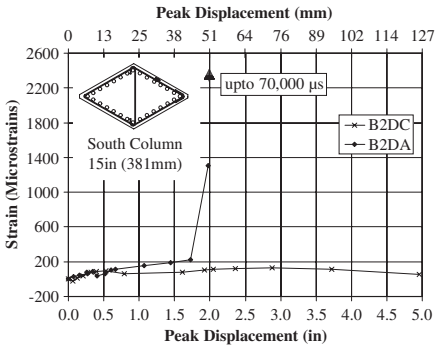

Figure 12. Strain in transverse steel at south column.

The tie bars at the top of the south column of the as-built specimen showed high strains during the last run which was consistent with the shear failure in the south column. But it is noted that the strains in the retrofitted column ties were very low and they remained low until the failure of B2DC (Fig. 12). This shows that the retrofit was successful in preventing shear failure of the south column. The strains in the CFRP jacket were very small and this justifies the fact that the column was in no danger of shear failure (Fig. 13). The north column tie bars had very small strains in both specimens (Fig. 14). This is consistent with the fact that no shear cracks were seen in the north column.

The longitudinal reinforcement in the columns had very high strains, exceeding yield strain in both specimens. The south column of B2DA had higher strains compared to the strains in the north column (Fig. 15). This is due the extensive plastic hinging in the south column which in turn caused the column to fail in shear. The strains in the longitudinal reinforcement in the beam of both specimens were similar (Fig. 16)

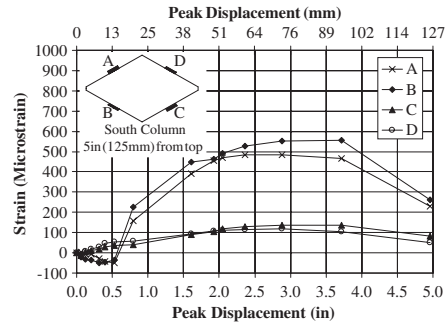

Figure 13. Strains in the CFRP jacket at south column.

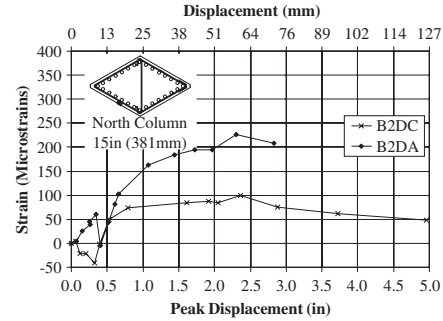

Figure 14. Strains in transverse steel at north column.

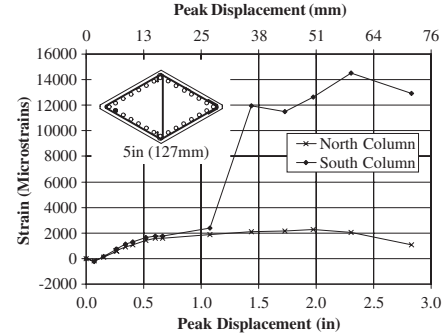

Figure 15. Strains in longitudinal reinforcement.

except that strains dropped in B2DC when the forces started shifting towards the joint.

The stirrups in the beam at the south and north end of both specimens had strains exceeding the yield

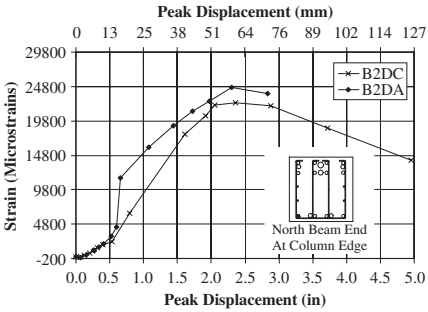

Figure 16. Strains in longitudinal steel at beam end.

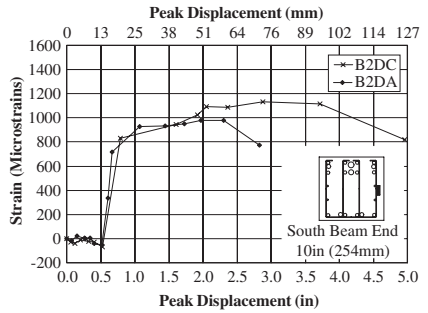

Figure 17. Strains in transverse steel at beam end.

strain. It was noted that the strains increased with displacement and then either dropped or remained the same (Fig. 17). This explains the formation of the shear cracks towards the joint region observed during testing as the input acceleration was increased. The shear cracks that formed during the initial runs did not widen or lengthen as new shear cracks formed closer to or at the joint and thus taking the stresses away from the existing cracks.

6 CONCLUSIONS

The following observations and conclusions were drawn from the experimental and analytical studies performed in the course of this research.

1. The measured displacement ductility capacity of the as-built bent was 5.5, which was substantially higher than the expected ductility capacity in substandard bridge bents.
2. The plastic hinge at the beam ends extended into the joint area during the latter events of the shake table test. This was because the joint was not fully rigid along its length due to the diamond shape of the column. This shift in plastic hinge controlled the increase in shear demand at the beam ends and thus prevented shear failure of the beam.
3. Unidirectional fibers in the CFRP jacket in the transverse direction did not increase the lateral load capacity of the bent and thus the shear demand in the columns. The stiffness of B2DA and B2DC were approximately the same.
4. The displacement ductility capacity of the retrofitted bent was 9.6. This is a 75% increase in displacement ductility to that achieved by the as built specimen. This confirms the effectiveness of this retrofit method to improve the seismic performance of the bent.
5. The CFRP jackets provided a large increase in shear capacity of the column and thus changed the mode of failure from shear failure of the column to failure of the beam-column joints.

ACKNOWLEDGEMENTS

The study presented in this paper was funded by grants from the Nevada Department of Transportation and Federal Highway Administration. The opinions expressed in this article belong solely to the authors and do not necessarily represent the view of others. The valuable support and comments of Mr. Bill Crawford, Mr. Troy Martin and other Bridge Division staff members are appreciated. The authors would also like to thank Dr. Patrick Laplace, Mr. Paul Lucas, Hoon Choi, Ersan Eldeleklioglu, and Jessica Gradick for their help in the construction and testing of the scaled columns. Mr. Ed Fyfe and Mr. Scott Arnold are thanked for their interaction in selection and application of the fiber reinforced plastic composites.

REFERENCES

California Department of Transportation, 1999. Memo to Designers 20-4 Attachment B, Engineering Services Center, Earthquake Engineering Branch, California, July 1999

Dong, G. 2003, Report on the analysis of Downtown Las Vegas Viaduct, A special project report submitted to Civil Engineering Department, University of Nevada, Reno

Johnson, N., Saiidi, M., and Itani, A., 2003, Seismic Retrofit of Octagonal Columns with Pedestal and One-Way Hinge at the Base, Civil Engineering Department, University of Nevada, Reno, Report No. CCEER-03-05

MacRae, G., Priestley, N., and Seible, F. 1994, Shake Table Tests of As-Built and Retrofitted Configuration, Report No. SSRP-94/18, Structural Systems Research Project, University of California, San Diego

Pantiledes, C., Gergely, J., Reaveley, L., and Volyy, V. 1999, Retrofit of RC Bridge Piers with CFRP Advanced

Composites, Journal of Structural Engineering, ASCE, Vol. 125, No. 10, pp 1094–1099
Pulido, C., Saiidi, M., Sanders, D., and Itani, A. 2001, "Seismic Performance and Retrofitting of Reinforced Concrete Bridge Bents", Report No. CCEER-01-xx, University of Nevada, Reno
Saiidi, M., and Mangoba, N. 2000, "Field Application of FRPs in Seismic Retrofit of a 16-Span Bridge with Flared Columns", 3rd International Conference, Ottawa, Ontario, Canada
Sexsmith, R., Anderson, D., and English, D. 1997, "Cyclic Behavior of Concrete Bridge Bents", ACI Structural Journal, Vol. 94, No. 2, pp 103–113
Seyed Mahan, M. 1999, "User's Manual for xSECTION", Version 2.40, California Department of Transportation, USA

FRP Composites in Civil Engineering – CICE 2004 – Seracino (ed)

Reinforced concrete squat walls retrofitted with carbon fiber reinforced polymer

Shyh-Jiann Hwang
Department of Construction Engineering, National Taiwan University of Science and Technology, Taiwan
National Center for Research on Earthquake Engineering, Taiwan

Tsung-Chih Chiou
Department of Construction Engineering, National Taiwan University of Science and Technology, Taiwan

Yaw-Shen Tu
Department of Civil Engineering, De Lin Institute of Technology, Taiwan

ABSTRACT: For seismically insufficient buildings, to retrofit the RC partition walls using the carbon fiber reinforced polymer (CFRP) is of particular interest at the present juncture in Taiwan after Chi-Chi earthquake. This paper describes theoretical and experimental studies related to the seismic retrofits of the RC frames containing walls using CFRP materials. Three "as built" RC frames with or without walls and two "retrofitted" RC frames with walls had been tested under simulated seismic actions. Experimental observations and theoretical analyses indicated that the shear resisting mechanism of the RC squat walls can be modeled as the struts and ties, and that shear strength of squat wall can be reasonably predicted by the softened strut-and-tie model. The test results of the retrofitted squat walls indicated that the CFRP with sufficient end anchorage is an effective retrofitting measure.

1 INTRODUCTION

The poor performances of the low-rise RC buildings with nonductile reinforcing details had been widely observed during the Chi-Chi earthquake. This simulates an urgent need of seismic assessment and retrofitting of these structures. However, seismic retrofitting of each component of the nonductile RC frames is extremely difficult and expensive. Fortunately, the existing low-rise buildings in Taiwan contain a lot of partition walls which are lightly reinforced RC walls. By retrofitting these walls as the lateral-force-resisting elements, the existing frames can be treated as members that are not proportioned to resist forces induced by earthquake motions. This retrofitting strategy may alleviate the strength and deformation requirements of a nonductile RC frame. Due to the greatly reduced cost, the retrofitting of the existing buildings with nonductile frames is more feasible.

Since these partition walls are detailed with temperature reinforcement only, which might result in insufficient strength. The common practice in Taiwan now is to tear down the partition walls then to recast with the RC structural walls. This retrofit scheme is time consuming and causes tremendous inconvenience to the residents. Seeking for the other alternative is of ever-increasing expectance.

The repair of understrengthed or damaged reinforced concrete members by the external bonding of carbon fiber reinforced polymer (CFRP) laminates is becoming increasingly popular in the construction industry. The use of CRFP laminates for this application offers several desirable attributes, such as high strength, resistance to corrosion, light weight, and ease of handling. Retrofitting the RC partition walls by the bonding of CFRP might be a feasible solution of the aforementioned problem.

This paper describes theoretical and experimental studies related to the seismic retrofits of the RC frames containing walls using CFRP materials. Experimental tests were conducted on wall specimens that were subjected to reversed cyclic inelastic deformations representative of earthquake loadings. Theoretical analyses, based on the softened strutand- tie model (Hwang and Lee 2002) and the ACI 318 building code (ACI 2002), were performed to evaluate the shear strength of the walls.

2 EXPERIMENTAL PROGRAM

2.1 *Test specimens*

In all, five large-scale isolated specimens, one frame and four walls, were tested. The test specimens are identified as PF, WF-12, WF-12-FV, WF-12-FHV, and WF-15. The dimensions and reinforcing details are given in Fig. 1. In order to focus attention on the failure behavior of walls, the ductile detailing requirements per ACI 318 building code (ACI 2002) was adopted for the design of frames for all specimens.

Specimen PF was a pure frame, which intended to draw a comparison between frame and wall. The details of Specimen PF, shown in Fig. 1 (a), were used repeatedly for the frames of the other wall specimens.

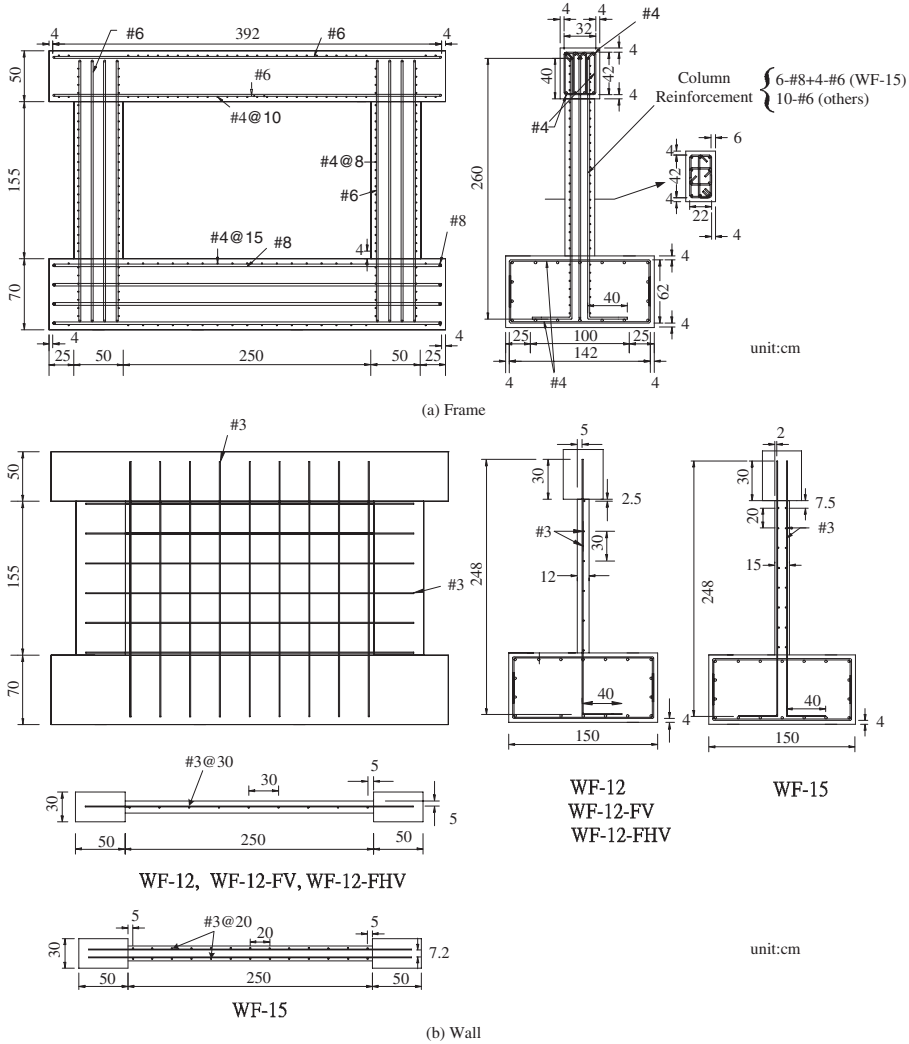

Figure 1. Geometry and reinforcement detail.

The test wall of Specimen WF-12 represented approximately 0.6 scale model of a prototype partition wall in a building. The test wall was 12 cm thick with 30 × 50 cm boundary elements. The overall length of the wall was 350 cm and the height was 155 cm. The vertical and horizontal reinforcement in the wall of Specimen WF-12 was 0.2 percent of the wall cross section [Fig. 1 (b)], which corresponded with the area of shrinkage and temperature reinforcement.

Specimens WF-12-FV and WF-12-FHV had the same existing wall dimensions as WF-12 but retrofitted with CFRP laminates. Specimen WF-12-FV was strengthened with four layers of CFRP laminates, two layers for each side of wall. The fibers of CFRP laminates for Specimen WF-12-FV were placed in the vertical direction and the thickness of each layer is 0.1375 mm. Total of eight layers of CFRP laminates were bonded to Specimen WF-12- FHV, four layers in the horizontal direction and four layers in the vertical direction. The end anchorages of the CFRP laminates were carefully considered and revealed in Fig. 2.

Specimen WF-15 contains a structural wall of thickness of 15 cm. The vertical and horizontal reinforcement in the wall of Specimen WF-15 was approximately 0.5 percent of the wall cross section [Fig. 1 (b)], which provided a threshold of the qualified wall behavior.

The test specimens were cast vertically in timber molds. Table 1 summarizes the material properties.

2.2 *Test setup and procedure*

The overall test setup is shown in Fig. 3. Horizontal load was applied with three double-acting servocontrolled actuators, 1000-kN capacity each. The top beams of the test specimens were clamped with two steel beams to simulate the mechanism that the lateral load is transferred from the strong diaphragm (Fig. 3). The footing was tied down to the test floor with 8 post-tension rods, and the horizontal movement of the footing was further restrained by two end reaction blocks. Fig. 4 presents the photo of the test setup in this study.

The specimens were subjected to a reversed cyclic loading based on displacement control. The loading

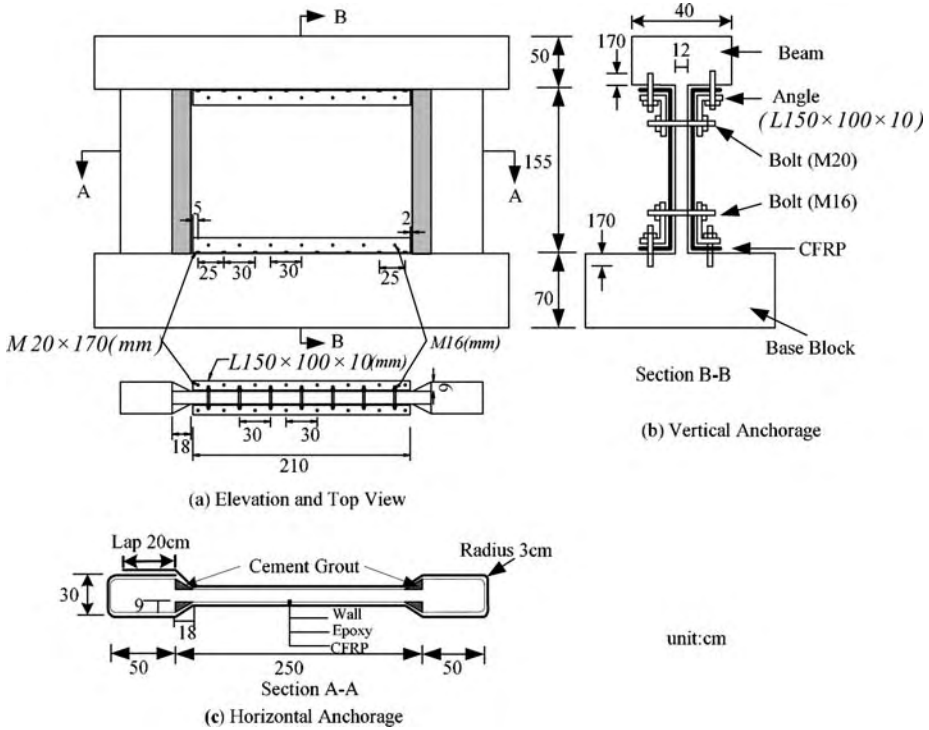

Figure 2. Detail of end anchorage of CFRP.

Table 1. Material properties.

Specimen	Concrete		Steel				CFRP (MRL-T7-250)		
	Wall & frame f'_c (MPa)	Base f'_c (MPa)	#3 f'_y (MPa)	#4 f'_y (MPa)	#6 f'_y (MPa)	#8 f'_y (MPa)	E_j (GPa)	f_{ju} (MPa)	ε_{ju} (%)
PF	22.8	23.4	–	443	571	466	–	–	–
WF-12	21.0	23.4	446	443	571	466	–	–	–
WF-12-FV	22.1	23.4	446	443	571	466	230	4102	1.8
WF-12-FHV	23.6	23.4	446	443	571	466	230	4102	1.8
WF15	22.6	23.4	446	443	571	466	–	–	–

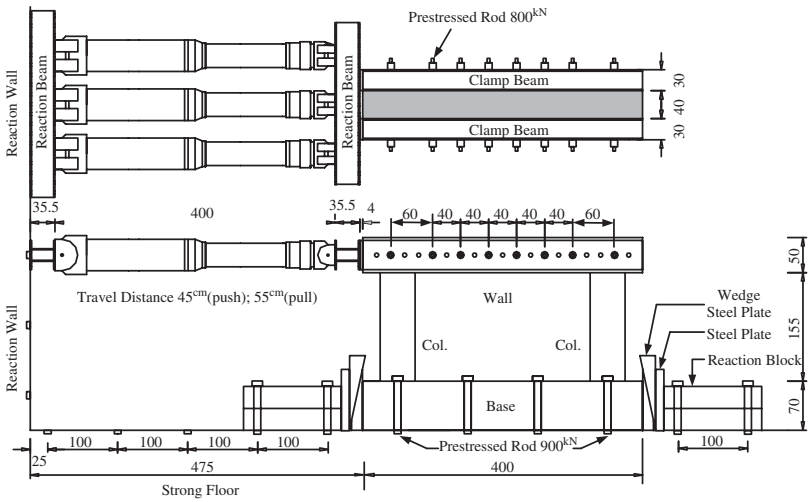

Figure 3. Schematic representation of the test setup.

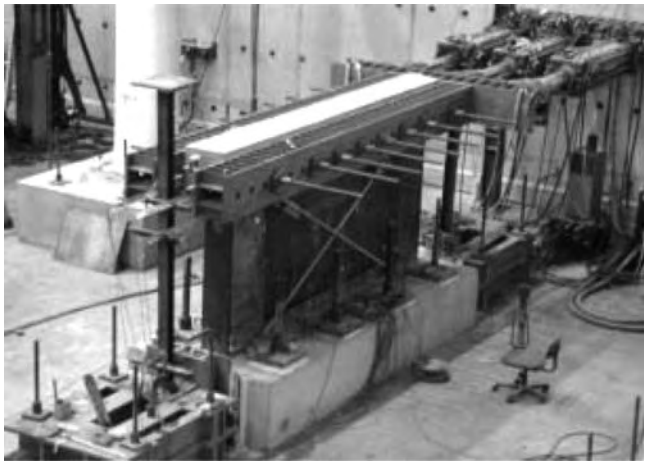

Figure 4. Photo of test setup.

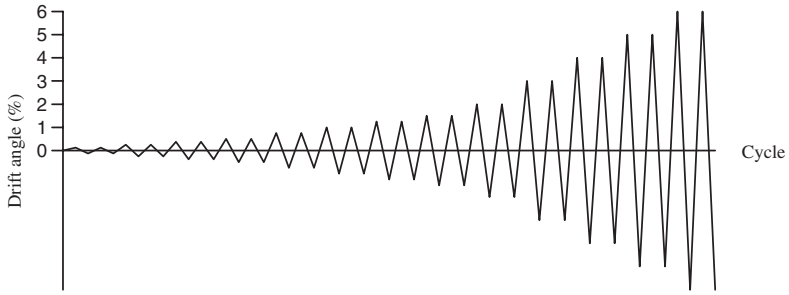

Figure 5. Loading history.

pattern for the specimens consisted of two cycles at lateral drift ratios, as shown in Fig. 5.

Applied horizontal forces were measured by calibrated load cells. Linear potentiometers were used to measure displacements. Strains in the reinforcement and CFRP were measured by means of electrical resistance strain gages.

3 OBSERVED BEHAVIOR

Horizontal force-displacement hysteretic response histories and final damage patterns for all specimens are shown in Fig. 6. All the test specimens were failed in shear. The failure mode of Specimen PF was the flexural shear failure of columns near the base. The failure mode of Specimens WF-12, WF- 12-FV and WF-12-FHV was the diagonal compression failure in the wall web due to shear. Specimen WF-15 was failed due to the interface shear at base.

Table 2 reports the peak measured strengths, P_{test}, as well as the calculated flexural strengths, P_y and P_n. Only the peak horizontal force of PF exceeded the calculated nominal flexural strength P_n. The maximum force-carrying capacities developed by other wall specimens were less than the calculated yield strength P_y, indicating insufficient shear strengths.

Figure 7 shows the envelopes of load-deflection response for all specimens. By comparing Figs. 7 (a) and (b), it is clearly shown that the partition wall could greatly enhance the stiffness and the strength of a RC frame. As revealed in Fig. 7, the retrofitted specimens WF-12-FV and WF-12-FHV developed much higher strengths than the as-built walls WF-12 and WF-15. The test results indicated that the retrofit of RC partition walls by the external bonding of CFRP laminates is quite effective.

Due to the nature of brittleness of the shear failures, the ductility issue is not pursued.

4 ASSESSMENT OF WALL SHEAR FAILURE

4.1 *Softened strut-and-tie model*

A rational model for determining the shear strength of shear walls for seismic resistance has been developed by Hwang et al. (2001). The proposed model, called the softened strut-and-tie model, is based on the concept of struts and ties and derived to satisfy equilibrium, compatibility, and constitutive law of cracked reinforced concrete. The proposed model adopts the softening behavior suggested by Zhang and Hus (1998) as the constitutive relationship of cracked reinforced concrete.

Three strut-and-tie load paths (Hwang et al. 2001) are proposed to model the force transfer within the wall, and they are the diagonal, horizontal, and vertical mechanisms as depicted in Fig. 8. The diagonal mechanism is a diagonal compression strut. The vertical mechanism includes one vertical tension tie and two steep compression struts, and the horizontal mechanism is composed of one horizontal tension tie and two flat compression struts. For diagonal comcompression failure, the shear strength of the wall is defined as the concrete compressive stress on the nodal zone reaching its capacity. The softened strut-and-tie model was found to reproduce the available test results of shear walls from the literature with reasonable accuracy (Hwang et al. 2001).

In order to facilitate the routine design, a simplified approach of the softened strut-and-tie model was also developed (Hwang and Lee 2002). It is found that the simplified model is a useful and practical tool for determining the shear strength of the walls failing in diagonal compressions. More details of the simplified softened strut-and-tie model are presented elsewhere by Hwang and Lee (2002).

4.2 *Evaluation of test results*

It was reported that the walls with a barbell or flanged section have a strength significantly higher than that

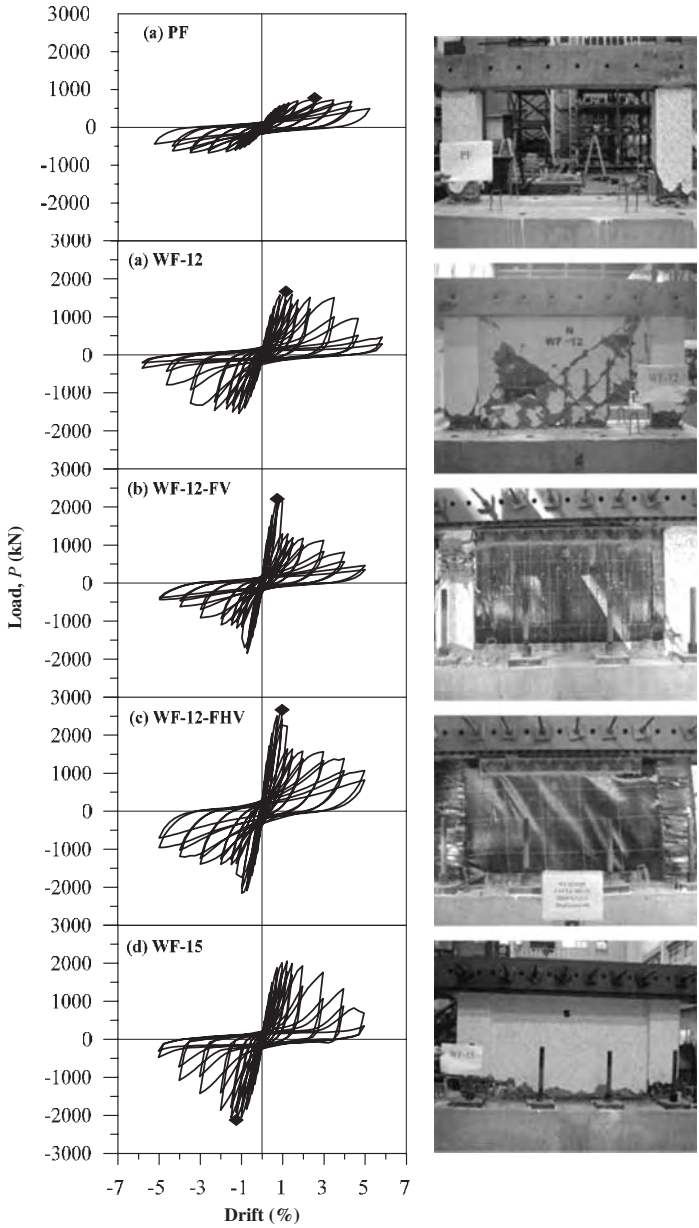

Figure 6. Load versus deflection responses and final damage patterns.

Table 2. Measured data and comparison.

Specimen	Measured P_{test} (kN)	Calculated P_y (kN)	Calculated P_n (kN)	Comparison: Softened strut-and-tie P_{SST} (kN)	Comparison: Softened strut-and-tie P_{text}/P_{SST}	Comparison: ACI 318-02 P_{ACI} (kN)	Comparison: ACI 318-02 P_{test}/P_{ACI}
PF	740.1	539	668.1	–	–	–	–
WF-12	1664	2789	3048	1352	1.23	912	1.82
WF-12-FV	2215	3149	4692	1797	1.23	925	2.4
WF-12-FHV	2669	3171	4670	1861	1.43	1368	1.95
WF-15	2122	3378	4260	2088	1.02	1671	1.27
				MEAN	1.23		1.86
				COV	0.12		0.22

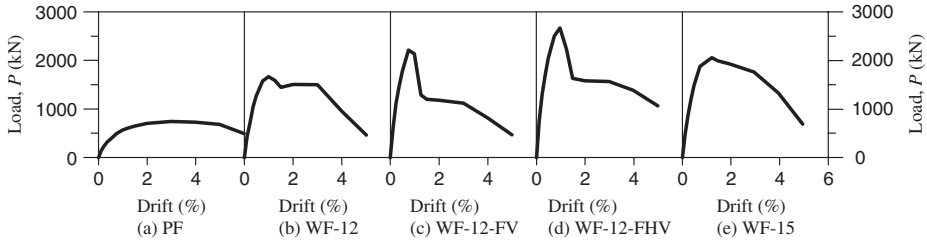

Figure 7. Envelopes of load-deflection response.

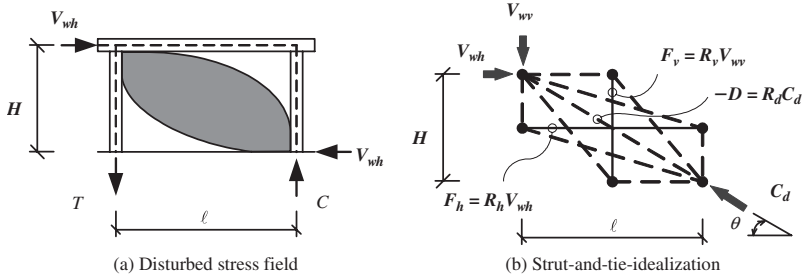

Figure 8. Softened strut-and-tie model.

of a rectangular section (Hwang et al. 2001). The higher strength for the wall with boundary elements is attributed to the improved end conditions of its diagonal strut provided by the compression boundary element. Web crushing usually occurs in the compressive struts that intersect the compression boundary element at the wall base. Therefore, load carried by crushed struts can be transferred to higher or lower struts depending on the stiffness of boundary element (Oesterle et al. 1984).

In light of above argument, the damage patterns of the boundary elements were clearly documented as shown in Fig. 9. The depth of the diagonal strut a_s of the softened strut-and-tie model is then defined as

$$a_s = \sqrt{a^2 + b^2} \tag{1}$$

where a is the depth of the compression zone at the base of the wall, and b is the depth of the compression zone provided by the boundary element. In this paper, a was determined by the sectional analysis for the stage when the extreme tensile steel reaches yielding, and b was estimated as (Hwang et al. 2004).

$$b = \frac{1}{5}\frac{h_b}{H_n t_w}\left(7 b_b h_b + \ell_n t_w\right) \le \frac{H_n}{2} \tag{2}$$

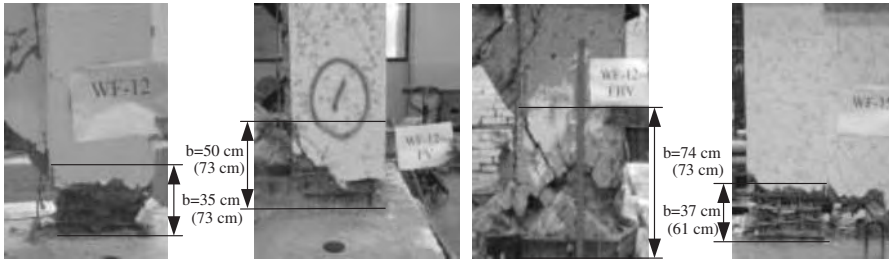

(a) WF-12 (b) WF-12-FV (c) WF-12-FHV (d) WF-15

Note: b = measured value(calculated value by Eq (2))

Figure 9. Damaged patterns of boundary elements.

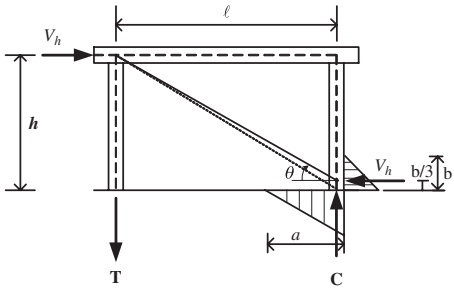

Figure 10. Angle of inclination for strut-and-tie modeling.

where h_b is the depth of the boundary element; b_b is the width of the boundary element; H_n is the clear height of wall web measured from the reaction beam to the wall base; t_w is the thickness of wall web; and ℓ_n is the clear length of the wall web in the direction of the shear force applied.

The angle of inclination θ of the diagonal compression strut becomes flatter due to the participation of the boundary element. According to Fig. 10, the value of θ is defined as

$$\theta = \tan^{-1}\left(\frac{h - b/3}{\ell}\right) \quad (3)$$

The shear strengths of test walls were calculated using the softened strut-and-tie model (P_{SST} in Table 2; Hwang and Lee 2002) and the ACI 318 method (P_{ACI} in Table 2; ACI 2002). For the prediction of the ACI 318 method, Eq. (21-7) was used and the strength reduction factor was taken as 1.0. The average strength ratio (P_{test}/P_{SST}) for the softened strut-and-tie model is 1.23 with a coefficient of variation (COV) of 0.12. The mean value and the coefficient of variation of the test-to-calculated shear strength ratio by ACI equations were found to be 1.86% and 22%, respectively (Table 2). As seen in Table 2, the softened strut-and-tie model (Hwang and Lee 2002) predicts the failure shears more accurately than the equation of the ACI 318 building code (ACI 2002).

5 CONCLUSIONS

The test results of the retrofitted squat walls indicated that the CFRP with sufficient end anchorage is an effective retrofitting measure. Experimental observations and theoretical analyses indicated that the shear resisting mechanism of the RC squat wall can be modeled as the struts and ties, and that the shear strength of squat wall can be reasonably predicted by the softened strut-and-tie model.

As an improvement to current wall retrofit design methodology, it is recommended that the softened strut-and-tie model be used to assess the shear strength of RC walls, and that the insufficient RC partition walls be retrofitted by using CFRP materials.

ACKNOWLEDGMENTS

This research study was sponsored by both the National Science Council and the National Center for Research on Earthquake Engineering of the Republic of China. The authors would like to express their gratitude for the support.

REFERENCES

American Concrete Institute (ACI). (2002), "Building Code Requirements for Structural Concrete," ACI 318-02 and Commentary (ACI 318R-02), Farmington Hills, Michigan.

Hwang, S. J., Fang, W. H., Lee, H. J., and Yu, H. W. (2001), "Analytical Model for Predicting Shear Strengths of Squat Walls," Journal of Structural Engineering, ASCE, Vol. 127, No. 1, January, pp. 43–50.

Hwang, S. J., and Lee, H. J. (2002), "Strength Prediction for Discontinuity Regions by Softened Strut-and-Tie Model," Journal of Structural Engineering, ASCE, Vol. 128, No. 12, December, pp. 1519–1526.

Hwang, S. J., Tu, Y. S., Yu, H. W. (2004), "Load Deflection Responses of Low Rise Reinforced Concrete Shear Walls," under preparation.

Oesterle, R. G., Aristizabal-Ochoa, J. D., Shiu, K. N., and Corley, W. G. (1984), "Web Crushing of Reinforced Concrete Structural Walls." ACI Journal, Vol. 81, No. 3, May–June, pp. 231–241.

Zhang, L. X. B., and Hsu, T. T. C., "Behavior and analysis of 100 MPa concrete membrane elements," Journal of Structural Engineering, ASCE, Vol. 124, No. 1, pp. 24–34 (1998).

FRP Composites in Civil Engineering – CICE 2004 – Seracino (ed)

Experimental study on the strengthening and repair of R/C wall-frame structures with an opening by CF-sheets or CF-grids

A. Kitano, O. Joh & Y. Goto
Graduate School of Engineering, Hokkaido University, Sapporo, Japan

ABSTRACT: In this study, the first story in a multi-storied reinforced concrete structural wall with openings was strengthened using carbon fiber sheets (CF sheets) and carbon fiber grids (CF grids). The effect of shear reinforcement and repair on earthquake resisting behavior were examined with a horizontal forcing experiment for several specimens having different opening positions and opening shapes. The maximum strength and deformability were improved by the CF grid reinforcement of the wall irrespective of opening positions, etc. The deformability was greatly improved by establishing vertical slits in the wall at the four corners of the opening, and reinforcing the columns and sleeve walls using CF sheets. It was possible to evaluate approximately the ultimate flexural and shear capacities of the test specimens in which the reinforcement method differs, by correlating with the fracture modes.

1 INTRODUCTION

Reinforced concrete structural walls overwhelmingly increase the share of the horizontal force in seismic force action in comparison with other members for high rigidity, and are not a negligible influence in the design of structural walls for the earthquake resistance of the whole structure. Therefore, it is desirable that the structural walls that are the original strength resistive members, show not only strength in earthquake action but can also be expected to show toughness and consequently high input energy absorption performance. We reported the possibility that reinforcing the opening with CF sheets could be expected to have a stiffening effect on those structural walls, having a window or door opening between the columns and a low shear capacity as designed according to previous Building Standards of Japan that had been applied until 1971. In this report, we examine new reinforcement methods using CF grids on walls and using CF sheets wrapped on flange walls separated by vertical slits set at the corners of window openings. The final purpose is to propose that the strengthening method produces both excellent strength and toughness in the wall-column structures by reinforcing the wall and adjacent columns.

2 TEST PROGRAMS

2.1 *Description of test specimens*

The configuration and bar arrangement are drawn in Figure 1. The list of test specimens and the mechanical properties of the materials are shown in Tables 1 and 2, respectively. The test specimens were assumed as the first story of a one-span structural wall in a three-story building, and were produced in a total of nine bodies reduced in models to about 1/3 size (the ten body minute in the test species). In these specimens, a total of six bodies, consisting of four bodies which had the window opening in the center of the wall and two bodies in which the (vertical) door opening was located in the column side as reported in a previous paper (Matsuura, 2002). The test specimens in this paper were the following: (a) a non-strengthened Specimen WA-04S-01 with a localization door opening (S-01), (b) Specimen WA-04S-RG that was repaired, after it gave a horizontal force to Specimen S-01 up to a drift angle R = about 10×10^{-3} rad, and the wall strengthened with a CF grid and the column with CF sheets (S-RG), (c) Specimen WA-04C-CWG (C-CWG) which had a center window opening and was strengthened in the same way as S-RG, (d) Specimen WA-04C-CW3s (C-CW3s) that had four vertical slits at the corners of the window opening and the columns and sleeve walls strengthened with CF sheets. The wall panels were 70 mm thick, had an inner width of 1600 mm, and an inner height of 1000 mm. An equivalent opening periphery ratio of 0.4 was established. The opening circumference was reinforced with reinforcing steel according to the AIJ-RC Standard (AIJ,1999). The cross sections of the columns on both sides were $200 \times 200\,mm^2$, and the inner heights were 1000 mm.

The column axial reinforcement was 10-D13 (SD345), hoops were 4f-@200 (expressed as a round bar of 4 mm in diameter and 200 mm spacing)

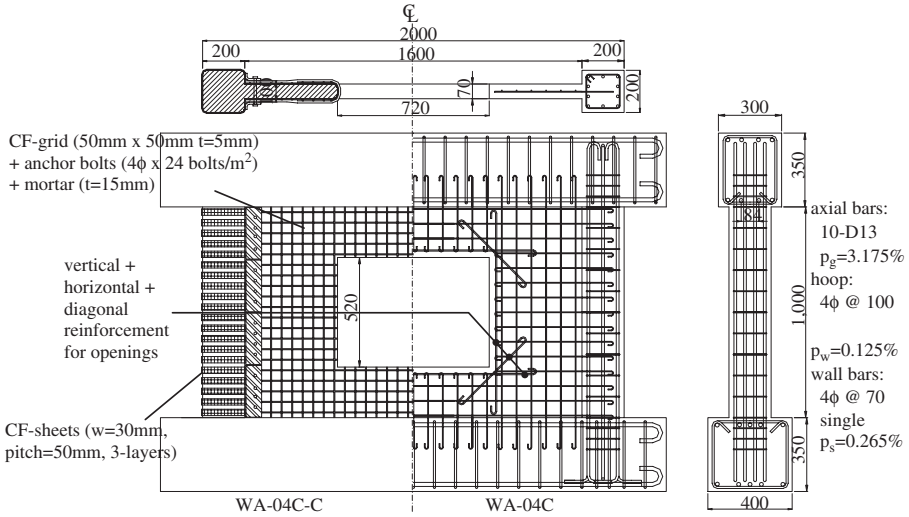

Figure 1a. Proportions and reinforcements of specimens.

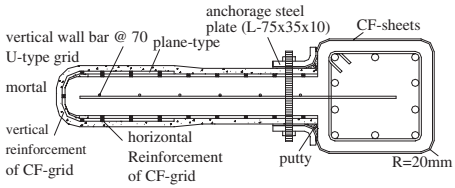

Figure 1b. Details of CF sheets and grids jacketing.

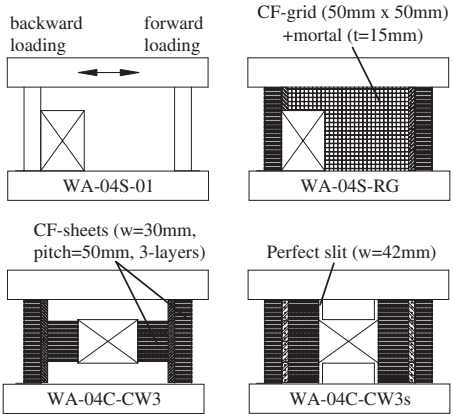

Figure 1c. Variables in four specimens.

(equivalent to SR295) and wall bars were arranged vertically and horizontally with 4f-@70 (SR295 equivalent, SR345 equivalent for Specimen C-CWG). The opening reinforcing bars were arranged with 2-6 f vertically, horizontally and diagonally. For Specimen S-RG, the severely flaking portions were replaced with a cross-section repairing material in the cement series, and the crack repair was carried out with epoxy series resin. As for the CF grid strengthening method of the wall of Specimens S-RG and C-CWG, firstly the wall surface was blasted for adhesion force security between the existing wall and the additional mortar. The CF grid was then fixed by steel anchors 4 mm in diameter and 200 mm apart on the wall surface. The mortar was sprayed on each side to a thickness of 15 mm. The total wall-thickness after the CF grid reinforcement was 100 mm. As for the CF sheet reinforcement method, after the surfaces of the concrete members had been blasted and chamfered, some epoxy-system backing-material was applied to the corner division (radius of 20 mm), and CF sheets of 30 mm width were stuck on after hardening using epoxy system resin at 50 mm intervals in three layers. The CF sheet was fixed using L form steel ($35 \times 75 \times 10$, outer size radius 20 mm) and M12 high strength bolts (@50 mm) in the wall edge. In Specimen C-CW3s, the vertical slits, starting at the four corners of the window opening in the wall, were established in order to separate perfectly the sleeve walls, the high waist-wall and the hanging wall. The columns and sleeve walls were reinforced using CF sheets.

Table 1. Variables of specimens.

Specimen	Opening conditions	Strengthening method	σ_B (MPa)
WA-04S-01	Door opening located	Non	17.5
WA-04S-R*	at bottom and left side	Repair + Column:S	25.5
WA-04S-CW3*	height = 720 mm	Column:S + Sleeve:S	23.5
WA-04S-RG	width = 520 mm	Repair + Column:S + Sleeve:G	21.8
WA-04C-00*	Window opening	Non	21.3
WA-04C-C3*	located at center	Column:S	24.6
WA-04C-CW3*	height = 520 mm	Column:S + Sleeve:S	21.8
WA-04C-CO3*	width = 720 mm	Column:S + Walls:S	22.6
WA-04C-CWG		Column:S + Sleeve:G	21.5
WA-04C-CW3s		Slits + Column:S + Sleeve:S	22.1

[Notes]*: reported in a previous paper, S: CF-sheets, G: CF-grids , Sleeve: sleeve-wall, Walls: two sleeve-walls + hanging-wall + high-waist-wall, σ_B: concrete strength, Repair: repaired cracks after pre-loading.

Table 2. Properties of materials.

Steel bar	Grade	Yield stress (MPa)	Yield strain (μ)	Young's modu. (GPa)	Elongation (%)
Column bar: D13	SD345	399	2020	194	20.3
Hoop & wall bar: 4ϕ	SR295	393	1990	195	24.2
Wall bar(C-CWG): 4ϕ	SR345	529	4780	189	9.7
Opeing reinforcement: 6ϕ	SR295	357	1760	201	20.8
CFRP	Tens. Strength (MPa)	Young's modu. (GPa)	Elongation (%)	Thickness for design (mm)	Sectional area (mm^2/string)
Carbon fiber sheet*	3480	230	1.5	0.111	–
Carbon fiber grid*	1400	100	1.5	–	26.5
Polymer mortal (example)	Comp. Strength σ_B (MPa)	Tens. Strength (MPa)	Bond strength (MPa)	Young's modu. at σ_B/3 (GPa)	Young's modu. at σ_B2/3(GPa)
WA-04S-RG	36.6	9.18	1.88	11.4	10.2
WA-04C-CWG	46.5	9.06	1.94	11	9.9

[Note]*: all values exhibited on catalog.

2.2 *Loading method*

Repeated static horizontal loads with displacement increments were applied at loading heights equivalent to a shear-span ratio of 1.13 in order to reproduce the first-story stress-diagram in a three-story structural wall which receives uniform horizontal forces at each floor. A constant axial force which corresponded to an axial force ratio of 1/6 ($=\sigma_0/\sigma_B$) was applied to both column heads. The loading program was one time forward and backward loading at $R = 0.5 \times 10^{-3}$ rad (hereafter, '$\times 10^{-3}$ rad' is omitted), and twice repeated forward and backward loadings at R = 1, 2, 5, 10, 15, 20, 25, where R was the story drift-angle measured between the top of the lower reaction-beam and the bottom of the upper loading-beam. Additional loading was then carried out at R = 30, 35, 40 for specimens which had relatively small damage.

3 EXPERIMENTAL RESULTS AND CONSIDERATIONS

3.1 *Destruction*

The loading system and common names for each part are shown in Figure 2. The final distraction of each specimen is shown in Figure 3. The whole deformations of the strengthened specimens at the ultimate stage (R = 30.0) are shown in Figure 4.

S-01 (forward loading): Shear cracks of the sleeve wall and of the lower part in the compressive column widened at R = 5.1, and lateral reinforcements of the wall and column around these cracks yielded. Finally, just after the specimen reached maximum strength, the lateral resistance rapidly lowered by shear failure around such yield positions.

S-01 (backward loading): In the whole sleeve wall, shear cracks were generated in great numbers, the

specimen reached maximum strength at R = 8.3, and the lateral resistance lowered by widening of these cracks. Another shear crack widened in the lower part of the independent column, which was in the compression side and without a sleeve wall, and the hoop near the shear crack yielded at maximum strength.

S-RG (forward loading): A horizontal bending crack starting from the opening side was generated at the bottom of the sleeve wall, and the main bars of the tensile column and vertical reinforcement in the bottom of the sleeve wall yielded. After that, the wall-column structure was rotated around the bottom of a compressive column. The displacement increased while the lateral resistance was maintained at an almost constant value, reaching its maximum strength at R = 19.3. In the region beyond the maximum strength, the compressive column collapsed, and the bottom of the sleeve wall and compressive column started sliding in the loading direction. The lateral resistance lowered.

S-RG (backward loading): The main bars of the tensile column yielded at R = 5.1, and the specimen reached maximum strength. The vertical boundary line

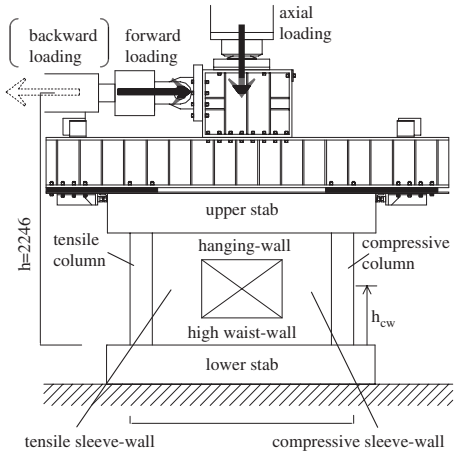

Figure 2. Schema of loading system.

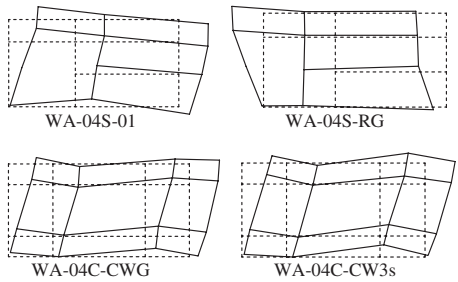

Figure 4. In-plane deformations of specimens at drift angle of 0.03 radian.

WA-04S-01

WA-04S-RG

WA-04C-CWG

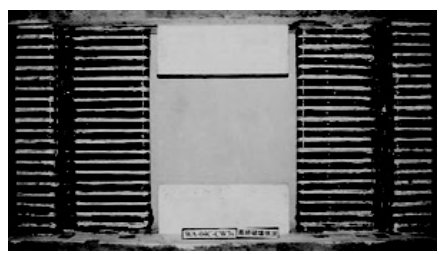

WA-04C-CW3s

Figure 3. Final failure of each specimen.

between the tensile column and the sleeve wall began to open in the forward loading under the effect of the bending crack that occurred at the bottom of the sleeve wall along the stub. The whole sleeve wall then started sliding in the loading direction, and the lateral resistance lowered. The CF sheet around the lower part of the tensile column broke due to this effect, and degradation of the lateral resistance increased, since the tensile column also started sliding with the sleeve wall in the loading direction.

C-CWG (forward and backward loadings): The main bars of the lower part in the tensile column yielded at R = 5.0, and the stiffness reduced. Bending cracks along the top and bottom stubs widened, the strain of the vertical wall bars increased, and the specimen reached maximum strength at R = 14.1. Afterwards, the concrete in the vicinity of the opening corner crashed by compressive stress. Consequently the right and left columns with the sleeve wall were deformed in bending separately to each other. The lateral resistance lowered with the progress of this collapse. The compressive column and sleeve structure wall then began to slip as with a one-body structure (without separation at the boundary between the column and the sleeve wall) in the loading direction at R = 20.0 along the bending cracks which occurred laterally at the top and bottom stubs.

C-CW3s (forward and backward loadings): bending cracks produced laterally along the bottom stub in the sleeve wall of the compression side and the top stub in the sleeve wall of the tension side, opened remarkably. The column and sleeve wall-structure in each side was deformed in bending as a one-body structure, and reached its maximum strength at R = 15.2. Afterwards, the sleeve walls near the top and bottom stubs collapsed, and the lateral resistance was gradually lowered.

3.2 *Deformation vs. load relationship*

Comparison of the envelope curves for all specimens is shown in Figure 5.

3.2.1 *Strengthening effect of structural walls with an asymmetric door opening*

The initial stiffness of repaired specimens S-RG and S-R lowered a little in comparison with that of the undamaged specimens, but remarkable differences in the initial stiffness could not be observed in all specimens. The maximum strengths of strengthened specimens in both the forward and backward loading directions were higher than those of the non-strengthened specimen S-01 without relation to repair and non-repair. Therefore, it can be said that when CF sheet strengthening of the columns is minutely carried out, the shear fracture in the early stages of the column can be prevented and lateral resistance increased.

In forward loading, S-RG maintained its lateral resistance higher than that of S-R by large deformation, while the maximum strength of S-R decreased by shear fracture of the sleeve wall at R = 10.0. These behaviors were caused by the effect in which the whole wall-column frame deformed in flexure and rotated around the bottom of the compressive column, since the CF grid strengthening of the walls prevented shear cracks widening of the sleeve walls of S-RG, and consequently raised the rigidity. In comparison with S-RG

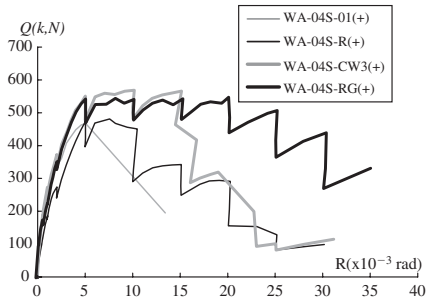

(a) Asymmetric door opening type under forward loading

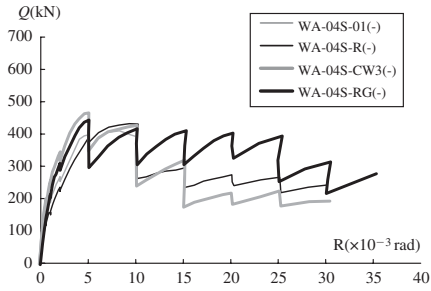

(b) Asymmetric door opening type under backward loading

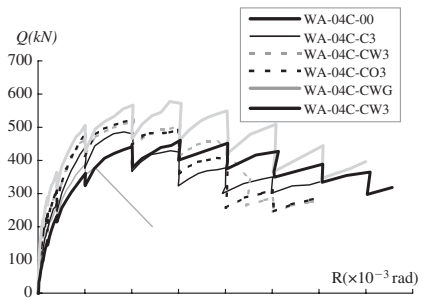

(c) Window opening type in wall center

Figure 5. Lateral load and drift angle relationships.

and S-CW3, the reduction of lateral resistance of S-RG caused by the bending crush around the lower part of the compressive column, was small even at R = 25.0, while the lower part of the compressive column in S-CW3 could not keep yielding and collapsed in bending crush at R = 15.0 which rapidly caused lateral resistance lowering. This performance of S-RG was the effect of the additional plastered mortar in the CF grid strengthening work, and was because the share of the bending compressive force by the sleeve wall, increased.

Lateral resistance rise of the strengthened specimens against the non-strengthened specimens in backward loading, was less than that in forward loading. This was due to the sleeve wall sliding in the opening side along the diagonal shear crack-line in the sleeve wall for S-R, and along the lateral-bending crack at the bottom of the sleeve wall for S-CW3 and S-RG after dividing at the boundary between the column and wall. Especially, since breaking the column CF sheets caused not only wall sliding but also column sliding for S-CW3 and S-RG, improvement in the strengthening method for sliding is a future problem.

3.2.2 *Strengthening effect of walls with a center window opening*

In C-CW3s, the initial stiffness lowered most in all specimens, because the wall was divided into four parts by the slits and a diagonal compression strut in the wall was not formed. Specimens C-CW3 and C-CO3 were able to prevent shear-crack widening in the strengthening portions. However, there was not a large improvement in lateral resistance and deformability, since the shear fracture in the non-strengthening portions progressed. The whole wall of Specimen C-CWG was strengthened by the CF grids and the wall shifted to the flexure fracture mode, since shear crack widening in the wall was prevented. Consequently, there was a rise of 18.9% at maximum strength, high lateral resistance was maintained in the large deformation, and there was an improvement in the deformability. When C-CW3s was compared with other strengthened specimens, although the maximum strength lowered, the mechanical properties of the sleeve wall and column structures became that of a one-body structure in each side by the slits set up at the four corners of the window opening. Therefore, the lateral resistance at R = 25.0 was the highest after C-CWG among all the specimens, and the deformability in large deformation was the best.

3.3 *Comparison between measured and calculated maximum strengths*

Table 3 shows the measured horizontal force and story drift-angle at maximum resistance with the calculated values.

3.3.1 *Ultimate flexural strength of RC structural wall* ${}_BQ$

${}_BQ$ is defined by Equation 1 as the minimum value between the ultimate flexural capacity of structural walls calculated as a one-body structure ${}_BQ_w$ (JBDPA, 2001) and the flexural capacity summing capacities of the columns and of the sleeve wall ${}_BQ_{cw}$.

$$ {}_BQ = \min\left[{}_BQ_w \ , \ {}_BQ_{cw} \right] \tag{1} $$

Ultimate bending capacity of RC column-wall structure evaluated as one-body system${}_BQ_w$ is defined by the following:

$$ {}_BQ_w = \frac{M_u}{h}, $$
$$ M_u = a_t \cdot \sigma_y \cdot l_w + \beta \cdot a_w \cdot \sigma_{wy} \cdot l_w + 0.5N \cdot l_w, \tag{2} $$

where,

β: factor according to opening location
h: reflection height of one-body system (mm) (=height of lateral loading, see Figure 2)
a_t: total cross-sectional area of column bars (mm^2)
σ_y: yield stress of column bars (N/mm^2)
σ_{wy}: yield stress of wall bars (N/mm^2)
a_w: total cross-sectional area of vertical wall bars (mm^2)
l_w: distance between both columns (mm)
N: column axial force (N)

Ultimate bending capacity of RC column-wall structure summing capacities of column-sleeve wall system ${}_BQ_{cw}$ is defined by the following:

$$ {}_BQ_{cw} = \sum {}_BQ_{cw}' $$

for door opening located eccentrically,

$$ {}_BQ_{cw} = {}_BQ_{cw}' + {}_BQ_c $$

for window opening located in center,

$$ \text{where, } {}_BQ_{cw}' = \frac{M_u}{h_{cw}} $$
$$ M_u = a_t' \cdot \sigma_y \cdot l_w + 0.5 \cdot a_w \cdot \sigma_{wy} \cdot l_w + 0.5N_e \cdot l_w \tag{3} $$

h_{cw}: reflection height of column with sleeve wall (mm) (it appears at mid-height of the column normally, see Figure 2),
a_t': vertical cross-sectional area in virtual column (mm^2),
N_e: column axial force considering with variable axial load (N).

A virtual column of which the width and depth were equal to the wall-thickness and column depth respectively, was established in the opening side of the sleeve wall, as shown in Figure 6, and ${}_BQ_{cw}$ was calculated using Equation 3. The height of the reflection point of the column with the sleeve wall, was evaluated as the height of the reflection point calculated in the portal

Table 3. List of experimental maximum strengths and calculated ultimate strength.

Specimen	σ_B (MPa)	r	Q_{exp} (kN)	R ($\times 10^{-3}$ rad)	${}_BQ_w$ (kN)	${}_BQ_{cw}$ (kN)	${}_BQ$ (kN)	${}_SQ_h$ (kN)	${}_SQ$ (kN)	Q_{cal1} (kN)	$\frac{Q_{exp}}{Q_{cal1}}$	Q_{cal2} (kN)	$\frac{Q_{exp}}{Q_{cal2}}$	Failure mode
WA-04S-01(+)	17.5	0.86	467	5.1	500	580	500	383	402	383	1.22	402	1.16	Shear failure in C&S
WA-04S-01(−)		0.76	410	8.3	522	506	506	339	341	339	1.21	341	1.20	Shear failure in S
WA-04S-R(+)	25.5	0.86	481	7.6	553	636	553	451	553	451	1.07	553	0.87	Shear failure in S
WA-04S-R(−)		0.76	432	9.3	555	566	555	399	488	399	1.08	488	0.88	Shear failure in S
WA-04S-CW3(+)	23.5	0.86	568	10.2	533	692	533	710	644	533*	1.07	533*	1.07	Bending failure of whole wall
WA-04S-CW3(−)		0.76	466	5.1	544	507	507	627	547	507*	0.92	507*	0.92	Sliding failure at wall bottom
WA-04S-RG(+)	21.8	0.86	547	19.3	523	651	523	835	721	523*	1.05	523*	1.05	Bending failure of whole wall
WA-04S-RG(−)		0.76	443	5.1	545	515	515	738	596	515*	0.86	515*	0.86	Sliding failure at wall bottom
WA-04C-00(−)	21.3	0.59	389	5.0	534	562	534	285	353	285	1.36	353	1.10	Shear failure in C&S
WA-04C-C3(−)	24.6	0.59	486	9.2	551	581	551	304	476	304	1.60	476	1.02	Shear failure in S
WA-04C-CW3(−)	21.8	0.59	516	10.1	537	565	537	477	512	477	1.08	512	1.01	Shear failure in hanging wall
WA-04C-CO3(−)	22.6	0.59	523	10.2	541	569	541	482	519	482	1.09	519	1.01	Shear failure in S
WA-04C-CWG(−)	21.5	0.59	578	14.1	543	571	543	587	552	543*	1.06	543*	1.06	Bending failure of whole wall
WA-04C-CW3s(−)	22.1	0.59	461	15.2	538	479	479	479	515	479*	0.96	479*	0.96	Bending failure of C&S
								Average			1.12		1.01	
								Standard deviation			0.19		0.11	

*: Values show ${}_BQ$

$Q_{cal1} = \min \cdot [{}_SQ_h, {}_BQ]$, $Q_{cal2} = \min \cdot [{}_SQ, {}_BQ]$

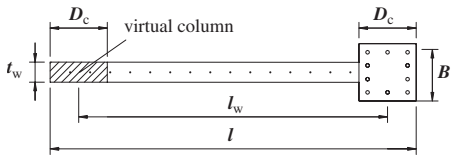

Figure 6. Notation of column with sleeve wall.

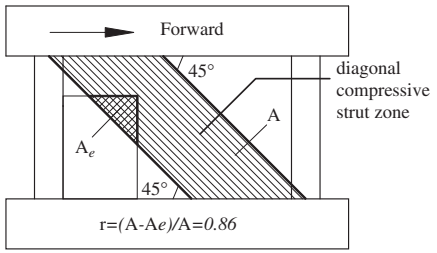

Figure 7. Evaluation of decreasing ratio by opening.

frame consisting of the columns with and without the sleeve wall and the beam with a hanging wall, by using the D-value Method. However, the height of the reflection point was reduced considering the rigid zone in the height direction and appeared by the high-waist-wall for the center window-opening specimen without the slits.

3.3.2 *Shear capacity based on Hirosawa's modified equation ${}_sQ_h$ (AIJ, 1990)*

${}_sQ_h$ was obtained by multiplying a reduction factor gamma γ to the shear capacity without any opening. The factor was defined as $(1 - A_e)/A$, where A_e was the area which the opening occupied in the compressive diagonal strut zone, and A was the area of the compressive diagonal strut zone, as shown in Figure 7. The CF grid strengthened specimens S-RG and C-CWG seemed to change from the shear fracture mode to the flexure fracture mode, since the shear capacity increased highly by the arch mechanism caused by the mortar used in the CF grid reinforcement, in addition to the increase of the shear capacity in the truss mechanism by the CF grid itself. The compressive strength of the concrete was then estimated as the weighted-average compressive strength of the existing wall-concrete and additional mortar in consideration of the weight given at both cross sectional areas, and shear-capacity increment by the arch mechanism of the concrete included in Equation 4.

$$ {}_sQ_h = r \cdot \left\{ \frac{0.068 \cdot p_{te}^{0.23} (\sigma_B + 17.7)}{\sqrt{M/(Q \cdot D)} + 0.12} + 0.85\sqrt{p_{wh} \cdot \sigma_{sy} + \alpha \cdot p_{wf} \cdot \sigma_f} + 0.1\sigma_0 \right\} b_e \cdot j \quad (4) $$

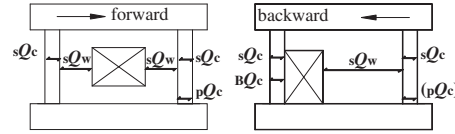

Figure 8. Relationship of shear capacities Q and their positions.

where,

p_{te}: reinforcement ratio of column axial bars ($= a_t/b_e \times l_w$),

p_{wf}: reinforcement ratio of CF sheets or CF grids ($= a_f/b_e \times x_f$),

x_f: spacing of CF sheet or CF grid (mm),

a_f: cross-sectional area of CF sheets or CF grids (mm^2),

b_e: equivalent thickness of wall-column structure (mm),

j: moment arm $= l_w$

σ_f: tensile strength of CF sheets or CF grids (MPa),

σ_B: equivalent compressive strength of concrete with polymer mortal (MPa),

σ_w: axial stress ratio of equivalent cross-section (MPa),

α: reduction factor for opening defined by Figure 7.

3.3.3 *Shear capacity based on summation of shear strengths of all resistant members ${}_sQ$*

${}_sQ$ was defined in the following so that the calculation formula would correspond to the strengthened position. The strengthening method and fracture pattern of each test specimen, and the relationship between each Q and its member is shown in Figure 8.

In the case of walls with a central opening:

$$ {}_sQ = [\,{}_sQ_c + {}_sQ_w\,]\text{tension} + \min[({}_pQ_c + {}_sQ_w), ({}_sQ_c + {}_sQ_w)]\text{comp.} \quad (5) $$

In the case of walls with an asymmetric opening:

$$ {}_sQ = \min[({}_sQ_c + {}_sQ_w), ({}_pQ_c + {}_sQ_w)]\text{column with sleeve wall} + \min[{}_bQ_c, {}_sQ_c]\text{independent column} \quad (5)' $$

where,

${}_sQ_c$: the shear capacity of the strengthened columns calculated from Hirosawa's Modified Equation (AIJ, 1990),

${}_sQ_w$: shear capacity of walls without columns calculated from the following equation (JBPDA, 2001),

$$ {}_sQ_w = [\,\sigma_B/20 + 0.5\,(p_s \times \sigma_{sy} + \alpha \times p_f \times \sigma_f)] \times t_w \times l_w \quad (6) $$

α: 1/10, which was assumed from the wall-sheet strain measured at the maximum resistance,
${}_pQ_c$: punching shear-strength of the side columns,

$$ {}_pQ_c = \tau_{min} \times \sigma_0 \times b_e \times D \quad (7) $$

${}_bQ_c$: flexural capacity of independent column (AIJ, 1900),

The calculated shear-capacities Q_{cal1} and Q_{cal2} of each specimen were defined by the following:

$$ Q_{cal1} = \min [{}_bQ, {}_sQ_h], \quad Q_{cal2} = \min [{}_bQ, {}_sQ] \quad (8) $$

It was possible that the calculated values Q_{cal1} and Q_{cal2} agreed with experimental values as well as the calculated fracture modes determined using Equation 8 since they corresponded to the experimental fracture modes. It was possible that the maximum strength of the specimens that failed in flexure, could be estimated approximately by Equation 1. The shear capacity of C-CW3s with the slits could be estimated by Equation 3 because it had a flexure fracture pattern. Equation 4 had no good correspondence to specimens of the shear-fracture type, since the representation in the equation does not include the effect of CF sheets on column strengthening. Therefore the calculated shear-capacity of C-C3 did not show good results. In the meantime, when the shear capacity was calculated using Equation 5, the increase in maximum strength caused by differences in the reinforcement position was evaluated, and good correspondence was shown.

4 CONCLUSIONS

We investigated by experimental tests, the development of a new method using carbon fiber sheets or grids to strengthen existing RC structural walls which were framed by strong beams and columns with weak shear capacity and which had a window opening in the wall center or a door opening beside one column asymmetrically. The test results conclude as follows.

(1) The strengthening method covered by CF-grids and polymer mortar on whole surfaces of walls in a frame, shifted the shear-fracture mode to the flexure-fracture mode, regardless of the asymmetry of the opening, since shear-crack widening in the walls was prevented. Thus, lateral shear-capacity and deformability of the wall structure could be improved.

(2) When the wall with a central window opening was set up with vertical slits at the four corners of the window opening and both the sleeve wall and column structures separated by the slits were strengthened by CF sheets, maximum strength and stiffness of the new structures became lower. However bending deformation that appeared individually in each of the sleeve wall and column structures predominated and the deformability was largely improved.

(3) The ultimate flexural-capacity of structural walls with an opening could be evaluated from the minimum value between the flexural capacity as a one-body structure and a calculated value summing the flexural capacities of the columns with the sleeve wall.

(4) The ultimate shear-capacity could be evaluated by summing the minimum shear capacities of the columns and the sleeve walls, because of estimating the strengthening effect of each member using CF sheets or grids.

ACKNOWLEDGMENTS

This study was subsidized by the Ministry of Education, Culture, Science and Technology (Grant-in-Aid for Scientific Research (A)(2), Subject No. 15201035). Nittetsu Composite Co., Ltd. provided financial supports and the FRP sheets and grids used for the experiment. Sapporo Sunkit Co., Ltd. repaired some specimens without compensation. We would like to express our deepest gratitude for this support.

REFERENCES

AIJ (Architectural Institute of Japan), 1990. Potential Resistance and Deformability on Seismic Design of Buildings, Tokyo, AIJ

AIJ (Architectural Institute of Japan), 1999. AIJ Standard for Structural Calculation of Reinforced Concrete Structures – Based on Allowable Stress Concept-. Tokyo, AIJ

JBDBA (Japan Building Disaster Prevention Association), 2001. Standard for Aseismic Diagnosis of R/C Existing Buildings and Guidelines for Rehabilitation of them. Tokyo, JBDPA

Matsuura, M., Kitano, A.,Goto, Y. and Joh, O. 2002. Experiment on Seismic Strengthening R/C Structural Walls with an Opening by Carbon Fiber Sheets. Proceedings of the Japan Concrete Institute 24(2): 1249–1254

Strengthening of beam-column joints

FRP Composites in Civil Engineering – CICE 2004 – Seracino (ed)
© 2005 Taylor & Francis Group, London, ISBN 90 5809 638 6

Evaluation of wrap thickness in CFRP-strengthened concrete T-joints

A. Parvin & S. Wu
Department of Civil Engineering, The University of Toledo, Toledo, OH, USA

ABSTRACT: This paper presents the results of a numerical study on the carbon fiber reinforced polymer (CFRP) wrapped beam-column joints subjected to axial and lateral cyclic loads. The numerical models include the beam-column joints wrapped with two, four, and six layers of CFRP fabric. The results showed the greatest improvement in ductility and strength for the beam-column joint with six layers of CFRP.

1 INTRODUCTION

The use of fiber composite wraps for concrete structures with damage or with insufficient reinforcement has been recognized as an effective upgrade technique to increase the strength and to extend the service life of the structures. Traditional methods of retrofitting beam-column joints include pressure epoxy injection into cracks under steel plates (Adin et al. 1993), steel and concrete jacketing (Alcocer & Jirsa 1993), and plain or corrugated steel jackets (Beres et al. 1992, Ghobarah et al. 1997). However, in recent years, fiber composites have received significant attention as a replacement for steel material both in new construction and existing structures. Comparing with traditional rehabilitation techniques, fiber composites or fiber-reinforced polymer (FRP) have high strength-to-weight ratio, superior resistance to corrosion, flexibility in design and replacement, and reduced life cycle cost. Furthermore, FRP reinforcement of structural members offers a means to protect the infrastructure from seismic damages by providing enhancement in strength and ductility. At present, the studies on application of composite materials for seismic strengthening of beam-column joints are limited (Mosallam 2000, Granata & Parvin 2001, Gergely et al. 2000, Antonopoulos & Triantafillou 2003), as compared with extensive investigations on FRP strengthened beam or column members. The goal of this research is to study the behavior of beam-column joints externally reinforced with CFRP wraps subjected to axial and lateral cyclic loads using nonlinear finite element analysis. The software MARC-MENTAT 2001 was employed for the numerical analysis study. In the following sections, the maximum lateral load and displacement results of the control joint model are compared with those of CFRP wrapped beam-column joints in order to observe the effect of wrap thickness.

2 FINITE ELEMENT ANALYSIS STUDY

2.1 *Description of model*

Four models were considered in the numerical study: one was the control model and the other three were CFRP wrapped exterior beam-column joints with various wrap thicknesses under combined axial and lateral cyclic loads. The column and the beam cross-section and height dimensions are $127 \times 127 \times 1067$ mm ($5 \times 5 \times 42$ in) and $76 \times 127 \times 610$ mm ($4 \times 6 \times 24$ in), respectively. For all beam-column joints, the strength of concrete is 27.6 Mpa (4,000 psi), with the modulus of elasticity of 20,690 Mpa (3×10^6 psi), and Poisson ratio of 0.17. The rebar strength is 414 Mpa (60,000 psi) with modulus of elasticity of 206,896 Mpa (3×10^7 psi), Poisson ratio of 0.3, and yield strain of 0.002. Concrete or steel is considered as isotropic materials. The CFRP is unidirectional, orthotropic elastic material with 0.18 mm (0.007 in) thickness per layer; the modulus of elasticity along the fiber direction and Poisson's ratio are 4,1379 Mpa (6×10^6 psi) and 0.22, respectively; the ultimate strain of CFRP is 0.016. An axial load value of 110 kN (25,000 lb), equivalent to $0.25 Agf'c$ and a cyclic lateral load sequence are applied to the top of the column.

2.2 *Control model of exterior beam-column joint (Model 1)*

Figure 1 represents a typical control beam-column joint. The column and the beam were modeled by 1325 and 528 three-dimensional solid brick elements, respectively. The total number of solid elements was 1753. The bottom of the column and the end of the beam were pinned (Figure 2). Three reinforcement types, namely four 9.525 mm (3/8 in) diameter

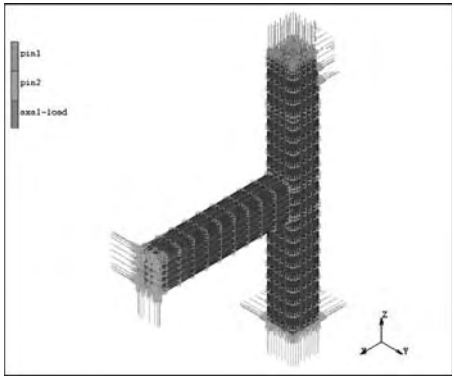

Figure 1. Exterior beam-column joint.

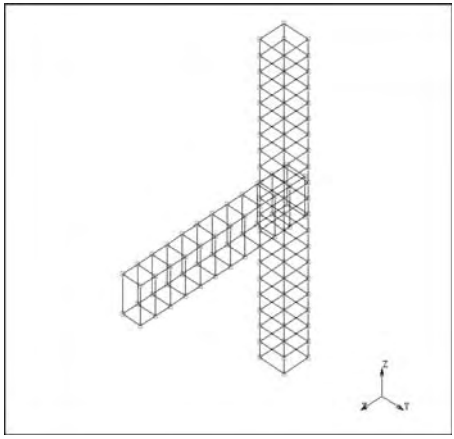

Figure 2. Beam-column joint reinforcement (truss element).

longitudinal rebars in the column, two 7.94 mm (5/16 in) diameter rebars in each side (top and bottom) of the beam, and 6.35 mm (1/4 in) stirrups were modeled by 80, 44, and 132 truss elements, respectively. The total number of truss elements was 256.

A maximum *x* displacement of 10.4 mm (0.41 in) in the push and 13.0 mm (0.51 in) in the pull direction was observed for the control joint model under combined axial and cyclic loads. The yield point displacement in push was 3.6 mm (0.14 in) while the same in pull was 3.4 mm (0.135 in). These two yield displacements were used to calculate the ductility of CFRP wrapped joint models, which amounted to 2.9 in the push and 3.8 in the pull for the control model. This joint carried 47 kN (10500 lb) in push and 45 kN (10080 lb) in pull as the maximum lateral load.

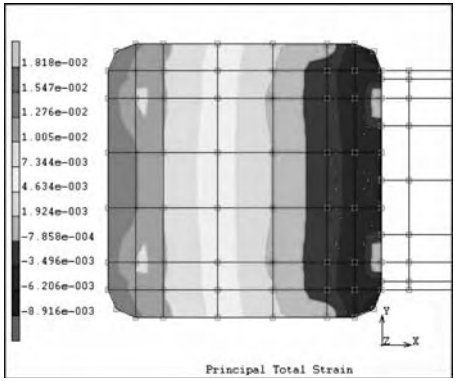

Figure 3. Total principal strain distributions in horizontal cut Section of control model.

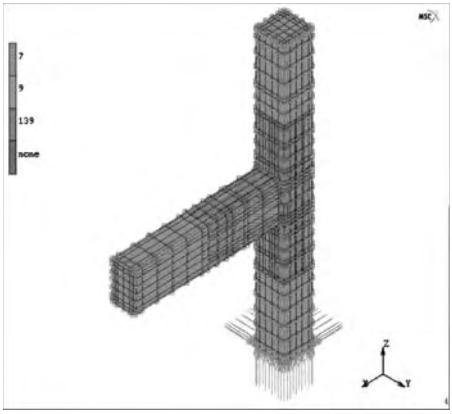

Figure 4. CFRP wrapped beam-column joint model.

A horizontal cut located at 25.4 mm (1 in) above the top of the beam equivalently 431.8 mm (17 in) from the top of the column was selected to demonstrate the strain distributions and to identify the failure location. The maximum principal tensile strain was observed at the outer side of the column in the vicinity of the joint due to a lateral load in the push direction at the failure point. The maximum compressive strain was observed at the inner side of the beam-column joint (Figure 3).

2.3 *Beam-column joint with 2 layers of CFRP (Model 2)*

Figure 4 shows a sketch of the beam-column joint where 14 in (355.6 mm) of column height and 203.2 mm (8 in) of beam length were wrapped around

the panel zone by 2 individual layers of CFRP in 0° and 90° directions with respect to circumferential direction of the column or beam member. This resulted in 0.36 mm (0.014 in) of CFRP total thickness. The wraps for the column and the beam were modeled by 194 and 48 shell elements, respectively. The total number of the joint elements including concrete, CFRP wrap and reinforcement elements was 2349.

The beam-column joint with 2 layers of CFRP exhibited a maximum lateral load of 52 kN (11700 lb) with a maximum lateral x displacement of 10.5 mm (0.414 in) and 13.2 mm (0.5187 in) in push and pull, respectively. This resulted in the ductility levels of 2.96 in the pull and 3.84 in the push directions. Comparing with the control model, the ultimate load capacity increased by 11% in the push and by 16% in the pull while the ductility increased by as little as 2%.

2.4 *Beam-column joint with 4 layers of CFRP (Model 3)*

The same (as in the Model 2) areas of column and beam around the panel zone of joint model 3 were wrapped by 2 layers of CFRP in 0° and 90° directions with respect to member circumferential direction while repeating two times: the total thickness of CFRP was equal to 0.71 mm (0.028 in). The finite element analysis results indicated ductility levels of 4.1 and 5.4, in the push and the pull, respectively. In terms of strength, the ultimate load capacity was determined as 64 kN (14400 lb) in the push or in the pull directions. Therefore, the ultimate load capacity increased by 37% in the push and by 43% in pull direction while the ductility increased by 39% in the push and by 42% in the pull direction as compared to the control model of the joint.

As shown in Figure 5, the distribution of strain indicates that high strain concentrations occur at the inner side around the top intersection of the beam and the column as the column bends under a pull force at failure. The total principal strain distribution of horizontal cut section shown in Figure 6 shows that the largest strain is at the tension side (inner side) while the maximum compression strain at the outer side of the column. The strains gradually shift from tension to compression.

2.5 *Beam-column joint with 6 layers of CFRP (Model 4)*

Same regions of the column and the beam (as in the model 2) around the panel zone were wrapped using 2 layers of CFRP in 0° and 90° directions with respect to circumferential direction of the member repeated three times. Consequently, the total thickness of CFRP became 1.07 mm (0.042 in).

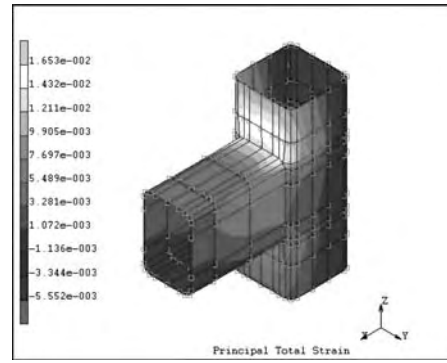

Figure 5. Total principal strain of beam-column joint with 4 Layers of CFRP.

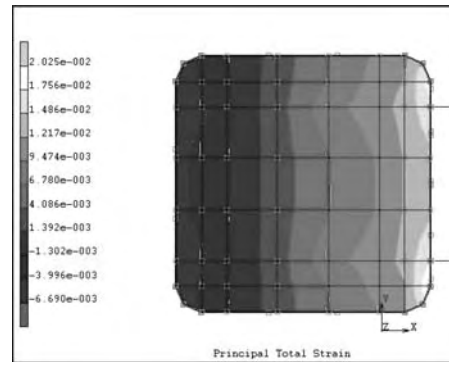

Figure 6. Total principal strain distributions in horizontal cut section of the joint with 4 layers of CFRP.

For this model, the maximum x displacement in the push and pull directions were 24.3 mm (0.958 in) and 22.4 mm (0.881 in), respectively. Accordingly, the ductility of the joint was equal to 6.8 and 6.5. The finite element analysis results indicated a maximum load capacity value of 69.4 kN (15600 lb) in the push and 64 kN (14400 lb) in the pull directions. Comparing with the control model, the ultimate strength increased by 49% and by 43% while the ductility improved by 133% and by 73% in the push and pull directions, respectively.

3 CONCLUSIONS

This investigation involved finite element analysis of beam-column joints retrofitted with CFRP under combined axial and lateral cyclic loadings, where the effect

of various wrap thicknesses was considered. Findings suggest that, in general, the external FRP reinforcement enhanced the lateral load capacity and ductility of the reinforced concrete joints. Preliminary results further indicated that the increase in the number of layers for the wrap resulted in higher strength and ductility. However, the gain in strength in the model with 6 layers of wrap as compared to the model with 4 layers is small. Therefore, if the designer's primary concern is to improve the strength with acceptable level of enhancement in ductility, the beam-column joint wrapped with 4 layers of CFRP will provide adequate retrofit efficiency while minimizing the cost.

ACKNOWLEDGMENTS

This research was partially supported by the National Science Foundation under NSF Grant No CMS-9753099. However, views and conclusions presented are those of the authors and do not necessarily represent those of the funding agency.

REFERENCES

Adin, M.A., Yankelevsky, D.Z. & Farhey, D.N. (1993). "Cyclic Behavior of Epoxy Repaired Reinforced Concrete Beam-Column Joints." *Struct. J.*, ACI, 90(2) 170–179.

Alcocer, S. & Jirsa, J.O. (1993). "Strength of Reinforced Concrete Frame Connections Rehabilitated by Jacketing." *Struct. J.*, ACI, 90(3), 249–261.

Antonopoulos, C.P. & Triantafillou, T.C. (2003). "Experimental Investigation of FRP-Strengthened RC Beam-Column Joints." *J. Compos. for Constr.*, ASCE, 7(1), 39–49.

Beres, A., El-Borgi, S., White, R.N. & Gergely, P. (1992). "Experimental Results of Repaired and Retrofitted Beam-Column Joint Tests in Lightly Reinforced Concrete Frame Buildings." *Technical Report NCEER-92-0025*, State Univ. of New York at Buffalo.

Gergely, J., Pantelides, C.P. & Reaveley, L. D. (2000). "Shear Strengthening of RCT-Joint Using CFRP Composites." *J. of Compos. for Constr.*, ASCE, 4(2), 56–64.

Ghobarah, A., Aziz, T.S. & Biddah, A. (1997). "Rehabilitation of Reinforced Concrete Frame Connections Using Corrugated Steel Jacketing." *Struct. J.*, ACI, 4(3), 283–294.

Granata, P.J. & Parvin, A. (2001). "An Experimental Study on Kevlar Strengthening of Beam-Column Connections." *Composite Structures*, 53, 163–171.

Mosallam, A.S. (2000). "Strength and Ductility of Reinforced Concrete Moment Frame Joints Strengthened with Quasi-isotropic Laminates." *Composites*: Part B, 31, 481–497.

FRP Composites in Civil Engineering – CICE 2004 – Seracino (ed)
© 2005 Taylor & Francis Group, London, ISBN 90 5809 638 6

CFRP-retrofitted RC exterior beam-column connections under cyclic loads

S.S. Mahini & H.R. Ronagh
Division of Civil Engineering, School of Engineering, The University of Queensland, Brisbane, QLD, Australia

S.T. Smith
Infrastructure and the Environment Group, Faculty of Engineering, University of Technology, Sydney, Australia

ABSTRACT: This study contains the results of experimental tests performed at the University of Queensland in order to evaluate the ability of CFRP wraps in strengthening an exterior beam-column connection subjected to cyclic loads. For this purpose, two specimens were designed based on the earthquake requirements of AS3600. One of these specimens was then wrapped with FRP while the other left untreated. Specimens were then tested to failure under a displacement-controlled regime. The displacement control had an ascending displacement amplitude as a multiplier of the yield displacement with a variable direction. The retrofitted specimen was found to behave in a satisfactory manner and was able to relocate the position of the plastic hinge away from the face of the column. The Hystersis curves, modes of failure, additional strength gain, etc. are presented in this paper.

1 INTRODUCTION

Beam-column connection failures that occurred during the El-Asnam earthquake in 1980 and the shear and anchorage failure at the exterior joints during the 1985 Mexico, the 1986 San Salvador, and the 1989 Loma Prieta earthquake brought about a universal awareness that beam-column connections may become critical zones in reinforced concrete (RC) structures.

Current standards of design take this view into account and have adequate provisions to combat against connection failure. One such provision is the concept of *weak-beam strong-column*, which results in the development of a plastic hinge close to the column face. Researchers recommend that beams should be designed in such a way that the required energy dissipation occurs in plastic hinges at a distance away from the connection core (Park & Pauly, 1975). If not, damage may penetrate into the core causing severe degradation of the connection's structural strength.

When a building's use changes (and in turn it's loading pattern), the plastic hinge location may move toward the connection core. Methods of avoiding this shall then be exercised. The recent advancement of Fibre Reinforced Plastics into the field of construction has provided a means for achieving this.

Carbon or glass fibres can be wrapped around the connection area or glued to the sides of the beam in order to strengthen the beam locally at the column face shifting the plastic hinge away from the strengthened region towards the beam.

The effectiveness of the method would depend on many parameters including the strength of FRP, strength of concrete, amount of reinforcement in the beam, the wrapping method and the extension length of FRP into the beam.

Compared to the considerable amount of research on strengthening of beams, slabs and columns with FRP composites (Teng et al. 2002), limited research has been undertaken on the application of FRP composites to RC beam-column connections (herein referred to as *connections*). This limited amount of research on connections is possibly due to the complex behaviour of connections, as well as difficulties in retrofitting, and complicated testing arrangements. The majority of research on connections has been limited to experimental studies. To date, both exterior and interior two-dimensional connections have been tested under monotonic or cyclic loads.

Of the research been conducted to date on retrofitting connections, externally bonded FRP composites have been used to enhance the shear capacity of the connection (i.e. Ghobarah and Said 2001, Antonopoulos and Triantafillou, Ouyang et al. 2003), improve the anchorage of inadequately anchored bottom longitudinal beam steel reinforcement (i.e. Geng et al. 1998), increase the flexural capacity of the beam at the connection (i.e. Granata and Parvin 2001), increase the overall load carrying capacity of the connection (Li et al. 1999) and increasing the joint ductility (Mosallam 2000). In all cases, externally bonded FRP was found to enhance the strength and ductility

of the connection. One study has been undertaken on the strengthening of three-dimensional connections (Antonopoulos and Triantafillou 2003), however the method of retrofit was not effective. To the best of the authors' knowledge, no tests have been performed on using externally bonded FRP to relocate the plastic hinge further along the beam away from the column face. Studies have however been conducted on relocating plastic hinges away from the column faces using other methods such as the use of headed reinforcing bars (Chutarat & Aboutaha 2003).

The experimental study reported in this paper is the first of its type and will consider common Australian construction practices while satisfying the design and detailing requirements of AS3600 (2001). The behaviour, strength, ductility and energy dissipation capacity of two-dimensional exterior connections retrofitted with externally bonded FRP, subjected to cyclic loading, are reported. Cyclic loading is used to simulate earthquake loading while an exterior connection is tested, as such connections attract higher shear forces than internal connections. A two-dimensional connection is modelled and the results will be applicable to retrofitting structures supported by two-dimensional framing. The research outcomes presented in this paper will be of interest to researchers throughout the world as well as owners, designers and users of RC structures.

2 EXPERIMENTAL DETAILS

2.1 *Details of test specimens*

The experimental program consisted of testing two 1:2.5 scale exterior RC beam-column connections as shown in Figure 1. The specimens represented a scaled down exterior connection of a typical RC residential building designed according to AS 3600. All connections consisted of 180 mm wide and 230 mm deep beams with 220 mm × 180 mm columns and the width of the columns and beams were equal. All beams were reinforced with high-strength 12 mm diameter (N12) longitudinal reinforcing steel bars, with two bars in the top and two bars in the bottom of the beam. All columns were reinforced with fours N12 reinforcing bars, with one bar positioned in each corner of the column. The beam stirrups and column ties were 6.5 mm bars at 150 mm centres. Ties were also placed in the connection region in accordance with the earthquake loading requirements of AS3600 (2001). Additional stirrups and ties were placed near the ends of the beam and columns in all specimens to ensure local failure will not occur at the load and support points respectively. The height of the column was taken as being corresponding to points of contraflexure in the actual structure.

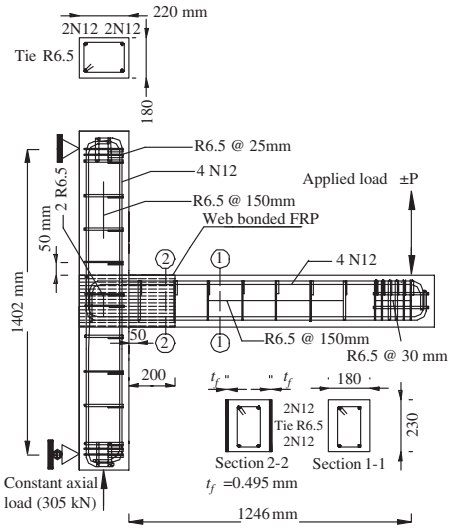

Figure 1. Specimen details.

The proposed retrofitting system consists of three plies of web-bonded CFRP sheet. All layers were unidirectional sheets and were applied in a length of 200 mm from the column face on the beam-end with fibre directions parallel to the longitudinal beam axis as shown in Figure 1. The fibres were applied to the beam using a solvent free epoxy resin after a careful surface preparation as follows.

Prior to the application of composite, the surface of specimen was ground and loose concrete pieces were removed using air jet pressure in order to assure a good bond between CFRP sheet and concrete. It was then buffed clean using Acetone. A film of primer (Thixotropic epoxy mortar) was applied to fill voids on the specimen. The primer was allowed to cure for 24 hours after application. The concrete surface was then ground smooth and uni-directional carbon fibre sheets were applied using the aforementioned epoxy resin.

2.2 *Material properties*

The material properties of the concrete; the concrete compressive strength; elastic modulus and splitting strength (Table 1) were determined on the day of testing each connection.

Yield strength of the N12 reinforcing steel bars and R6.5 mm stirrups and ties were also tested as being 500 MPa and 380 MPa. Carbon fibres used had a thickness of 0.165 mm with a maximum elongation of 1.55% and a tensile strength of 3900 MPa according to the manufacturers specifications.

Table 1. Mechanical properties of concrete.

Specimen	Compressive strength (Mpa)	Modulus of elasticity (Gpa)	Tensile strength (Mpa)
CSC1	40.73	30.17	3.29
RSC1	36.44	29.70	3.62

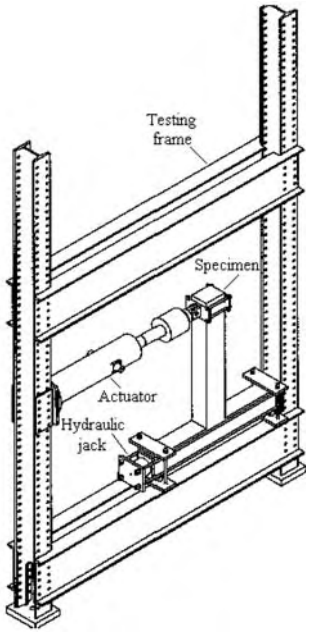

Figure 2. Test set-up.

2.3 *Test set-up and instrumentation*

Figure 2 shows the experimental set-up. The connection that has been orientated to the length of the column is parallel and the beam is perpendicular to the ground. The free end of the beam was loaded and the connection between the beam and the actuator was carefully designed in order to ensure that the load could be applied in a push-pull manner. Axial loading of the column was simulated by stretching four high-strength low-elongation steel bars placed outside the column by the use of a hydraulic jack while a load cell was utilised to measure the applied load. The column was subjected to a simulated axial gravity load of 305 kN and this load was scaled down from the load experienced in the actual structure. The columns were supported at each end with specially designed supports that ensured their ends were free to rotate but not to translate.

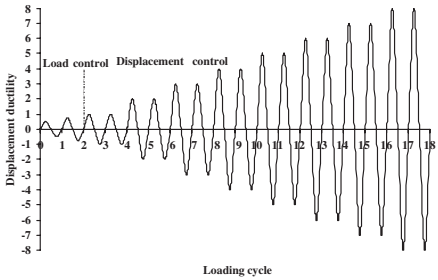

Figure 3. Loading regime.

Both the control specimen CSC1 and the retrofitted specimen RSC1 were tested to failure in order to determine the ultimate load carrying capacity, cracking patterns, hysteresis behaviour and energy dissipation characteristics, ductility and rigid-body-rotation of the beam at the column face.

A reversible load, measured with a load cell, was applied at the beam tip using a hydraulic actuator ± 125 mm. The load was applied in two phases as shown in Figure 3. In the first phase, the load was applied in a load-control manner up to the first yield of steel reinforcement for which the displacement corresponding to first yield, Δ_y, was recorded. The manner in which Δ_y is determined is described in detail in the following paragraph. The second phase of load application consisted of displacement-control by displacing the tip of the beam with the tip displacement, Δ, increasing in magnitude with each push-pull until failure of the connection occurred. The amount of tip displacement for each push-pull was a multiple of Δ_y as shown in Figure 3 where the displacement ductility μ is Δ/Δ_y.

The displacement at first yield is a difficult quantity to measure as determination of the point of first yield is complicated by concrete cracking and strain localisation in the reinforcing steel. The load corresponding to first yield of reinforcing bars was therefore partly based on theory and experiment. The load corresponding to first yield was firstly calculated. Seventy-five percent of this load was then applied and the corresponding tip displacement recorded in both of the push and pull cycle. Both of theses displacements were then averaged and multiplied by 4/3 to give the displacement at first yield. The displacement at the tip of the beam as well as mid-length of the beam and 200 mm along the beam, from column face, as shown in Figure 4, were measured using linear variable displacement transducers (LVDT). Four LVDTs were placed at the end of the beam and at the end of the CFRP strengthening region (200 mm for the column face in the beam) as shown in Figure 4. These LVDTs were positioned to record the displacement

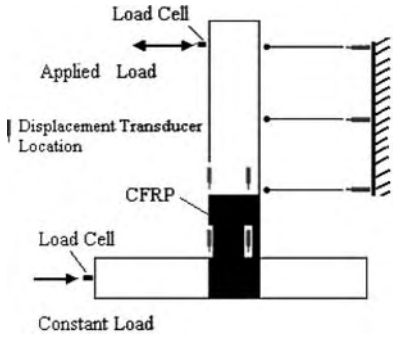

Figure 4. Typical instrumentation on test specimens.

at the level of the beam reinforcement and the opposite concrete face. The strains of steel and concrete were extracted from the relative displacements of two transducers placed close to each other, only 15 mm apart.

3 EXPERIMENTAL RESULTS

In the following, the results of tests performed on the aforementioned specimens are described and the effectiveness of the retrofitting scheme is evaluated.

3.1 *Control specimen CSC1*

As mentioned previously, the specimens were subjected to a load-control regime that was followed by a displacement-control regime after the first yielding of the beam longitudinal reinforcement is reached. In the first loading cycle, the specimen was loaded to 9.0 kN pull and push. The first crack was observed at the column face at a load of about 5.1 kN.

In the second cycle, a load of 13.5 kN was applied (pull and push) to the specimen. This load was around 75% of the expected theoretical load at first yield. The corresponding displacement at this load cycle was used as a base from which the displacement at first yield was guessed as being equal to 15.8 mm (being 4/3 of the measured one at 13.5 kN). At this load, new flexural cracks were formed along the beam. The estimated displacement of 15.8 mm was then used in the displacement-controlled phase of the loading.

The specimen, CSC1, was then subjected to an increasing displacement-control loading using multiples of displacements recorded at the initial yield of the steel Δ_y. Two cycles were applied at each ductility ratio level starting from $\mu = \Delta/\Delta_y$ equal to 1, then 2, 3, 4, etc, where, Δ is the beam-tip displacement and μ is the displacement ductility ratio. In the seventh cycle

Figure 5. Failure pattern of specimen CSC1.

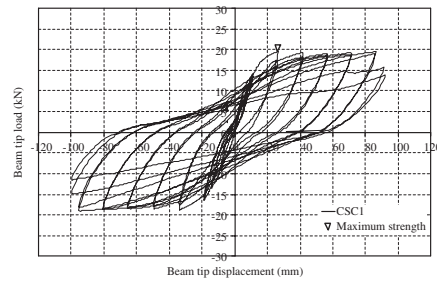

Figure 6. Load versus displacement for CSC1.

at the beam's tip displacement of 47.4 mm, vertical cracks were formed in the connection area close to the back of column due to the bond deterioration between the column top reinforcements and concrete. Cracking of the concrete due to the flexural deformation of the beam was initiated from the beam end at the column face and grew along the beam length. Some cracks were penetrated into the connection core at beam's tip displacement of 31.6 mm. Crushing and spalling of the concrete occurred in the thirteenth cycle at the tip displacement of 94.8 mm and the corresponding load of 19 kN (pull). This load was the maximum load that the specimen held. The specimen failed soon after when buckling of the beam's top rebar occurred at the column's face. Consequently the load on the specimen started to descend. The final failure pattern is shown in Figure 5.

Examining the hysteretic behaviour of the specimen showed severe pinching, stiffness degradation during the test and strength deterioration in the final two cycles followed by spalling of the concrete and the subsequent full buckling of the steel reinforcements at the column face, as shown in Figure 6. The plastic hinge was formed at the face of the column. Figure 7 presents the envelope curves that pass through the maximum loads in both push and pull.

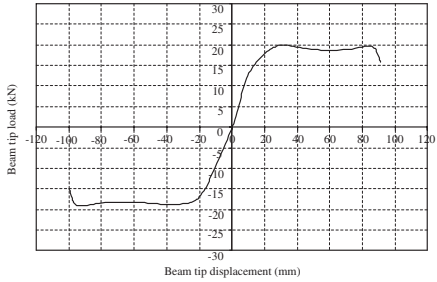

Figure 7. Envelope curves for CSC1.

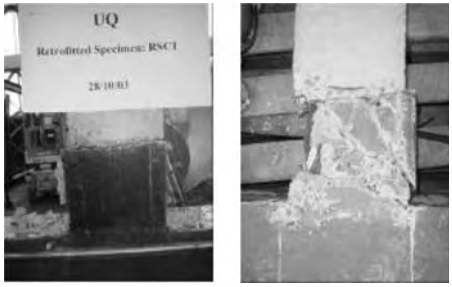

Figure 8. Failure pattern of specimen RSC1.

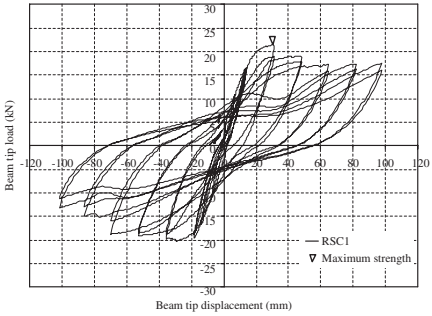

Figure 9. Load versus displacement for RSC1.

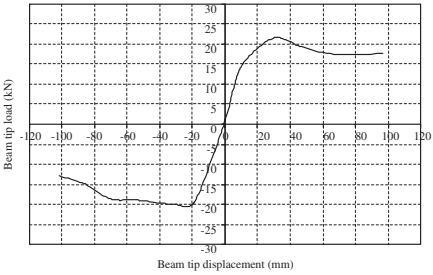

Figure 10. Envelope curves for RSC1.

The retrofitting scheme was totally effective in relocating the plastic hinge. Rigid body rotations of beams confirmed this re-location visually.

3.2 *Retrofitted specimen RSC1*

Specimen RSC1 was subjected to the same loading sequence as specimen CSC1. The first crack occurred during the first cycle at a load of 6.4 kN at the FRP cut-off point. In the second cycle, the specimen was loaded to 16.35 kN (pull and push). This load was again 75% of the theoretical load at which the first yield of steel was expected. The displacement at this load (17.5 mm) was then used as the basis for guessing the displacement at first yield after which the displacement-control regime started.

During the first cycle of displacement control, no crack was observed at the column face. In fact all cracks shifted beyond the cut-off of CFRP. The loading continued to the seventh cycle without any debonding of FRP sheets and only then the first signs of debonding were observed at the mid-height of the beam close to the column face.

In the cycles that followed, as the tension in FRP was lost due to de-bonding, steel bars started to carry the developed tensile force. In the ninth cycle, the top steel bars of the beam started to buckle. This buckling occurred around 150 mm away from the column face.

The position of buckled steel rebar can arguably be thought of as the centre of plastic hinge. Assuming this, FRPs have been able to shift the location of plastic hinge 150 mm away from the column face. This is about 65% of the section depth and three quarter of the length of FRP coverage.

As for the load, the specimen reached a maximum load of 21.33 kN (pull) and 20.16 kN (push) in fifth cycle and then experienced a decreasing trend to a load of 19 KN in the seventh cycle. The strength of the specimen was almost maintained up to failure. The final failure conditions before and after removing the CFRP from concrete surface are shown in Figure 8.

Examining the hysteretic loops of the specimen (Figure 9) shows that the energy absorbing capacity is maintained as the maximum loads hold to a healthy plateau up to the end. No considerable pinching, stiffness degradation or strength deterioration was observed in the final two cycles as was the case for the plain RC specimen. This obviously is a result of plastic hinge region being confined by the FRP sheet to some extent.

Figure 10 contains the envelope curve that passes through the maximum points both in push and pull.

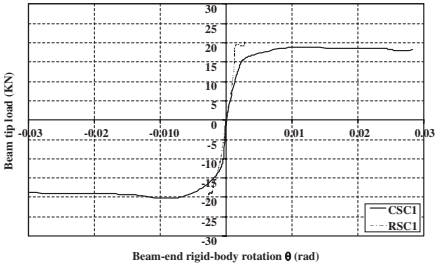

Figure 11. Beam tip load versus rotation.

Beam CSC1 rotated at the column face while beam RSC1 about an axis located almost 150 mm away from the column face within the beam. Elastic movements away from the plastic hinge were small compared to the plastic deformations and therefore the final deformed shape was basically a function of plastic hinge rotations.

Figure 11 presents the envelope of the rigid-body rotations of the beam's end at the column face. Beam RSC1 shows very little rotation while the rotation of CSC1 extends to around 0.03 radians at failure.

4 CONCLUSIONS

Two 1:2.5 scale-down reinforced concrete exterior beam-column sub-assemblages in a one-way frame were tested under cyclic loads. The objectives were to investigate the effect of web-bonded CFRP on energy absorbing capacity of RC beam-column connections and to evaluate the possibility of relocating the position of the plastic hinge away from the face of the column. The results showed that the CFRP-retrofitted specimen developed a plastic hinge at a distance of 150 mm from the column face within the beam. No bond deterioration was occurred in the connection region in the retrofitted specimen. The overall strength, stiffness and energy dissipation of the original specimen was regenerated in the retrofitted specimen with the additional benefit of the plastic hinge region being confined and as such spalling of concrete being kept to a minimum.

Overall, the method seemed very effective in relocating the plastic hinge away from the column face.

ACKNOWLEDGEMENTS

Authors would like to express their thanks to MBT Australia for making carbon fibres and other materials available to them at a subsidised rate. The first author is supported by a combined IPRSUQIPRS scholarship from the Australian Federal government and the University of Queensland for the duration of his PhD. This support that has enabled him to perform the current research is gratefully acknowledged.

REFERENCES

Antonopoulos, C.P. & Triantafillou, T.C. 2003. Experimental investigation of FRP-strengthened RC beam-column joints. *Journal of Composites for Construction, ASCE 7*(1): 39–49.

AS3600, 2001, *Concrete Structures*, Standards Australia, Homebush Bay, Australia.

Chutarat, N. & Aboutaha, R.S. 2003. Cyclic response of exterior reinforced concrete beam-column joints reinforced with headed bars-experimental investigation. *ACI Structural Journal* 100(2): 259–264.

Geng, Z.J., Chajes, M.J., Chou, T.W. & Pan, D.Y.C. 1998. The retrofitting of reinforced concrete column-to-beam connections. *Composites Science and Technology* 58:1297–1305.

Ghobarah, A. & Said, A. 2001 Seismic rehabilitation of beam-column joints using FRP laminates. *Journal of Earthquake Engineering* 5(1): 113–129.

Granata, P.J. & Parvin, A. 2001. An experimental study on Kevlar strengthening of beam-column connections. *Composite Structures*, 53(2): 163–171.

Li, J., Bakoss, S.L., Samali, B. & Ye, L. 1999. Reinforcement of concrete beam-column connections with hybrid FRP sheet. Composite Structures 47:805–812.

Mosallam, A.S. 2000. Strength and ductility of reinforced concrete moment frame connections strengthened with quasi-isotropic laminates. *Composites Part B Engineering*, 31(6–7): 481–497.

Quyang, Y., Gu, X.X.L., Huang, Y.H. & Qian, Z.Z. 2003. Seismic behaviour of reinforced concrete beam-column joint strengthened with GFRP. In K.H. Tan (ed.) *Sixth International Symposium on Fibre-Reinforced Plastics for Reinforced Concrete Structures, FRPRCS-6; Proc. Intern. Conf., Singapore, 8–10 July 2003.* World Scientific.

Park, R. & Paulay, T. 1975. *Reinforced Concrete Structures.* Christchurch: Johan Wiley & Sons.

Paulay, T. & Priestley, M.J.N. 1992. *Seismic Design of Reinforced Concrete and Masonry Buildings*. John Wiley Johan Wiley & Sons.

Teng, J.G., Chen, J.F., Smith, S.T. & Lam, L. 2002 FRP-*Strengthened RC Structures*. Johan Wiley & Sons.

FRP Composites in Civil Engineering – CICE 2004 – Seracino (ed)
© 2005 Taylor & Francis Group, London, ISBN 90 5809 638 6

Flexural repair of RC exterior beam-column joints using CFRP sheets

S.S. Mahini, H.R. Ronagh & P.F. Dux
Division of Civil Engineering, School of Engineering, The University of Queensland, Brisbane, QLD, Australia

ABSTRACT: A practical technique for flexural repairing of exterior beam-column joints using CFRP wraps is presented. The procedure is to restore the flexural capacity of the damaged joint. An experimental study is conducted in order to evaluate the performance of a 1:2.5 scale reinforced concrete external beam-column joint sub-assemblage belonging to an OMRF RC structure (Ordinary Moment Resisting Frame) designed to Australian Concrete Code, and then repaired using the proposed technique. The beam-column joint is tested under monotonic load applied at the free end of the beam and under a constant axial column load. The proposed repair procedure is applied to the tested specimen. The Unidirectional CFRP sheet system proved to be effective in upgrading the flexural capacity of the damaged beam-column joint. Comparison between the behaviour of the specimen before and after repair is presented and the results are checked against a non-linear finite element analysis using ANSYS.

1 INTRODUCTION

In the event of a severe earthquake, many modern RC buildings may experience small to moderate damage at their joints. Repairing of the joints is often the most economical solution that can be performed at a fraction of the cost of demolition and re-building.

When damage to the joint is low, epoxy injection may be sufficient to restore the strength and stiffness. Small cracks, intact steel and a concrete that is neither crashed nor spalled identify a low level damage. In a high-level damage identified by crack widths of more than 5 mm, heavily deformed steel and a concrete that is crushed, epoxy injection would not work and some means of external support for the system is required. Fibre composites investigated in the current study could be a good candidate.

During the last decade, fibre composites have gradually entered the construction market. A lot of studies have been performed on their use in repair and retrofitting applications particularly in strengthening beams, columns, piers and walls. These noncorrosive, light-weight materials are made of carbon, glass or aramid fibres and can be glued to the surfaces of a reinforce concrete element in order to increase it's strength. The fibre combined with epoxy (or resin) is then called FRP, which stands for Fibre Reinforced Plastic.

While, one may find many studies in the literature on the application of FRPs in shear, axial and flexural strengthening of beams and column, studies on strengthening of the joints is very limited. Of the few that exist, the majority are concentrated on the shear strengthening of joints. The performance of FRPs in flexural strengthening is yet to be fully addressed.

In order to design a joint in an earthquake prone region, the methodology of *strong-column-weak-beam* is usually utilised. This design methodology ensures that the joints and the columns remain elastic under lateral loads up to failure while beams undergo large localised plastic deformations in order to ensure adequate energy dissipation. This design concept when implemented ensures that the damage is contained within the beam where the beam's end meets the joint. In this situation, FRPs can be used to repair the beam (and the joint) back to its original strength.

In the repairing, however, one would not only look at the strength but at the ductility and stiffness of the system as these may affect the intended energy dissipation mechanism and the redistribution of loads at the time higher cyclic loads re-occur.

Of the two main types of FRP (carbon and glass), carbon fibres are utilised in the current study in order to investigate their ability in repairing the joints.

2 PAST STUDIES

Epoxy and resin injection techniques were used in the past after the Anchorage earthquake in Alaska, the San Fernando earthquake in the US and the Managua

earthquake in Nicaragua. These techniques were investigated by Popov & Bertero (1975). Several severely cracked test specimens of RC joints were repaired using either epoxy resin or concrete in their research. The results showed that the repairing technique was able to restore the destroyed bond between the concrete and reinforcing steel. Filiatrault & Lebrun (1996) also used the epoxy pressure injection to rehabilitate exterior RC beam-column joints. Two full-scale specimens were subjected to cyclic loads above cracking limit and then repaired with epoxy. The repaired specimens were then loaded with the same load-history applied to original specimens. Filiatrault & Lebrun (1990) showed that the epoxy injection was effective in restoring the strength; stiffness and energy-dissipation capacity of the RC exterior joins.

The epoxy and resin injection techniques are usually employed when the damage level is low. When buildings are moderately damaged, other means of rehabilitation are required. During the 1990s, several attempts were made to repair damaged RC structures by FRP sheets or plates. David et al. (1998) performed an investigation into the repair and strengthening of RC beams using composite materials. They examined the effect of thickness of FRP sheet and plate on the flexural behaviour of the repaired and retrofitted RC beam. Test results indicated that all beams had significant increases in flexural stiffness and ultimate capacity. Moreover, the results showed that the glass or carbon fibre transform the ductile flexural failure of the specimen into a brittle failure after repairing. Duthinh & Stranes (2001) tested seven concrete beams repaired with FRP laminates and showed that FRP could enhance the flexural capacity of repaired beams. Recently, Mosallam (2000) investigated the strength and ductility of RC moment frame connections strengthened with quasi-isotropic laminates. Two half-scale specimens repaired with carbon and E-glass quasi-laminates were examined in his investigation. Mosallam indicated that the composite overlays increase the stiffness, strength and ductility of repaired RC joints. In the second phase of his research program, the damaged specimens were repaired with both CFRP overlays and wraps and tested under cyclic loading. Test results indicated that the repairing method was efficient in restoring the ultimate capacity and enhancing the stiffness of the repaired specimen. In some cases, however, some stiffness and strength degradation for the repaired specimens was observed due to the fact that the steel reinforcements were already yielded. The effects of U-shaped wrapping and complete wrapping on the joint behaviour were also investigated in this pilot study. Results demonstrated that as the U system did not cover the top of pre-cracked concrete surfaces, high tensile and compressive stresses occurred in this area. The complete wrapping on the other hand was able to increase the initial stiffness and strength of the joint although this method is impractical due to the presence of the floor slab in a real situation.

3 EXPERIMENTAL PROGRAM

3.1 *Specimens*

The test specimens were three 1:2.5 scale models of the prototype. The prototype structure was a typical eight story residential RC building located in Brisbane. The controlling design criterion for this structure was the strength required to resist the applied gravity and lateral loads. The prototype was designed as an Ordinary Moment Resisting Frame (OMRF), according to the Australian Concrete Code AS 3600 (2001), with details similar to non-ductile RC frames designed to ACI-318, American standard. A scaled-down frame was modelled by the application of the similitude requirements that relate the model to the prototype using the Buckingham theorem (Noor & Boswell, 1992). The scaled-down joints were extended to the column mid-hight and beam mid-span, corresponding to the inflection points of the bending moment diagram under lateral loading. Figure 1 shows a specimen under load in the testing frame. The specimen is rotated 90 degrees for ease of testing. Code provisions have been used to determine the spacing of steel stirrups and ties. The specimen size and reinforcement were limited by the hydraulic actuator size and the ultimate capacity of hydraulic jacks that apply the loads to the column and the testing frame. Special hinge support was designed to simulate the real performance of the sub-assemblies at the inflection points as well as applying the constant load into the column as shown in Figure 1. Yield strength of the main steel reinforcements was around 500 Mpa and the modulus of elasticity was equal to 194 Gpa. Four N12 rebars (ϕ12 mm) were used for both the column vertical

Figure 1. Beam-column joint testing set-up.

reinforcement and the beam longitudinal reinforcement. R6.5 bars (ϕ6.5 mm) were used for stirrups with a spacing of 150 mm in both column and beam. The joint detail was designed according to AS3600-2001. Figure 2 shows the specimens' details. The concrete had a compressive strength around 40, 52 and 48 MPa and a modulus of elasticity around 27.6, 35.7 and 35.2 Gpa for plain (CSM0) and repaired specimens (RPSM1 & RPSM2) respectively. The cross-sectional dimensions of beams and columns were about 180 by 230 mm and 180 by 220 mm respectively.

One connection specimen was tested as control specimen to failure. Two other specimens were precracked, repaired and then retested under a similar loading regime.

3.2 *FRP composite system*

Carbon Fibre Reinforced Polymer (CFRP) sheets that were used in the experiments were unidirectional. The sheets were glued to the web of the beam with the fibre orientation parallel to the beams' longitudinal axis. The beams were not fully wrapped as it could have been impractical in real situations due to the interface with the concrete slab. Wraps were extended over the joint core area to the back of the column in order to minimize the possibility of premature delamination.

Beams were either wrapped with one layer of CFRP or two, named RPSM1 and RPSM2 respectively. CFRP was an MBrace Fibre sheeting from MBT, which possesses a tensile strength of about 3900 MPa, a modulus of elasticity of 240 GPa and an ultimate tensile elongation of 1.55%. The MBrace Saturant (adhesive) was also used for warping the MBrace sheet using a wet lay up method. The saturant had a minimum tensile strength of 50 MPa and a minimum compressive strength of more than 80 MPa. It's modulus of elasticity was around 3000 MPa and it's ultimate elongation around 2.5%.

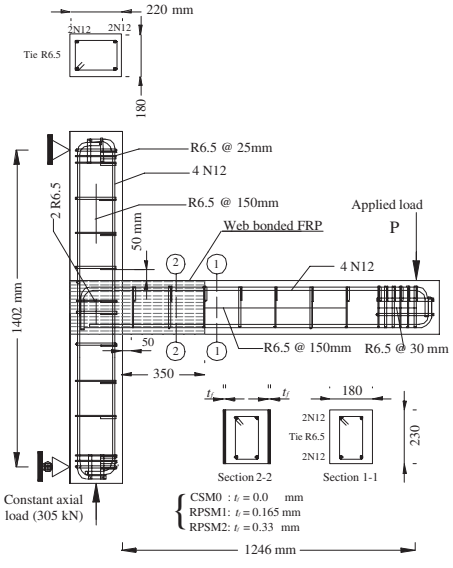

Figure 2. Specimens' details.

3.3 *Test fixtures and instrumentation*

The specimens were tested in a 2D testing frame. This test frame was equipped with a hydraulic actuator of 100 kN capacity and a hydraulic jack with a maximum capacity of 500 kN. Although the loading was applied monotonically, the actuator was capable of applying cyclic loads in both load and displacement control regimes. Load and deflections were automatically recorded using a computerized data acquisition system. The relative displacement of a primary point at the beams' end and a secondary point located 15 mm apart was captured using four LVDTs placed on the concrete surface at the reinforcement position and the extreme fibres of the concrete compressive zone in other to obtain the strain in the main steel bars and the concrete.

3.4 *Loading regime*

Lateral loads were applied to the beam tip using a 100 kN hydraulic actuator. A constant 305 kN load was applied to the column using a hydraulic jack. The control specimen CSM0 (Control Specimen under Monotonic load – number 0) was loaded monotonically. The load control regime was used to capture the steel reinforcement yielding point. After yielding, the test was continued using a displacement control regime up to displacements that were corresponding to a ductility ratio of 5.

The two repaired specimens were tested twice. Once prior to repair where they were called control specimens CSM1 and CSM2 and once after the repair was performed, where they were called RPSM1 and RPSM2. CSM1 and CSM2 were loaded in a similar manner to CSM0 to first yield under a load control regime and then to a ductility ratio of 2 in a displacement control manner. At that ductility level, the specimens were cracked significantly, but not destroyed. They were then repaired and retested to failure in a manner similar to that described before.

4 EXPERIMENTAL RESULTS

4.1 *Control specimen CSM0*

The first plain control specimen was tested to failure in order to determine it's capacity, flexural stiffness,

Figure 3. Ultimate failure of specimen CSM0.

Figure 4. Ultimate failure of specimen RPSM1 & RPSM2.

and failure mode (see Figure 1). Firstly, the load corresponding to steel yielding was calculated from a nonlinear numerical analysis performed by ANSYS as being equal to 17 kN. The tip displacement corresponding to this load was also calculated as 18.4 mm. When this load level was reached in the experiments, flexural cracks were developed at the beam-end close to the column face ranging from 1.5 mm to 10 mm in width. Larger cracks of up to 20 mm were observed at a distance of 85 mm from the column face.

Some propagation of cracks (around 30 mm deep) into the joint region was also visible. The ultimate load for the specimen was about 24.6 kN with a corresponding displacement of 70 mm. The ultimate failure mode of CSM0 is shown in Figure 3 and the load-displacement in Figure 7. As is seen, the behaviour is linear up to a load of 5 kN. The initial stiffness measured from the curve is around 1.11 kN/mm.

4.2 *CFRP-repaired specimen RPSM1*

Prior to the application of composite systems, the surface of pre-cracked specimen CSM1 was ground and loose spalled concrete pieces were removed using air jet pressure to assure a good bond between CFRP sheet and concrete. It was also buffed clearly using Acetone. A film of primer was applied to fill cracks and voids on the damaged areas of the specimen. The primer was allowed to cure for 24 hours after application. The concrete surface was then ground smooth and unidirectional MBrace CF130 sheets were applied using MBrace Saturant adhesive.

The repaired specimen was first loaded to initial yield under load control and then to failure under a displacement control regime. The behaviour was linear up to a load of about 2.5 kN which is about 50% less than plain specimen CSM0. After this load a slight nonlinearity was observed up to a load of 20.15 kN (and the corresponding vertical displacement of 16.4 mm), which was corresponding to steel yielding. At this point, the repaired cracks were reopened slightly

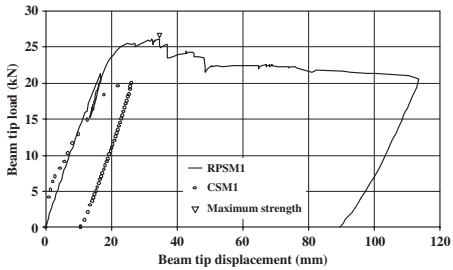

Figure 5. Load versus displacement for CSM1 & RPSM1.

whereas the main cracks relocated from the column face to the cut-off point of the wrap.

The maximum load recorded in this test was 26.4 kN. As compared to the strength of the control specimen (24.6 kN), an increase in the ultimate strength of about 7% was achieved repairing with one-ply CFRP sheets. At ultimate, concrete crushing occurred at the column face. Subsequently, the beam was rotated about the fulcrum and the specimen was failed suddenly by the rupture of CFRP on the tension side. A loud crackling sound was heard indicating the initiation of concrete crushing and the subsequent rupture of the CFRP. No shear cracks were observed in the wrapped area. Figure 4 shows the failure mode of specimen RPSM1. Figure 5 contains the load-displacement curves for CSM1 and RPSM1.

4.3 *CFRP-repaired specimen RPSM2*

In order to improve the performance of the CFRP web-bonded repair system, a new specimen was precracked and repaired, but this time with two plies of CFRP sheets. The same loading regime, as in specimen RPSM1 was applied. Under loading, the repaired cracks did not reopen but new cracks started to develop

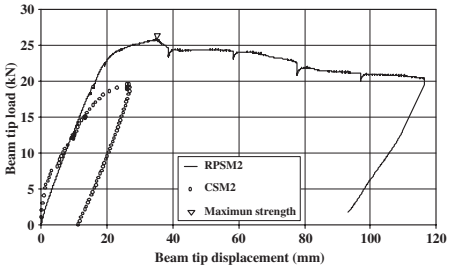

Figure 6. Load versus displacement for CSM2 & RPSM2.

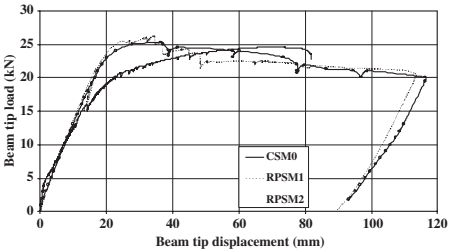

Figure 7. Load versus displacement for all specimens.

beyond the cut-off point of CFRP. The failure occurred by concrete crushing followed by the yielding of steel reinforcement in the plastic hinge region at a distance of around 270 mm away from the column face. FRP remained intact up to failure without any visible debonding.

Some shear deformation within the wrapped region was also observed. The ultimate failure mode of RPSM2 is shown in Figure 4 and the load-displacement of CSM2 and RPSM2 in Figure 6.

The maximum load recorded in this test was about 25.9 kN. The strength of the repaired specimen RPSM2 is 5.3% more than the plain specimen CSM0. The stiffness of the specimen was also improved.

The beams' tip load versus displacement curves for all connection specimens is shown in Figure 7.

Comparison of the load-displacement curves indicates that the integrity of the cracked beam-column joints could be completely restored by CFRP web-bonded repair system.

5 NUMERICAL INVESTIGATION

A nonlinear numerical analysis using ANSYS was performed in order to numerically recreate the observed failure mechanisms. To perform the analysis, a three dimensional model was used. The concrete was

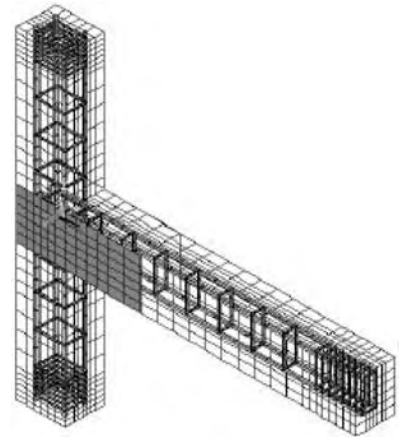

Figure 8. Typical FE mesh of the retrofitted Joint.

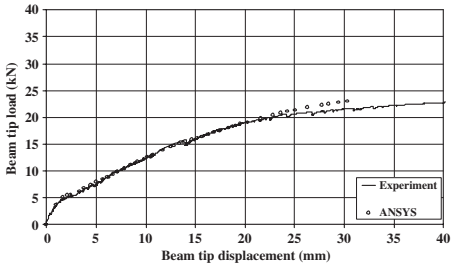

Figure 9. Comparison between ANSYS predictions and the test result for CSM0.

modelled using solid65 that is ANSYS specifically designed element for reinforced concrete. This element is capable of modelling plasticity, cracking and crushing of the concrete. The stress-strain curve presented by Kwak and Fillippou (1990) was employed in order to model the concrete properties. Steel reinforcements were modelled using space truss elements (ANSYS element link8). Material properties of link8 elements include a multilinear stress strain curve to account for plastic deformation and strain hardening of the steel reinforcing bars. CFRP sheets were modelled using a three dimensional solid element (ANSYS element solid45) which possesses anisotropic plasticity. Figure 8 shows a typical FE mesh of retrofitted joint.

Figures 9, 10 and 11 contain a comparison between ANSYS predictions and the test results. As is seen, the agreement is reasonable. The results of ANSYS match the plain RC beam better than the repaired specimens. This may be a result of bond slip between FRP and concrete that is ignored in the current analysis.

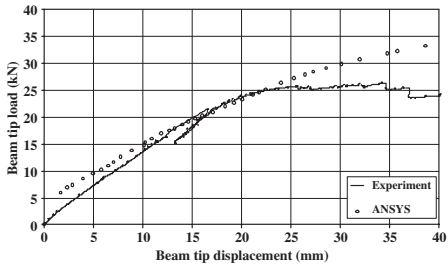

Figure 10. Comparison between ANSYS predictions and the test result for RPSM1.

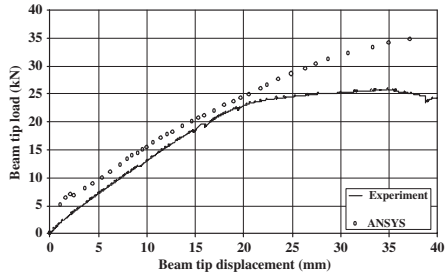

Figure 11. Comparison between ANSYS predictions and the test result for RPSM2.

Nevertheless, as results are reasonably close, ANSYS can be used as a tool in order to understand the behaviour and to design the appropriate amount of CFRP in order to relocate the plastic hinge while maintaining a ductile failure mode.

6 SUMMARY AND CONCLUSIONS

Based on the experimental results, it evident that the web-bonded CFRP repair system is capable of a full restoration or even enhancement of the original capacity of damaged beam-column joints. Table 1 summarizes the experimental test results and the percentage strength gain obtained in this study.

The test results reported herein have led to the following conclusions concerning the efficiency of CFRP sheets for repairing damaged RC beam-column joints:

1. The repair process restores the integrity of the specimen.
2. Both the rotational stiffness and the ultimate flexural strength of the damaged RC joint were increased after repair.
3. The repaired specimen may be stiffer than the original, and the loss of ductility need to be considered.

Table 1. Summary results for CFRP-repairing.

Specimen	Ultimate load (kN)	Strength increase (%)	Failure location
CSM0	24.6	–	Beam-end
RPSM1	26.4	7.0	Beam-end
RPSM2	25.9	5.3	Within the beam

4. The ductility of the repaired specimen can be maintained when enough FRP is utilised to ensure a ductile failure due to the development of a plastic hinge at the FRP cut-off point.
5. Using a supporting U-wrap system is recommended in order to confine the retrofitting wraps thus ensuring a complete transfer of plastic hinge away from the column towards the beam.

ACKNOWLEDGEMENT

Authors would like to express their gratitude to MBT Australia for making the carbon fibres and other materials available to them at a subsidised rate. The first author is supported by a combined IPRS-UQIPRS scholarship from the Australian Federal government and the University of Queensland for the duration of his PhD. This support that has enabled him to perform the current research is gratefully acknowledged.

REFERENCES

AS3600. 2001. *Concrete Structures*, Standards Australia, Homebush Bay, Australia.

David, E., Djelal, C. & Buyle-Bodin, F. 1998. Repair and strengthening of reinforced concrete beams using composite materials, *2nd Int. PhD symposium in civil engineering*. Budupest: 1–8.

Duthinh, D. & Starnes, M. 2001. *Strength and ductility of Concrete Beams Reinforced with Carbon FRP and Steel.*: National Institute of Standards and Technology, Technology Administration US Department of commerce.

Filiatrault, A. & Lebrun, I. 1996. Seismic rehabilitation of reinforced concrete joints by epoxy pressure injection technique. In: *G.M. Sabnis, Shroff, A.C and Kahn, L.F. (Editor), Seismic rehabilitation of concrete structures.* ACI: 73–92.

Kwak, H.G. & Fillippou, F., 1990. Finite Element Analysis of Reinforced Concrete Structures under Monotonic Loads. Tech. Report No.UCB/SEMM-90/14, Dept. of Civil Engineering, University of California, Berkeley, California.

Mosallam, A.S. 2000. Strength and ductility of reinforced concrete moment frame connections strengthened with quasi-isotropic laminates. *Composites Part B-Engineering* 31(6-7): 481–497.

Noor, F.A. & Boswell, L.F. 1992. *Small scale modelling of concrete structures*. Elsevier Applied Science.

Popov, E.P. & Bertero, V.V. 1975. Repaired R/C members under cyclic loading. *Earthquake Engineering and* and structural dynamics, 4: 129–144.

FRP Composites in Civil Engineering – CICE 2004 – Seracino (ed)
© 2005 Taylor & Francis Group, London, ISBN 90 5809 638 6

Multi-level seismic rehabilitation of existing frame systems and subassemblies using FRP composites

S. Pampanin
Department of Civil Engineering, University of Canterbury, Christchurch, New Zealand

D. Bolognini, A. Pavese, G. Magenes & G.M. Calvi
Department of Structural Mechanics, University of Pavia, Italy

ABSTRACT: The feasibility and efficiency of a retrofit intervention on gravity load-designed frame systems using externally bonded FRP composites is herein presented, through both analytical and experimental investigations. A multi-level retrofit strategy is proposed to achieve the desired performance, based on hierarchy of strength considerations. The expected sequence of events can be visualized through demand-capacity curves within M-N Performance-Domains. An analytical procedure able to predict the enhanced non-linear behaviour of the panel zone region, due to the application of CFRP laminates, in terms of shear strength (principal stresses) vs. shear deformation, is developed and proposed as a fundamental step for the definition of a proper retrofit strategy. The experimental results from quasi-static tests on 2/3 scaled beam-column subassemblies (either interior and exterior) in as-built and retrofitted configuration, provided very satisfactory confirmations of the viability and reliability of the retrofit solution adopted as well as of the proposed analytical procedure.

1 INTRODUCTION

Extensive experimental-analytical investigations on the seismic performance of existing reinforced concrete frame buildings, designed for gravity loads only, as typically found in most seismic-prone countries before the introduction of adequate seismic design code provisions in the 1970's, confirmed the expected inherent weaknesses of these systems (Aycardi et al., 1994; Beres et al., 1996; Hakuto et al., 2000; Park, 2002; Pampanin et al., 2002; Bing et al., 2002; Calvi et al., 2002a,b). As a consequence of poor reinforcement detailing, lack of transverse reinforcement in the joint region as well as absence of any capacity design principles, brittle failure mechanisms were observed. At a local level, most of the damage is likely to occur in the beam-column joint panel zone while the formation of soft-story mechanisms can greatly impair the global structural performance of these RC frame systems. An appropriate retrofit strategy is therefore required, which is capable of providing adequate protection to the joint region while modifying the hierarchy of strengths between the different components of the beam-column connections according to a capacity design philosophy.

Alternative retrofit and strengthening solutions have been studied in the past and adopted in practical applications. A comprehensive overview of traditional seismic rehabilitation techniques was presented by Sugano (1996). Conventional techniques which utilize braces, jacketing or infills as well as more recent approaches including base isolation and supplemental damping devices have been considered. Most of these retrofit techniques have evolved in viable upgrades. However, issues of costs, invasiveness, and practical implementation still remain the most challenging aspects of these solutions. Preliminary investigations on a non-invasive and economical retrofit solution based on metallic haunch connections have, for example, been recently presented by Pampanin & Christopoulos (2003).

In the past decade, an increased interest in the use of advanced non-metallic materials, including Shape Memory Alloys, SMA (Dolce et al., 2000), or Fibre Reinforced Polymers, FRP (*fib* 2001), has been observed.

In this contribution, the feasibility and efficiency of a retrofitting intervention using FRP composite materials, according to a multi-level performance-based approach will be presented. Depending on the joint typology (interior or exterior) and on the structural details adopted, alternative objectives can be achieved in terms of hierarchy of strength within the beam-column-joint system.

The theoretical developments of the retrofit strategy as well as the characteristic of the simplified

analytical model adopted to evaluate the increase in shear strength in the joint panel zone region will be described. The results from experimental quasi-static tests on as-built and CFRP retrofitted beam-column subassemblies (either exterior and interior), 2/3 scaled, will be presented. Extremely satisfactory performance of the retrofitted specimens was observed: the desired hierarchy of strength and sequence of events, according to the proposed multi-level design strategy, were achieved as targeted and well-predicted by the analytical methods.

2 SEISMIC RESPONSE OF EXISTING POORLY DETAILED BUILDINGS

2.1 *Experimental results*

The first phase of the research project involved the assessment, through analytical and experimental investigations, of the seismic vulnerability of existing reinforced concrete frame systems, primarily designed for gravity-loads as typical of the period between 1950s & 1970s, before the introduction of modern seismic design provisions in the mid-1970s.

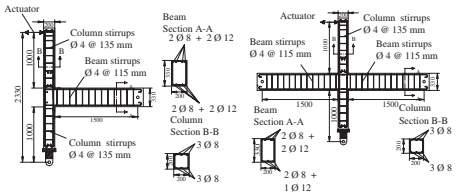

Figure 1. Geometry and reinforcement details in exterior joint specimen T1 and interior specimen C2.

The experimental program, part of a co-coordinated national project, comprised of quasi-static tests carried out at the Laboratory of the Department of Structural Mechanics of the University of Pavia on six, 2/3 scaled, beam-column joint subassemblies (two exterior knee-joints, two exterior Tee-joints and two interior joints, Fig. 1) as well as on a three-storey three bays frame system. Particular attention was given to the vulnerability of the panel zone region. An overview of the results will be herein given while more details can be found in Pampanin et al. (2002) and Calvi et al. (2002b).

Table 1 reports the fundamental geometric and reinforcement details of section of the beam-column subassemblies specimens: both identifications corresponding to as-built and retrofitted configurations (discussed later in the contribution) are indicated.

The testing loading protocol for the beam-column subassemblies (set-up shown in Fig. 2, left side) consisted of increased level of lateral top displacements (series of three cycles) combined with a variation of axial load as a function of the lateral force, as would

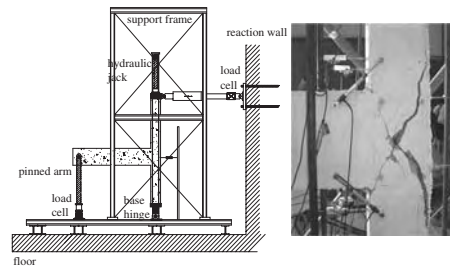

Figure 2. Test set-up and shear hinge mechanism in exterior joint (specimen T1).

Table 1. Specimen reinforcement and section geometry.

Joint type	Specimen		Section dimensions	Longitudinal reinforcement	Transverse reinforcement
Exterior tee	T1A, T1B**	Beam	330 × 200 mm*	Top $2\phi8 + 2\phi12$; Bottom $2\phi8 + 2\phi12$	$\phi4$@115 mm*
		Column	200 × 200 m*	$3\phi8 + 3\phi8$*	$\phi4$@135 mm*
	T2A, T2B**	Beam		Top $2\phi8 + 1\phi12$; Bottom $2\phi8 + 1\phi12$	
		Column			
Interior	C1**, C3**	Beam		Top $2\phi8 + 3\phi12$; Bottom $2\phi8 + 1\phi12$	
		Column			
	C2, C4	Beam		Top $2\phi8 + 2\phi12$; Bottom $2\phi8 + 1\phi12$	
		Column			

* Equal for all specimens.
** Reinforced with FRP.

occur in a beam-column subassembly during the sway of the frame.

The exterior tee-joint specimens showed (at both subassembly and frame system level) a particular brittle hybrid failure mechanism given by joint shear damage combined with slippage of beam longitudinal (plain round) bars within the joint region with concentrated compressive force at the end-hook anchorage. As a result, a concrete "wedge" tended to spall off (Fig. 2 right side), leading to a brittle local failure and loss of bearing-load capacity (Fig. 3).

Conversely, the interior joint specimens showed significant resources of plastic deformation (Fig. 4), even without specific ductile structural details.

A marked pinching was still observed, due to slip of the column longitudinal reinforcement bars. According to preliminary capacity design considerations, shear joint cracking and column hinging were predicted to be relatively close events. The concentration of flexural damage in the column at early stages, thus, acted as a structural fuse for the joint panel zone, which did not suffer significant cracking and damage. However, it should be recalled that the global frame system response can be seriously impaired if column hinging leads to a soft-storey mechanism.

2.2 *Shear hinge mechanism and global response*

The experimental quasi-static tests on the three storey-three bays frame system (Calvi et al., 2002b) confirmed the high vulnerability of the panel zone region as observed at a subassembly level (particularly in exterior joints) and the tendency to develop undesirable global mechanisms, due to the absence of an adequate hierarchy of strength.

In particular, an interesting peculiar mechanism at global level was observed, when compared to a weak-column strong-beam mechanism (which would lead to a soft storey mechanism), typically expected in existing building.

Based on the experimental evidences and numerical investigations, the concept of a shear hinge mechanism has been proposed as an alternative to flexural plastic hinging in the beams (Pampanin et al., 2002, 2003). The concentration of shear deformation in the joint region, through the activation of a so-called "shear hinge", can reduce the deformation demand on adjacent structural members, postponing the occurrence of undesirable soft-storey mechanism (see Fig.5).

The drawback of this apparent favourable effect on the global response is the increase in shear deformations in the joint region which can possibly lead (depending on the joint typology and structural details adopted) to strength degradation and loss of vertical load-bearing capacity. The post-cracking behaviour of the joint depends, in fact, solely on the efficiency of the compression strut mechanism to transfer the shear within the joint. Thus, while rapid joint strength degradation after joint diagonal cracking is expected

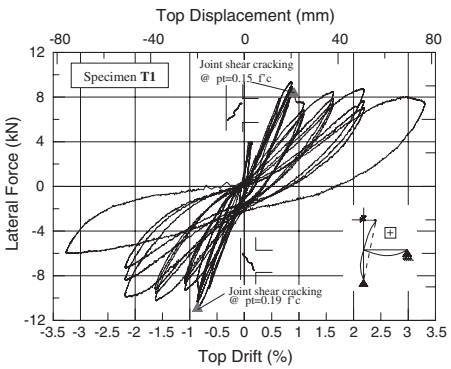

Figure 3. Hysteresis loop of exterior Tee-joint (specimen T1).

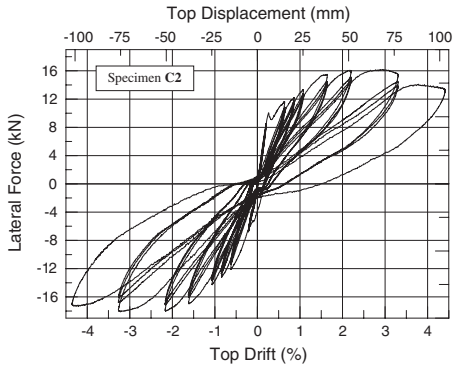

Figure 4. Experimental hysteretic response of interior joint (specimen C2).

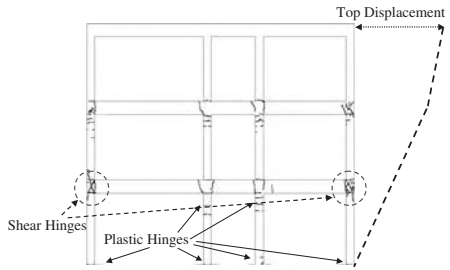

Figure 5. Frame response global mechanism: plastic hinges and shear hinges (top drift 1.6%, Calvi et al., 2002b).

in exterior joints, an hardening behaviour after first diagonal cracking can be provided by an interior joint.

A critical discussion on the effects of damage and failure of beam-column joints in the seismic assessment of frame systems has been given in Calvi et al. (2002a). Limit states based on joint shear deformations have recently been defined and are reported in Pampanin et al. (2003). Based on a detailed assessment of the local damage and corresponding global mechanisms, a more reliable seismic rehabilitation strategy can be defined.

3 MULTI-LEVEL RETROFIT STRATEGY

Independently on the technical solution adopted, the efficiency of a retrofit strategy strongly depends on a proper assessment of the internal hierarchy of strength of beam-column joints as well as of the expected sequence of events within a beam-column system (shear hinges in the joints or plastic hinges in beam and column elements). The effects of the expected damage mechanisms on the local and the global response should also be adequately considered.

3.1 *Performance-based retrofit strategy*

An ideal retrofit strategy would not only protect the joint panel zone region, identified critically weak point in older frames, but would further upgrade the structure to exhibit the desired weak-beam strong-column behaviour which is at the basis of the design of new seismic resistant RC frames. However, due to the disproportionate flexural capacity, in gravity load dominated frames, of the beams when compared to the columns a complete inversion of hierarchy of strengths is difficult to achieve in all cases and for all beam-to-column connections without major interventions. This is especially true for interior beam-to-column connections where the moment imposed on interior columns from the two framing beams is significantly larger than for exterior columns. As indicated in the previous paragraph, interior joints are less vulnerable than exterior joints and exhibit a much more stable hysteretic behaviour with hardening after first cracking. It is thus conceivable, in a bid to protect the interior columns from hinging, to tolerate some joint damage. According to a multi-level retrofit strategy approach suggested by Pampanin & Christopoulos (2003), two levels of retrofits can therefore be considered, depending on whether or not interior joints can be fully upgraded.

A *complete retrofit* would consist of a full upgrade by protecting all joint panel zones and developing plastic hinges in beams while columns are protected according to capacity design principles. A *partial retrofit* would consist of protecting exterior joints, forming plastic hinges in beams framing into exterior columns, while permitting hinging in interior columns or limited damage to interior joints, where a full reversal of the strength hierarchy is not possible. The viability of the partial retrofit strategy must be investigated on a case-by-case basis to assure that the localized damage to interior joints does not severely degrade the overall response of the structure or jeopardize the ability of the interior columns to safely carry gravity loads.

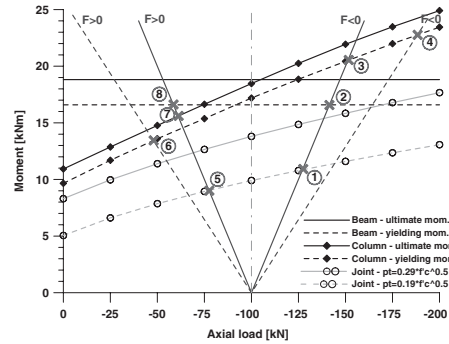

Figure 6. Evaluation of hierarchy of strengths and sequence of events: M-N performance-domain (exterior Tee-joint T1 in as-built configuration).

3.2 *Assessment of sequence of events: performance domains*

A simple procedure to compare the internal hierarchy of strengths within a beam–column-joint system is herein presented. The evaluation of the expected sequence of events is then proposed to be carried out through comparison of capacity and demand curves within a M-N (moment-axial load) performance-domain.

Figure 6 shows, as an example, the M-N performance domain adopted to predict the sequence of events and level of damage in the joint panel zone expected for the exterior specimen T1.

The capacities of beam, column and joints are referred to a given limit state (e.g. for joints: cracking, equivalent "yielding" or extensive damage and collapse) and evaluated in terms of equivalent moment in the column at that stage, based on equilibrium considerations within the beam-column joint specimen. While the evaluation of M-N curves for beams and columns is a relatively simple task, the definition of an "equivalent" curve to represent the joint panel zone can rely on the procedure described below.

The capacity or damage level of a joint is typically expressed in terms of nominal shear stress

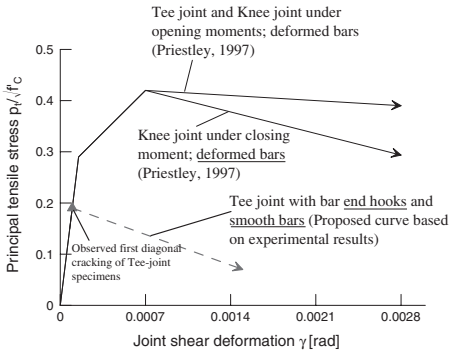

Figure 7. Strength degradation curves for exterior joints in terms of principal tensile stress-shear deformation.

(v_{jn}) or principal compression/tensile stresses (p_c, p_t). Although current codes (e.g. ACI 318-02, AIJ, EC8, NZS3101) tend to adopt simplified provisions which limit the nominal shear stress v_{jn} expressed as function of the concrete tensile strength, $k_1\sqrt{f'_c}$, or the concrete compressive strength, $k_2 f'_c$, where k_1 and k_2 are empirical constants, it is commonly recognized that principal stresses, by taking into account the contribution of the actual axial compression stress acting in the column, can provide more accurate indications on the stress state and thus damage level in the joint region.

Typical strength degradation models, available in literature and based on research on poorly designed joints (e.g. Priestley, 1997, Pampanin et al., 2002, shown in Fig. 7) can be adopted to define limit states in a joint panel zone subjected to shear and axial load.

According to the simplified analytical model proposed by Pampanin *et al.* (2003) to describe the joint non-linear behaviour, based on a rotational spring within a concentrated plasticity approach, the equivalent moment-rotation curve of the joint region (i.e. monotonic characteristics of the spring model) can be derived from the corresponding principal tensile stress-shear deformation curve using equilibrium considerations: for any given level of principal tensile (or compression) stress in the joint, the corresponding "joint moment" M_j, which is either the sum of the beam moments or the sum of the column moments at that stage, can be evaluated.

So doing, M-N capacity curves corresponding to the different joint limit states can be plotted within a performance domain where "equivalent column" capacity are represented.

As shown in Fig. 6 (as-built exterior specimen T1), demand curves should account for the variation of axial load due to the effects of lateral forces in a frame system (for either opening and closing of the joint). Incorrect and non-conservative assessment of the sequence of events can otherwise result, leading to inadequate design of the retrofit intervention

Table 2. Sequence of events for exterior specimen T1 (as-built configuration).

Specimen T1 (as-built)			
Type of lateral force	No.	Event	Lateral force [kN]
Open joint F < 0	1	Joint cracking and deterioration starting $p_t = 0.19\sqrt{f'_c}$	−10.94
	2	Beam yielding	−16.59
	3	Upper column yielding	−20.50
	4	Lower column yielding	−22.75
Close joint F > 0	5	Joint failure	9.37
	6	Lower column yielding	13.50
	7	Upper column yielding	14.50
	8	Beam yielding	16.59

In the case of specimen T1, in the as-built configuration, a pure shear hinge mechanism, with extensive damage of the joint, was thus expected (using a proper demand curve) prior to any hinging of beams or columns (Table 2), as confirmed by the experimental tests. However, the order and "distance" of the events strongly depends on the demand curve assumed. If a constant axial load curve was used (as shown in Fig. 6 for N = −100 kN), only a minor increase in the column strength (in addition to the joint strengthening) would have appeared necessary, leading to a column hinging occurring before the formation of a beam hinge (i.e. high risk of a soft storey mechanism even after the retrofit intervention).

The concept of a performance-domain could thus be extended from the purpose of assessing as-built systems and adopted to evaluate and control the feasibility and efficiency of any retrofit strategy on beam-column joints, provided that the effects of the retrofit solution on the single elements (beams, column or joint panel zone) can be simply and independently evaluated as described in the following paragraphs.

4 FRP STRENGTHENING EFFECTS: ANALYTICAL MODEL

The effects of a retrofit intervention with FRP composite materials, in the form of externally bonded reinforcement (EBR), on beam-column joint, in terms of flexural or shear capacity in beams, columns and panel zone region, is carried out through a step-by-step procedure. The occurrence of defined limit states (cracking, yielding, debonding, crushing and spalling of concrete, failure within the adopted materials)

corresponding to given stress or strain value can thus be properly evaluated and controlled when designing the retrofit intervention. As mentioned and shown, an accurate prediction of the expected sequence of events, can thus be obtained through M-N performance-domains.

Analytical procedures available in literature are adopted and properly modified to account for debonding phenomena as well as, more importantly, for the effects of the variation of axial load onto the joint panel zone behaviour (critical issue typically neglected).

4.1 *Flexural FRP retrofit of beams and columns*

The enhanced flexural behaviour of a FRP retrofit beam or column critical section was evaluated though a fibre section analysis. Bernoulli-Navier hypothesis on plane sections remaining plane was assumed, considering fully composite action (bond) between the external FRP laminates and the concrete. Debonding was taken into account according to the model proposed by Holzenkämpfer (1994) (and adopted by the *fib* guidelines of FRP retrofit, 2001), and thus expected to occur at a strain limit level $\varepsilon_{deb} = c_1 \cdot \sqrt{\frac{f_{ctm}}{E_f t_f}}$, where E_f is the FRP E-modulus, f_{ctm} the mean value of concrete tensile strength, s the thickness of the FRP laminate and c_1 an empirical coefficient taken as 0.64 for CFRP as suggested by Neubauer & Rostasy (1997).

The material behaviour was defined through proper stress-strain relationships, as follows: Mander *et al.* (1988) model for concrete; Dodd-Restrepo model (1995) for steel and a linear-elastic rule for the FRP composite material, consistent with the properties supplied by the provider.

The moment-curvature behaviour of the critical section in presence of externally bonded FRP laminate can thus be evaluated for different level of axial load (Fig. 8) using an iterative procedure as typically done for R.C. sections.

The position of the neutral axis is estimated until both compatibility and equilibrium conditions are satisfied. M-N capacity curves for beams and columns corresponding to a given limit state can be derived and plotted in a performance-domain to define the sequence of events.

The confinement effects of the FRP on the section curvature ductility capacity can be taken into account following procedures available in literature (e.g. Spoelstra & Monti 1999).

4.2 *Shear FRP retrofit of joint*

The evaluation through analytical models of the strengthening effects on the panel zone (joint) shear is a more complex task with limited research available in the literature. An overview of alternative procedures has been given by Antonopoulos & Triantafillou (2002). Typical over-simplified approaches consider the contribution of the FRP equivalent to external "stirrups" (analogy with steel transverse reinforcement). Upper limits of the maximum strain in the FRP material are used in the calculations, either corresponding to the declared ultimate tensile capacity (Gergely et al. 1998) or to a constant strain values depending on the preparation of the concrete surface (Tsonos & Stylianidis, 1999; Gergely et al., 2000).

A more rigorous model, based on stress equilibrium and strain compatibility equations of the panel zone region (idealized as a three-dimensional element) has been presented by Antonopoulos & Triantafillou (2002) as an extension of the model for RC joint behavior without FRP proposed by Pantazopoulou & Bonacci (1992). Satisfactory validation of the analytical model was obtained on the experimental results on a total of 15 beam-column exterior beam-column subassemblies, tested by the authors (Antonopoulos & Triantafillou, 2003) or available in literature (Gergely et al., 2000).

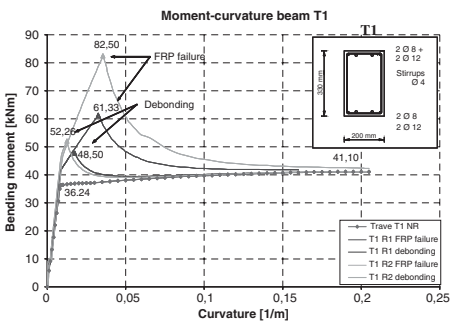

Figure 8. Effects of FRP on the moment-curvature curve of a member (beam) critical section.

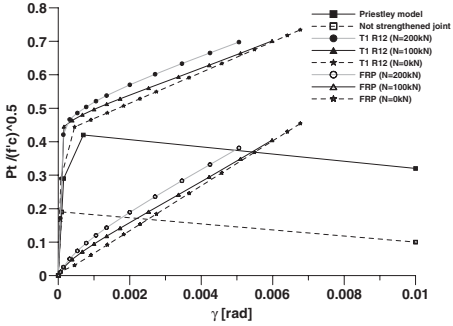

Figure 9. Joint strength degradation curve: contributions of FRP and concrete. (exterior speciment T1).

It is however important to underline that, as typically done in most experimental tests on beam-column joints, no variation of axial load as a function of the lateral force during the lateral sway of a frame system was considered during the tests. The implications of assuming a constant load in the assessment of sequence of event prior or after a retrofit intervention has been briefly discussed in the previous paragraphs.

In the present contribution the step-by-step iterative procedure proposed by Antonopoulos & Triantafillou (2002) is adopted as a sound basis tool and extended after simple modifications, to separately evaluate the contribution of FRP on the concrete compression strength in terms of principal tensile-shear deformation curve of the joint. As shown in Figure 9, the overall joint strength degradation curve would thus be given by the combination of the contributions of FRP and the concrete.

In terms of modelling according to a plasticity concentrated approach, two rotational springs (with moment-rotation curves derived, as mentione, according to the method proposed by Pampanin et al., 2003) can be adopted to represent the two independent contributions.

It is in fact expected (later confirmed by the experimental tests) that the cracking and damage of the joint can still occur underneath the protection given by the FRP laminates, whose major effect is to increase the overall joint strength, avoiding local failure mechanism (as the "concrete wedge" mechanism) and achieving an enhanced global behaviour by developing a more desirable sequence of events (e.g. weak-beam strong-column mechanism if a total retrofit strategy is followed).

Details on the analytical procedure and simplified design method can be found in Vecchietti (2001) and Nassi (2002).

5 DESIGN OF RETROFIT INTERVENTION

According to the proposed multi-level retrofit strategy, a full retrofit was adopted for the exterior joint (protection of the joint and plastic hinge in the beam) while a partial retrofit was adopted for the interior joint specimen (partial protection of the column hinging while some damage in the joint region can be accepted).

Issues related to the expulsion of the concrete wedge in the exterior joints as well as to the premature debonding of the fibres were carefully considered as explained in the following sections.

5.1 *Retrofit solutions*

Alternative FRP retrofit solutions (relying on different form or properties of the composite material) have been successfully proposed in literature and available. As mentioned, extensive experimental investigations on exterior beam-column joint retrofitted with FRP (in the form of laminates or strips) have been carried out by Triantafillou & Antonopouos (2003). Due to the scope of that investigation (evaluation of FRP contribution to the joint shear strength), the design of the retrofit strategy aimed at guaranteeing that the damage occurred in the joint region. A selective seismic strengthening technique for gravity load designed frames, relying on both FRP laminates and NMS (Near Mounted Surface) has been recently proposed by Prota et al. (2002).

In this contribution, uni-directional carbon fiber laminates (high-modulus CFRP, Table 3) were adopted in the configurations illustrated in Figures 10 and 11, for exterior joint and interior joint, respectively.

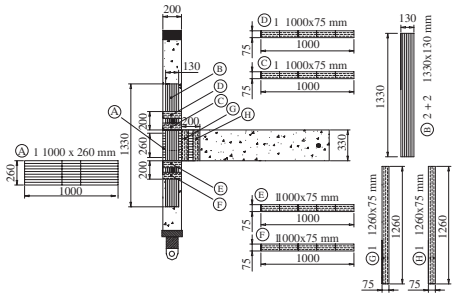

Figure 10. FRP-retrofit solution for exterior joint (specimen T1B).

Table 3. Properties of high modulus carbon fibre with unidirectional fabric (MBrace CFRP C5-30).

Fibre	Density [kg/m^3]	Effective thickness of 1 layer [mm]	Characteristic tensile strength [MPa]	Characteristic modulus of elasticity [MPa]	Ultimate strain [%]
High modulus carbon	1820	0.165	3000	390000	0.8

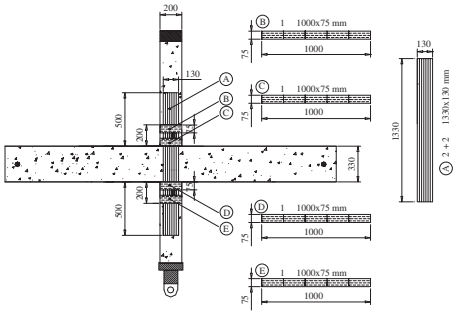

Figure 11. FRP-retrofit solution for interior joint (specimen C3).

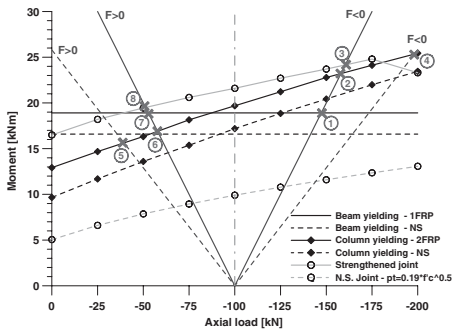

Figure 12. Evaluation of hierarchy of strengths and sequence of events: M-N performance-domain (exterior Tee-joint T1B joint after retrofit).

Vertical FRP laminates were used on the external face of the column in both interior and exterior joints (2 layers per side) in order to increase the column flexural capacity as well as the joint shear strength. In addition, in the exterior joint specimen, a U-shape horizontal laminate, wrapped around the exterior face of the specimen at the joint level, was used to increase the joint shear strength as well as prevent the expulsion of a concrete wedge.

An adequately limited anchorage length within the beam was calculated in order to guarantee sufficient shear strengthening in the joint without excessively increasing the beam capacity (as per Fig. 6). Although the evaluation of strengthening effects was carried out including debonding effects (when non-conservative), additional smaller strips were used to wrap the main FRP laminates and provide proper anchorage. In the case of the interior joint, the FRP laminate crossing the joint was intentionally left unprotected from debonding in the joint panel zone region.

Table 4. Sequence of events for exterior specimen T1 (retrofit configuration).

Specimen T1B (strengthened)			
Type of lateral force	No.	Event	Lateral force [kN]
Open joint	1	Beam yielding	−18.91
F < 0	2	Upper column yielding	−23.11
	3	Joint cracking (no strength degradation)	−24.15
	4	Lower column yielding	−25.32
Close joint	5	Lower column yielding	15.75
F > 0	6	Upper column yielding	16.98
	7	Beam yielding	18.91
	8	Joint failure	19.67

The target performance of the retrofit solution was controlled using the proposed procedure and M-N performance-domain as shown in (Fig. 12) and Table 4 for the exterior specimen T1B.

6 EXPERIMENTAL RESULTS

The results of the experimental quasi-static tests on three beam column joints in the retrofitted configurations (namely T1B, T2B, and C3, with the test on C1 being under preparation) provided very satisfactory confirmations of the efficiency of the adopted retrofit solution as well as of the reliability of the analytical procedure developed to design the intervention and assess the expected sequence of events and performance. A summary of the results is herein given, while more details are available in Nassi (2002) and will be reported in future publications.

In all cases, the retrofit objective based on a multi/level retrofit strategy was achieved, leading to a significantly improvement in the behaviour of the subassemblies, which ultimately imply an enhanced behaviour of the frame system (adequate global inelastic mechanism).

As shown in Figure 13, a properly designed FRP-retrofit solution can protect and avoid the formation of a brittle shear hinge mechanism and reestablished a more desirable hierarchy of internal strengths and sequence of events, enforcing a beam plastic hinge mechanism (total retrofit).

As a result, an improved and more stable hysteresis behaviour was observed with increased ductility and energy dissipation capacity (Figs 14 and 15).

The values of lateral force corresponding to the occurrence of the critical events were well-predicted by the analytical methods (presented in Fig. 12 and Table 4).

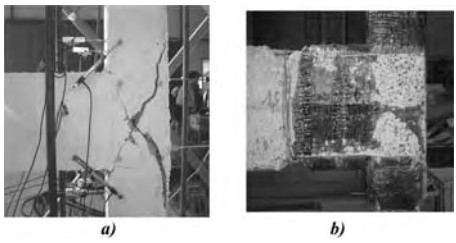

Figure 13. Alternative damage mechanisms; a) shear hinge (as-built T1); b) beam plastic hinge (retrofitted T1B).

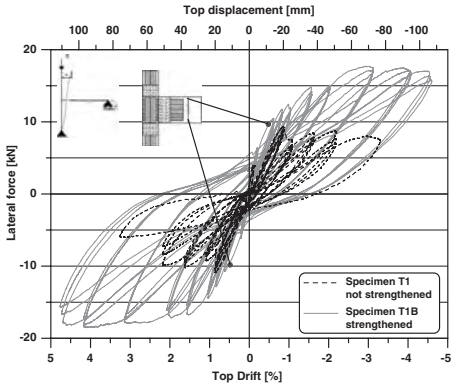

Figure 14. Comparison of hysteresis behavior of as-built and FRP-retrofitted configuration: exterior specimen T1B.

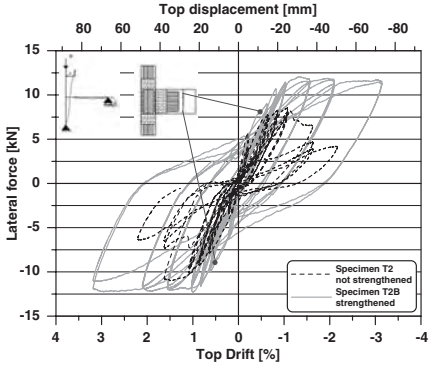

Figure 15. Comparison of hysteresis behavior of as-built and FRP-retrofitted configuration: exterior specimen T2B.

Similar considerations can be derived for the interior joint (specimen C3, Fig. 16) where the partial retrofit strategy led to a controlled debonding of the column vertical fibres crossing the joint. The

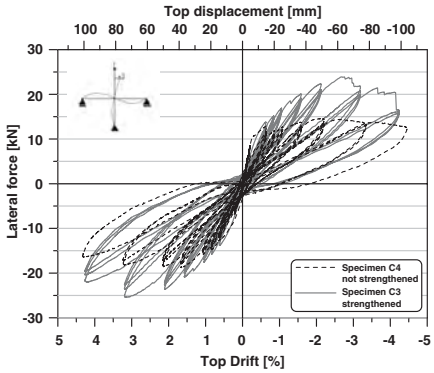

Figure 16. Comparison of hysteresis behavior of as-built and FRP-retrofitted configuration: exterior specimen T2B.

formation of flexural damage in the column was thus postponed. In addition to the increased overall strength, the FRP provided a favourable confinement effects in the column plastic hinge region avoiding the premature crushing and spalling of concrete cover, protecting from strength degradation, buckling of the longitudinal bars and consequent failure.

Moreover, preliminary analytical-experimental comparison of the joint behaviour in terms of principal tensile stress vs. shear deformation curve confirmed the efficiency of the adopted analytical model in evaluating the strengthening effects of FRP on the joint shear strength.

7 CONCLUSIVE REMARKS

The preliminary results of quasi-static tests on beam-column joint specimens, designed for gravity load only and retrofitted with CFRP laminates, provided very satisfactory confirmation of the efficiency of similar solutions for existing buildings.

A multi-level retrofit strategy depending on the subassemblies type and structural details has been proposed to achieve the desired performance with a feasible intervention. A simplified procedure to evaluate and control the sequence of event using M-N performance-domain has been presented.

In the exterior joint, the occurrence of a brittle joint shear mechanism was adequately protected and a more desirable hierarchy of strengths and sequence of events achieved, leading to a more ductile and dissipating hysteresis behaviour.

Similar retrofit procedure and solutions have been adopted on a three storey frame system, whose experimental quasi-static tests is on preparation and will be conducted by middle of the year. The results from

the test on the retrofitted configuration as well as comparisons with the performance of the as-built configurations (Calvi et al., 2002b), will allow to further validate the efficiency of the proposed retrofit strategy concept and methods.

Ultimately, as discussed in the introduction, issues of accessibility of the joint region and invasiveness will be faced in real applications. It is worth however noting that a typical geometrical and plan configuration of existing buildings designed for gravity load only in the 1950s–1970s period consist of frames running in one direction only and lightly reinforced slab in the orthogonal direction, the latter being quite typical of the construction practice in Mediterranean countries. In these cases, the adoption of the proposed retrofit intervention can be somehow facilitated, when compared with more recently designed buildings with frames in both directions and cast-in-situ concrete slabs providing flange effects.

ACKNOWLEDGEMENTS

The financial support provided by the Italian Ministry of the University and the University of Pavia, under a coordinated national Project (PRIN 2001), as well as by the European Community (SPEAR G6RD-CT-2001-00525) is gratefully acknowledged. The authors wish to thank the MAC S.p.a. Treviso for providing the materials and technical assistance for the retrofit intervention. The assistance and cooperation, during different phases of the project, of the postgraduate students Mr. A. Vecchietti and Mr. R. Nassi are also kindly acknowledged.

REFERENCES

ACI Committee 318 2002. Building Code Requirements for Structural Concrete (ACI 318-02), *American Concrete Institute*, Farmington Hills, Mich., 391 pp.

AIJ, Architectural Institute of Japan 1997. Design Guidelines for Earthquake-Resistant R.C. Buildings Based on Inelastic Displacement Concept (draft, in Japanese).

Aycardi, L.E., Mander, J.B. & Reinhorn, A.M. 1994. Seismic Resistance of R.C. Frame Structures Designed Only for Gravity Loads: Experimental Performance of Subassemblages, *ACI Structural Journal*, Vol. 91, No.5, 552–563.

Antonopoulos, C.P. & Triantafillou, T.C. 2002. Analysis of FRP-strengthened RC beam-column joints, *Journal of Composites for Construction*, Vol. 6, no.1, pp. 41–51.

Antonopoulos, C.P. & Triantafillou, T.C. 2003. Experimental Investigation on FRP-Strengthened RC Beam-Column Joints, *J.l of Composites for Construction*, 7(1), pp. 39–43.

Beres, A., Pessiki, S., White, R. Gergely, P. 1996. Implications of Experimental on the Seismic Behaviour of Gravity Load Designed RC Beam-Column Connections, *Earthquake Spectra*, Vol. 12, No.2, May, pp. 185–198.

Bing. L, Yiming W. & Tso-Chien P. 2002. Seismic Behavior of Non-Seismically Detailed Interior Beam-Wide Column Joints. Part I: Experimental Results and Observed Behavior, ACI Structural Journal, Vol. 99, N. 6.

Calvi G.M., Magenes G. & Pampanin S. 2002a. Relevance of Beam-Column Damage and Collapse in RC Frame Assessment. *J. of Earthq. Engng (JEE), Special Issue 1*, pp. 75–100.

Calvi, G.M., Magenes, G. & Pampanin, S. 2002b. Experimental Test on a Three Storey R.C. Frame Designed for Gravity Only, *12th ECEE*, London, paper n. 727.

Dolce, M., Cardone, D. & Marnetto, R. 2000. Implementation and testing of passive control devices based on shape memory alloys. *Earthq. Engng. & Struct. Dyn*., 29, 7, 945–968.

Dodd, L.L., & Restrepo, J.I. 1995. Model for Predicting Cyclic Behavior of Reinforcing Steel. ASCE *Journal of Structural Engineering*, Vol. 121, No. 3, pp. 433–445.

Eurocode 8, 2003 Design Provisions for Earthquake Resistance of Structures, *European Committee for Standardization*, Brussels.

fib (Federation International du Beton) 2001. Externally Bonded FRP Reinforcement for RC structures, *fib Bulletin n.14*, Lausanne.

Gergely, J., Pantelides, C.P., Nuismer, R.J. & Reaveley, L.D. 1988. Bridge Pier Retrofit Using Fibre Reinforced Plastic Composites, *Journal of Composite Constructions*, ASCE, 2(4), 165–174.

Gergely, J., Pantelides, C.P. & Reaveley, L.D. 2000. Shear Strengthening of RC T-Joints Using CFRP composites, *Journal of Composite Constructions*, ASCE, 4(2), 56–64.

Hakuto, S., Park, R. & Tanaka, H. 2000. Seismic Load Tests on Interior and Exterior Beam-Column Joints with Substandard Reinforcing Details, *ACI Structural Journal*, V. 97, N.1, 11–25.

Holzenkämpfer, P. 1994. Ingenieurmodelle des verbundes geklebter bewehrung für betonbauteile, *Dissertation*, TU Braunshwieg (in German).

Mander, J.B., Priestley, M.J.N. & Park R., 1988. Theoretical Stress-Strain Model for Confined Concrete, *ASCE Journal of the Structural Division*, Vol. 114, No. 8, pp. 1804–1826.

Nassi, R. 2002. Seismic Retrofit Strategy for Under-Designed Beam-Column Subassemblies Using FRP, *Laurea Thesis*, Dept. of Struct. Mech., Un. of Pavia (in Italian).

Neubauer & Rostásy, 1997. Design aspects of concrete structures strengthened with externally bonded CFRP-plates, Concrete+Composites, *7th International Conference on Structural Faults and Repair*, 2, 109–118.

NZS3101, 1995. Part 1 The design of Concrete Structures, Standards New Zealand.

Pampanin, S., Calvi, G.M. & Moratti, M. 2002. Seismic Behaviour of R.C. Beam-Column Joints Designed for Gravity Loads, *12th ECEE,* London, paper n. 726.

Pampanin, S., Christopoulos, C. 2003. Non-invasive Retrofit of Existing RC Frames Designed for Gravity Loads only, *fib2003 Symp. Concrete Struct. in Seismic Regions*, Athens.

Pampanin, S., Magenes, G. & Carr, A. 2003. Modelling of Shear Hinge Mechanism in poorly Detailed RC Beam-Column Joints, *Proceedings of the fib Symposium Concrete Structures in Seismic Regions*, Athens, paper n. 171.

Pantazopoulou, S.J. & Bonacci, J.F. 1994. On earthquake-resistance reinforced concrete frame connections. *Canadian Journal of Civil Engineering*. 21, 307–328.

Park, R. 2002. A Summary of Results of Simulated Seismic Load Tests on Reinforced Concrete Beam-Column Joints, Beams and Columns with Substandard Reinforcing Details. *Journal of Earthquake Engineering*, Vol. 6, No. 2, 1–27.

Priestley, M.J.N. 1997. Displacement-based Seismic Assessment of Reinforced Concrete Buildings", *Journal of Earthquake Engineering*, Vol. 1, No. 1, 157–192.

Prota, A., Manfredi, G., Nanni, A. & Cosenza, E. 2002. Capacity Assessment of GLD RC Frames Strengthened with FR, *12th European Conference on Earthquake Engineering*, London, paper n. 241.

Spoelstra, M.R. & Monti, G. 1999. FRP-Confined Concrete Model. *J. of Composites for Constr.*, ASCE, 3(3), 143–150.

Sugano, S. 1996. State of the art in Techniques for Rehabilitation of Buildings, *Proceedings of the 11th World Conf. on Earth. Engng.*, Acapulco, Mexico, Paper no. 2175.

Tsonos, A.D. & Stylianidis, K.A. 1999. Pre-Seismic and Post-Seismic Strengthening of Reinforced Concrete Structural Subassemblages Using Composite Materials (FRP), Proceedings, 13th Hellenic Concrete Conference, Rethymno, Greece, 1, 455–466 8in Greek).

Vecchietti, A. 2001. Seismic Rehabilitation of Concrete Frame Systems Designed for Gravity Loads Only Using FRP Composite Materials, *Laurea Thesis,* Dept. of Structural Mechanics, University of Pavia (in Italian).

Strengthening of masonry and timber structures

FRP Composites in Civil Engineering – CICE 2004 – Seracino (ed)
© 2005 Taylor & Francis Group, London, ISBN 90 5809 638 6

Numerical simulation of FRP strengthened unreinforced masonry

S.H. Xia & D.J. Oehlers
Department of Civil and Environmental Engineering, Adelaide University, Adelaide, Australia

ABSTRACT: In this paper, a numerical simulation method was used to study the effect of interface model between Fiber Reinforced Polymer (FRP) plates and masonry on the structural response of FRP strengthened unreinforced masonry (URM) beams. Interfacial shear stress versus slip relationship was determined from a series of pullout tests. A numerical simulation was developed to model the debonding formation of FRP strengthened URM beams. For simplicity, bricks were assumed to be linear elastic while brick-to-brick through mortar and masonry-to-FRP interface were modeled by an interface element with a bi-linear constitutive relationship. The program was then used to investigate the debonding mechanism in FRP strengthened URM structures subjected to out-of-plane bending. Parametric analysis results showed that decrease in ascending and increase in descending stiffness can significantly improve strength and deformation capacities of FRP strengthened URM beams and strains at which the debonding failure occurred varied.

1 INTRODUCTION

Interfacial model plays an important role in analyzing the behaviour of FRP strengthened reinforced concrete (RC) and URM structures and in predicting structural strength and ductility. While intensive research has been carried out worldwide in investigating debonding failure mechanisms and the bonding characteristics of the interface for FRP strengthened RC structures (Chen & Teng, 2001; Oehlers & Seracino 2004), to the best of authors' knowledge, there is no published work on interface model and how debonding processes to lead to final failure for FRP strengthened URM; although much existing research on FRP strengthened URM has reported that debonding is a major premature failure mechanism in FRP strengthened URM.

Testing of FRP plated masonry specimens under out-of-plane load has primarily been performed by Saadatmanesh (1997). During out-of-plane bending tests of FRP plated URM wall specimens, Gilstrap and Dolan (1998) observed that, as a result of early failure due to debonding, predicted failure loads exceeded experimental wall strengths by anywhere between 25–800%. Recent experimental studies have focused on making FRP retrofitting a viable alternative to conventional retrofitting techniques, and in the derivation of semi-empirical formulae to predict the response of FRP retrofitted URM walls. The effect of varying FRP material and layout on the load carrying capacity and ductility of FRP plated URM walls under out-of-plane bending was investigated by Hamoush *et al.* (2002) and Albert *et al.* (2001). Holberg & Hamilton (2002) improved the ductility by combining a Glass FRP composite system with conventional structural steel and reinforcing steel connections to ensure steel yield before rupture of the brittle FRP. Hall *et al.* (2002) introduced ductility into the FRP retrofitted masonry walls by using a hybrid strengthening system. Kuzik *et al*. (2003) found that the amount of Glass FRP sheets significantly affected the behaviour of the retrofitted URM walls, and walls with small cracks under successive out-of-plane loading cycles could still maintain their integrity. A simple method to predict the overall moment-deflection response of FRP retrofitted walls was presented, in which, the ultimate FRP strain was derived from regression analysis of test data with one variable being the amount of FRP reinforcement.

The bonding characteristics of the interface between FRP composites and the surface of parent structures have usually been investigated experimentally by examining the effect of certain key parameters on the debonding failure mechanism. One such representative experiment is the pullout test. The main purpose of the pullout test is to determine the shear stress distribution and slip along the interface as the load increases and debonding forms. A shear stress and slip relationship or interface law is then correlated and is adopted in finite element simulation and in deriving analytical solutions of debonding strengths.

In this paper, based on an interface mode obtained from the results of a series pullout tests carried out for FRP strengthened masonry recently at the University of Adelaide (Xia & Oehlers, 2004), a numerical simulation was developed to model the debonding

formation of FRP strengthened URM beams. For simplicity, bricks were assumed to be linear elastic while mortar and masonry-to-FRP interface were modeled by an interface element with bi-linear constitutive law. The program was then used in a parametric study to investigate debonding mechanism in FRP strengthened masonry structures subjected out-of-plane bending. It is worth noting that only debonding failure was investigated in this paper.

2 FINITE ELEMENT ANALYSIS

2.1 *Elements*

A finite-element program has been developed to simulate the interfacial shear stress distribution, and the propagation of debonding along the plate bond length, and the debonding strain at which failure occur. For simplicity, the linear elastic response of the mortar was smeared with that of the brick into a masonry block which was assumed to be linear elastic. A four-node plan stress quadrilateral iso-parametric element was adopted to divide each masonry block into identical meshes. FRP composites were represented using either 4-node plane stress quadrilateral iso-parametric elements (if thickness of FRP composites can not be ignored) or bar elements. The brick-to-brick and masonry-to-FRP bond joints were modeled by interface elements, as illustrated in Figure 1. The interface element had four nodes but zero thickness, with two upper nodes connected to masonry and two lower nodes to FRP in the case of masonry-to-FRP joint, while two right nodes connected to right masonry and two left nodes to left masonry at mortar joint. At each end of the interface element, interaction between the two nodes were represented by two springs: with a tangential (shear) spring (K_t) representing shear-slip in the form of mode II fracture and a normal (tension-compression) spring (K_n) representing tension-opening in the form of mode I fracture.

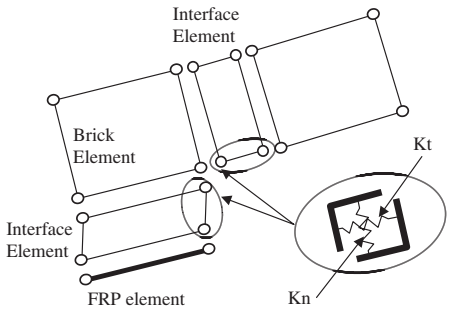

Figure 1. Interface element.

2.2 *Constitutive laws for interface elements*

Under general loading conditions, mixed-mode interface debonding with large displacement discontinuity can occur. For example, the shear strength and stiffness of the mortar are likely to be influenced by the normal stress. For sake of simplicity, in this paper two springs of the interface element were assumed to be independent before the full degradation of the interface resistance is reached either in tangential direction ($s \geq s_f$) or in normal direction ($w \geq w_f$). The yield surface is given in Figure 2a, where peak shear stress $t^- = t^+$, and peak normal stress $n^- \neq n^+$, which reflects the nature of both interfaces. The constitutive law of all the spring elements consisted of a linearly ascending branch followed by a linearly descending branch to capture the softening nature in the brittle material. If necessary, a horizontal branch can be used to represent residual stress resulted from aggregate interlock, as illustrated in Figure 2b, where s_0 and w_0 are the displacement discontinuities in correspondence to the maximum shear t_f and the maximum traction n_f, respectively. Non-penetration of normal spring was enforced through non-deformable spring and unlimited compressive strength, as shown Figure 2c.

For the mortar joints, the initial K_n and K_t of the brick-to-brick interface can be either assumed to be infinite as elastic response of mortar can be smeared into that of the masonry block, or calculated to reflect the normal and shear stiffness of the mortar through the tributary area that a spring represents. The stiffness of the tangential spring K_t was assumed to be zero when mortar opening exceeded w_f. The maximum tensile of the normal spring were calculated from the tensile strength of mortar through the tributary area that a spring represents. The maximum shear strength of the tangential spring was obtained from the shear strength

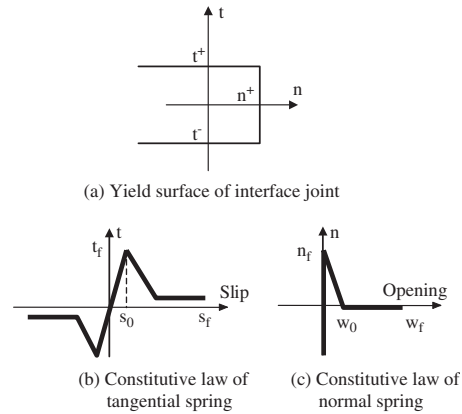

Figure 2. Constitutive laws.

of mortar that was taken as the lesser of 1.25f′t and 0.35 MPa (f'_t is the tensile strength of mortar) in the numerical simulation.

The dominating failure mode at the FRP-masonry interface is the mode II fracture failure. It is therefore reasonable to assume a constitutive relationship for the tension-compression spring of the FRP-masonry interface so that no yield would occur before the shear debonding failure and the penetration between FRP and masonry can be minimized. The constitutive relationship of tangential spring along the FRP-masonry was calculated from the shear stress and slip curve obtained from test results (Xia and Oehlers, 2004).

2.3 *Solution scheme*

The framework of the numerical approach to accommodate softening of bond strength mode lies at the intersection of three broad areas: elastoplasticity, interface modeling and complementarity theory. In effect, complementarity, an ingredient common to the first two mentioned areas, provides a unifying framework (theoretical and computational) for the solution of a large number of practical and important engineering mechanics problems. Based on the work in Tin-Loi & Xia (2001 & 2003), a finite-element simulation has been developed to accommodate the behaviour peculiar to FRP strengthened masonry as described above. A unified formulation describing interface behaviour can be written as

$$\dot{z} \geq 0; \quad F(z) \geq 0; \quad \dot{z}^T F(z) = 0 \tag{1}$$

This particular mathematical programming problem is known as a nonlinear complementarity problem (NCP) and is characterized by two sign-constrained and orthogonal vectors, where, for a given, usually continuously differentiable, nonlinear function of variable **z**, it is required to find in a finite-dimensional real vector **z**, or to show that no such z exists. A linear complementarity problem (LCP) is recovery if $F(z)$ is a linear function. For the problem dealt with here, **z** defines plastic multipliers or internal variables that describe a post-peak softening behaviour in relation to normal/shear stress with opening/slip, $F(z)$ represents yield function describing the progress of yielding surface or the fracture processing zone, and $\dot{z}^T F(z) = 0$ describes yield condition. It is worth noting that the constitutive law of both the normal spring and the tangential spring are assumed to be irreversible. A rate formulation thereby was used in Eq. (1) to handle unloading phenomena.

The nonlinear analysis was conducted for subsequent finite load increments. The computation of the response to each step was carried out using a predictor-corrector method through an iterative procedure consisting of a linear prediction phase and a nonlinear correction phase. The linear prediction was carried out under displacement control so that the entire equilibrium path can be traced. The PATH solver (Dirkse & Ferris, 1995) was employed to solve the resulting NCP in the nonlinear correction phase.

3 PARAMETRIC STUDY

To date, many experiments have been conducted to investigate the effect of certain physical parameters have on the ultimate load capacity and deformation capacity of FRP strengthened URM beams and walls under out-of-plane loading. However, no study has examined the shear stress-slip relationship along the length of the plate and how changes in the shear stress-slip relationship and shear-span may affect the behaviour of FRP strengthened URM beams. Therefore it was desirable to conduct parametric analyses into the properties of interface model and the shear span to determine the effect they have on the performance of FRP strengthened URM beams. Simply supported beam strengthened with a 1.2 mm thick and 50 mm wide FRP on its tension side under a point load, as illustrated in Figure 3, was used in the parametric study. For the purpose of the current study, the FRP reinforcement was designed to ensure no FRP rupture would occur. Table 1 lists all the relevant geometrical and material parameters that are constant for all the analyzed beams.

3.1 *Validation of the numerical model*

A series of beam test were conducted (Xia and Oehlers, 2004) in order to investigate failure modes under

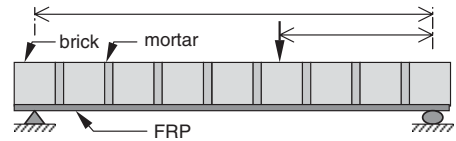

Figure 3. Beam.

Table 1. Constant test specimen properties.

Parameter	Symbol	Value
FRP elastic modulus	E_p	160 MPa
Beam width	b	230 mm
Beam depth	d	110 mm
Mortar thickness	t_m	8 mm
Brick thickness	t_b	62 mm
Masonry elastic modulus	E_m	9 GPa
Masonry compressive strength	f_{mc}	27 MPa
Mortar tensile strength	f_{mt}	0.37 MPa
Mortar elastic modulus	E_{mor}	1.23 GPa

Table 2. Varied spans and shear spans of beams.

Specimen number	Span (L) (mm)	Right span (a) (mm)
s1	560	241
s2	1042	451
s3	1462	661
s4	1952	871

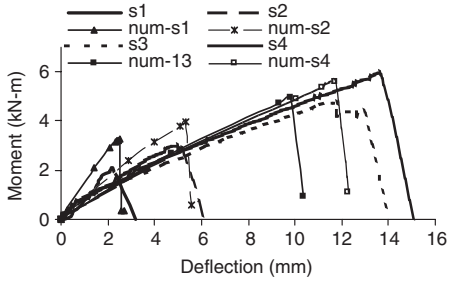

Figure 4. Comparison between predicted and experimental bending moment and deflection curves.

various parameters and to validate numerical model. Four beams with varying spans listed in Table 2 were analyzed with the typical shear stress and slip obtained from test results. All beam test specimens were plated with a 1.2 mm thick and 50 mm wide FRP plate. Load versus deflection for all beam specimens are plotted in Figure 4 in comparing with the experimental results. Overall, there is consistent trend for numerical load-deflection curves in comparison with that from the experimental results. Initial stiffness of the curves from both results is very closed. Up to half maximum load, numerical load versus deflection curves were stiffer than that of experiment, especially for short span beams in which larger shear forces are required to produce the same amount of bending moment as it in long-span beams. This difference is resulted from assigning relatively large shear stiffness and shear strength to the tangential spring at mortar joint to avoid shear failure of mortar, which restricted the shear deformation of mortar to be developed. It is noticeable in Figure 4 that the predicted capacity for short span beam is higher than experimental result. This is due to the fact that short span beams in test did not fail in the mode numerical simulation attempted but in shear which typically occurred at the first mortar joint near a support where very little shear can be sustained through masonry-to-FRP interface. As vertical flexural crack caused radical change within the cross-sectional geometry of the mortar joint, relatively large shear force in specimen s1 eventually caused the

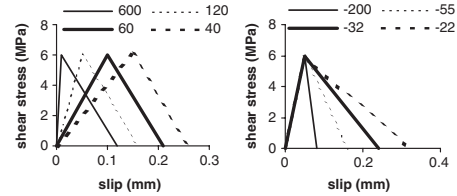

(a) Ascending branch (b) Descending branch

Figure 5. Shear stress end slip relationship.

blocks to split, and the two pieces translate laterally away from one another.

3.2 *Interface model of FRP-masonry joint*

The interface model used in the parametric study was linearly ascending, before a maximum shear was reached, followed by a linear descending to accommodate the degradation of the interface resistance. Figure 5 lists the variation of stiffness in both ascending and descending branches. The thin dash line in Figure 5 is a typical shear stress and slip relationship obtained from pullout tests of FRP strengthened masonry with material properties given in Table 1 (Xia and Oehlers, 2004). Values given in Figure 5a are the stiffness of ascending branch with a fixed descending stiffness of −55 N/mm while in Figure 5b are the stiffness of descending branch with a fixed ascending stiffness of 120 N/mm. Both stiffnesses are characteristic of masonry-to-FRP interface. In the parametric study, beams analyzed had a constant span of 560 mm and shear span of 241 mm and the maximum shear stress remained unchanged along the interface. Residual stress in the shear stress and slip curve was ignored in analyzed beams unless mentioned.

Figure 6 illustrates applied load (P) against deflections at the point of the applied load for varying stiffness in ascending branch (Figure 6a) and in descending branch (Figure 6b). Overall, the beams responded in a very linear fashion and failed rapidly when debonding cracks approached the beam support on the short span side. It can be seen from Figure 6 that the load carrying capacity and the deformation capacity of FRP strengthened masonry significantly increased as the ascending stiffness was decreased and the descending stiffness increased (note: negative value for descending). Although the change in the stiffness of the ascending branch did affect the initial stiffness of FRP strengthened URM beams, it had little effect on the overall beam stiffness. As expected, the change in stiffness of the descending branch did not influence much the initial response. Given a residual stress of 10% of maximum shear stress in the shear stress and slip relationship, the beam with a descending

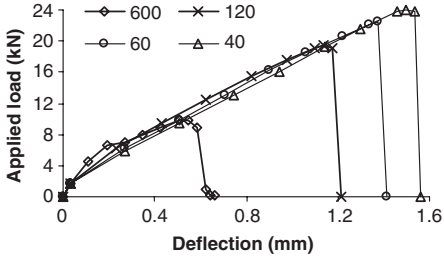

(a) Ascending branch

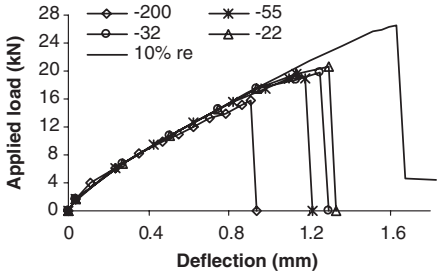

(b) Descending branch

Figure 6. Applied load and deflection relationships for varying stiffness in shear stress and slip curve.

stiffness of −22 MPa was reanalysed. The solid line in Figure 5(b) displayed how a residual stress can further improve the performance of FRP strengthened masonry beam. Due to the brittle nature of masonry, it is unlikely that a favourable combination of the stiffness of the descending branch and the residual stress can be achieved to improve the performance of FRP strengthened URM beams. However, decrease in ascending stiffness is possible by reducing the shear stiffness of adhesive layer or increasing adhesive layer thickness.

3.3 *Shear span*

Four beams with varying spans listed in Table 2 were analyzed with the typical shear stress and slip given in previous section. Figure 7a showed the shear capacity versus span-to-depth ratio while Figure 7b the moment capacity versus span-to-depth ratio. Without the consideration of other potential failure modes reported from experimental study (Gilstrap and Dolan,1998), Figure 7 suggested that, the moment capacity of a beam can be increased with the increase of beam span-depth ratio. It was noticed from the numerical results that the moment when debonding started to initiate from the vertical flexure crack where the moment was the maximum was almost the same for all four beams.

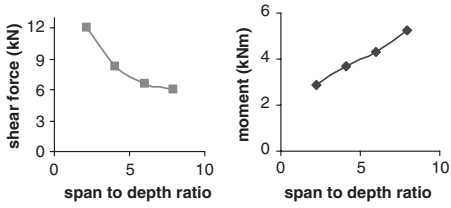

Figure 7. Relationships between moment capacity versus span-to-depth, and shear capacity versus span-to-depth.

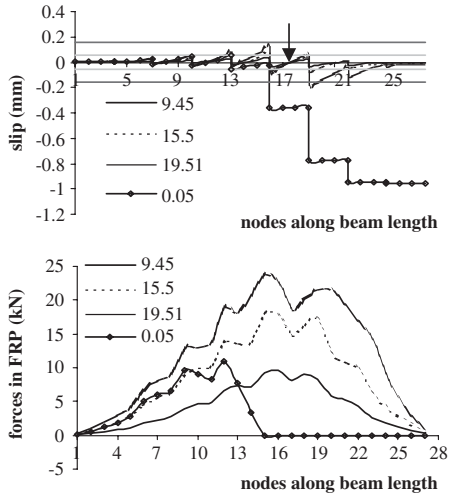

Figure 8. Force distributions in FRP and slip distributions along the beam length for Beam s1 with untrapped support.

The applied load or the moment capacity can be further increased as debonding started to form at other mortar joints along the masonry-to-FRP interface until either these debonding cracks met each other or no further increase in the shear force transferred through masonry-to-FRP can be sustained.

3.4 *Slip and FRP force distributions*

Beam s1 was analyzed under two support conditions: a) with FRP plate trapped under support and b) untrapped to investigate the effect that plate end anchorage has on FRP strengthened masonry beams. In the case of the trapped support, the shear stiffness and maximum shear force that the tangential spring has at the support are five times the stiffness of the tangential springs in other regions to represent the trapped mechanism. Figures 8–9 display force distribution in

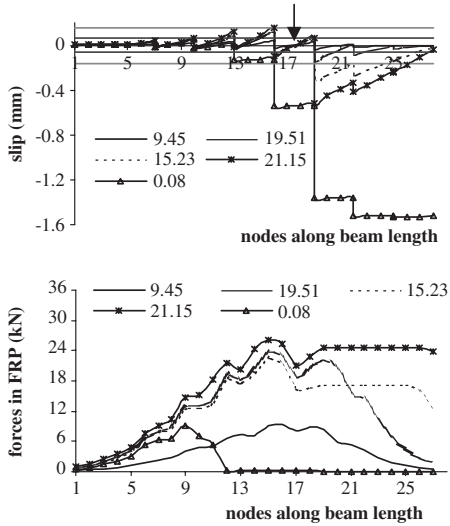

Figure 9. Force distributions in FRP and slip distributions along the beam length for Beam s1 with trapped support.

FRP plate and slip distribution along beam length at different load levels which are given in loading order. The Moment versus deflection curves at the point of applied load are also plotted for Beam s1 and s3 in Figure 10. Two horizontal lines on the upper and lower sides of the x-axis in the slip distribution diagrams are used to indicate the slip levels at which its shear stress reaches the maximum and its shear resistance fully degradates. Numerical results revealed that a uniform distribution of vertically flexural cracks developed at early stage of loading at most of mortar joints due to the low strength of mortar joints. Thus the debonding could develop at any mortar joint and propagate along the interface towards both supports as shown in Figures 8 and 9 after load level approached 15.5 kN, which is different from intermediate flexural debonding in a flexural test of FRP strengthened RC beam where the debonding usually develops at one or two major flexural cracks and propagates to meet other flexural and flexural-shear cracks. In both types of supports, force distribution in FRP and slip distribution along masonry-to-FRP interface are almost the same before applied load reached 19.51 kN where full degradation of the shear resistance at the first mortar next to applied load has been reached.

Beyond 19.51 kN, in the case of the untrapped support, debonding propagated rapidly towards the end of the short shear span as the shear force needed to be transferred through the interface cannot be sustained

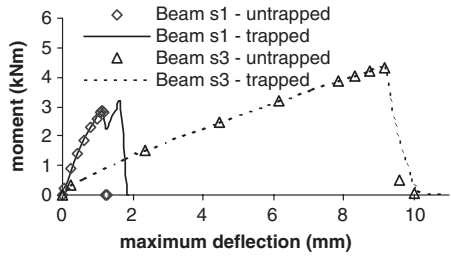

Figure 10. Moment and deflection at the position of applied load.

due the zero residual stress and steep softening branch in the shear stress and slip curve. A drop in forces in the FRP and an increase of slip can be seen from Figure 8. It is worth mentioning that it is assumed in the numerical modelling that no shear failure of the mortar would occur to allow a full development of debonding. If any one of the mortar joint failure in shear, FRP rupture and brick failure occurs before the full development of debonding, the load capacity of the FRP strengthened beam would be smaller than that at the point of debonding failure.

In the case of the trapped support as shown in figure 9, debonding propagates across the short shear span first. The applied load decreases to a load level of 15.23 kN at which the shear force transferred through the masonry-to-FRP interface is sustained by the trapped mechanism and the uniformly distributed forces in FRP over the short span indicated the full degradation of the interface over short span. The applied load continues to increase until the maximum shear force that the trapped support can carry is reached. It is apparent that, apart from improving the behaviour of masonry-to-FRP interface, the proper design of end anchorage system is extremely important in maintaining strength and increasing ductility for FRP strengthened masonry walls subjected to out-of-plane load. The support entrapment, however, had less effect on beams response as beam span increased as shown in Figure 10.

3.5 *Debonding strain*

It has been reported by (Kuzik *et al*., 2003) that strains in FRP varied when FRP strengthened masonry beams or walls fail before their ultimate capacity reaches and it is critical to provide accurate debonding strain predictions upon which an analytical model can be based to calculate the capacity of FRP strengthened beams. Debonding strains for all numerically analyzed FRP strengthened beams has been summarized in Table 3. It can be seen from Table 3 that debonding strains change

Table 3. Debonding strain.

Ascending stiffness	Debonding strain 10^{-3}	Descending stiffness	Debonding strain 10^{-3}	Beam no.	Debonding strain 10^{-3}
600	1.238	−200	1.949	s1	2.346
120	2.346	−55	2.346	s2	3.274
60	2.811	−32	2.396	s3	3.879
40	2.853	−22	2.521	s4	4.618

with the physical parameters of masonry-to-FRP interface model, beam span and span-depth ratio. It may not be rational that this strain is only a function of the amount of FRP reinforcement as in Kuzik *et al*. (2003).

4 CONCLUSION

The following conclusions can be drawn from numerical simulations and a parametric study:

- Comparison between numerical simulation and experimental results shows that the proposed numerical model provides reasonably accurate prediction on the response of FRP plated masonry beam when a failure is governed by debonding.
- Parametric study revealed that strength and deformation capacities of FRP plated URM beams can be enhanced through reducing ascending stiffness and increasing descending stiffness in bi-linear interface mode.
- Trapping at the plate ends appeared to have great effect on the strength and ductility of FRP strengthened masonry beams with short spans, and to become less effect as span increased. However, these may be affected by other parameters, such as distributed load over beam, and masonry and masonry-to-FRP properties. Therefore, more parametric study needs to be undertaken before the conclusion can be drawn.
- The debonding strain varied as change in stiffness of bi-linear interface mode and in shear-span. It is therefore critical to provide accurate debonding strain predictions upon which an analytical model can be based to predict capacity of FRP plated URM beam.

ACKNOWLEDGEMENT

The authors gratefully acknowledge the financial support provide by the University of Adelaide through small grant scheme.

REFERENCES

Albert, ML, Elwi, AE, Cheng JJR. (2001) Strengthening of Unreinforced Masonry Walls Using FRPs, *J COMPOS CONSTR*, **5**(1) 76–84.

Chen, JF, Teng, JG (2001) Anchorage strength models for FRP and steel plates bonded to concrete, *Journal of Structural Engineering*, ASCE, **127**(7), 784–791.

Dirkse, SP, Ferris, MC 1995. The PATH solver: a non-monotone stabilization scheme for mixed complementarity problem. *Optimization Method & Software* **5**, 123–156.

Gilstrap, JM, Dolan, CW (1998) Out-of-plane bending of FRP-reinforced masonry walls, *Composites Science and Technology*, **58**, 1277–1284.

Hall JD, Schuman PM, Hamilton, HR (2002) Ductile anchorage for connecting FRP strengthening of under-reinforced masonry buildings, *J COMPOS CONSTR* **6** (1), 3–10.

Hamoush, SA, McGinley, MW, Mlakar, P, Terro, MJ (2002) Out-of-plane behavior of surface-reinforced masonry walls, *Construction and Building Materials*, **16**(6), 341–351.

Holberg, AM, Hamilton, HR (2002) Strengthening URM with GFRP composites and ductile connections, *Earthquake Spectre*, **18** (1): 63–84.

Kuzik, MD, Elwi, AE, Cheng, JJR (2003) Cyclic Flexure Tests of Masonry Walls Reinforced with Glass Fiber Reinforced Polymer Sheets, *J COMPOS CONSTR*, **7**(1) 20–30.

Oehlers, DJ, Seracino, R (2004) *Design of FRP and Steel Strengthened RC Structures: retrofitting beams and slabs for strength, stiffness and ductility*. Accepted by Elsevier, due to be published September 2004.

Russo, S, Gottardo, R, Codato, D (2003) Effect of FRP mesh reinforcement on shear capacity and deformability of masonry walls, *FRPRCS-6 proceedings*, Ed. by Tan, KH, World Scientific Publishing Company, 1239–1248.

Saadatmanesh, Hamid (1997). "Extending the Service Life of Concrete and Masonry Structures with Fiber Composites." *Construction and Building Materials*, Vol.11, No. 5–6, 327–335.

Tin-Loi, F, Xia, SH (2001) Holonomic softening: models and analysis, *Mechanics of Structures and Machines*, **29**, 65–84.

Tin-Loi, F, Xia, SH (2003) An iterative complementarity approach for elastoplastic analysis involving frictional contact, *Int. J. Mechanical Sciences*, In press, accepted date: 11/02/2003.

Xia, SH, Oehlers, DJ (2004) Tests on debonding mechanisms in FRP plated masonry (in writing).

FRP Composites in Civil Engineering – CICE 2004 – Seracino (ed)

Diagonal tests on tuff masonry strengthened with CMF systems

G. Marcari, G. Fabbrocino, A. Prota & G. Manfredi
Department of Structural Analysis and Design, University of Naples Federico II, Naples, Italy

C. Aldea
Saint Gobain Technical Fabrics, St. Catharines, Canada

ABSTRACT: The paper deals with an innovative strengthening technique applied to tuff masonry panels. Tuff is a volcanic stone that has been commonly used as building material in the Mediterranean area since Roman age. Particularly over the past few decades, interest in preserving and strengthening heritage tuff masonry structures has led to develop specific and non-invasive architectural and engineering strategies. Within this contest an experimental research program has been initiated. In the present paper results of diagonal compression tests are presented; comparative experimental analysis between as-built and strengthened panels is discussed. Strengthening is based on use of a cement matrix–fabric (CMF) system externally applied to the masonry panels. Review of experimental tests points out the effectiveness of adopted strengthening layout in terms of strength and ductility of panels.

1 INTRODUCTION

Tuff masonry structures have been built since old times in countries located in the Mediterranean areas and constitute a significant part of the existing masonry building inventory including historical architecture of Central-South Italy.

Tuff represents a very attractive material from a technological point of view due to its outstanding workability, low cost, good mechanical and physical (good thermal and acoustic insulation) properties. It has been widely used in order to build solid and/or faced structural walls having different textures and shape of units.

It is a rock composed of volcanic particles, ranging from ash size to small pebble size, compacted or cemented in a consolidated state. Tuff stones show a quite high porous frame and are available in different types, sizes and colours. Usually, in the past they were bonded in a running bond of pozzolanic mortar (mix of ground lime and volcanic ash) with rather low strength.

Physical and mechanical properties of tuff units widely vary according to quarry locations. Moreover, a remarkable reduction in strength is observed with an increase in degree of saturation of stones, as confirmed in many experimental programs (Evangelista & Pellegrino 1990).

In addition, the construction sequence and strengthening applications are often unknown, and significant changes may occur in the core and constitution of structural walls, especially when they belong to historical constructions.

Yellow tuff stone represents the main volcanic product widely spread in the Campania region, South Italy and in particular around Naples. Therefore, a challenging structural problem is seismic protection of a large number of tuff construction located in medium and high seismicity environment.

From a seismic standpoint, the analysis of tuff structures is a complex task due to interaction between plan arrangement of walls, percentage and location of openings and type and features of floor diaphragms.

Furthermore, due to age of examined constructions many former interventions can interact and lead to complex structural layout or even drop seismic resistance of the buildings.

Typically, existing buildings have been strengthened with traditional techniques, i.e. diaphragms stiffening, typing walls to floor diaphragms or adding steel ties.

In such cases the floor acts as a rigid diaphragm which distributes the lateral loads to the walls depending on their in-plane stiffness. Combination of vertical and horizontal loads produces complex stress distributions in the wall and can activate floor failure mechanisms. This aspect is well confirmed by the observation of earthquake damage on masonry structures, and it can be analysed by means of different modelling approaches (Penna 2001, Lourenço 2002).

Structural masonry shear walls can exhibit distinct failure mechanisms, mainly depending on wall geometry, mechanical properties of units and mortar,

the interaction among them, and the type of loads applied (Drysdale et al. 1994).

Therefore, main emphasis can be attributed to the analysis of the response of shear masonry walls. The selection of reliable strengthening techniques of such structures may be then carried out upon the prediction of the in-plane wall performance. Nowadays, retrofitting and strengthening tuff structures is becoming a key issue in Italy.

Most of them mainly suffered the effects of seismic loads or structural deterioration as results of weathering. Problems caused by loss of integrity are well known for tuff units consisting of very high porosity matrix, and are likely to be significant in cases of historical and monumental buildings that institutions aim to preserve for future generations.

Within this context, Fiber Reinforced Polymers (FRP) represent an interesting option for strengthening and rehabilitation of existing buildings, due to their negligible influence on global mass, their outstanding mechanical performance, easy handling and installation that improve on-site productivity, and durability (Triantafillou & Fardis 1997, Triantafillou 1998, Neale 2000).

Many studies at various levels have shown that FRP materials, used in form of both laminates and strips, provide a significant increase of load carrying capacity of flexural and shear walls made of concrete blocks or clay units (Ehsani et al. 1999, Valluzzi et al. 2002, Marshall et al. 1999, Grando et al. 2003, Patoary & Tan 2004), while the knowledge about application of FRP systems to tuff masonry is still lacking (Manfredi et al. 2003, Manfredi et al. 2004).

Because of porosity and low resistance to abrasion, the surfaces should be pre-treated by proper coating primers in order to consolidate the support and improve the adhesion of strengthening FRP materials. Moreover, high compatibility and reversibility of strengthening methods using FRP are requested. The concept of reversibility is of particular relevance for applications on historical structures that are supervised by National offices for Historical Heritage Preservation; such institutions allow only the use of strengthening techniques that could be removed anytime if any problem is detected or a better solution is identified.

The present paper discusses the potential of an innovative strengthening technique consisting of a cementitious matrix – fabric (CMF) system (SRG 45® system) externally applied to the masonry wall surface. The fabric is an Alkaline Resistant (AR) Glass coated fabric, SRG 45® (structural reinforcing grid) and the matrix is a polymer modified glass fiber reinforced mortar.

This composite material is highly compatible in terms of chemical, physical and mechanical properties with the substrate, e.g. tuff masonry.

Among the advantages of the CMF strengthening system, the following can be mentioned: ease of installation, no need for any surface preparation or high levels of workmanship, fire resistance, excellent bond with the substrate, breathebility of the system, which allows transport of air and moisture through the matrix, and reversibility.

Besides, for strengthened walls exposed to high temperature or environmental effects, the application of a thick layer of cementitiuos mortar substantially ensures a protection for the SRG grid and improves the long-term behavior of the strengthening system.

These are some key advantages and unique properties which make it a potential alternative to the traditional techniques for masonry structures. Full scale tests using this system and unreinforced masonry units (URM, artificial masonry) were conducted at the US Army Core of Engineers-CERL (Marshall 2002).

1.1 *Research objectives*

The present work is a part of a larger research program "TE.M.P.E.S.: Innovative Technologies and Materials for the Seismic Protection of Historical Masonry Structures" under development, realized with the financial support of the Italian "Ministero dell'Istruzione, dell'Università e della Ricerca". The main purpose is to cover the gaps in knowledge of the behaviour of tuff masonry structures strengthened with FRP, via an integration of comprehensive experimental investigations on the behaviour of strengthened tuff masonry walls and numerical models. In this paper, some experimental results of diagonal compression tests on yellow tuff panels are presented.

2 EXPERIMENTAL PROGRAM

The primary goal of the work is the evaluation of the performances in terms of shear capacity provided by a strengthening technique based on use of CMF system (SRG 45® system) bonded to external surfaces of tuff masonry walls.

Six tests on tuff panels are reported: four as-built masonry panels tested as reference specimens and two panels strengthened with CMF system. Summary of results from all the tests is given in Table 1, where each test is designated by the series (P), followed by the test number.

The strengthened walls are identified adding the letter (S). The shear failure mechanisms detected are also indicated.

2.1 *Test specimens and set up*

All panels have been built with the same size and type of masonry units and mortar.

Table 1. Summary of results of the diagonal compression tests.

Specimen Type	FRP system	V_{max} [kN]	τ_{max} [MPa]	ν	γ_{el} %	G [Mpa]	Ductility factor μ	Failure mechanism (*) S
P#1	USP	80.65	0.22	0.16	0.018	318	2.22	S
P#2	USP	128.54	0.35	0.10	0.022	535	–	S-T
P#3	USP	76.92	0.21	0.36	0.014	515	2.54	S
P#4	USP	70.04	0.19	0.45	0.011	690	3.03	S
PS#1	Grid	196.36	0.54	0.40	0.029	620	4.51	SPL
PS#2	Grid	234.18	0.64	0.50	0.026	747	2.05	SPL

* S = sliding along mortar joint.
S-T = combined sliding along mortar joint and tensile rupture of units.
SPL = splitting.

Masonry units were supplied from the same local quarry to avoid localized materials properties. They have been stacked clear of the ground and covered to protect them from contaminations. Because of the highly water absorptive properties of tuff units, layer of mortar at the interface may completely dry out, resulting in poor bond. For this reason the stones have been pre-wetted before any panel construction according to erection practice.

Test on the basic components were performed according to Italian standards. Different types of setup were adopted and data analyses are made in order to obtain mean values from the tests. The compressive strength of the natural stones was determined as 2.00 MPa using 100-mm cube specimens. Moreover, uniaxial compression tests were performed on tuff prisms $370 \times 60 \times 90$ mm in order to evaluate the elastic modulus that ranged between 1800 and 2000 MPa.

The mortar mix proportion was as follows: 310 kg/m^3 of binder, 1245 kg/m^3 of sand, 195 kg/m^3 of water. The mortar mixture was set in order to obtain an average strength close to the one typical of the pozzolanic mortar used in existing tuff buildings.

Mortar prisms were moulded from sample of mortar used to build the specimens; they were stored under the same conditions as the relevant specimens and cured for 28 days.

Standard $160 \times 40 \times 40$ mm prisms and 50-mm cubes were used for bending and compression test, respectively. A mean value of the flexural strength of 1.57 MPa and an average compressive strength equal to 5 MPa, resulted.

All panels, included PS#1 and PS#2 specimen were allowed to cure for 28 days. The stones ($370 \times 120 \times 250$ mm) were laid in a running bond so that a final mortar joint thickness of 15 mm mortar was attained. Each panel was eight courses high and two and one half tuff blocks wide. The resulting dimensions were $1030 \times 1030 \times 250$ mm as shown in Figure 1.

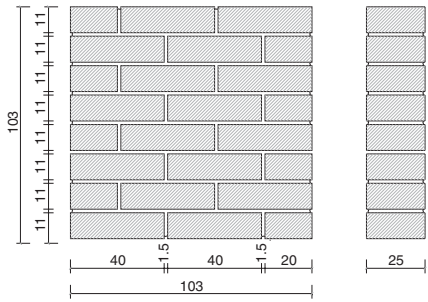

Figure 1. Panel geometry.

Figure 2. AR-Glass fabric.

The CMF system is using a bi-directional AR-glass coated fabric, SRG 45®, (Fig. 2) manufactured by Saint-Gobain Technical Fabrics. The properties of the fabric are the following: tensile strength 1700 MPa or 45k N/m as per ASTM D 6637, Young's Modulus 72 GPa and ultimate strain equal to 2.4%. SRG 45® fabric is embedded in a cementitious matrix, which is

a polymer modified glass fiber reinforced mortar produced by Quickrete Companies, which is compatible with masonry applications. The mechanical properties of the matrix after 28 days of curing are the following: compressive strength 13.9 MPa; flexural strength 3.9 MPa and tensile strength 1.2 MPa.

Two plies of fabric were used and were applied symmetrically over the whole surfaces of the masonry (Fig. 3). The wall was accurately wetted and the mortar, previously mixed with water and an acrylic fortifier, was then trowelled onto the wall of 5 mm thick layer. A first 900 mm squared fabric was firmly pressed into the wet binder by hand to ensure its adequate anchorage to the support. Then, a second layer of mortar was applied by trowelling an additional 5 mm thick layer; an offset of 15 mm of the second ply with respect to the first was ensured in order to avoid that any fracture plane could originate from the overlap. Finally, the second ply of fabric was applied and covered by a relatively smooth surface (Fig. 3). The nominal thickness of the CMF system was of about 10 mm.

The panels were tested in a four column testing frame (Fig. 4a), characterized by a 1000 mm wide and 4000 mm long steel base floor, and capable of testing specimens more than 4 m high. Its load capacity is 3000 kN both in tension and in compression with a total stroke equal to 150 mm.

The tests have been carried out under displacement control, in order to follow the post-peak response of the panels; the displacement rate was equal for all the tests and equal to 0.02 mm/sec. Tests were stopped when the reduction in strength with respect to the peak value was of about 50%.

Two steel loading shoes placed on two diagonally opposite corners of the panels were used; the test layout basically fits the requirements of ASTM E 519-81, even though some changes have been introduced in order to properly account for the dimensions of tuff blocks. To avoid a premature splitting failure of panel edges, the spaces between the specimen and steel plates were filled with fast setting and shrinkage free mortar. A particular care and specific devices have been used in order to avoid misalignments and assembly eccentricities.

The 90° rotation of the panels has been carried out as shown in Figure 4b; horizontal and vertical ties have been set in combination with diagonal bars to uplift the specimen and avoid any damage. Multiple direction prestressing has been used in order to ensure compressive stresses (about 10–15% of the compressive strength of the panel) all over the panel during the handling phase; upper steel beams have been also used to balance specimens during rotation.

Vertical load was transferred to the specimen via a spherical hinge put between the actuator steel end and the load cell used to measure the applied load. The instrumentation layout ensured measure of loads, changes in wall geometry and strains profiles in the FRP reinforcement. An overview of the test setup and instrumentation is shown in Figures 5a, b.

For all tested panels, five linear displacement variable transducers (LVDT) were used: four, two on each side, were placed along the diagonals in order to monitor the shear deformation over a gauge length of 400 mm (LVDTs 3 and 4 in Fig. 5b); the other was

(a) (b)

Figure 4. Test layout (a) and lifting phase of the panel (b).

Figure 3. CMF installation.

(a) (b)

Figure 5. Test setup and instrumentation (a) for as-built panels and (b) for strengthened specimens.

placed perpendicular to the panel surface in order to monitor out-of plane displacements, if any.

In addition to those five, two more LVDTs were placed on one side of both PS#1 and PS#2 specimens in order to measure strains along grid fibers over a gage length of 100 mm gauge length (LVDTs 5 and 6 in Figure 5a).

3 EXPERIMENTAL RESULTS

Preliminary results of the experimental work are here reported. The analysis of displacements recorded on the opposite surfaces of the specimens enabled to recognize that load–displacement distributions were very similar. This confirmed that the amount of out of plane displacements was negligible apart from a slight initial settlement of the specimens.

Test results are first discussed in terms of mean shear strength, τ_{max}, computed on the net section area A_n of the uncracked section of the panels ($A_n = 0.257\ m^2$), according to ASTM standard test method: $\tau_{max} = 0.707\ V_{max}/A_n$, where V_{max} is the peak experimental load. As-built panels P#1, P#3 and P#4 showed a similar mean strength ranging between 0.19 MPa and 0.22 MPa (Table 1). Panel P#2, instead, gave the highest mean strength equal to 0.35 MPa (Table 1). This value was probably due to a particular failure mechanism that will be discussed later. The average shear strength of 0.20 MPa, assumed as reference in the following, will refer only to P#1, P#3 and P#4 specimens and is associated to a CV of 6.1%. If P#2 was included, a mean shear strength equal to 0.24 MPa and a CV of 26% would have been obtained.

Values of mean strength underline that the shear capacity of the strengthened walls was substantially increased by the CMF reinforcement (Table 1), with a gain in strength of about 170% and 220% for PS#1 and PS#2 specimens, respectively.

Typical failure modes observed for all tested panels are summarized in Table 1, where S denotes the shear slip failure along the mortar joints, and S-T denotes a failure resulting from combined slip of the mortar joints and splitting of stones. Finally, SPL indicates the splitting of the stones and the mortar joints.

At the ultimate stage, the stress field in the as-built panels tends to force the fracture cracks to follow the line of least resistance rather than the line of action of the splitting load. As indicated in Table 1, for panels P#1, P#3 and P#4 the failure resulted typically in shear slip between the units and the mortar along the joints. Thus, the shear capacity is governed by the weak bond between mortar and tuff stones. For panel P#2 the failure plane had a marked stepped appearance due to a combination of debonding along the mortar joints and tensile failure of tuff units. This is the reason for the higher shear strength above mentioned. In fact, the failure plane ran through a greater surface compared to the case of the sliding along the mortar joints that caused the full separation of the panel in two pieces (Fig. 6). It is underlined that no failure at the loaded edges was observed for the as-built panels.

The presence of the CMF system changed the mode of failure of panels from a shear slip along the mortar joints to a more uniform crack pattern along the splitting line. A sketch of the wall crack pattern at failure can be seen in Figure 7a. The elastic modulus of glass fibers lead to a better redistribution of the lateral load on the panel, and a more uniform stress level was achieved.

Generally, the bond between the masonry and the externally bonded strengthening system plays a crucial role in order to ensure an adequate load carrying capacity to the whole composite system. This is emphasized especially when strengthening systems are applied in situ on roughly squared tuff stone surfaces, using hand lay up technique. When the development length of the strengthening system cannot be assured, adequate mechanical anchorage needs to be installed. Even though no mechanical anchorage system of SRG45® was provided, no premature debonding of CMF reinforcement occurred, confirming the high compatibility between the proposed CMF strengthening system and the tuff masonry substrate. Besides, except some visible cracks, the panel kept its structural integrity throughout the entire test (Fig. 7b) and

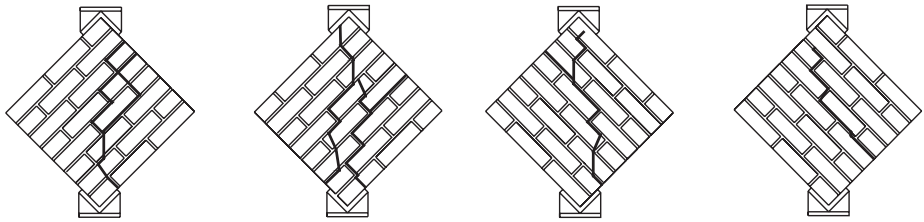

P#1 - Peak load 80.65 kN P#2 - Peak load 128.54 kN P#3 - Peak load 76.92 kN P#4 - Peak load 70.04 kN

Figure 6. Crack pattern of the control panels at ultimate stage.

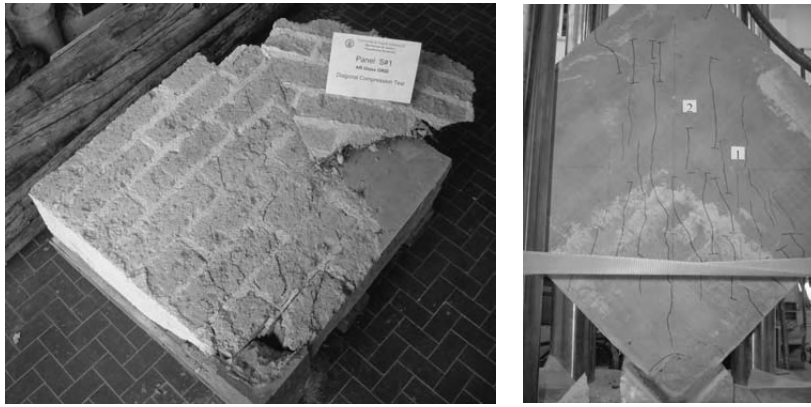

(a) (b)

Figure 7. Typical failure of strengthened panels.

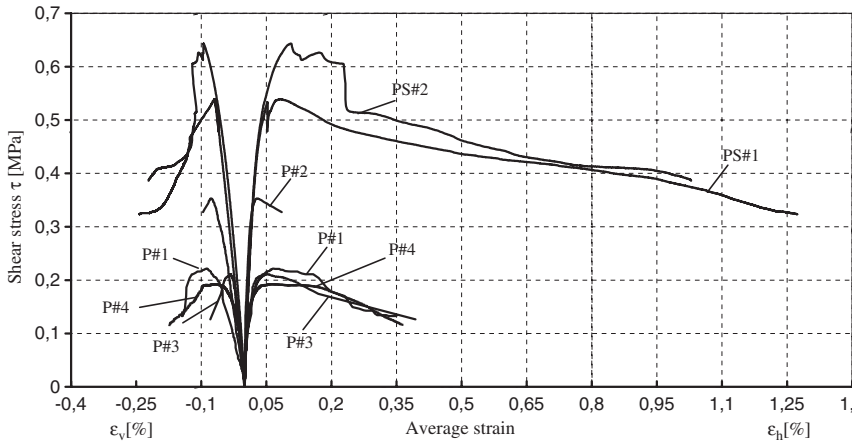

Figure 8. Shear strength vs. diagonal strains curves.

it would have been able to carry further load if no local failure close to the loading shoes happened. For this reason, the ultimate values determined with the tests represent a lower bound of the shear capacity of tested specimens.

The behavior of tested panels can be also analyzed in terms of shear stress-average strain, and shear stress-average shear strain curves. The shear stress, τ, can be obtained as $\tau = 0.707\,V/A_n$, where V is the current experimental load. The average strains, ε_v and ε_h, have been computed as the average displacement on the two sides over the gauge length (400 mm) along the compressive and tensile diagonals, respectively. The shear strain, γ, can be then computed according to ASTM E519-81 standard method as $\gamma = \varepsilon_v + \varepsilon_h$. Figures 8 and 9, depict curves of shear stress-average strain, and shear stress-average shear strain of tested panels.

At low load levels, as-built panels show a very similar behavior in terms of shear stress versus horizontal strain relationship (Fig. 8). Up to 0.1 MPa a relatively linear behaviour is noted. From this stage P#1, P#3 and P#4 suddenly change in slope and experience greater stiffness degradation than P#2. They reach the shear strength at about the same horizontal strain (i.e., 0.059%); at 80% of the peak load on the descending branch, they give an average shear strain

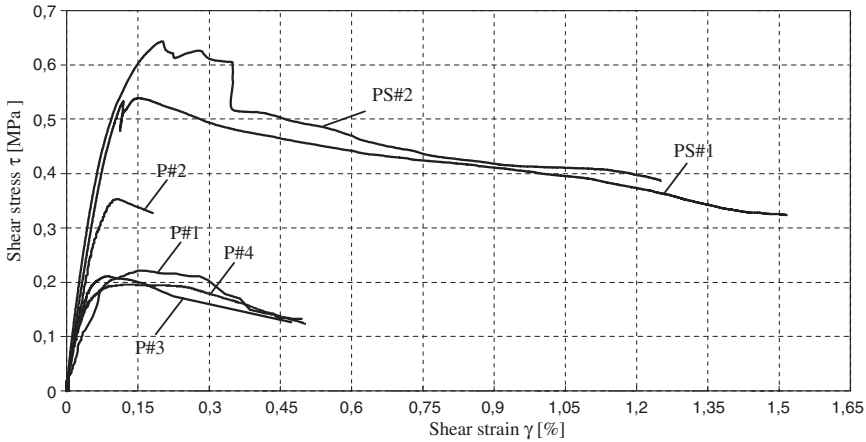

Figure 9. Shear strength vs. shear deformation curves.

of about 0.21%, which is about 3.5 times higher than the mean peak horizontal strain (Fig. 8).

Panel P#2, instead, shows a more or less linear loading branch up to its maximum shear stress of 0.35 MPa, corresponding to a horizontal strain of 0.029%. At 93% of the peak load on the descending branch, the horizontal strain is approximately 1.5 times higher than the strain corresponding to the maximum shear stress (Fig. 8). Brittle failure mechanism determined a data acquisition problem that did not allow to record data beyond such percentage (i.e. 93%) of the peak load on the softening branch.

The strengthened specimens exhibit the same initial trend up to a shear stress level (i.e., 0.35 MPa) higher with respect to that of those as-built and this is due to the full composite action between the masonry and the CMF system. Moreover, the analysis of the shear-average strain curves (Fig. 8) highlights that the influence of the CFM system along the tensile diagonal direction determines a more stable softening response with regard to the relevant post peak behaviour observed on the shear stress-vertical strain plots (Fig. 8).

Similarly, in terms of shear stress-shear strain curves (Fig. 9), a linear behavior is detected at very low level of stress for both as-built and strengthened panels. After a stress of about 0.1 MPa, a cracking phenomenon of masonry starts to develop in the P#1, P#3 and P#4 specimens (Fig. 9), followed by a non linear trend. Only P#2 panel exhibits a very limited deformation after reaching the maximum stress.

The presence of the grid determines that PS#1 panel has an almost linear behavior up to about 75% of its shear strength. After that, the shear stress increases with a slight slope change; a sudden drop in strength occurs at a stress of about 0.52 MPa (Fig. 9), due to the local compression failure of the masonry near the lower edge of the panel. After that drop, the panel is able to sustain further load up to the peak stress of 0.54 MPa (Table 1). The descending branch starting from that point is characterized by inelastic deformations until a shear strain of 0.64% reached at 80% of the peak.

PS#2 panel reveals an approximately linear elastic phase up to 35% of its shear strength and a subsequent stiffness degradation up to the maximum shear stress of 0.64 MPa. On the softening branch, a less stable behavior than PS#1 specimen is observed, due to the cracks that started to develop near the bottom edge of the panel close to 80% of the shear peak associated to a shear strain is of 0.35%.

Moreover, a sudden loss in strength occurs when the loaded edge is almost fully cracked (Fig. 9), even though the panel still maintains the load-carrying capacity up to large deformations.

In Figure 10, the apparent Poisson's ratio with the shear percentage τ/τ_{max} is plotted. During the loading process, the horizontal strain ε_h to vertical strain ε_v ratio is affected by the cracking phenomenon as the load increased. In particular, the crack propagation is denoted by a sudden increment of ν. In Figure 10, the as-built panels showed first cracks at a loading level varying from $0.3\tau_{max}$ to $0.6\tau_{max}$; for strengthened panels this level reached $0.75\tau_{max}$.

From this observation the evaluation of the elastic parameters (i.e., elastic shear strain, γ_{el}, and Poisson's ratio, ν) of each panel can be calculated based on a shear stress corresponding to one third of the relevant shear strength. In addition, the modulus of rigidity, G, has been calculated as secant modulus

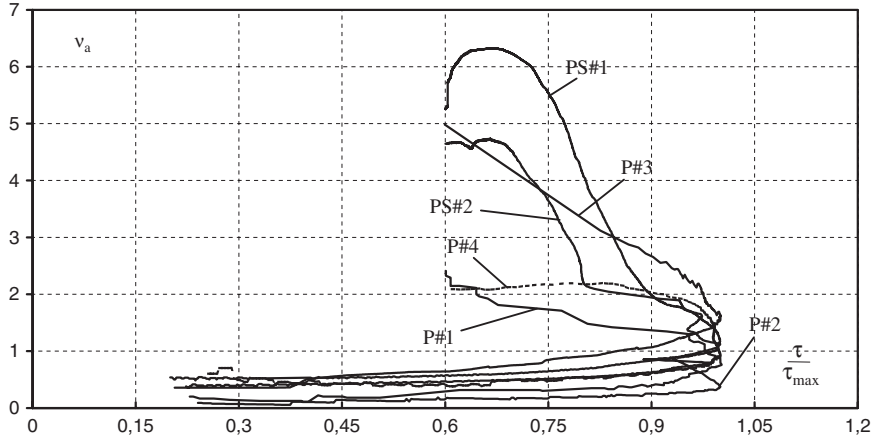

Figure 10. Poisson modulus vs. shear load percentage.

between the origin and the stress equal to 30% of the peak stress on the shear-strain curves in Figure 8. Values of such elastic parameters are summarized in Table 1. The modulus of rigidity of the as-built panels approached a mean value of 513 MPa, whereas the strengthened ones showed a mean value of 683 MPa. The latter revealed a stiffer behaviour with respect to the as-built specimens. This underscores that the initial stiffness of the strengthened panels was affected by the grid reinforcement. The Poisson's ratio results of the as-built panels gave a significant CV of 53%; however, a mean value equal to 0.26 can be assumed. The strengthened panels went from 0.40 to about 0.50 and averaged 0.45.

The effectiveness of the proposed strengthening technique can be assessed by computing the ductility of tested panels. An exact evaluation of the strain corresponding to the shear stress from which the cracking phenomenon takes place is not simple to detect accurately, as can be seen in Figures 8 and 9.

Therefore, the deformation capacity is herein conventionally analysed considering a ductility factor μ, as the ratio γ_u/γ_{max}, where γ_u is defined as the shear strain when the shear stress drops to 80% of τ_{max}; γ_{max} is the shear strain corresponding to τ_{max}.

Comparing ductility rates of as-built panels, an average value of 2.6 is obtained. Panel P#2 failed at an ultimate shear stress equal to 93% of the maximum stress, so any ductility ratio cannot be provided. Conversely, the strengthened panel PS#1 increased its deformation capacity, as demonstrated by the ductility factors of about 4.51 reported in Table 1. No significant gain in ductility was reached by PS#2.

4 CONCLUSIONS

The present paper has focused on the experimental behaviour of tuff masonry panels commonly used in many constructions in the Mediterranean area. The experimental program is still in progress and the preliminary conclusions here proposed will need to be confirmed by the outcomes of further tests. An interesting strengthening technique based on the use of a CMF system to the panels with a cementitious mortars has been analysed.

The overall shear performance of the tuff masonry specimens externally reinforced by the CMF (SRG 45®) system was very satisfactory. Test results indicate that strengthening of as-built structures with composite grids could be a very effective option to enhance the shear strength and even the ductility of such elements. Observed failure mechanisms of strengthened walls, related to crushing of the loading edges, indicate that diagonal tests can be useful to compare overall performances of tuff masonry, but cannot give exhaustive results. Such crushing of loading edges cannot be easily prevented since the strength enhancement due to CMF leads to very high compressive stresses that are not compatible with internal stone strength. Further biaxial and shear-compression tests can improve the knowledge and help extending the promising results herein discussed.

ACKNOWLEDGMENTS

The authors would like to gratefully acknowledge the support of the Italian Government funding the Research Project TE.M.P.E.S., Saint–Gobain

Technical Fabrics Canada Ltd (SRG 45® system patent pending) and Quickrete Company.

REFERENCES

ASTM E 519-81. 1981. Standard test Method for Diagonal Tension (Shear) in Masonry Assemblages. American Society for Testing Materials.

Drysdale, R.G., Hamid, A.A. & Baker, L.R. 1994. *Masonry structures, behaviour and design*. In Prentice Hall (ed.). Englewood Cliffs, New Jersey.

Ehsani, M.R., Saadatmanesh, H. & Velazquez-Dimas, J.I. 1999. Behavior of Retrofitted URM Walls under Simulated Earthquake Loading. *ASCE Journal of Composites for Construction*, 3(3): 134–142.

Evangelista, A. & Pellegrino, A. 1990. Caratteristiche geotecniche di alcune rocce tenere italiane. In SGE (ed.), *Proc. 3° Ciclo di conferenze di Meccanica e Ingegneria delle Rocce, Torino, 26–29 November 1990.*

Grando, S., Valluzzi, M.R., Modena, C. & Tumialan, J.G. 2003. Shear strengthening of URM clay walls with FRP systems. *Advancing with Composites*: 179–186.

Lourenço, P.B. 2002. Computations on historic masonry structures. *Prog. Struct. Engng. Mater.*, 4: 301–319.

Manfredi, G., Pecce, M., Marcari, G. & Ceroni, F. 2003. Experimental and theoretical behaviour of masonry elements externally reinforced with FRP laminates. *Proc. Int. Conf. Composites in Constructions*, University of Calabria, Rende (Cs), 16–19 September 2003.

Manfredi, G., Marcari, G. & Pecce, M. 2004. In-plane shear performance of stone masonry panels strengthened with FRP. *ASCE Journal of Structural Engineering, under revision.*

Marshall, O.S., Sweeney, S.C. & Trovillion, J.C. 2000. Performance testing of Fiber-Reinforced Polymer Composite Overlays for Seismic Rehabilitation of Unreinforced Masonry Walls. *Int. Report*, U.S. Army Construction Engineering Research Laboratory (CERL), Champaign IL.

Marshall, O.S. 2002. *Int. Report*, U.S. Army Construction Engineering Research Laboratory (CERL), Champaign IL.

Neale, K.W. 2000. FRPs for structural rehabilitation: a survey of recent progress. *Prog. Struct. Engng. Mater*, 2: 133–138.

Patoary, M.K.H. & Tan, K.H. 2004. Strengthening of masonry walls against out-of plane loads using fiber-reinforced polymer reinforcement. *ASCE Journal of Composites for Construction*, 8(1): 79–87.

Penna, A. 2001. Una procedura a macroelementi per l'analisi dinamica non lineare di edifice in muratura. *PhD Thesis*, University of Milan, Italy.

Triantafillou, T.C. 1998. Strengthening of masonry structures using epoxy-bonded FRP laminates. *ASCE Journal of Composites for Construction*, 2(2): 96–104.

Triantafillou, T.C. & Fardis, M.N. 1997. Strengthening of historic masonry structures with composites materials. Materials and Structures, 30: 486–496.

Valluzzi, M.R., Tinazzi, D. & Modena, C. 2002. Shear behavior of masonry panels strengthened by FRP laminates. *Construction and Building Materials*, 16: 409–416.

FRP Composites in Civil Engineering – CICE 2004 – Seracino (ed)

FRP jacketing of masonry columns

T. Krevaikas & T.C. Triantafillou
University of Patras, Patras, Greece

ABSTRACT: The application of fiber reinforced polymers (FRP) as a means of increasing the axial capacity of masonry through confinement, a subjected not addressed before, is investigated in this study. Four series, a total of 42 specimens, of uniaxial compression tests were conducted on model masonry columns, with variables the number of layers, the radius at the corners, the cross section aspect ratio and the type of fibers. It is concluded that, in general, FRP-confined masonry behaves very much like FRP-confined concrete. Confinement increases both the load-carrying capacity and the deformability of masonry, almost linearly with the average confining stress. The uniaxial compression test results enabled the development of a simple confinement model for strength and ultimate strain of FRP-confined masonry. This model is consistent with test results obtained here, but should attract further experimental verification in the future, to account for types of masonry materials other than those used in this study.

1 INTRODUCTION

Masonry structures in need of intervention through strengthening constitute a significant portion of the building stock throughout the world, as either they have suffered from the accumulated effects of inadequate construction techniques and materials, seismic and wind loads, foundation settlements and environmental deterioration, or they need to be upgraded in order to meet more stringent seismic design requirements, often combined with change in use.

In the past decade or so, traditional strengthening techniques for masonry (e.g. filling of cracks and voids by grouting, stitching of large cracks and other weak areas with metallic or brick elements or concrete zones, application of reinforced grouted perforations, external or internal post-tensioning with steel ties, and single- or double-sided jacketing by shortcrete or by cast in-situ concrete, in combination with steel reinforcement) have been supplemented with the FRP strengthening technique, which involves epoxy-bonding of strips or sheets mainly in the direction of principal tensile stresses.

Studies on the use of FRP as strengthening materials of masonry have been numerous. A detailed review of the literature reveals that the application of FRP as a means of increasing the axial capacity of masonry, e.g. through confinement, has not been explored, except in Triantafillou & Fardis (1993, 1997), through the introduction of external prestressing, and Valluzzi et al. (2003), through the use of horizontally placed near-surface mounted (in the bed joints) FRP strips. Despite the great potential of FRP-based confinement, which has received substantial attention in concrete structures, and despite the urgent need to develop effective methods of masonry confinement as a means of preventing catastrophic failures e.g. during earthquakes or even due to creep effects, no studies have been reported in this area, namely masonry confinement through FRP wrapping. It is this gap that the authors intend to fill in this study, through both experimental and analytical developments.

2 EXPERIMENTAL PROGRAMME

2.1 *Test specimens and material properties*

A total of 42 model masonry column specimens in four series were prepared using clay bricks with dimensions 55 mm (width), 40 mm (height) and 115 mm (length), bonded together with a mortar containing cement and lime as binder, at a water:cement:lime:sand ratio equal to 0.9:1:3:7.5 by weight. The cross sectional area of the specimens was 115×115 mm (aspect ratio 1:1) in the first two series, 172.5×115 mm (aspect ratio 1.5:1) in the third and 230×115 mm (aspect ratio 2:1) in the fourth. Each model column comprised bricks placed in seven rows with six bed joints in between, as shown in Figure 1. The thickness of mortar was, in general, 10 mm, except in some of the head joints, where it was slightly reduced, in order to maintain the desired cross section aspect ratio. The corners of all specimens were rounded using a grinding machine at a radius of 10 mm in the first, third and fourth series, and at a radius of 20 mm in the second series. Within each series, specimens were wrapped with one, two or

three layers of unidirectional CFRP sheets or with five layers of unidirectional GFRP sheets, applied through the use of a two-part epoxy adhesive.

Details about the model columns in each series are given in Table 1. In this table, each specimen type is given the notation FN_A_RX, where F = fiber type (C for carbon and G for glass), N = number of layers (1, 2 or 3 for carbon, 5 for glass), A = aspect ratio of cross section dimensions (1 or 1.5 or 2) and X = radius at corners (10 mm or 20 mm). For instance, C2_1_R20 denotes specimens with square cross section (aspect ratio 1), corners rounded at 20 mm and wrapping with two layers of carbon fabrics; G5_1.5_R10 denotes specimens with cross dimensions of aspect ratio 1.5, corners rounded at 10 mm and wrapping with five layers of carbon fabrics. For specimens without wrapping (control), FN is denoted as Co. The number of identical specimens tested was either two or three (column [2] in Table 1).

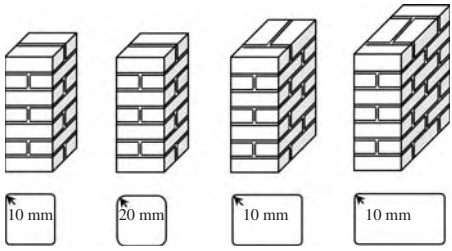

Figure 1. Configuration of masonry walls tested: (a) square cross section, corner radius 10 mm; (b) square cross section, corner radius 20 mm; (c) cross section with aspect ratio 1.5:1, corner radius 10 mm; cross section with aspect ratio 2:1, corner radius 10 mm.

The configurations described above allow the investigation of the role of various parameters on the effectiveness of FRP jacketing as a means of confining masonry; these parameters include the aspect ratio of the cross section, the radius of rounding at the corners, the type of fibers, the number of layers and the stiffness/strength characteristics of the jacket.

Before wrapping the FRP sheets, masonry surface defects were filled with epoxy putty. A layer of epoxy resin was next applied on the surface of each specimen and then wrapping of the sheets was applied with the fibers in the hoop direction. After the wrapping of each lap of a fiber sheet a layer of epoxy resin was applied and a roller was used to remove air voids and to allow a better impregnation of the resin. The finishing end of the sheet overlapped the starting end by approximately 100 mm. Wrapping of the sheets took place after curing of the specimens (actually the mortar) for at least one month in laboratory conditions and testing started approximately one month after application of the FRP jackets.

The strength of mortar was determined from compression testing of three 50 × 50 × 50 mm cubes for each mortar mix; 28-day average strength results

Table 1. Specimen notation and summary of test results.

Specimen notation	No. of specimens	Compr. strength, f_{Mc} (MPa)	f_{Mc}/f_{Mo}	Ultimate strain, ε_{Muc}	$\sigma_{\ell u}/f_{Mo}$
Series 1					
Co_1_R10	*3*	*12.07*	*1.000*	*0.0018*	*0.000*
C1_1_R10	3	13.63	1.129	0.0190	0.328
C2_1_R10	2	16.92	1.402	0.0223	0.656
C3_1_R10	3	25.42	2.106	0.0373	0.984
G5_1_R10	2	40.00	3.314	0.0644	1.484
Series 2					
C1_1_R20	2	16.87	1.398	0.0255	0.429
C2_1_R20	2	23.91	1.981	0.0375	0.858
C3_1_R20	2	34.69	2.874	0.0529	1.287
G5_1_R20	2	44.87	3.717	0.0623	1.941
Series 3					
Co_1.5_R10	*3*	*6.65*	*1.000*	*0.0045*	*0.000*
C2_1.5_R10	3	11.90	1.789	0.0093	0.833
C3_1.5_R10	3	17.29	2.600	0.0485	1.250
G5_1.5_R10	3	24.37	3.665	0.0690	1.885
Series 4					
Co_2_R10	*3*	*6.21*	*1.000*	*0.0044*	0.000
C2_2_R10	3	11.79	1.899	0.0102	0.579
C3_2_R10	2	12.00	1.932	0.0340	0.869
G5_2_R10	2	17.81	2.868	0.0604	1.310

were as follows: 2.85 MPa, 2.15 MPa, 1.93 MPa and 1.98 MPa in series 1, 2, 3 and 4, respectively. The bricks had an average compressive strength of 23.5 MPa, obtained through testing of six 55 mm long orthogonal prisms (cut from bricks) of cross section 40 × 40 mm. Finally, the following properties (average values) were provided by the supplier of the fiber sheets: elastic modulus and tensile strength of CFRP jackets = 230 GPa and 3500 MPa, respectively; elastic modulus and tensile strength of GFRP jackets = 70 GPa and 2000 MPa, respectively.

2.2 *Experimental setup and procedure*

The main objective of testing was to record the axial stress–strain curve and the failure mode of all the masonry specimens, which were subjected to axial loading applied monotonically under a displacement control mode in a compression testing machine of 1200 kN capacity. Loads were measured using a load cell and displacements were obtained using external linear variable differential transducers (LVDT) mounted on the walls, at a gauge length of 200 mm in the middle part of each specimen.

3 RESULTS AND DISCUSSION

3.1 *σ–ε behaviour, strength, deformability, failure modes*

The stress–strain diagrams for series 1, 2, 3 and 4 are presented in Figures 2, 3, 4 and 5 respectively. It can be observed that, in all cases, the diagrams are nearly bilinear with a curved transition curve between the two linear parts; no descending branch was recorded. The first linear part of the diagrams is similar in most cases, whereas the second linear part depends very much on the cross section aspect ratio, the corner radius and the jacket characteristics: it becomes steeper and longer as the number of layers or the radius at the corner increases. The average values of axial strength (peak stress in the stress–strain diagram) and ultimate strain in each series of identical specimens are given in columns (3) and (5), respectively, of Table 1.

The control specimens failed in a brittle manner by the formation of vertical cracks through the head joints and the bricks (Figs 6a, b). Despite the fact that material properties were quite similar, specimens with square cross sections (series 1 and 2) were stronger but failed at lower strain compared to those with cross section aspect ratio of 1.5 or 2 (series 3 and 4). The failure modes of FRP-wrapped specimens were identical in all cases. After their formation through mortar joints and bricks, vertical cracks became increasingly wide and the masonry in between those cracks crushed. This was continued until the lateral expansion reached the capacity of FRP, which failed by fracture at the corners (Figs 6c, d).

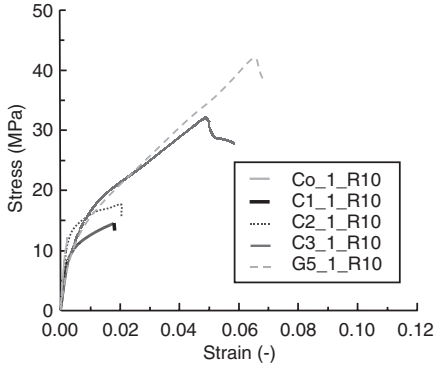

Figure 2. Typical stress–strain curves for specimens in series 1.

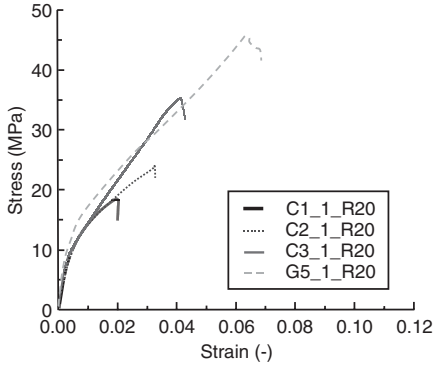

Figure 3. Typical stress–strain curves for specimens in series 2.

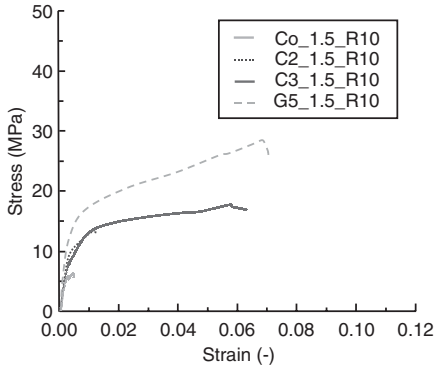

Figure 4. Typical stress–strain curves for specimens in series 3.

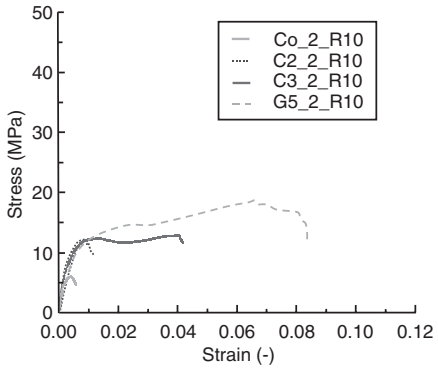

Figure 5. Typical stress–strain curves for specimens in series 4.

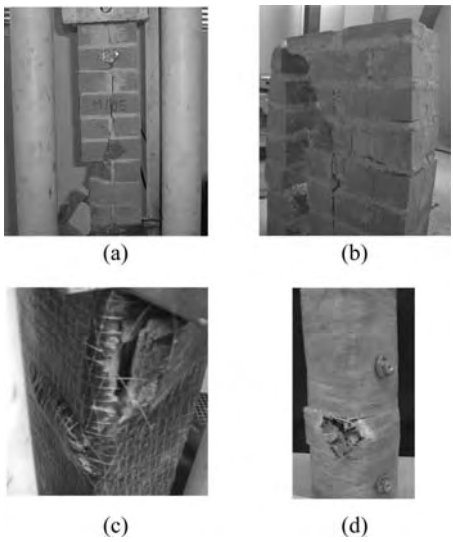

Figure 6. Failure modes of unconfined and FRP-confined masonry: (a) vertical cracking in specimens with square cross section; (b) vertical cracking in specimens with cross section aspect ratio 2:1; (c) fracture of CFRP at corner; (d) fracture of GFRP at corner.

3.2 *Discussion of results*

By examining the stress–strain curves and the results given in Table 1 in terms of strength and ultimate strain, the following observations can be made:

General: FRP jackets can significantly enhance both the strength and the deformability of masonry under axial load. Confinement effectiveness for strength, defined as the ratio of peak stress of FRP confined masonry to that of the unconfined masonry, exceeded 3 [column (4) in Table 1]. Enhancement in deformability was much more pronounced than gain in strength, as the ultimate strain of confined masonry exceeded that of unconfined masonry by a factor more than 30.

Number of layers: In most cases, particularly when the cross section aspect ratio was 1, strength and deformability increased almost linearly with the number of layers. In specimen series 1, strength increased by about 13%, 40% and 110%, and ultimate strain by a factor of 10, 12.5 and 20, for one, two and three layers of CFRP. The respective increases in series 2 were 40%, 100% and 185% for strength and by a factor of 14, 21 and 29 for ultimate strain. In series 3, strength increased by 80% and 160%, and ultimate strain by a factor of 2 and 10, for two and three layers of CFRP. In series 4, strength increased by about 90% and 95%, and ultimate strain by a factor of 2.5 and 7.5, for two and three layers of CFRP, respectively.

Corner radius: When the corner radius was increased from 10 mm to 20 mm (series 1 versus series 2), the strength increased by about 25–40% with CFRP jackets and by about 12% with the very thick GFRP jackets. Hence the beneficial effect of increasing the corner radius was verified.

Aspect ratio: Due to the large difference in control specimen strength and ultimate strain values between series 1 and 3 or 4, a direct comparison of the results for all three aspect ratios is not possible. However, this comparison can be made between series 3 and 4, where it is observed that for all cases but one (when 2 layers of CFRP were used) the reduction in confinement effectiveness when the aspect ratio becomes 2 from 1.5 is about 20–25% for strength and about 10–20% for strain.

Type of fibers: As far as axial stiffness in the hoop direction is concerned, five layers of GFRP fall somewhere in between two and three layers of CFRP. Yet, the effectiveness of GFRP jackets with five layers was superior to that of CFRP, even if the comparison is made with the three layer CFRP jacket. This proves that the higher deformability of glass fibers, compared to carbon, makes them more effective as jacketing materials if comparisons are made for the same stiffness.

Overall, it may be argued that the response and failure of axially loaded masonry confined with FRP has many similar characteristics to that of concrete. Hence, the development of a confinement model could be based on existing knowledge and experience for concrete. This is attempted in the next section.

4 CONFINEMENT MODEL

The basis of the FRP contribution to the strength and deformability of confined masonry is, in analogy to

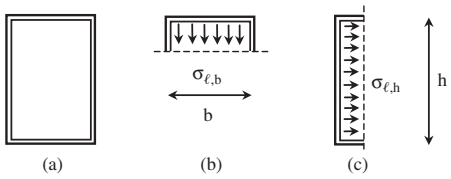

Figure 7. Approximate confining stresses in rectangular cross sections.

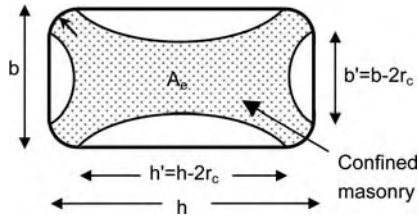

Figure 8. Effectively confined masonry in columns with rectangular cross section.

confined concrete, the transverse passive pressure σ_ℓ developing in the masonry in response to the jacket forces. This pressure is, in general, non-uniform, especially near the corners of rectangular cross sections. As an average value for σ_ℓ in a cross section with dimensions b and h one may write (Fig. 7):

$$\sigma_\ell = \frac{1}{2} k_e \left(\frac{2t_f}{h} E_f \varepsilon_f + \frac{2t_f}{b} E_f \varepsilon_f \right) = k_e \frac{(b+h)}{bh} t_f E_f \varepsilon_f \quad (1)$$

where E_f = elastic modulus of FRP; ε_f = circumferential FRP strain; t_f = thickness of FRP; and k_e = effectiveness coefficient. For continuous FRP jackets with fibres in the direction perpendicular to the member axis, k_e is defined as the ratio of effectively confined area (A_e in Fig. 8) to the total cross sectional area A_g (e.g. *fib* 2001).

Compressive failure of FRP-confined masonry occurs when the FRP jacket fractures at a hoop stress equal to the hoop tensile strength, f_{fe}, which is, in general, less than the uniaxial tensile strength of FRP (due to the multiaxial state of stress, stress concentrations etc.). Hence, the confining stress at failure, $\sigma_{\ell u}$, is given by Equation (1) with $E_f \varepsilon_f$ replaced by f_{fe}:

$$\sigma_{\ell u} = k_e \frac{(b+h)}{bh} t_f f_{fe} \quad (2)$$

The model proposed here for FRP-confined masonry is based on the well-known form of models typically adopted for FRP-confined concrete (see,

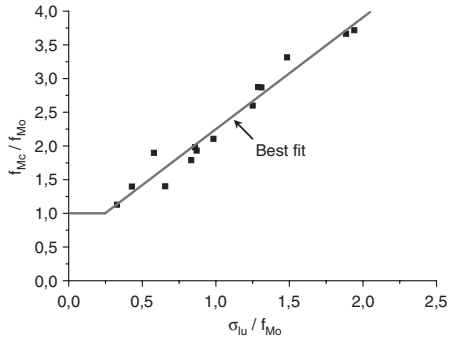

Figure 9. Normalized compressive strength of confined masonry in terms of lateral confinement.

for instance, De Lorenzis & Tepfers 2003, for a comparative study of confinement models):

$$f_{Mc} = f_{Mo}\left(1 + k_1 \frac{\sigma_{\ell u}}{f_{Mo}}\right) \quad (3)$$

$$\varepsilon_{Muc} = \varepsilon_{Muo} + k_2 \frac{\sigma_{\ell u}}{f_{Mo}} \quad (4)$$

where f_{Mc} = compressive strength of confined masonry; f_{Mo} = compressive strength of unconfined masonry; ε_{Muc} = ultimate strain of confined masonry; ε_{Muo} = ultimate strain of unconfined masonry; and k_1, k_2 = empirical constants. Experimental evidence both for concrete and for masonry confined with low volumetric fractions of transverse (confining) reinforcement suggests that for very low values of the confining stress the confined compressive strength does not exceed the unconfined value. Hence, Equation (3) can be re-written as follows:

$$f_{Mc} = f_{Mo}\left(\alpha + k_1 \frac{\sigma_{\ell u}}{f_{Mo}}\right) \le f_{Mo} \quad (5)$$

with $\alpha < 1$, to ensure continuity of f_{Mc} at the level of confining stress beyond which $f_{Mc} \ge f_{Mo}$.

The aforementioned confinement model for masonry is defined fully by determining the empirical constants k_1, k_2 and α from testing. Test data obtained in this study for the ratio of confined to unconfined strength, f_{Mc}/f_{Mo}, in terms of the normalized confining stress, $\sigma_{\ell u}/f_{Mo}$ [see column (6) in Table 1] are plotted in Figure 9. The best fit linear equation to these data resulted in $\alpha = 0.6$ and $k_1 = 1.65$. Substituting these values in Equation (6) and taking $f_{Mc}/f_{Mo} = 1$, the ratio $\sigma_{\ell u}/f_{Mo}$ becomes equal to 0.24. Hence, the proposed

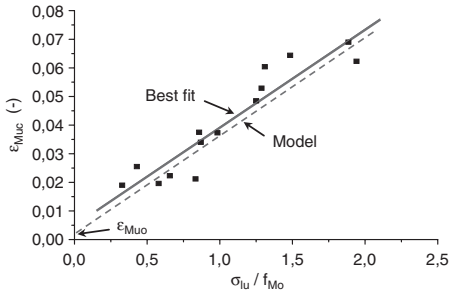

Figure 10. Ultimate compressive strain of confined masonry in terms of lateral confinement.

model for strength, shown by the solid lines in Figure 9, is written as follows:

$$f_{Mc} = f_{Mo} \quad \text{if} \quad \frac{\sigma_{\ell u}}{f_{Mo}} \le 0.24 \tag{6}$$

$$f_{Mc} = f_{Mo}\left(0.6 + 1.65\frac{\sigma_{\ell u}}{f_{Mo}}\right) \quad \text{if} \quad \frac{\sigma_{\ell u}}{f_{Mo}} \ge 0.24 \tag{7}$$

The experimental data for the ultimate axial strain of confined masonry, ε_{Muc}, in terms of $\sigma_{\ell u}/f_{Mo}$ are plotted in Figure 10. Again, the best fit linear equation to these data was obtained as follows:

$$\varepsilon_{Muc} = 0.005 + 0.034\frac{\sigma_{\ell u}}{f_{Mo}} \tag{8}$$

Hence, k_2 in Equation (4) may be taken equal to 0.034, so that the proposed model for ultimate strain is as follows:

$$\varepsilon_{Muc} = \varepsilon_{Muo} + 0.034\frac{\sigma_{\ell u}}{f_{Mo}} \tag{9}$$

Note that the line plot of Equation (9) maintains the slope of the best fit (solid line in Fig. 10) but is shifted a bit downwards, so that the intersection with the vertical axis becomes equal to the unconfined strain ε_{Muo} (dashed line in Fig. 10).

5 CONCLUSIONS

Confinement of masonry with FRP has not been investigated in the past. This study presents an experimental investigation on the behaviour of axially loaded short masonry columns confined with FRP jackets, followed by the development of an analytical model for the prediction of confined strength and ultimate strain. Four series, a total of 42 specimens, of uniaxial compression tests were conducted on specimens with variables the number of layers, the radius at the corners, the cross section aspect ratio and the type of fibers. The results are summarized as follows:

(1) In general, FRP-confined masonry behaves very much like FRP-confined concrete. The confinement provided by FRP improves considerably both the load-carrying capacity and the deformability of masonry columns of rectangular cross section.
(2) For the specimens tested in this study the gain in performance (strength and deformability) increases almost linearly with the average confining stress. Increasing the corner radius or decreasing the cross section aspect ratio is beneficial to the strength and strain capacity of rectangular masonry columns. Being more deformable, glass fibers are more effective than carbon fibers if the gain in strength and deformability is compared for the same FRP hoop stiffness.
(3) Test results enabled the development of a simple confinement model for strength and ultimate strain of FRP-confined masonry. This model is consistent with test results obtained here, but should attract further experimental verification in the future, to account for types of masonry materials other than those used in this study.

REFERENCES

De Lorenzis, L. and Tepfers, R. 2003. Comparative study of models on confinement of concrete cylinders with fiber-reinforced polymer composites. *Journal of Composites for Construction* 7(3): 219–237.

fib 2001. *Externally bonded FRP reinforcement for RC structures*. Bulletin 14, International Federation for Structural Concrete, Lausanne, Switzerland.

Triantafillou, T. C. and Fardis, M. N. 1993. Advanced composites as strengthening materials of historic structures. In *Structural preservation of the architectural heritage*; *Proc. IABSE Symp.,* Rome, 541–548.

Triantafillou, T. C. and Fardis, M. N. 1997. Strengthening of historic masonry structures with composite materials. *Materials and Structures* 30: 486–486.

Valuzzi, M. R., Tinazzzi, D. and Modena, C. 2003. Strengthening of masonry structures under compressive loads by using FRP strips. In K. H. Tan (ed.), *Fibre-Reinforced Plastics for Reinforced Concrete Structures; Proc. 6th Intern. Conf.,* Singapore, World Scientific Publishing Co., 1249–1258.

FRP Composites in Civil Engineering – CICE 2004 – Seracino (ed)

Strengthening of timber structures in-situ with an application of fiber-reinforced polymers

K.U. Schober & K. Rautenstrauch
Bauhaus-University of Weimar, Department of Timber and Masonry Engineering, Weimar, Germany

ABSTRACT: Upgrading structures for higher working loads or restoring original design strength is an engineering task for structures of any material. This paper presents a study of reinforcement techniques for restoration and strengthening of existing timber floors and bridge girders under bending loads, based on the use of structural adhesives on the building site, whereby the removal of the overhanging part of the structure as well as the inserted ceiling is not necessary. Commercial adhesives, as well as products modified for this particular application, were tested. The tests showed the arrangement of the reinforcement and the stiffness of the materials transmitting the loads, i.e. wood, carbon fiber reinforcement and the bonding agent, were of decisive influence for the overall strength of the specimen. Not all influence parameters could be checked in the executed experiments. Therefore, a numerical investigation based on a finite-element model with nonlinear timber properties was applied.

1 INTRODUCTION

Rehabilitation of buildings has an increasing economical and social importance particularly in countries with great abundance of traditional buildings that require specific attention when consolidation is needed. A great number of these buildings need specific interventions to restore the damages for renovation. Particularly old timber structures in residential houses have a couple of damages. They are designed for lower live loads as specified in performance and design standards and need new technologies to increase the load-carrying capacity of the members for state-of-the-art housing conditions, including reinforcement or repair due to previous overloading, insect and fungal attack.

Besides, many historical timber structures require urgent and proper maintenance and repair works and often, the structures have been directly substituted or, if maintained, recovered only for aesthetic purposes without respecting their original structural role and conception. Frequently neither decision makers nor building contractors have the necessary knowledge on suitable reinforcement techniques and damaging interventions are often made. Therefore, a study of reinforcement techniques for restoration and strengthening of existing timber floors under bending loads has been carried out. The experimental and numerical study based on the use of structural adhesives on the building site, whereby the removal of the overhanging part of the structure as well as the inserted ceiling is not necessary.

The first results and insights have been used successfully for renovation and reconstruction of historic roof and floor constructions shown in the next figures (Rautenstrauch 2004).

Figures 1–2. Damaged spire of the Merseburg cathedral (D) due to high wind loads and weathering. Cantilever joint after strengthening with CFRPs.

2 BACKGROUND

Rehabilitation based on the formation of a composite system has found frequent applications in the case of timber floor beams with a concrete slab, but may have different forms depending on the concerned structural element. Reinforcement techniques for structural timber elements, based on the use of structural adhesives on site, have been applied for some decades as an

Figure 3. CFRP and polymer concrete strengthening of a historic ceiling joist in waffle slab, Mansfeld castle (D).

extension of procedures that became very common for the repair or the upgrading of other structures. Adhesives can be used either on their own or in conjunction with steel plates, rods, or fiber-reinforced materials. Such techniques are very promising as they minimize disturbance of the building and to its occupants during the intervention. Repair techniques involving the use of adhesives are versatile and effective, less time and cost consuming than alternative traditional methods and materials. However, some problems have prevented the wider use of structural adhesives, particularly in historical timber structures, where sufficient reliability cannot yet be guaranteed. One reason is that a life-long service life has not yet been fully proven for synthetic adhesives, since the oldest bonded joints are around sixty years and greater ages cannot be simulated by existing accelerated ageing tests. Besides, although the failure of a structural bonded joint may be responsible for the collapse of the whole structure, short and long-term performance of glued bonds highly depends on the bonding process and conditions as shown in the tests performed, which are especially difficult to control on the building site.

Although epoxy based adhesives have been used in most cases for on-site repair jobs, most formulations were developed for other materials. These adhesives are generally too rigid for bonding timber and there is no chemical bonding or suitable mechanical anchorage in wood. The bond line is prone to fail because of dimensional changes in the wood induced by moisture content variations, even under Service Class 2 applications (moisture content of timber up to 18%). However, this group of adhesives has the potential to be the most suitable one for on-site bonding. Therefore, it is necessary to improve the existing adhesives or to develop alternative adhesive formulations, suitable for indoor (and even outdoor) jobs on site where the use of pressure is generally not available and clean regular bond lines are difficult to achieve. Moreover, the existing test methods to evaluate bond line performance were developed for other types of industrially used adhesives, especially phenol or amino plastic based products, and have repeatedly proved to be inadequate to assess the behavior of epoxy type adhesives or epoxy bonded products. The application of existing European or national test and performance standards to epoxy bonded products are much too penalizing, since they merely impose severe stresses which do not describe the glue performance on site as far as it has been reported. Extensive pre-normative research and thorough consideration of these problems are still required. Moreover, on-site application of adhesives is somewhat difficult and the consequent quality of adhesive bond is not easy to evaluate. Since properties of reinforced elements very much depend on the care put in the work, such difficulties have to be overcome. Procedures for applying and controlling are needed and must be established.

These techniques generally resort to the use of other materials, which are made to collaborate with the original timber according to various modalities. These are amenable to two basic approaches discussed here: the use of reinforcement materials embedded in the wood, and the use of external reinforcement resulting in a system of composite type.

3 BENDING TESTS

3.1 *Aim and scope*

Six series of un-reinforced and carbon FRP-reinforced old solid wooden beams with different location and direction of the reinforcement were tested to study the specific influence on the load-carrying and fracture behavior. The main task of the test series performed was gathering and generating qualitative and quantitative knowledge on structural adhesives suitable for on site repair of timber structures. This will enable the effective and safe application of reinforcement techniques based on the use of structural adhesives, especially in high demanding situations where the present lack of knowledge and reliability of these products restrain their application. Commercial adhesives were tested. The tests showed the arrangement of the reinforcement and the stiffness of the materials transmitting the loads, i.e. wood, CFRP and the bonding agent, were of decisive influence for the overall strength of the specimen, also influenced by the wood structure and the nature of the wood surface. Questions exist concerning the proportion of the quality, influenced by the properties of the wood surface, and how adhesion and the forming of the interface between adhesive and the wood surface really work. We have studied three practical solutions of bonding on the building site in order to investigate the different performance of the composite structure and to attain the highest possible quality of the bond line.

Figures 4–5. Typical cross-section of tested beams.

Table 1. Cross-sectional data of used timber.

Specimen	Height [cm]	Width [cm]	$I_{y,mean}$ [cm^4]	I_y [cm^4]	$I_y/I_{y,mean}$ [%]
S02/1-uv	16.62	15.39	5049	3916	77.57
S02/2-uv	18.76	15.30	5599	4411	78.77
S03/1-uv	19.33	14.59	5003	4158	83.10
S03/2-uv	21.28	15.76	6942	5517	79.48
S04/1-uv	17.67	15.14	5110	4187	81.83
S04/2-uv	21.09	15.00	5932	4545	76.62
S05/1-uv	18.07	16.00	6168	5280	85.60
S05/2-uv	20.11	16.11	7007	5444	77.69
S07/1-uv	15.42	20.30	10,750	9788	91.05
S08/1-uv	14.64	18.28	7452	6573	88.20
S09/1-uv	15.74	17.74	7323	6758	92.28
S11/1-uv	15.56	19.33	9365	7410	79.12
Mean value	17.86	16.58	6808	5666	82.61

3.2 *Specimen*

For practice related investigations, a carefully election of the test specimen was required. In this case a couple of preloaded spruce rafters and ceiling joists with an age of more than 100 years where removed from an old residential house in Bavaria/Germany. The influencing factors like pre-ageing/weathering, moisture content when bonding, wood species, density, cross-section, existing cracks, knots and damages were analyzed. For determination of the strengthening effect after bonding and the Young's modulus of the specimen the real cross-sectional data including cracks and damages A, I_y and the averaged properties A_{mean}, $I_{y,mean}$ where taken into account. Due to the usual existing cracks in historic timber beams a reduction of the moment of inertia and the bending stiffness of about 17% can be observed (Table 1).

The old solid wood beams were reinforced with a continuous carbon fiber lamella S&P 150/2000 with intermediate modulus fibers from S&P Reinforcement Ltd. and 3.15 m length within the clear span for reinforcement type Vh, otherwise over the full length of 3.50 m.

The CFRP layer with a cross-section of 1.4 × 50 mm was glued/embedded by means of the commercially available epoxy resin StoPox SK 41 from StoCretec Ltd, which has a technical approval for gluing together with the carbon fiber lamellas. As a result of the tests and the fracture modes observed, the resin will be modified for this special application on timber members. The epoxy resin consisted of two parts of component A and B mixed in a ratio of 4:1 by volume, as required in the technical description. The mean mechanical properties are shown in Tables 2–3.

Table 2. Mean material properties of used CFRP-lamellas.

Property	Unit	Epoxy matrix	Carbon fiber	Lamella S&P 150/2000
Tensile strength	MPa	75	4800	2200–2500
Tensile MOE	GPa	2.8	2400	164
Ultimate elongation	%	3.5	2.00	1.4
Density	g/cm^3	–	1.73	–

Table 3. Mean material properties of used epoxy resin.

Property	Unit	StoPox SK 41	StoJet IHS
Tensile strength	MPa	≥30	–
Tensile MOE	GPa	11	–
Density	g/cm^3	1.75	1.07

Three different reinforcement schemes were evaluated in the testing program (Table 4):

- Reinforcement of series 1 = series 4
  Type Vh: 1 × 1.4 × 50 mm bonded centrally to the tension zone, horizontal on bottom
- Reinforcement of series 2 = series 5
  Type Vs: 2 × 1.4 × 25 mm bonded laterally to the tension zone 3 cm from bottom in slot
- Reinforcement of series 3 = series 6
  Type Vh: 1× 1.4 × 50 mm bonded centrally to the tension zone, vertical on bottom

The gluing of the lamellas was done under practice-related conditions. For reinforcement type Vh, the wood surface must be even, unweathered and clean by planning the surface until sound wood is reached to ensure a continuous bound. The CFRP lamellas were cleaned by using acetone. The timber surface was primed using StoJet IHS to avoid desiccation of the resin and to ensure a full compound between resin and wood surface.

3.3 *Testing*

For investigating the strengthening effect of the carbon fiber reinforcement in different, practice-related positions three series of un-reinforced and reinforced old solid wood beams were tested. Test series 1–3 were

accomplished to determine the bending stiffness and MOE of the un-reinforced specimen within the elastic range. After unloading the same specimen were reinforced described above already and the tests were executed on each beam again within the elastic range for MOE and bending stiffness examination of the reinforced specimen. The applied loads were increased till specimen failure to evaluate the fracture behavior and ultimate load. There were four beams in each series with a length of the specimen of 3.50 m, span 3.25 m and with cross-sections shown in Table 1. All beams were surveyed for geometric dimensions and wood damages. The humidity ratio was measured on different locations. The average value of the humidity ratio was 13.49% with a COV of 6%.

The tests were executed as a four-point bending test according to EN 408. The load span was equal to 6 h_m. The beams were loaded with a 200 kN actuator and a spreader beam. The spreader beam, centered about the mid-span, created a zone with constant moment and zero shear. The vertical displacements of the beams were measured using six inductive transducers in the span and 2 IT on the supports, additionally using a photogrammetric approach by analyzing the deflection field in the midspan of the specimen Fig. 6, Rautenstrauch et al. 2003, 2004). For measuring the horizontal deflection in the midspan area 10 IT were used. For test series 4–6 the longitudinal deflection between the specimen and the CFRP lamella were measured using inductive transducers at the face of the specimen. In test series 4 (reinforcement type Vh) additional 25 strain sensors were applied on the bottom of the specimen to obtain the elongation of the lamella itself. The results have been used to calculate the bonding stresses in the resin and for an examination of the load-slip rule of the groove.

Two tests were executed on each beam within the elastic range to determine the bending stiffness and MOE of the un-reinforced and reinforced specimen and a third test to evaluate the fracture behavior and

Figure 6. Photogrammetric measurement of deflections.

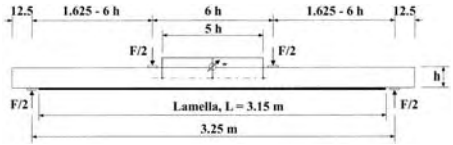

Figure 7. Load arrangement.

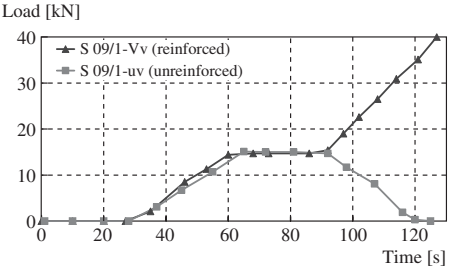

Figure 8. Exemplified load-time curve for MOE and bending stiffness examination within the elastic range. Here specimen S 09/1 with and without reinforcement.

Table 4. Test series.

Specimen	Series	Reinforced	Series	Reinforcement	ρ^* [%]
S03/1	1	None	4	Vh	0.274
S04/1					0.293
S05/1					0.276
S07/1					0.254
S02/2	2	None	5	Vs	0.272
S03/2					0.232
S05/2					0.243
S08/1					0.280
S02/1	3	None	6	Vv	0.309
S04/2					0.245
S09/1					0.266
S11/1					0.267

* Reinforcement ratio $\rho = A_{CFK}/A_{ef}$.

ultimate load. The Young's modulus of the specimen was measured by recording the load deflection behavior of all beams between two load levels according to EN 408 with a maximum load value of 12 kN. Loads for the measurement of the flexural capacity of the wood beams were applied monotonically to failure. The test for the evaluation of the bending stiffness achieves failure in 10 to 15 minutes. The results for the un-reinforced beams are reported solely for quantitatively evaluating the effectiveness of the interventions through a comparison with the results for strengthened beams.

4 RESULTS AND DISCUSSION

Several experimental tests (Triantafillou 1997, Borri et al. 2003) showed that the most frequent fracture mechanism is caused by the failure of the traction zone without the complete plasticization of the compression region, depending on the quality of the wood. However, under particular conditions it is possible to note the other failure mechanism, which is theoretically preferable for several reasons. First, the section shows a more ductile behavior, while the stresses in the FRP material with reinforcement are highly increased and therefore, the composite material is more involved. Initially the load defection is shown to be linear elastic up to local failures induced by the presence of defects e.g. knots and cracks. Wood yield produced a non-linear response terminated by a sudden drop of the load as a result of CFRP rupture. CFRP rupture was immediately followed by wood fracture in the tension zone, resulting in the collapse of the beams. The load-deflection behavior of the different reinforcement schemes is shown in Figures 10–12. Failure occurred at a load level between 35 kN and 87 kN (mean 53.16 kN) due to the different fracture behavior and sections. The tests have shown that the most frequent failure mechanism is the one in which traction failure and shear failure occurs with or without partial plasticization of the compressed zone.

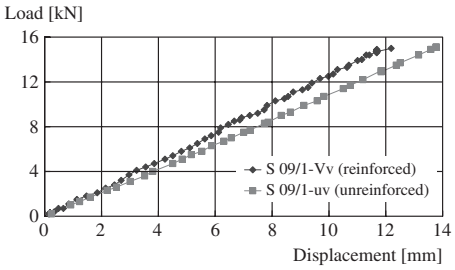

Figure 9. Exemplified load-deflection curve within the elastic range. Here specimen S 09/1 with and without reinforcement.

Generally, for all tests on reinforced specimens a linear phase could be observed until reaching the maximum Service Load F_s with low creak and first small cracks in the specimen. Depending on the wood quality and reinforcement scheme a linear or non-linear phase until the Ultimate Load F_u where the first good visible cracks occurred and a further increasing of the deflection until reaching the Maximum Load F_m with brittle failure of the specimen follows the linear phase. The different load levels are shown in Table 6. It could be ascertained that on all tests in series 4 and 6 the Ultimate Load is reached within the linear range and on all tests of series 5 the specimen could not support further load increments after the first break.

The determination of the flexural strength of the composite structure has been done in the elastic range.

Table 5. Different fracture modes of specimen observed during the tests till the maximum load is reached.

Series	Specimen	Ultimate load F_u[kN]	Shear failure in timber	Crushing failure in timber	Tension failure in bottom chord	Fracture in middle part	Deflection failure	Embedding failure	Failure out of knots	Lamella torn off
4	S03/1-Vh	50.46		☐	☐		☐			☐
	S04/1-Vh	44.46	☐		☐			☐		☐
	S05/1-Vh	38.06	☐			☐	☐	☐	☐	☐
	S07/1-Vh	66.23	☐		☐	☐		☐		
5	S02/2-Vs	58.93	☐		☐		☐	☐		
	S03/2-Vs	57.03			☐			☐		
	S05/2-Vs	47.03			☐		☐			
	S08/1-Vs	35.03				☐	☐			
6	S02/1-Vv	38.96		☐		☐			☐	
	S04/2-Vv	41.76	☐		☐					
	S09/1-Vv	73.86	☐			☐				
	S11/1-Vv	86.13	☐			☐				

Table 6. Different load levels observed at the tests.

Specimen	F_{DIN} [kN]	F_s [kN]	F_u [kN]	F_m [kN]
S03/1-Vh	11.89	22.00	50.46	53.46
S04/1-Vh	11.61	18.00	44.46	44.46
S05/1-Vh	12.57	21.00	38.06	38.06
S07/1-Vh	17.25	39.00	66.23	66.23
S02/2-Vs	12.64	22.00	58.93	58.93
S03/2-Vs	15.43	25.00	57.03	57.03
S05/2-Vs	15.44	21.00	47.03	47.03
S08/1-Vs	15.52	18.00	35.03	35.03
S02/1-Vv	11.52	22.00	38.96	41.06
S04/2-Vv	13.70	27.00	41.76	46.16
S09/1-Vv	15.53	32.00	73.86	73.86
S11/1-Vv	18.99	49.00	86.13	86.13
Mean	14.58	26.33	53.16	53.95
COV	16.06	35.49	29.71	28.45

*F_{DIN} = max. DL according to German code DIN 1052 (4.88).

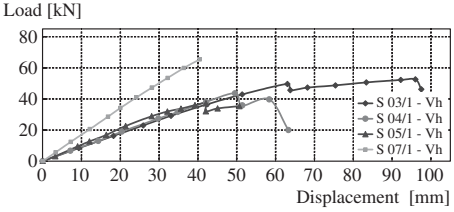

Figure 10. Load-deflection curves for series 4–reinf. type Vh.

Ehlbeck & Colling (1987) gave the increase of the bending stiffness as:

$$k_{EI} = \frac{ef\ EI}{EI} \tag{1}$$

where ef EI = effective bending stiffness of the composite structure is. The increasing of EI by applying CFRP reinforcement can been done also by defining a fictitious modulus of elasticity, calculated from the cross-section data of the un-reinforced specimen according to EN 408:

$$E_{fict} = \frac{a \cdot l_1^2 \cdot (F_2 - F_1)}{16 \cdot I \cdot (w_2 - w_1)} \tag{2}$$

where $F_2 - F_1$ = load increase in elastic range, $w_2 - w_1$ = equivalent deflection values. The increase of the bending stiffness is shown in Table 7. The reinforcing scheme increased the capacity (E_{fict}) by mean 5.86% in comparison to the values measured for the un-reinforced wood beams. The measured data correlate with the experimental results published by Blaß

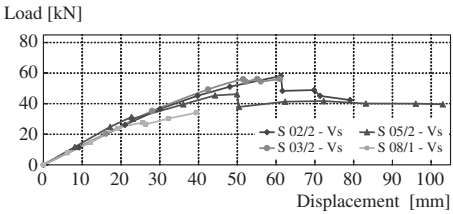

Figure 11. Load-deflection curves for series 5–reinf. type Vs.

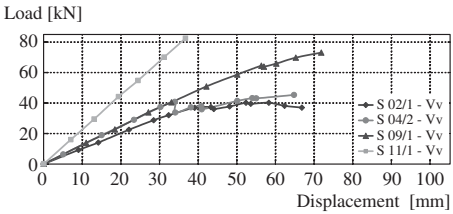

Figure 12. Load-deflection curves for series 6–reinf. type Vv.

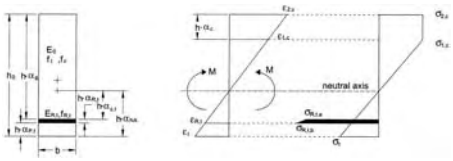

Figure 13. Notation and stress-strain relationship for a cross-section with plastic compression area.

& Romani (2000, 2001) for horizontal reinforcement. Here, the bending stiffness is calculated in the linear-elastic range and plastic deformations are not considered, since the stiffness is used for serviceability limit states. The factor k_{EI} indicates the stiffness increase for horizontal reinforced beams with an reinforcement over the full with.

$$\begin{aligned} k_{EI} = {} & 12 \cdot \alpha_g \cdot \left(\frac{1}{2} + \frac{\alpha_{R,t} + \alpha_{P,t}}{2} - \alpha_{NA} \right)^2 \\ & + n_t \cdot \alpha_{R,t}^3 + 12 \cdot n_t \cdot \alpha_{R,t} \cdot \left(\alpha_{z,t} + \frac{\alpha_{R,t}}{2} \right)^2 \\ & + \alpha_{P,t}^3 + \alpha_g^3 + 12 \cdot \alpha_{P,t} \cdot \left(\alpha_{NA} - \frac{\alpha_{P,t}}{2} \right)^2 \end{aligned} \tag{3}$$

The wood beams reinforced with CFRP lamellas revealed more ductile behavior with respect

Figures 14–15. Section ripping due to horizontal cracks.

Table 7. Comparison of un-reinforced and reinforced specimen.

Specimen	F_u[kN]	E [MPa]	E_{fict} [MPa]	E_{fict}/E[%]
S03/1-Vh	50.46	12,622	14,390	113.99
S04/1-Vh	44.46	14,900	15,546	104.34
S05/1-Vh	38.06	13,229	14,875	112.45
S07/1-Vh	66.23	10,744	12,163	113.20
S02/2-Vs	58.93	17,675	17,891	101.22
S03/2-Vs	57.03	13,954	14,762	105.79
S05/2-Vs	47.03	16,373	16,982	103.72
S08/1-Vs	35.03	11,156	11,642	104.36
S02/1-Vv	38.96	15,837	16,742	105.71
S04/2-Vv	41.76	18,747	17,823	095.07
S09/1-Vv	73.86	10,837	11,427	105.45
S11/1-Vv	86.13	17,770	18,604	104.96
			Mean	105.86
			COV	5,03

*$E_{fict}/E = ef\,EI_{reinf}/EI$.

to un-reinforced beams. The presence of CFRP reinforcement arrest crack opening, confines local rupture and bridges local defects in the timber. Therefore, the specimen can support higher loads before failure. Moreover, as can be observed from the load-deflection curves of the reinforced and un-reinforced specimen and the calculation of the fictitious MOE E_{fict}, there is an increase of the load-carrying capacity as a consequence of the quoted crack opening arrest. Especially in reinforcement type Vs and Vh, with in wood embedded lamellas, an improvement of the load-carrying behavior can be observed. The failure of the structure in this cases occurred by shear due to ripping of the section in longitudinal direction between cracks. To avoid this an additional shear strengthening with connectors usable under practice-related conditions should be applied in further test series.

In the midspan the horizontal deflection on the timber faces was measured with inductive transducers and close range photogrammetry. The results have been used to compare the measurement data with stress-strain laws given by Plevris & Triantafillou. A linear strain distribution over the specimen height could be observed in the elastic range for all test series.

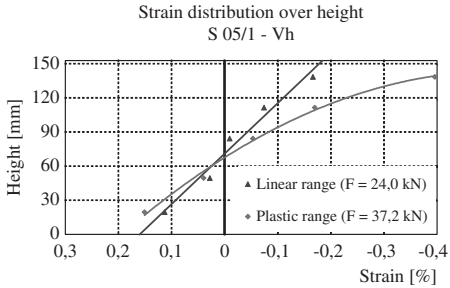

Figure 16. Typical strain distribution for reinforcement type Vh.

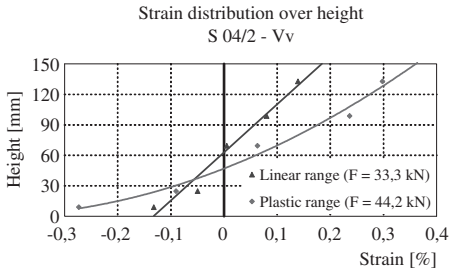

Figure 17. Typical strain distribution for reinforcement type Vv.

Where plastic behavior in the compression zone was reached a non-linear strain distribution nearby the state of failure could be observed. At the time, numerical investigations of this phenomena are carried out.

5 CONCLUSIONS

New requirements in the restoration and strengthening of timber structures force the use of new materials. The use of CFRP as a strengthening technique can be applied without necessitating the removal of the overhanging part of the structure. It is very promising in many cases of reinforcement of old, historical structural wood parts. Upgrading traditional timber structures of old solid wood with carbon fiber reinforcement on different locations are described and discussed here on the basis of experimental investigations. For practice related investigations effective cross-sectional data including existing cracks, knots and damages were used with a reduction of the initial bending stiffness/moment of inertia of about 17% compared to the cross-sections without defects. The results of the experiments have highlighted the limitations of the composite structure as well as the

advantages of the various reinforcement positions and present numerous interesting aspects.

However, not all influence parameters could be checked in the executed experiments. The various theories of bonding developed so far are not able to explain comprehensively the observed effects. Chemical bonding always has been seen as the optimal form of combining two surfaces with each other, but its contribution to the overall bonding mechanism is still unclear. The properties of the glue line can be described among other methods by the analysis of the microstructure of the bond line. This includes the adhesive penetration into the wood surface, the effect of ageing of a glue bond as well as the description of the cohesive strength of the glue line in terms of an optimization of the brittle and elastic ratio of the glue line.

The wood beams reinforced with CFRP lamellas revealed more ductile behavior with compared to unreinforced beams. The presence of CFRP reinforcement arrests crack opening, confines local rupture and bridges local defects in the timber especially for reinforcement types other than on the bottom face. The failure of the structure in this cases occurred by shear due to separating of the section in longitudinal direction between cracks. To avoid this, an additional shear strengthening with connectors usable under practice-related conditions should be applied in future test series. These investigations are currently going on and will be supplemented by using further practical boundary conditions.

ACKNOWLEDGEMENTS

The authors wish to thank Mr. D. Grunewald from S&P Reinforcement Ltd. for supplying the carbon fiber lamellas and resin. Special thanks to Mr. J. Frobel from Bennert Ltd. and Ms. K. Grund for assistance with the experiments.

REFERENCES

Baldassino, N. et al. 1996. In situ evaluation of the mechanical properties of timber structural elements. In: *10. Int. Symposium on Nondestructive Testing of Wood, Lausanne, CH:* 369–377. Engineering 2000, Whistler, British Columbia, Canada.

Bazan, I.M.M. 1980. *Ultimate Bending Strength of Timber Beams.* PhD thesis. Nova Scotia Technical College. Halifax, Canada.

Blaß, H.J. & Romani, M. 2000. Trag- und Verformungsverhalten von Verbundträgern aus Brettschichtholz und faserverstärkten Kunststoffen. *Research report: Schlussbericht AiF-Vorhaben 11407/N.* Karlsruhe.

Blaß, H.J. & Romani, M. 2001. Design model for FRP reinforced glulam beams. *International Council for Research and Innovation in Building and Construction. Working Commission W18-Timber Structures. Paper CIB-W18/34-12-3.* Venice.

Bodig, J. & Jayne, B.A. 1982. *Mechanics of Wood and Wood Composites.* New York: Van Nostrand.

Borri, A. et al. 2003. FRP reinforcement of wood elements under bending loads. In: Proceedings, *Structural Faults and Repair.* London.

Buchanan, A.H. 1990. Bending strength of lumber. *Journal of Structural Engineering 116(5)*: 1213–1229. ASCE.

Dziuba, T. 1985. The ultimate strength of wooden beams with tension reinforcement. *Holzforschung und Holzverwertung 37(6)*: 115–119.

Ehlbeck, J. & Colling, F. 1987. *Tragfähigkeit von mit Glasfaser-Verbundprofilen verstärkten Brettschichtholzträgern.* Versuchsanstalt für Stahl, Holz und Steine, Universität Fridericana Karlsruhe.

EN 408: 1995. Timber structures – Structural timber and glued laminated timber. Determination of some physical and mechanical properties. CEN European Committee for Standardization.

Kobetz, R.W. & Krueger, G.P. 1976. Ultimate strength design of reinforced timber Biaxial stress failure criteria. *Wood Science 8(4)*: 252–262.

Kropf, F.W. & Meierhofer, U. 2000. Strengthening, Retrofitting and Upgrading of Timber Structures with High-Strength Fibres, *SEI* 3/2000.

Krueger, G.P. 1973. Ultimate strength design of reinforced timber: state of the art. *Wood Science 6(2)*: 175–186.

Larsen, K.E. & Marstein, N. 2000. *Conservation of Historic Timber Structures*., Oxford: Butterworth-Heinemann.

Piazza, M. 1994. Restoration of timber floors via a composite timber-timber solution. *Proceedings of the Technical Workshop Timber: A Structural Material from the Past to the Future*: 167–187. Trento: RILEM.

Piazza, M. & del Senno, M. 2001. Proposals and criteria for the preliminary evaluation, the design and the execution of works on ancient load bearing timber structures. In: *Wooden Handwork/Wooden Carpentry: European Restoration Sites*: 263–277. Paris: Elsevier.

Plevris, N. & Triantafillou, T.C. 1992. FRP Reinforced wood as structural material. *Journal of Materials in Civil Engineering 4(3)*: 300–315.

Rautenstrauch, K. et al. 2003. Strain analysis of solid wood and glued laminated timber constructions by close range photogrammetry. In: *International Symposium: Non-Destructive Testing in Civil Engineering*. Berlin.

Rautenstrauch, K. et al. 2004. Beanspruchungsanalyse von Bauteilen aus Voll- und Brettschichtholz durch Nahbereichsphotogrammetrie. *Bauingenieur.* Düsseldorf: Springer VDI-Verlag. In press.

Rautenstrauch, K. 2004. Standsicherheitsgutachten zur Unterzugsanierung Schloss Mansfeld. Unpublished work.

Triantafillou, T.C. & Plevris, N. 1991. Post-strengthening of r/c beams with epoxy-bonded fibercomposite materials. *Proceedings ASCE Specialty Conference on Advanced Composites for Civil Engineering. Structures*: 245–256. ASCE.

Triantafillou, T.C. 1997. Shear reinforcement of wood using FRP materials. *Journal for Materials in Civil Engineering 9(2)*: 65–69. ASCE.

FRP Composites in Civil Engineering – CICE 2004 – Seracino (ed)
© 2005 Taylor & Francis Group, London, ISBN 90 5809 638 6

Improving the structural performance of timber beams with FRP composites: a review

J.R. Gilfillan, S.G. Gilbert & G.R.H. Patrick
Faculty of Engineering, Queen's University, Belfast, N Ireland

ABSTRACT: This paper provides a selected review of the extensive research that has been carried out on the reinforcement of timber beams over the last three decades. The work indicates that reinforcement is an effective means of improving the performance of solid and laminated beams. Recent research has highlighted the advantages of fibre reinforced polymers as reinforcement in strip or rod form. A primary objective of much of the work was to promote the use of low quality timber. For such material tension reinforcement bonded to the soffit of a beam is an effective way to suppress brittle collapse and, instead, induce a ductile type of failure. In addition to the review, this paper describes some aspects of a theoretical and experimental programme at Queen's University Belfast, concentrating on the use of locally-grown Sitka spruce. It has been established that the strength of reinforced beams depends primarily on the behaviour of the timber in compression, resulting in more consistent performance and a considerable increase in flexural stiffness.

1 BACKGROUND

1.1 *Timber as a native resource*

The sustainability of timber is a positive factor in promoting its structural use. Sitka spruce (*Picea sitchensis*) is the most abundant species grown in the United Kingdom and Ireland.

Sitka spruce is characterised by lower strength grades compared with imported timber of similar species. This is largely due to its fast growth rate and relatively low density. The need to use larger section sizes to achieve the same structural performance often eliminates the cost advantage over imported timber.

1.2 *Timber composites*

Structural timber composites (STCs) are vital to the competitiveness and growth of the timber industry worldwide. Those manufactured from the increasing supply of locally grown timber are a particularly attractive proposition and their utilisation is important for economic, political and environmental reasons. Composites take many forms, reconstituted from particles, fibres, flakes, strands, veneers and laminates. The most common form is glue-laminated timber (glulam).

Laminated beams have higher strength, increased stiffness and lower performance variation than the donor timber from which they were made. The difference is most marked for the lower strength grades of timber.

Although laminating overcomes many of the problems associated with timber and homegrown Sitka spruce in particular, there is a tendency for beams to fail prematurely due to defects in the lowest tension laminate. The authors (Patrick 2004) have observed this brittle type of failure many times when testing solid and laminated beams made with Irish Sitka spruce (Fig. 1).

Figure 1. Brittle tension failure of solid timber beam.

2 REINFORCEMENT TECHNIQUES

2.1 *General*

The addition of reinforcement can increase the strength and stiffness of beams and is a means of both avoiding the brittle tension failure and producing a more consistent failure mode. The disposition of the reinforcement in the cross section depends on the quality of timber in the beam.

A beam of clear timber beam will fail in compression, as the strength of such timber is higher in tension than in compression. In contrast, lower grade timber, like home-grown Sitka spruce, will fail in tension because defects such as knots reduce the strength of the timber in tension more than in compression. Since

clear timber is only available in limited quantities, there have been relatively few studies of singly reinforced beams with the reinforcement located above the neutral axis in order to suppress compression failure in the timber (2.4.).

2.2 *Use of steel reinforcement*

Various researchers have examined the reinforcement of glulam beams using both steel bars and plates placed in machined grooves prior to laminating. Lantos (1964) placed reinforcing bars in the tension timber or, as double reinforcement, in tension and compression areas. Increases for ultimate load of up to 40% were observed. Steel plates were used to reinforce horizontally laminated beams by Borgin, Ledoff and Saunders (1968). These were located in the compression zone only, or in both compression and tension zones. Increases in strength and stiffness were recorded along with an alteration to the mode of failure. Using defect-free timber and the same total area of reinforcement, the doubly reinforced beams displayed higher strengths and stiffness than beams with tension only reinforcement. Gilfillan (1978) worked on preflexing timber/plywood box beams with laminated flanges. A 22 m span beam with reinforcement equally divided between tension and compression flanges displayed increases of 120% and 36% in strength and stiffness respectively.

Bulleit (1989) used steel reinforcing bars embedded in flakeboard, to replace a laminate in the tension zone of glulam timber beams. These displayed increases of up to 32% in stiffness and 30% in strength but suffered from bond failure at high moisture contents.

Buchanan (1990) developed a doubly reinforced system with deformed steel reinforcing bars placed between the outer laminations of the beam and also for reinforcement of connections in glulam frame buildings (Buchanan & Fairweather 1994).

Gardner (1991, 1994) placed deformed steel bars in machined voids between the outer laminates at the top and bottom of glulam beams. A high strength epoxy resin created a physical bond to the timber and a mechanical bond on the deformations on the steel bar. Increases in stiffness of 100 to 200% were reported. The failure modes of the beams varied between yielding of the steel and horizontal shear in the timber and rupturing of the webs. The reinforcement of the beams also significantly reduced their creep deflections. The level of creep was lowered from 50% to 15% of the initial elastic deflection. Based on long-term tests performed, it was suggested that long-term creep would be negligible.

Tasbeam (2002), an Australian company based in Brisbane, fabricates steel-reinforced glulam beams commercially using this technique. The important features of the product, according to the manufacturers,

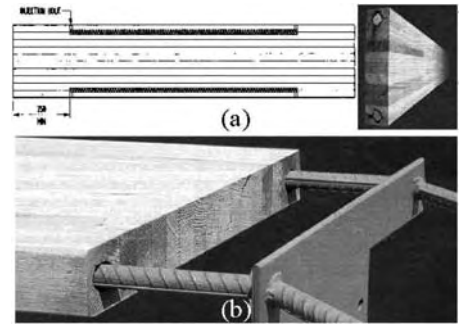

Figure 2. Tasbeam: (a) position of reinforcing bars and (b) moment joint.

are additional strength and stiffness with reduced variability and small creep deflections. The reinforced timber also displays a non-catastrophic failure mode, unlike that of non-reinforced beams which fail without warning.

A 'new age flitch beam' has been developed recently by TRADA (2002) using shot fired dowels for the timber to steel connection. The purpose of this work was to provide 'a means of utilising UK-grown Sitka spruce to produce a high performance structural engineered product.'

There are problems in achieving a good bond to timber and concerns about durability. Nevertheless, steel was a popular choice due to its relatively low cost, availability and good stiffness properties. However, where steel is used as a reinforcing material the timber will not reach its full strain capacity prior to the yielding of the reinforcement. The yield strain for high yield steel at 0.2% is approximately half that of timber at 0.4%. The yielding of the steel will cause it to debond from timber, resulting in the subsequent tensile failure of the beam.

2.3 *Fibre reinforced polymers (FRPs)*

The successful use of FRP reinforcement is perhaps the most significant development in laminated beam technology during the last 40 years. One of the most important steps in this progress is that of matching the strain of FRP composites to timber. The FRP reinforcement used by Tingley (1996) exhibited linear stress–strain behaviour in tension and failed about 1.7% strain. This is approximately double the strain of the clear timber at failure. The high strain capacity of the reinforcement allows the compression fibres to reach their yield points and the tension laminates to reach their ultimate tensile capacity, fully utilising the strength of the timber.

In recent years attention has focussed on the use of lower quality timber for which tension reinforcement

is most effective. FRP-timber composites have been developed at the University of Maine, USA (Landis & Dagher 1997) and in Japan (Ogawa 2000) to use poorer quality timber. An FRP is, of course, itself a composite material in which high strength fibres of glass, aramid or carbon are combined with a resin matrix by a pultrusion process to produce a strip or rod in which the fibres are aligned uniaxially.

FRPs have other properties that make them particularly suitable for use with timber. For example, timber and FRPs both have a similar low coefficient of thermal expansion, so that any differential strain caused by temperature variation is well within the tolerance for the bond line between the two materials and the low rate of creep of FRPs will improve the long-term cyclic loading performance of timber structures.

2.4 *Use of glass fibre reinforced polymer (GFRP) reinforcement*

Fibres have been used in many different forms and arrangements. FRP composite pultrusions were not available for the earliest applications, which were based on fibres alone. As early as the 1960s Theakston (1965) reinforced laminated timber beams with various types of glass fibre mats impregnated with epoxy resin, of which the unidirectional non-woven mats were found most suitable. The members displayed increases in strength and stiffness both when wrapped in the reinforcement and also when it was placed between the horizontal laminates.

Some time later, Boehme (1976) investigated the behaviour of reinforced beams made from solid timber, plywood and particleboard. A polyester resin was used to impregnate glass fibre that was added to the upper and lower edges of the beams. A significant reduction in creep deflection was reported.

Bulleit (1983) used surface mounted unidirectional non-woven glass fibre mat impregnated with phenol-resorcinol formaldehyde to reinforce particleboard. The beams exhibited significant increases in both stiffness and strength together with significant strength retention beyond the peak moment capacity.

Rowlands et al (1986) considered FRP composites suitable for reinforcement of timber beams. Douglas fir beams were reinforced with three types of FRP: glass, carbon and aramid (in the form of Kevlar). Tension reinforcement of the beams with 18% by weight of GFRP increased stiffness by 40% and moment capacity by 100%. The CFRP and AFRP offered further improvements in performance but the cost of these materials was significantly higher than GFRP.

Van de Kuilen (1991) showed that there were only small gains in strength and stiffness from the use of tension and compression reinforcement compared with tension reinforcement only. Using the same total area of GFRP reinforcement, the improvements in performance between single and doubly reinforced beams were similar. The resulting gains in strength and stiffness over unreinforced beams were 58% and 32% respectively for doubly reinforced beams, compared with 49% and 27% increases for beams with tension reinforcement only.

Plevris (1992) concluded that the use of FRP in the compression zone of timber is not justified unless the size of the beam is a critical design issue. This is due to the fact that FRP composites have a lower axial strength in compression, approximately 60% of that in tension, and also due to stiffness disparities between the timber and FRP that can cause delamination of the reinforcement. Relatively few researchers have considered the use of FRP as compression reinforcement (Davalos & Barbero 1991; Kim, Davalos & Barbero 1997).

Tasbeam is now experimenting with GFRP rod. The substitution of FRP for steel rod in their current production results in beams with a higher moment capacity, lower weight allowing more convenient handling and a section that is easier to saw to length. A prerequisite for the GFRP is that it should possess an axial stiffness value (EA) at least equal to that of the steel it is replacing, since most of the designs are governed by deflection limitations.

GFRP rods have been used to reinforce solid Douglas fir beams (Gentile, Svecova & Rizkalla 2002). Rods of 5, 10 and 13 mm diameter were installed close to the bottom edge in 4 and 10 m span beams producing reinforcement area ratios ranging from 0.27% to 0.82%. The rods were placed in routed grooves that were filled with an epoxy resin. The increase in flexural strength was between 18% and 46%. The failure mode of all beams was ductile compression-based and there was no delamination or debonded of the reinforcement outside regions where tension cracks occurred. This technique was proposed for the strengthening of a timber bridge near Winnipeg, Canada.

Lindyberg (2000) produced 90 no. beams of 6.7 m span from Douglas fir and Western hemlock. The beams were reinforced with GFRP, in equal numbers, in ratios of 0, 1.1 and 3.3%. The reinforcement was positioned above the bottom laminate. The highest ratio of reinforcement, 3.3% which was obtained using three layers of the GFRP, was found to increase bending strength by nearly 120%.

2.5 *Use of carbon and aramid reinforced polymers (CFRP and AFRP) as reinforcement*

The higher strength and stiffness properties of carbon and aramid reinforced polymers (CFRP and AFRP) compared to those of glass have provided greater increases in performance using lower volumes of reinforcement. A number of investigators reinforced glulam beams by placing various types of CFRP plates on their tension face.

Plevris and Triantafillou (1992) demonstrated that the bending strength increases approximately linearly with the area of FRP up to a certain level, beyond which moment capacity remains almost constant. It was shown that as little as 1% CFRP of the cross-sectional area of the timber can the increase strength by 60% before compression yield occurred.

Ogawa (2000) has concentrated on finding a suitable use for the dominant native Japanese species, Cryptomeria and Larch, which have low strength and stiffness values. A CFRP composite sheet was sandwiched between resin impregnated pulp paper so that standard laminating glues could be used to bond it to the timber. The beams were doubly reinforced and, for 1.3% CFRP content, displayed a flexural modulus and moment capacity twice that of the donor beams.

With a similar intention, Landis and Dagher (1997) focused on developing FRP reinforced glulam, as it was suitable for transforming the low-grade, low-strength timber that was abundant locally in Maine, USA, into high strength and stiffness composite beams. The addition of CFRP reinforcement increased the bending strength of the beams by up to 60% and the flexural stiffness by approximately 30%.

Tingley (1994) has developed and patented a technology to fabricate a product known as FiRP glulam. These glulam beams are reinforced with aramid, carbon, glass FRPs or hybrids containing more than one type of fibre. The FRP is bonded to the glulam with conventional timber adhesives along the full beam or on particular zones of high bending moment. The typical amount of reinforcement used is in the range of 0.3% to 2.5%. From tests on full-scale reinforced glulam beams Tingley found that AFRP was the most suitable in strength applications compared to other FRPs containing carbon and glass fibres. Hybrid reinforcement combining aramid and carbon was also investigated.

Flavre and Tingley (2001) contend that the coefficient of variation for reinforced beams compared with unreinforced beams is significantly reduced in relation to the predicted and experimental ultimate moment values: typically 8–16% relative to 16–25%. Ten AFRP reinforced beams, with a 1000×200 mm cross-section, have been used for a commercial building with a span of 26 m. These beams proved to be significantly lighter than conventional beams. On-site deflection testing showed good agreement between the measured and predicted deflections.

3 RECENT WORK AT QUEEN'S UNIVERSITY

3.1 *Materials*

On-going work has concentrated on the reinforcement of locally grown Sitka spruce. The strength and stiffness properties of structural size 'in-grade' timber samples were established and used for the theoretical prediction of elastic and ultimate load behaviour of test beams. The results from axial tests produced the data presented in Figure 3. The stress–strain relationship in compression is of particular significance; it is linear up to the limit of proportionality and then displays clear non-linearity beyond the elastic range. This behaviour has been simplified to a bi-linear plot (Gilfillan, Gilbert & Patrick 2001).

The properties of the FRP materials selected for use in the programme were established by test and are given in Table 1.

Various types of adhesives were used in a series of shear block tests on small cube specimens to evaluate the reinforcement/timber bond. A 'filled' two-part epoxy resin system was selected which ensured that all shear failures took place in the timber (Fig. 4).

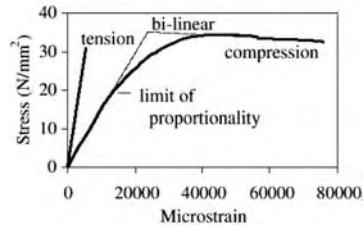

Figure 3. Axial stress–strain plot for strength class C16 Sitka spruce.

Table 1. Material properties.

Material	Axial E ($N/mm^2 \times 10^3$)	Ultimate strength (N/mm^2)	
		Tension	Compression
CFRP (epoxy m.)	165	3050	–
$GFRP_1$ (polyester m.)	23	400	–
$GFRP_2$ (phenolic m.)	52	1120	–
Steel	210	460 (yield)	–
Sitka spruce	9	35	34.2

3.2 *Theoretical assessment*

The failure model adopted assumes that initial failure occurs at the outer fibres on the compression edge. Further loading causes a redistribution of stresses through the depth of the beam as these fibres lose some of their stress-sustaining capacity due to the bi-linear nature of the stress–strain plot.

A theoretical study was carried out to examine the influence of reinforcement type, location and percentage area on the strength and stiffness of timber beams for both the elastic and ultimate behaviour states. It was possible to predict flexural stiffness, shear capacity, moment of resistance and neutral axis position. The analysis was designed to facilitate a parametric study of the various cases (Gilfillan, Gilbert & Patrick 2001).

3.3 *Beam testing*

The test arrangement for a series of 6 m span beams, is shown in Figure 5. These beams had a cross-section measuring 70 × 300 mm, made up with 10 no. 30 mm thick laminates. Strain profiles were recorded carefully in order to verify the assumptions made during the theoretical modelling. A typical strain profile for a tension-reinforced beam close to failure is shown in Figure 6.

3.4 *Discussion of results and comparison with prediction models*

3.4.1 *Elastic behaviour*

The measured stiffness of all the reinforced laminated beams showed good agreement with the predictions, Figure 7. The solid lines indicate theoretical predictions. The experimental values show increases in flexural stiffness over the donor beams ranging from 24% to 55%. The donor beams are represented by 0% area of reinforcement.

3.4.2 *Ductile failure*

The tension-reinforced beams displayed a high degree of ductility approaching failure. A close-up view of a typical failure zone is shown in Figure 12. The ductility ratio compares the deflection at failure to that at the elastic limit. For these beams it was approximately 2.3. In contrast, unreinforced control beams displayed a linear load-deflection curve until sudden failure occurred, resulting in a ductility ratio of 1.0.

3.4.3 *Ultimate load behaviour*

The unreinforced beams failed suddenly due to tension in the timber. Tension-reinforced beams exhibited clear evidence of timber crushing in the upper laminate

Figure 4. Typical failed shear cube sample.

Figure 5. Beam testing arrangement.

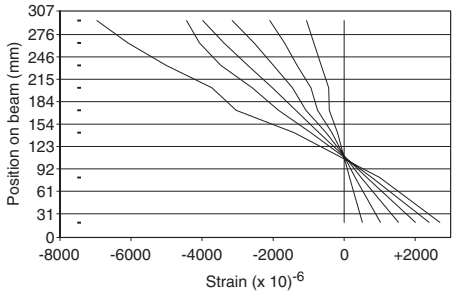

Figure 6. Typical strain profile for 10 laminate beam.

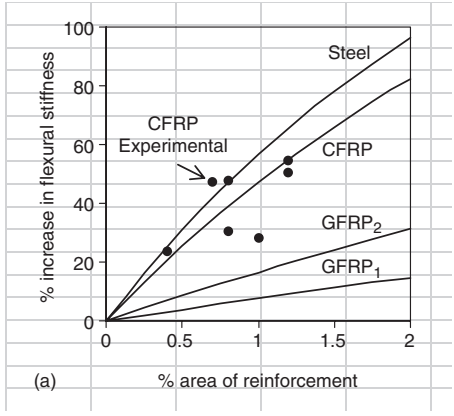

Figure 7. Experimental results and theoretical predictions for flexural stiffness.

Figure 8. Initial compression failure in upper laminates followed by tensile failure in lower laminates.

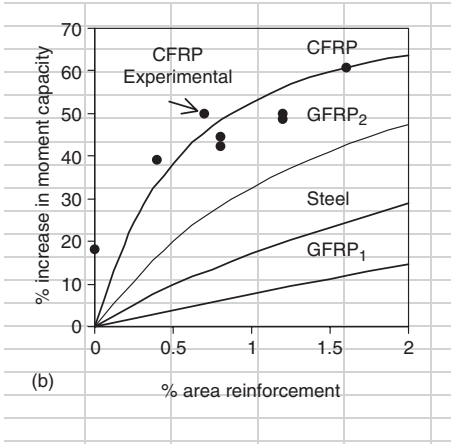

Figure 9. Experimental results and theoretical predictions for ultimate moment.

as shown in Figure 8. This was followed by secondary failure in which the timber split longitudinally.

There was generally good agreement between the experimental and predicted values, Figure 9. The stress profiles obtained for the more heavily reinforced beams indicate that compression yield extended only to approximately 2/3 of the section depth, even though the area of reinforcement provided was sufficient, in theory, to mobilise all the timber in compression. This limit on the amount of timber in compression explains why the predicted ultimate moments for a number of beams that were effectively 'over-reinforced' by different amounts, are similar (Gilfillan, Gilbert & Patrick 2002).

4 CONCLUSIONS

This review of work on FRP reinforced timber indicates that reinforcement is an effective means of increasing the strength and stiffness of solid and laminated beams. In the case of low quality timber the use of tension reinforcement is the most effective approach to suppress brittle tension failure in the timber and produce more consistent behaviour.

Recent work has focused on the use of high strength fibres, particularly glass, aramid and carbon in the form of pultruded reinforced polymers. The high strain capacity of the reinforcement allows the compression fibres to reach their yield points and the tension laminates to reach their ultimate tensile capacity, fully utilising the strength of the timber. Pultruded strip is compatible with the fabrication process of laminated timber and increased demand has started to reduce costs, particularly in the case of CFRP.

Recent work at Queen's University Belfast has concentrated on the reinforcement of home-grown Sitka spruce with the general intention of promoting this timber in higher value end uses. The findings indicate that this timber is particularly suited to the addition of reinforcement due to the resulting ductile compression mode of failure. Strength and stiffness behaviour is significantly improved.

REFERENCES

Boehme, C. 1976. The constructive behaviour of GFK-wood sandwiches – Comparison of experimental results with various computational methods. *Holz Roh-Werst*, 32(7): 250–256.

Borgin, K. B., Loedolff, G. F. & Saunders, C. R. 1968. Laminated wood beams reinforced with steel strips. *ASCE J. Struct. Div.*, 94(ST7): 1681–1705.

Buchanan, A. H., Moss, P. J. & Townsend, P. K. 1990. Reinforcing bars epoxy bonded in glued laminated timber. *In Proceedings of the International Timber Engineering Conference, October 23–25, 1990. Tokyo, Japan.* The Steering Committee of the 1990 International Timber Engineering Conference, Tokyo, Japan.

Buchanan, A. & Fairweather, R. 1994. Glulam connections for Seismic Design. *Proceedings of the Pacific Timber Engineering Conference, Gold Coast Australia, July 11–15, 1994.* Timber Research and Development Advisory Council, Queensland, Australia.

Bulleit, W. M. 1983. Reinforcement of wood materials: A review. *Wood and Fibre Science*, 16(3): 391–397.

Bulleit, W. M., Sandberg, L. B. & Woods, G. J. 1989. Steel-reinforced laminated timber. *Journal of Structural Engineering*, 115(2): 433–444.

Davalos, J. F. & Barbero, E. J. 1991. Modeling of glass-fiber reinforced glulam beams. *In Proceedings of the*

International Timber Engineering Conference, September 2–5, 1991. London, England. Timber Research and Development Association, High Wycombe, United Kingdom, 1991, Vol 3, pp. 3.234–3.241.

Favre, P. A. & Tingley, D. A. 2001. Compression Based Design of FRP Reinforced Glulam Beams. *Proceedings of the International Conference on FRP Composites in Civil Engineering, December 2001 Hong Kong*, Vol II, pp. 1379–1396.

Gardner, G. P. 1991. A reinforced glued laminated timber system. *In Proceedings of the International Timber Engineering Conference, September 2–5, 1991. London England*. Timber Research and Development Association, High Wycombe, United Kingdom, Vol 3, pp. 3.218–3.225.

Gardner, G. P. 1994. Reinforced glued laminated timber system – epoxy/steel/timber composite material. *In Proceedings of the Pacific Timber Engineering Conference, Gold Coast Australia, July 11–15, 1994.* Timber Research and Development Advisory Council, Queensland, Australia, Vol 1, pp. 548–557.

Gentile, C., Svecova, D. & Rizkalla, S. 2002. Timber Beams Strengthened with GFRP Bars: Development and Applications. *Journal of Composites for Construction*, 6(1): 11–20.

Gilfillan, J. R. 1978. A new prestressing concept applied to a 72 feet span timber box beam. *Thesis (Ph.D.) The Queen's University of Belfast.*

Gilfillan, J. R., Gilbert, S. G. & Patrick, G. 2001. The use of FRP composites to enhance the structural performance of timber beams. *Proceedings of the International Conference on FRP Composites in Civil Engineering, December 2001, Hong Kong*, Vol II, pp. 1371–1378.

Gilfillan, J. R., Gilbert, S. G. & Patrick, G. 2002. The improved performance of home-grown timber glulam beams using fibre reinforcement. *Journal of the Institute of Wood Science (IWSc)* Vol 15 No. 6 Issue 90.

Kim, Y., Davalos, J. F. & Barbero, E. J. 1997. Delamination buckling of FRP layer in laminated wood beams. *Composite Structures*, 37(3/4): 311–320.

Plevris, N. & Triantafillou, T. C. 1992. FRP-reinforced wood as structural material. *Journal of materials in Civil Engineering*, 4(3): 300–317.

Landis, E. N. & Dagher, H. G. 1997. NDE and Performance Monitoring of FRP-Wood Hybrid Structures. *Structures Congress Proceedings*, 2: 1504–1507.

Lantos, G. 1964. Test results on mild steel reinforced glulam beams. *Civil Engineering* London.

Lindyberg, R. F. & Dagher, P. E. 2000. Probabilistic Nonlinear Model for Reinforced Glulam Beams. *World Timber Engineering Conference Whistler, Canada*.

Ogawa, H. 2000. Architectural application of carbon fibres Development of new carbon fibre reinforced glulam. *Carbon*, 38: 211–226.

Patrick, G. R. H. 2004. The structural performance of FRP reinforced glue laminated beams made from homegrown Sitka spruce. *Thesis (Ph.D.) Queen's University Belfast.*

Plevris, N. & Triantafillou, T. C. 1992. FRP-reinforced wood as structural material. *Journal of materials in Civil Engineering*, 4(3): 300–317.

Rowlands, R. E., Van Deweghe, R. P., Laufenberg, T. L. & Krueger, G. P. 1986. Fibre-reinforced wood composites. *Wood and Fibre Science*, 18(1): 39–57.

Tasbeam. 2002. *http://www.tasbeam.com.au/prod_des.htm*

Theakston, F. H. 1965. A Feasibility Study for Strengthening Timber Beams with Fibreglass. *Canadian Agricultural Engineering.*

Timber Research & Development Association, 2002. New Age Flitch. *http://www.trada.co.uk/frames_timber.asp*

Tingley, D. A. & Leichti, R. 1994. Glued-laminated Timber Beams having a High Strength Fibre Reinforcement: The Bimaterial Interface. *Proceedings of the Pacific Timber Engineering Conference, Gold Coast Australia, July 11–15.* Timber Research and Development Advisory Council, Queensland, Australia.

Tingley, D. A. 1996. The stress–strain relationships in wood and fibre-reinforced plastic laminae of reinforced glued laminated wood beams. *Thesis, Oregon State University*.

Van de Kuilen, J. W. G. 1991. Theoretical and experimental research on glass fibre reinforced laminated timber beams. *In Proceedings of the International Timber Engineering Conference, September 2–5, 1991. London, England*. Timber Research and Development Association, High Wycombe, United Kingdom, Vol 3, pp. 3.226–3.233.

Strengthening of steel structures

FRP Composites in Civil Engineering – CICE 2004 – Seracino (ed)
© 2005 Taylor & Francis Group, London, ISBN 90 5809 638 6

Evaluation and construction of composite strengthening systems for the Sauvie Island Bridge

Ayman S. Mosallam
University of California at Irvine, California, USA

ABSTRACT: This paper presents the results of a multi-phase project aiming at developing fiber-reinforced-polymer (*FRP*) composite systems for structural upgrade of the flexural capacity of steel girders. This study is divided into three phases; namely i) large-scale verifications tests of two strengthening systems, ii) field application of the composite systems on some girders of the Sauvie Island Bridge (*Portland, Oregon, USA*), and iii) long-term monitoring of the performance strengthening system using either strain gages and/or fiber optical system with either wire or wireless data collection system. The two composite systems that were evaluated in this program are i) precured carbon/epoxy (*CFRP*) strips, and ii) the innovative composite sandwich system (*H-Lam*©). This paper describes the results of first two phases of the study that includes large-scale verification tests and description the field application of the composite systems.

1 INTRODUCTION

Despite its great potential, limited information is available on bonded FRP composite-to-steel. The proposed project aims at investigating the feasibility of using a combination of polymer composites, high-strength adhesives as strengthening system for upgrading the structural performance of bridge steel members.

In addition to the benefit of upgrading the structural capacity of steel members, results of a prior FHWA research study sponsored by the Federal Highway Administration (FHWA) indicated that attaching a cover plate to the tension flange of a steel girder with longitudinal welds along the central region, and with friction-type high-strength bolted connections at the non-welded ends, could increase the fatigue life by a factor of 21 over that of conventionally end-welded cover plate (Albrecht et al. (1984)). Accordingly, end-bolted cover plates have Category B fatigue strength, whereas end-welded cover plates have Category E strength. The large increase in life is possible due to the fact that friction-type bolted connections transfer forces from one plate to another with lesser stress concentration compared to rigid welded connections. Based on this observation, one would expect an increase in the fatigue strength of structural bridge member when adhesives are added to assist in distributing and transferring the load over a larger area, thus reducing the stress concentration.

The use of adhesives provides attractive features for strengthening existing under-rated bridge steel members.

This includes the ease of applications, minimizing heavy equipment, minimizing or eliminating the need for making holes or using bolts. As a result, this approach can provide the structural engineers with quick and low cost fix for different members such as bridge steel girders and columns.

2 RELATED RESEARCH WORK

A pioneering research project on the use of composites and high-strength adhesives in seismic repair and rehabilitation of welded steel moment frame connections was initiated by Mosallam et al. (1999). The fullscale test results indicated that the used of bonded carbon/epoxy stiffeners resulted in an increase of more than 25% of the undamaged welded steel connection strength. In addition, the ductility of the repaired connections was enhanced with a plastic rotation capacity of more than 0.025 rad. One of the first investigations on the use of carbon/epoxy strips in strengthened steel girders was reported by Sen and Liby (1994). A case study on the use of composites in upgrading the structural capacity of steel girders was reported by Garden, and Shahidi (2002). In this case study, the steel girders were heavily corroded and were repaired, after cleaning and geometrical restoration, by composites that were applied using vacuum bagging method. Whether this repair was appropriate given the advanced corrosion stage of the repaired, is still questionable.

The majority of the research work and field applications for cast iron members' rehabilitation were performed in Europe and with the majority in England. For example, Silvia and Church (2002) reported a case study on the use of carbon/epoxy composites for structural upgrade of three cast iron bridges in England. Tavakkolizadeh and Saadatmanesh (2003) presented the results of a study on repairing steel girders using precured carbon/epoxy strips. In this study, a total of three large-scale composite (*steel/concrete*) girders were repaired using different composite strengthening ratios with different degrees of simulated damages were evaluated. A similar study was conducted by Photiou et al. (2004) on artificially degraded steel box beams using prepreg carbon/glass U-shaped laminates. The test results showed a significant increase in the strength and stiffness of the repaired beams. The use of prestressed composite patches for repair of cracked steel members was analyzed by Colombi et al. (2003). Progress in the technique of upgrading metallic structures with advanced polymer composites was reported by Hollaway and Cadei (2002).

3 COMPOSITE STRENGTHENING SYSTEMS

A total of five (5) tests were conducted on three (3) half-scale wide flange steel beams (*W8 × 35A36*). The control specimen was tested up to failure with no initial cyclic loadings. However, for each of the strengthened beams, initial cycling tests were performed followed by quasi-static tests up to failure.

3.1 *CFRP strips*

The precured CFRP strips were made of unidirectional carbon/epoxy. The adhesive used to bond these strips was a two-part ambient temperature epoxy system that is originally designed to bond composites to concrete surfaces. Per the supplier data, the mixing ratio of this epoxy is 100 parts of component A to 30 parts of component B by volume (or 100 parts of component A to 25 parts of component B by weight). The carbon/epoxy strips used in this evaluation were 101.6 mm (4″) × 1.9 mm (0.075″) [*width* × *thickness*]. The mechanical properties of the precured CFRP strips provided by the supplier are shown in Table (1). It should be mentioned that during construction, a glass mat was added to one surface of the strips for galvanic corrosion protection (refer to Figure (1)).

3.2 *H-LAM© panels**

The reinforcing honeycomb polymer composite panels consist of high strength composite facing sheets bonded to a lightweight high-density/high-strength core material. The H-Lam© panels were designed such that they are both thermally and mechanically balanced. The face sheets of the composite sandwich panels are comprised of 0°/90° carbon/epoxy laminates with E-glass/epoxy thin laminates at the interface with the steel girder and the aluminum honeycomb core. The reason for using 90° cross laminates is for stability of the unidirectional laminates during both the fabrication and during service.

As mentioned earlier, the H-Lam© used in this study also has an E-glass/epoxy cover layers to protect the carbon-based composite panel from galvanic corrosion (*the galvanic corrosion occurs upon direct contact of the carbon/epoxy to steel in the presence of moisture, which in this application is unavoidable*). In addition, the H-Lam© panels have an E-glass peel-ply to protect the pretreated face sheet to be bonded to the steel bottom girder (*refer to Figure* (2)). This functions of the added peel-plies are: i) to ensure a high quality shop surface preparation of the composite face, ii) to protect the composite panels from damages and

Table 1. Mechanical properties of the CFRP strips.

Property	Typical test value
σ_{11}	2.79 GPa [405,000 psi]
E_{11}	155.1 GPa [22.5 × 10^6 psi]
ε_{11}	1.8%
σ_{22}	Zero

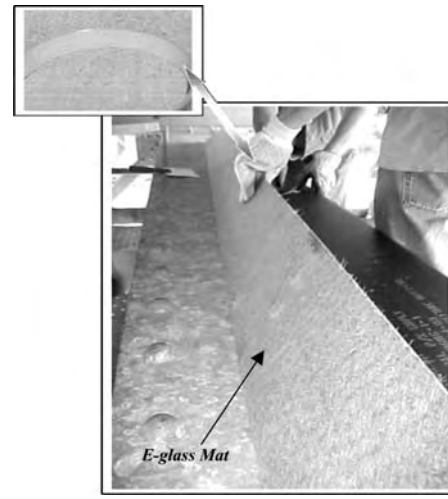

Figure 1. SCCI carbon/epoxy strips with E-glass chopped Fibers Mat.

*US Patent Pending # 60-146,830.

surface contamination while handling and shipping and iii) to minimize the field surface treatment.

Unlike the general-purpose epoxy used for the off the-shelf CFRP strips system, which was originally developed for concrete and masonry, the H-Lam© adhesive system was engineered specifically for steel strengthening application. In designing the adhesive system, several criteria were considered including: i) the surface preparation and treatment requirements (ease of field application), ii) viscosity (workability), iii) temperature variation, and long-term durability requirements including wet environment, iv) toughness and strain compatibility with steel and composites, v) fatigue resistance and vi) strength and stiffness requirements. Instead of the general-purpose epoxy adhesives used for bonding the CFRP strips, a methacrylate adhesive system was engineered and used for bonding the H-Lam© panels. Properties of the H-Lam© adhesive system are presented in Table 2 and Figure (3).

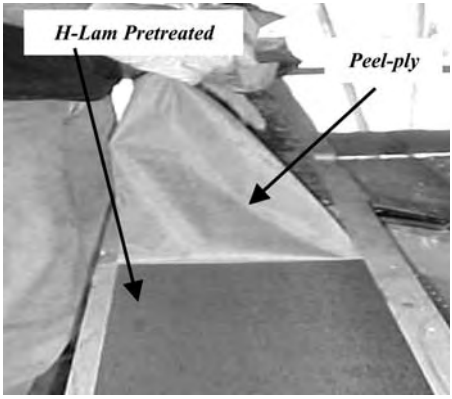

Figure 2. The H-Lam© Peel-ply.

Table 2. Mechanical properties of H-Lam© adhesives.

Tensile strength (psi)	Tensile modulus (psi)	Tensile elongation (%)	Lop shear strength* (psi)
3,500–3,800	75,000–100,000	0.9–1.1	2,200–2,700

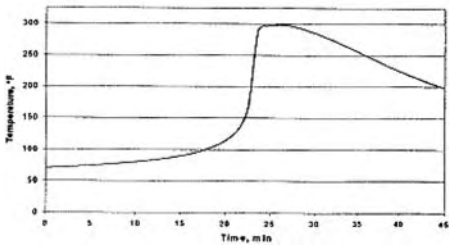

Figure 3. Typical exotherm curve for H-Lam© adhesive at 24°C (75°F).

4 DESCRIPTION OF THE EXPERIMENTAL VERIFICATION PROGRAM

Figures (4) and (5) show the test setup details used for evaluating all the beam specimens under both cyclic and quasi-static loads. As shown in these figures, the load was applied in a four-point load configuration. Both deflection and strain measurements were collected continuously during each test.

The load was applied using a 445-kN (100-kip) MTS which was connected to a 445-kN (100-kip) load cell with ±76.2 mm (3″) stroke. The hydraulic actuator total load was applied in the form of two concentrated loads via a transfer steel beam. The two concentrated loads were positioned at equal distance

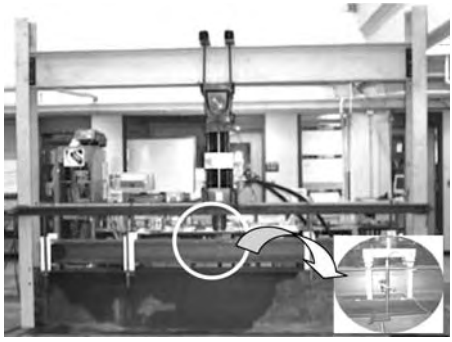

Figure 4. Typical test setup and stiffeners details.

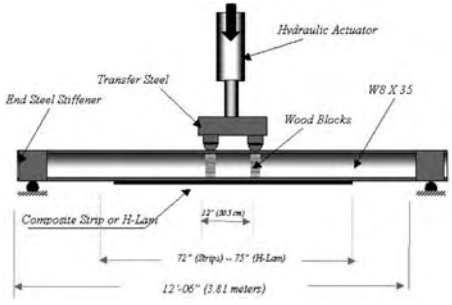

Figure 5. Dimensions and typical test setup.

from the beam centerline of 30.5 cm (12″). The original experiment design called for welded steel stiffeners under the applied loads to minimize the stress concentration at these locations and to avoid premature web buckling. However, it was decided to use wooden blocks instead which were snugly fitted to support the flanges and minimize the stress concentration effects (*refer to Figure* (5)).

All data was monitored and recorded using data acquisition software, which also provided real-time monitoring of data during testing. The deflection data was captured using a ±25.4 mm (1″) Linear Variable Differential Transducer (LVDT). Strains were measured using several electronic strain gages bonded to both the steel and the composites at different locations (*refer to Figure* (6)). Load/deflection (P/δ) and Load/strain (P/ε) curves were developed for each specimen and both localized and ultimate failure modes were recorded and then analyzed.

4.1 *Loading regime*

Cyclic Loading: The cyclic loading test was performed only on the two beam specimens strengthened with polymeric composites (*i.e., Strips and H-Lam*©). The purpose of the cyclic tests was to evaluate the strength of the adhesive bond line when subjected to repeated loading cycles. The average value of the cyclic load was 70 kN (15.75 kips) which was applied to the strengthened beam specimens. The mid-span deflection corresponding to the cyclic load was 6.35 mm or 0.25″ (L/600). The frequency used in all cyclic tests was 1.43 Hz to simulate traffic load over time. It was estimated that 547,500 cycles simulate 5 years of bridge traffic. The cyclic tests duration of the CFRP strips was 122 hours, while the duration for the HLam© test was 166 hours. The second test was longer because it was run continues over the Thanksgiving Holiday rather than having someone come in to stop the testing.

Quasi-Static Ramp Loading: This type of test was conducted for all three steel beam specimens evaluated in this program. These tests were conducted on the same strengthened beam specimens that were used in the cyclic test. The quasi-static loads were applied in a form of a ramp until failure. However, the loading was halted several times for a few minutes to perform inspections. The definition of failure load used in this study is the point at which the beam could no longer resist any additional load.

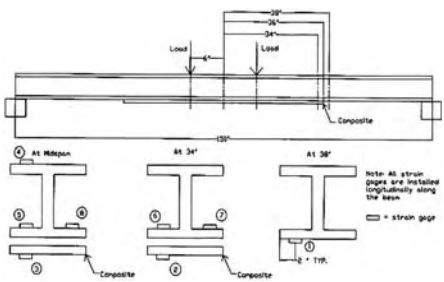

Figure 6. Locations of deflection and strain gages.

5 CYCLIC BEHAVIOR OF STRENGTHENED BEAMS

5.1 *CFRP strengthened beam*

This beam specimen was identical to the control specimen in both dimensions and mechanical properties, except that two 101.6 mm (4″) CFRP strips were bonded to middle 1.83 m (72″) of the beam bottom flange using epoxy adhesives described *earlier*. Prior to the application of the CFRP strips and the *bottom flange was* sand blasted and cleaned.

As mentioned earlier, the average value of the cyclic load was 70 kN (15.75 kips). The average mid-span deflection corresponding to the cyclic load was 6 mm or 0.234″ (L/641). The frequency used in all cyclic tests was 1.43 Hz to simulate traffic load over time. The cyclic duration of this test was 122 hours (5.083 days) with a total number of cycles of 628,000.

The strain versus time for this specimen is shown in Figure (7). As shown in this figure, the starting value of the mid-span CFRP tensile strain was 297.85 μ-strain and the maximum value was 314 m-strain that occurred after sixty-one (61) hours of cyclic loading. The minimum value of the CFRP tensile strain measured at the mid-span location was 295.4 μ-strain. In general, there was no significant drop in the strain that

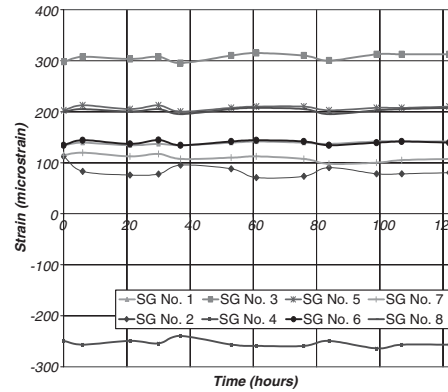

Figure 7. CFRP strengthened beam strains vs. time curves.

would imply local or global debonding at the mid-span location where shear stresses are zero. However, towards the ends of the CFRP strips strain values were unstable. This unstable behavior may be attributed to the inherent brittleness and the lack of toughness of the Tyfo™ epoxy adhesives used in bonding the CFRP strips to the steel bottom flange indicating the development of microcracks at the bondline. Figure (8) shows the percentage of tensile strain variation near the ends of the CFRP strips [*@ 0.87 m (34″) from the Centerline.*]

5.2 *H-Lam© strengthened beam*

The test setup for this specimen was identical to the CFRP strips strengthened beam specimen described earlier.

The duration of this test was 36% longer than the duration of the CFRP strips strengthened beam specimen (*166 hrs vs. 122 hrs*). The total number of cycles for this test was 855,000. The average value of the cyclic load was 694.4 kN (15.50 kips). The average mid-span deflection corresponding to the cyclic load was 6.4 mm or ¼″(*L/600*). The same frequency of 1.43 Hz was used to simulate traffic load over time.

The strain versus time for this specimen is shown in Figure (9). It should be noted that the H-Lam© tensile strains mid-span and at 34″ from the centerline are captured by strain gage #3 and gage #4, respectively. As shown in Figure (9), there were no significant drops in the strain values (that would imply local or global debonding) at the mid-span location where shear stresses are zero or at the H-Lam© ends where shear stresses are maximum.

As compared to the behavior of the CFRP strips strengthened specimen, one can see that the H-Lam© strengthened strain vs. time behavior is very stable indicating the complete bond between the H-Lam© and the steel bottom flange and the enhanced toughness characteristics of the methacrylate adhesives used in bonding the composites to the steel.

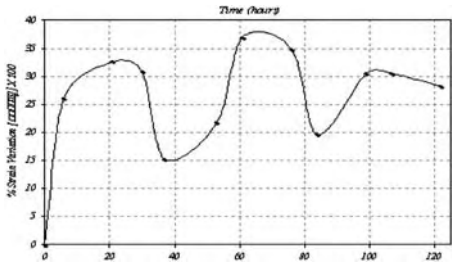

Figure 8. Percentage of tensile strain variation near the ends of the tyfo™ CFRP strips [*@ 0.87 m (34″) from the centerline*].

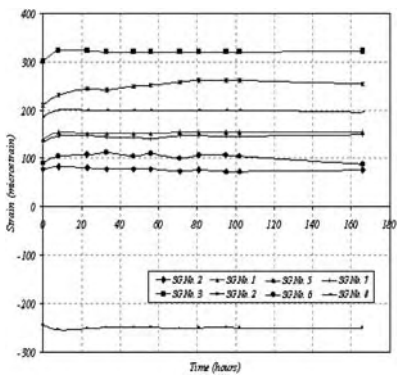

Figure 9. H-Lam© strengthened beam strains vs. time curves.

6 QUASI-STATIC AND ULTIMATE BEHAVIOR FRP STRENGTHENED BEAMS

6.1 *CFRP strengthened beam*

Following the cyclic test, the CFRP strips strengthened specimen was visually inspected and then subjected to quasi-static failure test. The ultimate failure test setup is identical to the cyclic test setup.

As shown in Figure (10), the behavior of this specimen was linear up to a load level of 370 MPa or 53.66 ksi (*proportional limit stress*), after which the behavior exhibited non-linearity up to the ultimate failure of the specimen. The net ultimate load of the strengthened specimen was 269 kN (*60.45 kips*) with a corresponding mid-span deflection of 41 mm or 1.62″ (*L*/92.5). It should be noted that deflection readings were limited by the available clearance between the bottom of the specimen and the testing frame ground girder. The failure was a combination of local buckling

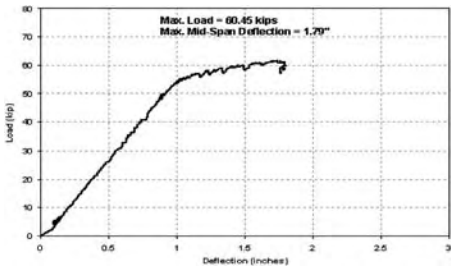

Figure 10. Experimental load-deflection curve of CFRP strips strengthened beam specimen.

of the top flange and an overall lateral buckling of the beam.

6.2 *H-Lam© strengthened beam*

Following the cyclic test, the H-Lam© strengthened specimen was visually inspected and was subjected to quasi-static failure test. The ultimate failure test setup is identical to the cyclic test setup (*refer to* Figure (4))

As shown in Figure (11), the behavior of this specimen was linear up to a load level of 367 MPa or 53.46 ksi (*proportional limit stress*), after which the behavior exhibited non-linearity up to the ultimate failure of the specimen. The net ultimate load of the strengthened specimen was 297 kN (66.79 kips) with a corresponding mid-span deflection of 68 mm or 2.71″ (L/55.4). No failure was observed in the bondline or the H-Lam©. Again, and due to the fact that the compression is not supported, the failure was a combination of local buckling of the top flange leading to an overall lateral torsional buckling of the beam (*refer to Figure* (11)).

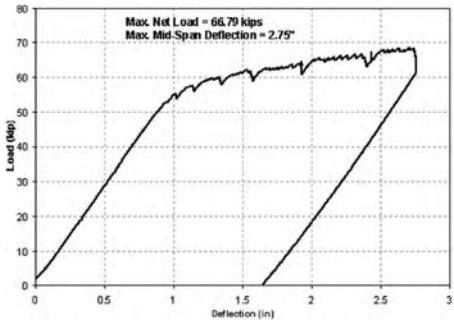

Figure 11. Experimental load–deflection curve of H-Lam© strengthened beam specimen.

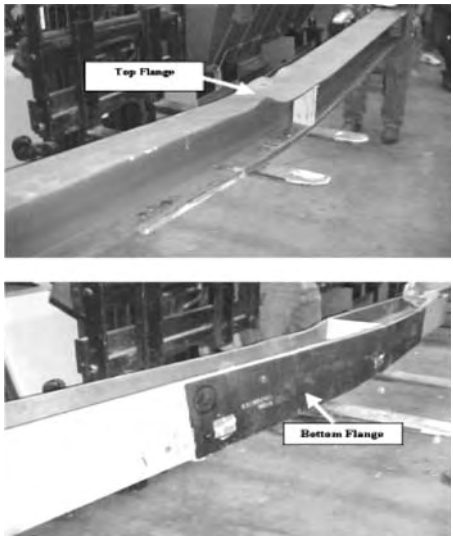

Figure 12. Ultimate failure of the H-Lam© strengthened beam specimen.

The maximum-recorded steel strains at the bottom flange locations (*Gage No. 5 and Gage No. 8*) were 3,322.8 μ-strain and 2,836.91 μ-strain, respectively. Again, the difference in the steel strain values is attributed to the development of lateral torsional buckling, as well as the unevenness of the applied load due to the large deformation at higher stresses. The maximum-recorded tensile strain at the bottom face laminate of the H-Lam© was 4,199.22 μ-strain at mid-span and only 359 μ-strain at a distance of 0.87 m (34″) from the beam's centerline.

Figure (13) shows the strain distribution along the depth of the H-Lam© strengthened beam specimens at two load levels. The first load level corresponds to an L/600 mid-span deflection of 6.35 mm (¼″) occurred at an applied load of 64.5 kN (14.5 kips).

The second strain distribution corresponds to the maximum load level applied to this specimen (*at a load of 304.7 kN or 68.5 kips*). As shown in this figure, at both low and high stress levels, the neutral axis (N.A.) shifted downwards to a distance of 13.2 mm (0.52″) relative to the beam centerline. This distribution also shows that there was an increase of 26% in the tensile strain level at the bottom laminate of the H-Lam© as compared to the tensile strain of the interior bottom flange face. This percentage could have been larger had shear connectors and concrete deck been used in combination with the adhesive which would reduces the percentage of the bypass strains that developed

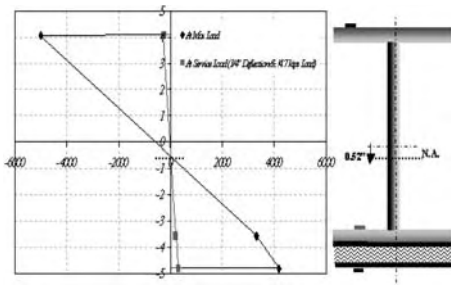

Figure 13. Mid-Span strain distributions along the H-Lam© strengthened beam depth at service and ultimate loading levels.

due to the shear deformation of the aluminum core. It should be noted that the linearized strain distribution at the maximum load is an approximation and is based on only three strain gage readings.

7 FIELD APPLICATION OF THE COMPOSITES SYSTEMS

Following the half-scale laboratory verification phase, the field application phase that included the application of the two verified systems was performed. The field application was performed on selected steel girders of a selected span of the Sauvie Island Bridge. The construction phase occurred in the summer of 2003.

All composite panels, adhesives and tools were transported to the site at the same day. The temperature was about 22°C (73°F) and increased towards the middle of the day to about 22°C (77°F). The field application took place during the weekend (*Sunday, June 29, 2003*) to ensure minimum traffic interruption. In addition, a restriction (*from 12 p.m. to 9 p.m.*) for all vehicles over 10 tons was posted in the bridge two weeks prior to the construction date (*refer to Figure* (14)). This was important to minimize the dynamic load that may affect the initial curing (*cross linking*) process of the adhesives. Temporary clamping steel/plywood fixtures were used for applying pressure to the composite panels during curing (*refer to Figure* (15)) and were removed after one day of application. The application was completed in 5 hours and the panels were instrumented with strain gages in different locations for the third ongoing health-monitoring phase. In addition to strain monitoring, several composite samples were adhered to steel using the same types of adhesives that were subjected to the same field environment. Frequent pull-off tests are being performed to monitor the long-term bondline strength at different environmental exposures.

Figure 14. Restriction of all vehicles over 10 tons was posted in the Sauvie Island Bridge one week prior the construction date.

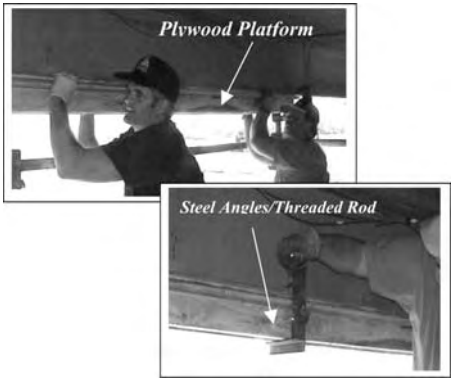

Figure 15. The temporary clamping system.

8 CONCLUSIONS

Cyclic and quasi-static test results obtained from half-scale steel beams indicated that the use of polymer composite is capable of enhancing the structural behavior of steel beams. However, one should note that these tests are a conservative modeling of the actual steel bridge girders for several reasons including the unsupported top flange configuration (no concrete deck) that was used in these tests described herein, while in the actual bridge, the top flanges are embedded in and supported by the bridge deck.

Despite the fact that no shear connector mechanism is provided between the actual top flange and the bridge deck, the major benefit of the deck is supporting the top flange and consequently preventing the occurrence of both local buckling of the top flange, and the lateral torsional buckling failures that were observed in all tests. Another issue is the high stress concentrations that were developed during the quasi-static tests due to four-point load configuration and the lack of sufficient supporting stiffeners under the point loads, except for the two unbonded wooden blocks described earlier in this report. The simply supported configuration contributed also in the occurrence of the lateral instability that does not exist in the Sauvie Island Bridge.

The cyclic results indicated the stability of the bond line of the H-Lam© strengthened beam at both zero and maximum shear stresses locations, while the CFRP strips may have shown instability, at end locations where shear stresses are maximum.

Ultimate test results indicated that the use of polymer composites increases the flexural capacity of the control beams. The net strength gain resulted from

using the H-Lam© was almost double of the strength of the beam strengthened with the CFRP strips (27.5% vs. 15.4% as compared to the ultimate capacity of the control steel beam). Although, test results indicated that the H-Lam© strengthened beam system resulted in an increase in toughness up to 45% as compared to the control specimen while the CFRP strips strengthened had 42% lower toughness as compared to the control specimen, this is not a final conclusion due to the fact that the CFRP strips strengthened beam test was stopped due to the clearance limitation between the bottom flange of the strengthened beam and the testing frame ground beam.

Based on the results obtained from both the quasi-static and cyclic loading tests, it is concluded that the use of composites succeeded in meeting the flexural demand. Accordingly, it is concluded that composites are found to be valuable and effective system to increase the capacity of the existing steel girders of the Sauvie Island Bridge.

A simplified analytical and design linear procedures, based on the transformed section methodology were developed and successfully predicted the linear portion of the behavior of the steel beam strengthened with H-Lam© composites.

The predicted strength of the steel beam strengthened with H-Lam© composites deviated only 6% from the experimental value. The predicted location of the neutral axis was 10.41 mm (0.41″) below the centroidal axis of the as-built beams while the actual experimental location was 13.2 mm (0.52″) with 26% deviation. The deviation is attributed to the fact that the analysis was performed for the elastic range while the experimental value included the nonlinear range resulting in additional downward movement of the neutral axis due to the local buckling of the top flange of the strengthened beam as witnessed in the laboratory test.

In order to capture the performance of the hybrid steel/composite beam during the nonlinear range (*post-buckling behavior*) both finite element analysis and progressive failure (PFA) simulation are required. For this reason, models for the control (*unstrengthened steel beam*) and the steel beam strengthened with H-Lam© composites were generated and both linear and non-linear finite element analysis were conducted using NASTRAN finite element code (*refer to Figure*(16)). The progressive failure analysis is being performed by the state-of-the-art virtual reality code GENOA developed jointly by NASA and Alpha Star Corporation. It is intended to extend the scope of the PFA analysis to cover durability and other service conditions for the actual applications and the final resulted will be reported after the demonstration application on the actual bridge.

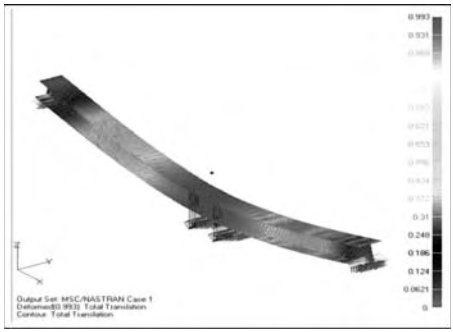

Figure 16. Displacement plot of the H-Lam© strengthened beam NASTRAN model.

ACKNOWLEDGEMENTS

This study was funded by the US Federal Highway Administration (FHWA) IBRC TEA-21 program. The contributions Mr. Ken Huntley of the Multnomah County Bridge Division in both the testing and the construction phases are highly appreciated. The author would like to acknowledge the contributions of Professor W. H. Mueller and both graduate and undergraduate students at the Portland State University where the experimental verification program was conducted. The in-kind support of Structural Construction Composites Incorporated (*SCCI*), ITW Plexus™ for donating the CFRP composite materials and adhesives for the field application, and Fyfe Company for donating the CFRP and epoxy for the CFRP beam test are appreciated. The contribution of Alpha Star Corporation, Long Beach, California in assisting in developing the PFA analyses is acknowledged.

REFERENCES

Albrecht et al. 1984. *Application of Adhesive to Steel Bridges*, Final Report, *FHWA-RD-84-037, Federal Highway Administration,* Washington, D.C., 106–147.

Colombi et al. 2003. Analysis of Cracked Steel Members Reinforced by Pre-Stress Composite Patch, *Fatigue and Fracture of Engineering Materials and Structures*, 26, 59–66.

Garden, H. N. and E. G. Shahidi. 2002. Steel Building Rehabilitation Using Composites, Proceedings of *the Advanced Polymeric Composites for Structural Applications in Construction ACIC'02*, Southampton, UK, April.

Hollaway, L.C. and J. Cadei. 2002. Progress in the Technique of Upgrading Metallic Structures with Advanced Polymer Composites, *Progress in Structural Engineering and Materials*, Vol. 4, Issue 2, pp. 131–148.

Mosallam, A. S. 2000. Seismic Retrofitting of Steel Beam-to-Column Joints with Polymer Composites & Steel Stiffeners, Proceedings of the *Composites in the Transportation Industry*, 14–18 February, Sydney, Australia, 198–203.

Mosallam et al. 1999. Making the Connections, *Civil Engineering Magazine*, ASCE, 69 (4), 56–59.

Photiou, N. et al. 2004. Strengthening of An Artificially Degraded Steel Beam Utilising a Carbon/Glass Composite System, Proceedings, *ACIC'2004 Conference*, University of Surrey, UK, 274–283.

Sen, R. and L. Liby. 1994. *Repair of Steel Composite Bridge Sections Using Carbon Fiber Reinforced Plastic Laminates*, Final Report, FDOT-510616, *Florida Department of Transportation*, Tallahassee, Florida, USA.

Silvia, D. and D. Church. 2002. Applications of Fiber Carbon Composites at Covered Ways 12 & 58 and Bridge EL 31, Proceedings of the *Advanced Polymeric Composites for Structural Applications in Construction ACIC'02*, Southampton, UK, April.

Tavakkolizadeh, A.M. and H. Saadatmanesh. 2003. Repair of Damaged Steel-Concrete Composite Girders Using Carbon Fiber-Reinforced Polymer Sheets, J*ournal of Composites for Construction*, ASCE, 7 (4), 311–322.

FRP Composites in Civil Engineering – CICE 2004 – Seracino (ed)

Strengthening of historic cast iron girders with bonded CFRP plates

F.S. Rostásy
Technical University of Braunschweig, Germany

U. Neubauer
Civil Engineering Materials Testing Institute, Braunschweig, Germany

R. Nothnagel
Technical University of Braunschweig, Germany

ABSTRACT: The New Museum in Berlin – built in the middle of the 19th century – is presently being rehabilitated. Its slabs consist of historic cast iron girders with masonry vaults in between. The increase of service loads of future use, damage of girders due to war, etc. warrant the strengthening of girders. Because of preservational reasons, CFRP plate bonding was chosen for that. Report describes the various steps needed to verify that method, seldom applied yet for cast irons structures.

1 INTRODUCTION

The Museum Isle in the center of Berlin represents the cultural heart of the city. There, several museums of renown are assembled. Most of them were built in the 19th century, and all of them were severely damaged during the 2nd world war. In the focus of this paper is the New Museum which formerly housed the collection of ancient Egyptian art. The New Museum is presently being rehabilitated. In addition to the damage by war, the neglect over decades did its share to the desolate condition of the building. Figure 1 shows its present state.

A special feature of this building are its slabs. These consist of flat masonry vaults between historic cast iron girders (HG). For large spans, the girders rest on tied arches made of cast iron; for short spans, the girders lie directly on masonry walls. Figure 2 presents a view of the partly intact structure. The cross-section of the HG is very similar to the one of newly manufactured girders (NG) for test purposes, shown in Figure 5. The HG have to be strengthened because of the increase of service loads of future use, internal defects in historic cast iron and because of potential cracks in the tensile zone of girders caused by falling debris etc.

Authors were engaged to elaborate a concept for the strengthening of the historic cast iron girders by bonded CFRP plates. Reasons for this method were its efficiency and the unobtrusiveness of plates. The concept required the assessment of on-site status of girders, comprehensive tests, rules for design, execution, and for the quality control of works.

Figure 1. The New Museum at present.

Figure 2. View of undamaged cast iron structure.

2 EXPERIMENTS

2.1 *Material values of cast iron*

Prior to test work, the girders were thoroughly investigated. Preservational reasons precluded the extraction of historic cast iron girders for tests. However, remnants could be salvaged for materials testing.

Cast iron from 1850 exhibits – with a carbon content of 3.4% – a lamellar graphite structure. When subjected to high tensile stress, it may fail in brittle manner and under a low failure strain. Its stress–strain lines in compression and tension are markedly non-linear. Scatter of mechanical properties is significant. The following values were measured for the HG:

$R_m = 124$ MPa — mean axial tensile strength
$V_R = 6.8\%$ — coefficient of variation
ε_u = min. 3.0 to max. $6.0 \cdot 10^{-3}$ [–] — ultimate strain

For comparison and the analysis of test results, the values for new cast iron NG (material GG 20 acc. to DIN 1691) also had to be established:

$R_m = 201$ MPa — mean axial tensile strength
$\varepsilon_u = 6.0$ to $7.5 \cdot 10^{-3}$ [–] ultimate strain

The progress in cast iron technology is obvious. Stress sensitivity was significantly mitigated over the past 150 years. Figure 12 shows examples of stress–strain lines in axial tension for HG and NG.

It must be pointed out, that the cylindrical test specimens for NG were machined from the bulk of seperate cast iron rods. Whether these specimens represent the texture and mechanical properties of cast iron near the bottom or top of girders could not be verified.

2.2 *Material values of CFRP plates*

CFRP plates – produced by Sika – with the breadth $b_p = 50$ mm were used. Two types of plate were investigated: CarboDurS (standard modulus fibers) with the thickness of $t_p = 1.2$ mm and CarboDur H (high modulus fibers) with $t_p = 1.4$ mm. The mean material values in axial tension are:

CarboDur S – nominal values
$f_c = 2800$ MPa — axial tensile strength
$E_c = 170$ GPa — elastic modulus
$\varepsilon_u = 16 \cdot 10^{-3}$ [–] failure strain

CarboDur H – based on test results
$f_c = 1890$ MPa — axial tensile strength
$E_c = 276$ GPa — elastic modulus
$\varepsilon_u = 6.9 \cdot 10^{-3}$ [–] ultimate strain

For bonding, the epoxy resin Sikadur 30 was selected.

2.3 *Bond strength tests*

The test specimen consists of 2 cast iron plates with the dimensions length/breadth/thickness 400/100/20 mm (double lap type). These plates were prepared by sandblasting and joined on either side by CFRP strips with the dimensions $2l_b/50\,\text{mm}/t_p$ The bond length l_b was varied: 50, 100 and 200 mm. S- and H-CFRP type plates were investigated. Specimens were instrumented with several electrical strain gages on both sides and along bond-length.

Specimens were tested in axial tension to failure. With these bond-lengths, 3 tests with each plate type were performed. Specimens failed in brittle manner where S-type plates exhibited failure in the adhesive close to the interface glue/CFRP. The H-types however failed by interlaminar CFRP-failure. Figure 3 shows the specimen with the H-type plate and bond-length of 200 mm after failure.

Within the investigated range, the bond failure forces were not significantly influenced by the bond length. This fact indicates that the maximum bond force is already associated with the bond transfer length of about 50 mm. The stiffness of plate exerted a significant influence. The mean bond failure force of joints with the high modulus H-type plates were $F_{u,m} = 48$ kN for all bond lengths and thus considerably higher than with the low-modulus S-type of $F_{u,m} = 30.9$ kN. The ratio of mean failure forces is about 1.56 which is in between the ratio of plate stiffnesses 1.9 and the square root thereof.

2.4 *Bending tests*

In the structure, the HG are single span beams with a span of up to 5.90 m. The extraction of girders from structure was rejected. In view of this fact, the assessment of bending strength of HG with and without CFRP plates based on calculations alone seemed to be too risky.

It was therefore decided to perform bending tests on un-strengthened and strengthened newly manufactured girders (NG), with and without artificial sharp notches in the tensile zone of girder. The existence of internal defects and cracks in the HG cannot be

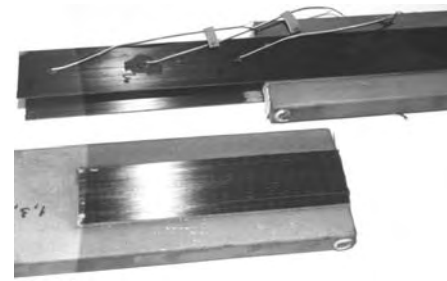

Figure 3. Specimen for bond testing after failure.

precluded. On basis of the tests, the relative gain in bending strength due to CFRP will be introduced into the strengthening concept.

Figure 4 shows the system and dimensions of specimen, Figure 5 the cross-section and Figure 6 the test set-up. The span was 1.40 m. The CFRP plates were bonded to both sides of girder and on entire free length. Instability of compression chord was obviated. In all, 13 beams were tested.

In Table 1 the main variables and results are listed. Specimens were either un-notched or artificially pre-notched. For the notched specimens, 2 notches of a depth of 4 mm and a breadth of 1 mm were cut into tensile zone. One notch was located in one of the force axes, the other one in the zone between forces. CFRP plates of S- and H-type were investigated. Besides the forces and vertical deformations, the longitudinal strains of girder and plates were measured with electrical strain gages in 6 elevations from bottom of girder, partly 2 gages in opposite in certain elevations.

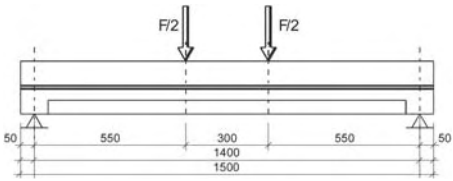

Figure 4. System and dimensions of specimen.

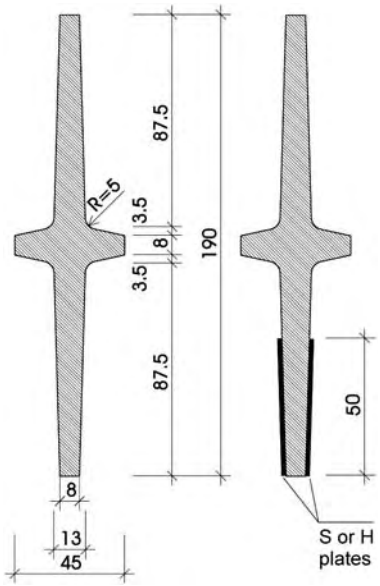

Figure 5. Cross-section of girder and CFRP plates.

3 MAIN RESULTS OF BENDING TESTS

3.1 *Modes and locations of failure*

A brief discussion of results is presented. All specimens failed suddenly in tension starting at the bottom of girder in the cast iron. This was caused and was immediately followed by a combination of rupture and bond failure of the CFRP plates.

Un-notched specimens failed within the zone M = const., notched specimen also failed within that zone, though always at one of the notches. In Figure 7, specimen No. 12 after failure is depicted. In Table 1 the failure loads meas F_u and the tensile failure strains meas ε_u 5 mm above bottom of girder are listed.

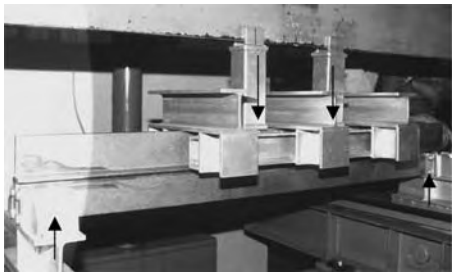

Figure 6. Set-up of four points bending test.

Table 1. Variables and main results of bending tests.

No.	CFRP type	Notch	Meas F_u [kN]	Meas ε_u [10^{-3}]
1	–	No	89.7	–
2	–	No	96.6	7
3	–	No	89.1	6.5
Mean	–	–	91.8	–
4	–	Yes	48.8	2
5	–	Yes	52.8	2
10	–	Yes	47.4	3
Mean	–	–	49.7	–
6	S	No	111.8	5
7	S	Yes	89.1	6
8	H	No	156.5	8
13	H	No	147.4	6.5
Mean	–	–	152.0	–
9	H	Yes	118.4	5
11	H	Yes	114.1	5
12	H	Yes	118.6	5
Mean	–	–	117.0	–

Figure 7. Girder No. 12 after failure, CFRP removed.

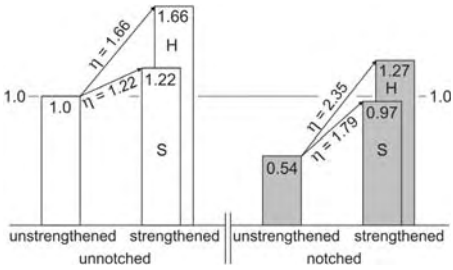

Figure 8. Normalized mean bending capacities and strengthening ratios of test girders.

3.2 *Influences on bending strength*

The notch reduced the bending strength of unstrengthened girders by 46%, meanwhile the reduction of the section modulus being only 3.5%.

The bending strength of both, un-notched and notched girders was noticeably increased by CFRP-plates, the stiffness of the latter being influential. The increase in bending strength by the CFRP plates can be expressed by the strengthening ratio η (meas-F_{uCFRP}/measF_u). In Figure 8 the observed bending capacities, normalized to the un-notched and unstrenghtened girder (1,0) and the strengthening ratios are shown. For un-notched beams this ratio with H-plates amounts to ≈1.66 and with S-plates ≈1.22. For notched beams the respective ratios are 2.35 and 1.79.

3.3 *Strains*

The strain measurements prove that specimens strictly deform in the vertical plane. The longitudinal strains in the zone M = const. are linearly distributed over the height of girder. Immediately prior failure, a certain plasticity of bottom strain can be observed. Figure 9

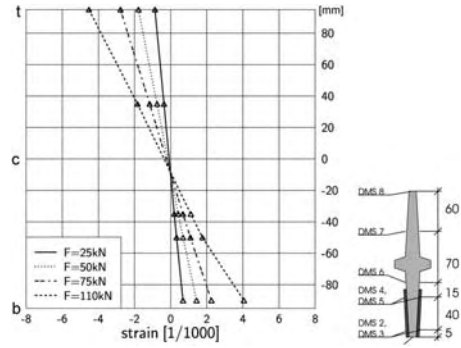

Figure 9. Strains dependent on force and location of strain gage DMS for girder No. 12.

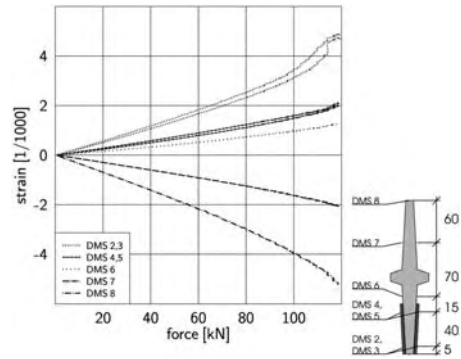

Figure 10. Strains dependent on distance above bottom of girder and on force for girder No. 12.

shows the strains in the zone M = const. for girder No. 12 dependent on force and distance from bottom of specimen (with DMS the strain gages are denoted). In Figure 10 the distribution of strains over the height of girder and dependent on force is depicted.

3.4 *Conclusions from experiments*

The fact, mentioned in 3.2, that in unstrengthened girders actual strength reduction by notching far exeeds the arithmetical reduction of the section modulus, illustrates the dramatic influence of the notch effect.

It is evident, that the strengthening effect in notched beams is significantly more pronounced, i.e. the strengthening ratio η is greater by the factor 1,42 and 1,47 resp., than in un-notched beams. By CFRP-strengthening the capacity of notched beams could be

restored to the level of un-notched beams (97% with S-plates) or even well above that (127% with H-plates).

These facts are strong indications for a significant mitigation of the notch effect by CFRP in addition to the increased cross-section. The CFRP-plates, acting compositely with the cast iron obviously impedes crack propagation. In terms of fracture mechanics, the CFRP-plates, glued over a – visible or invisible – crack, reduce the stress intensity factor by reducing the relative portion of the crack-affected beam width.

4 MODEL OF BENDING STRENGTH

4.1 *On the state of art*

Strengthening with CFRP plates has evolved from strengthening of concrete. For this, mechanical models, especially for the bond between plate and beam have been developed, e.g. Neubauer (2000). Regarding the strengthening of steel and light metal structures with CFRP plates or fabrics, less literature sources exist e.g., Buyukozturk et al. (1998) report on the effect of CFRP patches to stop the growth of fatigue cracks in steel girders. The strength of historic cast iron structural members was dealt with by Frey & Kaepplein (1993).

Practical applications of cast iron strengthening with CFRP-plates are kown from UK, where girders have been temporarily secured in the London subway, Barnes (1997). Two historic cast iron bridges have been permanently strengthened with high-modulus CFRP-plates, Sika Ltd. (2001).

4.2 *Engineering of model*

The aim of modeling is the forecast of bending strength of strengthened historic girders with adequate reliability. Thereby, the existence of defects, cracks, etc. cannot be precluded. For various reasons already mentioned, the strengthening and testing of HG could not be realized. But, also the theoretical analysis of the problem seems insurmountable, as its solution would require a fracture mechanics approach. For that, however, the necessary pre-requisites are not available.

It was therefore decided, to forecast the bending strength of NG – strengthened with the more efficient H-plates – on basis of a classical engineering approach. With the model, the mean strength will be forecast which then can be compared with the test results. Provided the comparison is satisfactory, the bending strength of strengthened HG can be calculated on basis of the σ–ε lines of historic cast iron.

4.3 *Assumptions and pre-suppositions*

The tests prove that the strains are linearly distributed over the height of girder. The stress–strainlines of the

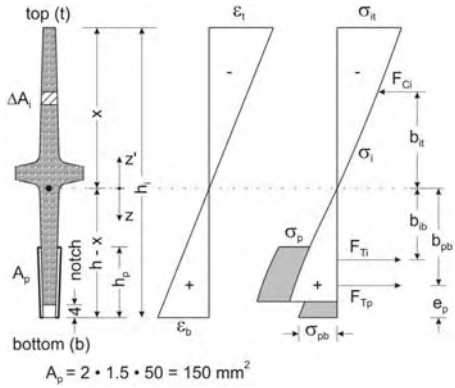

Figure 11. Geometry, notations, strains, stresses and internal forces of strengthened girder.

historic and new cast iron must be modeled on basis of tests. Between CFRP plate and girder, rigid bond is pre-supposed.

Furthermore, it is pre-supposed that the HG are-in the zone of max M not more severely notched (cracked) than the NG girder in the bending tests.

4.4 *Relationships of model*

Figure 11 shows the notations, dimensions, distributions of strains and stresses for the notched and strengthened girder. The neutral axis x can – for a chosen set of edge strains – be expressed by:

$$x = -h\frac{\varepsilon_t}{\varepsilon_b - \varepsilon_t} \tag{1}$$

As the bending strength is to be determined, for the bottom strain ε_b the ultimate strain ε_u or a limit strain lim ε_b of the cast iron can be inserted. With that, the internal forces are (i for cast iron; p for CFRP-plate):

$$F_T = F_{Tp} + F_{Ti} = 2t_p E_p \Sigma\varepsilon_p(z)\Delta z + \Sigma\sigma_i(z)\Delta A_i(z) \tag{2}$$

$$F_C = \Sigma\sigma_i(z')\Delta A_i(z') \tag{3}$$

Equilibrium is attained if: $F_T + F_C = 0$. The loss of cross-section caused by the notch is taken into consideration. For the determination of the inner lever arms, the distances of internal forces from the neutral axis must be known:

$$b_{it} = \frac{1}{F_{Ci}}\Sigma\sigma_i(z')z'\Delta A_i(z') \tag{4}$$

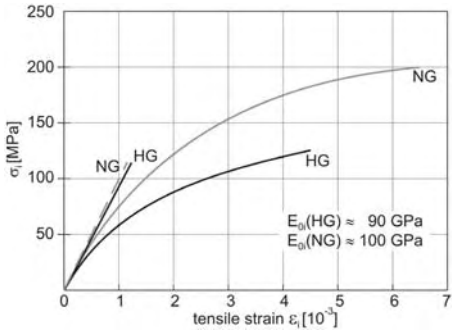

Figure 12. Stress–strainlines in axial tension for section analysis.

Table 2. Measured and calculated failure forces.

NG no.	Notched	Strengthened (H)	Meas F_{um}/ cal F_{um}
1–3	No	No	1.26
8, 13	No	Yes	1.04
9, 11, 12	Yes	Yes	1.04

$$b_{ib} = \frac{1}{F_{Ti}} \Sigma \sigma_i(z) z \, \Delta A_i(z) \tag{5}$$

$$b_{pb} = h - x - e_p \tag{6}$$

In Figure 12 the stress–strain lines in axial tension of HG and NG are depicted. The stress–strain lines in axial compression were assumed to be linear with the virtual secant modulus $E_v \approx 0.9E_{0i}$.

With Equations (1) to (6), the bending moment $M(\varepsilon_b)$ can be derived:

$$M(\varepsilon_b) = F_{Tp}(b_{pb} + b_{it}) + F_{Ti}(b_{ib} + b_{it}) \tag{7}$$

It can be compared with measured moments

$$meas\ M(\varepsilon_b) = meas\ F(\varepsilon_b)\ 0.55\ /2 \tag{8}$$

with 0.55 m lever arm of support force, Figure 4.

Equations (1) to (8) were evaluated with the stress–strain lines of NG shown by Figure 12, inserting the maximum bottom strain associated with the measured failure force.

4.5 *Comparison between measured and computed ultimate bending moments*

In Table 2, the ratios meas F_{um}/cal F_{um} are listed. For strengthening only the results with H-plates are evaluated.

For the strengthened girders, irrespective of notches, the model is confirmed by the test results. For the un-notched and un-strengthened girders, the model significantly underestimates the observed bending strength. It is believed, that the stress–strainlines of Figure 12 – derived from axial tensile tests – underestimate the actual tensile capacity of tensile zone of the girders. Strengthened girders though are much less affected by this shortcoming, because due to the composite action between the cast iron and the high-modulus CFRP-plates, the behaviour of the tensile zone is less dominated by the cast iron.

4.6 *Limit design of CFRP-strengthened historic cast iron girders*

It is pre-supposed that besides the geometrical data of HG, the mean stress–strain line in axial tension of cast iron including the scatter of ultimate strain and axial tensile strength can a priori be assessed (see section 2.1 and Figure 12).

The computation of characteristic bending moment cal M_{uk} must be based on the limit tensile strain ε_{uk} (5%-quantile value) of bottom fibre of HG. Frey & Kaepplein (1993) recommend – on basis of comprehensive experimental investigations – the value of $\lim \varepsilon_{uk} = 3.5 \cdot 10^{-3}$. At this value, the stress–strain line in tension, as for instance depicted in Figure 12, is cut-off. The calculation procedure of the characteristic moment follows section 4.4.

Although shear stress in the adhesive is unlikely to be relevant for design, it must be proved to be below the adhesive's shear strength, given by the manufacturer, e.g. 18.0 MPa. For girder No. 8, having withstood the highest load, an adhesive shear stress at bending failure of 3.35 MPa was calculated.

The admissible moment for service loads can be determined either with a global safety or with partial safety factors. This decision is within the realm of the responsible structural engineer.

5 QUALITY CONTROL OF ON-SITE WORK

The CFRP-plate strengthening technique – although well established for concrete members – is still quite novel for historic cast iron. Therefore, besides safe design, good workmanship together with a rigid quality control of execution is required. The quality control concept, elaborated by the Materials Testing Institute includes

- selection of the most suitable method of surface preparation from tests, carried out before work commences, with special regard to protection of adjoining historic stuccowork etc.
- assignment of works to an experienced contractor with proven record in CFRP-strengthening

- use of approved CFRP and adhesive
- continuous control of surface preparation by visual inspection and adhesion tests
- continuous control of ambient conditions, relevant for glueing, mainly temperature, humidity, dew point
- regular control of work during execution
- regular mechanical tests on adhesive specimen, taken on site
- intermediate and final visual inspection for levelness of plates, cleanness etc.

6 CONCLUSIONS

Historic cast iron girders can be strengthened with CFRP-plates, bonded to the tensile zone. Due to their greater efficiency high-modulus plates are to be preferred.

For the assessment of structural safety of historic cast iron girders in view of current and future loads and consequently for the diagnosis of strengthening demand, section analysis, assuming linear distribution of strains can be applied. The stress–strain line of the cast iron should – if at all possible – be gained from carefully extracted small specimens from non-critical locations. Bending capacity of e.g. girders is then governed by the ultimate tensile strain. Safety factors for unstrengthened historic cast iron must take the considerable scatter – especially of its tensile properties – due to internal notching effects, caused by lamellar graphite inclusions etc. into account.

Section analysis for strengthening design follows the above-mentioned classical engineering approach, assuming rigid bond between cast iron and CFRP. Material safety factors for strengthened cast iron can be less conservative than for unstrengthened, because composite action with stricly elastic CFRP impedes notch-triggered crack propagation in the cast iron and therefore mitigates uncertainties and scatter.

Quality control of strengthening works, especially careful surface preparation, i. e. cleaning and roughening to ensure unweakened adhesive bond is essential.

REFERENCES

Barnes, F. 1997. CFRPs for strengthening and repair. *Construction Repair* 11 (3): 41

Buyukozturk, O., Gunez, O., Martland, C. 1998. *Use of Fiber Reinforced Polymer (FRP) Composites in Repair and Strengthening of Steel Railway Bridges*. AAR Affiliated Lab, Paper 98-2, Center for Transportation Studies, Massachusetts Institute of Technology

Frey, A., Käpplein, R. 1993. Beitrag zum rechnerischen Nachweis der Tragfähigkeit alter Biegeträger aus Gußeisen. (Theoretical proof of load bearing capacity of historic cast iron girders. (in German)). *Stahlbau* 62 (8): 129–136

Neubauer, U. 2000. *Verbundtragverhalten geklebter Lamellen aus Kohlenstoffaser-Verbundwerkstoff (Bond Behaviour of Plates of Carbon Fiber Reinforced Plastics for the Strengthening of Concrete Structures (in German))*. PhD-thesis, Technical University Braunschweig

Sika Ltd. 2001. Carbon fibre solution. *The Structural Engineer* 79 (12): 36

FRP Composites in Civil Engineering – CICE 2004 – Seracino (ed)
© 2005 Taylor & Francis Group, London, ISBN 90 5809 638 6

Investigation into the bond between CFRP and steel tubes

S. Fawzia, X.L. Zhao & R. Al-Mahaidi
Department of Civil Engineering, Monash University, Clayton, Victoria, Australia

S.H. Rizkalla
North Carolina State University, Raleigh, North Carolina, USA

ABSTRACT: CFRP material has been widely used to strengthen concrete structures. There is an increasing trend of using CFRP in strengthening steel structures. The bond between steel and CFRP is a key issue. Relatively less work has been done on the bond between CFRP and a curved surface which is often found in tubular structures. This paper reports a study on the bond between CFRP and steel tubes. A series of tensile tests were conducted with different bond lengths and number of layers. The types of adhesive and specimen preparation methods varied in the testing program. High modulus CFRP was used. Tests were carried out to measure the modulus and tensile strength of CFRP. Strain gages were mounted on different layers of CFRP. The stress distributions across the layers of the CFRP were established. Models were developed to estimate the maximum load for a given CFRP arrangement.

1 INTRODUCTION

Carbon fiber reinforced polymer (CFRP) have been successfully used to strengthen structural elements made of concrete [Teng et al. 2000]. A limited amount of research has been conducted on the application of CFRP to steel structures [Moriarty & Barnes 1998, Tani et al. 2000, Moy 2001, Miller et al. 2001, Tavakkolizadeh & Saadatmanesh 2003a,b, Jiao & Zhao 2004]. Carbon fiber composites, that weigh approximately one-tenth of what steel does, can be adhesively bonded, and can have stiffnesses comparable to that of steel. Their high strength-to-weight ratio has played a significant role in creating interest in strengthening, repair and rehabilitation of metallic structures [Hollaway & Cadei 2002, Tumialan et al. 2002, Cederquist 1999]. In addition, their nonreactive and corrosion resistant properties mean that the materials can be used in areas where deterioration from environmental conditions pose a problem for traditional materials [Andres & Torres-Acosta 2002, Karbhari & Shulley 1995, Tavakkolizadeh & Saadatmanesh 2001, Bassetti et al. 2000]. Research has shown the potential of using CFRP overlays for prolonging the fatigue life of steel sections [Tavakkolizadeh & Saadatmanesh 2003b, Bassetti et al. 2000, Sean et al. 2003]. Some research has also been conducted for steel bridge [Miller et al. 2001, Liu et al. 2001], steel beams [Nikouka et al. 2002, Moy 2000], and steel concrete composite structures [Tavakkolizadeh & Saadatmanesh 2003b,c, Rajan et al. 2001]. It is important to note that life cycle costs associated with composite structures become attractive to owners because of the limited need for continual maintenance and future rehabilitation. Recently CFRP was used to strengthen butt welded very high strength (VHS) tubes [Jiao & Zhao 2004]. The strength reduction in the heat-affected-zone was successfully recovered using the CFRP technique. However there is a lack of understanding of the bond characteristics between CFRP and steel tubes. In the present study the bond behaviour of CFRP and steel circular tubes is investigated.

Tensile tests were conducted to measure the modulus and stress–strain relationship of the CFRP used. Several tests were carried out to examine the bond between CFRP and steel tubes. Load transfer and slip between the top layer and steel tubes are discussed. The strain distributions across CFRP layers and along the CFRP length were established. The load carrying capacity was predicted with reasonable accuracy.

2 MATERIALS

2.1 *CFRP*

In the present research, MBrace fiber CF530 was chosen. Mbrace CF530 is so called high modulus (640 GPa) CFRP as compared with CF130 (240 GPa).

The specified properties of Mbrace CF530 are listed in Table 1.

2.2 *Adhesives*

High strength Araldite 420 adhesive was selected. Experiments showed that this was a suitable adhesive for steel structures [Jiao & Zhao 2004].

Table 1. Properties of MBrace CF 530 specified by the manufacturer.

Fibre reinforcement	Carbon – high modulus
Fibre density	2.1 g/cm^3
Fibre modulus	640 GPa
Fibre weight (CF)	400 g/m^2
Thickness	0.19 mm
Tensile strength	2650 MPa
Tensile elongation, ultimate	0.4%
Design tensile force @ 0.2% strain/m width	200 kN
Roll length	50 m
Sheet width	300 mm

2.3 *Steel tubes*

The steel tubes were provided by One Steel Market Mills Australia. They are similar to those used in a previous research project on strengthening butt-welded tubes [Jiao & Zhao 2004].

3 MEASUREMENT OF MATERIAL PROPERTIES OF CFRP

Tensile tests were conducted to verify the modulus and tensile strength specified by the manufacturer. Three tensile tests were conducted separately for the FRP with and without epoxy.

The length and width of the specimen were 400 mm and 50 mm, respectively. At the two ends of CFRP sample, steel plates were attached to grip the CFRP to the machine. Two strain gages were fixed on both sides of the CFRP and positioned at the centre of the sample. Figure 1 shows the test setup for the tensile test.

The stress vs strain curves are shown in Figure 2. Measured properties are summarized in Table 2. The large values of COV reflect possible variations in the test setup. Tests are being carried out to investigate this further.

Figure 1. Typical test specimen of tensile test.

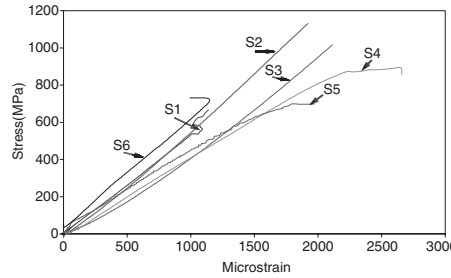

Figure 2. Stress vs. strain curves.

Table 2. Measured properties of CFRP.

Sample ID	With epoxy	Length (mm)	Width (mm)	Modulus E (MPa)	Maximum strain ε_{max} (microstrain)	Maximum stress σ_{max} (MPa)
S_1	Yes	400	50	530397	1139	666
S_2	Yes	400	50	581250	1921	1130
S_3	Yes	400	50	475905	2113	1016
S_4	No	400	50	409264	2660	858
S_5	No	400	50	449537	1970	698
S_6	No	400	50	603962	1148	720
Average				508386	1825	848
COV				0.1505	0.3232	0.2237

4 SPECIMENS FOR BOND TESTING

The first step in sample preparation was the preparation of steel surface to which the CFRP sheets were bonded. Surface grinders or sandblasters were used to remove all rust, paint, and primer from the tube surface along the bond length and the cross sectional surfaces where the two tubes were joined together. Another purpose of using grinder or sandblaster was to make the surface rough to ensure better bonding. The cross sectional surfaces of the tubes were then cleaned using Acetone. Adhesive was then used at these surfaces of the tubes to join two tubes. The sample was cured for one day and postcured for about 24 hours at a controlled temperature of about 70°C.

The tube surfaces were cleaned using acetone to apply adhesives. Thin coat of adhesive was applied uniformly to the CFRP sheet and on steel tube surfaces up to the bond length mentioned in Table 3. The selection of bond length is based on the findings by Jiao and Zhao 2004. The findings also suggested that any anchorage length beyond 65 mm would produce similar results. Steel tubes were then wrapped by one layer CFRP sheet. The excess epoxy and air (if any) were removed using a ribbed roller, applying it in the direction of the fiber. Sufficient time was allowed to settle the bonding before adding another layer to avoid the possible void between two layers. In this manner, five layers of CFRP were wrapped on the tubes. The whole specimen was then cured for at least one week and postcured for about 24 hours at about 70°C.

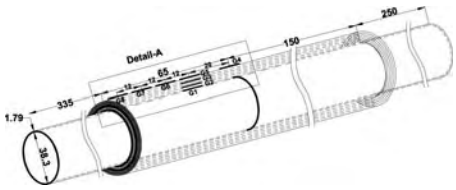

Figure 3(a). Location of strain gages.

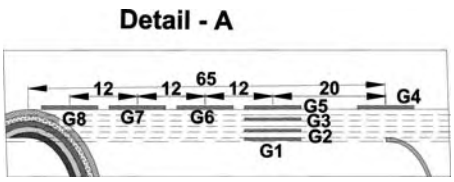

Figure 3(b). Detail-A of Figure 3(a).

Figure 3(c). Typical specimen with strain gages.

5 BOND TESTS

5.1 *Instrumentation*

Several 'student type' strain gages were attached to each test specimen. Figures 3(a), (b) and (c) show the location of each gage. Strain gages were placed at the short side of the bonded CFRP to capture the longitudinal strain development along the CFRP and the tube. One strain gage (G1) was placed inside the tube at a position 20 mm from the joint. The 2nd strain gage (G2) was placed on the 1st layer of CFRP laminate, at 20 mm from the joint. The 3rd strain gage (G3) was placed on the 3rd layer, 20 mm away from the joint. The 4th strain gage (G4) was applied at the top layer at the joint of the two tubes. The 5th strain gage (G5) was applied at the top layer, 20 mm away from the joint. All other strain gages at the top layer were applied along the tube at 12 mm distance from each other. The number of gages used in each sample, thus, depends on the bond length of that specimen.

LVDT was instrumented to record the relative slip between CFRP and steel. String pot was placed to measure the gross vertical movement of the tube. Crack propagation in CFRP was recorded by a high speed video recorder.

5.2 *Test setup and test procedure*

Each tube was loaded in a Baldwin Universal Testing machine as shown in Figure 4, at a loading rate of 2.0 mm/min and 500 kN load range. The test procedure consisted of applying increasing tensile loads to the specimen and recording the accompanying strain data. The test was continued until failure of the specimen.

6 TEST RESULTS

The failure modes and ultimate loads obtained in the tests are presented in Table 3 where t is the tube thickness. The failed specimens are shown in Figure 5.

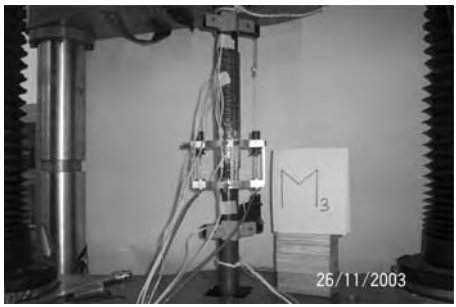

Figure 4. Test setup for steel tube wrapped with CFRP under tensile loading.

Table 3. Test results.

Specimen label	D (mm)	t (mm)	l_1 (mm)	l_2 (mm)	P_u (kN)	Failure mode
M_1	38.24	1.84	85	150	84.9	Fiber break
M_2	38.22	1.83	75	150	42.2	Fiber break & adhesive failure
M_3	38.30	1.79	65	150	74.1	Fiber break
M_4	38.10	1.60	62	112	77.5	Fiber break
M_5	38.27	1.74	50	100	67.3	Fiber break

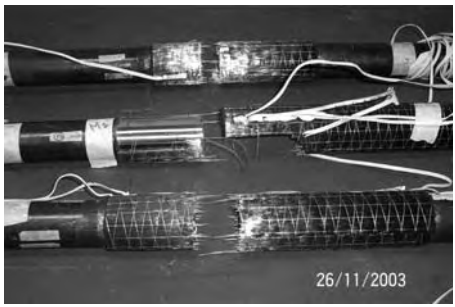

Figure 5. Typical failure mode of test specimen.

Specimen M_2 shows different failure mode from other specimens. Fiber break failure together with adhesive failure were observed in this specimen. This specimen failed at much lower load than other specimen. It is believed that when part of the adhesive failed, probably because of improper wrapping, then the CFRP couldn't hold the rest of the load and failed by fiber break at a lower load. This phenomena clearly indicates that preparation of specimen is very much important in CFRP bonding as it can influence the ultimate bond strength.

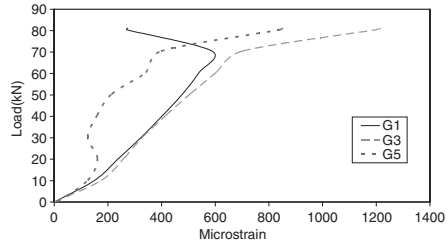

Figure 6. Microstrain vs. load curve for a typical specimen.

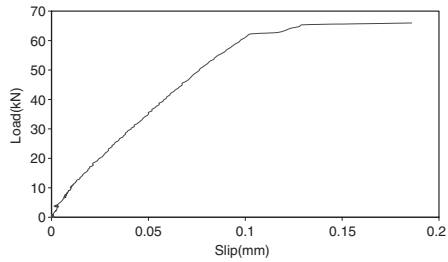

Figure 7. Relationship of slip between CFRP and steel tube [specimen M_5].

7 LOAD TRANSFER

The rehabilitation/repair or strengthening scheme, to a great extent, depends upon load transfer. From the strain distribution profiles the evolution of the load transfer process can be determined. Load is transferring from steel to the CFRP first layer then the CFRP second layer up to the top layer. Thus, there is load sharing between CFRP and steel. The dominant failure mode observed here is 'fiber break failure'. For a typical test, the strain readings at different load level recorded by different strain gages through the layers of CFRP are shown in Figure 6. In the case of G3 and G5 the whole fibre did not break or tear at once. When a portion of the fibre was broken, the remaining portion of fiber carried the additional load before the final failure. Figure 6 shows that when load is transferred to the remaining portion of the CFRP, strain on these fibres increased significantly.

G1 and G3 show almost identical strain distribution before failure starts. In the case of G1, the gage installed on the steel tube, the strain reading after failure is different from the strain reading G3 and G5, gages installed on CFRP. In G1, the strain decreases rapidly during failure, because, unlike CFRP, there is no additional fibre to carry the load. The strain pattern before failure in G5 is different from that of G1 and G3. The strain pattern of G5 before failure shown in

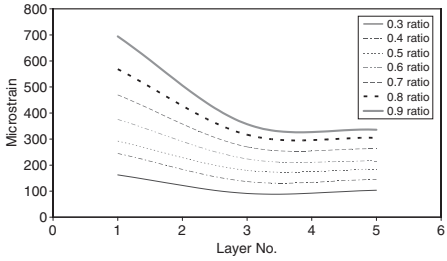

Figure 8. Distribution of strain through FRP layers at different load level.

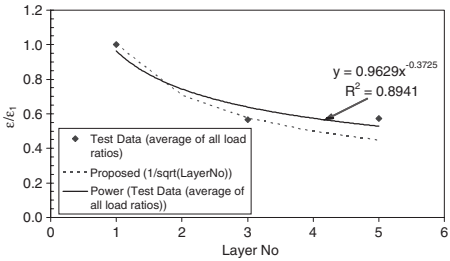

Figure 9. Non-dimensional strain versus CFRP layer numbers.

figure is mainly because of slip between the top layer and the steel tube, as can be seen in Figure 7. That's why the top layer reading is lower than the inside layer reading. The strain distributions are as used later in the paper. Whether the same results could have been established by using flat steel plates with CFRP bonding is under investigation at present.

8 STRAIN DISTRIBUTION

8.1 *Distribution across layers*

One of the main objectives of this study is to determine the distribution of strain across the CFRP layers and also along the CFRP. To perform this task, strain was measured at 1st (bottom), 2nd, 3rd and 5th (top) layer of CFRP (G1, G2, G3 and G5) at same location away from the joint. Strain was also measured at different locations away from the joint on top layer (G4, G5, G6, G7 and G8). The strain gage locations are shown in Figures 3(a) (b) & (c).

Figure 8 shows the variation of strain at different CFRP layers under different load ratio. The load ratio is defined as ratio of applied load to the maximum load achieved in the text. Figure 8 is based on the average strain readings of all specimens. There is a general trend of decreasing in strain from the bottom layer to

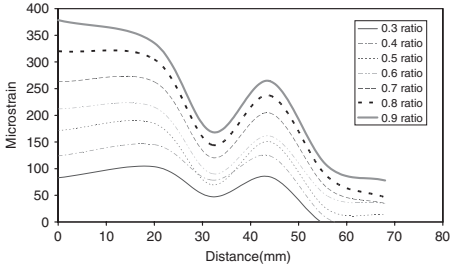

Figure 10. Distribution of strain at top layer at different load level.

the top layer. The trend is very much the same for all load ratios. In order to derive an expression of strain in terms of layer numbers, non-dimensional strains ($\varepsilon/\varepsilon_1$ where ε_1 is the strain in layer one) are plotted against layer numbers in Figure 9. A regression line can be determined using Excel as shown in Figure 9 where y refers to the vertical axis and x represents the horizontal axis. This regression expression is simplified in this paper to the following equation:

$$\varepsilon_i = \frac{\varepsilon_1}{\sqrt{i}} \quad (1)$$

where i is the layer number (i = 1, 2, 3, 4, or 5), ε_i is the strain in the ith layer.

8.2 *Distribution along CFRP*

To study the distribution of strain along the length of CFRP, strain at different distances away from the joint in the top layer is shown in Figure 10. Similar to Figure 8 the strain distribution is plotted at different load levels. It is clear from the figure that strain generally decreases with the distance away from the joint. The decreasing trend do not seem to be consistent because the reading in gage G7 located about 44 mm away from the joint is higher than that in G6 located about 32 mm away from the joint. More tests are needed in order to obtain a reliable expression of strain distribution along CFRP length.

9 LOAD CARRYING CAPACITY

9.1 *Stress distribution at the ultimate state*

The strain at the ultimate state can be expressed as:

$$\varepsilon_{i,u} = \frac{\varepsilon_{1,u}}{\sqrt{i}} \quad (2)$$

where $\varepsilon_{i,u}$ is the ultimate strain in the ith layer, $\varepsilon_{1,u}$ is the ultimate strain in the first (bottom) layer.

Table 4. Comparison of load carrying capacity.

Specimen label	P_u (kN)	P_p (kN)	P_p/P_u
M_1	84.9	75.7	0.891
M_3	74.1	75.8	1.023
M_4	77.5	75.4	0.973
M_5	67.3	75.7	1.125
Mean			1.003
COV			0.098

The corresponding stress in the ith layer can be written as:

$$\sigma_{i,u} = E \cdot \varepsilon_{i,u} = E \cdot \frac{\varepsilon_{1,u}}{\sqrt{i}} \quad (3)$$

where E is the modulus of CFRP.

9.2 *Load carrying capacity*

The load carried by each CFRP layer (P_i) can be calculated as the product of the area of that layer (A_i) and the ultimate stress in that layer ($\sigma_{i,u}$). The total predicted load carrying capacity (P_p) can be written as:

$$P_p = \sum A_i \cdot \sigma_{i,u} = \sum A_i \cdot E \cdot \frac{\varepsilon_{1,u}}{\sqrt{i}} \quad (4)$$

The value of $\varepsilon_{1,u}$ is taken as the maximum strain (2113 microstrain) obtained in the tensile test of CFRP with epoxy given in Table 2. The corresponding modulus of 457,905 MPa is taken as E in the calculation of P_p in this paper.

The predicted load carrying capacity is listed in Table 4 where specimen M_2 is not included due to a premature failure. The predicted values are compared in Table 4 with experimental ultimate load (P_u). A mean ratio (P_p/P_u) of 1.003 is achieved with a coefficient of variation (COV) of 0.098.

10 CONCLUSIONS

The following conclusions and observations are made based on the limited test results.

1. The average measured modulus of CFRP was found to be 508 GPa which is slightly lower than the manufacturer specified modulus 640 GPa. The measured tensile strength of CFRP was found to be significantly less than 2650 MPa specified by the manufacturer.
2. The dominant failure mode observed in the CFRP bond test was fiber break failure. The method of specimen preparation was found to be important.
3. The slip between the top layer and steel tubes might be the reason for non-uniform strain distribution among the layers.
4. The strain distribution across the layers was established as shown in Eq. (1).
5. The strain was found to generally decrease along the CFRP length away from the joint.
6. The estimated load carrying capacity was found to be in close agreement with that obtained experimentally.

ACKNOWLEDGEMENT

The authors acknowledge the contribution of Graeme Rundle and Kevin Nievaart for the setup of the test equipment. MBT, Vantico & OneSteel Market Mills, Australia Pte Ltd provided Fiber, Epoxy and steel tubes, respectively.

REFERENCES

Andres, A. and Torres-Acosta, 2002. Galvanic Corrosion of Steel in Contact with Carbon-Polymer Composites. I: Experiments in Mortar. Journal of Composites for Construction, ASCE, May 6(2): 112–122.

Bassetti, A., Nussbaumer, A. and Manfred, A. 2000. Crack Repair and Fatigue Life Extension of Riveted Bridge Members Using Composite Materials. Bridge Engineering Conference, ESE-IABSE-FIB, 26–30 March. Vol 1, 227–238.

Cederquist, S.C. 1999. Repairing America's deteriorating bridges. Materials Performance, 38(5): 20–25.

Hollaway, L. and Cadei, J. 2002. Progress in the technique of upgrading metallic structures with advanced polymer composites. Progress in Structural Engineering and Materials, 131–148.

Jiao, H. and Zhao, X.L. 2004. CFRP Strengthened Butt-Welded Very High Strength (VHS) Circular Steel Tubes. Thin-Walled Structures, 42: 963–978.

Karbhari, V.M. and Shulley, S.B. 1995. Use of Composites for Rehabilitation of Steel Structures – Determination of Bond Durability. Journal of Materials in Civil Engineering, ASCE, November 7(4): 239–245.

Liu, X., Silva, P.F. and Nanni, A. 2001. Rehabilitation of Steel Bridge Members with FRP Composite Materials. Proc., CCC2001, Composites in Construction, Porto, Portugal, October 10–12, 613–617.

Miller, T.C., Chajes, M.J., Mertz, D.R. and Hastings, J.N. 2001. Strengthening of a Steel Bridge Girder using CFRP Plates. Journal of Bridge Engineering, ASCE, 6(6): 514–522.

Moriarty, J. and Barnes, F. 1998. The Use of Carbon Fiber Composites in the London Underground Limited Civil Infrastructure Rehabilitation Program. SAMPE Journal, 34(2): 23–28.

Moy, S.S.J. 2000. Early Age Curing Under Cyclic Loading – A Further Investigation into Stiffness Development in Carbon Fibre Reinforced Steel Beams. Department of Civil

and Environmental Engineering, University of Southampton, UK, September.
Moy, S.S.J. 2001. FRP Composites: Life Extension and Strengthening of Metallic Structures. ICE Design and Practice Guides. London: Thomas Telford. 64.
Nikouka, F., Lee, M. and Moy, S. 2002. Strengthening of Mettalic Structures using Carbon Fibre Composites. IABSE Symposium, Melbourne.
Rajan, S., Larry, L. and Gray, M. 2001. Strengthening Steel Bridge Sections using CFRP Laminates. Composites Part B: Engineering, Vol 32, 309–322.
Sean, C.J., Scott, A.C. and Civjan, P.E. 2003. Application of Fiber Reinforced Polymer Overlays to Extend Steel Fatigue Life. Journal of Composites for Construction, ASCE, November 7(4): 331–338.
Tani, K., Matsumura, M., Kitada, T. and Hayashi, H. 2000. Experimental Study on Seismic Retrofitting Method of Steel Bridge Piers by using Carbon Fiber Sheets. In 6th Korea–Japan Joint Seminar on Steel Bridges. Tokyo, Japan. 437–445.
Tavakkolizadeh, M. and Saadatmanesh, H. 2001. Galvanic Corrosion of Carbon and Steel in Aggressive Environments. Journal of Composites for Construction, ASCE, August 5(3): 200–210.
Tavakkolizadeh, M. and Saadatmanesh, H. 2003a. Strengthening of Steel-Concrete Composite Girders using Carbon Fiber Reinforced Polymers Sheets. Journal of Structural Engineering, ASCE, 129(1): 30–40.
Tavakkolizadeh, M. and Saadatmanesh, H. 2003b. Fatigue Strength of Steel Girders Strengthened with Carbon Fiber Reinforced Polymer Patch. Journal of Structural Engineering, ASCE, 129(2): 186–196.
Tavakkolizadeh, M. and Saadatmanesh, H. 2003c. Repair of Damaged Steel-Concrete Composite Girders using Carbon Fiber-Reinforced Polymer Sheets. Journal of Composites for Construction, ASCE, November 7(4): 311–322.
Teng, J.G., Chen, J.F., Smith, S.T. and Lam, L. 2000. FRP Strengthened RC Structures. New York: Wiley.
Tumialan, G., Nanni, A., Ibell, T. and Fukuyama, H. 2002. FRP composites for strengthening civil infrastructure around the world. SAMPE Journal, 38(5): 9–15.

FRP Composites in Civil Engineering – CICE 2004 – Seracino (ed)
© 2005 Taylor & Francis Group, London, ISBN 90 5809 638 6

An ultra-high modulus carbon/glass fibre composite system for structural upgrading of steel members

N.K. Photiou, L.C. Hollaway & M.K. Chryssanthopoulos
School of Engineering – Civil Engineering, University of Surrey, Guildford, Surrey, UK

ABSTRACT: The paper discusses the stress analysis of the flexural strengthening of an artificially degraded steel member by utilising a hybrid ultra high-modulus carbon fibre/glass fibre/epoxy composite prepreg; this system is compared with one utilising a hybrid high-modulus carbon fibre/glass fibre/epoxy composite prepreg. The fabrication technique involves the hybrid composites being formed as a U-shaped unit bonded to the tensile region of the steel member by a compatible film adhesive; this fabrication technique is also compared with a plate system formed from a hybrid ultra-high modulus carbon fibre/glass fibre/epoxy composite prepreg and bonded to the soffit of the beam. The tests were carefully monitored, up to failure, in terms of strains and deflections at strategic positions. These critical values have been compared with those of a linear and non-linear finite-element analysis. It has been shown that there is a decided advantage in encapsulating a part of the beam's web with the glass fibre component of the hybrid composite as it is then possible to increase the steel strain to twice its yield value before failure of the ultra-high modulus carbon fibre composite, without any severe adhesive shear strains developing at the composite/steel interfaces.

1 INTRODUCTION

There are many steel bridge structures throughout Europe which are in need of (i) rehabilitation due to either corrosion, fatigue or lack of proper maintenance or (ii) upgrading due to a change in loading requirements. A repair and a retrofit option should be considered before a decision is made to replace a bridge; the cost for the former is far less than that for the latter, and usually requires less time. The traditional procedure for upgrading a steel member is to attach steel plates to it through bolting or welding but there are some disadvantages to this method; (i) the procedure is labour intensive and time consuming, (ii) it requires drilling and extensive lap splice detailing, (iii) there is a potential for weld fatigue cracking at the cover plate ends, (iv) traffic management would be required and there could be possible traffic delays and bridge closures, (v) an increased dead weight will act on the structure. Therefore, the need to adopt new materials, fabrication techniques and cost effective methods is evident.

Advanced polymer composites (APCs) are arguably the newest material to enter the construction industry but its utilisation is growing rapidly. The most highly developed application to date is the repair and upgrading of reinforced concrete (RC) bridge beams and slabs utilising the plate bonding technique. Currently, only a small number of metallic structures, compared with RC ones, have been upgraded using composite materials. The superior mechanical and physical properties of fibre reinforced polymer (FRP) makes them excellent candidates for repair and rehabilitation of steel bridges, particularly the carbon fibre reinforced polymer composites (CFRP). However, it is necessary to consider: (i) The type of carbon fibre to be used, ranging from the high modulus to the ultra high modulus fibre, to form the composite; (ii) the type of adhesive to be used, and (iii) the degree, if any, of encapsulation that the CFRP composite should afford to the steel member to ensure that early adhesive failure, particularly end debonding, does not occur. It should be mentioned that the high stiffness carbon fibre has a lower modulus of elasticity value compared to steel (typically about 60–70%) whereas the ultra-high stiffness carbon fibre, which can have a modulus value of up to twice that of steel, has a low ultimate strain, typically 0.4%.

There are three methods for the manufacture of CFRP composite plates for the rehabilitation of steel members, these are: (i) the pultrusion technique, (ii) the pre-pregnated fibre with a resin matrix (prepreg), (iii) the vacuum assisted resin transfer process. The majority of strengthening applications using CFRP composites employs the pultrusion system, which is a pre-formed plate, bonded to the soffit of the steel beam. The advantage of utilising a prepreg or a vacuum assisted resin transfer process is that the steel beam can be wrapped with a designed composite lay-up irrespective of its geometrical shape. There are two added advantages in the use of the prepreg material over that of the resin transfer system, these are: (i) The

matrix material may be combined with the fibre in the factory under ideal conditions, consequently there is much less site work to perform, (ii) The prepreg material may be bonded to the steel beam by means of a compatible film adhesive which is cured at the same time as the prepreg material.

This paper will describe and compare the effectiveness of two methods of fabrication for flexural upgrading a steel beam using an ultra high and a high modulus carbon fibre/epoxy composite prepreg; both composite materials were developed specifically for the construction industry. Of particular interest will be their capacity for strengthening steel girders to improve the latter's ultimate load carrying capacity and their stiffness before and after yield of the steel. The fabrication systems consist of (i) a partial encapsulation of the beam by the prepreg, which is bonded to the steel beam by a compatible film adhesive and (ii) a prepreg forming a plate only bonded to the soffit of the beam with the compatible film adhesive.

It should be noted that the definition of *Strengthening* metallic structures has been given in the CIRIA, RP 645 (2004) as a generic term to describe all applications of externally-bonded strengthening, including stiffening or repairing a structure, extending its life or increasing its load capacity.

2 PREVIOUS WORK ON REHABILITATION OF STEEL STRUCTURES USING COMPOSITES

Only a limited number of research papers have been published, these include Mertz & Gillesbie 1996, Mosallam & Chakrabarti 1997, Lui et al. 2001, Hill et al. 1999, Moy et al. 1999, Tavakkolizadeh & Saadatmanesh 2003a, b, Photiou et al. 2004a; in addition, two design guides have been published in the UK, ICE (2001) and CIRIA RP 645 (2004). Nevertheless, the high tensile strength and modulus of elasticity of CFRP composites make them ideal candidates for upgrading steel structures, although it is necessary to appreciate the possible limitations of their mechanical properties, their interaction with the steel substrate and their long term behavior in harsh environments. It is thus important to investigate the best possible combination of CFRP and adhesive, in terms of stiffness and strength criteria but also in terms of ease and reliability of manufacturing as well durability.

One of the earliest studies of utilising CFRP composites for upgrading a steel-concrete composite bridge was conducted at the University of South Florida (Sen & Libby 1994). A total of six number 6 m long steel-concrete composite beams, comprising steel sections and 711 mm wide by 115 mm thick concrete slabs under four-point bending. The CFRP sheets were 3.65 m long and 150 mm wide; two sheets of thickness 2 and 5 mm were used. It was reported that the addition of CFRP laminates improved the ultimate capacity of the composite beam by up to 50%.

At the University of Delaware, Mertz & Gillespie (1996) investigated the advantages of using advanced composite materials for the rehabilitation of deteriorated bridges. A series of small-scale tests were performed on eight 1.5 m long steel beams using five different retrofitting schemes: they reported a 60% increase in the use of CFRP systems. In addition, they showed a 25% increase in stiffness and a 100% increase in the ultimate load-carrying capacity of two 6.4 m long corroded steel girders. The beams were of a typical American Standard I-shape section of depth 610 mm and 230 mm width flange.

Tavakkolizadeh & Saadatmanesh (2003a) have presented the results of an experimental and analytical study on the behavior of steel-concrete girders strengthened with CFRP sheets. The test results showed that the epoxy-bonded CFRP sheet increased the ultimate load-carrying capacity of the girders by up to 75%, though the effect on stiffness was not significant. The final failure mode was concrete crushing, although one girder failed by premature debonding of two of the three CFRP layers. An analytical model of the moment–curvature response was also developed and was shown to provide conservative predictions compared to the test results. The study was further extended (Tavakkolizadeh & Saadatmanesh 2003b) to investigate the fatigue response of retrofitted steel girders.

In these studies, the CFRP composites used had a modulus of between 120 and 140 GPa, and a failure strain well over 1.5%. The adhesives used were two-part epoxies, usually selected on the recommendation of the CFRP manufacturer. Typically, the CFRP plate was fitted to the underside of the tension flange, where from a theoretical point of view it would provide maximum contribution to the bending stiffness and strength.

3 SCOPE OF PRESENT INVESTIGATION

So far, three beam tests have been undertaken in the present study. The objective was to compare the effectiveness of two carbon fibre polymer prepregs and two possible fit-ups. Specifically, an ultra-high stiffness carbon fibre/polymer (CFRP) U-shaped hybrid composite prepreg system (Beam 1) was compared to a high stiffness CFRP U-shaped hybrid composite prepreg system (Beam 2). The effect of alternative fit-ups was investigated by comparing the former (Beam 1) to an ultra-high stiffness CFRP hybrid composite system bonded to the soffit of the steel beam only (Beam 3). Given the number of parameters and their possible variation the tests are then simulated

numerically through the development of a non-linear finite element model, which, subject to validation, can be used in wider parametric studies.

4 MATERIALS AND SPECIMEN PREPARATION

4.1 *Prepregs*

CFRP composites are corrosion resistant, but if they are in contact with metals, galvanic interaction between the two materials could take place if an exposed carbon fibre were to touch the metal. In addition, to aid a uniform stress transfer from the steel to the CFRP, a layer of glass fibre composite was placed between the metal and the carbon composite to prevent direct contact between the two materials. This enabled an examination of the actual bonding mechanism between the glass fibre composite/steel interface to be made. The effectiveness of stress transfer when using a GFRP composite between the steel and CFRP composite adherends under a direct tension situation has been discussed in Photiou et al. (2004b).

The two types of carbon fibre/polymer composite prepreg materials and the glass fibre/polymer composite used in this investigation were manufactured by ACG (Advanced Composites Group Ltd., Heanor Gate Industrial Estate, Derbyshire, DE76 7SI). The matrix resin system and the adhesive film, whose typical thickness is about 110–120 microns, were made from a low temperature curing resin system (cure temperature 65°C); this is a relatively low temperature and can be readily accommodated on site by using a heated enclosure.

The CFRP composite material used in the investigation was made from two double laminate layers, comprised of unidirectional carbon fibre prepregs. Inter-leaved with these laminate layers were three single GFRP laminate layers each made from ±45° fibre prepregs positioned along the longitudinal direction of the beam. The overall lengths of the three types of CFRP prepregs were identical and measured 1600 mm. The width of the CFRP composite was 70 mm for Beams 1 and 2; this virtually covered the flange of the steel section with the exception of the curved corners. The width of the CFRP composite was 60 mm for Beam 3. The developed width of the GFRP prepregs was 210 mm, as these extended up the sides of the beam to its centroidal height; it is noted that no CFRP laminates were placed in the webs of the beam. It was anticipated that the U-shaped GFRP composite unit would prevent a peel failure at the free end of the reinforcement or a peel failure following a strain failure of the carbon fibre composite. In Beams 1 and 3, an ultra-high stiffness CFRP was used, each layer being 0.3 mm thick. For Beam 2, a high modulus CFRP was used, each layer being 0.6 mm thick. Table 1 gives tensile stress–strain characteristics for both the CFRP and the GFRP prepregs, obtained from tension coupon tests.

Table 1. Mechanical properties of the composite strengthening system.

	Spec. No.	Max. stress (MPa)	Max. axial strain	Modulus of elasticity (GPa)	Poisson ratio
2-Layer	01	2083.6	16383.0	136.0	
(high CFRP)	02	2124.8	16130.0	132.0	
t = 1.2 mm	03	2119.5	15239.0	138.0	
Average		2109.3	15917.0	135.3	0.28
4-Layer	01	956.4	3616.0	261.5	
(ultra CFRP)	02	1269.2	4615.2	279.5	
t = 1.2 mm	03	1136.8	4286.3	269.2	
Average		1120.8	4172.5	270.1	0.32
2-Layer	01	202.9	16298.9	17.8	
(high GFRP)	02	218.6	17666.5	15.5	
t = 0.8 mm	03	224.3	18217.6	15.6	
Average		215.2	17394.3	16.3	0.15
Adhesive film t = 0.1 mm		32.0	8600.0	3.7	0.37

t = the thickness of the specimen.

4.2 *Steel beams*

The first operation in the test programme consisted of cutting the hollow steel sections, 120 mm × 80 mm, to a length of 1800 mm and machining 2.5 mm thickness of material off the flange to simulate a degraded beam. Multiple low speed passes performed this operation, in order to minimise distortions induced by heat input and residual stress release. The corners between the flange and web faces were rounded to a radius of 10 mm. Subsequently, all exposed surfaces of the rectangular shaped hollow section steel beams were grit blasted to the Swedish Code SA $2^{1/2}$ Grade 3 Dirk grit. Immediately before applying the adhesive film, the surface of the steel was solvent degreased using acetone to remove any contaminant materials. Small tension specimens were cut from the main beam section and tension tests were undertaken to determine the mechanical characteristics of the steel. The average values were 375 MPa for 0.2% proof strength, 205 GPa for the modulus of elasticity and 0.3 for the Poisson ratio.

4.3 *Beam upgrading process*

The hybrid composite laminates including the adhesive film were cut to size and were stacked onto the soffit surface of the steel beam as follows, (a) the adhesive film, (b) a single glass fibre laminate, (c) one

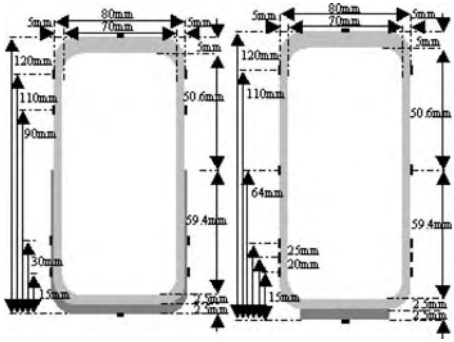

Figure 1a. Schematic diagram of a rectangular hollow cross-section ultra and high modulus CFRP, also showing strain gauge positions (not to scale).

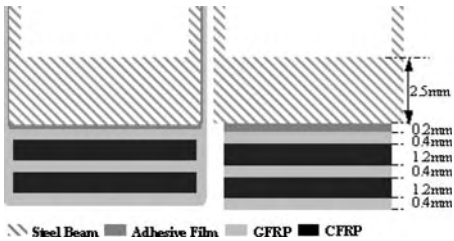

Figure 1b. Schematic diagram of the stacking sequence of the FRP composite components (not to scale).

double laminate of carbon fibre, (d) a single glass fibre laminate, (e) the other double layer carbon fibre, and (f) another single glass fibre laminate. Between items (c) and (d) the system was de-baulked. At the end of the laying-up procedure a halar film and breather blanket covered the beam and the whole unit was placed in a vacuum bag. The bag, under vacuum assisted pressure of 1 atm., was transferred to an oven at 65°C for 16 hours. After curing, the temperature of the oven and sample were reduced to room temperature at a steady rate. The beam was then ready for testing. Figures 1a and 1b show the stacking sequence of the FRP composite system on the steel beams.

5 TEST PROCEDURE

The beams were placed on to the test rig on a span of 1700 mm. The two external loads were positioned at a distance of 200 mm on either side of the centre line of the beam. Strain gauges were bonded at strategic positions on both sides of the beams at mid-span and down the depth of the beams. The test arrangement is shown in Figure 2. Two displacement transducers were placed

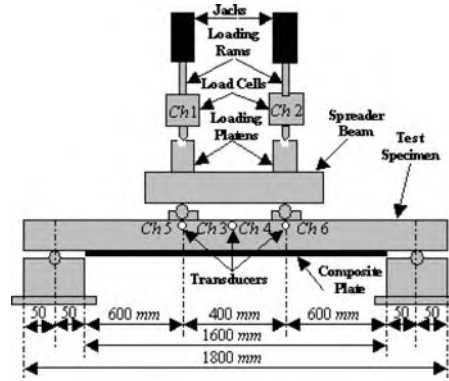

Figure 2. Test arrangement for beam tests.

on either side of the beam at mid-span to determine the deflections and to indicate any inconsistency in these readings. Displacement transducers were also placed at the two external load positions to determine the curvature of the beams over the pure moment region. A series of four cyclic loading increments were applied to a value one eighth of the estimated failure load before the beams were taken to failure; the load increments were 1 kN.

6 SUMMARY OF TEST RESULTS

The maximum load on Beam 1, reached immediately before failure, was 46 kN per jack and was concentrated in the CFRP composite within the pure moment region, this was equivalent to an ultimate strain of about 0.4%, which corresponds to the failure strain of the ultra-high stiffness CFRP. At this point there was no apparent bond failure between the composite and the steel members on either side of the failed section, therefore, complete composite action still existed between the two components, apart from the location of the failed section. Figure 3 shows the average load per jack versus average deflection response of the strengthened beam and the non-linear response can be observed from about 23 kN; this corresponds to the bottom region of the steel beam commencing to exhibit softening characteristics due to yielding. The central deflection at this point was 8 mm. As can be seen, the load increased to almost twice this value before failure of the CFRP composite, at this point the central deflection was 24 mm. In fact, the ultimate load of the artificially degraded CFRP-strengthened beam reached the theoretical plastic collapse load corresponding to the full steel beam section. As mentioned above, the tension flange of the original steel beam had been reduced by 50% (from 5 mm thick

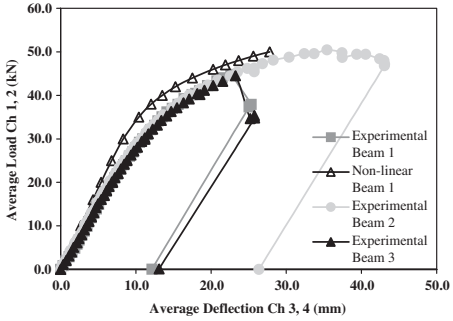

Figure 3. Average load–deflection (per jack) response of the strengthened Beams 1, 2, 3.

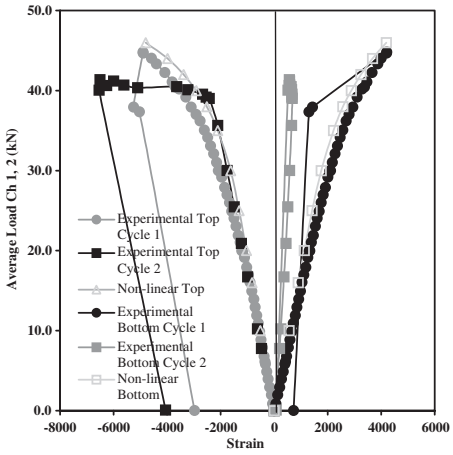

Figure 4. Load–strain response of the strengthened Beam 1.

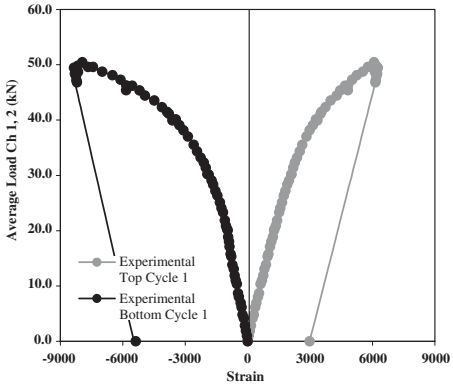

Figure 5. Load–strain response of the strengthened Beam 2.

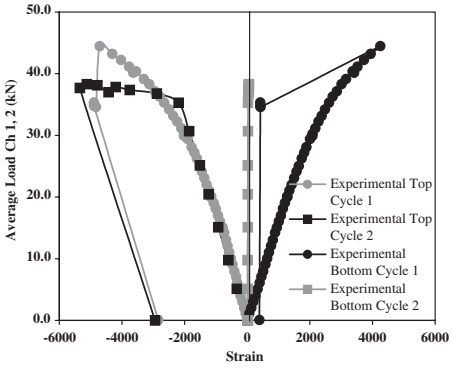

Figure 6. Load–strain response of the strengthened Beam 3.

to 2.5 mm) to represent a degraded beam. Hence, this test demonstrated the ability of the CFRP/GFRP composite prepreg system to restore the full bending capacity of the steel beam. On removing the loads the permanent deflection was 12 mm.

Beam 2, strengthened with a U-shaped high stiffness CFRP, displayed a ductile response up until the maximum load and beyond. The steel reached its 0.2% proof stress at a load of 23 kN per jack and at a deflection of 8 mm. The beam continued to deform under the application of an increasing load to a value of 50 kN per jack, at which point the test was stopped due to excessive deflection at the centre of the beam; the deflection value at this maximum load was 42 mm. Figure 3 shows the average load per jack versus average central deflection. As the strain in the CFRP composite had not reached its ultimate value of about 1.7% no failure of the composite occurred. Clearly, this case, the maximum load was in excess of the full plastic collapse load of the original steel beam, and the ductility of the beam was not impaired, at least not up to the deflection level reached in the test. On unloading the beam, the permanent deflection was 26.3 mm.

The failure load of Beam 3 was almost identical to that of Beam 1, i.e. the beam collapsed when the ultimate strain of the CFRP composite reached a value of about 0.4%, Furthermore, the load–deflection path followed a similar pattern to that of Beam 1, as can be seen from Figure 3. At failure, there was a complete de-bonding of the composite system from the soffit of the steel beam. Thus, unlike Beam 1, after failure no residual composite action between the CFRP and steel beam remained. On unloading, the permanent deflection was 13 mm.

Figures 4–6 present typical load–strain responses for the three beams, whereas Figures 7–9 show the

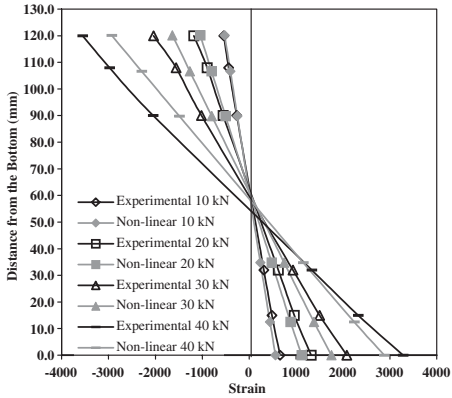

Figure 7. Strain distribution response of the strengthened Beam 1.

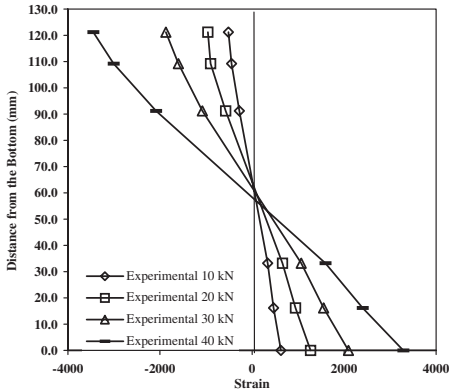

Figure 8. Strain distribution response of the strengthened Beam 2.

strain distribution across the depth of the section at the centre of the beam. The results confirm the observations made above regarding the non-linearity of the response and the type of final failure reached in each of the three beams.

7 NUMERICAL STUDY

The next phase of the current investigation involves the development of a finite element model to simulate the physical tests. A model has been set up using the commercial software package ABAQUS Version 6.3 (2002). The model uses 20 node brick, reduced integration elements (C3D20R) to model all the parts of

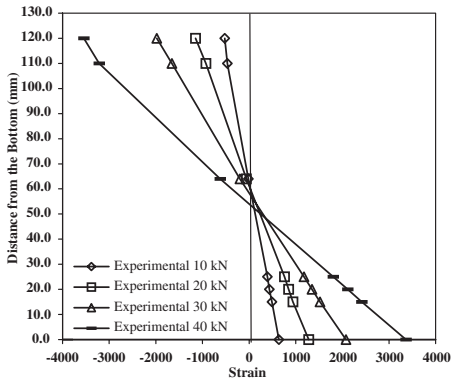

Figure 9. Strain distribution response of the strengthened Beam 3.

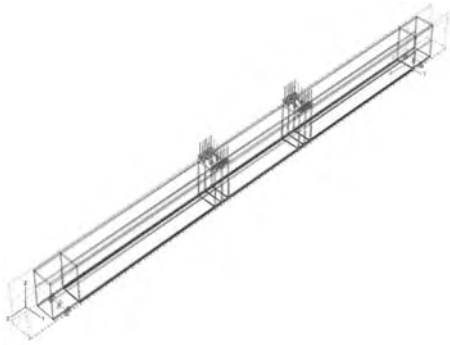

Figure 10. A complete view of the model.

the strengthened beam. Both geometric and material non-linearities are included, the latter being only in the material characteristic of the steel. Both adhesive and FRP materials are modelled through a linear elastic stress–strain curve. Although more efficient elements could have been used for the steel and FRP materials, it was decided to use the same type for all parts, in order to mitigate the risk of compatibility problems. A view of the complete model is shown in Figure 10. The whole length of the beam is modelled in order to simulate as closely as possible the actual boundary conditions of the beam ($U_2 = 0$, $U_3 = 0$ LHS and $U_2 = 0$ RHS). It is also envisaged that the same model could then be used in cases where partial debonding (say, on one side) needs to be investigated. Numerical analysis has so far been undertaken for Beam 1 only. Initial results are shown for load–deflection in Figure 3 and for load–strain in Figure 4. Furthermore, the predicted strain distribution across the depth

of the cross-section is shown in Figure 7. As can be seen, the FE model is able to reproduce the trends observed in the experiments, both in terms of overall characteristics (i.e. load–deflection) and in terms of local response (i.e. load–strain at the bottom of the section in the middle of the beam). The strain distribution across the depth is also in reasonable agreement, especially in the linear range. However, discrepancies are also apparent, for example in beam stiffness (Fig. 3), and in the strain distribution during non-linear response (Fig. 7). These could be attributed to (i) unavoidable rig flexibilities and (ii) the effect of thermal stresses induced during the curing of the composite system. Further work is currently under way to improve the correlation between numerical predictions and experimental measurements.

8 CONCLUSIONS

This paper has presented two different hybrid prepreg composite systems for the flexural stiffening of a closed section steel beam. The hybrid systems consist of ultra-high modulus CFRP and high-modulus CFRP, both composites being interleaved with GFRP prepregs and the whole bonded to individual steel beams. (These beams are referred to as Beams 1 and 2.) Two different fabrication methods were employed, the first one used U-shaped hybrid composites, which were bonded to the tension sides of Beams 1 and 2, and in the other method the ultra-high modulus CFRP/GFRP hybrid composite flat plate was bonded to the soffit of the Beam 3. A compatible adhesive film was used to bond the hybrid composites to the steel section during the final stages of curing the composites at an elevated temperature. The beam loading arrangement consisted of a four point loads on a span of 1700 mm.

Within the linear range of the experimental loading tests undertaken on the three beams, there is close agreement with the value of the stiffness and the strain distributions of the rehabilitated beams.

Within the non-linear range of the beam, upgraded with U-shaped ultra-high stiffness CFRP/GFRP composite (Beam 1), the carbon fibre reached its ultimate strain at a total load of 46 kN per jack; there was no apparent bond failure between the composite and the steel member on either side of the fracture point. The maximum load reached was 92% of the defined failure load of Beam 2. The latter beam continued to take more load up to a maximum value of 50 kN per jack when the test was stopped due to excessive deflection of the beam; at this point the ultimate strain of 1.7% of the high modulus carbon fibre had not been reached.

Beam 3, which had the ultra-high stiffness CFRP/GFRP hybrid composite prepreg bonded to the soffit of the beam only, failed in a similar way to that of Beam 1. At the ultimate strain of the carbon fibre of 0.4%, the composite plate failed and there was a complete de-bond of the hybrid composite system from the steel beam.

From the results of Beams 1 and 3, it is clear that the area geometry of the upgrading material does not affect the ultimate load that the upgraded beam is able to support; this is governed by the ultimate strain of the carbon fibre. However at post failure, the U-shaped composite has the advantage of continuing to support the full load once the bond length from the failure region has been fully developed; this situation does not exist for the soffit plate.

The finite element analysis is able to reproduce the trends observed in the experiments, in both load–strain and load–deflection responses and are in reasonable agreement in the linear range. The discrepancies, between the two techniques in the non-linear regions, which have already been mentioned in the paper, are currently being investigated.

It will be realised that, unlike concrete upgrading, the peel stresses developed at the free ends of a composite plate bonded to a steel adherend are not a serious concern provided sufficient bond length is developed. What must be realised is the complete de-bond of the soffit bonded composite system at the carbon fibre failure. It has been shown this de-bond can be prevented by using a U-shaped upgrade to cover the tensile region of the steel beam.

REFERENCES

ABAQUS Version 6.3, 2002. Hibbit, Karlson & Sorensen, Inc.

CIRIA RP 645 2004 (Publication No. C595). Cadei, J., Stratford, T.J., Hollaway, L.C. & Duckett, W.G. Strengthening metallic structures using externally bonded fibre reinforced polymers. Published by CIRIA: London, UK.

Hill, P. S., Smith, S. & Barnes, F. J. 1999. Use of high modulus carbon fibres for reinforcement of cast iron compression struts within London Underground: Project details: *Conference on Composites and Plastics in Construction. Held at Building Research Establishment.* UK.

ICE design and practice guides 2001. FRP composites life extension and strengthening of metallic structures. In S.S.J. Moy (ed), Thomas Telford: London.

Liu, X., Silva, P.R. & Nanni, A. 2001. Rehabilitation of steel bridge members with FRP composite materials. In J. Figueiras, L. Juvandes & R. Furia (ed), *Proc. Composites in Construction CCC 2001*. 613–617. Porto, Portugal.

Mertz, D. & Gillespie, J. 1996. Rehabilitation of steel bridge girders through the application of advanced composite material. NCHRP 93-ID11. *Transportation Research Board*. 1–20. Washington, D.C.

Mosallam, A.S. & Chakrabarti, P.R. 1997. Making connection. *Civil Engineering: ASCE*: 56–59.

Moy, S.S.J., Barnes, F., Moriarty, J., Dier, A.F., Kenchington, A. & Iverson, B. 1999. Structural upgrade and life extension of cast iron struts using carbon fibre

reinforced Composites. *Proc. of the Conference on Composites and Plastics in Construction, Held at Building Research Establishment*. UK.

Photiou, N.K., Hollaway, L.C. & Chryssanthopoulos, M.K. 2004a. Strengthening of an artificially degraded steel beam utilising a carbon/glass composite system. In L.C. Hollaway, M.K. Chryssanthopoulos & S.S.J. Moy (ed), *Proc. of the Conference Advanced Polymer Composites for Structural Applications in Construction-ACIC 2004*. Woodhead Publishing.

Photiou, N.K., Hollaway, L.C. & Chryssanthopoulos, M.K. 2004b. Selection of CFRP Systems for steelwork upgrading. *Held at Innovative Materials and Technologies for Construction and Restoration (IMTCR), Lecce, 7–9 June 2004*. Italy.

Sen, R. & Libby, L. 1994. Repair of steel-composite bridge sections using carbon fibre reinforced plastic laminate. FDOT–510616. *Florida Department of Transportation*. Tallahassee Florida.

Tavakkolizadeh, M. & Saadatmanesh, H. 2003a. Strengthening of steel-concrete composite girders using carbon fibre reinforced polymer sheets. *Journal of Structural Engineering: ASCE* January 2003: 30–40.

Tavakkolizadeh, M. & Saadatmanesh, H. 2003b. Fatigue strength of steel girders strengthened with carbon fibre reinforced polymer patch. *Journal of Structural Engineering: ASCE* February 2003: 186–196.

FRP Composites in Civil Engineering – CICE 2004 – Seracino (ed)
© 2005 Taylor & Francis Group, London, ISBN 90 5809 638 6

Suppression of local buckling in steel tubes by FRP jacketing

J.G. Teng & Y.M. Hu
Department of Civil and Structural Engineering, The Hong Kong Polytechnic University, Hong Kong, China

ABSTRACT: Circular steel tubes are widely used in many structural forms and local buckling in the elephant's foot mode can occur when they are subject to axial compression alone or in combination with monotonic or cyclic lateral loading. The appearance of this inelastic local buckling mode, generally near the ends of a uniform-thickness tube, signifies not only the exhaustion of the load-carrying capacity but also the end of ductile response. To delay or prevent the appearance of this local buckling mode, external confinement by an FRP jacket is proposed in this paper and demonstrated to be effective through a series of exploratory axial compression tests on circular steel tubes. The test results show conclusively that even with the provision of a thin FRP jacket, the ductility of the steel tube can be greatly enhanced, so FRP confinement provides an effective means to enhance the ductility of circular steel tubes in both retrofitting applications and new construction. The test results also show that the enhancement in the ultimate load is limited, which is desirable in seismic retrofit so that the retrofitted tube will not attract forces that are so high that adjacent members may be put in danger. It is worth noting that the same benefit can be expected when FRP confinement is used in much thinner shells (e.g. liquid storage tanks and silos) to delay/prevent failure in the elephant's foot buckling mode when subject to combined axial compression and internal pressure.

1 INTRODUCTION

Over the past decade, fiber-reinforced polymer (FRP) has gained wide acceptance as a new structural material. In particular, many possibilities of combining FRP and concrete in structural applications have been explored, including the external bonding of FRP to concrete structures for the enhancement of strength and ductility, concrete structures reinforced or prestressed with FRP, concrete-filled FRP tubes as columns and piles as well as FRP-concrete composite beams/bridge decks (Teng et al. 2002, 2003, Hollaway 2003, Mufti 2003, Van Den Einde and Seible 2003). By contrast, much less has been explored about possible combinations of FRP with steel in structural applications, although a significant amount of research exists on the external bonding of FRP to steel/metallic members for flexural strengthening purposes (Hollaway 2002). This paper presents the results of a series of exploratory axial compression tests on circular steel tubes confined with an FRP jacket. It is well known that FRP confinement can lead to significant enhancement in the strength and strain capacity of axially compressed concrete, and this study shows that a similar benefit exists when an FRP jacket is used to confine a steel tube to prevent/delay the appearance of the well-known elephant's foot buckling mode.

2 RESEARCH SIGNIFICANCE

There is a great potential for the application of FRP jacketing to steel tubes and shells in both retrofitting and new construction. For example, in the 1995 Kobe earthquake in Japan, many circular steel bridge piers failed by local buckling in the elephant's foot buckling mode when they were subject to cyclic lateral loads in addition to axial compression (Usami and Ge 2000). The ductility of these steel bridge piers can be greatly enhanced by the external wrapping of FRP in regions near the base. Hollow circular tubes in other applications which may suffer local buckling failures (e.g. Elchalakani et al. 2002, 2004) can benefit similarly from FRP wrapping. A recent proposal for the construction of concrete-filled steel tubular columns is to confine the end portions using FRP jackets (Xiao 2004), which is another example of FRP confinement of steel tubes. Here, by providing an FRP jacket, the steel tube is prevented from deforming inwards by the concrete core and outwards by the FRP jacket and the ductility of the steel tube can be greatly enhanced. The above discussion relates to circular tubes but rectangular tubes can also benefit from FRP jacketing although the effectiveness is expected to be significantly reduced. This is analogous to the FRP confinement of concrete columns where the

effectiveness of confinement is significantly reduced if the section is non-circular.

The idea of FRP jacketing of circular steel tubes can be extended to circular cylindrical shells (or even shells of revolution) in general if the elephant's foot buckling mode is the critical failure mode. It is well known that large thin steel cylindrical shells such as liquid storage tanks and steel silos for storage of bulk solids may fail in the elephant's foot buckling mode when subject to the combined action of axial compression and internal pressure (Rotter 1990). Many such failures have been observed during earthquakes. For such steel cylindrical shells, FRP confinement provides an almost ideal method of retrofitting and may also become a standard feature of new tank/silo designs.

3 EXPERIMENTAL DETAILS

3.1 *Specimens*

To demonstrate the effect of FRP confinement of steel tubes, four steel tubes with or without an FRP jacket were recently tested at The Hong Kong Polytechnic University in an exploratory study. The four tubes were cut from a single long tube and their details are shown in Table 1.

One of the tubes (tube ST1) was tested as a bare steel tube (without FRP jacketing), while the other three tubes (tubes ST2, ST3 and ST4) were each provided with an FRP jacket with a different number of plies (Table 1). The FRP jacket was formed in a wet lay-up process, and each ply consisted of a single lap of a glass fibre sheet impregnated with epoxy resin. For each steel tube, two continuous glass fibre sheets were used without any vertical overlap as the width of the fibre sheets was smaller than the height of the tube. Each continuous glass fibre sheet was wrapped around the steel tube to form a jacket with the required number of plies, with its finishing end overlapping its starting end by 150 mm to ensure circumferential continuity. Before the wrapping of FRP, the surface of the steel tube was appropriately cleaned.

Steel coupon tests were conducted to obtain the tensile properties of the steel. The coupons for the tensile tests were cut from the same long steel tube directly (Fig. 2) and details of test coupons are given in Table 2. Two 8 mm strain gauges were attached to the two sides of each coupon respectively at the mid-length to measure strains during the tensile test.

The tensile tests showed that the steel had a Young's modulus of 206.0 GPa, a yield stress of 338.6 MPa with a long plastic plateau and an ultimate elongation of 0.347. The FRP used had a nominal thickness of 0.17 mm, a Young's modulus of 76 GPa and a tensile strength of 2,300 MPa based on the nominal thickness, according to data supplied by the manufacturer.

3.2 *Instrumentation and loading*

For the bare steel tube, four unidirectional strain gauges with a gauge length of 8 mm were installed

Figure 1. Steel tube confined with an FRP jacket.

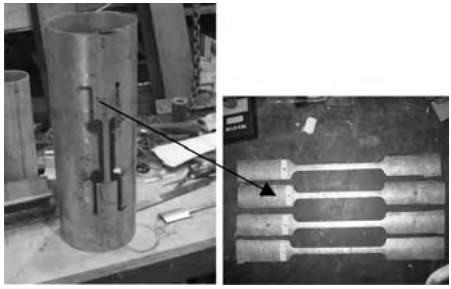

Figure 2. Coupons for tensile tests.

Table 1. Specimen details.

Tube specimen	ST1	ST2	ST3	ST4
Outer diameter (mm)	165	166	165	165
Length (mm)	450	450	450	450
Tube thickness (mm)	4.2	4.2	4.2	4.2
FRP jacket thickness	NA	1 ply	2 plies	3 plies

Table 2. Details of coupons for tensile tests.

Test coupon	CT1	CT2	CT3	CT4
Thickness (mm)	4.22	4.24	4.19	4.20
Average width b (mm)	12.10	12.12	12.01	12.20
Cross-sectional area	51.06	51.39	50.32	51.24

Table 3. Results of tensile tests.

Specimen	Yield stress (MPa)	Young's modulus (GPa)	Elongation
CT1	355.7	206.2	0.340
CT2	329.6	206.3	0.320
CT3	369.1	184.3	0.400
CT4	330.6	205.5	0.380
Average(excluding CT3)	338.6	206.0	0.347

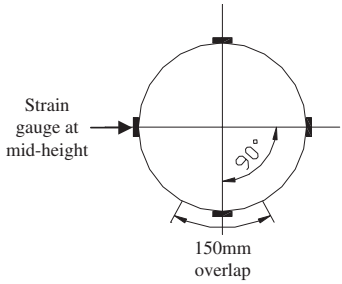

Figure 3. Layout of strain gauges.

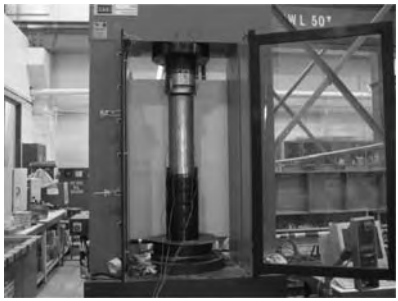

Figure 4. Test set-up.

at the mid-height to measure longitudinal strains. For each FRP-confined steel tube, four bidirectional strain gauges with a gauge length 20 mm were installed at the mid-height of the FRP jacket. The layout of strain gauges is shown in Fig. 3. The compression tests were all conducted using an MTS machine with displacement control (Fig. 4).

4 TEST RESULTS AND OBSERVATIONS

The failure mode of the bare circular steel tube was outward buckling around the circumference. This

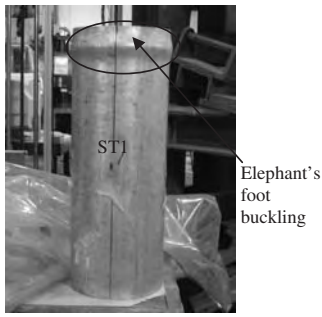

Figure 5. Bare steel tube after ccompression test.

Figure 6. FRP-confined steel tubes after compression test.

local buckling occurred near the end and is widely known as the elephant's foot buckling mode (Fig. 5). This buckling mode is normally found in steel tubes whose diameter-to-thickness ratio is relatively small.

The three FRP-confined tubes after failure are shown in Fig. 6. Two failure modes were observed in these FRP-confined steel tubes. For the steel tube with a single-ply FRP jacket, failure occurred by the rupture of the FRP jacket when its hoop strain in the local buckling zone exceeded the ultimate tensile strain of the FRP in the hoop direction. Once rupture of the FRP jacket occurred, the confinement effect of the FRP jacket disappeared and the load the tube was able to carry reduced rapidly. From the data supplied by the manufacturer, the FRP used in this study had an ultimate tensile strain of 2.8%, but the average ultimate hoop rupture strain achievable in a circular jacket is expected to be significantly lower due to the detrimental effect of curvature and non-uniform deformation,

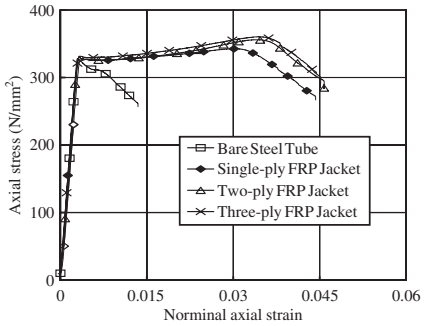

Figure 7. Axial stress–axial strain curves of bare and FRP-confined steel tubes.

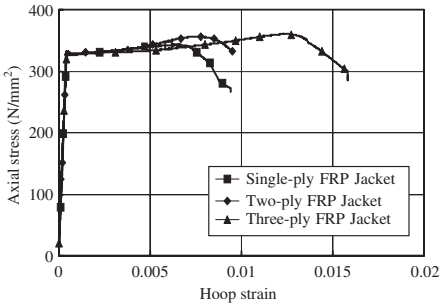

Figure 8. Axial stress–hoop strain curves of FRP-confined steel tubes.

similar to the phenomenon observed in FRP-confined concrete cylinders (Lam and Teng 2004).

For the other two tubes confined with a two-ply jacket and three-ply jacket respectively, failure was by the inward buckling of the steel tube wall. In these tubes, the expanding local buckling deformations near the ends were unable to break the thicker FRP jackets. Since the tube was prevented from deforming outward by a strong FRP jacket, the tube instead failed by inward buckling. Rupture of the FRP jacket was also observed in this failure mode in the tube with a two-ply jacket, as a result of the inward buckling deformation. This jacket rupture is however not the cause of the failure of the steel tube. The FRP jacket was thus very effective in preventing the development of the elephant's foot buckling mode.

The axial stress–strain curves of all four specimens are shown in Fig. 7, where the nominal axial strain found from the total axial shortening between the loading platens is shown instead of the strain gauge readings as the nominal axial strain represents the overall response of the steel tube better. It is clear that the axial stress-axial strain curve of the bare steel tube features a descending branch immediately after the linear ascending branch, while those of the three FRP-confined tubes all feature a long and slowly ascending branch before reaching the peak load, showing great ductility. Fig. 7 shows that the tube confined with a single-ply FRP jacket is almost as ductile as those with a two-ply or a three-ply jacket. For practical applications, methods need to be developed to achieve optimum designs of FRP jackets.

Table 4. Summary of test results.

Specimen	ST1	ST2	ST3	ST4
P_{co} (kN)		718.6		
P_u (kN)	699.2	726.8	753.3	762.9
P_u/P_{co}	0.97	1.01	1.05	1.06
ε_{co}		0.00327		
ε_u	0.00327	0.0312	0.0351	0.0358
$\varepsilon_u/\varepsilon_{co}$	1.00	9.54	10.73	10.95

Fig. 8 shows the axial stress–hoop strain curves of the three FRP-confined tubes. The hoop strains shown here are average values of the readings from the three strain gauges located outside the overlapping zone. Since the buckling deformations were localised, it is difficult to relate these hoop strains to the development of buckling deformations. Nevertheless, the hoop strains at the tube mid-height did reach around 50–80% of the expected hoop rupture strain of around 1.9% based on tests conducted on FRP-confined concrete cylinders (Teng et al. 2004), indicating that the jackets were well mobilised.

Key test results are summarized in Table 4, where P_{co} is as the yield load defined as the yield stress of the steel from tensile coupon tests times the cross-sectional area of the steel tube and P_u is the ultimate loads of the FRP-confined steel tubes obtained from the tests. ε_{co} is the nominal axial strain of the bare steel tube at peak load from the bare steel tube compression test, while ε_u is the nominal axial strain of the FRP-confined steel tube at peak load. It can be found that P_u and ε_u increase with an increase in the thickness of the FRP jacket.

The confinement effectiveness of the FRP jacket can be judged by examining enhancements in the ultimate load and the strain at peak load. As seen in Table 4, the ultimate load of the steel tube was enhanced by 1% to 6% by FRP jackets of different thicknesses. The ultimate load increases with the thickness of the FRP jacket, although this increase is generally very limited. Table 4 and Fig. 7 both show that the ductility of the steel tube was greatly enhanced by FRP confinement. The nominal axial strain at the peak load is enhanced by 9–10 times through FRP confinement.

5 CONCLUSIONS

In this paper, the use of FRP confinement to enhance the ductility and hence the seismic resistance of circular steel tubes has been proposed. A series of exploratory axial compression tests has been presented to demonstrate the effectiveness of FRP confinement of steel tubes whose ductility is otherwise limited by the development of the elephant's foot buckling mode. The test results have shown conclusively that even with the provision of a thin FRP jacket, the ductility of the steel tube can be greatly enhanced. The test results also show that the enhancement in the ultimate load is very limited, which is desirable in seismic retrofit so that the retrofitted tube will not attract forces that are so high that adjacent members may be put in danger. It is worth noting that the same benefit can be expected when FRP confinement is used in much thinner shells (e.g. liquid storage tanks and silos) to delay/prevent failure in the elephant's foot buckling mode when subject to combined axial compression and internal pressure.

ACKNOWLEDGEMENTS

The authors are grateful for the financial support provided by The Hong Kong Polytechnic University (Project No: 1ZE-06).

REFERENCES

Elchalakani, M., Zhao, X.L. and Grzebieta, R. (2002). Bending tests to determine slenderness limits for cold-formed circular hollow sections. *Journal of Constructional Steel Research*, 58(11), 1407–1430.

Elchalakani, M., Zhao, X.L. and Grzebieta, R. (2004). Cyclic bending tests to determine fully ductile section slenderness limits for cold-formed circular hollow sections. *Journal of Structural Engineering*, ASCE, 130(7), 1001–1010.

Hollaway, L.C. (2003). The evolution and the way forward fro advanced polymer composites in the civil infrastructure. *Construction and Building Materials*, 17(6&7), 365–378.

Hollaway, L.C. and Cadei, J. (2002). Progress in the technique of upgrading metallic structures with advanced polymer composites. *Progress in Structural Engineering and Materials*, 4, 131–148.

Lam, L. and Teng, J.G. (2004). Ultimate condition of FRP-confined concrete. *Journal of Composites for Construction*, ASCE, 8(6).

Mufti, A.A. (2003). FRPs and FOSs lead to innovation in Canadian civil engineering structures. *Construction and Building Materials*, 17(6&7), 379–387.

Rotter, J.M. (1990). Local collapse of axially compressed pressurized thin steel cylinders. *Journal of Structural Engineering*, ASCE, 116(7), 1955–1970.

Teng, J.G., Chen, J.F., Smith, S.T. and Lam, L. (2002). *FRP Strengthened RC Structures*, John Wiley & Sons Ltd.

Teng, J.G., Chen, J.F., Smith, S.T. and Lam, L. (2003). Behaviour and strength of FRP-strengthened RC structures: a state-of-the-art review. *Proceedings of the Institution of Civil Engineers – Structures and Buildings*, 156(SB1), 51–62.

Teng, J.G., Yu, T. and Wong, Y.L. (2004). Behaviour of hybrid FRP-concrete-steel double-skin tubular columns, *Proceedings, 2nd International Conference on FRP Composites in Civil Engineering*, Adelaide, Australia, 8–10 December 2004.

Usami, T. and Ge, H.B. (2000). Failure predictions of thin-walled steel structures under cyclic loading. *Proceedings, 7th International Symposium on Structural Failure and Plasticity (IMPLAST 2000)*, 4–6 October, Melbourne, Australia, 43–52.

Van Den Einde, L., Zhao, L. and Seible, F. (2003). Use of FRP composites in civil structural applications. *Construction and Building Materials*, 17(6&7), 389–403.

Xiao, Y. (2004). Application of FRP composites in concrete columns. *Advances in Structural Engineering*, 7(4), 335–341.

Concrete structures reinforced or prestressed with FRP

FRP Composites in Civil Engineering – CICE 2004 – Seracino (ed)
© 2005 Taylor & Francis Group, London, ISBN 90 5809 638 6

Modelling of arching action in FRP reinforced concrete

S.E. Taylor & D.R. Robinson
Queen's University, Belfast

ABSTRACT: It has been recognised for some time that laterally restrained slabs exhibit strengths far in excess of those predicted by most design codes. This enhancement in slab strength is due to Compressive Membrane Action (CMA). Previous research has also shown that CMA has a beneficial influence on the service behaviour of laterally restrained slabs. Therefore, by utilising the benefits of new reinforcing materials, such as FRPs, in combination with CMA, it should be possible to produce more economic and durable concrete slabs. This paper presents the results of NLFEA modelling of arching action concrete slabs reinforced with either steel or Glass Fibre Reinforced Polymer (GFRP) bars.

1 INTRODUCTION

In the past 30 years it has become increasingly evident that corrosion of reinforcement due to the effects of de-icing salts has been one of the major factors in the deterioration of reinforced concrete bridge decks. One solution to the corrosion problem is the use of alternative materials to steel reinforcement that do not corrode, such as Fibre Reinforced Polymer (FRP). The majority of recent research using FRP reinforcement has concentrated on simply supported slabs (e.g. ACI Committee 440, 2001; Farreira et al, 2001 and Alsayed et al, 2000). By taking advantage of CMA in laterally restrained slabs such as those in bridge decks, it is possible to reduce the dependency of the slab on reinforcement. Developments in Canada of a novel reinforcing system (Mufti and Newhook, 1998) have shown that the in-plane restraint to the slab, provided by external steel 'reinforcement' had a beneficial effect on both the serviceability and the cost of the deck slab. More recent research in Canada (Mufti et al, 2002) has investigated the use of carbon fibre reinforced polymers to replace conventional reinforcement. However, the Canadian system is not applicable to decks with concrete beams which tend to be significantly more popular in the UK and Europe.

This research uses previous laboratory test results (Mullin and Taylor, 2003) on six reinforced concrete slab strips with both steel and Glass Fibre Reinforced Polymer (GFRP) reinforcement. The variables were the boundary conditions, reinforcement type and concrete strength. A primary objective of the numerical modelling was to develop suitable modelling strategies to enable reliable and predictive estimates of the strength of laterally restrained concrete slabs reinforced with FRP. Slab deflections and reinforcing bar strains were used to correlate the numerical models with experimental data at both service and ultimate load levels. A correlated finite element model will complement the test data by providing a more complete understanding of the load transfer mechanism occurring in laterally restrained slabs.

Following development of an appropriate modelling strategy, and correlated numerical models, a second objective of the numerical modelling element was to extend the experimental data by consideration of the relative sensitivities of the slabs to various variables. In particular, the external lateral restraint stiffness, as this has shown to be more critical to the service and ultimate behaviour of the slab than the type of reinforcement used i.e. steel or GFRP. In the experimental slabs it is comparatively complex to vary the degree of the external lateral restraint.

2 BACKGROUND TO ARCHING ACTION

The arching phenomenon occurs in concrete due to the significant difference between its tensile and compressive strengths. The weak strength in tension causes cracking due to the application of load. This shifts the neutral axis towards the compression face. If the edges of the slab are restrained by a stiff boundary, internal arching action or Compressive Membrane Action is induced as the slab deflects (Fig. 1). This enhances the flexural capacity of the slab. The fraction of the load that is carried by arching action is dependent upon several variables such as the degree of external restraint, the concrete compressive strength and the span to depth ratio. It has been shown that the arching effect is relatively greater in slabs with lower reinforcement percentage, low span to depth ratio and a high

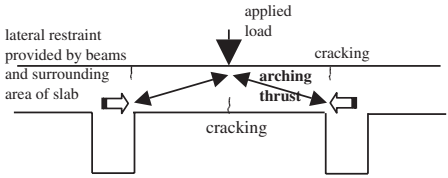

Figure 1. Compressive membrane action.

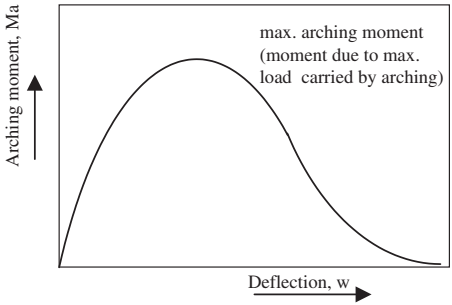

Figure 2. McDowell et al's idealised mode of action for restrained masonry strips.

degree of lateral restraint. That is, in comparison to the flexural or yield line predicted ultimate strengths which do not consider membrane effects.

Rankin & Long (1997) first developed a method for assessing the strength of laterally restrained slab strips as part of their rational approach to predicting the enhanced punching strength of slab and column specimens. They extended the theory of McDowell, McKee and Sevin (1956) which focused on the geometry of deformation of laterally restrained masonry walls. The idealised mode of action is depicted in Figure 2.

The similarities in the material properties of masonry and concrete provided a justifiable basis for the extension of their theory to restrained reinforced concrete slab strips. Although McDowell et al (1956) had ascertained the various stress-strain responses over the full range of deformation and material states, only two were considered applicable to the arching strength in RC slabs, that is, the elastic and the elastic-plastic state.

A previous paper (Taylor et al, 2001) outlined an arching theory developed by the author for one-way spanning laterally restrained slab strips with steel reinforcement. This predicted an enhanced flexural capacity by including an arching component and led to a subsequent investigation of GFRP in slab strips The arching theory was found to be valid for certain parameters.

Table 1. Experimental variables.

Slab no.	Concrete strength (N/mm^2)	Reinforcement		Boundary conditions
S-40-SS	39.7	Steel	0.5% centre	S/S
S-40-LR	41.0	Steel	0.5% centre	F/E + L/R
S-70-LR	85.0	Steel	0.5% centre	F/E + L/R
G-40-SS	39.9	GFRP	0.5% centre	S/S
G-40-LR	38.6	GFRP	0.5% centre	F/E + L/R
G-70-LR	67.9	GFRP	0.5% centre	F/E + L/R

GFRP = glass fibre reinforced polymer.
F/E = fixed end.
L/R = laterally restrained.
S/S = simply supported.

The interaction of arching and flexure in a reinforced concrete element is complex. By using NLFEA and correlating to known test result it should be possible to provide a means of assessing arching action in slabs with many variations. This has large potential as a tool for design where enhanced strength under arching action can be recognised.

3 EXPERIMENTAL PROGRAMME

3.1 *Test slabs*

Six one-way spanning slabs with varying reinforcement type and slab boundary conditions were tested (Table 1). Previous work by Taylor (2003) found that when lateral restraint was provided, the slabs could be efficiently reinforced with the bars located centrally. All the slabs were detailed with centre reinforcement.

A line load was applied at midspan of each test slab (Fig. 3). A steel frame used in previous tests at Queen's University provided restraint (Ruddle, 1989). Electronic displacement transducers were located directly below the position of the knife-edge load, 25 mm in from the side faces of the slab. Strain gauges were also mounted on each of the reinforcing bars at various locations. The test slabs were loaded incrementally up to failure and the development of cracking was monitored.

3.2 *Test results*

Control samples were taken and the reinforcement types are compared in Figure 4. The stress-strain characteristics for the two reinforcement types highlights the difference in the elastic modulus of the two reinforcement types although the strengths were of a similar order.

In the simply supported slab the material properties of the reinforcement were the overriding criteria for

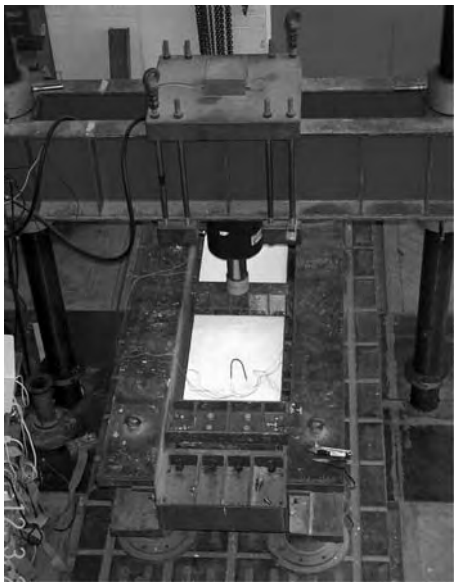

Figure 3. Test slabs set-up.

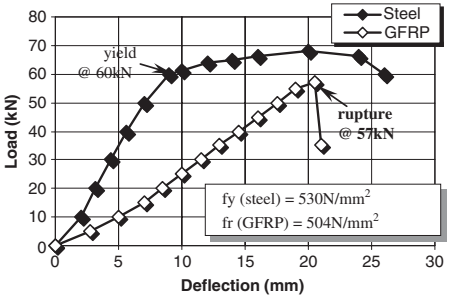

Figure 4. Material strengths.

the service behaviour and the ultimate capacity of the slab. The strain results also showed that the yield and rupture strains of the reinforcement had been reached.

However, for the laterally restrained slabs, the concrete material properties had a far greater influence compared to the simply supported slabs. It can be seen from Table 2 that the laterally restrained GFRP slabs had strengths similar to, or in excess of, the laterally restrained steel slabs. Additionally the deflections were similar to, or lower, than the equivalent steel reinforced slab. This is in contrast to the majority of reported results for the service behaviour of FRP reinforced slabs and is due to the beneficial influence of arching action.

Table 2. Experimental results.

Slab no.	Concrete strength (N/mm^2)	Failure load (kN)	Deflection @failure (mm)	Failure mode
S-40-SS	39.7	37.4	22	Steel yielding
S-40-LR	41.0	129.8	22	Crushing/ bending
S-70-LR	85.0	210	30	Crushing/ bending
G-40-SS	39.9	33	28	Crushing
G-40-LR	38.6	145	20	Crushing
G-70-LR	67.9	200	21	Crushing

GFRP = glass fibre reinforced polymer.
F/E = fixed end.
L/R = laterally restrained.
S/S = simply supported.

4 NLFEA MODEL

4.1 *Introduction*

The focus of this research was to attempt to use NLFEA to model the arching effect in both steel and FRP reinforced slabs. As a result NLFEA could be used to optimise the design of such slabs. This will ultimately lead to a more cost effective and sustainable solution for laterally restrained concrete slabs. The 'Abaqus' NLFEA package was chosen on the basis of previous work by the Author and due to the new enhanced models for reinforced concrete. The solution approach is similar to other packages and uses the Newton Rahpson method for solving non-linear equations. However this has been enhanced by Rik's procedure to aid convergence with softening materials. Other options have been tested but the detailed findings are not presented in this paper.

In addition to the above implicit approach the Abaqus package has extensive facilities for solving dynamic problems by the use of explicit algorithms. The explicit method uses very small load increments which require significantly less computation than the alternative implicit method. Although the explicit method was developed for dynamic problems, it can be applied to static problems if the inertia effects are minimised.

4.2 *Model specification*

The basic geometry of the slab is illustrated in Figure 5. As the strength of a laterally retained slab is more dependent upon the concrete compressive strength the reinforcement was positioned in the centre. The same reinforcing bar acts to resist both the hogging and sagging flexural moments giving a 50% saving in

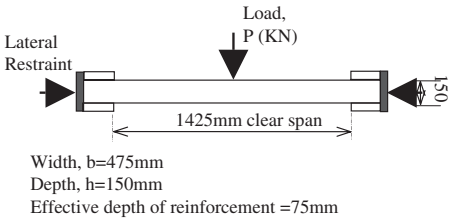

Figure 5. Slab test load arrangement for partial F/E & finite L/R boundary conditions.

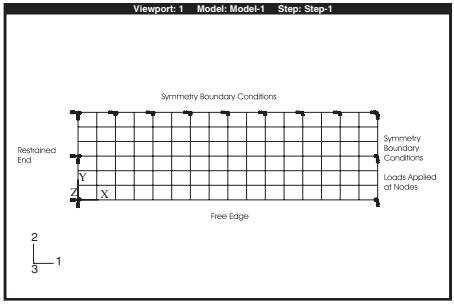

Figure 6. NLFEA model geometry.

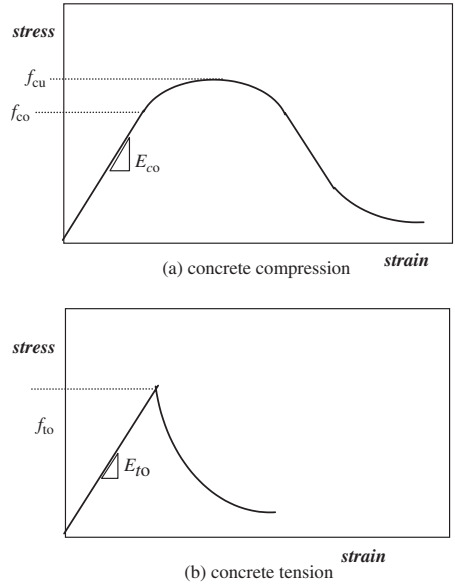

Figure 7. Response of concrete to uniaxial loading in compression and tension.

the material costs. This has been modelled by four node shell elements with integration points through the depth and length of the element. The use of shell elements allowed the physical behaviour throughout the thickness of the slab to be modelled without the thickness being geometrically defined. This provided a computationally efficient model with allowance for slab geometrical variations.

The actual support conditions were as indicated in Figure 5, that is, partially fixed end with finite lateral restraint or simply supported with no lateral restraint. The boundary conditions were modelled as either simply support, simply supported with lateral restraint or fully fixed end. On going research to establish a model with end conditions to represent restraint with finite stiffness is currently being undertaken and it is intended to present these findings at the conference. The model was set up with shell elements and a mesh as indicated in Figure 6.

4.3 *Material properties*

For a simply supported slab the material properties of the reinforcement will be the overriding criteria for the service behaviour and the ultimate capacity of the slab. The amount of cracking in the GFRP simply supported slabs was far more extensive than in the equivalent steel reinforced slab. It is essential to model the characteristics of the materials under service loads as this could be the overriding design consideration, particularly in the simply supported GFRP reinforced slabs.

In a laterally restrained slab the concrete material properties have a far greater influence on the ultimate capacity compared to the simply supported slab. It is therefore essential to model the concrete material properties accurately. The damaged concrete plasticity model was chosen in which the uniaxial stress-strain curves were converted into stress versus plastic-strain curves based upon the user defined tension and compression strengths (Figure 7). The elasticity of the concrete is changed according to the level of cracking or the level of plasticity that has been developed.

Abaqus gives the stress-strain relationship for the three-dimension multi-axial condition by using a scalar damage plasticity equation:

$$\text{stress} = (1 - d)D_o:(\varepsilon - \varepsilon^{pl}) \quad (1)$$

where D_o is the initial undamaged elasticity.

The damaged elasticity was implemented in the package to allow for cyclic loading, although cyclic loading has not been presented here, it is the facility that will be needed for future work. More relevant for this work, the potential and yield functions have been upgraded in this model allowing for a non-associated

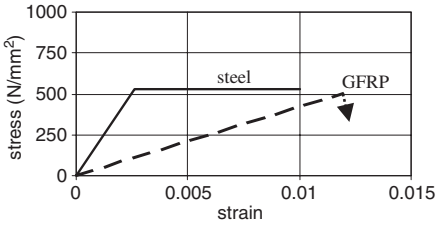

Figure 8. Idealised reinforcement material properties for NLFEA input.

flow model that is more representative of concrete. In addition the damaged model is available in both the implicit and explicit versions of the package.

The material properties of the reinforcing bars used in the NLFEA model were based upon the experimental control samples. The elastic modulus for the steel and GFRP bars was 205 kN/mm^2 and 42 kN/mm^2 respectively as indicated in Figure 8. The reinforcement was defined as one-dimensional rods in a single layer and considered independently to the surrounding concrete.

The model assumes the two main failure mechanisms are compressive crushing and/or tensile cracking. The failure surface is controlled by hardening variables linked to the tensile and compressive strains. The post failure mechanism is modelled using concrete tension stiffening with user defined strain softening behaviour for cracked concrete which is based upon the cracking strain or stress.

Tension stiffening is dependent upon the bond between the reinforcement and the concrete and requires some calibration for these models the actual failure stresses, for example, 1.8 N/mm^2 for model S-40-SS, from the measured indirect tensile stresses were used. A linear loss of strength was assumed for post cracking behaviour.

Additionally, the degree of cracking from the NLFEA can be dependent upon the fineness of the mesh adopted. That is, there may be some mesh sensitivity particularly where there is high level of cracking such as the simply supported GFRP reinforced slabs.

4.4 *Yield function*

The NLFEA model is based upon the yield function of Lublier et al (1989) with modification by Lee and Fenves (1998) to account for differing strengths under tension and compression. The yield function is governed by the material hardening variables and is described by Lee and Fenves (1998) in terms of the effective stresses by:

$$F = [1/(1-a)]\{q - 3\alpha p + \beta(\varepsilon^{p})(\sigma_{max}) - \gamma(\sigma_{max}\} - \sigma_c(\varepsilon_c^{pl}) = 0 \quad (2)$$

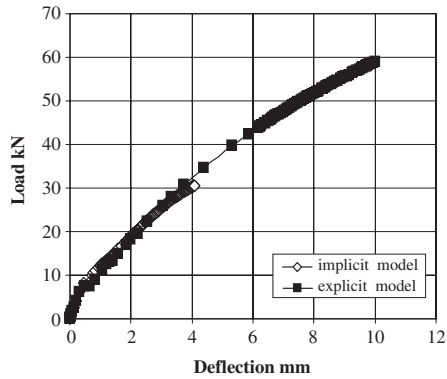

Figure 9. Comparison between the smeared creak and the damaged plasticity model for model S-40-SS.

Convergence problems associated with the implicit analysis are overcome in the explicit method. Figure 9 shows the problems with convergence under the implicit method which failed to converge beyond an applied load of 30 kN compared to the same analysis under the explicit method which went to beyond the maximum applied load value.

The implicit method requires the systems of nonlinear equations to be satisfied at the end of each load increment. This is difficult to achieve in the extensively cracked regions throughout the slab. The explicit method does not require the equations to be satisfied at each load increment but relies on the selection of the appropriate load increment. This selection is based on element size and wave velocity.

The explicit method allows the convergence difficulties to be eliminated but there is greater speculation regarding the integrity of the solution. As a safe guard the solution obtained by the implicit and explicit methods are compared. It can be seen that the two analyses give virtually the same results up to an applied load of 30 kN.

5 COMPARISON WITH EXPERIMENTAL RESULTS

5.1 *Load–deflection characteristics*

The results for the steel reinforced simply supported, simply supported with lateral restraint or fully fixed end NLFEA analyses under the explicit or damaged model are compared to the experimental results for the 40 N/mm^3 concrete compressive strength in Figure 10. The simply supported model showed a close relationship with the actual load-deflection results although

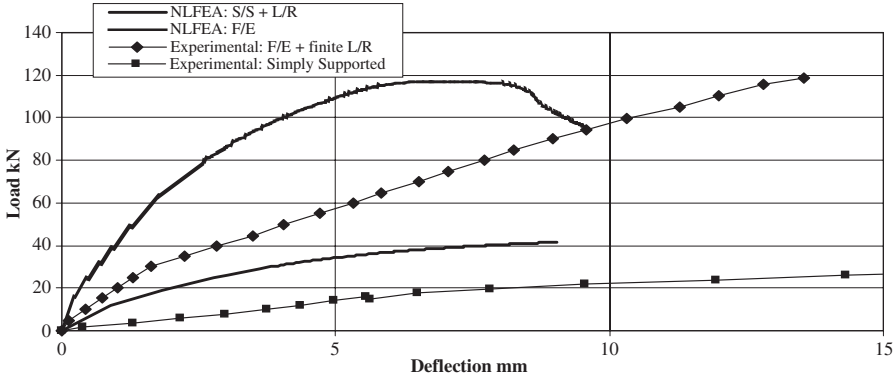

Figure 10. Comparison of 40 N/mm^2 steel reinforced models – NLFEA explicit model – with experimental results.

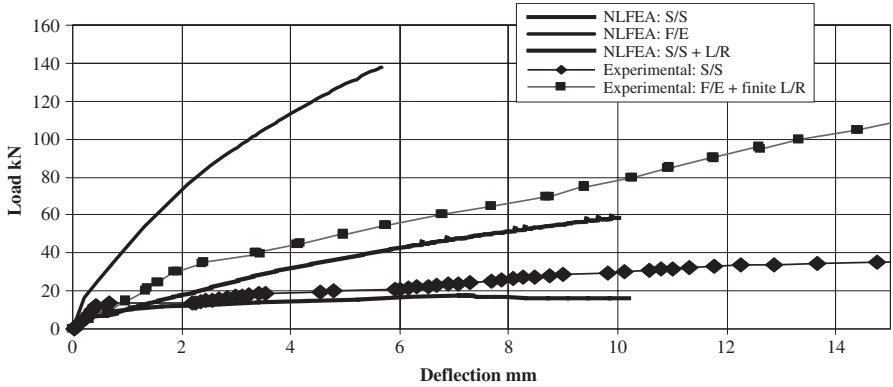

Figure 11. Comparison of 40 N/mm^2 GFRP reinforced models – NLFEA explicit model – with experimental results.

it tended to be slightly conservative in predicting the failure load of the slab.

The experimental results lie between the results for the simply supported with lateral restraint and the fully fixed end NLFEA analyses. The ratio of the external restraint stiffness to that of the slab is 0.41. From previous research by the authors, this would equate to approximately 50% of the arching capacity that would be present in an infinitely rigidly restrained slab. As discussed earlier, one aim of this research is to model the effect of varying external lateral restraint stiffness and this is on going at the time of writing this paper.

The degree of arcing action could be modelled by applying spring supports representing the real external restraint stiffness. Previous work (Taylor et al, 2001) used an arching theory which uses the geometry of the section and an equivalent rigidly restrained arch to establish the contact area at the support. It is intended to use this as basis for establishing the restraint conditions in the NLFEA model.

The results for the GFRP reinforced simply supported with lateral restraint or fully fixed NLFEA analyses under the explicit or damaged model are compared to the experimental results for the 40 N/mm^3 concrete compressive strength Figure 11. The results underestimated the deflection in the GFRP reinforced slab and this is due to the rigid lateral restraint support conditions which will enhance the arching action and thus reduce the level of deflection at the midspan region.

6 DISCUSSION AND CONCLUSIONS

The results clearly showed that the load-defection characteristics of simply supported models were highly

dependent upon the reinforcement type. The low value of elastic modulus in the GFRP caused greater deflections at the same value of applied load compared to the equivalent steel reinforced slab although the failure loads were of a similar order. In the steel reinforced model the steel had reached yield strain prior to reaching the maximum predicted ultimate load as indicated by the experimental results.

However, when external lateral restraint is introduced the failure mechanism is one of compressive failure and it is the concrete compressive strength that governed the failure load. This was reflected in the NLFEA analysis. The GFRP and steel reinforced model with lateral restraint had similar predicted load-deflection characteristics as the yield function was due to a compressive failure. The rupture strain in the NLFEA with GFRP had not been reached at maximum predicted load in the results as indicated by the experimental strain results. Similarly the NLFEA with steel reinforced model had not reached yield strain prior to the maximum predicted ultimate load.

7 FUTURE RESEARCH

This is on-going research and clearly there is much scope for improving the NLFEA for less than rigid external lateral restraint. For slabs where arching action is present, modelling the external lateral restraint stiffness and contact areas at the support and midspan regions is principal to achieving a realistic model. It should then be easier to investigate the interaction of arching action and flexure within such slabs.

REFERENCES

ACI Committee 440. (2001), *ACI440.1R-01 – Guide for the design and construction of concrete reinforced with FRP bars*, American Concrete Institute, Detroit, USA, 2001.

Alsayed, S.H., Al-Salloum, Y.A. and Almusallam, T.H. (2000) Performance of glass fiber reinforced plastic bar as a reinforcing material for concrete structures, *Composites:* Part B, V.31, 2000: 555–567.

Farreira, A.J.M., Camanho, P.P., Marques, A.T. and Fernandes, A.A. (2001) Modelling of concrete beams reinforced with FRP re-bars, *Composite Structures*, V.53, 1, July 2001: 815–823.

Hassan, T., Abdelrahman, A., Tadros, G. and Rizkalla, S. (2000) Fibre reinforced polymer reinforcing bars for bridge decks, *Canadian Journal of Civil Engineering*, V.27, 5, October 2000: 839–849.

Lee, J. and Fenves, L.G. (1998) Plastic-damage concrete model for earthquake analysis of dams, *Earthquake Engineering & Structural Dynamics*, V.27, 9, Sep 1998: 937–956.

Lubliner Oliver, J., Oller, S. and Onate, E. (1989) Plastic-damage model for concrete, *International Journal of Solids and Structures*, V.25, 3, 1989: 299–326.

McDowell, E.L., McKee, K.E. and Sevin, E. (1956) Arching action theory of restrained masonry walls, *ASCE Journal of Structural Engineering*, V.82, ST2, 1956: 915-1–915-18.

Mufti, A.A. and Newhook, J.P. (1998) Punching shear strength of restrained concrete bridge deck slabs, *ACI Structural Journal*, V.95, No.4, Jul–Aug 1998: 375–338.

Mufti, A.A., Labossiere, P., Neale and Kenneth, W. (2002) Recent bridge applications of FRPs in Canada, *Structural Engineering International, Journal of the International Association for Bridge and Structural Engineering (IABSE)*, V.12, No.2, 2002: 96–98.

Mullin, B. and Taylor, S.E. (2003) Arching action in concrete slabs with novel reinforcement *The Structural Engineer*, V.81, 2, 2003: 15–18.

Rankin, G.I.B. and Long, A.E. (1997) Arching action strength enhancement in laterally restrained slabs, *ICE Proceedings – Structures and Buildings*, 122, Nov 1997: 461–467.

Ruddle, M. (1989) *Arching action and the ultimate capacity of reinforced concrete beams*, PhD thesis, Queen's University of Belfast, Northern Ireland, 1989.

Taylor, S.E., Rankin, G.I.B. and Cleland, D.J. (2001) Arching action in high strength concrete slabs, *Proceedings of the Institution of Civil Engineer – Structures and Buildings,* V.146, Issue 4, Nov. 2001: 353–362.

Taylor, S.E., Rankin, G.I.B. and Cleland, D.J. (2003) High performance concrete bridge deck slabs, *Proceedings of the Institution of Civil Engineers, Bridge Engineering*, V.156, Issue BE2, June 2003: 81–90.

FRP Composites in Civil Engineering – CICE 2004 – Seracino (ed)

Fatigue behaviour of second generation of steel-free concrete bridge deck slab

A.H. Memon
Ph.D. Candidate, Department of Civil Engineering, University of Manitoba, Winnipeg, Manitoba, Canada

A.A. Mufti
Professor of Civil Engineering and President of ISIS Canada, University of Manitoba, Winnipeg, Manitoba, Canada

ABSTRACT: This paper describes the fatigue behaviour of the cast-in-situ full-scale model of a bridge deck slab. Although cast monolithically, this deck slab was divided into three segments (A, B and C). Segment A was reinforced according to the conventional design with steel reinforcement. Segments B and C were reinforced internally with a CFRP crack control grid and a GFRP crack control grid respectively and externally with steel straps. This hybrid CFRP/GFRP and steel straps design is called the second generation of the steel-free concrete bridge deck slab. This hybrid system reduced the development of longitudinal crack width and eliminated corrosion completely from the concrete bridge deck slabs. All three segments were tested under 25 ton cyclic loading to investigate fatigue behaviour. The performances of all three segments were measured through a number of sensors, including: linear variable displacement transducers (LVDTs), pi-gauges and strain gauges. The findings are reported in this paper.

1 INTRODUCTION

This paper describes a study to replace the steel reinforcement completely from the deck slab with hybrid internal either CFRP or GFRP and external steel straps as an alternative solution to increase the service life of bridges. The decline in North American infrastructure has never been more prevalent than it is today. In particular, the highway system and its bridges have been adversely affected by age and weathering over the past two decades. Since the majority of highway bridges have reinforced concrete decks supported on steel or concrete girders, concrete has been the choice for highway bridge decks for many years. Over the years, the weather has taken its toll on these reinforced concrete decks. Rainwater and de-icing chemicals applied to roadway surfaces during the winter months have seeped through many concrete decks and caused corrosion of the reinforcing steel. To avoid the corrosion of steel reinforcement Mufti et al. (1993), proposed the concept of a steel-free concrete deck slab entirely free of any internal steel reinforcement. This concept has been applied to four highway bridges and one forestry bridge in Canada (Bakht and Mufti (1998)).

During the lifetime of a bridge deck slab, it is subjected to a very large number of wheels of different magnitudes. By contrast, the laboratory investigation of the fatigue resistance of a bridge deck slab is usually conducted under wheel loads of constant magnitude. The design codes (AASHTO (1998), and CHBDC (2000)) are not explicit with respect to the design of fatigue loads on deck slabs. An analytical method was developed by Mufti et al. (2002) for establishing the equivalence between fatigue test loads and a given population of wheel loads. While the method is general enough to be applicable to all deck slabs of concrete construction, it was developed especially for steel-free concrete deck slabs Mufti et al. (1993) and Bakht and Mufti (1998), which are relatively new and do not have a long track record of field performance.

The performance comparison of all three segments under a 25 ton cyclic load is reported in this paper, while performance under a 60 ton cyclic load will be published in the Ph.D. dissertation of Memon (2004). Observation showed that Segment C with a GFRP crack control grid had the highest fatigue resistance of 420,682 cycles under a 60 ton cyclic load followed by Segment B with CFRP crack control grid, which had a fatigue resistance of 198,863 cycles under a 60 ton cyclic load and Segment A with steel reinforcement had the lowest fatigue resistance of 23,162 cycles under a 60 ton cyclic load Memon (2004).

2 CONCEPT OF STEEL-FREE DECK SLAB

In a steel-free concrete bridge deck slab, the steel straps are placed at the top flange of the girder providing

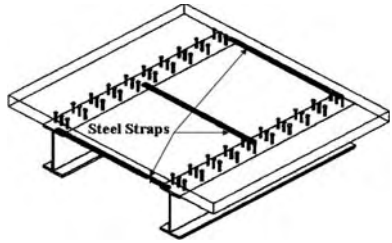

Figure 1(a). Steel-free concrete bridge deck slab.

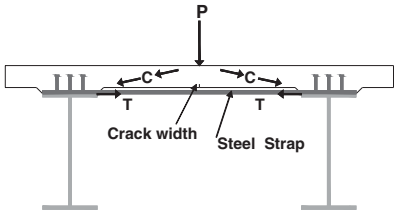

Figure 1(b). Cross-section of a steel-free concrete bridge deck slab.

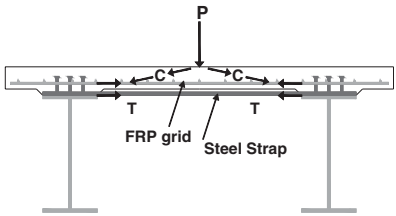

Figure 2. Cross-section of a second generation steel-free concrete bridge deck slab.

lateral restraint, which develops compressive membrane force in the deck slab, as shown in Figure 1(a). In operation, as the bridge deck withstands the stress of traffic loads, the deck will deform and stresses will develop. Eventually the loads will reach a magnitude where the tensile stresses will cause the concrete to crack. Once the bridge deck cracks, it resists traffic loads through arching action. Such arching action is characterized by compressive membrane action, as shown in Figure 1(b), and failure by punching shear. This concept led to the world's first steel-free concrete bridge deck slab over the Salmon River on the Trans-Canada Highway in Nova Scotia, which was opened to traffic in December 1995 (Mufti et al. 1999). Six months later, approximately 1 mm wide longitudinal cracks were observed on the soffit of the deck slab, roughly midway between the girders. Periodical visual inspection has shown that the widths and pattern of the cracks have not changed significantly during the past eight years. Since these cracks are aesthetically unpleasing and public sector engineers are not comfortable with them, a number of methods for controlling the widths and distribution of cracks in steel-free concrete deck slabs are being investigated experimentally. One of these methods involves the use of a FRP (fibre reinforced polymers) crack control grid of either CFRP or GFRP near the bottom surface of the slab, as shown in Figure 2.

3 THEORETICAL APPROACH

Many theoretical approaches (Kinnunen and Nylander (1960); Hewitt and Batchelor (1975); Marzouk and Hussein (1991); and Mufti and Newhook (1998)) have been developed for predicting the punching strength in reinforced concrete deck slabs. The models generally relied on stresses developed in the steel reinforcement as a key parameter. Therefore, it became necessary to develop a model that could predict the behaviour of laterally restrained deck slabs containing no internal reinforcement. A finite element model study done by Wegner and Mufti (1994) was very successful in providing guidance for further experimental work; however, the model was found to be very complex and sensitive to modelling parameters. The model developed by Kinnunen and Nylander (1960) and enhanced by Hewitt and Batchelor (1975) to include lateral restraint conditions was adapted for steel-free concrete deck slab conditions. The full mathematical formulation of this model can be found elsewhere, Newhook et al. (1995) and Newhook (1997); only the basic elements of the model are reviewed here.

The important components of the system geometry are the depth of the concrete deck, the spacing of the support girders, the spacing and cross-sectional area of the transverse straps, and the dimensions of the loaded area. The essential parameters are the modulus of the transverse strap, area of strap, the yield strain of the straps, the compressive strength of the concrete, and the influence of three dimensional stresses on the compressive strength of concrete, girder spacing and thickness of deck slab.

Newhook (1997) and Newhook and Mufti (1998) developed a computer program called the PUNCH Program to predict the ultimate capacity of restrained deck slabs under concentrated loads. A comparison of the theoretical and experimental work is presented in Mufti and Newhook (1998). The comparison reveals that the PUNCH Program can predict, with reasonable accuracy, the punching failure load of a restrained, fibre-reinforced concrete slab-on-girder bridge deck.

Khanna et al. (2000) reported the ultimate capacity of his model deck slab reinforced with steel and designed by an empirical design method similar to

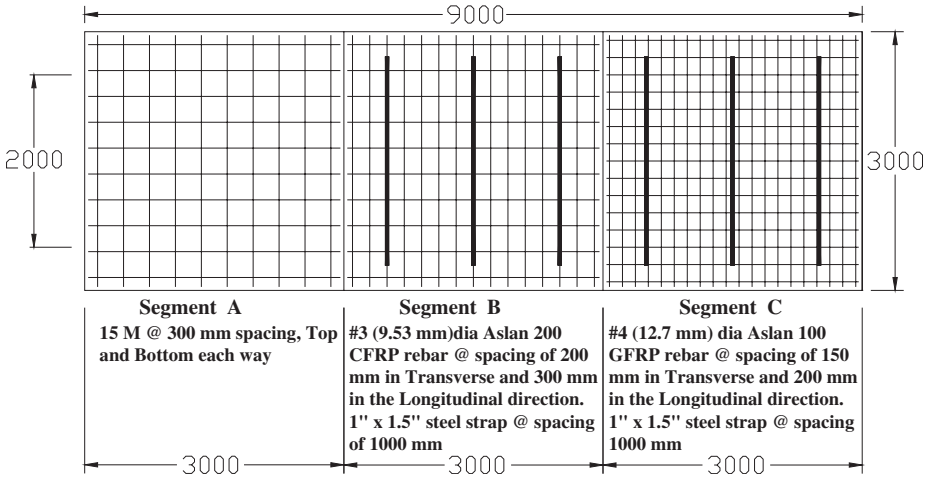

Figure 3(a). Schematically reinforcement detail of the deck slab.

Segment A. When the experimental results were compared with the theoretical model PUNCH Program developed by Newhook and Mufti (1998), it showed very good agreement between the results Mufti et al. (1999). Furthermore, the experimental and theoretical results of Segment A were comparable with the nonlinear finite element program (ANACAP) Mufti et al. (2001). Segments B and C were designed according to the provisions of CHBDC (2000) Section 16 and analysed by PUNCH Program. Therefore all three segments A, B and C were designed with an almost equal ultimate capacity so that a direct comparison between the segments under fatigue could be made.

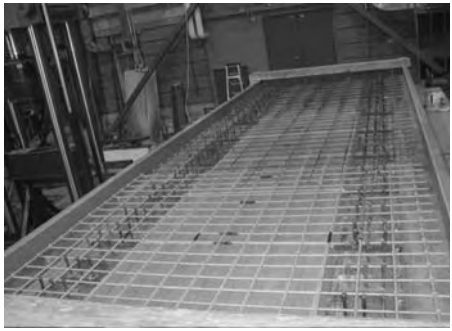

Figure 3(b). Reinforcement detail of the deck slab and formwork.

4 EXPERIMENTAL PROGRAM

4.1 *Details of bridge deck slab*

The full-scale model of the bridge deck slab consisted of three segments of 3000 mm each with overall dimensions of 9000 × 3000 mm and a slab thickness of 175 mm. The bridge deck slab was tested under cyclic loading to investigate fatigue behavior as shown schematically and before casting in Figures 3(a) & 3(b).

The deck slab was cast-in-situ compositely on two steel girders at a center-to-center spacing of 2000 mm through the use of shear connectors and had a 500 mm long cantilever overhang beyond the center of the each girder. In the longitudinal direction (i.e.: parallel to the girders), the deck slab was 9000 mm long. Although cast monolithically, the slab was conceptually divided into three segments, as shown in Figure 3(a). Segment A of the bridge deck slab was reinforced with steel reinforcement by empirical design method according to the CHBDC (2000). Segment A contained two layers of steel reinforcement with 15 M bars spaced at 300 mm in each direction in each layer, providing total reinforcement of 1.2%, as shown in Figures 4(a) & 4(b).

Segment B of the bridge deck slab was reinforced with hybrid CFRP crack control grid internally and externally with steel straps. CFRP bars with a modulus of elasticity of 121 GPa and ultimate tensile strength of 1310 MPa were used. Segment B contained one CFRP bar with a diameter of 9.53 mm (#3) spaced at 200 mm in the transverse direction, providing a reinforcing ratio of 0.19%, and one 9.53 mm (#3) spaced at 300 mm in the longitudinal direction, providing a reinforcing ratio of 0.13% and a steel

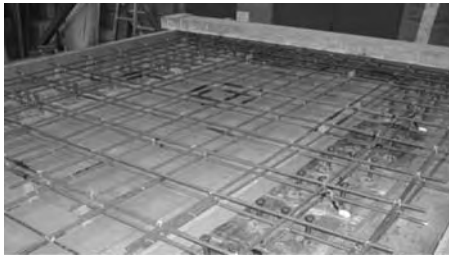

Figure 4(a). Reinforcement detail of Segment A.

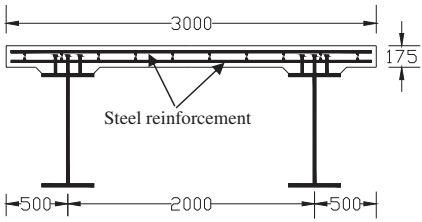

Figure 4(b). Cross-section of Segment A

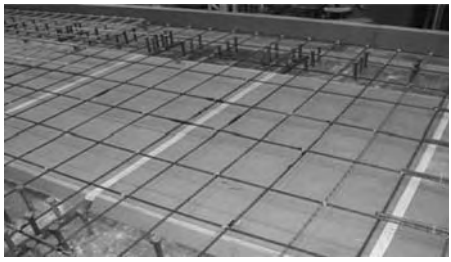

Figure 5(a). Reinforcement detail of Segment B.

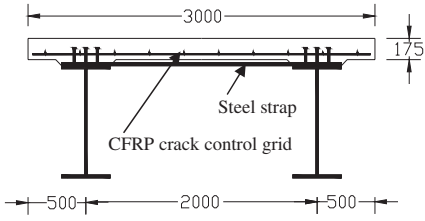

Figure 5(b). Cross-section of Segment B.

strap having dimensions 25.4 × 38.1 mm (1″ × 1.5″) spaced at 1000 mm in the transverse direction only, providing a reinforcing ratio of 0.55%, as shown in Figures 5(a) & 5(b).

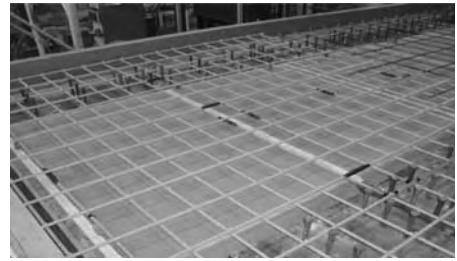

Figure 6(a). Reinforcement detail of Segment C.

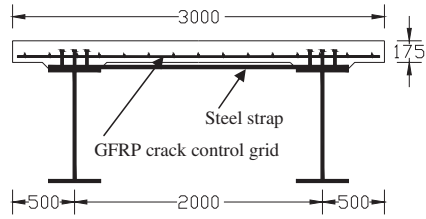

Figure 6(b). Cross-section of Segment C.

Segment C of the bridge deck slab was reinforced with hybrid GFRP crack control grid internally and externally with steel strap. The GFRP bars with a modulus of elasticity of 40.8 GPa and the ultimate tensile strength of 690 MPa were used. Segment C contained one GFRP bar with a diameter of 12.7 mm (#4) spaced at 150 mm in the transverse direction, providing a reinforcing ratio of 0.48%, and one 12.7 mm (#4) spaced at 200 mm in the longitudinal direction, providing a reinforcing ratio of 0.36% and steel strap having dimensions of 25.4 × 38.1 mm (1″ × 1.5″) spaced at 1000 mm in the transverse direction only, providing a reinforcing ratio of 0.55%, as shown in Figures 6(a) & 6(b).

A steel-free concrete deck slab on a girder bridge derives its strength from an arching action, which is harnessed by both the longitudinal and transverse confinement system. To control the temperature and thermal cracking, concrete is mixed with 0.3% chopped polypropylene fibers.

4.2 *Instrumentation*

To investigate performance under cyclic loading, each segment of a bridge deck slab was monitored through a number of sensors including: linear variable displacement transducers (LVDTs), strain gauges, and pi-gauges. Vertical deflection of each segment was measured by LVDTs. To monitor the internal performance of each segment of the bridge deck slab an electrical resistance strain gauges were mounted on

Figure 7(a). Typical bottom view of Segments B & C and instrumentation.

Figure 7(b). Bottom view of Segment A and instrumentation.

few bars of steel reinforcement, CFRP and GFRP. The instrumented bars were then placed under the cyclic load and away from it in transverse and longitudinal directions, as shown in Figures 4(a), 5(a) & 6(a). In order to monitor the performance of the steel straps, an electrical resistance strain gauge was mounted on the middle of each strap, as shown in Figure 7(a). To monitor the longitudinal crack width of each segment of a bridge deck slab, pi-gauges were used and mounted on the bottom surface of each segment of the bridge deck slab under the load, as shown in Figures 7(a) & 7(b).

4.3 *Testing procedure*

To understand the fatigue behaviour of a cast in situ concrete bridge deck slab, a cyclic test was conducted at a 25 ton load level. For this dynamic test, the load was applied at 1 Hz frequency and the data were recorded through Data Acquisition System. The deck slab was tested under a central rectangular patch load measuring 610 × 305 mm, with the later dimension being in the longitudinal direction of the deck slab. The typical test setup for each segment is shown in Figure 8.

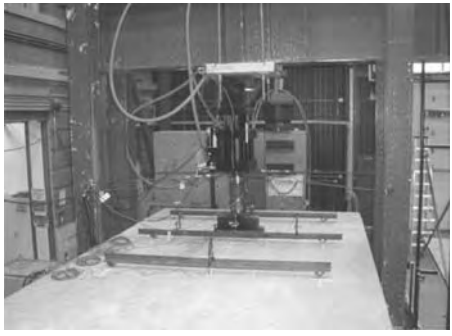

Figure 8. Typical test setup and instrumentation.

5 WHEEL LOAD DATA

Commentary Clause C3.6.1.4.2 of the AASHTO (1998), notes that the Average Daily Traffic (ADT) in a lane is physically limited to 20,000 vehicles and the maximum fraction of trucks in traffic is 0.20. Thus, the maximum number of trucks per day in one direction (*ADTT*) is 4000. When two lanes are available to trucks, the number of trucks per day in a single lane, averaged over the design life, ($ADTT_{SL}$) is found by multiplying *ADTT* by 0.85, giving 3400. It is assumed that the average number of axles per truck is four (a conservative assumption), and that the life of a bridge is 75 years. Therefore the maximum number of axles that a bridge deck would experience on one lane during its lifetime is 372 million.

Matsui and Tei (2001) described the maximum axle load observed in Japan as 32 ton, or 314 kN. The close correspondence between the expected annual maximum axle load in Canada Mufti et al. (2002), and the maximum observed axle load in Japan indicates a similarity between the axle loads in the two countries. Matsui and Tei (2001), also provided a histogram of wheel loads observed on 12 bridges in Japan. In the absence of data for Canadian trucks, their histogram was used to construct the wheel load statistics, as shown in Table 1. Table 1 also includes the numbers of wheels of various magnitudes corresponding to a total of 372 million wheel passes. Any fatigue test load on a bridge deck slab should cause the same damage in the slab as the damage caused by all the wheel loads included in this or any similar table. An analytical method for estimating equivalent number of cycles at two load levels, as shown in Equation 1, was

Table 1. Statistics of maximum number of wheel loads in a lane during a lifetime of 75 years.

Wheel load (ton)	Percentage of total (%)	No. of wheels (million)
1	21.25	79.05
2	32.06	119.3
3	21.61	80.39
4	12.60	46.87
5	6.48	24.11
6	3.24	12.05
7	1.44	5.37
8	0.54	2.01
9	0.32	1.19
10	0.18	0.67
11	0.11	0.41
12	0.07	0.26
13	0.04	0.15
14	0.02	0.07
15	0.01	0.04
16	0.003	0.01

Table 2. Lifetime number of cycles equivalent to 25 ton wheel load.

Load (P_1) (ton)	No. of cycles (n_1) @ P_1 (million)	Load (P_2) (ton)	No. of cycles (n_2) @ P_2 (million)
1	79.05	25	0.016
2	119.3	25	0.034
3	80.39	25	0.032
4	46.87	25	0.027
5	24.11	25	0.020
6	12.05	25	0.014
7	5.37	25	0.009
8	2.01	25	0.005
9	1.19	25	0.004
10	0.67	25	0.003
11	0.41	25	0.003
12	0.26	25	0.003
13	0.15	25	0.002
14	0.07	25	0.001
15	0.04	25	0.001
16	0.01	25	0.0004
Total no. of cycles (n_2) @ 25 ton			0.174

developed by Mufti et al. (2002) and it is valid for reinforced and steel-free concrete bridge deck slabs.

$$n_2 = n_1 e^{\left(\frac{P_1 - P_2}{P_s}\right)30} \quad (1)$$

where P_1 and P_2 are two different wheel loads; n_1 and n_2 are the corresponding number of passes of P_1 and P_2 respectively; while P_s is the static failure load.

The ultimate capacity of the deck slab can be predicted by using the Punch Program developed by Newhook and Mufti (1998). The reliability of this program is discussed in Mufti and Newhook (1998). According to the Punch Program, the ultimate capacity of each segment of a bridge deck slab is about 827 kN (84.4 ton).

Consider that a bridge deck slab has a static failure load (P_s) of 84.4 ton, while P_1, P_2 and n_1 are 1 ton, 25 ton and 79.1 million, respectively. By using Equation 1, n_2 will be 0.016 million, as shown in Table 2. From Table 2, it is clear that the maximum number of axles that a bridge deck would experience in one lane, during its lifetime, is 372 million. This includes the number of wheels of various magnitudes from 1 ton to 16 ton. The equivalent number of cycles at a 25 ton load level will be approximately 174,000 cycles.

6 RESULTS AND DISCUSSION

Test results show that under 25 ton cyclic loading, all three segments of a bridge deck slab completed one million cycles without significant damage. As mentioned earlier, during the lifetime of a bridge deck slab, it is subjected to about 372 million cycles of different magnitudes. By using the analytical approach, which was explained earlier, 372 million cycles are equivalent to 174,000 cycles at 25 ton cyclic load as shown in Table 2. This shows that all three segments of the bridge deck slab have much higher fatigue resistance than required.

Vertical deflection of all three segments of the bridge deck slab were measured by displacement transducers and the maximum deflection was found to be approximately 2 mm when completing one million cycles, as shown in Figure 9. It was also observed, for all three segments, the deflection was increasing with the increasing number of cycles.

In order to measure the internal and external response of each segment of a bridge deck slab, strain gauges were mounted on some of the steel, CFRP and GFRP bars as well as on the steel straps, and maximum response was measured under the applied load in transverse direction, as shown in Figure 10. From Figure 10, it is clear that all strain values are lower than 1200 micro-strain, therefore serviceability criteria were met. Since the serviceability limit for either CFRP or GFRP is 2000 micro-strain, based on the test results, it is suggested that there can be a reduction of up to 40% in the use of either CFRP crack control grid or GFRP crack control grid.

To see the effect of either CFRP or GFRP crack control grid on the growth of crack width, a longitudinal crack was measured with an increasing number of cycles under the applied load, as shown in Figure 11. From Figure 11, it can be seen that the maximum crack width for all three segments was

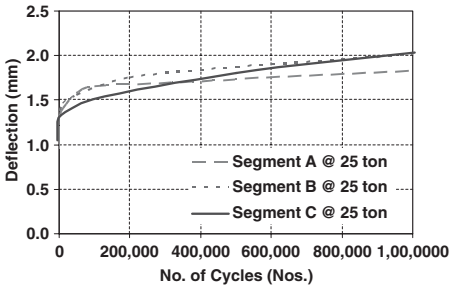

Figure 9. Deflection behaviour with increasing number of cycles.

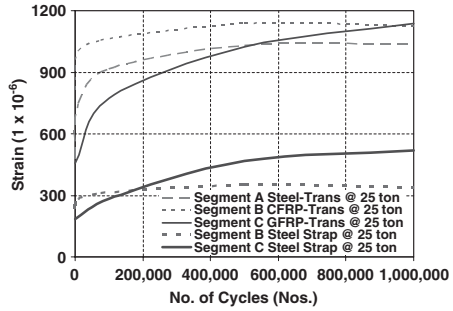

Figure 10. Strain behaviour with increasing number of cycles.

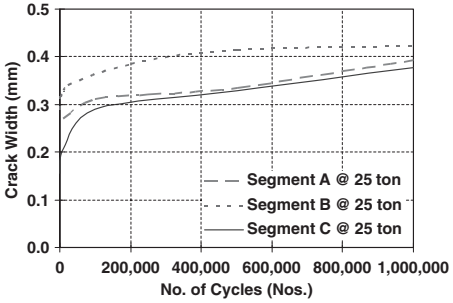

Figure 11. Crack width behaviour with increasing number of cycles.

approximately 0.4 mm, when completing one million cycles under 25 ton cyclic load. ACI Committee 440 (2001) reported that, for steel reinforced structures, the allowable crack width limits are 0.3 mm for exterior exposure and 0.4 mm for interior exposure. Since FRP rods are corrosion resistant, the maximum crack width limitation can be relaxed. However, excessive crack width is undesirable aesthetically as well as for other reasons including contribution to the damage or deterioration of structural concrete.

7 CONCLUSIONS

Based on the findings of this investigation, the following conclusions can be drawn:

(a) The presence of internal CFRP crack control grid or GFRP crack control grid and external steel straps in a bridge deck slab reduced the development of longitudinal crack width and eliminated corrosion completely.
(b) Experimental results suggested that the area of CFRP or GFRP can be reduced by up to 40%.
(c) Experimental results show that fatigue damage induced under 25 ton cyclic load is within permissible limits.
(d) Analytical results show that, during a bridge deck's lifetime, it is subjected to 372 million cycles of different magnitudes, which are equivalent to about 174,000 cycles under 25 ton cyclic wheel load.
(e) Experimental results showed that all three segments completed one million cycles under 25 ton cyclic load without significant damage, this suggested that all three segments have a fatigue resistance higher than required.
(f) Since GFRP is much cheaper than CFRP, internal GFRP crack control grid and external steel straps are the most economical solution to reduce the development of longitudinal crack width and eliminate corrosion. The first field application of this hybrid system was introduced in the Red River Bridge in Winnipeg, Manitoba, Canada in 2003.

ACKNOWLEDGEMENT

The financial assistance provided by ISIS Canada, a Network of Centres of Excellence, and the Cement Association of Canada are gratefully acknowledged. The authors are thankful to Dr. Baidar Bakht for providing the statistics on wheel loads. The GFRP bars (Aslan 100) and CFRP bars (Aslan 200) are manufactured by Hughes Brothers, Inc. USA. The authors are gratefully acknowledged Vector Construction Group for providing GFRP bars for this research. Special thanks to Moray Mcvey, Grant Whiteside and Liting Han for their assistance during fabrication and testing of the bridge deck slab and the administrative support provided by ISIS Canada.

REFERENCES

AASHTO, LRFD. 1998. Bridge Design Specifications. *American Association of State Highway and Transportation Officials*. Washington, D.C.

ACI 440.1R-01. 2001. Guide for the Design and Construction of Concrete Reinforced with FRP Bars. *Reported by ACI Committee 440.*

Bakht, B., and Mufti, A.A. 1998. Five Steel-Free Bridge Deck Slabs in Canada. *Journal of the International Association for Bridge and Structural Engineering (IABSE).* Vol. 8, No. 3, pp. 196–200.

CHBDC. 2000. Canadian Highway Bridge Design Code. *Canadian Standards Association International*. Toronto.

Hewitt, B.E., and Batchelor, B. 1975. Punching Shear Strength of Restrained Slabs. *ASCE, Journal of the Structural Division*. 101(STP9), pp. 1837–1853.

Khanna, O.S., Mufti, A.A., and Bakht, B. 2000. Experimental Investigation of the Role of Reinforcement in the Strength of Concrete Deck Slabs. *Canadian Journal Of Civil Engineering*. Vol.27(3), pp. 475–480.

Kinnunen, S., and Nylander, H. 1960. Punching of Concrete Slab without Shear Reinforcement. *Transactions of the Royal Institute of Technology, Stockholm, Sweden*. No. 158.

Marzouk, H., and Hussein, A. 1991. Punching Shear Analysis of Reinforced High-Strength Concrete Slabs. *Canadian Journal of Civil Engineering*. Vol. 18, pp. 954–963.

Matsui, S., and Tei, K. 2001. Researches and Japanese Developments on Highway Bridge Slabs and Contribution of Wheel Running Machines. *Proceedings, Third International Conference on Concrete under Severe Conditions*, Vancouver, June 18–20, V. 1, pp. 992–1008.

Memon, A.H. 2004. Fatigue Behaviour of Steel-Free Concrete Bridge Deck Slabs under Cyclic Loading. *Ph.D. dissertation to be submitted to the University of Manitoba, December*.

Mufti, A.A., Newhook, J.P., and Mahoney, M.A. 1999. Salmon River Bridge Field Assessment. *Proceedings of the Canadian Society for Civil Engineering Annual Conference*. Vol. I, pp. 51–61.

Mufti, A.A., and Newhook, J.P., 1998. Punching Shear Strength of Restrained Concrete Bridge Deck Slabs. *ACI Structural Journal*. 95(4), pp. 375–381.

Mufti, A.A., Hassan, T., Memon, A., and Tadros, G. 2001. Analytical Study of Punching Shear Strength of Restrained Concrete Slabs. *Proceedings of the Canadian Society of Civil Engineering (CSCE) Annual Conference*. Victoria, British Colombia, CD-Rom.

Mufti, A.A., Jaeger, L.G., Bakht, B., and Wegner, L.D. 1993. Experimental Investigation of FRC Slabs without Internal Steel Reinforcement. *Canadian Journal of Civil Engineering*. Vol. 20 No.3, pp. 398–406.

Mufti, A.A., Memon, A.H., Bakht, B., and Banthia, N. 2002. Fatigue Investigation of the Steel-Free Bridge Deck Slabs. *ACI International SP- 206, American Concrete Institute*, pp. 61–70.

Mufti, A.A., Newhook, J.P., and Khanna, O.S. 1999. Predicting the Punching Behaviour of Reinforced Concrete Bridge Decks. *Proceedings of the Canadian Society for Civil Engineering Annual Conference*. Vol. I, pp. 95–104.

Newhook, J.P. and Mufti, A.A. 1998. Punch Program User Manual. *Nova Scotia CAD/CAM Centre Dalhousie University*. Halifax, Nova Scotia, September.

Newhook, J.P., Mufti, A.A., and Wegner, L.D. 1995. Fibrereinforced Concrete Deck Slabs without Internal Reinforcement – Half-Scale Testing and Mathematical Formulation. *Research Report No. 1-1995, Technical University of Nova Scotia – Nova Scotia CAD/CAM Center.*

Newhook, J.P. 1997. The Behaviour of Steel-Free Concrete Bridge Deck Slabs under Static Loading Conditions. *Doctor of Philosophy Thesis, Technical University of Nova Scotia, Hallifax, Nova Scotia, Canada*.

Wegner, L. D., and Mufti, A.A. 1994. Finite Element Investigation of Fiber-Reinforced Concrete Deck Slabs without Internal Steel Reinforcement. *Canadian Journal of Civil Engineering*. Vol. 21, pp. 231–236.

FRP Composites in Civil Engineering – CICE 2004 – Seracino (ed)

Crack widths during sustained flexural loading of small-scale GFRP reinforced concrete beams

Charles E. Bakis & Matthew A. Ogden
Dept. of Engineering Science and Mechanics, The Pennsylvania State University, University Park, PA, USA

ABSTRACT: Small-scale concrete beams reinforced with steel bars and glass fiber reinforced polymer (GFRP) bars manufactured with either thermoplastic or thermoset matrix materials were subjected to sustained flexural loadings while flexural crack widths were monitored. Separate sets of beams were kept under load at temperatures of 23 and 60°C for time periods of 10 and 3 months, respectively. A nondimensional bond parameter that is considered to be independent of bar modulus and reflective of the tendency for bond slip was fit to the time dependent crack width data and used to compare time dependent bond behavior of the three bars. The thermoplastic GFRP bar demonstrated the highest or nearly the highest bond slip at both test temperatures and the least variation in bond slip with temperature. The thermoset GFRP bar had the least bond slip at both test temperatures. All three types of bar had increased bond slip at the higher test temperature.

1 INTRODUCTION

Fiber reinforced polymer (FRP) materials are being used increasingly as concrete reinforcement in harsh environments that limit the lifetime of conventional steel reinforcement and in structures where steel reinforcement is not permitted for various functional reasons. FRP reinforcement bars are typically made with a thermosetting matrix material, such as vinylester, where polymer chains are irreversibly cross-linked by strong chemical bonds. Thermoplastic bars, where no cross-linking occurs and polymer chains can be rearranged at suitably high temperatures could prove to be useful in construction on account of their ability to be heated and bent in the field. Even though design guidelines for using FRP reinforcements in concrete have been published (Bakis et al. 2002), the long term performance of FRP reinforcements remains an area on ongoing investigation. The width of flexural cracks over extended periods of time is one topic that has received little attention in the literature. Crack widths in structures containing no steel are considered important mainly for aesthetic reasons and possibly for reasons related to water ingress. Current ACI and Canadian design guides recommend that flexural crack widths be no greater than 0.5 mm for exterior exposures and 0.7 mm for interior exposures when FRP reinforcements are used (ACI 440 2003). Flexural crack widths are dependent on many factors, one of which is bond between the reinforcement and concrete.

Masmoudi et al. (1996) investigated crack widths versus quasi-statically applied moment in concrete beams reinforced with two different types of GFRP bars at reinforcement ratios of 0.50 to 1.07%. The Gergely–Lutz equation (Gergely and Lutz 1973) was adopted for characterizing crack widths as a function of beam cross section parameters and bar stress level:

$$w = K_g f_s \beta (\sqrt[3]{d_c A}) \quad (1)$$

where w is the crack width at the tensile face of the beam, K_g is an empirical constant that accounts for different types of bars, f_s is the bar stress calculated by elastic cracked section theory (MPa), β is the ratio of the distance from the neutral axis to the extreme tension fiber to the distance from the neutral axis to the centroid of the tensile reinforcement, d_c is the thickness of concrete cover measured from the bottom of the beam to the center of the closest reinforcement bar (mm), and A is the effective tension area of the concrete surrounding the main tension reinforcement and having the same centroid as that reinforcement, divided by the number of bars (mm^2). The constant K_g was determined by best-fitting the equation to the crack width data measured during monotonically increasing moment. Thus, the value of K_g is dependent on the modulus of elasticity of the reinforcement. The value of K_g was found to be between 4.7 and 6.4 times that for conventional steel reinforcement, leading to the conclusion that crack widths with the GFRP bars are 4.7 to 6.4 times greater than those for comparably sized steel bars, all else the same. Considering that the modular ratio of steel to GFRP is between 4 and 5, most of the extra crack width seen in the GFRP reinforced beams

in relation to the steel reinforced beams is accounted for by factoring in the bar modulus. Crack widths were not measured over extended periods of time in this investigation.

Vijay and GangaRao (1998) investigated the creep behavior of beams reinforced with two types of GFRP bars, each with different reinforcement ratios (0.61% and 0.96%). The beams were subjected to sustained four-point flexure at 20–50% of ultimate moment for up to 655 days while the concrete strain, beam deflection, bar strain, and flexural crack width were monitored. Although no specific crack width data were presented for any of the bars tested, it was claimed in the paper that the time-dependent increase in crack width was less than or equal to the magnitude of crack width upon initial loading.

Masmoudi et al. (1998) investigated crack widths in concrete beams reinforced with either steel or E-glass GFRP bars with reinforcement ratios ranging from 0.42 to 2.15%. Crack widths were measured under short term quasi-static loading. Using equation (1), it was found that K_g for the GFRP bars increased with decreasing reinforcement ratio, whereas K_g for steel bars did not depend on reinforcement ratio. The values of K_g for the GFRP bars ranged from 3 to 5.2 times that of steel, which to a certain extent can be explained by the modular ratio of steel and GFRP bars.

In general, there are insufficient data on flexural crack widths over time in FRP-reinforced concrete beams. In addition, there is little information on the performance of thermoplastic FRP bars, particularly in terms of bond and crack width. Thus, the objective of the present investigation is to evaluate the bond capabilities of thermoplastic and thermoset GFRP reinforcement bars as they relate to flexural crack width in reinforced concrete beams subjected to sustained loading. The bond properties of the bars were analyzed using a modified form of the Gergely–Lutz crack width equation, which allows for a quantitative comparison of the bond behavior of reinforcements in relation to steel with special consideration given to the modular ratio of the reinforcements. Crack widths were monitored for extended periods of time while the beams were kept in room-temperature (23°C) and elevated temperature (60°C) environments under a constant moment.

2 EXPERIMENTAL INVESTIGATION

The experimental investigation involved fabricating the beams, pre-cracking the beams in three-point flexure to induce one or more flexural cracks, holding the beams under four-point flexure using spring loaded rigs, and measuring crack widths over the designated holding time.

Table 1. Properties of reinforcement bars.

Bar type	Nom. dia. (mm)[a]	Nom. area (mm^2)[a]	Young's modulus (GPa)[a]	Tensile strength (MPa)
S	12.6	125	204	>586[b]
G	13.7	147	40.6	689[c]
B	13.8	150	39.0	896[d]

[a] Measured in present investigation.
[b] Based on data acquired in the current investigation.
[c] (ISOROD, undated).
[d] (Vanderpool, 2002).

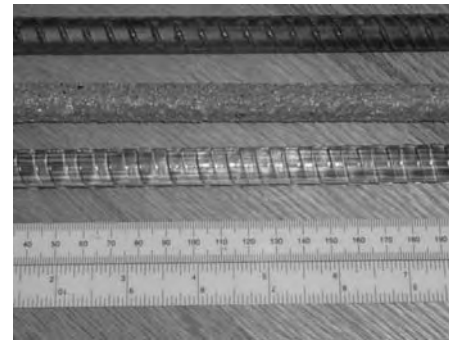

Figure 1. Steel, thermoset, and thermoplastic GFRP bars (top to bottom).

2.1 *Materials*

The thermoset GFRP bars, denoted type G, were manufactured by Pultrall (Thetford Mines, Quebec) and consist of E-glass fiber and a vinlyester matrix (ISOROD, undated). The thermoplastic GFRP bars, denoted type B, were manufactured by Dow Chemical (Midland, MI) and consist of approximately 54% E-glass fiber and 46% thermoplastic polyurethane (Vanderpool 2002). The polyurethane matrix, formed by a reaction of diisocyanate and diol (Anon 2003), has a glass transition temperature of 90°C (Fulcrum, undated). The physical properties of the GFRP and black steel (denoted type S) reinforcements used in this research are shown in Table 1 and a photograph of the bars is shown in Figure 1. The nominal diameters and nominal areas were found by volume displacement, and the Young's moduli were determined by loading one specimen of each bar in tension. Three LVDTs positioned every 120 degrees around the circumference of the bar were used to obtain bending-compensated bar strains. For purposes of data analysis, the bar moduli were all assumed to be constant over the 23–60°C temperature range of the sustained loading experiments. The concrete beams were 890-mm

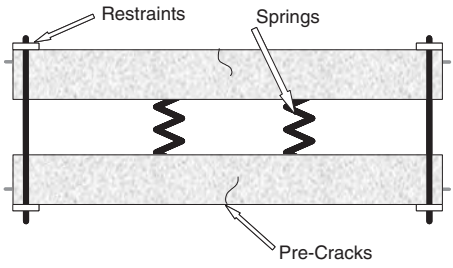

Figure 2. Schematic of sustained loading rig.

long, 100-mm deep, and 89-mm wide and had one bar centered 31.8 mm from the bottom. The compressive strength and coefficient of variation of the concrete measured at an age of 6 months using four 10-cm-dia. cylinders were 41 MPa and 3%, respectively. The reinforcement ratio of the beams varied from 1.7% for the GFRP bars to 1.4% for the steel bar. The balanced reinforcement ratios for the GFRP and steel bars are roughly 0.3 and 2%, respectively.

2.2 *Beam testing*

At an age of one month, each of the beams was pre-cracked in symmetric three-point flexure using a hand pumped hydraulic actuator. Pre-cracking moments averaged 0.92 kN-m, with a range of 0.76–1.25 kN-m. Loading was continued until the visual observation of the first instance of cracking. One or two cracks were formed in each beam in this manner. After the beams had been pre-cracked, they were unloaded and placed as pairs in four-point flexure loading rigs to allow the monitoring of crack widths over time (Fig. 2). The inner and outer load spans measured 28 and 84 cm, respectively. Coil springs held a sustained load of 1.90 kN at each load point and a sustained moment of 0.53 kN-m in the center span with an accuracy of ±2%. The sustained bar force, stress, and strain for the three types of reinforcement, estimated using a standard section analysis that assumes plane sections remaining plane, linear elastic bars, perfect bonding, zero tensile strength in concrete, and parabolic concrete stress–strain behavior (Lin and Burns 1997), are listed in Table 2.

Two pairs of loaded beams containing one steel bar (designated SL), one thermoset bar (GL), and two thermoplastic bars (BL) were tested in an air-conditioned laboratory and thus served as the control specimens. The temperature and relative humidity for the control specimens were kept in the range of roughly 20–25°C and 40–60%, respectively, for a period of 320 days. Four pairs of beams containing two steel, two thermoset, and four thermoplastic bars were placed in a convection oven held at 60 ± 2°C for 89 days.

Table 2. Calculated bar force, stress and strain during sustained loading.

Bar	Bar force (N)	Bar stress (MPa; % of ult.)	Bar strain (με)
S	8710	69.7; <12	340
G	8180	55.6; 8	1370
B	8170	54.5; 6	1400

These specimens are designated BO, GO, and SO, respectively.

The width of each crack was measured at regular time intervals using a 50 × hand-held microscope with a 25.4 μm minimum scale and a 25.4-mm field of view. The cracks were measured on both sides of the beams, as close to the outermost tensile surface as possible. Due to the roughness of the crack surfaces being measured, the repeatability of crack opening measurement is estimated to be ± 50 μm. For the heated beams, the specimens were removed from the heated environment 3–4 hours prior to measuring the cracks in order to obtain the measurements at room temperature. When subsequent flexural cracks appeared over the course of testing, these new cracks were included in the results along with the pre-cracks. Some beams had as many as four flexural cracks in total.

3 DATA ANALYSIS

A useful tool for the analysis of bond characteristics of different FRP bars is a modified Gergely–Lutz equation (ACI 440 2003). This equation relates the maximum crack width at the bottom of a beam, w (mm), to the stress on the bar, f_f (MPa), and the longitudinal modulus of elasticity of the bar, E_f (MPa):

$$w = \frac{2.2\beta k_b f_f}{E_f}\sqrt[3]{d_c A} \qquad (2)$$

where k_b is the bond parameter of interest in the present investigation, and w is normally the upper 90th percentile crack width. The parameters A and d_c were defined in reference to equation (1) and, in this investigation, have respective values of 5650 mm^2 and 31.8 mm. The parameter β, also defined previously, was determined by calculation to be 1.57, 1.58, and 1.74 for bar types B, G, and S, respectively. Note that the ratio f_f/E_f in equation (2) is equal to the strain in an unconstrained bar. Crack width in a beam varies inversely with bar modulus if all other terms in equation (2) are held constant. Hence, by comparing bars to each other on the basis of k_b, one effectively factors out the influence of bar modulus. The bond-related parameter k_b is normally taken as 1.0 for deformed

black steel reinforcement. However, if bond slip of an FRP bar is less than that of steel, k_b is less than 1.0. On the other hand, if bond slip is greater than that of steel, k_b is greater than 1.0. According to the current ACI design guide (ACI 440 2003), some typical k_b values for deformed GFRP bars are between 0.71 and 1.83. The ACI guide suggests that designers use a value of 1.2 for deformed GFRP bars unless more specific information is available.

In the current investigation, k_b was calculated using the measured widths of flexural cracks located in the constant moment zone of the beams. The growth of these cracks was measured over time at load, allowing the calculation of a time-dependent k_b. Because the beams in the present investigation contained only four cracks or less, the mean crack width (rather than 90th percentiles) for a given set of measurements was used to assign a value of k_b at each measurement interval. The range of data scatter in graphical representations of k_b data over time is represented in the results with error bars.

4 RESULTS

4.1 *Crack width*

Crack width data for the 23°C specimens tested in four-point flexure are shown in Table 3. Listed are the number of data points collected and the mean crack widths for all the cracks measured. The beam with a steel bar had one crack (providing two data points), the beam with a thermoset bar had two cracks (four data points), and the two beams with thermoplastic bars each had three cracks (six data points) within 16 days of initial loading. Although the four-point sustained moment existing over the central third of the beams was as much as 40–70% of the three-point pre-cracking moment that was previously exerted in three-point flexure during the pre-cracking procedure, only the beams reinforced with GFRP bars exhibited one or two subsequent flexural cracks over the 10-month loading period. Crack widths in the SL specimen did not change significantly over time. Crack widths in the GL specimen increased slightly, whereas those in the BL specimens increased by nearly a factor of two.

Crack width data for beams subjected to sustained loading at 60°C are shown in Table 4. After stabilization of subsequent cracking, which took as long as 14 days at this temperature, the two SO specimens each had two cracks and the two GO specimens each had four cracks. Two of the BO specimens had two cracks and two had three cracks. At 60°C, crack widths with all types of bars increased in proportion to loading time. Crack widths for all three types of bars increased substantially over the three month loading period.

At both test temperatures, steel bars had the smallest crack widths, followed by the thermoset bars and the thermoplastic bars. Crack width growths over roughly three months of loading at both temperatures are compared in Table 5, where it can be seen that the steel and thermoset bars had negligible crack growth at 23°C. Each of these bars had greater crack growth at the higher temperature. The thermoplastic bar had the most crack growth on a numerical basis at either temperature, yet the amount of growth was not significantly affected by the 37°C temperature difference.

Table 3. Number of data points, N, and mean crack widths, w, for 23°C tests.

	Steel (SL)		Thermoset (GL)		Thermoplastic (BL)	
Day	N	w (μm)	N	w (μm)	N	w (μm)
0	2	89	4	76	4	229
16	2	76	4	102	6	271
45	2	76	4	89	6	343
80	2	76	4	89	6	394
160	2	76	4	89	6	406
205	2	76	4	89	6	406
320	2	89	4	127	6	457

Table 4. Number of data points, N, and mean crack widths, w, for 60°C tests.

	Steel (SO)		Thermoset (GO)		Thermoplastic (BO)	
Day	N	w (μm)	N	w (μm)	N	w (μm)
0	8	51	12	123	14	259
7	8	67	14	165	20	271
14	8	89	16	175	20	310
26	8	102	16	191	20	344
40	8	108	16	211	20	370
56	8	105	16	219	20	394
89	8	124	16	238	20	417

Table 5. Change in mean crack width over three months.

	80 days @ 23°C			89 days @ 60°C		
	SL	GL	BL	SO	GO	BL
Change (μm)	−13	13	165	73	115	158
Change (%)	−15	17	72	143	93	61

4.2 *Bond parameter*

Raw crack widths, while useful in and of themselves, are not an appropriate metric for evaluating bond behavior across different types of bars because of differences in the longitudinal moduli of elasticity of the bars, as explained earlier. Therefore, subsequent

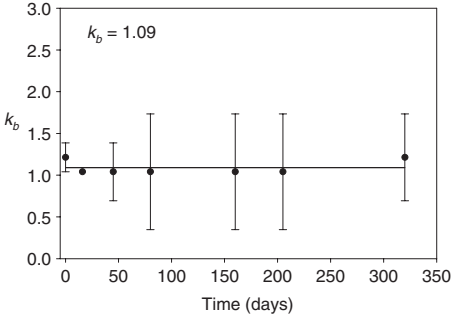

Figure 3. Bond parameter for steel bar at 23°C (SL).

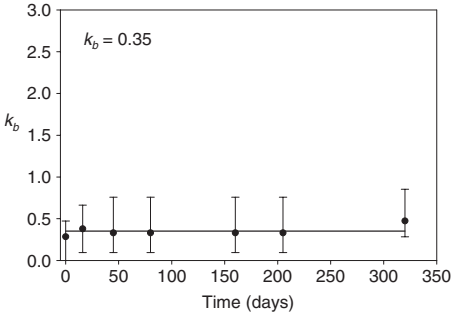

Figure 4. Bond parameter for thermoset GFRP bar at 23°C (GL).

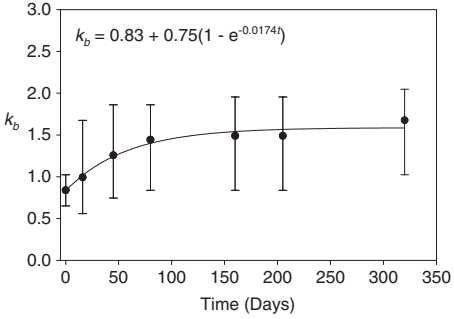

Figure 5. Bond parameter for thermoplastic bar at 23°C (BL).

discussions focus on the nondimensional bond constant, k_b, defined in equation (2).

Figures 3–5 show k_b over a 320-day loading period at 23°C. It can be seen that k_b for the SL and GL beams did not change significantly during this time period.

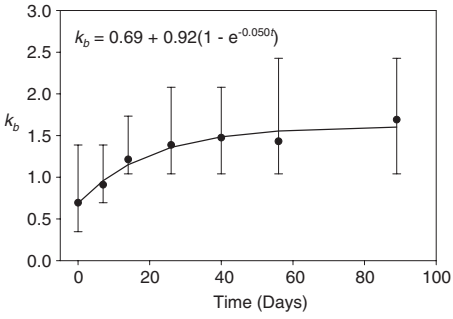

Figure 6. Bond parameter for steel bar at 60°C (SO).

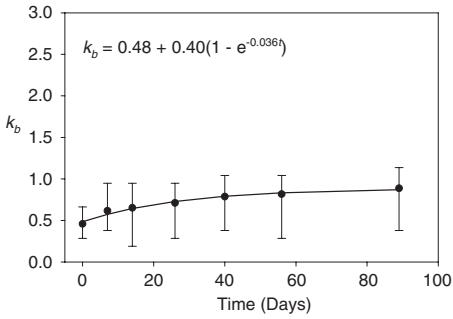

Figure 7. Bond parameter for thermoset GFRP bar at 60°C (GO).

Assuming constant values of k_b for these cases, the mean values for the steel and thermoset bars are 1.09 and 0.35, respectively. A value of k_b near 1.0 for a steel bar is expected according to the theory behind the modified Gergely–Lutz equation (ACI 440 2003). The value of 0.35 for the thermoset bar indicates less bond slip in comparison to the steel bar. The best-fit value of k_b for the thermoplastic bar begins near 0.83 (slightly less bond slip versus the steel bar) and grows in an exponential manner to a value of about 1.6 (more bond slip than steel). The three-parameter exponential type of equation fit to the thermoplastic bar data in Figure 5 was selected simply to illustrate the trend in the available data and is not meant to imply a particular bond slip mechanism or longer term trend.

Figures 6–8 illustrate trends of k_b over 89 days of testing at 60°C for the three types of bars. Differences between the 0-time data in these figures versus the 0-time data in Figures 3–5 for 23°C tests reflects the extent of crack width scatter among different groups of specimens before immersion into their respective testing environments. In the high temperature specimens, the best-fit initial k_b value for steel was only 0.69,

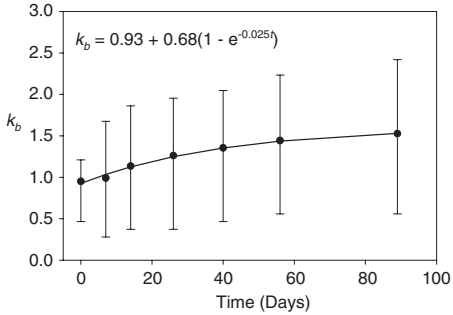

Figure 8. Bond parameter for thermoplastic GFRP bar at 60°C (BO).

which is substantially less than the expected value of 1.0. The best-fit initial values of 0.48 and 0.93 for k_b of the thermoset and thermoplastic bars, respectively, were comparable to initial values observed among their respective counterparts in the 23°C tests.

One immediately apparent conclusion that can be drawn from the trends in k_b at 60°C is that bond slip increases over time for all three types of bar, including steel, as evidenced by increasing k_b. After three months at load, the values of k_b for the steel bar stabilize to a greater extent than those for either GFRP bar. This result suggests that the contribution of concrete to bond slip nearly ended in three months, since it is unlikely that steel itself contributes measurably to bond slip at 60°C. By extension, one can conclude that time-dependent bond slip mechanisms in the GFRP bars are active for at least three months at 60°C.

Table 6 summarizes the average values of k_b recorded initially and after about three months under load (80 days for 23°C and 89 days for 60°C). As one would expect, the percent change in k_b over three months for a given type of bar is identical, within round-off error, to the corresponding percent change in crack width in Table 5. Comparing values of k_b across bar types gives new information about bond that cannot be discerned by considering only crack widths, however. In particular, k_b values for the thermoset bars are the lowest of the three bars initially and after three months of testing at either test temperature. While the thermoplastic bar had a higher k_b value than the steel bar initially, the thermoplastic as well as thermoset GFRP bars had lower k_b values than steel after three months of 60°C testing.

The best-fit equations for k_b based on all the experiments are compared in Figure 9. It can be concluded that, at the 23°C test temperature, the thermoplastic bars demonstrated time dependent bond slip that was not evident in either steel or thermoset bars, although further bond slip had nearly ceased after 10 months of loading. After three months of loading at 60°C, bond slip with the steel bar had nearly stopped, whereas it continued to increase with both GFRP bars. Bond slip was significantly less with the thermoset GFRP bar than with the thermoplastic bar at both test temperatures.

Table 6. Change in mean k_b over three months.

	Temp (°C)	Initial	3 month	Change	% Change
SL	23	1.21	1.04	−0.17	−14
GL	23	0.28	0.33	0.05	18
BL	23	0.84	1.44	0.60	71
SO	60	0.69	1.69	1.00	145
GO	60	0.46	0.89	0.43	93
BO	60	0.95	1.53	0.58	61

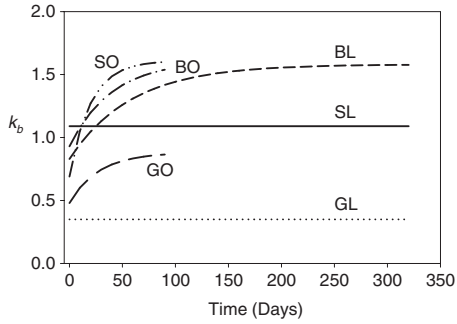

Figure 9. Best-fit equations for k_b for all experiments.

5 DISCUSSION

While there is abundant evidence that the strength and stiffness of mechanical interlock play prominent roles in the bond slip behavior of FRP reinforcement inside of concrete (eg. Bakis et al. 1998), some underlying complications operating in the present set of experiments carried out at various temperatures should be mentioned. For instance, the radial pressure induced at the interface between concrete and an internal bar due to a temperature change varies in direct proportion to the difference in coefficients of thermal expansion (CTE) and the individual transverse moduli of the bar and concrete (Gentry and Husain 1999). The isotropic CTEs of concrete and steel are both in the range of 10–11 με/°C, whereas the longitudinal and transverse CTEs of undirectionally reinforced GFRP bars are typically 6–8 με/°C and 30–40 με/°C, respectively. The difference in longitudinal CTEs of the GFRP bars and concrete is considered insignificant for the present discussion. In the transverse direction, however, the CTE mismatch is significant for GFRP bars. Based on a

simple friction argument, it can be easily imagined that interfacial pressure and, therefore, resistance to bond slip, increases with GFRP reinforcements when the temperature increases, whereas not much change in transverse pressure is expected with steel reinforcement. Clearly, if such a "tightening" mechanism was operative in the present set of elevated temperature experiments, it was overridden by contrary mechanisms such as elastic softening and time dependent creep and relaxation of the interfacial region of the concrete and GFRP bars. Supporting observations of degraded bond behavior at elevated temperatures were made by Katz and coworkers using pull-out tests of GFRP reinforcements in concrete (Katz et al. 1999).

Another mechanism that could increase the bond slip of GFRP bars in comparison to steel is Poisson's effect. In the present investigation, longitudinal strains were roughly four times greater in the GFRP bars than in the steel bars, despite slightly lower bar forces in the former. Since the Poisson's ratios for steel and unidirectionally reinforced GFRP bars are both near 0.3, the transverse contraction and consequent loss of frictional bond strength can therefore be expected to be greater in the GFRP bars than in the steel bars regardless of temperature. Since the experimental data do not support this hypothesis, however, it cannot be concluded that the Poisson effect is a major governing mechanism for slip at flexural cracks in the short or long term.

6 CONCLUSIONS

The findings presented in this paper, though preliminary in scope and limited to the particular materials, geometries, and temperatures investigated, provide new information on the flexural bond slip behaviors of two types of GFRP reinforcement bars as they relate to crack width in concrete beams under a sustained moment loading. Bond behavior was characterized in terms of a non-dimensional parameter in the Gergely–Lutz equation, k_b, which is normally assumed to be 1.0 when bond slip at flexural cracks is similar to that of deformed black steel reinforcement, greater than 1.0 when bond slip exceeds that of steel, and less than 1.0 when bond slip is less than that of steel. The k_b values in these conclusions refer those obtained by best-fitting smooth curves to the data.

After 310 days 23°C, one beam with a steel bar had an invariant k_b of 1.09, one beam with a thermoset GFRP bar had an invariant k_b of 0.35, and two beams with thermoplastic GFRP bars had k_b values increasing from 0.83 to 1.57 over the test duration. Thus, of these three bar types, only the thermoplastic GFRP bar had time dependent bond slip at 23°C. However, even the thermoplastic bar reached a nearly steady value of k_b after 310 days at load.

All beams tested for 89 days at 60°C had k_b values increasing over the test time: 0.69–1.60 for steel; 0.48–0.86 for thermoset GFRP; and 0.93–1.54 for thermoplastic GFRP. Only the beams with steel bars reached a nearly steady k_b value in the 89 days of testing at 60°C. The values of k_b in both GFRP bars were still increasing at the conclusion of the 60°C test, albeit at a much lower rate than initially.

The thermoplastic GFRP bar demonstrated the highest or nearly the highest values of k_b of all bars tested and also the least dependence of k_b on temperature. The thermoset GFRP bar had the lowest values of k_b for both test temperatures.

For future research, it is recommended that sustained load on beams with various designs (eg., reinforcement ratios, confinement), types of reinforcement, and load levels be used to determine crack widths over longer times to better characterize the time dependent bond parameter, k_b, and to broaden the database currently available to designers. Additionally, more temperatures should be used to determine the functional form of temperature dependence of k_b.

ACKNOWLEDGEMENTS

Dow Chemical, Midland, MI (USA), financially supported this research and provided the reinforcement bars. The encouragement and support of Mr. Chris Edwards, formerly of Dow Chemical and currently with Fulcrum Composites, Midland, MI, is appreciated. Mr. Seung Chul Lee and Mr. Haink Tu assisted with specimen fabrication and data collection, respectively.

REFERENCES

ACI 440 2003. *Guide for the Design and Construction of Concrete Reinforced with FRP Bars*, ACI 440.1R-03. Farmington Hills, MI: American Concrete Institute.

ISOROD, undated product data sheet. Thetford Mines, Quebec: ADS-Pultrall Inc.

Anon. 2003. Dow Establishes FULCRUM facility at the National Composite Center. *Composites Technology*, 9(2):11.

Bakis, C.E., Uppuluri, V.S., Nanni, A. & Boothby, T.E. 1998. Analysis of bonding mechanisms in smooth and lugged FRP rods embedded in concrete. *J. Composites Science and Technology*, 58(8):1307–1319.

Bakis, C.E., Bank, L.C., Brown, V.L., Cosenza, E., Davalos, J., Lesko, J.J., Machida, A., Rizkalla, S., & Triantafillou, T. 2002. FRP composites for construction – state of the art review. *J. Composites for Construction*, 6(2):73–87.

Fulcrum, undated product data sheet No. 030402. Midland, MI: Fulcrum Composites, Inc.

Gentry, T.R., & Husain, M. 1999. Thermal compatibility of concrete and composite reinforcements. *J. Composites for Construction*, 3(2):82–86.

Gergely, P., & Lutz, L.A. 1973. Maximum crack width in reinforced concrete flexural members. In *Causes, Mechanism and Control of Cracking in Concrete*, SP-20: 87–117. Farmington Hills, MI: American Concrete Institute.

Katz, A., Berman, N., & Bank, L.C. 1999. Effect of high temperature on bond strength of FRP bars. *J. Composites for Construction*, 3(2):73–81.

Lin, T.Y., & Burns, N.H. 1997. *Design of Prestressed Concrete Structures*, 3rd ed., New York: John Wiley & Sons.

Masmoudi, R., Benmokrane, B., & Chaallal, O. 1996. Cracking behavior of concrete beams reinforced with FRP bars. In Saadatmanesh, H., & Ehsani, M.R. (eds), *Fiber Reinforced Composites in Infrastructure, ICCI'96*:374–388. Tucson, AZ: University of Arizona.

Masmoudi, R., Thériault, M., & Benmokrane, B. 1998. Flexural behavior of concrete beams reinforced with deformed fiber reinforced plastic reinforcing rods. *ACI Structural Journal*, 95(6):665–676.

Vanderpool, D. 2002. Dow Chemical Co., Midland, MI, pers. comm., June 12, 2002.

Vijay, P.V., & GangaRao, H.V.A. 1998. Creep behavior of concrete beams reinforced with GFRP bars. In *Durability of Fibre Reinforced Polymer (FRP) Composites for Construction*: 661–668. Sherbrooke, Quebec: University of Sherbrooke.

FRP Composites in Civil Engineering – CICE 2004 – Seracino (ed)
© 2005 Taylor & Francis Group, London, ISBN 90 5809 638 6

Load–deflection response of high strength concrete beams pretensioned by carbon fibre reinforced polymers

Patrick X.W. Zou
The University of New South Wales, Sydney, Australia

ABSTRACT: The high tensile strength and non-corrosion nature of carbon fibre reinforced polymers (CFRP) make it suitable to prestressing concrete structures. This paper presents the test results of the load–deflection responses of ten high strength concrete beams pretensioned by CFRP tendons. Furthermore, a theoretical prediction of load–deflection response is also presented as a comparison to the experimental results. It is concluded that the load–deflection relationship of high strength concrete beams pretensioned by CFRP is in a bi-linear fashion that is linear before cracking and linear after cracking but with a reduced sectional stiffness. It is also concluded that finite strip strain compatibility method is a suitable means for predicting the load–deflection responses of such beams. Furthermore, the residual deflection of CFRP prestressed beams is about 10–15% of the original deflection and the energy stored in the beam was mainly elastic until failure.

1 INTRODUCTION

The problem of corrosion of steel reinforcement/tendon in concrete structures has led to researchers in searching for alternative reinforcements or tendons. Fibre reinforced polymers (FRP), with its non-corrosive nature and high tensile strength make itself suitable for such purpose. Some research has been conducted in this topic (Abbdelrahman 1995, Abbdelrahman and Rizkalla 1995, Fam 1995, Park and Naaman 1999, Naaman 2003, Agyei et al 2003 and Zou 2003), however, in order to understand the behaviour of FPR reinforced or prestressed concrete beams and to develop a comprehensive design guideline, further research is still needed (ACI 440 2003). Furthermore, since CFRP has a tensile strength as high as up to 3000 MPa (Abbdelrahman 1995, Zou 2003), it would seem logical to consider using higher strength concrete in conjunction to CFRP tendons. This paper is therefore focused on the behaviour (such as load–deflection responses) of high strength concrete beam pretensioned by CFRP tendons.

2 EXPERIMENTAL PROGRAM

This section describes the processes of constructing the beams and the test set-up for both sustained service load and ultimate flexural strength tests.

2.1 *Beam construction*

Ten full-scale beams with rectangular cross-sections (300 mm deep by 150 mm wide) and with spans of 6000 mm (overall length is 6400 mm) were fabricated and tested in the study (Figure 1).

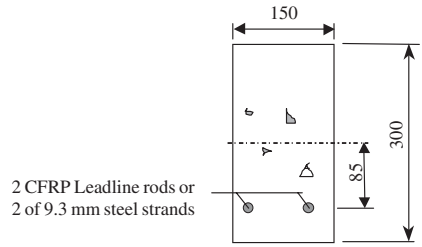

Figure 1. Cross sectional details of 6.4 m long beam with CFRP/steel tendon.

The beams contained only two CFRP rods (or 2 steel strand) and no stirrups nor other longitudinal reinforcement. A particular type of CFRP rods (trade name "Leadline"), with slightly indented surface, 8 mm in diameter with a manufacturer guaranteed tensile strength of 2250 MPa and elastic modulus of 147,000 MPa was used in eight of the beams. 7-wires steel strand, with smooth surface, 9.3 mm in diameter with the tensile strength of 1860 MPa and elastic modulus of 200,000 MPa was used in the other two beams for comparison purpose. The eccentricity of the tendons was 85 mm along the beams. The two CFRP rods or steel strands were stressed to the range 40–60% of the manufacturer's guaranteed tensile strength to achieve a total jacking force of range 80–120 kN. All beams were pretensioned in 8 m long prestressing

Table 1. Beam specification.

ID	Beam designation	f'_c (MPa)	E_c (GPa)	P_j (kN)
1	C40-80-S	45	32.2	83.8
2	C80-120-S	77	48.7	114.6
3	C80-120-L-U	74	40.5	122.3
4	S80-120-L-U	74	40.5	125.3
5	C40-120-L-U	52	38.1	123.1
6	S40-120-L-U	52	38.1	124.5
7	C40-80-L-U	45	32.2	82.3
8	C80-80-L-C	77	48.7	74.9
9	C40-80-L-C	37	27.3	79.3
10	C40-120-L-C	37	27.3	121.9

bed. Load cells were used to monitor the prestress in the tendon from the time of prestressing till the release (transfer) of prestress. Commercial ready-mixed concrete with a 28-day characteristic compressive strength of either 40 MPa or 80 MPa and a slump of 100 mm was used. The beam details including their designation, the initial prestressing force, concrete properties are listed in Table 1.

The specifications of the beams are as follows (see Table 1): the first letter "C" or "S" indicates the type of tendon used in the beam ("C" for CFRP and "S" for steel). The first digital number represents the concrete strength in MPa, and the second digital number refers the total prestress in the tendon before the release in kN. The letter "L" following the second digital number indicates that the beams have been subjected to long-term sustained service load. The letter following "L" (i.e. the last letter) indicates the cracking situation of the beam ("C" for cracked, 'U" for uncracked) under the long-term service tests.

The prestressing force was transferred to the concrete by cutting the rods/strands at concrete age 9 days. The beams were simply supported immediately after the transfer of prestress and deflection and strain measurements commenced.

2.2 *Test set up*

Beam C80-120-S was tested to failure at the age of 57 days and Beam C40-80-S was tested at 100 days to obtain load–deflection response and ultimate flexural strength (note apart from their self-weight these two beams did not subject do any sustained service load prior to this test). The deflections at midspan were measured using a LVDT linked to a computer and the concrete strains at midspan were measured using a demec gauge and/or a LVDT.

The other eight beams were loaded with a sustained service load, in the form of two concentrated point loads, 1 meter or 2 meters apart, and centrally located in the span. The bending moment at midspan created by this load varied from slightly less than the cracking moment to about 1.2 times the cracking moment

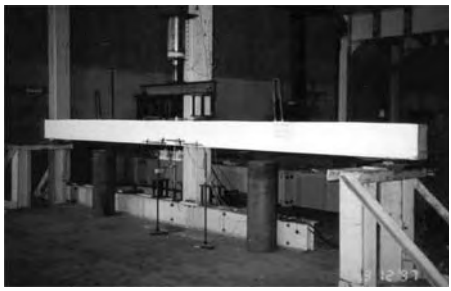

Figure 2. Ultimate flexural test set up.

at midspan for different beams. This sustained service load was maintained for at least 250 days. Two points should be noted here. One is that Beams C40-120-L-U and S40-120-L-U were subjected to two stages of loading, the first loading stage was maintained for a period of 259 days (where the beams remained uncracked during this period). At this time, more load was added so that the beams cracked and were then monitored for a further period of 260 days. The second point is that Beam C40-80-L-C was quite heavily loaded (about 1.4 times the cracking moment) for experimental purpose and this level of loading may not be appropriate in the real structural applications at service load level.

During the sustained service load tests, deflections at midspan and quarter span were measured using dial gauges while the crack width was measured using a microscope with a magnification factor of 40. The cracking behaviour in terms of number of cracks, crack height and crack spacing were also recorded. The slippage of the tendon at the ends of each beam was monitored using dial gauges. The beams were then loaded to failure for the ultimate flexural behaviour.

The test results of the sustained service load condition have been reported in Zou (2003) and this paper will concentrate on the results of the load–deflection response under the ultimate flexural testing. Figure 2 shows the ultimate flexural test set up. During the tests, most beams were subjected to between 5 and 10 cycles of slow loading to study the ability of recovery of deflection and energy absorption. The unloading was carried out at first cracking, then at deflections of 15, 25, 40, 60, 80, 100, 120 mm, and finally immediately before failure.

3 RESULTS AND DISCUSSIONS

The experimental results of the concrete beams prestressed by CFRP rods with different concrete strengths are presented in this section. In addition, two comparisons are made: comparison of load–deflection response of beams prestressed by CFRP rod to those

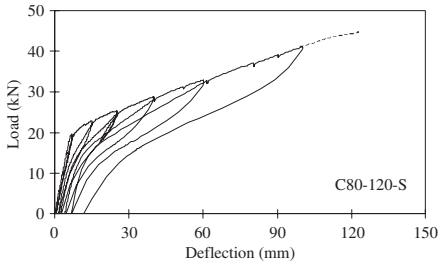

Figure 3. Load–deflection of Beam C80-120-S.

by steel strands and the comparison between the experimental results to the theoretically calculated results. Furthermore, effect of level of prestressing, concrete strength, sustained service load on ultimate flexural strength are also discussed.

Generally, the beams prestressed by CFRP had a linear load–deflection relationship before cracking. The beams cracked near the predicted cracking–loading levels. After cracking, these beams showed a reduced stiffness but still followed a linear load–deflection relationship up to failure. This was because of the linear stress–strain relationship of the CFRP tendon up to failure. The general observation in flexure of each beam is described below.

3.1 *Beam C80-120-S*

The load–deflection relationship of this beam is shown in Figure 3. A bilinear load–deflection relationship was observed up to failure. The deflection increased linearly with an increase of load before cracking. The beam cracked at a load of 19.6 kN. With an increase of load, the deflection increased more rapidly but still followed a linear relationship up to failure. The number of cracks increased with the increase of load. At a load of 22.8 kN, the two cracks in the constant moment zone propagated to a height of 150 mm from the soffit of the beam. With a further increase in load, these two cracks bifurcated and extended at an angle of about 30° to the longitudinal axis of the beam.

The flexural-shear cracks outside the constant moment zone developed towards the loading points from both sides. Near ultimate, there were nine cracks in the beam with a maximum height of about 270 mm. The crack spacing was in the range of 300 to 500 mm. The maximum crack width was more than 4 mm (at the soffit of the beam). The failure load was 47.8 kN and the ultimate deflection was 131.5 mm (1/46 of the span).

At the point of failure, a horizontal crack developed at the tendon level and the concrete below the tendon spalled. This was because the release of the elastic energy stored in the beam upon the rupture of the CFRP rods (as discussed later the energy stored in the beams was mainly elastic). The CFRP rods were debonded from the concrete and the surface between the concrete and the CFRP rods was quite smooth. This indicates that the friction component of the bond strength maybe inferior to that steel or sand coated AFRP.

It should be pointed out that the failure was caused by the rupture of the CFRP rods at the section where the major flexural-shear crack developed. In other words, the failure was caused by the bending moment together with the shear force. According to the shear strength calculation using the current code method, the beam should not have failed in this manner. This indicated that the dowel action of the CFRP rod was lower than that of steel due to its lower transverse stiffness/strength. More discussion on this aspect follows at later sections.

The ratios of residual deflection to original deflection after unloading were approximately the same for different deflection levels and it was about 10 to 12%. This meant that the energy stored in the beam was mainly elastic. This elastic energy is responsible for the horizontal crack development after the rupture of the CFRP rods. The unloading path did not follow the initial loading path. The stiffness of unloading path was slightly higher the loading path. Close to complete unloading the stiffness increased rapidly approaching the initial stiffness.

3.2 *Beam C40-80-S*

The initial prestressing force in this beam was 83.8 kN and the concrete strength was 45 MPa. The beam cracked first at a load of 13.6 kN in the constant moment zone. With an increase in load, one more crack appeared within the constant moment zone and two more appeared just near the loading points. The number of cracks increased as the load increased; so did the height of the cracks. Two cracks in the centre region bifurcated at a height of 150 mm at a load level of 15.9 kN while the other two cracks bifurcated at about 200 mm height from the soffit at a load level of 19 kN (Figure 4). There were 10 cracks in the beam near ultimate and the crack spacing was in the range of 230 to 440 mm. The beam failed at a load of 37.7 kN with a corresponding deflection of 137 mm. The failure was, however, caused by a flexural-shear crack propagating up to the top of the beam near the loading point. This is a typical flexure-shear failure. There was no horizontal crack found after the rupture of the CFRP rods.

3.3 *Beam C40-80-L-U*

This beam was subjected to a service load (60% of the cracking load) for 330 days before being tested to ultimate. At a load of 17 kN, the beam cracked

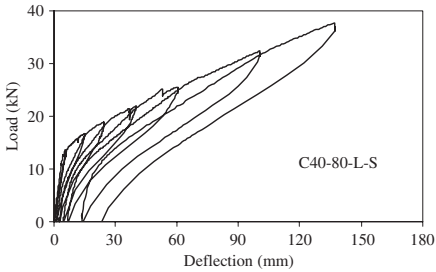

Figure 4. Load–deflection of Beam C40-80-S.

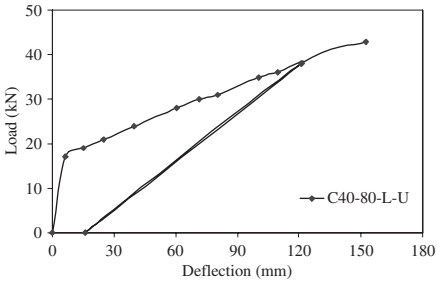

Figure 5. Load–deflection of Beam C40-80-L-U.

at one of the loading points. At this point the beam was unloaded in order to install the LVDT for measuring crack widths. Upon reloading to a load of 18 kN, two new cracks formed in the constant moment zone. At a load of 19 kN, one more crack formed and the deflection reached 15 mm. The beam was unloaded again and the residual deflection was 1.6 mm. However, one new crack appeared after reloading back to 19 kN. Additional cracks formed at increasing loading levels. The beam was subjected to seven cycles of loading and unloading and the residual deflections were about 10 to 15% irrespective of the original deflection levels. The failure was caused by flexural-shear cracking near the loading point. At failure, there were 13 cracks in the beam. The ultimate load was 43 kN and the ultimate deflection was 152.5 mm (Figure 5).

The concrete strains at the top fibre and at the tendon level were 0.00182 and −0.0106 respectively. It should be pointed out that the load–deflection relationship was recorded manually during the test since the computer collected data were lost due to a technical problem in the computer system.

3.4 *Beam C80-120-L-U*

Before being tested to failure, this beam was subjected to a sustained service load in the form of two point

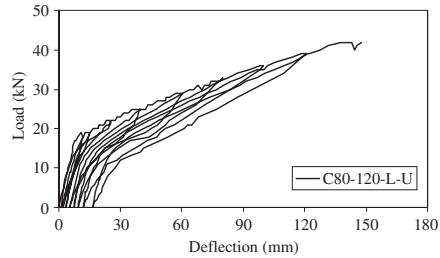

Figure 6. Load–deflection of Beam C80-120-L-U.

loads, applied 2 m apart at the centre of the beam. Five fine cracks appeared two weeks after the application of the sustained service load. When tested to ultimate, the load was applied to the beam using two equal point loads 500 mm apart in the centre. The existing cracks first opened at a load of 6 kN. The number of cracks increased to 12 at the ultimate state. A 5 m long horizontal crack appeared at the tendon level upon the rupture of the tendon. The concrete below the tendon level spalled off. The failure was caused by the shear force cutting off the tendons near the loading point on one side of the beam. The ultimate load was 42 kN and the ultimate deflection was 142 mm or 1/42 of the span as shown in Figure 6. The maximum crack width was about 5 mm at failure and the crack spacing was in the range of 230 to 450 mm while the height of the crack was more than 270 mm near failure.

3.5 *Beam S80-120-L-U*

This beam contained two 9.3 mm 7-wire steel strands with an initial prestressing force of 125.5 kN. The concrete strength and the loading history were the same as that of Beam C80-120-L-U, but the beam was uncracked before being tested to ultimate. The test set up for ultimate testing was identical to Beam C80-120-L-U.

Two cracks with a height of 120 mm appeared simultaneously in the constant moment region at a load of 17 kN. The mid-span deflection at the first crack was 7.8 mm. One more crack appeared at a load of 18 kN. These cracks bifurcated at a height of 150 mm from the soffit of the beam. Three more cracks appeared at load levels of 21, 23 and 27 kN. Near ultimate, at 30 and 31 kN of loads, two fine cracks occurred at the shear span. With an increase of load, the crack located inside the constant bending moment zone developed as wide as 10 mm and more than 250 mm in height, and led to the rupture of the steel strand at this section.

The residual deflection increased with increase of deflection level, from 7% at 40 mm deflection to 32% at 143.8 mm (close to ultimate), as shown in Figure 7. This indicated that the energy was consumed more and

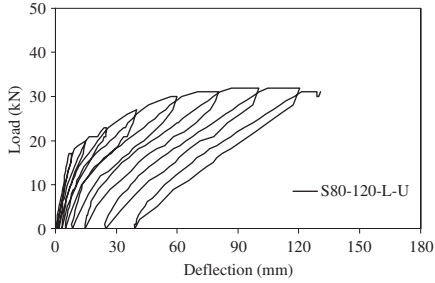

Figure 7. Load–deflection of Beam S80-120-L-U.

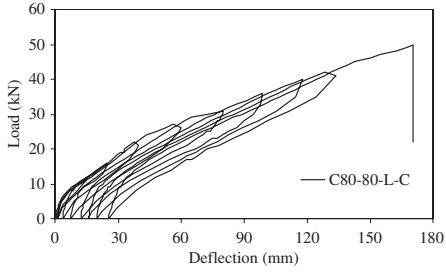

Figure 8. Load–deflection of Beam C80-80-L-C.

more by the beam with an increase of deflection (especially after the steel yielded), i.e. the elastic energy stored in the beam became less and less towards the ultimate state. At ultimate, there were eight cracks over the length of 2.5 m and the spacing ranged from 200 to 540 mm. No horizontal crack appeared and no concrete spalled off the beam after the rupture of the steel strands. The deflection at ultimate was 143.8 mm.

3.6 *Beam C80-80-L-C*

There were seven cracks in the beam due to the sustained service load which was greater than the cracking load. No new cracks formed and the crack height did not increase up to a load of 25 kN. Four new cracks developed as the load was increased from 25 kN to 50 kN (ultimate). The total number of cracks at ultimate was 11. The maximum crack width at midspan was 3.7 mm. The deflection at ultimate was 170 mm or 1/35 of the span (Figure 8).

A 4 m long horizontal crack occurred at the tendon level at failure, but at this point the tendons were not completely ruptured. The residual deflections were only about 15% of the original deflections. The failure was initiated by a flexural-shear crack forming near one loading point. The concrete strain at the top fibre at mid span near failure was about 0.002.

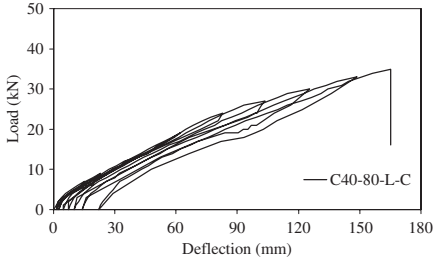

Figure 9. Load–deflection of Beam C40-80-L-C.

3.7 *Beam C40-80-L-C*

The beam was loaded under a service load equal to 1.6 times the cracking load for 270 days before being tested to failure and 10 cracks with the maximum height was 230 mm appeared in the beam due to this load. Figure 9 shows the load–deflection response. When tested under two point loads, the beam deflected 15 mm at a load of 7 kN. The beam showed a linear load–deflection relationship. One new crack developed at a load of 27 kN. The beam failed at a load of 35 kN with a corresponding deflection of 165.4 mm. The concrete strain at the top fibre was 0.00252. The failure of the beam was caused by the rapid development of a flexural-shear crack located 750 mm away from the loading point. At this stage, the CFRP rods did not rupure but the concrete spalled off.

The residual deflections were low after unloading at different deflection levels as shown in Figure 9, being about 10% of the original deflection up to 100 mm. With increasing deflection, the residual deflection only increased to about 15% near ultimate. This indicated that the energy stored in the beam was mainly elastic energy.

3.8 *Beam C40-120-L-C*

The prestressing force in this beam was 50% higher than that of Beam C40-80-L-C. The beam was subjected to a sustained service load equivalent to 1.2 times its cracking load for 270 days before being tested to failure. There were six cracks in the beam during the long term testing. When tested to failure, two point loads were applied to the beam 460 mm apart at the centre region.

The two cracks at the constant moment zone opened at a low load level. The flexural-shear cracks also opened and developed towards the top and inclined to the loading point with the increase of load. Two flexural-shear cracks developed quickly on one side of the beam at the loading level of 30 kN. At a load of 37 kN, the beam failed by rupture of the CFRP rods in the flexural-shear section and the deflection at failure

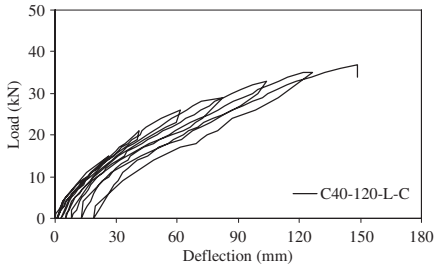

Figure 10. Load–deflection of Beam C40-120-L-C.

was 148.3 mm (or 1/40 of the span). The failure was quite sudden and accompanied by a loud noise. Apart from the six cracks due to the sustained load, three more cracks appeared at loads of 26, 29 and 33 kN. The residual deflections at different deflection levels were small, about 13% at 140 mm deflection (Figure 10). This meant that the energy restored in the beam was mainly elastic energy.

3.9 *Comparison of tested to predicted load–deflections of beams prestressed with CFRP tendons*

A strain compatibility approach and a finite strip method is suitable to predict the flexural response of beams with FRP tendons. In this approach, the cross-section is divided into a number of strips. The concrete is assumed to be subjected to uniaxial strains uniform over the entire width of the section, and the strains are linear over the depth of the section, which means that plane sections remain plane after bending. Perfect bond between the tendon and concrete is assumed. This method is widely used for prestressed concrete beams and is described in many textbooks (e.g. Collins and Mitchell, 1991). From the flexural response, the cracking moment, deflection at first crack, ultimate load and deflection at ultimate can be determined.

The load–deflection relationships of Beams C40-80-S and C80-120-S were predicted using the strain compatibility approach described previously. Figure 11 (a) shows the comparison of the predicted curve to the curve obtained from the experiment of Beam C40-80-S. It is clear that the predicted curve is in good agreement to the experimental results. It should be pointed out that the LVDT was removed before the beam failed to prevent the possible damage. This is why the theoretical curve extended longer than the experimental curve.

Similar to Beam C40-80-S, the load–deflection of Beam C80-120-S is also predicted using the same method and the comparison between the predictions and the experimental results is shown in Figure 11 (b).

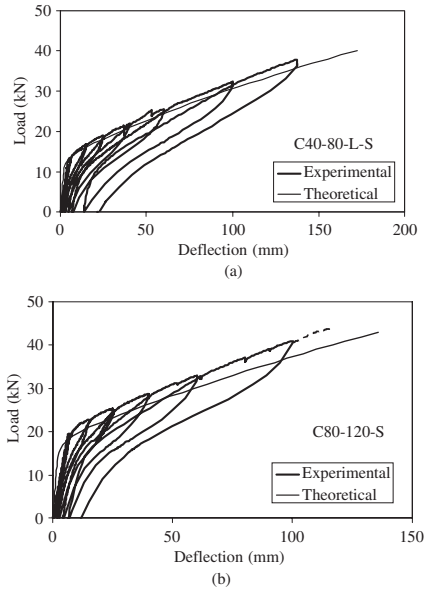

Figure 11. Comparison of predicted and tested load–deflection.

Figure 12. Cracking pattern and failure mode.

It can be seen that before cracking, the theoretical prediction was slightly less than the test values, however, after cracking, the prediction slightly overestimate the measured deflection but the difference was very small. In general, the load–deflection of beams prestressed by CFRP rod tendons can be predicted using the strain compatibility method, for both normal strength and high strength concrete.

3.10 *Cracking behaviour*

All beams first cracked near the theoretically predicted loading level in the pure flexural region (Figure 12). The cracks extended upward with an increase of load and the number of cracks also increased. At high loading levels, a major flexure-shear crack near

the loading point developed leading to the failure of the beams. A horizontal crack at the tendon level also developed after the rupture of CFRP rods in most of the beams this was due to the release of the energy when the tendons snapped and part of the energy was absorbed by the concrete. This observation was also confirmed by Abbdelrahman (1995). An inspection of the beams after failure showed that the tendons were completely debonded from the concrete. The surface between the CFRP rods and the concrete was quite smooth. This indicated that the friction component in bond strength was not sufficient. However, no slip was recorded from the dial gauges attached to the tendons at the end of the beams up to failure. The number of cracks was about 10 to 12 at ultimate in all beams despite the difference in concrete strength and prestressing force in each beam. The crack width at ultimate was as high as 5 mm. The crack spacing in beams with CFRP were similar to that in beams with steel strand, about 300 to 500 mm.

3.11 *Failure mode*

The failure of the beams prestressed by CFRP rods was due to the development of flexural-shear cracks near the loading point (i.e. due to shear) while the beam prestressed by steel failed due to the rupture of steel in the constant moment zone (refer Figure 12). According to the shear strength calculation, these beams should not have failed in shear. The shear failure modes of the beams prestressed by CFRP indicated that the dowel action of CFRP is less than that of steel due to the low transverse stiffness of the CFRP rods. However, the depth of neutral axis at ultimate was relatively small in all cases. The concrete strain at the top fibre reached 0.003 in some cases. The ultimate deflections were large enough (1/40 of the span) to give a physical warning. The energy released from the beams prestressed by CFRP was mainly elastic at failure.

3.12 *Ultimate moment of resistance*

Table 2 summarised the test results of Beams C40-80-S and 80-120-S, together with the theoretical values. It can be seen that the test results are in close agreement with the calculated values. The failure of the beams prestressed by CFRP was due to the rupture of the CFRP rods in the shear span as described above.

3.13 *Residual deflections*

The residual deflections when unloaded after first cracking were relatively small for all beams. The residual deflections as a percentage of the original deflection after each loading cycle are plotted against the original deflection level in Figure 13. The residual

Table 2. Comparison of test results and theoretical values of beams with CFRP.

Beam ID	C40-80-S	C80-120-S
Cracking load, $P_{cr,\ exp.}$ (kN)	13.6	19.6
Cracking load, $P_{cr,\ theo.}$ (kN)	15.5	18.7
Ultimate load, $P_{u,\ exp.}$ (kN)	37.7	47.8
Ultimate load, $P_{u,\ theo.}$ (kN)	35.4	46.2
Deflection at first crack, $\Delta_{cr,\ exp.}$ (mm)	5.64	6.25
Deflection at ultimate, $\Delta_{u,\ exp.}$ (mm)	137	131.5
$P_{u,\ exp.}/P_{cr\ exp.}$	2.77	2.44
$\Delta_{u,\ exp.}/\Delta_{cr\ exp.}$	24.29	21.04

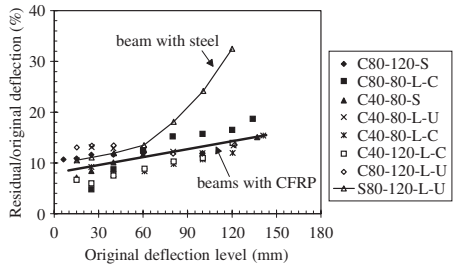

Figure 13. Residual deflections of beams prestressed by CFRP and by steel.

deflections were only about 10 to 12% of the original deflection which means the beams prestressed by CFRP showed a very good recovery when unloaded at different levels. Beam T-4-0.5-V tested by Abbdelrahman (1995) also resulted in a residual deflection equal to 11.4% of the original deflection when unloaded at 91.8 mm of deflection. This behaviour is attributed to the linear elastic stress–strain behaviour up to the failure of the CFRP tendon. The high recovery of deflection behaviour is an advantage in terms of serviceability, but is a disadvantage in term of energy absorption at the ultimate limit state, i.e. more energy will be released at failure when the failure was caused by rapture to tendons. From the figure, for the beams prestressed by CFRP, it is accurate enough to assume that the residual deflection is in the range of 8 to 15% of the original deflection when unloaded. The elastic and inelastic energies can be calculated based on this residual deflection.

In the case of beams prestressed by steel, before the steel yielded, the residual deflection was also about 12% of the original deflection. However, after the steel yielded, the level of residual deflection (in terms of percentage of original deflection) increased rapidly up to 35% of the original deflection.

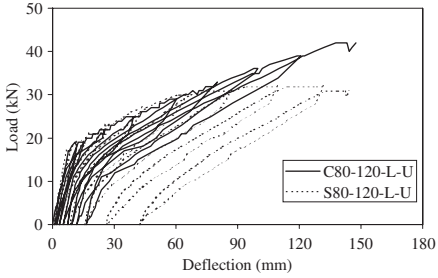

Figure 14. Comparison of load–deflection of beams prestressed by CFRP and steel.

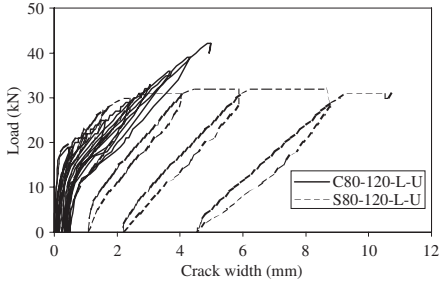

Figure 15. Comparison of load–crack width of Beams C80-120-L-U and S80-120-L-U.

3.14 *Comparison of beams prestressed by CFRP rods and by steel strands*

3.14.1 *Load–deflection relationships*

The load–deflection relationship of the beam prestressed by CFRP (Beam C80-120-L-U) is compared to the beam prestressed by steel (Beam S80-120-L-U) in Figure 14. The behaviour of the two beams was similar before cracking. Both beams cracked at similar load levels. After yielding of the steel, the deflection of Beam S80-120-L-U increased rapidly while there was not much increase in load. The Beam C80-120-L-U showed a different behaviour. The load continued to increase with in increase of deflection up to failure. This is due to the stress–strain relationship of the CFRP being almost linear up to failure. This behaviour led to Beam C80-120-L-U reaching a higher load carrying capacity at ultimate than Beam S80-120-L-U, although the area of tendon and the total breaking force was similar for both beams.

As describe previously, before the steel strands yielded, the recovery of deflections (or residual deflections) was similar for both beams. After the steel yielded, the beam prestressed by steel showed more residual deflection, i.e. the recovery of deflection was as good as for the beam prestressed by CFRP. Again, this is because the stress–strain relationship of the CFRP is linear up to failure. This indicates that at ultimate, the energy stored in the beam prestressed by steel strands is mainly inelastic while it is mainly elastic in the beam prestressed by CFRP rods.

3.14.2 *Crack widths*

Figure 15 shows the development of the width of a major crack in the constant moment zone for both beams. For the loads in the range corresponding to first cracking until the steel yielded in Beam S80-120-L-U, Beam C80-120-L-U had a larger crack width than Beam S80-120-L-U at the same loading level. This is because the Young's modulus of CFRP is lower than that of steel. After the steel yielded, the crack width of Beam S80-120-L-U developed very rapidly while the crack width in Beam C80-120-L-U developed at a constant rate up to failure. At ultimate, the crack width in Beam C80-120-L was about 5 mm while Beam S80-120-L-U reached 10.7 mm. The load–crack width relationship of Beam C80-120-L-U may be described as linear while it is non-linear for Beam S80-120-L-U. The recovery of crack width of Beam S80-120-L-U was good before the steel yielded and it was poor after the steel yielded. However, the recovery of the crack width of Beam C80-120-L-U was good up to failure.

3.14.3 *Failure mode*

The failure of the beam prestressed by steel strands (Beam S80-120-L-U) was due to the rupture of the steel strands in the constant moment zone. This is because of the beam was under-reinforced and the concrete strength was as high as 75 MPa. In the case of Beam C80-120-L-U, the failure was due to the rapid development of the flexural-shear crack located 500 mm away from the loading point. At ultimate state Beam C80-120-L-U deflected 152 mm with the load of 42 kN, while Beam S80-120-L-U deflected 143.8 mm with a load of 32 kN.

3.15 *Effect of concrete strengths*

The effect of concrete strengths on the load–deflection behaviour for the Beams prestressed by CFRP rods is shown in Figure 16. The cracks in beam C40-80-L-C were much more extensive than that in beam C80-80-L-C under the sustained service load in terms of both crack width and crack height. There were 10 cracks in Beam C40-80-L-C and only 7 in Beam C80-80-L-C when they were subjected to the UDL. The deflection was smaller at the same loading level when higher concrete strength was used. However, the ultimate deflections were not affected much by the concrete strength. At the ultimate state, the number of cracks was the same for both beams and the crack spacing

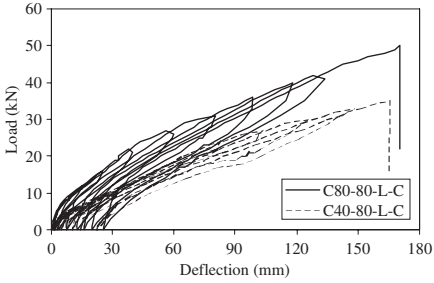

Figure 16. Comparison of beams with different concrete strengths.

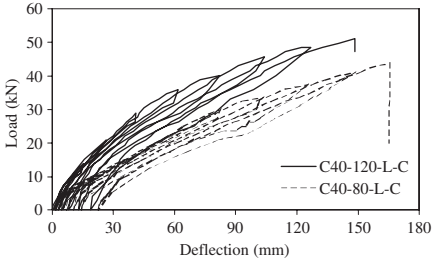

Figure 17. Comparison of load–deflection of beams with different prestress.

was also similar, ranging from 250 to 400 mm. With the higher concrete strength, the maximum crack width reduced from 4.3 to 3.7 mm (14% reduction). The concrete strain at the top fibre was reduced from 0.0025 to 0.002. At failure, the CFRP rods in Beam C40-80-L-C were not cut off and no horizontal cracks appeared in the beam. However, the CFRP rods in Beam C-80-80-L-C ruptured at the flexure-shear section and a 4 m long horizontal crack appeared at the level of the tendons after the rupture of the CFRP.

3.16 *Effect of level of prestressing force*

The effect of the level of prestressing force on load–deflection relationship can be seen by comparing the load–deflection of Beams C40-80-L-C and C40-120-L-C as shown in Figure 17.

The cracking was more extensive in Beam C40-80-L-C than that in Beam C40-120-L-C due to sustained service load before being tested to the ultimate. With a higher prestressing force, the deflection at the same loading level was lower but the residual deflection was similar for both beams after unloading. The deflection at ultimate of beam with higher prestress was slightly

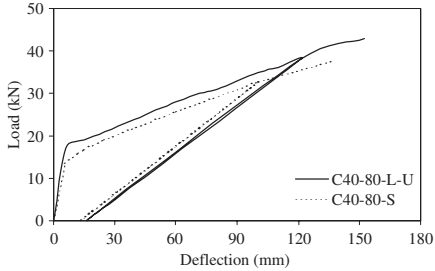

Figure 18. Comparison of load–deflection of Beams C40-80-S and C40-80-L-U.

less than the beam with lower prestressing force. The crack width was smaller at a higher prestressing force at the same loading level but was similar at ultimate.

3.17 *Effect of sustained service load*

The load–deflection relationship of Beams C40-80-S and C40-80-L-U are compared in Figure 18 and the effect of sustained service load on the ultimate strength is insignificant. The stiffnesses before and after cracking were similar for both beams, so was the recovery of deflection upon unloading. Beam C40-80-L-U failed at a slightly higher deflection level and this was due to the creep of concrete with time. The ultimate load was also slightly higher for beam C40-80-L-U and this was possibly due to the increase of concrete strength with time. The number of cracks and the crack spacing were also similar for both beams.

3.18 *Effective sectional stiffness*

For the beams prestressed by CFRP rods and without any additional steel reinforcement, current investigation showed that the load–deflection behaviour was linear before cracking and still linear after cracking with a reduced sectional stiffness. Abbdelrahman and Rizkalla (1995) also reported similar behaviour in their studies. Hence for simplicity purpose the load–deflection behaviour of beams prestressed by CFRP can be simplified as a bilinear relationship. Given the slope of the load–deflection curve before cracking is Ω_0, and the slope of the curve after cracking is Ω_1, the bilinear behaviour can be modelled by establishing a simple relationship between Ω_1 and Ω_0:

$$\Omega_1 = a\,\Omega_0 \qquad (1)$$

where a is a factor which depends on the material properties and the sectional geometry. Ω_0 is easily determined using the gross sectional stiffness $E_c I_g$ and the cracking load P_{cr}. The present study showed a

Table 3. Slope of load–deflection curves of concrete beams prestressed by CFRP.

Beam ID	Ω_1/Ω_0 (%)	Source
C40-80-S	11.6	Current research
C80-120-S	11.5	Current research
T-4-.5-H	9.8	Abbdelrahman (1995)
R-4-.5-H	14.2	Abbdelrahman (1995)
T-4-.5-V	7.4	Abbdelrahman (1995)
R-4-.5-V	10.3	Abbdelrahman (1995)
T-4-.7-V	8.9	Abbdelrahman (1995)
R-4-.7-V	11.5	Abbdelrahman (1995)
R-2-.5-V	7.5	Abbdelrahman (1995)
TR-1-7.5/7	13.5	Fam (1995)
TR-2-5/1	13	Fam (1995)
TR-3-5/7	13.3	Fam (1995)
LL-4-2B	13.2	Fam (1995)
LL-5-1B	12.8	Fam (1995)

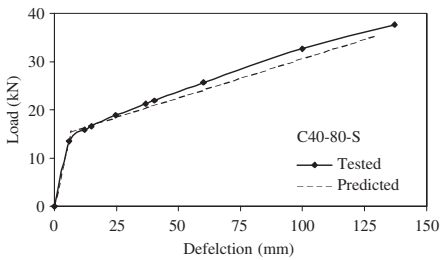

Figure 19. Comparison of tested and predicted load–deflection curves of C40-80-S.

is 11.5% for the beams tested as shown in Table 3. The results obtained by Abdelrahman (1995) and Fam (1995) are also quoted in Table 3 for comparison. From this table, it can be seen that the slope after cracking is in the range of 7.4 to 13.5% of the slope before cracking. The ultimate load can be easily calculated using the current code methods, hence the load–deflection of beams prestressed by CFRP is readily determined when the slope of the curve after cracking is known.

Considering a concrete beam prestressed by CFRP rods, the cracking moment, ultimate moment and gross sectional stiffness can be easily calculated based on the material properties and the geometry of the cross section. Hence the deflection at first cracking is also obtained. If the slope of the load–deflection curve after cracking is known, then the load–deflection relationship can be determined. Using Equation 1 and taking $a = 11.5\%$, the predicted and tested curves of load–deflection relationships of C40-80-S, are shown in Figure 19. A good agreement between the test results and the predicted curves are seen in this figure.

4 CONCLUSIONS

In summary, this study could derive the following conclusions:

- The load–deflection relationship of beams prestressed by CFRP rods was linear before cracking and almost linear after cracking with a reduced stiffness and this is different from the load–deflection of the beam prestressed by steel. The slopes of the load–deflection curve before and after cracking (denoted as Ω_0 and Ω_1, respectively) are related as follows: $\Omega_1 = (0.1 \sim 0.15)\ \Omega_0$. Large deflection near failure of 1/40 of the span of the beams prestressed by CFRP give sufficient warning before failure. The residual deflection was about 10 to 15% of the original deflection for beams prestressed by CFRP rods and the energy stored in the beams was mainly elastic up to failure. In comparison, the beam prestressed by steel showed the residual deflection to be as mush as 35% of the original deflection.
- The cracking load was in close agreement with the theoretical value. No slip of tendons was found at the end of the beams up to failure. The crack widths in the beams prestressed by FPR t\rods were larger than that of the beam prestressed with steel strand, within the service loading level. The number of cracks of the beams prestressed by CFRP was 9 to 12 at ultimate and the crack spacing was in the range of 230 mm to 500 mm with the maximum height of 270 mm. The crack width was more than 4 mm at failure. The horizontal crack due to the rupture of the CFRP rods indicated that the energy stored in the beam was mainly elastic up to ultimate.
- The strain compatibility method is suitable for predicting the load–deflection relationship of beams prestressed by CFRP rods for both normal and high strengths concrete.
- An increase of concrete strength led to a higher cracking load and less deflection at the same loading level. However, neither the total number of cracks nor the deflection at ultimate was affected significantly.
- With an increase of the level of prestressing force, the cracking load increased while the deflection at ultimate reduced, but the ultimate moment carrying capacity was not affected.
- There was no evidence that the sustained service load would affect the ultimate limit state if the beam did not crack under the sustained service load.

The shear failure of the beams prestressed by CFRP rods indicated that the dowel action of CFRP in prestressed concrete beams was less than that of steel due to the low transverse shear strength of CFRP. Further investigation is needed in this area.

REFERENCES

Abbdelrahman, A.A. (1995), Serviceability of concrete beams prestressed by Carbon Fibre Reinforced Plastics tendons (*PhD thesis*), University of Manitoba, Canada.

Abbdelrahman, A.A. and Rizkalla, S.H. (1995), Serviceability of concrete beams prestressed by carbon fibre plastic rods, *Non-metallic (FRP) reinforcement for concrete structures*, Taerwe L. (Ed.), E & FN Spon, pp. 403–412.

ACI 440.1R-03 (2003), *Guide for the Design and Construction of Concrete Reinforced with FRP Bars*, American Concrete Institute (ACI) Committee 440, technical committee document 440.1R-03, Michigan, USA, 42 pp.

Agyei B.B., Lees J.M. and Terrasi G.P. 2003, "Fatigue of high strength concrete beams pretensioned with CFRP tendons", Fibre-reinforced polymers reinforcement for concrete structures (*Proceeding of FRPRCS 6 International symposium*), July 2003 Singapore 935–944.

Dolan C., Hemiltom H.R., Bakis E and Nanni A. (2001), Design recommendations for concrete structures prestressed with FRP tendons (*FHWA Contract DTFH61-96-C-0009 Final report*), Parts 1, 2 and 3.

Fam A, 1995, "Carbon fibre reinforced plastics prestressing and shear reinforcements for concrete highway bridges; MSc Thesis, University of Manitoba, Winnipeg, Manitoba, Canada.

Park S.Y. and Naaman A.E. 1999, Shear behaviour of concrete beams prestressed with FRP tendons, *PCI Journal* 4491, 73–85.

Naaman A.E. 2003, "FRP reinforcement in structural concrete: assessment, Progress and Prospects" Fibre-reinforced polymers reinforcement for concrete structures (*Proceeding of FRPRCS 6 International symposium*), July 2003 Singapore. 1–23.

Zou P.X.W. (2003), "Long-term deflection and cracking behaviour of concrete beams prestressed with fiber reinforced polymer tendons", *ASCE Journal of Composite Construction*, 7(3), 187–193.

FRP Composites in Civil Engineering – CICE 2004 – Seracino (ed)

Predicting the long-term behaviour of concrete beams pretensioned by fibre reinforced polymers – Part A: a theoretical framework

Patrick X.W. Zou
The University of New South Wales, Sydney, Australia

ABSTRACT: The corrosion-free property of fibre reinforced polymers (FRP) has attracted researchers worldwide to study the feasibility of using FRP as reinforcement or prestressing tendons in concrete structures. However the majority of these studies up-to-date have been in the form of experimental. This paper proposes an analytical method to predict the time-dependent behaviour, including concrete strains, curvature and deflection as well as loss of prestress, of concrete beams prestressed by FRP tendons, under sustained service load condition.

1 INTRODUCTION

In prestressed concrete flexural members the prestressing force is applied to the concrete in order to reduce the curvature, the deflection and the extent of cracking. Over a period of time the prestressing force in the member will progressively decrease due to creep and shrinkage of the concrete, as well as relaxation of the tendons, i.e. the loss of prestress increases with time. The loss of prestress results in a gradual increase in the deflections which affects the serviceability of the member.

If FRP tendons are to be used as alternatives to steel tendons in prestressed concrete, it is important to understand the implications and effects on the time-dependent structural behaviour. The material properties of the tendons that most affect the service load performance of prestressed structures are the elastic modulus E_p and the final percentage relaxation R (or creep coefficient, ϕ_p). Some FRP tendons may relax or creep more than prestressing steel tendons and the elastic modulus may be substantially lower than that of steel. Higher creep in the tendons results in a greater loss of prestress (due to relaxation), whilst a lower elastic modulus means that the time dependent deformations of the concrete (due to creep and shrinkage) cause less loss of prestress.

Many researchers have provided test results indicating that FRP in fact could be an alternative to steel to prestress concrete beams (Jeong 1994, Abdrehraman 1995, Abdrehraman and Rizkalla 1995, Brown 1997, Dolan et al 2003, Zou 2003) at service load level. In this paper, analytical methods are presented for determining the short-term and time-dependent behaviour of fully or partially prestressed cross-sections under sustained bending and axial force. The Age-adjusted Effective Modulus Method (AEMM) is used to model the creep behaviour in the concrete and the relaxation in the FRP prestressing tendons. A tension-stiffening model proposed by Zou (2003) which was modified based on Gilbert (1988) was adopted for the calculation of the effective section stiffness of the cracked beams.

2 CROSS-SECTIONAL ANALYSIS METHOD

This section discusses methods of cross-sectional analysis, including un-cracked and cracked sections.

2.1 *Determination of analysis method*

Two cross-sectional analysis methods have been considered here, and these are dependent on the magnitude of the service load that is applied to the beam. These are uncracked section analysis, and cracked section analysis.

The method used to ascertain whether an uncracked section analysis or a fully cracked section analysis is to be undertaken is to first calculate the cracking moment M_{cr} required to cause flexural tensile cracking (The moment at which cracking first occurs is called the cracking moment). If the service moment applied to the cross-section of the beam M_s is less than the cracking moment, then an uncracked section analysis is undertaken, otherwise a fully cracked section analysis must be used.

The cracking moment M_{cr} is calculated using the following equation:

$$M_{cr} = P_e\, e + \left(f_r + \frac{P_e}{A_g} \right) Z_b \qquad (1)$$

where P_e is the effective prestressing force; e is the eccentricity of the prestressing tendons based on the gross cross-sectional properties; f_r is flexural strength of concrete; A_g is gross cross-sectional area; and Z_b is section modulus.

2.2 *Short-term analysis of an uncracked pretensioned section*

The short-term analysis of a cross-section can be carried out by transforming the bonded reinforcement into equivalent areas of concrete and performing a simple, elastic analysis on the equivalent concrete section. Consider the transformed section shown in Figure 1.

The area A, the first and second moments B and $\bar{I}$ respectively of the transformed section about the top fibre are given by the following equations:

$$A = bD + (n_p - 1)A_p + (n_{s1} - 1)A_{s1} + (n_{s2} - 1)A_{s2} \quad (2)$$

$$B = \frac{1}{2}bD^2 + (n_p - 1)A_p d_p + (n_{s1} - 1)A_{s1} d_{s1} + (n_{s2} - 1)A_{s2} d_{s2} \quad (3)$$

$$\bar{I} = \frac{1}{3}bD^3 + (n_p - 1)A_p d_p^2 + (n_{s1} - 1)A_{s1} d_{s1}^2 + (n_{s2} - 1)A_{s2} d_{s2}^2 \quad (4)$$

The ratios n_p, n_{s1} and n_{s2} are the modular ratios of the prestressing tendon or ordinary reinforcements to the concrete, and are given by (E_p/E_c), (E_{s1}/E_c) and (E_{s2}/E_c) respectively. A_{s1} and A_{s2} represent the areas of additional steel reinforcements at the top and bottom of the section.

The initial strain and stress distributions of uncracked sections are shown in Figure 2. The concrete strain at top fibre ε_{oi} and the initial curvature κ_i are given by (Gilbert and Mickleborough, 1990):

$$\varepsilon_{oi} = \frac{B M_i - \bar{I} N_i}{E_c\left(B^2 - A\bar{I}\right)} \quad (5)$$

and

$$\kappa_i = \frac{B N_i - A M_i}{E_c\left(B^2 - A\bar{I}\right)} \quad (6)$$

where the stress resultants N_i and M_i for the cross-section are

$$N_i = -P_i \quad (7)$$

$$M_i = M_s - P_i d_p \quad (8)$$

The initial concrete strain and stress at y below the top fibre are

$$\varepsilon_i = \varepsilon_{oi} + y\kappa_i \quad (9)$$

$$\sigma_i = E_c \varepsilon_i = E_c(\varepsilon_{oi} + y\kappa_i) \quad (10)$$

The corresponding stresses in the tendons and the reinforcement can be determined using the linear material properties for FRP prestressing tendon or reinforcement.

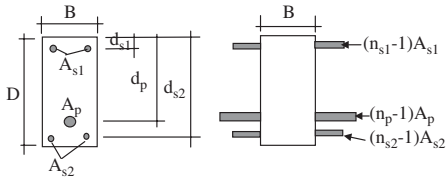

Figure 1. Actual and transformed uncracked cross-sections.

2.3 *Short-term analysis of a cracked pretensioned section*

If the applied moment at a section is greater than the cracking moment at any time t, cracking will occur and at each crack the concrete below the neutral axis

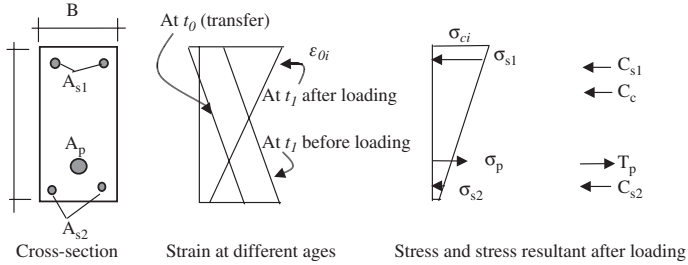

Figure 2. Distribution of initial strain and stress of an uncracked section.

is ineffective. The short-term behaviour of the cracked cross-section may be calculated using a simple elastic analysis with the following assumptions:

1. Plane sections remain plane and therefore the strain distribution is linear over the depth of the section.
2. Perfect bond exists between the concrete and FRP tendons and reinforcements.
3. Instantaneous material behaviour is linear-elastic for concrete, steel and FRP.

The instantaneous strains and stresses on a cracked section are shown in Figure 3.

The horizontal equilibrium and moment equilibrium can be used in the cross section to find the concrete strain at top fiber ε_{oi} and the depth of neutral axis d_n, that is:

$$T_p + T_s + C + C_s = 0 \tag{11}$$

$$M_s = T_p d_p + T_s d_{s2} + C d_z + C_s d_{s1} \tag{12}$$

where C, C_s, T_s and T_p may be expressed as functions of d_n and ε_{oi}, as follows:

$$C = \frac{1}{2} E_c \varepsilon_{oi} b d_n \tag{13}$$

$$C_s = E_{s1} A_{s1} \frac{-\varepsilon_{oi}\left(d_n - d_{s1}\right)}{d_n} \tag{14}$$

$$T_s = E_{s2} A_{s2} \frac{-\varepsilon_{oi}\left(d_{s2} - d_n\right)}{d_n} \tag{15}$$

$$T_p = E_p A_p \left(\varepsilon_{pe} + \left|\varepsilon_{ce}\right| + \frac{-\varepsilon_{oi}\left(d_p - d_n\right)}{d_n} \right) \tag{16}$$

where

$$\varepsilon_{pe} = \frac{P_e}{A_p E_p} \tag{17}$$

$$\varepsilon_{ce} = \frac{1}{E_c}\left(-\frac{P_e}{A_g} - \frac{P_e e^2}{I_g} \right) \tag{18}$$

By a trial and error procedure, the depth of neutral axis d_n and the strain at top fibre ε_{oi} can be found. Hence the curvature κ_i can be determined:

$$\kappa_i = -\frac{\varepsilon_{oi}}{d_n} \tag{19}$$

After d_n is determined, the properties of the fully cracked transformed section with respect to the top reference surface (A, B and $\bar{I}$) may be calculated and the short-term strain at the top fibre, the curvature and hence the distribution may be found by Equations 5 and 6, respectively. Furthermore, when d_n and ε_{oi} are known, the strains and stress in the tendons or reinforcements are also readily determined.

2.4 *Time-dependent analysis of cross-section*

In pretensioned concrete beams, the bonded tendons and the reinforcement provide restraint to the time-dependent shortening of concrete caused by creep and shrinkage. The tendon and reinforcement are gradually compressed. Equal and opposite tensile forces are applied to the concrete at each level of the bonded tendon and reinforcement, thereby reducing the compression caused by prestress. It is the tensile forces applied gradually at each level of bonded reinforcement that result in significant time-dependent changes in curvature and deflection (Gilbert and Mickleborough, 1990). The sum of the time-dependent change of strain at any depth y below the top fibre of the cross-section ($\Delta\varepsilon$) may be expressed in terms of the change in the top fibre strain ($\Delta\varepsilon_o$) and the change of curvature ($\Delta\kappa$):

$$\Delta\varepsilon = \Delta\varepsilon_o + y\Delta\kappa \tag{20}$$

The time analysis of the cross-section considered here uses the AEMM together with a relaxation approach. The application was proposed by Gilbert (1988).

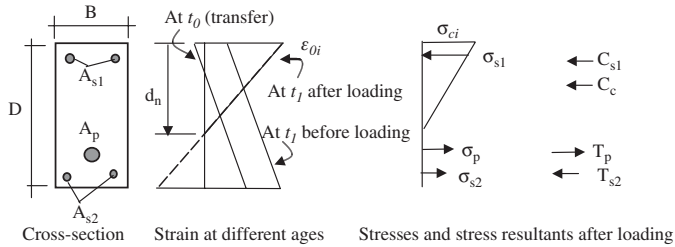

Figure 3. Distribution of strain and stress of a cracked section.

In the relaxation procedure, the strain state is assumed to be held constant throughout a given time interval. If the total strain is held constant and the creep and shrinkage strains change, then the instantaneous component of strain must also change by an equal and opposite amount. As the instantaneous strain changes, so too does the concrete stress. The concrete stress on the cross-section is therefore allowed to vary due to relaxation. As a result, the internal actions change and equilibrium is not maintained. An axial force ΔN and a bending moment ΔM must, therefore, be applied to the cross-section to restore equilibrium. The actions required to restrain creep and shrinkage in the concrete and creep in the prestressing tendon are given by

$$\Delta N = \overline{E}_{ec}\left[\phi_{cr}\left(A_c\varepsilon_{oi} + B_c\kappa_i\right) + \varepsilon_{sh}A_c\right] + E_{ep}\phi_p\left(A_p\varepsilon_{oi} + A_p d_p\kappa\right) \quad (21)$$

$$\Delta M = \overline{E}_{ec}\left[\phi_{cr}\left(B_c\varepsilon_{oi} + \overline{I}_c\kappa_i\right) + \varepsilon_{sh}B_c\right] + E_{ep}\phi_p\left(A_p d_p\varepsilon_{oi} + A_p d\right) \quad (22)$$

where $\overline{E}_{ec}$ is the age-adjusted effective modulus for concrete and E_{ep} is the effective modulus of the prestressing tendons.

The variables A_c, B_c and I_c are the area, first moment of area and second moment of area of the concrete part of the cross-section, with respect to the top surface. The change of strain in the top fibre and the change of curvature with time are calculated using the equivalent properties $\overline{A}_e$, $\overline{B}_e$ and $\overline{I}_e$ of the age-adjusted transformed section and the equations below:

$$\Delta\varepsilon_o = \frac{\overline{B}_e\Delta M - \overline{I}_e\Delta N}{\overline{E}_{ec}\left(\overline{B}_e^{\,2} - \overline{A}_e\overline{I}_e\right)} \quad (23)$$

$$\Delta\kappa = \frac{\overline{B}_e\Delta N - \overline{A}_e\Delta M}{\overline{E}_{ec}\left(\overline{B}_e^{\,2} - \overline{A}_e\overline{I}_e\right)} \quad (24)$$

The modular ratios of the age-adjusted transformed section are given by $\overline{n} = E_{ep}/\overline{E}_{ec}$, $\overline{n}_{s1} = E_{s1}/\overline{E}_{ec}$ and $\overline{n}_{s2} = E_{s2}/\overline{E}_{ec}$ and are used to determine the transformed area of the tendons and the non-prestressed reinforcements (if any).

The change in stress in the concrete at any depth y is

$$\Delta\sigma = -\overline{E}_{ec}\left[\phi_{cr}(t,t_0)\left(\varepsilon_{oi} + y\kappa_i\right) + \varepsilon_{sh} - \left(\Delta\varepsilon_o + y\Delta\kappa\right)\right] \quad (25)$$

and the change in stress in the tendon is

$$\Delta\sigma_p = -E_{ep}\left[\phi_p\left(\varepsilon_{oi} + d_p\kappa_i\right) - \left(\Delta\varepsilon_o + d_p\Delta\kappa\right)\right] \quad (26)$$

After the time-dependent changes of strains, curvatures and stresses are determined, the final strains, curvatures and stresses at the cross-section are readily found by

$$\varepsilon(t) = \varepsilon_{oi} + \Delta\varepsilon(t) \quad (27)$$

$$\kappa(t) = \kappa_i + \Delta\kappa \quad (28)$$

$$\sigma(t) = \sigma_{oi} + \Delta\sigma \quad (29)$$

Note it is assumed here that the neutral axis position remains constant with time. When a fully cracked cross-section is subjected to a period of sustained loading, creep causes a change of position of the neutral axis. In general, the depth to the neutral axis increases with time and so too does the area of concrete in compression. However, to include this in the calculations requires an iterative numerical solution that leads to increased complexity with little increase in accuracy. This assumption is in fact necessary, if the short-term and time-dependent stress and strain increments are to be calculated separately and added together to obtain the final stresses and deformations. The assumption greatly simplies the analysis and usually results in relatively little error.

3 DEFLECTION CALCULATION

Direct integration of curvature can be used to calculate the deflection of the beam. By obtaining a variation of curvature at a number of sections using the method described in previous section, the deflection at midspan can be obtained by integrating the curvatures $\kappa(x)$ twice.

$$\Delta = \int_0^L\int_0^L \kappa(x)\,dx\,dx \quad (30)$$

This equation is a general equation and applicable for both elastic and inelastic material behaviour. It is also suitable for short-term and long-term deflection calculations.

For cracked beams, the deflection can be calculated with and without accounting for tension stiffening. (Note that the calculation that takes tension stiffening effect into account will lead to more accurate results).

3.1 *Integration of curvature*

In this method the deflection was determined by integration of the curvature from the support to the midspan section to obtain the maximum deflection due

to the sustained service load. The curvature integration is performed numerically using Equation 31 and is illustrated in Figure 4 (with $x_1 = 0$).

$$\Delta = \frac{\kappa_1 x_1 + \kappa_2 x_2}{2}(x_2 - x_1) + \frac{\kappa_2 x_2 + \kappa_3 x_3}{2}(x_3 - x_2) + \frac{\kappa_3 x_3 + \kappa_4 x_4}{2}(x_4 - x_3) \quad (31)$$

In this case, the integration of curvature is performed at four distinct sections for one half of the beam, namely at the support, cracking moment, location of the concentrated load and midspan (see Figure 4). It should be noted that increasing the number of sections increases the accuracy of the calculations.

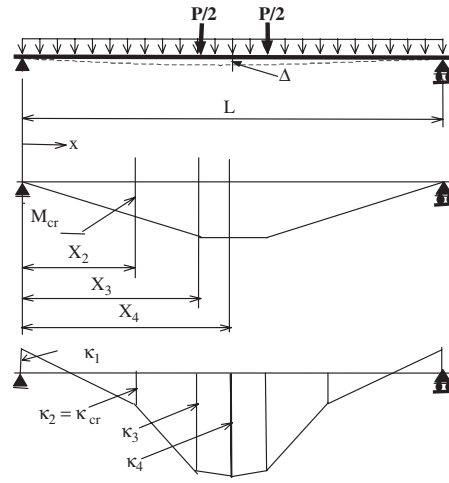

Figure 4. Integration of curvature at 4 key sections.

3.2 *Tension stiffening*

Immediately after first cracking, the intact concrete between adjacent primary cracks carries considerable tensile force, mainly in the direction of the tendon or reinforcement, due to the bond between the tendon or reinforcement and the concrete. The average tensile stress in the concrete is a significant percentage of the tensile strength of concrete. The stress in FRP tendon/reinforcement is a maximum at a crack, where the FRP carries the entire tensile force, and drops to a minimum between the cracks. The bending stiffness of the member is greater than that based on a fully-cracked section, where concrete in tension is assumed to carry zero stress. This tension stiffening effect may be significant in the service-load range of performance of beams. Noting that concrete has the ability to carry tensile stress between cracks in the tension zone due to the bond between the FRP and concrete, a tension stiffening model should therefore be used in the cracked cross-sectional analysis of the beams.

Gilbert (1988) proposed a tension stiffening model for concrete members with steel reinforcement or steel tendons. The approach for modelling tension stiffening is to assume that an area of concrete located at the tensile steel level is effective in providing stiffening. Figure 5 shows an average cross-section of a singly reinforced member. The properties of this average section are between those of fully-cracked cross-section and the uncracked cross-section between the primary cracks. The tensile concrete area A_{ct}, is assumed to contribute to the beam stiffness after cracking and depends on the magnitude of the maximum applied moment M_s, the area of tendon or tensile reinforcement A_{st}, the amount of concrete below the neutral axis, the tensile strength of the concrete (i.e., the cracking moment M_{cr}), and the duration of the sustained load. The tensile concrete area A_{ct}may be calculated using Equation 32:

$$A_{ct} = \beta_1 \beta_2 \left(0.21 b_w - n A_{st}\right)\left(\frac{M_{cr}}{M_s}\right)^2 \quad (32)$$

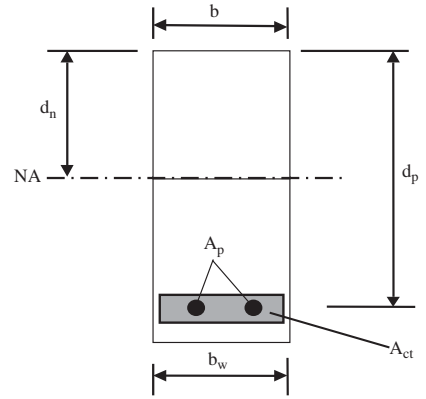

Figure 5. Tension stiffening model (Gilbert, 1988).

where $\beta_1 = 1.0$ for deformed bars/tendons and 0.5 for round bars; $\beta_2 = 1.0$ for initial loading and 0.5 for long-term load or cycles of load.

The above mentioned Gilbert's model (Gilbert 1988) was modified by Zou (2003) for its application to FRP pretensioned concrete beams, through the introduction of a material parameter, β_3, as follows:

$$A_{ct} = \beta_1 \beta_2 \beta_3 \left[0.21 b_w d - n A_{st}\right]\left(\frac{M_{cr}}{M_s}\right)^2 \quad (33)$$

where β_1 is the reinforcement surface condition parameter, β_2 is the load history parameter, and β_3

is the material parameter. Zou (2003) recommended values of these parameters, as given in Table 1.

There are also other tension stiffening models and some of these are described below. The tension stiffening model specified in ACI 318-95 (1999) involves the calculation of the transformed second moments of the cracked and uncracked critical sections and calculating an effective second moment of area which depends on the ratio of applied service moment to cracking moment at the cross-section being considered. The model is based on that of Branson (1964) which was originally developed for reinforced concrete. In this model, the effective second moment of area, I_e as:

$$I_e = I_{cr} + \left(I_g - I_{cr}\right)\left(\frac{M_{cr}}{M_s}\right)^3 \leq I_g \tag{34}$$

The CEB-FIP (1983) has also proposed an alternative approach for reinforced concrete and was modified for cracked, prestressed sections by Gilbert (1990) as below:

$$I_e = \left(1-\zeta\right)I_u + \zeta I_{av} \tag{35}$$

where

$$\zeta = 1 - \beta_1\beta_2\left(\frac{M_{cr}}{M_s}\right)^2 \tag{36}$$

Here $\beta_1 = 1.0$ when deformed non-prestressed bars are present; 0.5 when plain round bars or bonded tendons only are present; $\beta_2 = 1.0$ for initial loading; 0.5 for long-term sustained loads or cycles of load.

3.3 *Long-term deflection*

Long-term deflections due to concrete creep and shrinkage are affected by many variables, including load intensity, concrete mix proportions, member size, age at first loading, concrete curing conditions, total quantity of compressive and tensile reinforcement, level of prestress, relative humidity and temperature (Gilbert and Mickleborough 1990). As for short-term deflection calculations, when the curvature at time t has been determined at each section, the long-term deflection at that time can be calculated by integrating the curvature twice.

There are also a number of approximate procedures for calculating the long-term deflection which are described in detail elsewhere (Gilbert and Mickleborough 1990). Gilbert and Mickleborough (1990) have pointed out that the long-term deflection multiplication factor specified in ACI 318-95 (1999) for reinforced concrete is not suitable for prestressed concrete members. This is because in prestressed concrete construction, a large proportion of the sustained external load is often balanced by the transverse force exerted by the tendons. Under this balanced load, the short-term deflection may be zero but usually the long-term deflection is not. The restraint to creep and shrinkage offered by non-symmetrically placed, bonded reinforcement on a section can cause significant time-dependent curvature and hence, significant deflection of the member.

Table 1. Values of β_1, β_2 and β_3 for FRP reinforcements.

Parameters	AFRP rod (Sand coated)	CFRP rod (indented)
β_1 (Surface)	1.0	0.5
β_2 (Short-term)	1.0	1.0
β_2 (Long-term)	0.5	0.5
β_3 (Material)	0.5	0.5

4 LOSS OF PRESTRESS

The losses of prestress that occur in a prestressed member can be illustrated in Figure 6.

When the prestress is transferred to the concrete, immediate losses of prestress occur. The difference between the prestressing force imposed at the jack, P_j, and the force in the tendon immediately after transfer at a particular section, P_i, is the immediate loss:

$$\textit{Immediate losses} = P_j - P_i \tag{37}$$

The gradual loss of prestress that takes place with time is called the time dependent loss. If P_e is the force in the prestressing tendon after all losses, then

$$P_e = P_i - \textit{time-dependent losses} \tag{38}$$

Both of these losses are made up of several components and are different for pretensioned members.

In a pretensioned member, the immediate loss is caused by elastic deformation of the concrete as the

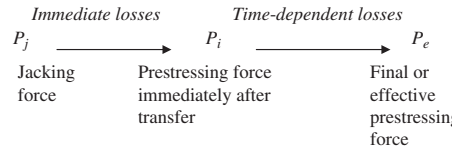

Figure 6. Losses of prestress (Gilbert and Mickleborogh 1990).

prestress is transferred. The change of strain in the tendon $\Delta\varepsilon_p$ caused by elastic shortening of the concrete is equal to the concrete strain at the tendon level, ε_{cp},

$$\varepsilon_{cp} = \frac{\sigma_{cp}}{E_c} = \Delta\varepsilon_p = \frac{\Delta\sigma_p}{E_p} \tag{39}$$

where σ_{cp} is the concrete stress at the tendon level, therefore, the loss of stress in the tendon is

$$\Delta\sigma_p = \frac{E_p}{E_c}\sigma_{cp} \tag{40}$$

The time-dependent losses are caused by the gradual shortening of the concrete at the tendon level due to creep and shrinkage, and by relaxation (creep) of the tendon and it can be calculated using the analysis described in previous section.

5 SUMMARY

This paper has provided a theoretical framework for calculating the time-dependent concrete strains, curvature and deflection of concrete beams prestressed by FRP tendons and loss of prestressing force. The framework uses the age-adjusted effective module method and takes into consideration the tension stiffening effects. The subsequent paper (Zou 2004) will provide illustrative examples how to predict the long-term behaviour of FPR pretensioned concrete beams using this framework.

REFERENCES

American Concrete Institute (ACI) (1999), "Building Coe requirements for reinforced concrete." ACI 318, Detroit.

CEB-FIP 1990, Model Code for concrete structures, Tomas Telford Editor, London.

Dolan C., Hemiltom H.R., Bakis E. and Nanni A. (2001), Design Recommendations for concrete structures prestressed with FRP tendons (FHWA Contract DTFH61-96-C-0009 Final report), Parts 1, 2 and 3.

Gilbert R.I. (1988), Time effects on concrete structures, Elsvier, New York, 321pp.

Gilbert R.I. and Mickleborough N.C. (1990), Design of prestressed concrete, Unwin Hyman, London, 504pp.

Jeong S-M (1994). Evaluation of ductility in prestressed concrete beams using fiber reinforced plastic tendons, (*PhD thesis*), The University of Michigan, USA.

Zou P.X.W. (2003), "Theoretical study on short-term and long-term deflection of fiber reinforced polymer prestressed concrete beams", *ASCE Journal of Composite Construction*, 7(4), 285–291.

Zou P.X.W. and Xing F. (2004), "predicting the long-term behaviour of concrete beams prestressed by FRP tendons-Part B: illustrative examples" paper submitted to the second international conference on FRP composites in Civil Engineering, 8–10 Dec 2004, Adelaide Australia.

FRP Composites in Civil Engineering – CICE 2004 – Seracino (ed)
© 2005 Taylor & Francis Group, London, ISBN 90 5809 638 6

Predicting the long-term behaviour of concrete beams pretensioned by fibre reinforced polymers – Part B: illustrative examples

Patrick X.W. Zou
The University of New South Wales, Sydney, Australia

ABSTRACT: This paper predicts the long-term concrete strains and deflections of concrete beams pretensioned by FRP tendons using the framework developed in Part A of the paper. Three examples are presented and these examples were chosen to reflect a range of practical issues, un-cracked sections versus cracked section, short span versus long-span. Based on the theoretical analysis carried out in this paper, it is concluded that FRP can be effectively used as prestressing tendon in concrete structures with acceptable level of long-term performance in term of deflection and concrete stains.

1 INTRODUCTION

In this Part (Part B) of the paper, three examples are presented and all three beams are pretensioned with CFRP rods. In example 1, the beam chosen is similar to the beam tested by Abdrehraman (1995), while in example 2, the cross-sectional details and the span are similar to the bridge built in Canada where CFRP were used as prestressing tendons (Abdrehraman and Rizkalla, 1995, and Abdrehraman et al, 1995) subjected to service loads less than the cracking load. The cross-sectional details and the span of Example 3 are identical to Example 1 but the beam is subjected to a service load greater than the cracking load which means the beams were cracked under sustained service load condition.

2 EXAMPLE 1: UNCRACKED SECTION ANALYSIS

A simply supported beam with a span of 5.8 m and a cross section shown in Figure 1 was subjected to its self weight and two symmetrical concentrated loads 1.0 m apart. The beam was prestressed (pretensioned) by four 8-mm diameter straight CFRP rods. The area of each tendon is 47.3 mm^2, while the guaranteed strength is 1970 MPa and the elastic modulus is 147 GPa.

At age 28 days, the concrete strength was 55 MPa, the elastic modulus was 37450 MPa and the modulus of rupture strength was 4.40 MPa. From the test results, the creep coefficient (ϕ_{cr}) and the shrinkage strain (ε_{sh}) may be expressed as a function of the age of concrete t (in days): $\phi_{cr} = (0.4939\ ln(t) - 0.9692)$, χ (aging coefficient) = 0.9, and $\varepsilon_{sh} = (88.913\ ln(t) - 169.94)/10^6$.

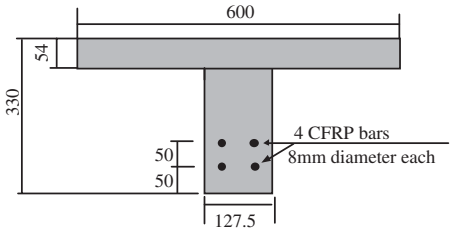

(a) Cross-section (units: mm)

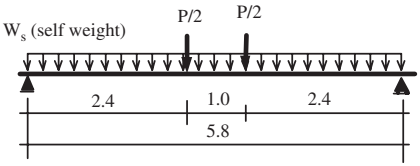

(b) Schematic of load distribution (units: m)

Figure 1. Example 1: beam cross-sectional details and loading arrangement.

The prestressing force was transferred to the concrete at an age of 9 days and the initial prestressing force, P_i was 155.6 kN. The superimposed load P was in the form of two point loads applied 1 m apart in the midspan range as shown in Figure 1. Load P is either of 20 or 24 kN.

It is required to calculate the short term and time-dependent concrete strains at the top fibre as well as the curvature and the deflection at midspan due to the self-weight and the superimposed load (either 20 or 24 kN). The long-term loss of prestress is also to be estimated.

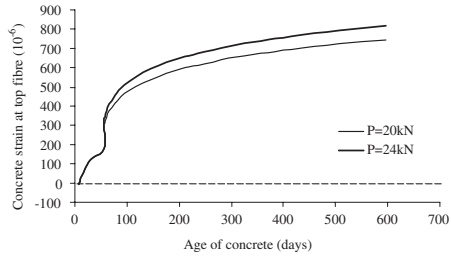

(a) Concrete strains at the top fibre at midspan section

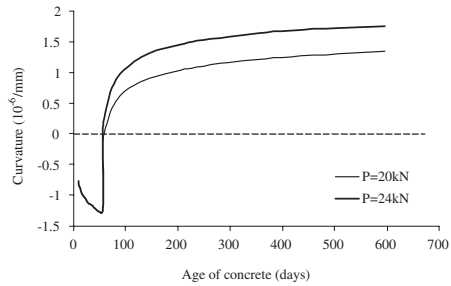

(b) Midspan curvature

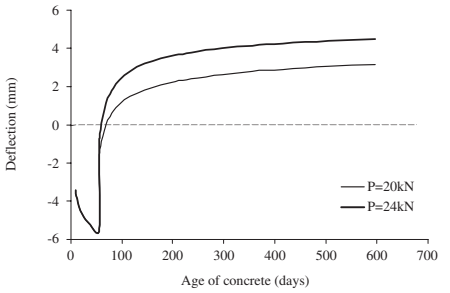

(c) Midspan deflection

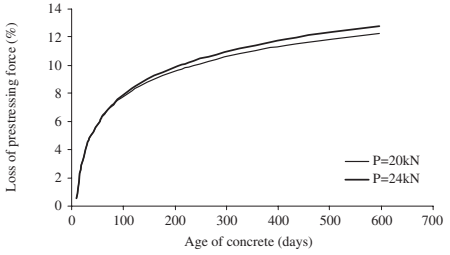

(d) Losses of prestress

Figure 2. Analytical results of Example 1.

Table 1. Comparison of effect of loading levels on deformations of Example 1.

Loading level	$P = 20$ kN	$P = 24$ kN
Immediately after loading		
ε_{oi} ($\mu\varepsilon$)	305	330
κ_i ($\times 10^{-6}$/mm)	−0.157	0.067
ε_{cpi} ($\mu\varepsilon$)	345	313
Δ_o (mm)	−1.72	−0.93
After 1.5 year of loading		
$\varepsilon_{o(t)}$ ($\mu\varepsilon$)	745	816
$\kappa_{(t)}$ ($\times 10^{-6}$/mm)	1.34	1.76
$\varepsilon_{cp(t)}$ ($\mu\varepsilon$)	403	367
$\Delta_{(t)}$ (mm)	3.18	4.49
After 100 year of loading		
$\varepsilon_{o(t)}$ ($\mu\varepsilon$)	1268	1375
$\kappa_{(t)}$ ($\times 10^{-6}$/mm)	2.17	2.52
$\varepsilon_{cp(t)}$ ($\mu\varepsilon$)	714	733
$\Delta_{(t)}$ (mm)	5.74	6.48

2.1 *Analysis*

Under the self weight of the beam and the superimposed load P of 20 kN, it is calculated that the bending moment at the midspan section is 30.8 kNm. The cracking moment of the beam is 39.3 kNm. Hence the total applied moment is about 78% of the cracking moment so the midspan section is not cracked.

The initial and long term behaviours at the midspan section, including concrete strain at the top fibre, the curvature, the deflection and the loss of prestress is shown in Figure 2. After one and a half years of loading, the calculated concrete strain at the top fibre, curvature at the midspan and the deflection at the midspan are 745 $\mu\varepsilon$, 1.341×10^{-6}/mm and 3.18 mm respectively, while the loss of prestress is 12.3%. After 100 years of service, these values increase to 1268.5 $\mu\varepsilon$, 2.172×10^{-6}/mm and 5.74 mm. The loss of prestress is 21.1%. The long-term deflection of 5.74 mm is about 1/1000 of the span and meets the deflection limit (1/800 of the span) for a bridge girder beam under the serviceability limit state.

If the superimposed load P is 24 kN, the moment at the midspan section would be 35.6 kN m which is about 90% of the cracking moment. The time-dependent behaviour of this beam is also shown in the relevant figures. The long term midspan deflection (after 100 years) is calculated to be 6.48 mm which is 1/670 of the span. Table 1 shows the critical values at different ages and the comparison between 20 kN and 24 kN of loading.

3 EXAMPLE 2: UNCRACKED SECTION ANALYSIS

The T-section beam shown in Figure 3 has a span of 22.85 m. The concrete strength at 28 days is 45 MPa

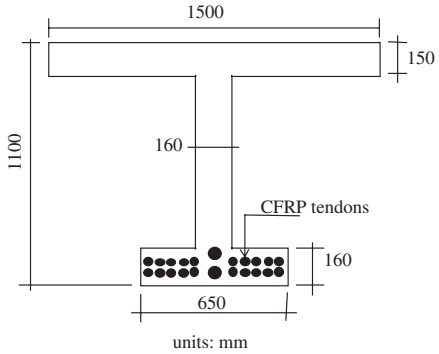

Figure 3. Example 2: Beam cross-sectional details.

and the elastic modulus is 33800 MPa. The beam is prestressed (pretensioned) by CFRP rods (Leadline) where Young's modulus of the CFRP is 147 GPa and the guaranteed ultimate tensile strength is 1970 MPa. The relaxation of the CFRP rod is considered negligible. There are 52 tendons in the cross section producing a total area of 2460 mm^2. The initial prestressing force P_i is 2907.7 kN which is equivalent to 60% of the guaranteed ultimate tensile strength of the CFRP rod. In addition to its self-weight, the beam is subjected to a sustained service load in the form of two point loads 3 m apart in the midspan region. The creep and shrinkage of the concrete may be modelled using the same relationship as described in Example 1. Under the three different levels of loading of P = 100, 150 and 200 kN, the time-dependent behaviour of the beam is to be calculated including the concrete strain at the top fibre and curvature at midspan, together with the deflections and loss of prestress at midspan.

3.1 *Analysis*

The bending moment induced by the self weight and the maximum superimposed point load of 200 kN is 1705.8 kN m at midspan and this is about 63% of the cracking moment of the beam (2721.8 kN m). The beam therefore remains uncracked throughout the period (550 days) of loading. The AEMM was used to model the creep behaviour of concrete. The short-term and time-dependent behaviour of the beam under these loading conditions are shown in Figure 4. These include the concrete strains at the top fibre and at the tendon level, the midspan curvature, the midspan deflection and the losses of prestress at midspan section. It can be seen in Figure 4 that with different loading levels the instantaneous concrete strain at the top fibre increased from 408.8 $\mu\varepsilon$ to 574.7 $\mu\varepsilon$ when the load increases from 100 kN to 200 kN. The rate of the time-dependent increase of concrete strain at the top fibre increases with an increase of load. At an age of 550 days, the concrete strain reaches 981.7 $\mu\varepsilon$ or 1462.4 $\mu\varepsilon$ depending on the loading level.

The change of concrete strain at the tendon level with time is shown in Figure 4. The instantaneous value was 500 $\mu\varepsilon$ and this increased to 920 $\mu\varepsilon$ just before the load P was applied. Immediately after the load P was applied, the strain became 678.8 $\mu\varepsilon$, 566.7 $\mu\varepsilon$ or 454.7 $\mu\varepsilon$ when the $P = 100$, 150 or 200 kN respectively. The time-dependent change of strain is also shown in the Figure. When $P = 100$ kN, the strain increased with time after an initial drop. When $P = 200$ kN, the strain decreased initially (for a period of about 2 months) then remained almost constant with time. When $P = 150$ kN, the strain slightly increased with time after an initial drop.

As shown in Figure 4, when $P = 100$ kN, the instantaneous curvature after loading remains negative (camber), and when $P = 150$ kN, it is close to zero. When $P = 200$ kN, the instantaneous curvature is 0.15×10^{-6}/mm. With time, the curvature increases, as shown, up to a maximum value of 1.15×10^{-6}/mm for $P = 200$ kN.

The midspan deflection is shown in Figure 4. Similar to the midspan curvature, when the applied load is 100 kN, the instantaneous and time-dependent deflection remains upward (camber) up to the age of 550 days. When the applied load increases to 150 kN, the instantaneous deflection is upward (camber), but the time-dependent deflection becomes downward due to creep and shrinkage of the concrete. If the applied load increases to 200 kN, the deflection reaches 48.7 mm which is 1/470 of the span after 550 days of loading.

As shown in Figure 4, the immediate loss and the time-dependent losses of the prestressing force are unaffected by the loading level. This is because the loss of prestress is caused by the shrinkage and creep of concrete at the tendon level (note the relaxation of the CFRP tendons negligible) and these are not significantly affected by the loading levels).

If loaded for 100 years with a sustained load of 200 kN, the concrete strain at the top fibre, the curvature at mid-span section and the deflection at midspan of this beam would reach 2030 $\mu\varepsilon$, 1.57×10^{-6}/mm and 65.7 mm respectively. This long-term deflection is about 1/350 of the span. The comparison of the beam under different levels of applied loads is shown Table 2.

4 EXAMPLE 3 – CRACKED SECTION ANALYSIS

The time-dependent behaviour of a beam with the cross-sectional dimensions and span shown in Figure 1, subjected to an applied load P of 35 kN is to be analysed using AEMM, with and without tension

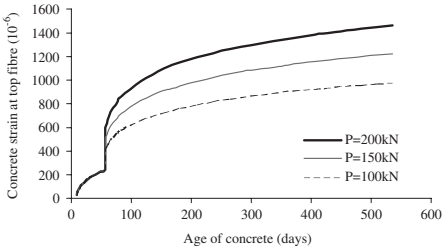

(a) concrete strain at the top fibre at midspan section

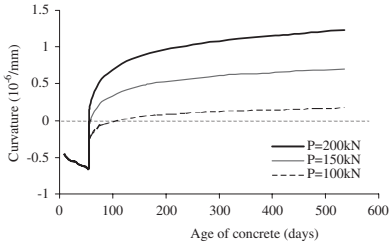

(c) Time-dependent midspan curvature

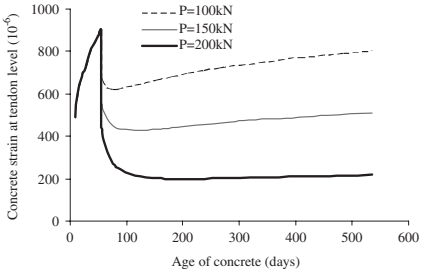

(b) Concrete strain at the tendon level at midspan section

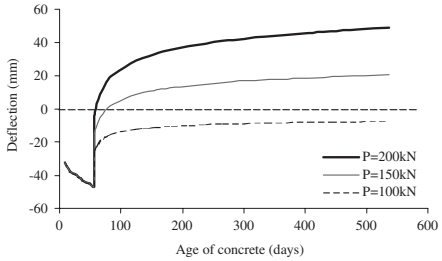

(d) mid-span deflection

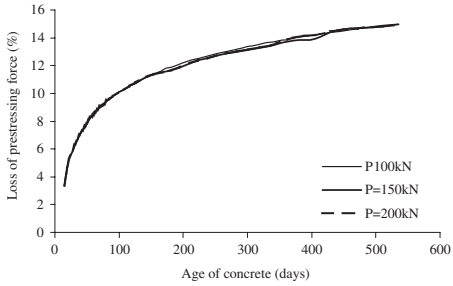

(e) loss of prestress

Figure 4. Example 2: Instantaneous and time-dependent behaviour.

stiffening. The cross-sectional details, the span and the concrete properties in this beam are the same as those in Example 1. The type of tendons to be used in the beam is to be chosen from CFRP rod or steel strand. The properties of these tendons are listed in Table 3. The total tendon area was selected such that the total breaking force of the tendons are similar for the two types of tendons. The selection is also based on the limitation (level) of prestressing of the tendons.

The relaxation of CFRP is negligible and the relaxation of steel strand can be expressed as

$$R = k_1 k_2 R_{1000}\left[\log\left(5.38t^{0.167}\right)\right] \quad (1)$$

where the coefficient k_1 depends on the initial stress level: For a stress level of 40–70% of the tensile strength:

$$k_1 = \frac{2}{3}\left(5\frac{\sigma_{pi}}{f_p} - 2\right) \quad (2)$$

For a stress level of 70–85% of the tensile strength:

$$k_1 = 0.5\frac{\sigma_{pi}}{f_p} + 0.65 \quad (3)$$

Factor k_2 is dependent on the average annual temperature T and may be taken as T/20 but not less than

Table 2. Comparison of effect of loading levels on deformations of Example 2.

Loading level	$P = 100$ kN	$P = 150$ kN	$P = 200$ kN
Immediately after loading			
ε_{oi} ($\mu\varepsilon$)	408.8	491.7	574.7
κ_i ($\times 10^{-6}$/mm)	−0.266	−0.0739	0.118
ε_{cpi} ($\mu\varepsilon$)	678.8	566.7	454.7
Δ_o (mm)	−26	−15.76	−5.53
After 550 days of loading			
$\varepsilon_{o(t)}$ ($\mu\varepsilon$)	981.7	1222.1	1462.4
$\kappa_{(t)}$ ($\times 10^{-6}$/mm)	0.174	0.700	1.226
$\varepsilon_{cp(t)}$ ($\mu\varepsilon$)	804.6	511.5	218.4
$\Delta_{(t)}$ (mm)	−7.23	20.74	48.72
After 100 years of loading			
$\varepsilon_{o(t)}$ ($\mu\varepsilon$)	1469.5	1749.7	2029.8
$\kappa_{(t)}$ ($\times 10^{-6}$/mm)	0.359	0.963	1.568
$\varepsilon_{cp(t)}$ ($\mu\varepsilon$)	1105	711.9	438.6
$\Delta_{(t)}$ (mm)	2.30	34.47	66.65

Table 3. Properties of tendons to be used in the beams.

Type of tendon	Trade name	Total tendon area (mm^2)	Elastic modulus E_p (GPa)	Tensile strength f_p (MPa)
CFRP	Leadline	189.2	147	1970
Steel strand	7-wire	200	195	1840

1.0. The basic relaxation R_{1000} is 2.5% for strand and is 2.0% for wire.

4.1 *Analysis*

As described in Example 1, the cracking moment of this beam is 39.3 kN m. Under the applied service load of 35 kN, the maximum bending moment is 48.8 kN m, which is about 1.25 times the cracking moment, and hence the beam is cracked under this load. From the calculation, the cracked region may be the centre region of 2.0 m.

The change of concrete strains at the top fibre and the deflections at the midspan section with time are calculated using the AEMM and discussed. The tension stiffening model proposed by Zou (2003) is used in the analysis. The designation of the beams is of the form C55-155-L-C and S55-155-L-C which is explained as follows: the first letter represents the type of the tendon ("C" for CFRP and "S" for steel). The first two digits indicate the concrete strength (eg 55 MPa) while 155 is the initial prestressing force in kN. "L" stands for long-term while "C" means the beam cracked under the service load.

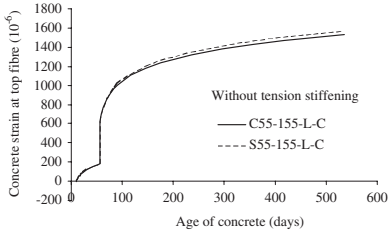

(a) Comparison of concrete strain at the top fibre for beams contained different tendons (without tension stiffening)

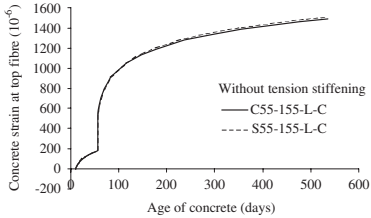

(b) Comparison of concrete strain at the top fibre for beams with different tendons (with tension stiffening)

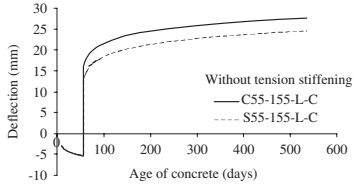

(c) Comparison of midspan deflections without tension stiffening

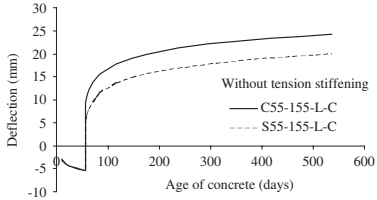

(d) Comparison of midspan deflections with tension stiffening

Figure 5. Comparison of long-term behaviour without or with tension stiffening (Example 3).

4.1.1 *Beam with CFRP: C55-155-L-C*

At the time the prestressing force is transferred, the concrete strain at the top fibre just reaches of $-5.2\,\mu\varepsilon$ (in tension) but it does not exceed the tensile strain capacity of concrete (Figure 5). Under the self weight and the prestressing force, the strain changes

to compressive strain and it increases with time. It reaches 178.7 με at an age of 56 days mainly due to the creep and shrinkage of concrete. Upon loading, the strain increases to 625.9 με (in compression). Under this service load, this top fibre strain increases rapidly at the early days and then slows down. After one and a half years of loading, the strain reaches 1527.1 με, which is more than twice the instantaneous strain.

Also shown in Figure 5 is the change of concrete strain when the tension stiffening is included in the calculation. It can be seen that both methods predict the same trends of strain development, but the value is slightly less when tension stiffening is taken into account as expected.

The change of midspan deflection with time of this beam is shown in Figure 5. The initial camber is −2.96 mm and it increases with time when the beam is only subjected to its self-weight and the prestressing force. At age 56 days, it reaches −5.43 mm, which is twice of the initial camber. Immediately after loading, the downward deflection (without tension stiffening) is 16.0 mm and it increases with time due to creep and shrinkage of the concrete. The deflection reaches 27.7 mm after one and a half years of loading. When tension stiffening is taken into account, the instantaneous downward deflection is only 10.8 mm and after one and a half years of loading, the deflection reaches 24.2 mm, which is about 1/250 of the span.

4.1.2 *Beam with steel strand: S55-155-L-C*

As with Beam C55-155-L-C, the concrete strain at the top fibre and the deflection at the midspan section are calculated. Figure 5 shows the long-term concrete strain at the top fibre and the long-term deflection. At the time of transfer of the prestressing force, the concrete strain is in tension at −4.8 με. Under the beam self-weight and the prestressing force, the strain becomes compressive and increases with time. At age 56 days, it had reached 181.4 με. Immediately after loading, the instantaneous strain is 624.4 με if no tension stiffening is taken into account and is 535.3 με if tension stiffening is taken into account. With time, the calculated maximum concrete strain increases and it finally reaches 1513.4 με or 1568.3 με depending on whether the tension stiffening is taken into account or not.

Regarding the long-term midspan deflection, while the initial camber at transfer is −2.92 mm, it increases to −5.15 mm at age 56 days. Upon loading, the initial downward deflection is 12.9 mm when tension stiffening is not taken into account and 6.9 mm if tension stiffening is considered. After one and a half years of loading, the deflection reaches 24.7 mm without tension stiffening or 20.1 mm with tension stiffening. These deflections are about 1/235 and 1/290 of the beam span, respectively.

Table 4. Comparison of deformations of Example 3, without tension stiffening effect.

Beam	S55-155-L-C	C55-155-L-C
Immediately after loading		
ε_{oi} (με)	624.4	625.9
Δ_o (mm)	12.9	16.0
After one and a half year of loading		
$\varepsilon_{o(t)}$ (με)	1568.3	1527.1
$\Delta_{(t)}$ (mm)	24.7	27.7

Table 5. Comparison of deformations of Example 3, with tension stiffening effect.

Beam	S55-155-L-C	C55-155-L-C
Immediately after loading		
ε_{oi} (με)	535.3	551.5
Δ_o (mm)	6.9	9.2
After one and a half year of loading		
$\varepsilon_{o(t)}$ (με)	1513.4	1488.8
$\Delta_{(t)}$ (mm)	20.1	24.2

4.1.3 *Comparison between beams with different tendons*

Under the above mentioned loading conditions, the concrete strains at the top fibre of beam C55-155-L-C and S55-155-L-C are compared in Figure 5. It can be seen that if the tension stiffening is not taking into account, the concrete strain of Beam C55-155-L-C is comparable to that of Beam S55-155-L-C. If tension stiffening is taken into account, the concrete strain of Beam C55-155-L-C is still comparable to that of Beam S55-155-L-C.

Figure 5 shows the comparison of deflections, with and without tension stiffening. It can be seen that with or without tension stiffening the deflection of Beam C55-155-L-C is slightly higher than that of Beam S55-155-L-C but the difference was only about 17% which was not significant. This behaviour is due to the difference in the elastic moduli of the tendons.

The calculated response of these beams at each stage of loading is listed in Tables 4 and 5. It is clear that the time-dependent behaviour of the concrete beams prestressed by CFRP is comparable to those beams prestressed by steel strand.

5 CONCLUSIONS

This paper presents calculation of the long-term concrete strains and deflections of concrete beams prestressed by FRP tendons using the framework developed in previous paper. The examples chosen reflected

a range of practical issues, un-cracked sections versus cracked section, short span versus long-span. From the theoretical studies conducted in this paper, it can be concluded that level of long-term performance of concrete beams pretensioned by FRP is acceptable, in term of deflection and concrete stains, despite the fact that the deflection may be slightly higher than those by steel strands when the section is cracked under service load condition.

REFERENCES

Abbdelrahman, A.A. (1995), Serviceability of concrete beams prestressed by Carbon Fibre Reinforced Plastics tendons, (*PhD thesis*), University of Manitoba, Canada.

Abbdelrahman, A.A. and Rizkalla, S.H. (1995), Serviceability of concrete beams prestressed by carbon fibre plastic rods, *Non-metallic (FRP) reinforcement for concrete structures*, Taerwe L. (Ed), E & FN Spon, p 403–412.

Abdelrahman, A.A., Tadros, G. and Rizkalla, S.H. (1995), Test model for the first Canadian smart highway bridge, *ACI Structural J*., 92 (4), p 451–458.

Zou, P.X.W. (2004), Predicting the Long-term Behaviour of Concrete Beams Prestressed by Fibre Reinforced Polymers – Part A: Theoretical Framework, CICE 2004 conference, Adelaide Australia, Dec. 2004.

Hybrid FRP structures

FRP Composites in Civil Engineering – CICE 2004 – Seracino (ed)

Behaviour of hybrid FRP–concrete–steel double-skin tubular columns

J.G. Teng, T. Yu & Y.L. Wong
Department of Civil and Structural Engineering, The Hong Kong Polytechnic University, Hong Kong, China

ABSTRACT: Hybrid FRP–concrete–steel double-skin tubular columns are a new form of hybrid columns recently proposed by the first author. The column consists of an outer tube made of fibre-reinforced polymer (FRP) and an inner tube made of steel, with the space between filled with concrete. In this new hybrid column, the three constituent materials are optimally combined to achieve several advantages not available with existing columns. In this paper, the rationale for the new column form together with its expected advantages is explained. Results from a series of stub column tests are presented and discussed to confirm some of these expected advantages. Results from a series of four-point bending tests are also described to demonstrate the application of this new hybrid section as a beam.

1 INTRODUCTION

In recent years, fibre reinforced polymer (FRP) composites have found increasingly wide applications in civil engineering, both in the retrofit of existing structures and in new construction. FRP composites possess several advantages over steel, including their high strength-to-weight ratio and good corrosion resistance. As a result, the use of FRP composites as externally bonded reinforcement for the retrofit of structures has become very popular in recent years (Teng et al. 2002). These same advantages can also be exploited in new construction, and indeed a large amount of research around the world is currently under way examining the performance of various forms of structures made of FRP composites alone (i.e. all FRP structures) or FRP composites in combination with other materials (i.e. hybrid structures). Examples include FRP bridge decks, concrete-filled FRP tubes as columns and piles, and FRP cables.

Compared with the two primary traditional structural materials, namely steel and concrete, FRP composites also have some disadvantages. These include their relatively high cost, linear-elastic-brittle stress–strain behaviour, low elastic modulus-to-strength ratio, and poor fire resistance. In retrofit applications, cost savings arise from a number of aspects that offset the higher material cost, but this is harder to achieve in new construction at the present.

The low elastic modulus-to-strength ratio is not critical in retrofit applications as the FRP is generally used to resist tension. The poor fire performance is also not an acute problem in retrofit applications as the FRP is generally not required to make any contribution to structural resistance during a fire. When FRP composites are deployed in new construction, the consequences of their weaknesses need to be minimized as in retrofit applications. Based on these considerations, it may be concluded that the successful application of FRP composites in new construction requires the following three criteria to be met: (a) cost effectiveness at least in terms of a life-cycle cost assessment; (b) FRP to be used in areas subject to tension as much as possible; (c) fire resistance to be non-critical. It should be noted that criterion (d) is easily met for bridge structures and other outdoor structures, while the first two requirements in general mean that FRP composites should be used in combination with other materials to form hybrid structures.

Based on the above discussion, it is apparent that the area of hybrid structures will be a major focus of future research on the use of FRP composites in new construction. Within the area of hybrid structures, the aim shall be to optimally combine FRP with traditional structural materials such as steel and concrete to create innovative structural forms that are cost-effective and of high-performance. To this end, simple duplications of existing structural systems are often inadequate. This paper presents the idea of a new form of columns, namely FRP-concrete–steel hybrid double-skin tubular columns (DSTCs), proposed by the first author of the paper, as well as test results to evaluate their axial and flexural behaviour.

2 NEW HYBRID COLUMN

Concrete-filled steel tubes have been a common form of columns. The simplest form of concrete-filled steel tubes consists of a single hollow steel tube filled with

concrete with or without internal steel reinforcing bars. A variation of this simple system is the double-skin tubular column, consisting of two generally concentric steel tubes with the space between filled with concrete. To the best of the authors' knowledge, such double-skin tubes were first reported in late 1980s (Shakir-Khalil and Illouli 1987). Since then, much research has been conducted on these columns (e.g. Shakir-Khalil 1991; Wei et al. 1995; Han et al. 1995; Yagishita 2000; Zhao et al. 2002; Tao et al. 2003). The inner void reduces the column weight without significantly affecting the bending rigidity of the section and allows the easy passage of service ducts.

More recently, hybrid FRP columns consisting of an FRP tube filled with concrete with or without internal reinforcement have received a great deal of research (Mirmiran and Shahawy 1997; Fam and Rizkalla 2001a, b; Hong et al. 2002; Zhang et al. 2000). Furthermore, double-skin hybrid FRP columns consisting of two FRP tubes and a concrete in-fill have been also been studied (Fam and Rizkalla 2001b). The advantages of simple concrete-filled FRP tubes over simple concrete-filled steel tubes include the lightweight and corrosion resistance of the FRP tube. Simple concrete-filled FRP tubes have been proposed for use as bridge columns and piles. Concrete-filled FRP tubes have a number of disadvantages particularly when used as building columns. These include poor fire resistance, difficulty for connection to beams, inability to support substantial construction loads, brittle failure in bending, and high cost as the tube needs to be relatively thick in order to resist axial loads. As a bridge column, the fire resistance and connection problems are not significant.

To overcome the existing disadvantages of concrete-filled FRP tubes, a new form of hybrid columns has recently been proposed by the first author and is being investigated in an ongoing research project at The Hong Kong Polytechnic University. The new column consists of a steel tube inside, an FRP tube outside and concrete in between. The inner void may be filled with concrete if desired. The FRP tube is provided with fibres which are predominantly oriented in the circumferential direction to provide confinement to the concrete. The new column is an attempt to combine the advantages of all three constituent materials and those of the structural form of DSTCs, so as to achieve a high-performance structural member.

The novel feature of the new column form compared to the existing DSTCs is that the inner tube is made of steel but the outer tube is made of FRP with fibres oriented mainly in the hoop direction to provide confinement to the concrete for enhanced ductility. This simple change to the existing DSTC forms offers many advantages, leading to a column which is easy to construct and highly resistant to corrosion and earthquakes. Direct comparisons can be made between the new column and the steel-concrete DSTC or between the new column and the FRP-concrete DSTC. Compared to the steel-concrete DSTC, the advantages of the new column include: (a) a more ductile response of concrete as it is well confined by the FRP tube which does not buckle; (b) no need for fire protection of the outer tube as the outer tube is required only as a form during construction and as a confining device during earthquakes; (c) no need for corrosion protection as the steel tube inside is well protected by the concrete and the FRP tube. Compared to the FRP-concrete DSTC, the advantages of the new column include: (a) ability to support construction loads through the use of the inner steel tube; (b) ease for connection to beams due to the presence of the inner steel tube; (c) savings in fire protection cost as the outer tube is required only as a form during construction and as a confining device during earthquakes; (d) better confinement of concrete as a result of the increased rigidity of the inner tube. Similarly, the new column also has many advantages over other composite/hybrid columns including concrete-filled steel tubes, concrete-filled FRP tubes and concrete-encased steel columns.

The section form shown in Figure 1(a) consists of two circular tubes, but many different combinations of tubes are possible. Figures 1(b) and 1(c) shows some of such variations. Needless to say, the section form can also be employed in a beam, in which case the inner steel tube may be shifted towards the tension side (Figure 1 (d)). It should be noted that if the column section with two concentric tubes is deployed in situations where axial compression does not dominate under service loading, the column should be provided with some longitudinal reinforcement to avoid the development of large tensile cracks.

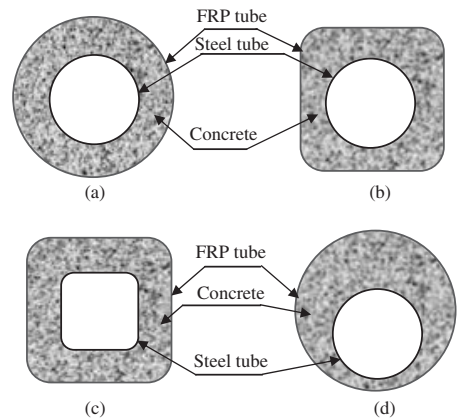

Figure 1. Typical sections of double-skin tubular members.

3 AXIAL COMPRESSION TESTS ON STUB COLUMNS

3.1 *General*

Obviously, for the new hybrid column to be accepted in practical applications, a great deal of research is required to develop knowledge of its structural behaviour and reliable design methods. As a first step, a series of stub column tests have been conducted at The Hong Kong Polytechnic University. Details of the test specimens and the test results are presented in this section.

3.2 *Specimens*

A total of six DSTC specimens of three different configurations were prepared and tested; two identical specimens were made for each configuration. The stub column specimens all had an outer diameter of 152.5 mm and a height of 305 mm. The steel tube inside each specimen was identical and was cut from the same long steel tube. The outer GFRP tube had three different thicknesses. Table 1 provides a summary of the specimens. In addition, 6 FRP-confined concrete (FCC) solid cylinders were prepared and tested for comparison, including specimens with one, two and three plies of FRP outside, respectively. Three hollow steel tubes also cut from the same long tube were tested under compression.

Tensile tests on steel coupons cut from the same original steel tube were conducted. These tests showed that the steel had a yield stress of 352.67 MPa, an ultimate strength of 380.4 MPa, a Young's modulus of 207.28 GPa and a long plastic plateau after yielding. The FRP used here had a nominal thickness of 0.17 mm per ply, a tensile strength of 2,300 MPa, and a Young's modulus of 76 GPa according to data supplied by the manufacturer. The three configurations had GFRP tubes made of 1 ply, 2 plies and 3 plies of GFRP. The elastic modulus, compressive strength and strain at peak stress of the concrete averaged from three concrete cylinder tests (152.5 mm $\times$ 305 mm) are 30.18 GPa, 39.64 MPa and 0.002628 respectively.

3.3 *Preparation of specimens*

The specimen preparation process included the following steps: (1) fabrication of the form, which consisted of a PVC tube outside and a steel tube inside; strain gauges on the steel tube were installed before the casting of concrete (Figure 2); (2) casting the concrete; (3) wet-layup formation of the FRP tube after the concrete had hardened and the PVC form removed (Figure 3).

It should be noted that the FRP tube was formed by the wrapping and resin impregnation of fibre sheets on concrete as is done in retrofit applications, instead of the use of a prefabricated FRP tube into which concrete is cast. The wrapping process was used as prefabricated FRP tubes with fibres oriented mainly in the hoop direction were not readily available to the authors. It is believed that there is little difference between the two ways of forming the FRP tube in terms of the performance of the hybrid column, based on previous research by Shahawy et al. (2000). In the present specimens, all fibres were oriented in the hoop direction; that is, no longitudinal fibres were present in these FRP tubes.

Table 1. Specimen details.

Specimens	FRP tube	Steel tube
DS1A, DS1B	1 ply	Outer diameter
DS2A, DS2B	2 plies	= 76.1 mm
DS3A, DS3B	3 plies	Thickness = 3.2 mm

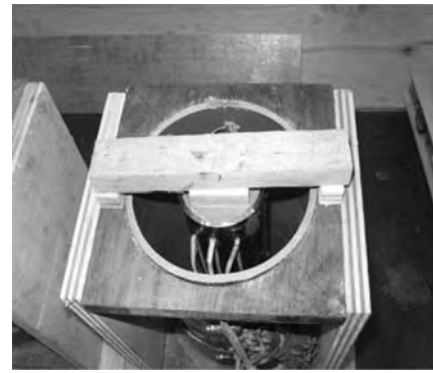

Figure 2. Form for casting concrete.

Figure 3. Formation of the FRP tube.

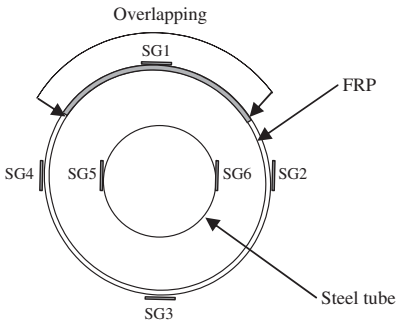

Figure 4. Layout of the strain gauges.

3.4 *Test set-up and instrumentation*

For each hybrid column specimen, two strain rosettes (gauge length = 10 mm) were installed at the mid-height of the outer surface of the steel tube and four strain rosettes (gauge length = 20 mm) were installed at the mid-height of the outer surface of the FRP tube. The circumferential layout of the strain gauges is shown in Figure 4, in which the overlapping zone spans a circumferential distance of 150 mm.

In addition, two linear variable displacement transducers (LVDTs) were used to obtain the axial deformation over a 120 mm mid-height region (Figure 5(a)). All the compression tests were carried out using an MTS machine with displacement control at a loading rate of 0.003 mm/sec. All the test data, including the strains, loads, and displacements, were recorded simultaneously by a data logger.

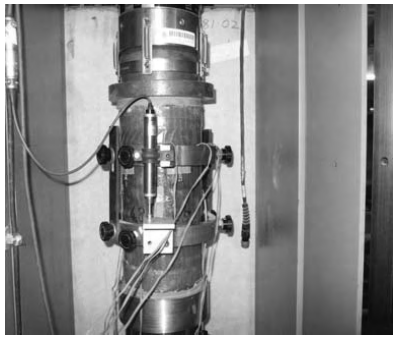

(a) before test

(b) after test

Figure 5. DSTC specimen before and after test.

3.5 *Test results and observations*

All six specimens displayed continuous load-displacement behaviour until ultimate failure which occurred by the rupture of the FRP tube as a result of hoop tension. Specimen DS2A before and after test is shown in Figure 5.

The test results of all 6 specimens are summarized in Table 2. In this table, P_{co} is equal to the unconfined concrete strength times the area of the annular concrete section (=543.5 kN), while P_s is equal to the average ultimate load of the three hollow steel tubes (=273.8 kN). Therefore, the ultimate load of the hybrid column is found to be 817.3 kN if the constituent parts do not interact and the confinement effect of the FRP tube is negligible. The ultimate load of the hybrid column from the test is denoted by P_c, while the ultimate strain is denoted by ε_u. For these specimens, the ultimate strain is the strain at the ultimate load. The strain of unconfined concrete at peak stress ε_{co} was found from tests on three 152.5 mm × 305 mm concrete cylinders to be 0.002628 and is used to normalize the test ultimate strain. The axial load-strain curves of the six DSTCs are shown in Figure 6 where the strains were found from the displacement transducer readings.

3.6 *Discussions*

From Table 2, it can be seen that the two single-ply DSTCs have approximately the same load capacity, and their average value is very close to the sum of the individual capacities of the concrete and the inner steel tube, which shows that the FRP confinement to the concrete has little effect on the ultimate load if the amount of FRP used is small. However, the load capacities of the DSTCs with two- or three-ply FRP tubes exceed the sum of the ultimate loads of the two constituent parts by a considerable amount. The 2-ply FRP tube led to a 27% increase in the ultimate load while the 3-ply FRP tube led to a 48% increase. This means that the strength enhancement is related to the thickness of the FRP tube, a phenomenon which is consistent with previous observations made on simple concrete-filled FRP tubes (Teng et al. 2002).

Table 2. Key test results of DSTCs.

Specimen	P_c (kN)	Average P_c (kN)	$P_c/(P_{co}+P_s)$ (MPa)	ε_u ($\times 10^{-6}$)	Average ε_u ($\times 10^{-6}$)	$\varepsilon_u/\varepsilon_{co}$
DS1A	793.75	811.51	0.99	14208	14542	5.53
DS1B	829.27			14875		
DS2A	1044.2	1034.5	1.27	22000	20204	7.69
DS2B	1024.8			18417		
DS3A	1214.0	1208.0	1.48	23416	23541	8.96
DS3B	1201.9			23666		

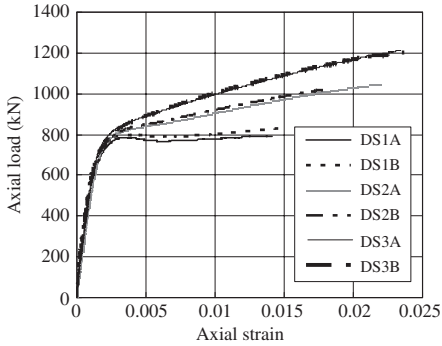

Figure 6. Axial load-strain behavior of DSTCs.

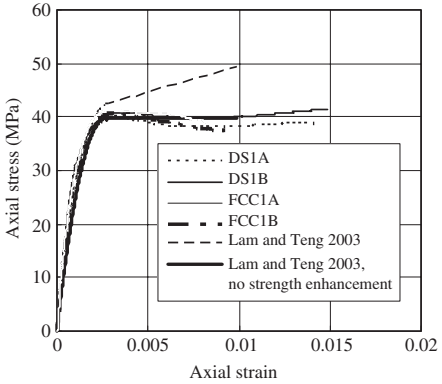

Figure 7. Comparison for the one-ply specimens.

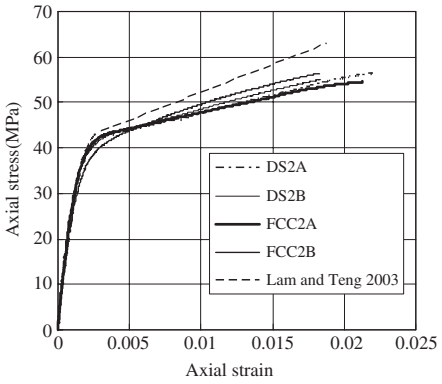

Figure 8. Comparison for the two-ply specimens.

Figure 6 shows that the 2-ply DSTCs and the 3-ply DSTCs have a bilinear load-strain curve while the 1-ply DSTCs have an almost elastic-perfectly plastic load-strain curve. All 6 specimens achieved large ultimate strains. The ultimate axial strains are 5.53, 7.69 and 8.96 times the strain at peak stress of the unconfined concrete for one-, two- and three-ply FRP tubes respectively (Table 2).

In order to evaluate the degree of confinement the concrete in DSTCs receives more directly, the stress–strain curves of the concrete in the test specimens are compared with those obtained from tests on the 6 FCC specimens and the predictions of the design-oriented stress–strain model recently proposed by Lam and Teng (2003). The axial stresses in the concrete in the DSTCs were found by dividing the load carried by the concrete by the cross-sectional area of the concrete. The load carried by the concrete was assumed to be equal to the difference between the load carried by the DSTC specimen and the load carried by the steel tube at the same axial strain as found from the compression tests on hollow steel tubes. Figures 7–9 show the comparisons for the one-, two- and three-ply specimens, respectively.

It can be seen from these figures that the stress–strain behaviour of the concrete in the DSTCs is almost the same as that of FRP-confined concrete solid cylinders for all specimens, which suggests that despite the inner void, the concrete in these DSTCs is confined as effectively as in a circular solid column. It should be noted that these deduced stress–strain curves for the

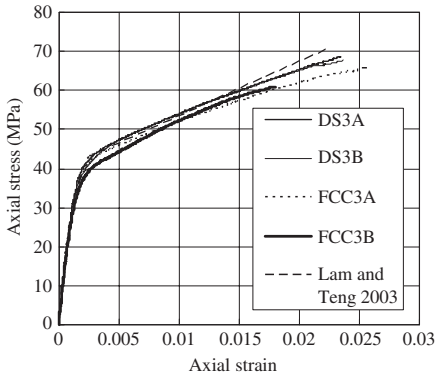

Figure 9. Comparison for the three-ply specimens.

concrete in the DSTCs have included any beneficial effect that may arise as a result of the steel tube being constrained by the external concrete and thus carrying a higher load at the same axial strain. Nevertheless, this effect is believed to be small. This demonstrates that the inner void in a DSTC does not lead to a significant degradation of the benefit of FRP confinement provided by the FRP tube.

It can also be seen from these figures that Lam and Teng's (2003) model predicts the stress–strain behaviour of the specimens with a 3-ply FRP tube closely but overestimates the performance of the specimens with a 1-ply FRP tube or a 2-ply tube. These predictions were made using the average hoop rupture strains from the FFC specimens. It should be noted that the confinement ratio of the specimens with a 1-ply FRP tube (=0.073) is nearly the same as the threshold value of 0.07 defined in Lam and Teng (2003). Lam and Teng (2003) suggested that no strength enhancement should be assumed when the confinement ratio is lower than this limit. Therefore, in Figure 7, a stress–strain curve predicted by Lam and Teng's model assuming no strength enhancement is also plotted for comparison, and this curve is in close agreement with the test results. These comparisons indicate that the accuracy of Lam and Teng's model needs to be improved when applied to concrete confined with a small amount of FRP.

4 FLEXURAL TESTS

4.1 *General*

A series of four-point bending tests were conducted to demonstrate the application of this new hybrid section as a beam and to provide a preliminary evaluation of the flexural behaviour of such beams. In these beams, the inner steel tube was shifted towards the tension side to leave more concrete in the compression zone and to place more steel in the tension zone. Details of the test specimens and the test results are presented in this section.

Table 3. Specimens for the bending tests.

Specimen	FRP tube	Steel tube
DSB1	No	Outer diameter = 76.1 mm
DSB2	1 ply	Thickness = 3.5 mm
DSB3	2 plies	

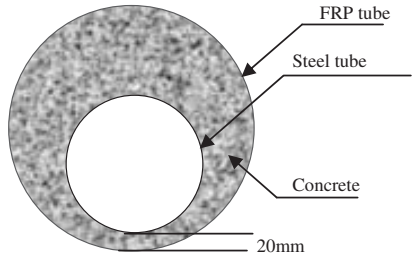

Figure 10. Cross-section of the beams.

4.2 *Specimens*

In total, three specimens have been prepared and tested. The specimens all had an outer diameter of 152.5 mm and a length of 1500 mm. The steel tube inside each specimen was identical and was cut from the same long steel tube. All three specimens had the same steel tube eccentricity: the centre of the steel tube was at a distance of 18.2 mm from the centre of the outer circumference of the concrete section. The only difference between the three specimens was the thickness of the FRP tube outside. Details of the specimens are summarized in Table 3 and the cross section of the beams is shown in Figure 10.

Tensile tests on steel coupons cut from the same original steel tube were conducted. These tests showed that the steel had a 0.2% proof stress of 340.3 MPa, a tensile strength of 444.5 MPa and a Young's modulus of 192.8 GPa. The FRP used here was the same as that used in the DSTC specimens. The compressive strength and the compressive strain at peak stress of the concrete averaged from three concrete cylinder tests (152.5 mm × 305 mm) are 33.37 MPa and 0.002502 respectively.

4.3 *Instrumentation and test set-up*

The test set-up is shown in Figure 11. The instrumentation included strain rosettes on the circumferences of Sections 1 and 2 (Figure 11) (section 1 only for specimen DSB1 without an FRP tube), five LVDTs

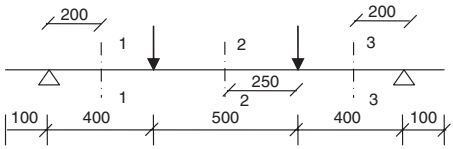

Figure 11. Bending test set-up.

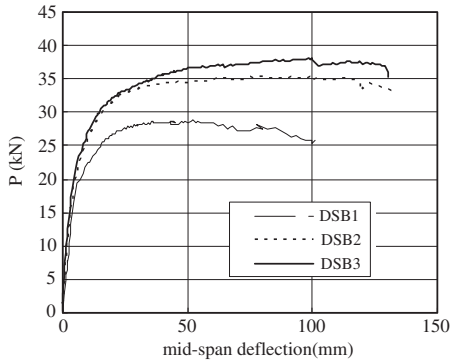

Figure 12. Mid-span load-deflection curves.

which were installed at Sections 1, 2 and 3 and the two loading sections (Figure 11) to measure deflections, and LVDTs at the ends of the specimen to measure the slips between the concrete and the steel tube and between the concrete and the FRP tube. Two load cells were used to measure the loads acting at the two loading points. The test data were collected by a data logger.

4.4 *Test results and observations*

All bending test specimens exhibited a smooth load-deflection curve (Figure 12). The tests were terminated due to the headroom limitation of the loading frame for specimens DSB2 and DSB3 (at a mid-span deflection of about 125 mm). For specimen DSB1, the test was terminated when various large cracks were found in many places (due to the absence of an FRP tube outside) and the whole loading system became somewhat unstable. Specimens DSB1 and DSB2 after test are shown in Figure 13.

Figure 12 shows the load-deflection curves of the specimens for the mid-span point, in which P is the average load recorded by the two load cells. It is evident that all the specimens showed good ductility. As the specimens did not collapse at the end of the test, they can be expected to possess a higher level of ductility than is indicated by these curves. It is also evident that the two specimens with a GFRP tube outside (DSB2 and DSB3) had a much larger loading capacity than the

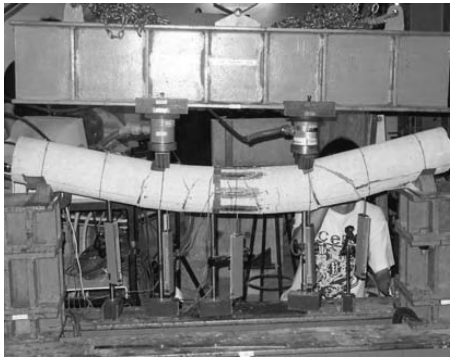

(a) Specimen DSB1

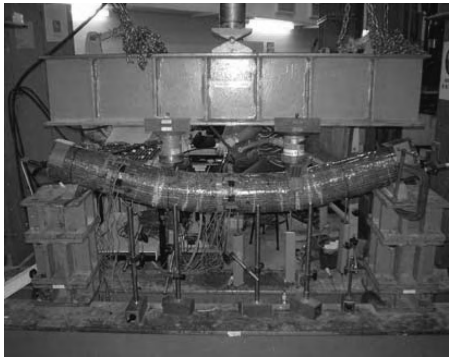

(b) Specimen DSB2

Figure 13. Specimens after test.

specimen without a GFRP tube (DSB1). In addition, in the second stage of deformation, the load gradually reduced for specimen DSB1 while it kept increasing or remained almost constant for specimens DSB2 and DSB3, which suggests a larger ductility for the latter two specimens. The poor behaviour of specimen DSB1 is at least partly due to the shear failure of the concrete section due to the absence of an outer GFRP tube as shear cracks are evident on the specimen (Figure 13(a)). The thickness of the GFRP tube has only a small effect on the load-carrying capacity of the member, as the load-deflection curve of the specimen DSB2 which had a 2-ply GFRP tube is only a little higher than that of specimen DSB3 which had a 1-ply GFRP tube. This further suggests that the GFRP tube in such beams enhances the structural behaviour by providing both confinement to the concrete and additional shear resistance.

As the mid-span deflection reached about 1/10 of the span length, cracks with large widths were

found in the final stage for all the specimens. For the two specimens with an outer GFRP tube, two major cracks were always found right below or very close to the two loading points, while other less prominent cracks were randomly distributed within and outside the pure-bending region of the specimen (Figure 13). For specimen DSB1, inclined shear cracks were found together with flexural cracks along the specimen. However, despite the large cracks found during the test, specimens DSB2 and DSB3 showed an almost linear behaviour in the initial loading stage until a load level close to the ultimate load, with a high flexural stiffness.

5 CONCLUSIONS

The details of the newly proposed hybrid FRP-concrete–steel double-skin tubular column have been introduced in this paper. The new column consists of an inner steel tube and an outer FRP tube, with the space between them filled with concrete. The new column possesses many advantages over existing columns including double-skin FRP-concrete columns and double-skin steel-concrete columns. These advantages include good ductility, corrosion resistance and ease for construction. In addition, fire protection is not needed as the outer FRP tube is not required to make any contribution to the structural resistance during a fire.

A series of stub column tests to confirm some of the expected advantages were conducted and the results have been presented and discussed in this paper. The test results confirmed that the concrete in the new column is very effectively confined, leading to a very ductile response. The inner void in the double-skin column was found to have almost no effect on the effectiveness of confinement provided by the FRP tube. A series of four-point bending tests have also been conducted on specimens with a hybrid section in which the inner steel tube was shifted towards the tension side to demonstrate the application of the hybrid section in a beam. These beams were found to show a very ductile behaviour. The results also showed that the GFRP tube in such beams enhances the structural behaviour by providing both confinement to the concrete and additional shear resistance.

ACKNOWLEDGEMENTS

The work presented in this paper has received financial support from The Hong Kong Polytechnic University through a research studentship of the Area of Strategic Development in Mitigation of Urban Hazards to the second author and through the Young Professorship Scheme (Project No: 1ZE-06), and from the National Science Foundation of China (Joint Research Fund for Hong Kong and Macao Young Scholars) (Project No. 50329802). The authors are grateful to both organizations for their financial support.

REFERENCES

Fam, A.Z. and Rizkalla, S.H. (2001a) "Confinement model for axially loaded concrete confined by circular fiber-reinforced polymer tubes", *ACI Structural Journal*, Vol.98, No.4, pp. 451–461

Fam, A.Z. and Rizkalla, S.H. (2001b) "Behavior of axially loaded concrete-filled circular fiber-reinforced polymer tubes", *ACI Structural Journal*, Vol.98, No.3, pp. 280–289

Han, B., Xia, J. and Zhao, J. (1995) "The strength of concrete filled double-skin steel tubes under axial compression", *Journal of Shijiazhuang Railway Institute*, Vol.8, No.3, pp. 75–80

Hong, W.K., Kim, H.C. and Yoon, S.H. (2002) "Experiment of compressive strength enhancement of circular concrete column confined by carbon tubes", *KCI Concrete Journal*, Vol.14, No.4, pp. 139–144

Lam, L. and Teng, J.G. (2003). "Design-oriented stress–strain model for FRP-confined concrete", *Construction and Building Materials*, 17(2003), pp. 471–489

Mirmiran, A. and Shahawy, M. (1997) "Behavior of Concrete Columns Confined by Fiber Composites", *Journal of Structural Engineering*, Vol.123, No.5, 583–590

Shahawy, M., Mirmiran, A. and Beitelman, T. (2000) "Tests and modeling of carbon-wrapped concrete columns", *Composites: Part B-Engineering*, Vol.31, No. 6–7, pp. 471–480

Shakir-Khalil, H. and Illouli, S. (1987) "Composite columns of concentric steel tubes", In *Proc. Non-Conventional Structures '87 Conf. on the Design and Construction of Non-Conventional Structures*, Vol.1, London, Dec. 1987, pp. 73–82

Shakir-Khalil, H. (1991). "Composite columns of double-skinned shells", *J. Construct. Steel Research*, 19(1991), pp. 133–152

Tao, Z., Han, L.H. and Huang, H. (2003). "Concrete-filled double skin steel tubular column with square section under eccentric loads", *China Civil Engineering Journal*, Vol. 36, No.2, pp. 33–40

Teng, J.G., Chen, J.F., Smith, S.T. and Lam, L. (2002) *FRP Strengthened RC Structures*, John Wiley & Sons Ltd

Wei, S., Mau, S.T., Vipulanandan, C. et al (1995) "Performance of New Sandwich Tube under Axial Loading: Experiment" *Journal of structural Engineering*, Vol.121, No.12, pp. 1806–1814

Yagishita, F., Kitoh, H., Sugimoto, M., Tanihira, T. and Sonoda, K. (2000). "Double skin composite tubular columns subjected to cyclic horizontal force and constant axial force", *Proceedings of the Sixth ASCCS International Conference on Steel-Concrete Composite Structures*, pp. 497–503

Zhang, D.X., Huang, L.N., Wang, R.G. and Zhao, J.H. (2000). "Experimental research on the mechanical properties of concrete filled FRP tubular column", *Journal of Harbin University of Civil Engineering and Architecture*, Vol.1, No.33, pp. 73–76

Zhao, X.L., Grzebieta, R. and Elchalakani, M. (2002) "Tests of concrete-filled double skin CHS composite stub columns", *Steel and Composite Structures*, Vol.2, No.2, pp. 129–146

FRP Composites in Civil Engineering – CICE 2004 – Seracino (ed)
© 2005 Taylor & Francis Group, London, ISBN 90 5809 638 6

Flexural performance of newly developed hybrid FRP–concrete beams

Wenxiao Li[1,2] & Zhishen Wu[1]
[1] *Department of Urban & Civil Engineering, Faculty of Engineering, Ibaraki University, Hitachi, Ibaraki, Japan*
[2] *School of Aeronautics, Astronautics and Mechanics, Tongji University, Shanghai, China*

ABSTRACT: A novel hybrid FRP–concrete structural system is recently proposed by the authors. Instead of conventional shear keys of hybrid systems, bonding technique with epoxy resin is adopted to ensure composite effect between FRP and concrete and hence avoid buckling failure mode of FRP shell. CFRP sheets with high strengths are axially bonded on the bottom surface of the concrete core to carry tensile load. GFRP sheets with high rupture strains are wrapped in hoop direction to bear the shear load, result in confinement effects to concrete core and prevent premature debonding of CFRP sheets. A minimum reinforcement ratio of rebars is used to control the localization and propagation of flexural cracks. In this paper a series of four-point bending experiments are carried out to study the feasibility of the proposed concept on a hybrid FRP-concrete beam system. Furthermore, based on the principles of strain compatibility and equilibrium, an iterative analytical method is used to analyze the flexure behavior of the specimens.

1 INTRODUCTION

Fiber Reinforced Polymers (FRPs) have been extensively used as externally bonded reinforcements in the maintenance, rehabilitation and upgrading of existing concrete structural members. FRP materials offer plenty of advantages such as excellent strength/self-weight ratio, easily handling, corrosion-free, low maintenance, durability, speed of construction and tremendous design flexibility. Being familiar with the value of combining materials into a composite structural system, civil engineers make great effort to introduce this attractive material into new constructions. Besides of direct material substitution in conventional reinforced concrete constructions where reinforcing bars are replaced by FRP rebars, some new hybrid FRP/concrete structural systems are also developed under 'material-adapted' principle that takes advantages of strengths inherent in each of its constituents (Keller, 2003).

Aiming at flexural applications, several hybrid systems of FRP and concrete have been proposed where CFRP or GFRP box and tubular sections have been used as permanent forms and reinforcements (Fam & Rizkalla, 2002; Yuan et al, 2002; Zhao et al, 2000, 2001; Ribeiro et al, 2003; Biddah, 2003). Although concrete filled FRP tube (CFFT) system has been applied as highway bridge girders (Zhao et al, 2001), the applications of FRP/concrete hybrid system have still been limited in a few demonstration projects. Higher initial cost and deformability are the main obstacles. Suffering from local buckling failure, the thickness of CFRP tube in CFFT system had to be increased which made the whole system to be too expensive. To ensure the composite action of FRP and concrete, mechanical interlocks such as inner helicoidal ribs or grooves in CFFT systems and nut bolts in FRP/concrete composite beam were proved to be indispensable to transfer shear force between FRP and concrete. (Samaan, 1997; Mirmiran et al, 1999, 2001; Aprile et al, 2000; Fam et al, 2001).

As an essential, convenient and effective joint method of FRP structures, bonding technology is widely used in the application of FRP in infrastructure. Related problems such as structural performances and debonding failure mechanics of reinforced concrete beams with externally bonded FRP sheets have been comprehensively studied (Wu & Niu, 2000; Niu & Wu, 2002).

To provide a new hybrid structure systems that can be potentially cost-competitive with conventional bridge construction practice, an innovative externally bonded FRP sheets/concrete hybrid system is proposed by the authors based on the research progress of bonding technology at Ibaraki University (Wu et al 2004). In order to develop a comprehensively high performances structural system and by considering that the higher initial cost of a hybrid system may be mainly influenced by the applied proportion of expensive composites as reinforcements, a hybrid composite material system is proposed by making the best of different kinds of continuous fibers in the viewpoints of mechanical behavior and cost performance. Also, instead of conventional interior shear connectors at

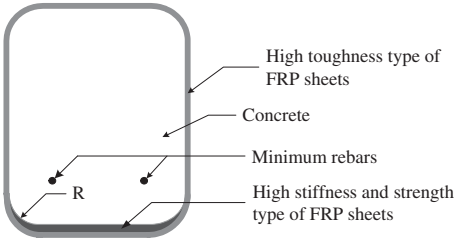

Figure 1. Concept for hybrid externally bonded FRP/concrete beam (Wu et al, 2004).

the interface of FRP and concrete, epoxy adhesive technique is adopted to ensure the composite effect between FRP and concrete.

As deformability is mainly influenced by elasticity of reinforcing materials and cross-sectional design, CFRP sheets with high strength are axially bonded on the bottom surface of the concrete core to carry tensile load and also to ensure the stiffness of the member (as shown in Fig. 1). GFRP sheets with a high rupture strain are wrapped in hoop direction outside the CFRP sheets to provide confinement to the whole concrete core and prevent the premature debonding of interior CFRP sheets. The application of glass fiber may reduce material cost of the whole system and provide better ductility and shear resistance for the webs. The hybrid CFRP/GFRP layers form an integrated jacket that can prevent inner concrete core from harsh environment. The encased concrete core carries compressive loads, stabilizes the thin FRP shell against buckling on the compression side, and allows the anchorage for possible connection with deck and column. Steel bars with minimum reinforcement ratio are used to control the localization and propagation of flexural cracks.

This paper intends to evaluate the flexural performance of externally bonded FRP sheets/concrete hybrid system by experimental and analytical investigations. Three different hybrid beams were manufactured and tested in four-point bending test. In addition, based on Euler-Bernoulli beam theory, an iterative analytical model was also developed to predict the flexural performances of the proposed hybrid beam system.

2 EXPERIMENTAL PROGRAM

2.1 *Materials and fabrications*

All the composite materials were provided by Nippon Steel Composite Co., Ltd.: T-glass fiber sheets FTS-GT-30, high strength carbon sheets FTS-C1-20, FTS-C1-30 and epoxy resin FR-E3PW (for winter). Conventional steel deformed rebars (SD295A) with a

Table 1. Summary of composite material properties.

Material	Thickness* (mm)	Tensile strength* (MPa)	Young's modulus* (GPa)	Ultimate strain (%)
FTS-C1-20	0.111	3400	230	1.60
FTS-C1-30	0.167	3400	230	1.60
FTS-C7-30	0.143	1900	540	0.45
FTS-GT-30	0.120	2700	86	3.20

* Based on manufacturer's specification.

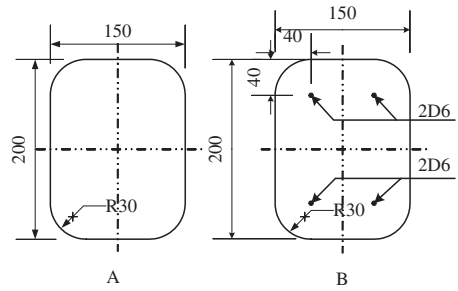

Figure 2. Cross-section configurations of test specimens.

Table 2. Scheme of hybrid FRP/concrete beam specimens.

Number	CFRP ratio as longitudinal reinforcement (%)	Number of layers and fiber types for side web*
A1	0.137	1G/1C
B1	0.148	2G
B2	0.273	1G/1C

* G for T-glass fiber, and C for high strength carbon fiber C1.

modulus of elasticity of 210 GPa and a tensile strength of 440 MPa was used. The corresponding mechanical properties of composite materials are listed in Table 1.

Two kinds of externally bonded FRP/concrete hybrid beams were tested. All concrete cores of hybrid beams had the same rectangular cross section of 200 × 150 × 2000 mm, and were pre-cast using normal concrete with a compressive strength of 35.0 MPa and a modulus of elasticity of 33.5 GPa. As shown in (Fig. 2), specimen of Type A adopted plain concrete core. Concrete core of Type B specimen was reinforced by D6 steel rebars and no steel stirrups were used. Concrete surface treatment was carried out in accordance with standard concrete surface treatment for upgrading of concrete structures with the use of continuous fiber sheets.

Table 2 lists the experimental scheme of hybrid beams. According to it, certain layers of carbon fiber

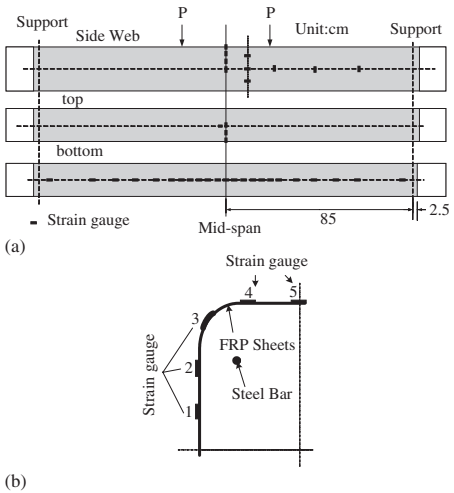

Figure 3. Strain gauge arrangements for (a) Hybrid beam; (b) Compressive zone in midspan.

sheets (width 90, 150 or 180 mm) were bonded along the axial direction (at 0° angle) at the bottom surface of the concrete core by epoxy resin, and then T-glass fiber sheets were wrapped in hoop direction around the beam (at 90° angle). Redundant resin was scraped off. Electro-thermal blanket was used to maintain the cure temperature above 25°C.

2.2 *Test procedure and instrumentation*

Figure 3(a) shows the four-point bending test set-up. The span of beam was 1700 mm and the distance between the loads was 400 mm. The simply supported beams were loaded with load rate of 1 kN/min. The beams were instrumented to record load, deflection and strain measurements. As shown in Fig. 3, in order to measure the strain distribution, a series of strain gauges were longitudinally bonded on the bottom surface of the CFRP sheets. Longitudinal strain on the top flanges at mid span was recorded for the calculation of the curvature. Strain gauges were transversally arranged along the center line of side web in shear span and in the compression zone of midspan. Two linear variable displacement transducers (LVDTs) were used to record the midspan deflection.

3 TEST RESULTS

3.1 *Experimental observations*

During the load procedure, white slender strips that indicated the development of the concrete cracks could

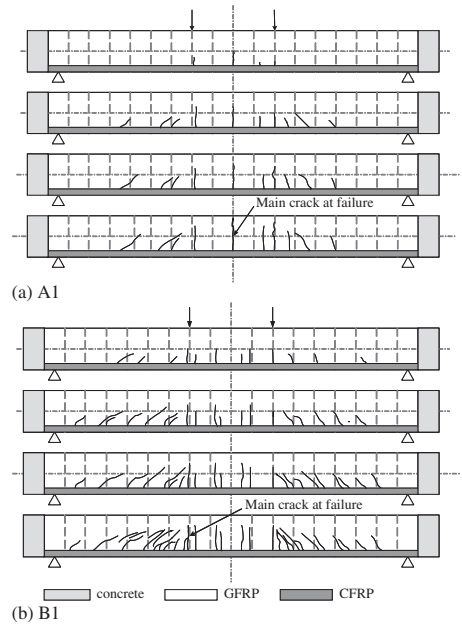

Figure 4. Typical progressive crack patterns of hybrid FRP/concrete beams.

be observed. It was difficult to find the occurrence of initial cracks because the lower part of the side web was covered by opaque carbon fiber sheets. (Fig. 4) shows the visible developments of cracking behavior of typical cases until final failure.

As shown in Fig. 4(a), the white strips which indicated flexural cracks appeared first, and then some declining strips which indicated the shear cracks occurred. The length and width of white strips extended with the increasing load, while the number of strips did not increase accordingly. The FRP sheets ruptured thoroughly at the sudden final failure. At the same time, the specimen broke into two parts completely.

Figure 4(b) shows the typical crack distribution and development of specimen series B. The flexural cracks appeared a little earlier than shear cracks, and then not only the length, but also the number of white strips gradually increased with load. The cracks of concrete could be heard discontinuously after the load exceeded about 30–40% ultimate load. Not as brittle as series A, failure was physically detectable and predictable. At the end of loading, CFRP sheets at the bottom flange were ruptured thoroughly in constant moment region.

No local buckling of FRP shell in compression area of midspan and slippage between FRP and concrete were observed in all the specimens.

Table 3. Summary of the test results.

Beam	Initial cracking load (kN)	Steel yielding load (kN)	Ultimate load (kN)	Deflection at failure (mm)
RC*	15.5	70.0	96.9	35.0
A1	18.5	/	89.9	25.7
B1	19.6	40.1	116.1	32.0
B2	21.4	44.7	166.1	43.0

* Reinforced concrete beam (Wu et al. 2002).

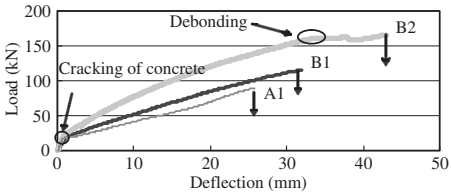

Figure 5. Load–deflection curves.

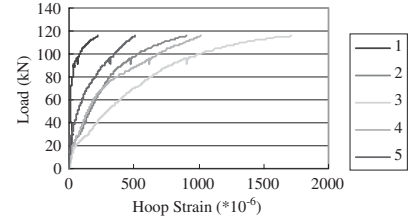

(a) Specimen B1

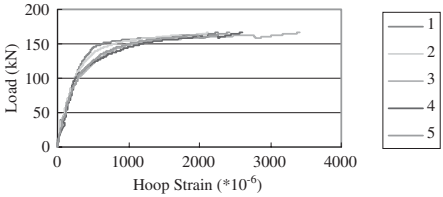

(b) Specimen B2

Figure 6. Load-lateral strain at midspan in compression zone.

3.2 *Load–deflection behaviors*

Test results are summarized in Table 3. The load–deflection behavior of all specimens is illustrated in Fig. 5. All three specimens failed in CFRP rupture, but the load–deflection behavior was different. As shown in (Fig. 5), load–deflection relations of specimen A1 and B1 were approximately linear after cracking. No debonding occurred in A1 and B1 before the final failure.

Small fluctuations are observed at the end of the load–deflection curve of beam B2. It is considered as a proof of debonding which occurred just a little before the occurrence of the final failure. The reduction on the stiffness of hybrid system after debonding is noticeable. Premature debonding of longitudinal CFRP sheets was effectively prevented by hoop wrapped FRP sheets which act as reliable anchors.

The effect of steel yielding on the load–deflection curve of specimen series B is not very obvious. The load–deflection behavior also suggests that the stiffness of the hybrid system after cracking and before debonding is proportional to the CFRP ratio of hybrid system.

4 DISCUSSION

4.1 *Effect of steel rebars*

First of all, steel rebars is proposed in this hybrid system to control the localization and propagation of concrete flexural cracks. The mechanism of this effect is the same as that of steel rebar in reinforced concrete beam. As mentioned in 3.1, the appearance and development of concrete cracks were more distributive in specimen B1 than in A1. In specimen without steel rebars, localized and wide-opened cracks resulted easily in local stress concentration of FRP sheets, and then caused premature FRP rupture and decreased the ultimate load of the hybrid system. Because steel rebars are not proposed to carry primary tensile load in specimen series B, only deformed steel bars with minimum allowable diameter (6 mm) were adopted. The observed behaviors of series B also proved that the effective steel reinforcement ratio could be as low as 0.27% to satisfy crack distribution.

Secondly, the existence of steel rebars can avoid the occurrence of dangerous collapse failure. The failure mode of specimen without steel rebars was a thorough breakdown where specimen broke instantly into two separate pieces. Linear-elastic response of FRP reinforcement often stores large amount of elastic energy in the structure, release of which may prove devastating. In contrast with this total collapse failure mode, the specimen with steel rebars can maintain its integrity even after the rupture of CFRP sheets.

Finally, due to the comparability of Young's moduli of CFRP and steel, the proportion of CFRP and steel in proposed hybrid system can be adjusted to achieve an acceptable balance of properties and cost. This effect is illustrated by a parametric study as presented in a following section.

4.2 *Effect of confinement*

Without axial load, the confinement of FRP reinforcements on concrete in pure flexure member was believed to be neglectable. To confirm the confinement in compression region, hoop strains was tested at midspan. As shown in (Fig. 6), hoop strains measured at midspan in the constant moment region evidently increases with load, especially near the round corner.

The confinement effects of FRP varied with the structure of hoop FRP sheets and load level. The maximum hoop strain at failure of Beam B2 is 0.0035 while that of beam B1 is only 0.0017. The variation of hoop strain was small under about 2/3 failure load, and then hoop strain increased rapidly. A majority of total hoop strain of B2 (about 75%) is developed near the ultimate load.

5 ANALYTICAL STUDY

5.1 *Analytical model*

An iterative analytical model was developed to predict the flexural behavior of the hybrid beam. As shown in (Fig. 7), this analytical model uses the principles of strain compatibility and equilibrium.

The assumptions include:

1. Euler-Bernoulli beam theory
2. Linear strain distribution throughout the full depth of the section
3. No slip between the longitudinal reinforcing steel and the surrounding concrete
4. No slip between the externally bonded FRP sheets and concrete
5. No Debonding or shear failure is accounted for.

Reinforcing bars is modeled by perfectly elastic-plastic curve in both tension and compression, and FRP materials are assumed to behave linear elasticity until failure (shown in Fig. 8). Classical laminate theory and maximum strain failure criterion of composite materials are adopted.

Considering the concrete tension stiffening effect, the model of Vecchio and Collins (1986) is used:

$$\begin{cases} f_{tc}^{'} = E_c \varepsilon_c & (\varepsilon_c \le \varepsilon_{cr}) \\ f_{tc}^{'} = \dfrac{f_{cr}}{1+\sqrt{200\varepsilon_c}} & (\varepsilon_{cr} < \varepsilon_c \le 0.016) \end{cases} \quad (1)$$

where f_{tc}' = tension strength of confined concrete; f_{cr} = cracking stress of concrete; ε_{cr} = the corresponding cracking strain of concrete.

To simulate the containment of the cracked concrete in tension, the limiting ultimate tensile strain of the concrete was taken as large as 1.60%.

Unconfined concrete is assumed to follow Hognestad's parabolic model (shown in Fig. 9), where

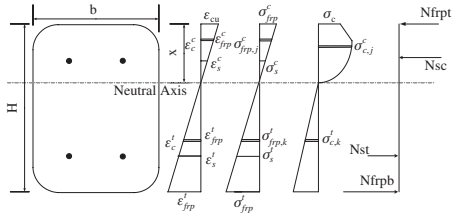

Figure 7. Assumed strain and stress distribution in hybrid beam.

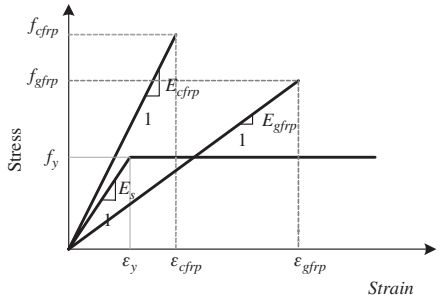

Figure 8. Constitutive relationships for steel and FRP sheets.

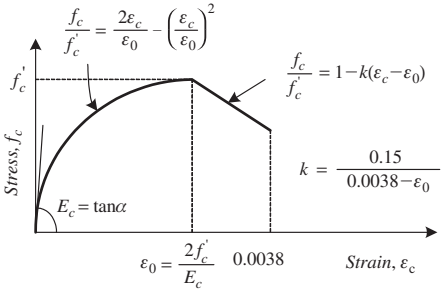

Figure 9. Constitutive relationships for concrete (Hognestad's).

f_c' = compressive strength of concrete; f_c = stress in concrete; ε_0 = strain in concrete corresponding to compressive strength; ε_c = strain in concrete; E_c = initial elastic modulus of concrete.

Due to the confirmed confinement effect of FRP sheets, this concrete model is reasonably modified to describe the behavior of confined concrete. As the effect of confinement on compressive strength of concrete is small in pure flexure, only the effect

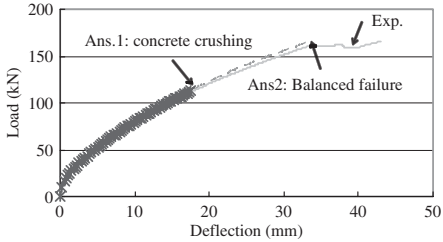

Figure 10. Load–deflection behaviors of B2 (Ans. 1 by using unconfined concrete model, Ans. 2 by using confined concrete model).

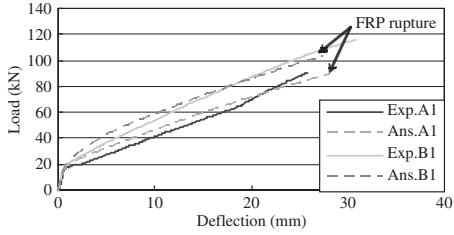

Figure 11. Load–deflection behaviors of A1and B1.

of confinement on the ultimate strain of concrete is considered:

$$k = \frac{0.15}{0.0038k_1 - \varepsilon_0} \qquad (2)$$

where k_1 = confinement coefficient equal to 2.

Figure 10 shows the influence of FRP confinement to the prediction of load–deflection relationship of beam B2. Using unconfined concrete model, the predicted failure mode of hybrid beam was compressive failure and the ultimate load is far below the experimental data. Adopting the confined concrete model, the predicted failure mode of hybrid beam is balanced failure where concrete crushing and CFRP rupture take place simultaneously. And before the occurrence of the debonding between CFRP and concrete, good agreement of experimental and analytical data is observed.

Figure 11 shows the validation of the analytical model by comparing the experimental and analytical load–deflection relationships of beam A1 and B1.

5.2 *Parametric study*

The analytical model was applied in a parametric study to examine the effects of CFRP ratio, stiffness of FRP sheets, steel reinforcement ratio and compressive strength of concrete on the flexure properties of hybrid FRP/concrete beam.

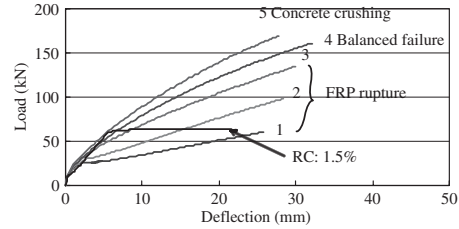

Figure 12. Load–deflection relationships of hybrid beams with longitudinal CFRP ratio of (1) 0.068%, (2) 0.137%, (3) 0.205%, (4) 0.273%, and (5) 0.342%.

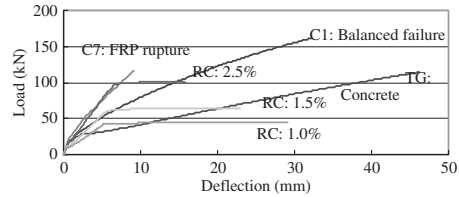

Figure 13. Load–deflection relationships of hybrid beams with different kinds of FRP sheets as longitudinal reinforcement and RC beams (TG: T-Glass fiber).

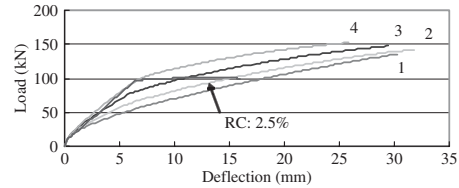

Figure 14. Load–deflection relationships of hybrid beams with different reinforcement ratio of rebars: (1) 0.264%, (2) 0.594%, (3) 1.06%, and (4) 1.66%.

The predicted load–deflection relationships are illustrated in (Fig.12–Fig.15). Material properties are as described earlier, the steel reinforcement ratio is assumed to be 0.27%.

5.2.1 *Longitudinal FRP ratio*

As shown in Fig. 12, the ultimate strength of hybrid beam increases with CFRP ratio, while the failure mode changes from tension failure to compressive failure.

Comparing a hybrid beam with 0.273% longitudinal FRP ratio with an equivalent conventional RC section with a 1.5% reinforcement ratio, the ultimate load of hybrid beam is 2.57 times of that of RC beam.

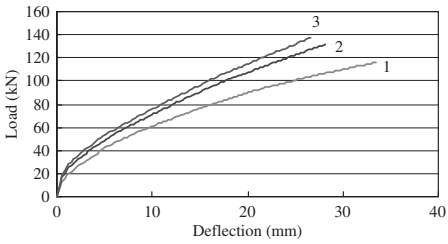

Figure 15. Load–deflection relationships of hybrid beams with different concrete compression strength: (1) 20, (2) 40, (3) 60.

Table 4. Predicted performance of hybrid beams with different longitudinal CFRP ratios.

Specimen number	Axial CFRP ratio (%)	Steel yielding load (kN)	Ultimate load (kN)
1	0.068	25.7	60.7
2	0.137	32.8	98.5
3	0.205	39.0	132.0
4	0.273	46.3	166.0
5	0.343	53.8	178.0
RC*	/	64.6	64.4

* With 1.5% reinforcement ratio.

Table 4 lists the predicted performances of proposed hybrid beams. The steel yielding loads of the proposed hybrid system are only about 27–42% of their ultimate loads. Due to the minimum reinforcement ratio, the steel yielding is no longer an appropriate failure criterion for hybrid system. It is evident that the proposed hybrid beam has a well performance in the load carry capability. The hybrid beam is also comparable in stiffness and ductility to this RC beam. The proposed hybrid system with adhesively bonding technique is confirmed to be effective as flexural members.

5.2.2 *Longitudinal fiber type*

The relationships between the type of longitudinal reinforcement and the flexural performances of hybrid system are shown in Fig. 13. The longitudinal FRP ratio is assumed to be 0.273. The load–deflection relationships of three equivalent conventional reinforced concrete beams with ordinary tensile reinforcement ratios are also illustrated.

The steel yielding loads are as follow: T-glass 27.2 kN, C1 carbon 39.0 kN, and C7 carbon 67.0 kN. Only the stiffness of hybrid beam reinforced by high modulus carbon fiber (C7) sheets is comparable to a RC beam of 2.5% reinforcement ratio. The reinforcement of high strength carbon fiber (C1) sheets makes the stiffness of hybrid beam comparable to a 1.5% equivalent conventional RC beam. Due to the low stiffness of GFRP, only 36% of the Young's modulus of CFRP, the proposed GFRP/concrete hybrid beam has the lowest stiffness.

Although it is illustrated in Fig 12 that the stiffness of hybrid beams increases with CFRP ratio after the cracking of concrete, the increment of stiffness of hybrid beam earned by increasing the layers of CFRP sheets is limited. It seems that a higher stiffness of CFRP/concrete hybrid beam may be obtained by a lavish usage of CFRP sheets. However, the excessive thickness of CFRP has been confirmed to be undesirable for the purpose of a fine bonding between CFRP and concrete (Wu & Niu, 2000). It is not an appropriate way to improve the stiffness by simply increasing the layers of CFRP sheets, because the induced debonding failure of FRP will destroy the composition effect of FRP and concrete. Therefore, the adoption of high modulus carbon fiber sheets in proposed hybrid beam is inevitable to obtain a satisfying stiffness and an acceptable cost of the system simultaneously.

The influence of fiber types on the deflection of hybrid beams is also very noticeable. Hybrid beam reinforced by high modulus carbon fiber sheets (C7) breaks down at very low deflection (9.08 cm) due to the low rupture strain of C7, 28% of that of C1. Meanwhile, the failure deflection of hybrid beam reinforced by GFRP sheets is 46 cm. Although the low stiffness of GFRP/concrete hybrid beam also influences the deflection, the high rupture strain of T-glass fiber is an important reason to the biggest failure deflection.

Hybrid beam reinforced by glass fiber has high toughness and low stiffness while hybrid beam reinforced by high modulus carbon fiber has a contrary performance. Material hybrid method might be the best way to resolve this conflict. (Wu et al, 2002). In order to ensure the stiffness and the ductility of hybrid beam, reduce the material cost of hybrid beam, the hybrid adoption of high modulus, high strength carbon fiber, and high toughness glass fiber should be considered.

5.2.3 *Steel reinforcement ratio*

The longitudinal CFRP ratio is assumed to be 0.205 in Fig. 14. As shown in Fig. 14, the stiffness of hybrid beams at service load level can be effectively increased by the increase of the steel reinforcement ratio in hybrid system. This also proves that the increase of reinforcement ratio may be an effective way to satisfy the stiffness demand and decrease the cost of hybrid system simultaneously.

5.2.4 *Compressive strength of concrete*

The longitudinal CFRP ratio is assumed to be 0.205 in Fig. 15. It illustrates that the adoption of high strength concrete is beneficial to get a hybrid beam system with

higher ultimate load. However, comparing with the effect of fiber ratio and fiber type, the influence of compression strength of concrete is not very obvious.

6 CONCLUSIONS

To study the effectiveness of a proposed hybrid beam system with externally bonded CFRP/GFRP sheets on the flexural behavior of hybrid beam, a series of four-point bending flexural tests were conducted. Moreover, an iterative analytical model was developed to evaluate the flexural behavior of the hybrid beams. The following conclusions can be deduced:

1. The proposed hybrid system with adhesively bonding technique is confirmed to be effective as innovative flexural members where a minimum reinforcement ratio of rebars is considered to be necessary to satisfy crack distribution.
2. The Euler-Bernouli beam theory is applicable to this proposed hybrid system, provided that composite action between FRP and concrete is fully developed. In addition, the confinement effect is confirmed to be important in the analytical model.
3. The load carrying capability, stiffness and ductility of the proposed hybrid FRP/concrete beam system can be realized through a rational design of different kinds of FRP composites.
4. In order to improve the stiffness performance of proposed hybrid beam, the adoption of the high modulus carbon fiber sheets is necessary.

ACKNOWLEDGEMENTS

The financial supports of partial work of this paper from Advance Technology Research in China (863 National Program) under 2001AA336010 and NSFC Joint Research Fund from Overseas Chinese Young Scholars under 50228828 are gratefully acknowledged.

REFERENCES

Aprile, A., Benedetti, A. & Camata, G. 2000. On the structural performance of concrete filled FRP tubes in flexure. *In Pascale G. (ed.) Advanced FRP materials for civil structures: design, quality control and realization European Conference, 19th October Bologna. Italy.*

Biddah, A. 2003. Experimental investigation of pultruded FRP section combined with concrete slab. *In Kiang Hwee Tan (ed.) Proceeding of the Sixth International Symposium on FRP Reinforcement for Concrete Structures (FRPRCS-6), 8–10 July, 2003, Singapore*, 715–724, Singapore: World Scientific.

Fam, A., Flisak, B. & Rizkalla, S. 2001. FRP tubes filled with concrete and subjected to axial loads, bending and combined loads. *In J.G. Teng (ed.), Proceedings of the International Conference on FRP Composites in Civil Engineering (CICE 2001), Hong Kong, 12–15 December 2001.* Oxford: Elsevier. 1307–1317.

Fam, A.Z. & Rizkalla, S.H. 2002. Flexural behavior of concrete-filled fiber-reinforced polymer circular tubes. *ASCE Journal of Composites for Construction*, 6(2): 123–132.

Keller, T. 2003. *Use of Fiber Reinforced Polymers in Bridge Construction, Structural Engineering Documents, 7.* IABSE-AIPC-IVBH, Zurich, Switzerland.

Mirmiran, A. & Shahawy, M. 1997. Behavior of concrete columns confined by fiber composites. *Journal of Structural Engineering, ASCE.* 123(5): 583–590.

Mirmiran, A., Shahawy, M. & Samaan M. 1999. Strength and ductility of hybrid FRP-concrete Beam-column. *Journal of Structural Engineering,* 25(10): 1085–1093.

Niu, H.D. & Wu, Z.S. 2002. Strengthening effects of RC flexural members with FRP sheets affected adhesive layers. *Journal of Applied Mechanics,* 5: 887–897.

Ribeiro, M.C.S., Ferreira, A.J.M. & Marques, A.T. 2003. Flexural behavior of GFRP-polymer concrete hybrid structural systems. *In Kiang Hwee Tan (ed.) Proceeding of the Sixth International Symposium on FRP Reinforcement for Concrete Structures (FRPRCS-6), 8–10 July, 2003, Singapore,* 695–705, Singapore: World Scientific.

Samaan, M.S. 1997. An analytical and experimental investigation of concrete-filled fiber reinforced plastics (FRP) tubes. *Ph.D. dissertation.* University of Central Florida, Florida.

Vecchio, F.J. & Collins, M.P. 1986. The modified compression-field theory for reinforced concrete elements subjected to shear. *ACI Structure J.*, 83(2): 219–231.

Wu, Z.S. & Niu, H.D. 2000. Study on debonding failure of RC beam strengthened with FRP sheet. *Journal of Structural Engineering, JSCE*, 46A(3): 143–144.

Wu, Z.S., Sakamoko K., Niu H.D., Shimada, M. & Murakami, S. 2002. Strengthening effects of concrete flexural members retrofitted with hybrid FRP composites. *The Third International Conference on Composites in Infrastructure*, (CD-ROM) *San Francisco, CA, June 10–12, 2002.*

Wu, Z.S., Li, W.X. & Sakuma, N. 2004. *Innovative Externally Bonded FRP/Concrete Hybrid Structure Systems. Composite Structure, (submitted)*.

Yuan, H., Xue, Y., Li, W. & Zhang, M. 2002. A novel concept of beam-study on a new hybrid GFRP/CFRP tube confined concrete beam. *Proceedings of the 2nd National Conference on Fiber Reinforced Plastic (FRP) for Civil Engineering, Kunming, China,* 296–305.

Zhao, L., Burgueno, R., Rovere, H., Seible, F. & Karbhari, V. 2000. Preliminary evaluation of the hybrid tube bridge system, Report No. TR-2000/4, California Department of Transportation under Contract No. 59AO032.

Zhao, L., Karbhari, V.M. & Seible, F. 2001. Development and Implementation of the Carbon Shell System for the Kings Stormwater Channel Bridge, *In J.G. Teng(ed.), Proceedings of the International Conference on FRP Composites in Civil Engineering (CICE 2001), Hong Kong, 12–15 December 2001.* Oxford: Elsevier.

FRP Composites in Civil Engineering – CICE 2004 – Seracino (ed)
© 2005 Taylor & Francis Group, London, ISBN 90 5809 638 6

A new fibre composite sandwich panel

M.F. Humphreys
Queensland University of Technology, Brisbane, Australia

ABSTRACT: Fibre composite materials are gaining a higher profile in infrastructure applications. Their use as a structural material may be grouped into three main areas; rehabilitation and retrofit, reinforcement for concrete and new fibre composite structures. Despite the considerable success of these materials in rehabilitation and retrofit they have enjoyed little success as new fibre composite civil structures. One reason for this is the relatively high cost of composite materials. One way to address this is to use fibre composite materials with other less expensive materials. Research is being undertaken at the Queensland University of Technology to investigate ways that fibre composite materials can be used with more traditional construction materials. This paper presents preliminary research into a novel fibre composite sandwich panel which uses autoclaved aerated concrete as the core material. Full scale fibre reinforced panels are fabricated and tested to destruction. Finite element analysis of the slabs is also carried out and compared to the results of the destructive testing. Conclusions are drawn on the suitability of autoclaved aerated concrete as a core material.

1 BACKGROUND

The use of fibre composite materials in civil and structural engineering applications continues to gain momentum. Their use in civil engineering has slowly evolved from glass fibre reinforced polyester rod reinforcement for concrete in the 1960's to fibre composite post tensioning cables, externally bonded reinforcement for rehabilitation of concrete and new fibre composite bridge decks.

Some of the characteristics of fibre composite materials most often espoused by proponents of the materials include light weight, high strength, good durability performance, versatility and good fatigue resistance. Whilst these traits may be true of some materials in some applications, the claims can be misleading. The popularity of fibre composite materials in rehabilitation and retrofit of existing structures is testament to characteristics such as light weight and versatility in terms of application, whilst durability or electromagnetic and radiowave transparency are often reasons for their use as reinforcement in concrete.

However, there are characteristics of fibre composite materials which work against their use in civil engineering. These characteristics include often higher initial cost than traditional materials, civil designer's lack of familiarity with the material and industry, composites industry not standardized, inadequate codes and specification and incomplete or irrelevant long-term durability data.

In order for fibre composite materials to gain acceptance as a mainstream construction material it is important that the material's shortfalls are minimized and the benefits that the material offers are realized. This cannot be achieved unless the material is designed with the characteristics of fibre composites in mind. Material traits which need to be exploited include the ability to design the material concurrently with the structure, versatility in geometry and suitability to mass production of light weight modular sections which can be assembled on site.

To civil engineers this should be nothing new. Steel reinforced concrete structures have been designed with these issues in mind for over a century as have timber structures.

Underpinning the appropriate use of composite materials by civil designers is the need for broad based education and continuing research into uses of fibre composite materials appropriate to construction applications. From this should flow forms of standardization suitable for a mature and sophisticated industry such as construction. Education of the composites industry will also be critical to providing commonality between the composites industry and the construction industry so that they can work together efficiently.

In certain areas of civil engineering the use of fibre composite materials has already proven successful. The widespread use of fibre composite materials in rehabilitation and retrofit of civil infrastructure is well known in both the construction and composites industries. It is an example of exploitation of the unique characteristics of composite materials and minimization of its shortfalls. The durability of fibre composite materials in a marine environment has been

exploited along with the material's ability to cope with non-circular pier cross sections with rehabilitation of bridge piers in South East Queensland (Carse, 1997) and novel installation methods have been developed to exploit the ability to strengthening bridge supports by wrapping them with CFRP tows (Toutanji and Balaguru, 1998).

But despite the considerable success of these materials in rehabilitation and retrofit applications they have enjoyed little success as new fibre composite civil structures. Reasons for this have been given previously, but may also include negative past experience with the material (which can often be attributed to inappropriate use rather than a fault with the material).

One way in which fibre composite materials can be used efficiently is by combining them with less expensive traditional materials. This can allow expensive high strength laminates to be used sparingly in conjunction with a less expensive bulking material that can also help to overcome stiffness challenges often faced in civil design.

To this end fibre composite materials suit sandwich panel construction and have been used in this form for decades by traditional composites industries such as marine and aerospace. However the soft cores used by these industries may not suit some applications in the construction industry.

A core material is required which not only provides adequate structural performance, but should also be durable, perform appropriately in fire and potentially provide thermal and sound insulation. One possible contender is autoclaved aerated concrete.

2 CORE MATERIALS FOR CIVIL APPLICATIONS

Core materials traditionally used in the composites industry include timber (balsa, plywood, sawn wood), foam (polystyrene, polyurethane) and honeycomb (aramid and aluminium). Each of these materials possesses characteristics which have made it well suited to certain applications based on, for example, the desire to provide durability or floatation, or to minimise weight. When considered for use in infrastructure applications, characteristics such as high strength and light weight may become secondary to low cost, compatibility with traditional construction materials and ability to provide the material in a suitably large quantity often required for large construction projects. Of the three core materials mentioned previously honeycomb is unlikely to gain widespread acceptance as a viable building material due mainly to its cost, lack of versatility and fragile nature. On the other hand whilst foam and balsa may not be able to provide a suitable solution in all cases, they do possess certain properties desirable to a civil designer.

Foams can be formulated to offer a high degree of durability and reasonable mechanical properties. A number of types are readily available in Australia and the composites industry is familiar with many of them. They have well-established processing techniques, are workable with common tools and can be obtained in forms which are relatively inexpensive. However, some well known brands such as Corecell and Divinycell can be relatively expensive and therefore may not provide an economic solution. Although some polyurethane foam can be less expensive and still possess reasonable mechanical properties, preliminary tests have shown that bonding of laminates to the foam can be difficult. This is critical to develop full laminate strength sandwich panel applications where the core is required to restraint thin strong faces from buckling.

On the other hand the relative affordability, availability, adequate mechanical properties, industry familiarity and workability characteristics of polystyrene foam could be considered distinct advantages over other foams. However polystyrene has a number of disadvantages including:

- Tendency to dissolve in contact with styrene
- Degradation of mechanical properties as temperature increases
- Low crushing strength
- Inability to take intermediate fixings
- Relatively low shear strength.

Compared to polystyrene foam, some of the mechanical properties of balsa makes it an excellent choice for a core material in civil structures including:

- Balsa's relatively high shear strength and shear rigidity
- Better resistance to lateral crushing
- Does not lose significant amounts of these properties at typical civil engineering service temperatures of up to 100°C
- The material is well known by the composites industry
- Can be worked with standard wood working machinery
- Readily available in many forms
- Unfavoured by insects
- Limited water ingress at laminate edges
- Tendency of balsa to char when burnt inhibits the spread of fire
- Available in a range of dimensions.

However balsa has characteristics that may limit its application in civil engineering and construction such as:

- Inability to cope well with localised loading (this can be accommodated by using localized hardpoints to facilitate introduction of load into the structure
- Tends to absorb resin into its fibres

- Limited compressive strength and stiffness across grain
- Limited sizes restrict versatility.

A new type of core material, based on what traditional composites industries call "syntactic foam" was proposed by researchers at USQ who refer to it more correctly as particulate filled resin (PFR) (Ayers and van Erp, 1999). The material is made by combining resin, which has been mixed with hardener or catalyst, with filler particles such as ceramic microspheres, hollow glass spheres or plastic beads. The material is generally castable and the viscosity can be varied by the addition of filler material. The objective of the addition of filler material is to provide a balance between cost, flowability and mechanical properties.

PFR offers a number of potential advantages over traditional core materials such as foam and end grain balsa. One of the main features of this material is that it is castable. PFR can be cast into blocks and machined into the desired shape, or, in the case of the trusses, cast in the finished shape of the core including hollow members. Tests (Ayers, 2001) indicated that PFR has relatively high shear strength and shear rigidity, reasonable tensile strength and tensile modulus and a high compressive strength and compressive strain at failure. It appears to be robust and capable of redistributing concentrated loads at load, support and intermediate fixing points.

Although tests provide positive reinforcement for PFR, it is a relatively new material in civil engineering contexts and as such there are a number of performance characteristics that are unknown. These include reaction to moisture (permeability and strength effects), temperature performance and long-term static and dynamic responses

Characteristics sought after in a core material to be used in civil engineering applications would ideally include:

- Low environmental impact
- Low cost
- High durability
- Tolerant of misuse and abuse
- Possess high axial stiffness and strength
- High shear strength and shear rigidity
- Robustness
- Ability to distribute concentrated loads into the laminate
- Geometric stability
- Versatility
- Stable temperature performance
- Compatibility with other materials.

Hebel meets a number of these criteria particularly low cost, high durability, geometric stability, versatility and compatibility. In addition it offers advantages such as sound and thermal insulations, it is non-toxic, light weight and easy to work as well as being familiar to designers and builders, fire resistant and suitable for modular construction. However it also possesses some characteristics which need to be considered in the design process such as low stiffness and strength and lack of ductility.

3 DESIGN AND ANALYSIS

There appears to be no previous research into the use of glass fibres to reinforce AAC spanning members. The two fundamental aims of this exploratory study were therefore to:

1. Study fabrication aspects of externally reinforcing AAC panels with fibre composite materials
2. Assess the effect of the external reinforcement on the structural behaviour of AAC spanning members.

Design and analysis was based on an "off-the-shelf" proprietary CSR Hebel AAC product, known as Powerpanel, and locally available E-glass fibres and epoxy resin.

Powerpanels are available in a range of lengths and thicknesses, the panels used in this study were 2700 mm long × 600 mm wide × 75 mm thick. These panels are nominally reinforced with light steel mesh primarily used to accommodate transport loads. The properties of the Hebel AAC material used in Powerpanels are provided in Table 1.

E-glass fibres were chosen for this study due to their cost, availability and the short term nature of the loading (Colan stitched 410 gsm). ADR246 epoxy resin with ADH106 hardener was chosen for reasons of cost, availability and industry familiarity with this particular product. Laminate properties are provided in Table 2.

Unidirectional (UD) fibres were used for the main longitudinal reinforcement and were applied to the top and bottom of the panels. Double bias (DB) fibres were used to help distribute loading evenly to all UD fibres

Table 1. Properties of AAC used in Hebel Powerpanels.

ρ (kg/m^3)	$\sigma_{ult.c}$ (MPa)	$\sigma_{ult.t}$ (MPa)	E_f (MPa)
600	4.5	0.44	2190

Table 2. Properties of fibre composite laminates used in this study.

Fibre form	$\sigma_{ult.c}$ (MPa)	$\sigma_{ult.t}$ (MPa)	E_f (GPa)	$\varepsilon_{ult.c}$ %	$\varepsilon_{ult.t}$ %
DB	200	320	17	1.3	2.0
UD	600	350	25	2.2	1.9

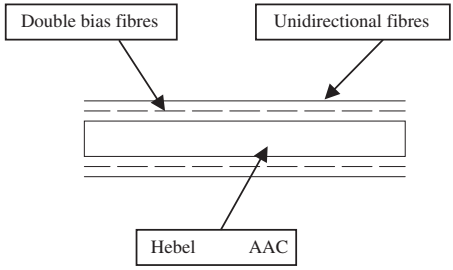

Figure 1. Typical schematic section through fibre reinforced Powerpanel.

and were provided as the initial layer on both sides of each panel. The basic fibre architecture used in this study is shown in Figure 1.

The compressive and tensile failure strains of the Hebel panels were derived using Hooke's Law and the flexural elastic modulus and the failure stresses ($\sigma_{ult.c}$ and $\sigma_{ult.t}$) given in Table 1. The failure strains of the AAC were predicted as $\varepsilon_{ult.c} = 0.21\%$ and $\varepsilon_{ult.t} = 0.02\%$. It can be seen by comparing these values of failure strain with those provided in Table 2 that the failure strains of the AAC core are significantly lower than the corresponding laminate failure strain.

This phenomenon has investigated previously by the author (Humphreys, 2003). It was found that in pure tension elements the low strength, low failure strain core had little effect on the strength and stiffness of the specimen. In the case of flexure it is likely that this will not be the case as the core is required to restrain the thin laminate faces from buckling and needs to remain in tact until failure of the laminates.

However, it is reasonable to assume that the amount of fibre reinforcement provided to the AAC panel will determine panel strength. For this preliminary investigation two external reinforcement configurations on identical cores were studied (an unreinforced Hebel Powerpanel (Type 1) was used in this study as a benchmark). The first external reinforcement configuration allowed a symmetrical/balanced sandwich panel to be produced using one layer of DB and one layer of UD laminate each side of the panel (Type 2). The second arrangement produced an unbalanced/unsymmetrical sandwich panel by reinforcing the top surface with a single layer of DB and UD laminate and the bottom surface with a single layer of DB and two layers of UD laminate (Type 3).

Hand calculations based on the assumptions that the core would remain in tact up to failure of the laminates, using a transformed AAC cross section and using the strain limits shown previously indicated that in both configurations the sandwich panel would be able to support significantly more load (greater than 50 times) than it would unreinforced.

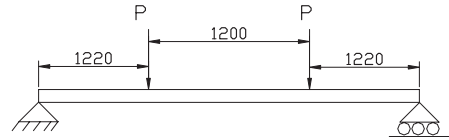

Figure 2. Schematic arrangement of FE model and test configuration.

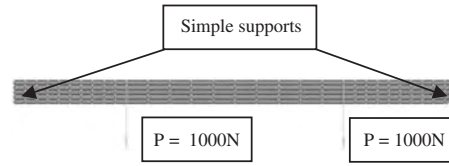

Figure 3. Finite element model (side elevation).

Figure 4. Principal stress contours.

However it was suspected that the core would fail well before the laminated faces, resulting in an instantaneous collapse. A simplified finite element analysis was undertaken investigate this. The geometry of the model (and test arrangement) shown schematically in Figure 2 and the basic finite element model is shown in Figure 3.

The simplified two-dimensional model used beam elements to represent the top and bottom fibre laminated faces and plate elements to represent the Hebel AAC core. Material properties are as shown in Tables 1 and 2. The model is based on a four-point bending system which will be adopted in physical testing and has nominal 1000N loads applied at points shown in Figure 2.

Results of a linear static analysis show that failure could be expected to occur at a location between the load application points and the supports in the form of shear failure. This is likely to manifest in inclined tensile cracks which will result in fracture of the core and separation of the top and bottom laminated faces. Figure 4 shows the principal (tensile) stress contours for this region.

Figure 5 shows the principle (tensile) stress vectors and an expected failure line has been produced

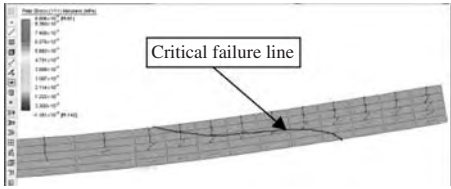

Figure 5. Principal stress vectors.

based on the magnitude and direction of the principal stresses.

This mode of failure would significantly reduce the load carrying capacity of the structure. Using the finite element model, stress limits from Table 1 and assuming failure of the core would result in complete failure of the structure, the maximum expected ram load to cause collapse would be approximately 7.1 kN. The extra layer of fibre reinforcement given to the bottom side of one of the specimens would tend to increase flexural rigidity somewhat, but was expected to have little effect on overall load carrying capacity due to the failure mode.

4 TESTING

Three specimens were prepared for the four-point bending test configuration shown in Figure 2. The first specimen was not reinforced externally with fibre composite material (Type 1), the second had a single layer of DB against the core top and bottom and a single outer UD laminate top and bottom (Type 2). The third specimen used the same basic configuration as Type 2 with an extra outer UD laminate on the bottom surface (Type 3).

Manufacture of the fibre reinforced test specimens consisted of brushing of the Hebel Powerpanel surface to remove loose material. A test had been performed on an area of Hebel AAC to determine the amount of resin that would be absorbed by the AAC. Hebel AAC appears to absorb a negligible amount of resin. The specimens were hand laminated using rushes and rollers. A small fibre reinforced Hebel AAC test sample was post cured to determine the effect of heat on the specimen. The test highlighted the potential for the Hebel AAC core to become damaged during the curing process, possibly due to the severe thermal gradient that would occur in the AAC specimen. For this reason the specimens fabricated for this study were not post cured. This could potentially affect the performance of the double bias layer, however it is unlikely to have a significant effect on the performance of the unidirectional fibres. The specimens are shown in Figure 6.

a)

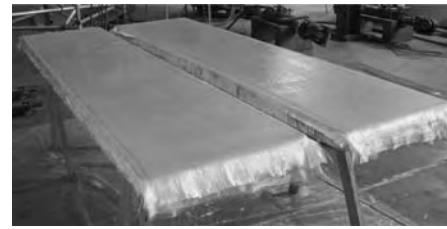

b)

Figure 6. a) Hebel AAC Powerpanel with no external reinforcement (Type 1) and b) Hebel AAC Powerpanel externally reinforced with E-glass/epoxy fibre composites (Type 2 and Type 3).

Figure 7. Typical specimen in test rig.

Strain gauges were installed onto the specimens at midspan top and bottom and linear varying displacement transducers were installed to measure midspan deflection. Pressure transducers were used to measure ram load. Monotonically increasing loading was applied at a rate of 2 mm/minute up to failure. A photograph of a finished specimens in the test rig is provided in Figure 7.

5 RESULTS

Three panels were tested to destruction. The unreinforced panel showed significant ductility during load and failed in a slow controlled manner. The mode of failure was tensile fracture of the AAC material on the

Figure 8. Powerpanel with no external reinforcement (Type 1).

a)

b)

Figure 9. a) Failed Hebel AAC Powerpanel – externally reinforced. b) Failed Hebel AAC Powerpanel – externally reinforced (close view of failure).

bottom surface of the panel near the loading points. Figure 8 shows the failed specimen.

The failure mode of the externally reinforced Powerpanels differs significantly from that of the plain Powerpanel. Both externally reinforced Powerpanels suffered identical failure modes.

Figure 10 shows a graph of the load versus displacement for each panel.

The maximum load carried by each specimen, the maximum midspan deflection and the maximum tensile and compressive strain generate at midspan top and bottom in each specimen is contained in Table 3.

The results show that whilst a significant increase in load carrying capacity is possible, it falls well short of the improvement which could be expected if the core remains intact up to failure of the laminated faces. Nevertheless an improvement of over 400% in terms of strength and over 800% in stiffness (kN/mm of midspan deflection) have been demonstrated. The

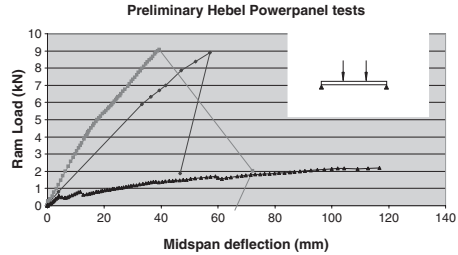

Figure 10. Graph of load versus midspan displacement for all three specimens.

Table 3. Maximum load, maximum tensile and compressive strain and midspan deflection at failure.

Specimen	Max ram load (kN)	Max tensile strain (%)	Max comp. strain (%)	Midspan deflection at failure (mm)
Type 1	2.18	0.021	−0.028	>100
Type 2	8.91	0.37	−0.21	57
Type 3	9.08	0.23	−0.20	39

following points are also noteworthy:

- The Type 3 panel deflected 30% less at failure than the type 2
- The extra layer of fibre reinforcement installed on the Type 3 panel did little to improve strength
- Very low strains were generated in the laminates
- No localized crushing was observed during loading
- Vertical flexural cracks in the core appearing at the bottom of the panel had little affect on the performance of the laminates or the structure as a whole
- The ductile behaviour of the Type 1 Powerpanel was not reproduced by the Type 2 or Type 3 panels.

6 CONCLUSIONS

It is possible to design and analyse externally reinforced panels as developed in this study using well-established engineering methods and simple finite element analysis. The fabrication of these panels was quite straight forward and did not require the use of any special tools or facilities. Locally available materials were used to produce the panels. The use of locally available materials was convenient and kept costs to a minimum.

This exploratory research showed that a significant increase in strength and stiffness can be produced in Hebel AAC Powerpanels by externally reinforcing them with E-glass/epoxy fibre composite laminates.

Potential strength gains above those achieved in this study are difficult to realize due to the low strength of the AAC core material. The configuration used in this test resulted in a loss of member ductility.

Within serviceability limits it may be possible to produce significant improvements in panel stiffness by increasing the amount of external fibre composite material. However this tends to result in an over reinforced section and hence inefficient material use in terms of strength. A more prudent approach would be to vary the depth of the cross section providing greater separation of the laminated faces and more balanced use of the laminates in terms of strength/stiffness although the weight of the panel will increase.

The level of improvement in strength performance of these panels equates to a load carrying capacity of around 5 kPa. The ability to improve the panels load capacity to this level could allow the panels to be used in a number of new horizontal and vertical spanning applications.

Despite the limitations imposed by the apparent inability to post cure the specimens, this study shows that, at this early stage of development, AAC can be considered as a suitable core material in terms of structural performance for fibre composite sandwich panels construction. However suitable applications would be limited to those which are not required to carry significant load.

7 FUTURE DIRECTIONS

The development of a more economically viable version of these panels is underway. The more efficient use of the expensive reinforcing to produce modest stiffness and strength improvements will allow this type of panel to be used as internal partitions in highrise buildings.

In addition to this, AAC beams externally reinforced with fibre composite materials are under investigation using innovative reinforcement patterns which aim to reduce the problem of shear failure in the core.

ACKNOWLEDGEMENTS

The author wishes to acknowledge the financial support of Queensland University of Technology and the support and CSR Hebel Australia for kindly donating the test materials.

REFERENCES

Aroni, S., de Groot, G.J., Robinson, M.J., Svanholm, G., Wittman, F.H., 1993, "Autoclaved Aerated Concrete Properties, Testing and Design", RILEM Technical Committee 78-MCA and 51-ALC, Chapmn and Hall, UK.

Ayers, S.R., Van Erp, G.M., 1999, "Development of a New Structural Core Material for Composites in Civil Engineering", Mechanics of Structures and Materials, Edited by Bradford M.A., Bridge, R.Q., Foster, S.J., Balkema, Rotterdam, The Netherlands, pp 367–372.

Ayers, S., 2001, "Material foundations for the application of fibre composite materials in civil and structural engineering", PhD Dissertation, University of Southern Queensland, Toowoomba, Australia.

Carse, A., 1997, "The Asset Management of a Long Bridge Structure Affected by Alkali-Silica Reaction", Proceedings of Concrete '97 Conference, Concrete Institute of Australia, Adelaide.

CSR Hebel, 1997, "Hebel Technical Handbook – 6th Edition", CSR Hebel, Australia.

Humphreys, M.F., 2003, "Development and Structural Investigation of Monocoque Fibre composite Trusses", Queensland University of Technology, Brisbane, Queensland, Australia.

Toutanji, H., Balaguru, J., 1998, "Durability Characteristics of Concrete Columns Wrapped with FRP Tow Sheets", Journal of Materials in Civil Engineering, Feb 1998, ASCE, USA, pp 52–57.

All FRP structures

FRP Composites in Civil Engineering – CICE 2004 – Seracino (ed)
© 2005 Taylor & Francis Group, London, ISBN 90 5809 638 6

Bending properties of secondary bonded pultruded I-shaped FRP beams

T. Kishima
Public Works Research Institute, Tsukuba, Ibaraki, Japan

T. Watanabe
Asahi Glass Matex, co. Ltd., Sagamihara, Kanagawa, Japan

S. Meiarashi
Public Works Research Institute, Tsukuba, Ibaraki, Japan

ABSTRACT: This paper presents the bending properties of the secondary bonded pultruded I-shaped FRP beams manufactured due to the restriction of FRP molding size. The properties of these beams may be different from those of the composite beams, because the adhesive layers have different properties. Firstly, comparison of the experimental results with the calculated results about the load–deflection curve showed that the bonded FRP beam could be assumed as a composite beam to some extent. Secondly, the shear deformation of the bonded beam gives the peel stress in the adhesive layer, but little effect was observed in the FEM results. Thirdly, the authors considered that the strength of the secondary bonded pultruded I-shaped FRP beam should be estimated by the three-dimensional analysis, through the comparison of the experimental results with the calculated results.

1 INTRODUCTION

Few cases have been observed where FRP materials are applied to bridge structural members. One main reason is why the cost of FRP materials is higher than the ordinary materials such as steel and concrete. The bridge structural member requires a large-cross-section when it is used as a bending structural member. The molding cost of a large-cross-section FRP structural member is higher than a small-cross-section one, because none of the appropriate molding box is generally used to mold a large-cross-section FRP structural member resulting in the introduction of a new large molding box. The development of the cost-effective molding method is required. One of the methods to manufacture a large-cross-section FRP structural member is to bond the small-cross-section FRP structural members molded by the existing FRP molding boxes. The secondary bonded FRP deck is one of the examples of bonding the small-cross-section FRP products to manufacture a large-cross-section FRP product. It can be a cost-effective method to manufacture a large-cross-section FRP structural member if the property of the adhesive layer is equivalent to that of the FRP material.

In this study, the authors focused on the secondary bonded pultruded I-shaped FRP beam which consists of four pultruded FRP structural members. Firstly, they conducted the bending test for the bonded pultruded I-shaped FRP beams and described the experimental results. After that, they compared them with the calculated results assuming the bonded beam as a composite beam. Secondly, they studied the stress properties in the adhesive layer because the strength of the adhesive layer is considered weaker than the FRP material. Finally, they conducted the FEM analysis and compared the calculated results with the experimental results.

2 EXPERIMENT

2.1 *Sample*

The secondary bonded pultruded I-shaped FRP beam consists of two channel pultruded FRP beams and two pultruded FRP plates. The bonding method of the FRP beams and the FRP plates are shown in Fig. 1. Firstly, the two channel pultruded FRP beams were bonded with each other to manufacture the I-shaped beam. Secondly, two pultruded FRP plates were bonded to the upper and the lower flange of the above I-shaped beam. The used resin in the FRP material is a vinyl-ester resin and the adhesive is an epoxy adhesive. Four cross-section types were used in the bending test. First one consists of upper GFRP plate, two channel GFRP

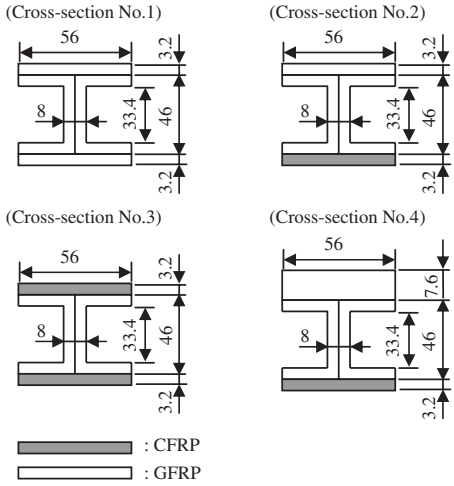

Figure 1. Cross-section types of the bonded beam.

Table 1. FRP material types of the channel beams and the plates.

	Channel beam	Upper plate	Lower plate
No.1	GFRP (M/R/M)	GFRP (M/R/M)	GFRP (M/R/M)
No.2	GFRP (M/B/C/R/C/M)	GFRP (M/R/M)	CFRP (M/T/M)
No.3	GFRP (M/B/C/R/C/M)	CFRP (M/T/M)	CFRP (M/T/M)
No.4	GFRP (M/B/C/R/C/M)	GFRP (M/R/M)	GFRP (M/R/M)

beams and lower GFRP plate. Second one consists of upper GFRP plate, two channel GFRP beams and lower CFRP plate. Third one consists of upper CFRP plate, two channel GFRP beams and lower CFRP plate (CGC beam). Fourth one consists of upper thick GFRP plate, two channel GFRP beams and lower CFRP plate (GGC beam). The bending stiffness of CGC beam is equivalent to that of GGC beam. Fig. 1 shows these cross-section types.

Table 1 shows the FRP material types composing the bonded beams for the cross-section No.1–No.4. Parentheses indicate the stacking sequences of the FRP channel beams and the FRP plates. In this expression, M indicates Mat layer, B indicates Bias layer, C indicates Cloth layer, R indicates Roving layer and T indicates Tow layer.

According to Table 1, the stacking sequence is Mat/Roving(Tow)/Mat, or Mat/Bias/Cloth/Roving (Tow)/Cloth/Bias/Mat. Mat layer consists of random

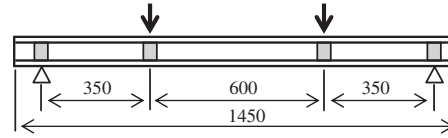

Figure 2. Bending test for the bonded beam.

Table 2. Test results (maximum load and Deflection).

	Maximum load (N)	Deflection (mm)
No.1	41,460	91.5
No.2	49,590	87.4
No.3	41,670	90.4
	(24,688)	(33.0)
No.4	(50,280)	(63.6)

oriented fibers and Bias layer consists of ±45° oriented fibers. Cloth layer consists of 0° and 90° oriented fibers. The fiber weaving types of Bias layer and Cloth layer are knitted types. CFRP includes carbon fibers in Tow layer and glass fibers in the other layers, while GFRP includes glass fibers in all layers.

2.2 *Bending test*

Figure 2 shows the configuration of the bending test with two concentrated loads. The loading speed is 6 mm/min. Table 2 shows the maximum loads and the deflections at the mid-span. The maximum load is the sum of two concentrated loads. The parentheses in the cross-section No.3 indicate the values when the upper CFRP plate was subjected to the compressive failure and the debonding under the loading. The parentheses in the cross-section No.4 indicate the values when the loading machine stopped under the loading.

For the cross-section No.1, the channel beams and the plates performed together without debonding until the final failure. At the final failure, the web was subjected to the shear failure and the plates were debonded at the same time.

For the cross-section No.2, the lower CFRP plate was partly debonded around the mid-span under loading. However, the channel beams and the plates performed together until the final failure. At the final failure, the flanges of the channel beams were subjected to the compressive failure around the loading point, and the debonding of the upper GFRP plate was also observed.

For the cross-section No.3, the upper CFRP plate was subjected to both the compressive failure and the debonding around the loading point, when the load reached about 25,000 N that is half of the final load. This location is between the supporting point and the

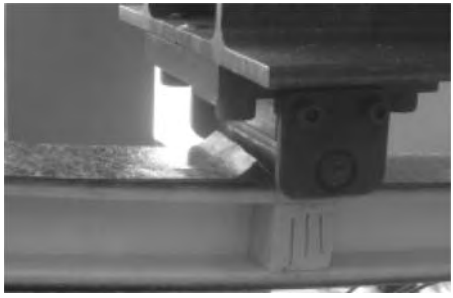

Figure 3. Compressive failure and debonding of the upper CFRP plate.

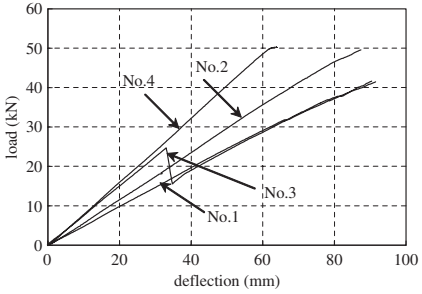

Figure 4. Load–deflection curve of the bonded beam.

loading point (Fig. 3). At the final failure, the upper CFRP plate was debonded all over and the flanges of the GFRP channel beams were subjected to the compressive failure around the loading point. The bonded FRP beam could not keep the initial condition after the failure of the upper CFRP plate.

Figure 3 shows the failure of the upper CFRP plate. No information was obtained through the test about whether the failure of the upper CFRP plate can be attributed to the compressive failure or the debonding.

For the cross-section No.4, the loading machine stopped at about 50 kN which we considered as the maximum load of the cross-section No.4. The channel beams and the plates performed together until the loading machine stopped. No debonding of the plates and no compressive failure of the upper plate was observed under the loading.

2.3 *Deflection at the mid-span*

Figure 4 shows the relationship between the load and the deflection at the mid-span for the cross-section No.1–No.4. The discontinuity of the load–deflection curve for the cross-section No.3 is due to the reduction of the bending stiffness by the failure of the upper

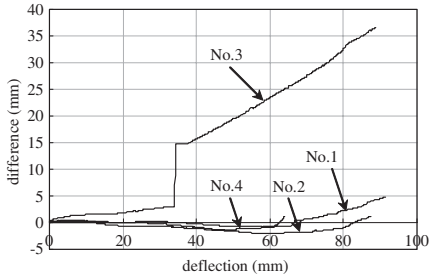

Figure 5. Difference between the experimental results and the calculation results for the deflection (difference = experiment − calculated).

Table 3. Elastic moduli of the FRP structural members.

	Channel beam (GPa)	Upper plate (GPa)	Lower plate (GPa)
No.1	30.15 (flange) 27.68 (web)	29.06	29.06
No.2	25.54 (flange) 18.09 (web)	29.06	80.79
No.3	25.54 (flange) 18.09 (web)	80.79	80.79
No.4	25.54 (flange) 18.09 (web)	29.06	80.79

CFRP plate. Figure 5 shows the difference between the experimental results and the calculated results for the deflection at the mid-span. The calculated results were obtained by assuming the bonded beam as a linear-elastic composite beam neglecting shear deformation. Equation 1 gives the calculation method of the deflection δ at the mid-span, where P is the sum of two concentrated loads, l is the span length, a is the length between the supporting point and the loading point, and $(EI)_T$ is the bending stiffness of the bonded beam.

$$\delta = \frac{Pl^3}{48(EI)_T} \times \frac{a}{l}\{3 - 4(\frac{a}{l})^2\} \quad (1)$$

Table 3 shows the elastic moduli of GFRP and CFRP in the beam axis direction. These moduli were calculated by the rule of mixtures.

According to Fig. 5, the difference is nearly equal to zero for the cross-section No.1, No.2 and No.4, especially at the initial stage of loading. The difference for the cross-section No.3 is also close to zero before the failure of the upper CFRP plate. The consideration through the load–deflection curve suggests that the secondary bonded I-shaped FRP beam can be assumed

as a composite beam neglecting shear deformation to some extent.

2.4 *Compressive stress in the upper plate*

The compressive stress at the middle of the upper plate can be easily calculated, by assuming the bonded beam as a composite beam neglecting shear deformation. In this case, the maximum compressive stress appears between the loading points. Table 4 shows the maximum compressive stress and the compressive strength of upper GFRP or CFRP plate. The values for the cross-section No.3 are at the failure of the upper CFRP plate. The values for the cross-section No.4 are at the stopping of the loading machine.

The maximum compressive stress is higher than the compressive strength only for the cross-section No.3. It suggests that the failure of the upper CFRP plate may be attributed to the compressive failure. However, if the compressive failure is a main factor, the location of the failure must be between the loading points. This location is between the supporting point and the loading point. Only this simple analysis cannot bring that the compressive failure of the upper CFRP plate is a main factor.

2.5 *Shear stress in the adhesive layer*

The shear stress can be calculated by Equation 2, where the composite beam consists of N layers shown in Fig. 6.

$$\tau_i = \frac{F\sum_{j=1}^{j=i}(E_j \cdot S_j)}{b_i\sum_{j=1}^{N}(E_j \cdot I_j)} \qquad (2)$$

τ_i is the shear stress in the i-th material. F is the shear force. b_i is the width of the i-th material. E_i is the elastic modulus of the i-th material. I_i is the second moment of the i-th material cross-section. S_i is the first moment of the i-th material cross-section.

The shear stress in the adhesive layer was calculated for the bonded beam shown in Fig. 2. In this calculation, it is assumed that the stress distribution in the bonded beam is two-dimensional. Figure 7 shows the shear stress in the adhesive layer for the maximum load. The maximum load for the cross-section No.3 is at the failure of the upper CFRP plate. The maximum load for the cross-section No.4 is at the stopping of the loading machine.

The shear stress in the upper adhesive layer is 3–4 MPa for the cross-section No.1–No.3, while that is about 6 MPa for the cross-section No.4. The shear stress for the cross-section No.3 is lower than the cross-section No.4 with same bending stiffness, while the debonding of the upper FRP plate was observed only for the cross-section No.3. It suggests that the shear stress in the adhesive layer is not a main factor of the failure of the upper CFRP plate.

Table 4. Maximum compressive stress in the upper plate and compressive strength of the upper plate.

	Maximum stress (MPa)	Strength (MPa)
No.1	337.9	450
No.2	409.5	450
No.3	335.8	300
No.4	271.3	450

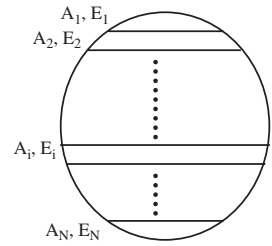

Figure 6. N layers as a composite beam.

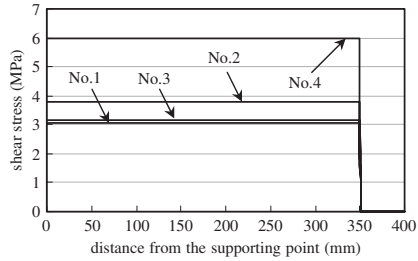

Figure 7a. Shear stress in the upper adhesive layer.

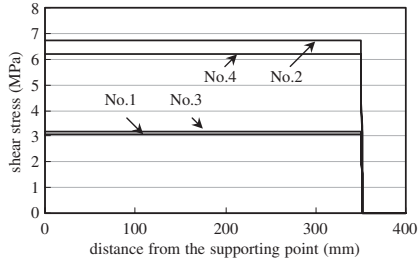

Figure 7b. Shear stress in the lower adhesive layer.

3 STRESS PROPERTIES IN THE ADHESIVE LAYER

The channel beams and the plates should be prevented from debonding before the entire bending failure in view of applying them to bridge structural members. This section focused on the stress properties in the adhesive layers by the formulation of the stresses in the adhesive layers for the bonded beam. The assumed bonded beam consists of three FRP beams bonded with each other. The formulation is based on the Smith and Teng's method for the concrete beam bonded with the FRP plate below. It contains the following assumptions.

1) The bonded beam is subjected to both bending deformation and shear deformation.
2) The stresses in the bonded beam are two-dimensional.
3) Each FRP beam is linear elastic.
4) Each FRP beam deforms with equal bending curvature.

The adhesives are only subjected to both shear stress and peel stress. The constant stress is assumed across the thickness of the adhesive layer. Figure 8 shows the differential element of the assumed bonded beam. It also shows the shear stress and the peel stress in the adhesive layers, bending moment, axial force and shear force in the FRP beams. The shear stress in the adhesive layer 1 and 2 is described as Equation 3.

$$\frac{d\tau_1}{dx} = \frac{G_{a1}}{t_{a1}}\left(\frac{du_2^U}{dx} - \frac{du_1^L}{dx}\right)$$
$$\frac{d\tau_2}{dx} = \frac{G_{a2}}{t_{a2}}\left(\frac{du_3^U}{dx} - \frac{du_2^L}{dx}\right) \quad (3)$$

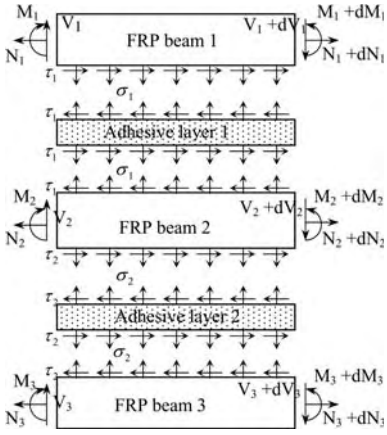

Figure 8. Differential element of the bonded beam.

The x axis is the beam axis. τ_i is the shear stress in the i-th adhesive layer. u_i is the displacement in the x direction of the i-th FRP beam. U and L mean the upper end and the lower end of the FRP beam, respectively. G_{ai} is the shear modulus of the i-th adhesive layer. t_{ai} is the thickness of the i-th adhesive layer.

The governing equation of the stress in the adhesive layer can be derived according to the Smith and Teng's method. The strains at the upper end and the lower end of the FRP beam in Equation 3 are expressed in terms of axial force, bending force and shear force. Assuming that the bending curvatures of the FRP beam 1, 2 and 3 are equivalent, the governing equation can be described as Equation 4.

$$R_1\frac{d^4\tau_1}{dx^4} + R_2\frac{d^2\tau_1}{dx^2} + R_3\tau_1 + R_4\frac{d\sigma_1}{dx} + R_5V_T + R_6\frac{d^2V_T}{dx^2} = 0$$
$$S_1\frac{d^4\tau_2}{dx^4} + S_2\frac{d^2\tau_2}{dx^2} + S_3\tau_2 + S_4\frac{d\sigma_2}{dx} + S_5V_T + S_6\frac{d^2V_T}{dx^2} = 0 \quad (4)$$

$$R_1 = 1$$

$$R_2 = -\frac{G_{a1}}{t_{a1}}b\left(\frac{y_1+y_2}{E_T}(y_1+y_2+t_{a1}) + \frac{1}{E_1A_1} + \frac{1}{E_2A_2}\right) - \frac{G_{a2}}{t_{a2}}b\left(\frac{y_2+y_3}{E_T}(y_2+y_3+t_{a2}) + \frac{1}{E_2A_2} + \frac{1}{E_3A_3}\right)$$

$$R_3 = \frac{G_{a1}}{t_{a1}}\frac{G_{a2}}{t_{a2}}b\left(\frac{y_1+y_2}{E_T}(y_1+y_2+t_{a1}) + \frac{1}{E_1A_1} + \frac{1}{E_2A_2}\right) \times b\left(\frac{y_2+y_3}{E_T}(y_2+y_3+t_{a2}) + \frac{1}{E_2A_2} + \frac{1}{E_3A_3}\right) - \frac{G_{a1}}{t_{a1}}\frac{G_{a2}}{t_{a2}}b\left(\frac{y_1+y_2}{E_T}(y_2+y_3+t_{a2}) - \frac{1}{E_2A_2}\right) \times b\left(\frac{y_2+y_3}{E_T}(y_1+y_2+t_{a1}) - \frac{1}{E_2A_2}\right)$$

$$R_4 = \frac{by_2}{G_2\alpha_2A_2} - \frac{by_1}{G_1\alpha_1A_1}$$

$$R_5 = -\frac{G_{a1}}{t_{a1}}\frac{G_{a2}}{t_{a2}}b\left(\frac{y_2+y_3}{E_T}(y_2+y_3+t_{a2}) + \frac{1}{E_2A_2} + \frac{1}{E_3A_3}\right) \times \frac{y_1+y_2}{E_T} + \frac{y_2+y_3}{E_T} \times \frac{G_{a1}}{t_{a1}}\frac{G_{a2}}{t_{a2}}b\left(\frac{y_1+y_2}{E_T}(y_2+y_3+t_{a2}) - \frac{1}{E_2A_2}\right)$$

$$R_6 = \frac{G_{a1}}{t_{a1}}\frac{G_{a2}}{t_{a2}}\frac{y_1+y_2}{E_T}$$

$$S_1 = R_1, \qquad S_2 = R_2, \qquad S_3 = R_3$$

$$S_4 = \frac{by_3}{G_3\alpha_3 A_3} - \frac{by_2}{G_2\alpha_2 A_2}$$

$$S_5 = -\frac{G_{a1}}{t_{a1}}\frac{G_{a2}}{t_{a2}} b\left(\frac{y_1+y_2}{E_T}(y_1+y_2+t_{a1}) + \frac{1}{E_1A_1} + \frac{1}{E_2A_2}\right) \times \frac{y_2+y_3}{E_T} + \frac{y_1+y_2}{E_T} \times \frac{G_{a1}}{t_{a1}}\frac{G_{a2}}{t_{a2}} b\left(\frac{y_2+y_3}{E_T}(y_1+y_2+t_{a1}) - \frac{1}{E_2A_2}\right)$$

$$S_6 = \frac{G_{a1}}{t_{a1}}\frac{G_{a2}}{t_{a2}}\frac{y_2+y_3}{E_T} \quad \left(E_T = E_1I_1 + E_2I_2 + E_3I_3\right)$$

σ_i is the peel stress in the i-th adhesive layer. G_i is the shear modulus of the i-th FRP beam. A_i is the cross-section area of the i-th FRP beam. y_i is the distance between the neutral line and the end line of the i-th FRP beam. α_i is the effective shear area multiplier of the i-th FRP beam. b is the width of the FRP beam.

Equation 4 suggests that the peel stress exists in the adhesive layer in addition to the shear stress when the shear deformation of the FRP beam can be involved. The shear modulus of FRP is lower than that of steel, which suggests that the existence of the peel stress may not be neglected. On the other hand, only the shear stress exists in the adhesive layer when the shear deformation of the FRP beam can be neglected. Involving shear deformations of the secondary bonded FRP beam, both the shear stress and the peel stress can be factors of the debonding in the adhesive layer.

4 FEM ANALYSIS

Equation 4 is difficult to solve in an explicit form. In addition to this, it is based on the several assumptions. The FEM analysis is considered as an effective method to obtain the accurate stresses, because few assumptions are required and the calculation is not complicated. This section focused on the failure mechanism of the upper CFRP plate for cross-section No.3 through the FEM results of the cross-section No.3 and No.4. The cross-section No.3 and No.4 have the equal bending stiffness, while only the cross-section No.3 lost its structural function before the entire bending failure due to the failure of the upper CFRP plate. The comparison of the FEM results for both cross-sections is to give the valuable basis of the failure mechanism.

The elastic moduli of CFRP and GFRP are shown in Table 5. x indicates the horizontal direction parallel to the beam axis. y indicates the horizontal direction normal to the beam axis. z indicates the vertical direction normal to the beam axis. Figure 9 shows the x, y and z axes. The FEM analysis was conducted for the maximum load. The maximum load for the cross-section No.3 is at the failure of the upper CFRP plate. The maximum load for the cross-section No.4 is at the stopping of the loading machine.

Table 5. Elastic moduli and poisson's ratios of the channel beams and the plates.

	Channel beam		Plate	
	Flange	Web	GFRP	CFRP
E_x	25.2 GPa	18.1 GPa	29.1 GPa	80.8 GPa
E_y	8.93 GPa	5.0 GPa	7.42 GPa	7.64 GPa
E_z	5.0 GPa	11.0 GPa	5.0 GPa	5.0 GPa
G_{xy}	5.0 GPa	4.0 GPa	4.0 GPa	4.0 GPa
G_{yz}	4.0 GPa	4.0 GPa	4.0 GPa	4.0 GPa
G_{xz}	4.0 GPa	6.0 GPa	4.0 GPa	4.0 GPa
ν_{xy}	0.3	0.3	0.3	0.3
ν_{yz}	0.3	0.3	0.3	0.3
ν_{xz}	0.3	0.3	0.3	0.3

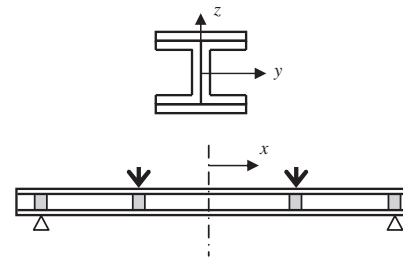

Figure 9. Coordinate axes of the bonded beam.

The calculated results for both cases show that the local stress is dominant around the loading point, where the failure of the upper CFRP plate was observed for the cross-section No.3. Figure 10 shows the shear stress in the upper adhesive layer around the loading point. The location in the y direction for Fig. 10(a) is at the center line and that for Fig. 10(b) is 16.5 mm away from the center line. According to the figures, the shear stress for the cross-section No.3 is smaller than the cross-section No.4, which suggests that the shear stress is not a main factor of the debonding.

Figure 11 shows the peel stress in the upper adhesive layer around the loading point. The location in the y direction for Fig. 11(a) is at the center line and that for Figure 11(b) is 16.5 mm away from the center line. Figure 11(a) shows that the peel stresses for both cases are below zero. Figure 11(b) shows that the maximum peel stress for the cross-section No.4 is about 2–3 MPa around the loading point and that for the cross-section No.3 is about 1–2 MPa. It suggests that the peel stress

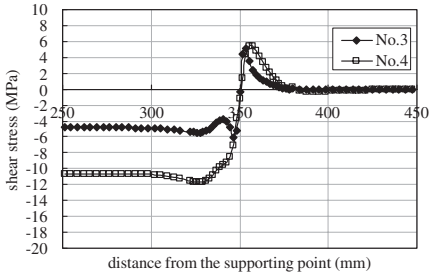

Figure 10a. Shear stress in the upper adhesive layer (center).

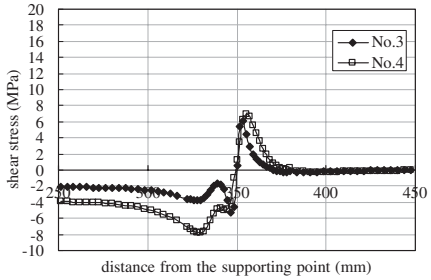

Figure 10b. Shear stress in the upper adhesive layer (side).

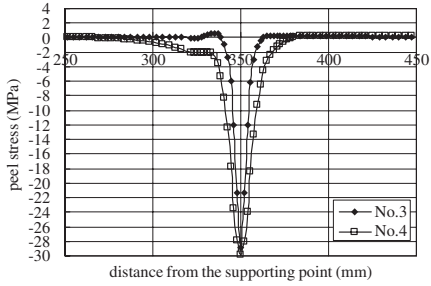

Figure 11a. Peel stress in the upper adhesive layer (center).

is not a main factor of the debonding. The shear deformation of the FRP beam gives little effect on the peel stress. The compressive failure and the debonding of the upper CFRP plate cannot be attributed to the stress in the adhesive layer.

Comparing the calculated shear stresses in the adhesive layer shown in section 2.5 with those shown in this section, they are recognized quite different. The two-dimensional analysis is assumed in section 2.5, but it may not give the accurate values because the stresses change across the x-y plane. The three-dimensional

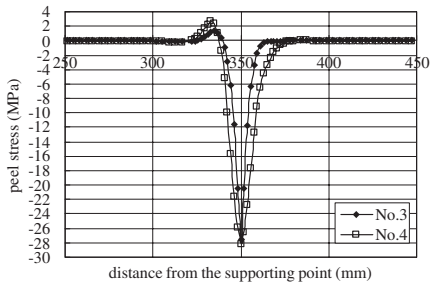

Figure 11b. Peel stress in the upper adhesive layer (side).

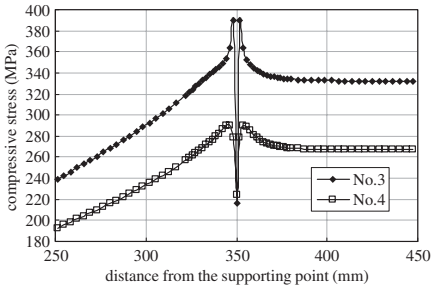

Figure 12. Compressive stress in the upper plate.

analysis such as the FEM analysis is required to obtain the accurate values.

Figure 12 shows the compressive stress in the upper plate. The location in the y direction is at the center line and that in the z direction is at the middle of the plate. The maximum compressive stress appears around the loading point. It means that the FEM analysis can give the local stress different from the calculation method shown in section 2.4. The figure tells that the maximum compressive stress for the cross-section No.3 is about 390 MPa while that for the cross-section No.4 is about 290 MPa. On the other hand, the compressive strength of the CFRP is around 300 MPa and that of the GFRP is around 450 MPa, as shown in Table 4. The compressive stress in the CFRP plate for the cross-section No.3 is higher than the compressive strength, while the compressive stress in the GFRP plate for the cross-section No.4 is much lower than the compressive strength. Fig. 3 also indicates the delamination of the upper CFRP plate in addition to the compressive failure and the debonding. For the cross-section No.3, it is considered that the upper CFRP plate was subjected to the compressive failure, leading to the delamination and the debonding. The compressive failure is considered as a main factor of the fracture and the debonding of the upper CFRP plate.

The authors considered that the strength of the secondary bonded pultruded I-shaped FRP beam should be estimated by the three-dimensional analysis including shear deformations such as the FEM analysis, because the two-dimensional analysis shown in section 2 could not give the accurate values. In this analysis, it is desired that the failure criterion is applied to both the FRP materials and the adhesive layers.

5 CONCLUSIONS

The study contains the following conclusions.

1) The secondary bonded FRP beam can be assumed as a linear elastic composite beam at the initial stage of loading when the FRP plate is not debonded.
2) The adhesive layer of the secondary bonded FRP beam is subjected not only to the shear stress but also to the peel stress when the shear deformation of the bonded beam is involved.
3) The shear deformation of the secondary bonded FRP beam gives little effect on the peel stress in the adhesive layer according to the FEM analysis.
4) The strength of the secondary bonded pultruded I-shaped FRP beam should be estimated by the three-dimensional analysis such as the FEM analysis.

REFERENCES

Bakis, C.E., Bank, L.C., Brown, V.L., Cosenza, E., Davalos, J.F., Lesko, J.J., Machida, A., Rizkalla, S.H. and Triantafillou, T. C. 2002. Fiber-Reinforced Polymer Composites for Construction – State-of-the-Art Review, Journal of Composites for Construction, ASCE, Vol. 6, No. 2, 73–87.

Smith, S.T. and Teng, J.G. 2001. Interfacial stresses in plated beams, Engineering Structures 23, 867–871.

FRP Composites in Civil Engineering – CICE 2004 – Seracino (ed)

Friction and load transfer in bolted joints of pultruded fibre reinforced polymer section

J.T. Mottram
School of Engineering, University of Warwick, Coventry, United Kingdom

ABSTRACT: A steel plate-to-plate joint test procedure is adapted so that it can be used to determine the approximate static coefficient of friction for Pultruded Fibre Reinforced Polymer (PFRP) on PFRP. By lubricating the steel bolts before their installation the coefficient is found to increase and, at 0.25, is similar to the coefficient of dry steel on steel. New results from a bolt tension relaxation test are present. These show that the loss in bolt tension in a PFRP bolted joint is likely to be >40% during the lifetime of the structure. Based on the paper's results, and other information, a worked example for a single bolted joint is used to show that we cannot develop a joint design procedure that relies on a pre-defined bolt torque to ensure that all the joint loading is transferred by friction.

1 INTRODUCTION

Pultruded Fibre Reinforced Polymer (PFRP) structural sections consist of thin-walled composite profiles having overall dimensions up to 1000 mm and wall thicknesses up to 25 mm (Anon 1989, Anon 1995, Anon 2001). Reinforcement is E-glass fibre in two forms, namely unidirectional (UD) rovings and continuous filament (or continuous strand) mats. The matrix is a thermoset resin such as polyester or vinylester, which often contains filler and other additives. PFRP structural sections are used in primary load-bearing structures with steel (galvanised stainless) bolts being the preferred method of connection (Turvey 2000). Primary joints are expected to provide strength and stiffness to the PFRP structure throughout its life (Clarke 1996). Failure of such joints would constitute major structural damage and be hazardous to life. The safe and reliable design of bolted joints is therefore a priority.

Mottram & Turvey (2003) have recently completed a review on the physical test research for plate-to-plate PFRP bolted joints. Its aim was to consider what the test data had to offer us for the appraisal of recognised connection design procedures (Clarke 1996, Hart-Smith 1985). In the review the authors present salient information on the 16 series of tests that have, for single-bolted and multi-bolted double lap joints, provided some 1700 ultimate strength results. They found that different joint variables had been studied, since the 16 series had different objectives. These differences reflect the current state of guidance on joint design and installation in the pultruders' design manuals (Anon 1989, Anon 1995, Anon 2001) and elsewhere (Clarke 1996).

A majority of the previously tested joints had the bolting tightened to the finger-tight condition and were failed subjected to monotonic stroke or load rates (Mottram & Turvey 2003). Of the many variables that can be changed the joint test series presented in the review did not considered how varying the bolt torque could effect the load transferred by friction (i.e. via shear forces over the contacting surfaces). Mottram, Lutz & Dunscombe (2004) conducted a small test series to determine the coefficient of friction for dry PFRP on PFRP to be about 0.2. It used a structural steelwork joint test method (Kulak, Fisher & Struik 2001) with the two bolt sizes of M12 and M16. They used current understanding on the behaviour of similar joints to conclude that a joint design procedure that relied on the entire joint force being transferred by friction could not be prepared. Additional physical tests were required, since the findings were very preliminary and the test procedure with the M16 bolt size did not conform to practice. In this paper the author presents a follow-on study which had the objective of providing new information to address a number of issues arising from the preliminary work by Mottram et al. (2004).

Justification for not recommending a high bolt torque (Clarke 1996) when assembling PFRP joints can be made since material creep, without the need to be exposed to elevated temperature (Scott & Zureick 1998), will undoubtedly allow the bolt tension (i.e. the clamping force) to reduce in the long-term. For the first time experimental measurements are presented

from a bolt force relaxation test which supports this recommendation.

2 BOLT TORQUE AND LOAD TRANSFER BY FRICTION

Cooper & Turvey (1995) showed that the clamping force generated by the bolt torque is beneficial in increasing the strength of PFRP bolted joints. This was because the onset of bearing failure was suppressed. Of the 1700 joint tests reported by Mottram & Turvey (2003) about 18% had a bolt torque higher than the finger-tight condition. This was because it is recognised that PFRP material creeps such that it would not, over the life of the structure, be prudent to rely on the clamping force to suppress the onset of bearing failure in the bolted joints.

Considering what current practice offers (Anon 1989, Anon 1995, Anon 2001), it is observed that PFRP joint detailing is likely to have a bolt pre-load, induced via a specified torque (there is, however, no consensus on what tension stress the bolt should experience). To comply with UK (European) steelwork practice (Anon 1985) and Clause 5.2.2.3(6) in EUROCOMP Design Code (Clarke 1996), it is, however, found that bolting is recommended to be tightened to the finger-tight condition. This low pre-load is expected to take into account factors such as poor on-site practice, the effect of long-term creep, cyclic loading, fatigue and vibration or their combination, and the likelihood that, with FRPs, little connection load is transferred by friction. For the reasons just given, the strength design of bolted FRP joints (Clarke 1996, Hart-Smith 1980) should not be expected to be based on including any additional resistance offered by the bolting having a high pretension that suppresses initiation of damage.

Both European (Anon 1985) and American (Kulak et al. 2001) structural steelwork practices recommend bolting to have a pre-load only when the joint is slip-critical (e.g., to design against fatigue failure). For bearing type joints, no pre-load is required and this is met by the bolting tightened to the snug-tight condition (Kulak et al. 2001). This condition is defined as the tightness that exists when all parts in a joint are in firm, but not necessarily continuous contact. It can be considered to be equivalent to the finger-tight condition recommended for PFRP joints (Mottram & Turvey 2003). There are also high-strength friction grip bolts (Anon 1985, Kulak et al. 2001), where slip in the steel connection is not permitted at the SLS or ULS and for these joints the load is carried entirely by static frictional (shearing) force. Given our reliance on transferring steelwork practice into PFRP practice, it is therefore not too surprising to hear that PFRP fabricators apply a high bolt torque, with the expectation that the friction between the contacting faces will aid in carrying the joint forces.

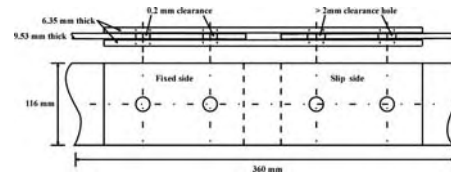

Figure 1. Test specimen for determination of static coefficient of friction of PFRP on PFRP.

To determine the static coefficient of friction of bolted connections Mottram et al. (2004) adapted a testing methodology from structural steelwork (Anon 1985). Figure 1 shows the PFRP plate-to-plate test specimen with two 1×2 bolted joints. The outer plates are of PFRP EXTREN® Series 525 flat sheet of 6.35 mm nominal thickness, while the two inner plates of nominal thickness 9.53 mm are taken from the web of a standard Pultex series 1525 wide flange profile (Anon 2001). Both PFRP materials have a polyester based matrix. The geometry of the specimen has end distance = 40 mm, bolt pitch = 80 mm, and width = 116 mm. The separation between the ends of the two inner plates is 40 mm.

The UD rovings are aligned to the concentric tension load. In the steel test procedure both inner plates are allowed to slip. As Figure 1 shows only the right-sided inner plates had clearance holes, which allows for the relative slip. At the 'fixed' side the clearance for the two bolt-holes in the three plates is about 0.2 mm, while at the 'slip' side it also 0.2 mm in the two outer 6.35 mm plates and 2 to 4 mm for the inner 9.35 mm plate. In the tests by Mottram et al. (2004) two bolt sizes of M12 and M16 were used. Non-lubricated (as-received) grade 8.8 bolts were used with standard steel washers against the nut and bolt head. For M12 bolting the washers had thickness of 1.45 mm and outer and inner diameters of 24 and 13 mm, respectively. Washers for the M16 bolting had thickness of 1.85 mm and outer and inner diameters of 29 and 17 mm, respectively.

Figure 2(a) shows a test specimen in the Dartec 9500 testing machine. To set-up the specimen the fixed side had the two bolts torque to >70 kNmm (Nm), after ensuring that the two bolts were bearing against the inner and outer plates (no slippage could occur). For the slip side the inner plate was pushed against the two bolts in the opposite sense to the tensile loading. This ensured that the slip distance could be 2 mm or higher. Testing was carried out with the bolt torque on the slip side increased in 10 or 20 kNmm increments. To set the torque a hand-held torque meter (wrench) was used, giving a maximum torque range of 0–150 kNmm.

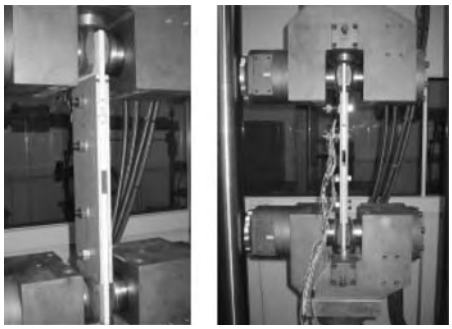

Figure 2. (a) Test specimen in Dartec grips (b) and with bolt load cells.

Figure 3. (a) Bolt tension load cell. (b) Set-up for calibration.

Tensile load was applied by way of a constant stroke rate of 0.01 mm/s. Testing continued until slip occurred (and static friction was overcome) and, later, there was additional load carried by bolt bearing on the slip side. During the slip stage of the test the frictional load remained constant, and the value of this dynamic load was the same as the load when static friction was overcome (Mottram et al. 2004). The test procedure was repeated three times at each torque increment.

It is well known that high strength bolts from the same lot yielded extreme values of bolt tension (±30%) from the mean tension desired by the pre-load applied (Kulak et al. 2001). The average variation is in general ±10%. This variance is caused mainly by the variability of the thread conditions, surface conditions under the nuts, lubrication, and other factors that cause energy dissipation without inducing tension in the steel bolt. Experience in field use of high strength bolts has confirmed the erratic nature of the torque versus tension relationship.

To establish what the bolt tension (and the clamping force) is, a simple bolt load cell was used. As Figure 3(a) shows it comprises a steel tube of length 25 mm and outer and inner diameters of 22 and 17 mm. The ends of the tube were machined smooth and parallel. Four 6 mm TML strain gauges (type FLA-6-120-11) were placed at 90° intervals around the tube to measure the axial strain. A load cell was calibrated,

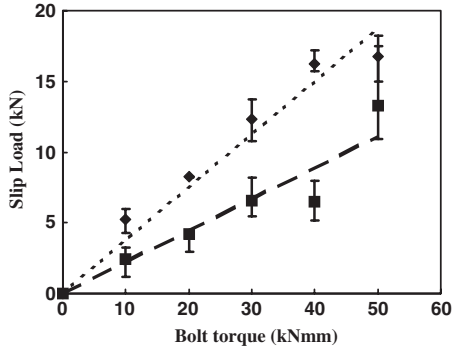

Figure 4. Previous load-slip test results (taken from Mottram et al. 2004), ♦ for M12 and ■ for M16 bolting.

as shown in Figure 3(b), by using the same bolts and torque method used in the coefficient of friction joint tests. Figure 2(b) shows a specimen with two load cells mounted and operational.

The results are preliminary as they are influenced by a number of error sources. Figure 4 shows the previous results from Mottram *et al*. 2004. The trendlines, with their intercept forced to go through 0,0, are the least square fits to the mean load slip values. The scatter bars give the ranges of the three measurements per torque value.

An approximate value to the static coefficient of friction can be determined from the test results. Mottram et al. (2004) established, using a calibrated bolt load cell, that the bolt tension (in kN) per bolt torque (in kNmm) is 0.44 and 0.40 kN per kNmm for M12 and M16 bolting, respectively. From the trendlines in Figure 4 the frictional force (per unit torque) when slipping commenced can be determined. Using the conventional relationship for the coefficient of friction these forces gave static values of 0.22 and 0.14 for the situation when the bolts were not lubricated.

The latter coefficient using the M16 bolting is considered unreliable. It can be seen from Figure 4 that these results give higher variation, and for a torque of 40 kNmm appear to be wrong. Because of a combination of the bolt length and the torque meter's dimensions the torque meter was attached to the bolt head to enable a bolt to be tightened. This is one reason why the M16 results in Figure 4 are unreliable.

In practice, bolting is always tightened by a torque wrench attached to the nut end (Kulak *et al*. 2004). This was the case for the M12 bolting test results in Figure 4. Figure 5 presents new results for the M16 bolting to the higher bolt torque of 110 kNmm. The torque was now correctly applied via the nut. Two new series are given, which are for the bolts without lubrication □ (as are the previous results in Figure 4) and fully lubricated with

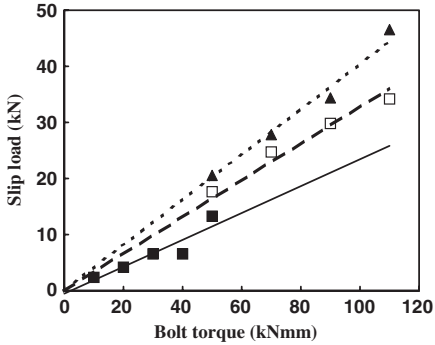

Figure 5. New load-slip test results for M16 bolting. □ is without lubrication and ▲ is with lubrication. ■ see Figure 4.

oil ▲. The trendlines are also given in the figure. It can be seen that the second series of tests without lubrication gives a trendline with a higher gradient to the previous data (in both Figures 4 and 5). As was expected this change in procedure demonstrates that by applying the torque to the nut a higher bolt tension is induced. It was observed that the load variation between the three repeated tests was similar to that found by Mottram et al. (2004). The coefficient increased from 0.14 to 0.21 on applying the torque to the nut.

The new results (▲) are those when the bolts were lubricated. This had the effect of reducing the load variation and increasing further the bolt load per unit torque. This finding can be directly associated to the variation of ±30% in bolt tension, which is known to exist when a constant bolt torque is used in steelwork erection (Kulak et al. 2001). Assuming the bolt tension per unit torque is the same as that when the bolt load cell (see Figures 2(a) and 3(a)) is used, the gradient of the short-dashed trendline in Figure 5 gives a coefficient of friction of 0.25. This M16 result is 14% higher than the coefficient determined when the M12 bolts were used without lubrication (see Figure 4 for the relationship between slip load and bolt torque).

A coefficient of 0.2 is typical of advanced polymeric composites on steel (Hyer, Hung & Cooper 1987) and between 0.2 to 0.3 for dry (non-lubricated) steel (Kulak et al. 2001). From the dry joint tests for PFRP on PFRP the static coefficient of friction is found to be similar that for dry steel on steel.

It is recommended, on page 717 of the EUROCOMP Design Code and Handbook (Clarke 1996), that the clamping force in Glass FRP bolted joints should not generate a bearing stress in excess of 68 N/mm^2. This limit on the average through-thickness compressive stress is to prevent the likelihood of material damage due to 'crushing'. A limit on the bolt tension is

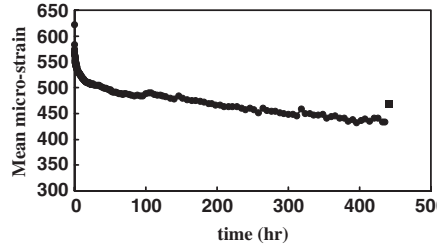

Figure 6. Mean axial strain with time.

therefore governed by the size of the bolt washer. For the standard sized washer used in the M16 tests the maximum bolt torque of 110 kNmm is estimated to subject the PFRP material to a compressive stress of 100 N/mm^2. After the test series had finished the bearing surfaces were visually inspected. The author did not observe crushing of the material, but did identify that there was a slight impression of the steel washer into the PFRP surfaces.

3 BOLT TENSION RELAXATION TEST

As PFRP material creeps (Scott & Zureick 1998) it can be reasoned that once a bolt has been torqued there will be relaxation of its tension force (and the clamping force) with time. A simple test procedure was used to determine the rate at which the compressive strain might be lost. A M16 bolt tightened to 70 kNmm was used to compress two 9.53 mm plates of PFRP material (the same material (Anon 2001) used in the friction load tests, discussed in Section 2). Between steel washers and between the bolt head and the PFRP a bolt load cell (see Figure 2(a)) was centrally placed to monitor the four axial strains at 90° spacings around the tube. An electronic datalogger was used to take compressive strain readings at increasing time increments over the test duration of 436 hrs (18 days).

Figure 6 shows the mean axial compressive strain with time from a single bolt relaxation test. The rate of decrease is very rapid in the first minutes and so the initial mean strain of $-620\,\mu\varepsilon$ is well below the maximum (estimated to be $-850\,\mu\varepsilon$) that will exist immediately the bolt was tightened to 70 kNmm.

It can be seen that the strain–time curve in Figure 6 has the expected exponential shape (Scott & Zureick 1998) and that, by smoothing out the ripples, the curve is smooth and continuous. Figure 7 shows how the laboratory room temperature varied during the same test duration. The ripples in the strain-time curve can be seen to correspond with the rapid changes in temperature. By plotting the mean strain and time on a log-log

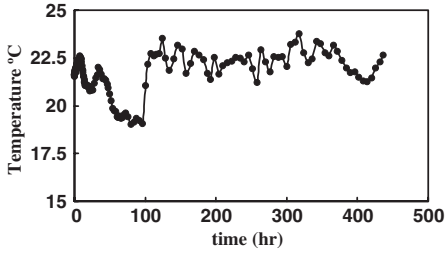

Figure 7. Laboratory temperature with time.

scale the curve is virtually a straight line. The equation for this relationship is

$$\text{mean compressive strain} = -17.6\ln(\text{hrs}) + 558 \quad (1)$$

with $R^2 = 0.964$.

Using Equ. (1) the loss of bolt tension is estimated to be 19% in 24 hrs, 25% in one week, 36%, 42%, and 44% in one, 10 and 20 years, respectively. Given that the loss in frictional force can be assumed to be directly proportional to the loss in bolt tension the effect of relaxation cannot be neglected when we are considering what is the maximum joint force that can be transferred by friction.

The single bolt relaxation test in Figure 6 was conducted with the compressed PFRP plates unstressed. The additional affect of long-term stressing and Poisson's ratio deformations might well increase the material creep and, therefore, the rate of compressive strain loss.

In Figure 6 there is a single data point (given by symbol ■), which was the new 'maximum' mean strain on re-tightening the M16 bolt to 70 kNmm, following the 436 hr bolt relaxation test. Axial compressive strain is only 30 $\mu\varepsilon$ above the last mean strain reading. This finding suggests that the strain loss cannot be recovered by maintaining the bolt torque at a specified level.

4 JOINT DESIGN RELYING ON FRICTION FOR LOAD TRANSFER

With high-strength friction grip bolts (Anon 1985, Kulak et al. 2001) slip in the connection is not permitted at the SLS or ULS, and for these joints the load is carried entirely by static frictional force (there is no bolt bearing). With the bolt not resisting any load in bearing, the maximum bolt tension is based on not exceeding 75% of the steel's proof stress. Grade 8.8 bolts have a proof stress of $>600\ \text{N/mm}^2$. Therefore, the maximum bolt tension is 71 kN for the M16 bolts (the tensile stress area is $157\ \text{mm}^2$).

Figure 8. Slip wear marks on the inner 9.53 mm thick PFRP plate.

To estimate the maximum tensile load, at which slip might be expected to occur, lets reduce by 30% the maximum bolt tension (to allow for the worse tightening condition due to the erratic nature of torque versus tension relationship), and assume the coefficient of friction is 0.25 (lubricated bolts). These conditions give for dry PFRP on PFRP a slip load per M16 bolt of about 12.5 kN; neglecting the effect of material creep. However, to achieve this static frictional load the average through-thickness compressive stress over the washer would need to be about 1.7 times higher than the recommended maximum of $68\ \text{N/mm}^2$ (Clarke 1996). Using $68\ \text{N/mm}^2$ as a limit on the bearing stress and $430\ \text{mm}^2$ as a the area for the standard washer, the maximum bolt tension is 28 kN (i.e. only 40% of the maximum 71 kN). The bolt slip load is now about 7 kN.

Using the limited physical test results in the literature it can be estimated that for M16 bolting, the ultimate load for a single bolted joint with concentric loading is above 40 kN. For this estimated bolt bearing failure load the PFRP thickness is 9.35 mm and the bolt torque is the finger-tight condition. If the safe working load is taken to be 30% of the ultimate load, it will be >12 kN. This is seen to be more than doubled the 5 kN load for slippage to occur when the M16 bolt has its recommended bolt torque and allowance is made for a 40% reduction in the bolt tension from creep relaxation.

After the testing was completed the specimen in Figure 2 was disassembled. Figure 8 shows the inner 9.53 mm plate from the slip. The lighter regions, appearing as longitudinal bands, show wear where the two mating surfaces made contact during the load-slip test. Such wear will only be realised after relative slip, under a higher enough clamping force, has occurred.

In practice such wear does not exist when a PFRP bolted frame structure is constructed of new beam and column PFRP sections, etc. The absence of a rough surface between the mating surfaces might mean the actual static coefficient of friction is <0.25. The

coefficient could also be reduced because of greasy surfaces or poor construction practice. To counteract such factors that might lower the coefficient of friction, it is practical to increase the bolt tension by increasing the size of the washer. Doubling its outer diameter, from 29 to 58 mm for M16 bolts, will ensure the bolt tension can be its maximum allowable while the clamping force will not create a mean bearing stress in excess of the limit of 68 N/mm^2 (Clarke 1996). Even with the best situation the maximum bolt load at slip, allowing for >10 years creep, will be 7.5 kN. This friction load is still below the working load of 12 kN for a single M16 bolted joint and 9.53 mm PFRP thickness when load transfer is by only bolt bearing.

Based on a preliminary evaluation it is clear that a joint design procedure cannot be developed which relies on a pre-defined bolt torque to ensure that the joint loading is transferred by friction without bolt bearing. It is therefore recommended that designers and fabricators continue to comply with current recommended design practice (Clarke 1996), in which bolt bearing is assumed to be the only mechanism for the load transfer in bolted plate-to-plate joints.

5 CONCLUSIONS

Using an experimental method devised for steel connections, and lubricating the M16 bolts, it is found that static coefficient of friction between PFRP flat sheets can be 0.25. By measuring the axial compressive strain over a period of 436 hrs (18 days) the bolt clamping force is shown to reduce as the PFRP material creeps. Re-tightening the bolt after the relaxation period does not recover the bolt strain to its initial value. The loss in pre-tension is estimated to be >40% in 10 years. It is shown, via a simple worked example, that it will be impractical to prepare a joint design procedure that relies on the entire joint force being transferred by friction. More research on PFRP bolt joints is required to confirm this finding and to refine existing design guidance, which assumes that pin-bearing is only mechanism for the load transfer.

ACKNOWLEDGEMENT

The author is grateful to technical support from Mr C. Banks.

REFERENCES

Anon. 1985. *European recommendations for bolted connections in structural steelwork*, Publication No. 38, 4th Ed., ECCS, CECM and EKS.

Anon. 1989. *EXTREN design manual*, Strongwell, Bristol, Va.

Anon. 1995. *Fiberline design manual for structural profiles in composite materials*, Fiberline Composites A/S, Kolding, Denmark.

Anon. 2001. *The new and improved Pultex pultrusion design manual of Pultrex standard and custom fiber reinforced polymer structural profiles*, Creative Pultrusions, Inc., Alum Bank, PA.

Clarke, J. L. (ed.), 1996. *Structural design of polymer composites – EUROCOMP Design code and handbook*, London: E. & F.N. Spon, London.

Cooper, C. & Turvey, G. J. 1995. Effects of joint geometry and bolt torque on the structural performance of single bolt tension joints in pultruded GRP sheet material, *Composites Structures*, 32(1–4): 217–226.

Hart-Smith, L. J. 1980. Mechanically fastened joints for advanced composites – Phenomenological considerations and simple analyses, *Proc. 4th Int Conf Fibrous Composites in Structural Design,* 1978. New York, Plenum. 543–574.

Hyer, M. W., Hung, C-L. & Cooper, D. E. 1987. Effects of pin elasticity, clearance and friction on the stresses in a pin-loaded orthotropic plate, *Journal of Composite Materials*, 21(3): 190–206.

Mottram, J. T. & Turvey, G. J. (eds.), 1998. *State-of-the-art review on design, testing, analysis and application of polymeric composite connections*, COST C1 Report, DG XII European Commission, Brussels & Luxembourg: Office for Official Publications of the European Communities.

Mottram, J. T. & Turvey, G. J. 2003. Physical test data for the appraisal of design procedures for bolted joints in Pultruded FRP structural shapes and systems, *Progress in Structural Engineering and Materials*, 5(4): 195–222.

Mottram, J. T., Lutz, C. & Dunscombe, G. C. 2004. Aspects on the behaviour of bolted joints for pultruded fibre reinforced polymer profiles, *Proc. 2nd Inter. Conf. on Advanced Polymer Composites for Structural Applications in Construction* (ACIC04). University of Surrey, UK, 20–22 April 2004. Cambridge: Woodhead Publishing Limited, 384–391.

Scott, D. W. & Zureick, A-H. 1998. Compression creep of a pultruded E-glass vinylester composite, *Composite Science and Technology*, 58(8): 1361–1369.

Turvey, G. J. 2000. Bolted connections in PFRP structures, *Progress in Structural Engineering and Materials*, 2(2): 146–156.

Kulak, G. L., Fisher J. W. & Struik, J. H. A. 2001. *Guide to design criteria for bolted and riveted joints*, 2nd Ed., Chicago: American Institute of Steel Construction.

FRP Composites in Civil Engineering – CICE 2004 – Seracino (ed)

GFRP for bridge structures in Russia

A.Ye. Ushakov
Professor, General Director, "ApATeCh", Russia

A.V. Pankov
Ph. D., Deputy General Director, "ApATeCh", Russia

Yu.G. Klenin
Director, "ApATeCh – Dubna", Russia

T.G. Sorina
Ph. D., Deputy Director, "ApATeCh – Dubna", Russia

ABSTRACT: The activity of ApATeCh Co. in introducing pultrusion technology to manufacture GFR profiles and apply them while constructing various infrastructure objects. Description of existing, designed and advanced bridge composite structures in Russia.

1 INTRODUCTION

Scientific & production enterprise "Applied Advanced Technology Company, ltd." (ApATeCh) was founded in 1991. Today it combines the functions of scientific center and mass production occupied with developing and manufacturing heavy-duty high-performance products for general and transport engineering using composite materials. Since the very beginning ApATeCh Co. implements the basic concept in its activity – it combines fundamental science with applied research and actual mass production.

The basic direction in ApATeCh Co. activity is transport engineering: railway, aircraft, automobile and urban transport as well as construction and city infrastructure. ApATeCh Co. presents in Russia one of very few examples of introducing technology and materials being developed and applied for high-performance aircraft structures into the railway and urban transport and construction.

For instance, in 1993–95 the enterprise in collaboration with Russian Railway Department has developed various options of composite fish-plates for insulating railway joints. Since that time ApATeCh Co. fulfils the orders of Russian Railway Department at the federal level that ensures the implementation of new insulating joint structures to enhance the reliability of railway tracks and safety of railway transportation. By the end of 2003 more than 400,000 insulating joints with ApATeCh fish-plates are operated throughout all the railways of Russian, Baltic countries and Kazakhstan. These fish-plates are mounted in the subways of Moscow, Saint-Petersburg, Novosibirsk, Nizhny Novgorod, Samara cities. Composite and metal-composite joints are operated in the railways of Belgium, France, Italy, China as well as in Paris metro. It should be stated that the introduction of such highly loaded fiberglass products like ApATeCh fish-plates is the meaningful event and it has no analogies in the world practice of applying composite materials for heavy- duty items.

2002 has resulted in the total of heavy-duty items delivered to different institutions of Russia and Baltic countries of over than 1500 tons in weight recalculation, that made ApATeCh Co. one of the largest Russian and world structural composite fabricators.

Thanks to activities in various productions fields ApATeCh Co. has accumulated significant experience in fabricating the products starting from single items up to mass production meeting the requirements of the customers. Much attention is paid to continuous in-service monitoring the fabricated products and to fulfilling the guarantees. ApATeCh Co. is the leader of home industry in developing and fabricating heavy-duty products using composite materials.

The achievements of ApATeCh Co. in the fields of science, production and service of heavy-duty products has got worldwide acknowledgement. Being the participant of many international conferences and shows ApATeCh Co. was awarded among more than 850 applicants at the JEC Composites Show 2002 in Paris, France, in the Transport nomination for the

introduction of composite fish-plates among the railways of Russian and Baltic countries.

ApATeCh Co. is recently occupied with new activity in Russia, i.e. the application of composite materials in the bridge structures.

Thus ApATeCh Co. is the enterprise being able to solve the problems in fabricating and production organization for heavy-duty and high-performance products that have the service parameters at the level of the best worldwide samples and event overpassing them.

2 PULTRUSION

Pultrusion today does not need any additional PR. Having been developed more than 40 years ago it is replacing other technological processes in the polymeric composites during the last two decades when the fabrication of long highly loaded profiles having constant geometric section is concerned. The success of this method results from the achievements in the field of processing structural fiber reinforcement: glass, carbon and basaltic fibers into various woven and non-woven structures having strict direction of reinforcement orientation in accordance with hypothetical field of applied stresses.

The continuous technology raises specific requirements to polymeric matrices. In this case it is the polymeric resin that affects the process productivity, the product integrity due to interaction with the fiber starting from the wetting stage till the final cure process. Finally, the cured resin and the resultant interface between the fiber and matrix define the following in-service reliability of pultruded item including the long-acting loads, climate, and chemical resistance in aggressive environments.

As far as applicability and efficiency of pultruded profiles are concerned as compared to metallic analogies, the bridge building and structural engineering are of most importance as they are recently developed fast in advance of the traditional applications of polymeric composites as well as electrical engineering and aerospace.

Though it is difficult to be uncommon both in generating new geometries, specific reinforcement structures and in developing new polymeric systems, there are some definite advantages of our own. The available pultrusion facility from Pultrex having 24 tons of loading enables to fabricate large-scale profiles being up to 0.35 m high and wall panels up to 1.4 m wide.

Figure 1 presents the profile configuration of the bridge deck from ApATeCh Co. A large number of FEM calculations in the 3-dimensional statement has been done to select the optimal cross section shape. The strength has been evaluated using Tsai-Wu criterion with regard for local stability effects. Table 1 compares principal parameters of the bridge deck made of ApATeCh profiles with the similar decks existing in the world.

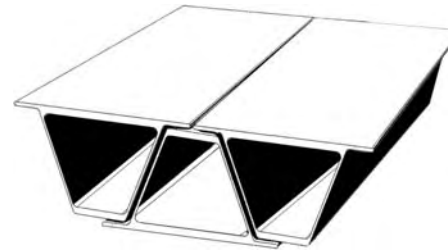

Figure 1. Composites bridge deck.

Table 1. Comparison of ApATeCh deck with similar decks.

Parameters	ApATeCh	Similar
Materials	glass fiber + vinylester	glass fiber + vinylester or polyester
Dead load, kN/m^2	1.1	0.9 ÷ 1.2
Deck thickness, mm	215	120 ÷ 225
Span in transversal direction, m	2	0.7 ÷ 2.7
Deflection to span length	1/1600	1/600 ÷ 1/2000
Surfacing	Polymer concrete	Polymer concrete, asphalt

The profiles consist of the well-known forms of fiber reinforcement, i.e. biaxial, multiaxial threat-piercing stripes and continuous mats, the layers of combined 3D material. Each layer of this material contains the crack stoppers whose space is calculated by the maximum crack resistance. No structure may avoid fasteners and the problem of enhancing the bearing strength in the items with stress concentrators can be solved by means of using combined material whose structure is shown in Figure 2.

The advantages of this developed combined reinforcement can be demonstrated by GFRP fish-plates for insulating railway joints where the material with the common reinforcement replaced by the combined one maintains both static and fatigue strength, and the rupture strength of the combined material containing stress concentrators is 1.5 times higher.

Our innovative concept of the hybrid material is implemented while using any continuous fibers: glass, carbon, basaltic, synthetic or their combinations. The crack stopper space is varied for each separate application depending on the crack resistance required parameters.

Alongside with epoxy systems introduced by us some modified vinylester resin is utilized for mass production monolithic bars 80 mm in diameter for

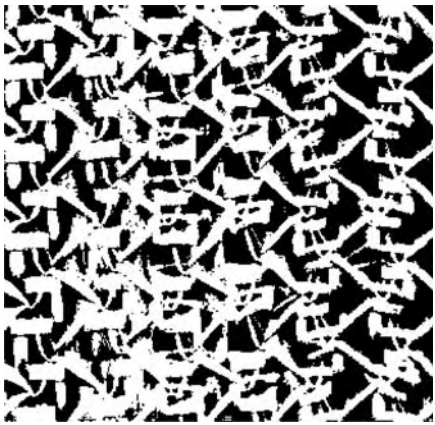

Figure 2. Combined material.

Table 2. Properties for the 80 mm Bar.

Property	E-glass	Basaltic
Density, g/cm^2	2,00–2,15	
Tensile strength (axial), MPa	1 200	1 200
Tensile modulus (axial), GPa	50	60
Comp. strength (axial), MPa	600	550
Impact strength, kJ/m^2	750	650
Water absorption, 24 h, 25°C, %	0,02	0,015
Electric strength, kV/mm	5,0	3,7
Resistance, O	10^{13}	10^{12}

electrical engineering whose properties are presented in Table 2 for heavy-duty products including bridge structures.

The feature of polymeric pultrusion system is that by means of modifying vinylester resin by bisphenol A and selecting the appropriate curing agent and catalyst some two-phase product has been generated. It means that the simultaneous curing of the selected resins can be considered as the binder synthesis being the system of interpenetrating networks. The initial polymers for this synthesis are selected so that the chemical interaction of different chains is excluded. In this case there is some topological isometry (only mechanical interweaving of chains with different chemical nature), and sequentially all the advantages of interpenetrating networks are implemented.

The taken efforts enabled to organize mass production of pultruded bridge profiles with the quality meeting the requirements to this type of products. The innovation originality is proved by the copyright. The performances of the profiles are listed in Table 3.

The continuity of pultrusion process has some negative effect on the structure of the polymer composite;

Table 3. Properties for the pultruded bridge profiles.

Property	ApATeCh (MPa)	Similar (MPa)
Tensile strength (axial)	450	200 ÷ 400
Tensile strength (transverse)	50	50 ÷ 60
Compression strength (axial)	400	200 ÷ 400
Compression strength (transverse)	144	70 ÷ 140
Shear	45	25 ÷ 30
Stiffness property	(GPa)	
Tensile modulus (axial)	26	20 ÷ 40
Tensile modulus (transverse)	13	5 ÷ 9
Shear modulus	3	3 ÷ 4
Density, g/cm^3	1.9	1.8 ÷ 1.9

first, due to impact cooling of the detail at the output of the hot die. Temperature gradient at the die cut may result in substantial residual stresses depending on the item thickness and flow rate. To optimize pultrusion modes a task was solved dealing with mathematical description of curing and temperature field distribution responsible for the final pultrusion performance. Some mathematical model has been developed describing heat conductivity changes resultant from phase transitions in the material while passing through the die, as well as some software simulating temperature field distribution and cure process for the details of different shapes.

3 SCIENTIFIC, METHODOLOGICAL AND CERTIFICATION BASE

Active introduction of composites in Russian aircraft industry has started since 1960ies. Theories and methods to predict composite properties are developed up to now when applied to primary structures and assemblies under static and dynamic loads with regard for the effects of both climatic factors (temperature difference, moisture, UV) and hostile environments (acids, alkali, salt solutions), erosion and contact wear. A comprehensive database has been accumulated in the actual composite behavior during their operation in different environments.

As most employees of the company are the experts from the aircraft industry, they accumulated their knowledge in the field and developed ApATeCh Design Manual Analysis for 2003–04 containing the methods to calculate static, fatigue and long-term strength, as well as buckling and joint strength.

To have the initial data for the analysis a great number of tests has been performed including climatic and long-term strength tests resulted in outlining the properties of pultruded profiles and their joints. The total number of tested specimens of various types and size was 1500.

The experience in designing actual bridge structures and accumulated methodological and scientific base enabled to get in 2003 two certificates of Russian State Building Department for applying GFRP profiles in the structural engineering, as well as for fabricating GFRP bridge structural profiles. These documents provide the certification base for wide pultruded profile application in the Russian construction engineering.

4 EXISTING OBJECTS

The first experience of ApATeCh Co. in the bridge construction may be considered the portable electrically insulating ladders made of GFRP pultruded profiles that are under mass production today, Figure 3. The ladders are fabricated 5 m and 7 m long, no corrosion is observed, they obtain better static and fatigue properties than those made of metal or wood, and at the same time they are easily portable for two workers. A 5-m ladder weighs 21 kg, and the 7-m one weighs 25 kg. The profile lifetime is over 70 years; in-service maintenance is affected by the life of the fasteners.

The full-scale fragment of the footway is manufactured shown in Figure 4. It is made of three type sizes of pultruded profiles with bolted joints. The steps are covered by the special non-slip surface. The footway has successfully passed the full cycle of static trials and it is now under in-service testing (for more than 3 years). The recent inspection of the structure has demonstrated no damages. The most important thing is that no traces are found of cleaning the structure to take away the ice and snow, though it was done using the standard set of tools common for Russia (i.e. crowbar and steel spade). Earlier the possibility of impact structural damage was one of the principal reasons for skeptical view on GFRP application in the bridge structures.

The developed compositions and technologies to lay up the appropriate cover are now used for bridge decks made of GFRP pultruded profiles to protect the profile material against the environment effects, to give to the deck non-slip and wear-resistant properties and to

Figure 4. Footway for the railway bridge.

Table 4. Wear-resistant, non-slip surface PB-M.

Property	
Flexural strength, MPa	>16
Wear resistance, g/cm^2	1.6
Frost resistance, cycles	200
Compression strength (axial)	50
Adhesive strength, MPa	>1

Figure 3. Electrically insulating ladder.

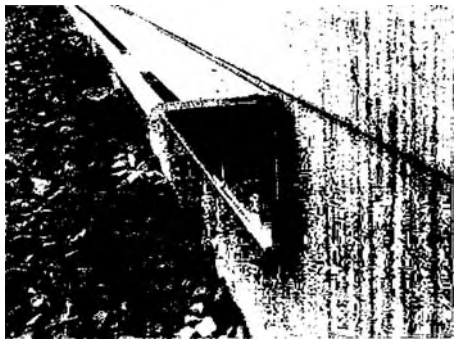

Figure 5. Electrically insulating profile.

ensure the safety of transport and foot-passers. Table 4 presents the principal parameters of wear-resistant, non-slip surface PB-M.

The technical decision is implemented in fabricating the elastic filling layer on non-ballast bridge deck for its reconstruction consisting of primary pultruded elements and elastic polyurethane layer. The latter dominates the total layer stiffness. The similar projects are under investigation to restore some other bridges in Russia.

Being damage safe this electrically insulating profile for railway platforms excludes the danger of passengers falling between the platform and the train. It is equipped by anti-sliding step, Figure 5.

For the needs of railway transport some trays for draining ground and waste waters from the rail ways and for electric cables have been developed and now mass produced. Composite trays have significant advantages as compared to common reinforced concrete ones as they are much lighter and may be hand laid up without any special equipment that results in large shortening of technological breaks in the traffic.

5 OBJECTS UNDER CONSTRUCTION AND DESIGN

5.1 *Bridge – barrage in Dubna*

"ApATeCh – Dubna" has awarded the first contest of innovative projects held to implement the development program for Dubna town as Russian scientific city assigned for 2002–06 within the theme: "Fabrication of bridge composite structures based on large-scale profiles made by pultrusion method". Within this project ApATeCh Co. has designed its own profile for automotive bridge decks, Figure 1. The deck was meant to restore the bridge – barrage across the Volga river for automotive transport in Dubna town. The task was to widen the carriage-way of the bridge, to organize two-way traffic and to enhance maximum tolerable load from 10 tons till 80 tons. The rest parameters of the old and new structures are given in Table 5. The bridge is situated on the only water stream of the region; hence the work should be conducted as fast as possible without complete traffic cancellation.

5.2 *Park bridge in Dubna*

ApATeCh Co. is building in the park region of Dubna town the pedestrian cable bridge of pultruded profiles, Figure 6. The bridge is 16 m long. The basic primary structural element of the bridge is a beam channel $400 \times 120 \times 18$, its feature parameters are listed in Table 3. As it is the first in Russia composite bridge it is planned to trial all the advanced ideas and systems. For instance, the bridge deck would include the heating system to eliminate the atmospheric precipitation (ice and water), as well as the system for the structural stress–strain state monitoring.

5.3 *Pedestrian bridge in Chertanovo*

The pedestrian bridge over the railway ditch ordered by Moscow railways is fabricated in collaboration with company Fiberline (Danish). The bridge rests on four supports and it has two spans 13.2 m each and one span 15 m long (Figure 7). The bridge is 3 m wide and it weighs about 10 tons, it is made of pultruded profiles with stainless steel arms. The bridge is assembled and ready to be mounted. The installation is planned for April–May 2004. The construction cost is equal to that of the bridge having steel primary structural elements. Six meters bridge fragment ready for full-scale static tests to determine the loads affecting the principal structural elements and to find the total structural deflection under the loads being 4 times as large as the

Table 5. Bridge properties before and after the reconstruction.

	At present	Plan
Max span length, m	21	21
Span number	9	9
Width, m	8,62	12
Load, ton	10	80
Material	Reinforced concrete	GFRP deck CFRP strengthening
Guide rail	Cast iron	GFRP pultruded profiles

Figure 6. Park bridge in Dubna.

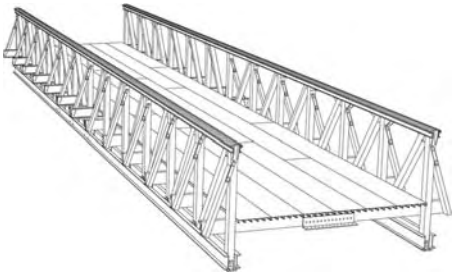

Figure 7. Pedestrian bridge in Chertanovo.

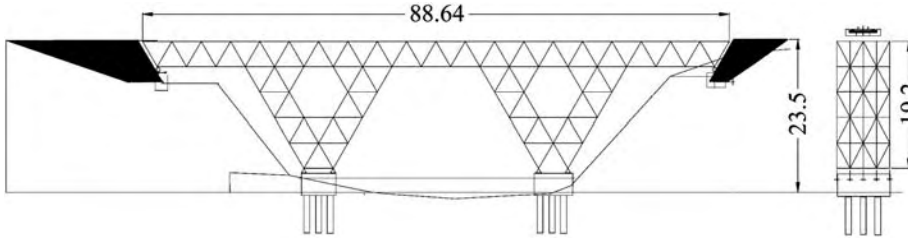

Figure 8. The drawing of railway bridge over the ditch.

design ones. The fatigue tests of main bridge units and assemblies have also been conducted.

5.4 *Railway bridge in Sakhalin island*

The potential of applying GFRP pultruded profiles for primary structural elements of the railway bridges has been evaluated. The study object was the bridge over the ditch 23.5 m deep and 84 m long. The analysis used finite element method for the bar 3D layout presented in Figure 8. The pin joint of elements has been considered, i.e. the bars act only in compression – tension. The bars had cross sections of 30 cm^2 to 150 cm^2. The bar modulus of elasticity in tension is 30 GPa, in shear 3 GPa.

Table 6 present the analytical results of finite element method application for the following options of the bridge girder:

- All the bars are A = 60 cm^2 in section. The areas of the lower half of V-shaped footings are 150 cm^2.
- Cross sections of the bars are selected based on stress distribution uniformity and deflection minimization. The bars having the area of 60 cm^2, 120 cm^2 and 150 cm^2 were used.
- Cross sections of the bars are selected based on stress distribution uniformity and weight minimization. The bars having the area of 30 cm^2, 60 cm^2, 70 cm^2, 100 cm^2 and 120 cm^2 were used.

In Table 6: σ_{max}, σ_{min} and δ_{max} – maximum and minimum values of stresses in the bars and maximum deflection of the upper bridge surface under the maximum static load, δ/L and $(\delta/L)_c$ – relative deflection of the whole bridge and the central span. Thus for all analyzed types the bar stresses and total structure deflections do not exceed tolerable values (tolerable stresses in tension 85 MPa and in compression −70 MPa, deflection limitation is 1/800 of the span length). Table 7 presents safety factors for the bars under different types of loading the girder having optimized weight (type 3 in Table 6).

Table 8 lists the bars utilized for most optimum third bridge type. It is clear in it that 91% of bars weigh less than 60 kg and maximum weight of one element is 101 kg that is the structure may be assembled using minimum additional equipment.

Table 6. Analytical results for three bridges types.

#	σ_{max}, MPa	σ_{min}, MPa	δ_{max}, mm	δ/L	$(\delta/L)_c$	Weight, tons
1	58,2	−63,2	55,5	1/3370	1/1445	90
2	29,2	−36,7	38,5	1/4870	1/2375	110
3	60,4	−60,5	59,5	1/3140	1/1564	68

Table 7. Safety factors.

	Safety factors for bars	
Loading type	Tensile	Compressive
Static strength	3.31	2.64
Fatigue strength	1.81	1.44
Creep	2.32	1.85
Buckling		1.54
Deflection	2	

Table 8. List of bar principal parameters.

No	Cross section, (cm^2)	Length, (m)	Number	Weight, (kg) of one	Weight, (kg) of all
1	30	2	212	11.4	2 420
2	60	2	56	22.8	1 300
3	60	4.86	352	55.4	19 500
4	70	4.43	595	58.9	36 100
5	100	4.43	116	84.2	9 780
6	120	4.43	4	101	404

Table 9 compares the price indexes for the following types of the bridge span:

- Typical through bridge. Material: painted steel.
- Girder of deck bridge (Figure 8). Material: galvanized steel.
- Girder of deck bridge (Figure 8). Material: primary structural elements – GFRP pultruded profiles;

Table 9. Cost comparison of different railway bridge types.

#	Material	Weight, tons	Price, (thousand ruble/ton)	Total cost (million rubles)
1	Steel + paint	660	42	27.7
2	Galvanized steel	220	60	13.2
3	Composite profiles	70	170	13.2
	Galvanized steel	22	60	

profile fasteners (brackets, fittings) – galvanized steel. All the fasteners of the load-bearing composite profile element are done using standard details (brackets, fittings) and galvanized steel bolts. It would allow decreasing the quantity of analytical, design and experimental activity required to provide and prove their strength and reliability.

The estimates are done only for structure fabrication. At the other stages of the structure life the costs for the railway composite bridge would be significantly lower than for the structure made of the traditional materials.

6 DESTINATION OF EXPERIMENTAL OBJECTS

There are strict standards in Russia like in most countries dealing with designing, calculating, fabricating and erecting heavy-duty constructions including the bridges and other structures. It is difficult and time-consuming to change these standards in order to add quite new material. The new standards should be based on the structures and materials manufacturing inside the country, i.e. the existing world experience in composite application for bridge structures cannot be directly used. Hence the important field of ApATeCh Co. activity at the contemporary stage is the participation in various bridge projects at different stages. Some examples follow:

- Railway bridge (Sakhalin Island) – analysis at the very early stage of the project selection.
- Modifying highway bridge (Dubna) – preparation of technical and economic assessment.
- Pedestrian bridge (Dubna) – experimental structure in the recreation area under low loading. It is designed to develop design & test methods, technology of fabricating the profiles and the complete structure, heating & monitoring systems etc.
- Pedestrian bridge (Chertanovo) – replacement of the actual bridge.

The participation in these projects often has no direct profits for the enterprise but it is useful in terms of:

- accumulating the experience of designing, fabricating and constructing being the basis for development of the enterprise certification base to fabricate and operate pultruded structures including: performance specifications for profiles, user's manual for designers, analysts, erectors and operators;
- certification base of the enterprise is used to form all-Russian certification base dealing with composite applications in structural engineering;
- it gives way for pictorial demonstration the feasibility of fabricating composite objects and their advantages, as even one actual object arises more confidence to the material than numerous reports with pictures and charts;
- direct contacts with design bureaus and construction plants while launching definite projects result in expand and share of knowledge among all the process participants. The construction engineers in this case start to realize the performance and advantage of new materials more thoroughly. Hence even the project resulting in no actual object gives rise to several new projects initiated by the former skeptics of composite applications in the structural engineering.

7 CONCLUSIONS

1. Modern composite structural material due to its unique property is highly competitive as compared to traditional construction materials like steel, aluminum, concrete, wood. Construction composites in some indexes exceed traditional materials in 2 to 10 times.
2. Cost of composite bridge structures does not often exceed the cost of similar objects made of traditional materials.
3. Russia has all necessary conditions for mass production of construction composites by pultrusion method both scientific, methodological and manufacturing bases to fabricate composite bridge structures have been created.

FRP Composites in Civil Engineering – CICE 2004 – Seracino (ed)

Web-flange junctions of pultruded GRP WF profiles: notched flange shear strengths

G.J. Turvey & Y. Zhang
Lancaster University, Lancaster, Lancashire, UK

ABSTRACT: A pultruded Glass Reinforced Plastic (GRP) Wide Flange (WF) profile was cut transversely into short lengths to provide test specimens to determine the longitudinal shear strengths of the web-flange junctions of the profile. In order to promote the formation of well defined shear failure planes within the junctions, pairs of part through-thickness notches were introduced into the flanges of the test specimens. The underlying principles and details are presented of a novel rig, which was used to carry out shear failure tests on the web-flange junction specimens. Examples of the load versus displacement response and the failure modes of a web-flange junction are also presented. It is shown that the shear strengths of the notched web-flange junction specimens are about 50% of those determined from previous tests on unnotched specimens and only about one-seventh of the shear strength of specimens cut out of the web and flanges of the profile.

1 INTRODUCTION

Structural grade pultruded GRP profiles, eg. I, H, channel, angle sections and flat plate, have been used in secondary structures for at least two decades. In more recent times, as the size of *off-the-shelf* profiles has increased, they have begun to be used in primary load-bearing structures such as building frames and bridge decks. The pressure to use pultruded profiles stems from their high specific strength, high specific stiffness, low self-weight, high corrosion resistance, low thermal conductivity, transparency to electromagnetic waves etc. Despite their many advantages, they do suffer from one significant disadvantage, viz. that the major elastic modulus of the material is relatively low, being almost an order of magnitude lower than that of steel. For this reason, limiting deflections and instability modes of failure are relatively more important than strength dominated failure modes. Consequently, there has been much interest amongst the research community in developing knowledge and understanding of the deflection and instability response of structural grade pultruded GRP beams and columns. Most of this research has been directed towards the development of formulae for predicting the onset of local and global buckling of columns, as, for example, in (Zureick & Shih 1998, Barbero & DeVivo 1999, Brown et al. 1998, Hashem & Yuan 2000) and lateral buckling of beams, as, for example, in (Mottram 1992, Turvey 1996). Little effort has been directed towards conducting research to establish the collapse behaviour of pultruded GRP beams and columns, most probably because it is regarded as being of lesser importance than the prediction of the buckling load itself. Whilst this may be true, it is, nevertheless, important to know how much the load may be increased beyond the buckling load to produce collapse and to understand the mode of collapse.

Recently, Bank & Yin (1999) took the first steps towards modelling the collapse behaviour of a pultruded GRP WF (Wide Flange) beam, which had been tested to failure in four-point bending. The test revealed that failure was triggered by local buckling of the beam's compression flange, which led to tearing of the flange from the web and collapse of the beam. Other evidence of this type of buckling-triggered failure mode has been observed in failure tests on axially loaded short pultruded GRP columns (Stubbs 1998, Yates 1999).

In their finite element (FE) analysis model, which was used to simulate the beam's collapse behaviour, Bank & Yin (1999) used strengths obtained from coupon tests in their failure criteria. The weakness of this approach is that coupon strengths over-estimate the strengths of the web-flange junction, where tearing separation occurs. This is because web-flange junctions have roving-rich cores and, moreover, the roving and Continuous Filament Mat (CFM) layers in the junction region are curved and sometimes wrinkled. Thus, it is vitally important to obtain true web-flange junction strengths if FE analyses are to yield more accurate predictions of the collapse loads and failure modes of pultruded GRP beams and columns.

In 2001 the authors began to address the issue of how to determine realistic web-flange junction strengths of pultruded GRP profiles. They concluded

that the simplest approach was to carry out failure tests on the web-flange junctions under a variety of simple load configurations. In the first instance, they focused their attention on the tensile or tearing strength of the web-flange junction. Recently, they reported the results of 43 tensile strength tests carried out on two sizes of pultruded GRP WF-section (Turvey & Zhang 2004a) and demonstrated that the values obtained were much lower than the tensile strengths of coupons cut transversely from either the web or flanges of the profiles.

Prior to separation of the flange from the web at the instant of collapse, the web-flange junction is subjected to a complex stress state. Therefore, it is not sufficient just to determine the tensile strength of the junction. Junction strengths subject to shear and bending stresses are also required. Recently, the authors built a new type of test rig for conducting shear strength tests on web-flange junctions (Turvey & Zhang 2004b). The rig was used to carry out 38 shear failure tests on the web-flange junctions of two sizes of WF section. Again, the test results showed that the shear strength of the junction is less than that obtained from asymmetric four-point bending tests on Iosipescu coupons cut from the web and flanges of the profiles. However, it was concluded that the test results were not entirely satisfactory, because visual examination of the failed specimens revealed that, in many instances, there was not a clearly defined shear failure plane. Therefore, it was decided to modify the specimens in order to try to promote a distinct plane of shear failure along the web-flange junction.

In this paper details are presented of the preparation of modified web-flange junction specimens, which were cut out of 203 × 203 × 9.5 mm (nominal dimensions) EXTREN® 500 Series pultruded GRP WF profile. The new test rig is also described together with its underlying theoretical background. The main features of the shear load versus shear deflection response of a typical test on a web-flange junction specimen are also explained. The shear strengths obtained from seventeen notched test specimens are compared with those of the unnotched strengths and with the shear strengths obtained from asymmetric bending tests on Iosipescu specimens. It is concluded that the notched specimens not only have lower shear strengths, but they also fail along more distinct and repeatable shear planes and, therefore, provide more realistic, i.e. lower bound, values of the shear strengths of the web-flange junctions of WF profiles.

2 MODIFIED TEST SPECIMENS

A band saw was used to cut transversely a single length of 203 × 203 × 9.5 mm WF profile into short lengths to provide a series of shear test specimens. Three specimen lengths, 25, 40 and 60 mm, were chosen.

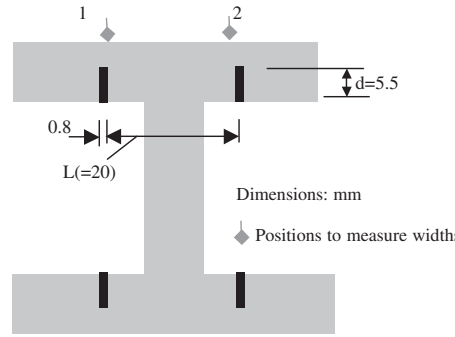

Figure 1. Sketch of notched web-flange junction test specimen.

A total of eleven specimens were cut out of the profile in the following order 25, 40, 60, 25, 40, ... mm. A fine to medium feed rate was used in order to minimise damage to the cut edges of the specimens. After all of the specimens has been cut from the WF profile, two notches, 0.8 mm wide, 5.5 mm deep and 20 mm apart were cut longitudinally and normal to the inside faces of the two flanges, as shown in Figure 1. The function of the notches was to promote a more clearly defined shear failure plane than was achieved in the tests on the unmodified shear specimens reported in (Turvey & Zhang 2004b).

Two of the eleven specimens were used to carry out preliminary tests. The purpose of these tests was to check that the notches did indeed promote more clearly defined shear failure planes and to check that the travel and sensitivity of the displacement transducer were appropriate. The remaining nine specimens were used to provide test data.

The nine WF profile specimens were sub-divided into three groups according to their lengths. Each group provided three top (T) and three bottom (B) web-flange junction test specimens. The following labelling scheme was used to identify each test specimen. The specimen label had the general form, I8-SJN1.m-Tn, where I8 denotes the profile size (8″ WF profile), SJN1 denotes notched junction shear test series 1, m denotes the specimen group number, T or B denotes the top or bottom junction and n denotes the specimen number.

3 THEORETICAL BACKGROUND TO SHEAR TESTS ON WEB-FLANGE JUNCTIONS

The method of testing the web-flange junction of a pultruded GRP WF profile is akin to loading a cantilever beam with a pair of opposing point loads applied close to the support. Figure 2(a) shows a beam loaded by opposing forces, F1 and F2, applied at A and

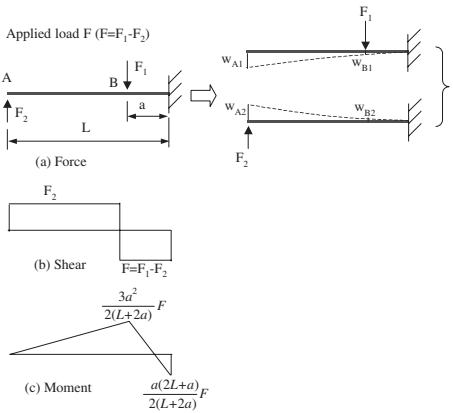

Figure 2. Propped cantilever model for determining the applied shear force in the web-flange junction test rig.

B, which are at distances a and L respectively from the rigid support. Also shown in Figure 2(a) are the deflections produced by each of the forces applied separately to the beam. The shear force and bending moment distributions are shown in Figures 2(b) and 2(c) respectively.

It is assumed that the rigidity of the test rig is much larger than that of the test specimen. Moreover, it is also assumed that during testing the deflections of the specimen at A and B are equal. Using classical beam theory it is a relatively simple matter to show that the shear force F at the web-flange junction is given as,

$$F = F_1 - F_2 \tag{1}$$

where

$$F_1 = \frac{2L^2 + 2La - a^2}{2\left(L^2 + La - 2a^2\right)}F \tag{2}$$

and

$$F_2 = \frac{3a^2}{2\left(L^2 + La - 2a^2\right)}F \tag{3}$$

By choosing the ratio of a to L carefully, the effect of the parasitic bending moment at the rigid support may be reduced. In (Turvey & Zhang 2004b), the effect of this bending moment on the shear strengths of the unnotched specimens was analysed and shown to be quite small.

4 TEST RIG DETAILS AND TEST PROCEDURE

A view of web-flange junction under test in shear is shown in Figure 3(a). More detailed sketches of the

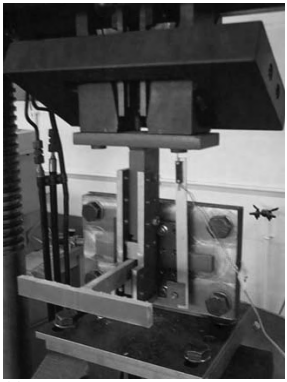

(a)

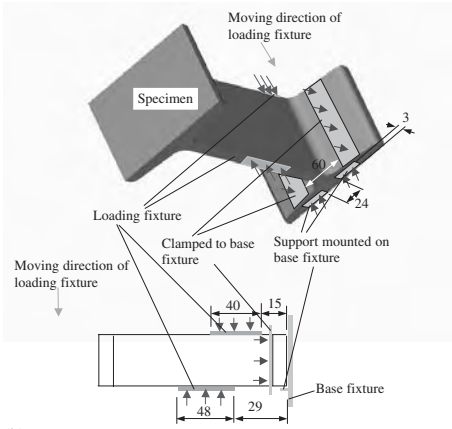

(b)

Figure 3. Web-flange junction test rig: (a) photograph of a specimen under test and (b) two sketches showing the load and support arrangements for a specimen and the principal dimensions.

test arrangement, including the main dimensions are shown in Figure 3(b).

The specimen set up procedure was as follows. The flange of the web-flange junction specimen was clamped by two steel bars to the vertical face of an L-shaped steel base. The base was bolted to the lower platen of the universal testing machine. Two small steel blocks, also fixed to the vertical face of the L-shaped plate, provided bearing support to the underside of the flange of the specimen. A T-shaped steel loading fixture was bolted to the upper platen of the testing machine. The web of the specimen passed through the loading fixture, as shown in Figure 3(a). A 40 mm long steel loading shoe was placed between the side plates

of the loading fixture and in contact with the upper surface of the web. A semi-circular steel rod between the loading shoe and the loading rod distributed the load uniformly into the upper surface of the web of the test specimen. Another steel block of length 48 mm was placed between the loading fixture and the underside of the web. This block was adjustable vertically in the loading fixture. Therefore when the upper platen moved downwards and the loading head came into contact with the semicircular bar and upper loading shoe, the lower steel block was adjusted to bring it into contact with the underside of the web of the test specimen. By so doing, rotation of the web was prevented. Loading of the specimen was then started until the web-flange junction failed in shear.

The vertical displacement of the upper platen of the test machine was monitored by means of an electronic displacement transducer which was mounted on the vertical face of the L-shaped base and had its tip in contact with the upper platen of the testing machine. The displacement transducer had a 10 mm travel. During the testing of each specimen the load and displacement data were recorded automatically at one-second intervals using an electronic data acquisition system.

5 TEST RESULTS AND DISCUSSION

Each of the eighteen web-flange junction specimens was set up in the test rig, as previously described, and loaded in shear until it failed. The loading rate used in the tests was approximately 0.87 kN/min, which corresponded to a displacement rate of about 0.1 mm/min.

A typical shear force versus displacement curve for specimen I8-SJN1.2-T2 is shown in Figure 4. The force–displacement response exhibits three stages, as was observed in the previous tests on unnotched web-flange junction specimens, which were reported in (Turvey & Zhang 2004b). In stage 1 the response was reasonably linear up to the maximum load of about 9 kN, which corresponded to a displacement of 1 mm. It was observed that as the load reached it peak value failure initiated in the web-flange junction. There was a small drop in load at the beginning of stage 2. This was followed by a gradual decrease in load as the displacement increased. During this stage, the crack in the web-flange junction gradually extended. When the displacement reached about 2.25 mm, there was a sudden loss of load, which signalled the start of stage 3 and the onset of total collapse as the web sheared off the flange.

Generally, failure initiated in the form of a delamination crack adjacent to the roving rich core at the centre of the web-flange junction. As the loading increased the crack extended around the core and along each flange until it intersected the notch and the web

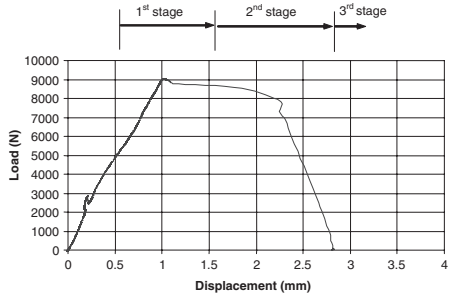

Figure 4. Typical load versus displacement response of a web-flange junction specimen tested in shear.

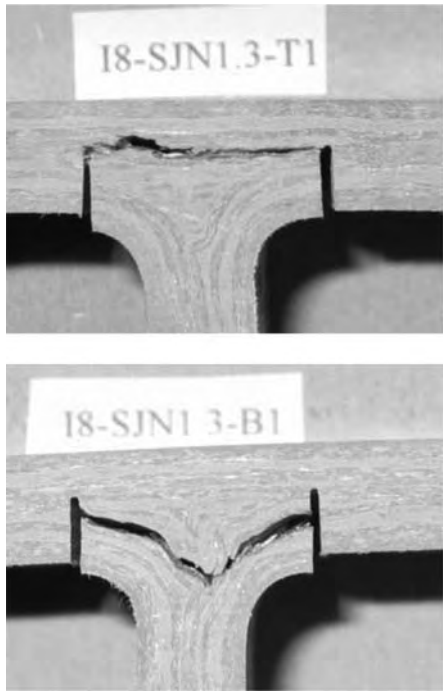

Figure 5. Shear failure modes of the top and bottom web-flange junctions of 203 × 203 × 9.5 mm pultruded GRP WF profiles.

sheared off. The failure modes of the top (T) and bottom (B) web-flange junctions of two specimens are shown in Figure 5.

The results of seventeen of the eighteen tests (one was invalid) on the web-flange junction specimens are given in Table 1.

Table 1. Results of shear tests on web-flange junction specimens cut from a 203 × 203 × 9.5 mm pultruded GRP WF profile.

Specimen	Dimensions of junction b (mm)	L (mm)	Failure load F_c (kN)	Failure stress τ_c (MPa)
I8-SJN1.1-T2	28.15	20.67	4.98	8.56
I8-SJN1.1-T3	26.51	20.17	5.68	10.62
I8-SJN1.1-B1	26.47	20.45	5.01	9.26
I8-SJN1.1-B2	26.68	20.17	5.01	9.31
I8-SJN1.1-B3	26.66	20.32	5.32	9.82
I8-SJN1.2-T1	39.54	20.21	8.90	11.14
I8-SJN1.2-T2	41.00	20.65	9.03	10.67
I8-SJN1.2-T3	42.23	20.39	10.21	11.86
I8-SJN1.2-B1	39.64	20.54	11.33	13.92
I8-SJN1.2-B2	41.46	20.46	10.71	12.63
I8-SJN1.2-B3	42.15	20.33	11.85	13.83
I8-SJN1.3-T1	59.97	20.02	15.18	12.64
I8-SJN1.3-T2	60.43	20.34	13.15	10.70
I8-SJN1.3-T3	60.36	20.06	10.54	8.71
I8-SJN1.3-B1	59.73	20.28	12.44	10.27
I8-SJN1.3-B2	60.46	20.25	16.07	13.13
I8-SJN1.3-B3	60.16	20.29	10.26	8.41

Table 2. Comparison of shear failure loads etc for unnotched and notched web-flange junction specimens and Iosipescu specimens.

Specimens Series	Nr	b (mm)	L (mm)	F_c (kN)	F_c/b (N/mm)	$\tau_c(=F_c/bL)$ (MPa)
I8-SJN1.1	5	26.89	20.36	5.20	193	9.51
I8-SJN1.2	6	41.00	20.43	10.34	252	12.34
I8-SJN1.3	6	60.18	20.21	12.94	215	10.64
I8-SJ1.1	6	24.83		9.62	387	
I8-SJ1.2	6	39.75		17.49	440	
I8-SJ1.3	6	59.89		26.05	435	
I8-S1	11					77.90

The average values of the shear failure loads etc obtained from the three series of web-flange junction tests on notched specimens (see Table 1) are compared with corresponding results obtained on unnotched specimens (Turvey & Zhang 2004b), denoted as I8-SJ1.n, and on Iosipescu specimens, denoted as I8-S1, in Table 2.

It is evident from Table 2 that the average of the average shear strength strengths of the three series of tests on notched web-flange junction specimens is approximately 11 MPa, which is only one-seventh of the value of the strength of the material remote from the web-flange junction, as determined from the tests on Iosipescu specimens.

Comparing the average of the average values of the shear strength per unit length obtained from the tests on the unnotched and notched specimens, it is clear that the effect of the notches reduces the shear strength per unit length by about 50%.

It is felt that the average notched shear strength is a more realistic measure of the shear strength of the web-flange junction, because it is associated with a more clearly defined failure plane than was evident from the tests on the unnotched specimens. Moreover, in the latter specimens, there was generally evidence of flexural-tension cracking in one or both surfaces of the curved transitions between the web and the flange.

A further and final point in favour of basing the shear strength per unit length of web-flange junctions on the average notched shear strength is that it would be a lower bound value, and, therefore, conservative for use in design analysis.

6 CONCLUDING REMARKS

Details have been presented of a series of tests on seventeen notched web-flange junction specimens cut out of a pultruded GRP WF profile. The specimens exhibited more clearly defined shear planes than a series of unnotched web-flange junction specimens tested earlier in the same test rig.

The notched specimens were tested at three nominal lengths, 25, 40 and 60 mm. The highest average strengths were obtained with the 40 mm long specimens, which were 30% and 16% higher respectively than the strengths of the 25 mm and 60 mm long specimens. It is unclear as to whether or not this observation is significant. The more so, as the highest specimen strength was 24% greater than the lowest strength for the 25 mm long specimens and the corresponding figures for the 40 mm and 60 mm long specimens were 30% and 56% respectively. Furthermore, as is evident from Figure 5 and similar images taken of the other test specimens, there is considerable divergence between the idealised and the real fibre architecture in the web-flange junctions and that is likely to account for the variability in the measured shear strengths.

The shear strengths of the web-flange junctions of the notched specimens were shown to be only about one-seventh of the shear strengths of the web or flange material, as measured in Iosipescu tests. Likewise, it was shown that the shear strength per unit length of the notched specimens was about 50% of that of the unnotched specimens.

Finally, it was suggested that the notched shear strengths, may be useful in design, since they are likely to be conservative.

ACKNOWLEDGEMENTS

The authors wish to record their appreciation to the United Kingdom's Engineering and Physical Sciences

Research Council (EPSRC) for funding their work through the award of a research grant (GR/R28386/01) under the auspicies of EPSRC's managed research programme on *Structural Integrity*.

REFERENCES

Bank, L.C. & Yin, J. 1999. Analysis of progressive failure of the web-flange junction in post-buckled I-beams. *Journal of Composites for Construction* 3(4): 177–184.

Barbero, E.J. & DeVivo, L. 1999. Beam-column design equations for wide-flange pultruded structural shapes. *Journal of Composites for Construction* 3(4): 185–191.

Brown, N.D., Mottram, J.T. & Anderson, D. 1998. The behaviour of columns for the design of pultruded frames: tests on isolated columns. In H. Saadatmanesh & M.R. Ehsani (eds), *Fiber Composites in Infrastructure; Proc. 2nd intern. conf., Tucson, 5–7 January 1998*. Tucson, University of Arizona.

Hashem, Z.A. & Yuan, R.L. 2000. Experimental and analytical investigations on short GFRP composite compression members. *Composites Part B: Engineering* 31(6 & 7): 611–618.

Mottram, J.T. 1992. Lateral-torsional buckling of thin-walled composite I-beams by the finite difference method. *Composites Engineering* 2(2): 94–104.

Stubbs, D. 1998. Buckling tests on pultruded GRP short columns in axial compression. *Final Year Project Report*, Engineering Department, Lancaster University.

Turvey, G.J. 1996. Lateral buckling tests on rectangular cross-section pultruded GRP cantilever beams. *Composites Part B: Engineering* 27(1): 35–42.

Turvey, G.J. & Zhang, Y. 2004a. Tearing failure of web-flange junctions in pultruded GRP profiles. *Composites Part A: Applied Science and Manufacturng*. In press.

Turvey, G.J. & Zhang, Y. 2004b. Shear failure strength of web-flange junctions in pultruded GRP profiles. In L. Hollaway, M. Chryssanthopoulos & S.S.J. Moy (eds), *Advanced Polymer Composites for Structural Applications in Construction – ACIC 2004; Proc. 2nd intern. conf., Guildford, 20–22 April 2004*. Cambridge, Woodhead Publishing Ltd.

Yates, R. 1999. Buckling tests on pultruded HF short columns in axial compression. *Final Year Project Report*, Engineering Department, Lancaster University.

Zureick, A-H. & Shih, B. 1998. Local buckling of fiber-reinforced polymeric structural members under linearly-varying edge loading – part 1, theoretical formulation. *Composite Structures* 41(1): 79–86.

FRP Composites in Civil Engineering – CICE 2004 – Seracino (ed)
© 2005 Taylor & Francis Group, London, ISBN 90 5809 638 6

Development and analysis of the large-span FRP woven web structure

P. Feng, L.P. Ye & R. Bao
Department of Civil Engineering, Tsinghua University, Beijing, China

J.G. Teng
Department of Civil and Structural Engineering, The Hong Kong Polytechnic University, Hong Kong, China

ABSTRACT: An innovative large-span structural system, namely the FRP woven web structure (FRPWWS), is introduced in this paper. In an FRPWWS, the high-strength FRP strips are "woven" like bamboo strips in a Chinese bamboo mat to form a plane web. The outer edge of the web is anchored on an outer ring beam, and an inner ring beam is provided to anchor the FRP strips at the center of the web. The stiffness of the web to resist various loads is derived from the initial prestressing during the "weaving" stage and the additional tensioning as a result of the out-of-plane movement of the inner ring beam. As a result of the high strength-to-weight ratio of FRP, this new structural form offers an attractive option for the construction of spatial structures with spans longer than are possible with conventional structural materials. In this paper, the basic layout and construction procedure for a simple FRPWWS is first presented. Three basic weaving patterns are next explained. Several variations of the basic structural system are also proposed. A simple mechanical model is presented for the deformation of individual FRP strips. Results from a finite element analysis of an example structure are also given. The results of these analyses confirm the feasibility of the FRPWWS.

1 INTRODUCTION

FRP is a new kind of structural material, whose use in civil engineering has been actively explored in recent years. Due to its favorable properties like corrosion resistance, high strength, low weight, good fatigue performance, and low maintenance cost, it is considered to be an ideal material for constructing long-span structures in the new century. However, its mechanical properties are distinctly different from those of traditional structural materials in some aspects, such as its anisotropy. Due to the unique properties of FRP, it is necessary to explore new forms of large-span structures for its efficient use and for achieving spans larger than are possible with traditional materials. For example, Maeda et al. (2002) have conceived a 5000 meter-span suspension bridge using FRP.

The FRP woven web structure, a new large-span structural system, is presented in this paper. This new system represents an attempt aimed at the efficient utilization of the unique characteristics of FRP in a large-span roof. In an FRPWWS, the high-strength FRP strips are woven like bamboo strips in a Chinese bamboo mat to form a plane web. The outer edge of the web is anchored on an outer ring beam, and an inner ring beam is provided to anchor the FRP strips at the center of the web. A small-scale model of a simple FRPWWS is shown in Figure 1. The FRP strips are initially prestressed to a limited extent to keep them straight during "weaving". Then, the FRP web is tensioned by a displacement of the inner ring beam in the out-of-plane direction, which is effected either by a set of prestressed tendons or by suspending a heavy mass from the inner ring beam. As a result, a tensioned FRP web, whose geometric stiffness is able to resist a variety of loads, forms a large-span roof system with the two rings.

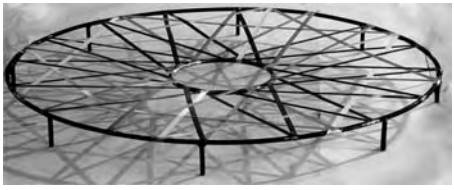

Figure 1. FRPWWS model.

The FRPWWS resembles the cable net structure and the cable-membrane structure: their members are flexible; and the geometric stiffness resulting from tension is utilized to resist loads. However, the FRPWWS has its unique advantages: (1) the FRP strips are ideal for super large-span structures due to their low self-weight and their superior material properties

in the lengthwise direction, which are efficiently utilized, while the weakness of inferior properties in the transverse directions is not exposed; (2) significant damping can be expected to arise from friction at joints between FRP strips, which can enhance the resistance of the structure to wind and earthquake loads; (3) the regular weaving pattern leads to an aesthetically pleasing surface; and (4) the corrosion resistance of FRP and the ease of installation because of its lightweight translate into low maintenance costs.

In this paper, the basic layout and construction procedure for a simple FRPWWS system is presented in detail. The weaving patterns in plane are summarized into three types. Some spatial FRPWWS forms for practical applications are also proposed. A simple mechanical model for individual FRP strips in the web is presented. Results from the finite element analysis of a simple FRPWWS are also described.

2 LAYOUT OF A SIMPLE FRPWWS

A simple FRP woven web structure is composed of a FRP woven web, an outer ring beam and an inner ring beam for anchorage, and an additional weight or a set of prestressed tendons, as shown in Figure 1.

The web is woven with FRP strips, and CFRP strips or other high-performance hybrid FRP strips are suggested. CFRP strips, which have been widely used to strengthen concrete structures in recent years, are manufactured by pultrusion in general, with a fiber volume ratio of about 65%. The properties of two representative products made in China and Switzerland respectively are listed in Table 1.

The strips can be curved and circumvoluted due to their small thickness. A typical CFRP strip with properties similar to those shown in Table 1 is able to resist a tensile force of 400 kN or more, while the weight of a 300 m long strip is less than 70 kg. In comparison, the self weight of a 300 m long high strength steel cable which can resist the same load is more than 500 kg.

The strips are arranged into a plane surface of a suitable pattern by some pre-defined rules. In the simplest weaving pattern, each strip passes over one crossing strip and under the next to form a web like a woven fabric. A part of such web is shown in Figure 2 (Peng et al. 2004). In a more general case, the number of strips meeting at a joint and the angles between these strips are the basic parameters of a weaving pattern: two strips at 90° to each other are shown in Figure 3(a), three strips at 60° shown in Figure 3(b), and four strips at 45° shown in Figure 3(c). At the joints, strips can be fully inter-connected by adhesive bonding after complete shape formation or left unbonded so that sliding between strips is allowed. In the latter case, the static friction between strips can contribute to the stiffness under static loading while the sliding friction can consume the kinetic energy of the structure under dynamic loading.

Table 1. Properties of two CFRP strip products.

Properties	Product 1	Product 2
Country of manufacturer	China	Switzerland
Width (mm)	100	120
Thickness (mm)	1.4	1.4
Specific gravity	1.5	1.6
Longitudinal strength (MPa)	≥2800	≥2400
Longitudinal modulus (GPa)	≥160	≥210
Ultimate elongation (%)	≥1.7	≥1.4
Thermal expansion coefficient (/°C)	0.2×10^{-6}	

Figure 2. Part of a woven web (After Peng et al. 2004).

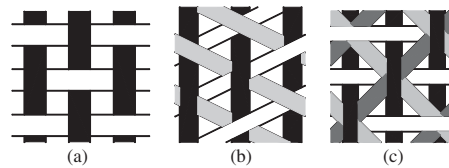

Figure 3. Weaving patterns.

3 CONSTRUCTION OF SIMPLE FRPWWS

Following the five construction steps as shown in Figure 4, a simplest FRPWWS can be completed.

First, the outer and inner ring beams on temporary supports are constructed. In general, the outer ring beam is in compression and the inner one is in tension when the web is in place. The outer ring beam is made of reinforced concrete while the inner ring beam is made of steel. The web which is woven with FRP strips is next fixed onto the ring beams with hinge joints and provided with some initial tension to form a plane surface. A tentative hinge joint scheme between the strip and the ring beam is shown in Figure 5, where the strip is tightly clamped between two stiff plates. The

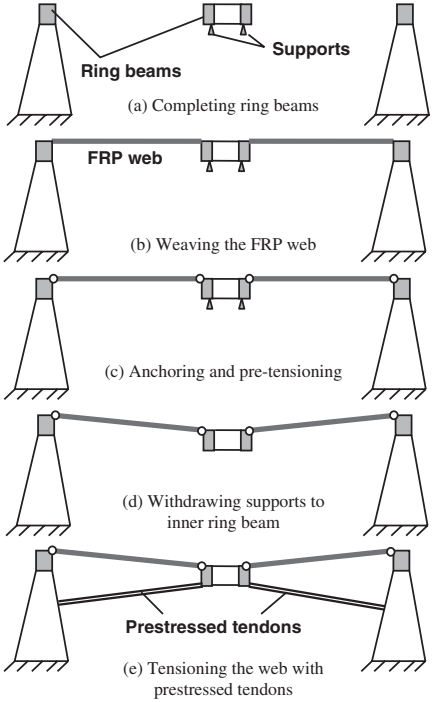

Figure 4. Construction steps.

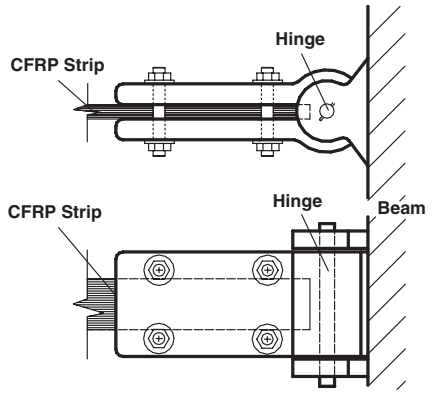

Figure 5. Tentative hinge joint scheme.

weaving of the strips should follow the rules of a specified weaving pattern which should have been designed by the structural engineer and the architect together. Weaving can be carried out easily due to the light

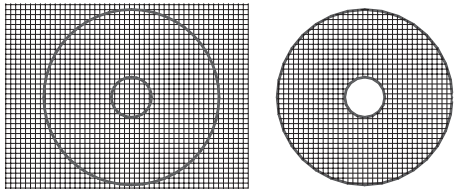

Figure 6. A tiled pattern with circular beams.

weight and small thickness of FRP strips. The temporary supports to the inner ring beam are now withdrawn and the inner ring beam moves in the out-of-plane direction by its self-weight plus an additional weight where necessary. This out-of-plane displacement of the inner ring beam can also be effected by a set of high strength tendons. The installation of these prestressed tendons completes the construction process. According to force decomposition, a small out-of-plane force causes a large in-plane component and enables the web to be tensioned, leading to a web of sufficient stiffness to resist various loads.

4 MORE COMPLEX FORMS OF THE FRPWWS

4.1 *Basic plane weaving patterns*

The FRP web is the main component in the FRPWWS system. Various weaving patterns can be adopted for the initial plane web, which will result in different mechanical behaviour. They may be classified into the following three types: tiled patterns, radiated patterns and polygonal patterns. A web weaving pattern that is independent of the boundaries is referred to as a tiled pattern as shown in Figure 6. The radiated pattern and the polygonal pattern are both made up of a number of repeated sets, each of which is composed of a number of line segments. Some examples of these two types are shown in Figures 7 and 8 respectively. Any pattern of these two types has its own defining rules. In practice, these three types of weaving patterns may be combined where appropriate in an FRPWWS system.

4.2 *Spatially curved outer ring beam*

In a real structure, a spatially-curved outer ring beam may be adopted to achieve a more appealing building shape. If the outer edge of the FRP web is anchored onto such a ring beam, the strips can form a smooth curved surface in space, as shown in Figure 9. The shape is that of a piece of stressed cloth placed on the curved beam. Because the web is composed of individual strips, it offers great flexibility in forming a curved surface with good mechanical behavior.

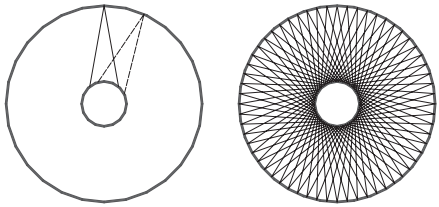

(a) Circular outer boundary

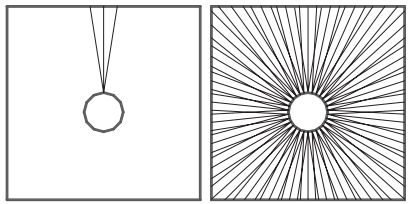

(b) Rectangular outer boundary

Figure 7. Radiated patterns.

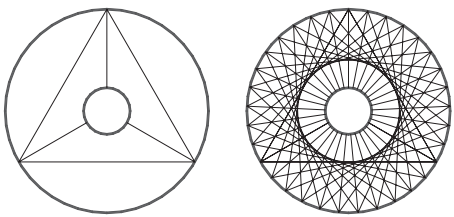

(a) Circular outer boundary

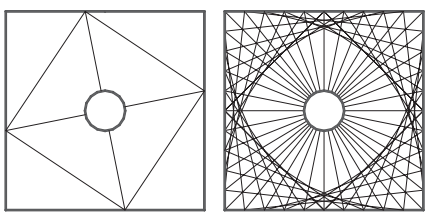

(b) Rectangular outer boundary

Figure 8. Polygonal patterns.

4.3 *Double web system*

The load carrying capacity of an FRPWWS is mainly provided by its geometric stiffness derived from the tensile forces in the FRP strips. The strips are pre-stressed in two steps: initial prestressing in plane before anchorage to the ring beams and second stage prestressing through the out-of-plane movement of the inner ring beam. The former is applied to each strip one by one, to achieve a plane web surface

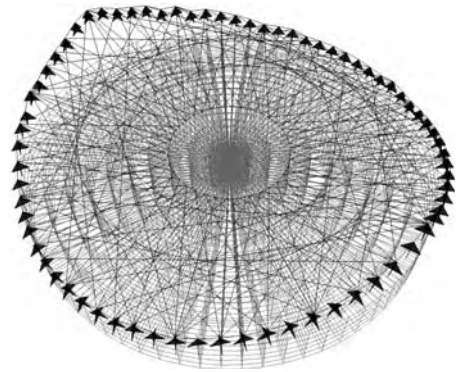

Figure 9. An FRPWWS with a spatially curved outer boundary.

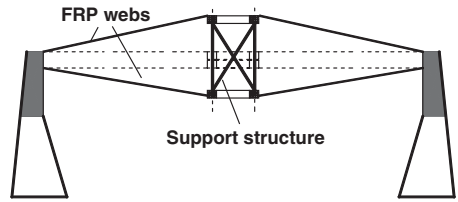

(a) Saucer-shaped double-web structure

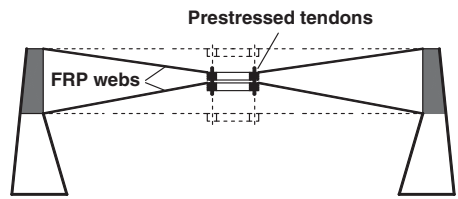

(b) Butterfly-shaped double-web structure

Figure 10. Double-web systems.

and to control the total displacement. The latter is applied to shape the web and to achieve a pre-defined stress level, which can be realized in many different ways, including the use of prestressed tendons as mentioned earlier, uplifting with a stay column and a hung heavy weight on the inner ring beam, which may be retractable roof equipment. An alternative to the above approaches is to form two webs, whose inner ring beams are then pulled together or pushed apart to induce tensile forces in the strips. Such a double-web structure is illustrated in Figure 10. Figure 10(a) shows a saucer-shaped FRPWWS achieved by pushing apart the two inner ring beams, while Figure 10(b) shows a

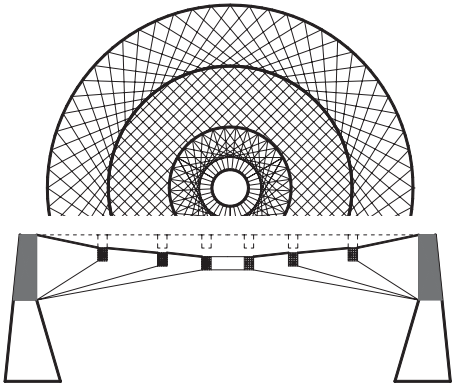

Figure 11. An FRPWWS with five ring beams.

Figure 12. Folded FRPWWS.

butterfly-shaped FRPWWS achieved by pulling together the two ring beams.

4.4 *FRPWWS with multiple ring beams*

There are only two ring beams in a simple FRPWWS. If more ring beams are used as shown in Figure 11, a large web will be divided into several shorter spans. The difficulty of construction and design will decrease as the length of continuous FRP strips becomes smaller. If a double-web system is provided with many ring beams, a folded-web system results (Figure 12).

The above are just some possible variations of the basic FRPWWS. In practical applications, many other forms/shapes can be explored. The FRPWWS may also be combined with other structural systems to become hybrid structural systems.

5 ANALYSIS OF A SIMPLE FRPWWS

5.1 *Individual FRP strip*

Each FRP strip in the web is mainly subject to tension if interaction between strips at joints is ignored. A pair of strips at 180° apart in a simple web can be modeled as two strips whose ends are connected to the outer beam and the inner ring beam respectively, as shown in Figure 13. The outer beam is regarded as a fixed

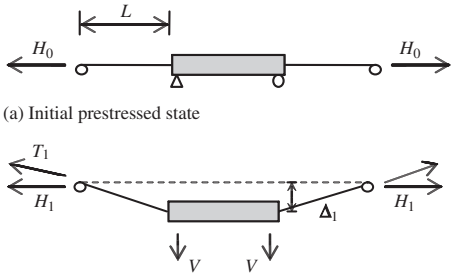

(a) Initial prestressed state

(b) Out-of-plane tensioned state

(c) Service loading state

Figure 13. Three states of a simple model of an FRPWWS.

point while the inner ring beam is treated as a rigid body. There are three states for the strips: initial prestressed state, out-of-plane tensioned state and service loading state.

It is assumed that the cross-sectional area of the strip is A, the elastic modulus is E, the difference between the radii of the inner and the outer ring beams is L, and the self weight and flexural stiffness of the FRP strip are neglected because they are very small.

In the first state as shown in Figure 13(a), a horizontal initial prestressing force H_0 is applied to the end of the strip. Then the strain of the strip is

$$\varepsilon_0 = \frac{H_0}{EA} \tag{1}$$

The initial length of the strip is

$$L_0 = \frac{L}{1+\varepsilon_0} \tag{2}$$

In the second state as shown in Figure 13(b), two vertical loads V are applied on the inner ring beam to move it down to tension the strips. The tensile force in the strip is T_1, whose horizontal component is H_1, and the displacement of the inner ring beam is Δ_1. Based on equilibrium consideration, there is

$$T_1 = \sqrt{H_1^2 + V^2} \tag{3}$$

If the strain of the strips at this time is ε_1, then

$$\varepsilon_1 = \frac{T_1}{EA} \tag{4}$$

$$\varepsilon_1 - \varepsilon_0 = \frac{\sqrt{L^2 + \Delta_1^2} - L}{L_0} \tag{5}$$

From the geometric relationship, there is

$$\frac{V}{H_1} = \frac{\Delta_1}{L} \tag{6}$$

Combining these equations, T_1, Δ_1, ε_1 can be found.

In the third state, the strips are required to support a service load $q(x)$ which is symmetrically placed with respect to the centre of the inner ring beam. The reaction at the fixed end can be decomposed into the horizontal force H_2 and the vertical force R. The total deflection of a point at a distance x from the fixed point is denoted by $z(x)$, the deflection due to the service load is denoted by $w(x)$, and the total displacement of the inner beam is denoted by Δ_2 Then,

$$R = \int_0^L q(x)\mathrm{d}x + V \tag{7}$$

The deflected shape is governed by the following cable equation (Shen 1997):

$$H_2 \frac{\mathrm{d}^2 z}{\mathrm{d}x^2} + q(x) = 0 \tag{8}$$

If $q(x)$ is a uniform load, the deflection curve can be found easily by double integration to be:

$$z(x) = \frac{q}{2H_2}(L - x)x + \frac{x}{L}\Delta_2 \tag{9}$$

and Equation (7) becomes

$$R = qL + V \tag{10}$$

The slopes at the strip ends are

$$\left.\frac{\mathrm{d}z}{\mathrm{d}x}\right|_{x=0} = \frac{R}{H_2} \tag{11}$$

$$\left.\frac{\mathrm{d}z}{\mathrm{d}x}\right|_{x=L} = \frac{V}{H_2} \tag{12}$$

Based on deformation compatibility, the total length change of each strip in the second stage is given by

$$\Delta s = \frac{1}{2}\int_0^L \left[\left(\frac{\mathrm{d}z}{\mathrm{d}x}\right)^2 - \left(\frac{\Delta_1}{L}\right)^2\right]\mathrm{d}x \tag{13}$$

but the second stage elongation found from strains is

$$\Delta s = \frac{(H_2 - H_1)L}{EA}\left[1 + \left(\frac{\Delta_1}{L}\right)^2\right] \tag{14}$$

Thus, H_2 and Δ_2 can be found from Equations (10–14).

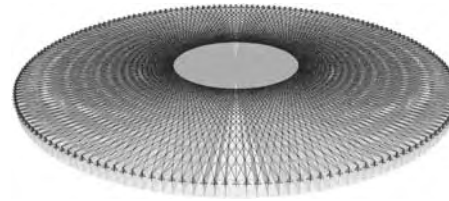

Figure 14. FRPWWS analysis model.

As an example, a pair of strips for a model FRPWWS as shown in Figure 13 is considered, where $L = 80$ m and the properties of the strips are the same as those of product 2 in Table 1. In the first stage, an initial stress of 500 MPa is induced in the strips, then $\varepsilon_0 = 0.0024$, $L_0 = 79.81$ m, and $H_0 = 84$ kN. In the second stage, an out-of-plane force $V = 30$ kN is applied. As a result, $\Delta_1 = 7.14$ m, $\varepsilon_1 = 0.0064$, $H_1 = 225.3$ kN and the stress in the strips is 1344 MPa. Finally, a uniform load $q = 0.5$ kN/m is applied on the strips, and consequently $\Delta_2 = 10.27$ m, $H_2 = 389.5$ kN, and the maximum stress in the strips is 2352 MPa and occurs near the outer fixed end.

From this simple analysis, the key parameters for an FRPWWS can be identified. These include the initial control stress or the prestressing force H_0, the out-of-plane force V or the deflection of the inner beam Δ_1. They control the deformation of the web under loading and the stress level in the FRP strips.

5.2 *A simple FRPWWS*

A simple FRPWWS as shown in Figure 14 was analyzed by the finite element method using the finite element package ANSYS (2000). It has a 150 m span, and the radius of the inner ring is 30 m. Product 2 listed in the Table 1 is employed in this structure, which is assumed to have a design value of 2000 MPa for the tensile strength. Only the radiated pattern is adopted. There are 360 repeated sets altogether, each of which is composed of three strips. Thus, there are 1080 FRP strips in the structure. The geometric nonlinearity from large deformation was considered in the finite element analysis, while interaction between strips was neglected. The self weight of the FRP web is ignored as it is only 177 kN which is much smaller the total load acting on the structure.

The stress level in the initial prestressed web is controlled to be no more than 210 MPa, while that after the downward movement of the inner ring beam no more than 1000 MPa. From the finite element analysis, under a vertical force of 14,400 kN for the second stage operation, the inner ring beam moves down by 5.08 m and the maximum stress in the strips reaches 995 MPa. The construction of the FRPWWS is now complete.

As the weight of each strip in this FRPWWS is less than 18 kg, which can be carried by an adult, the construction of this structure is expected to be easy. The total weight of the strips in the FRPWWS is estimated to be about 19,440 kg.

The completed FRPWWS was next subject to a factored uniform load of 1.8 kN/m^2 over the entire area enclosed by the outer ring beam, which is intended to include the self-weight of the roofing material, wind loading and snow loading. Under this loading, the maximum deflection increase is 1.22 m and the total maximum stress in the FRP strips is 1542 MPa, which is about 85.7% of the design stress. The structure is thus strong enough to resist this loading.

6 CONCLUSIONS

The FRP woven web structure (FRPWWS), which represents a new application of FRP in long-span structures, has been presented in this paper. The key aspects of this new system are listed below.

i. The FRP woven web, the ring beams and the out-of-plane tension system are the basic components of the FRPWWS.
ii. There are five construction steps for a simple FRPWWS as illustrated in Figure 4.
iii. The plane weaving patterns can be summarized into three types: tiled patterns, radiated patterns and polygonal patterns.
iv. Following the same basic principle, many different forms can be constructed. The paper has discussed several such possibilities, including the use of a spatially curved outer ring beam, the double-web system and systems with multiple ring beams.
v. An FRPWWS experiences three distinct stress states: the initial prestressed state, the out-of-plane tensioned state and the service loading state, all of which should be considered in design.

ACKNOWLEDGEMENTS

The authors are grateful to the Natural Science Foundation of China for their support to the research presented here through a national key project on the application of FRP composites in civil engineering in China (Project No. 50238030) and through the Joint Research Fund for Hong Kong and Macao Young Scholars (Project No. 50329802).

REFERENCES

ANSYS, Inc. 2000. *ANSYS User's Manual*.

Maeda, K., Ikeda, T., Nakamura, H., Meiarashi, S. 2002. Feasibility of ultra long-span suspension bridges made of all plastics. *Proceedings of IABSE Symposium (CD-ROM), Melbourne, Australia, 2002*.

Peng, X.Q., Cao, J., Chen, J., Xue, P., Lussier, D.S., Liu, L. 2004. Experimental and numerical analysis on normalization of picture frame tests for composite materials. *Composites Science and Technology* 64(1):11–21.

Shen, S.Z., Xu, C.B., Zhao, C. 1997. *Cable-suspended structure design.* Beijing: China Building Industry Press (In Chinese).

FRP Composites in Civil Engineering – CICE 2004 – Seracino (ed)
© 2005 Taylor & Francis Group, London, ISBN 90 5809 638 6

The effect of non-classical behaviors on the measurement of the Timoshenko shear stiffness

M.D. Hayes & J.J. Lesko
Department of Engineering Science and Mechanics, Virginia Tech, Blacksburg, VA, USA

ABSTRACT: A number of researchers have encountered difficulty in measuring the Timoshenko shear stiffness of thin-walled structural beams in the laboratory. Large errors in the measured values relative to analytical estimates have been attributed to error in the deflection measurements and to shear warping effects. It has been hypothesized that warping incompatibilities at loading points and supports result in local increases in the apparent shear stiffness. In this study, the influence of warping on beams under various types of loading and boundary conditions was considered using finite element analysis (FEA). In particular, a solid beam test case and a commercially available thin-walled FRP beam were investigated. The results suggest that warping has a negligible effect for thin-walled beams at reasonable span lengths. However, transverse compression at the load points and supports is found to reduce the effective shear stiffness significantly at shorter span lengths.

1 INTRODUCTION

1.1 *Background*

Fiber-reinforced polymeric (FRP) composites are increasingly finding use in the areas of civil infrastructure and construction. Specifically, composites are being considered for structural elements in bridge construction as lighter, more durable alternatives to steel and concrete. The design of FRP structures in infrastructure applications is typically stiffness-controlled, since large deflections can pose problems for overlay and connection durability. Furthermore, FRP structural beams will exhibit appreciable shear deformation at low aspect (span-to-depth) ratios, due to the relatively low shear modulus of FRP materials. In order to minimize cost and to design efficient structures using FRP beams, it is important for the manufacturers to be able to precisely specify stiffness design allowables. Therefore, it is imperative to be able to measure the stiffness quantities accurately in the laboratory and to be able to estimate them analytically.

The current study is motivated by the need to understand and predict the performance of a particular structural member that has been developed for the infrastructure market. Strongwell Corporation of Bristol, Virginia has developed a 91 cm (36 inch) deep pultruded double web beam (DWB) for use in bridge construction (Figure 1). The beam is a hybrid laminated composite, composed of both E-glass and carbon fibers in a vinyl ester resin. The DWB is intended for unsupported spans from 9.14 m to 18.3 m (30 to 60 feet) and has been implemented in the rehabilitation of a 12.2 m (40 ft) long bridge (Restrepo 2002). Experimental results indicate that at the 9.14 m span, shear accounts for 15% of the total deformation under four-point loading with loads applied at the third points (1/3 and 2/3 span).

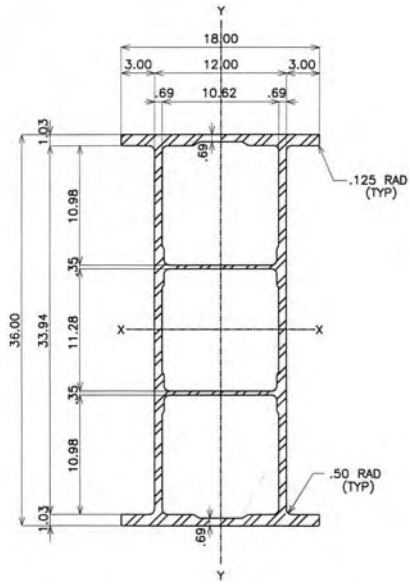

Figure 1. The 91 cm (36 inch) DWB (dimensions in inches).

Figure 2. Four-point bend test set-up for 91 cm (36 inch) DWB.

Waldron (Waldron 2001) examined eleven 91 cm (36 inch) double-web beams in a static four-point bending geometry to measure the bending and shear stiffness values. The measured Timoshenko shear stiffness *kGA* value was as much as 59% less than the analytically calculated value for 13 beams tested, and the scatter was considerable. At the time, the error was attributed mainly to imprecision in the deflection measurements caused by the low bit resolution of the data acquisition system.

More recently, Schniepp .(Schniepp 2002) tested 15 beams at spans ranging from 9.1 m to 17.7 m (30 ft to 60 ft), as shown in Figure 2. Care was taken to obtain accurate deflection measurement, and the issue of precision was alleviated greatly by switching to a higher resolution data acquisition system. Still, the mean *kGA* values were 15–27% higher than the analytical value, and the scatter was high. These results highlight the difficulty in measuring the Timoshenko shear stiffness *kGA*.

1.2 *Timoshenko shear stiffness*

Since Timoshenko's modification of beam theory to account for shear deformation in the 1920's, a number of analytical techniques have been devised to calculate the shear correction factor, k, which was introdced to correct the strain energy resulting from the assumption of a constant shear profile. In particular, Cowper developed an alternate derivation of Timoshenko beam theory that leads to a comprehensive definition for k (Cowper 1966). For homogeneous isotropic beams, he found that k depends only on the geometry and the Poisson's ratio, ν. For a solid rectangular section, k approaches the well-known value of 5/6 as ν approaches zero. For laminated composite beams, the material properties and therefore the shear stress will vary through the depth of the beam, e.g. (Dharmarajan and McCutchen 1973; Teh and Huang 1979; Madabhusi-Raman and Davalos 1996).

Determining the value of k for a thin-walled composite beam is more difficult, since the shear stress distribution is less easily obtained. The common practice is to estimate the shear stiffness *kGA* by multiplying the transverse shear modulus G by the shear area A and assuming a value of $k = 1$ (Nagaraj and GangaRao 1997). However, the definition of shear area for a thin-walled beam is not always clear. It is usually considered to be only the areas of the vertical members, since thin flanges carry very little shear. However, this assumption may no longer be valid as the thickness of the flanges increases. Furthermore, since the factor k is used to correct the Timoshenko strain energy as computed over the shear area, k and A are coupled. To estimate values of *kGA* for thin-walled composite beams, Bank (Bank 1987) and Bank and Melehan (Bank and Melehan 1989) extended Cowper's method to thin-walled beams made of anisotropic panels such as laminated FRP beams.

In References (Cowper 1966; Dharmarajan and McCutchen 1973; Teh and Huang 1979; Bank 1987; Bank and Melehan 1989; Madabhusi-Raman and Davalos 1996; Omidvar 1998), the shear is considered to act on the entire cross-sectional area of the beam. Since the shear stress distribution in a thin-walled beam is piecewise parabolic and the shear stress is very small in the flanges, the shear correction factor k can be much smaller than that found considering only the area of the vertical members.

For instance, the Mechanics of Laminated Beam (MLB) model developed by Barbero et al. (Barbero, Lopez-Anido et al. 1993) neglects any shear stiffness contributions from the horizontal walls, and the shear stiffness *GA* is simply equal to the sum of the in-plane shear stiffnesses of the vertical panel(s). Furthermore, only the shear flow over the vertical members is considered in computing the shear correction factor. The result is that the shear correction factor is approximately equal to 1 for moderately tall sections with thin flanges, as expected.

The shear flow across the entire section is found *a posteriori* by integrating the appropriate equilibrium equation in terms of stress resultants. The shear correction factor k is found by equating the shear strain energy computed from the shear flow over the web section only to the Timoshenko shear strain energy. In computing the latter, the shear force is taken to be the resultant of the shear stress over the web area only.

In summary, it is important to recognize that the value of k is dependent upon or coupled with the definition of the shear area. Consider, for example, the shear stress distribution for an isotropic wide flange calculated using the mechanics of materials approach. The MLB model yields a value of $k \cong 1$ for a homogeneous, isotropic I-beam with an aspect ratio of 1 (Barbero, Lopez-Anido et al. 1993). For the same section, Bank (Bank 1987) calculates a value of $k \cong 0.3$.

1.3 *Experimental determination of kGA*

It is clear that the section shear stiffness and the shear flow depend on the material properties and geometry of the beam. Therefore, simply performing coupon

shear tests on the web or vertical wall material of the beam is not sufficient to accurately determine the global section shear stiffness of the beam for use in Timoshenko beam theory. Full section tests on the beam itself are preferred, and two methods are available to determine the shear stiffness *kGA* experimentally.

In the first method, referred to here as the "back calculation method", a single four-point bend test is performed. The bending stiffness *EI* is first determined from strain readings on the outer flange surfaces at mid-span (in the constant moment region):

$$EI = \frac{Mc}{\varepsilon} \tag{1-1}$$

where M is the moment from equilibrium, c is the largest distance from the neutral axis, and ε is the measured strain. Once *EI* is known, the measured deflection can be used to back calculate *kGA* from the appropriate Timoshenko equation. For instance, the Timoshenko equation for a four-point bend test with the loads applied at the third points is

$$\delta_{\max} = \frac{23PL^3}{648EI} + \frac{PL}{3kGA} \tag{1-2}$$

where P is the is the load applied at both points and L is the span length. Solving for *kGA*,

$$kGA = \frac{PL}{3\left(\delta_{\max} - \frac{23PL^3}{648EI}\right)} \tag{1-3}$$

This method, while quick and simple, is generally avoided as it is very sensitive to error in the deflection measurement.

In the "simultaneous method", also referred to as the "graphical" method, multiple bending tests at different spans are run for each beam. Each test generates an additional Timoshenko equation with two unknowns, *EI* and *kGA*, since the measured deflection is known. Theoretically, only two span lengths are required to solve for the two unknown stiffness parameters, but additional tests are normally run to reduce the error. If the Timoshenko equation is modified by dividing by PL^3, then the equation can be interpreted as being that of a line, with $1/L^2$ being the independent variable on the abscissa and $\delta_{\max}/PL^3$ being the dependent variable on the ordinate. This is the "graphical" interpretation of the simultaneous approach. For example, Equation (1–2) becomes

$$\frac{\delta_{\max}}{PL^3} = \frac{23}{648EI} + \frac{1}{3kGA}\frac{1}{L^2} \tag{1-4}$$

Then the deflection quantity δ_{max}/PL^3 can be plotted versus $1/L^2$ for different tests run at different spans, L. The slope of a fitted line will be proportional to the *kGA* and the intercept will be proportional to the *EI*.

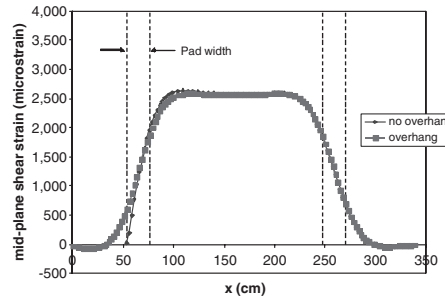

Figure 3. Shear strain profiles from the FE models of the DWB with pad supports, showing the decay near a support and at a load patch. The support is located between x = 53.3 and 76.2 cm, while the load patch is located between x = 248 and 271 cm. Only half of the span is shown.

Alternately, one can divide the Timoshenko equation by *PL*, and the slope and intercept will be proportional to *EI* and *kGA*, respectively. The simultaneous method has been used by a number of researchers to characterize solid beams, thin-walled beams, and sandwich panels (Allen 1969; Fischer, Roman et al. 1981; Sims, Johnson et al. 1987; Bank 1989; Barbero, Fu et al. 1991; Cosenza, Lazzaro et al. 1996; Davalos, Salim et al. 1996).

1.4 *Experimental error*

Both experimental methods are very sensitive to error in the deflection measurement. Furthermore, the inherent limitations of Timoshenko beam theory may introduce additional error. Non-classical effects caused by warping, transverse flexibility, and complex boundary conditions are neglected by Timoshenko beam theory and will affect deflections slightly. For example, "warping incompatibilities" caused by loading and boundary conditions or non-uniform bending cause additional axial displacements or warpings (Bauchau 1985). Through the strain-displacement relations, these warping displacements cause a local increase in the outer fiber axial strains and a reduction in the shear strain. The effect decays over a finite length, which depends upon the test geometry, beam geometry (aspect ratio), and material properties (degree of anisotropy).

To understand the effects of the boundary conditions on the effective *kGA* values, it is useful to observe the behavior of the beam in the vicinity of the supports and the loading points. Figure 3 shows the mid-plane shear strain along half of the length of a 6.1 m (20 ft) long DWB for two FE models using elastomeric pads at the supports. The shear strain undergoes a smooth decay at the load patch as the resultant shear force decreases from $P/2$ to 0. The pads have nearly the same

effect as the loading patches. The decay patterns are identical for longer spans, but it is obvious that this non-classical effect impacts a longer portion of the beam span at shorter spans.

The local reduction in shear strain caused by an incompatibility can be viewed as an increase in the local apparent Timoshenko shear stiffness, leading to an increase in the effective shear stiffness for the beam as a whole. Alternately, one can view the increase in axial strain as a decrease in the apparent bending stiffness. This view was taken by Lopez-Anido and GangaRao (Lopez-Anido and GangaRao 1996). They developed a thin-walled beam theory including out-of-plane warping and calculated an effective axial modulus, which varies along the length of the beam. The effective modulus is shown to decrease in the vicinity of load points, and the effect decays in the far field. According to the authors, this observation explains why so many researchers have difficulty calculating the shear stiffness using Timoshenko beam theory. This argument was again echoed by Bank (Bank 1987) in the context of calculating the shear correction factor.

1.5 *Summary*

Experimental determination of the Timoshenko shear stiffness of thin-walled composite beams has proven to be difficult due to the sensitivity of the calculation to small changes in the deflection measurement. This difficulty is likely a direct result of the type of non-classical behaviors that Euler and Timoshenko beam theories neglect, including warping and transverse flexibility. While several authors have acknowledged the importance of these factors, few have attempted to quantify the effects.

The objective the current study is to understand the difficulties in measuring *kGA* experimentally. In particular, the effects of boundary conditions, loading conditions, and test geometry are considered. At the onset of this study, it was hypothesized that these factors influence the beam response primarily through warping and warping restraint, and finite element analysis was utilized to test this hypothesis. The effects of transverse compressibility were also considered. A simple test case using a solid rectangular beam was considered, in addition to the 36 inch (91 cm) DWB. First, however, to provide exact reference values of the Timoshenko shear stiffness for later calculations, laminated beam theory and finite element analysis were applied to these beams.

2 SHEAR STIFFNESS CALCULATIONS

2.1 *Composite beams*

A simple solid beam was modeled to explore the effects of warping and compression without the additional complexity of width-direction geometric and material variations. The beam was assumed to have a narrow, rectangular cross-section with homogeneous, orthotropic properties. Thus, computation of the Timoshenko shear stiffness is straightforward. This beam also permits a high degree of mesh refinement in a finite element model. Aspect ratios varying from 3 to 30 and orthotropy ratios E/G of 2.5 and 37 were considered. The first orthotropy ratio corresponds to the ratio of the effective bending modulus of the DWB to its effective shear modulus, as calculated using the MLB model. The second orthotropy ratio corresponds to the properties of a carbon/vinyl ester uni-directional ply with a volume fraction of 55%.

The theoretical shear stiffness of the solid beam is calculated simply as kGA, the shear modulus G multiplied by the total cross-sectional area A, and the shear correction factor k. The value of k is calculated using the method of Cowper extended to homogeneous specially-orthotropic solid beams by Dharmarajan and McCutchen (Dharmarajan and McCutchen 1973):

$$k = \frac{5E_{zz}}{6E_{zz} - \nu_{xz}G_{xz}} \tag{2-1}$$

where E_{zz} is the axial modulus, G_{xz} is the transverse shear modulus, and ν_{xz} is the transverse Poisson's ratio. The shear correction factor is calculated to be 0.847 and 0.905 for the orthotropy ratios of $E/G = 2.5$ and 37, respectively.

2.2 *Thin-walled Laminated Beam*

Next, the 91 cm (36 inch) DWB was considered. The lay-up of the DWB was estimated using the fiber thread-up schematics provided by the manufacturer, and the ply-level engineering properties were estimated using standard micromechanics models. While the lay-up is proprietary, the web is essentially a quasi-isotropic panel with some random-fiber continuous strand mat (CSM). The flanges are comprised of two sub-laminates: the outer sub-laminate, which consists of carbon fiber and CSM, and half of the web panel material which is folded 90 degrees to form the inner sub-laminate. This all-glass portion terminates at two external tapers on the inner surface of the flanges (Figure 1). The Timoshenko shear stiffness kGA of the 91 cm (36 inch) DWB was calculated using the Mechanics of Laminated Beam (MLB) model of Barbero et al. (Barbero, Lopez-Anido et al. 1993) and finite element analysis. The results of the FEA k calculation are not presented here.

2.2.1 *Laminated beam theory*

The details of the MLB model are not presented here, but the "uncorrected" shear stiffness GA is essentially

the in-plane shear stiffness of the web panels as calculated using CLT. The reader is referred to Barbero et al. (Barbero, Lopez-Anido et al. 1993) for further details. The shear correction factor is found following the classical definition, i.e. by equating the shear strain energy predicted by Timoshenko beam theory to that obtained from the "actual" shear stress distribution over the cross-section. Because the MLB analysis neglects shear deformation in the flanges and assumes a constant shear strain distribution through the web, the actual wall shear stress resultant and shear strain across *all* walls is estimated *a posteriori* by integrating the z-direction resultant force equilibrium equation for each panel.

Barbero et al. give a general equation for k in terms of wall stiffness parameters and the contour definition. It is important to note that to be consistent with the underlying assumptions of MLB, only the shear flow over the web panels is used to compute k. That is, only part of the total shear flow is used to compute the shear strain energy. Furthermore, the shear resultant force used in the calculation is actually slightly less than the total shear force. These are subtle but important details which can cause large errors in the k calculation, if they are not carefully considered.

Using the MLB model, the total shear stiffness of the DWB (neglecting flange and sub-flange contributions) was found to be $GA = 176$ MPa-m^2 (39.6 Msi-in^2). The double web feature forces k to 0.997. Thus, the Timoshenko shear stiffness kGA is calculated to be 175 MPa-m^2 (39.5 Msi-in^2). Henceforth, this value will be referred to as the *reference value*.

3 WARPING EFFECTS

Next, the concept of apparent shear stiffness is revisited. This local phenomenon is caused by discontinuities or gradients in the resultant shear force. Depending upon the strength of the disturbances, which are controlled by the lay-up and geometry of the beam, integration of these local changes in kGA over the entire beam may impact the *effective kGA*. This effective shear stiffness is the quantity measured in experiments, and it should depend upon the loading and geometry. For instance, a beam loaded in three-point bending might exhibit a different effective kGA than a beam of equal length under four-point loading. In addition, distributed loads should have a different effect than concentrated loads. In this way, the Timoshenko shear stiffness is viewed as being not only a material or structural property, but also a geometry-dependent quantity.

The simplest way to characterize the impact of these non-classical effects on the shear response is to measure the change in deflection when the loading conditions are changed. Finite element models of the two composite beams were utilized to simulate the actual beam deflection measured in a lab test. The effective Timoshenko shear stiffness for a given test geometry was then back-calculated using this "actual" deflection. A primary advantage of applying this approach is that errors due to inaccurate deflection measurements are eliminated, if the FEA mesh is sufficiently refined to ensure convergence. Furthermore, FEA can account for actual loading conditions and boundary conditions, and it provides the real three-dimensional response of the beam.

3.1 *Finite element analysis*

Finite element models of the solid beam test case in four-point loading at varying span lengths were constructed. Two types of boundary conditions were considered: nodal fixity at the neutral axis and nodal fixity along the bottom edge. The FE models were constructed in ANSYS® using the PLANE42 element type, a 2-D planar 4-noded element for modeling plane stress problems. The beam was modeled with a 2.54 cm × 2.54 cm (1 inch × 1 inch) square cross-section and lengths ranging from 7.62 cm to 76.2 cm (3 inch to 30 inches). An element size of 1.27 mm × 1.27 mm (0.05 in × 0.05 in) was selected to provide a high degree of mesh refinement. The bending stiffness was computed analytically as $[E \cdot I]$, and then kGA was back-calculated from the FEA predicted deflections.

The DWB was modeled in full 3-D in ANSYS® using the SOLID46 8-noded, 3-D layered solid element. A full length FE model was constructed for a 12.2 m (40 ft) long beam under four-point bending with the loads applied near the third points. The mesh was sufficiently refined to provide convergence on the mid-span deflection, calculated on the bottom surface of the bottom flange. To accurately simulate the real test conditions, the load patches were modeled in detail (Hayes 2003).

Again, the two boundary conditions above were applied. Following the experimental procedure, the bending stiffness was calculated using Equation (1-1) and the axial strain from the outer surface of the top flange. This value was checked using the theoretical bending stiffness calculated with MLB beam theory. This analysis was conducted for the three spans tested by Schniepp (Schniepp 2002), as well as two additional span lengths (6.1 m and 15.2 m, or 20 ft and 50 ft).

3.2 *Results*

3.2.1 *Solid beam test case*

The back-calculated kGA values determined using the two nodal fixity boundary conditions for the low orthotropy example are shown in Figure 4. For the

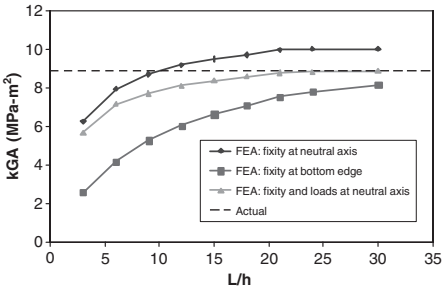

Figure 4. Back-calculated *kGA* values for a solid rectangular beam in four-point loading with E/G = 2.5 as determined by FEA.

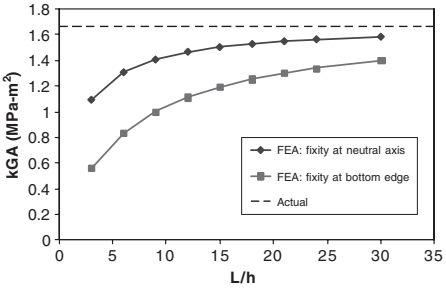

Figure 5. Back-calculated *kGA* values for a solid rectangular beam in four-point loading with E/G = 37 as determined from FEA.

case of nodal fixity at the neutral axis, the effective *kGA* value is much lower than the theoretical value at short spans and then overshoots the theoretical value at longer spans. When nodal fixity is enforced at the bottom edge of the beam, *kGA* is reduced by 20 to 50% relative to the former case, approaching the theoretical value at longer span lengths. As indicated in Figure 4, the location of the load, e.g. at the neutral axis or on the top surface, can have a significant effect as well.

These results suggest a significant effect of non-classical behavior on the effective *kGA* value, especially at shorter spans. For instance, at an aspect ratio of 10, the model using nodal fixity at the bottom edge yields an effective *kGA* value which is 40% less than the theoretical value. However, the source of this effect does not appear to be warping, since the FEA results show a clear trend of increasing *kGA* with span. This trend is contrary to the hypothesized trend due to warping. To further illustrate this point, the *kGA* versus span curves for the high orthotropy example are shown in Figure 5. The results again yield low *kGA* values at short spans which then approach the theoretical value at longer spans. It is noted, however, that much

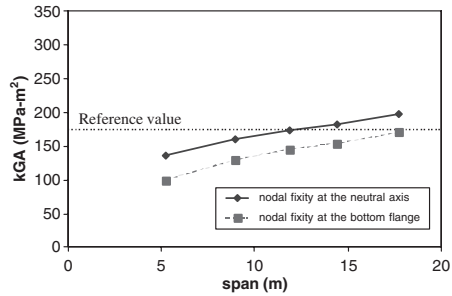

Figure 6. The effect of span on the effective *kGA* back-calculated from the FE results for the four-point loading geometry and the two cases of discrete supports.

longer spans are required to achieve a match with the theoretical value.

3.2.2 *DWB*

The resulting effective *kGA* values versus span length for the DWB are shown in Figure 6. As in the case of the solid beam, the results show a clear trend of increasing *kGA* with span. Again, this trend is contrary to the hypothesized increase in effective *kGA* with decreasing span due to warping. The case of the boundary conditions applied at the bottom edge yields a *kGA* value 14 to 26% lower than the case where the boundary conditions applied at the neutral axis.

4 TRANSVERSE FLEXIBILITY EFFECTS

The results of the previous section suggest that an effect other than warping causes a reduction in the effective *kGA* value at shorter spans. The effect appears to be dependent upon where the loads and boundary conditions are applied through the depth of the beam, suggesting a dependence upon the transverse properties. Based on observations in the sandwich beam literature (Frostig, Baruch et al. 1992), it is now hypothesized that transverse compressive deformation near the external loads and reactions can increase global deflections enough to decrease the measured Timoshenko shear stiffness at short spans.

To check for a transverse compressibility effect, a simple parametric study using the four-point loaded solid beam FE model was conducted. The transverse modulus E_z was varied between 5 MPa and 445 MPa (1.11 Msi and 100 Msi), the modulus of the carbon/vinyl ester ply in the DWB and the modulus of a nearly "infinitely stiff" material, respectively. The effective *kGA* was back-calculated as usual and compared to the theoretical value. This analysis was conducted for both orthotropy cases considered previously.

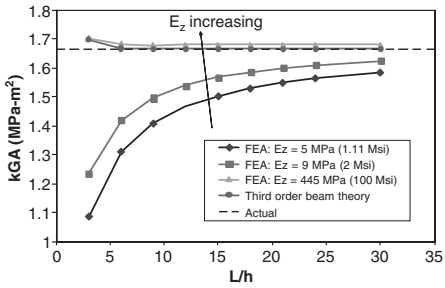

Figure 7. Influence of the transverse compressive modulus on the effective *kGA* value (solid beam test case, four-point loading).

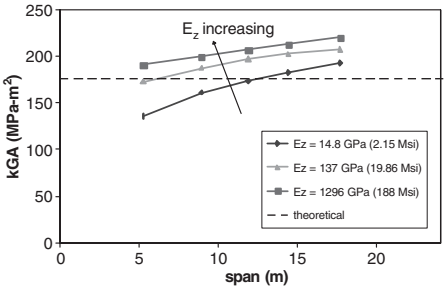

Figure 8. Effect of transverse stiffness on the effective *kGA* value of the DWB (finite element results).

A similar parametric study was undertaken to assess the influence of the transverse stiffness on the behavior of the DWB. The fiber-direction modulus E_{11} of the 90° plies in the web panels was increased to 689 GPa and 6.89e6 GPa (100 Msi and 1e6 Msi) to increase the panel stiffness in the *z*-direction from 14.8 GPa (2.15 Msi) to 138 GPa and 1296 GPa (20 Msi and 188 Msi), respectively. This approach does not affect the shear stiffness of the panels – an observation that can easily be verified by CLT. A check of the FE predicted shear strains also confirmed this.

4.1 *Results*

The results of the four-point loading FEA parametric study for the high orthotropy case are shown in Figure 7. The results clearly indicate that as the transverse stiffness is increased, the effective *kGA* value increases and approaches the theoretical value. Furthermore, as E_z becomes very large, the warping behavior is recovered and the slight short span stiffening effect is observed. This effect correlates well with the warping effect predicted using a third order laminated beam theory developed in (Hayes 2003). Thus, it appears that the reduction in *kGA* at short spans can be explained by transverse compression.

As noted previously, the amount of transverse deformation depends upon how the loads and boundary conditions are applied. Incidentally, the location where the mid-span deflection is "measured" is also important. In the previous results, the deflections were taken from the bottom surface. However, if the absolute maximum deflection is used instead, the resulting *kGA* values are shifted downward slightly [31].

The effect of the transverse stiffness on the back-calculated *kGA* value of the DWB is shown in Figure 8. The results clearly show an increase in *kGA* with transverse stiffness with the curves approaching a limit, although this limit is higher than the theoretical value. The reason for this discrepancy is unclear.

4.2 *Other FRP beams*

The DWB is a unique structural beam due to the use of carbon fiber in the flanges and the double web design. Therefore, the degree of orthotropy and behavior of this beam may be different than that of more common FRP beams. In Hayes (Hayes 2003), a third order laminated beam theory was derived to estimate the amount of the warping effect for a series of standard off-the-shelf wide-flange beams, I-beams, and box-beams. Due to the lower degrees of orthotropy, the magnitude of warping was estimated to be less than that of the DWB, confirming that warping will have a negligible effect on the measurement of *kGA* for most FRP shapes.

On the other hand, the transverse compressive stiffness depends on the amount of fiber oriented along the transverse direction of the web panel(s), and since off-the-shelf pultruded products typically utilize a high volume fraction of continuous strand mat, the compressive modulus will be less than that of the DWB. For instance, Strongwell's standard EXTREN® beams have a transverse compressive modulus equal to 6.89 GPa (1 Msi), compared to the 14.8 GPa (2.15 Msi) modulus of the DWB web panels (Strongwell 2000). Therefore, the transverse flexibility effect will likely be more pronounced in standard beams. Further study is required to verify this hypothesis.

"Soft" core sandwich panels are an example of a beam type structure with both low compressive stiffness and low shear stiffness. Both the warping and compression effects are expected to influence the measured shear stiffness. The low shear modulus of the core will yield a very high degree of orthotropy, so that warping effects may be much greater. In fact, the decay length over which the warping effect occurs can be many times the thickness of the panel or beam [31]. Therefore, the error in *kGA* measurements is likely to be even more pronounced in sandwich panels. The magnitude and sign of the resulting error in

the effective *kGA* will depend upon the strength of these two competing effects.

5 CONCLUSIONS

The purpose of this study was to identify factors which hinder accurate measurement of the Timoshenko shear stiffness. This study considered in great detail the issue of shear warping, which had been cited as a possible cause for *kGA* measurement errors by several sources. Specifically, an increase in the measured *kGA* value was expected at shorter spans. It has been shown that small changes or errors in the deflection measurement can significantly affect the back-calculated *kGA* values. Furthermore, the FE analyses also suggest that boundary conditions may play a role through non-classical behavior effects. However, the effect of shear warping was found to be negligible. This conclusion is supported by analyses using the third order laminated beam theory in Hayes (Hayes 2003).

The parametric studies in which the transverse stiffness was varied revealed that transverse compressibility has a significant local softening effect on a beam and reduces the effective Timoshenko shear stiffness, confirming the trend found in the finite element analyses: a decrease in effective *kGA* with decreasing span length. Furthermore, the boundary conditions and loading conditions were shown to significantly impact the back-calculated *kGA* by affecting the amount of transverse deformation. The fact that transverse deformation can have such a significant effect on the *kGA* measurement represents a significant contribution to the current understanding of the problem. Current on-going research by the authors is aimed at predicting this error using soft core sandwich theory.

REFERENCES

Allen, H. G. (1969). *Analysis and design of structural sandwich panels*. Oxford, Pergamon Press.

Bank, L. C. (1987). "Shear coefficients for thin-walled composite beams." *Composite Structures* **8**(1): 47–61.

Bank, L. C. (1989). "Flexural and shear moduli of full-section fiber reinforced plastic (FRP) pultruded beams." *Journal of Testing and Evaluation* **17**(1): 40–45.

Bank, L. C. and T. P. Melehan (1989). "Shear coefficients for multicelled thin-walled composite beams." *Composite Structures* **11**(4): 259–276.

Barbero, E. J., Fu, et al. (1991). "Ultimate Bending Strength of Composite Beams." *Journal of Materials in Civil Engineering* **3**(4): 292–306.

Barbero, E. J., R. Lopez-Anido, et al. (1993). "On the mechanics of thin-walled laminated composite beams." *Journal of Composite Materials* **27**(8): 806–829.

Bauchau, O. A. (1985). "A Beam Theory for Anisotropic Materials." *Journal of Applied Mechanics-Transactions of the ASME* **52**: 416–421.

Cosenza, E., F. Lazzaro, et al. (1996). *Experimental Evaluation of Bending and Torsional Deformability of FRP Pultruded Beams*. Advanced Composite Materials in Bridges and Structures, Montreal, Quebec.

Cowper, G. R. (1966). "The Shear Coefficient in Timoshenko's Beam Theory." *Journal of Applied Mechanics*: 335–340.

Davalos, J. F., H. A. Salim, et al. (1996). "Analysis and design of pultruded FRP shapes under bending." *Composites Part B:Engineering* **27**(3-4): 295–305.

Dharmarajan, S. and H. McCutchen (1973). "Shear Coefficients for Orthotropic Beams." *Journal of Composite Materials* **7**: 530–535.

Fischer, S., I. Roman, et al. (1981). "Simultaneous Determination of Shear and Young's Moduli in Composites." *Journal of Testing and Evaluation* **9**(5): 303–307.

Frostig, Y., M. Baruch, et al. (1992). "High-Order Theory for Sandwich-Beam Behavior with Transversely Flexible Core." *Journal of Engineering Mechanics-Asce* **118**(5): 1026–1043.

Hayes, M. D. (2003). Structural Analysis of a Pultruded Composite Beam: Shear Stiffness Determination and Strength and Fatigue Life Predictions. *Engineering Mechanics*. Blacksburg, Virginia, Virginia Polytechnic Institute and State University.

Lopez-Anido, R. and H. V. S. GangaRao (1996). "Warping Solution for Shear Lag in Thin-Walled Orthotropic Composite Beams." *Journal of Engineering Mechanics* **122**(5): 449–457.

Madabhusi-Raman, P. and J. F. Davalos (1996). "Static shear correction factor for laminated rectangular beams." *Composites Part B:Engineering* **27**(3-4): 285–293.

Nagaraj, V. and H. V. S. GangaRao (1997). "Static Behavior of Pultruded GFRP beams." *Journal of Composites for Construction* **1**(3): 120–129.

Omidvar, B. (1998). "Shear coefficient in orthotropic thin-walled composite beams." *Journal of Composites for Construction* **2**(1): 46–56.

Restrepo, E. S. (2002). Determination of AASHTO Bridge Design Paramters through Field Evaluation of the Rt. 601 Bridge: A Bridge Utilizing Strongwell 36 in. Fiber-Reinforced Polymer Double Web Beams as the Main Load Carrying Members. *Civil and Environmental Engineering*. Blacksburg, Virginia Polytechnic Institute and State University: 164.

Schniepp, T. J. (2002). Design Manual Development for a Hybrid, FRP Double-Web Beam and Characterization of Shear Stiffness in FRP Composite Beams. *Engineering Mechanics*. Blacksburg, Virginia, Virginia Polytechnic Institute and State University.

Sims, G. D., A. F. Johnson, et al. (1987). "Mechanical and Structural Properties of a GRP Pultruded Section." *Composite Structures* **8**: 173–187.

Strongwell (2000). EXTREN DWB^{TM} Design Guide.

Teh, K. K. and C. C. Huang (1979). "Shear Deformation Coefficient for Generally Orthotropic Beam." *Fiber Science and Technology* **12**: 73–80.

Waldron, C. (2001). Determination of the Design Parameters for the Route 601 Bridge: A Bridge Containing the Strongwell 36 inch Hybrid Composite Double Web Beam. *Civil Engineering*. Blacksburg, VA, Virginia Polytechnic Institute and State University.

FRP Composites in Civil Engineering – CICE 2004 – Seracino (ed)
© 2005 Taylor & Francis Group, London, ISBN 90 5809 638 6

Strength and life prediction for a composite structural beam

M.D. Hayes & J.J. Lesko
Department of Engineering Science and Mechanics, Virginia Tech, Blacksburg, VA, USA

ABSTRACT: The purpose of this study was to develop a tool to assess the long-term durability of a particular composite structural beam developed for the civil infrastructure market. The fatigue performance under transverse loading is of particular interest. A global-local finite element stress analysis was utilized to examine the possibility of both delamination and compression failures. The results of the analysis were compared with experimental test data. Despite the appearance of a delamination failure, the predictions based on the assumption of compression failure proved most successful. Next, a remaining strength approach was followed to predict the fatigue life of the structure. The damage kinetics of the critical and sub-critical elements were modeled using coupon laminate test data. Full-scale fatigue tests were conducted to validate the predictions.

1 INTRODUCTION

Composites are being considered for structural elements such as girders and deck panels in bridge construction as lighter, more durable alternatives to steel and concrete. However, the durability of FRP materials in critical, load-bearing structures under the influence of variable environmental factors is not well understood. Most durability studies have been limited to coupon-level testing, and the development of life predictions for structures based on the kinetics of damage mechanisms in coupon specimens is rare. Furthermore, failure often occurs by buckling or delamination as opposed to fiber fracture. Therefore, macro-level coupon studies may fail to predict the ultimate failure at the structural level. Careful identification of the competing failure mechanisms in the actual structure is crucial to accurate strength and life predictions.

1.1 *Background*

The current study is motivated by the need to understand and predict the performance of a particular structural member that has been developed for the infrastructure market. Strongwell Corporation of Bristol, Virginia has developed a 91 cm (36 inch) deep pultruded double web beam (DWB) for use in bridge construction (Figure 1). The beam is a hybrid laminated composite, composed of both E-glass and carbon fibers in a vinyl ester resin. The DWB is intended for unsupported spans from 9.14 to 18.3 m (30 to 60 feet).

Virginia Tech collaborated with Strongwell, the Virginia Department of Transportation (VDOT), and the Virginia Transportation Research Council (VTRC) to construct a bridge using the 36 inch DWB. The team rehabilitated a short span bridge on Route 601 over Dickey Creek in Smyth County, Virginia with the 36 inch DWB.

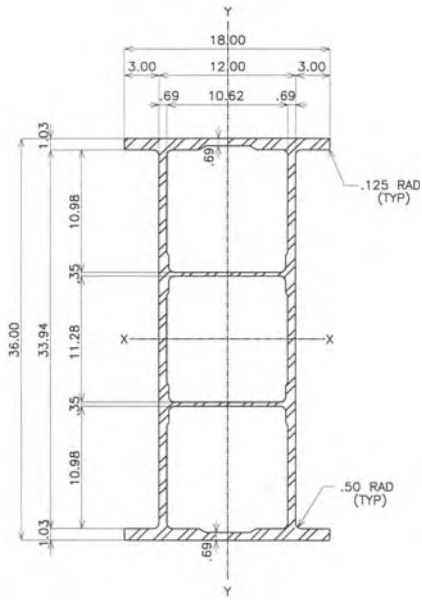

Figure 1. Strongwell's 36 inch DWB (dimensions in inches).

Schniepp (Schniepp 2002) tested nineteen 36 inch DWB's to failure under four-point bending (Figure 2). Tests were conducted on the 36 inch DWB at spans ranging from 5.5 m to 17.7 m to capture any span

Figure 2. Four-point bend test set-up for 36 inch DWB.

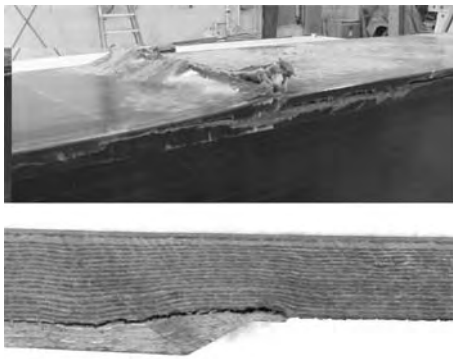

Figure 3. Failure of the compressive flange of a 36 inch DWB.

dependence of the moment capacity. The test set-up included two actuators located at roughly third points with 23 cm (9 inch) long steel-reinforced elastomeric bearing pads at both the supports and at the loading points to reduce the severity of the load concentrations. The failure mechanism was considered to be delamination within the compressive flange (Figure 3), initiating at the load patches. As reported by Schniepp (Schniepp 2002), the shear load at failure followed a linear dependence upon span length or aspect ratio, suggesting that the failure is moment controlled. However, the moment to failure was also found to vary with span.

The flange is relatively thick, and it is comprised of both material and geometric discontinuities, which generate high interlaminar stresses. The lay-up is proprietary, but the flange can be represented as two sub-laminates: the outer sub-laminate essentially consists of alternating layers of unidirectional carbon tows and glass fiber continuous strand mat (CSM), while the inner sub-laminate is formed from half of the web material and is basically a quasi-isotropic lay-up of glass fibers only. Possible delamination initiation sites include the free edge at the interface between the two sub-laminates, where the innermost carbon ply is adjacent to a [0/90] glass fabric, or the inner flange taper.

1.2 *Delamination*

A brief overview of free edge problem and analysis methods was given by Senne (Senne 2000). More exhaustive reviews can be found in (Kant and Swaminathan 2000; Tahani and Nosier 2003). The earliest work by Pipes and Pagano (Pipes and Pagano 1970) and others demonstrated the free edge effect in which large interlaminar stresses can develop at the free edge of a laminate at the interface between two dissimilar plies. These stresses decay over some distance away from the edge (the "boundary layer"), and if the loading is in-plane, the plane stress state predicted using CLT is recovered. The phenomenon is due to mismatches in Poisson's ratio and coefficients of mutual influence between adjacent plies. Later work revealed that the stresses can be singular at the free edge (Pagano and Pipes 1971; Wang and Crossman 1977).

Large interlaminar stresses can also develop at internal or external ply drop-offs. A review of analytical and numerical modeling studies of ply drop-offs and tapered laminates was given by He et al. (He, Hoa et al. 2000). A number of studies have confirmed that the interlaminar normal and shear stresses also control failure in these situations and that singular stresses occur in the corner regions of a "stepped" drop-off (Wu and Webber 1986; Her 2002).

Stress-based criteria for delamination initiation require accurate stress calculations and interlaminar strength measurements, both of which can be difficult. An alternate approach to strength prediction is to use fracture mechanics concepts in which the nature of the stress field around an existing crack tip is considered. This energy based approach was not considered in the current study due primarily to difficulties in measuring the critical strain energy release rate (Hayes 2003).

1.3 *Fatigue life prediction*

Predictions developed for fatigue durability are most commonly based on residual strength degradation. In this approach, fatigue failure is assumed to occur when the residual strength is equal to the applied stress. In particular, Reifsnider and Stinchcomb (Reifsnider and Stinchcomb 1986) postulated that remaining strength is a state variable and can be used as a measure of the damage. The remaining strength will depend upon the load level and number of fatigue cycles (or time). In general, the reduction in strength can be non-linear, so that the sequence of damage events can affect the length of life. The ability of this approach to capture such path-dependence is a distinct advantage over linear type models such as Miner's rule for metals.

In Reifsnider's approach, the remaining strength of a "critical element" governs the life of the entire structure. Examples of critical elements include the 0° plies in a [0/90] laminate loaded axially or the boundary

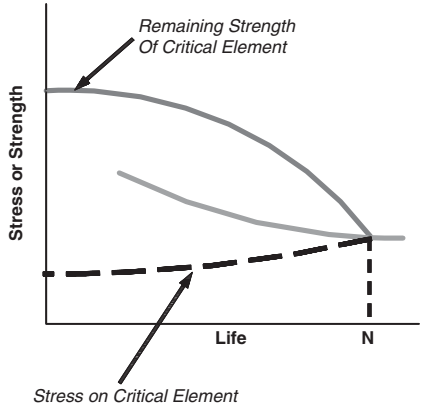

Figure 4. Residual strength approach to life prediction.

layer in a delamination problem. The remainder of the material, e.g. the 90° plies, comprises the "sub-critical elements". Degradation of the sub-critical elements serves only to redistribute the stress to the critical elements, eventually causing ultimate failure of the structure.

Using a non-linear kinetic/rate equation to describe the damage processes in the critical element, Reifsnider and his coworkers derived a strength evolution integral which has been tested extensively for a variety of problems and materials. This equation has the form

$$Fr = 1 - \int_0^{\tau} (1 - Fa) j \tau^{j-1} d\tau \qquad (1)$$

where Fr is the normalized remaining strength, Fa is the applied stress (or more generally, the failure function such as maximum stress, Tsai-Hill, etc.), τ is a characteristic time which describes the damage process, and j is considered to be a material constant. Thus, the equation can be applied to creep or other time-dependent processes. For the case of fatigue, $\tau = n/N$, where n is the number of fatigue cycles and N is the number of cycles to failure for the given Fa. Note that as damage occurs in the sub-critical elements, the stress level in the critical element increases, and Fa increases with time or cycles.

To apply the strength evolution integral to predict fatigue life, the fatigue S-N curve for the critical element is required, along with stiffness changes in the sub-critical elements due to fatigue cycles.

1.4 *Summary*

The first objective of this study is to identify the failure mechanism of the DWB. The second objective is to predict the fatigue life of the DWB as tested under transverse loading, using the remaining strength and critical element concepts. Failure is hypothesized to occur by delamination at either the free edge or the inner flange taper. The possibility of compression failure of the carbon fiber plies is also investigated.

2 STRENGTH PREDICTION: METHODS

Observations from the static failure tests by Schniepp (Schniepp 2002), post-failure inspection of the beams, and finite element analysis were used to attempt to identify the controlling failure mechanism for the DWB. The plausibility of compression failure was investigated using a 3-D global FE model of the DWB. To investigate the possibility of a delamination failure, a global-local FE solution was developed using a successive sub-model approach. The use of local sub-models allows a more detailed representation of the regions, which is necessary when calculating interlaminar stresses. The free edge and flange taper regions near the load patch were considered as potential "critical elements". The critical stresses were expected to be the interlaminar normal stress, σ_z, and the interlaminar shear stress, τ_{xz} where the x-axis is along the beam's length, the y-axis is across the width of the beam, and the z-axis is through the depth of the beam, in the direction of loading.

2.1 *Finite element analysis*

FE models of the DWB under four-point loading geometry for spans of 9.14, 11.9, and 17.7 m (18, 30, 39, and 58 ft) were constructed in ANSYS®. The walls of the beam were modeled using the SOLID46 element, a 3-D 8-noded layered solid brick/continuum element. Next, a sub-model was constructed to model the local behavior of the flange under and near a load patch. The free edge was idealized with perfectly flat and uniform plies.

The procedure actually consisted of two sub-modeling steps. In the first step, a small section of the top flange centered at the edge of the pad was modeled (EDGESUB1). The pad and plate volumes and the applied pressure on the steel plate were included. EDGESUB1 was meshed using solid 3-D elements with each ply was modeled as a single layer of elements. Even greater mesh refinement using multiple elements per ply is recommended to obtain accurate interlaminar stresses, but this becomes computationally intensive for very thick laminates as the DWB flange.

In order to provide additional refinement at the free edge, where gradients in stress are known to be very large, a second sub-model, EDGESUB2, was constructed. This sub-model was a 2.54 cm long

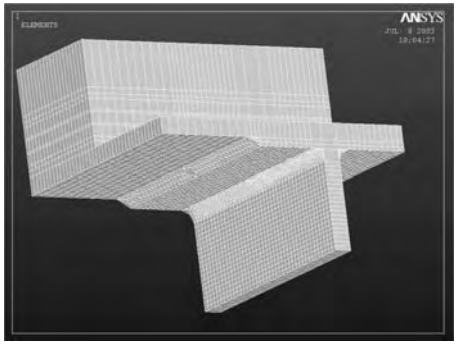

Figure 5. FE submodel (TAPERSUB2) used in taper analysis.

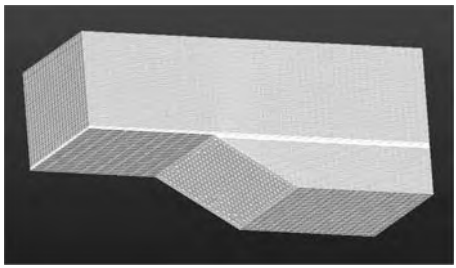

Figure 6. TAPERSUB3 used in the taper analyses.

by 2.54 cm wide by 2.62 cm thick (1 inch × 1 inch × 1.032 inch) volume that could be positioned along the free edge at any location of interest within the region modeled using EDGESUB1. Submodel boundary conditions were obtained from the nodel results along the cut boundary as determined in the previous submodel or model.

To assess the influence of thermal residual stresses and to estimate the failure load, the thermal and mechanical loadings were simulated separately. The thermal only loading was modeled by applying the change in temperature $\Delta T = -205°F$ ($-114°C$) and a very small load to the load patch. The mechanical loading was modeled by applying 445 kN (100 kips) per patch and setting $\Delta T = 0$. The two effects were then combined via superposition.

A similar successive sub-modeling approach was used to model the flange taper region (Figure 5 and Figure 6).

2.2 *Strength prediction*

2.2.1 *Compression failure*

The maximum stress failure criterion was applied to the outer carbon fiber ply in the top flange. The stresses along the length of the beam were determined from the appropriate global models for each test geometry considered. The failure loads were predicted by scaling the mechanical stresses and determining the load at which $Fa = 1$.

Compressive strength data for the carbon/vinyl ester plies were obtained by testing 26 specimens machined from the outer flange sublaminate, which is composed of carbon fiber and CSM. The Wyoming End-Loaded Side Supported (ELSS) test method (Adams and Finley 1997) was chosen due to its relative ease of use. Classical laminate theory was used to back calculate the carbon ply stresses at the failure load of each specimen. The resulting strength was found to be low relative to other available date (Lesko 1994; Verghese 1999).

2.2.2 *Free edge delamination failure*

Due to the sudden, catastrophic failure mechanism observed experimentally, ultimate failure was defined as the onset of delamination, as determined using the Quadratic Strength Criterion:

$$\left(\frac{\sigma_{zz}}{S_z}\right)^2 + \left(\frac{\tau_{xz}}{S_{xz}}\right)^2 + \left(\frac{\tau_{yz}}{S_{yz}}\right)^2 = 1 \qquad (2)$$

Following the average stress approach of Whitney and Nuismer (Whitney and Nuismer 1974) and Kim and Soni (Kim and Soni 1984), the interlaminar stresses at the free edge were averaged over a characteristic length across the width of the flange. This length was taken as the length over which the normal stress remains tensile, e.g. from the free edge to the point that the normal stresses changes sign. Again, the average stresses due to mechanical and thermal loading were superimposed, and the mechanical contribution was scaled to obtain the predicted failure load at $Fa = 1$.

The interlaminar tensile strength S_z was taken from the work of Williams et al. (Williams, Hayes et al. 2002), which utilized a tensile pull-off test method. The interlaminar shear strength S_{xz} of the flange material was estimated using the short beam shear (SBS) three-point bending test coupled with FEA.

2.2.3 *Taper delamination failure*

A similar procedure was followed to assess failure at the taper location. However, due to the strength of the taper wedge singularities, the stress concentrations were observed to decay over a much larger distance than the free edge singularity. In the free edge problem, the free edge stresses can quickly change magnitude and sign through the thickness of the laminate as the ply properties or orientations change. In the drop-off problem, all of the surrounding plies above and below the geometric discontinuity experience high stress levels. Therefore, the concept of volume

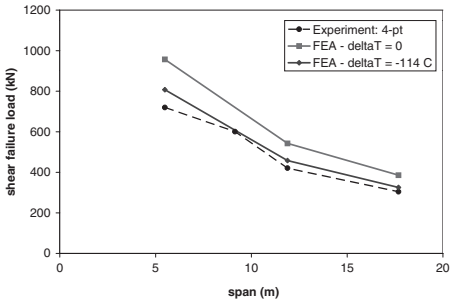

Figure 7. Comparison of the predicted shear capacity vs. span for the compressive failure mode and the experimental results.

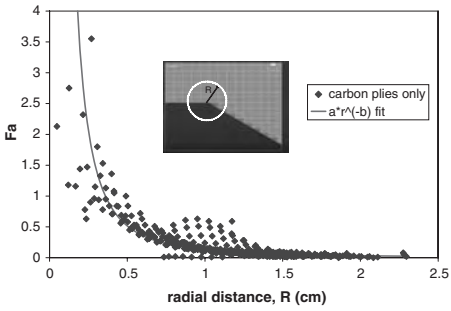

Figure 8. Fa in carbon plies in the taper region as a function of distance from the free edge of the taper.

averaging was utilized as an alternate means of predicting the strength. This concept also captures the observed effect that delamination strength is dependent upon the laminate thickness (O'Brien 1987), i.e. delamination resistance is volume-dependent.

To volume average the stresses within a certain radial distance of the taper's end, the stresses from each element were inserted into the Quadratic Strength Criterion to calculate the element failure function *Fa*. The product of *Fa* and the element volume for each element were then summed, and the average *Fa* value was obtained by simply dividing by the total volume of the elements. The resulting failure function versus distance is shown in Figure 8 for the 11.9 m case. The data points were empirically fit with a power law curve, which is the form of the stress concentration encountered in fracture mechanics. A length of 1.75 cm (0.688 inch), the thickness of the outer flange sub-laminate, was chosen as the characteristic averaging length. This length corresponds to about a 95% decay of the stress concentrations.

3 STRENGTH PREDICTION: RESULTS

3.1 *Compression*

The predicted shear loads at failure for the compression failure mode are plotted against the experimental data in Figure 7. Excellent agreement is found between the FEA prediction and the experimental results, and the span dependence of the moment capacity is also captured. It is noted that the load patch causes a stress concentration equal to approximately $Fa = 0.12$, an increase of between 10 and 30% over the mid-span stress level, depending upon the span.

3.2 *Free edge delamination*

At the primary carbon-glass interface, the normal stress σ_z was observed to become tensile at a short distance away from the free edge and then decrease to a compressive (singular) value at the free edge. Averaging over the tensile region, the maximum value of σ_z (occurring just inside the pad) was very low: only 262 kPa (38 psi) for the 11.9 (39 ft) span length. Similarly, the width-averaged shear stresses τ_{xz} and τ_{yz} were found to be relatively low.

On the other hand, the FE results indicate very high tensile normal stresses at the free edge in some of the glass plies. For example, large interlaminar normal and shear (τ_{xz}) stresses were observed at the interfaces between the $\pm 45°$ plies. Averaging over the tensile region only, the average interlaminar normal stress is 8.83 MPa (1280 psi). This high value suggests failure may occur within the all-glass portion of the flange (sub-laminate 2), contrary to experimental observations.

3.3 *Flange taper delamination*

The maximum stresses at the taper were found to be located just outside the load patch. A contour plot of the interlaminar normal stress σ_z at the tip of the flange taper is shown in Figure 9. The figure indicates stress concentrations at not only the end of the taper, but also at two locations within the all-glass inner sublaminate. These last two locations correspond to interfaces between 0 and 45° plies.

Despite relatively good agreement at the 12.2 and 18.3 m (40 and 60 ft) spans, the predicted strength at the 6.10 m (20 ft) span was in gross error of the experimental results. Furthermore, the stress profiles were found to be very sensitive to the characteristic averaging length, which in turn was very sensitive to the presence of residual thermal stresses. Additionally, high stresses were observed in the all-glass region, although failure was never observed to occur at this interface in the laboratory. The alternate, volume averaging method yielded similar problems.

Figure 9. Contour plot of interlaminar-normal stress σ_z in the flange taper region.

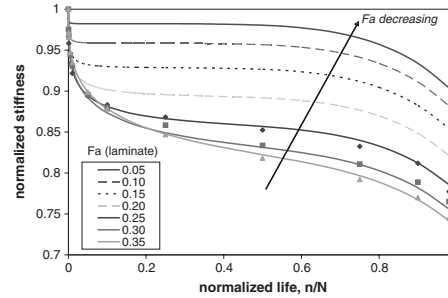

Figure 10. Estimated stiffness reduction curves extrapolated from the dynamic stiffness data of (Post and Bausano 2003).

3.4 *Summary*

The results of the failure analysis of the DWB suggest that the failure in four-point loading occurs by compression failure of the carbon fiber plies in the top flange near a load patch. The high compressive stresses, coupled with the relatively low measured compression strength for the carbon fiber plies leads to a relatively simple strength prediction. The evidence for compression failure is further reinforced by the span-dependence of the moment capacity.

While the failure has the appearance of a delamination event, the detailed analyses conducted in this study do not support this hypothesized failure mode. The free edge analyses at the 11.9 m (39 ft) span indicate relatively small interlaminar stresses at the primary carbon/glass interface. Furthermore, in both cases, large interlaminar stresses were predicted within the all-glass inner flange sub-laminate at a location not consistent with the observed failure surfaces. Furthermore, the results of the delamination analyses are considered inconclusive due to the sensitivity of the free edge stresses to mesh refinement, lay-up, material properties, and thermal effects, as well as the considerable material variability in the actual beam.

4 FATIGUE LIFE PREDICTIONS

To develop fatigue life predictions for the DWB, the global finite element model developed in the previous sections was integrated into a code that accounts for stiffness reductions with fatigue cycles due to matrix cracking in the off-axis plies of the tensile flange (sub-critical elements). Empirical expressions for the stiffness reduction were taken from glass/vinyl ester coupon data. The remaining strength of the critical element, the carbon fiber in the top flange, was tracked using the approach of Reifsnider et al. (Reifsnider and Stinchcomb 1986).

Only the outermost ply was tracked, as the outer fibers experience the largest axial strain in bending. The variation of *Fa* in the carbon fiber plies along the length of the beam was recorded at each cycle, but the maximum value near the load patch controlled failure. The remaining strength of each critical element was calculated using an iterative form of the remaining strength evolution integral suggested by Case (Case 2003).

The fatigue life of the carbon fiber plies was taken from fatigue data by Verghese (Verghese 1999) for the case of notched unidirectional laminates comprised of unsized carbon fibers in a vinyl ester matrix with a volume fraction between 55 and 59% fatigued at 10 Hz and a load ratio $R = -1$ (tension-compression). The data was fit to a log-linear form suggested by (Reifsnider and Case 2002) and extrapolated to lower stress levels (neglecting any endurance limit).

4.1 *Off-axis stiffness reductions*

Following the work of Senne (Senne 2000), stiffness reduction due to matrix cracking was assumed to occur only in the tensile flange and in the tensile sub-flange. Furthermore, damage was only assumed to occur in the off-axis uni-directional glass plies. Coupon level stiffness reduction data for quasi-isotropic glass/vinyl-ester laminates was obtained from Post et al. (Post and Bausano 2003), as shown in Figure 10.

The data indicate a clear stress level dependence. To apply the data, however, it is necessary to estimate the ply-level stresses or failure functions *Fa(ply)* in the off-axis plies which are degrading over time. Classical laminate theory and the maximum stress criterion were used to back-calculate *Fa(ply)* as a function of the laminate levels, *Fa(lam)*. However, the CLT analysis indicated that the failure functions in the off-axis plies of the test laminates were much than those of the DWB. Therefore, the coupon level stiffness reduction data was extrapolated to the lower stress levels.

Using non-linear regression, the data was fit to the following form, similar to that used commonly in the area of visco-elasticity to model reductions in mechanical properties caused by temperature changes (Aklonis, MacKnight et al. 1972):

$$\hat{E} = \left(\hat{E}_1 - \hat{E}_2\right)\exp\left[-\left(\frac{\hat{n}}{N_1}\right)^{m_1}\right] + \left(\hat{E}_2\right)\exp\left[-\left(\frac{\hat{n}}{N_2}\right)^{m_2}\right]$$

$\hat{E}$ is the normalized stiffness, which is a function of the normalized life, $\hat{n}$. The other parameters are empirically fit.

The *Fa(ply)* values vary along the length of the beam, because of the gradient in moment resultant. It would be impractical to attempt to apply separate stiffness reductions to each element, so a simpler scheme was taken. The half-span length was divided into 10 zones, so that the change in strain in any given zone was around 10%. The stresses for all elements in a zone were averaged to obtain an average zone stress level, and the appropriate extrapolated stiffness reduction curve was applied.

This procedure was employed to generate a fatigue-life (*S-N*) curve for the DWB under the transverse loading at the 11.9 m (39 ft) span length. Normalized stiffness reduction curves for the effective bending modulus of the DWB were constructed using the maximum deflection at mid-span for each cycle increment.

4.2 *Fatigue tests*

Two DWB's were tested in fatigue using MTS actuators and control system. The first beam was tested in four-point geometry with loads applied at the third points, as in the static testing. The beam length was slightly over 12.2 m (40 ft). The beam was loaded to a maximum deflection equal to 1.52 cm (0.6 inches), approximately two times the maximum predicted service deflection in the Route 601 Bridge. The corresponding load was 133 kN (30 kips) per actuator, which corresponds to about 30% of the ultimate static failure load (94.5 kips). A load ratio of $R = 0.1$ and a frequency of 1.1 Hz was used. The second beam was loaded to approximately 60% of the ultimate failure stress. A three-point loading geometry with a larger 890 kN (200 kip) actuator was necessary to apply the higher load.

In both tests, stiffness reduction was monitored by periodically interrupting the fatigue cycling to perform quasi-static loading tests. During the quasi-static tests, the axial flange strains were measured and the effective bending modulus was calculated. This yields the change in the actual bending stiffness only, which is slightly different than the change in effective bending stiffness calculated using the FEA results.

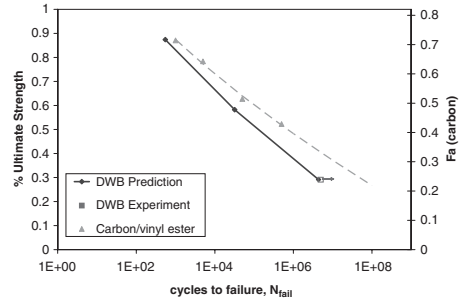

Figure 11. Predicted fatigue life curve, compared with experimental data and coupon data (Verghese 1999).

4.3 *Results*

The resulting fatigue life curve for the 11.9 m (39 ft) four-point test geometry is shown in Figure 11. The results suggest that at the 133 kN (30 kip) load level, failure is predicted to occur at 4.4 million cycles, while the experimental test (indicated as a run-out in the figure) was stopped 4.9 million cycles with no signs of damage. The second beam tested at the 363 kN (81.6 kip) load level was predicted to fail at 32,000 cycles, but the beam had not failed after 72,000 cycles.

The predicted stiffness reductions are quite small, e.g. a maximum of only 0.5% at the 133 kN (30 kip) load level. The result is that the stress level in the critical element, the carbon plies, essentially remains constant over the entire life of the beam. This fact makes the life prediction trivial, as the cycles at failure can be estimated by simply determining *Fa* from the stress analysis and picking off the cycles at failure from the *S-N* curve for the carbon/vinyl ester ply.

It is important, however, to consider the effect of the stress concentration on the fatigue life. A 30 to 45% increase in the carbon ply *Fa* at the load patch may decrease the fatigue life by one or two decades on a logarithmic scale. Therefore, the use of beam theory which cannot capture this effect will cause large errors in the predicted fatigue performance.

5 CONCLUSIONS

A strength based approach to predict delamination onset was followed in which average interlaminar stresses at the critical locations were compared to the interlaminar strengths using the Quadratic Strength Criterion. Detailed finite element analysis of the free edge, utilizing successive sub-models, did not indicate failure at that location. The analysis of the taper region was inconclusive, as the ply-averaged stresses were found to be very sensitive to the definition of the characteristic length.

On the other hand, the predicted beam strengths assuming compression failure in the carbon plies of the top flange demonstrated excellent agreement with the experimental data. In addition, this analysis was able to capture the span dependence of the moment capacity which was observed experimentally. Therefore, despite the appearance of a delamination failure, the analyses suggest that the actual failure mode is compression.

Based on the assumption of compression failure, a fatigue life prediction was conducted using a remaining strength damage model. Stiffness reductions in the off-axis plies of the tensile flange and sub-flange were modeled using data extrapolated from coupon tests, but the resulting change in the stress level of the critical element was negligible. Therefore, the life at a given applied load level can be predicted simply by determining the stress level in the carbon plies and determining the corresponding cycles to failure from the fatigue curve for the carbon/vinyl ester material. The validity of the prediction has not yet been verified due to limited fatigue test data.

REFERENCES

Adams, D. F. and G. A. Finley (1997). "Analysis of Thickness-Tapered Unidirectional Composite Compression Specimens." *Journal of Composite Materials* **31**(22): 2283–2308.

Aklonis, J. J., W. J. MacKnight, et al. (1972). *Introduction to Polymer Viscoelasticity*. New York, Wiley-Interscience.

Case, S. (2003). Personal Communication: Alternate Forms of the Strength Evolution Integral.

Hayes, M. D. (2003). Structural Analysis of a Pultruded Composite Beam: Shear Stiffness Determination and Strength and Fatigue Life Predictions. *Engineering Mechanics*. Blacksburg, Virginia, Virginia Polytechnic Institute and State University.

He, K., S. V. Hoa, et al. (2000). "The Study of Tapered Laminated Composite Structures: a Review." *Composites Science & Technology* **60**: 2643–2657.

Her, S. -C. (2002). "Stress Analysis of Ply Drop-off in Composite Structures." *Composite Structures* **57**: 235–244.

Kant, T. and K. Swaminathan (2000). "Estimation of Transverse/interlaminar Stresses in Laminated Composites – a Selective Review and Survey of Current Developments." *Composite Structures* **49**: 65–75.

Kim, R. Y. and S. R. Soni (1984). "Experimental and Analytical Studies on the Onset of Delamination in Laminated Composites." *Journal of Composite Materials* **18**: 70–80.

Lesko, J. J. (1994). Interphase Properties and Their Effects on the Compression Mechanics of Polymeric Composites. *Engineering Mechanics*. Blacksburg, Virginia, Virginia Polytechnic Institute and State University.

O'Brien, T. K. (1987). "Generic Aspects of Delamination in Fatigue of Composite Materials." *Journal of the American Helicopter Society* **32**: 13–18.

Pagano, N. J. and R. B. Pipes (1971). "The Influence of Stacking Sequence on Laminate Strength." *Journal of Composite Materials* **5**: 50–57.

Pipes, R. B. and N. J. Pagano (1970). "Interlaminar Stresses in Composite Laminates Under Uniform Axial Extension." *Journal of Composite Materials* **4**: 538–548.

Post, N. and J. Bausano (2003). Personal communication: Stiffness reduction data for a glass/vinyl ester laminate.

Reifsnider, K. and W. W. Stinchcomb (1986). A Critical Element Model of the Residual Strength and Life of Fatigue-Loaded Composite Coupons. *Composite Materials: Fatigue and Fracture, ASTM STP 907*. H. T. Hahn. West Conshohocken, PA, American Society for Testing and Materials: 298–303.

Reifsnider, K. L. and S. W. Case (2002). *Damage Tolerance and Durability of Material Systems*. New York, Wiley-Interscience.

Schniepp, T. J. (2002). Design Manual Development for a Hybrid, FRP Double-Web Beam and Characterization of Shear Stiffness in FRP Composite Beams. *Engineering Mechanics*. Blacksburg, Virginia, Virginia Polytechnic Institute and State University.

Senne, J. (2000). Fatigue Life of Hybrid FRP Composite Beams. *Engineering Science and Mechanics*. Blacksburg, Virginia Tech.

Tahani, M. and A. Nosier (2003). "Free Edge Stress Analysis of General Cross-ply Composite Laminates Under Extension and Thermal Loading." *Composite Structures* **60**: 91–103.

Verghese, K. E. (1999). Durability of Polymer Matrix Composites for Infrastructure: The Role of the Interphase. *Materials Engineering Science*. Blacksburg, VA, Virginia Polytechnic Institute and State University.

Wang, A. S. D. and F. W. Crossman (1977). "Some New Results on Edge Effects in Symmetric Composite Laminates." *Journal of Composite Materials* **11**: 92–106.

Whitney, J. M. and R. J. Nuismer (1974). "Stress Fracture Criteria for Laminated Composites Containing Stress Concentrations." *Journal of Composite Materials* **8**: 253–265.

Williams, B. Y., M. D. Hayes, et al. (2002). Measurement of the Interlaminar Strength of the 36" Double Web Beam Flange. Blacksburg, VA, Virginia Tech: 11.

Wu, C. M. L. and J. P. H. Webber (1986). "Analysis of Tapered (In Steps) Laminated Plates Under Uniform Inplane Load." *Composite Structures* **5**: 87–100.

Durability

FRP Composites in Civil Engineering – CICE 2004 – Seracino (ed)
© 2005 Taylor & Francis Group, London, ISBN 90 5809 638 6

The response and modeling of composite structures under fire exposure

S. Boyd, J. Bausano, J. Lesko & S. Case
Virginia Tech, Blacksburg, VA, USA

H. Halverson
The University of Connecticut, Storrs, CT, USA

ABSTRACT: In this work, we describe our attempts to characterize and model the response of structural composite materials subjected to fire loading conditions. Experimental and modeling results are presented for E-glass/DERAKANE 510A composites subjected to compression loading with a one-sided heat flux. In addition, shear compliance curves are presented a function of temperature to support the modeling of the compression creep and strength response. Finally, we model the response of a structural composite bulkhead subjected to fire loading conditions. Measured in-plane and out-of-plane responses are compared with those predicted using a finite element analysis with temperature dependent material properties. Deficiencies in the modeling effort are discussed.

1 INTRODUCTION

As composites enter the civil infrastructure in the form of repair, strengthening, decking and exposed structural members, the need for understanding how these systems respond structurally to fire exposure becomes necessary. As an example of how to account for fire exposure on a structural system this paper addresses some of the issues relevant to the structural response of fiber reinforced polymer composite sandwich structures with balsa cores subjected to fire exposure. These materials might be utilized in Navy deck house such as floors and bulk-heads. As a general approach we seek in this developing program to understand the physics of fire damage in E-glass/vinyl ester material composite systems. Ultimately, we seek to develop an understanding of how these fundamental phenomena influence structural behavior under fire exposure.

From a practical stand point, design engineers have expressed concerns about the integrity of FRP bridge structures exposed to fire. For buildings the same has held true, however these has been some guidance. The building community, when examining walls and columns strengthened with FRP retrofits for seismic considerations, have relied on the ASTM equivalents to the Uniform Building Code (UBC) as a qualification for building materials when considering fire. Specifically, the standards for fire resistance (ASTM E119 = UBC 43-1), flame-spread and smoke density (ASTM E84 = UBC 42-1) and non-combustibility of building materials (ASTM E136 = UBC 4-1) form the basis for selecting building materials.

As of yet, there are no comprehensive codes, or guidelines for specifying codes, concerning fire resistance and structural integrity. This is with exception to safety provisions in the ACI 440F code which requires a new factored nominal moment larger than 1.2 dead plus 0.85 live load to address structural integrity of bonded repairs. More comprehensive and validated guidelines will be required as routine use of these materials is sought. Such provisions will be introduced as the industry matures and other FRP housing structures are designed and evaluated for routine use.

A considerable amount of work has been undertaken to examine materials that do hold promise under conditions of fire, e.g., the phenolic matrices. Mechanics that describe the thermochemical and the resulting mechanical properties have been expanded over the years (first studied by Bumford et al., 1946). This work has motivated examination of fire durability and mechanical integrity in anisotropic composites (Griffis et al., 1981; Griffis et al., 1986; Henderson & Wiecek, 1987; Milke & Vizzini, 1991; McMannus & Springer, 1992a, 1992b; Caplan et al. 1996). Although the community still lacks a complete description of relationships between polymer composition/microstructure and fire behavior (Sorathia et al., 1996), some success at combining the thermochemical processes to residual physical properties of composites has been achieved.

Given the examination of the thermal-physical nature of the material itself, there has also been a considerable amount of work done to understand the materials aspects of how polymeric composites respond to fire in terms of heat of ignition, self

extinguishing characteristics, and heat release rate (Kinsella et al. 1997; Gibson et al., 1994). Yet with these works together, little has been accomplished to understand the effects of fire on the structural properties and how to model such effects. Thus, the main feature of our current effort is the accurate combination of all aspects of the thermal and structural problem. Thermal boundary conditions resulting from a fire simulation (FDS) are used to define the residual thermal-mechanical-damage response of the material, and therefore the structural capacity during and post fire can be predicted using the ANSYS analysis.

Again, this example analysis is conducted on a quasi-isotropic E-glass fiber reinforced vinyl ester polymer composite (12 mm thick face sheets) sandwich structures with balsa cores (end on 3" thick) subjected to fire exposure much like the systems under investigation for U.S. Navy deck house applications (e.g. floors and bulkheads). The procedure and methods employed are applicable to other systems more in line with civil applications given the availability of property evolution information as a function of temperature. Thus, we begin this discussion with the details of thermal physical mechanical material properties for those material systems used in the study. We then discuss the specific bulkhead structure, the testing conducted and the subsequent modeling and comparison of results.

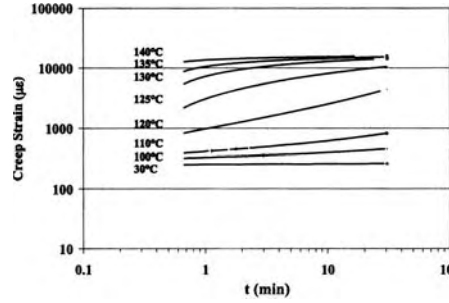

Figure 1. Shear creep strain at a shear stress of 1.38 MPa.

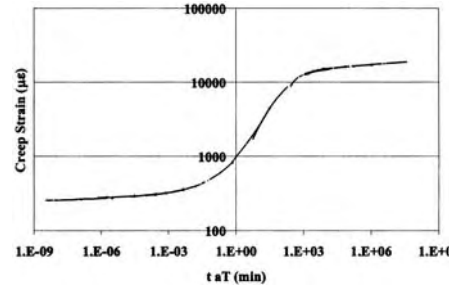

Figure 2. Shear creep master curve for E-glass/DERAKANE 510A.

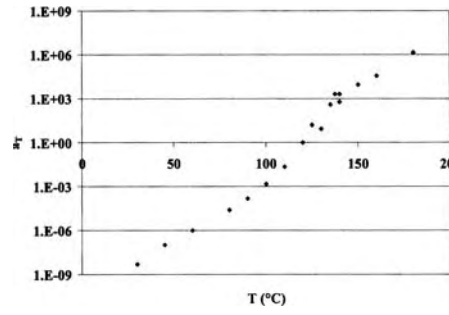

Figure 3. Temperature shift factor plot for E-glass/DERAKANE 510A.

2 VISCOELASTIC CHARACTERIZATION

In order to accurately describe structural response and to predict local composite failure, it is essential that we have an understanding of the viscoelastic response of the material. To develop such an understanding, we have been conducting short-term creep and recovery tests on panels of a $[\pm 45]_{2S}$ composite made using Derakane 510A and Saint-Gobain/Vetrotex 24 oz./yd^3 E-glass woven roving (using the VARTM process). The results of such tests, conducted at shear stress of 1.38 MPa, are shown in Figure 1. We may then reduce the results and create a shear creep compliance master curve, as illustrated in Figure 2 (using standard principles of time–temperature superposition). The corresponding temperature shift factor plot is then given in Figure 3.

3 ONE-SIDED HEAT FLUX TESTS

The motivation for conducting this test is to characterize the response of a composite exposed to a worst case scenario. The test combines elevated temperatures with mechanical loading. The mechanical loading was a constant compressive load. Compression was chosen because the matrix polymer is highly dependent on the temperature and dominates the compression and buckling failure modes. That is, the compression properties are affected more by elevated temperatures than are fiber dominated tensile properties. Also many applications of composites are subject to compressive loading situations and investigations into the mechanisms of there response and collapse under combined loading must be determined.

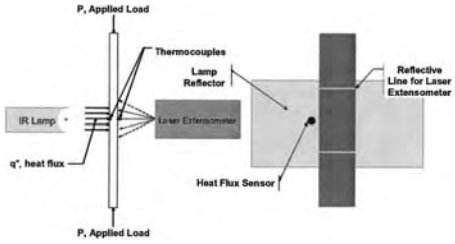

Figure 4. Combined thermal and mechanical loading setup.

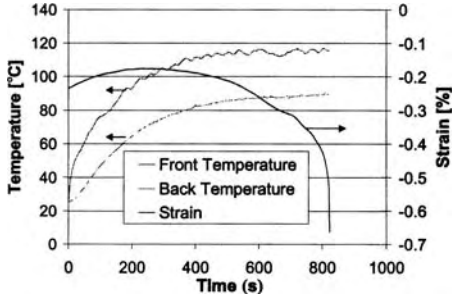

Figure 5. Experimental temperatures and strain.

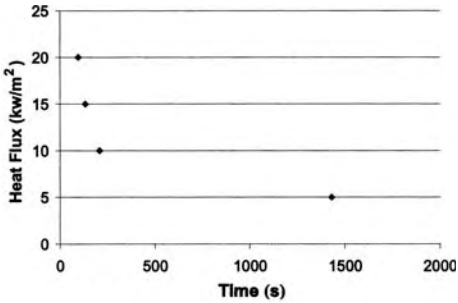

Figure 6. Heat flux versus time to failure for a sustained compressive stress of 57 MPa.

3.1 *Test description*

The test was performed using multiple load applicators (thermal and mechanical), and was instrumented to record various test parameters over the duration of the test. The samples were 6.4 mm thick and were machined to approximately 100 mm long by 25 mm wide. Samples were subjected to compressive stress levels from 20 to 100 MPa, while also being exposed to a steady heat flux of 5 to 30 kW/m^2. The samples were first gripped longitudinally in a servo – hydraulic testing frame, exposing a 50 mm gage length. A constant compressive load was then applied to the sample. After the compressive load was ramped to its final constant value, an IR strip heater manufactured by Research Inc. applied a constant heat flux to one side of the sample as depicted in Figure 4. The IR heater uses a quartz lamp and a parabolic reflector to produce an approximately uniform heat flux. The samples were painted black with a high temperature manifold paint to achieve an absorptivity of approximately 0.95. Multiple gages and probes were used to monitor and control the test. Front (side exposed to the heat flux) and back side temperatures were recorded using small gage K-type thermocouples that were adhered to the surface using a dot of a standard epoxy. The applied heat flux was monitored and recorded using a Vatell HFM7-E/H heat flux gage that was mounted to the side of the sample. To achieve a constant applied heat flux, the gage was monitored during each run; if the heat flux drifted the power to the lamp was adjusted accordingly to keep the heat flux as stable as possible. The strains on the back side of the sample were measured with a non-contact laser extensometer manufactured by Fiedler Optoelektronik GmbH of Germany, over a gage length of approximately 45 mm. The laser extensometer used two reflective strips placed on the sample as references for the strain measurement. A standard 89 kN load cell was used to monitor the applied mechanical loads. All data channels were wired into a National Instruments Multiplexor Data Acquisition System, the system allowed for the real time monitoring of the variables and storage of the data.

3.2 *Test results*

Results for a typical one-sided heat flux test that was conducted at constant heat flux of 5 kW/m^2 and compressive stress of 57 MPa is presented in Figure 5. At time 0 seconds the heat flux was applied and the front and back face temperatures began to increase. For the first 250 seconds the specimen expanded due to the increases in temperature, which can be seen from the positive increase in strain in Figure 5. After 250 seconds the elevated temperature distribution of the specimen induced significant stiffness loss. The strain began to decrease due to this stiffness loss. Once the strain began to decrease, small wrinkles started to form on the surface exposed to the heat flux. The strain continued to decrease until the specimen ultimately failed.

The influence heat flux level has on times to failure was examined. Multiple samples were tested under the same compressive stress of 57 MPa, but the heat flux was varied form 5 to 20 kW/m^2. As expected the times to failure decrease as the applied heat flux is increased (Figure 6). The samples exposed to the higher heat fluxes reach elevated temperatures faster and therefore become more compliant quicker which resulted in quicker failures. The times to failure steadily increased

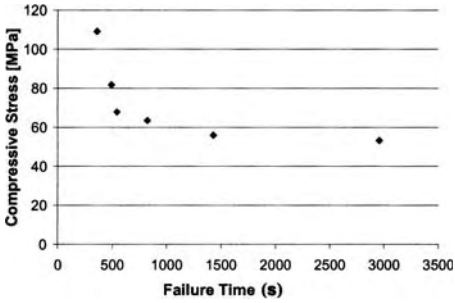

Figure 7. Times to failure vs. compressive stress.

as the heat flux was lowered from 20 to 10 kW/m^2, but at 5 kW/m^2 the time to failure increased by a factor of 7. The samples tested at the higher heat fluxes continued to increase in temperature throughout the experiment but, the sample tested at 5 kW/m^2 achieved thermal equilibrium. This suggests that the failure of the sample that was tested at 5 kW/m^2 failed due to creep, not just temperature effects.

The effect of the stress level had on the times to failure of specimens exposed to a heat flux of 5 kW/m^2 was investigated and the results are shown in Figure 7. As the applied stress in increased the failure times decrease.

4 STRUCTURAL RESPONSE MODELING

The final portion of our effort has been devoted to integrating our knowledge of material property changes into a structural analysis package to describe the behavior of structural composites subjected to fire. As an example, we consider a 2.7 m × 4.3 m (9 ft. × 14 ft.) interior bulkhead with stiffeners loaded at the top edge (6000 lbs./ft.) and exposed to a UL 1709 profile in a vertical furnace. The bulk-head and the stiffeners consist of a 90 mm (3.5") balsa core sandwiched by 6.4 mm (1/4") composite panels. Placed on the surface of the structure exposed to the temperature profile are two layers of 15.9 mm (5/8") Structo-gard insulation. On the test article are a total of 34 thermocouples and three deflection meters. Fourteen thermocouples were placed on the unexposed composite surface with varying degrees of additional insulation to simulate the effect of material placed against the wall (Figure 8), and are not germane to this analysis.

Seven thermocouples are used to obtain a temperature profile through the bulkhead. Four are placed at the interfaces (insulation/insulation, insulation/composite, and two balsa/composite), two are on the outer wall surfaces, and a seventh is located in the

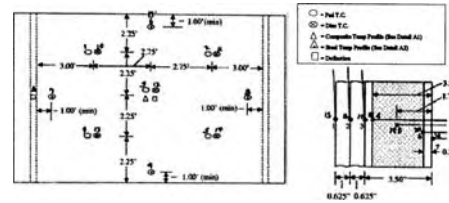

Figure 8. Bulkhead test article and associated instrumentation.

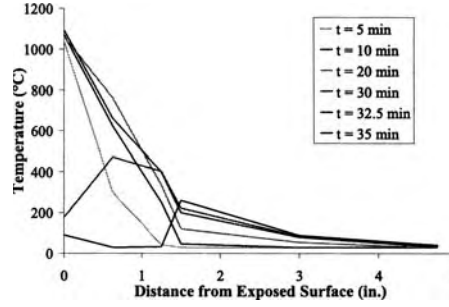

Figure 9. Temperature profile in the bulkhead as a function of time.

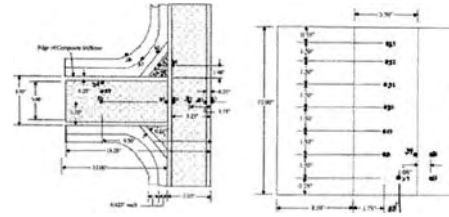

Figure 10. Thermocouple locations.

center of the balsa core. The temperature profiles at a variety of times are shown in Figure 9.

Note that the thermocouple located at the exposed insulation surface did not produce a reading, and the mean oven temperature is used instead. As heat transfer into the wall is due to both radiation and convection, this is almost certainly an overestimate of the wall temperature. This chart demonstrates the efficacy of the insulation and that the peak temperature moves into the structure as the test proceeds.

Thirteen thermocouples are used to obtain a temperature profile in the balsa/composite stiffener as illustrated in Figure 10. These thermocouples are arrayed vertically as well as through the thickness of the structure. The temperatures measured by thermocouples 29–33 remain at room temperature throughout

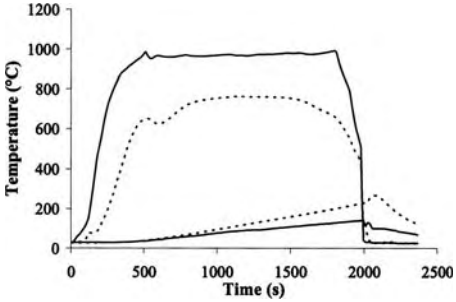

Figure 11. Thermocouple readings at first composite/balsa interface and insulation/insulation interface.

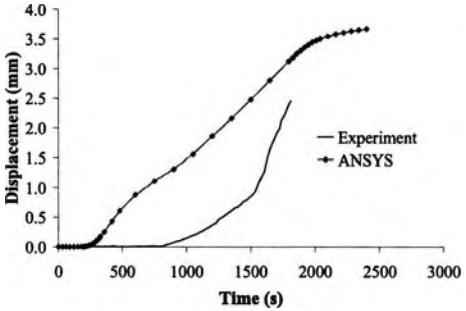

Figure 12. Experimental and analytical displacement at bulkhead center.

the course of the test. Thermocouples 22, 23, 25, 34, and 28 are approximately analogous to the bulkhead thermocouples. However, the temperatures measured in these locations are very different from the bulkhead measurements. Examples are shown in Figure 11.

4.1 *Model*

The finite element model produced in ANSYS is slightly simplified from the true geometry. Specifically, the wedge of balsa/composite at the connection between the bulkhead and the stiffener is not included. This is done to reduce the number of elements in the model and thus the time required to generate results. The bottom of the structure is fixed in the three translational degrees of freedom. The free vertical edge is allowed to move unconstrained. Load is applied through a 'stiff' plate attached to the top of the structure and constrained to move only in the vertical direction. Material properties used in the modeling were discussed above in Section 1a. The creep behavior of the constituents is not included in the model due to lack of data.

4.2 *Model results and comparison*

Two primary results from the model are temperature distributions and displacements. The temperature distributions are similar to those measured experimentally, but still differ from measured results by approximately 20–30% for the insulation/insulation interface with increasing error as the distance into the structure increases. Figure 14 shows the experimental and FEA results for temperatures at various locations within the structure. The results from the two dimensional joint model were similar to those of the stiffened bulkhead model. The reason for the differences between the measured temperatures at the two locations within the structure remains unknown. The displacement at the center of the structure is shown in Figure 12. Again, there is some difference between the magnitude of the measured and the model results however the shape/trend and direction appear to be comparable. Figure 13 shows the out-of-plane displacement as a function of time.

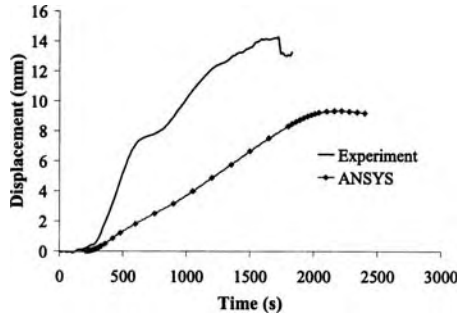

Figure 13. Out-of-plane displacement.

5 SUMMARY AND CONCLUSIONS

In this paper, we have presented an overview of our efforts to model the response of structural composites subjected to mechanical and fire loading. As part of this effort, we have characterized the shear creep behavior of these composites. This information will ultimately feed into the modeling of the response in the one-sided heat flux tests, as well as the structural response. In addition, we have presented our initial efforts at modeling the response of a structural bulkhead subjected to fire loading. Results for predicted temperatures are in relatively good agreement with measurements; the predicted displacements do not agree as well. We suspect that some of the discrepancy may be due to viscoelastic response that has not (to date) been included in the analysis.

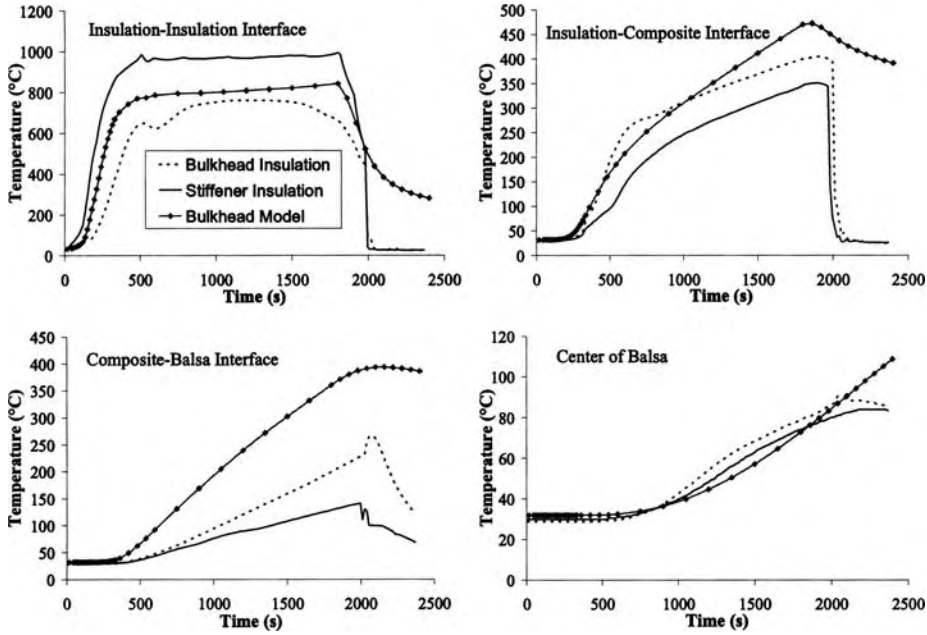

Figure 14. Experimental and analytical temperatures.

ACKNOWLEDGEMENTS

The authors would like to acknowledge the support of the Office of Naval Research through grant number N00014-03-1-0151.

REFERENCES

Bumford, C.H., Crank, J. & Malan, D.H. 1946. "The combustion of wood, part 1," Cambridge *Phil. Soc. Proc.* 42, 166.

Caplan, I., Sorathia, U. & Rollhauser, C. 1996. "Navy programs in fire materials," *Proc. International SAMPE Symp.* 41.

Gibson, A.G., Chandler, H.W. & Wu, Y.-S. 1994. In *Structural Materials in Marine Environments* (Ed.: I. o. M. (UK)), 1994, pp. 35–46.

Griffis, C.A., Masumura, R.A. & Chang, C.I. 1981. "Thermal response of graphite epoxy composites subjected to rapid heating", *Journal of Composite Materials* 15, 427–443.

Griffis, C.A., Nemes, J.A., Stonesifer, F.R. & Chang, C.I. 1986. "Degradation in strength of laminated composites subjected to intense heating and mechanical loading," *Journal of Composite Materials* 20, 216–235.

Henderson, J.B. & Wiecek, T.E. 1987. "A mathematical model to predict the thermal response of decomposing, expanding polymer composites," *Journal of Composite Materials* 21, 373–393.

Kinsella, K., Markham, J.R. & Nelson, C.M. 1997. "Thermal decomposition products of fiberglass composites: Ftir analysis," *Journal of Fire Science* 1997, 15, 108–125.

McMannus, H.L.N. & Springer, G.S. 1992a. "High temperature thermomechanical behavior of carbon-phenolic and carbon-carbon composites, i. Analysis," *Journal of Composite Materials* 26, 206–229.

McMannus, H.L.N. & Springer, G.S. 1992b. "High temperature thermomechanical behavior of carbon-phenolic and carbon-carbon composites, ii. Results," *Journal of Composite Materials* 26, 230–255.

Milke, J.A. & Vizzini, A.J. 1991. "Thermal response of fire-exposed composites," *J. Comp. Tech. and Rsch*. 13, 145.

Sorathia, U., Lyon, R., Gann, R. & Gritzo, L. 1996. "Materials and fire threat," *SAMPE Journal* 32, 8–15.

FRP Composites in Civil Engineering – CICE 2004 – Seracino (ed)
© 2005 Taylor & Francis Group, London, ISBN 90 5809 638 6

A study on the fire behavior of multifunctional and fire resistant FRP building components

T. Keller, C. Tracy & A. Zhou
Composite Construction Laboratory (CCLab), Swiss Federal Institute of Technology, Lausanne, Switzerland

ABSTRACT: A new fiber reinforced polymer (FRP) building system is under investigation that attempts to mitigate high material costs and improve building performance through the integration of structural, architectural, and physical functions into single components, while at the same time offer an effective fire resistance system. The system employs internal water-cooling. The concept has been blended with the well-established under-floor heating techniques to create a fire resistance system that can be used for climate control under normal conditions. This paper presents the behavior of components of the system that are currently being investigated through a variety of fire exposure experiments. Our experiments show that pultruded GFRP laminates are vulnerable under ISO-834 fire conditions, the temperature gradient is very steep through the thickness, and the fire-resistance effect of charring of the resin is insignificant. Liquid cooling was demonstrated to be an efficient way to improve fire-resistance of pultruded GFRP components.

1 INTRODUCTION

Today, fiber-reinforced polymers (FRPs) are used in building construction primarily for the strengthening of girders, columns and masonry walls. There is also, however, some interests in the use of these materials for load-carrying structures of buildings. The favorable characteristics of FRP materials can lead to substantial innovations in building construction. Fiber reinforced materials are characterised by a high specific strength. Glass fiber reinforced polymers (GFRPs) have the added benefit of a low thermal conductivity. The high specific strength results in thinner structural elements and therefore a lower mass of inertia, which is favorable in high-risk earthquake zones. Due to their low thermal conductivity, GFRP load carrying components can act as insulating elements, in addition to their structural function. Furthermore, GFRP elements can be translucent or transparent and come in a large range of colors. The possibility of integrating different functions into individual building components can allow the load-carrying structure to be merged with the facade into a single-layer load-carrying building envelope. This re-opens for architects the lost conceptual and structural possibilities of the "Bauhaus" or modern architectural style.

This new function-integrated envelope concept was developed at the CCLab on two projects – the Eyecatcher Building and the Dock Tower project, both situated in Basel, Switzerland (Keller 2002). As these projects showed, for FRP buildings, the main challenge is to provide a sufficient fire resistance of the FRP load-carrying components. For the Dock Tower project, a concept for building components (walls and floors) was developed which integrates the following functions: structural support, fire resistance and climate control. The load-carrying components consisted of a cellular FRP structure with exterior face sheets and interior webs. The fire safety would be ensured by liquid cooling. By circulating water through internal cells of the wall and floor panels, the energy from a fire would be transferred through the FRP composites and into the relatively cool water.

This concept and design provides fire protection of structures and buildings through three mechanisms. The first mechanism is that, at the beginning of fire, circulating water increases the thermal mass of the component by taking away heating energy from the fire-affected area. If the first mechanism is not sufficiently effective, a second mechanism will be triggered. As fire continues and the temperature of the FRP rises to a level that causes boiling in the water (and if this really happens), large amounts of energy will be used to change the state of the water from liquid to gas. This latent energy stored in the water vapour will be carried away from the heated areas by its natural buoyancy and by the flowing water. Under severely uncontrollable fire, if the inner face sheets were damaged, a third mechanism will be triggered: the water in the internal cells will run out, providing assisting fire-fighting measures; while the outer face sheet and vertical stiffeners provide necessary structural load

carrying capability. In addition, this system of fire protection can be used for climate control. Under normal conditions, by regulating the temperature of the water in circulation, the air temperature in the rooms can be controlled and, therefore, is perfectly suited to heating and cooling a building.

The rationale for such a building construction system originates from three sources: (1) Water-cooled steel structures: numerous buildings worldwide have been constructed using exposed structural steel tubes with water filling as the fire protection system (Bond 1975). (2) FRP sprinkler pipes: recent research on the exposure of filament-wound glass-reinforced pipes to hydrocarbon fires suggests the survivability of FRP materials at high temperatures by water cooling. Failure times of approximately 2 minutes resulted for the empty condition, approximately 10 minutes for the stagnant condition, and greater than 120 minutes for the flowing condition (Davies et al. 1999). (3) Underfloor heating and cooling systems: for decades, networks of water pipes have been embedded in concrete to provide comfortable, efficient and architecturally liberating climate control.

To demonstrate the feasibility of the proposed concept of FRP fire resistance by liquid cooling, experiments on GFRP laminates, small-scale unloaded liquid cooled cellular GFRP components and large-scale loaded liquid cooled cellular GFRP components were performed. This paper reports the results from experiments on fire behavior of GFRP laminates and small-scale unloaded liquid cooled cellular GFRP components.

2 CHARRING EXPERIMENTS ON GFRP LAMINATES

2.1 *Experiment details*

The goals of the charring experiment (CE) on GFRP laminates were to measure the temperature profile through the thickness of the specimen over time, to observe the high-temperature behavior, and to examine the effect of charring on laminates' fire behavior.

The specimens under investigation were cut from DuraSpan® 766 bridge deck (MMC 2002). The glass-reinforced polyester section is produced by the pultrusion process and consists of two face sheets separated by webs (Fig. 1). The cellular panels have been initially designed and fabricated for rehabilitation and new construction of bridge decks. Recently, the interest of modifying and applying this kind of cellular panel as wall and floor elements for building construction is growing. Therefore, this study focuses on this kind of cellular panel system. The basic element of the cellular panel is the trapezoidal dual-cell profile, which is formed through a pultrusion process. E-glass fibers in forms of rovings and mats were used as the

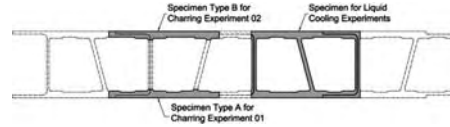

Figure 1. Origin of specimens.

Figure 2. CE specimen with thermocouples slots.

reinforcement and isophthalic polyester was used as the resin. The dual-cell profiles are bonded together by polyurethane adhesive to form the panel.

The fiber weight fraction of the pultruded GFRP cellular panel is 62%, which was obtained by burn-off tests. The E-glass has a softening temperature (T_s) of around 830°C. The E-glass/polyester composite was further investigated through dynamic mechanical analysis (DMA) and thermogravimetric analysis (TGA). The DMA data showed a glass transition temperature (T_g) of 117°C. From TGA tests, the decomposition temperature (T_d) of 300°C was determined for the material.

The dimensions of the specimens were 32.5 × 41.0 cm, which included one adhesively bonded joint. The top face sheet and the bottom face sheet are different in fiber lay-up and thickness due to the structural design and the pultrusion process. Therefore, two types of specimens were obtained: type 'A' for the bottom sheet and type 'B' for the top sheet as shown in Figure 1. The average thickness is 16.1 mm for Type A specimens and 17.3 mm for Type B specimens.

Thermal couples were installed in the specimens for temperature recording. In order to install the thermocouples within the thickness of the face sheets, 40 × 2.5 mm slots were cut into the cold faces. Using a computer-piloted router, two slots were cut at each depth of 3.8, 7.6, 11.4, and 15.2 mm from the cold face. Figure 2 provides an overview of a specimen with slots. After an exploratory burning experiment on one laminate, two more groups of specimens (four for each group) were prepared and tested, referred as groups CE01 and CE02 respectively. Type A specimens were used for group CE01, and type B specimens were used for CE02. Thermocouples were placed at the bottom of the slots and on the cold faces of the specimens. Sikadur® 330, a two-part epoxy adhesive, was mixed with powdery grindings of the specimen to fill

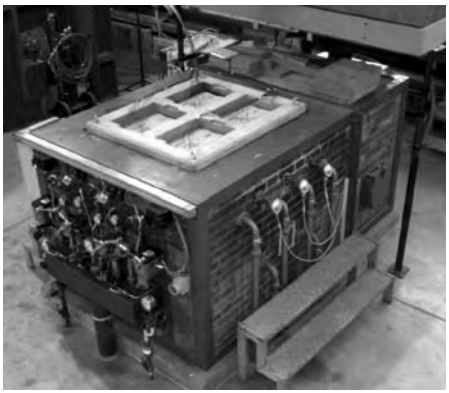

Figure 3. Horizontal oven with CE specimens and custom-built concrete cap.

in the slots over the thermocouples. The adhesive was allowed to cure at least 24 hours. The thermocouples have an accuracy of ±2.2°C or 0.75% of the measured temperature.

The specimens were placed in the four exposure windows of a small horizontal oven (Fig. 3) and thermally loaded according to the ISO-834 temperature curve. The burners were automatically controlled by a computer, which read the oven temperature from the six internal thermocouples and adjusted the intensity of the burners to follow the ISO-834 temperature curve as closely as possible. The first specimens were removed from the oven after 15 minutes, the second at 30 minutes, the third at 45 minutes, and the fourth at 60 minutes. Temperatures where measured by 10 thermocouples on and within each specimen, as well as by 6 thermocouples in the oven. Pictures were taken throughout the duration of the experiments.

2.2 *Experiment observations*

The progression of damage to the hot face seemed to have proceeded in stages. In the first stage occurring in the first 9 minutes, the surface was heated past its decomposition temperature and turned to black as the resin decomposed (Fig. 4-a). The next stage began as the fuel created by this decomposition was combusted until roughly 2 minutes later when the fuel was exhausted. A third stage, also roughly 2 minutes in duration, followed as decomposition continued to a deeper level (Fig. 4-b) and the scoured fibers near the surface began to turn to a whitish char. A final fourth stage began with the flaming combustion of gases from the decomposition occurring deeper within the laminate. This phase continued for the remainder of the experiment, as the reinforcement layers closer

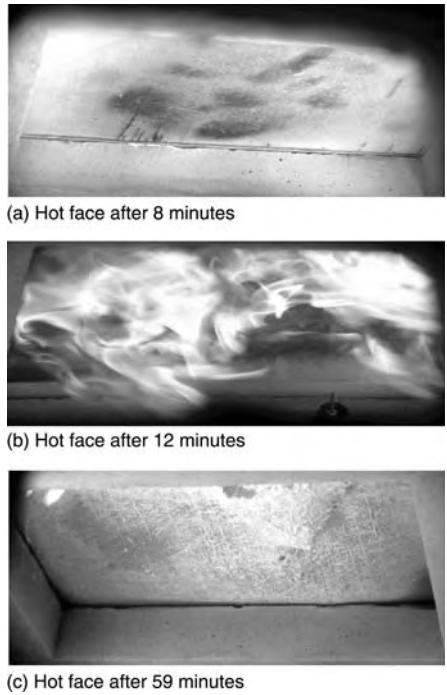

Figure 4. Fire behavior of the hot face of the CE specimens.

to the surface turned to the whitish char and the resin at deeper levels was decomposed (Fig. 4-c).

The persistence of flaming combustion suggests that no steady-state condition was reached and that the entire thicknesses would have eventually been consumed. The whitish char that remained was only the char from the burnt fibers. The black char from the resin did not remain on outermost reinforcement layers, and appeared only as a kind of powdery fiber coating on the deeper layers. It did not seal the surface or close the gaps between the fibers to prevent the escape of decomposition gasses from the deeper level. Thus, there was no significant fire-resisting effect from the charring of the resin. The burnt-out reinforcement layers, however, provided some level of protection by blocking the radiation of the oven and reducing the ablative effects of the exhaust system.

During the experiment, the hot faces of the specimens showed varying levels of damage depending on the location (Fig. 5). While the area towards the center was the most severely damaged on the hot faces, the opposite was true on the cold faces. This was due to the uneven distribution of oven temperature: the

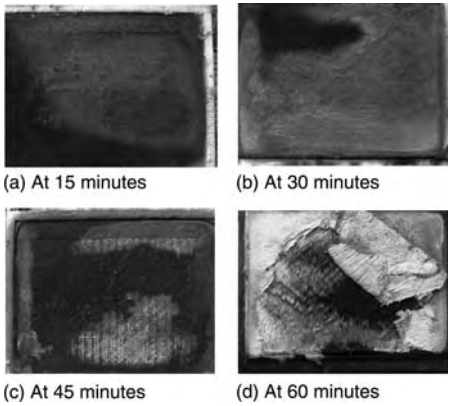

Figure 5. Hot faces of CE specimens.

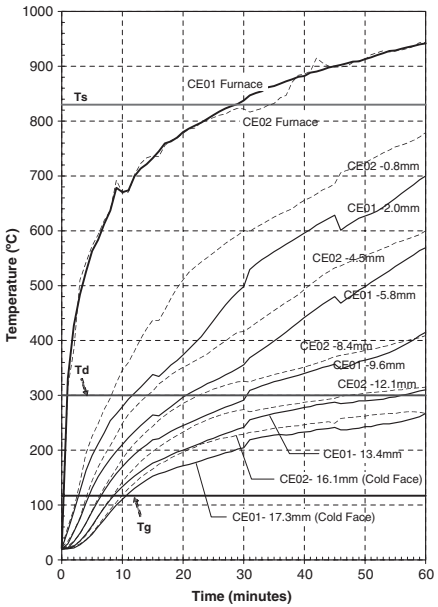

Figure 6. Temperatures through the thickness of GFRP panels (numbers such as "0.8" indicate the distance to the hot face).

locations close to the burners have higher temperatures than those far from the burners.

Figure 6 shows the temperature profiles within the laminate thickness. It indicates a direct correlation between thickness of material and temperature. The differences between curves of similar depth ranges show the extreme sensitivity of depth of measurement to temperature, as the temperature gradient is extremely steep through the thickness.

During the CE experiments, debonding of the polyurethane joint was evident in one of the eight specimens. It would be prudent to expect no strength from bonded joint of this type at elevated temperatures under fire exposure. It was also observed that viscous liquid slowly bubbled up through cold face of specimens. This was due to the releasing of liquid styrene monomer at elevated temperatures.

3 SMALL-SCALE UNLOADED LIQUID COOLING EXPERIMENTS

3.1 *Experiment preparations*

Small-scale unloaded liquid cooling (LC) experiments continue the investigation into the behavior of a GFRP section exposed to high temperatures. Following the investigations where the cold face was cooled by natural convection of ambient air in experiments described in Section 2, the LC experiments have been conducted to observe the thermal behavior of the same material when cooled by flowing water. All variables were kept as constant as possible in the three LC experiments except the water flow rate, which varied from 0.16 m^3/hr to 4.00 m^3/hr. The temperature profiles measured in both the CE and LC experiments will be used to calibrate the heat transfer of the theoretical model which is being developed to solve the heat transfer problem. In addition, the small-scale experiments were helpful in discovering and resolving the issues that would be encountered in the large-scale experiments. With the threat of hundreds of liters of water suddenly pouring into the 1000°C large oven facility during the large-scale experiments, the LC experiments provided a lower risk method to verify the safety of the procedures for both the people and the equipment.

Specimens for liquid cooling (LC) were sections from the pultruded cellular GFRP panel as shown in Figure 1. Specimen dimensions and instrumentation of thermal couples for LC experiments are shown in Figure 7. To obtain the distance of thermal couples to the cooling face, one subtracts the slot depth shown in the figure from the total thickness (17.3 mm). The dimensions of the specimens were chosen to be 0.32×1.13 m so that two full deck cells would be included and that the specimens would fit on the test furnace. Three specimens were prepared for LC experiments, hereafter referred as LC01, LC02, and LC03. The Type B sheet side was exposed to fire for the LC specimens during the experiments.

In order to measure the temperature gradient between the oven interior and the flowing water, thermocouples were placed throughout the thickness of

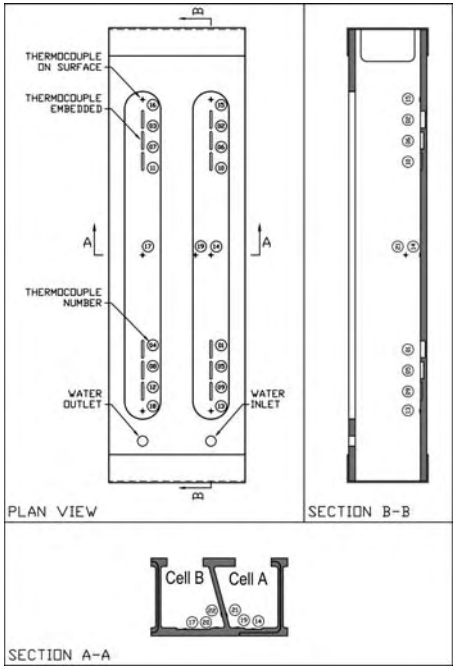

Figure 7. Thermocouple layout for LC specimens.

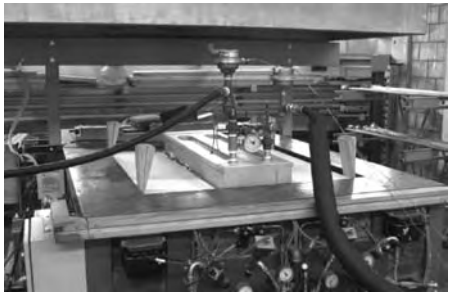

Figure 8. Setup for liquid cooling (LC) experiments.

the lower flange (Fig. 7). This was accomplished by routing slots from the interior face (cold face), which necessitated the cutting of access holes in the top flange. As the thermal performance of the top flange was not under study, the cutting of the holes had little effect on the experimental performance. When the machining was completed and the thermocouples were installed, the holes were sealed by bonding thin FRP plates to the interior face of the top flange. In an attempt to maintain the thermal continuity in the vicinity of the temperature readings, the slots that were cut to receive the thermocouples were refilled using a mixture of the previously mentioned epoxy adhesive and a powder made by grinding down other samples of the deck material.

Figure 8 shows the experimental setup for liquid cooling experiments. Water was supplied by either the standard or the high-pressure fire plumbing of the test laboratory, depending on the required flow rate. The water passed through a calibrated and certified digital flow rate meter (accurate to 0.001 m^3/hr) before entering the specimens. Special pipe elbows that suspended thermocouples amidst the flowing water were placed just above the inlet and outlet couplings. An analog graphic recorder plotted water inlet and outlet temperatures versus time. An analog manometer was also installed just above the outlet coupling to observe the water pressure within the specimen for the high-flow experiment. After passing through the specimen, water passed through approximately 25 m of 2.5 cm diameter rubber hose to a drain. A second outlet coupling was installed for the high-flow experiment to reduce the internal pressure. For the low-flow experiment, the end of the outlet hose was elevated 0.5 m above the specimen to maintain a positive pressure within. Summarizing, the path of the water was therefore: inlet hose → flow rate control valve → flow rate meter → inlet thermocouple → interior of specimen Cell A → interior of specimen Cell B → manometer → outlet thermocouple → outlet hose.

3.2 *Experiment proceedings*

The first experiment, LC01, was conducted at a modest flow rate of 0.800 m^3/hr (or 1.0 cm/s water velocity in cell A or B). The second experiment, LC02, was conducted at a rather high flow rate of 4.000 m^3/hr (or 5.0 cm/s), which is five times the flow rate of LC01. The third experiment, LC03, was conducted at a very low flow rate of 0.160 m^3/hr (or 0.2 cm/s), which is one-fifth the flow rate of LC01.

The experiments began with the circulation of water at the desired flow rate for approximately 10 minutes. This time permitted the water and the specimen temperatures to stabilize before the fire loading. Time began with the firing of the oil burners. The burners were automatically controlled by a computer to follow the ISO-834 temperature curve. Oven and specimen temperatures were automatically logged every 60 seconds by a central digital unit, while water temperature was continuously recorded by a graphical unit. Notes and photos were taken through the observation window of the oven.

In each of the experiments, two criteria were set to ensure safety: that water must not leak into the furnace and that the water must not approach boiling.

To enforce the first criterion, the limit was set that none of the four thermal couples 4–5 mm below the cold face of the burning flange could approach the decomposition temperature and were thus limited to 200°C (100°C below T_d). This ensured that a minimum of 4 mm of material would remain to contain the water. The second criterion was enforced by limiting the temperature of the water at the outlet to 70°C to ensure the safety of experiment personnel. Fortunately, neither of these criteria was needed for any of the experiments. Taking caution in the first experiment, LC01 was stopped after 90 minutes, though neither of the limits had been exceeded. Gaining confidence from the post-experimental evaluation of the LC01 specimen, LC02 and LC03 were both run for a full 120 minutes, which corresponds to the code-maximum endurance time required of structural components for most categories of buildings.

3.3 *Experiment observations*

The hot faces of the three specimens differed significantly from those of the charring experiments. The surface damages of LC specimens were different from the CE experiments, in which the charring of resin was not observed. For LC specimens, the cooling water lowered the temperature on the cold face, which helped the resin close to the cold face to form char during the decomposition process.

On the hot sides of LC specimens, the glass reinforcement appeared to have first melted and then drooped down directly into the burner flames. From there, it was completely oxidized into a sort of lightweight, brittle, foam-like char and eventually fell away (Fig. 9). For the LC03 specimen (which had the lowest flow rate), the lower flange was reduced to roughly one-half of its original thickness of 17.3 mm (Fig. 10). Large quantities of charred glass reinforcement were found at the bottom of the oven. For the LC01 specimen (which had the medium flow rate), more flange thickness was retained and less material was found at the oven bottom. For the LC02 specimen (which had the highest flow rate), it appeared that only the first of the four unidirectional roving layers was oxidized in this manner and nearly no material was found at the bottom of the oven.

In LC experiments, no debonding of the polyurethane joint was observed during the burning process.

3.4 *Heat transfer to water*

Using the recorded input and output temperatures of the flowing water, the amount of energy removed from the specimens by liquid cooling can be approximated. Taking a linear approximation of the change in temperature (T, °C) versus time (t, minute) curves, we obtain

Figure 9. Reinforcing roving layers drooping down and oxidizing (LC experiment).

Figure 10. Post-fire hot face of LC03 specimen.

the following functions:

$$\text{LCO1: } T = 0.5 + 0.0675 \cdot t \tag{1}$$

$$\text{LC02: T=no measurable change} \tag{2}$$

$$\text{LC03: } T = 0.5 + 0.2542 \cdot t \tag{3}$$

The change in temperature is related to energy absorbed through the equation:

$$H = m \cdot C_p \cdot \Delta T \tag{4}$$

where H (kJ) is the energy required to change a mass m (kg) of material with specific heat capacity C_p (kJ/(kg · °C) by ΔT degrees. Because varies with time, an average change in temperature, ΔT_{AVG}, will be used. Thus, Eq. (4) becomes:

$$H = m \cdot C_p \cdot \Delta T_{AVG} \tag{5}$$

The value of ΔT_{AVG} is found by integrating the change in temperature with respect to time and then dividing by the total time:

$$\Delta T_{AVG} = \frac{1}{t_1} \int_0^{t_1} T dt \tag{6}$$

Evaluating this equation for = 120 minutes and substituting into equation (5) we obtain:

$$\text{LC01: } H_{LC01} = 15.3\text{MJ} \tag{7}$$

LC03: H_{LC03}=10.6MJ (8)

If we assume that for LC02, $\Delta T_{AVG} \approx 2°$, the accuracy of the measurement, we find:

LC02: H_{LC02}=33.6MJ (9)

As expected, the amount of heat transferred to the water increased as the flow rate increased. This is explained by two factors. The first is that the convection heat transfer coefficient increases with increasing water flow rate. The second is that the water remained cooler as the flow rate increased, which maintained a larger temperature gradient between the materials and thus a higher rate of heat transfer. This verifies that, within the range of water flow rates used, increasing the flow rate increases the cooling effect.

4 DISCUSSIONS

4.1 *Damage to hot faces*

The hot faces of the LC specimens appeared to be more severely damaged than the CE specimens. This is due to two factors: the exposure time and geometrical shape of the specimens. The most harshly tested CE specimens were exposed to 1 hour of the ISO temperature curve, while LC specimens continued for another 30–60 minutes. The geometric differences were also an important factor because of the drooping effect in the reinforcement layers. In the charring experiments, the specimens were small rectangles that were supported on all edges. This meant that the layers of reinforcement were less likely to droop down after the resin was removed and the glass was melted. The LC specimens, in contrast, were only supported on the short ends and were approximately 3.5 times longer than the LC specimens. This configuration made the reinforcement layers more susceptible to the drooping behavior (due to dead load from self-weight and the contained water inside the cells). As each layer sagged and fell down, the radiation shielding that it provided was lost and the damage was allowed to penetrate further.

4.2 *Temperature profiles*

The comparisons of through-thickness temperatures for LC specimens and CE02 specimens are shown in Figure 11. The LC specimens remained substantially cooler than the CE specimens. This effect is most prominent towards the cold faces, the greatest differences registering at the cold faces themselves. This effect was more pronounced as the exposure time increased. While the curves all appeared similar during the first 5 minutes, the cold faces differed by ~200°C at 60 minutes.

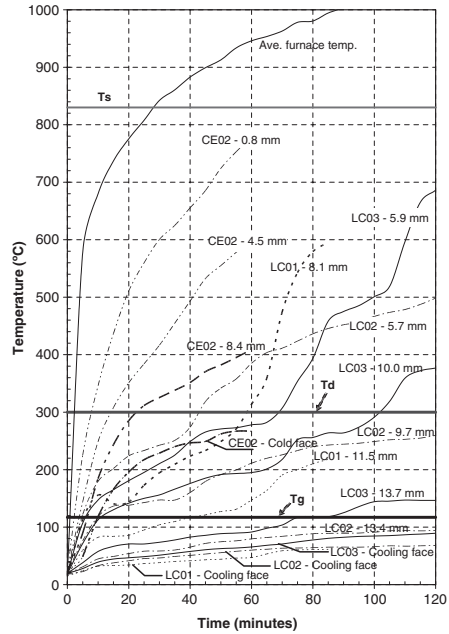

Figure 11. Comparison of liquid cooling (LC) experiments to charring experiments (CE) [the numbers before mm indicate the distance to the hot face].

In Figure 11, comparing the steep slope of the "CE02 – Cold face" curve to the relatively flat "LC0X – Cooling face" (X = 1, 2, 3) curves, it is likely that this discrepancy would have augmented even further with additional exposure of time. The "CE02-8.4 mm" and "LC01-8.1 mm" curves represent the middle of the thickness of CE02 laminates and the burnt sheet of LC01 respectively. It is seen that, without cooling, the temperature at the middle of CE02 laminates could surpass the decomposition temperature within 20 minutes. With liquid cooling, the half of LC01 burnt sheet did not exceed the decomposition temperature at 55 minutes. More significantly, the temperature of the cold face of CE specimens exceeded the T_g of the material at 10 minutes; while for liquid cooled specimens, none exceeded the T_g even at the end of experiments on the cooling faces.

Figure 12 shows the temperature distributions through the thicknesses of the CE specimens and the burnt side of the LC specimens, where the temperature at a certain distance to the hot face is an average value from all measurements on all specimens (eight specimens for a CE curve and three specimens for a LC curve).

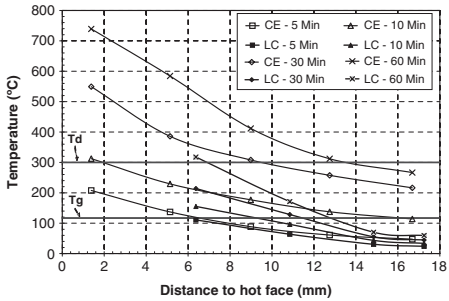

Figure 12. Through-the-thickness temperature distributions.

The "LC02-13.4 mm" curve in Figure 12 shows that, at about 4 mm from the cooling face, the temperature was still below T_g after 120 minutes. Since the total sheet thickness is 17.3 mm, the above results suggest that liquid cooling could allow more than 20% of material to provide structural resistance after two hours of exposure to ISO-834 fire conditions.

Figure 12 also shows that at 5 minutes, the CE and LC specimens had similar temperature distributions through the thickness. As the time of exposure to fire grew, the temperature distribution difference also grew. After 30 minutes, the temperature in more than half of the thickness of CE specimens exceeded the decomposition temperature. It is also interesting to compare the temperatures 12.3 mm to hot face (or 5 mm below the cold face) in Figure 12. The temperatures of the LC specimens were still below the glass transition temperature after 60 minutes, while those of the CE exceeded this limit in less than 8 minutes. Therefore, a significant gaining of liquid cooling for fire-resistance of FRP structures has been obtained.

5 CONCLUSIONS

The following conclusions can be drawn from the charring experiments and the small-scale liquid cooling experiments:

1. No significant fire resistant effect from the charring of the resin was observed for the pultruded GFRP laminates.
2. Temperature gradient is very steep through the thickness of pultruded GFRP laminates.
3. Following the ISO-834 curves, the pultruded GFRP laminates started decomposition and burning after 8–9 minutes during the CE experiments. The persistence of flaming combustion suggests that no steady-state condition was reached and that the entire thicknesses would have eventually been consumed.
4. In the small-scale unloaded liquid cooling experiments, water cooling has been demonstrated to be an effective way of improving fire-resistance of pultruded GFRP components. Temperatures within the lower flanges of the specimens remained significantly lower in the liquid cooling experiments than in the charring experiments.
5. The cooling effect improved with increased flow rates. The liquid temperature was always far below boiling temperature for up to 120 minutes at very low flowing rate. Liquid cooling for fire resistance of FRP structures only requires low to moderate flowing rates (0.2–1.0 cm/s).

ACKNOWLEDGMENT

The authors would like to thank the Swiss National Science Foundation and Martin Marietta Composites for supporting this research. Testing facility and technical support from EMPA, Dübendorf, Switzerland, are greatly appreciated.

REFERENCES

Bond, G.V.L. (1975). Fire and steel construction- Water cooled columns. Steel Construction Institute, Ascot, Berkshire, UK.

Davies, J.M., Dewhurst, D.W.(1999). The fire performance of GRP pipes in empty and dry, stagnant water filled, and flowing water filled conditions. In: Composites in Fire, Proceedings of the International Conference on the Response of Composite Materials to Fire (Edited by Gibson, A.G.), Reprinted in 2001 by Woodhead Publishing Ltd., Cambridge, UK: 69–84.

Keller, T. (2002). Fiber reinforced polymers in building construction. International Association for Bridge and Structural Engineering (IABSE), Symposium Towards a Better Built Environment, Melbourne, Australia.

MMC. (2002). DuraSpan fiber-reinforced polymer bridge deck systems. Martin Marietta Composites, Raleigh, USA. (The documents is available online at http://www.martinmarietta.com/Products/DuraspanV1.pdf, 14/08/2004)

FRP Composites in Civil Engineering – CICE 2004 – Seracino (ed)
© 2005 Taylor & Francis Group, London, ISBN 90 5809 638 6

Temperature effect on bonding and debonding behavior between FRP sheets and concrete

Z.S. Wu, K. Iwashita & S. Yagashiro
Ibaraki University, Urban & Civil Engineering, Japan

T. Ishikawa & Y. Hamaguchi
The Japan Aerospace Exploration Agency (JAXA), The Institute of Space Technology and Aeronautics

ABSTRACT: Generally, epoxy resin will be softened and its bond capacity will decrease remarkably under a high temperature environment near to or higher than the glass transition temperature (T_g) or deflection temperature under load (HDT) of epoxy resin. This paper summarizes a series of investigations for confirming the temperature effect on bonding behavior between fiber reinforced polymers (FRP) sheets and concrete. An experimental program is designed by using prism specimens subjected to a direct tensile load. The temperature around the concrete prism and the types of epoxy resin are considered as the experimental parameters. The experimental results are exploited to determine the debonding fracture energy (G_f), failure mode, and effective bonding length (L_e) of the test specimens. It is observed from results that the value of G_f decreases and L_e increases largely at temperatures near to or higher than T_g or HDT. Moreover, the newly developed epoxy resin presents higher temperature-resistance behavior than ordinary epoxy resin.

1 INTRODUCTION

Recent studies have reported a variety of fiber reinforced polymers (FRP) premature debonding problems (Wu et al, 2000a, 2000b, 2001). Moreover, FRP bonding properties under different severe environmental conditions are still an important issue that should be addressed. In these circumstance, this paper aims at investigating clearly the bonding behavior of carbon fiber reinforced polymers (CFRP) sheets bonded to concrete under a high temperature environment over 30°C.

Generally, epoxy resin is softened and its bond capacity decrease under temperatures higher than glass transition temperature (T_g) or deflection temperature under load (HDT). Accordingly, an interface between FRP and concrete can also fail under temperature near to or higher than T_g and HDT. In this paper firstly, a series of experimental investigations are summarized. Then, the effect on bond strength is characterized by conducting the relationship between environmental temperature and maximum bond strength. Beside this, a concept based on nonlinear fracture mechanics is proposed to discuss the debonding mechanism under different environmental temperatures and to evaluate the bond behavior of FRP sheets. Finally, a bond capacity of a newly developed thermo-resistant epoxy under temperature near to or higher than T_g and HDT is investigated, and a relationship between bond capacity and environmental temperature is found expressed clearly.

2 MATERIALS PROPERTIES AND THERMO-TOLERANCE OF EPOXY RESINS

CFRP sheets present many advantages such as high tensile strength and high stiffness-to-weight ratio as shown in Table 1. However, the tensile strength is not displayed often due to premature debonding between FRP sheet and concrete. Thermo-tolerance capacity of epoxy is characterized by T_g and HDT (See Table 2). These values are investigated and calculated based on

Table 1. Summary of material properties.

Carbon fiber sheets	
Guarantee tensile strength (MPa)	3400
Nominal modulus of elasticity (GPa)	235
Nominal design thickness (mm)	0.128
Ordinary epoxy resin	
Guarantee tensile strength (MPa)	51.9
Nominal modulus of elasticity (GPa)	3.43

ISO standards (1993a, 1993b, 1999). The value of T_g means a critical temperature when epoxy softens and its tensile stiffness decreases by the influence of the temperature. The value of HDT means a temperature when a specimen is bended. It is observed that T_g and HDT values of the newly developed thermo-resistant epoxy are about 10°C higher than the values of ordinary epoxy as shown in Table 2.

Table 2. Summary of material properties.

Type of epoxy	Curing condition	T_g (°C)	HDT (°C)
Ordinary epoxy	80°C 3hour	38	48
	60°C 3hour	34	43
Ordinary primer	80°C 3hour	42	*
	60°C 3hour	34	*
Thermo-resistant epoxy	80°C 3hour	38	55
	60°C 3hour	40	57
Thermo-resistant primer	80°C 3hour	46	68
	60°C 3hour	55	76

*HDT of ordinary primer is not measured.

3 EXPERIMENTAL PROGRAM

In accordance with the experimental method of JSCE Recommendations for Upgrading of Concrete Structures with Use of Continuous Fiber Sheets (JSCE, 2000), prism specimens with 450 mm long are used in these investigations. The details of the prism specimens are schematically shown in Figure 1. CFRP sheets are bonded to both sides of the concrete block along the axial direction. A tensile load is applied by pulling both ends of the steel rod embedded in the concrete block, on which CFRP sheets are bonded. The steel rod is cut off at the position of the notch (Pre-crack). Before bonding of CFRP sheet, the concrete surface preparation is treated with a diamond sander, and an epoxy primer is painted after wiping with cloth soaked with acetone. In this investigation, Instron 8502 series fatigue testing machine was used. And a 100 kN load cell is used to measure the load acting on the specimen and a SVDT attacked on the test machine is used to measure the displacement of the specimens. The arrangement of wire strain gages to measure CFRP strains is shown in Figure 1. A cup oven is used to maintain the temperatures of prism specimens. The

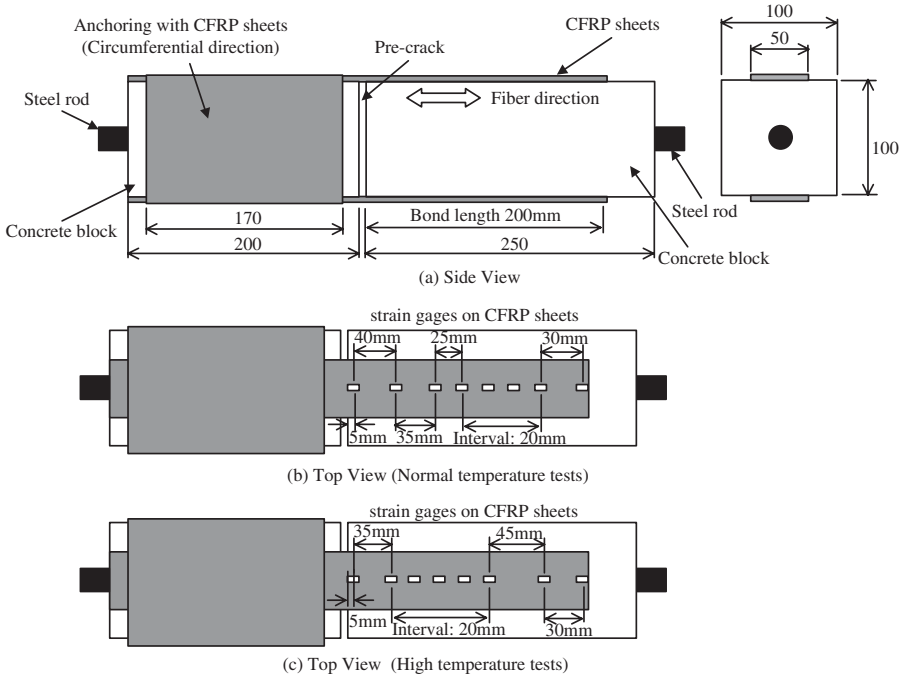

Figure 1. Detail of CFRP sheet-concrete bonding joints (Double-lap shear test).

temperatures in the cup oven are raised with a rubber heater and maintained with an aluminum sheet, paste-board and sponge rubber (Figure 2). Testing of prism specimens with ordinary epoxy resin were conducted in the cup oven at temperature levels ranging from 26°C to 50°C while testing of specimens with thermo-resistant epoxy resin were conducted in the cup oven at temperature levels ranging from 26°C to 60°C. Before applying the load, each specimen was kept under the test temperature for at least 6.5 hours.

4 EXPERIMENTAL RESULTS AND DISCUSSIONS

Figure 3 show the debonding propagating process, and Figure 4 and Figure 5 show the load–displacement relationships of specimens with both ordinary and thermo-resistant epoxy resins under different temperatures. At first, micro-debonding initiate at the tensile end of bonded FRP sheets. The micro-debonding propagates gradually and as a result macro-debonding occur. Once macro-debonding area is formed about 20–30 mm, debonding propagates toward to the free end of bonded FRP sheet. Finally, a final FRP sheet debonding occurs when debonding propagation reaches a critical location. And the maximum applied load and elastic modulus decrease gradually with temperatures ranging from 26°C to 60°C. The distance

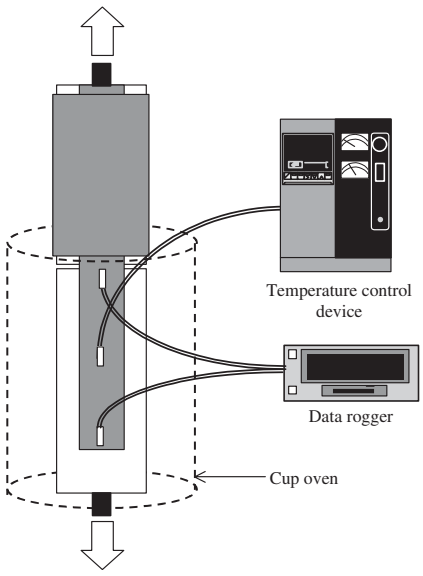

Figure 2. Details of the tensile test under different temperatures.

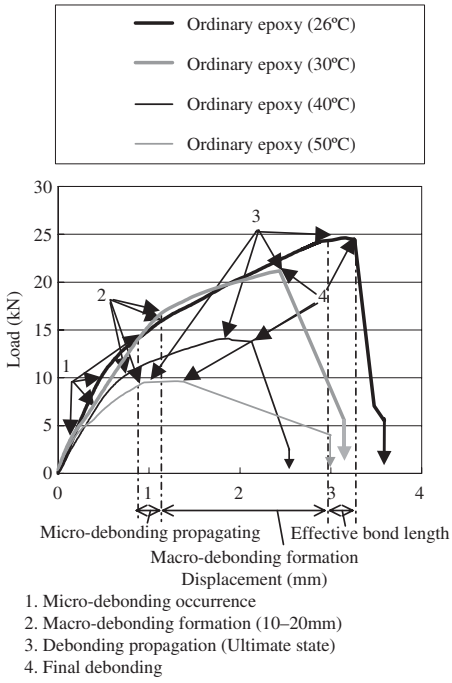

Figure 4. Load–displacement curve (Ordinary epoxy).

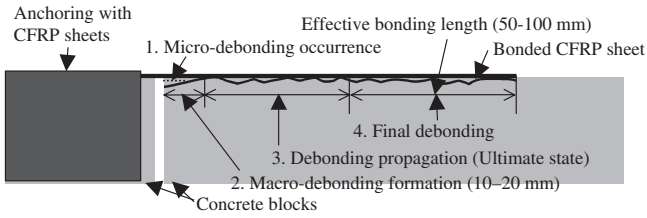

Figure 3. Debonding propagating process.

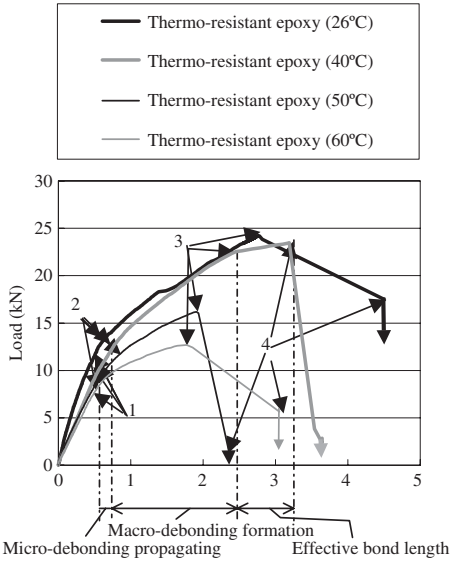

1. Micro-debonding occurrence
2. Macro-debonding formation (10–20mm)
3. Debonding propagation (Ultimate state)
4. Final debonding

Figure 5. Load–displacement curve (Thermo-resistant epoxy).

from this critical location to the free end of bonded FRP sheet is considered being effective bonding length about 50–100 mm. The debonding behavior is nearly same for both specimens used ordinary epoxy and thermo-resistant epoxy. The results of prism tests are investigated for the determination of interfacial fracture energy (G_f), average bond strength (σ_{bs}), failure mode, and effective bonding length (L_e). G_f and average bond strength are calculated from eq. (1) and eq. (2) respectively as given below [3,4].

$$G_f = \frac{P^2_{\max}}{8b^2E_f t} \quad (1)$$

$$\sigma_{bs} = \frac{P_{\max}}{2bt} \quad (2)$$

where P is the maximum transferable force in CFRP sheet; E_f, b and t are modulus of elasticity, width and thickness of CFRP sheets respectively. The average bond strength σ_{bs} and interfacial fracture energy G_f of bonded FRP sheet by using both ordinary and thermo-resistant epoxy resins decrease approximately in direct ratio with temperatures ranging from 26°C to

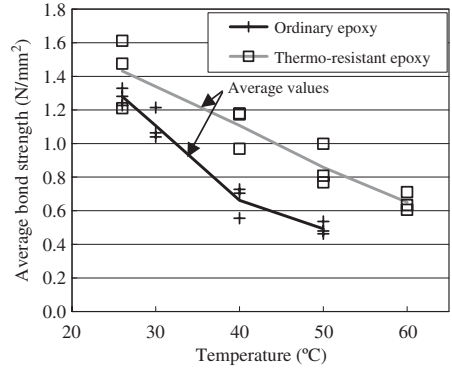

Figure 6. Average bond strength under different temperatures.

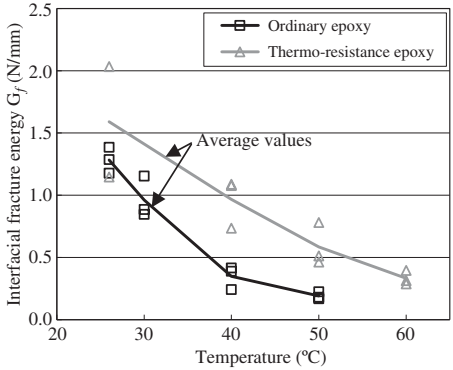

Figure 7. Interfacial fracture energy under different temperatures.

60°C (Figure 6 and Figure 7). Generally, the minimum value of G_f for normal bending situations under normal temperature condition (26°C) can be identified to be 0.5N/mm from a lot of prism tests of CFRP sheets [3,4]. Therefore here $G_f = 0.5$ N/mm is used as a criterion value. G_f for specimens by using ordinary epoxy under temperature 40°C which is higher than T_g (=38°C) is lower than the minimum value (=0.5 N/mm) under normal temperature 26°C.

Meanwhile, G_f for specimen by using thermo-resistant epoxy under temperature which is higher than T_g (=46°C) is lower than the minimum value. It is observed that two epoxy resins under temperatures higher than T_g and HDT start softening and deflection. However, the newly developed epoxy resin has higher thermo-tolerance of debonding. By investigating the

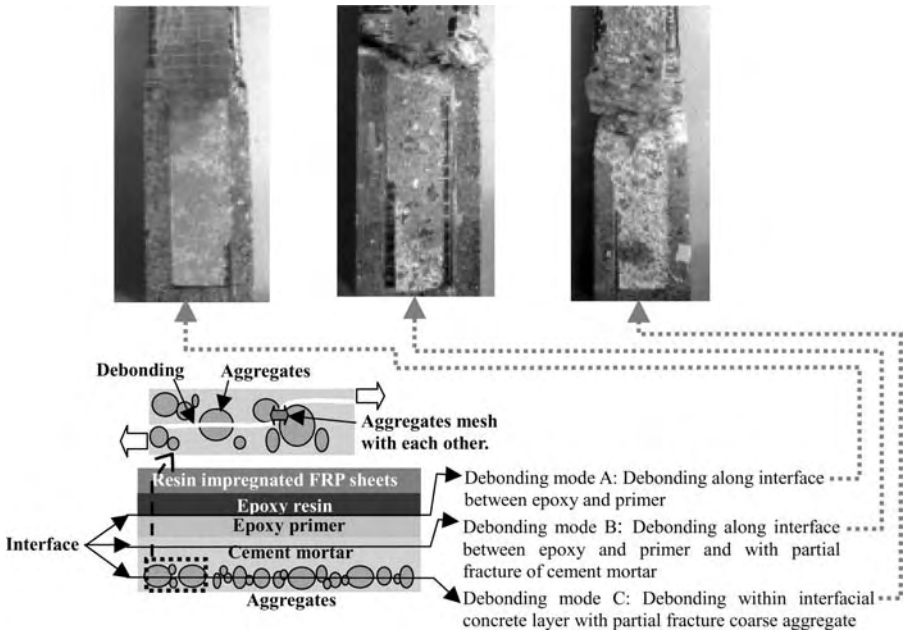

Figure 8. Different debonding modes along CFRP-concrete interface.

detail debonding location and situations, debonding failure in appearance can be classified into three modes such that debonding mode "A" has debonding along interface between epoxy and primer, and debonding mode "B" has debonding along interface between epoxy and primer and with partial fracture of cement mortar, while debonding mode "B" has debonding within interfacial concrete layer with partial fracture of coarse aggregate, but it is similar to the case "C" roughly (Figure 8). Debonding modes in temperatures lower than T_g and HDT were partially "B" or "C" and in temperatures higher than T_g and HDT were almost "A" are found clearly (Table 3). Figure 9 and Figure 10 show strain distribution of specimens with ordinary epoxy resin along the fiber direction under temperature about 26°C and 40°C. The strain distribution of specimens with thermo-resistant epoxy about 26°C and 50°C are shown in Figure 11 and Figure 12. In accordance to the reference [1,2], effective bonding length is defined as the distance from the pre-crack of prism specimen to the position where 97% strain of the value at the pre-crack is occurred. Figure 13 shows the effect of temperature on effective bonding length of specimens. It is observed that the effective bonding lengths in temperatures about 26°C are longer than those under temperatures higher than T_g and HDT (Figure 13).

Table 3. Results of CFRP-concrete bonding test.

Type of epoxy	Temperature (°C)	No.	Debonding mode
Ordinary epoxy	20	1	B
	20	2	B
	20	3	C
	30	1	C
	30	2	B
	30	3	A
	40	1	A
	40	2	A
	40	3	A
	50	1	A
	50	2	A
	50	3	A
Thermo-resistant epoxy	20	1	C
	20	2	B
	20	3	B
	30	1	A
	30	2	A
	30	3	C
	40	1	A
	40	2	A
	40	3	A
	50	1	A
	50	2	A
	50	3	A

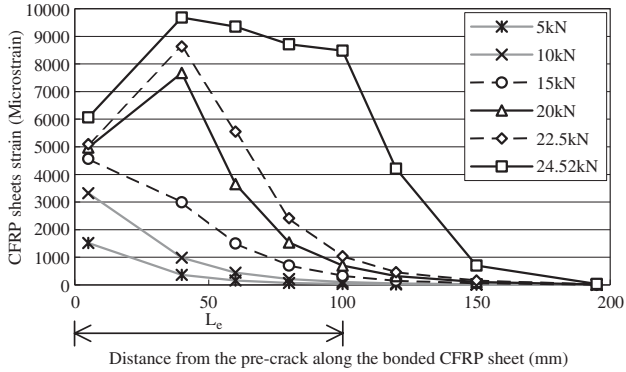

Figure 9. Strain distribution along bonded CFRP sheet for a specimen by using ordinary epoxy resin (26°C).

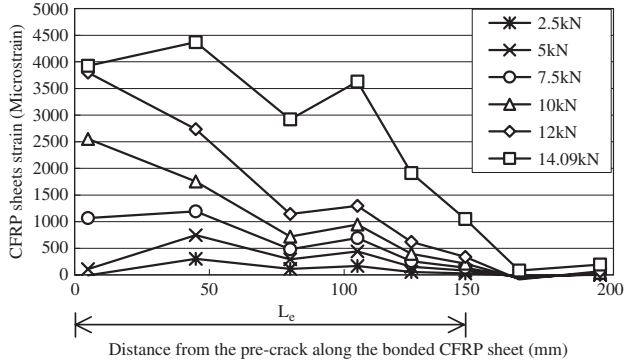

Figure 10. Strain distribution along bonded CFRP sheet for a specimen by using ordinary epoxy resin (40°C).

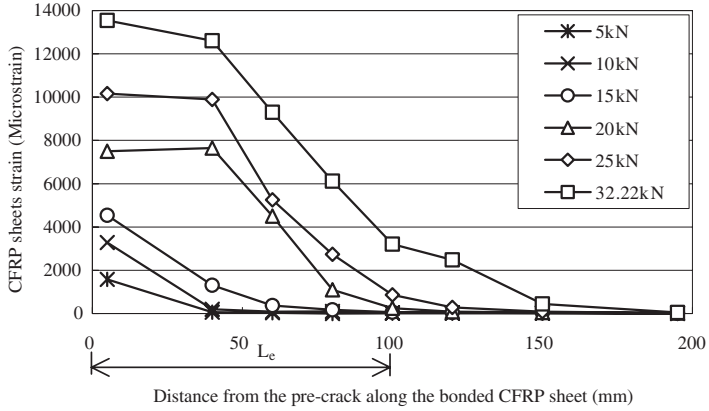

Figure 11. Strain distribution along bonded CFRP sheet for a specimen by using thermo-resistant epoxy resin (26°C).

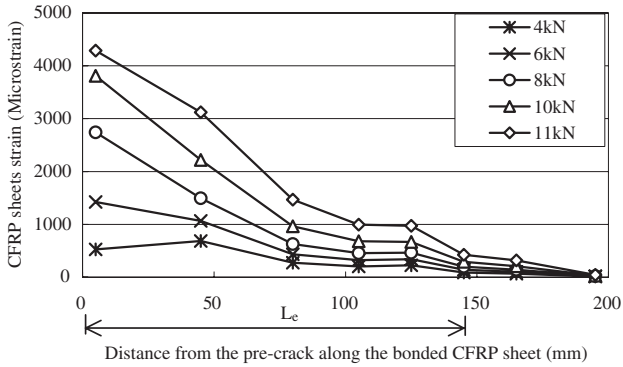

Figure 12. Strain distribution along bonded CFRP sheet for a specimen by using thermo-resistant epoxy resin (50°C).

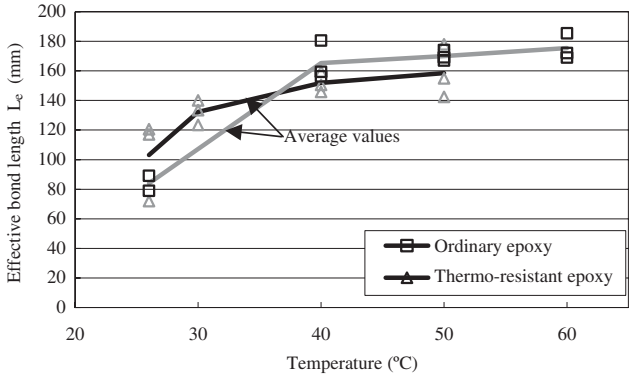

Figure 13. Effective bond length under different temperatures.

5 CONCLUSIONS

Based on the results of this experimental study, the following conclusions are obtained:

1. Maximum applied load and elastic modulus decrease gradually with temperatures ranging from 26°C to 60°C. Average bond strength σ_{bs} and interfacial fracture energy G_f of bonded FRP sheet by using both ordinary and thermo-resistant epoxy resins decrease approximately in direct ratio with temperatures ranging from 26°C to 60°C.
2. The value of G_f becomes lower than 0.5 N/mm under temperatures from 40°C for the ordinary epoxy resin while this critical temperature increases to 50°C for the thermo-resistant epoxy resin.
3. The debonding modes under temperatures lower than T_g and HDT are normally "B" or "C" while the debonding modes under temperatures near to or higher than T_g and HDT turn to be almost "A".
4. The effective bonding lengths of CFRP sheets get longer with increasing FRP–concrete interface temperatures.

ACKNOWLEDGEMENTS

Developing and investigating thermo-resistant epoxy supported by Toho Earthtech inc., Japan is gratefully acknowledged. Moreover, authors would also like to thank all the members of the P-PUT R&D consortium for their useful advices.

REFERENCES

Wu, Z. S., Yuan, H., Yoshizawa, H. and Kanakubo, T. 2001, "Experimental/Analytical Study on Interface Fracture Energy and Fracture Propagation along FRP-Concrete Interface," ACI International SP, *Fracture Mechanics and its Applications*.

Yoshizawa, H., Wu, Z. S., Yuan, H. and Kanakubo, T. 2000a, "Study on FRP-Concrete Interface Bond Performance," *Journal of Materials, Concrete Structures and Pavement*, JSCE, No.662/V-49, pp.105–119.

JSCE, 2000, *Guideline of Repairing and Strengthening on Concrete Structure with Externally Continuous Fiber Sheets*, Concrete Library 101.

Z. S. Wu and H. D. Niu, 2000b, Study on Debonding Failure Load of RC Beams Strengthened with FRP Sheets, *Journal of Structural Engineering*, JSCE, Vol. 46A, 1431.

Plastics - Thermomechanical analysis (TMA) - Part 2 1999, Determination of linear thermal expansion coefficient and glass transition temperature ISO 11359-2.

Plastics -Determination of temperature of deflection under load- Part 1 1993a, General test method, ISO 75-1.

Plastics -Determination of temperature of deflection under load- Part 2 1993b, General test method, ISO 75-2.

FRP Composites in Civil Engineering – CICE 2004 – Seracino (ed)
© 2005 Taylor & Francis Group, London, ISBN 90 5809 638 6

Durability of reinforced concrete structures with externally bonded FRP sheets

T. Shimomura & K. Maruyama
Nagaoka University of Technology, Niigata, Japan

ABSTRACT: This study focuses on long-term performance of reinforced concrete structures with externally bonded FRP sheet, which is carbon or aramid textile bonded with epoxy resin. Laboratory tests were carried out to investigate the durability aspect of concrete member retrofitted with FRP sheet. It was experimentally verified that the FRP sheet can reduce chloride ingress into concrete. Diffusivity of chloride ions in the layer of FRP sheet was identified by the numerical analysis of the test results. It was clarified that FRP sheet can improve mechanical performance of deteriorated concrete members due to reinforcement corrosion and associated concrete crack. Consequently, retrofit of FRP sheet is effective to improve durability, i.e. to extend service-life, of existing concrete structures.

1 INTRODUCTION

In the last ten years, upgrading of existing concrete structures by externally bonded fiber reinforced plastic (FRP) sheet has been increasingly adopted in Japan (JCI 1998, JSCE 2001, Ueda et al 2001). Continuous fiber sheets, which are carbon or aramid fiber textiles, are bonded on the surface of existing concrete structures with epoxy resin. The principal purpose of this upgrading technique is to improve mechanical performance of existing concrete structures, namely load-carrying capacity and ductility. Therefore, most of research projects on FRP sheets so far were based on this point of view.

However, durability of concrete structures with FRP sheet has not yet been well clarified. Though residual service-life of the upgraded structure is often discussed in practical design, there has been no verification method for its durability. Considering this situation, this study focuses on durability of concrete structures with FRP sheet.

Since epoxy resin has originally very low permeability, FRP sheet bonded on concrete surface can protect concrete from ingress of aggressive agents, such as chloride ions, and consequently extend service-life of the structure. Permeability test of reinforced concrete (RC) specimens with FRP sheet was carried out to examine the effectiveness of FRP sheet to reduce chloride ingress into concrete, as well as to increase mechanical performance. Diffusion coefficient of chloride ions within FRP sheet was quantified from the test results and the numerical analysis.

On the other hand, FRP sheet is normally applied on existing structures under service. In most studies, sound concrete structures are considered without any fatal material deterioration. However, in actual existing concrete structures, material deteriorations, such as reinforcement corrosion or associated concrete crack, have been sometimes induced before retrofitting FRP sheet. In order to investigate the influence of reinforcement corrosion on strengthening of RC member by FRP sheet, uniaxial tensile tests of RC specimens were carried out in this study. Reinforcement corrosion and corrosion crack were induced in the laboratory. Tensile behavior of RC specimens with FRP sheet was examined.

Finally in this study, numerical simulation of performance of concrete structures after retrofitting FRP sheet is demonstrated as a function of time based on the knowledge obtained from the experiments.

2 DIFFUSIVITY OF CHLORIDE ION IN FRP SHEET WITH EPOXY RESIN

2.1 *Outline of experimental study*

It is difficult to measure the diffusivity of aggressive agents, such as chloride ions or water, within the layer of epoxy resin on the surface of concrete under the normal condition because epoxy resin has very low permeability and may hardly allow chloride ingress. Therefore, the electrical permeability test was employed (Shimomura et al 2004).

Cylindrical concrete specimens shown in Figure 1 were used in the test. Twelve specimens, whose experimental parameters are water-cement ratio of concrete, thickness of concrete cover and wrapping of carbon

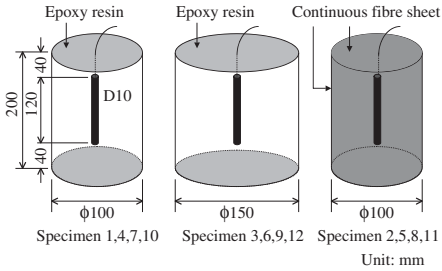

Figure 1. Cylindrical specimen for permeability test.

Table 1. Conditions of specimens.

Specimen no.	W/C of concrete (%)	Thickness of cover (mm)	FRP sheet wrapping
1	60	45	No
2	60	45	Yes
3	60	70	No
4	50	45	No
5	50	45	Yes
6	50	70	No
7	40	45	No
8	40	45	Yes
9	40	70	No
10	30	45	No
11	30	45	Yes
12	30	70	No

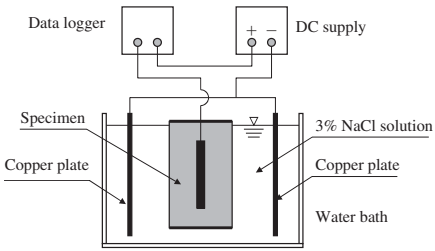

Figure 2. Setup for chloride permeability test.

FRP sheet on the surface, were tested. Testing conditions of the specimens are indicated in Table 1.

Setup for the permeability test is shown in Figure 2. Constant electric voltage of 30V was applied to the specimen in NaCl solution. Time-dependent direct current penetrating the concrete was measured.

2.2 *Test results*

Concrete cracks were generated in the specimens 1 and 4 around 100 hours by corrosion of reinforcements

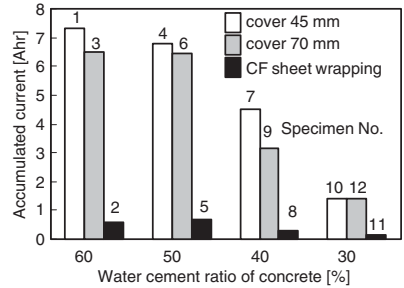

Figure 3. Accumulated electric current of the specimens until 90 hours.

in concrete. Electric resistance of concrete cover was suddenly lost after cracking. In order to compare permeability of all the specimens under the unified condition, therefore, accumulated electric current until 90 hours is taken as an index for permeability of specimen as shown in Figure 3.

Comparing the obtained accumulated electric current without FRP sheet in Figure 3, it is clear that permeability of concrete decreases with decreasing of water-cement ratio and increasing of thickness of concrete cover. These tendencies are very reasonable. In cases that FRP sheet is attached on the surface of concrete, accumulated current became very small in spite of water-cement ratio of concrete. It is verified that the system of FRP sheet and epoxy resin is effective as a surface insulator against ingress of materials into concrete.

2.3 *Numerical analysis of transport of chloride*

The authors have developed a computational model for the transport process of water and chloride ions in concrete based on pore structure of concrete and thermodynamic behavior of water in porous media (Shimomura and Maekawa 1997, Shimomura and Maruyama 2000). Mass conservation equations of water and chloride are respectively expressed as follows:

$$\frac{\partial w}{\partial t} = -div(J_v + J_l) \tag{1}$$

$$\frac{\partial C_{Clt}}{\partial t} = -div\left(J_{Cldif} + C_{Clf}\frac{J_l}{\rho_l}\right) \tag{2}$$

where, w = mass concentration of water per unit concrete volume, t = time, and J_v and J_l = mass flux of vapor and liquid water respectively, C_{Clt} = total mass concentration of chloride per unit concrete volume, J_{Cldif} = mass flux of chloride by molecular diffusion

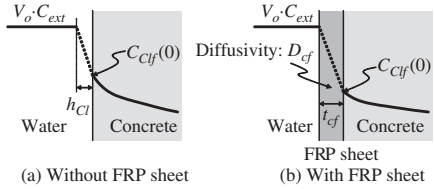

(a) Without FRP sheet (b) With FRP sheet

Figure 4. Profile of mass concentration of chloride near the boundary.

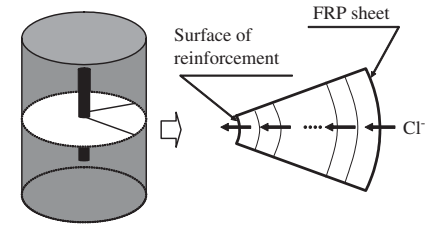

Figure 5. Numerical analysis of transport of chloride ion in cylindrical specimen.

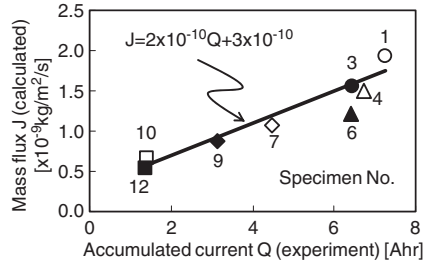

Figure 6. Correlation between the experimental and the analytical results.

and C_{Clf} = mass concentration of free chloride. The last term in Equation (2) expresses mass flux of chloride ions carried by liquid water that can be obtained from the moisture transport analysis.

It is necessary to execute coupling analysis of water and chloride to evaluate transport of chloride in non-saturated concrete in the atmosphere. However, in case of saturated concrete, molecular diffusion is dominant as transport mechanism of chloride in concrete. The mass flux of chloride by molecular diffusion is formulated as:

$$J_{Cldif} = -K_{Cl} D_{Cl} \, grad \, C_{Clf} \tag{3}$$

where, K_{Cl} = non-dimensional material factor of concrete as a function of its pore structure, D_{Cl} = diffusivity of chloride ion in liquid water.

Mass flux of chloride by molecular diffusion at the boundary surface is formulated as:

$$J_{Cldif} = -D_{Cl} \frac{C_{Clf}(0) - V_o \cdot C_{ext}}{h_{Cl}} \tag{4}$$

where, $C_{Clf}(0)$ = mass concentration of free chloride in concrete at the surface, V_o is porosity of concrete, C_{ext} is mass concentration of chloride in external solution and h_{Cl} is thickness of boundary-layer for mass concentration of chloride, in which local gradient of mass concentration of chloride is developed as shown in Figure 4.

When FRP sheet is bonded on the surface of concrete with epoxy resin, mass flux of chloride through the sheet is calculated as:

$$J_{Cldif} = -D_{cf} \frac{C_{Clf}(0) - V_o \cdot C_{exy}}{t_{cf}} \tag{5}$$

where, D_{cf} = diffusion coefficient of chloride ion in the layer of FRP sheet and epoxy resin and t_{cf} = thickness of the layer of FRP sheet and epoxy resin. Profile of mass concentration of chloride near the boundary is schematically shown in Figure 4.

2.4 *Evaluation of diffusion coefficient*

Diffusion processes of chloride in the cylindrical concrete specimens that were used in the electric permeability test were analyzed by the proposed diffusion model. Finite differential method was employed to solve the governing equations numerically (Figure 5).

Material parameters for concrete were determined based on the previous study (Shimomura and Maekawa 1997). The driving force in the experiment is the gradient of electric potential, while the driving force assumed in the computational model is the gradient of chloride concentration. Though they are different phenomena in fact, these two transport phenomena may have some correlation with each other since they are both transport phenomena of ions in concrete. Hence, before discussing permeability of FRP sheet, the correlation between the experiment and the analysis is verified using the results of the specimens without FRP sheet (Figure 6).

Figure 6 shows the relationship between the experimental and the analytical results performed in this study. Accumulated electric current until 90 hours (Q) is taken as the index of the experimental result, while mass flux of chloride in the steady state (J) is taken as the index of the analytical result. It is clear that the experimental results (Q) and the analytical ones

Table 2. Diffusion coefficient of FRP sheet.

Specimen no.	W/C of concrete (%)	Experimental Q (Ahr)	D_{cf} ($\times 10^{-14}$ m2/s)
2	60	0.56	2.29
5	50	0.68	2.99
8	40	0.28	3.03
11	30	0.13	4.69

(J) have good correlation in spite of water-cement ratio of concrete and thickness of concrete cover. This result implies that the hypothesis on the correlation between the experiment and the analysis is correct. In Figure 6, an empirical equation between the experimental results (Q [Ahr]) and the analytical ones (J [kg/m^2/s]) is indicated.

$$J = 2\times10^{-10}Q + 3\times10^{-10} \quad \left(kg/m^2/s\right) \tag{6}$$

It is assumed that this empirical correlation may be adapted to the specimens with FRP sheet. Then, diffusion coefficient of FRP sheet can be determined by trial and error so that the obtained analytical result (J) and the experimental result of the specimen (Q) satisfy the empirical equation. In the analysis, the thickness of FRP sheet (t_{cf}) was set 1 mm.

The diffusion coefficients of FRP sheet, which were obtained by this method from the experimental results of the specimens with FRP sheet, are shown in Table 2. Close values were obtained from the four specimens. The obtained diffusion coefficient of FRP sheet was approximately 3×10^{-14} m^2/s.

3 STRENGTHENING RC MEMBER WITH REBAR CORROSION BY FRP SHEET

3.1 *Outline of experimental study*

Figure 7 shows the dimensions of reinforced concrete specimens with and without continuous fiber sheet (Shimomura et al 2003). Conditions of specimens are given in Table 3. The $100 \times 100 \times 1000$ mm concrete prismatic specimens with single deformed steel bar (ϕ19 mm) in their center were prepared. After casting of concrete, specimens were wrapped with wet cloths and had been kept in the laboratory room for four weeks.

After four weeks of curing, the specimens RC3 and RC4 were exposed to the electrolytic corrosion test. The test setup is shown in Figure 8. Only the corrosion length of the specimen, which is 800 mm at the middle of the specimen, was placed in a 3% NaCl solution, while the rest part of the specimen was kept out of the solution to ensure anchorage of the reinforcement at

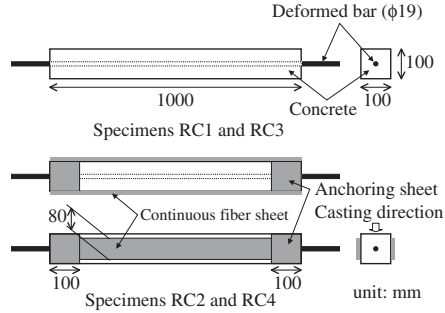

Figure 7. Specimens for uniaxial tensile test.

Table 3. Condition of specimens.

Specimen	Corrosion	FRP sheet
RC1	No	No
RC2	No	Yes
RC3	Yes	No
RC4	Yes	Yes
Bare bar A	No	–
Bare bar B	Yes	–

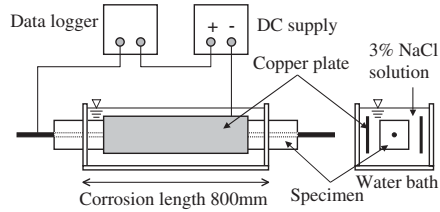

Figure 8. Test setup for electrolytic corrosion test.

the ends of specimen by avoiding corrosion. Constant direct current of 0.7A was provided by a DC supply with an embedded reinforcement as an electrode.

The corrosion test was continued until the cumulative current reaches the target value, which was set according to the previous test data (Matsuo et al 2001) so that the average corrosion in the corrosion length is about 1 mg/mm^2. In fact, longitudinal corrosion crack was observed at one of the concrete surface in both specimens after the electrolytic corrosion test. Actual amount of corrosion were measured by weight of the reinforcements taken out from the concrete after the loading tests. Electrolytic corrosion test of bare steel bar specimen B was also carried out with the same amount of cumulative current.

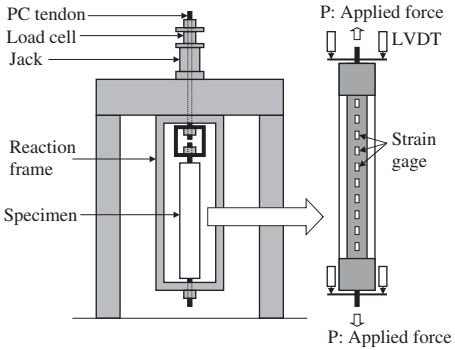

Figure 9. Test setup for uniaxial tensile test.

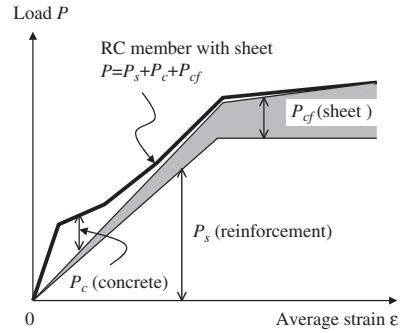

Figure 10. Load-sharing in RC member retrofitted with FRP sheet.

Carbon FRP sheets were bonded on the two side surfaces of the specimens RC2 and RC4 as shown in Figure 7. The sheets on RC4 were bonded just after curing of concrete, while the sheets on RC4 were bonded after the electrolytic corrosion test. One of the sheets on RC4 was bonded just over the longitudinal corrosion crack that had been induced by the corrosion test. Before bonding the sheets, the concrete surface was chipped and coated with a primer. Thereafter, the continuous fiber sheets were bonded with an epoxy resin.

As shown in Figure 7, anchoring sheets of 100 mm width were wrapped in both ends of the specimen to avoid delaminating of the longitudinal sheets from the ends. Aramid FRP sheets were used as the anchoring sheets because of their high flexibility.

The test setup for the uniaxial tensile test is shown in Figure 9. Tensile force was applied in the vertical direction in order to avoid eccentric load due to gravity as much as possible. Average strain of specimen was calculated from displacements measured with LVDT at the upper and bottom ends of the specimen. Local strains of continuous fiber sheets were measured with strain gages attached every 50 mm. Monotonic tensile force was applied. Tensile tests of the bare bar specimens A and B were also performed with this test setup.

3.2 *Formulation*

At an arbitrary section of a uniaxial specimen, applied force is carried by reinforcement, concrete and FRP sheets:

$$P = P_s(x) + P_c(x) + P_{cf}(x) \tag{7}$$

where, P = applied force, $P_s(x)$ = force carried by reinforcement at section x, $P_c(x)$ = force carried by concrete at section x and $P_{cf}(x)$ = force carried by FRP sheets at section x. $P_s(x)$, $P_c(x)$ and $P_{cf}(x)$ vary with respect to x because of concrete cracks and delaminating of sheets due to loading. By integrating Equation (7) with respect to x from the one end of the specimen to the other and dividing it by the length of the specimen, we obtain:

$$P = P_s + P_c + P_{cf} \tag{8}$$

where, P_s = average force of reinforcement, P_c = average force of concrete and P_{cf} = average force of FRP sheets. By dividing P_s, P_c and P_{cf} by corresponding cross sectional areas, we obtain average stress of reinforcement, concrete and FRP sheet in RC member respectively.

Figure 10 illustrates the state of load sharing of reinforcement, concrete and sheet in a RC member with FRP sheet. In the conducted uniaxial tensile tests, applied force (P) and average strain (ε) of specimens were measured.

When the reinforcement is not yielding at any points, average force of reinforcement (P_s) is given by:

$$P_s = A_s E_s \varepsilon_s \tag{9}$$

where, A_s = cross sectional area of reinforcement, E_s = elastic modulus of reinforcement and ε_s = average strain of reinforcement. The products of cross sectional area and elastic modulus of reinforcement ($A_s E_s$) in both corroded and non-corroded specimens were determined based on the tensile tests of bare steel bars. The results are shown in Table 4.

The amount of corrosion in the specimens RC3 and RC4 indicated in Table 4 were directly measured from the reinforcements taken out from concrete after the loading tests. As these measured amounts of corrosion were found to be close to that of the bare bar B,

Table 4. Mechanical properties of reinforcement.

	Corrosion (mg/mm^2)	A_sE_s (kN)	Yielding force (kN)	As (mm^2)
Bare bar A	0	54500	97.8	286.5*
Bare bar B	1.18	44700	94.2	277.5**
Bar in RC3	1.27	–	–	276.8**
Bar in RC4	1.12	–	–	277.9**

* Nominal cross sectional area.
** Calculated from nominal cross sectional area and loss of cross section estimated from corrosion.

the value A_sE_s of the bare bar B is adopted in computing the specimens RC3 and RC4. Average strain of reinforcement (ε_s) in Equation 9 is assumed to be equivalent to average strain of specimen (ε), which was measured in the experiment. Since Equation 9 is true when reinforcement is in elastic stage, test data only before yielding are used in the computation in this study.

As FRP sheet is elastic material, its average force (P_{cf}) is given by:

$$P_{cf} = A_{cf} E_{cf} \varepsilon_{cf} \tag{10}$$

where, A_{cf} = cross sectional area of FRP sheet, E_{cf} = elastic modulus of FRP sheet and ε_{cf} = average strain of FRP sheet. Though the distribution of sheet strain is not uniform after cracking, average values always satisfy Equation 10 independently of strain distributions. In the computation, average value of measured strain distribution of sheet is used as ε_{cf}.

Consequently, we can calculate P_s and P_{cf} from measured values. Substituting them into Equation 8, we obtain average force of concrete (P_c) or average stress of concrete (σ_c):

$$\sigma_c = \frac{P - P_s - P_{cf}}{A_c} \tag{11}$$

where, A_c = cross sectional area of concrete.

3.3 *Test results and discussion*

Figure 11 shows obtained relationships between the applied force and the average strain of all the uniaxial test specimens. Concrete strengths at the age of loading test were between 27 and 30 N/mm^2.

The specimen RC1 is the standard one for comparison, which has neither reinforcement corrosion nor continuous fiber sheet.

The specimen RC2, which was strengthened with FRP sheets, had high stiffness than RC1 after cracking in concrete. Total applied load in RC2 increased even after yielding of reinforcement because FRP sheet is an elastic material.

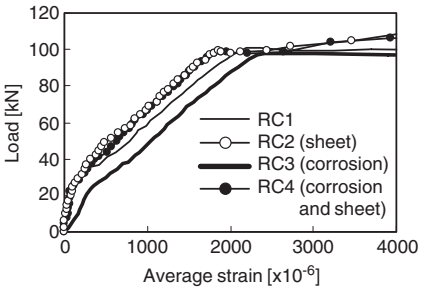

Figure 11. Load–strain curves for the uniaxial test specimens.

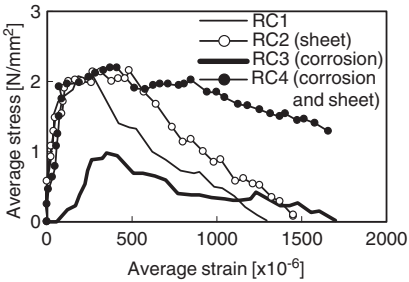

Figure 12. Average stress–strain curves of concrete.

The specimen RC3 with reinforcement corrosion had an apparent low stiffness from the initial stage. This is because cross sectional area of reinforcement was reduced due to corrosion.

The specimen RC4 showed almost same loadstrain curve with RC2 though the reinforcement in RC4 had been corroded, while RC2 had no corrosion.

This result suggests that FRP sheets bonded on RC member cannot only simply strengthen the RC member but also recover the deterioration of mechanical performance of the RC member due to reinforcement corrosion. This possibility shall be investigated more in detail in terms of stress carried by concrete in the specimens calculated from the experimental data.

Figure 12 shows the average stress-strain curves of concrete in the four specimens. The average stress of concrete was calculated by Equation 11. The average strain was measured by LVDT.

Comparing the average stress-strain curves of RC1 and RC2 in Figure 12, it is found that concrete stress increased when FRP sheet is retrofitted. The reason of this may be that bonding between concrete and reinforcement is improved because FRP sheet confines

concrete externally. However, as the difference in the average stress-strain curves of RC1 and RC2 is small, the improvement of the tensionstiffness of concrete by FRP sheet may not be remarkable.

It is clear that the tension-stiffness of concrete in RC3 is smaller than that in RC1 because of reinforcement corrosion. Rust products on the surface of reinforcement and corrosion crack in concrete, both of which reduce bonding between concrete and reinforcement, may cause the degradation of the tensionstiffness of concrete.

4 NUMERICAL SERVICE-LIFE SIMULATION OF RC STRUCTURES WITH FRP SHEET

4.1 *Outline*

In order to verify the advantage of taking into account the insulating effect of FRP sheet as well as its strengthening effect in service-life prediction, numerical simulation of time-dependent performance change of reinforced concrete structure with FRP sheet was carried out. The flowchart of the calculation is shown in Figure 13. At each time step, chloride ingress into concrete, corrosion of reinforcement in concrete and load-carrying capacity of the member are calculated. As results, load-carrying capacity of the member is evaluated as a function of time. After retrofitting FRP sheet on the structure, its roles, as surface insulator and as external mechanical reinforcement, are taken into account on the basis of the experimental results shown in this paper.

4.2 *Analytical conditions*

Flexural capacity of RC beam with FRP sheet shown in Figure 14 under various conditions were calculated as a function of time. Material properties used in the analysis are shown in Table 5. Six cases were analyzed as indicated in Table 6.

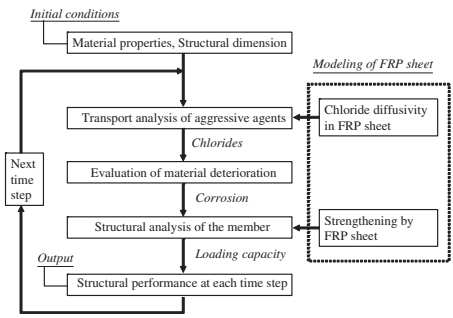

Figure 13. Flowchart of numerical service-life simulation of RC beam with FRP sheet.

The structure was assumed to stand under the corrosive environment with airborne salt from the sea. One-dimensional transport analysis was employed to evaluate chloride ingress into concrete as shown Figure 14. Corrosion of reinforcement in concrete caused by chloride and loss of cross-sectional area of the reinforcement due to corrosion were considered.

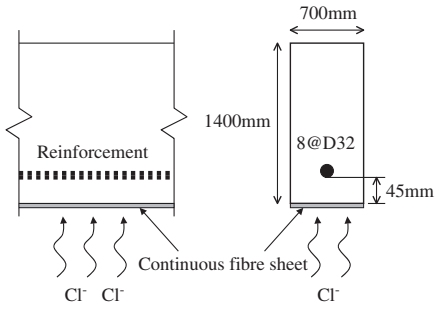

Figure 14. RC beam with FRP sheet.

Table 5. Material properties.

Concrete	
Unit water	165 kg/m^3
Water-cement ratio	50%
Compressive strength	38 N/mm^2
Other mechanical properties	Presumed from compressive strength
Parameters for mass transport	Presumed from mix proportion
Reinforcement	
Yield strength	400 N/mm^2
Elastic modulus	200000 N/mm^2
FRP sheet	
Thickness	1 mm (including epoxy resin)
Tensile strength	3500 N/mm^2
Elastic modulus	2.7×10^5 N/mm^2
Diffusion coefficient	3×10^{-14} m^2/s

Table 6. Analytical cases.

Case no.	Time of retrofit of FRP sheet	Effect of FRP sheet to be considered
1	Without FRP sheet	–
2	From the initial stage	Insulating and strengthening
3	At 10 years	Insulating and strengthening
4	At 20 years	Insulating and strengthening
5	From the initial stage	Only insulating
6	From the initial stage	Only strengthening

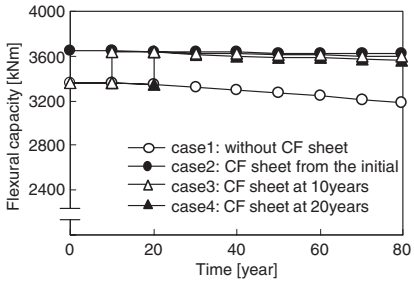

Figure 15. Analytical results 1: flexural capacity of beam as a function of time.

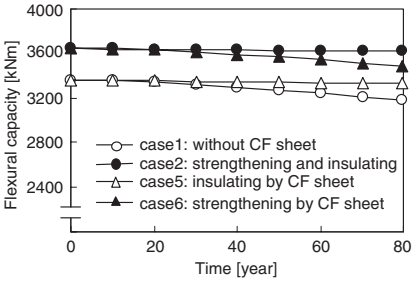

Figure 16. Analytical results 2: flexural capacity of beam as a function of time.

Strengthening effect of FRP sheet was evaluated by the conventional beam theory. Delamination of the sheet was not considered.

Based on the experimental results shown in this paper, tension-stiffening effect of concrete cover is reduced as a function of corrosion of reinforcement. However, after FRP sheet is bonded on concrete, tension-stiffening effect of concrete cover is not reduced even if reinforcement is corroded.

4.3 *Results and discussion*

Figures 15 and 16 show the analytical results, in which flexural capacity of the beams as a function of time are plotted. In case 1, in which FRP sheet is not attached, flexural capacity of the beam decreases gradually because of reinforcement corrosion. In cases 2, 3 and 4, in which FRP sheet is attached, flexural capacity is increased by the strengthening effect of the sheet and the time-dependent decreasing of flexural capacity is avoided by the insulating effect. The 'jump' in flexural capacity in the cases 3 and 4 in Figure 15 is attributable to the retrofitting of sheet.

As shown in Figure 15, the rate of deterioration after retrofitting of the sheet is a little different depending on the time of retrofitting. This is due to the difference of chloride concentration in concrete at the time of retrofitting.

The advantage to take into account the effectiveness of FRP sheet both as surface insulator and as external reinforcement is much clear in comparison of the results of cases 1, 2, 5 and 6 in Figure 16. The flexural capacity in case 2, in which both effectiveness are taken into account, is kept the highest level among these four cases.

5 CONCLUSIONS

Concerning durability and service-life prediction of reinforced concrete structures with FRP sheet, following conclusions were obtained through this study.

The effectiveness of FRP sheet bonded on concrete to reduce chloride ingress was experimentally verified by the electric permeability test.

Coupling the electric permeability test and numerical diffusion analysis, diffusion coefficient of chloride in the layer of FRP sheet with epoxy resin was quantified.

FRP sheet bonded on concrete, as it is well-known, can strengthen the existing concrete member by carrying tensile stress. This strengthening mechanism of FRP sheet is effective both in sound member and deteriorated member by reinforcement corrosion.

FRP sheet bonded on concrete can recover the tension-stiffness of concrete that was once degraded by reinforcement corrosion. This recovery may be achieved by the confinement effect of FRP sheet on concrete.

Through the numerical service-life simulation of RC structure with FRP sheet, the advantage to take into account the effect of FRP sheet both as surface insulator and as external reinforcement was verified.

REFERENCES

Japan Concrete Institute. 1998. Technical Report on Continuous Fiber Reinforced Concrete.

Japan Society of Civil Engineers. 2001. Recommendations for Upgrading of Concrete Structures with Use of Continuous Fiber Sheets, Concrete Engineering Series 41.

Ueda T., Shimomura T. and Maruyama K. 2001. Latest Design Method for Upgrading of Concrete Structures in Japan – JSCE Guidelines –, *Proceeding of the Eighth East Asia-Pacific Conference on Structural Engineering and Construction (EASEC8)*., *5–7 December 2001*. Singapore.

Shimomura T., Kasahara H. and Maruyama K. 2004. Numerical simulation of long-term behaviour of concrete structures with externally bonded continuous fibre sheet, *Proceeding of the International Conference on Advanced*

Polymer Composites for Structural Applications in Construction (ACIC2004)., 20–22 April 2004. Guildford.

Shimomura T. and Maekawa K. 1997. Analysis of the drying shrinkage behaviour of concrete using a micromechanical model based on the micropore structure of concrete, Magazine of Concrete Research, 49(181): 303–322.

Shimomura T. and Maruyama K. 2000. Service life prediction of concrete structures subjected to chloride attack by numerical simulation, *Proceedings of the International RILEM Workshop on Life Prediction and Aging Management of Concrete Structures*, Cannes, RILEM Publications S.A.R.L.

Shimomura T., Kasahara H. and Okazaki M. 2003. Effectiveness of continuous fiber sheet in strengthening of reinforced concrete member with rebar corrosion, *Proceedings of the JCI International Symposium on Latest Achievement in Technology and Research on Retrofitting Concrete Structures -Interface Mechanics and Structural Performance*, Kyoto.

Matsuo H., Gokaku W. and Shimomura T. 2001. Tension Stiffness of Reinforced Concrete Member with Corroded Reinforcement, *Proceeding of the JCI*, 23(3), 1327–1332, (in Japanese).

FRP Composites in Civil Engineering – CICE 2004 – Seracino (ed)
© 2005 Taylor & Francis Group, London, ISBN 90 5809 638 6

Determining hydrolysis behavior and durability from short term water sorption data

T. Wells & R.E. Melchers
School of Engineering, The University of Newcastle, Callaghan, NSW, Australia

ABSTRACT: This paper outlines a procedure for estimating long term hydrolytic aging of polyesters from short term water sorption data. Following calibration of the diffusion/hydrolysis model against sorption data obtained at ambient temperatures spatial and temporal evolution of network scissioning and small organic molecules concentration were determined for 50 mm thick composite samples under a variety of conditions. The simulations reveal that network fragmentation will be concentrated near the exposed composite faces while small organic molecules will concentrate in regions a short distance from the exposed composite faces making this region the most likely to suffer initial osmotic cracking. Simulation results also reveal markedly different damage distribution in thicker composite sections to that experienced by thinner composite samples. Consequently caution must be used when ascribing long term trends observed for some thin coupon mechanical properties to thicker samples. Several areas of improvement for the model were also identified for future work.

1 INTRODUCTION

It is widely acknowledged that a significant deficit exists in our ability to predict the long-term degradation of FRP materials when subjected to prolonged contact with moisture (Liao et al. 1998, Weitsman & Elahi 2000, Karbhari et al. 2003). The reasons for such a shortfall are many. Environmental aging mechanisms are complex and poorly understood. The effects involving breakdown of the resin, interface and reinforcing fibers are wide ranging and not easily categorized as they arise from the interplay of many environmental and material factors. Additionally durability studies by their nature require long term commitments of time which are often not practical. As a result durability data is sparse and findings from different studies are not easily compared thereby making the development of general models of the breakdown process difficult.

The aging process, particularly for polyester based composites is dominated by the corrosive action of water. Long term contact can result in resin swelling, hydrolytic breakdown of the resin and resin fiber interface, and osmotic cracking resulting in fiber debonding, delamination, loss of mechanical strength and premature failure. Some of the consequences of contact with moisture can be observed over relatively short periods of time (a few years) during water sorption studies in which the net weight change of composite coupons exposed to moisture is recorded. Figure 1 for example shows some typical water sorption trends

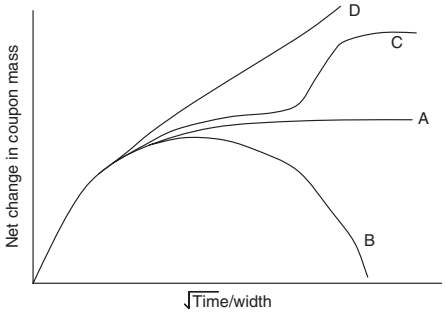

Figure 1. Examples of short term water sorption profiles. A – Linear Fickian behavior; B – sorption with hydrolysis/ leaching; C – two stage diffusion process; D – diffusion with increasing hydrophilic nature.

observed for polyester based composite materials. Linear Fickian diffusion (curve A) is a reasonable approximation for many composite materials however assumptions of Fickian diffusion will generally fail if structural and/or chemical changes to the resin occur on the same time scale as moisture diffusion (Springer 1981).

Such changes include relaxation of the polymeric structure (resulting in a two stage process as illustrated by curve C), increases in the hydrophilic nature of the

resin (due to chemical changes to the polymeric structure such as induced by hydrolysis – curve D) or the breakdown and leaching of resin and interface components (again via hydrolysis). In this last scenario an overall decrease in mass will be observed if mass loss due to leaching outstrips mass increase due to moisture uptake (curve B).

The form of the short term sorption profiles therefore contains information about the susceptibility of the resin/composite to water induced degradation and consequently can be used to help predict the long term aging of the material (Camino et al. 1998). To fully determine the effects of prolonged exposure to moisture not only must water sorption trends be modeled over time but also any accompanying physical and chemical changes to the matrix which not only have a bearing on the mechanical properties of the composite material but also influence future water sorption trends.

In this paper we will explore the hydrolysis of polyester resins, examining the interplay between the diffusion process and hydrolytic damage produced. The aim of this study is to calibrate a hydrolysis/diffusion physical model against short term sorption data gathered at ambient conditions and use the model obtained to predict the spatial and temporal distribution of polyester network disruption, depletion of ester sites and build up of hydrolysis products within the composite over the long term. The roles of different material and environmental properties on the aging process will also be considered.

2 HYDROLYSIS MODEL

Polyester resins have a high number of ester sites that are vulnerable to hydrolysis. Hydrolysis of those ester sites scissions the polyester chains leaving behind two "dangling chains" one with a alcohol end group and one with a carboxylic acid end group. Hydrolysis results in disruption of the polyester network system and osmotic cracking of the polyester resin both of which lead to resin embrittlement (e.g. see Ashbee et al. 1967, Apicella et al. 1983, Abeysinghe et al. 1982). Recently Gautier and co-workers (Gautier et al. 2000, 2001) proposed a simple kinetic model of the hydrolytic process which we will use as a starting point in our considerations. The pseudo-first order model proposed by Gautier is applicable to thin, permanently saturated composite samples in which the (equilibrium) water and ester concentrations within the polyester network are not significantly altered by time or the hydrolytic process. For thicker polyester samples exposed for longer time periods such assumptions may not be adequate so we have generalized the model to take into account spatial/temporal variation in water and ester levels throughout the hydrolysis process. The equations used to model the hydrolytic process are as follows:

$$\frac{\partial W_{(x,t)}}{\partial t} = D_w \frac{\partial^2 W_{(x,t)}}{\partial x^2} - k_h W_{(x,t)} E_{(x,t)} \qquad 0 < x < h \qquad (1)$$

$$\frac{\partial n_{(x,t)}}{\partial t} = \frac{-\partial E_{(x,t)}}{\partial t} = k_h W_{(x,t)} E_{(x,t)} \qquad (2)$$

where W = water concentration; D_w = diffusion coefficients of water (here assumed constant); x = distance from face of composite; k_h = second order hydrolysis reaction rate constant; E = concentration of ester groups within the resin; n = polyester chain scissions (hydrolysis events) per volume and h = the thickness of the composite.

In Equation 1 a second term is added to the Fickian expression describing the diffusion of water which takes into account the removal of water from the system as it is consumed in the hydrolysis reaction. The hydrolysis reaction which creates the chain scission event (n) and removes a reactive ester site (E) is described as a second order rate process (Equation 2).

Gautier et al. (2000, 2001) proposed that small organic molecules (SOCs) are formed when chain scissions occur close to the end of "dangling chains" and that the build up of SOCs is responsible for the initiation of osmotic cracking processes within polyester matrices, in itself an important aging process. In this work the formation and distribution of the hydrolysis breakdown products will also be examined. The expression used to determine the rate of formation of SOC material follows from the work of Gautier et al. (2001) with the added consideration that once formed such molecules are themselves free to diffuse throughout the matrix structure (albeit more slowly than water). The distribution of the hydrolysis product is then described via Equation 3:

$$\frac{\partial \gamma_{(x,t)}}{\partial t} = D_\gamma \frac{\partial^2 \gamma_{(x,t)}}{\partial x^2} + \frac{2\phi n_{(x,t)}}{E_{(x,t=0)}} \frac{\partial n_{(x,t)}}{\partial t} \qquad 0 < x < h \qquad (3)$$

where $\gamma_{(x,t)}$ = the free SOC concentration; D_γ = SOC diffusion coefficient; ϕ = the number of reactive ester groups located near the terminus of dangling chains.

When formulating the initial and boundary conditions for Equations 1–3 it was assumed that the composite was initially dry. It was also assumed that water and SOC concentrations were symmetrical about the central plane of the sample and that the contribution of polymer relaxation to the diffusion process could be expressed in the form proposed by Pritchard & Speake (1987). The considerations lead to the following initial and boundary conditions:

$$W(x,0) = 0 \qquad x \neq 0 \qquad (4)$$

$$E(x,0) = E_0; n(x,0) = n_0; \gamma(x,0) = \gamma_0 \quad x \neq 0 \tag{5}$$

$$\frac{\partial W\left(\frac{h}{2},t\right)}{\partial x} = 0; \frac{\partial \gamma\left(\frac{h}{2},t\right)}{\partial x} = 0 \tag{6}$$

$$W(0,t) = W_{t=0}^{sat} + W_{t=\infty}^{sat}(1 - \exp(-k_r t^2)) \tag{7}$$

where E_0 = the initial ester content (which can be calculated from the resin formulation); n_0 and γ_0 represent the initial number of dangling chain ends and SOCs initially present in the matrix respectively, (Gautier et al. 2000) and k_r is the polymer relaxation coefficient (Pritchard & Speake 1987).

3 RESULTS

3.1 *Calibration against ambient polyester + water sorption data*

The bulk of work undertaken on hydrolytic degradation of polyester resins has focused on degradation at temperatures significantly higher than ambient (Bélan et al. 1997a, Gautier et al. 2000, 2001) where osmotic cracking of the resin can be induced over relatively short periods of time. Analysis of immersion bath fluid in studies undertaken at near ambient temperatures however has revealed the presence of low molecular weight polyester species with hydroxyl end groups indicating that hydrolytic breakdown of polyester resins, while slower, still takes place at these lower temperatures (Kootsookos & Mouritz 2004). In the absence of osmotic cracking these species diffuse to the external surfaces of the composite material.

In this study we wish to focus on the aging of polyester material employed in infrastructure applications and thus our interest lies with long term behavior at ambient conditions. An assessment of the long term durability of these materials will involve looking at the long term consequences of a slow build-up of hydrolytic activity and products. As a first step in examining this scenario Equations 1–7 were calibrated against water sorption data obtained for polyester composite samples immersed at near ambient conditions. The model was then used to predict the hydrolytic aging of the same polyester composite over longer time frames.

Equations 1–3 were used to model the water sorption data reported for 1.6 mm thick fully cured E-glass reinforced isophthalic polyester composites samples immersed in 30°C seawater over a 2 year period (Kootsookos & Mouritz 2004). The overall change in mass of the polyester composite in the simulation was determined by comparing the fluxes of water and SOCs through the exposed faces of the composite (Equation 8):

$$\Delta M_{(t)} = \frac{-2}{h}\left(D_\gamma MW_\gamma \int_0 \left.\frac{\partial \gamma_{(x,t)}}{\partial x}\right|_{x=0} dt + D_w MW_w \int_0 \left.\frac{\partial W_{(x,t)}}{\partial x}\right|_{x=0} dt\right) \tag{8}$$

where ΔM_t = the overall change in mass (kg.m^{-3}); MW_w and MW_γ are the molecular weights of water and the SOC species respectively.

Additionally the following assumptions were made:

1. For the purposes of the mass balance it was assumed that the leached species could be represented as propylene glycol ($MW_\gamma = 76$ kg/kmol). This follows from analysis of leaching products which indicates a significant presence of low molecular weight polyester species with hydroxyl end groups (Kootsookos & Mouritz 2004).
2. A constant ratio, $D_\gamma/D_w = 40$, was assumed. This ratio was estimated from solubility data reported for water, propylene glycol, ethylene glycol and diethylene glycol in Gautier et al. (2000).
3. Transport of leached species from the surface of the composite coupon to the surrounding bath fluid was assumed to be significantly faster than the rate at which the SOC species diffuse to the exposed surfaces of the composite. Additionally the concentration of SOC species within the bath fluid is sufficiently dilute that the concentration of SOCs at the composite surface remains negligible throughout the course of the study.
4. The relaxation constant 'k_r' used in Equation 7 was that obtained for an isophthalic polyester resin immersed at 30°C in the same study. The ratio of $W^{sat}(t=\infty)/W^{sat}(t=0)$ employed in Equation 7 was set to ~3 (again as suggested by the data of Pritchard & Speake 1987).

The initial ester concentration (E_0) in the isophthalic polyester resin was estimated at 10 kmol/m^3. The values of the remaining parameters (D_w, k_h, n_0, γ_0 and $W^{sat}(t=0)$) were then varied until a satisfactory fit to the data was obtained (see Figure 2). The parameter values employed are listed in Table 1.

Calibration of the above model against the sorption data gathered at 30°C provides an insight into the relative effects of water diffusion (feeding moisture to the interior of the composite) and hydrolysis (removing moisture from the system as it reacts with polyester reactive sites) at near ambient conditions. Calculation the characteristic times of hydrolysis (τ_h) and diffusion (τ_d) then provides the means of directly comparing the kinetics of the two processes, (Bellenger et al. 1995):

$$\tau_h = \frac{1}{k_h E_{(x,t)}} \approx \frac{1}{k_h E_0} \tag{9}$$

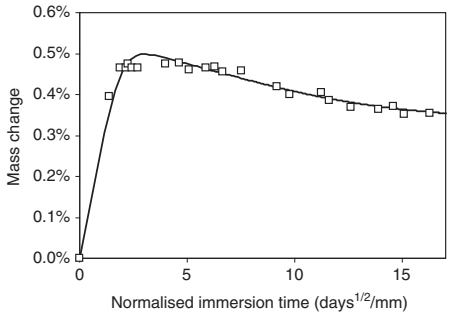

Figure 2. Fit of hydrolysis model to 100% cured polyester composite waster sorption profiles. (Data: Kootsookos & Mouritz 2004.)

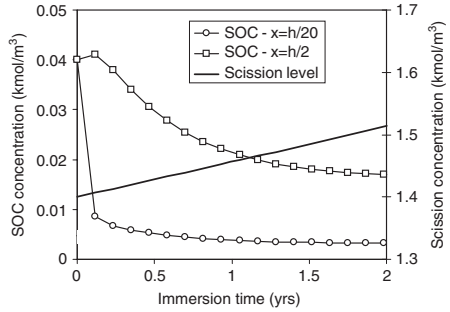

Figure 3. Predicted scission density and small organic molecule distribution in a 1.6 mm polyester coupon as a function of immersion time at 30°C and distance × from the exposed faces of the sample.

Table 1. Values used in modeling of polyester water sorption.

Parameter		Values
D_w	(m^2/s)	6×10^{-13}
$W^{sat}(t=0)$	(wt%)	0.55
k_h	(m^3/kmol.s)	3.8×10^{-10}
E_0	(kmol/m^3)	10
n_0	(kmol/m^3)	1.4
γ_0	(kmol/m^3)	0.04
k_r	(s^{-2})	7×10^{-18}

$$\tau_d = \frac{h^2}{D_w} \qquad (10)$$

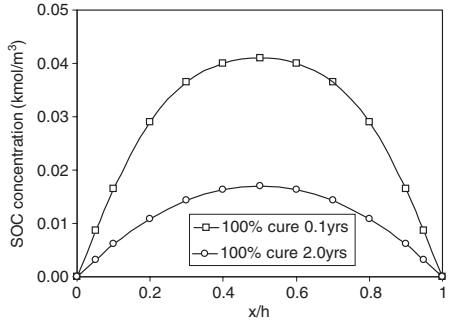

Figure 4. Spatial distribution of small organic molecules in 1.6 mm polyester coupons at 30°C at various times.

Comparison of the two time constants for the 1.6 mm coupons reveals that $\tau_h \gg \tau_d$ implying that in this case the diffusion process dominates the hydrolysis process enabling water to penetrate to the core relatively unhindered.

Solving Equations 2 and 3 for $n_{(x,t)}$ and $\gamma_{(x,t)}$ allows determination of the temporal and spatial distribution of scission damage and SOCs (Fig. 3). Over the course of the 2 year immersion period the level of chain breakage is predicted to have increased slowly with time in a near linear fashion (increasing by 5∼10% over that time). The narrowness of the coupon coupled with the low hydrolysis reaction rates at 30°C ensures that water levels quickly approach the saturation level (prior to relaxation) and that the level of ester sites available for hydrolysis is not significantly reduced in the first few years. These two factors combine to ensure that the scission concentration is uniform across the cross-section of the coupon and increases in a linear fashion within the time period.

The concentration of SOCs (Figs. 3 and 4) follows a more complicated evolution. The SOC concentration at any point in time and space is the result of two competing effects; the extent of hydrolysis (creating the SOCs) and SOC diffusion (dispersing SOCs to the sinks at either composite face). The balance of competing processes at the conditions experienced in the study result in a maximum SOC concentrations along the central plane of the coupon. The greater dispersive nature of this system however results in an overall decrease in SOC levels over time (Fig. 4).

3.2 *Extending the model to thicker sections over longer lifetimes*

Having calibrated the hydrolysis/diffusion model against the short term sorption data it is now possible to extend the range of the model to consider the long term effects of hydrolysis on more substantial polyester

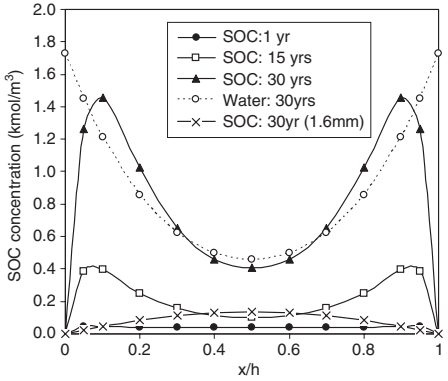

Figure 5. Evolution of the spatial distribution of small organic molecules in a fully cured 50 mm thick polyester composite at 30°C.

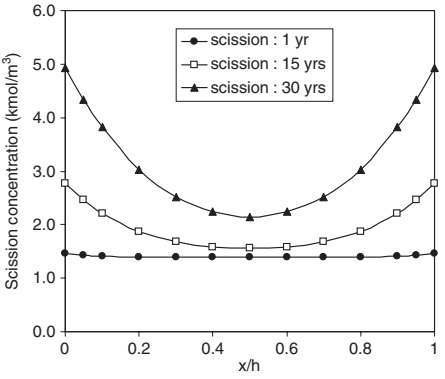

Figure 6. Evolution of scission levels in a fully cured 50 mm polyester composite at 30°C.

specimens possessing the same characteristics as the above mentioned material.

To do this the hydrolysis model was rerun to examine the behavior of a sample 50 mm thick exposed for 30 year period at 30°C. Figure 5 shows the evolution of SOC levels in the thicker composite over that time period. The distribution pattern evolves over time for the larger section to produce local maxima of SOC material ∼5–10 mm below the exposed faces of the member. The profile develops in this way because the relative balance between the water diffusion, SOC diffusion and hydrolytic processes has shifted. With the thicker sample section the characteristic time of diffusion is now greater than that of hydrolysis and consequently the hydrolytic depletion of moisture proceeds more rapidly relative to the diffusion process which feeds moisture to the interior of the composite with the net result of lower moisture levels near the central plane of the composite.

This in turn lowers the rate of scission and SOC production near the central plane of the composite. Simultaneously diffusion of the SOC material near the exposed surfaces out into the surrounding fluid reduces SOC levels in the region adjacent to the exposed composite faces producing SOC maxima in the intervening region. Scission levels (Fig. 6) show the same central minima with the majority of network disruption being predicted at the exposed composite faces.

The magnitude and position of SOC maxima is an important factor when considering the longevity of the composite specimen as it has been postulated (Gautier et al. 2000) that once $\gamma_{(x,t)}$ exceeds a critical value osmotic cracking is initiated at that site. The position of the SOC concentration maxima therefore suggests that the initiation of osmotic cracking is most likely to occur slightly inside the exposed faces. The magnitude and position of the maxima is clearly dictated by many parameters ($k_h, D_\gamma, D_w \ldots$), however application of the aforementioned equations to short term data enables an estimate of the time it would take to reach a critical SOC level (provided this is known) and the positioning of the first levels of damage once cracking begins.

The above results demonstrate that water distribution pattern observed for thin coupons commonly employed in laboratory studies are not representative of those to be expected in more substantial samples particularly when hydrolytic processes are also active. A comparison of data obtained for both the 1.6 mm and 50 mm composite samples over a 30 year period (Fig. 5) for instance reveals that the patterns of damage also are markedly different, even though the two situations involve identical material characteristics. Consequently caution must be used in extrapolating mechanical properties observed for thin coupons to thicker composite components.

3.3 *Effect of altering climatic conditions and materials properties*

The calibration of Equations 1–7 also allows exploration of the effect of changes in climatic and material properties on the long term hydrolysis of the polyester composite. A brief examination of the consequence of small changes in temperature, resin chemistry and level of cure follows.

3.3.1 *Temperature*

A change in the temperature at which the component is exposed to moisture alters the rates of hydrolysis, relaxation and diffusion of both of water and SOC material. To examine the effect of a modest change

Table 2. Activation energies used in calculating diffusion, hydrolysis and relaxation rates at 35°C.

Process	Activation energy (kJ/mol)	Source
Water/SOC diffusion	75.0	Pritchard & Speake (1987)
Hydrolysis	90.0	Bélan et al. (1997a)
Polymer relaxation	180.0	Pritchard & Speake (1987)

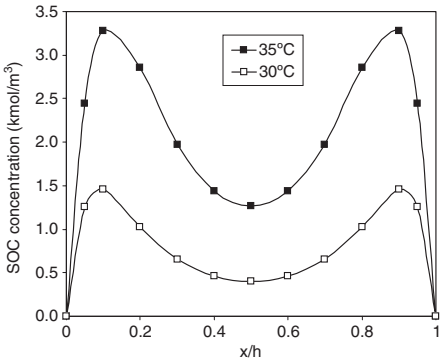

Figure 7. Predicted spatial distribution of small organic molecules in a fully cured 50 mm thick polyester composite at 30 and 45°C after 30 years immersion.

in temperature a comparison of scission and SOC levels in a 50 mm thick polyester sample exposed at 30 and 35°C were compared after 30 years of immersion. In this instance it was assumed that all of the above processes obey an Arrhenius relationship with temperature. Activation energies used to calculate diffusion, relaxation and rate reaction constants at 35°C and their sources are listed in Table 2.

It is clear from Figures 7 and 8 that even moderate changes in temperature can have a significant influence on the aging of the composite, with a 5°C increase more than doubling SOC levels and increasing scission levels by more than 50%. Once again the effect is not uniform but concentrated at the exposed faces (scission) and points just interior (SOC levels). Clearly the overall effect of changes in temperature is heavily dependent on the relative values of the activation energies chosen – knowledge of these values is crucial if temperature dependency of long term aging is to be evaluated.

3.3.2 *Effect of resin chemistry*

Changing the polyester resin formulation can significantly alter the vulnerability of the resin to

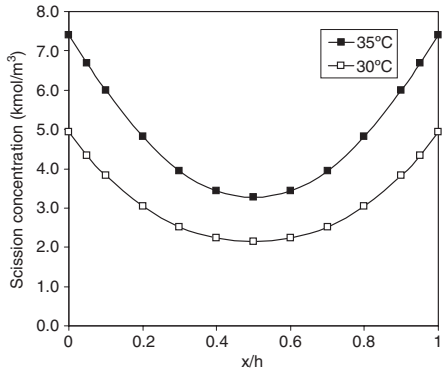

Figure 8. Predicted distribution of scission concentration in a fully cured 50 mm thick polyester composite at 30 and 35°C after 30 years immersion.

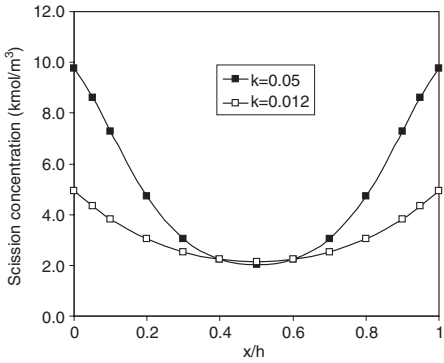

Figure 9. Effect of change in susceptibility to hydrolysis to the predicted scission distribution within a 50 mm thick polyester composite after 30 years immersion.

hydrolytic attack. Recently for instance Bélan et al. (1997b), examined the relationship between structure and the hydrolysis rate of polyester prepolymers and observed a large range of hydrolysis rates (second order reaction rate constants ranging from ~0.2 to 12.1 $kg.mol^{-1}s^{-1}$).

The consequences of increasing the reaction rate constant by a factor of 4 are shown in Figures 9 and 10. As expected there are significant increases in both the levels of network scission and levels of hydrolysis product. Once more degradation effects are concentrated at the exposed faces (scission) and in the regions slightly interior to the exposed faces (SOC levels) while the core of the composite is relatively unaffected by the increased hydrolytic attack suggesting that mechanical properties which are dependent

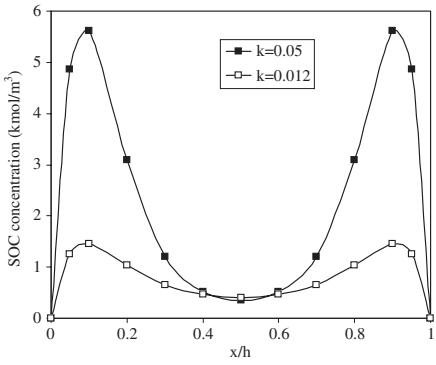

Figure 10. Effect of change in susceptibility to hydrolysis to the predicted small organic molecule distribution within a 50 mm thick polyester composite after 30 years immersion.

on damage location rather than average damage levels (e.g. flexural properties) will be more adversely affected.

3.3.3 *Cure level*

In the hydrolysis model the degree of cure is principally manifested in the value of γ_0, the level of water-soluble molecules such as catalyst residues and unreacted monomers initially present in the composite. To examine the role of cure level the water sorption behavior of under-cured (88%) polyester coupons reported in the same study as the aforementioned fully cured 1.6 mm polyester coupons (Kootsookos & Mouritz 2004) was undertaken. The fully cured and under cured samples were identical except for the level of curing so only the value of γ_0 was altered in our attempts to model the behavior.

Figure 11 shows curve of best fit ($\gamma_0 = 0.09$ kmol/m^3). The fit is less satisfactory than that obtained in the fully cured case however the best fit value obtained for γ_0 is higher than obtained for the fully cured polyester data, and thus agrees with the perception that the initial levels of water soluble organic material would be higher in under-cured samples. Never the less there exists considerable room for improvement in simulating the magnitude and trends of the sorption data. The suppression of the maximum mass gain observed by Kootsookos & Mouritz (2004) ($\sim$0.48% in the fully cured sample and $\sim$0.38% in the 88% cured sample) is considerably greater than that predicted by the model and the predicted slope of the mass change curve after the maxima has been reached does not match that observed. Given the variation between the predicted and observed values and trends with time, long term predictions of the effect of cure with the above model are of limited value.

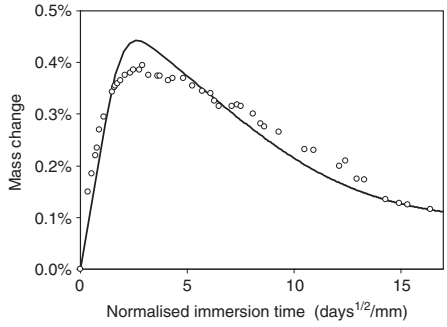

Figure 11. Fit of model to 88% cured data. (Data: Kootsookos & Mouritz 2004.)

4 DISCUSSION AND FUTURE WORK

The hydrolysis/diffusion modeling discussed in this paper is very much a work in progress. As evidenced by the results obtained for low cure sorption behavior the simple model described above does not adequately explain all aspects of the sorption data observed. A further issue arises with the manner in which sorption data is normalized for coupon thickness. It is the general practice in sorption studies to normalize the sorption data for the coupon thickness by plotting mass change as a function of ($t^{1/2}$/h) where t is the immersion time and h is the coupon thickness (as has been done above in Figures 2 and 11). However sorption data reported for polyester samples of varying thicknesses by Kootsookos & Mouritz (2004) and Camino et al. (1996) indicate that the sorption data cannot be successfully normalized in this fashion (normalization is achieved when sorption data is plotted against $\sim t^{1/2}/h^2$). Simulations carried out with the hydrolysis/diffusion model discussed in this paper do not predict this behavior but rather the more traditional $t^{1/2}$/h relationship still holds during the initial stages of the sorption process. Whether this is a consequence of the simplicity of the model employed in this study is not clear and will be the focus of future work. The introduction of additional factors such as the concentration dependence of D_w and D_γ, the autocatalytic nature of the hydrolysis process and increasing hydrophilicity of the resin material due to chemical changes will be considered in future versions of the model.

5 CONCLUSIONS

A procedure for estimating the long term hydrolytic aging of polyester from trends observed in short term water sorption trials has been outlined.

Spatial and temporal evolution of network scissioning and concentrations of small organic molecules (a precursor to osmotic cracking) predicted by the hydrolysis/diffusion model for 50 mm composite section in prolonged contact with moisture has revealed that network damage will be concentrated near the exposed composite faces while small organic molecules will be most concentrated in regions that lie a small distance into the composite. Model predictions have also revealed that modest increases in temperature and hydrolytic susceptibility greatly increase the level of damage in those same areas in the long term while the core of the composite is relatively unaffected.

The model results clearly indicate that the pattern of damage in thicker composite sections will be quite different to that experienced by thinner composite samples exposed to moisture over the same time frame. Trends in mechanical properties observed for thin sectioned composite samples which are influenced by the distribution of damage (rather than the average damage over the composite cross-section) are therefore likely to differ for thicker samples of the same material.

Analysis of the effect of cure on sorption behavior indicates that aspects of the model need improvement. Future work will investigate the incorporation of additional factors such as concentration dependence of diffusion coefficients to improve the fit of the model to observed data.

ACKNOWLEDGEMENT

The work presented in this paper was undertaken within the research program of the Cooperative Research Centre for Advanced Composite Structures Ltd., Australia.

REFERENCES

Abeysinghe, H.P., Edwards G., Pritchard G. & Swampillai G.J. 1982. Degradation of crosslinked resins in water and electrolyte solutions. Polymer 23: 1785–1789.

Apicella, A., Migliaresi C., Nicolais L., Iaccarino L. & Roccotelli S. 1983. The water ageing of unsaturated polyester-based composites: influence of resin chemical structure. Composites 14(4): 387–392.

Ashbee, K.H.G., Frank F.C. & Wyatt R.C. 1967. Water damage in polymer resins. Proceedings of the Royal Society A. 300: 415–419.

Bélan, F., Bellenger V. & Mortaigne B. 1997a. Hydrolytic stability of unsaturated polyester networks with controlled chain ends. Polymer Degradation and Stability 56: 93–102.

Bélan, F., Bellenger V., Mortaigne B. & Verdu J. 1997b. Relationship between the structure and hydrolysis rate of unsaturated polyester prepolymers. Polymer Degradation and Stability 56: 301–309.

Bellenger, V., Ganem M., Mortaigne B. & Verdu J. 1995. Lifetime prediction in the hydrolytic ageing of polyesters. Polymer Degradation and Stability 49: 91–97.

Camino, G., Luda M.P. & Polishchuk A.Y. 1996. Chemical structure and water diffusion in polyester resin glass fibres composites. Composites 18: 40–50.

Camino, G., Polishchuk A.Y., Luda M.P., Revellino M., Blancon R. & Martinez-Vega J.J. 1998. Water ageing of SMC composite materials: a tool for material characterisation. Polymer Degradation and Stability 61: 53–63.

Gautier, L., Mortaigne B., Bellenger V. & Verdu J. 2000. Osmotic cracking nucleation in hydrothermal-aged polyester matrix. Polymer 41: 2481–2490.

Gautier, L., Mortaigne B., Bellenger V. & Verdu J. 2001. Osmotic cracking in unsaturated polyester matrices under humid environment. Journal of Applied Polymer Science 79(14): 2517–2526.

Karbhari, V.M., Chin J.W., Hunston D., Benmokrane B., Juska T., R. M., Lesko J.J., Sorathia U. & Reynaud D. 2003. Durability gap analysis for fiber-reinforced polymer composites in civil infrastructure. Journal of Composites for Construction 7(3): 238–247.

Kootsookos, A. & Mouritz A.P. 2004. Seawater durability of glass- and carbon-polymer composites. Composites Science and Technology 64(10–11): 1503–1511.

Liao, K., Schultheisz C.R., Hunston D.L. & Brinson L.C. 1998. Long-term durability of fiber-reinforced polymer-matrix composite materials for infrastructure applications: a review. Journal of Advanced Materials 30(4): 3–40.

Pritchard, G. & Speake S.D. 1987. The use of water sorption kinetic data to predict laminate property changes. Composites 18(3): 227–232.

Weitsman, Y. & Elahi M. 2000. Effects of fluids on the deformation, strength and durability of polymeric composites – an overview. Mechanics of Time-Dependent Materials 4: 107–126.

FRP Composites in Civil Engineering – CICE 2004 – Seracino (ed)
© 2005 Taylor & Francis Group, London, ISBN 90 5809 638 6

Service life prediction of GFRP pipes in aggressive environments

M. Farshad*, A. Necola & P. Flüeler
Swiss Federal Laboratories for Materials Testing and Research, EMPA, Switzerland

ABSTRACT: In this contribution, results of long-term creep tests of Glass Fiber Reinforced Polymer (GFRP) pipe samples in wet condition, acid, and alkaline environments are reported. Two sample groups were pipes produced by centrifugal casing and filament winding process. Regression analysis of the data related to the tests in wet condition to 50 years showed a reduction of strength by more than 50% of the dry strength in short-term loading. Long-term regression of strain corrosion tests revealed a 50-year strain at failure of less than 0.2%. Long-term extrapolation of the tests in alkaline medium to 50 years showed dramatic reduction of strength to about 1% of the initial strength. In all cases, low failure strain and brittle mode was observed. It was concluded that in design of GFRP pipes and service life prediction the strength values as well as the strain criteria under the influences of medium should be considered.

1 INTRODUCTION

Glass Fiber Reinforced Polymer (GFRP) pipes are composite constructions consisting of short and/or long glass fiber and thermosetting materials such as unsaturated polyester (or vinyl ester) as their main constituents. These pipes are normally produced through centrifugal casting with short fibers or filament winding of long fibers. In addition to the structural layer, the pipes may also have internal and external protection layers, which mainly consist of the resin material.

Glass Fiber Reinforced Polymer (GFRP) pipes have applications in pressure pipelines as well as in drainage and sewerage piping systems. In these applications the pipe is in contact with various fluids that, in some cases, may have aggressive effects on the material components of the pipe. The mechanism of action of the environmental conditions on the pipe material depends on the individual medium. For example, action of an alkaline medium produces leaching, pitting, and corrosion of glass fibers. The corroding influence of the alkaline environment on such pipes has been reported by Zhang (1999) and Karbhari (2000).

The contact of the loaded pipe with acid environment may lead to the so called *strain corrosion*. Some attention has been given to this effect has been reported by Woo (1988). Long-term strain corrosion studies in acid environments were carried out under constant diametrical deflection of pipe ring samples as reported by Farshad (in press, 2004). The action of water on the pipe behavior may also be qualitatively anticipated. It can be conceived that the long-term water action would weaken some types of resin components and would lead to debonding of the fiber-resin system as reported by Fried (1967) and Woo (1988). In a previous work the effect of aqueous environment on the long-term behavior of GFRP pipes was investigated by Farshad (in press, 2004).

Determination of the long-term response of Glass Fiber Reinforced Polymer GFRP) pipes in wet conditions and the theoretical long-term extrapolation is of great importance in the design of these pipes. The experimental data are normally obtained over a time period of up to about 2 years. These data should be extrapolated to much longer time periods including 50 years, which is considered the service life of pipelines.

This work has been carried in the framework of a joint European project in which various European partners were involved. The creep tests on samples immersed in water were carried out by a number of partners. In this sense, a collective correlation and benchmarking was achieved and the results were validated. The results reported in this paper, however, relate only to the work done in the institution of the authors.

∗Corresponding author: Professor M. Farshad, Swiss Federal Laboratories for Materials Testing and Research, EMPA, 129 überlandstrasse, 8600 Dübendorf, Switzerland, Tel. (++41) 01 8234491, Fax 00411 8216244, E-Mail: mehdi.farshad@empa.ch

2 TESTING EQUIPMENTS

To perform the long-term experiments a number of testing devices were developed and constructed. Two

types of experimental equipment were constructed: one type was used for the direct creep testing of GFRP pipes in wet condition and also in the alkaline medium; another type was used for the stress relaxation tests of GFRP pipes under the influence of acid environment.

For testing of the pipe ring samples in wet condition the preconditioned GFRP pipe segments were immersed in water container and were subjected to diametrical compressive force. For testing of the pipe ring samples in alkaline medium the GFRP pipe segments were immersed in container with high alkali content and were subjected to diametrical compressive force. A typical testing system of both tests consisted of a dead weight loading device, a container, and a

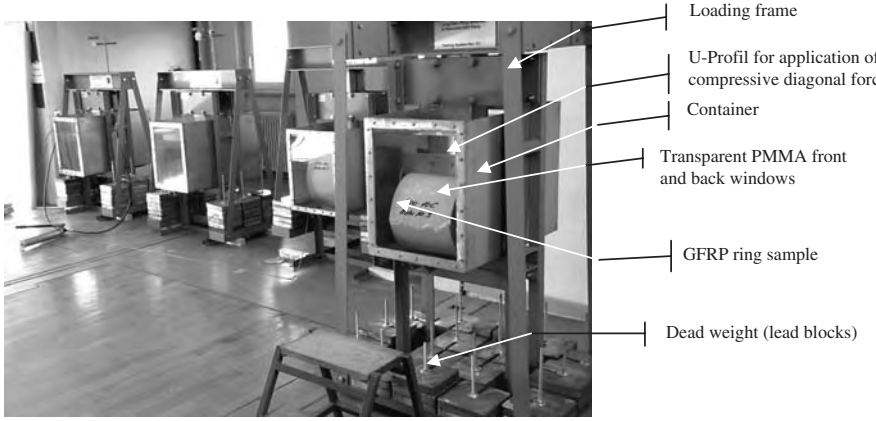

Figure 1. Testing equipment for long-term tests of GFRP pipe ring in saturated condition (water medium as well as alkaline medium).

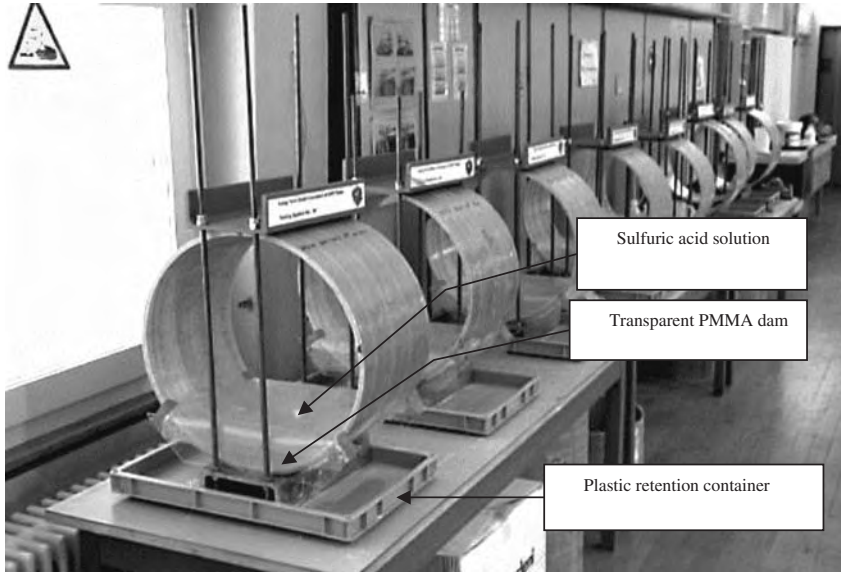

Figure 2. Series of experimental set-ups for long-term strain corrosion tests.

structural frame. Figure 1 shows one of the testing set-ups for the long-term creep tests of GFRP pipe samples in wet condition as well as for the testing of samples in alkaline medium. For efficient parallel testing, a total number of nine such systems were constructed. The diametrical deflection of the pipe samples was periodically monitored by the external measurement devices.

To investigate the influence acid environment on the long-term behavior of GFRP pipes, another type of equipment capable of applying constant diametrical deflection was constructed. GFRP pipe ring samples were exposed to the acid medium at the lower part of the section. Figure 2 depicts a number of such testing apparatus.

3 TEST SAMPLES AND TESTING PROCEDURE

3.1 *Creep behavior of GFRP pipes in wet condition*

Ring sections were taken from short glass fiber-reinforced pipes with unsaturated polyester resin produced by a centrifugal casting procedure. They constituted the *first* batch of the two available batches of this pipe type. The specimens used had a nominal diameter of 500 mm. The length of each sample was about 300 mm. Prior to experiment, samples were stored at room temperature of $22 \pm 3°C$ and $50 \pm 5\%$ relative humidity. A number of selected specimens were conditioned in a container filled with circulating drinking water at $20 \pm 2°C$. The specimens were kept in the container for at least 1000 hours. To establish reference values, short-term diametrical compression tests were performed on a number of dry as well as conditioned samples. Testing was carried out in compatibility with an existing guideline, see EN 1227 (1997). For the long-term tests, using the reference values, various loading levels were chosen. The diametrical loading covered a range of 6.0 to 17.1 kN and resulted in failure times in the range of 0.2 to 6000 hours.

3.2 *Strain corrosion of GFRP pipes in acid environment*

Samples made of Glass reinforced thermosetting (GFRP) plastics with polyester resin were tested. The pipes were produced by a filament winding process. The specimens used for the strain corrosion tests consisted of GFRP pipe segments had nominal diameter of 500 mm. The nominal stiffness of the ring samples amounted to 10,000 N/m^2. The length of each sample was about 300 mm.

3.3 *Long-term behavior of GFRP pipes in alkaline medium*

Samples of GFRP pipes produced by centrifugal casting were tested. They belonged to the second batch of the centrifugally cast pipe. The specimens used had a nominal diameter of 500 mm. The length of each sample was about 300 mm. To establish a basis, short-term diametrical compression tests were carried out on three samples from this batch group. The tests were performed on the dry pipes with no preconditioning. The mean of the maximum diagonal force obtained from these short-term tests amounted to 11.6 kN. This value was considerably lower than the maxim force of 17.1 kN obtained for the first batch of the centrifugally cast pipes.

Prior to testing, samples were stored at room temperature of $22 \pm 3°C$ and $50 \pm 5\%$ relative humidity. At the testing time, samples were directly immersed in the container of the testing apparatus, which had been also used for testing of the wet samples (Fig. 1). For these tests, however, the container was filled with alkali medium with alkali grade of PH 12.5.

4 STATISTICAL ANALYSIS AND LONG-TERM EXTRAPOLATION OF DATA

4.1 *Long-term behavior of GFRP pipe in wet condition*

Figure 3 shows the results of creep tests on the conditioned GFRP pipe ring samples tested in wet conditions. It shows data points for the diametrical force and the corresponding maximum creep deformation at break as a function of the time. The ordinate of each point, on a logarithmic scale, depicts the diametrical force and the abscissa designates the time to failure on a logarithmic scale.

To analyze the experimental data, according to EN 705 (1995) a linear regression analysis was carried out. In this analysis, a linear regression curve was fitted into the data relating the diametrical force (F in Newton) to the failure time (t in hours). As the result of this analysis, the following mathematical relation between the above-mentioned quantities was found.

$$\mathrm{Log}_{10} F = 4.16 - 0.05 \, \mathrm{Log}_{10} t \qquad (1)$$

Figure 3 shows the plot of this regression curve together with the experimental data points. The solid line shown in Figure 3 is the regression curve up to the 6400 hours. The dotted line shown in Figure 3 is the geometrical extension of the regression line up to 50 years. According to this extrapolation, strength of about 7550 N for the submerged pipe after 50 years was estimated.

4.2 *Long-term strain corrosion of GFRP pipes*

Figure 4 shows the results of strain corrosion tests on the GFRP pipe ring samples presented by a diagram with a double logarithmic scale. The ordinate of the

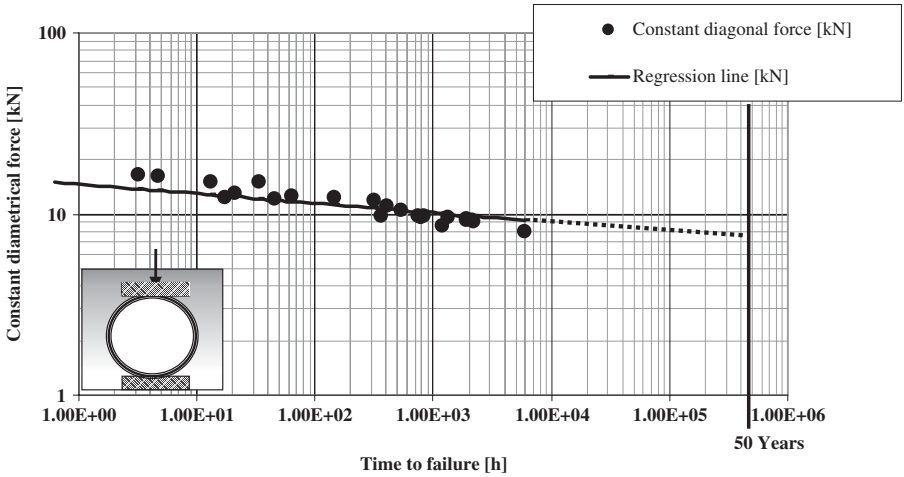

Figure 3. Long-term creep response of GFRP ring specimens in wet condition under vertical diagonal compressive force.

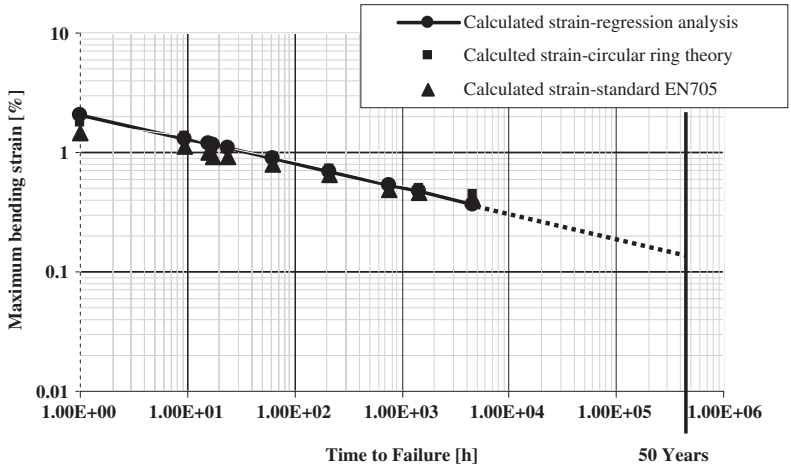

Figure 4. Long-term strain corrosion behavior of GFRP pipe in acid environments; strain at failure: the experimentally based calculation, the regression curve, and the long-term extrapolation.

diagram signifies the relative diametrical deflection (in %) and the abscissa designates the time to failure (in hours). The relative diametrical deflection (in %) was calculated as the measured diametrical deflection multiplied by 100 divided by the mean pipe diameter.

To analyze the experimental data, a linear regression analysis was performed by Woytowich (1991). Figure 2 shows the regression curve together with the experimental data points. From this analysis, the following mathematical relation between the vertical deflection (y in mm), the nominal pipe diameter (D = 500 mm) and time to failure (t in hours) was deduced.

$$\mathrm{Log}_{10}\,(y/D) = 1.37\text{-}0.20\ \mathrm{Log}_{10}\,t \qquad (2)$$

The solid line in Figure 4 shows the regression curve of the experimental data up to the 4600 hours. The dotted line is the geometrical extension of the regression line up to 50 years. Using the maximum diametrical deflection, the strain at failure was calculated. For this

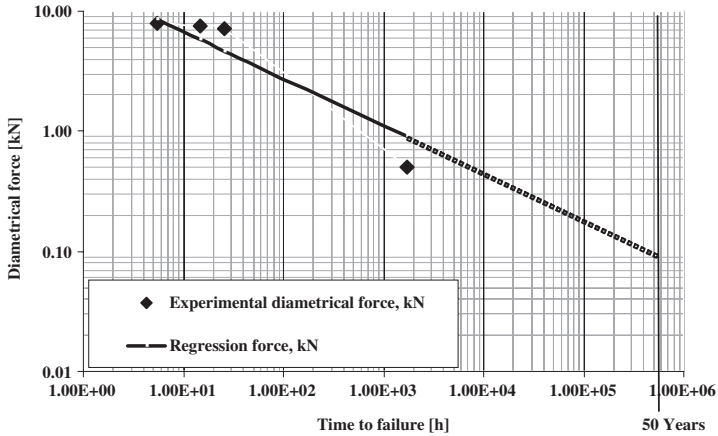

Figure 5. The experimental data for the second batch of the centrifugally cast GFRP pipe samples in the PH 12.5 alkali environment and the linear regression curved fitted to the data points.

purpose, the theory of an elastic ring acted upon by a pair of diametrical forces (F in Newton) was used. According to this theory, the maximum diametrical deflection and the maximum bending moment (M in N · mm) in the ring would be related to F via the following formula [1]:

$$y = 0.15\ F \times R^3 / E \times I \quad (3)$$

$$M = 0.32\ F \times R$$

where E is the modulus of elasticity (in MPa), I is the second moment of area of the ring wall section (in mm^4), and R is the mean radius of the ring (in mm).

Using the above relations and employing the classical elastic rod theory, the maximum strain (ε) would be related to other parameters as follows:

$$\varepsilon = 4.28\ (h/D) \times (y/D) \quad (4)$$

For the pipe sections under investigation, the above relation becomes:

$$\varepsilon = 0.09\ (y/D) \quad (5)$$

Finally, using the statistical correlation of relation (1), the following relation was obtained.

$$\mathrm{Log}_{10}\ (\varepsilon) = 0.33\text{-}0.20\ \mathrm{Log}_{10}\ t \quad (6)$$

Figure 4 shows the maximum bending strain as a function of the time to failure according to the above relation and also by a modified formula proposed in by Woytowich (1991). Figure 4 also shows the extrapolation of the linear regression curve to 50 years.

4.3 *Long-term alkaline resistance of GFRP pipe*

Figure 5 shows the experimental data for the second batch of the centrifugally cast GFRP pipe samples tested in PH 12.5 alkali environment. It also depicts the linear regression curved fitted to these data points.

5 SUMMARY OF RESULTS

5.1 *Long-term behavior in water*

The test results presented in Figure 3 show a clear decreasing trend of pipe strength as function of time. The long-term extrapolation by the regression curve showed that the 50 years strength for the continuously submerged pipe was about 7.5 kN. Hence it was found that the 50-years strength of wet pipes reduced to more than 50% of the dry strength in short-term loading.

The data points related to the creep deformation at break showed a more or less constant trend. The average value of the diametrical deflection at break amounted to about 20% of the pipe nominal diameter. The relatively constant temporal trend of deflection showed that the maximum creep strain in the pipe under wet conditions did not vary too much. Hence, one may conclude that the continuous contact of the composite pipe with water would mainly affect the strength and not the maximum strain. The strength reduction could be attributed to the composite debonding caused by diffusion of water into the layers and the interfaces between the fibers and the resin.

5.2 *Strain corrosion*

The results of strain corrosion study showed a decreasing regression trend of maximum strain as a function

of time to failure. According to the statistical extrapolation shown in Figure 4, for a pipe continuously exposed to sulfuric acid, a critical diametrical deflection of about 1.7% after 50 years was obtained. On the other hand, the short-term static tests performed on the dry ring sections of this pipe revealed a 23.4% diagonal deflection at break. Hence, according to these results, a deformation capacity reduction of about 90% relative to the short-term deformation of dry pipes was deduced.

The bending strain calculation, using the experimental data and the elastic ring theory, revealed a short-term maximum strain of about 2.1%. Under the influence of constant diametrical deflection and the sulfuric acid, the maximum strain reduced to about 0.5% after 1000 hours. Furthermore, the long-term extrapolation showed that after 50 years of continuous exposure to sulfuric acid and diametrical loading, the strain at failure of the ring could reduce to the value of about 0.16%.

5.3 *Alkaline resistance*

The trend curve in Figure 5 shows a relatively sharp drop of the load bearing capacity of the pipe submerged in the alkaline environment. The extrapolation to 50 years of the pipe service life showed a dramatic reduction of strength of the pipe strength. According to this extrapolation, the pipe in alkaline environment was less than 1% of its initial strength! This dramatic reduction of the strength could be attributed to the corrosion of the short glass fibers and the interaction of polyester matrix with the alkaline medium.

6 PIPE DESIGN AND SERVICE LIFE PREDICTION

From the long-term experiments on the GFRP pipe ring samples in various environments namely water, acid and alkaline medium and the long-term extrapolation of data number of general conclusions were reached. It was found that the strain capacity of the GFRP pipe would generally decrease and would fall much below the short-term maximum strain of the dry sample. This strain degradation in a material with relatively low ductility would bring a warning, which should be taken into consideration in the design as well as in the service life prediction of these pipe types. According to these results, the common philosophy of designing the GFRP pipes on the basis of strength should be reevaluated. It is proposed that, as an engineering measure for design and for service life assessment, the deformation and strain criteria should also be equally be considered. Accordingly, appropriate safety factors are to be imposed on the long-term strength as well as the strain limits of the pipe.

ACKNOWLEDGEMENTS

This work was carried out in the framework of the 5th European research program. The EMPA project was financed by the Swiss Board of Education and Research (BBW) and EMPA. Authors are grateful for useful discussions and exchange of information among various project partners and EMPA collegues. They also appreciate the cooperation of the GFRP pipe companies that provided the test specimens.

REFERENCES

EN 1227, 1997. *Plastics piping systems – Glass-reinforced thermosetting plastics (GRP) pipes – Determination of the long-term ultimate relative ring deflection under wet conditions*.

EN 705, 1994 (AC 1995. *Plastics Piping Systems – Glass-reinforced thermosetting plastics (GRP) pipes and fittings – Methods for regression analysis and their use*.

Farshad, M. & Necola, A. 2004 (in press). Effect of aqueous environment on the long-term behavior of glass fiber-reinforced plastics pipes, *Polymer Testing*, Vol. 23, No. 2, pp163–167.

Farshad, M. & Necola, A. 2004 (in press). Strain corrosion of glass fiber-reinforced plastics pipes, *Polymer Testing*.

Fried, N. 1967. Degradation of Composite Materials: The Effect of Water on Glass Reinforced Plastics, *Proc. of the 5th Symposium on Naval Structural Mechanics*, Philadelphia, pp813–837.

Karbhari, V., Rivera, J. & Dutta, P. 2000. Effects of short-term freeze-thaw cycling on composite confined concrete, *Journal of Composites for Construction*, Vol. 4, No. 4, pp191–197.

Karbhari, V., Murphy, K. & Zhang, S. 2002. Effects of concrete based alkali solutions on the short-term durability of E-glass/vinylester composites, *Journal of Composite Materials*, Vol. 36, No. 17, pp2101–2121.

Pr-EN 1120. 2001. Plastics piping systems – Glass-reinforced thermosetting plastics (GRP) pipes and fittings – Determination of the resistance to chemical attack from the inside of a section in a deflected condition.

Roark, R. 1965. *Formulas for Stress and Strain*, McGraw-Hill Book Company, New York, p175.

Van de Velde, K. & Kiekens, P. 2001. Effects of chemical environments on pultruded E-Glass reinforced polyester, *Journal of Composites Technology@Research*, JCTRER, Vol. 23, No. 2, pp92–101.

Woo, M.S.W. 1988. Water absorption of resins and composites II: diffusion in carbon and glass reinforced epoxies, *Journal of Composites Technology and Research*, Vol. 9, No. 4, pp162–166.

Woytowich, D.L., King, M.W., Britton, M.G. & Oleszkiewicz, J.A. 1991. Accelerated testing of a filled polyester E-glass composite in acid environments, *Canadian Journal of Civil Engineering*, Vol. 18, No. 5, pp799–809.

Zhang, S. & Karbhari, V.M. 1999. Effects of Alkaline Environments on the Durability of E-Glass Fiber Composites for Use in Civil Infrastructure, *Proc. of the American Society for Composites* (Whitney, Ed), pp12–20.

Practical applications

FRP Composites in Civil Engineering – CICE 2004 – Seracino (ed)
© 2005 Taylor & Francis Group, London, ISBN 90 5809 638 6

A case study of application of FRP composites in strengthening of the reinforced concrete headstock of a bridge structure

A. Nezamian & S. Setunge
CRC for Construction Innovation, School of Civil and Chemical Engineering, RMIT University, Melbourne, Victoria, Australia

ABSTRACT: A worldwide interest is being generated in the use of fibre reinforced polymer composites (FRP) in rehabilitation of aged or damaged reinforced concrete structures. The service life of concrete bridges is often reduced due to the deterioration and increased traffic volume. Strengthening of an existing concrete structure may also become necessary because of required increase in load carrying capacity. As a replacement for the traditional steel plates or external post-tensioning in strengthening applications, various types of FRP plates, with their high strength to weight ratio and good resistance to corrosion, represent a class of ideal material in externally retrofitting. This paper describes a solution proposed to strengthen the reinforced concrete headstock of Tenthill Creeks Bridge, Queensland, Australia, using FRP composites. Shear and flexural cracks were observed at some locations on the beam. Thus, a decision was made to consider strengthening of the headstock using bonded FRP laminates to increase load carrying capacity of the headstock in shear and bending. The relevant guidelines and design recommendations were adopted in accordance with AS 3600 (2002) to estimate the shear and flexural capacity of a rectangular cracked FRP reinforced concrete section.

1 INTRODUCTION

Rehabilitation and upgrading of existing civil engineering infrastructure has recently become a major issue which often requires immediate attention of asset managers. There are a number of situations where an increase in structural capacity or rehabilitation of a bridge structure is required due to environment effects, overloads, aging and design and construction errors. Cost of repair and replacement of the deficient structures are continuously rising. Even when resources are available, extended time is often required for performing needed remedies, causing distribution of traffic and inconvenience to the traveling public. Traditional repair, strengthening or replacement of bridge components to resist higher design loads, correct deterioration-related damage, or increase ductility has been accomplished using conventional materials and construction techniques. Externally bonded steel plates, steel or concrete jackets and external post tensioning are just some of the many traditional techniques available. Recent developments in fiber reinforced polymer (FRP) composites have opened up another cost-efficient alternative for rehabilitation and strengthening of the aged concrete structures.

Strength of FRP composites come largely from the fibers, which are usually glass, carbon, or aramid. FRP materials are lightweight, non-corrosive, non-magnetic and exhibit high tensile strength. Additionally, these materials are readily available in several forms ranging from factory made laminates to dry fiber sheets that can be wrapped to conform to the geometry of a structure before adding the polymer resin. The relatively thin profile of cured FRP systems is often desirable in applications where aesthetics or access is a concern (Nystrom et al. 2003).

Whilst there have been a number of reinforced concrete bridge girder strengthening projects completed in Australia using FRP materials, in each occasion, an overseas consulting company or an academic institution has been engaged to perform the structural design and consultancy advice using different design guidelines (Kalra and Neubauer, 2003 and Shepherd and Sarkady 2002). However, these are most of the time one-off applications which did not lead to establishment of general guidelines for designing strengthening schemes using the innovative FRP systems in Australia.

This paper covers a case study of strengthening of the Tenthill creek bridge headstock in Queensland using FRP composites. The relevant guidelines and design recommendations were adopted for the headstock in accordance with AS 3600 (2002) and Austroad Bridge design code (1992) to estimate the shear and flexural capacity of a rectangular reinforced concrete section strengthened with FRP reinforcement. These

recommendations may be used for the similar rehabilitation or strengthening cases in a state controlled road network of Queensland, Australia.

2 DESCRIPTION OF THE CASE STUDY

The case study was selected after a number of discussions with the Queensland Department of Main Roads and identifying that the headstock of reinforced and pre-stressed concrete bridge structures is currently the weak link, which requires strengthening to satisfy the current requirements of traffic and other loading.

The bridge studied in this report used to carry traffic between Ipswich and Toowoomba over Tenthill Creek in Gatton (Gatton Helidon Rd), Queensland, Australia. This simply supported reinforced concrete, pre-stressed-beam structure was built in 1970s. The bridge is 82.15 m long and about 8.6 m wide and is supported by a total of 12 pre-stressed 27.38 m long beams over three spans of 27.38 m. Side and cross views of the Tenthhill Bridge are shown in Figure 1. The beams are supported by two abutments and two headstocks. A headstock elevation view is shown in Figure 2.

Figure 1. Photos of Tenthill bridge.

3 PRELIMINARY STRUCTURAL ASSESSMSNT

The first stage of the rehabilitation of the bridge headstock is identifying the headstock deficiencies. Queensland Department of Main Roads (QDMR) has a comprehensive asset management system of inspections, condition data, analysis and prioritization tools, maintenance manuals, and heavy load routing systems (Fenwick & Rotolone 2003).

The asset management system aims to maintain the bridges in a condition that allows heavy vehicles free access to all parts of the network. In other words, avoid placing load restrictions on any bridge in the primary (state-controlled roads) network. The Tenthill Bridge has been observed to require immediate strengthening to avoid such restriction.

The suitable rehabilitation system for the headstock is decided based on condition assessment of the existing structure including establishing its existing load-carrying capacities, and determining the condition of the concrete substrate. The overall evaluation included a thorough field inspection, review of existing design or as-built documents, and a structural capacity analysis in accordance with AS 3600 and Austroads Bridge Design Code (1992). Existing construction and operational documents for the bridges was reviewed, including the design drawings, project specifications, as-built information and past repair

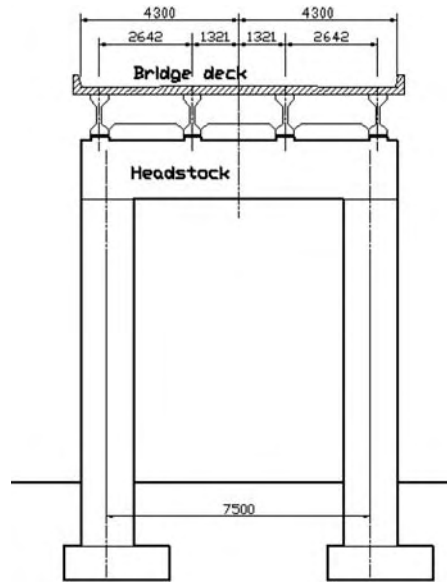

Figure 2. Schematic view of the headstock.

documentation. Austroads bridge design code (1992) was used for assessment of the bridge to ascertain the capacity of the bridge. The Gatton Helidon road over Tenthill Creek is selected as functional Class 3 from the Table 2.3.4 of Austroads code (1992).

3.1 *Structural analysis*

The headstock has been analysed as a portal frame considering all necessary design situations and load combinations according to Austroad Bridge Code (1992) for ultimate limit state and serviceability limit state. The grillage analysis (lane analysis) was used to calculate traffic load on the headstock. The traffic loading models of T44 and Heavy Load Platform HLP 320 in one and two lanes were used in grillage analysis. The computer program SAP2000 has been used for structural analysis. Pre-stressed beams were analyzed as simply supported beams to determine the applied dead load from the secondary beams on the headstock.

The strengthening target for ultimate bending moment and shear force resulted from combination of ultimate traffic loads of HLP 320 and permanent effect (dead load). The ultimate bending moment of 5520 kN-m and ultimate shear force of 2525 kN and serviceability bending moment of 2526 kN-m and serviceability shear force of 1797 kN were then calculated for the load combination.

3.2 *Existing capacity of the headstock*

In accordance with the Australian codes of practice for structural design, the capacity analysis methods contained in this section are based on ultimate limit-state philosophy. This ensures that a member will not become unfit for its intended use. The capacity analysis results would be compared with structural analysis results to identify the deficiencies. This approach sets acceptable levels of safety against the occurrence of all possible overload situations. The nominal strength of a member is assessed based on the possible failure modes and subsequent strains and stresses in each material.

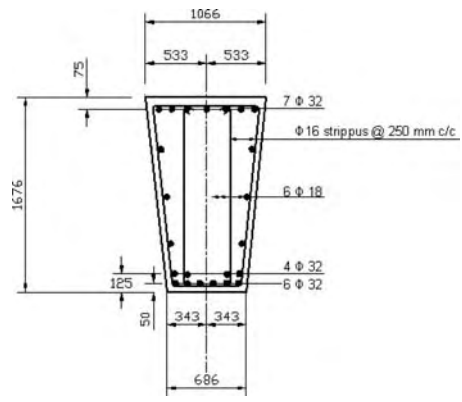

Figure 3. The headstock cross-section.

A typical beam section of the headstock is shown in Figure 3. The positive and negative flexural and shear capacities of the section were calculated in accordance with Australian standards AS 3600. The nominal steel–rebars areas, nominal steel yield strength of 400 MPa for longitudinal reinforcement and 240 MPa for shear reinforcement and nominal concrete compressive strength of 20 MPa were used in the section capacity analysis. The degradation due to corrosion of the steel and creep and shrinkage of the concrete were ignored.

The following assumptions form the basis for the calculation of the ultimate strength of the concrete element strengthened in flexure.

- Design calculations are based on the actual dimensions, internal reinforcing steel arrangement, and material properties of the existing member.
- The strain in reinforcement and concrete are directly proportional to the distance from the neutral axis, that is, a plane section before loading remains plane after loading.

The residual flexural capacity of 3840 kN-m and shear capacity of 2065 kN then calculated for the headstock in accordance with Austroads Bridge design code clause 5.8.1.2, clause 5.8.1.3 and clause 5.8.2. Although calculated applied bending moments and shear force in serviceability limit state are relatively lower than structural capacity of the headstock, a decision was made to strengthen the headstock for ultimate bending moments and shear and to contain the cracking. The capacity analysis is based on strength of the un-cracked reinforced concrete beam. Design codes do not provide any guidelines on calculation of the shear strength of a reinforced concrete beam with a diagonal crack. This area requires further research. A literature review indicated that a 15 to 20% reduction in capacity could be expected in a beam with a diagonal crack compared to un-cracked shear strength of the beam (Duthinh, 1999).

3.3 *Observed cracks*

The bridge has two headstocks supporting the pre-stressed concrete beams. In headstock 1, flexural cracking only is observed while headstock two, both flexural cracking and shear cracking are observed. A photo of the damaged headstock and a schematic figure of the cracked beam are shown in Figure 4.

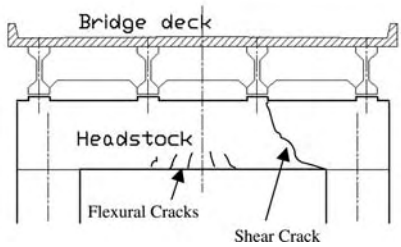

Figure 4. Observed cracks in the headstock.

An overload case higher than HLP 320 most likely caused the shear cracks.

4 FRP STRENGTHENING OF THE HEADSTOCK

The structures division of QDMR has developed a conventional solution for rehabilitation of the bridge structure using external post-tensioning. After preliminary analysis, it was decided to develop an innovative new solution using Fibre Reinforced Polymer composites for strengthening for purpose of comparison. The details of the calculations are given identifying the decisions faced by the designer at various stages of the development of the innovative solution.

The applicability of FRP composites to concrete structure for rehabilitation or capacity enhancement has been actively studied in numerous research laboratories and professional organization around the world (ACI 440, 2002, CEB-FIB 14, 2002 and Bakis et al. 2002). FRP reinforcements offer a number of advantages such as corrosion resistance, non-magnetic properties, high tensile strength, light weight and ease of handling.

Initial discussion with the structures division of QDMR has indicated that the there are some specific concerns which inhibited ready acceptance of FRP composites for regular strengthening schemes. These stem from concerns about the lack of design guidelines in accordance with the Austroads code (1992), brittleness of the failure modes in flexure as well as de-bonding, lack of information on durability and fire-resistance and difficulty in selecting a product to suit a given application without completely relying on the supplier of FRP products. In addressing these issues, the published research on the topic has been reviewed and a strengthening procedure was developed to apply these outcomes systematically to the practical strengthening project of the Tenthill bridge.

4.1 *Design guidelines*

Since the use of FRP composites for strengthening of reinforced concrete structures is a relatively new technique, the development of design guidelines for externally bonded FRP systems is ongoing in Europe, Japan, Canada and the United States. Within the last ten years, many design guidelines have been published to provide guidance for the selection, design and installation of FRP systems for externally strengthening of concrete structures. Applications of provisions of the two major guidelines of Task Group 9.3 of the international Federation for Structural Concrete published bulletin 14 (FIB 14) and ACI Committee 440 in rehabilitation of the headstock were already covered and compared (Nezamian and Setunge 2004). The following conclusions were drawn from the design calculations and the comparison of the two guidelines.

- Both design guidelines adopt the same principal of design to estimate shear and flexural capacity enhancements of the strengthened member.
- The ACI guideline is more conservative in prediction of flexural capacity enhancement for the strengthened headstock. This is mainly due to the use of an additional strength reduction factor of 0.85 applied to the contribution of FRP reinforcement.
- The FIB guideline uses a more accurate approach to check de-bonding of FRP laminates from the concrete substrate, which covers all possible bond failure modes.
- Both design guidelines predicted almost the same shear capacity enhancement for the strengthened member.

In view of above finding, it was concluded that the use of ACI 440 design guideline may be more appropriate for FRP strengthening applications in Australia. The design concepts and philosophy used by ACI is similar to those adopted by AS3600 (2002). However, in considering the failure of FRP composites in debonding and anchorage zones, use of FIB appears to be more appropriate since it systematically covers all possible scenarios.

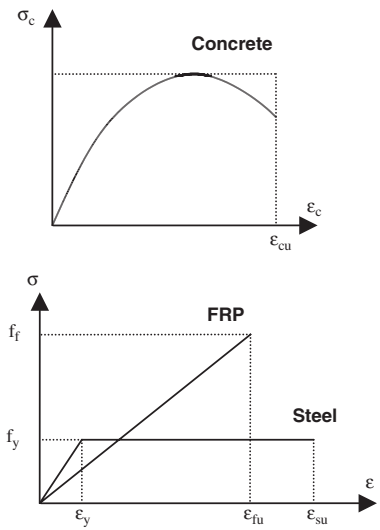

Figure 5. Idealised stress–strain curves for constitutive materials at ULS.

4.2 *Design of FRP system*

In accordance with the Australian codes of practice for structural design, the design methods are based on limit-state design philosophy. This ensures that a strengthened member will not fail at an accidental overload during its design life with 95% confidence. All necessary design situations and load combinations would be considered, which were already outlined. This approach sets acceptable levels of safety against the occurrence of all possible failure modes.

The nominal strength of a member is assessed based on the possible failure modes and subsequent strains and stresses in each material (see Figure 5).

The design of the FRP composites involves assessing the effects of the additional FRP reinforcement provided to the section (designed assuming full composite action) and the ability of transferring forces by means of the bond interface. All possible failure modes should be investigated for a FRP strengthened section (Ganga Rao and Vijay 1998). In general, the failure modes can be subdivided to those assuming full composite action between the reinforced concrete/pre-stressed concrete member and the FRP and those verifying the different de-bonding mechanisms that may occur. The state of the structure prior to strengthening is taken as a reference for the design of the externally bonded FRP reinforcement. The strength of strengthened member depends on the controlling failure mode.

Table 1. Material properties of the Sika CFRP systems.

Type	Tensile strength (MPa)	Elastic modulus (MPa)	Elongation at break (%)
CarboDur Type S	2800	165000	1.7
Sika-Wrap 230C	3500	230000	1.5

Table 2. Material properties of the Mbrace CFRP systems.

Type	Tensile strength (MPa)	Elastic modulus (MPa)	Elongation at break (%)
Mbrace CFK laminates 150/2000	2700	165000	1.4
Mbrace CF 130	3800	240000	1.55

Among the available FRP materials, carbon was chosen for its better long-term performance. It was decided to bond CFRP laminates to the tension face of the beam section (bottom fibre) of the headstock with fibres oriented along the length of the member for positive flexural strengthening and use a complete wrapping scheme with fibres oriented along the transverse axis of the beam section for the shear strengthening. After consulting with suppliers of FRP materials in Australia, it was decided to use Sika CFRP laminate CarboDur type S for flexural strengthening and Sika CFRP wet lay up type Sika-Wrap-230C. Table 1 shows material properties of the proposed Sika systems.

The Sika CFRP materials can be replaced by similar MBT CFRP products of MBrace CFK laminate 150/2000 for flexural and MBrace CF 130 for shear strengthening. Table 2 shows material properties of the proposed Mbrace systems.

4.3 *Flexural strengthening*

In the section analysis for the ultimate state in flexure, the ACI guideline follows well established procedures using the idealised stress–strain curves for concrete, FRP and longitudinal reinforcement.

These curves, along with the following assumptions, form the basis for the capacity analysis of a concrete element strengthened in flexure.

- Design calculations are based on the actual dimensions, internal reinforcing steel arrangement, and material properties of the existing member being strengthened.

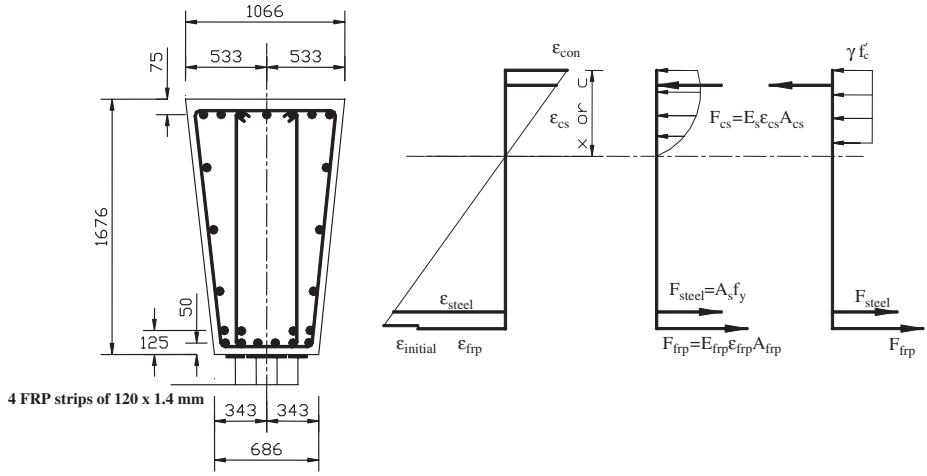

Figure 6. Internal strain and stress distributions for the beam cross section of the headstock.

- The strain in reinforcement and concrete are directly proportional to the distance from the neutral axis, that is, a plane section before loading remains plane after loading.
- There is no relative slip between external FRP reinforcement and the concrete.
- The shear deformation within the adhesive layer can be neglected since the adhesive layer is very thin with slight variations in its thick.

The cross section analysis identifies all possible failure modes. Failure of the strengthened element may then occur as a result of various mechanisms as follows:

- Crushing of the concrete in compression before yielding of the reinforcing steel.
- Yielding of the steel in tension followed by rupture of the FRP laminates.
- Yielding of the steel in tension followed by concrete crushing.
- Shear/tension de-lamination of the concrete cover.
- De-bonding of the FRP from the concrete substrate.

The cross section analysis indicated that the failure mode of the beam section of the headstock would be the yielding of the longitudinal steel reinforcement followed by concrete crushing, while the FRP is intact. This is the most desirable failure mode, which satisfy the safety requirements in ultimate state for a reinforced concrete section. The design bending moment for the strengthened member was then calculated in accordance with each design guideline based on well established principles of flexural design of reinforced concrete beams. The design principles are shown in Figure 6.

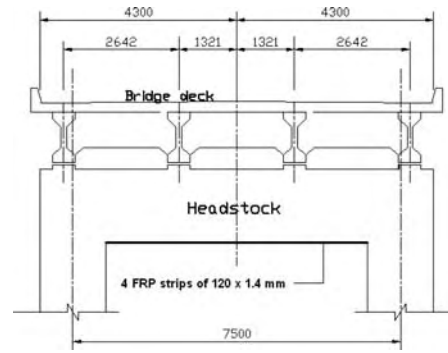

Figure 7. Flexural strengthening scheme.

The design bending moment capacity was then calculated based on the ACI design guideline. The design bending moment capacity of 5854 kN-m was calculated for strengthened section (see Figure 7)

4.4 *Anchorage*

Experimental investigations show that the FRP rupture is a rare event and de-lamination of FRP strips is more likely to occur before stress in the FRP reach

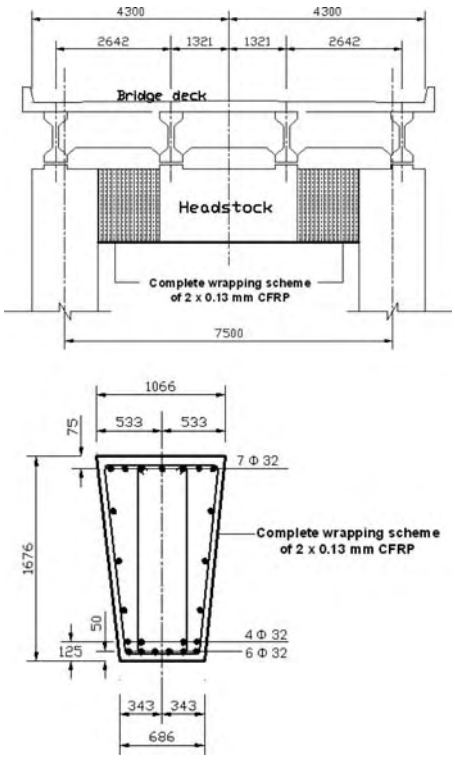

Figure 8. Shear strengthening scheme.

the ultimate level. De-bonding implies the complete loss of composite action between the concrete and FRP laminates. Bond failure will be a brittle failure and should be prevented. The ACI guideline place a limitation on the strain level in the laminate to prevent de-lamination of FRP from the concrete substrate. De-bonding of CFRP strips was checked based on the ACI guidelines. The calculations indicated that the strengthening system satisfies the requirements to prevent the de-bonding failure.

Regarding the conclusions of the comparison between the ACI and the FIB guidelines (Nezamian & Setunge 2004), the following failure modes were also considered to prevent de-lamination of FRP in accordance with the FIB guideline.

- De-bonding in an un-cracked anchorage zone
- De-bonding caused at flexural cracks
- De-bonding caused at shear cracks

However the de-bonding failure of CFRP strips in the strengthening of the headstock will be also controlled by applying CFRP wrapping scheme for shear strengthening (see Figure 8).

4.5 *Shear strengthening*

The design for shear strengthening of a reinforced concrete member is based on truss model and superposition principle with some considerations for the orthotropic behaviour of the CFRP material. The shear strength of a strengthened member is determined by adding the contribution of the CFRP reinforcing to the contributions from the concrete and shear reinforcement.

$$\phi V_n = \phi\left(V_{uc} + V_{us} + \psi_f V_f\right) \qquad \text{(Equation 1)}$$

Use of CFRP wrapping system increases the design shear capacity of the strengthened member by 323 kN based on the ACI design guideline. The CFRP shear reinforcement is considered as contact critical shear reinforcement. Hence, the ultimate failure does not occur with de-bonding (see Figure 8).

4.6 *Other issues*

The ACI guideline suggested imposing reasonable strengthening limits to guard the strengthened member against failure of the FRP strengthening system and collapse of the structure due to fire, vandalism, or other causes. It is recommended that the existing strength of the structure be sufficient to a level of load as described by below Equation 2.

$$\left(\phi R_n\right)_{existing} \geq \left(1.2S_{DL} + 0.85S_{LL}\right)_{new} \qquad \text{(Equation 2)}$$

where S_{DL} is dead load and S_{LL} is live load. It is also recommended that the strength of a structural member with a fire-resistance rating before strengthening should satisfy the conditions of Equation 3.

$$\left(R_{n\theta}\right)_{existing} \geq S_{DL} + S_{LL} \qquad \text{(Equation 3)}$$

$(R_{n\theta})_{existing}$ is the nominal resistance of the member at an elevated temperature, which can be determined using the ACI 216R guideline.

Environmental conditions affect the performances of the FRP system. The mechanical properties of FRP systems degrade under exposure to certain environments, such as alkalinity, salt water, chemicals, ultralviolet light, high temperatures, high humidity and freezing and thawing cycles. The ACI guideline accounts for this degradation using the environmental reduction factor for the design material properties of CFRP. The environmental reduction factor of 0.85 was used in design of shear and flexural strengthening systems.

4.7 *Summary of strengthening scheme*

The design of FRP strengthening system for the Tenthill bridge headstock can be summarized as follows:

- The flexural strength of the headstock can be increased from 3800 kN-m to 5854 kN-m by bonding four FRP unidirectional strips of 120 × 1.4 mm to the tension face of the beam section (bottom fibre) of the headstock with fibres oriented along the length of the member (Figure 7).
- The shear strength of the headstock can be increased from 2065 kN to 2711 kN by complete wrapping of the beam with two layers of 0.13 mm thick carbon fibres oriented along the transverse axis of the beam section (Figure 8).

5 CONCLUSIONS

The use of CFRP laminate and CFRP wrapping appears to be an effective way to strengthen the Tenthill bridge to provide additional flexural and shear capacities. The proposed strengthening scheme for the bridge using FRP technology can be used as a basis for the development of a decision support tool for rehabilitation of reinforced concrete bridge structures using Fibre Reinforced Polymer composites. Through the case study an appropriate design basis for use FRP in strengthening has been developed comply with the Austroad Bridge design code (1992) and in accordance with the ACI design guideline.

ACKNOWLEDGEMENTS

The case study of strengthening of the headstock of the Tenthill bridge is part of a research project entitled "Decision Support Tools for Concrete Infrastructure Rehabilitation". The Department of Main Roads Queensland, Queensland, Australia supports the project as the major industrial partner. QDMR also provided required information regarding the structural assessment of the Tenthill bridge. The project is funded by Cooperative Research Center for Construction Innovation.

REFERENCES

ACI 216R, "Guide for Determining the Fire Endurance of Concrete Elements"

ACI 318-99 (1999). "Building Code Requirements for Structural Concrete and Commentary"

American Concrete Institute Committee 440 (2003). "Guide for the Design and Construction of Externally Bonded FRP Systems for Strengthening Concrete Structures"

AS3600 (2002) "Concrete Structures", Australian Standard, Standards Association, Australia

Austroads (1992), "Bridge Design Code", Section 2: Design loads

Bakis, C.E., Bank, L.C., Brown, V.L., Cosenza, E., Davalos, J.F., Lesko, J.J., Machida, A., Rizkalla, S.H. and Triantifillou, T.C. (2002). "Fiber-Reinforced Polymer Composites for Construction-State-of-the-Art Review", *Journal of Composites in Construction*, Vol. 6, No. 2, pp. 73–87.

Duthinh, D. (1999). "Sensitivity of Shear Strength of Reinforced Concrete and Prestressed Concrete Beams to Shear Friction and Concrete Softening According to Modified Compression Field Theory", *ACI Structural Journal*, Vol. 96, No. 4, pp. 495–508

Fenwick, J.M. and Rotolone, P. (2003). "Risk Management to Ensure Long Term Performance in Civil Infrastructure" *21st Biennial Conference of the Concrete Institute of Australia*, Brisbane, Australia, pp. 647–656

GangRao, H.V.S. and Vijay, P.V. (1998). "Bending Behavior of Concrete Beams Wrapped with Carbon Fabric", *Journal of Structural Engineering*, Vol. 124, No.1, pp. 3–10

Kalra, R. and Neubauer, U. (2003). "Strengthening of the Westgate Bridge with Carbon Fibre Composites – A Proof Engineer's Perspective" *21st Biennial Conference of the Concrete Institute of Australia*, Brisbane, Australia, pp. 245–254

Nezamian, A., Setunge, S. and Kumar, A. (2004). "Decision Support in Using Fiber Reinforced Polymer (FRP) composites in Rehabilitation of Concrete Bridge Structures", *Proceeding of Innovative Materials and Technologies for Construction and Restoration*, June 6–9, 2004, Lecce, Italy

Nezamian, A. and Setunge, S. (2004). "Comparison between ACI 440 and FIB 14 Design Guidelines in Using CFRP for Strengthening of Concrete Bridge Headstock", *Proceeding* 4th International Conference on Advanced Composite Materials in Bridges and Structures, July 20–23, 2004, Calgary, Canada

Nystrom, H.E., Walkins, S.E., Nanni, A. and Murray, S. (2003). "Financial Viability of Fiber-Reinforced Polymer (FRP) Bridges", *Journal of Management in Engineering*, Vol. 19, No. 1, pp. 2–8

Shepherd, B. and Sarkady, A. (2002) "Carbon Fibre Fabric Strengthening of Little River Bridge" *Proc. IABSE Symposium*, September 11–13, 2002. Melbourne, Australia

Sika Australia Pty Limited "Heavy-Duty CFRP strengthening system" Product Guide Specification, February 2004. Web site: http://www.sika.com.au

The international federation for structural concrete (CEB-FIB), technical report bulletin 14 (2002). "Externally bonded FRP reinforcement for RC structures"

FRP Composites in Civil Engineering – CICE 2004 – Seracino (ed)
© 2005 Taylor & Francis Group, London, ISBN 90 5809 638 6

Retrofit of the Louisa-Fort Gay Bridge using CFRP laminates

C.C. Choo, T. Zhao & I.E. Harik
University of Kentucky, Lexington, Kentucky, USA

ABSTRACT: The Louisa-Fort Gay Bridge, in Lawrence County, Kentucky, is a four-span monolithic reinforced concrete slab-girder bridge. It is located in the coal mining area in Eastern Kentucky. Inspection of the bridge revealed severe flexural cracks in the girders. The initial analysis of the bridge indicated that the crack formation may have resulted from heavily loaded trucks. A detailed moment–curvature relation analysis was carried out and a flexural retrofitting scheme was conceived in which CFRP laminates were used. The retrofit of the bridge started and finished in Fall 2003. Crack gauges were installed at the affected areas for post-strengthening monitoring. The bridge will be monitored for a period of three years. This paper presents details of the bridge analysis and description of the retrofitting scheme.

1 INTRODUCTION

1.1 *Background*

The use of fiber-reinforced polymer (FRP) composites as repair and rehabilitation alternative in structures is gaining significant worldwide acceptance due to their multitude of attractive qualities, i.e. corrosion-resistant, high strength-to-weight ratio, flexibility, etc. Some of the common retrofit applications involving FRP composites are: strengthening and repairing of reinforced and prestressed concrete beams; repairing of seismically deficient reinforced concrete columns, piers, and bents; and retrofitting of walls and slabs (Avramidou et al. 1999, Chajes et al. 1994, Ehsani et al. 1999, Hamilton & Dolan 2001, Holloway & Leeming 1999, Hutchinson & Rizkalla 1999, Khalifa & Nanni 2000, Karbhari et al. 1999, Lam & Teng 2001, Norris et al. 1997, Tan 1997, Yamakawa et al. 1999, and Zhao et al. 2002). Repair of bridge structures involving FRP system has the added benefit that includes reduction in the disruption of traffic due to shorter construction time, and sometimes, allowing traffic while work is being performed underneath the superstructure (Simpson et al. 2004).

1.2 *Objective and scopes*

In this paper, the flexural repair and strengthening project of the Louisa-Fort Gay Bridge using carbon fiber-reinforced polymer (CFRP) laminates will be presented. This paper details the four tasks of the retrofitting process: (1) initial investigation which includes field inspection, load and strength investigation, etc.; (2) detailed plans for the retrofitting scheme; (3) construction phases and details; and (4) post-retrofit bridge inspection and monitoring.

2 THE LOUISA-FORT GAY BRIDGE, KENTUCKY, USA

2.1 *Bridge description*

The Louisa-Fort Gay Bridge is located in the mining community of Lawrence County, Kentucky, USA. The multi-span bridge crossing the Big-Sandy River is composed of spans with steel plate girders and spans with cast-in-place reinforced concrete girders acting compositely with cast-in-place concrete bridge deck. The approach spans (heading towards Louisa and Fort Gay in Figs. 1 & 2) at both ends are steel composite bridge spans, whereas the middle portion (Spans 4-5-6-7) is reinforced concrete span. A schematic sketch of the middle span is shown in Figure 3.

2.2 *Preliminary investigation*

Routine inspections of the 25-year old Louisa-Fort Gay Bridge are performed on regular basis with inspection intervals not more than 2 years apart. They revealed severe flexural cracks in almost the entire middle reinforced concrete portion (see Figs. 4 & 5). Cracks in girders are likely due to heavily loaded trucks – 5-axle trucks as heavy as 1000 kN has been recorded traversing the bridge. The legal limit for such truck is approximately 712 kN.

A finite element (FE) model was created for the middle RC portion shown in Figure 3. Live load analysis for the spans was performed based on the recorded

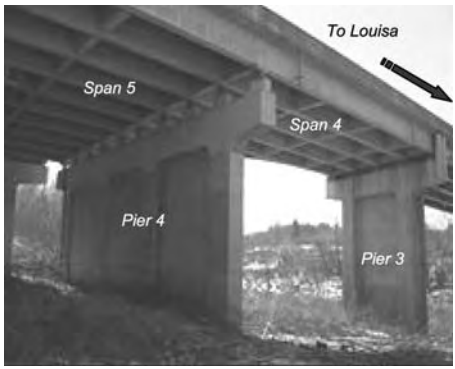

Figure 1. Direction towards Louisa.

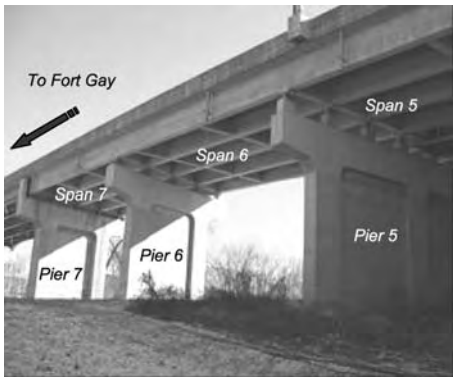

Figure 2. Direction towards Fort Gay.

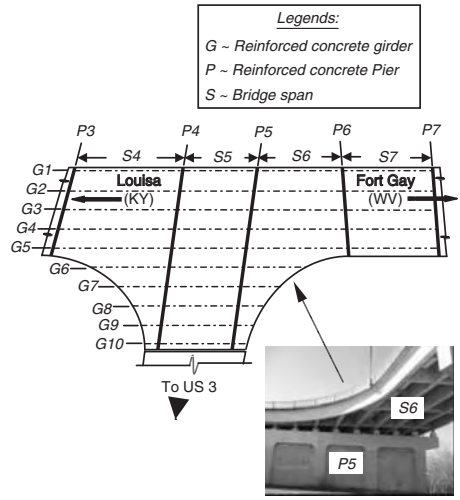

Figure 3. Middle reinforced concrete span of the Louisa-Fort Gay Bridge.

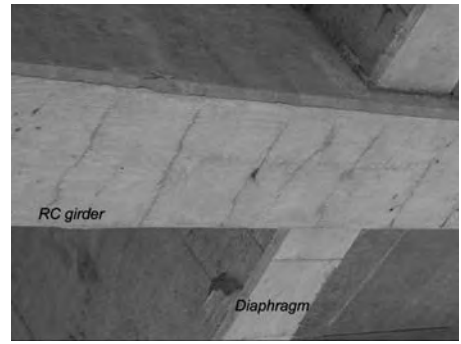

Figure 4. Flexural cracks in RC girder.

weight of the 5-axle truck (1000 kN total). The strength of respective girders was determined based on available bridge plans by conducting a moment–curvature relation analysis. A '*layered method*' was used in the analysis taking the nonlinear concrete stress/strain relation into consideration. Steel stress/strain relation includes the strain-hardening effect was used. For flexural strengthening, the CFRP laminate stress/strain model was characterized as linearly-elastic until failure. In the analysis, the failure of the section is initiated when either concrete reaches its pre-defined ultimate compression strain (AASHTO assumes 0.003) or CFRP laminate reaches its ultimate tensile strain.

The analytical results confirmed that, except for the girders in Span 5, all girders were indeed overloaded to an extent where service limits allowed in the current AASHTO provisions were close to being or have been exceeded. As an illustration, service moment-curvature and factored moment–curvature diagrams were generated for one particular girder in the middle RC portion (Girder 4 of Span 4), and the results are presented in Figures 6, 7, & 8, respectively.

2.3 *Retrofitting schemes*

Studies conducted at the University of Kentucky (Alagusundaramoorthy et al. 2002a & b) and successful field applications (Simpson et al. 2004) in the state of Kentucky, as well as at other research institutions, have demonstrated that FRP retrofitting of concrete structures is a viable option. Additionally, exploration

Figure 5. Flexural crack located at the bottom of RC beam.

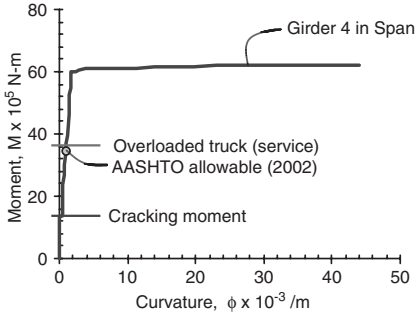

Figure 6. Service moment–curvature relation.

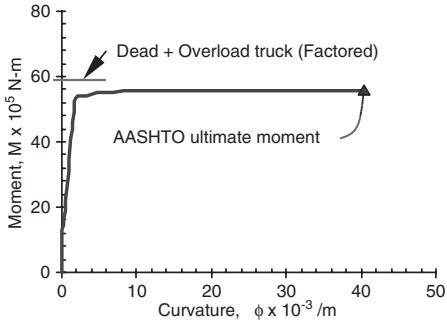

Figure 7. Factored moment–curvature relation.

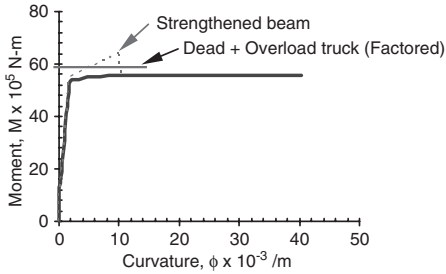

Figure 8. Moment–curvature relation for girder 4 in Span 4.

Table 1. Physical properties of CFRP laminates and fabric.

Sika® CFRP laminate			
Product	Thickness (mm)	Width (mm)	Area (mm^2)
S 1012	1.2	100	120

Ref: Sika Corporation. 2003. Construction Products Catalog. Lyndhurst, New Jersey, USA.

of alternative repair techniques and encouragement at the state and federal agencies with programs such as the Innovative Bridge Research and Construction (IBRC), etc, has made the restoration of the Louisa-Fort Gay Bridge with FRP composites a reality.

At present, repair of the bridge is the only option as replacement of the superstructure, in addition to being very costly, will cause tremendous inconvenience to the public and the local industries – this is especially true for the coal industry. The bridge connects two cities located at the border of Kentucky (Louisa) and West Virginia (Fort Gay), and is one of the few essential routes for coal trucking in the region.

For this project, CFRP laminates produced by Sika® Corporation were used as the primary repair material. The physical and mechanical properties of the CFRP laminates are presented in Tables 1 & 2. CFRP laminates were used primarily to increase flexural capacity of RC girders by attaching laminates to the bottom of the beam. Scheduling of CFRP laminates is presented in Table 3. Analytical results indicated that all girders in Span 5, and griders 6 to 10 of Spans 4 and 6 did not require any retrofit.

As an example, the moment–curvature response of Girder 4 in Span 4 strengthened with three CFRP laminates is presented in Figure 8.

2.4 *Construction work*

The flexural strengthening process is a two-step operation: (1) surface preparation; and (2) FRP application.

Table 2. Mechanical properties of CFRP laminates and fabric.

Sika® CFRP laminate			
	Tensile properties		
Product	Strength (MPa)	Modulus (GPa)	Strain (%)
S 1012	2800	165	1.69

Ref: Sika Corporation. 2003. Construction Products Catalog. Lyndhurst, New Jersey, USA.

Table 3. Scheduling of CFRP laminates for flexural strengthening.

	Number of laminates required		
	Span 4	Span 6	Span 7
Girder 1	1	2	2
Girder 2	1	2	2
Girder 3	3	2	3
Girder 4	3	2	3
Girder 5	2	2	3

Figure 9. Surface preparation: grinding.

Since FRP application is bond-critical, the bonded surfaces must be properly prepared. Surface preparation includes these additional operations: (a) surface grinding and cleaning; and (b) concrete surface pull-off strength testing. The grinding process resulted in a sound surface that is rid of loose concrete and other particles that may have accumulated over the years. The process was successfully accomplished by utilizing a hand-grinder as shown in Figure 9.

The cleaning process followed immediately after surface grinding. This process was to ensure the cleanness of the concrete surfaces by removing any stain, debris, or other contaminants that might affect bond. Mobile high pressure washer was used in this case thoroughly clean the application areas of the girders.

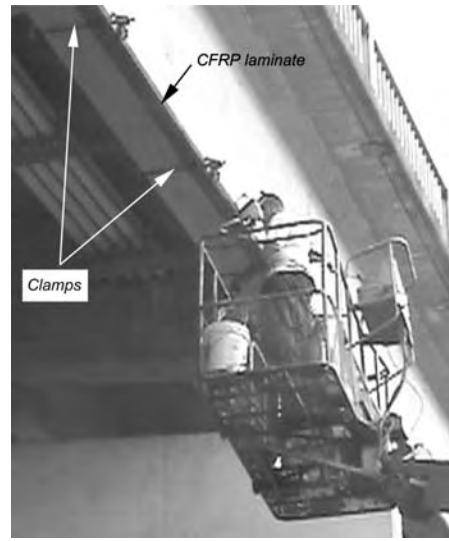

Figure 10. Application of CFRP laminates to the bottom of Girder 5 in Span 6 by a trained worker on a movable crane.

The adhesive strength of the concrete substrate was then verified by conducting pull-off testing according to ACI 503 (1992). The test was performed at various surface locations and confirmed that the concrete substrate had tensile strength greater than the minimum required of 1.4 MPa.

CFRP laminate application was performed after the surfaces have been cleaned and dry. The process began by first priming the concrete surface with epoxy. CFRP laminates were also saturated with epoxy before attaching them to the concrete surface. Once the laminates were in place, they were lightly pressed with a roller. Figure 10 shows a worker attaching a CFRP laminate to the bottom of Girder 5 in Span 6.

Figure 10 shows that clamps are used to secure the laminates in place along the girders as the resin hardened.

2.5 *Bridge monitoring after strengthening*

The Louisa-Fort Gay Bridge is being monitored on a regular basis, for a period of three years following the retrofit completion in December 2003. Any distress in the bridge will be detected by monitoring crack propagation and movement. For that purpose, Avongard crack gauges (Fig. 11) were installed on the affected areas of the girders. The crack gauge shown in Figure 11 consists of two overlapping plexiglass/acrylic

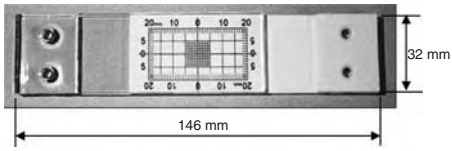

Figure 11. The avongard crack gauge.

plates. One plate is white with a black millimeter grid, while the other is transparent with red crosshairs centered over the grid. Any movement of the crack will be tracked if the crosshairs shift.

3 SUMMARY AND CONCLUSION

This paper reported the retrofit project of the 25-year old Louisa-Fort Gay Bridge which is located in a mining community in Eastern Kentucky, USA. The bridge, connecting the cities of Louisa in Kentucky and Fort Gay in West Virginia, is one of the most vital routes for coal transportation in this region. The bridge is multi-span having both steel composite portions at the two approaches and a cast-in-place reinforced concrete construction as its middle portion.

Field inspection of the bridge revealed severe flexural cracks in the girders in the middle RC portion. Initial indication was that these cracks may have been caused by heavily loaded trucks. This notion was later confirmed when detailed analyses were carried out. A decision was finally made to strengthen the bridge with funds provided by the Federal Highway Administration (FHWA) as replacing the superstructure is not a viable option. The flexural strengthening was successfully executed by using CFRP laminates.

From the experience with the Louisa-Fort Gay Bridge, the following observations can be made: (1) short construction time – the project started in Fall of 2003 and was completed within weeks; (2) minimal man power – only light-weight hand tools were used and, two skilled workers were involved in the retrofitting process; and (3) no traffic disruption – the work was performed without closing any lanes to normal daily traffic.

Crack monitoring gauges were installed at several locations to monitor crack propagation and movement. Thus far, no sign of distress has shown. The bridge will be inspected on a regular basis for a period of three years.

REFERENCES

AASHTO. 2002. Standard Specifications for Highway Bridge. 17th Ed. American Association of State Highway and Transportation Officials. Washington, D.C.

ACI. 1992. 503.1-92: Standard specification for bonding hardened concrete, ste, wood, brick and other materials to hardened concrete with a multi-component epoxy adhesive. American Concrete Institute.

Alagusundaramoorthy, P., Harik, I.E., & Choo, C.C. 2003. Flexural Behavior of RC Beams Strengthened with CFRP Sheets or Fabric. ASCE Journal of Composites for Construction, Vol. 7, Issue 4. pp. 292–301.

Alagusundaramoorthy, P., Harik, I.E. & Choo, C.C. 2002. Shear Strength of RC Beams Wrapped with CFRP Fabric. Research Report (KTC-02-14/SPR 200-99-2F), Kentucky Transportation Center (KTC), University of Kentucky, Lexington, Kentucky.

Avramidou, N., Drdacky, M.F. & Prochazka, P.P. 1999. Strengthening Against Damage of Brick Walls by Yarn Composites. *Proceeding of the 6th International Conference on Inspection, Appraisal, Repairs & Maintenance of Buildings & Structures*, Melbourne, Australia.

Chajes, M. J., Thomson, T. A., Januszka, T. F. & Finch, W. W. Jr. 1994. Flexural Strengthening of Concrete Beams Using Externally Bonded Composite Materials. Construction and Building Materials, Vol. 8, No. 3.

Ehsani, M.R., Saadatmanesh, H. & Velazquez-Dimas, J.I. 1999. Behavior of Retrofitted URM Walls under Simulated Earthquake Loading. ASCE Journal of Composites for Construction. Vol. 3, Issue 3. pp. 134–142.

Hamilton III, H.R. & Dolan, C.W. 2001. Flexural Capacity of Glass FRP Strengthened Concrete Masonry Walls. ASCE Journal of Composites for Construction. Vol. 5, Issue 3. pp. 170–178.

Holloway, L.C. & Leeming, M.B. 1999. Strengthening of Reinforced Concrete Structures using Externally-Bonded FRP Composites in Structural and Civil Engineering. 1st Ed., Cambridge: Woodhead Publishing Limited.

Hutchinson R.L. & Rizkalla, S.H. 1999. Shear Strengthening of AASHTO Bridge Girders Using Carbon Fiber Reinforced Plastic Sheets. *Fourth International Symposium – Fiber Reinforced Polymer Reinforcement for Reinforced Concrete Structures*, Amercian Concrete Institute, ACI International SP-188, Farmington Hill, Michigan.

Khalifa, A. & Nanni, A. 2000. Improving Shear Capacity of Existing RC T-section Beams Using CFRP Composites. Cement and Concrete Composites. Vol. 22.

Karbhari, V.M., Seible, F., Seim, W. & Vasquez, A. 1999. Post-Strengthening of Concrete Slabs. *Fourth International Symposium – Fiber Reinforced Polymer Reinforcement for Reinforced Concrete Structures*, American Concrete Institute, ACI International SP-188, Farmington Hill, Michigan.

Lam, L. & Teng, J.G. 2001. Strengthening of RC Cantilever Slabs Bonded with GFRP Strips. ASCE Journal of Composites for Construction. Vol. 5, Issue 4. pp. 221–227.

Norris, T., Saadatmanesh, H., & Ehsani, M. 1997. Shear and Flexural Strengthening of R/C Beams with Carbon Fiber Sheets. *Journal of Structural Engineering*, American Society of Civil Engineering (ASCE), Vol. 123, N. 7.

Simpson, J.W., Choo, C.C. & Harik, I.E. 2004 (Pending). Shear Repair and Reinforcement of Precast Prestressed Box Beams using Carbon Fiber Reinforced Polymer Fabric. Research Report, Kentucky Transportation Center (KTC), University of Kentucky, Lexington, Kentucky.

Tan, K.H. 1997. State-of-the-Art Report on Retrofitting and Strengthening By Continuous Fibers – Southeast Asian Perspective – Status, Prospects and Research Needs.

Non-Metallic (FRP) Reinforcement for Concrete Structures – Proceedings of the Third International Symposium, Vol. 1.

Yamakawa, T., Satoh, H. & Zhong, P. 1999. Seismic Performance of Hybrid Reinforced Concrete Circular Columns Confined in Aramid Fiber Reinforced Polymer Tube. *Fourth International Symposium – Fiber Reinforced Polymer Reinforcement for Reinforced Concrete Structures*, American Concrete Institute, ACI International SP-188, Farmington Hill, Michigan.

Zhao, T., Zhang, C.J. & Xie, J. 2002. Study and Application on Strengthening the Cracked Brick Walls with Continuous Carbon Fibre Sheet. *Advanced Polymer Composites for Structural Applications in Construction, Proceedings of the 1st International Conference*, University of Southampton, UK.

FRP Composites in Civil Engineering – CICE 2004 – Seracino (ed)
© 2005 Taylor & Francis Group, London, ISBN 90 5809 638 6

Progressive failure analysis of a composite army bridge

Ramki Iyer
U. S. Army – TARDEC, Warren, Michigan, USA

Ayman Mosallam
University of California at Irvine, California, USA

Frank Abdi
Alpha Star Corporation, Long Beach, California, USA

ABSTRACT: Military composite bridges offer many unique advantages for the army including its lightweight (high strength-to-weight ratio), as compared to current steel and aluminum bridges, as well as their superior corrosion and fatigue resistance properties. This paper presents the results of a part of a comprehensive research program sponsored by the US Army to develop innovative field repair techniques for military composite bridges. In this paper, results of virtual testing and progressive failure analysis (*PFA*) simulation conducted on a Composite Army Bridge (*CAB*) prototype are presented. The simulation was conducted using the state-of-the-art simulator, GENOA, developed jointly by Alpha Star Corp and NASA. The virtual tests were performed on the composite treadway under three different loading cases. The three cases used in this study are: (i) maximum static shear loading case, (ii) maximum static flexural loading case and (iii) fatigue progressive failure analysis for the maximum moment case loading. The simulation results matched well the full-scale laboratory test results. For example, the variation between the maximum deflections predicted by the GENOA simulation for the maximum shear and those obtained from the full-scale tests was only 3.2%. In addition, the location and type of damages at the ultimate load were very close to those obtained from the full-scale laboratory tests.

1 INTRODUCTION

In the recent years, the use of advanced composites in building bridges and bridge components for both military and civilian applications became an attractive topic of research for many structural engineers *(DARPA (2000), Iyer (2002) and Mosallam and Haroun (2003))*. Composite bridges (Figure 1) provide several attractive features including its lightweight (*high specific stiffness and strength*), compared to current steel and aluminum bridges, as well as its superior corrosion resistance properties that is preferred in harsh environmental conditions. The lightweight features of composites are attractive and essential property in order to fulfill the goal of rapid operational mobility of army vehicles. However, during hostile battlefield conditions, damages are likely to occur due to a variety of reasons including punctures from rocks, impact loads from deployment/ handling, dropping the structure from moderate heights and various battlefield threats (*Iyer (2002)*).

In order to develop an effective repair methodology for military composite bridges, and in order to verify its validity through virtual testing, one should identify (i) the most potential loading scenarios that would cause damages to the bridge including extreme live loading conditions, and (ii) loads that the "repaired" bridge should withstand after being repaired.

Figure 1. The composite army bridge (DARPA (2000)).

The first part of this study involved calibrating the materials constituent properties of the composite army bridge that will be used in demonstrating and virtually verifying the smart repair technology for military bridges. In the second part of the study,

GENOA virtual testing and progressive failure simulations were performed on the composite treadway under three different loading cases.

The three cases used in this study are: (i) Maximum static shear loading case (*Load Case 1*), (ii) Maximum static flexural loading case (*Load Case 2*), and (iii) fatigue progressive failure analysis for the maximum moment case loading (*Load Case 3*).

2 CALIBRATION OF MATERIALS CONSTITUENT PROPERTIES USING GENOA MCA & PFA CODES

2.1 *Objective*

The objective of this analysis is to calibrate the materials constituent properties of the CAB that are used in demonstrating and verifying the smart repair technology for army composite bridges. This calibration process is essential in developing both the NASTRAN finite element (FE) and the GENOA Progressive Failure Analytical (PFA) models of the composite army bridge before and after damage occurs as well as after performing the smart repair process.

In order to gain confidence in the material properties that are used in evaluating the field repair methodology and to ensure reliable results, calibration of materials constituent properties that include weighing the effect of the braided tri-axial properties was preformed.

2.2 *Background*

Material calibration is a backbone process of constituent properties based on the laminate test data. The purpose of this calibration process is to build a databank to be used in for structural analysis of the bridge structure. In addition, material calibration is necessary because lamina and laminate manufacturing processes involve many unknowns and variables that influence product properties. The use of mechanical properties supplied by vendors usually results in overestimating both the lamina and laminate properties. The numerical material calibration is similar to the concept of coupon tests (*virtual testing*).

In this process, the GENOA code is used to calculate the mechanical properties of each ply using best available constituent data (*e.g. fibers, matrix, etc.*). If the calculated ply properties do not match the experimental data, then the constituent properties are adjusted until the experiments and predictions are in agreement. Ply properties are calculated from algebraic equations that are functions of the constituent properties. For a single set of fiber and matrix properties, there are almost 50 different values that can be changed in order for each of the ply properties to match any available data. Fortunately, each of the ply properties only depends on about 2 to 10 different constituent properties, and is highly sensitive to only a few of those constituent properties. Therefore, in trying to match up each ply property at a time, only two or three variables are manipulated between each prediction. The calibration process is performed by calculating ply properties, comparing them to experimental results, manipulating the constituent properties as needed. This process is repeated until predictions match experimental results. First, it should be assumed that the experimental results are reliable and are measured from a ply whose constituent properties were not measured at the time of the experiment. The rest of the calibration process/prediction matching occurs in series. The experimental results are then set equal to the same results that would be obtained from a mathematical, mechanics of materials model of the ply of concern. Finally, the fiber and matrix properties that would give similar mathematical results are then sought. This becomes a root finding problem, not a curve fitting process, for each of the ply properties. At some point in the design space for each ply property, the prediction will match the experiment. Calculating ply properties using mathematical models of composite materials and these inputs and having the values match up to experiments is a good accomplishment. It states that a set of fiber and matrix properties, or design point, has been found that could possibly be the same set of properties that might have been measured from the plies tested experimentally.

2.3 *Calibration procedure*

The following are the typical procedure used in the calibration process:

1. Prepare a databank with fiber/matrix properties as close as possible to the calibrated fiber/matrix properties. The closer, the faster the calibration process. Otherwise, the fiber/matrix properties provided by vendors are used.
2. Understand the dependency of lamina properties on constituent properties using the sensitivity module in GENOA-MUA (Materials Uncertainty Analyzer).
3. Using GENOA-MCA (Material Constituent Analyzer), adjust fiber/matrix moduli in the databank until the calibrated lamina moduli agree with the lamina test data.
4. Adjust fiber/matrix strengths in the databank until the calibrated lamina strengths agree with the lamina test data.
5. If the composite laminate coupon test data is available, simulation may be conducted for further confirmation of the calibrated databank using GENOA-PFA.

Steps 2 and 3 can be switched because the calibrations of lamina moduli and strengths are not obviously

coupled. Figure (2) shows the flowchart of the GENOA calibration procedure.

2.4 *Calibrated materials*

A total of four different composite materials were calibrated in this task that comprise the structure of the CAB (*refer to* Figure 3). Prior to performing the calibration process, original mechanical information were identified from DARPA (2000) report.

2.5 *Calibration results*

The results of the calibration process identified several variations between the calculated properties and those obtained from ASTM laboratory coupon tests, especially in the shear moduli, strength and Poisson's ratios. As expected, the original and the calibrated results for unidirectional laminates agreed well. Figures (4) through (7) present graphical presentation of the results obtained from the calibration analysis for different materials.

3 PROGRESSIVE FAILURE ANALYSIS

The maximum shear loading case (*Load Case 1*) and the maximum bending loading case for MLC 100 described in DARPA (2000) report were simulated using the GENOA code. In addition, a fatigue progressive failure analysis was conducted for the maximum flexural loading case (*Load Case 2*).

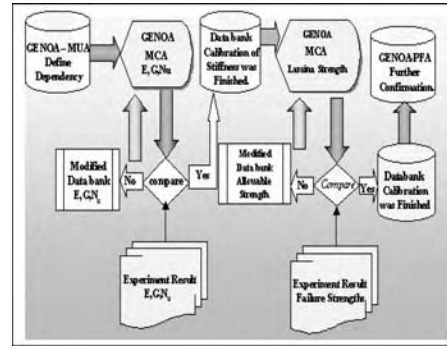

Figure 2. GENOA calibration procedure.

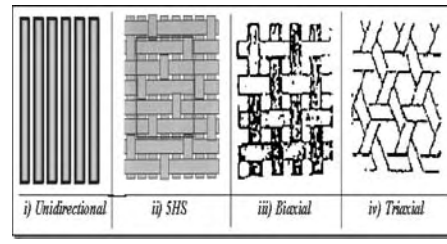

Figure 3. Types and geometry of fibers used in the FEM analysis.

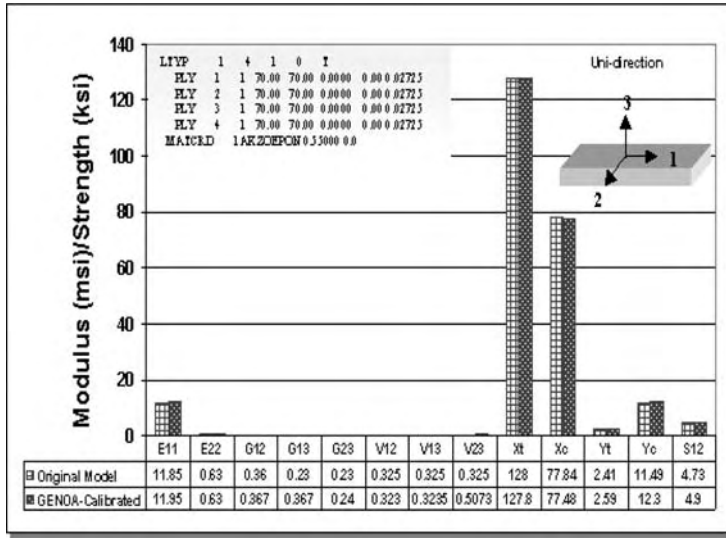

Figure 4. A comparison between calibrated and original mechanical properties of unidirectional laminates.

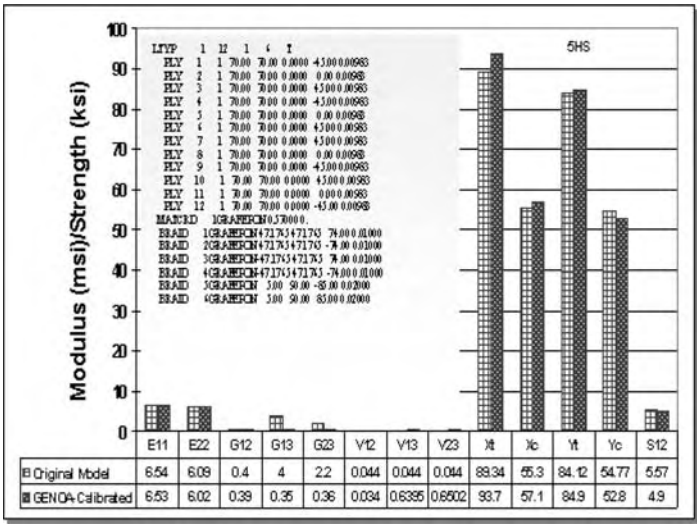

Figure 5. A comparison between calibrated and original mechanical properties of 5HS laminates.

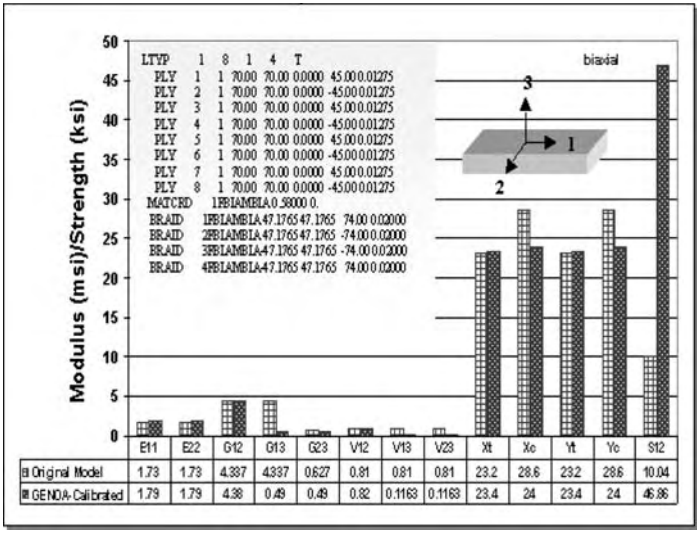

Figure 6. A comparison between calibrated and original mechanical properties of the biaxial laminates.

3.1 *Load Case 1 (Maximum Shear)*

The NASTRAN FEM model of the composite bridge treadway was transformed into a GENOA numerical model. The model consisted of 14,514 mixed elements. A Progressive Failure Analysis (PFA) was performed on this model for Load Case 1 (Max Shear) shown in Figure (8).

Unlike the NASTRAN FEA, the GENOA analysis is non-linear. Any damage or fracture calculated to have occurred in the structure causes the model

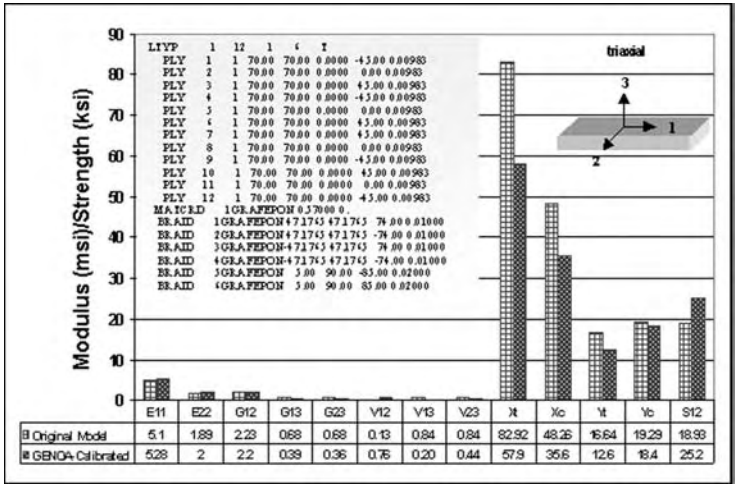

Figure 7. A comparison between calibrated and original mechanical properties of the triaxial laminates.

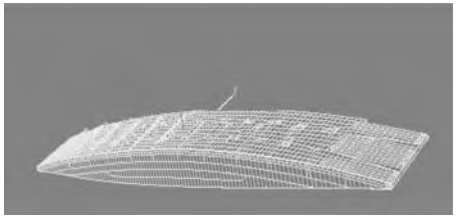

Figure 8. Static shear loading pattern (*Load Case 1*).

stiffnesses to change and the internal loads to redistribute. Larger deflections would, therefore, result. In the case of the CAB model, some damage occurs at the working pressure level. In GENOA parlance, damage and fracture failure are distinctly different phenomena. Damage is defined as an intra-lamina event. One or more plies in a laminate have failed. The laminate still has a load bearing capacity albeit at a lower level. The laminate properties are reduced for subsequent GENOA analyses. Fracture occurs in GENOA when laminate level failure has been reached at a node. The GENOA model is modified at a fractured node by disconnecting it from adjacent, non-fractured elements. This also results in an altered load path. When the accumulation of damage and fracture causes the structure's load bearing capacity to drop to zero, it is considered to have failed.

The maximum deflection at the working pressure was 3.31″ (84 mm) as compared to 3.42″ (86.86 mm) experimental value presented in DARPA (2000) report. The variation between the experimental and

Figure 9. Generalized N_{xy} (lb-in) shear stress distribution at the ultimate load [*280 kips* (*1,245.44 kN*)].

GENOA predicted maximum displacement was 3.4%. The ultimate failure was a combination of local damage of both the balsa wood and the composite sidewalls of the bridge (refer to Figure 9). A summary of both experimental and simulated results for the maximum shear loading case is shown in Table (1).

3.2 *Case 2 – Maximum moment*

Similar to Load Case Load 1, the NASTRAN FEM model was transformed into a GENOA numerical model. A progressive failure analysis (PFA) using GENOA simulation code was performed on the bridge model for Load Case 2 (*Max Flexural Loading)* shown in Figure (10) which is identical to the loading pattern

Table 1. Summary of experimental and PFA results for Load Case 1 (Max Shear).

Experimental Service Load	151 kips (672 kN)
GENOA Ultimate Load	280 kips (1,245.5 kN)
Experimental Ultimate Load	Not Available
Maximum Displacement at Service Load (GENOA)	3.31 inches (84.10 mm)
Maximum Displacement at Service Load (Experimental)	3.42 inches (86.87 mm)
Maximum Displacement at Ultimate Load (GENOA)	6.26 inches (159 mm)
Maximum Displacement at Ultimate Load (Experimental)	Not Available

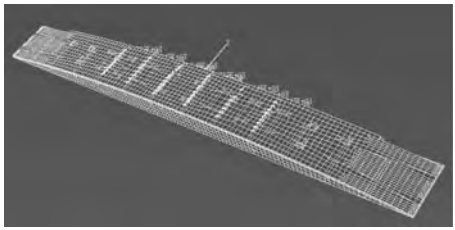

Figure 10. Static flexural loading pattern (Load Case 2).

Figure 11. Nodes damage distribution at initial loading level.

used in the full-scale laboratory tests performed and described in DARPA (2000) report.

The GENOA-PFA simulation was initiated at a single actuator load level of 107 kips (*476 kN*). At this initial loading, no fractured nodes were formed. However, a total of 105 local damages were calculated. Although, no fractured nodes were observed, the number of local ply damages increased (*refer to* Figure 11).

The last equilibrium was achieved at a load level of 202 kips/898.50 kN per loading actuator which was set to be the ultimate failure load. At this load level, a total of 11 nodes were fractured resulting in ultimate

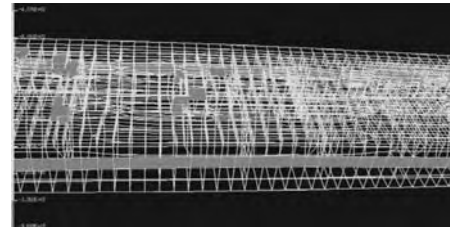

Figure 12. Zoom-In top view of damage distribution just before the ultimate failure.

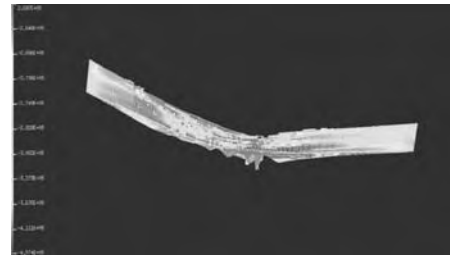

Figure 13. Ultimate failure of the composite bridge treadway.

failure of the bridge. The node damage distribution just before the ultimate failure is shown in Figure (11).

As mentioned earlier, the majority of the local damages were concentrated at the span's mid-third in both the deck balsa wood core and the composite sidewalls/web as shown in Figure (12). The concentration of these localized damages led to the ultimate failure of the bridge treadway as shown in Figure (13). The location and mode of simulated failure were close to those observed in the laboratory test that were reported in DARPA (2000). The simulated maximum displacement at failure was 6.87″ (*174.50* mm) as compared to 6.80″ (172.72 mm) as reported in Figure 142 of the DARPA (2000) report. A comparison between the simulated and experimental actuators loads are presented in Figure (14).

3.3 *Progressive fatigue failure analysis (Load Case)*

The GENOA computational simulation is implemented by the integration of three distinct computer codes that are used as the modules of a progressive fracture tracking code. These computational modules are: (1) composite mechanics, (2) finite element analysis, and (3) damage progression tracking. The overall evaluation of composite structural durability is carried out in the damage progression module that keeps track of composite degradation for the entire structure.

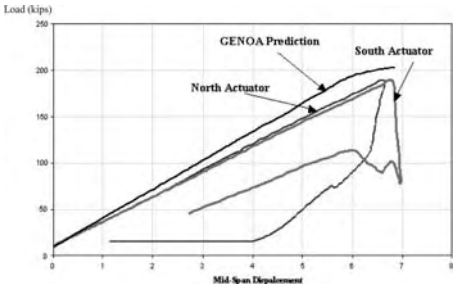

Figure 14. Comparison between full-scale experimental and GENOA predicted results for Load Case 2 (*Max Flexural Loading Case*).

Figure 15. Generalized normal stress N_x distribution after 128,140 cycles (*Fatigue Life*) – *top view*.

The damage progression module relies on a composite mechanics code (*Nakazawa et al.* (1987)) for composite micromechanics, macromechanics, laminate analysis, as well as cyclic loading durability analysis, and calls a finite element analysis module that uses anisotropic thick shell and 3-D solid elements to model laminated composites.

The composite bridge treadway was subjected to a cyclic loading up to failure. The fatigue analysis was performed for the maximum moment load case (Case 2) as shown in Figure (10). The GENOA-PFA simulation started at 5,000 cycles and was continued until ultimate failure occurred. In this analysis, a degradation factor of 0.1 was used to construct the assumed S–N relation with a stress ratio (R) equal to zero.

At the end of 11,250 cycles, the accumulative number of fractured nodes was five. As the number of cycles increased, the number of fractures increased. After 25,312 loading cycles, a total of 12 nodes were fractured. The last equilibrium prior to the ultimate failure was achieved after 128,140 cycles, which is the predicted fatigue life of the composite treadway. Figures (15) and (16) show the generalized N_x (lb-in) stress distributions after 128,140 cycles. The damage

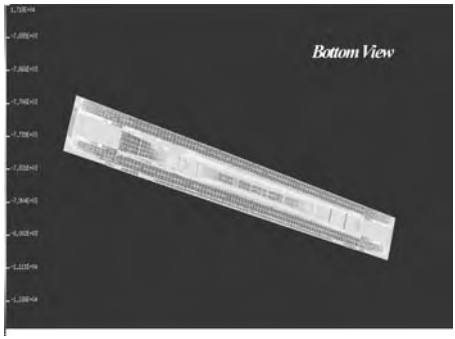

Figure 16. Generalized normal stress N_x distribution after 128,140 cycles (*Fatigue Life*) – *bottom view*.

growth was monitored using the modified-distortion-energy-damage criteria.

The second part of the paper presented the numerical results that was accomplished using GENOA progressive failure simulation of the composite treadway under three different loading cases. The simulated results matched well the full-scale experimental results reported in DARPA (2000). For the fatigue case, a comprehensive study is now in progress that compares the simulated fatigue data with both the full-scale laboratory and field cyclic tests that were performed on both the treadway and a CAB prototype that was subjected to actual field loading conditions.

4 SUMMARY AND CONCLUSIONS

In this paper, the results of two studies were presented. The first part of this paper focused on calibrating the materials constituent properties of the composite army bridge that will be used in demonstrating and virtually verifying the smart repair technology for military bridges. This calibration process is essential in refining both the NASTRAN finite element (FE) and the GENOA Progressive Failure Analytical (PFA) models of the composite army bridge before and after damage as well as after performing the smart repair process. The results of the calibration process identified several variations, especially in the shear moduli, strength and Poisson's ratios. As expected, the original and the calibrated results for unidirectional laminates agreed well.

ACKNOWLEDGEMENTS

This work is a part of a multi-phase SBIR research project funded by the U.S. Army – TARDEC, Warren, Michigan. The support and encouragement of Mr. Brain Hornbeck is highly appreciated. The information reported in this paper reflects the authors'

opinions and does not necessary imply endorsement of the sponsoring agency.

REFERENCES

1. Advanced Composites for Bridge Infrastructure Renewal-Phase II, DARPA Agreement 0030, Volume II-Task No. MDA972-94-3-14, March 2000, Submitted to DARPA by Advanced Composites Technology Transfer/Bridge Infrastructure Renewal Consortium.
2. Mosallam, A.S. and M.A. Haroun, 2003. Structural Evaluation, Repair and Construction of a Composite Highway Bridge Deck, 2nd International Workshop on Structural Composites for Infrastructure Applications, NSF/HBRC, Cairo, Egypt, December 17–18, CD ROM, 2003.
3. Iyer, R. 2002. Composite Army Bridge, a *Distinguished* Paper, Proceedings of the 9th International Conference on Composites Engineering (ICCE/9), San Diego, California, July.
4. Abdi, F., Surdenas, J., Mosallam, A. and J.J. Wang, 2003. Field Repair Technology For Composite Bridges, Final Report, Phase I, Submitted to U.S. Army TACOM, July, 90ps.
5. Murthy, P.L.N. and C.C. Chamis, 1986. Integrated Composite Analyzer (ICAN): Users and Programmers Manual, NASA Technical Paper 2515.
6. Nakazawa, S., Dias J.B., and M.S. Spiegel, 1987. MHOST Users' Manual, Prepared for NASA Lewis Research Center by MARC Analysis Research Corp.

FRP Composites in Civil Engineering – CICE 2004 – Seracino (ed)

CFRP strengthening and monitoring of the Gröndals Bridge in Sweden

B. Täljsten[1,2] & A. Hejll[1,3]
[1] *Department of Civil Engineering, Luleå University of Technology, Luleå, Sweden*
[2] *Skanska Teknik AB, Solna, Sweden*
[3] *EMPA Structural Engineering Research Laboratory, Dubendorf, Switzerland*

ABSTRACT: The Gröndal Bridge, is a large freivorbau bridge (pre-stressed concrete box bridge), approximately 400 meters in length with a free span of 120 m. It was opened to tram traffic in 2000. Just after opening cracks were noticed in the webs, these cracks have then increased, the size of the largest cracks exceeded 0.5 mm, and at the end of 2001 the bridge was temporarily strengthened. This was carried out with externally placed pre-stressed steel stays. The reason for cracking is still debated and will be further discussed in this paper. Nevertheless, it was clear that the bridge needed to be strengthened. The strengthening methods used were CFRP laminates in the Service Limit State (SLS) and pre-stressed dywidag stays in the Ultimate Limit State (ULS). The strengthening was carried out during 2002. At the same time monitoring of the bridge commenced, using LVDT crack gauges as well as optical fibre sensors.

To date, a large amount of data has been collected and the data is still under evaluation. Primary results show that the largest stress can be referred to the temperature load and that the contribution from the live load is minor. The results from the monitoring show that the CFRP laminates work as intended and that the cracks are not propagating.

1 INTRODUCTION

1.1 *Background*

Over the past decade, the issue of deteriorating infrastructure has become a topic of critical importance in Europe, and to an equal extent in North America and Japan. FRP (Fibre Reinforced Polymers) are today used for various applications, such as reinforcement in RC and PC structures, stay cables and newly built structures. However, by far the most extensive application is in repair and strengthening of existing structures. This strengthening technique may be defined as one in which composite sheets or plates of relatively small thickness are bonded with an epoxy adhesive to, in most cases, a concrete structure to improve its structural behaviour and strength. The sheets or plates do not require much space and give a composite action between the adherents. The adhesive that is used to bond the fabric or the laminate to the concrete surface is normally a two component epoxy adhesive. The old structure and the newly adhered material create a new structural element that has a higher strength and stiffness than the original.

The motivation for research and development into repairing, strengthening and restoration of existing structures, particularly concrete systems, is increasing. If consideration is given to the capital that has been invested in the existing infrastructure, it is not always economically viable to demolish and rebuild a deficient structure.

The challenge must be to develop relatively simple measures such as restoration, reparation and strengthening that can be used to prolong the life of structures. This challenge places a great demand on both consultants and contractors. Also, there could be difficulties in assessing the most suitable method for an actual repair; for example, two identical columns within the same structure can have totally different lifespan depending on their individual microclimate.

The use of epoxy as the bonding medium for the adherent has proven to give excellent force transfer. Not only does epoxy bond to concrete, steel and composites, it has also shown to be durable and resistant to most environments.

1.2 *History*

The method of strengthening existing concrete structures with the use of epoxy adhesives originates in France in the nineteen-sixties (L'Hermite, 1967), (Bresson, 1971), where tests on concrete beams with epoxy bonded steel plates were conducted. Even though the method was used widely, it was not considered very successful.

The drawbacks such as corrosion, the need for overlap joints, the heavy working loads during installation and the need for pressure on the adhesive during hardening could not be overcome. In the last decade the plate bonding method has gone through a revival. The reason for this is mainly the increased need for retrofitting of our existing buildings and bridges. However, another very important factor is the introduction of advanced composites to the civil engineering arena. Fibre composites and reinforced plastics offer unique advantages in applications where conventional materials cannot supply a satisfactory service life (Agarwal & Broutman, 1990).

The high strength to weight ratio and the excellent resistance to electrochemical corrosion of composites make them attractive materials for structural applications. In addition, composites are formable and can be shaped to almost any desired form and surface texture. One interesting application of currently available advanced composite materials is the retrofitting of damaged or structurally inadequate building and bridges. In Switzerland, (Meier, 1987), one of the first applications with the use of carbon FRP (CFRP) was carried out at the end of the 1980's, and since then several thousand applications have been carried out worldwide.

Clearly there is a great potential for, and considerable economic advantages in FRP strengthening. However, if the technique is to be used effectively, it requires a sound understanding of both the short-term and long-term behaviour of the bonding system. It also requires reliable information concerning the adhesion to concrete and composite. The execution of the bonding work is also of great importance in order to achieve a composite action between the adherents. Of the utmost importance is to know the practical limits of any proposed strengthening method.

1.3 *Research at Luleå University of Technology*

At Luleå University of Technology, Sweden, research has been carried out in the area of plate bonding. The research work started in 1988 with steel plate bonding and is now continuing with FRP materials. Both comprehensive experimental work and theoretical work have been carried out.

Initially steel plates were used to strengthen members. Currently, however, all research is focussed on plate bonding using fibre reinforced polymer (FRP) composite materials in which, carbon fibre composite is the favoured material.

The laboratory tests have included strengthening for bending as well as for shear (Täljsten, 2001). Full-scale tests on strengthened bridges have also been performed (Täljsten, 1994, Täljsten & Carolin, 1999 and Täljsten, 2000). In particular, the theory behind the development of peeling stresses in the adhesive layer at the end of the strengthening plate has been studied, as has the theory of fracture mechanics to explain the non-linear behaviour in the joint (Täljsten, 1994, Täljsten, 1996 and Täljsten, 1997).

In Sweden the FRP strengthening methods have been used in the field for almost 10 years now, and both laminates and wrap systems are used. Sweden is also one of the first countries in the world where a national code exists for FRP strengthening (Täljsten, 2003).

2 THE GRÖNDAL BRIDGE

2.1 *Background*

The main span of the Gröndals Bridge is 120 meters with two adjacent spans each of 70 meters (see Figure 1). The bridge carries two railway tracks which are placed symmetrically about the cross-section of the bridge. The bridge has no footpath.

Bridge inspection carried out on the newly built, 2000, Gröndals Bridge revealed extensive cracking in the webs of its concrete hollow box-girder section. The bridge is a part if a light-rail commuter line which is located in the south of Stockholm. The cause of cracking is still under investigation and has resulted in several articles in Swedish construction industry magazines (Sundquist, 2002 and Hallbjörn, 2002).

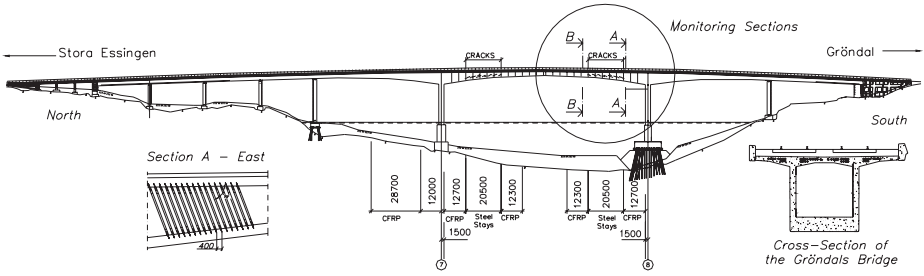

Figure 1. The Gröndals Bridge, CFRP strengthening and monitoring area.

The bridges were designed to the currently applicable Swedish codes, BRO 94 and BBK 94. On the basis of these regulations, it was possible to erect the bridges with extraordinarily slender webs. Relatively high shear stresses and principal stresses are generated by the small web widths although the webs are fully compressed considering the normal stresses caused by pre-stressing in the longitudinal direction. Furthermore, the permanent loads on the structure are dominant. As the permanently exerted principal tensile stresses reached the value of the tensile strength of the concrete, shear cracks were finally created. In addition, restraining bending moments have been superimposed in the webs due to sun radiation. Assuming a linear temperature difference of 10 to 15 K, this, together with the other transverse bending moments, additionally causes vertically directed tensile stresses in the inside of the web amounting to approximately, $s_z = 2$ to 3 MPa. The positions of the cracks in longitudinal direction of the bridges correspond to the areas of the maximum principal tensile stresses, (König, 2002).

The cracks first appeared after only a few years of service and subsequent inspections showed that the number and size of the cracks were increasing, (James, 2004). The cracks widths were between 0,1–0,3 mm and in a few isolated cases between 0,4–0,5 mm in the most cracked sections.(when was this- in 2000 or 2004?)

Preliminary investigations as to the cause of the cracking suggested that they were due to inadequate shear reinforcement in the webs. The webs are slender with a thickness of 350 mm and a total height of the box girder close to the main span supports of approximately 7,5 m. In addition to that the flanges are quite thick, the bottom flange at most is about 1300 mm. The reasons for cracking can be summarised as follows:

- Due to the slender webs high tensile stresses are developed.
- The principal stresses, due to high permanent loads, are the main cause for cracking.
- The location of the cracks is in accordance with the highest principal stresses.
- The cross-sections are under-reinforced due to shear reinforcement.

To increase the safety level of the bridge strengthening was decided.

Because of the progressive nature of the cracking in combination with wariness for shear cracks, the bridge was temporarily closed for traffic towards the end of 2001.

2.2 *Strengthening*

The bridge required strengthening in several sections, strengthening was needed both in the ultimate limit state (ULS) and in the service limit state (SLS), but in different sections. Strengthening in the ultimate limit state was carried out by prestressed dywidag-stays and in the service limit state by CFRP laminates. Strengthening in the SLS was in this case particularly complicated since for this type of structure the portion of the dead load is considerable, approximately 85% of the total load. It was decided to use high modulus carbon fibre laminates to strengthen the bridge. The purpose of strengthening in the SLS was to inhibit existing cracks and prevent new cracks from developing.

Therefore the existing crack widths would be reduced to no more than 0.3 mm (maximum allowed crack width in the Swedish code in the SLS). The design of the CFRP strengthening in the SLS is not covered by existing codes and a fracture mechanics approach was here applied where considerations to the total energy to open up new cracks over a unit distance was taken. The design, due to limited space, is not presented in this paper but the design philosophy is discussed. The sections strengthened with CFRP laminates had no or only very small cracks, $<0{,}05$ mm, at time of strengthening. In this particular case strengthening performed in the SLS state will also contribute in the ULS state. Carbon fibre strengthening was chosen to prevent and minimise future cracks in areas where minor or no cracking had developed. In the calculations the strain in the existing steel stirrups has been calculated due to sectional forces. In the calculation the following assumptions have been made:

- Calculation in Stadium I, non-cracked concrete.
- The crack widths are the limited factor.
- The cracks are not allowed to become larger than 0.3 mm after strengthening.
- The effect of pre-stressing has in the crack calculation been neglected but is accounted for when calculating the internal forces.
- The concrete is only exposed to tensile stresses perpendicular to the crack plane.
- Only vertical reinforcement in the webs has been considered.
- The concrete starts to crack at approximately 100 μs.
- The first visible crack arises at approximately 0.05–0.10 mm.
- Characteristic material data has been used in the calculations.

The material data for concrete, steel and CFRP laminates is given in Table 1. In the design it has been assumed that the steel reinforcement may yield in the crack tip for a crack width of 0.3 mm. However, bonding CFRP laminates to the surface of the concrete at development of cracks gives a stress (and strain) distribution between the steel and composite. The bridges are very important for the commuters going from the south parts of Stockholm into the centre of the town.

Table 1. Material data for CFRP strengthening.

	Characteristic value		Design value	
Concrete	E_{ck}	33.0 GPa	E_c	22.9 GPa
	f_{cck}	32.0 MPa	f_{cc}	17.8 MPa
	f_{ctk}	2.10 MPa	f_{ct}	1.17 MPa
	ε_{cu}	*3.5 ‰*		
Steel	E_{sk}	200.0 GPa	E_s	173 GPa
	f_{yk}	490.0 MPa	f_{st}	371 MPa
			A_s	2010 mm^2/m
BPE® laminates 1412M	E_{fk}	250 GPa	E_f	189 GPa
(1.4 × 120 mm)	ε_{fk}	11.0 ‰	ε_{fd}	5.0 ‰
Dimensions	b	1.0 m	d	3.8 m

For that reason it was undesirable that the bridges were closed during strengthening. However, it has been shown that strengthening with CFRP laminates can be carried out during traffic (Hejll and Norling, 2002); therefore it was decided to permit traffic during strengthening.

Before the strengthening work started the concrete surfaces were sandblasted and holes were drilled in the upper and lower flanges for anchorage of the laminates. Laminates were only placed on the inside of the bridge.

The surfaces were thoroughly cleaned with pressurised air and vacuum cleaners. The surfaces to be bonded were treated with a primer for the system to enhance the bond. The laminates were bonded to the surface, the webs of the structure with a high quality epoxy adhesive, BPE® Lim 567, specific for the strengthening system used. The Young's modulus of the adhesive is approximately 6.5 GPa at 20°C. The average thickness of the adhesive was 2 mm. A total of 2 500 meters of CFRP laminates was used for the bridge. The placement of the CFRP laminates in the Gröndal Bridge in section A, the east side is shown in Figure 1.

It can also be noticed in Figure 1 that the CFRP laminates have been bonded at an angle of 70° to the horizontal plane. This was in order that for the laminates to be bonded perpendicular to the direction of the cracks.

In Figure 2 the anchorage system is shown. Here, steel plates with welded steel bars that were anchored by epoxy bonding in pre-drilled holes in the top and bottom flanges. The anchor length was approximately 250 mm.

The final result after strengthening is shown in Figure 3.

To follow up the behaviour of the bridge over time a monitoring system was installed. The system and some results from the monitoring are explained in the next section.

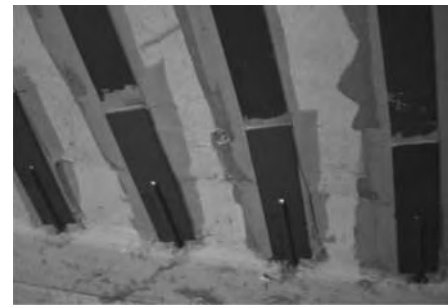

Figure 2. Anchor system for the CFRP laminates. The anchorages are bonded with an epoxy adhesive in pre-drilled holes in the flanges.

Figure 3. Result after strengthening – seen from inside the bridge. This photo shows strengthening approximately from section A to the column no. 8.

3 MONITORING THE BRIDGE

3.1 *SHD system*

When the first crack in the webs of the bridge was found it would have been preferable if measurements had been undertaken immediately. A visual inspection has been carried out regularly, but unfortunately no real measurements have been carried out. In spite of this it has been decided to measure the behavior of the bridges after strengthening, and in particular the future crack developments. Consequently a monitoring program has been put together. In this program measurements have been suggested to be taken at specific locations to measure crack development and strain on the CFRP laminates.

To obtain the most out of a measurement program it is important to carry out SHD (Structural Health Diagnostics) in a structured way and that a well-planned procedure is followed. Luleå University of Technology has worked out a method termed Structural Health

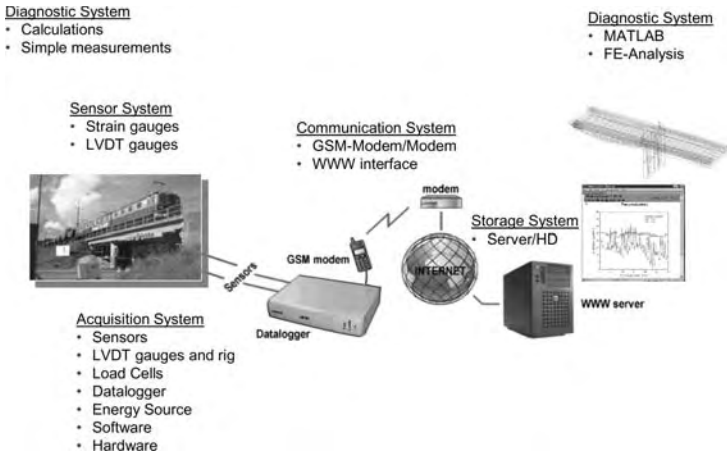

Figure 4. Structural Health Diagnostic system.

Diagnostics (SHD), which in short implies that a rough diagnosis is made on the structure; this can be simple calculations, on site visual inspections or minor measurements. Next it is decided what is to be measured and the purpose with the measurement. In this phase the acquisition system is also decided. Sensors and communications systems are established as well as hard- and software. On top of this, an evaluation system is connected which connects the data from the measurement to a model of the structure. From this action plans are then suggested. In Figure 4 an example on a SHD for a railway bridge is shown.

3.2 *SHD system for the Gröndals Bridge*

Two monitoring systems have been installed on the Gröndals Bridge, one traditional monitoring system using LVDTs (Linear Vertical Displacement Transducers), and one with Fibre Optic Sensors (FOS). The first is used for continuously monitoring and the second for periodic monitoring. The traditional system is installed for monitoring the long term effect of the crack development. The FOS system was installed for two purposes; first to monitor crack development and strain changes due to temperature and tram traffic, second to increase the practical experience by using FOS in field. In addition to this a comparison between the two systems have been made. The traditional system has been installed and followed up by the Royal Institute of Technology (KTH) in Stockholm, (James, 2004) and the FOS system has been installed and followed up by Luleå University of Technology in collaboration with City University in London, UK. (Täljsten & Hejll, 2004).

There are a total if six LVDT's mounted on the Gröndals Bridge, one of which is a dummy used to verify the accuracy of the traditional monitoring system. With exception of the dummy and a sensor, which is positioned between the top flange and the web of the box girder, all the LVDT's are positioned across and perpendicular to a crack so as to measure the opening and closing of a crack. The placement of the gauges can be seen in Figure 5. Four of the LVDT's are mounted on the inside on the west web of the box girder, one of which is the dummy. One of the LVDT's is mounted on the inside of the east web. The last of the LVDT's is mounted between the top flange and the web of the box-girder and measures the relative displacement of the bridge deck to the web.

In addition two temperature sensors, thermocouples, have been installed on the bridge and they are both positioned on the east web of the box girder, one on the inside and one on the outside, both belonging to the traditional system.

In total 32 FOS gauges have been installed on the Gröndals Bridge, they are all installed in section A and section B, see Figure 1 and Figure 5. In section A, 12 sensors have been installed on the west side where three were used to compensate for the temperature. Two of these sensors (including temperature compensation) are positioned on a section of CFRP laminates, the others on different locations of concrete cracks. On the east wall in thesame section seven sensors are installed, five on the concrete (including temperature compensation) and two on a CFRP laminate also here including temperature compensation. In section B, west side, four sensors have been positioned on the concrete, one of which is for temperature compensation and two have been

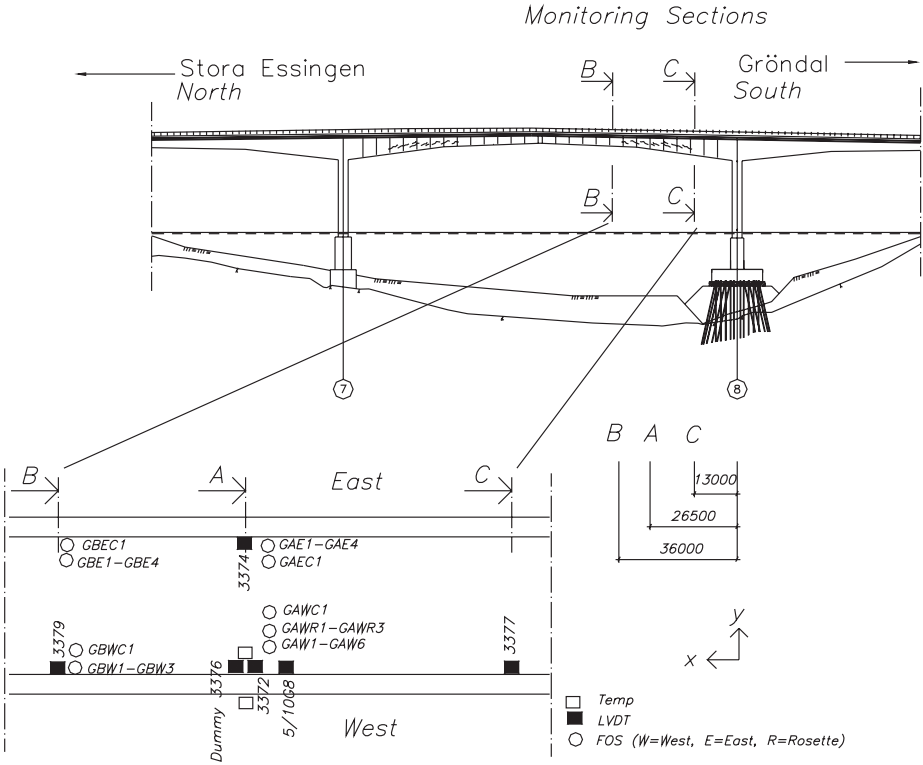

Figure 5. Position of gauges on the Gröndals Bridge.

Table 2. Sensors for monitoring.

Sensor	Measure	Sensor	Measure
Section A (and C)			
3372	Crack opening	GAW1-6	Crack opening
3374	Crack opening	GWR1-3	Strain concrete
3376	Dummy	GAWC1	Strain CFRP
5/10G8	Displacement	GAE1-4	Crack opening
		GAEC1	Strain CFRP
Section B			
3379	Crack opening	GBW1-3	Crack opening
		GBWC1	Strain CFRP
		GBE1-4	Crack opening
		GBEC1	Strain CFRP

positioned on a CFRP laminate, where one is for temperature compensation. On the east side in the same section six sensors have been positioned on the concrete, one for temperature compensation and two on a CFRP laminate, of which one is for temperature compensation. The placement of all the gauges is shown in Figure 5.

As can be noticed in Figure 5 many gauges have been placed on the bridge. The filled rectangular blocks represent the LVDT's and the open rectangular blocks represent the thermocouples for the traditional system. The FOS are represented by open circles. In Table 2 the sensors are presented systematically. For the FOS system the previously mentioned sensors for temperature compensation shall also be included, however, this is not recorded in Table 2.

4 RESULT FROM MONITORING

It is not possible to present all the results from the measurements and therefore only the most interesting values are presented, however all data from the monitoring up to March 2004 may be found in James, 2004 and Täljsten & Hejll, 2004.

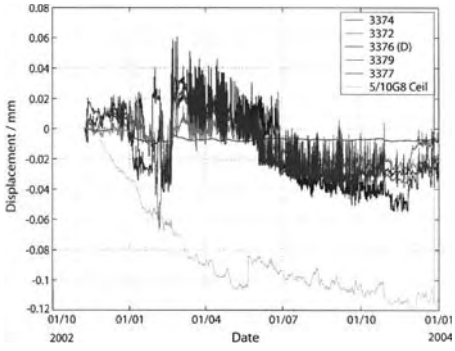

Figure 6. Result from crack-displacement with traditional monitoring system, from (James, 2004).

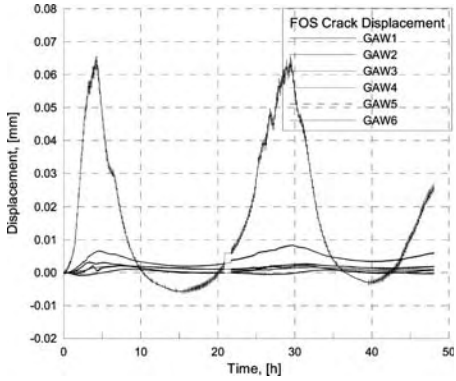

Figure 7. Result from crack-displacement with FOS system (Täljsten & Hejll, 2004). Start date for monitoring 21-05-04.

The results from the monitoring are presented for the traditional and FOS systems respectively.

4.1 *Results from the traditional monitoring system*

The result from the entire year 2003 for the Gröndals Bridge is shown in Figure 6 (James, 2004). It is not easy to extract a single value of the crack behaviour. However, from the figure it is possible to see that the cracks in the webs (indicated by sensors 3374, 3372, 3379 and 3377) do not appear to be of a progressive nature but rather that the cracks open and close depending on daily and seasonal temperature changes.

The crack widths of these gauges are not significantly different at the start of 2004 than at the start of 2003, with the variation in the order of 0.02–0.03 mm. The LVDT sensor (5/10G8) mounted between the underside of the top flange and the inside of the west web measures the longitudinal displacement in the top flange in relation to the web. The displacement appears from these results to be progressive even if the growth rate has decreased over the later half of the year.

4.2 *Results from FOS system*

Before we discuss the result from the FOS system, a brief discussion about the installation procedure and the SHD system used will be presented. Before installation calculation of stresses in the chosen sections had been carried out (Hallbjörn, 2002), however, these calculations also considered the dead load of the bridge. The monitoring systems installed can only follow the relative changes with regard to temperature and live load. The FOS system used has been developed at City University in London and the University also took part in the installation work, calibration and monitoring of data. The FOS sensors are of type Bragg grating and at most 7 sensors were written on one fibre, the length of each senor was approximately 20 mm. The total time for installing and calibrating all the FOS sensors was approximately 10 days, this corresponds with the time it took to grind the concrete and CFRP laminate and bond and protect the fibres. Monitoring was carried out during May 2003 and over a time period of 3 days (periodic monitoring). It was not possible at that time to carry out a continuous monitoring due to the high cost of the system. Nevertheless, to store the data a portable hard disk was used, which was then transported from the bridge to the office for further evaluation of the data. Not all data has been evaluated up to date and has been planned to repeat the monitoring sequence during the next winter. However, it was found that using this FOS system was convenient and the installation procedure was quite simple.

This paper will not present results from all sensors however, in Figure 7 crack displacement from sensors GAW1 to GAW6 is shown. From Figure 7 it can be seen that crack displacement for GAW3 is considerably larger than for the others, here the FOS sensor is placed in the same crack as the LVDT gauge 3372, however during this time the crack displacement for the LVDT is approximately 0,035 mm (this can not be seen in Figure 6 due to the scale). The large variation over time is due to daily variation in temperature. In Figure 7 small jumps may also be noticed, approximately 0,001 mm wide.

This is due to the tram traffic, it seems that the effect of the temperature on opening and closing of the cracks is tenfold to the traffic load.

Over the same crack as in Figure 7 a CFRP laminate has been bonded, in Figure 8 the strain is recorded in this laminate in the same position as the crack.

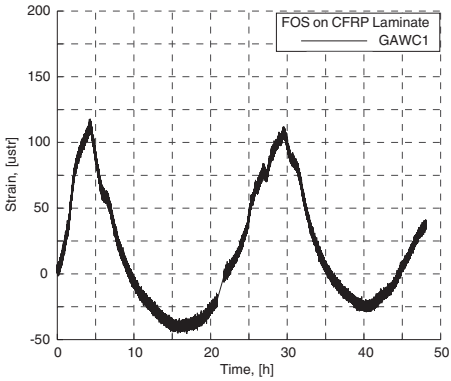

Figure 8. Result from crack-displacement with FOS system (Täljsten & Hejll, 2004).

A calculation of stress gives a level of approximately 30 MPa in the laminate.

5 SUMMARY AND CONCLUSIONS

In this particular project the most innovating part was not to use CFRP laminates for strengthening, it was the way the design of strengthening was carried out. By using fracture mechanics in design and in combination with CFRP laminates it was possible to (theoretically) use the energy needed to open a crack to a certain size and transfer that energy to the CFRP laminate, which then redistributes the cracks and the distance between the cracks over the length of the laminate. Therefore a cost effective solution for strengthening in the SLS (also contributing to the ULS) could be chosen and finally carried out.

Both monitoring systems installed on the bridge showed that the cracks were not propagating and that the opening for the cracks was more or less negligible The largest crack opening measured was approximately 0.06 mm. Furthermore, the temperature effect was approximately 10 times larger than the effect from the tram traffic. Monitoring will continue and it will be interesting to follow the bridge over time.

ACKNOWLEDGEMENT

The research presented in this paper has been funded by several organisations. Here the Swedish National Road Administration, the Development fund of the Swedish Construction Industry, Stockholm Transport (SL) and Skanska Sverige AB should be acknowledged.

REFERENCES

Agarwal B.D. and Broutman L.J., 1990, Analysis and Performance of Fibre Composites, John Wiley & Sons Inc. ISBN 0-471-51152-8, 1990, p 449.

Bresson J., 1971, Novelles resherches et applications concernant lútilisation des collages dans les structures. Betong plaque, Annales de l+institute technique, No. 278, 1971.

Hallbjörn L., 2002, Sprickor I Gröndalsbron och Alviksbron I Stockholm, Betong No. 2, 2002, pp 8–12. (In Swedish).

Hejll A Norling, 2002, O "Betongbalkar förstärkta med kolfiberkomposit: Dynamisk belasting under limmets härdningsförlopp" Luleå University of Technology, Division of structural engineering, ISSN:1402-1617.

L'Hermite R., 1967, Lápplication des colles et resins dans la construction. La betong coffrage portant, Annales línstitut technique, No. 239, 1967.

James G., 2004, Long term monitoring of the Alvik and Gröndal Bridges, TRITA-BKN Rapport 76, Byggkonstruktion, 2004, www.byv.kth.se, p 48.

König G., 2002, Expert Opinion about the cracks in the webs of the Gröndals bridge, Sweden. Report prepared by König und Heunisch, Planungsgesellschaft mbH, p 48.

Meier U., 1987, Repair of bridges with high performance composite materials, Material + Technik, Vol. 15, No. 4, 1987, pp 125–128.

Sundquist H., 2002, Hur mår våra Frevorbau broar egentligen? Betong No. 1, 2002, pp 4–5 (In Swedish).

Täljsten B., 1994, Plate Bonding, Strengthening of Existing Concrete Structures with Epoxy Bonded Plates of Steel or Fibre reinforced Plastics Doctoral Thesis 1994:152D, Div. of Structural Engineering, Luleå University of Technology, ISSN 0348 - 8373, 308 pp.

Täljsten B., 1996, Strengthening of concrete prisms using the plate-bonding technique, International Journal of Fracture 82: 253–266, 1996, 1996 Kluwer Academic Publishers, Printed in the Netherlands.

Täljsten B., 1997, Strengthening of Beams by Plate Bonding, Journal of Materials in Civil Engineering, November 1997, pp. 206–212.

Täljsten B. and Carolin A., 1999, Strengthening of a concrete railway bridge in Luleå with carbon fibre reinforced polymers – CFRP: load bearing capacity before and after strengthening, Technical Report 1999:18, Luleå: Luleå University of Technology, Structural Engineering. 61 pp.

Täljsten B., 2000, Förstärkning av befintliga betongkonstruktioner med kolfiberväv eller kolfiberlaminat, Dimensionering, material och utförande, Teknisk Rapport, Luleå tekniska universitet, Avdelningen för Konstruktionsteknik, 1999:12, ISSN 1402-1536, 1999, p 122 (In Swedish).

Täljsten B., 2001, "Design guidelines – a Scandinavian approach", International Conference on FRP Composites in Civil Engineering CICE 2001 Ed. J.G. Teng, Hong Kong, ISBN: 0-08-043945-4

Täljsten B., 2003, FRP Strengthening of Existing Concrete Structures. Design Guideline Division of Structural Engineering, Luleå University of Technology, Luleå 2003, Second edition, 228 pp, ISBN 91-89580-03-6.

Täljsten B. and Hejll A., 2004, "Evaluation of the monitoring of the Gröndal and Alvik bridges", Report to be published.

FRP Composites in Civil Engineering – CICE 2004 – Seracino (ed)
© 2005 Taylor & Francis Group, London, ISBN 90 5809 638 6

Condition evaluation and strengthening techniques for Kayakapi ruins in Turkey

A. Turer & T. Eroglu
Civil Engineering Department, Middle East Technical University, Ankara, Turkey

ABSTRACT: Ruins of Kayakapi, which is located at Urgup town of Nevsehir-Turkey, will be converted to a museum by Urgup municipality. The ruins include more than 70 (commonly multistory) residential blocks of arched masonry construction and rectangular set of rooms carved into rocks. In addition to buildings, mosques, Turkish bath, fountains, and churches exist including the house of St. Yuhannes who is a sacred figure for the Orthodoxes. The restoration work is carried out by participants from private organizations, government, academia and planned to be completed in 4 years. Structural integrity/stability of critically unstable portions and retrofitting of the ruins are the focus of the study. This paper concentrates on the visual condition evaluation, emergency measures, and strengthening techniques for Kayakapi ruins. Visual inspection of the existing masonry structures and caves are carried out, structural emergency precautions and strengthening techniques are grouped under separate headings for each predefined emergency type.

1 INTRODUCTION

1.1 *Location of Kayakapi ruins*

Kayakapi, a village of Urgup Town, is located in Nevsehir-Turkey in Central Anatolia. Kayakapi is located on Esbelli Rock, which is directly seen at the town entrance. Kayakapi ruins settled on an area of 16 km^2 with more then 200 buildings in about 70 blocks. The location and general view of the Kayakapi ruins are shown in Figure 1.

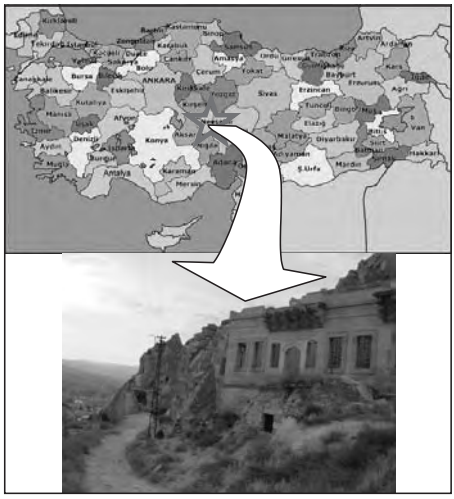

Figure 1. The location and a general view of Kayakapi.

1.2 *Historical importance of Kayakapi*

In 1969 Kayakapi was declared as a "disaster area" and the quarter has been abandoned since that time. In 2001 Kayakapi has been selected a reservation and restoration site by the Turkish Government.

The first church in Urgup carved into rock is located among the ruins. In addition, there are two mosques (one of them was caved into rock), a Turkish bath and wells.

Long time ago, respectable Turkish and Greek families were living together in this neighborhood. St. Yuhannes who is believed to be a sacred person by Greeks lived in Kayakapi. Every year on May 27th, the house of St. Yuhannes is visited by many visitors leaded by a Greek Patriarch. Kayakapi ruins are also one of the Capadoccian sites, which have been defined as a World Cultural Heritage by UNESCO. Seven of Kayakapi structures have been included among World Cultural Heritages so far.

1.3 *Historical background of ruins*

A series of eruptions about 100 thousand years ago from the Mt. Erciyes and Mt. Hasan covered the area with a thick layer of volcanic ash. Volcanic ash is a relatively soft material which can be carved. This property of ground has allowed residents to shape rocks into

today's invaluable houses, churches, mosques, baths, and caves. Earliest residents of the region go back to VII millennium B.C. when Neolithic peoples settled in Hacilar and Catalhoyuk. Cappadocia records indicate settlements V century B.C. (Paleolithic era) which became a Persian satrapy in the mid VI century B.C. Earliest written records regarding Kayakapi have dates 451 A.C.

1.4 *Current study regarding the renovation*

After Kayakapi has been declared as a conservation area the municipality invited tenders to restoration and open Kayakapi for tourism.

KA.BA – Conservation of Historic Buildings and Architecture Ltd. is a private organization which started working on "Urgup – Kayakapi Cultural and Natural Environment Conservation and Revitalisation Project" with a restoration team including participants from academia, private organizations, and municipality.

The project is planned to be completed in 4 years. The house of St. Yuhannes will be converted to a museum in future and other buildings will be renovated without changing their original properties.

1.5 *Scope and objective of our team*

The aim of METU structural team was to visit the ruins, assess the condition of buildings in each separate block, determine the emergencies – risky conditions, and develop short-term/long-term precautions and strengthening techniques.

Figure 2. Erosion and dislocation of stones.

Figure 3. Eroded stones at the slopes.

2 CONDITION ASSESSMENT AND COMMON DEFICIENCIES

The assessment work carried out by our team can be grouped under four headings: "walls", "arches", "caves", and "rocks". Walls and arches sections list the common deficiencies and problems observed. Caves section includes and MS-Excel based small software to approximately determine the safety and load rating of cave roofs. The rocks section has suggestions on slope stabilization for cracked unstable large rock piece located at the entrance of the Kayakapi ruins.

2.1 *Walls*

Almost all of the garden walls, which are on the side of road, have been eroded. Mortar between stones has been lost. Stones forming the walls became smaller and some fell down from their original places leaving gaps in the walls (Fig. 2). Some walls are partially collapsed, others are unstable.

A number of load carrying house walls have diagonal shear cracks which are attributed to differential support settlements. Some of the walls are used as retaining walls to support steep slopes. The retaining walls especially supporting road sides should be repaired after dismantling and reassembling using similar stone blocks. The erosion associated with the mortar and stone blocks are mainly due to rain water. Discharge of excessive rain water is required for prevention of further erosion and safety of road carrying steep slopes.

The lower parts of the walls (i.e. about 1 m height from the ground) has larger extent of erosion which is again attributed to humidity coming from the ground. Temporary supported or unsupported wall segments are unstable and exhibit very dangerous conditions (Fig. 3).

Lintels are commonly used at window and door openings to support the upper portion of the openings. Although small arches are also common, two lintel types and damages are frequently seen at Kayakapi. These are wooden and stone lintels.

Almost all of the wooden lintels were taken out from their places by poor local residents as burning material. The remaining wooden lintels are decayed and sagged.

Figure 4. Lost lintels, impending walls for collapse.

Figure 5. Arch feet erosion.

The stone lintels are either broken in to two pieces with a deep vertical crack in the middle due to bending forces and/or less commonly eroded if exposed to external agents such as water, freezing and thawing, wind, etc. The stone pieces above damaged lintels are in impending collapse stage, presenting threat for the walls and visitors (Fig. 4). Urgent precautions and repair work will be explained in the following sections.

2.2 *Arches*

Most commonly noticed deficiencies on arches can be grouped under three headings:

2.2.1 *Stone disintegration at arch supports*

Dissolutions at arch feet would allow vertical instability and lateral displacements, which are both very dangerous for integrity of arches (Fig. 5). Emergency measures and possible strengthening techniques for stone disintegration at arch feet are described in the following sections.

Figure 6. Arch keystone erosion.

Figure 7. Laterally unsupported arches.

2.2.2 *Dissolved/dislocated keystones at upper parts of the arches*

The upper portions of the arches are sometimes eroded due to type of the stone piece or water discharge (Fig. 6).

2.2.3 *Laterally unsupported arches*

If supporting structure behind an arch has been lost due to partial collapse or erosion, the arch would be laterally unstable and may experience total collapse especially when other conditions coexist such as support decay (Fig. 7).

2.3 *Caves*

Majority of the caves are carved into soft rock which easily disintegrates into a powder looking material. The roofs of the caves are not carved into arch shapes

Figure 8. Room carved into rock with thin slabs.

but they are rather rectangular. Multi storey rooms are carved into rocks leaving thin slabs in between which are partially collapsed (Fig. 8). Some of the houses had residents until very recently. The houses carved into stone had better condition if there were residents in them. The residents of these houses applied regular maintenance which affected the condition of those houses in a positive way. Some caves that were abandoned long time ago had experienced total or partial collapses or were in very bad condition.

Some caves are carved underneath roads. The roads become narrow trails; however a small car can easily enter to the road at the entrance level. Small pickups can enter to the site during restoration work and carved spaces under roads can be dangerous.

A small spreadsheet program is developed to approximately evaluate the load capacities of cave roofs under their own weight and a point load acting above them. The excel sheet calculates the load capacities for 1) shear, 2) tension (45° to shear), 3) bending, 4) punching, and 5) compression strut failure conditions; different factors of safety 6, 6, 2, 2, and 2 are used, respectively and can be updated as necessary. The smallest allowable load P is calculated by subtracting self-weight effect from the total capacity of the cave roof. Allowable tensile (S_c) and compressive stresses (S_b), shear stress capacity (T), unit weights of cave roof rock (W_k) and overlaying earth fill (W_t), effective roof width (b), rock depth (h), earth fill depth (t), and length (L) are taken as variables.

2.4 *Cracked unstable large rock blocks*

Kayakapi ruins had numerous large massive boulders rumbled down the hills. Several rocks at the higher elevations look stable, but likely to come down some time in the future if precautions are not taken.

At the entrance of Kayakapi region, there is a large massive rock (Fig. 10) which has vertical cracks showing indications of instability and presenting a

L=	2.5	m
b=	1.5	m
h=	0.75	m
t=	2	m
T=	10	kgf/cm2
Sç=	12	kgf/cm2
Sb=	95	kgf/cm2
Wk=	1.3	t/m3
Wt=	1.8	t/m3

	F.S.	P
Bending	2	7.78125
Shear	6	10.17188
Tension	6	13.92188
Comp. strt.	2	174.711
Punching	2	115.7886
P=	**7.78125**	**tons**

Figure 9. Excel sheet to calculate approximate capacity.

Figure 10. Partially instable large massive rocks.

dangerous condition. A number of solutions are developed for the stabilization of the large entrance rock, which are discussed in Section 3.3.

3 RETROFITTING

This section concentrates on the emergency measures for structural safety of the Kayakapi ruins. The retrofitting techniques commonly cover unstable walls, arches, and rocks. The long time strengthening and restoration work is also mentioned as method development stage.

3.1 *Arches*

The common problems about arches are summarized in the previous section. Supports of an arch should be carefully placed such that the axial load flow is not disturbed. Therefore, probing directly underneath the arch is not recommended in any case since some of the arch stones can be dislocated and lost leading to total collapse. Arches can be 45° probed from the front or rear (Fig. 11a), close-to-vertically supported at the support level (Fig. 11b), cross braced at the bottom side of the curved section (Fig. 11c), or fully supported underside with scaffolding (Fig. 12).

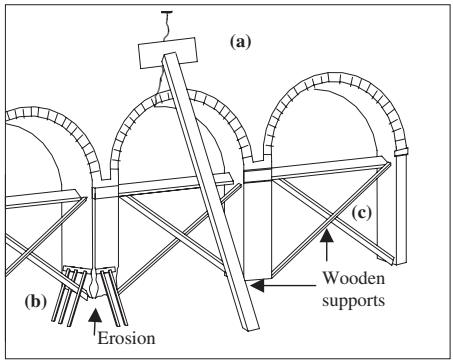

Figure 11. Emergency measures for unstable arches.

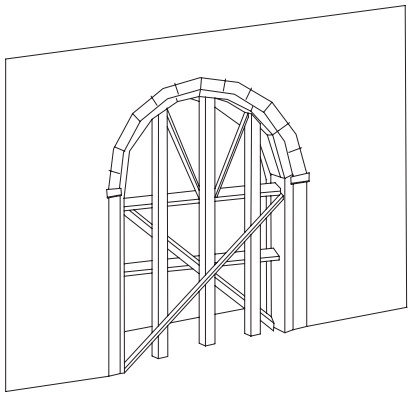

Figure 12. Full scaffolding support for arches.

The cross braces and horizontal supports at the support level ensures the lateral stability of the feet which otherwise might sway sideways and initiate total collapse. The complete scaffolding underneath an arch should be used when some of the load carrying stones are significantly eroded or the arch shows indications of poor load carrying capacity or instability such as extreme deformation in its curved shape. The stone erosion at the upper parts of the arch can be repaired as the arch is fully supported underneath and top pieces are replaced with new stones.

The erosion and section loss at the arch supports is a problematic condition since the arch and all supporting structure should be dismantled and rebuild after the support is repaired, which is a too intrusive and costly approach. Replacement of supports without complete rebuilding is possible with full scaffolding and vertical direct and friction supports at the footing level (Fig. 13).

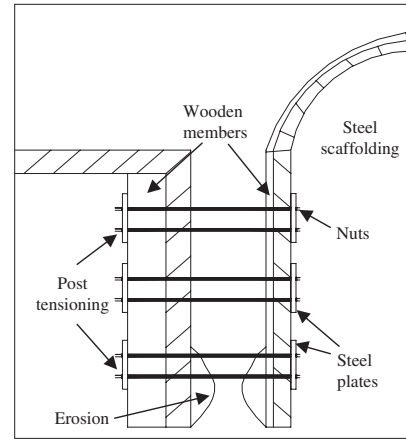

Figure 13. Replacement of support stones.

To strengthen or replace an eroded arch or column foot, firstly whole area should be totally propped up with steel members. To avoid smashing, wood members can be placed on both sides of stones. Afterwards eroded foot can be replaced or strengthen. An important thing is that the material, which is used for renovation, must look like the same as original. If loading on the area is too much, firstly loading must be decreased if possible. This can be made through taking down overlaying heavy stones.

The eroded support stone can also be retrofitted using CFRP coating. The eroded portion is first wrapped using a cylindrical CFRP layer and inside is filled with expanding mortar. The confined portion would be able to withstand large axial forces and the view of the retrofitted section can be improved with plastering outer surface with a mixture close to the original stone material. The laboratory tests on axial load capacity of wrapped mortar using FRP is planned to be concluded by 2005.

A few instances of half arches are observed which should be supported with props having angles close to the discontinuous arch stone's angle. Usage of at least two props would enhance the stability of supported node (Fig. 14). Props should be at least 10 cm by 10 cm wooden sections or steel pipes.

Assuming the props will be slender, load carrying capacities can be determined by Equation 1 and allowable axial load capacity of $P = A * \sigma_{allowable}$.

$$P_{cr} = \frac{\pi^2 EI}{L^2} \quad (1)$$

where E = modulus of elasticity, I = Moment of inertia, L = span length, and P_{cr} = critical axial load.

Figure 14. Supporting half arches.

Figure 15. Massive and unstable walls.

3.2 *Walls*

There are several types of strengthening and preventive measures, which should be applied individually or in combination with others.

3.2.1 *Propping with 45° inclined wood blocks*

This precaution can be applied to walls, which have stability problems. The area, where the prop supports the wall, should be covered with a wood panel in order to spread the pressure. The end of the prop, which delivers loads to the soil, should also be fixed to ground. The prop may be on both sides of the wall for improved stability. Missing lintel locations should not be supported underneath but inclined, similar to arches.

Heavy walls (Fig. 15) or propping over long distances can be achieved by use of steel profiles instead of wooden blocks. Large distances can be supported using built-up columns with battened or latticed connections.

3.2.2 *Removal of unstable stones over the walls*

Unstable stones over the walls can easily fall down due to wind or earthquake. They should be fixed or lowered to the ground level.

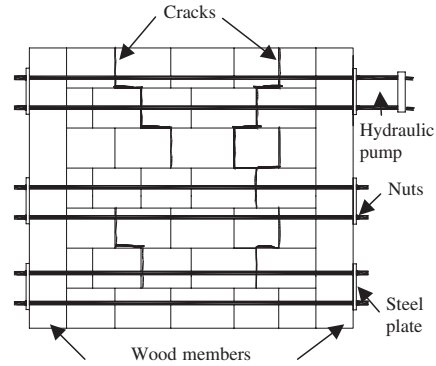

Figure 16. Wall post-tensioning.

3.2.3 *Void fills*

Empty spaces in the walls can be filled with mortar or similar stone pieces based on the void/gap nature. Vertical props can also be used as a short term remedy. Temporary fixes are aimed to secure the remains while long term permanent modifications should not change original look of the walls. In some extreme cases, the walls can be carefully disintegrated and rebuilt close to its original form

3.2.4 *Post tensioning*

Some walls can be located next to a steep slope, where propping is not suitable. If the wall is in a dangerous condition, the wall can be stabilized by compression through post-tensioning. Steel bars, steel plates, bolts, hydraulic pump, and wood cushion members can be used to post-tension a masonry wall. A 30 tons hydraulic pump would be sufficient to sequentially tense three layers of tension belts as shown in Figure 16. The bars are locked in place using nuts at either side of the wall after the wall is compressed by the hydraulic pump. The wooden members on both ends allow equal pressure distribution and prevent damage to the wall members. The out-of-plane stability is achieved by even pressure distribution among masonry blocks in horizontal direction. Additional propping can be placed on one side only this time which may carry tension or compression.

3.2.5 *Strengthening bottom portions of walls*

Some walls have dissolutions particularly on bottom portion up to level of 1 meter. The reason of this issue is most probably due to soil moisture. At some walls dissolution problem threatens the stability of the wall. Water level should be lowered (using pumps at wells) and lower portions of the walls should be protected against moisture using chemical moisture repellents, surface coatings, or penetrant type strengthening agents. The penetrant type chemicals fill cracks

and air pores inside the stone and develop crystal structure. Under this effect the resistance of stones increases and water impermeability is achieved. But since this application is irreversible, the effects of the chemical should be investigated in detail conducting experiments on test rocks at the site. Previous research showed that chemical treatment may sometimes cause more damage than normal aging.

3.3 *Cracked unstable large rock blocks*

The large rock blocks shown in Figure 10 can be stabilized using a number of different approaches. The most radical solution would be controlled demolition of dangerous rock. The demolition can be carried out using limited amount of explosives at a time or hammered excavators after the neighborhood is evacuated.

Because the surface of the parent rock block is very smooth, anchorage holes on the rock can be opened. Through these holes tension bars can be extended to the deep parts of the parent rock and fixed with anchorages achieved by high strength concrete injection. On the surface of the rock around anchorage holes steel plates can be used in order to prevent bars from developing stress concentrations.

The parent rock and the sliding rock block can be stabilized together by surrounding them with many web-like steel straps which are anchored to many footings at the parent rock. High strength grouting can be injected to the crack in an attempt to increase adhesion between two rocks. Compressive forces developed by tensed steel straps will increase the friction forces on the cracked surface improving the behavior.

Another alternative is supporting the sliding rock block using an oversized reinforced concrete support. This support may not look very nice, however it can also become a mascot, marking the enterance of the Kayakapi ruins.

4 CONCLUSIONS

The historic buildings in Kayakapi region are heavily damaged in general with the exception of buildings in which people lived until recent times. The remains suffered from material degradation and erosion. Looting wooden lintels caused partial or full collapse of the walls. Many arches resisted demolishing effects of about two thousand years and still able to support multi-storey houses. Mosques, churches, and Turkish bath may still be considered as in good condition. Rooms carved in soft rock suffer from material degradation similar to majority of the rocks forming walls.

The main structural elements are grouped under walls, arches, and caves. Walls suffered from total or partial collapse due to wakening around the openings, material erosion, and support related problems. Arches dominantly have support and erosion problems. Caves have large cracks and many have collapsed.

Retrofitting suggestions presented in this paper are mostly short-term remedies to prevent premature collapses and related possible personal injuries. The suggested techniques generally target to stabilize the about-to-collapse cases. A few options are developed to repair critical parts of structural systems in a cost efficient and quick way, such as suspending upper structure while replacing footing stone blocks instead of complete dismantling-rebuilding or CFRP wrapping and grout injection while plastering outer surface with some mortar layer that have material properties close to the stone's original texture without replacing the stone and staying loyal to its original. Post-tensioning of walls would increase out-of-plane stability since brittle tensile bending stresses are transformed into small and large compressive forces on either face of the wall with constant, overall post-tensioning stress.

A simplified spreadsheet evaluation program is prepared in order to rate a number of cave roofs that exist under the main road. The variables defining the geometric and material properties of cave roofs are easily modified, and the most critical loading type and capacity can be approximately calculated. Structural strengthening of caves is left out of this study since caves with collapse risk will be filled with boulders and concrete grout. Those risky caves which are too valuable to lose may be strengthened using concrete arches or steel frames which may also be covered by plaster that looks like the original rock formations. The decision will be made based on architectural and conservational approaches.

ACKNOWLEDGMENTS

The authors kindly acknowledge the contributions of KABA Ltd. workers especially Gulgun Kabaoglu Faruk Zarshati for their initiative and support during this study. Partial support is obtained from World Bank DM2003, Project #1451. Additional thanks goes to Sinasos Gul Konaklari for their hospitality during our stay at Urgup.

FRP Composites in Civil Engineering – CICE 2004 – Seracino (ed)
© 2005 Taylor & Francis Group, London, ISBN 90 5809 638 6

Author index